AGARD-CP-422

AGARD

ADVISORY GROUP FOR AEROSPACE RESEARCH & DEVELOPMENT

7 RUE ANCELLE 92200 NEUILLY SUR SEINE FRANCE

AGARD CONFERENCE PROCEEDINGS No.422

Combustion and Fuels in Gas Turbine Engines

NORTH ATLANTIC TREATY ORGANIZATION

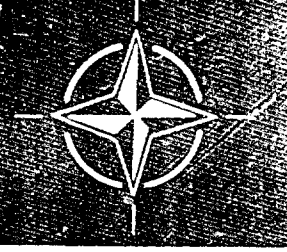

DISTRIBUTION AND AVAILABILITY
ON BACK COVER

AGARD-CP-422

NORTH ATLANTIC TREATY ORGANIZATION

ADVISORY GROUP FOR AEROSPACE RESEARCH AND DEVELOPMENT

(ORGANISATION DU TRAITE DE L'ATLANTIQUE NORD)

AGARD Conference Proceedings No.422

COMBUSTION AND FUELS IN GAS TURBINE ENGINES

Papers presented at the Propulsion and Energetics Panel 70th Symposium held in Chania, Crete, Greece, on 19—23 October 1987.

THE MISSION OF AGARD

According to its Charter, the mission of AGARD is to bring together the leading personalities of the NATO nations in the fields of science and technology relating to aerospace for the following purposes:

- Recommending effective ways for the member nations to use their research and development capabilities for the common benefit of the NATO community;
- Providing scientific and technical advice and assistance to the Military Committee in the field of aerospace research and development (with particular regard to its military application);
- Continuously stimulating advances in the aerospace sciences relevant to strengthening the common defence posture;
- Improving the co-operation among member nations in aerospace research and development;
- Exchange of scientific and technical information;
- Providing assistance to member nations for the purpose of increasing their scientific and technical potential;
- Rendering scientific and technical assistance, as requested, to other NATO bodies and to member nations in connection with research and development problems in the aerospace field.

The highest authority within AGARD is the National Delegates Board consisting of officially appointed senior representatives from each member nation. The mission of AGARD is carried out through the Panels which are composed of experts appointed by the National Delegates, the Consultant and Exchange Programme and the Aerospace Applications Studies Programme. The results of AGARD work are reported to the member nations and the NATO Authorities through the AGARD series of publications of which this is one.

Participation in AGARD activities is by invitation only and is normally limited to citizens of the NATO nations.

Published June 1988

ISBN 92-835-0465-8

Printed by Specialised Printing Services Limited
40 Chigwell Lane, Loughton, Essex IG10 3TZ

RECENT PUBLICATIONS OF THE PROPULSION AND ENERGETICS PANEL

Conference Proceedings

Testing and Measurement Techniques in Heat Transfer and Combustion
AGARD Conference Proceedings No.281, 55th *A* Meeting, May 1980

Centrifugal Compressors, Flow Phenomena and Performance
AGARD Conference Proceedings No.282, 56th *B* Meeting, May 1980

Turbine Engine Testing
AGARD Conference Proceedings No.293, 56th Meeting, Sep/October 1980

Helicopter Propulsion Systems
AGARD Conference Proceedings No.302, 57th Meeting, May 1981

Ramjets and Ramrockets for Military Applications
AGARD Conference Proceedings No.307, 58th Meeting, October 1981

Problems in Bearings and Lubrication
AGARD Conference Proceedings No.323, 59th Meeting, May/June 1982

Engine Handling
AGARD Conference Proceedings No.324, 60th Meeting, October 1982

Viscous Effects in Turbomachines
AGARD Conference Proceedings No.351, 61st *A* Meeting, June 1983

Auxiliary Power Systems
AGARD Conference Proceedings 352, 61st *B* Meeting, May 1983

Combustion Problems in Turbine Engines
AGARD Conference Proceedings 353, 62nd Meeting, October 1983

Hazard Studies for Solid Propellant Rocket Motors
AGARD Conference Proceedings 367, 63rd *A* Meeting, May/June 1984

Engine Cyclic Durability by Analysis and Testing
AGARD Conference Proceedings No.368, 63rd *B* Meeting, May/June 1984

Gears and Power Transmission Systems for Helicopters and Turboprops
AGARD Conference Proceedings No.369, 64th Meeting October 1984

Heat Transfer and Cooling in Gas Turbines
AGARD Conference Proceedings No.390, 65th Meeting, May 1985

Smokeless Propellants
AGARD Conference Proceedings No.391, 66th *A* Meeting, September 1985

Interior Ballistics of Guns
AGARD Conference Proceedings No.392, 66th *B* Meeting, September 1985

Advanced Instrumentation for Aero Engine Components
AGARD Conference Proceedings No.399, 67th Meeting, May 1986

Engine Response to Distorted Inflow Conditions
AGARD Conference Proceedings No.400, 68th *A* Meeting, September 1986

Transonic and Supersonic Phenomena in Turbomachines
AGARD Conference Proceedings No.401, 68th *B* Meeting, September 1986

Advanced Technology for Aero Engine Components
AGARD Conference Proceedings No.421, 69th Meeting, September 1987

Working Group Reports

Aircraft Fire Safety
AGARD Advisory Report 132, Vol.1 and Vol.2. Results of WG11 (September and November 1979)

Turbulent Transport Phenomena (in English and French)
AGARD Advisory Report 150. Results of WG 09 (February 1980)

Through Flow Calculations in Axial Turbomachines
AGARD Advisory Report 175. Results of WG 12 (October 1981)

Alternative Jet Engine Fuels
AGARD Advisory Report 181. Vol.1 and Vol.2. Results of WG 13 (July 1982)

Suitable Averaging Techniques in Non-Uniform Internal Flows
AGARD Advisory Report 182 (in English and French). Results of WG 14 (June/August 1983)

Producibility and Cost Studies of Aviation Kerosines
AGARD Advisory Report 227. Results of WG 16 (June 1985)

Performance of Rocket Motors with Metallized Propellants
AGARD Advisory Report 230. Results of WG 17 (September 1986)

Lecture Series

Non-Destructive Inspection Methods for Propulsion Systems and Components
AGARD LS 103 (April 1979)

The Application of Design to Cost and Life Cycle Cost to Aircraft Engines
AGARD LS 107 (May 1980)

Microcomputer Applications in Power and Propulsion Systems
AGARD LS 113 (April 1981)

Aircraft Fire Safety
AGARD LS 123 (June 1982)

Operation and Performance Measurement of Engines in Sea Level Test Facilities
AGARD LS 132 (April 1984)

Ramjet and Ramrocket Propulsion Systems for Missiles
AGARD LS 136 (September 1984)

3-D Computation Techniques Applied to Internal Flows in Propulsion Systems
AGARD LS 140 (June 1985)

Engine Airframe Integration for Rotorcraft
AGARD LS 148 (June 1986)

Design Methods Used in Solid Rocket Motors
AGARD LS 150 (April 1987)

Other Publications

Airbreathing Engine Test Facility Register
AGARD AG 269 (July 1981)

Rocket Altitude Test Facility Register
AGARD AG 297 (March 1987)

Manual for Aeroelasticity in Turbomachines
AGARD AG 298/1 (March 1987)

Application of Modified Loss and Deviation Correlations to Transonic Axial Compressors
AGARD Report 745 (November 1987)

THEME

Combustion in the gas turbine engine was last considered at an AGARD meeting in 1983. Since that time, apart from the continuing need to ever increase engine operating conditions, the attention of combustor designers and researchers has focussed upon two main factors: the identification of the significance of fuel degradation upon combustion design and performance, and the potential prizes to be gained by the development of better design techniques.

The aim of the meeting was to review the progress made in these areas under four main subject headings, namely, alternative fuels and fuel injection, combustor development, soot and radiation, and the development of mathematical models for the design of gas turbine combustors.

***

La combustion dans les moteurs à turbines à gaz a été examinée pour la dernière fois lors d'une réunion AGARD en 1983. Depuis lors, et mis à part le besoin continuel d'améliorer les conditions de fonctionnement des moteurs, l'attention des chercheurs et des concepteurs de systèmes de combustion s'est concentrée sur deux facteurs principaux: la détermination de l'importance de la dégradation en matière de combustion du carburant dans la conception et les performances, et les avantages potentiels résultant de meilleures techniques de conception.

Le but du symposium était de passer en revue les progrès réalisés dans ces domaines sous quatre rubriques principales, à savoir: les différents types de carburant et de systèmes d'injection, la réalisation des systèmes de combustion, les résidus de combustion et le rayonnement et le développement de modèles mathématiques pour la conception de systèmes de combustion des turbines à gaz.

PROPULSION AND ENERGETICS PANEL

Chairman: Dr W.L.Macmillan
Project Manager
EHF Communications Satellite
Defence Research Establishment
Ottawa, Ontario K1A 0Z4
Canada

Deputy Chairman: Ing. Principal de l'Armement P.Ramette
Direction de Recherches, Etudes et Techniques
26 Boulevard Victor
75996 Paris Armées, France

PROGRAMME COMMITTEE

Professor R.S.Fletcher (Chairman)
Pro Vice Chancellor
Cranfield Institute of Technology
Cranfield, Bedford MK43 0AL, UK

Professor L.De Luca
Politecnico di Milano
Dipartimento di Energetica
Piazza Leonardo da Vinci 32
20133 Milano, Italy

Major M.Metochianakis
Commander, Maintenance Squadron
115 Combat Wing
Chania, Crete, Greece

Professor M.N.R.Nina
CTAMFUL
Instituto Superior Tecnico
Avenida Rovisco Pais
1096 Lisboa Codex, Portugal

M.l'Ing. Principal de l'Armement P.Ramette
Direction des Recherches, Etudes et Techniques
26 Boulevard Victor
75996 Paris Armées, France

Professor G.Winterfeld
DFVLR
Institut für Antriebstechnik
Postfach 90 60 58
5000 Köln 90, Germany

HOST NATION COORDINATION

Major M.Metochianakis

PANEL EXECUTIVE

Dr Egbert Ricster
AGARD-NATO-PEP
7 rue Ancelle
92200 Neuilly sur Seine
France

ACKNOWLEDGEMENT

The Propulsion and Energetics Panel wishes to express its thanks to the National Delegates from Greece for the invitation to hold this meeting in Chania, Crete, and for the facilities and personnel which made the meeting possible.

CONTENTS

*Presented in Session II.

TECHNICAL EVALUATION REPORT
COMBUSTION AND FUELS IN GAS TURBINES

by

George Opdyke, Jr
Textron, Lycoming

1. INTRODUCTION

The design of gas turbine combustion chambers is becoming increasingly more sophisticated as demands on performance increase and combustor operating conditions become more and more harsh. The design compromises which account for much of the art in successful combustor design have become more difficult as gas turbine cycles reach higher pressure and temperature levels and design objectives become more rigorous. This is particularly true for military applications of gas turbines, for both manned and unmanned aircraft. Concurrently, there is significant pressure for the combustor designer to reduce development time and cost, reduce life cycle costs, increase fuel tolerance and continue to minimize the environmental impact of the combustion process.

In the past two decades, an increasing amount of fundamental knowledge of chemical, aerodynamic and thermal phenomena, plus a more detailed understanding of sprays, has been applied with considerable success to practical combustor design. This 70th Symposium coordinated by the AGARD Propulsion and Energetics Panel (PEP) held in Chania, Crete, October 19—23, 1987, is another contribution to the growing collection of scientific literature which addresses the difficult problem of designing better combustors which must operate under more and more difficult conditions.

The papers presented at this symposium "Combustion and Fuels in Gas Turbine Engines" are categorized under the following four subject headings:

- Alternative Fuels and Fuel Injection,
- Combustor Development,
- Soot and Radiation, and
- Combustion Modeling. Keywords: NATO Furnished, Afterburners, Alternative Fuels, Atomization, Drops, Distribution, Soot, Cra

Each subject area is discussed in Sections 2 through 5, respectively. The papers are categorized slightly differently than in the published program and they are tabulated in Tables I to IV. These indicate the major subject content of each paper.

2. ALTERNATIVE FUELS AND FUEL ATOMIZATION

The eleven papers grouped under this heading are listed in Table I.

Alternative fuels experience in engine and combustor tests has shown that the effects of fuel can be conveniently divided into two categories; chemical effects and physical effects. The latter are of overwhelming practical importance, largely because of the impact of the change in physical characteristics of the fuel on fuel atomization and vaporization and the resultant effects on combustor performance.

The papers presented in this group represent a continuation of the work reported on alternative fuels at the PEP meeting in 1983 in Cesme, Turkey. The general conclusion from both that earlier symposium and this one is that no projected alternative fuel helps combustor performance, and the combustor design problem becomes more difficult, particularly for the fuel injection system.

There are only two reported areas where alternate fuels have only a minimal effect. They are:

1. Experience with the TF30 afterburner showed negligible fuel effects on performance, ostensibly because this is a premixed type of combustor where atomization effects are absent.
2. Extensive experience with main burners shows that alternate fuels have only a minor or negligible impact on the combustor pattern factor or on radial temperature distribution.

The combustor characteristics which are affected by fuel type were reported in considerable detail.

Soot production in the combustor is the major change in combustor operation caused by fuel chemistry. Since exhaust smoke is the difference between soot production and soot burnup, the aerothermal design of the combustor, as well as the operating conditions of the combustor, will affect these processes. There is evidence, also, that a reduction in spray drop size will have a small beneficial impact on exhaust smoke.

Engine exhaust smoke has been correlated quite well with fuel hydrogen content, with the sensitivity to fuel type being a function of combustor design. The ASTM smoke point test is also a good measure of the soot formation tendency of a fuel if hydrogen content data is not available. The radiation flux from the primary zone increases with soot production and the resultant increase in liner wall temperature will shorten the low cycle fatigue (LCF) life of the combustor liner.

The effects of changes in fuel physical characteristics on combustor performance far overshadow the effects of chemistry.

A decrease in atomization quality occurs primarily because of the higher viscosity of most alternate fuels and the resultant larger drop sizes with their increased evaporation times will worsen lean limit and ignition, combustor efficiency and CO and UHC emissions at low power conditions, and slightly worsen NOx emission at high power. A quantitative measure of these changes can be approximated by using the empirical expressions given in the papers by Lefebvre and by Odgers. The quantitative impact of the effect of injector characteristics on combustor performance is also influenced significantly by both the design of the injector and the design of the combustor, i.e., there is a requirement to match the injector to the combustor. This has been characteristically done by combustor development tests after the injector specifications have been drawn up and after bench tests have shown that the injectors meet the specification. Additional effort in the future is required to predict the match of the injector spray characteristics to the flow pattern in the combustor at all operating conditions at the time the specification is written. Highly atomized, well distributed sprays are desired for high efficiency and good pattern factor, but some non uniformity is helpful in achieving good ignition and broad stability limits. The performance of several types of fuel injection systems was reported. These types included pressure atomizing, airblast and vaporizing styles. The performance of these different types of fuel injectors was examined primarily from the point of view of how combustor operating conditions and fuel characteristics would affect their spray characteristics. Eight papers, all listed in Table I, cover fuel injector or spray performance at some length.

Lefebvre pointed out that despite a hundred years of theoretical study of the breakup of a liquid jet it is still not possible to predict spray characteristics satisfactorily from first principles. Even empirical correlations, of which there are many, have significant shortcomings, particularly for sophisticated injector designs. The effects of air velocity and turbulence in the region surrounding the spray also influence injector performance, and this is dominated by the swirler design. Although a well designed airblast injector should have less performance deterioration with more viscous alternate fuels than does a pressure atomizer, the average SMD can still increase by 20% to 30%, with a resultant increase in average droplet vaporization time of the order of 50%, possibly more for the largest drops in the spray.

The sensitivity to fuel physical characteristics varies with the styles of fuel injector, with those types which rely on air pressure drop for fine spray formation being the least sensitive. Since the airblast style of injector relies on combustor pressure drop to provide the air energy for atomization, it is difficult to achieve good atomization at the low pressure drops associated with light off conditions. Hebrard and Jasusja point out that the so-called vaporizing injector style has performance trends and atomization capabilities that are generally similar to those of conventional airblast atomizers. It is usual to provide some supplementary means for igniting this type of combustor. The impact of combustor operating conditions on the performance of the dual swirler type of airblast injector was discussed in detail. Here droplet inertia and aerodynamic forces cause an increase in spray angle with increasing engine power, just opposite from the decrease in spray angle characteristic of pressure atomizers. It was also clearly pointed out that small variation in manufacturing of injectors or their associated swirlers would have a negative, non-trivial impact on the spray.

Gulder presented a practical scheme to correct for the effect of multiple scattering in a dense spray when using the forward light scattering technique for measuring drop size.

These papers on the subject of atomization generated considerable interest, and it is worth noting that there were no representatives of fuel injector manufacturing companies in the audience.

3. COMBUSTOR DEVELOPMENT

The papers in this category are listed in Table II. As usual, these papers were case studies of experiences encountered in the development of a combustor, something which is always useful to understand since the point of gas turbine combustor research is to assure better combustor design and development. These case studies illustrated the degree to which some engineers are able to use the advanced design techniques.

Two papers described afterburner development in some detail, particularly emphasizing the range of stable operation of modern afterburner designs. The point was very clearly made that lean extinction cannot be correlated solely by the flameholder blockage in the duct, but is also affected by the geometry and location of the V gutters. Tests of development afterburners should model the engine geometry accurately to ensure that proper test results are obtained.

The two papers about main combustors described diametrically opposed development approaches, one using a modern 3D flow field prediction method, and the other an imaginative series of development tests. Both represented successful beginnings, but as these programs progress to completion, the development methodology used will probably become more similar. Additional papers of this sort are needed to continue to demonstrate the practical value (or lack of value) of modern combustor modeling methods.

4. SOOT AND RADIATION

The papers grouped under this heading are listed in Table III.

The increased radiation flux which usually occurs with alternate fuels results from the increased soot production in the primary combustion zone. If this soot is not subsequently consumed in the combustor, an increase in exhaust smoke results.

While smoke correlates well with fuel hydrogen content, the point was made that fuels with low hydrogen content may have their smoking tendencies increased because of the presence of other compounds. The prediction of radiation from soot is not straightforward and it was pointed out that soot particles outside of the formation region tend to block some of the radiation. In addition, knowledge of soot particle size can be important in predicting turbine wear, and methods of particle size measurement were described. Measurement of engine exhaust smoke with precision is difficul, and standard procedures do not give data in real time or measure smoke during transients. Investigators at Pyestock have developed a smoke generator which can be used for instrument calibrations. Samuelson described a surrogate fuel which could be used as a repeatable standard.

Empirical equations were presented for the formation and burnup of soot, with indications that soot forms at an equivalence ratio of 1.5 and above, with this onset value increasing as temperature increases above 1500K. Data was presented on the effect of pressure and temperature on soot production as well as measurements of emissivity with temperature. Laminar flamelet modeling of turbulent combustion indicated a soot formation rate proportional to $p^{1.5}$, with soot formation restricted to about a 3/1 range of lower mixture fractions. This compares with earlier data indicating rates proportional to p^2.

A summary of alternate fuel radiation on hot section durability showed that a 1/2% reduction in fuel hydrogen content, which has occurred in JP-5 fuel in the past 20 years, can shorten combustor liner life by 10% to 60%, depending on the liner design. Intermittent use of fuel with 1/2% lower hydrogen content will reduce the combustor life by 1.1 to 2.0 hours for every hour the low hydrogen fuel is used, depending on how benign the mission is. The impact on maintenance depends on current liner life and maintenance frequency. Some engines will be nearly unaffected, while others, like the T58, F404 and J59 (high smoke) may require increased maintenance as fuel quality decreases.

Despite difficulties, it appears that sooting flames and their impact on flame radiation can be estimated to a degree which is useful in design, but considerable work remains to be done before soot concentration and radiation predictions can be incorporated with confidence into combustor design models.

5. COMBUSTOR MODELLING

The 15 papers grouped under this heading are listed in Table IV. This group can be subdivided into those papers dealing with design of combustors and a larger group addressing methods of modeling some elements of combustion.

Combustor multi dimensional design models can now better match combustor geometry, since body fitted coordinates with adaptive grids are replacing cartesian coordinates, and this permits more accurate representation of geometric details. Despite some inaccuracies, predictions of exit temperature distribution have been shown to be reasonably good, and the promise of these models being effectively used in combustor design appears to be nearer at hand. Errors still exist because of limited knowledge of boundary conditions, spray characterization, for example, plus the ever present possibility of numerical inaccuracies. However, advanced numerical schemes are now being employed, both for improvement in accuracy and for cost reduction by shortening computer run time. There is a clear tendency to increase the number of grid nodes ten fold from the 20K to 35K currently used to 250K or even 500K, a step which requires very large, high speed computer capability

Burrus presented details of the development of combustor models at General Electric and their application to CFM56 annular combustor. A similar presentation was made by the university of Sheffield team with both can and annular combustor examples, while Wittig described the modeling of a reverse flow combustor. In all cases the authors were encouraged with the results.

Mongia presented a somewhat different approach based on a background of 12 different combustors of several styles. He suggested a combination of the best of semi-analytical and multi dimensional numerical modeling techniques. In this approach, macro volume models for efficiency, blowout, ignition, exit temperature, soot and radiation interface with a 3-D model of a combustor, which has been designed in a preliminary way using semi-analytical correlations. This approach is claimed to have given good agreement with data from a number of combustors, and the data shown is for the most part as good as experimental accuracy. Advanced numerical schemes to reduce computer time, a PDF approach to turbulence modeling and a modeling approach to atomization and spray transport processes are all discussed.

As a complement to this last item, Blümcke showed that the complex flowfield from a counter swirl airblast atomizer can be predicted with reasonable accuracy.

The various combustion models discussed in the remaining paper in this group detail procedures which sooner or later can be used to improve the numerical solution of gas turbine combustor problems. Several papers dealt with flame modeling including flame stretch in non uniform flow and with the prediction of the turbulence levels within the flames. The value of adaptive gridding for the numerical simulation of premixed flames was demonstrated. Predictions of flow in a simplified primary zone showed only small differences between the burning and non-burning cases, and a simple model for CO oxidation in a diluent zone was shown to give better agreement with experimental results than the chemical equilibrium model. Limitations of applicability of this latter model were given, a most desirable service by the author. The optimism concerning the utility of both combustor and combustion modeling is certainly encouraging, and yet a significant amount of validation is still required with both practical combustors and with benchmark quality experimental data. Many years of effort will be required before combustor design can be attempted with these models with a significant degree of confidence, and we should expect to hear more in this regard at the next AGARD symposium on combustion. Advances are required in numerics, to increase accuracy and reduce computational costs, as well as in turbulence models and in characterization of atomization and spray droplet transport and vaporization processes.

6. CONCLUSIONS AND EVALUATION OF THE MEETING

This symposium plus the associated panel meeting were attended by 144 delegates from a total of 15 NATO countries. The questions and discussions of each paper were of considerable interest and helped to increase the understanding of the author's subject. The resulting exchange of information among the many combustor experts present added significantly to the value of the symposium.

The reason for the symposium was to aid combustor designers to cope with more difficult operating conditions, and the symposium met its objective of reviewing progress made under the four main subject headings. The delegates were appreciative of the Propulsion and Energetics Panel and the Program Committee for coordinating the presentation of these papers. The subjects were not nearly exhausted, and remain candidates for future symposia, particularly the subjects of combustor modeling, fuel injection systems, and combustor durability.

7. RECOMMENDATIONS FOR FUTURE MEETINGS

Future conferences should feature papers about design or design methods which demonstrate how the negative effects of poor quality fuels can be minimized or eliminated. Since these design approaches will involve fuel system and fuel injection design, these should be featured subjects in the next symposium.

The design of advanced fuel injection and preparation systems which will guarantee highly reliable ignition, plus high combustor efficiency in the transient between ignition and idle is of interest. The operation of these systems at low ambient temperatures, high altitudes and with fuels of high viscosity should be addressed.

The further advancements in combustor numerical design models and submodels will be of continuing interest for many years. The solutions obtained with these models to meet detailed combustor design objectives, including fuel injector performance, liner wall temperatures for long life, reduced pattern factors and other performance requirements particularly under difficult operating conditions, should be delineated, along with experimental validation of the results in meeting these objectives. While combustor design models will not give pefect solutions in the near future, the imperfect solutions presently possible appear to be satisfactory for many engineering purposes. Repeated assurances of the practical value of these models are needed to help justify the cost of their development.

Reports of combustor and after burner designs which are both lower weight, long lasting and require only minimal cooling air would be a desirable addition to the next symposium.

Experience gained in combustor operation at high inlet pressures and temperatures, and with exit temperatures approaching stoichiometric, would be of great interest, particularly if multi-dimensional models are shown to be helpful in the design of these combustors.

There are indications that significant advances in gas turbine design will be taking place during the next decade, and major combustor design and operational improvements will be required. The dissemination of information about these combustor design advances is an important function of the AGARD Propulsion and Energetics Panel.

TABLE I - MAJOR SUBJECTS CONTAINED IN THE PAPERS

ALTERNATIVE FUELS AND FUEL INJECTION

No.	Author	Effects of Fuels	Injectors, Sprays	Model or Analysis	Experimental	Bench Tests	Comb or Engine Tests	Review
70-1	Mosier, Karpovich	X			X		X	
70-2	Peters-Asheim		X	X	X	X		
70-3	Lefebvre	X	X				X	X
70-4	Lavergne, Hebrard		X		X	X		
70-5	Wittig, Klausmann, Noll		X	X		X		
70-6	Rosfjord, Eckerle		X		X	X		
70-7	Gulder	X	X	X				
70-8	Simon, Joos, Eickhoff, Cao		X		X	X		
70-9	Jasuja, Low		X		X	X		
70-10	Kretschmer, Odgers	X			X		X	
90-41	Odgers, Kretschmer	X			X		X	

TABLE II - MAJOR SUBJECTS CONTAINED IN THE PAPERS ON

COMBUSTOR DEVELOPMENT

No	Authors	Exprm.	Model or Bench Tests	Full Scale Tests	Analytical	Main Burner	Reheat Burner
70-11	Cadiou	X		X			X
70-12	Southeran	X		X			X
70-13	Joon-Simon	X		X	X	X	
70-14	Whitelaw, Bicen, Tse	X	X			X	
70-42	Collin	X		X		X	

TABLE III MAJOR SUBJECTS CONTAINED IN THE PAPERS ON

SOOT AND RADIATION

No	Authors	Radiation	Soot	Exptl.	Analysis	Combustor Modelling
70-15	**Moses, Karpovich**	X	X	X		
70-16	Samuelson, Wood, Smith		X	X		
70-17	Faeth, Gore, Swathani	X	X	X	X	
70-18	Moss, Stewart, Syed	X	X	X	X	
70-19	Carvalho, Coelho	X				X
70-20	Girling		X	X		
70-21	Wittig-Feld		X	X		
70-22	Gerhardt etal		X	X	X	
70-23	Williams-Simmons Mullins		X	X	X	
70-24	Wagner		X		X	
70-32	Kakaros, et al	X	X		X	

TABLE IV MAJOR SUBJECTS CONTAINED IN THE PAPERS ON

COMBUSTOR MODELLING

No	Authors	Reviews	Mathematic Modelling	Aerodynamics	Kinetics	Combustor or Component
70-25	Burrus et al	X	X	X		X
70-26	Mongia	X	X	X		X
70-27	Wild, Boysan, Swithenbank & Lu	X	X	X		X
70-28	Wittig, Bauer, Noll		X	X		X
70-29	Markatos					X
70-30	Gal' tti, Bruno, Belli		X		X	
70-31	McGuirk		X	X	X	
70-33	Candel, Darabiha, et al		X		X	
70-34	Giovannini		X	X	X	
70-35	Larrouturou		X		X	
70-36	Cambray, et al				X	
70-37	Bruel, et al					X
70-38	Sheppard, et al		X		X	
70-39	Scherrer		X	X		X
70-40	Bluemcke, et al		X	X		X

FUEL PROPERTY EFFECTS ON THE U.S. NAVY'S TF30 ENGINE

S. A. Moster
Pratt & Whitney
Engineering Division
West Palm Beach, FL 33410-9600
USA

P. A. Karpovich
U.S. Navy
Naval Air Propulsion Center
Trenton, NJ 08628
USA

SUMMARY

The TF30 engine was introduced into Navy service in 1972 and is scheduled to continue to power the carrier-based F14 "Tomcat" for some time. Although the engine was designed and developed to operate on specification-grade JP-5 fuel, it is conceivable that during its lifetime, the TF30 might have to operate on out-of-specification/broadened-specification fuels. This contingency could arise should the availability of high-grade petroleum crude oil used for aircraft fuel production be decreased. Therefore, a program of experimentation and analysis was conducted to evaluate the effects of broadened-specification petroleum fuels on the performance, durability and operability of the TF30-P-414A engine. As fuel quality deteriorated, some reductions in engine performance characteristics were observed. However, based upon limited-duration testing, the TF30-P-414A engine was shown to be capable of operating on liquid petroleum fuels having a wide range of properties.

NOMENCLATURE

API	American Petroleum Institute	Max	Maximum
ARTS	Automated Recording Temperature System	N_2	High Rotor Speed
ATP	Alternate Test Procedure	NAPC	Naval Air Propulsion Center
B/M	Bill-of-Material	NATOPS	Naval Air Training
DFM	Diesel Fuel Marine (F-76)		Operations Procedure
EFH	Equivalent Flight Hours		Standard
EP	End Point	P	Pressure
f/a	Fuel-to-Air Ratio	ΔP	Differential Pressure
FCP	Fuel Characterization Parameter	r^2	Coefficient of Determination
FPR	Fuel Parameter Ratio	r	Stoichiometric Ratio
F_n	Thrust	SLTO	Sea-Level Takeoff
F-76	Diesel Fuel Marine	SMD	Sauter Mean Diameter
H	Heat of Combustion	SN	Smoke Number (SAE ARP
H_2	Hydrogen Content, %		1179A; Reference 11)
HO No. 2	Heating Oil No. 2	Sun A,B	Suntech Fuel Blend A,B
IBP	Initial Boiling Point	T	Temperature
IOC	Initial Operational Capability	ΔT	Differential Temperature
IRP	Intermediate Rated Power	T/C	Thermocouple
JFTOT	Jet Fuel Thermal Oxidation Tester	VI	Vaporization Index
LCF	Low-Cycle Fatigue	W	Flow Rate
LSP	Liner Severity Parameter	Z	Afterburner Zone
m	Meter	η	Combustion Efficiency

SUBSCRIPTS

f	Fuel	S	Static
g	Gas	90	Value at 90% Distillation Point
I	Idle	T	Total
l	Liquid	o	Initial
L	Liner	2	Engine Inlet
REF	Reference	4	Combustor Inlet
10	Value at 10% Distillation Point	5	Combustor Exit

1. INTRODUCTION

Gas turbine fuel costs have stabilized in recent years and the world fuel supply has been abundant; however, the fuel shortages of 1973 and 1979 demonstrated how quickly this situation can change. The unstable economic and political conditions of the world petroleum market have caused the Navy to evaluate its dependency on middle distillate petroleum fuels. The potential threat of disruption to the Navy's aviation turbine fuel supply has prompted efforts to conserve fuel and to identify alternative sources of jet fuel.

While it is predicted that the Navy will be dependent primarily on petroleum crudes as the source of JP-5 for some time, it is expected that there will be significant changes in the type and quality of crudes available to refiners. The changes in the petroleum supply market (i.e., increased use of more highly aromatic crudes, the additional refining necessary to process these crudes, and supplemental use of fuel derived from shale or coal) are likely to exert influence to broaden jet fuel specifications.

Several solutions have been proposed for obtaining adequate, reliable supplies of the Navy's aviation turbine fuels, i.e.:

- Relaxing the current JP-5 specification to include a larger fraction of the petroleum barrel could increase availability. This action, however, together with the introduction of new crudes from Alaska and Mexico, or previously undesirable residual crudes, and the changes in processing necessary to refine some of these crudes may result in specification changes to fuel properties and composition.

- The Navy will likely begin to use fuels refined from non-petroleum sources such as oil shale. This will help to improve fuel availability, but may produce additional pressure for specification changes.

- In emergency situations, the temporary use of non-aviation fuels such as F-76(Diesel Fuel Marine), or F-76 blended with JP-5, has been suggested as a means of extending supplies of JP-5. The use of such fuels must also be investigated with respect to performance characteristics.

Due to the logistics of Navy aircraft operations, future jet fuels will undoubtedly be obtained from a combination of these sources. The many scenarios for future jet fuel supplies dictate the requirement for establishing a technical information base from which fuel acceptance and usage decisions can be made and future gas turbine engine technology can evolve.

The TF30 engine was introduced into Navy service, following its Initial Operational Capability qualification in 1972, as the propulsion system for the twin-engine, carrier-based F14 "Tomcat" fighter. The engine was designed and developed to operate on JP-5 fuel. To date,fuel quality has been well within specification and the engine has performed as intended.

The TF30 is classified as being mature; however, it will not be phased out of Navy service for some time. Although the engine went out of production last November, the Navy has 1200 TF30s in its inventory; the engine is scheduled to be there past the year 2000. Therefore, there is the possibility that during its lifetime, the TF30 engine now in service could be required to operate on out-of-specification fuels. This contingency might arise should the availability of high-grade petroleum crude oil for JP-5 production be decreased: possibly necessitating the use of aircraft fuels having property values broader than those of JP-5. Therefore, a program of experimentation and analysis was conducted to evaluate the effect of broadened-specification fuels on the performance, durability, and operability of the TF30-P-414A engine. This paper describes some of the results of the evaluation program.

2. TEST APPROACH

A TF30-P-414A engine was tested at sea-level and simulated altitude conditions using six liquid hydrocarbon fuels, described in a later section. The sea-level tests were conducted at Pratt & Whitney's Government Products Division at operating conditions corresponding to idle, takeoff, and two high-rotor speeds (87 and 92 percent N_2).

Engine start and transient demonstrations were also conducted at sea-level conditions; however, no afterburner testing was undertaken during sea-level operation. All simulated altitude testing was conducted at the U.S. Navy's Naval Air Propulsion Center. Testing at NAPC consisted of hot and cold-day ground start and altitude airstart evaluations, mainburner and afterburner steady-state and transient operations and afterburner operability characterizations.

3. TEST ENGINE

The TF30-P-414/P-414A is a 92.97 kN maximum thrust afterburning turbofan engine, Figure 1. It powers the Grumman F-14A, one of the Navy's highest performance fighter aircraft. This engine incorporates a three-stage fan, a six-stage low pressure compressor, a seven-stage high pressure compressor, a can-annular combustor, a cooled one-stage high pressure turbine and an uncooled three-stage low pressure turbine. The afterburner system incorporates a five-zone fuel injection system, and a flameholder consisting of an annular vee gutter with radial spokes. The nozzle is a convergent/divergent variable iris type.

4. FUEL SELECTION

Six test fuels were used in the TF30-P-414A engine/afterburner evaluation program. JP-5, the fuel of choice for naval aircraft, served as the baseline. JP-7, a very high thermal stability fuel for special aircraft applications, was used as a high-quality baseline. Heating oil No. 2 (HO No.2) and F-76 represented emergency fuels; compared to the baseline JP-5, they had lower thermal stability, decreased volatility and higher viscosity. Suntech A and B were special fuel blends having higher aromatic and lower hydrogen contents than the emergency fuels. The test fuels were selected to exhibit pronounced variations in properties predicted to affect engine/afterburner operation significantly. Properties of the fuels are presented in Table 1. NAPC Fuel No. 22 (JP-5) and No. 17 (F-76) were used in the nonafterburning tests; NAPC Fuel No. 27 (JP-5) and No. 26 (F-76) were used in the afterburning tests.

5. EXPERIMENTAL RESULTS

A significant amount of experimental data was obtained during conduct of the engine test program. No attempt will be made, however, to present all of the data or the resulting analyses. This information is available in contractor reports through the sponsoring agency. The objective of this paper is to provide a somewhat limited assessment of the effect of liquid hydrocarbon fuels, having a wide range of properties, on selected engine component and system performance and operation. This assessment is provided in the following paragraphs.

Reference has been made throughout the discussion of results to the Alternate Test Procedure (ATP). The Pratt & Whitney version of the ATP consists of a set of fuel effect correlations that quantify changes in engine system and component performance and durability that result from changes in fuel properties. The objective of the ATP is to provide means for qualifying new fuels for Navy aircraft with a minimum of costly full-scale engine testing and for determining the acceptability of nonspecification fuels in emergency situations. The ATP modeling effort has concentrated on defining fuel effects for the TF30 engine while generally outlining approaches that could be applied to other systems.

A. COMBUSTOR

The TF30-P-414A combustor is a can-annular design having eight individual burner cans which discharge into an annular transition duct. The burner cans are arranged about the engine centerline and are interconnected through crossover tubes to allow propagation of flame from one can to another. There are two ignitors that are positioned in each of the two burners at the bottom of the engine: cans 4 and 5. Each ignitor is aligned with a fuel nozzle to ensure a fuel rich mixture for ignition. From the lower burner cans, flame propagates through the crossover tubes to the remaining six cans.

The improved durability/low smoke combustor embodies co-rotating "hollow-spray cone" air swirlers, an increased pressure drop liner and a tailored cooling and dilution hole pattern compared to the B/M version. In addition, the number 4 and 5 burner cans have a reduced flow air swirler at the ignitor position for improved lighting. Aside from the ignitor bosses; ignitor swirler and different dilution hole patterns for the two lower cans; and the afterburner squirt injection port in the number 4 can; all eight cans are identical.

Fuel is introduced in the dome of each can through a cluster of four pressure atomizing nozzles mounted on a support that anchors the front end of the can. Primary combustion air enters the dome through swirlers concentric with the fuel nozzles and through a center

tube. Of the flow entering the center tube, swirl is imparted to only approximately 40 percent of this airflow. Dilution air to reduce the average gas temperature and to tailor the temperature distribution to produce a profile that is acceptable for the turbine is introduced through radial holes in the walls of the can. Cooling air is introduced in the annular slots formed where the cylindrical louvers are welded together.

TABLE 1.
FUEL ANALYSIS

NAPC Fuel No. Fuel type Description	Spec Reqmts. MIL-T-5624L	22 JP-5	16 JP-7	17 F-76	18 HO No. 2	19 Sun. A	20 Sun B	26 F-76	27 JP-5
****Composition****									
Paraffins		82.2	96.6	72.8	67.3	62.3	68.4	71.5	81.3
Aromatics, Vol percent	25.0 max	17	2.6	26.4	30.8	37.1	30.7	27.8	17.9
Olefins, Vol percent	5.0 max	0.8	0.8	0.8	1.9	0.8	0.9	0.9	0.8
Sulfur, Total, Wt percent	0.40 max	0	0	0.37	0.12	0.21	0.07	0.63	0.07
Acidity, Total, mm KOH/g	0.015 max	0.003	0.001	0.07	0.023	0.017	0.017	0.068	0.003
Hydrogen Content, Wt percent	13.50 min	13.7	14.5	13.3	13.4	12.2	12.9	13.17	13.7
Nitrogen, ppm, Wt/vol		5	< 1.0	67	94	178	78	–	–
****Volatility****									
Distillation, K									
IBP		457	469	449	460	448	445	455	445
10 percent	478 max	472	480	486	491	469	476	502	466
20 percent		476	482	504	506	479	486	516	473
50 percent		489	488	537	542	514	513	552	488
90 percent		515	507	587	595	581	556	605	513
EP	563 max	534	536	603	614	600	593	616	537
Residue, ml	1.5 max	1.0	0.8	1.0	1.5	2.0	1.5	3.0	1.0
Loss, ml	1.5 max	1.0	0.2	1.0	0.0	0.4	0.5	2.5	0.0
Flash Point, K	333 min	341	344	344	344	338	343	358	334
Density		0.821	0.801	0.838	0.839	0.863	0.843	0.847	0.818
API Gravity at 288K	36.0 — 48.0	40.9	45.2	37.4	37.1	32.5	36.3	35.6	41.5
Surface Tension, N/m(x10^3)		5.140	5.186	5.384	5.308	5.246	5.344	5.380	4.740
****Fluidity****									
Viscosity at 273K, m^2/s (x10^6)		3.3	3.5	7.21	6.05	4.80	4.53	10.21	3.51
Freeze Point, K	227	225	228	266	270	259	255	266	227
Viscosity at 310.8K		1.57	1.67	2.74	2.85	2.06	1.91	3.37	1.57
Temperature at 12 x 10-6m^2/s, K		237	237	260	265	248	247	268	236
Pour Point, K		216	222	252	247	241	236	268	216
****Combustion****									
Aniline - Gravity product	4,500 min	5,845	7,417	5,950	6,009	3,777	4,298	6,566	5,922
Net Heat of Combustion, MJ/kg	42.555 min	42.897	43.425	42.639	42.729	42.066	42.390	42.599	42.906
Net Heat of Combustion, MJ/m^3		35105.3	34655.3	35465.3	35776.0	36175.8	35674.0	36114.8	35064.0
Smoke Point, mm	19.0 min	19	30	16	16	13	11	15	20
****Corrosion****									
Copper Strip, 2 hr at 373 K	1B max	1B	1A	1A	1A	1A	1A	1A	1B
****Stability****									
JFTOT Breakpoint Temp, K		644	>589	461	494	483	494	516	525
****Contaminants****									
Existent Gum, mg/100 ml	7.0 max	1.2	0	15.2	1.4	34.6	12	6.0	0.8
Particulates, mg/liter	1.0 max	1.73	0.1	8.45	1.77	4.18	1.02	2.42	1.56

(1) Exit Temperature Distribution

Combustor exit temperatures were recorded using the Automated Recording Temperature System (ARTS) package that consisted of a set of completely instrumented first-stage turbine vanes with 240 thermocouples (five per vane). ARTS data were used to calculate the turbine inlet pattern factor for each test fuel burned at each of the four power settings at sea-level conditions. Pattern factor is defined as $(T_{T5\,max} - T_{T5}) / (T_{T5} - T_{T4})$ where $T_{T5\,max}$ is the maximum temperature in the plane of the first stage vane; T_{T5} is the average combustor exit temperature in the same plane and T_{T4} is the combustor inlet temperature. Weibull techniques were used to determine $T_{T5\,max}$ where $T_{T5\,max}$ was assumed to equal the temperature of 99.7 percent of the cumulative data (mean fit, 50 percent confidence) as shown in Figure 2. This technique eliminates much of the uncertainty that results from having a reduced number of thermocouples, and is particularly helpful if the number of functioning thermocouples diminishes during the course of the testing.

The range of combustor pattern factor measured at sea level for the six fuels as shown in Figure 3. The pattern factor at intermediate power, 98 percent N_2, is considered to be the most significant value because of the effect of high T_{T5} on turbine vane durability. Pattern factors were lower when the aviation-type fuels JP-5 and JP-7 were burned than when the emergency fuels HO No. 2 and F-76 were used.

The Weibull pattern factor results measured for various fuels in the TF30-P-414A engine were correlated with 90 percent distillation fuel vaporization index ratio as shown in Figure 4. The ATP prediction and burner rig results of Reference 1 were also corrected to the same parameters for comparison. The comparison indicates the data from engine testing show less pattern factor variation than for the rig data or the ATP prediction. The difference may be attributed to improved operating conditions (i.e., higher fuel temperature) in engine testing and to the temperature measurement techniques used (i.e., engine ARTS vanes versus rig transversing rake).

The ATP correlation of pattern factor was based on TF30 fuel effect sensitivity anchored to previous TF30 engine data. The

Reference 1 data are single-can rig data which typically show much lower pattern factors than engine data. The difference in the effect of fuel property variations on pattern factor for the engine results are attributed to better aerodynamic mixing for the improved durability/low-smoke combustor and higher fuel temperatures with the engine fuel system as compared to the TF30 rig.

The fuel effect on average radial temperature profile at sea level intermediate power is shown in Figure 5. The average radial profile is significant between zero and 50 percent span because of its influence on turbine blade yield strength. The maximum difference, 3.8K, in radial profile at the 50 percent span location due to fuel effects is considered to be insignificant for the TF30 engine.

(2) Combustor Liner Temperature

Any changes in the combustion process which results in a change in the heat transfer to the combustor liner will effect combustor durability. The effect of fuel property variations on the local combustion gas temperature and the resultant liner temperature is of concern.

The temperature of the combustor liner is dependent on convective and radiative heating, as well as cooling air temperature. To isolate these separate effects, the temperature of the combustor liner was correlated with the rise in burner temperature, $T_{T5} - T_{T4}$. This parameter is used in heat transfer analysis to determine the cooling film temperature and the convective heat loading for a louver liner design, such as the TF30 combustor. This term accounts for differences in gas temperature, represented by T_{T5} changes, and for deficiencies in coolant temperature, T_{T4}. By comparison of fuel effects data at a constant burner temperature rise, the radiative heating effects due to fuel property variation were determined. The fuel radiative heating effect on the highest combustor liner temperature over the range of combustor ΔT operation is shown in Figure 6. The aviation JP-type fuels showed the lowest radiative heating effect, and the Suntech blend fuels with low hydrogen content had the highest effect. The results indicate the highest combustor liner temperatures occur at intermediate power, the condition at which life predictions were made.

Higher combustion flame radiation caused an increase in combustor liner metal temperature. Increased liner temperature caused by fuel combustion effects has commonly been correlated with liner severity parameter, LSP, defined as:

$$\text{Liner Severity Parameter (LSP)} = \frac{T_{L\,max} - T_{T4}}{T_{T5} - T_{T4}} \qquad (1)$$

Where:

T_{T4} = Compressor discharge temperature

$T_{L\,max}$ = Maximum liner temperature

T_{T5} = Combustor exit temperature

Correlation of combustor LSP with hydrogen content for the latest engine data is compared with the ATP correlation (Reference 2) in Figure 7. A good correlation was obtained for the LSP as a function of hydrogen content. The trend toward increased radiation with decreasing hydrogen content is evident for the TF30 combustor. Since it is the change in LSP which determines changes in liner life, the agreement in the slopes of the data trends confirm the original ATP prediction.

(3) Combustor Life

The ATP prediction of fuel effects on combustor liner temperature was based on the TF30-P-414A bill-of-materials combustor and fuel effects data of Reference 1. The improved durability/low-smoke combustor proposed for the TF30-P-414A engine incorporates several improvements to increase life, including local cooling changes and louver posts to prevent liner overheating due to louver cooling passage closure. Based on the current TF30 fuel effects data and improved durability combustor geometry, a life prediction analysis was conducted. Using this analysis of the effect of maximum liner temperature on cyclic life, the effect of fuel hydrogen content on liner life was determined. The resulting correlation is shown in Figure 8. Relative to the JP-5 baseline, the fuel with the lowest hydrogen content (1.5 percent less hydrogen) reduced TF30 liner life by 20 percent. The percent reduction in liner life with decreased hydrogen content is similar to that predicted by the ATP correlation.

(4) Altitude Airstart

The ability to restart an engine in flight is dependent on the aerodynamic conditions within the combustor and on the condition of the fuel spray near the ignitor. The aerodynamic variables at standard day conditions include: inlet pressure, Mach number, altitude, airflow rate and air temperature. Using any two of these variables, the other variables may be defined from a standard day windmill map. The critical fuel properties and flow factors which determine the condition of the fuel spray near the ignitor are typically fuel viscosity, surface tension, density, volatility, flowrate and flow split in dual orifice injectors.

Altitude airstart limits as defined by flame propagation to all burner cans were determined for each of the test fuels by finding the boundary between complete (i.e. successful) and partial lights, no lights, and/or hot starts (i.e. unsuccessful). Comparison of results for each fuel is plotted on the TF30 windmilling airstart envelope, shown in Figure 9. A comparison between fuels is made along lines of constant high rotor speed at windmilling. The aviation JP-type fuels, which are more volatile and less viscous than the other blend fuels, have the higher airstart altitude limits.

Under the ATP, an altitude ignition correlation was developed based upon the relationship derived by Ballal and Lefebvre for minimum ignition energy in a heterogeneous flowing stream (Reference 3). The correlation was developed by explicitly combining fuel properties into a single parameter referred to as the fuel characterization parameter (FCP): Reference 4.

A simplified correlation was developed in order to compare results from simulated altitude ignition rig operations and TF30 engine operations. The change in altitude ignition limit as a function of FCP was determined for the highest rotor speed line (35 percent N_2) of the engine results and for the equivalent air flow line of the TF30 rig results (Reference 5). The ignition data consisted of only those points that were determined to be no lights or single burner can lights (i.e., only one burner can ignited). FCP for a fuel in question was normalized by dividing it by the FCP value for JP-5 to obtain the fuel parameter ratio, FPR:

$$FPR = \frac{FCP_{fuel}}{FCP_{JP-5}} \quad (2)$$

A correlation comparison of the effect of fuel properties on TF30 altitude ignition for the latest engine results and for the ATP model is shown in Figure 10. A larger fuel effect variation is seen for the improved durability/low smoke combustor than for the bill-of-materials combustor. The difference may be attributed to an aerodynamic change to improve ignition capability of the improved durability/low-smoke combustor used in the TF30-P-404A engine and to better conditions for ignition relative to component rig testing (Reference 1). The fuel temperature was also a contributing factor; the temperature ranged from 304 to 372 K during engine testing, but was controlled at 278 K during component testing. The altitude ignition correlation for the TF30 engine with the B/M P-414 combustor is expected to lie between the current component rig results and the engine results for the improved durability/low smoke combustor.

(5) Ground Start

During prior ATP studies, a correlation was developed based on TF30 combustor rig data of minimum fuel flow at three different air flowrates to obtain ground start ignition characteristics. A correlation of ground start minimum fuel-air ratio as a function of normalized vaporization index, calculated for 10 percent distillation temperature, is presented in Figure 11.

During this program, data on ground starts were obtained for the TF30-P-414A engine by varying the ambient temperature for the highest viscosity fuels: F-76 and HO No. 2. The ground start limits were defined as full lights: determined by flame propagation between cans. Since different criteria were employed to evaluate ground start limits (i.e., minimum ambient temperature versus minimum fuel-air ratio), the TF30 engine results could not be directly compared with those of the combustor rig (ATP correlation). Using the TF30 engine results, a correlation was developed for minimum ambient temperature as a function of fuel volatility similar to other investigators (Reference 6). The effect of fuel 10 percent distillation temperature on TF30 ground start is shown in Figure 12. Since the ambient temperature is the cold soak temperature for the engine, it represents both the combustor inlet air temperature and fuel temperature.

(6) Smoke

The influence of the fuel on this particulate formation is exerted through both the fuel chemistry and the physical properties involved in fuel-air mixture preparation. Aromatic molecules have been shown to readily undergo condensation reactions that eventually lead to graphitic structure (Reference 7). Additionally, long droplet lifetimes increase the change for liquid pyrolysis and create locally fuel-rich conditions under which the condensation reactions may dominate the oxidative reactions. The cumulative effect of changes in both physical and chemical properties of the fuel is shown in Figure 13 where smoke number is plotted against high rotor speed. The operating conditions of the TF30-P-414A engine that yields the highest smoke is a part power setting. The higher smoke at part power conditions is attributed to low secondary nozzle fuel pressure drop and correspondingly poor fuel atomization. The largest fuel effects on smoke formation also occurs at part power setting for the P-414A engine. This result implies that fuel effects become more pronounced under less favorable operating conditions.

A TF30 smoke comparison at intermediate power is shown in Figure 14 for the test fuels at different flight points. The smoke results have been plotted against fuel hydrogen content. Earlier studies (References 1, 2, 5 and 8) have indicated a strong dependence of smoke number on hydrogen content. The change in smoke with flight point is attributed to differences in fuel preparation (i.e., fuel temperature and nozzle pressure drop) and combustor operating conditions (i.e., inlet temperature, pressure and fuel-air ratio).

The TF30-P-414A engine smoke results for the improved durability/low-smoke combustor measured at intermediate power for several flight points were correlated with hydrogen content of the fuel in Figure 15. The ATP smoke prediction is indicated as a shaded region through the JP-5 (baseline fuel) data. Comparison shows slightly larger effects of fuel property variation on smoke for the engine results than predicted with the ATP correlation. The ATP smoke correlation was based on higher smoke number results of engine and rig testing of the TF30-P-414 and P-3 bill-of-materials combustors (References 1, 5 and 9).

Extrapolation of the low smoke combustor data indicates that a zero smoke number corresponds to a hydrogen content of approximately 15.0 percent. This extrapolation is probably not valid above about 15.0 percent hydrogen. However, the trends do indicate that over the range of interest, 12.0 to 15.0 percent hydrogen, the effect of hydrogen content on smoke number is linear, and the slope is approximately proportional to the smoke number at some reference hydrogen content. The expression for smoke number from Reference 5 was modified for the proposed combustor and is given as follows:

$$SN = SN_{REF}\left[1 + \frac{(H_{2_{REF}} - H_2)}{(15 - H_{2_{REF}})}\right] \quad (3)$$

A correlation was also developed to evaluate the effect of variations of fuel physical properties on smoke formation. The physical property effects were calculated based on a relative fuel droplet size. The fuel droplet Sauter mean diameter (SMD) was normalized by dividing the SMD for JP-5 fuel calculated at 289 K. The smoke data for other fuels were adjusted to a reference smoke number for a 13.7 percent hydrogen content fuel using the above correlation. The effect of SMD ratio on TF30 smoke number is shown in Figure 16. A comparison of the smoke correlations indicates a stronger dependence on hydrogen content than on droplet size.

(7) Transient Operation

Engine acceleration from idle to intermediate power is set by the operation of the main fuel control. Fuel flow rate is metered to an acceleration schedule until engine speed nears intermediate N_2. The rate of acceleration is dependent on combustor heat release during the acceleration period. The heat release, in turn, is influenced by fuel effects parameters, such as combustion efficiency, fuel flow rate and lower heating value. Analysis of transient data from snap accelerations with the test fuels indicates acceleration times to reach 98 percent of intermediate N_2 at the Mach No. 0.5/3,048 m flight point to range from 29 to 41 percent of the specified maximum sea-level transient time for the control.

The minimum burner fuel-air ratio for evaluating blowout was determined by performing snap intermediate-to-idle decelerations at altitude for each of the test fuels. During engine deceleration, the fuel flow is set by the main fuel control to a minimum W_f/P_{S4} schedule until engine speed nears idle N_2. A typical deceleration transient is shown in Figure 17. Analysis of the transient data indicates a minimum fuel-air ratio of 0.0055 occurs within 1.2 seconds of the throttle pull back. The engine speed reached 98 percent of idle-setting N_2 within 12

seconds of the throttle change. A lean blowout fuel air ratio of 0.0030 was measured for JP-5 fuel in rig tests at idle conditions. A comparison of minimum fuel-air ratio during snap deceleration at Mach No. 0.8/15,240 m with the measured lean blowout value indicates at the least a 45 percent margin. No burner lean blowouts were experienced during the snap deceleration transient testing with any of the fuels.

B. AFTERBURNER

The afterburner of the TF30-P-414A consists of five independent zones that are engaged individually depending on the level of thrust augmentation required. Fuel flow to each zone is supplied through independent fuel manifolds and sprayrings. The fuel is injected upstream against a splash plate through fixed area orifices in each sprayring. The sprayrings for zones III and V consist of single concentric rings and are located in the fan stream. The three concentric sprayrings for zone IV are in the vitiated core stream, and the single rings of zone I and II are located near the interface between the fan and core streams. The locations of the sprayrings and flameholders are shown in Figure 18.

The flameholder consists of an annular vee gutter with radial spokes. There are six equally spaced flameholders that extend radially inward from the annular vee gutter across the core stream. An additional six vee gutters extend from the annular vee gutter halfway across the core stream. Seventeen radial vee gutters extend from the annular flameholder outward into the fan stream.

The annular flameholder acts as a pilot providing an ignition source and flame stabilization. The combustion process is distributed axially downstream to the nozzle throat. The hot combustion gases are surrounded by a liner to reduce the heat transfer to the engine case. This liner is 2.20 m in length and consists of two sections: a screech portion designed to suppress high frequency acoustic oscillations, and a conventional louvered portion. The screech section contains a total of 30 rows of holes in three groups with an axial hole spacing of 0.019 m between each group. Eleven louvered panels are located downstream of the screech section.

(1) Lighting Disturbances

The TF30-P-414A afterburner uses a main and auxiliary fuel squirt system and zone 1 fuel sprayring during ignition. During the lighting sequence, the afterburner fuel control starts filling the zone 1 sprayring, and begins flowing the auxiliary squirt that injects fuel into the air stream at the turbine exhaust. A zone I manifold fuel pressure signal initiates the main squirt that injects fuel into the No. 4 burner can causing a momentary rich fuel-air mixture and a hot streak flame. This flame propagates through the turbine and lights the auxiliary squirt and zone I fuel flow. The ignition of the squirt flow along with the zone I lighting fuel flow can result in relatively high lighting pressure spikes due to the sudden gas temperature rise with a choked exhaust nozzle.

Zones II through V are scheduled independently at a minimum fuel flow ratio (W_f/P_{S4}) by the afterburner fuel control. The introduction of these zones will also cause a pressure disturbance because of sudden temperature change in the afterburner. The amount of pressure disturbance depends on the size of the zone, the sequence order and the combustion efficiency. The TF30-P-414A engine uses an afterburner soft light system to reduce this over suppression by preopening the engine exhaust nozzle. As a result, the turbine pressure ratio is suppressed prior to the introduction of each zone; so that it is still within stall margin limits with the addition of lighting spikes for each zone.

Data taken with five fuels at the Mach No. 0.5/3,048 m point displayed no significant differences in pressure spikes during lighting of the different zones. Table 2 summarizes the maximum pressure spike from the nominal steady state pressure levels. The data indicate that there should be a minimal change in afterburner lighting disturbance with these fuels.

TABLE 2.
IGNITION SPIKES FOR TEST FUELS
(Relative to JP-5 operation)

Fuel Type	NAPC No.	Zone I	Zone II	Zone III	Zone IV	Zone V
JP-7	16	1.057	1.018	1.013	1.006	1.009
F-76	17	0.968	0.958	1.065	1.018	0.973
HO No. 2	18	0.967	0.975	1.070	1.011	1.013
Sun A	19	0.971	0.912	1.109	1.014	1.002
JP-5	27	Base	Base	Base	Base	Base

(2) Afterburner Performance

Combustion efficiency of the afterburner is determined by the flame spreading process downstream of the flameholder. For a turbofan engine afterburner, such as the TF30, better vaporization in the core stream leads to higher combustion efficiency than in the fan stream. The influence of fuel property variations is to change in the rate of fuel vaporization and fuel droplet combustion.

The afterburner combustion efficiency was determined for the test fuels from measurements of carbon monoxide and unburned hydrocarbon concentrations at the nozzle exit. Data were obtained at the following testing points: Mach No. 0.5/ 3,048 m, Mach No. 0.8/ 10,668 m and Mach No. 0.8/ 12,192 m. The afterburner combustion efficiency variation with fuel type for the Mach No. 0.8/12,192 m test point is shown in Figure 19. The solid line indicates the expected efficiency for operation of each afterburner zone with JP-5 fuel. The efficiency results for the other test points show a similar fuel effects trend.

In correlating the afterburner combustion efficiency data, the properties of the fuel relating the burning rates of fuel droplets were studied. An ATP correlation for combustion efficiency was developed using the 10 percent and 90 percent distillation temperatures (Reference 5). The 10 percent distillation temperature is considered to affect the vaporization rate and burning of the lighter fuel ends in the flameholder wake, and the 90 percent distillation temperature is related to vaporization and droplet burning of the heavier fuel ends downstream of the flameholder. A linear regression was used to develop an expression for the change in combustion efficiency relative to JP-5 as follows:

$$\eta = \eta_{REF} - (0.148\ \Delta T_{10} + 0.0274\ \Delta T_{90})\ f/a + 0.0102\ \Delta T_{10} - 0.00342\ \Delta T_{90} \quad (4)$$

Where, $\Delta T_{10} = (T_f - T_{REF})$ at 10 percent distillation (°F)
$\Delta T_{90} = (T_f - T_{REF})$ at 90 percent distillation (°F)
f/a = Afterburner fuel-air ratio
η_{REF} = Combustion efficiency of reference fuel (percent).

The coefficients of this correlation differ from those of the previous ATP correlation. The detrimental fuel effects are shown by the net negative coefficients for both the 10 percent and 90 percent distillation temperature difference. The results of this correlation are compared with the efficiency data and the previous ATP prediction in Figure 20 for F-76.

These curves indicate that the above correlation agrees well with the measured efficiency data; the coefficient of determination (r^2) is 0.975 for all of the alternative fuel data. The ATP prediction was based on previous fuel effects sector rig testing. These tests were apparently not representative of full engine tests. The above correlation better reflects expected fuel effect trends and should be used for predicting afterburner combustion efficiency changes in place of the previous ATP prediction.

(3) Flameholder Temperature

The TF30 afterburner flameholder consists of an annular pilot vee gutter with radial vee gutters extending into the core and fan streams. The flameholders acts as a bluff body to maintain a combustion flame within its wake. In performing this function, the flameholder is heated by convective heat transfer from the airstream and by radiative heat transfer from the combustion flame. The influence of fuel property variations on flameholder temperature is through changes in engine operating temperature (i.e., turbine exit temperature differences) and through changes in radiative heating due to differences in fuel chemistry.

The flameholder metal temperatures were measured by thermocouples installed on the annular and radial vee gutters at several locations. The highest temperature reading occurred for the core stream radial flameholder at the Mach No. 0.5/3048 m maximum afterburner point. The variation in the highest flameholder temperature with fuel type is shown in Figure 21.

A fuel effect correlation for the maximum flameholder temperature was obtained from the measurements (reference Figure 21) by applying a correction to 0.052 afterburner fuel-air ratio. The flameholder temperature correlation at maximum afterburning is shown in Figure 22. The actual data corrected to the appropriate afterburner fuel-air ratio setting are indicated. The results show a radiative heating effect of the fuel on temperature of the flameholder due to fuel property variation. Only a minor effect on durability is expected with the use of alternative fuels since the flameholder is a low maintenance part requiring weld repair of trailing edge cracks at periodic overhaul periods.

(4) Afterburner Liner

The afterburner liner, which is a conventional louver design, uses a portion of fan airflow for cooling. Liner heating is through convective and radiative heat transfer from hot combustion gases. The amount of heating depends on afterburner fuel-air ratio, particularly that of zone V since it is the most outboard zone located nearest the liner. The influence of fuel property variations on liner temperature is through changes in afterburner operating fuel-air ratio and changes in radiative heating due to differences in fuel chemistry. The afterburner liner temperatures were measured at several locations along the length of the liner. The highest liner temperatures were recorded at the Mach No. 0.5/3,048m maximum afterburner test point. Measurements of typical liner temperatures are shown in Figure 23.

A fuel effect correlation of afterburner liner temperature was determined from the measurements (reference Figure 23) by applying the correction for afterburner fuel-air ratio. The afterburner liner temperature correlation is shown in Figure 24. Actual data corrected to the appropriate afterburner fuel-air ratio setting are included. The results indicate that afterburner liner temperature is slightly dependent on radiative heating effects. Using an afterburner liner life prediction model (Reference 9), the change in LCF life was determined for the alternative fuels relative to JP-5. The results shown in Figure 25, indicate 13.5 percent LCF life improvement for JP-7 and a deficit for the other alternative fuels.

(5) Afterburner Exhaust Nozzle

The afterburner exhaust nozzle is a convergent/divergent area type. It has hydraulically driven nozzle segments located aft of the afterburner combustion chamber duct. Seals are installed internally between adjacent segments by guides, seal locks and bolts. This arrangement allows the segments to travel in both a radial and an axial direction while maintaining surface contact between the seals and segments. Both nozzle segments and seals are exposed to convective and radiative heating by hot combustion gases when the nozzle is fully opened; this occurs at the maximum afterburner operating point.

The afterburner exhaust nozzle temperatures were measured by installing thermocouples on the backside of the nozzle segments. Due to relative travel between the overlapping seals and segments on the inside (i.e., hot side) surface, it was necessary to install the thermocouples on the outside segment surface. Although the measured temperatures are lower than experienced on the hot side, the trends with fuel property variation can be determined. A typical nozzle segment temperature is shown in Figure 26.

A fuel effect correlation of exhaust nozzle temperature was determined from the measurements (reference Figure 26) by applying the correction for afterburner fuel-air ratio. The exhaust nozzle temperature correlation at maximum afterburning is shown in Figure 27. Actual data corrected for appropriate fuel-air ratio are included. The results show a small fuel radiative heating effect. The correlation indicates an 18K difference in nozzle temperature between alternative fuels and agrees with previous results (Reference 10). This would result in a small influence of fuel property variation on exhaust nozzle life.

(6) Spraying Coking and Fouling

The TF30 afterburner fuel sprayrings consist of fixed orifice injectors and splash plates for fuel distribution. The sprayrings are empty of fuel until afterburner operation is selected. The core stream sprayring (i.e., zones I, II and IV) are exposed to 1460K turbine temperature both during intermediate and afterburner operation. The sprayring hot wall and fuel temperatures lead to conditions that cause internal coking, particularly during initiation and cancellation of the zone.

The core stream sprayrings are also subject to the build-up of external surface deposits through formation of combustion related compounds carried in the fuel as impurities (i.e., sulfur and metals). These compounds may be deposited by the turbine exhaust flow, or they may be formed when fuel spray collects on the sprayring surface and is heated. The build-up of the surface deposit around the fuel orifices can restrict the fuel flow rate through the sprayring.

The severity of afterburner sprayring coking and orifice fouling was evaluated by conducting post-test flow calibrations. Results indicated flow reductions of 12.8 and 3.5 percent in the Zone II and III sprayrings, respectively; the remaining sprayrings were within flow specifications. This amount of sprayring fouling is not untypical for the amount of afterburner testing conducted in the engine fuel effects investigation.

Following post-test inspection of the engine, the flow capacities of the sprayrings were fully restored through chemical and pyrolytic cleaning techniques. It is likely that some pyrolitic cleaning of zone I and IV sprayrings occurs when installed in the afterburner since these sprayrings are directly exposed to turbine exhaust temperatures.

(7) Smoke

Carbon particles are generally consumed during afterburner operation due to multiple diffusion flame fronts and relative long residence time at high temperature in the afterburner duct. The smoke reduction with afterburner setting at Mach No. 0.5/3,048 m is shown in Figure 28. The results indicate a 40 percent reduction in intermediate smoke level through zone 3 operation and an 85 percent smoke reduction for maximum afterburner operation. The amount of smoke reduction is independent of fuel type and is associated with the amount of combustion coverage of the core stream zones (i.e. zones I, II and IV).

(8) Transient Operation/Operability

Rapid transients require the afterburner control system to initiate zone I ignition, compute and meter fuel flow, select individual fuel zones for operation, and change the exit area to maintain the desired engine pressure ratio. During a transient to zone V operation, the nozzle area is scheduled to lead the fuel flow. There is a scheduled pause as each individual fuel zone comes in to allow enough fill and light time before nozzle area and fuel flow are increased. The influence of fuel property variations is to change the scheduled flow rates through specific gravity differences and/or to change afterburner temperatures (i.e., desired nozzle opening) due to fuel vaporization and combustion efficiency differences. The afterburner control must be tolerant of these fuel property variations to prevent fan stall due to over suppression (i.e., high engine pressure ratio) or low rotor overspeed due to undersuppression (i.e., low engine pressure ratio).

The capability of the P-414A afterburner control to accommodate various fuels was evaluated by performing intermediate to maximum afterburner snap transients. A series of five snaps were attempted for each fuel in each of five test regimes: Mach No. 0.5/3,048 m, and Mach No. 0.8 at 10,668; 12,192; 13,716; and 15,240 m. The results indicate successful intermediate to maximum transient operation for all attempts, except for the Mach No. 0.8/15,240 m point. A slow intermediate to maximum transient was performed for each fuel at this point, and it was found that fan stall occurred during the afterburner reduction to intermediate setting. Analysis of transient data of the stall indicates the fan was oversuppressed due to the nozzle area change leading the afterburner fuel flow reduction. The stalls during afterburner cancellation at the Mach No. 0.8/15,240 m point were considered to be a result of the fuel control schedule, and were not attributed to fuel property variations.

The time to complete the intermediate to maximum afterburner transient is a function of afterburner fuel control schedule, and is independent of fuel type. Analysis of the snap transient data indicates the mean times to achieve 98 percent maximum nozzle area were 3.9 and 5.2 seconds for the Mach No. 0.5/3,048 m and Mach No. 0.8/13,716 m points respectively. These test points represent the afterburner fuel flow range over which transient testing was accomplished. These transient times are within the fuel control specifications.

An assessment of the effect of fuel property variation was made for those aspects of the TF30 afterburner which affect its ability to fulfill the requirements of an aircraft mission, i.e., operability. The most critical condition is the upper left-hand corner of the flight envelope (low Mach number, high altitude conditions). Afterburner operation at these conditions requires: (1) ignition of the pilot zone, (2) subsequent flame propagation to the remaining zones, and (3) stable, efficient combustion. Efforts were directed at defining fuel effects on the ignitions, stability and transient operation of the afterburner under these conditions.

The fuel effects testing of afterburner lighting indicated zone 1 ignition with the hot squirt system occurred for all fuels for the test points of 3,048 through 15,240 m altitude. Previous afterburner lighting testing with a spark ignitor at the zone 1 circumferential flameholder location found a limit in ignition altitude due to variations in fuel properties (Reference 5). Comparison of these results indicate that the hot squirt system has superior lighting capability to the spark igniter and no fuel effects are apparent with the hot squirt ignition system.

6. CONCLUSIONS

Based upon the results of the TF30-P-414A engine testing, and the analysis of fuel effects data, the following conclusions are made with regard to the effect of fuel property variation.

a. A significant loss in altitude airstart capability was seen for fuels with higher fuel characterization parameter, FCP. The primary factors which caused this change are differences in fuel viscosity and 10 percent distillation temperature. Altitude ignition was found to occur at or above NATOPS ceiling for all of the test fuels, except for F-76. The flame propagation between burner cans was determined to be the lighting criteria limiting altitude airstart capability. The flame propagation limit shows a similar fuel effect trend and a dependence on combustor conditions (i.e., inlet air temperature).

b. Cold day ground start may become difficult with viscous, low volatility fuels.

c. The burner combustion efficiency, gaseous emissions and pattern factor for the TF30 low smoke combustor were slightly affected by fuel property variation through changes in fuel viscosity and volatility.

d. Exhaust smoke was found to be strongly influenced by the hydrogen content in the fuel. Smoke was also seen to be influenced by relative fuel droplet size through fuel viscosity and fuel temperature changes.

e. Increased flame radiation with the decreased fuel hydrogen content reduced the projected low cycle fatigue life of the combustor liner. Relative to the JP-5 baseline, Suntech A fuel, which had the lowest hydrogen content (i.e. 1.5 percent less hydrogen), reduced the TF30 liner life by 20 percent.

f. The durability of the afterburner components (i.e., flameholder, liner and exhaust nozzle) were only slightly influenced by variation in fuel properties.

g. Relative to JP-5 the afterburner combustion efficiency with alternative fuels was found to vary with 10 percent and 90 percent fuel recovery temperatures and fuel-air ratio. The revised correlation predicts a small efficiency loss with less volatile fuel.

h. Ignition of the afterburner at high altitudes with the hot squirt system was 100 percent reliable to 15,240 m altitude with all of the fuels tested.

i. Comparisons with the ATP predictions indicate the previous analyses and rig results can be used to project fuel effect trends however the actual levels may be different due to limitations of rig testing.

7. REFERENCES

1. Beal, G.W., "Effect of Fuel Composition on Navy Aircraft Engine Hot Section Components," NAPC-PE-74C, May 1983.

2. Ernst, R. C. and Andreadis, D., "Fuel Effects on Gas Turbine Engine Combustion," AFWAL-TR 83-2048, January 1983.

3. Ballal, D.R. and Lefebvre, A. H., "Ignition and Flame Quenching of Flowing Heterogeneous Fuel-Air Mixtures," Combustion and Flame, Vol 35, pp.155-168, 1979.

4. Mosier, S. A., "Fuel Effects on Gas Turbine Combustion Systems", AGARD Conference Proceedings No. 353 on Combustion Problems in Turbine Engines, 1983.

5. Masters, A. I., Beal, G. W., Biddle, T. B., Warner, P. A., and Weiss, C. G., "Alternate Test Procedure for Navy Aircraft Fuels - Phase II," NAPC-PE-108C, May 1985.

6. Jackson, T. A., "The Evaluation of Fuel Property Effects on Air Force Gas Turbine Engines - Program Genesis" ASME 81-GT-1, 1981.

7. Blazowski, W.S., "Dependence of Soot Production on Fuel Blend Characteristics and Combustion Conditions," ASME 79-GT-155, 1979

8. Herrin, J.R., Longenecker, K.O., and Biddle, T.B., "Alternate Test Procedure for Navy Aircraft Fuels - Phase I," NAPC-PE-63C, January 1982.

9. Gleason, C.C., Oller, T.L., Shayeson, M.W., and Bahr, W.D., "Evaluation of Fuel Character Effects on F101 Engine Combustion System," AFAPL-TR-79-2018, June 1979.

10. Russell, P.L., "Fuel Character Effects on USAF Gas Turbine Engine Afterburners, Part II - TF30 Afterburner," AFWAL-TR 82-2114, June 1983.

11. SAE Aerospace Recommended Practice 1179A, "Aircraft Gas Turbine Engine Exhaust Smoke Measurement," Society of Automotive Engineers, New York, N.Y., July 16, 1979.

8. ACKNOWLEDGEMENT

One of us wishes to acknowledge support of the United States Navy in sponsoring the engine evaluation and ATP programs from which this paper is derived. He would specifically like to thank his coauthor, Pete Karpovich, who served as the Navy's Program manager for his technical and managerial guidance, and patience.

We both wish to acknowledge the many people at Pratt & Whitney and at the Naval Air Propulsion Center who contributed to the success of the TF-30 engine program. These include John Weston, Paul Russell, George Beal, Art Masters and Bob Pangborn at Pratt & Whitney; and G.H. Chun, A. Miguelez, M. Marx and J. Ricciardelli from the Naval Air Propulsion Center.

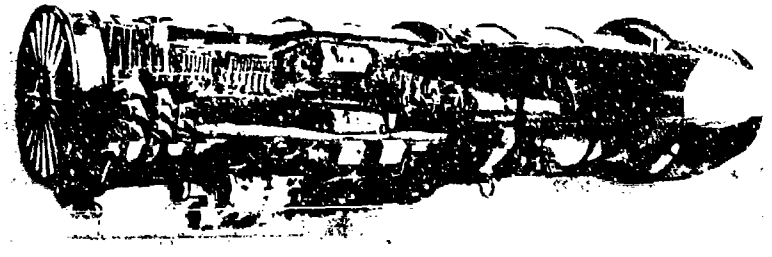

Figure 1 TF30-P-414/P-414A Afterburning Turbofan Engine

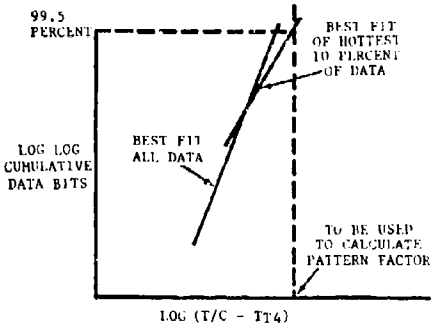

Figure 2. Weibull Estimation Of $T_{T5\ max}$

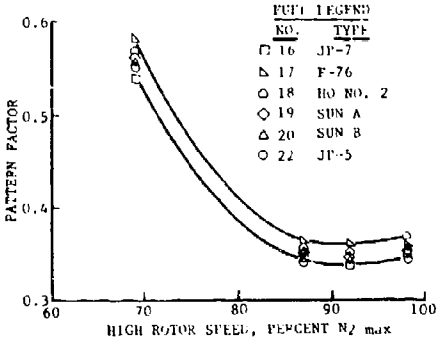

Figure 3 Combustor Pattern Factor Variation With Rotor Speed

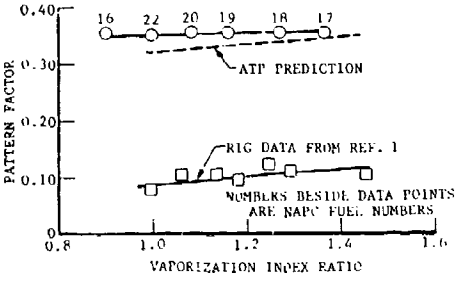

Figure 4. TF30 Pattern Factor Correlation

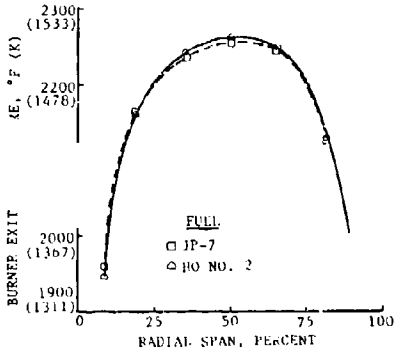

Figure 5. Average Radial Temperature Profile Variation

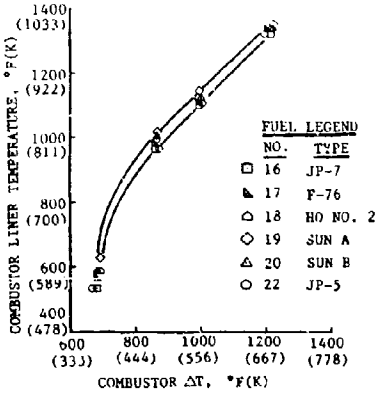

Figure 6. Combustor Liner Temperature Variation

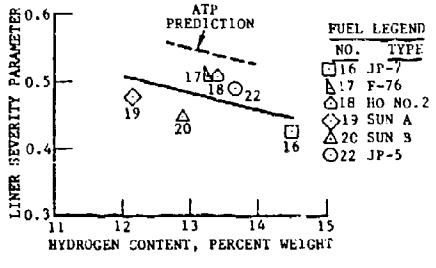

Figure 7. Combustor Liner Severity Parameter Correlation

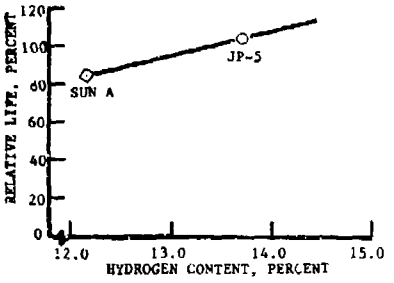

Figure 8. Effect Of Fuel Hydrogen Content On TF30 Liner Life

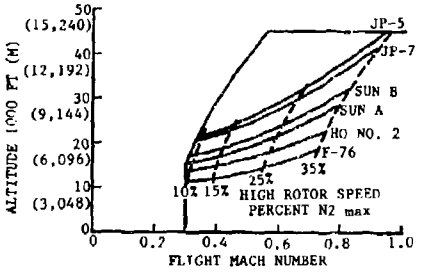

Figure 9. TF30 Altitude Airstart Comparison

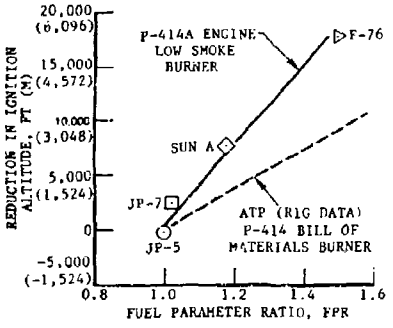

Figure 10. Effect of Fuel Properties on TF30 Altitude Ignition

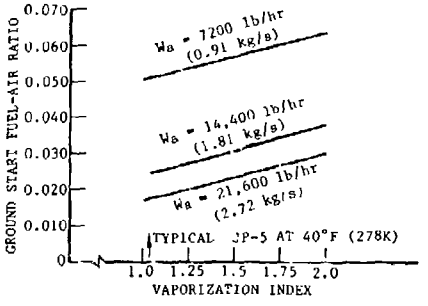

Figure 11. Effect of Vaporization Index on Ground Start Fuel Air Ratio

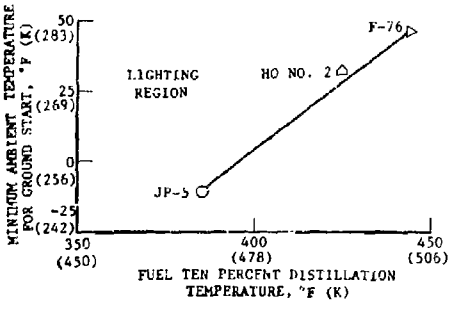

Figure 12. Effect of Fuel Volatility on Engine Ground Start

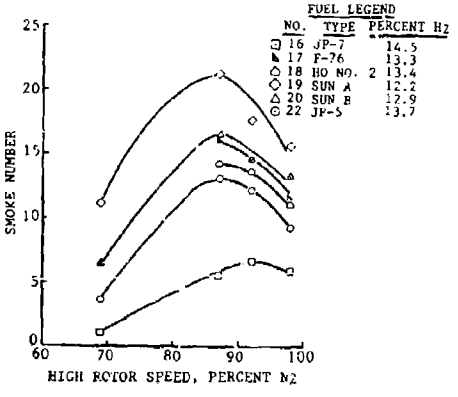

Figure 13. Variation in Smoke Number With Engine Power Setting

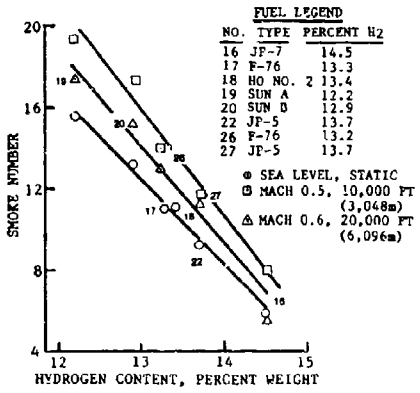

Figure 14. Variation in Smoke Number With Fuel Hydrogen Content

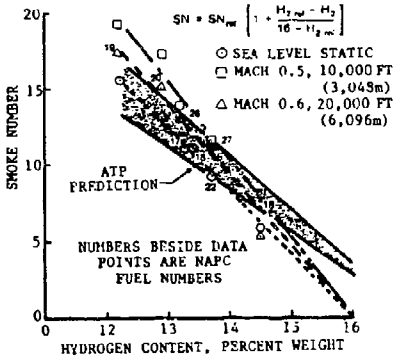

Figure 15. TF30 Smoke Correlation For Improved Durability/Low Smoke Combustor

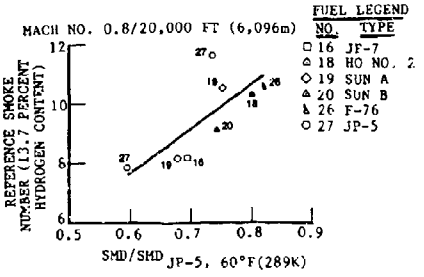

Figure 16. Effect of SMD Ratio on TF30 Smoke

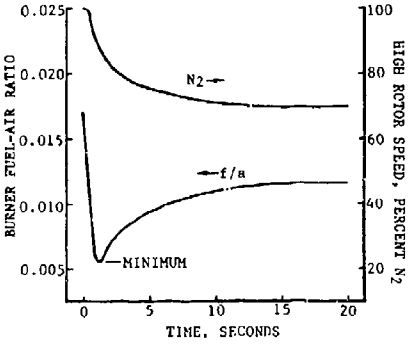

Figure 17. Engine Typical Deceleration Transient

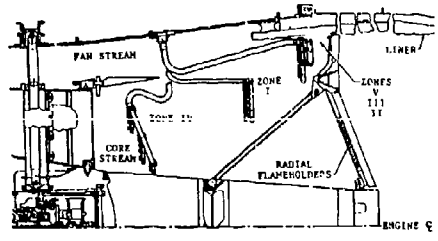

Figure 18. TF30-P-414A Afterburner

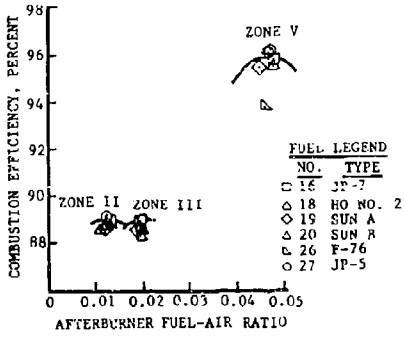

Figure 19. Afterburner Combustion Efficiency Variation

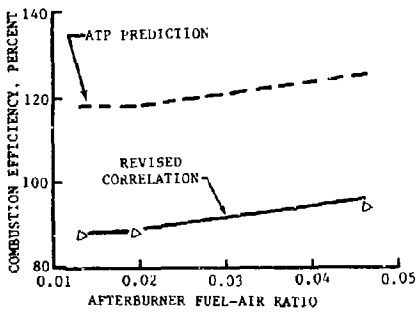

Figure 20. Afterburner Combustion Efficiency Correlation For F-76 Fuel

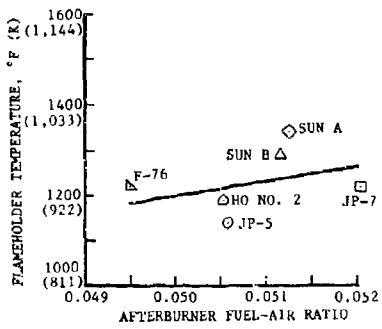

Figure 21. Variation In Flameholder Temperature

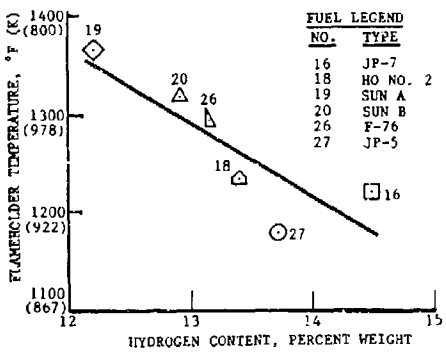

Figure 22. Flameholder Temperature Correlation

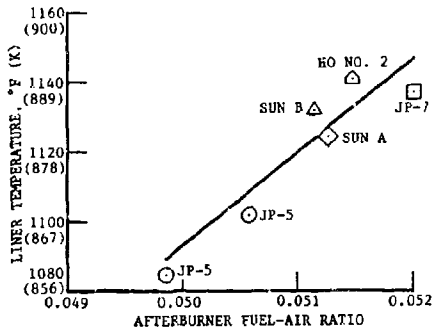

Figure 23. Afterburner Liner Temperature Variation

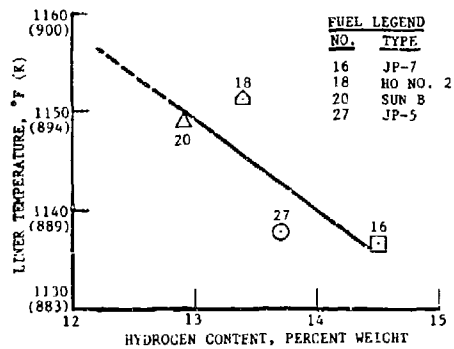

Figure 24. Afterburner Liner Temperature Correlation

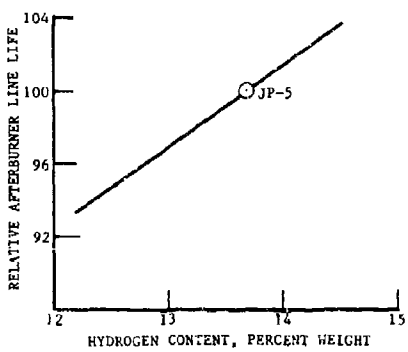

Figure 25. Afterburner Liner Relative Life Correlation

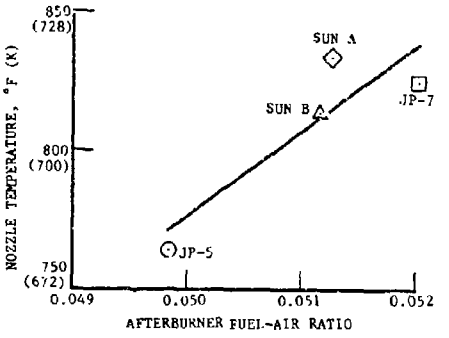

Figure 26. Afterburner Exhaust Nozzle Temperature Variation

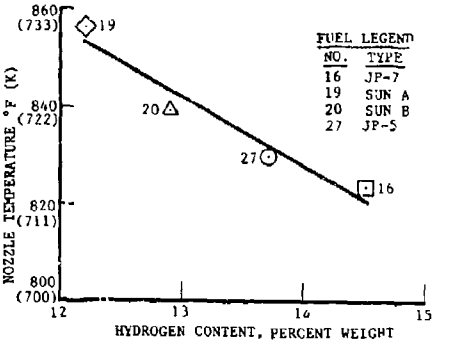

Figure 27. Exhaust Nozzle Temperature Correlation

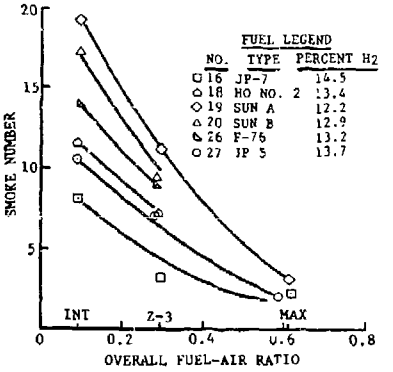

Figure 28. Variation in Smoke Number With Afterburner Setting

DISCUSSION

G.Grienche, FR

How can you explain that the maximum smoke number doesn't appear at the maximum power?

Author's Reply

The variation in smoke number with power setting for the TF30 engine is a unique characteristic of that engine. The measure relationship for the two variables constitutes a "fingerprint" for this particular engine. Each engine has its own "fingerprint" which is a function of variables such as fuel injection characteristics; combustor geometry; combustor inlet air flowrate, temperature and pressure; and, of course, the fuel being used. No attempt has been made to determine the interaction of these variables to produce a unique "fingerprint". Instead, the smoke number-power profile was acquired using the fuel of choice for US Navy engines, viz. JP-5. The measured deviation from this baseline characteristic, when other fuels were burned, served to indicate their impact on smoke production in the TF30 engine.

A.Winterfeld, GE

If we agree that the physical properties of the fuels are the main source of problems in the main combustor, it would be interesting to know whether there has also been carbon deposition at the combustor walls.

Author's Reply

After 94 hours of operation at sea-level conditions during which six test fuels were burned, an inspection of the fuel nozzles and burner cans was made. No unusual carbon deposits were seen as a result of using four poor quality fuels. Again, after approximately 131 hours of operation at simulated altitude conditions there was no excessive carbon formation on the burner liners, with one exception. There was a carbon clinker at the ignitor swirler location in one can. Because the total amount of engine operating time was relatively small, however, it is not inconceivable that carbon deposits observed were likewise small. There is great concern that carbon deposition both on liners and within, and on, fuel injectors will increase noticeably if poor quality fuels are used in today's aircraft gas turbine engines for extended periods of time. This concern must be addressed in the design and development of new and upgraded combustion systems.

J.Odgers, CA

What was maximum combustion efficiency for the afterburner?

Author's Reply

The afterburner maximum combustor efficiency, on the slide that was displayed, was approximately 96 percent when all five zones were engaged. The operating condition that was simulated in this case was Mach No. 0.8/40,000 ft (12,192 m).

J.Odgers, CA

This fits with our observation that 'chemical' effects are small (approx. 3%) whereas 'physical' effects are much more significant.

G.Bayle-Laboure, FR

How do you measure smoke in reheat conditions?

Author's Reply

During engine operation under reheat conditions, cooled, multiple-point entry, traversing probes were used to acquire a portion of the exhaust gas in a continuous manner.

Exhaust gas was treated in compliance with SAE Aerospace Recommended Practice No. 1179A (1980) to obtain the actual smoke number.

ALTERNATIVE FUEL SPRAY BEHAVIOR

J. P. Ashelm and J. E. Peters

Department of Mechanical and Industrial Engineering
University of Illinois at Urbana - Champaign
1206 West Green Street
Urbana, Illinois 61801

ABSTRACT

In this paper the effects of alternative fuels on the combustion characteristics of a liquid fuel spray are examined. Fuel properties are systematically varied and the effects of these variations on the structure (drop histories, temperatures and species concentrations) of the spray flame are calculated. In addition, a comparison is made of the differences in two spray flames fueled by the standard NATO F - 40 fuel and a proposed alternative fuel, the AGARD Research Fuel. The calculations are performed using a reacting, two phase, two dimensional flow code which utilizes a Lagrangian calculation of droplet trajectories and an Eulerian approach (with the k - ε turbulence model) for the gas phase flowfield. Interactions between the drops and the gas phase are accomplished through the particle-source-in-cell technique with exchange of mass, momentum and energy between the two phases. A global reaction scheme is used with the reaction rate determined by the minimum of either an Arrhenius rate or mixing rate.

Fuel property changes which affect droplet size and volatility are shown to have significant effects on droplet trajectory patterns. However, for the flowfield examined in this paper (where the fuel spray core is very rich and the mixing of air with the fuel occurs at a relatively slow rate) these trajectory changes only moderately modify the fuel vaporization pattern within the spray. In addition, the majority of the fuel is vaporized in an extremely fuel rich environment so that the energy release throughout most of the flowfield is controlled by the gas phase phenomena of mixing and chemical kinetics. The exception to this is the location of the ignition point which is shown to move downstream with reduced evaporation rates associated with higher fuel boiling points. Increasing the width of the inlet droplet size distribution significantly increases the length of the droplet trajectories due to the presence of large drops in the spray but it does not affect the overall structure of the spray since all the droplets still evaporate in highly fuel rich regions. Turbulent dispersion of the droplets and droplet collisions are shown to have little effect on the spray flame for this flowfield.

NOMENCLATURE

a	air mass fraction
A_1	empirical constant
B_M	mass transfer number
B_T	thermal transfer number
C_D	drag coefficient
C_1, C_2, C_μ	turbulence model constants
C_p	specific heat
D	droplet diameter
$\bar{D}$	Rosin Rammler mean droplet diameter
D_T	tunnel diameter
F_D	drag force
f	fuel mass fraction
H_f	fuel's heat of combustion
h	enthalpy
i	stoichiometric air/fuel ratio
k	kinetic energy of turbulence
k_g	gas thermal conductivity
L	latent heat of vaporization
L_e	eddy length
m	mass
$\dot{m}_d$	droplet mass flow rate
$\dot{m}_{evap}$	droplet evaporation rate
MW	molecular weight
N	Rosin Rammler exponent
N_d	number of droplets in a parcel
P	pressure
p	product mass fraction
Pr	Prandtl number
R_f	fuel reaction rate per unit volume
$R_{f,kin}$	kinetic limited reaction rate
$R_{f,mix}$	mixing limited reaction rate
r	radial coordinate
Re	Reynolds number
S	source term
SMD	Sauter Mean Diameter
T	temperature
T_b	boiling temperature
t	time
t_e	eddy lifetime
t_t	transit time
$\vec{u}$	total velocity
u	axial velocity component
v	radial velocity component
$\vec{x}$	position vector
x	axial coordinate
τ	droplet relaxation time
Γ	diffusion coefficient
μ	gas viscosity
ν_f	fuel viscosity
ε	dissipation rate of turbulence
ρ	density
ϕ	general flow variable
σ	standard deviation
σ_1,σ_2	fuel surface tension
σ_k,σ_ε,σ_f, σ_h,σ_p	turbulence model constants
α	number of carbon atoms
β	number of hydrogen atoms

Subscripts

d	droplet
eff	effective
f	fuel
g	gas phase
i	inlet
o	outlet
s	droplet surface
ϕ	general variable
α	number of carbon atoms
β	number of hydrogen atoms

Superscripts

ϕ	general variable
$\bar{}$	time averaged value

INTRODUCTION

Spray flame behavior can strongly depend on the fuel's physical properties such as boiling point, vapor pressure, viscosity and surface tension because of the influence of these parameters on fuel evaporation rate. This has been demonstrated frequently in the literature from a global point of view as emissions, flame stability and efficiency have been shown to depend on physical properties of

the fuel [1 - 3]. In addition, detailed studies of spray flames have also revealed fuel property effects on flame structure as spray flames have been observed to vary from gas diffusion burning of the fuel vapor (when the fuel evaporates rapidly resulting in a fuel rich vapor core) to individual droplet burning (when large, slowly evaporating droplets penetrate beyond the central spray region and progress into the oxygen rich environment surrounding the spray) [4].

These results can be cause for concern when alternative fuels are substituted for conventional fuels because of the potential for changes in the flame structure and, hence, changes in the performance of the combustion device in terms of global parameters such as emissions, flame stability, etc. Therefore, in this paper the structure of a spray flame is modeled as fuel properties are varied through a realistic range corresponding to the changes that would be encountered in switching from a relatively volatile kerosene type fuel to a heavy fuel oil. In particular, droplet trajectories, temperature profiles, equivalence ratio profiles and evaporation rates are examined as key fuel properties are independently varied.

MODEL DESCRIPTION

In this paper we consider a geometry similar to the one used in the experiments by Yule and Bolado [4] because of our interest in eventually comparing our computational work with their experimental results on spray flame structure. As shown in Fig. 1, the configuration consists of an air blast atomizer from which fuel and air are injected through a 1 cm diameter orifice at the centerline. A 7.5 cm circular flame stabilization disk is located at the atomizer exit plane. The duct is 27 cm in diameter and 1.5 meters long.

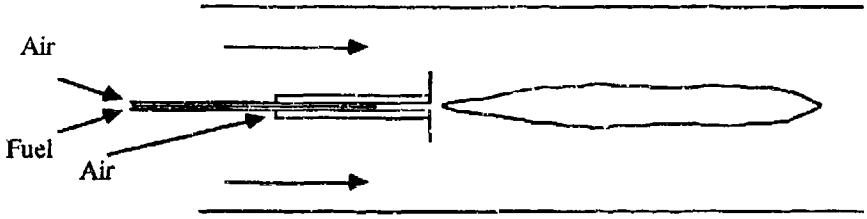

Figure 1. Schematic of the combustion test rig of Yule and Bolado [4].

In the following sections the model details are briefly described. The approach is fairly conventional and draws on our past work and the work of others for the various submodels. We do not intend to "break new ground" with the model formulation but rather to use existing modeling techniques to examine the particular problem of alternative fuel effects on spray structure.

Gas Phase Model

In modeling the gas phase, we employ a TEACH-based code [5] which solves axisymmetric, two-dimensional, time-averaged turbulent mean flow gas phase equations. The code uses a hybrid differencing scheme and a tri diagonal matrix algorithm equation solver with relaxation. The k-ε model provides for turbulence closure.

Eight conservation equations are solved simultaneously, one each for u- and v-momentum, mass, enthalpy (h), turbulent kinetic energy (k) and its rate of dissipation (ε), fuel mass fraction (f) and product mass fraction (p). The general form of these conservation equations is

$$\frac{\partial}{\partial x}(\bar{\rho}\,\bar{u}\,\phi) + \frac{1}{r}\frac{\partial}{\partial r}(r\,\bar{\rho}\,\bar{v}\,\phi) = \frac{\partial}{\partial x}\left(\Gamma_\phi \frac{\partial \phi}{\partial x}\right) + \frac{1}{r}\frac{\partial}{\partial r}\left(\Gamma_\phi\, r \frac{\partial \phi}{\partial r}\right) + S^\phi + S_d^\phi \qquad (1)$$

where ϕ is any one of the eight general flow variables, Γ_ϕ is the effective diffusion coefficient for ϕ, and S_d^ϕ and S^ϕ are the sources for ϕ from the droplets and gas phase, respectively. Specific expressions for the eight flow variables are shown in Table 1.

Table 1. Transport coefficients and source terms for the variable ϕ.

ϕ	Γ_ϕ	S^ϕ	S_d^ϕ
1	0	0	$\Sigma\,(\dot{m}_{d,i} - \dot{m}_{d,o})N_d(I,J)$
$\bar{u}$	μ_{eff}	$\frac{\partial}{\partial x}(\mu_{eff}\frac{\partial \bar{u}}{\partial x}) + \frac{1}{r}\frac{\partial}{\partial r}(\mu_{eff}\, r \frac{\partial \bar{v}}{\partial x}) - \frac{\partial \bar{P}}{\partial x}$	$\Sigma\,(\dot{m}_{d,i}u_{d,i} - \dot{m}_{d,o}u_{d,o})N_d(I,J)$
$\bar{v}$	μ_{eff}	$\frac{\partial}{\partial x}(\mu_{eff}\frac{\partial \bar{u}}{\partial r}) + \frac{1}{r}\frac{\partial}{\partial r}(\mu_{eff}\, r \frac{\partial \bar{v}}{\partial r}) - 2\mu_{eff}\frac{\bar{v}}{r^2} - \frac{\partial \bar{P}}{\partial r}$	$\Sigma\,(\dot{m}_{d,i}v_{d,i} - \dot{m}_{d,o}v_{d,o})N_d(I,J)$
k	$\frac{\mu_{eff}}{\sigma_k}$	$G - \rho\varepsilon$	0
ε	$\frac{\mu_{eff}}{\sigma_\varepsilon}$	$C_1\frac{\varepsilon}{k}G - C_2\rho\frac{\varepsilon^2}{k}$	0
f	$\frac{\mu_{eff}}{\sigma_k}$	$-R_f$	$\Sigma\,(\dot{m}_{d,i} - \dot{m}_{d,o})N_d(I,J)$
h	$\frac{\mu_{eff}}{\sigma_h}$	$H_f R_f$	$\Sigma\,\{\dot{m}_{d,i}C_{p,f}(T_{f,i} - T_{ref}) - \dot{m}_{d,o}C_{p,f}(T_{f,o} - T_{ref}) - (\dot{m}_{f,i} - \dot{m}_{f,o})L\}N_d(I,J)$
p	$\frac{\mu_{eff}}{\sigma_p}$	$(1+i)R_f$	0

Notes

1. All S_d^ϕ are source terms for computational cell (I,J) in the finite difference equations.
2. $G = \mu_{eff}\{2[(\frac{\partial \bar{u}}{\partial x})^2 + (\frac{\partial \bar{v}}{\partial r})^2 + (\frac{\bar{v}}{r})^2] + (\frac{\partial \bar{u}}{\partial r} + \frac{\partial \bar{v}}{\partial x})^2\}$
3. $\mu_{eff} = \mu + C_\mu \rho k^2/\varepsilon$
4. $C_1 = 1.44$, $C_2 = 1.92$, $C_\mu = .09$, $\sigma_h = 1.0$, $\sigma_k = 1.0$, $\sigma_\varepsilon = 1.22$, $\sigma_f = 1.0$, $\sigma_p = 1.0$

In calculating the droplet source terms, we employ the Particle-Source-In-Cell [6] method. When a droplet leaves a finite difference cell, the mass, momentum, and energy are compared to their values upon entering that cell; the difference in the entering and exiting values become droplet source terms for the Eulerian gas phase equations.

Combustion Model

The combustion model determines the fuel consumption rate (R_f) for each finite difference cell. As Table 1 shows, this rate produces a source (or sink) term in the energy, fuel mass fraction, and product mass fraction equations. The model assumes that the fuel and oxygen combine irreversibly in a single global reaction given by

$$C_\alpha H_\beta + (\alpha + \frac{\beta}{4})(O_2 + 3.76\, N_2) \rightarrow \alpha\, CO_2 + \frac{\beta}{2} H_2O + 3.76\,(\alpha + \frac{\beta}{4})\, N_2. \qquad (2)$$

The fuel consumption rate is then determined from the slower of either the mixing rate of the reactants or the chemical reaction rate.

We chose to use the eddy mixing model of Magnussen and Hjertager [7] because it requires only the evaluation of mean fuel and oxidizer concentrations; additional equations of concentration fluctuations (as required by the eddy breakup model [8], for example) need not be solved. With this model the fuel reaction rate per unit volume, as determined by the intermixing of the fuel and oxygen eddies, can be expressed using the mean mass fractions of the species. In regions in which the time mean fuel mass fraction is very low, the dissipation of the fuel eddies limits the combustion rate. Similarly, the dissipation of the oxygen eddies limits R_f in regions where the mass fraction of fuel is high and the oxygen mass fraction is low. Consequently, the mixing limited fuel reaction rate per unit volume ($kg/s/m^3$) is given by

$$R_{f,mix} = A_1 \rho \frac{\varepsilon}{k} \min\left(f, \frac{a}{i}\right) \qquad (3)$$

where ε/k has units of sec^{-1}, i is the stoichiometric air/fuel ratio, A_1 is an empirical constant set equal to 4, ρ is the mass weighted gas density (kg/m^3) of the fuel vapor, products, and air, and f and a are the fuel and air mass fractions, respectively.

The fuel consumption rate may also be controlled by chemical kinetics when the fuel and oxidizer mixing is rapid. An Arrhenius expression taken from [9] provides the chemical limited fuel reaction rate ($kg/m^3/s$) which is given by

$$R_{f,kin} = 1.73 \times 10^6 MW_f^{0.75} f^{0.25} a^{1.5} \rho^{1.75} \exp(-15115/T_g) \qquad (4)$$

where T_g is the gas temperature in K, MW_f is the molecular weight of the fuel (kg/kmole), and ρ, a and f are the same as in Eq (3).

Using equations (3) and (4), the fuel reaction rate is then determined from

$$R_f = \min(R_{f,mix}, R_{f,kin}). \qquad (5)$$

Droplet Model

The spray is followed by employing a discrete droplet model which represents the spray by a statistically meaningful number of individual droplets. Each of the computational droplets represents a parcel of droplets all having the same velocity, temperature, position, and size. A droplet's velocity is calculated by integrating Newton's second law

$$\vec{F}_D = m_d \frac{d\vec{u}_d}{dt} \qquad (6)$$

where $\vec{F}_D$ is the drag force on the droplet given by

$$\vec{F}_D = \frac{\pi}{8} C_D \rho_g |\vec{u}_g - \vec{u}_d| (\vec{u}_g - \vec{u}_d) D^2. \qquad (7)$$

The drag coefficient, C_D, is a function of the Reynolds number based on the relative drop velocity and the drop diameter. The specific values used are given by Dickerson and Schuman [10]. Once a new droplet velocity is found, the new droplet position is determined from integrating

$$\frac{d\vec{x}_d}{dt} = \vec{u}_d. \qquad (8)$$

As developed by Gosman and Ioannides [11] and discussed by Faeth [12], the turbulence effects on droplet motion are simulated stochastically by superimposing upon the gas field turbulent eddies, each having a length, lifetime, and u- and v-velocity fluctuations. As determined by the dissipation scale in the k-ε model, the length of each eddy is

$$L_e = C_\mu^{1/2} k^{3/2}/\varepsilon \qquad (9)$$

with its lifetime given by

$$t_e = \frac{L_e}{(2k/3)^{1/2}}. \qquad (10)$$

The droplet interacts with an eddy for a time taken to be the smaller of either t_e or the transit time, t_t, required for the droplet to traverse the eddy. Following Brown and Hutchinson [13], the transit time is determined from a linearized form of the droplet equation of motion and is given as

$$t_t = -\tau \ln\left(1 - \frac{L_e}{\tau\,|\vec{u}_g - \vec{u}_d|}\right) \tag{11}$$

where τ is the droplet relaxation time defined as

$$\tau = \frac{\frac{4}{3}\rho_f D}{\rho_g C_D |\vec{u}_g - \vec{u}_d|}. \tag{12}$$

When $L_e > \tau|\vec{u_g} - \vec{u_d}|$, equation (11) has no solution and the droplet is assumed to have been captured by the eddy.

To find the velocity fluctuations associated with each eddy, random numbers are generated by a Gaussian probability density function (PDF) centered about zero with a standard deviation of one. A fluctuating velocity component is then set equal to the product of the PDF random number and the actual standard deviation given by

$$\sigma = \left(\frac{2k}{3}\right)^{1/2} \tag{13}$$

where k is the interpolated value at the drop's current position. The u- and v-velocity fluctuation calculations for a particular eddy use two different PDF random numbers.

The droplet evaporation rate is given by

$$\dot{m}_{evap} = \frac{2\pi D k_g}{C_{pg}}(1 + 0.276\,Re_d^{1/2} Pr_g^{1/3}) \ln(1 + B_M) \tag{14}$$

which is the d^2 law expression with Frossling's [14] correction for forced convection. Re_d is the Reynolds number based on the relative velocity between the droplet and the gas. The gas thermal conductivity, k_g, and specific heat, $C_{p,g}$, are found by mass weighting the air and fuel vapor values. The values for these two quantities are highly dependent on the temperature and fuel vapor mass fraction at which they are evaluated. Chin and Lefebvre [15] recommended using Sparrow's "1/3 rule" [16] which employs a reference temperature equal to the droplet surface temperature plus 1/3 of the difference between the surrounding gas and droplet surface temperature. A reference value for the fuel vapor mass fraction is found similarly. The droplet temperature, which is assumed to be spatially constant within the droplet, is found by integrating the following

$$\frac{dT_d}{dt} = \frac{\dot{m}_{evap} L}{C_{p,f} m_d}\left(\frac{B_T}{B_M} - 1\right). \tag{15}$$

B_T and B_M are the thermal and mass transfer numbers, respectively, given as

$$B_T = \frac{C_{p,g}(T_g - T_d)}{L} \tag{16}$$

and

$$B_M = \frac{f_s - f_g}{1 - f_s}. \tag{17}$$

Note that in order to determine f_s, the mass fraction of fuel at the surface, relations of vapor pressure as a function of temperature were developed for the fuels of interest from data presented in [17]. Also a single boiling point is used which implies that the constituents in the droplet do not change as evaporation occurs. Thus distillation curve effects have been neglected.

Finally, the droplet diameter can be found by integrating

$$\frac{dD}{dt} = \frac{-4 k_g}{\rho_f C_{p,g} D}(1 + 0.276\,Re_d^{1/2} Pr_g^{1/3}) \ln(1 + B_M). \tag{18}$$

Computational Mesh and Boundary Conditions

The geometry under consideration has already been described and is shown in Fig. 1. The finite difference mesh starts at the atomizer exit plane and extends 1.5 m axially with 32 cells and 13.5 cm radially with 35 cells. The axial dimensions of the cells were uniform (1.7 cm) up to 1.5 tunnel diameters downstream at which point they continually expanded in the axial direction. In the radial direction, 5 cells were placed in the center jet and then the radial dimensions of the cells were uniform (0.4 cm) up to 0.33 tunnel diameters at which point they expanded in the radial direction. (The results are considered to be independent of the grid configuration since similar results were obtained with other grid configurations with reduced resolution.)

At the tunnel's wall, a no-slip condition is imposed which requires that the turbulent kinetic energy and the u- and v-velocites be set to zero. The wall temperatures are approximated from measurements presented by Yule and Bolado [4]. Along the tunnel's centerline, the radial gradients of all variables are zero. For the secondary air flow between the stabilization disk and the wall, the inlet

u- and v-velocity are 2 m/s and 0 m/s, respectively, and the inlet k and ε are determined by assuming a turbulence intensity of 1.5 percent and a turbulence length scale equal to 3 percent of the tunnel's diameter. The u- and v-velocity of the primary air flow from the atomizer are 21.4 m/s and 0.374 m/s, respectively. This provides a trajectory half angle of 1°. For this primary flow region, k and ε are determined as stated above except that the turbulence length scale is set equal to 3 percent of the orifice diameter. Between the radial distances of 0.5 cm and 3.75 cm, the stabilization disk is modeled with a no-slip wall condition. The temperature of the primary and secondary air flow as well as the stabilization disk wall are set to 383 K. Finally, at the computational outlet, a fully developed profile is assumed by imposing a zero v-velocity along with a zero axial derivative for the remaining variables.

Droplet Initial Conditions

A Rosin-Rammler (RR) distribution is assumed for the inlet droplet sizes so that

$$\text{volume \% of droplets larger than diameter } D = 100 \exp[-(D/\bar{D})^N]. \tag{19}$$

For a given RR distribution, the spray is divided into 20 size classes with each class representing 5 % of the fuel on a mass basis. Twenty droplet parcels for each size class are fired into the flowfield. (The results are considered independent of the number of droplet parcels since 50 parcels for each size class were injected for one test run with no noticeable difference in the results between the 50 and 20 parcel runs.) The total fuel flow rate is constant at 3.14×10^{-4} kg/s which gives an overall equivalence ratio is 0.29 and an equivalence ratio for the inner jet of 18.8.

Each droplet parcel has the same initial temperature of 383 K. The initial u- and v-velocity for each droplet parcel is arbitrarily chosen from a Gaussian distribution with a mean drop velocity equal to that of the center jet air velocity given above and a standard deviation given by Eq. (13). As a result, every droplet parcel for all of the sets will have different u- and v- initial velocities though the velocity distribution used is the same for each parcel.

After injecting droplets into the gas phase, the droplet source terms of mass, momentum, and energy are used to obtain a new converged gas phase solution. Droplets are then injected into this new gas phase solution, thus producing new source terms and a subsequent new gas phase solution. This iterative procedure is repeated until the results converge.

FUEL PROPERTIES AND TEST CASES

As discussed in the introduction, the purpose of this paper is to consider the effect of potential alternative fuels on spray flame structure. With this goal in mind, fuel properties were selected to range from those for a conventional fuel (NATO F-40), to a likely alternative fuel (AGARD Research Fuel) and to a heavy fuel oil. Some key fuel properties for these fuels are shown in Table 2. Note that the SMD values were determined by arbitrarily choosing 40 μm for the NATO fuel and then calculating the SMD for the other two fuels by using the following empirical equation from Lefebvre [18] for pressure swirl atomizers.

$$SMD_2 = SMD_1 \left(\frac{\sigma_2}{\sigma_1}\right)^{0.25} \left[\frac{(v_f \rho_f)_2}{(v_f \rho_f)_1}\right]^{0.20} \tag{20}$$

Within the fuel property constraints of Table 2, specific test cases were designed to determine the effect of three key variables on the spray flame structure. These variables were the mean drop size, the drop size distribution width and the fuel volatility; their values for all the cases are indicated in Table 3. The base case corresponds to the NATO F-40 fuel. Cases 2 and 3 isolate the effects of the mean drop size changes for the fuels and cases 4 and 5 address the boiling point changes. Case 8 considers the combined effects of all the fuel properties in changing from the NATO F-40 fuel to the AGARD Research Fuel. Finally, cases 6 and 7 were included to examine the effects of the drop size distribution on the spray with the mean drop size held constant.

Table 2. Fuel properties.

Property	NATO F-40	ARF[a]	Heavy Fuel Oil
Viscosity[b], cs	0.89	3.0	11.0
Surface Tension[b], dyn/cm	21.4	24.3	25.2
Density[b], kg/m^3	756.	838.	862.
Mean Boiling Point[c], K	373.	473.	573.
Sauter Mean Diameter, μm	40.	55.	70.

[a]AGARD Research Fuel
[b]evaluated at 25 °C
[c]temperature at which the vapor pressure is 0.1 MPa

Table 3. Description of computational cases.

Case	Description	Fuel	SMD (μm)	$(\bar{D},N)$ (μm)	T_b (K)
1	Base Case	F-40	40	(71.2)	373
2	Drop Size Variation	"	55	(97.5,2)	"
3	Drop Size Variation	"	70	(124.2)	"
4	Boiling Point Variation	"	"	"	473
5	Boiling Point Variation	"	"	"	573
6	Monodisperse	"	"	(40,∞)	"
7	Wide Distribution	"	"	(107.1.5)	"
8	Fuel Variation	ARF	55	(97.5,2)	473

[a]same as base case

RESULTS AND DISCUSSION

Fuel Property Effects

The general structure of the spray flames to be discussed here are illustrated in Fig. 2 which shows droplet trajectories, isotherms and gas phase equivalence ratio profiles for the base case. The mixture ignites rapidly (within 0.1 diameters downstream of the injector) as shown by the high temperatures near the injection point and the reaction region spreads as the mixture proceeds downstream. The droplet trajectories show the dispersion of the droplets due both to the random nature of their inlet velocities and the influence of the turbulent velocity fluctuations. Note that all the droplets evaporate within 2 diameters downstream in an extremely fuel rich environment. Thus, the flame structure is similar to a gaseous jet diffusion flame in that the mixing of the fuel and oxidizer is limited by the gas phase behavior rather than the droplet evaporation rates. We now wish to examine the spray flame structure as the fuel spray properties are changed as discussed in the previous section.

The effects of the increase of the mean drop size (due to increased viscosity and surface tension of the fuels) on the spray flame are indicated in Figs. 3 - 5. Fig. 3 illustrates the change in droplet trajectories as the mean drop size is changed. As expected, the increase in droplet lifetime for the larger drops of cases 2 and 3 can be seen from the longer trajectories for those cases. However, even

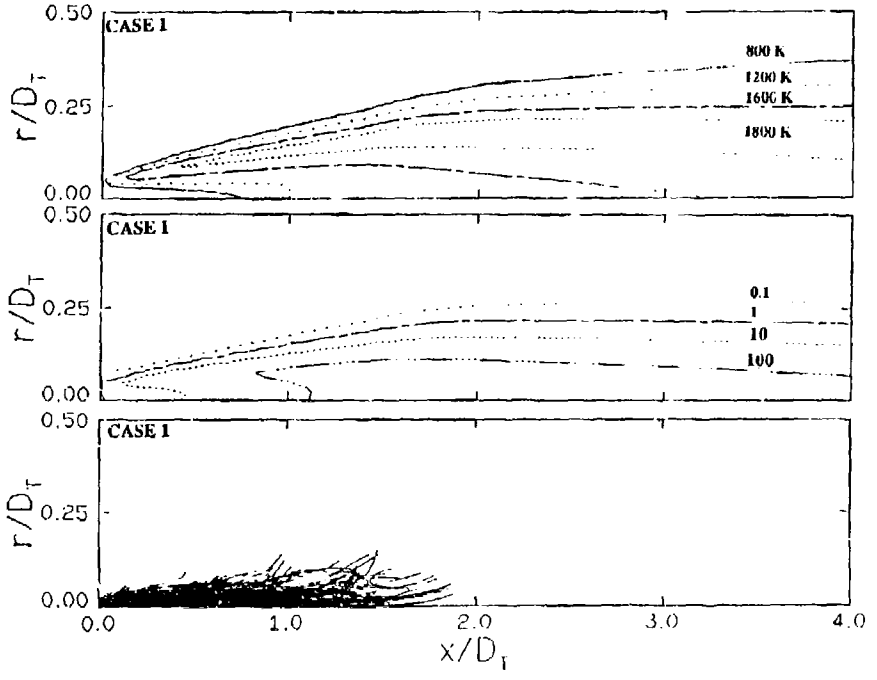

Figure 2. Flame structure in terms of droplet trajectories and temperature and equivalence ratio profiles for Case No. 1.

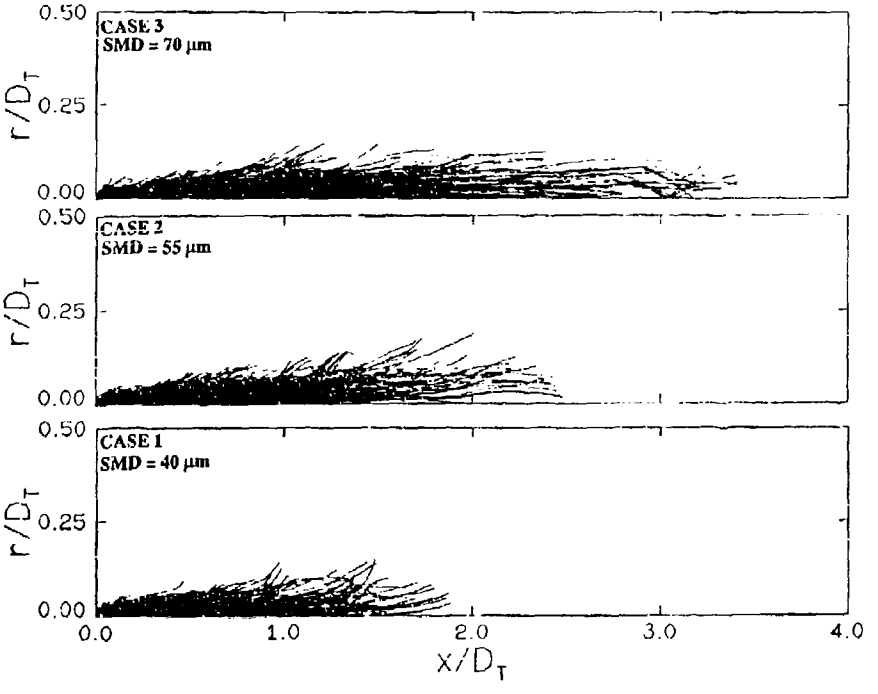

Figure 3. The effect of initial drop size on droplet trajectories.

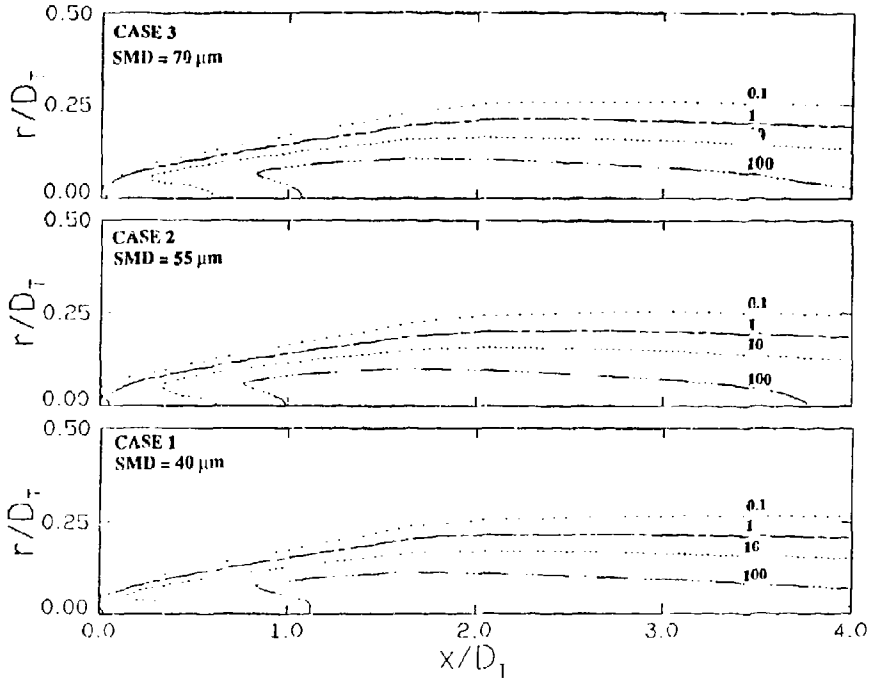

Figure 4. The effect of initial drop size on equivalence ratio profiles.

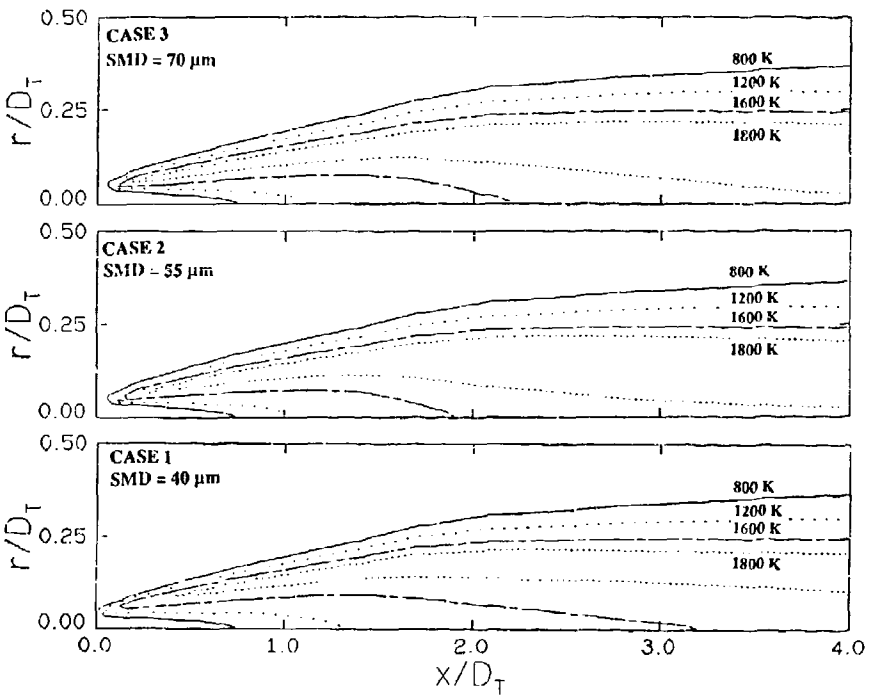

Figure 5. The effect of initial drop size on temperature profiles.

though the trajectories of case 3 are nearly twice as long as those of case 1, this does not drastically change either the temperature or equivalence ratio profiles as shown in Figs. 4 and 5. The ignition point does move slightly downstream for cases 2 and 3 and the temperature is somewhat cooler at the centerline for case 1. Both of these effects are due to the reduced evaporation rate for the larger droplets but, in general, the flame structure is still very similar for all three cases. Again this indicates that droplet evaporation is rapid enough so that the energy release is limited by gas phase phenomena rather than droplet effects even for the largest drop sizes. This is further illustrated in Fig. 6 where the cumulative percent of mass evaporated is plotted versus axial distance for cases 1, 2 and 3. The similarities of these curves, where in all three cases over 70 % of the fuel is evaporated by one diameter downstream, indicates that the large differences in the droplet trajectory curves can be somewhat misleading.

The effects of the variation of boiling point on the spray flame are shown in Figs. 7 - 9. The droplet trajectories are very similar with only a slight increase as the boiling point increases by 200 K. As indicated in Fig. 8, the equivalence ratio profiles beyond one diameter downstream are similar but within 0.5 diameters downstream of the injector the region near the centerline is much leaner for case 5 as compared to case 1 due to the slower evaporation rate of case 5. This difference is also evident in Fig. 9 where the ignition point moves downstream for the higher boiling point but the downstream temperatures for the three cases are similar (somewhat cooler at the centerline for case 1 as previously mentioned). Although the initial region where the temperature and equivalence ratios vary significantly from case 1 to case 5 is small, it becomes more important when one considers Fig. 10. Note, for example, that for case 5

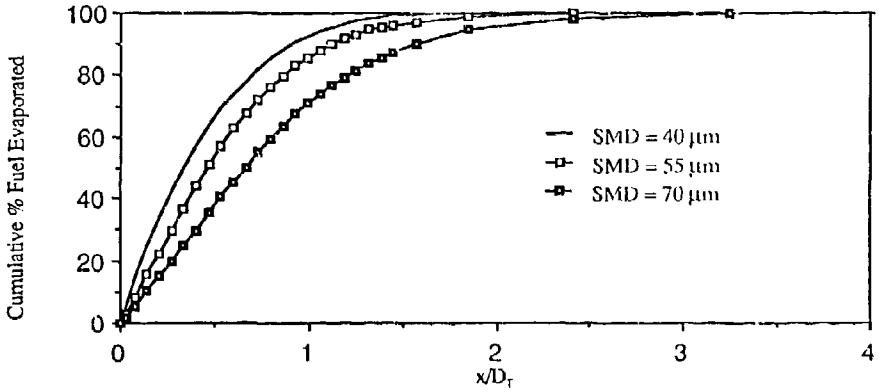

Figure 6. The effect of initial drop size on percent of fuel evaporated.

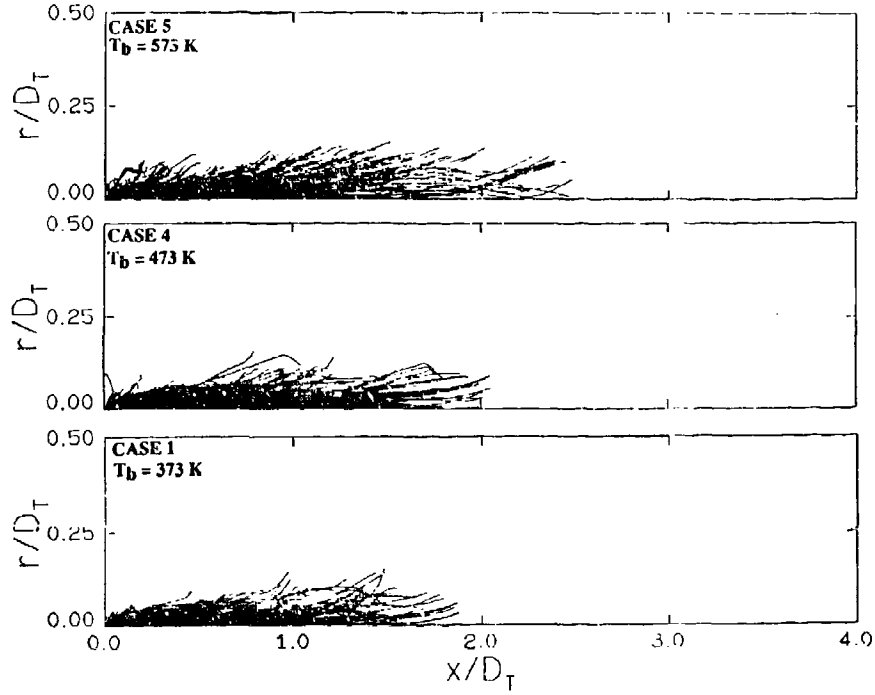

Figure 7. The effect of boiling point on droplet trajectories.

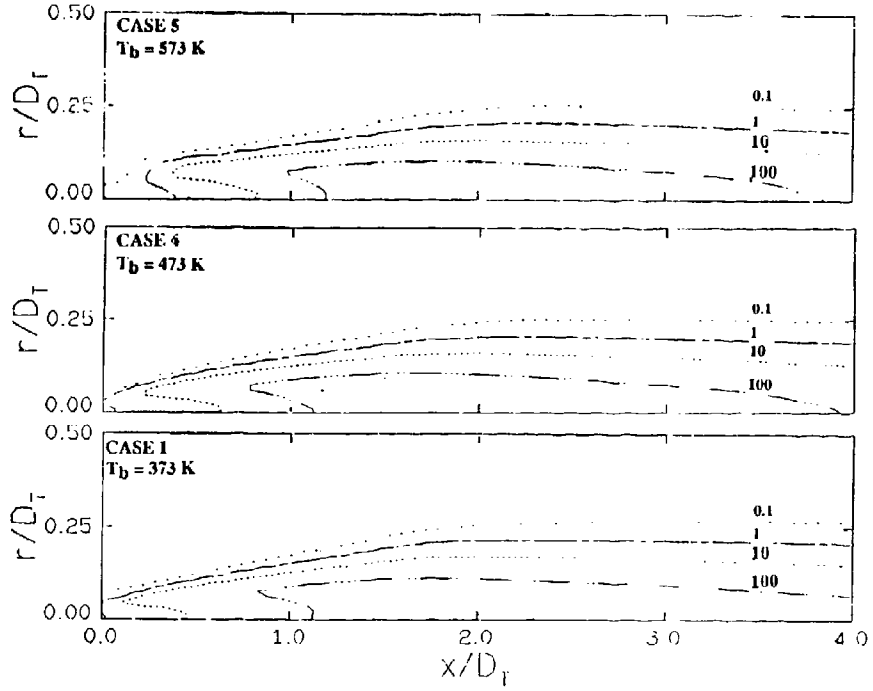

Figure 8. The effect of boiling point on equivalence ratio profiles.

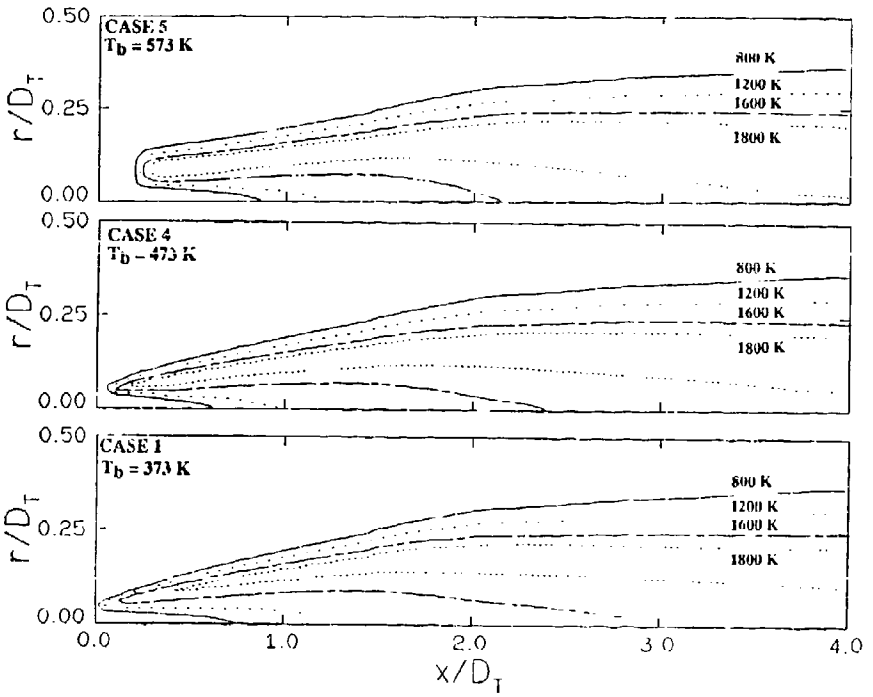

Figure 9. The effect of boiling point on temperature profiles

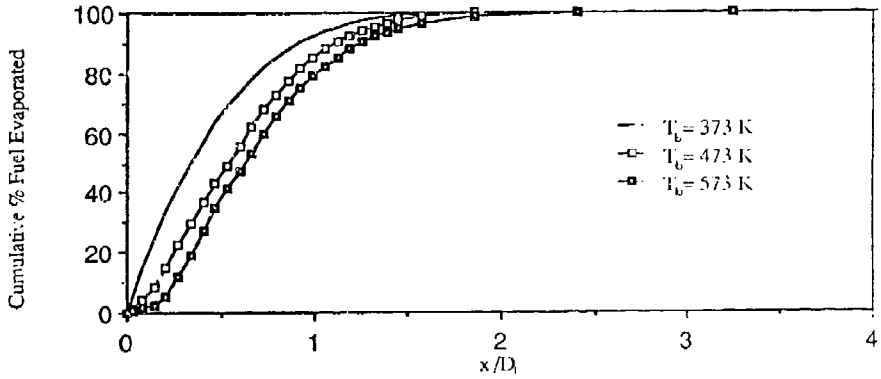

Figure 10. The effect of boiling point on percent of fuel evaporated.

nearly 40 % of the fuel is evaporated prior to 0.5 diameters downstream. Thus, a significant fraction of the evaporation occurs in a fuel lean, rather than rich, gas phase environment.

The combined effects of boiling point, drop size and other fuel property variations are shown in Figs. 11 - 13 for a comparison of the AGARD Research Fuel and the NATO F - 40 fuel. These figures show trends similar to those already discussed where the larger drop size results in longer droplet trajectories for the AGARD Research Fuel. In addition, the higher boiling point delays evaporation rate so that the ignition point is further downstream and the initial phases of evaporation occur under much leaner conditions for the AGARD Research Fuel.

Additional Considerations

In addition to considering the effect of fuel property variations on the spray flame structure, some additional cases were examined to investigate the effects of drop size distribution width (cases 6 and 7 in Table 3), the effects of the turbulent eddies and the effects of droplet collisions on the results.

Figures 14 and 15 show the effects of drop size distribution on the spray flame. First, note that for the monodisperse case the droplet trajectories are extremely short in comparison to the other two cases. This is due to the fact that there are no large droplets present in the monodisperse case to extend the droplet trajectories. Figure 15 indicates that similar amounts of fuel are evaporated in the initial regions of the flowfield so that the temperature and equivalence ratio profiles (not shown here due to space limitations) in the upstream region are virtually identical. One might expect that the monodisperse case would have limited evaporation in the initial region of the flow because of the lack of small droplets. However, this is evidently compensated by the lack of large droplets which would otherwise carry significant fractions of the fuel downstream. In the downstream region, the drops in all three cases are evaporating (or have evaporated) in a very fuel rich region so that the gas phase phenomena are again controlling and the temperature (and equivalence ratio) profiles are similar for all three cases.

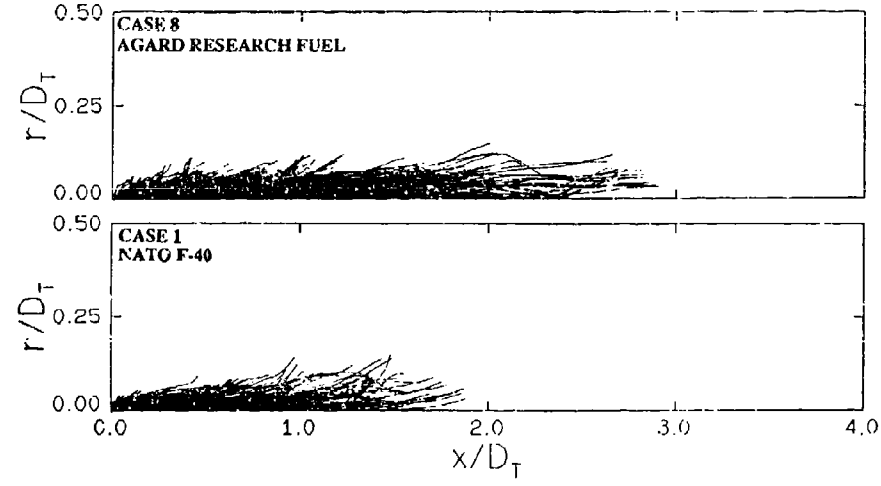

Figure 11. The effect of fuel type on droplet trajectories.

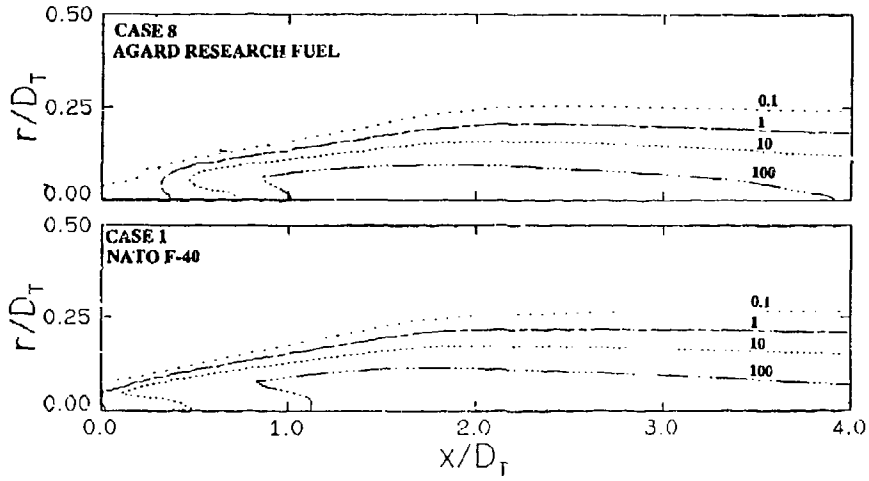

Figure 12. The effect of fuel type on equivalence ratio profiles.

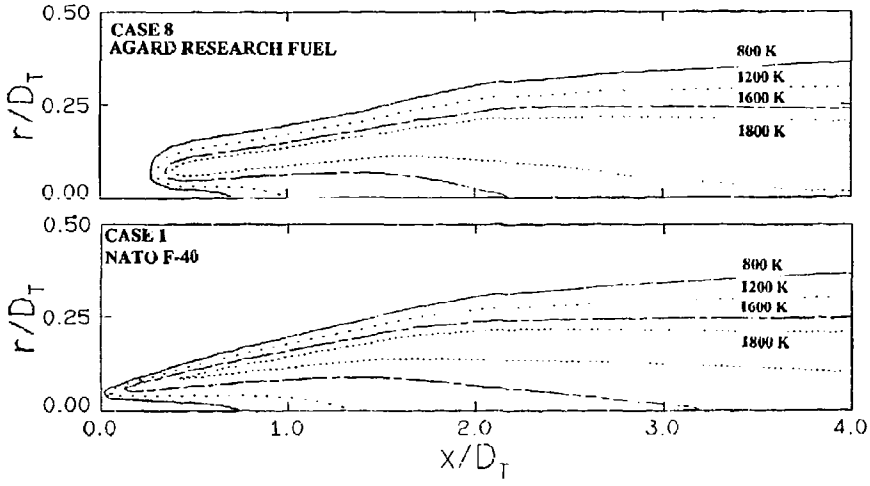

Figure 13. The effect of fuel type on temperatures.

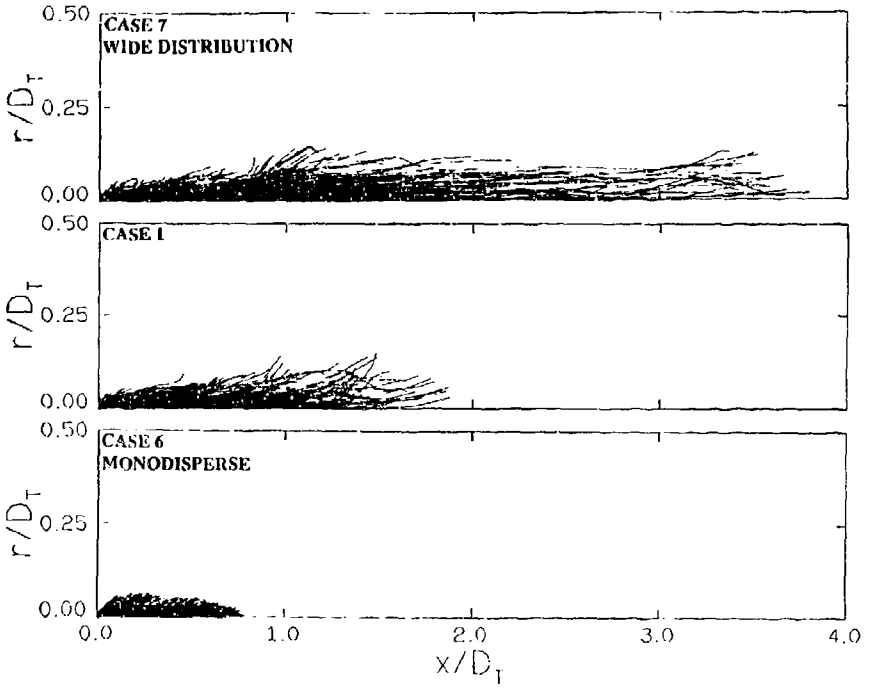

Figure 14. The effect of drop size distribution on droplet trajectories.

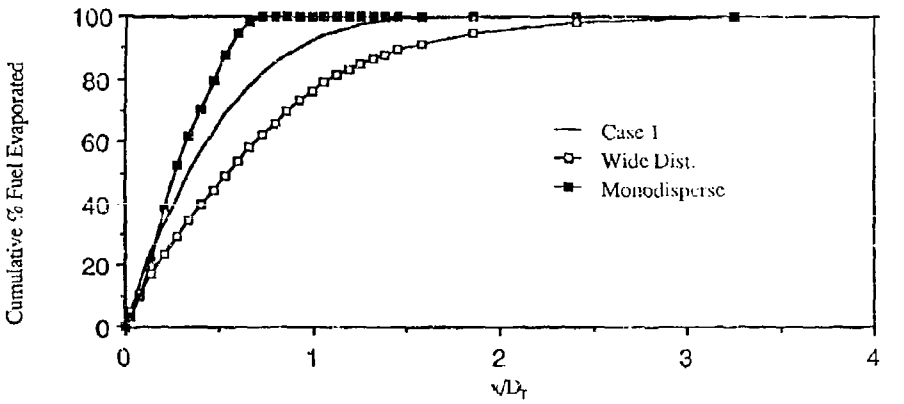

Figure 15. The effect of drop size distribution on percent of fuel evaporated.

Finally, Figs. 16 and 17 are included to show the effects of the turbulent eddies and droplet collisions, respectively. In Fig. 16 the turbulent eddies are shown to promote the spreading of the liquid droplets. However, they do not have a significant effect for this flowfield on the overall evaporation rate of the spray so that the flame structures in terms of temperature and equivalence ratio profiles (not shown) are virtually identical.

The effects of doplet collisions were briefly examined with the model developed by Bracco and O'Rourke [19] and as used by Asheim et al. [20]. This model employs a Poisson probability distribution in determining whether two or more droplets have collided with the result of a collision being coalescence or breakup. Because of the small number density (approximately 20,000 per cm^3) of the droplets leaving the injector only a small percentage (5 to 10 %) of the droplets collide. Over 90% of the collisions involve one drop with a diameter less than 40 μm and one drop with a diameter greater than 100 μm and 95% of these collisions result in coalescence. For these large size differences, most of the fuel mass is contained in the large drop and the combined drop diameter is only a few percent larger than the original large drop. Therefore, these infrequent collisions do not radically alter the drop size distribution. Consequently, Fig. 17 shows little change in the droplet trajectories with only a few increased trajectory lengths due to the collision effects. This small change in trajectories resulted in no differences in the temperature or equivalence ratio profiles of the two flames.

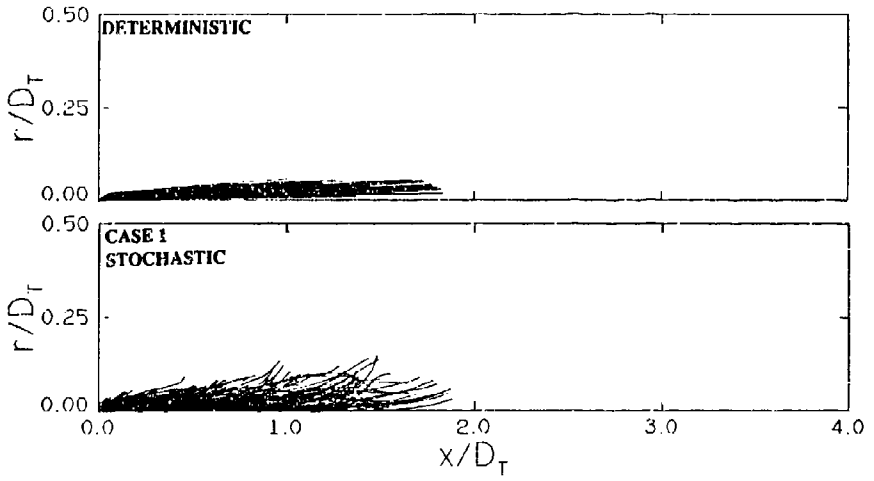

Figure 16. Comparison of stochastic and deterministic droplet trajectories.

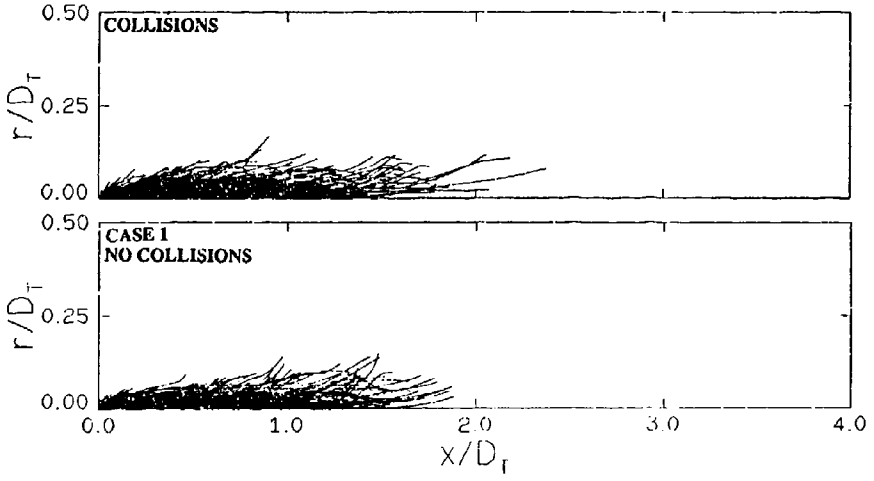

Figure 17. The effect of droplet collisions on droplet trajectories.

CONCLUSIONS

In general, fuel property changes which influence drop size and volatility were shown to have significant effects on the droplet trajectory patterns. However, for the flowfield examined in this paper these trajectory changes only moderately modified the fuel vaporization pattern within the spray. In addition, the majority of the fuel was always vaporized in an extremely fuel rich environment so that the energy release was (throughout most of the flowfield) controlled by the gas phase phenomena of mixing and chemical kinetics. The exception to this was the location of the ignition point which was shown to move downstream with reduced evaporation rates associated with higher fuel boiling points.

Other parameters investigated included size distribution effects, turbulent eddy effects and droplet collisions. Increasing the width of the inlet droplet size distribution significantly increased the droplet trajectories due to the presence of large drops in the spray but did not affect the overall structure of the spray since all the droplets still evaporated in highly fuel rich regions. Turbulent dispersion of the droplets and droplet collisions were shown to have little effect on the spray flame.

The conclusions noted above and the results reported in the paper should be remembered to be limited to the particular spray flame considered, one in which the fuel spray core is very rich with relatively slow mixing of the air with the fuel. In other situations, with relatively lean spray interiors and rapid intermixing of air, changes in droplet trajectories could have a more pronounced influence on the flame structure with the possibility of transition from gaseous diffusion flame behavior to some individual droplet burning. Along these lines, further work could address the effect of varying the same fuel properties in a different flowfield with leaner interior spray conditions plus a more detailed look at the effects of other important variables such as boiling point distributions of the fuels.

REFERENCES

1. Peters, J. E., "Current Gas Turbine Combustion and Fuels Research and Development," ASME Paper No. 87-GT-107, 1987.

2. Reeves, C. M., and Lefebvre, A. H., "Fuel Effects on Aircraft Combustor Emissions," ASME Paper No. 86-GT-212, 1986.

3. Mellor, A. M., "Semi-Empirical Correlations for Gas Turbine Emissions, Ignition, and Flame Stabilization," Progress in Energy and Combustion Science, Vol. 6, No. 4, 1981, pp. 347 - 358.

4. Yule, A. J., and Bolado, R., "Fuel Spray Burning Regime and Initial Conditions," Combustion and Flame, Vol. 55, No. 1, 1984, pp. 1-12.

5. Gosman, A. D., and Ideriah, F. T. K., "TEACH-2E: A General Computer Program for Two-Dimensional, Turbulent, Recirculating Flows," Imperial College, London, England, Mechanical Engineering Report (unnumbered), June, 1976.

6. Crowe, C. T., Sharma, M. P., and Stock, D. E., "The Particle-Source-In-Cell (PSI-CELL) Model for Gas-Droplet Flows," Journal of Fluids Engineering, Vol. 99, No. 2, 1977, pp. 325-332.

7. Magnussen, B. F., and Hjertager, B. H., "On Mathematical Modeling of Turbulent Combustion with Special Emphasis on Soot Formation and Combustion," Sixteenth Symposium (International) on Combustion, The Combustion Institute, Pittsburgh, 1976, pp. 719-729.

8. Spalding, D. B., "Development of the Eddy-Break-Up Model of Turbulent Combustion," Sixteenth Symposium (International) on Combustion, The Combustion Institute, Pittsburgh, 1976, pp. 1657-1663.

9. Westbrook, C. K., and Dryer, F. L., "Chemical Kinetic Modeling of Hydrocarbon Combustion," Progress in Energy and Combustion Science, Vol. 10, No. 1, 1984, pp. 1-58.

10. Dickerson, R. A., and Schuman, M. D., "Rate of Aerodynamic Atomization of Droplets," J. Spacecraft and Rockets, Vol. 2, No. 1, 1965, pp. 99-100.

11. Gosman, A. D., and Ioannides, E., "Aspects of Computer Simulation of Liquid-Fuelled Combustors," AIAA Paper No. 81-0323, 1981.

12. Faeth, G. M., "Evaporation and Combustion of Sprays," Progress in Energy and Combustion Science, Vol. 9, No. 1, 1983, pp. 1-76.

13. Brown, D. J., and Hutchinson, P., "The Interaction of Solid or Liquid Particles and Turbulent Fluid Flow Fields - A Numerical Solution," Journal of Fluids Engineering, Vol. 101, No. 2, 1979, pp. 265-269.

14. Frossling, "On the Evaporation of Falling Drops," Gerlands Beitrage Zur Geophysik, Vol. 52, 1938, pp. 170-216.

15. Chin, J. S., and Lefebvre, A. H., "The Role of the Heat-up Period in Fuel Drop Evaporation," AIAA Paper No. 83-0068, 1983.

16. Sparrow, E. M., and J. L. Gregg, "The Variable Fluid-Property Problem in Free Convection," ASME Trans., Vol. 80, 1958, pp. 879-886.

17. Coordinating Research Council, "Handbook of Aviation Fuel Properties," CRC Report No. 530, 1983.

18. Lefebvre, A. H., "Influence of Fuel Properties on Gas Turbine Combustion Performance," Report No. AFWAL - TR - 84 - 2104, 1985.

19. O'Rourke, P. J., and Bracco, F. V., "Modeling of Drop Interactions in Thick Sprays and a Comparison with Experiments," Stratified Charge Automotive Engineering Conference, The Institute of Mechanical Engineering, London, 1980.

20. Asheim, J. P., Kirwan, J. E., and Peters, J. E., "Modeling of a Hollow-Cone Liquid Spray Including Droplet Collisions," AIAA Paper No. 87-0135, 1987.

DISCUSSION

B.Noll, GE

Which convergence criterion did you use to stop the iterative procedure which accounts for droplet/gas phase interaction?

Author's Reply

We iterated between the liquid and gas phases until the results changed by less than one percent for all variables. In many cases, most of the variables were converged to within a much smaller tolerance than one percent.

A.M.Mellor, US

Why is there so little calculated effect of turbulent dispersion? Were gas-phase radial turbulent intensities reported for the experiment? If not, what values were assumed for the calculations shown?

Author's Reply

The effect of turbulent dispersion is small because even with dispersion of the droplets, they all evaporate in a fuel rich core so that the gas phase phenomena still control most of the spray flame structure.

No radial turbulent intensities were reported in the original experimental work so we assumed a turbulence intensity of 1.5% as noted in the paper.

A.Williams, UK

The properties attributed to the heavy fuel oil do not allow for the presence of high boiling point components which are present in real heavy fuel oils, therefore the computed burning rates will be faster than the real case. Has any comparison been made with experimental results to check the accuracy of the prediction?

Author's Reply

The results presented in the paper are based on the assumption of a *single* boiling point for the fuel. The boiling point temperature that was used is the temperature for which the vapour pressure of the fuel is one atmosphere. If, in actuality, the evaporation process is better approximated with a distillation type of evaporation behaviour, then the initial evaporation rate is actually *under* predicted by the model and the final evaporation rate is overpredicted.

We have not yet compared our calculations with experimental results but we plan to do so. Also we plan to look at the effects of distillation curve behaviour on the results by relaxing the assumption of a single boiling point temperature and using distillation curve data.

A.Lefebvre, US

To what extent are your results and conclusions influenced by your assumptions of a Rosin-Rammler drop-size distribution parameter?

Author's Reply

The use of some other appropriate drop-size distribution function (such as an upper limit distribution function, for example) would not change our results or conclusions. This is due to the fact that for this particular flow field the structure of the spray flame is primarily controlled by the gas phase phenomena. In other spray flame situations, where droplet effects are more pronounced, the form of the drop-size might be important. This could be determined by comparing computed spray flame structures for different assumed drop-size distribution forms.

A.Ormancey, FR

A propos de votre modèle stochastique de dispersion des gouttelettes, vous utilisez une densité de probabilité gaussienne pour déterminer les valeurs des fluctuations de vitesse de l'écoulement vues par les gouttelettes. Est-ce une hypothèse fondée et valable lorsque les gouttelettes se trouvent:

1. Près de l'injecteur?
2. Près des parois?

Author's Reply

We have only worked with a Gaussian probability density function for velocity fluctuation calculations and cannot comment on the applicability of other forms of PDFs for this part of the model.

C.Moses, US

Do all the droplets initially have the same velocity or is there a distribution of velocities correlated to the sizes?

Author's Reply

All the droplet parcels have the same initial *mean* velocity but each individual drop has its own velocity which is the sum of the mean velocity and a fluctuating component which is randomly selected as discussed in the paper. We recognize that for many injection processes there is a correlation between drop sizes and velocity (in many cases, large drops have large velocities) but for this particular injector we have no such evidence and believe that using the same initial mean velocity for all drop-sizes is appropriate for this injector.

ATOMIZATION OF ALTERNATIVE FUELS

by
Arthur H. Lefebvre
Reilly Professor of Combustion Engineering
School of Mechanical Engineering
Purdue University, West Lafayette, IN 47907, USA

SUMMARY

The influence of atomisation quality on several key aspects of combustion performance is reviewed. The performance parameters considered include combustion efficiency, lean blowout, and lean lightup, and also the pollutant emissions of carbon monoxide, unburned hydrocarbons, oxides of nitrogen, and smoke. The fuel properties of importance are described and equations are presented for estimating the effects of changes in fuel properties on spray characteristics for the main types of fuel nozzle employed in aero gas turbines, namely plain orifice, pressure-swirl, and airblast atomizers. The anticipated effects on atomisation of changes from conventional to alternative fuels is discussed.

LIST OF SYMBOLS

A_p	total inlet ports area, m^2
AFR	air/fuel mass ratio
D_o	Sauter mean diameter, m
D_h	hydraulic mean diameter of air exit duct, m
D_p	prefilmer diameter, m
D_s	swirl chamber diameter, m
d_o	discharge orifice diameter, m
f	fraction of total combustor airflow
FN	flow number $\dot{m}_L/(\Delta P_L/\rho_L)^{0.5}$, m^2
LCV	lower calorific value of fuel, J/kg
L_c	characteristic dimension of airblast atomizer, m
L_s	length of swirl chamber, m
MMD	mass median diameter, m
$\dot{m}$	flow rate, kg/s
P	pressure, Pa
ΔP_F	injection pressure differential across nozzle, Pa
ΔP_L	liner pressure drop, Pa
Q	volumetric flow rate, m^3/s
q_{LBO}	fuel/air ratio at lean blowout, g fuel/kg air
q_{LLO}	fuel/air ratio at lean lightup, g fuel/kg air
Re_F	Reynolds number based on fuel properties $(U_F \rho_F d_o/\mu_F)$
SMD	Sauter mean diameter, m
T	temperature, K
U	velocity, m/s
V	volume, m^3
We_F	Weber number based on fuel properties $(\rho_F U_F^2 d_o/\sigma)$
ρ	density, kg/m^3
λ_{eff}	effective value of evaporation constant, m^2/s
μ	dynamic viscosity, kg/ms
ν	kinematic viscosity, m^2/s
σ	surface tension, kg/s_2

Subscripts

A	air
F	fuel
L	liquid
R	air relative to liquid
c	combustion zone
pz	primary zone
3	combustor entry conditions

INTRODUCTION

Until comparatively recently an abundance of mid-distillates from petroleum has been made available for jet fuel. Future demand for jet fuel is expected to increase at a time when there is severe competition for the available mid-

distillates. The measures now being taken to ensure future supplies of fuels for aero gas turbines include the exploitation of alternative fuel sources and the acceptance of a broader specification for aviation fuels. Compared to present specification jet fuels, future jet fuels may exhibit any combination of the following property changes: higher freezing point, higher aromatic content, lower hydrogen content, lower volatility, higher viscosity, and poorer thermal stability [1-3].

In the late 1970's the USAF, Army, Navy and NASA, along with engine manufacturers, initiated programs to determine the effects of anticipated future fuels on existing engines [4-8]. As a result of these studies, data became available that yielded new and useful insights into fuel property effects on combustion performance. The fuels employed ranged from aviation gasoline (JP4) thru diesel oil (DF2) and were chosen to achieve a range of hydrogen content from 14 to 12 percent by mass.

The rationale for the diesel fuel was to approximate the Experimental Referee Broad Specification (ERBS) aviation fuel that emanated from the NASA-Lewis Workshop on Jet Aircraft Hydrocarbon Fuel Technology [9]. The JP4, JP8 fuels, and their blends were chosen to span systematically the possible fuel variations in key properties that might be dictated in the future on grounds of availability and cost, and the use of non-petroleum sources for jet fuel production.

The experimental data acquired in these programs provided much useful information on the influence of fuel chemistry on many important aspects of combustion performance. Analysis of these data [10-14] also highlighted the significance of fuel viscosity and surface tension which affect both the atomization quality and the cone angle of the fuel spray. Equations were derived from which quantitative assessments could be made of the impact of any change in atomization quality on combustion performance and pollutant emissions. The main results of this analytical study are summarized below.

COMBUSTION PERFORMANCE

The three main facets of combustion performance are combustion efficiency, lean blowout li nits, and lean lightoff limits.

Combustion Efficiency

This is expressed as the product of the reaction rate efficiency η_ℓ and the evaporation rate efficiency η_e, i.e.

$$\eta_c = \eta_\ell \times \eta_e \tag{1}$$

where
$$\eta_{c\ell} = 1 - \exp\left[\frac{-0.022 P_3^{1.3} V_c \exp(T_c/400)}{f_c \dot{m}_A}\right] \tag{2}$$

and
$$\eta_{ce} = 1 - \exp\left[\frac{-38 P_3 V_c \lambda_{eff}}{T_c D_o^2 f_c \dot{m}_A}\right] \tag{3}$$

Comparison of measured and predicted values of combustion efficiency for the TF33 combustor are shown in Fig. 1.

Lean Blowout

An expression for the fuel/air ratio at lean blowout was derived as

$$q_{LBO} = A\left[\frac{f_{ps}}{V_{ps}}\right]\left[\frac{\dot{m}_A}{P_3^{1.3}\exp(T_3/300)}\right]\left[\frac{D_o^2}{\lambda_{eff} LCV}\right] \tag{4}$$

The first term on the right-hand side of the foregoing expression is a function of combustor design. The second term represents the combustor operating conditions. The third term embodies the relevant fuel-dependent properties. The value of the constant A depends on the geometry and mixing characteristics of the combustion zone and must be arrived at experimentally.

The correlation of lean blowout limits provided by Eq. (4) for an F101 combustor, using a value for A of 0.54, is shown in Fig. 2.

Ignition

The minimum fuel/air needed for ignition can also be expressed in terms of combustor dimensions, combustor operating conditions, fuel properties, and mean fuel drop size. An appropriate equation is the following:

$$q_{LLO} = B\left[\frac{f_{ps}}{V_{ps}}\right]\left[\frac{\dot{m}_A}{P_3^{1.5}\exp(T_3/300)}\right]\left[\frac{D_o^2}{\lambda_{eff} LCV}\right] \tag{5}$$

This equation is almost identical to Eq. (4), except for a higher pressure dependence: $P_3^{1.5}$ versus $P_3^{1.3}$. The correlation of data obtained with Eq. (5) for an F100 combustor using a value for B of 0.70, is illustrated in Fig. 3.

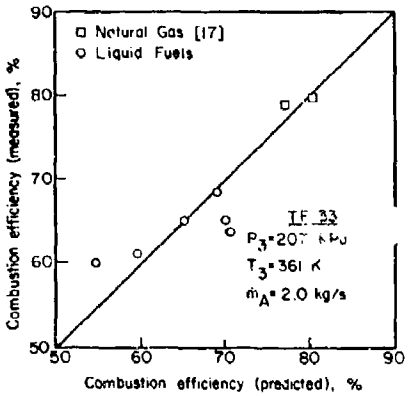

Fig. 1 Comparison of measured and predicted values of combustion efficiency for the TF 33 combustor.

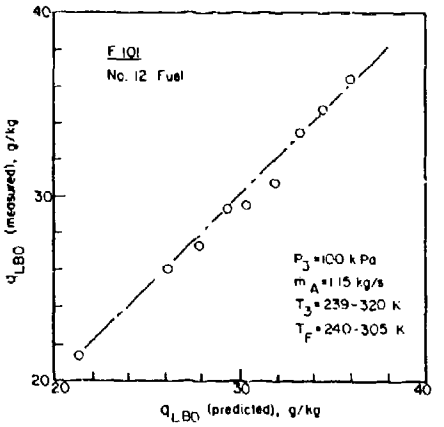

Fig. 2 Comparison of measured and predicted values of lean blowout limits for the F101 combustion.

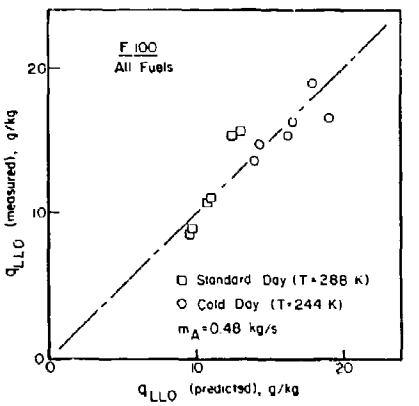

Fig. 3 Comparison of measured and predicted values of lean lightup limits for the F100 combustor.

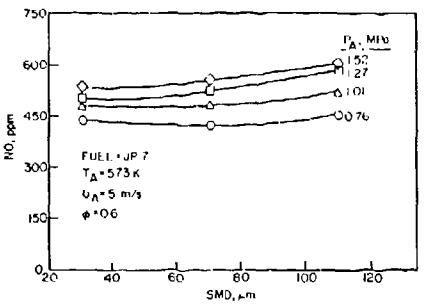

Fig. 4 Influence of mean drop size on NO emissions [19].

Other examples that demonstrate the ability of Eqs. (1), (4) and (5) to predict combustion efficiencies, lean blowout limits, and lean lightoff limits, respectively, for a wide range of aircraft combustors, are contained in references 11 and 14.

POLLUTANT EMISSIONS

The pollutant emissions of most concern for the aircraft gas turbine are oxides of nitrogen (NO_x), carbon monoxide (CO), unburned hydrocarbons (UHC), and smoke. The concentration levels of these pollutants can be related directly to the temperature, time, and concentration histories of the gases within the combustor. These histories vary from one combustor to another and, for any given combustor, with changes in operating conditions. The nature of pollutant formation is such that the concentrations of carbon monoxide and unburned hydrocarbons are highest at low-power conditions and diminish with increase in power. In contrast, oxides of nitrogen and smoke are fairly insignificant at low power settings and attain maximum values at the highest power condition. The basic causes of these pollutants, and the various methods employed to alleviate them have been fully discussed elsewhere [15]

Most modeling of emission characteristics has been concerned with oxides of nitrogen, NO_x, but efforts have also been made to predict the formation of other pollutant species. The high cost and complexity of the more sophisticated mathematical models have encouraged the development of semi-empirical models for predicting the effects on emissions of variations in the dimensions, design features, and operating conditions of gas turbine combustors [16-18].

Oxides of Nitrogen

Lefebvre's semi-empirical model for the prediction of pollutant emissions [10], based on considerations of mixing rates, chemical reaction rates, and combustor residence time, leads to the following expression for NO_x.

$$NO_x = \frac{9 \times 10^{-8} P_3^{1.25} V_c \exp(0.01 T_{st})}{\dot{m}_A T_{ps}} g/kg \qquad (6)$$

Equation (6) demonstrates that the only influence of fuel type on NO_x formation is via the two temperatures terms T_{ps} and T_{st}. The former is calculated as

$$T_{ps} = T_3 + \Delta T_{ps}$$

where ΔT_{ps} is the temperature rise due to combustion corresponding to the inlet temperature, T_3, and the primary-zone fuel/air ratio. T_{st} is the stoichiometric flame temperature corresponding to the inlet temperature, T_3. Equation (6) suggests that in the combustion of heterogeneous fuel-air mixtures, it is the stoichiometric flame temperature that determines the formation of NO_x. However, for the residence time in the combustion zone, which is also significant to NO_x formation, the appropriate temperature term is the bulk value, T_{ps}, as indicated in the denominator of Eq. (6).

The justification for the use of stoichiometric flame temperature in Eq. (6) is that a significant proportion of the total combustion process occurs in the form of envelope flames surrounding the larger drops in the spray, where combustion takes place preferentially at the stiochoimetric fuel/air ratio. If this hypothesis is correct then a reduction in mean drop size should, by eliminating some of the largest drops in the spray, lead to a reduction in NO_x. Recent work by Rink et al. [19] has, in fact, shown that improvements in atomization quality result in lower NO_x emissions, as shown for aviation kerosine (JP7) in Fig. 4.

Carbon Monoxide

For the estimation of CO emissions we have [13].

$$CO = \frac{86 \dot{m}_A T_{ps} \exp - (0.00345 T_{ps})}{\left(V_c - 0.55\ 10^{-6} \frac{f_{ps} \dot{m}_A}{\rho_{ps}} \frac{D_o^2}{\lambda_{eff}}\right)\left(\frac{\Delta P_L}{P_3}\right)^{0.5} P_3^{1.5}} g/kg \qquad (7)$$

Atomization quality affects CO emissions through its influence on the rate of evaporation of the fuel spray. As CO emissions are most important at low pressure conditions, where evaporation rates are relatively slow, it is necessary to reduce the combustion volume, V_c, by the volume occupied in fuel evaporation, V_e. This was evaluated [11] as

$$V_e = 0.55\ 10^{-6} f_{ps} \dot{m}_A D_o^2 / \rho_{ps} \lambda_{eff} \qquad (8)$$

The influence of mean fuel drop size on CO emissions is illustrated for a high aromatic fuel in Fig. 5.

Unburned Hydrocarbons

Unburned hydrocarbons are normally associated with poor atomization and inadequate burning rates. Increase in engine power setting usually reduces the emission of unburned hydrocarbons, partly through improved fuel atomization but also through the effects of higher inlet air pressure and temperature, which together enhance chemical reaction rates in the primary combustion zone. Analysis of the experimental data contained in references 4 thru 9 yielded an equation of the form [13]

$$UHC = \frac{11{,}764 \dot{m}_A T_{ps} \exp - (0.00345 T_{ps})}{\left(V_c - 0.55\ 10^{-6} \frac{f_{ps} \dot{m}_A}{\rho_{ps}} \frac{D_o^2}{\lambda_{eff}}\right)\left(\frac{\Delta P_L}{P_3}\right) P_3^{2.5}} g/kg \qquad (9)$$

This equation is very similar to Eq. (7) for the prediction of CO emissions. It shows that the primary influence of atomization quality on the emissions of unburned hydrocarbons is manifested through its effect on fuel evaporation rates. Increase in mean drop size slows down the rate of fuel evaporation so that less time is available for chemical reaction.

Smoke

Exhaust smoke is caused by the production of finely-divided soot particles in fuel-rich regions of the flame, and may be generated in any part of the combustion zone where mixing is inadequate. With pressure atomizers, the main soot-forming region lies inside the fuel spray at the center of the combustor. This is the region in which the recirculating burned products move upstream toward the fuel spray, and where local pockets of fuel vapor are enveloped in oxygen-deficient gases at high temperature. In these fuel-rich regions, soot may be produced in considerable quantities.

Rink et al. [20] have examined the influence of combustor operating conditions, fuel chemistry, and fuel mean drop size on soot formation in a continuous flow combustor. Their results for JP4 fuel, at a combustion pressure of 1.01 MPa (10 atmos.) are shown in Fig. 6. They indicate that small but worthwhile reductions in exhaust smoke can be realized by improved fuel atomization.

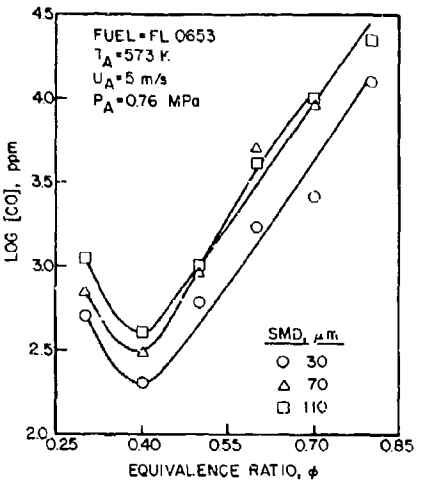

Fig. 5 Influence of mean drop size on carbon monoxide emissions [19].

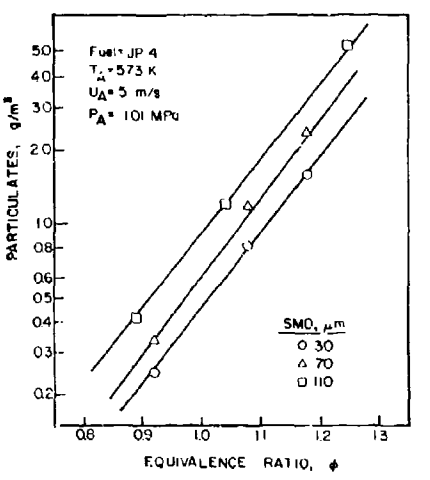

Fig. 6 Influence of mean drop size on particulates formation [20].

SUMMARY OF EFFECTS OF FUEL ATOMIZATION ON COMBUSTION PERFORMANCE

From the preceding discussion it is clear that atomization quality has a significant effect on many important aspects of combustion performance. These effects stem directly from the pronounced influence of mean drop size on evaporation rates. At low combustion pressures, where spray quality is relatively poor, ignition performance and lean blowout limits are both limited by inadequate concentrations of fuel vapor in the primary combustion zone. In a similar manner, combustion inefficiency and the accompanying emissions of carbon monoxide and unburned hydrocarbons, are due mainly to the time absorbed in fuel evaporation which, at low combustion pressures, represents a significant proportion of the total residence time of the combustor. These considerations highlight the need to take full account of changes in fuel spray characteristics when assessing the impact of any change in fuel type on combustion performance.

ATOMIZATION

The spray properties of interest for gas turbines include mean drop size, drop-size distribution, radial and circumferential patternation, droplet number density, cone angle, and penetration. Of these the mean drop size is of paramount importance through its influence on fuel evaporation rates. Various definitions of mean drop size are available of which the most widely used is the Sauter mean diameter which represents the surface/volume ratio of the spray.

Unfortunately, the physical processes involved in atomization are not yet sufficiently well understood for mean diameters to be expressed in terms of equations derived from basic principles. The simplest case of the breakup of a liquid jet has been studied theoretically for more than a hundred years, but the results of these studies have been unable to predict the spray characteristics to a satisfactory level of accuracy. The situation in regard to the complex sprays produced by more sophisticated types of atomizers is, understandably, even worse. As the physical structure and dynamics of a spray are the result of many interwoven complex mechanisms, none of which are fully understood, it is hardly surprising that mathematical treatments of atomization have so far defied successful development. In consequence, the majority of investigations into the drop size distributions produced in atomization have, of necessity, been empirical in nature. Nevertheless, they have yielded a considerable body of useful information from which a number of general conclusions on the effects of fuel properties, gas properties, and injector dimensions, on mean drop size can be drawn.

The properties of a fuel most relevant to atomization are surface tension, viscosity, and density. For a fuel injected into a gaseous medium, the only thermodynamic property generally considered of importance is the gas density. The turbulence characteristics of the air or gas may also influence atomization, but no systematic study of this effect has yet been undertaken.

For plain-orifice injectors, the key geometric variables are the orifice length and diameter. Final orifice diameter is also of prime importance for pressure-swirl atomizers. For prefilming-type airblast atomizers the dimensions that have

most influence on mean drop size are the prefilmer diameter and the hydraulic mean diameter of the atomizer air duct at the exit plane. For twin-fluid injectors, another variable affecting atomization is the fuel/air mass ratio.

The absence of any general theoretical treatment of the atomization process has led to the evolution of empirical equations to express the relationship between the mean drop-size in a spray and the variables of fuel properties, gas properties, flow conditions, and atomiser dimensions. The equations presented below are considered to be the best available for engineering calculations of mean drop sizes for the types of atomizers of relevance to gas turbines.

ATOMIZERS

The atomizers employed in aircraft gas turbines include plain-orifice, pressure-swirl, and airblast types. Plain-orifice nozzles are unsuitable for main combustors because their spray cone angles are too small (< 15°), but they are widely used in ramjets and afterburners, where the fuel injection system normally consists of one or more circular manifolds supported by struts within the jet pipe. Fuel is sprayed into the flame zone from holes drilled in the manifolds. Sometimes "stub pipes" are used instead of manifolds, and many fuel-injector arrays consist of stub pipes mounted radially on circular manifolds. In all cases the objective is to provide a uniform distribution of fuel drops throughout the portion of the gas stream that flows into the combustion zone.

The problem of narrow cone angle that besets the plain-orifice atomizer is eliminated in the pressure-swirl atomizer by imparting a swirling motion to the fuel. As soon as the fuel emerges from the exit orifice, it spreads out into a hollow conical sheet which rapidly disintegrates into ligaments and drops. The simplest form of pressure-swirl atomizer is the simplex nozzle, as illustrated in Fig. 7a. Another widely-used type of pressure-swirl atomizer is the dual-orifice nozzle, as shown in Fig. 7b. Essentially, it comprises two simplex nozzles which are fitted concentrically, one inside the other. This nozzle has the ability to provide good atomization over wide ranges of fuel flow rate. Its main drawback is a tendency to generate copious amount of soot at high combustion pressures. For this reason airblast atomizers are generally preferred for engines of high pressure ratio. Most airblast atomizers are of the prefilming type in which the fuel is spread into a thin sheet before being exposed on both sides to high velocity air. Also used occasionally is the plain-jet airblast atomizer in which the fuel is injected into a high-velocity airstream in the form of one or more discrete jets. These two alternative forms of airblast atomizer are shown schematically in Fig. 7c and 7d.

DROP-SIZE EQUATIONS

The following equations for mean drop size are normally expressed in terms of the Sauter mean diameter (SMD). However, some workers prefer to express their results in terms of the mass median diameter (MMD), which is defined as the drop diameter below or above which lie 50 percent of the mass of the drops. For many practical sprays, the mass median diameter is about 20 percent larger than the Sauter mean diameter.

Plain-Orifice Atomizers

With this type of injector atomization takes place as the fuel jet is first converted to ligaments and then to drops. Disintegration of the jet is promoted by an increase in flow velocity, which increases both the level of turbulence in the issuing jet and the aerodynamic drag forces exerted by the surrounding medium; it is opposed by an increase in fuel

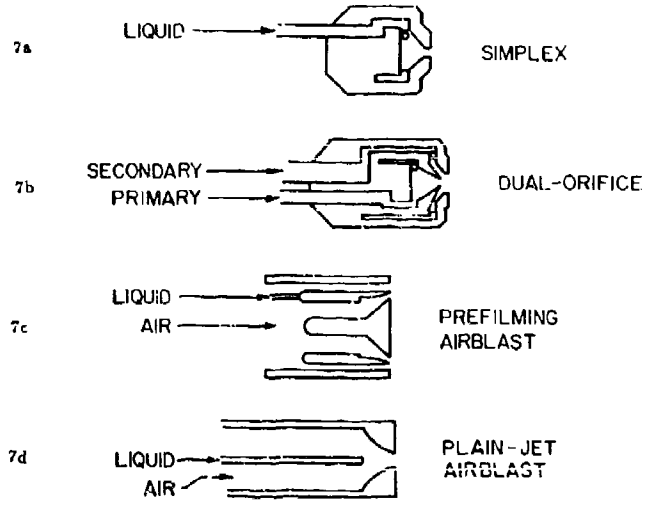

Fig. 7 Atomisersused in gas turbines.

viscosity which delays the onset of atomization by resisting breakup of the ligaments. Merrington and Richardson's [21] experiments on sprays injected from a plain circular orifice into stagnant air yielded the following relationship for mean drop size.

$$SMD = \frac{500\, d_o^{1.2}\, \nu_F^{0.2}}{U_F} \qquad (10)$$

Most of the research carried out on plain-orifice atomizers has been directed toward the types of injectors employed in compression ignition (diesel) engines. With these injectors, jet breakup is due mainly to aerodynamic interaction with a highly turbulent jet. In an early study, Panasenkov [22] examined the influence of turbulence on the breakup of a liquid jet and determined mean drop sizes for jet Reynolds numbers ranging from 1,000 to 12,000. Drop sizes were correlated in terms of discharge orifice diameter and liquid Reynolds number as

$$MMD = 6\, d_o\, Re_L^{-0.15} \qquad (11)$$

Harmon's [23] equation for SMD takes account of ambient gas properties as well as fuel properties. We have

$$SMD = 3330\, d_o^{0.3}\, \mu_F^{0.07}\, \rho_F^{-0.648}\, \sigma^{-0.15}\, U_F^{-0.55}\, \mu_G^{0.78}\, \rho_G^{-0.052} \qquad (12)$$

An unusual feature of this equation is that an increase in surface tension is predicted to give finer atomization.

The above equations for plain-orifice atomizers apply strictly to the injection of fuels into quiescent air. Two other cases of practical importance are (1) injection into a co-flowing or contra-flowing stream of air, and (2) transverse injection across a flowing stream of air.

The influence of air or gas velocity is important because the atomization process is not completed as soon as the jet leaves the orifice. Instead, the process continues in the surrounding medium until the drop size falls to a critical value below which no further disintegration can occur. For any given fuel this critical drop size depends not on the absolute velocity of the fuel jet, but on its velocity relative to that of the surrounding medium. If both are moving in the same direction, penetration is augmented, atomization is retarded, and mean drop diameter is increased. When the movements are in opposite directions, penetration is decreased, the cone angle widens, and the quality of atomization is improved. Thus, insofar as gaseous flow affects the formation and development of the spray and the degree of atomization achieved, it is the relative velocity that should be taken into consideration.

The above discussion on the effects of air motion on the spray characteristics of plain-orifice atomizers is relevant only to situations in which the air velocity is not sufficiently high to change the basic nature of the atomization process. If, however, the issuing jet is subjected to a high-velocity airstream, the mechanism of jet disintegration changes and corresponds to airblast atomization. Ingebo and Foster [24] used a plain-jet type of airblast atomizer, featuring cross-current air injection, to examine the break-up of iso-octane, JP-5, benzene, carbon tetrachloride and water. They derived an empirical relationship for correlating their experimental data which they expressed in the following form:

$$SMD/d_o = 5.0\, (We_F\, Re_F)^{-0.25} \qquad (13)$$

Substituting for We_F and Re_F gives

$$SMD = 5.0 \left(\frac{\sigma\, \mu_F\, d_o^2}{\rho_A\, U_R^3\, \rho_F} \right)^{0.25} \qquad (14)$$

According to Ingebo [25] the above equations are valid for $We_F\, Re_F < 10^6$. For $We_F Re_F > 10^6$ he recommends the following expression for mean drop size

$$SMD/d_o = 37 (We_F\, Re_F)^{-0.4} \qquad (15)$$

or

$$SMD = 37 \left[\frac{\sigma \mu_F d_o^{0.5}}{\rho_A U_R^3 \rho_F} \right]^{0.4} \qquad (16)$$

Only water jets were used in deriving these dimensionally-correct empirical expressions.

Equations (13) to (16) are highly relevant to the design of ramjets and turbojet afterburners which commonly employ radial fuel injection from plain orifice atomizers into high velocity, cross-flowing streams of air or gas.

In situations where transverse penetration of fuel into the gas stream is unnecessary or undesirable, a "splash-plate" type of injector is generally preferred. With this device a round fuel jet is arranged to impinge at the center of a small plate. As the fuel flows over the edge of the plate it is atomized by the high velocity gas stream in which it is immersed. Essentially the device functions as a simple prefilming airblast atomizer.

Ingebo [26] has studied the atomizing performance of this type of injector for air pressures ranging from 0.10 to 2.1 MPa (1 to 20 atmos). His tests were confined to water, for which the effects of liquid velocity and air properties on mean drop size conformed to the relationship

$$SMD = \left[2.67 \times 10^{4} U_L P_A^{-0.33} + 4.11 \times 10^{3} \rho_A U_A P_A^{-0.75}\right]^{-1} \qquad (17)$$

Pressure-Swirl Atomizer

Owing to the complexity of the various physica nomena involved in pressure-swirl nozzles, the study of atomization has been pursued principally by empirical m ds, yielding correlations for mean drop size of the form

$$SMD \propto \sigma^{a} \nu^{b} \dot{m}_F^{c} \Delta P_F^{d} \qquad (18)$$

One of the earliest and most widely quoted expressions is that of Radcliffe [27]

$$SMD = 7.3\, \sigma^{0.6} \nu_F^{0.2} \dot{m}_F^{0.25} \Delta P_F^{-0.4} \qquad (19)$$

This equation was derived from analysis of experimental data obtained by Needham [28], Joyce [29], and Turner and Moulton [30]. Subsequent work by Jasuja [31] yielded the expression

$$SMD = 4.4\, \sigma^{0.6} \nu_F^{0.16} \dot{m}_F^{0.22} \Delta P_F^{-0.43} \qquad (20)$$

However, the variation of surface tension in these experiments was very small and was accompanied by wide variations in viscosity. Thus the exponent of 0.6 has no special significance in Eqs. (19) and (20).

From a series of tests conducted on twenty-five different fuels, using six different simplex nozzles of large flow number, Kennedy [32] derived the following correlating parameter for nozzles operating at Weber numbers larger than 10.

$$SMD = 10^{-3} \sigma_F \left[6.11 + 0.32 \cdot 10^{5}\, FN \sqrt{\rho_F} - 6.973 \cdot 10^{-3} \sqrt{\Delta P_F} + 1.89 \cdot 10^{-6}\, \Delta P_F\right] \qquad (21)$$

In estimating Weber number, Kennedy [32] used the film thickness in the final orifice as the characteristic dimension.

Equation (21) implies a very strong dependence of mean drop-size on surface tension, while viscosity appears to have no effect at all. Kennedy attributes this, and other differences between his results and those of other workers, to the larger Weber numbers resulting from his use of nozzles of exceptionally high flow number. According to Kennedy, "for Weber numbers greater than 10, a different atomization process occurs, i.e. "shear-type breakup, which results in much finer atomization than predicted by previously-reported correlations." However, Jones [33] using large industrial nozzles of much higher flow numbers than those employed by Kennedy, found the effects of surface tension and viscosity on mean drop size to be fully consistent with all previous observations on small-scale nozzles.

Jones [33] used a high-speed photographic technique to investigate the effects of changing liquid properties, operational variables, and geometric parameters on the drop sizes produced by large pressure-swirl atomizers. Analysis of the experimental data yielded the following equation for mean drop size:

$$MMD = 2.47\, \dot{m}_F^{0.315} \Delta P_F^{-0.47} \mu_F^{0.16} \mu_A^{-0.04} \sigma^{0.25} \rho_F^{-0.22} \times \left(\frac{L_s}{D_s}\right)^{0.07} \left(\frac{A_p}{D_s d_o}\right)^{-0.13} \left(\frac{D_s}{d_o}\right)^{0.21} \qquad (22)$$

Lefebvre's [15] analysis of the flow processes in the final orifice of a simplex nozzle led to the following equation for SMD:

$$SMD = A\, \sigma^{0.25} \mu_F^{0.25} \rho_F^{0.125} d_o^{0.5} \rho_A^{-0.25} \Delta P_F^{-0.375} \qquad (23)$$

Substituting $d_o \propto \dot{m}_F^{0.5} / (\Delta P_F / \rho_F)^{0.25}$ into Eq. (23) and using Jasuja's [31] data to determine the value of A, gives

$$SMD = 2.25\, \sigma^{0.25} \mu_F^{0.25} \Delta P_F^{-0.5} \rho_A^{-0.25} \qquad (24)$$

Airblast Atomizers

The first major study of airblast atomization was conducted over 40 years ago by Nukiyama and Tanasawa [34] on a plain-jet airblast atomizer, as illustrated in Fig. 7. The drop sizes were measured by collecting samples of the spray on oil-coated glass slides. Drop-size data were correlated by the following empirical equation for the SMD:

$$SMD = \frac{0.585}{U_R} \left(\frac{\sigma}{\rho_L}\right)^{0.5} + 53 \left(\frac{\mu_L^2}{\sigma \rho_L}\right)^{0.225} \left(\frac{Q_L}{Q_A}\right)^{1.5} \qquad (25)$$

This equation is not dimensionally correct but could be made so by introducing a term to denote length, raised to the 0.5 power. One obvious choice for this length is the diameter of the liquid orifice or air nozzle. However, from tests carried out with different sizes and shapes of nozzles and orifices, Nukiyama and Tanasawa concluded that these factors have virtually no effect on mean drop size. Thus, the absence of atomizer dimensions is a notable feature of Eq. (25).

Another significant omission is air density, which was kept constant (at the normal atmospheric value) in all experiments. This represents a serious limitation, since it prohibits the application of Eq. (25) to the many types of atomizers that are required to operate over wide ranges of air pressure and temperature.

Further studies on plain-jet airblast atomization have been made by Lorenzetto and Lefebvre [35], Jasuja [36], and Rizk and Lefebvre [37]. The latter workers derived the following dimensionally-correct equations for mean drop size

$$\frac{SMD}{d_o} = 0.48 \left(\frac{\sigma}{\rho_A U_R^2 d_o}\right)^{0.4} \left(1 + \frac{1}{AFR}\right)^{0.4} + 0.15 \left(\frac{\mu_F^2}{\sigma \rho_F d_o}\right)^{0.5} \left(1 + \frac{1}{AFR}\right) \qquad (26)$$

This equation was shown to provide an excellent data correlation, especially for low-viscosity fuels.

Rizkalla and Lefebvre [38] carried out the first detailed study of the atomizing performance of prefilming airblast atomizers. They used dimensional analysis to derive the following equation for mean drop size; the various constants and indices being deduced from the experimental data.

$$SMD = 3.33 \times 10^{-3} \frac{\left(\sigma \rho_F D_p\right)^{0.5}}{\rho_A U_A} \left(1 + \frac{1}{AFR}\right)$$

$$+ 13.0 \times 10^{-3} \left(\frac{\mu_F^2}{\sigma \rho_F}\right)^{0.425} D_p^{0.575} \left(1 + \frac{1}{AFR}\right)^2 \qquad (27)$$

For fuels of low viscosity, such kerosine, the first term predominates; the SMD thus increases with increases in fuel surface tension, fuel density, and atomizer dimensions, and decreases with increases in air velocity, air/fuel ratio, and air density. For fuels of high viscosity, the second term acquires greater significance; in consequence, the SMD becomes less sensitive to variations in air velocity and density.

Jasuja [36] subsequently examined the airblast atomization characteristics of kerosine, gas oil and various blends of gas oil with residual fuel oil. The experimental data correlated well with the equation

$$SMD = 10^{-3} \left[1 + \frac{1}{AFR}\right]^{0.5} \left[\frac{(\sigma \rho_F)^{0.5}}{\rho_A U_A} + 0.06 \left(\frac{\mu_F^2}{\sigma \rho_A}\right)^{0.625}\right] \qquad (28)$$

This equation is very similar to Eq. (27), except for the absence of a term representing the atomizer dimensions and a somewhat lower dependence of the SMD on air/fuel ratio.

The effect of atomizer scale on mean drop size was examined by El Shanawany and Lefebvre [39]. They used three geometrically similar nozzles having cross-sectional areas in the ratio of 1:4:16. Their experiments were confined mainly to water and kerosine, but they also used some specially prepared liquids of low viscosity. From an analysis of all the experimental data, El Shanawany and Lefebvre [39] concluded that the mean drop sizes produced by prefilming airblast atomizers could be predicted by the following dimensionally correct equation:

$$\frac{SMD}{D_h} = \left[1 + \frac{1}{AFR}\right] \left[0.33 \left(\frac{\sigma}{\rho_A U_A^2 D_p}\right)^{0.6} \left(\frac{\rho_F}{\rho_A}\right)^{0.1} + 0.068 \left(\frac{\mu_F^2}{\rho_F \sigma D_p}\right)^{0.5}\right] \qquad (29)$$

Wittig and his colleagues [40] have also examined the spray characteristics of a prefilming type of airblast atomizer in which the liquid sheet is injected into the outer air stream. Their results are generally consistent with those obtained for other types of prefilming airblast atomizers.

DISCUSSION

From inspection of all the available experimental data on pressure atomizers, including both plain-orifice and pressure-swirl types, some general conclusions concerning the effects of air and fuel properties on mean drop size can be drawn. Drop sizes increase with reduction in ambient air density according to the relationship SMD α $\rho_A^{-0.25}$. The fuel properties of importance are surface tension, viscosity, and density. In practice the significance of surface tension is diminished by the fact that gas turbine fuels exhibit only minor differences in this property. This is also true for density, as indicated by the values listed for various alternative fuels in Table 1. However, viscosity varies by more than an order of magnitude, so its effect on mean drop size can be appreciable.

Table 1 Atomizing potential of jet fuels derived from shale oils, tar sands, and coal syncrudes

Fuel	ρ at 288 K kg/m^3	μ at 293 K kg/ms	SMD ratio		
			Plain orifice	Pressure swirl	Prefilmer airblast
Aviation kerosine	800	0.00130	1.00	1.00	1.00
Shale oils					
Tosco low-yield (boiling range, 250-550K)	807	0.00547	1.33	1.43	1.14
Tosco low-yield (initial boiling point, 550K)	795	0.00376	1.24	1.30	1.08
Tosco high-yield (boiling range, 250-550K)	804	0.00565	1.34	1.44	1.15
Tosco high-yield (initial boiling point, 550K)	787	0.00341	1.22	1.27	1.07
Marine diesel produced by Paraho process to Mil-F-16884-G	801	0.00693	1.40	1.52	1.19
Jet-A/JP-5 produced by Paraho process to MIL-F-5624	805	0.00217	1.11	1.14	1.03
Green River high-grade shale	911	0.02200	1.72	2.03	1.17
Tar sands					
Alberta Shell Canda	860	0.01100	1.51	1.71	1.32
Alberta GCOS, pilot plant	837	0.00320	1.19	1.25	1.07
Alberta Sun Oil, pilot plant	900	0.00360	1.20	1.29	1.08
Alberta Sun Oil, DF #2	882	0.00544	1.31	1.43	1.14
Coal derived					
Utah A-seam	866	0.00350	1.31	1.43	1.14
Pittsburgh seam	919	0.01500	1.59	1.84	1.44

The results obtained by many workers on the many different types of airblast atomizer allow the following conclusions to be drawn:

1. The mean drop size of the spray increases with increasing fuel viscosity and surface tension and with decreasing air/fuel ratio. Ideally, the air/fuel mass ratio should exceed 3, but little improvement in atomization quality is gained by raising this ratio above a value of about 5.
2. Fuel density appears to have little effect on the mean drop size.
3. The air properties of importance in airblast atomization are density and velocity. In general, the mean drop size is roughly inversely proportional to air velocity. The effect of air density may be expressed as SMD $\propto \rho_A^{-n}$, where n is about 0.3 for plain-jet atomizers and between 0.6 and 0.7 for prefilming types.
4. For plain-jet nozzles, the initial fuel jet diameter has little effect on mean drop size for fuels of low viscosity; but, for high-viscosity fuels, the atomization quality deteriorates with increasing jet size.
5. For prefilming atomizers, the mean drop size increases with increasing atomizer scale (size) according to the relationship SMD $\propto L_c^{0.4}$.
6. For any given size of prefilming atomizer (i.e. for any fixed value of L_c), the finest atomization is obtained by making the prefilmer lip diameter D_p as large as possible.
7. Minimum drop sizes are obtained by using atomizers designed to provide maximum physical contact between the air and the fuel. With prefilming systems the best atomization is obtained by producing the thinnest possible liquid sheet of uniform thickness.
8. The performance of prefilming atomizers is superior to that of plain-jet types, especially under adverse conditions of low air/fuel ratio and/or low air velocity.

Atomizing Properties of Some Alternative Fuels

Drop size estimates have been made for the three main types of fuel injectors most widely used in aircraft gas turbines, namely, the plain-orifice pressure atomizer, the pressure-swirl (simplex) atomizer, and the prefilming airblast atomizer. Drop sizes for normal atmospheric pressure were calculated for these three types of atomizers, using Eqs. (10), (23), and (29) respectively. All of the airblast atomizer calculations were based on an atomizing air velocity of 100 m/s, corresponding to a liner pressure drop of 2.5 percent, and an atomizing air/fuel ratio of 2. Data on fuel properties, as listed in Table 1, were drawn from Lefebvre et al. [41]. Unfortunately, this source of data contains no information on surface tension. However, Lefebvre et al. [41] quote a value of 0.041 kg/s^2 for shale-derived fuels, and this value was used in all calculations of mean drop size for alternative synthetic fuels.

For all three types of atomizers, the constants in the equations were adjusted to give an SMD of unity for aviation kerosine. Thus, the numbers listed in the three right-hand columns of Table 1 represent for each fuel the ratio of its SMD to that of kerosine under the same operating conditions.

CONCLUDING REMARKS

Inspection of Table 1 reveals that for all fuels the atomization quality is markedly inferior to that of normal aviation kerosine. It is also apparent that the airblast atomizer is characterized by significantly lower values of SMD than the swirl atomizer, thus confirming previous observations on the reduced sensitivity of airblast atomizer performance to variations in fuel type. The superior atomizing performance of the airblast atomizer would, of course, show up to even greater advantage on engines of high pressure ratio, since SMD values for airblast nozzles diminish much more rapidly with increase in ambient gas pressure than for swirl atomizers. Thus, to some extent the problems to be anticipated with alternative and synthetic fuels may be alleviated by the use of efficient and well-designed airblast atomizers.

For any given atomizer the effect of changing from kerosine to some alternative fuel will be to increase the fuel/air ratios corresponding to lean blowout and lean lightoff, as indicated by Eqs. (4) and (5) respectively. As these two fuel/air ratios are both proportional to the square of mean drop size, the effect of changing fuel will be more pronounced than is suggested by the SMD ratio in Table 1. Combustion efficiency at idle, altitude cruise, and altitude relight could also be adversely affected by the use of alternative fuels.

The larger drop sizes obtained with alternative fuels will lead to lower evaporation rates and hence to higher emissions of carbon monoxide and unburned hydrocarbons. The anticipated effect on the emissions of NO_x and smoke is much less. Although increase in mean drop size is known to increase smoke, the main effect of a change in fuel type on soot formation and smoke is manifested through the influence of fuel chemistry, notably the aromatic content and/or hydrogen/carbon ratio.

REFERENCES

1. Macfarlane, J. J., "Future Fuels for Aviation," AGARD Lecture Series No. 9b, Aircraft Engine Future Fuels and Energy Conservation, 1979, pp. 2/1-12.
2. Lewis, A., "Future Avaiation Fuels-Fuel Suppliers Views," AGARD Lecture Series No. 9b, Aircraft Engine Future Fuels and Energy Conservation, 1979, pp. 3/1-22.
3. Rudey, R. A. and Grobman, J. S., "Characteristics and Combustion of Future Hydrocarbon Fuels," AGARD Lecture Series No. 9b, Aircraft Engine Future Fuels and Energy Conservation, 1979, pp. 5/1-22.

4. Gleason, C. C., Oller, T. L., Shayeson, M. W., and Bahr, D. W., "Evaluation of Fuel Character Effects on J79 Engine Combustion System," AFAPL-TR-2015, June 1979.

5. Gleason, C. C., Oller,T. L., Shayeson, M. W., and Bahr, D. W., "Evaluation of Fuel Character Effects on F101 Engine Combustor System," AFAPL-TR-2018, June 1979.

6. Vogel, R. E., Troth, D. L., and Verdouw, A. J., "Fuel Character Effects on Current High Pressure Ratio, Can-Type Turbine Combustion Systems," AFAPL-TR-79-2072, April 1980.

7. Gleason, C. C., Oller, T. L., Shayeson, M. W., and Kenworthy, M. J., "Evaluation of Fuel Character Effects on J79 Smokeless Combustor," AFWAL-TR-80-2092, November 1980.

8. Oller, T. L., Gleason, C. C., Kenworthy, M. J., Cohen, J. D., and Bahr, D. W., "Fuel Mainburner/Turbine Effects," AFWAL-TR-2100, May 1982.

9. Longwell, J. P., ed. "Jet Aircraft Hydrocarbon Fuels Technology," NASA CP-2033, 1978.

10. Lefebvre, A. H., "Fuel Effects on Gas Turbine Combustion," Air Force Wright Aeronautical Laboratories Report, AFWAL-TR-2004, January 1983.

11. Lefebvre, A. H., "Influence of Fuel Properties on Gas Turbine Combustion Performance," Air Force Wright Aeronautical Laboratories Report, AFWAL-TR-84-2104, January 1985.

12. Lefebvre, A. H., "Fuel Effects on Gas Turbine Combustion-Liner Temperature, Pattern Factor, and Pollutant Emissions," AIAA Journal of Aircraft, Vol. 21, No. 11, November 1984, pp. 887-898.

13. Reeves, C. M., and Lefebvre, A. H., "Fuel Effects on Aircraft Combustor Emissions," ASME Paper 86-GT-212, 1986.

14. Lefebvre, A. H., "Fuel Effects on Gas Turbine Combustion - Ignition, Stability, and Combustion Efficiency," Trans ASME Journal of Engineering for Gas Turbines and Power, Vol. 107, 1985, pp. 24-37.

15. Lefebvre, A. H., Gas Turbine Combustion, Hemisphere Press, New York, 1983.

16. Hammond, D. C. Jr. and Mellor, A. M., "Analytical Calculations for the Performance and Pollutant Emissions of Gas Turbine Combustors," Combustion Science and Technology, Vol. 4, No. 3, 1971, pp. 101-112.

17. Hammond, D. C. Jr. and Mellor, A. M., "Analytical Predictions of Emissions from and within an Allison J-33 Combustor," Combustion Science and Technology, Vol. 6, No. 5, 1973, pp. 279-286.

18. Mellor, A. H., "Semi-Empirical Correlations for Gas Turbine Emissions, Ignition, and Flame Stabilization," Progress in Energy Combustion Science, Vol. 6, 1981, pp. 347-358.

19. Rink, K. K., Lefebvre, A. H., and Graves, R., "The Influence of Fuel Composition and Spray Characteristics on NO_x Formation," International Conference on Combustion in Engines, London, May 1988.

20. Rink, K. K., Lefebvre, A. H., and Graves, R., "The Influence of Fuel Composition and Spray Characteristics on Particulate Formation," SAE Fuels and Lubricants Meeting, Toronto, Ontario, November 1987.

21. Merrington, A. C. and Richardson, E. G., "The Break-Up of Liquid Jets," Proc. Phys. Soc. London, Vol. 59, No. 33, 1947, pp. 1-13.

22. Panasenkov, N. I., Zhur. Tekh. Fiz., Vol. 21, 1951, p. 160.

23. Harmon, D. B., J. Franklin Inst., Vol. 259, 1955, p. 519.

24. Ingebo, R. D. and Foster, H. H., "Drop-Size Distribution for Cross-Current Break-Up of Liquid Jets in Air Streams," NACA TN 4087, 1957.

25. Ingebo, R. D., "Capillary and Acceleration Wave Breakup of Liquid Jets in Axial Flow Airstreams", NASA Technical Paper 1791, 1981.

26. Ingebo, R. D., Atomization of Liquid Sheets in High Pressure Airflow", ASME Paper HT-WA/HT-27, 1984.

27. Radcliffe, A., "Fuel Injection, Vol. XI,High Speed Aerodynamics and Jet Propulsion, Princeton University, Press, Princeton, N.J., 1960.

28. Needham, H. C., Power Jets R and D Report, No. R1209, 1946.

29. Joyce, J. R., Report ICT 15, Shell Research Ltd., London, 1949.

30. Turner, G. M. and Moulton, R. W., Chem. Eng. Prog., Vol. 49, 1943, p. 185.

31. Jasuja, A. K., "Atomization of Crude and Residual Fuel Oils," ASME Journal of Engineering for Power, Vol. 101, No. 2, 1979, 250-258.

32. Kennedy, J. B., "High Weber Number SMD Correlations for Pressure Atomizers," ASME Paper 85-GT-37, 1985.

33. Jones, A. R., "Design Optimization of a Large Pressure-Jet Atomizer for Power Plant," Proceedings of International Conference on Liquid Atomization and Sprays (ICLASS), Madison, Wisconsin, 1982, pp. 181-185.

34. Nukiyama, S. and Tanasawa, Y., "Experiments on the Atomization of Liquids in an Airstream," Trans. Soc. Mech. Eng. Jpn. Vol. 5, 1939, pp. 68-75.

35. Lorenzetto, G. E. and Lefebvre, A. H., "Measurements of Drop Size on a Plain Jet Airblast Atomizer," AIAA Journal, Vol. 15, No. 7, 1977, pp. 1006-1010.

36. Jasuja, A. K., "Plain-Jet Airblast Atomization of Alternative Liquid Petroleum Fuels Under High Ambient Air Pressure Conditions," ASME Paper 82-GT-32, 1982.

37. Rizk, N. K. and Lefebvre, A. H., "Spray Characteristics of Plain-Jet Airblast Atomizers," Trans. ASME Journal of Engineering for Gas Turbines and Power, Vol. 106, July 1984, pp. 639-644.

38. Rizkalla, A. and Lefebvre, A. H., "The Influence of Air and Liquid Properties on Air Blast Atomization," ASME Journal of Fluids Engineering, Vol. 97, No. 3, 1975, pp. 316-320.

39. El-Shanawany, M.S.M.R. and Lefebvre, A. H., "Airblast Atomization: The Effect of Linear Scale on Mean Drop Size," J. Energy, Vol. 4, No. 4, 1980, pp. 184-189.

40. Wittig, S., Aigner, M., Sakhani, Kh. and Sattelmayer, Th., "Optical Measurements of Droplet Size Distributions: Special Considerations in the Parameter Definition for Fuel Atomizers," Paper presented at AGARD meeting on Combustion Problems in Turbine Engines, Cesme, Turkey, Oct. 1983. Also Aigner, M. and Wittig, S., "Performance and Optimization of an Airblast Nozzle, Drop-Size Distribution and Volumetric Air Flow," Proceedings of International Conference on Liquid Atomization and Sprays, London, England, July 1985, pp. IIC/3/1-8.

41. Lefebvre, A. H., Mellor, A. M., Peters, J. E., "Ignition, Stabilization, Atomization; Alternative Fuels in Gas Turbine Combustors," Alternative Hydrocarbon Fuels: Combustion and Chemical Kinetics, edited by C. T. Bowman and Jorgen Birkeland, Vol. 62, Progress in Astronautics and Aeronautics, 1979.

DISCUSSION

T.Rosfjord, US

While distinct atomizer types do exist, in real gas turbine applications, an airflow is present. Even pressure atomizers have an airflow across its face to prevent mists from depositing. Data show that this *small* airflow has a very significant influence on spray pattern and atomization. Hence, even for this injector, there is an aerating characteristic. While certain classical pressure atomizer features will persist, a useful correlation must consider the airflow influence. Perhaps a (modified) aerating form of correlation would be suitable.

Author's Reply

I am well aware that shroud air can influence spray characteristics at low fuel flow conditions where the air/fuel momentum ratio is relatively high. It is surprising to learn that this minute air flow can have significant effects on spray pattern and spray aeration at high fuel injection pressures, as your data suggest.

G.Grienche, FR

Vous ne parlez pas dans votre étude des injecteurs de type "canne à prévaporisation. Ne pensez-vous pas que vaporiser le carburant, même particellement, avant son injection dans la chambre, soit un élément favorable d'adaptation aux differents carburants?

Author's Reply

Problems of coking and carbon buildup within the vaporizer tubes restrict its useful application to light distillate fuels such as kerosine and DF2. It would be quite unsuitable for the alternative fuels described in my paper. Mr George Opdyke of Textron Lycoming has had many years of practical experience with vaporizers. I woul I like to invite his comments on this question.

G.Opdyke, US

The first vaporizer which I tested was a MAMBA can, using a residual fuel. The vaporizers lasted about 15 minutes because of internal coking and subsequent burnout. I have never since tried such a heavy fuel in a vaporizer.

C.Moses, US

You showed a significant effect of drop size on particulates. I've not seen this effect in my own combustor work or in my analysis of the combustor programs sponsored by the US. Air Force and Navy. Do you consid- r this to be an artifact of your combustor or would you get a general conclusion from it?

Author's Reply

The results we show on the influence of mean drop size on particulates were obtained using a continuous plug flow combustor. This device does not simulate conditions in a gas turbine combustor in which combustion takes place in two stages, i.e. a soot-forming zone followed by a soot oxidation zone. I believe that fuel drop size has a small but significant effect on soot formation in the primary combustion zone, but this effect is masked by the soot oxidation process occurring further downstream. The net result, as you rightly point out, is that soot concentrations measured at the combustor exit exhibit very little influence of fuel drop size.

G.Faeth, US

In your atomization correlations, you indicated the effects of Reynolds number, although other characteristics must also be important. Do you have correlations which account for length/diameter ratio surface finish, etc.?

Author's Reply

No. Although many physical characteristics of the nozzle affect the quality of the spray, I have used Reynolds number because it is something that can be quantified, is non-dimensional, and is related to first order effects. I believe that further down the road the second order effects will have to be included in an equation for mean drop size.

ETUDE PAR SIMULATION DES PHENOMENES DE PULVERISATION, DE RUISSELLEMENT ET DE VAPORISATION LIES A L'INJECTION DE CARBURANT

par P. HEBRARD, G. LAVERGNE
ONERA/CERT/DERMES
2 avenue Edouard Belin 31055 Toulouse Cédex
FRANCE

RESUME

La modélisation de la combustion nécessite la connaissance des conditions aux limites et des modèles physiques que souvent, seule l'expérience peut fournir. Une telle approche expérimentale pour les phénomènes liés à l'injection, obtenue par simulation à partir de mesures réalisées au moyen de matériels spécifiques développés au CERT, est présentée. L'évaluation des performances de différents types d'injecteurs utilisés dans des chambres de combustion est effectuée à partir d'essais de granulométrie : distribution locale de taille et diamètre moyen de Sauter (DMS), et de mesures de concentration de gouttes.

Des modèles décrivant les phénomènes d'évaporation,de mise en vitesse et d'impact de gouttes sur une paroi chauffée sont testés expérimentalement.

La modélisation de l'injection prémélangée de carburant dans un injecteur du type "canne à prévaporisation", qui utilise ces résultats expérimentaux, est un exemple d'application d'une telle démarche.

NOTATIONS

C_d	: coefficient de traînée
C_v	: chaleur spécifique du gaz
d	: diamètre de la goutte
D.M.S.	: diamètre moyen de Sauter $\Sigma n\, d^3 / \Sigma n\, d^2$
g	: grossissement
L	: chaleur latente de vaporisation
$\dot{M}_F$	: débit évaporé
n	: indice de réfraction
R_e	: nombre de Reynolds = $VR\, d/\nu$
S	: seuil de numérisation
T_∞	: température de l'air
T_L	: température du liquide
T_u	: taux de turbulence
V_a	: vitesse de l'air
$U_{\ell n}$	: composante normale de la vitesse de la goutte
V_ℓ	: vitesse de la goutte
VR	: vitesse relative = $(V_a - V_\ell)$
W_r	: nombre de Weber = $\rho_\ell U_{\ell n}^2\, d/\sigma$
ΔP_j	: pression d'injection du liquide
ρ_a	: masse volumique du gaz
ρ_ℓ	: masse volumique du liquide
λ	: longueur d'onde
$\alpha = \pi d/\lambda$	: facteur de diffusion
σ_j	: tension superficielle du liquide
ν	: viscosité cinématique

I - INTRODUCTION

Les performances d'une chambre de combustion sont fortement liées à la qualité de la pulvérisation du carburant injecté. Les caractéristiques du jet de carburant (expansion, tailles et vitesses des gouttes) sont nécessaires à la modélisation de la combustion.

Récemment, de nombreuses techniques de granulométrie par mesures optiques (par mesures de l'intensité de la lumière diffusée par les gouttes, par anémométrie laser...) ont été développées (Réf. 4).

Plusieurs techniques utilisant le traitement d'images ont été mises au point au CERT en couplant des moyens de visualisation : caméra vidéo ou C.C.D. et microcalculateur. Ces méthodes, appliquées à l'étude de jets de gouttelettes, permettent d'obtenir des résultats en temps réel relatifs à la granulométrie et aux concentrations de gouttes. Le principe consiste à numériser une image du jet fortement grossie, un traitement donne ensuite en temps réel la forme du panache, la distribution spatio-temporelle de taille de gouttes, (diamètre moyen de Sauter (DMS))...

Après une description rapide de ces techniques, nous présenterons quelques applications relatives aux études de chambres de combustion. Les performances d'injecteurs élémentaires sont étudiées par la détermination des lois d'évolution du diamètre moyen de Sauter et de la forme du panache en fonction des paramètres principaux : pression d'injection ΔP_j, vitesse de l'air V_a, tension superficielle σ_j. D'autres résultats concernent l'injection dans des maquettes simplifiées de turboréacteurs en simulation aérodynamique et en écoulement isotherme. Dans le cadre des recherches sur les instabilités de combustion, des études sont actuellement menées sur l'influence d'une perturbation acoustique sur la distribution de tailles de gouttes.Enfin, plusieurs expériences de base sur l'évaporation et la mise en vitesse des gouttes, sur l'impact des gouttes et le ruissellement sur une paroi chaude permettent de valider des modèles physiques qui seront par la suite incorporés au code de calcul.

II - ETUDE EXPERIMENTALE

II.1 Granulométrie

Pour évaluer le taux d'évaporation d'un jet de gouttelettes, la connaissance du D.M.S. n'est pas suffisante, il faut prendre en compte les distributions locales et spatiales des tailles de gouttes. Le comportement des gouttes dans cette première phase a une influence primordiale sur la répartition de carburant dans les différentes zones de la chambre de combustion.

II.1.1. Principe de mesure

La méthode de granulométrie est décrite sur la figure 1. L'écoulement diphasique est éclairé soit avec une tranche lumineuse générée par un laser He/Ne de 15 mwatt, soit par un diode laser. La lumière diffusée par les gouttes est visualisée à 90° par une caméra par l'intermédiaire d'un banc optique comportant un télescope (diamètre 100 mm, focale 600 mm) et un microscope (grossissement 8 à 4) qui assure un grossissement suffisant.

Avec ce dispositif optique, le champ objet analysé est de quelques mm^3 ($<10\ mm^3$) avec une profondeur de champ de 100 µm. Les tailles mesurées sont comprises entre 10 µm et quelques centaines de microns. Les images des gouttes traversant le volume élémentaire de mesure peuvent être analysées en temps réel par le microcalculateur à partir de deux types de traitements.

a) Première méthode
Cette méthode a déjà été décrite dans la référence 2. A chaque trame (16 ms), les images grossies des diverses gouttes présentes dans le champ observé sont numérisées sur un bit. Le principe consiste à superposer les contours de ces images au "maillage" défini par le balayage (ligne) de la caméra et l'horloge interne du calculateur (colonne).
Le diamètre moyen de Sauter DMS = $\Sigma n d^3 / \Sigma n d^2$ peut s'exprimer par la relation :

$$D.M.S. = \frac{3\ P_P}{P_L}$$

P_P : nombre de points situés à l'intérieur des images des gouttes
P_L : nombre de points situés à l'intersection du maillage et de la périphérie des images

A partir de l'analyse d'un nombre suffisant de trames (200 à 1000), le DMS est calculé en temps réel et une première approche de la distribution de tailles peut être obtenue après un temps voisin de 2 minutes. Ce type d'acquisition est limité du fait qu'il n'est pas possible d'accéder à la position et à la taille de chaque goutte. Ainsi avons-nous développé une deuxième technique pour augmenter les possibilités de cette méthode.

b) Deuxième méthode
L'extraction de contour de chaque image est effectuée en temps réel à partir de la méthode des gradients de Robert et l'utilisation d'une ligne de retard. Pour pouvoir traiter un nombre important de trames sans utiliser une capacité mémoire trop importante, un système d'acquisition d'image "compressée" est utilisé. Le principe consiste à sauvegarder les coordonnées des points ou des lignes dont la brillance est supérieure à un niveau fixé. Un "triplet" de valeurs est acquis par segment (coordonnées du 1er point et longueur du segment) et est transmis à un bus 32 bits et ensuite mémorisé.
Ce système développé sur IBM PC utilise un traitement permettant d'obtenir les informations suivantes :

- taille de chaque goutte,
- diamètre moyen de Sauter (D.M.S.) et différents moments,
- distance moyenne entre gouttes à partir de l'obtention des coordonnées des centres.

II.1.2. Etalonnage du banc granulométrie

Un étalonnage est nécessaire pour relier la taille des images de gouttes vues par la caméra à leur taille réelle.

Pour un faisceau de lumière incidente (intensité I_0, longueur d'onde λ) et un angle d'observation θ donnés, le facteur d'étalonnage dépend de l'optique (g : grossissement), du seuil de numérisation S, de l'indice de réfraction n. Des billes de verre de tailles comprises entre 50 et 200 µm sont généralement utilisées. Les résultats sont en bon accord avec ceux déduits de la théorie de Mie pour $\alpha = \pi d/\lambda > 10$ (Réf. 4).

II.2. Mesures de concentration de gouttes

Principe de mesure :

Le principe de mesure utilisé dans le cas d'un traceur coloré injecté dans l'eau a déjà été décrit (Réf. 2). Les principales modifications présentées ici portent, d'une part sur l'électronique et, d'autre part, sur l'application à un milieu diphasique. Le principe repose sur le fait que l'intensité de la lumière diffusée est proportionnelle à la surface d'analyse. Une telle surface générée sur l'écran du microcalculateur, matérialise la zone à étudier. Cette hypothèse suppose une concentration faible pour assurer une diffusion indépendante par chaque particule. Le signal vidéo intégré dans la fenêtre d'analyse est proportionnel à la brillance locale de l'image et donc à la concentration des gouttes. Cette technique nécessite un étalonnage préalable.

II.3. Exemples d'applications

Depuis plusieurs années, des études expérimentales et de modélisation concernant les chambres de combustion sont menées au CERT/DERMES (Réf.12). Dans ces études, la partie expérimentale est effectuée par simulation en écoulement isotherme à partir de maquettes simplifiées de chambres de combustion.
La démarche choisie est la suivante :

- simulation hydraulique pour étudier l'aérodynamique interne,
- simulation aux conditions atmosphériques de l'injection, sur banc aérodynamique,
- modélisation de la combustion utilisant des modèles de cinétique chimique et en prenant comme conditionsaux limites, les résultats expérimentaux de simulation.

La modélisation de la phase liquide nécessite aussi la connaissance de lois élémentaires telles que l'évaporation en milieu gazeux surchauffé de gouttes, l'impact et l'évaporation de gouttes sur un paroi chaude.

II.3.1. Performances d'injecteurs élémentaires

Dans ce premier exemple, les caractéristiques d'injecteurs élémentaires, utilisés dans des chambres de combustion, sont étudiés en fonction des conditions expérimentales. De tels résultats ont été obtenus dans une veine aérodynamique (figure 1) usinée en plexiglass de section carrée (150mm x 150mm). Cette installation offre la possibilité de faire varier les conditions expérimentales (vitesse et taux de turbulence de l'air, pression d'injection, nature du fluide injecté...). Certains résultats ont déjà été présentés dans la référence 12.
Des exemples de résultats montrant la variation de D.M.S. en fonction de la vitesse de l'air et de la tension superficielle du liquide injecté sont présentés sur les figures 2 et 3.
Tous ces résultats peuvent être rassemblés sous la forme d'une corrélation :

$$D.M.S. = K\, V_a^{-0.38}\, \Delta P_j^{-0.23}\, \sigma_j^{0.42} \quad ....$$

Une telle corrélation montre les rôles importants de la vitesse de l'air et de la tension superficielle. Ces résultats ont été complétés par l'étude de l'évolution radiale de la taille des gouttes. Nous pouvons remarquer sur la figure 4, des variations importantes de tailles. La figure 5 montre un exemple de distribution de tailles de gouttes comparée aux lois de TANASAWA TESIMA et de ROSIN RAMLER (Réf.6).

Dans le cadre d'études d'instabilité de combustion, nous avons été amenés à étudier l'influence de perturbations acoustiques d'amplitude et de fréquences données sur les performances d'un injecteur élémentaire. La perturbation acoustique provient d'un haut parleur qui peut fournir une puissance de 135 db à des fréquences comprises entre 200 et 500 Hz. Des études ont été réaliaées au CERT montrant que le mécanisme de formation des gouttes peut-être modifié si on superpose à l'écoulement aérodynamique une excitation de forte amplitude à une fréquence bien définie (Réf.10). Un exemple d'influence est montré sur la figure 6 pour lequel les effets suivant apparaissent lorsque la puissance acoustique augmente :

- la dispersion de la distribution est plus faible,
- le D.M.S. diminue.

II.3.2. Performances d'un injecteur double vrille placé dans une maquette bidimensionnelle de chambre de turboréacteur

Pour déterminer l'influence locale de l'aérodynamique sur les caractéristiques du jet de carburant provenant d'un injecteur double vrille, des expériences ont été réalisées dans une maquette bidimensionnelle en écoulement aérodynamique isotherme. La distribution radiale de D.M.S. obtenue à différentes distances de l'injecteur et pour une richesse donnée montre (figure 7), les éléments suivants ;

- une variation radiale importante de DMS près de l'injecteur liée à l'aérodynamique des jets,
- une diminution de DMS lorsque la distance à l'injecteur augmente.

Les petites gouttelettes subissant une accélération plus importante que les grosses, suivent mieux l'écoulement aérodynamique. Dans la zone centrale (zone de recirculation) et dans la zone des jets d'air, les grosses gouttes sont sous représentées, ce qui se traduit par un DMS plus faible. Très près de l'injecteur, la valeur importante de DMS peut s'expliquer par l'accumulation de grosses gouttes non encore entraînées par l'écoulement. Ce type de résultats a aussi été obtenu dans la référence 6.Une étude paramétrique a été effectuée en prenant en compte l'influence sur le DMS du débit liquide, du débit d'air et de la vitesse de l'air au niveau de l'injecteur. A titre d'exemple, la figure 8 montre l'influence peu importante du débit liquide injecté sur le DMS. Ce résultat indique que c'est l'aérodynamique qui semble avoir une influence primordiale sur le DMS.
Ces résultats nous ont permis d'exprimer la variation de tailles de gouttes sous la forme d'une corrélation :

$$D.M.S. = \frac{K}{U_a^{0.19}} \left(1 + \frac{\dot{m}_L}{\dot{m}_a}\right)^{0.4}$$

U_a : vitesse débitante des jets d'air

$\dot{m}_L$: débit masse liquide

$\dot{m}_a$: débit masse d'air

K : constante

Ce type de corrélation a aussi été obtenu par Lefebvre (Réf.13).

Ces résultats ont été complétés par des mesures de concentration de gouttes. Des sondages verticaux et horizontaux de concentration (figure 9) effectués sur un rayon et pour deux richesses injectées différentes, montrent des variations très importantes entre l'axe du swiler et le plan de symétrie entre deux swileis.
Un résultats semblable a été aussi obtenu par Yamanaka (Réf. 16). L'augmentation importante de la concentration à la périphérie dans le plan horizontal correspond à l'apport du liquide de l'injecteur adjacent. Une dissymétrie importante entre le sondage vertical (influence des parois) et le sondage horizontal (influence

de l'injecteur voisin) est à remarquer. Ces profils de concentration de gouttes évoluent rapidement avec le rapport des débits d'air entre les deux vrilles de l'injecteur. La fermeture de la vrille externe ayant pour effet de diminuer le taux de "swirl", provoque une augmentation importante de la concentration sur l'axe (figure 10).

II.3.3. Etude de l'évaporation d'un liquide

Une autre application de ces techniques est l'étude de l'évaporation de gouttelettes liquides se déplaçant dans un écoulement d'air surchauffé. Une telle expérience est intéressante pour vérifier les lois utilisées dans les différents codes de calcul. Dans l'expérience représentée sur la figure 11, de l'air chaud à température et débit variables s'écoule dans un tube de pirex de longueur 2 m et de diamètre 60 mm. Les gouttelettes sont introduites dans l'écoulement par un petit injecteur. L'évaporation des gouttes qui est le résultat de l'écart de température et de vitesse entre les phases liquide et gazeuse est étudiée par l'analyse, en différentes sections, de la distribution des tailles des gouttes. En parallèle, il a été nécessaire d'étudier à chaque section test, la vitesse locale des gouttes et de l'air. Les résultats obtenus se rapprochent des résultats ci-dessous obtenus par Dickerson et Schuman

$$\frac{dV_R}{dt} = -\frac{3}{4}\,\frac{C_d}{D}\,\frac{\rho_g}{\rho_\ell}\,V_R^2$$

avec $V_R = |V_a - V_\ell|$

et $C_D = \frac{24}{R_e}$ pour $R_e < 0{,}48$

$C_D = 27\,R_e^{-0.84}$ $\quad 0{,}48 < R_e < 78$ $\quad R_e = \frac{V_R\,D}{\nu}$

$C_D = 0{,}27\,R_e^{0.27}$ $\quad R_e > 78$

Pour comparer les résultats obtenus expérimentalement à des résultats théoriques, un modèle monodimensionnel a été utilisé dans lequel différentes lois de vaporisation ont pu être testées. La loi qui semble être en bon accord avec nos résultats est celle de Frossling (Réf. 9).

$$\dot{M}_F = \dot{M}_O\,(1 + 0{,}244\,R_e^{0.5}) \quad \text{avec } M_O = \pi\,d\,\frac{\lambda}{C_V}\,\mathrm{Log}\,(1+B)$$

$$B = \frac{T_\infty - T_f}{L}$$

La figure 11 indique un exemple d'évolution d'histogramme avec la distance de l'injection et montre une décroissance du diamètre moyen. La comparaison de ces résultats avec les résultats du modèle de calcul avec la loi de Frossling comme loi d'évaporation est satisfaisante (Figure 12).

II.3.4. Etude de l'impact et du ruissellement des gouttelettes

Les premiers résultats sur le comportement d'une goutte impactant sur une paroi chaude et le transfert de chaleur qui en découle ont été obtenus par Wachers et Westerling (Réf.14) avec de l'eau. Les phénomènes observés sont fortement liés au nombre de Weber défini par l'expression suivante :

$$We = \frac{\rho_L \cdot U_{Ln}^2\,d}{\sigma}$$

Pour une température de plaque de 400° C et pour des gouttes d'eau, les auteurs proposent le modèle suivant :

- $We < 30$ la goutte rebondit sur la paroi sans éclater
- $30 \leq We \leq 80$ la goutte subit des déformations considérables lors de l'impact mais retrouve une forme presque sphéroïdale après le rebond
- $We > 80$ la goutte s'étale sur la paroi en formant un film

$We = 80$ est la valeur critique pour l'eau.

Ces résultats bibliographiques obtenus pour l'eau ne concernent que quelques températures de paroi. Une étude expérimentale a été entreprise à partir d'une plaque chauffante fournissant une température maximale de 300° C pour connaître l'évolution "éventuelle" du nombre de Weber critique, d'une part, avec la température de paroi et, d'autre part, avec la nature du liquide.

Les résultats présentés sur la figure 13 font apparaître une évolution notable de ce nombre de Weber critique avec la température de la plaque. A température fixée, le nombre de Weber critique du kérosène est plus important que celui de l'eau. Un autre exemple d'application est l'évolution du temps d'évaporation d'une goutte en fonction de la température de la plaque. Les résultats obtenus pour l'alcool, l'eau et le kérosène font apparaître une zone de température critique appelée température de "Leidenfrost" pour laquelle il y a changement de mode de transfert thermique (figure 14).

D'autres résultats concernant les caractéristiques physiques et le taux de ruissellement d'un film liquide ont été obtenus mais ne sont pas présentés dans cette communication.

III - EXEMPLE DE MODELISATION SIMPLIFIEE D'UN ECOULEMENT DIPHASIQUE

L'écoulement diphasique dans une canne à prévaporisation est un écoulement type pour lequel la plupart des modèles physiques cités ci-dessus doivent être pris en compte. Le but de cette modélisation est d'obtenir, à partir d'un calcul simplifié, les caractéristiques du mélange air-carburant en sortie d'une canne à prévaporisation. Pour ce type d'injecteur, les résultats bibliographiques peu nombreux ne sont que qualitatifs (Réf. 15).

Devant les difficultés d'effectuer des mesures in situ, nous avons choisi la simulation en essayant d'étudier individuellement les phénomènes présents dans la canne à partir d'expériences de base.

Les phénomènes physiques à prendre en compte et qui ont été simulés sont les suivants :

- pulvérisation du carburant (taille et vitesse initiales des gouttes),
- mise en vitesse et évaporation des gouttes,
- impact d'une goutte sur la paroi chaude de la canne,
- ruissellement sur les parois,
- taux d'évaporation du film sur une paroi chaude,
- caractéristiques du film liquide (vitesse, épaisseur...),
- transformation film-goutte,
- aérodynamique de la canne.

Ce programme de calcul de l'écoulement dans la canne que nous avons proposé, est constitué de la juxtaposition des différents modèles testés expérimentalement au CERT et d'un calcul simplifié de l'aérodynamique (écoulement bidimensionnel plan, fluide parfait). Ce modèle du type Lagrangien permet, pour des conditions d'injection données (vitesse d'air, vitesse de carburant) de restituer les trajectoires de gouttes, à partir des conditions initiales obtenues expérimentalement par simulation, et de calculer le taux d'évaporation dans différentes sections de la canne. La figure 15 montre l'influence de la taille moyenne des gouttes injectées sur le taux d'évaporation du carburant en sortie de canne. L'intérêt de ce code de calcul est la prise en compte de la plupart des phénomènes physiques existants dans la canne et la possibilité d'effectuer des études de tendances (géométrie de la canne, diamètre et orientation des orifices de l'injecteur, richesse injectée...). Actuellement, ce code de calcul, bien que validé seulement par injection d'eau, fournit des résultats réalistes. Des améliorations de l'aérodynamique d'un tel écoulement sont en cours par la prise en compte de la turbulence à partir d'un programme d'écoulement diphasique tridimensionnel du type K ε .

IV - CONCLUSION

Des techniques simples de granulométrie et de concentration de gouttes permettent d'évaluer les performances de différents types d'injecteurs et peuvent être appliquées à des expériences de base simulant certains phénomènes physiques existants dans les chambres de combustion. Ce type de démarche est actuellement étendu aux écoulements tridimensionnels.

REFERENCES

1. J.M. Vateau, R. Charlot,
Techniques de mesure des aires interfaciales dans les écoulements à bulle
Rapport CEA - R - 5075 1983

2. Y. Biscos, P. Hébrard, G. Lavergne, G. Toulouse
Digital video image processing application to drop size and concentration measurements
International symposium on visualization, Paris 1986

3. P. Hébrard, G. Lavergne
Etude d'injection de carburant
Internal report, n° 2243/DERMES, 1986

4. H.C. Van der Hulst
Light scattering by small particles
Chapman and Hall, 1957

5. A.H. Lefebvre, Rizkalla
The influence of air and liquid properties on airblast atomization
ASME Journal of fluids engineering, 1975

6. S. Nukizama, Y. Tanasawa
An experiment on the atomization of fluid
Trans SME Japan 6, vol. 4 n° 14, 1938

7. S. Witig, M. Aigner, K.H. Sakbaw and Th. Sattelmayer
Optical measurement of droplet size distribution : special consideration in the parameter definition for fuel atomizers
AGARD C.P. 353, 1983

8. M. El Kotb
Fuel atomization for spray modelling
Prog. energy, combustion, Vol. 8, 1982

9. N. Frossling
Geophysics 52, 170, 1938

10. P. Hébrard, B. Platet
Etude et analyse du comportement dynamique d'un injecteur soumis à une perturbation d'origine acoustique
Internal report n°2/2249/DERMES, 1986

11. Y. Biscos, F. Bismes, P. Hébrard, G. Lavergne,
Optical particle sizing application
Intern. Symposium on "optical particle sizing : theory and practice", Rouen 12-15 May

12. G. Frager, P. Hébrard, G. Lavergne, A. Mir
Etude aérodynamique de la combustion dans les foyers de turbomachines : approches expérimentales et théoriques
AGARD n° 353, Combustion problems in turbine engines, Turkey, 3-6 october 1983

13. A.W. Lefebvre
Gas turbine combustion
Mr Graw Hill series in Energy, combustion and Environment 1983

14. L.H.J. Watchers, N.A.J. Westerling
Chemical engeneering science, Vol. 21 pp 1047

15. H.C. Low
Recent research on the efflux of the Rolls Royce vaporiser fuel injector
AGARD n° 353 Combustion problems in turbines engines, Turkey 3-6 October 1983

16. Yamanaka
Combustion characteristics in gas turbine combustor with airblast type fuel injectors
Gas turbine society of Japan Juin 1983

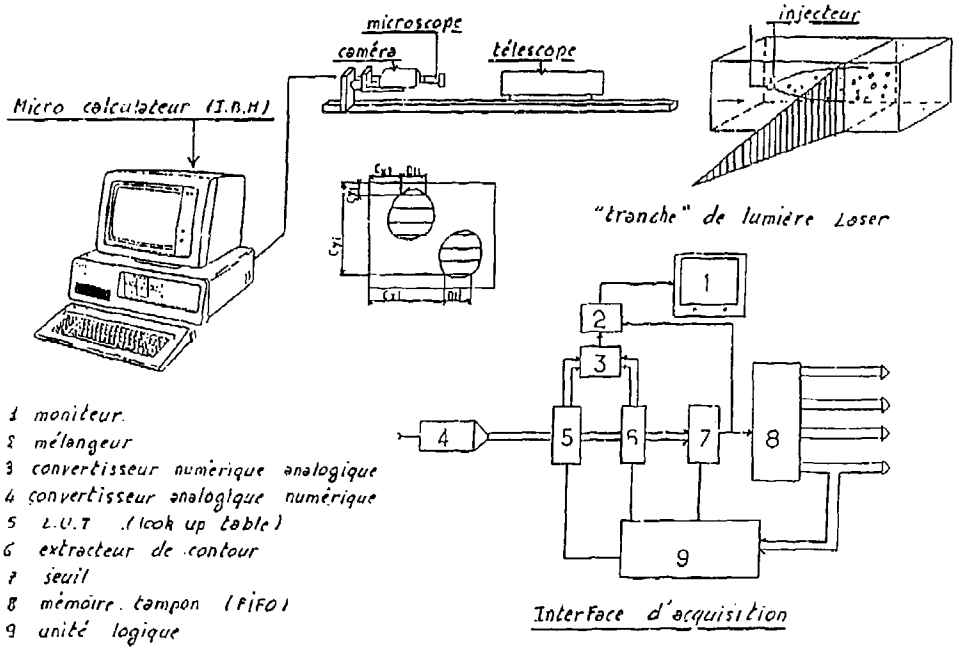

FIGURE 1 : BANC DE GRANULOMETRIE

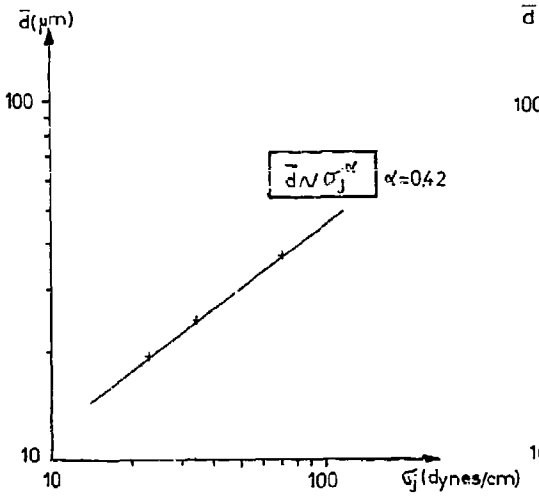

FIGURE 2 : INFLUENCE DE LA TENSION SUPERFICIELLE SUR LE D.M.S.

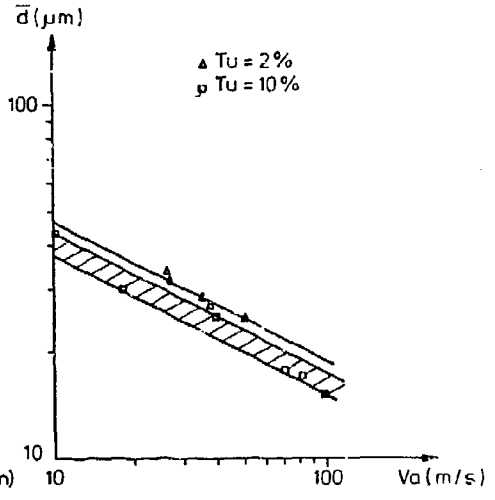

FIGURE 3 : INFLUENCE DE LA VITESSE DE L'AIR SUR LE D.M.S.

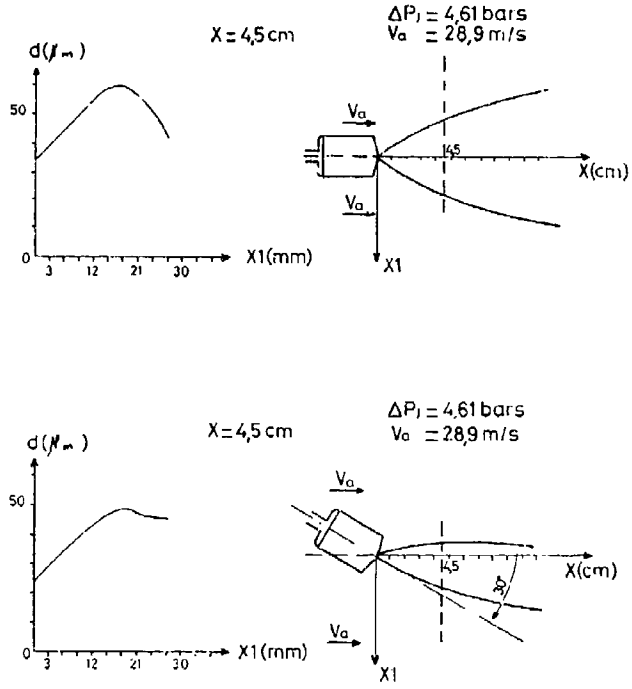

FIGURE 4 : EVOLUTION RADIALE DE D.M.S.

RR $$f(D) = \frac{1}{D}\left(\frac{D}{D_{3v}}\right)^{n-1} e^{-\left(\frac{D}{D}\right)^{n}}$$

TT $$\frac{dn}{n\, d(D/D_{32})} = a\left(\frac{D}{D_{32}}\right)^{\alpha} e^{-b\left(\frac{D}{D_{32}}\right)^{\beta}}$$

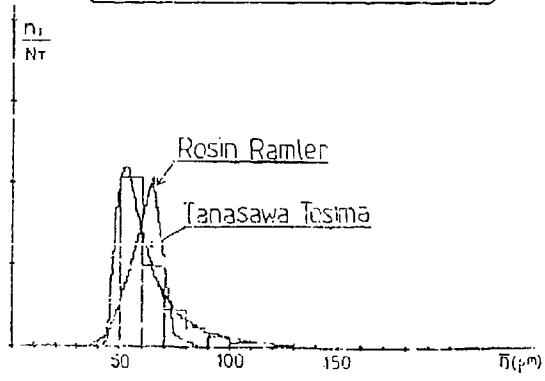

FIGURE 5 : EXEMPLE DE DISTRIBUTION DE TAILLES DE GOUTTES

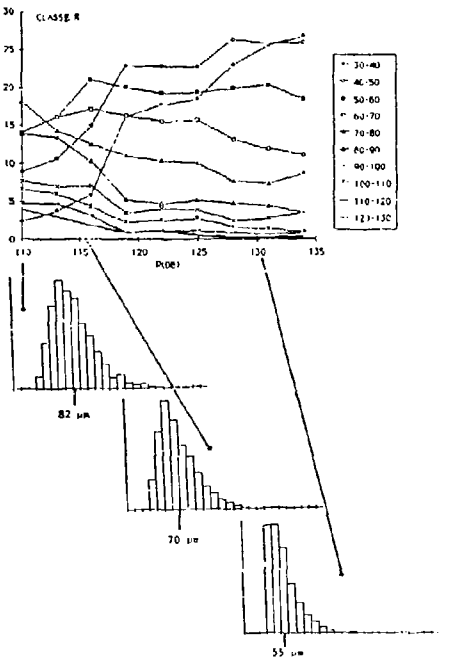

FIGURE 6 : INFLUENCE D'UNE EXCITATION ACOUSTIQUE SUR LA DISTRIBUTION DE TAILLES

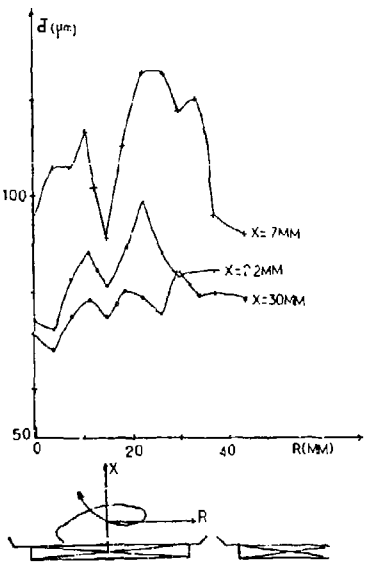

FIGURE 7 : INJECTEUR DOUBLE VRILLE - EXEMPLE DE DISTRIBUTION SPATIALE DE D.M.S.

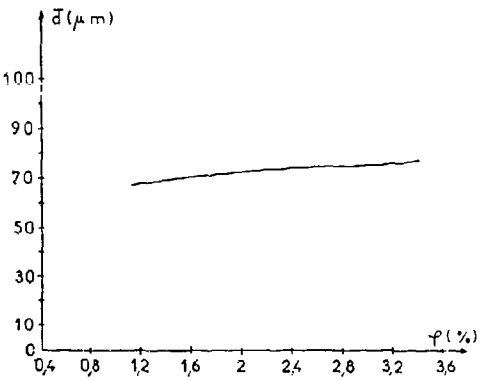

FIGURE 8 : INJECTEUR DOUBLE VRILLE - EVOLUTION DE D.M.S. EN FONCTION DE LA RICHESSE INJECTEE (DEBIT D'AIR CONSTANT)

SONDAGE HORIZONTAL SONDAGE VERTICAL

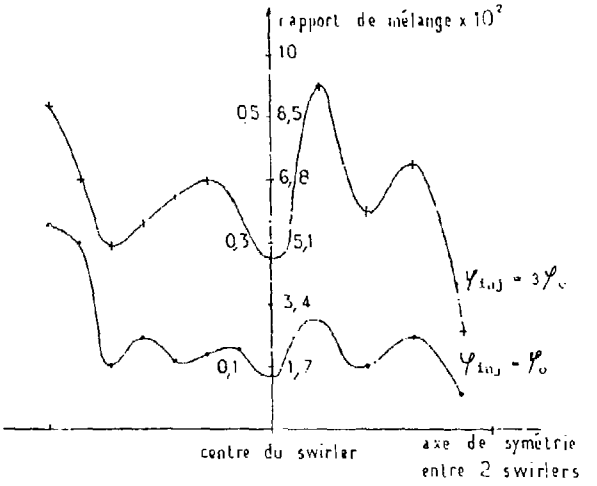

FIGURE 9 : INJECTEUR DOUBLE VRILLE - EXEMPLE DE DISTRIBUTION SPATIALE DE CONCENTRATION DE GOUTTES

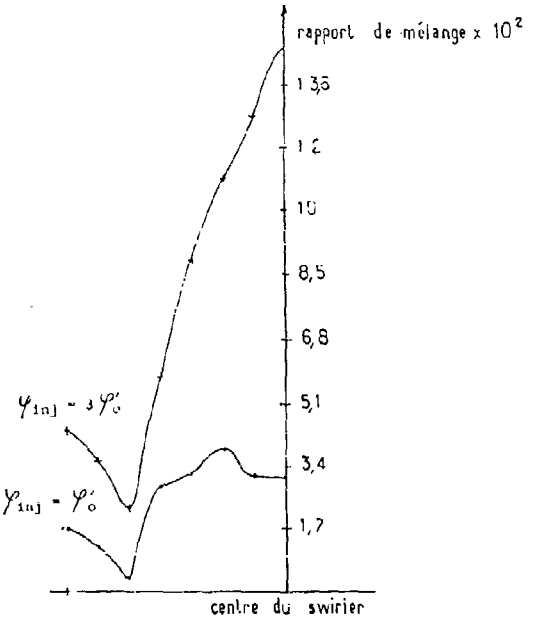

FIGURE 10 : INJECTEUR DOUBLE VRILLE - DISTRIBUTION SPATIALE DE CONCENTRATION DE GOUTTES DANS LE CAS VRILLE EXTERNE FERMEE

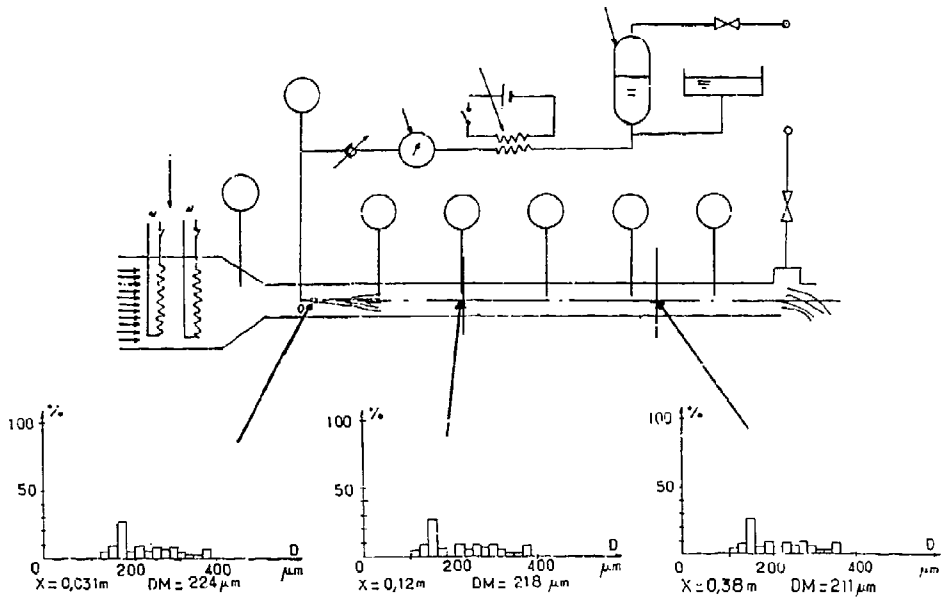

FIGURE 11 : DISPOSITIF EXPERIMENTAL POUR L'ETUDE DE L'EVAPORATION DE GOUTTES D'EAU

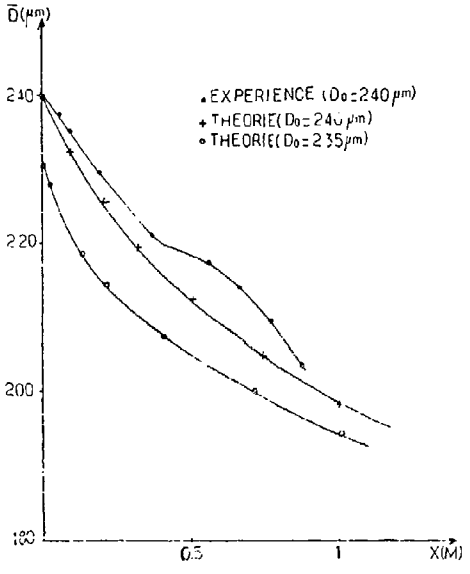

FIGURE 12 : COMPARAISON ENTRE LES RESULTATS EXPERIMENTAUX ET THEORIQUES DE L'EVOLUTION DU D.M.S. AVEC LA DISTANCE A L'INJECTEUR

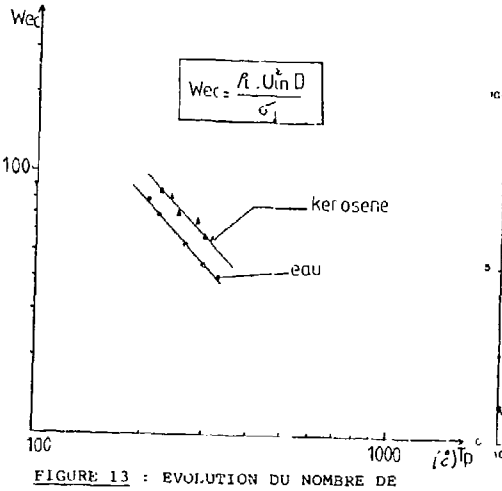

FIGURE 13 : EVOLUTION DU NOMBRE DE WEBER CRITIQUE AVEC LA TEMPERATURE DE

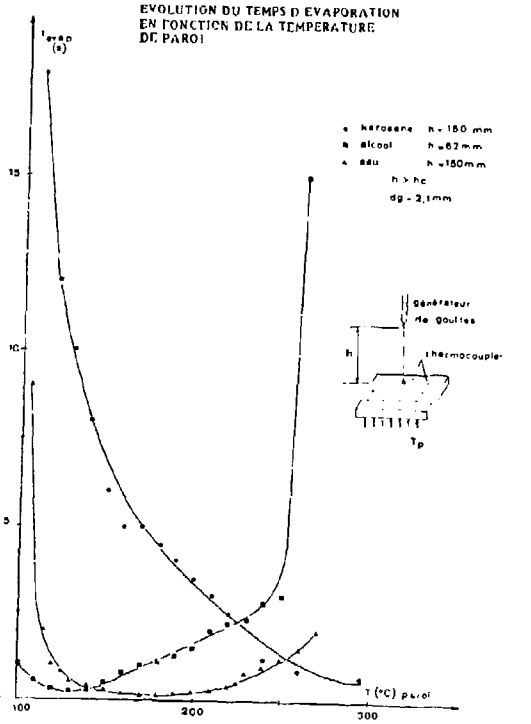

FIGURE 14 : DETERMINATION DE LA TEMPERATURE DE "LEIDENFROST"

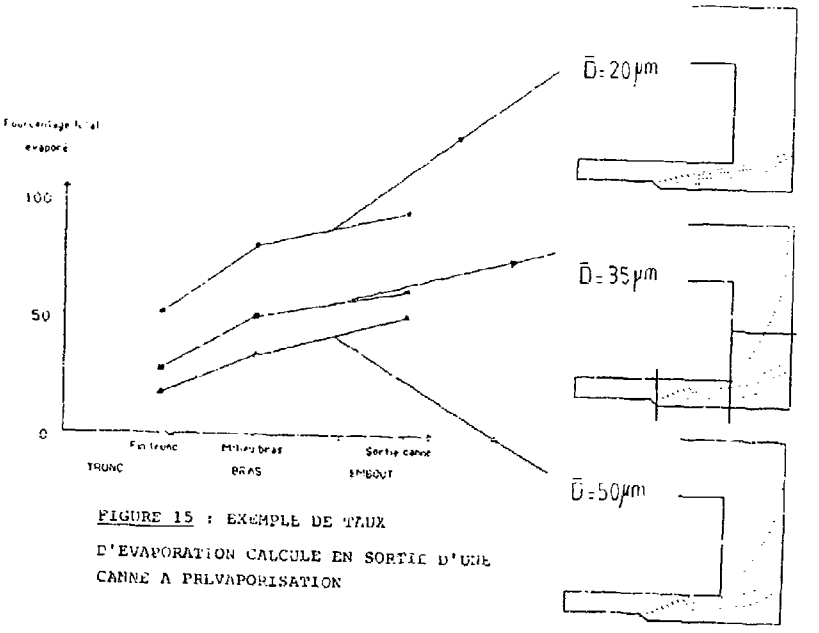

FIGURE 15 : EXEMPLE DE TAUX D'EVAPORATION CALCULE EN SORTIE D'UNE CANNE A PREVAPORISATION

DISCUSSION

A.K.Jasuja, UK

I wish to draw the meeting's attention to the last paper of the day covering spray performance of a vaporiser injector. In our work, which will be reported fully later today, we have also observed high degrees of vaporisation in addition to high degrees of atomization.

A.Lefebvre, US

How important is the quality of atomization in the primary injector upon the quality of atomization leaving the vaporizer?

A.Jasuja, UK

To answer Prof. Lefebvre's question, earlier papers show that the primary atomization is not important.

Turbulence Effects on the Droplet Distribution Behind Airblast Atomizers

by
S. Wittig, W. Klausmann and B. Noll
Lehrstuhl und Institut für Thermische Strömungsmaschinen
Universität Karlsruhe (T.H.)
Kaiserstr. 12, D-7500 Karlsruhe (West-Germany)

SUMMARY

Turbulent fluctuations of the airflow in gas turbine combustion chambers have decisive influence on the mixing of fuel droplets and air both in premixing regions and primary zones.

In the present work, detailed measurements in a recirculating, droplet charged airflow in a combuster model are conducted with an optical diffraction-type particle sizer. These investigations yield information about the local fuel concentrations as well as the local concentration weighted diameter distributions under cold and hot airflow conditions. The spray is produced by a prefilming airblast nozzle, which is built into the combustor model. The calculation of the above-mentioned quantities using a new computational model shows that in considering turbulence fluctuations significant improvement of the results is obtained and excellent agreement between predicted and measured values is achieved. Therefore, the results indicate that turbulence can be one of the major influencing parameters on droplet distribution.

NOMENCLATURE

A	area
B	transfer number
c_D	drag-coefficient
c_p	specific heat
d	depending on droplet diameter
D	drop diameter
D_{10} ; D_{50}	characteristic diameters corresponding to a drop-size distribution, index indicates the % by volume with smaller diameter
F (α)	distribution of droplet volume flow rate over the spray angle
Fr	Frössling factor
h	height
H	latent heat of gasification
i	index for summation
k	index for summation over different size classes
k	kinetic energy of turbulence
K	evaporation rate constant
M (d)	distribution of droplet volume flow rate
n	exponent in the Rosin-Rammler drop size distribution
N	number of drops in a computational cell
Nu	Nusselt number
Pr	Prandtl number
Q	liquid volume fraction with diameter smaller than d
Re	Reynolds number
SC	sample concentration
t	time
T	temperature
u	time averaged velocity component, horizontal
v	time averaged velocity component, vertical
$\dot{V}$	volume flow rate
W	width
x	space coordinate, horizontal
y	space coordinate, vertical
Z	droplet number flow rate, number of droplets leaving the atomization edge per unit time in one direction
α	spray angle
λ	thermal conductivity
ε	dissipation rate of turbulence
ν	viscosity
ρ	density

SUBSCRIPTS

air	corresponding to the air-flow
Boil	boiling point
d	droplet
l	liquid
rel	relative
s	slot

INTRODUCTION

In a large variety of applications concerning fuel atomizers, it is of major importance to match the geometry of the nozzle and the duct with the flow field. This is of special consideration in the combustion of liquid fuels where the proper mixing of air with the fuel dominates the combustion and the formation of pollutant emissions /1/. In the context of a major research program directed towards the understanding of the phenomena governing airblast atomizers, the influence of individual parameters such as the shear stresses driving the film and the pressure gradients etc. has been analysed and correlated yielding the droplet size distribution as generated with these atomizers /1,2,3,4/. In continuing this work, the emphasis of the present study is extended towards the computation of the mixing of the liquid fuel with the air under prototype combustor conditions. Appropriate models are clearly necessary for the selection and arrangement of the atomizers and their matching with the primary as well as the secondary air flow within a flame tube or in premixing regions. For reaching the optimal performance of the atomizer -i.e. the produced droplet size spectra - it is necessary to describe the motion and evaporation of the liquid phase within the flow field.

Up to now, detailed experimental information on the local mixing of fuel droplets with air under conditions found in gas turbine combustors is scarce. The present paper, therefore, describes measurements of the local liquid concentration and the local size distribution of a typical two-phase flow behind an airblast nozzle. The measurements are primarily intended to provide accurate information which could serve as a data base for comparison with numerical codes recently introduced by us as well as by other research groups. One of the dominant questions was whether the interactive coupling of the two phases must be considered in the model. In addition the role of turbulence in the airflow and its effect on the droplet motion is of major interest as this is a key question in typical combustor flow.

EXPERIMENTAL SETUP

A schematic view of the entire test facility for the experimental investigations is given in Figure 1. Compressed air with temperatures up to 600 K is supplied by a compressor via an electrical air heater and passes a settling chamber before reaching the test section with the atomizer. Following the test section, the two-phase flow is separated in a trap-box before entering the exhaust fan. All temperature and pressure signals are recorded by a PDP 11/34 mini-computer.

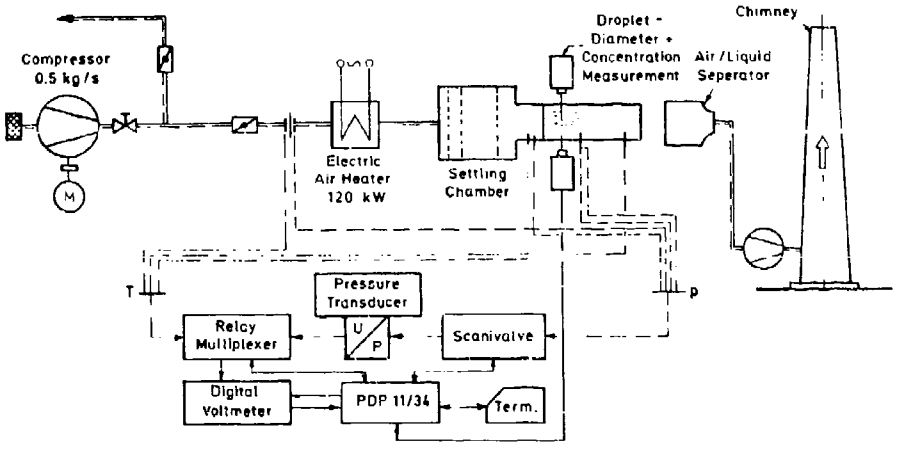

Figure. 1: Test Facility with Data Aquisition

Figure 2 gives a detailed view of the test section which has a cross sectional area of 100 x 300 mm^2. A prefilming airblast nozzle with two-dimensional character is installed into the test section as shown. The airflow passes though four slots, two of which carry the film, and reaches the atomizer edges. The liquid flow is controlled by callbrated volumeters. It is admitted to the atomizer plate's surface via a row of holes perpendicular to the main flow direction, thus poviding homogeneous flow distribution along the plate's surface (Figure. 2). The liquid is driven to the atomization edge by the shear stress at the phase interface. With the aid of a second air stream the liquid film disintegrates to single droplets.

The length of the air gaps is sufficient to ensure fully developed flow conditions near the atomization edge. The relations between the flow parameters within the nozzle and the disintegration of the liquid film, as well ar the formation of droplets under comparable flow conditions are derived from our earlier studies /2,3,4/.

The flow in the combustor model itself is characterized by a recirculation zone induced by the centerbody of the nozzle. Variations of the characteristic geometrical parameters such as the gap and centerbody heights are possible, leading to flow fields with differing recirculation zones. In order to obtain characteristic air velocities for droplet formation, as well as typical flow fields in the combustor model, proper adjustment is required. Volumetric mean velocities in the combustor model in the range from 6 to 18 m/s with corresponding mean velocities at the atomization edge from 30 to 120 m/s were achieved. The liquid mass flow rate was scaled to the air mass flow in a typical range for combustion processes to provide realistic liquid-charged air flows. In addition, high liquid loads ($\dot{m}_{air}/\dot{m}_l$ = 2) were produced to study the influence of the droplets on the air flow.

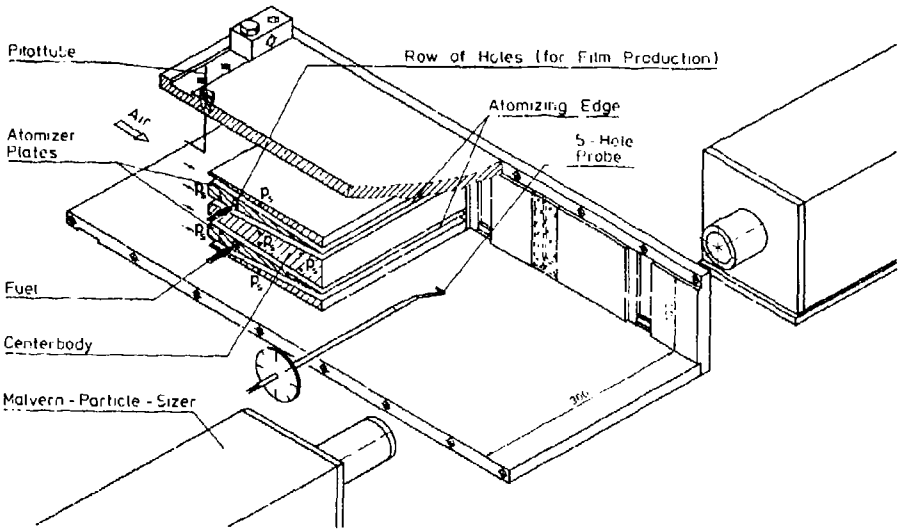

Figure. 2: 2-D Combustor Model

MEASURMENT TECHNIQUE AND DIAGNOSTICS

A systematic approach in analyzing the flow was attempted: In the first step, the flow parameters of the unloaded air jets - i.e. without fuel - at the atomizing edge were recorded in defining the inlet flow conditions. Using a five-hole probe of 2.9 mm OD, profiles of the velocity distribution in the duct were obtaind at eight different axial locations This data is of predominant interest for the verification of the numerical codes, as shown later.

In the second phase, the droplet diameter distribution and liquid concentrations in the loaded air flow were measured using an optical diffraction-type particle sizer (Malvern Type 2600c) /5/. With the laser-beam arranged parallel to the atomization edge (see Figure. 2), the measurements provide the local drop size distribution as well as the liquid concentration, assuming the flow field behind the nozzle is two-dimensional. In order to avoid side wall effects on the droplet motion, only the central regime of the atomization edge (60 mm) was wetted, within a 300 mm wide duct.

Diffraction light measurements of drops in a probe volume over a certain time period provide time-averaged diameter distributions. Due to the velocity differences of droplets with different diemeters, the sampled diameter distribution is biased towards the slower droplets, as previously discussed by us /6/ and confirmed later by Chin et al. /7/. The velocity of each droplet size class, therefore, influences the results of the local diameter distribution, which is weighted by the concentration.

DROPLET MOTION AND EVAPORATION.

It should be noted that the main purpose of the present study was not to provide a new model for the calculation of droplet motion and evaporation. However, using detailed knowlege of the atomization process, a comparison can be obtained between calculated and measured values of local liquid concentration and diameter distribution in turbulent recirculating flows, thus revealing the capabilities of the codes and the importance of the determining parameters. Direct comparison between predictions and measurements are provided.

The air flow field in the combustor model is calculated by utilizing a Finite Volume method as has been frequently applied in solving the time averaged conservation equations for the momentum and the turbulence quantities k and ε. The results of the predictions include the field quantities of the velocity components as well as pressure, temperature and turbulence parameters.

The propagation of a polydisperse spray is described by superposing the trajectories of single droplets. In a two-dimensional arrangement the droplet velocity components and trajectories are calculated in the Lagrangian domain by solving a system of four ordinary differential equations (1-4) /8/:

$$\frac{dx_d}{dt} = u_d \tag{1}$$

$$\frac{dy_d}{dt} = v_d \tag{2}$$

$$\frac{du_d}{dt} = \frac{3}{4}\frac{\rho}{\rho_d}\frac{c_D}{D_d} c_{rel}\,(u - u_d) \tag{3}$$

$$\frac{dv_d}{dt} = \frac{3}{4}\frac{\rho}{\rho_d}\frac{c_D}{D_d} c_{rel}\,(v - v_d) \tag{4}$$

$$c_{rel} = \sqrt{(u - u_d)^2 - (v - v_d)^2} \tag{5}$$

with:

$$c_D = c_D(Re) = 0{,}36 + 5{,}48\,Re^{-0{,}573} + \frac{24}{Re} \tag{6}$$

and

$$Re = \frac{c_{rel}\,D_d}{\nu}$$

The influence of the turbulence of the air can be incorporated by superposing the time mean air velocity and the fluctuating components as presented by Gosman et al. /16/. Local turbulence quantities, therefore, are required. The interaction time of a droplet with an eddy, which is characterized by a random instantaneous velocity, is the lower of two time scales: the eddy dissipation time given by Hinze /11/ and the droplet transit time through an eddy. The transit time is estimated from a simplified linearized equation of motion of the droplet /10/.

The description of droplet heating and evaporation is added to the computational model using two equations. This equations are solved separately assuming that during the first phase the droplet is heated to an equilibrium temperature, followed by the second phase in which the evaporation process causes a decrease in diameter. By neglecting evaporation during the heating phase, the temperature change of the droplet is determined by:

$$\frac{dT_d}{dt} = \frac{6\,Nu\,\lambda\,(T - T_D)}{\rho_d\,c_{p,d}\,D^2} \tag{7}$$

After reaching the boiling point the temperature remains constant and the diameter decreases according to the following equation (see /12/):

$$\frac{dD_d}{dt} = -\frac{K\,Fr}{2\,D_d} \tag{8}$$

$$K = \frac{8\,\lambda}{\rho_d\,c_p}\,\ln(1+B) \tag{9}$$

$$B = \frac{c_p\,(T - T_{d,Rout})}{R} \tag{10}$$

Here 'Fr' present the Froessling factor which describes the enhancement of heat transfer due to forced convection /13/.

$$Fr = 1 + 0{,}276\,Re^{0.5}\,Pr^{0.33} \tag{11}$$

$$Nu = 2\,Fr \tag{12}$$

This factor is comparable to corrections used by other authors in determining the influence of forced convection. It should be mentioned that other evaporation models were tested as well. In the context of the present paper, however, a detailed description is not possible.

MODELLING A SPRAY.

In modelling a spray, the liquid volume flow is distributed over the various initial conditions at the atomization edge. For each combination of initial conditions at least one trajectory is calculated. Experimental results show that the liquid volume concentrations follow a normal distribution over the spray angle F(α) /3/. For each initial direction, the volume flow is divided into specified size classes according to a diameter distribution function M(d). A series of previous investigations at our Institute have shown the correspondence between the air flow parameters of comparable nozzles and the resulting droplet size spectra. Information concerning the spray angle has also been provided /2,3,4,15/. Measurements of the liquid film thickness /3/, along with the liquid flow rate, provide the mean volumetric film velocity. The initial velocity of the drops is assumed to be close to the film velocity. Thus the distribution of the liquid volume flow leads to a droplet number flow rate Z for each trajectory:

$$Z\,(d,\alpha) = F(\alpha)\,M(d)\,\frac{\dot{V}_l / W}{\pi/6\,D^3} \tag{13}$$

The droplet number flow rate determines the number of drops leaving the atomizing edge per unit time and unit width in a specific angle and diameter range. A typical set of initial conditions is given in Figure 3. In this way, 'a group of trajectories (here 210 trajectories)' results from the computation of one trajectory for each initial condition.

In calculating the local diameter distributions and concentrations, the placement of 'observation cells' correspond to the measuring positions as shown in Figure 4.
For all observation cells, the transit times of the droplets are determined. The number of droplets in a particular diameter class in one cell can then be calculated using the drop number flow rate and the corresponding transit time (14):

$$N(d) = \sum_{i=1}^{i_{max}} (Z\,(d,\alpha_i)\,\Delta t_i) \tag{14}$$

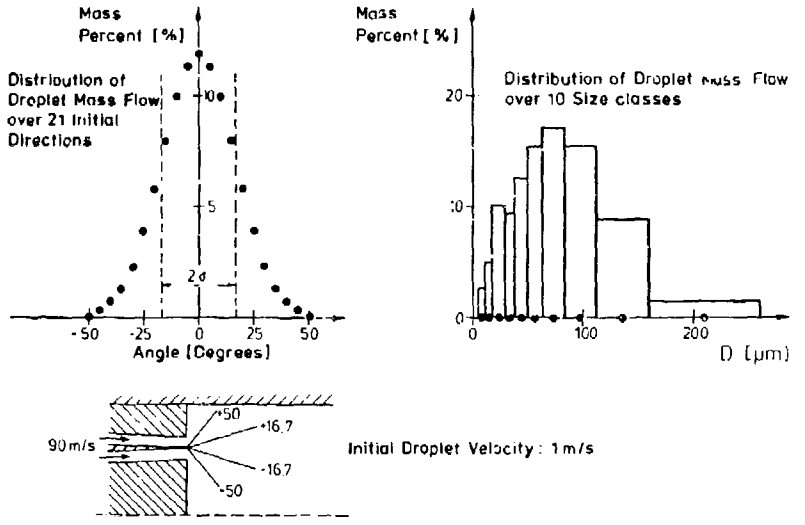

Figure 3. Droplet Initial Conditions

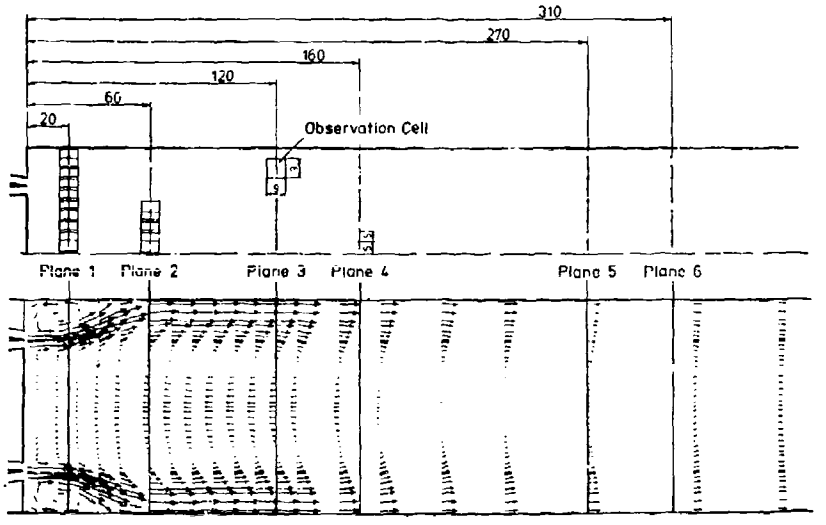

Figure 4: Position of Measurement Planes and Observation Grid

As the diameter along the trajectory decreases, the number N(d) of the droplets is related to the corresponding (lower) size class. The values of N(d) are used to determine the liquid concentration in the observation cells (15):

$$SC = \sum_{k=1}^{k_{max}} \left(N\,(d_k)\, D_k^2 \frac{\pi}{6\,A\,W} \right) \tag{15}$$

After the spray calculation is completed - i.e. 'a group of trajectories' is determined - the weighting factor for the liquid volume in each diameter range is calculated for each observation cell (16):

$$W\,(d) = \frac{N\,(d)\,D^3}{\sum_{k=1}^{k_{max}} N\,(d_k)\,D_k^3} \tag{16}$$

Local diameter distributions can be calculated by fitting a diameter distribution curve to the summed values of W(d). Here, the well known Rosin-Rammler diameter distribution is used (17).

$$Q = 1 - exp\left(-\left(d/d_{63.2}\right)^n\right) \tag{17}$$

Two characteristic diameters are needed to completely define the chosen diameter distributions. In presenting the results, the volumetric mean diameter D_{30} and a characteristic diameter for small droplets D_{10} are used. Again it should be noted that the calculated distributions as well as the measured distributions depend on the velocity in each size class.

In considering turbulent fluctuations, the computation of one trajectory for each initial condition is insufficient. Despite similar initial conditions, turbulence leads to different trajectories. For realistic results, a larger number of trajectories for each initial conditions - i.e. several 'groups of trajectories' - must be considered. After each complete calculation of a 'group of trajectories', the mean value of the liquid concentration is determined taking into account the data from preceding runs. This process is repeated until the difference between the mean values in each observation cell is within a chosen tolerance. The diameter distribution is then calculated using the above curve-fitting method.

RESULTS

As has been shown, local flow field parameters are required in predicting the droplet motion. This data is obtained using a two-dimensional Finite Volume method as indicated earlier. Accurate calculations of the flow field, therefore, are a necessity.

AIR FLOW FIELD

Data obtained by the measurements in eight different planes are shown in Figure 5 along with the corresponding calculations. These results reveal the typical air flow field in the model combustor. High velocities are obtained behind the gaps of the nozzle and a recirculation zone is present with high velocity gradients. Further downstream, the velocity gradients decrease rapidly and a nearly parallel flow field is obtained at the chamber exit. In the calculations a 28*31 computational grid is employed along with the QUICK-scheme /17/ for the discretization of the convection terms in the momentum equations. This scheme is completely free of numerical diffusion. As can be seen from Figure 5, the agreement between measurement and calculations is quite encouraging. The high velocity gradients observed in the initial planes are accurately calculated. The velocities within the recirculation zone are slightly underpredicted. Comparisons of predicted and measured flow fields with different boundary conditions, for example, different gap heights or air mass flow rates show comparable results. Together with detailed measurements over the chamber width, the results verify the existence of a two-dimensional air flow field with a closed recirculation zone in the combustor model. After verification of the two-dimensionality, it is possible to take local measurements of the dispersed droplets.

DROPLET SIZE MEASUREMENTS

As shown in Figure 4, droplet size measurements were taken at six planes located downstream from the nozzle as indicated: The first four planes are located in the region with strong forward and reverse flow. The study of the droplet-charged airflow was performed in two phases. First, in analyzing the droplet motion detailed measurements were taken using water as the experimental liquid. In the second step, Ethanol was used under cold and hot air flow conditions to study the evaporation processes.

The experiments with water demonstrate that the local liquid concentrations are proportional to the liquid flow rate under constant inlet air velocities and geometric

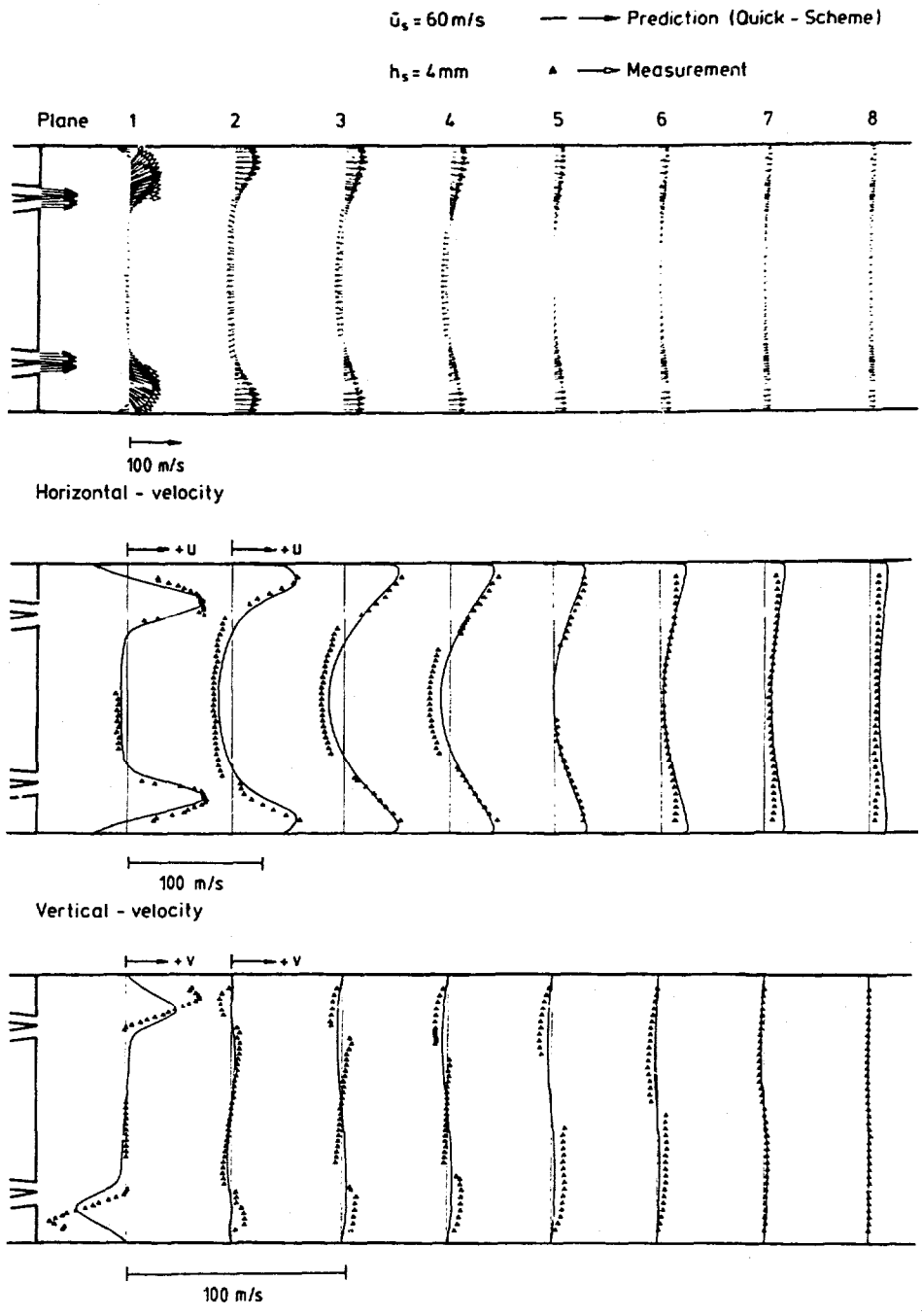

Figure 5: Comparison between Predicted and Measured Flow Field Parameters

conditions. As the liquid concentration depends largely on the droplet velocity, which in turn is a function of the air velocity, it follows that the air flow field is not altered by higher liquid flow rates. In other words, the momentum transfer to the air from the droplets is small under the conditions chosen. Based on these results, the effects of the droplets on the air flow are neglected in the following analysis. However, close attention is paid to the influence of the air turbulence on the droplet motion.

In extending the measurements, Ethanol was used as the test fluid due to its high evaporation rate. The local liquid concentrations in the combustion chamber at an air temperature of 320 K are presented in Figure 6 with the highest concentrations occuring close to the atomization edge. The concentration decreases rapidly toward the center of the chamber (recirculation zone). Furthermore, the concentration becomes more uniform over the chamber height. Along with the measurements, results are presented from calculations of 210 trajectories for a 'group of trajectories'. Here, turbulence fluctuations are not yet considered. As can be seen, the concentrations within the outer regions of the duct are overpredicted whereas zero concentrations are obtained in the recirculation zone.

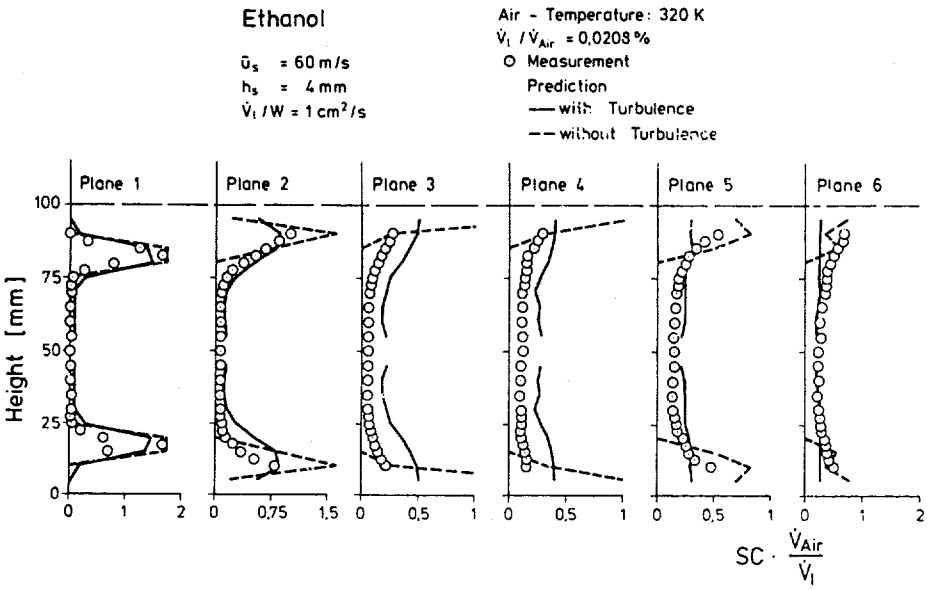

Figure 6: Predicted and Measured Local Liquid Concentrations - Influence of Turbulence

The predictions are clearly improved by the inclusion of turbulent fluctuations. Concentrations and gradients calculated by the computational model described above, show good agreement with measurements. Local diameter distributions can only be calculated when turbulence is considered: The turbulent fluctuations, together with a higher number of calculated trajectories, provide a sufficient number of droplets in each size class in the observation cells. A comparison of predicted and measured diameter distributions is given in Figure 7. As shown by the characteristic diameters D_{10} and D_{50} the recirculation zone is predominantly occupied by smaller droplets because of the turbulent dispersion, while the forward flow region is dominated by larger droplets. The initial conditions at the atomizer were determined using our earlier correlations /15,18/. With 60 m/s mean air velocity at the atomization edge and using the surface tension of Ethanol, the initial drop-size spectrum is described by the characteristic parameters D_{10} = 19 µm and D_{50} = 52 µm. Measurements as well as calculations reveal changes in the local size distribution relative to the initial size distribution, which is caused by different inertia of the various drop size classes. The good agreement of predicted and measured diameter distributions shown in Figure 7, in addition, indicates accurate predictions of the local droplet velocities in each size class. The width of the local size spectra in each measuring plane is illustrated by the distance between the lines of the characteristic diameters. As indicated in Figures 6 and 7 the droplet motion can be calculated with sufficient accuracy as long as turbulent fluctuations are taken into account.

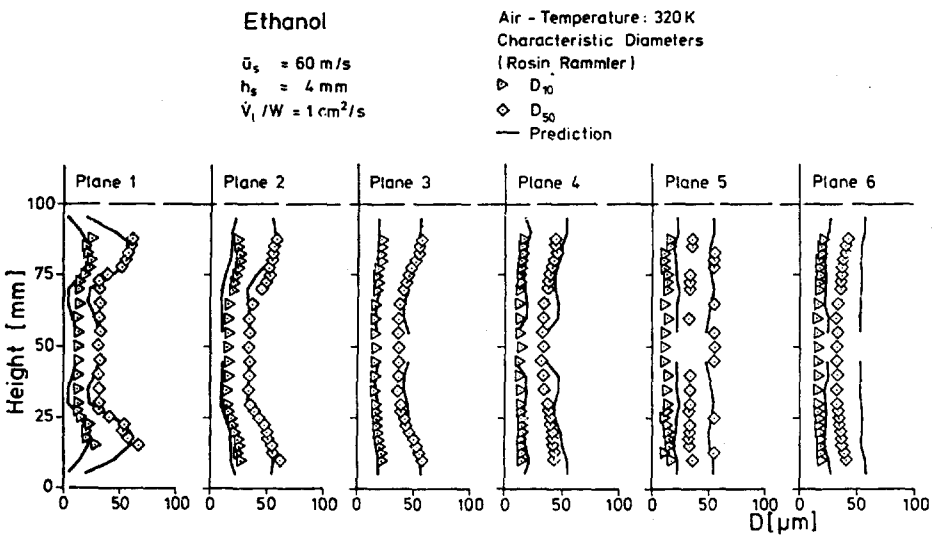

Figure 7: Local Diameter Distributions - Prediction and Measurement

Similar measurments were made under identical geometric conditions at an elevated temperature level (520 K). Due to the lower density of the driving air the size spectrum of the droplets produced is shifted towards larger diameters (D_{10} = 25 µm and D_{50} = 65 µm) according to the relation $D \sim (1/\rho_l)^{0.5}$as already mentioned by other authors /18,19/. Figure 8 illustrates the typical behaviour of two evaporating droplets, water and Ethanol, at 520 K under simplified flow conditions. It is clear from this example that the diameter decreases rapidly for Ethanol within the length of the test section (400 mm).

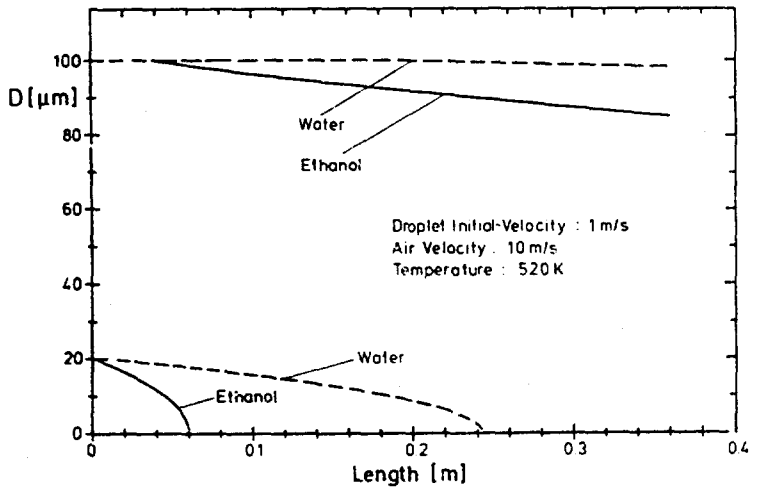

Figure 8: Evaporation of Water and Ethanol Droplets

For hot air flow conditions local size distributions within the combustion chamber obtained from computations and measurements are compared in Figure 9. The drop size distributions in this Figure show larger characteristic diameters than under cold flow conditions. One reason for this is that the initial diameters are larger and in addition, the smaller droplets evaporate faster. The computational results presented, again account for turbulent fluctuations. The computation of the local diameter distribution at the elevated temperature, indicating that the employed evaporation model is of sufficient accuracy at the conditions chosen .

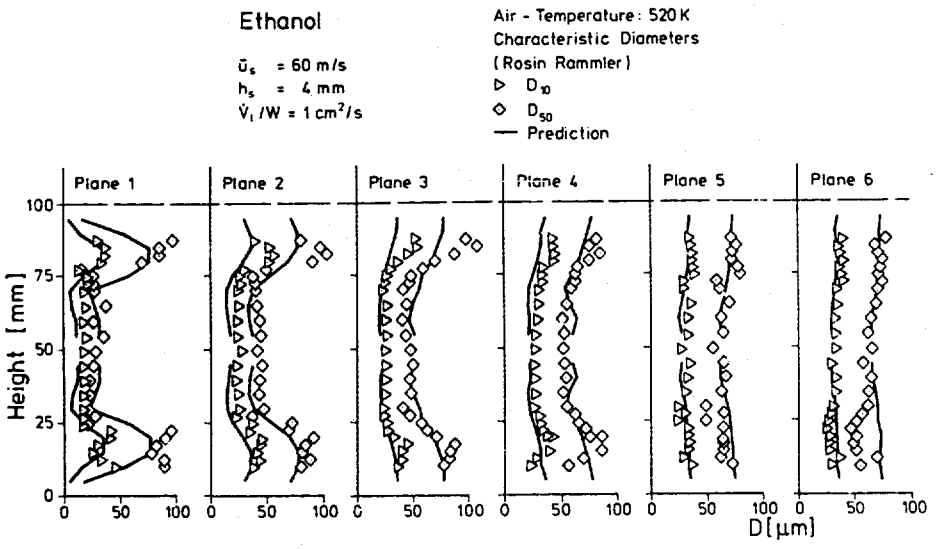

Figure 9: Local Diameter Distributions

CONCLUSIONS

The results of the present study illustrate that in utilizing well-known principles in describing the droplet motion and evaporation the important parameters of the typical combustor two-phase flow can be accurately computed. Detailed measurements confirm the chosen methodology: The numerical code allows the calculation of the motion and evaporation of droplet clouds in the turbulent flow field starting from the initial conditions determined by the fuel nozzle. In addition, local fuel vapor sources can be obtained in the entire flow regime which can be used for subsequent combustion calculations. Good agreement between experiment and theory has been obtained over a broad range of parameters, i.e. temperature , flow velocities and fuel concentration.

ACKNOWLEDGMENTS.

Thanks are due to the Forschungsvereinigung Verbrennungskraftmaschinen, e.V. for initiating this research program on 'Zerstäubung und Gemischaufbereitung in Gasturbinenbrennkammern' (Atomization and Air-Fuel Mixing in Gas Turbine Combustors) and to the Deutsche Forschungsgemeinschaft DFG (German National Science Foundation) for its support on various aspects of the study within the larger context of the 'Sonderforschungsbereich SFB 167, High Intensity Combustors'.

REFERENCES

/1/ Wittig, S.; Kutz, R.; Steinebrunner, K. (1985):
Einfluß des Strömungsfeldes und der Brennstoffzerstäubung
auf die Schadstoffemissionen aus ölgefeuerten Kleinbrenneranlagen.
VDI-Berichte Nr. 274, 12. Deutscher Flammentag, Karlsruhe 1985

/2/ Sattelmayer, Th. (1985): Zum Einfluß der ausgebildeten, turbulenten Luft-Flüssigkeitsfilm-Strömung auf den Filmzerfall und die Tropfenbildung am Austritt von Spalten geringer Höhe. Dissertation, Universität Karlsruhe

/3/ Sattelmayer, Th.; Wittig, S. (1986): Internal Flow Effects in Prefilming Airblast Atomizers: Mechanisms of Atomization and Droplet Spectra. Transactions of ASME (86-GT-150)

/4/ Wittig, S.; Sattelmayer, Th.; Aigner, M.; Sakbani, K. (1985): Strömungsvorgänge und Tropfenbildungsmechanismen in luftgestützten Zerstäubungsdüsen. Brennstoff Wärme Kraft; Band 37; Nr. 10 Oktober 1985

/5/ Swithenbank, J.; Beer, J.M.; Taylor, D.S.; Abbot, D.; Mc Greath, C.G. (1977): A Laser Diagnostic Technique for the Measurements of Particle Size Distribution. AIAA, Prog. in Astron. and Aeron., Vol. 5

/6/ Wittig, S.; Aigner, M.; Sakbani, K.; Sattelmayer, Th. (1983): Optical Measurements of Droplet Size Distribution. Special Considerations in the Parameter Definition of Fuel Atomizers. ARGARD, 62nd PEP-Symposium on Combustion Problems in Turbine Engines, Turkey, Conference-Proceedings No. 353

/7/ Chin, J.S.; Nickolaus, D.; Lefebvre, A.H. (1986): Influence of Downstream Distance on the Spray Characteristics of Pressure-Swirl Atomizers. Journal of Engineering for Gas Turbines and Power; Vol. 108; p. 219 - 224

/8/ Noll, B.E. (1986): Numerische Berechnung brennkammertypischer Ein- und Zweiphasenströmungen. Dissertation, Universität Karlsruhe

/9/ Stein W.A. (1973): Berechnung der Verdampfung von Flüssigkeiten aus feuchten Produkten im Sprühturm. Verfahrenstechnik 7, Nr.9 1973

/10/ Gosman, A.D.; Ioanides, E. (1983): Aspects of Computer Simulations of Liquid-Fueled Combustors. Journal of Energy, No. 7, p. 483-490

/11/ Hinze, J.O. (1975): Turbulence; McGraw-Hill

/12/ Law, C.K. (1982): Recent Advances in Droplet Vaporization and Combustion. Prog. Energy Combustion Sci.; Vol. 8; p. 171-201

/13/ Frössling, N. (1938): Über die Verdunstung fallender Tropfen. Gerlands Beiträge zur Geophysik; Band 52; Leipzig: Akademische Verlagsgesellschaft

/14/ Faeth, G.M. (1977): Current Status of Droplet and Liquid Combustion. Prog. Energy Combustion Sci.; Vol. 3

/15/ Aigner, M.; Wittig, S. (1985): Performance and Optimization of an Airblast Nozzle: Drop Size Distribution and Volumetric Air Flow. Proceedings of the International Conference on Liquid Atomization and Spray Systems, p. IIC/3,1-8 London

/16/ Björk; Dahlquist (1979): Numerische Methoden 2. Auflage; Oldenburg Verlag GmbH, München 197-, p. 254

/17/ Leonard, B.P. (1979): A Stable and Accurate Convective Procedure based on Quadratic Upstream Interpolation. Computer Methods in applied Mechanics and Engineering 19, 59

/18/ Aigner, M. (1986): Charakterisierung der bestimmenden Einflußgrößen bei der luftgestützten Zerstäubung: Physikalische Grundlagen und meßtechnische Erfassung. Dissertation, Universität Karlsruhe

/19/ Aigner, M.; Wittig, S. (1987): Swirl and Counterswirl Effects in Prefilming Airblast Atomizers Transactions of ASME (87-GT-204)

DISCUSSION

G.Faeth, US

I have a suggestion. Your calculation method assumes Stokes flow, which most droplets do not satisfy. In our work we have found it easier to calculate trajectories by determining the interactions from the full drag characteristics of the flow and you might want to try that.

J.Peters, US

Could you comment on any corrections needed when using the forward scattering system while evaporation was occurring?

Author's Reply

We used the corrections for the lower angles.

NOZZLE AIRFLOW INFLUENCES ON FUEL PATTERNATION

T. J. Rosfjord
Senior Research Engineer
United Technologies Research Center
East Hartford, Connecticut 06108 USA

W. A. Eckerle
Associate Professor
Clarkson University
Potsdam, New York 13676 USA

SUMMARY

The velocity and turbulence levels downstream of eight variations of a model gas turbine, aerating, fuel nozzle have been measured. The nozzle configurations were assemblies which purposefully altered the airflow through the nozzle by mis-aligning swirlers, changing the number of vanes in a swirler or contouring swirl vane trailing edges. Data were acquired by a traversing, two-component laser velocimeter in planes 0.060 in. and 2.50 in. downstream from the nozzle exit. Analyses of these data indicated that very symmetric flowfields can be produced. Such control was easier to achieve for the airflow than the fuel, supporting the position that nozzle patternation quality is more dependent on the fuel distribution in the nozzle. The presence of swirler wakes could always be discerned at the nozzle exit; the extreme variations imposed by coarse swirlers could dominate the flow. Such airflow influences were not apparent in the velocity profiles at downstream locations. However, their influence in convecting a higher fuel mass flux persisted from the nozzle exit and produced extreme variations in the spray pattern.

INTRODUCTION

Gas turbine combustors are complex devices. While apparently mechanically simple, they contain a very hostile environment; pressures exceed 20 atmospheres and temperatures exceed 4000 F. The flow is multi-phase, three-dimensional, turbulent, at times grossly unsteady, and reacting. Advances in computational fluid dynamics are helping to understand the role of key processes in the burner but to date this knowledge is not sufficiently based to permit final definition of the device without developmental testing. The spray formed by the fuel nozzle can exhibit a strong influence on the performance, durability and operability of the combustor. Highly-atomized, well-distributed sprays are desired both to achieve high performance levels and to avoid temperature regions which might distress components of the burner and turbine. In contrast, some level of fuel-air non-uniformity is necessary to achieve adequate light-off and stability characteristics. It is not known how to specify the spray requirements to satisfy all these demands. Further, even if limited criteria were established, a complete set of nozzle design guidelines does not exist which would assure meeting the goals.

Most modern gas turbine combustor systems use an aerating fuel nozzle. In such a device, the fuel is injected as a thin annular sheet with high velocity airflows adjacent to both the inner and outer surfaces of the sheet. Unlike a pressure-atomizing nozzle, the aerating nozzle (sometimes referred to as an airblast nozzle) does not rely upon achieving a high fuel velocity, as produced by a high fuel path pressure loss, to atomize and distribute the liquid. Rather these responsibilities are assigned to the airflows which shear the fuel film and carry the droplets along the airflow trajectory. The airflows are driven by the pressure drop established by the combustor liner; for a nominal 3-pct-loss liner, airflow velocities in excess of 350 ft/sec would be produced at a high power condition. Because the aerating nozzle performance principally depends on the airflow and not the fuel flow, it has demonstrated the ability to achieve high levels of atomization for wide ranges of fuel flowrate and with relative insensitivity to the properties of the fuel. Both of these features represent distinct advantages over the pressure-atomizing nozzle. In contrast, the aerating nozzle promotes a coupling between the air and fuel flowrates which can be disadvantageous. For example, atomization and distribution are harder to achieve at light-off conditions, and this coupling could result in undesirable heat release profiles for transient operation. Since the nozzle uses a delicate balance of air and fuel momenta to achieve atomization and distribution characteristics, it also displays a greater sensitivity to improper design and manufacturing practices; non-symmetric sprays can easily result.

A previous UTRC study, sponsored by the USAF Aero-Propulsion Laboratory and USN Naval Air Propulsion Center, documented the influences of design and manufacturing practices on the circumferential uniformity of the spray formed by an aerating nozzle.

Detailed liquid patternation data were acquired for 33 nozzle configurations including nine which purposely imposed alterations on the nozzle airflow patterns. This paper reports the results of a complementary study which focused on measuring the airflow velocities for eight of those airflow configurations, and relating the results to the fuel patterns produced by them. Data were acquired for the three velocity components, the normal turbulent stresses and, for some cases, the correlated Reynolds stress in planes 0.060-in. and 2.50-in. downstream from the nozzle exit.

PREVIOUS STUDY

The sensitivity of aerating nozzle performance to design and manufacturing practices was studied at UTRC by documenting the spray patterns produced by a Baseline and 32 other configurations of a model aerating nozzle (Ref. 1). Detailed patternation data were acquired by use of a unique sampling system to determine critical influences on spray circumferential uniformity. The model nozzle used in this study (Fig. 1) was sized as a nomimally 850 lb/hr fuel flow device which delivered inner and outer clockwise swirled airstreams on either side of the annular fuel sheet. Alternative forms of each of the seven components indicated in the figure were assembled to provide the 33 configurations. Fuel, delivered to the nozzle by two 0.050-in. ID tubes, filled the plenum formed by the core air pipe and swirl chamber. Clockwise swirl was imparted to the fuel by passing it through a swirler constructed from a metal ring with six equally-spaced, canted slots machined on the outer edge. The swirler and swirl chamber components were machined and piloted to avoid flow past the endwalls. The fuel exit area ("pinch point gap") was defined by the tip of the core air pipe and the position of the filming lip of the swirl chamber. A spacer provided the means to alter this gap, with different thickness devices directly changing the gap width and wedge-shaped spacers producing misaligned components. The outer airflow was swirled by curved vanes with a final turning angle of 50 deg. The endcap imparted a radial-inflow component to this stream; a velocity vector normal to the minimum flow area formed a 60-deg angle with the nozzle axis. The inner swirler also contained 50-deg vanes. The core air pipe exit was a 0.44-in. dia circular area; the aircap exit was a 0.91-in. dia circle.

The configurations studied imposed alterations on eight nozzle features including: (1) Fuel exit annulus, (2) Fuel swirl chamber angular alignment, (3) Fuel filming lip shape, (4) Fuel filming lip imperfections, (5) Fuel swirler strength and obstruction, (6) Number of airflow swirler vanes, (7) Outer airflow swirler angular alignment, (8) Outer airflow swirler trailing edge shape.

A detailed discussion of the role of each of these alterations on fuel circumferential uniformity can be found in the above reference. In general, it was concluded that the fuel exit annulus was a critical feature in achieving symmetric spray patterns. A very uniform gap was required to achieve a high quality spray; non-uniform gaps resulted in non-symmetric sprays which could not easily be corrected by airflow alterations. Such gap variations were produced either by translating the core air pipe or by ovalizing its exit shape (Fig. 2). Results from these and other configurations were the basis of the conclusion that the concentricity of a nominal 0.040-in. wide gap ought to be controlled to within 0.002 in. and component angular misalignments kept below 2 deg to produce acceptable patterns. While these tolerances may be easy to achieve in the nozzle design, manufacturing and assembly practices must assure retaining them. Airflow influences had a generally lesser impact on fuel patternation although severe non-uniformities can be imposed by poorly designed airflow management components.

These several features are illustrated in Fig. 3 which contains contour plots of sprays formed by the Baseline (Fig. 3a), an ovalized fuel gap configuration (Fig. 3b), a mis-aligned aircap configuration (Fig. 3c) and an altered outer airflow swirler configuration (Fig. 3d). The Baseline contained symmetric components, aligned to the best degree achieved in the study, with the ovalized unit containing a core air pipe as shown in Fig. 2. The deviations of the major and minor axes from circular produced a fuel gap variation of 0.040 +0.003/-0.002 in. The outer aircap was mis-aligned by 2.5 deg in the third configuration. The fourth configuration resulted from removing alternate vanes from the 14-vane outer air swirler. The contour plots represent the fuel mass flux distribution in a plane 2.5-in. downstream from the nozzle as obtained in tests with the UTRC Ambient Spray Test Facility. The fuel and air flowrates used were scaled from a high power condition by both matching the air velocity and perserving the fuel-to-air momentum ratio. An automated patternation system (Ref. 2) collected samples at ten radial positions for 10-deg increments around the spray; 360 samples were collected in the 2-in. dia spray. The contour plots of Fig. 3 display lines of equal fuel mass flux. The quality of circumferential uniformity achieved in the spray was assessed by considering the variation of the fuel flux contained in a 45-deg sector of the spray; the consideration of this and other criteria are discussed in Ref. 2. Near axi-symmetric spray patterns were acheived for the Baseline while gross non-uniformities resulted from seemingly minor variations of the fuel gap. Comparison with a nozzle manufacturing acceptance limit, indicated that the Fig. 3b pattern was marginally unacceptable. This

and other results led to concluding that fuel gap concentricity must be controlled to within 0.002 in. The mis-aligned aircap appeared to divert the fuel off axis while the pattern produced by the altered airflow swirler configuration displayed seven regions of high fuel mass flux in direct correspondence with the removal of the seven swirler vanes. The spray quality criteria would not accept the diverted airflow pattern but pass the "seven-island" profile. These last two assemblies were among those which emphasized an airflow variation. Detailed study of the airflow directly ought to aid in interpreting these liquid fluxes; that was a goal of the complementary study.

It should be noted that the influence of airflow on a spray pattern is not limited to an aerating device. That is, while a pressure-atomizing nozzle primarily depends on the fuel pressure drop for atomization and distribution, airflow influences can be present. Figure 4 depicts fuel mass flux contours for an in-service aircraft duplex nozzle when evaluated with fuel spray alone and with both spray and a minute airflow directed across the nozzle face. This latter airflow is commonly used to prevent mists from wetting the nozzle and building carbon deposits. In this case, the airflow was 0.1 pct of the total airflow to this can combustor. More importantly, this anti-carboning air was directed by a cap which was secured to the nozzle by six short struts. The influence of this "minor" airflow and the presence of these struts is quite evident in the second spray pattern.

TEST PROGRAM

The focus of this effort was to measure and interpret air velocity and turbulence levels for the model nozzle configurations which imposed variations on the nozzle airflow. The alterations emphasized the following three features (Baseline and altered components are indicated).

1. Airflow Alignment
   a. Baseline: Perfectly axially aligned
   b. Variation: Endcap and outer swirler were canted 2.5 deg from the nozzle axis
2. Number of Swirler Vanes
   a. Baseline: Inner-6 vanes; outer-14 vanes
   b. Variation: (1) Three-vane inner swirler achieved by removing alternate blades. (2) Seven-vane outer swirler swirler achieved by removing alternate blades. (3) Tandem combinations of six vane swirlers.
3. Air Swirler Trailing Edge Shape
   a. Baseline: Rounded trailing edge
   b. Variation: (1) Square or (2) knife-edge shape

Including the original Baseline and a modified-Baseline to accept the tandem core swirlers (2.b.3 above), eight nozzle assemblies were documented. The test apparatus used in this study consisted of a conventional air supply system, a velocimeter system, and a precision positioning system. All of the tests were conducted in the UTRC Jet Burner Test Stand with the airflow discharging into the atmosphere; the nozzle airflow pressure drop was held constant at 7-in. H_2O. Measurements included axial, radial and tangential velocities and normal turbulent stresses; in some cases correlated axial-radial and axial-tangential Reynolds stress were also obtained. These measurements were performed along 5-deg increment circumferential traverses at typically nine radial positions. Such measurements were performed in a plane 0.060-in. downstream of the nozzle for every configuration; they were also obtained in a plane 2.5-in. downstream for limited configurations. Table 1 indicates the type and location of data acquired for the eight configurations; the identification number is the one retained from the original liquid patternation study.

Table 1 Airflow Data Sets

Configuration	Data Plane, z (in.)	Data Type
1. Baseline	0.060, 2.50	$U_z, U_r, U_\theta, u_z', u_r', u_\theta', \overline{u_z'u_r'}, \overline{u_z'u_\theta'}$
8. Mis-aligned endcap	0.060	$U_z, U_r, U_\theta, u_z', u_r', u_\theta'$
18. Reduced outer vanes	0.060, 2.50	$U_z, U_r, U_\theta, u_z', u_r', u_\theta'$
17. Reduced inner vanes	0.060, 2.50	$U_z, U_r, U_\theta, u_z', u_r', u_\theta'$
23. Extended core Baseline	0.060, 2.50	$U_z, U_r, U_\theta, u_z', u_r', u_\theta', \overline{u_z'u_r'}, \overline{u_z'u_\theta'}$
31. Tandem inner swirler	0.060	$U_z, U_r, U_\theta, u_z', u_r', u_\theta', \overline{u_z'u_r'}, \overline{u_z'u_\theta'}$
19. Square-edge outer swirler	0.060	$U_z, U_r, U_\theta, u_z', u_r', u_\theta', \overline{u_z'u_r'}, \overline{u_z'u_\theta'}$
20. Knife-edge outer swirler	0.060	$U_z, U_r, U_\theta, u_z', u_r', u_\theta', \overline{u_z'u_r'}, \overline{u_z'u_\theta'}$

The velocity measurements were made using a TSI Model 9100-7, two channel velocimeter. A two-watt argon-ion laser was used with frequency shifting by Bragg cells in both the blue and green beams to permit resolution of negative velocities. When used in the coincidence mode, the coincidence window was set to approximately 10 microseconds. Processor parameter settings were optimized for the velocity ranges of interest:

Channel	Blue	Green
Measured component	Axial	Tangential or Radial
Velocity range	-20 to +200	-200 to +200
Bragg shift	10 MHz	40 MHz
Hi filter	30 MHz	Off
Low filter	3 MHz	10 MHz
Cycles/burst	2**4	2**5

The seed material was titanium dioxide having a characteristic size less than 1 micron. Standard seeding techniques were used with the seed being introduced far upstream from the model nozzle. Seed rates were adjusted to achieve processor count rates of 100 to 300 Hz. In order to perform the measurements as close to the nozzle face as possible, a small beam convergence angle (1.67 deg) for the rays in the plane normal to the injector face (i.e, axial velocity) was used, producing an elongated probe volume. As a consequence, off-axis collection optics were required to achieve the desired spatial resolution. A forward-scatter, 30-deg off-axis system was used with the collection optics mounted rigidly to the velocimeter platform.

Figure 5 depicts the geometric orientations used to acquire the data. A flange on the aircap was used to mount the nozzle on the end plate of a cylindrical plenum. This assembly was mounted on a stepper-motor-driven rotary table (0.02 deg/step resolution) in a manner to precisely align the nozzle axis with the axis of revolution. The velocimeter was always oriented with the blue beams producing fringe patterns normal to the nozzle face, and the green beams producing fringe patterns parallel to the face and oriented to measure a vertical velocity. Hence the blue beams always sensed the axial velocity component (U_z). If the measurement volume was place on the y-axis, the green beams sensed the radial velocity (U_r). If the measurement volume was placed on the x-axis, the green beams sensed the tangential velocity (U_θ). Then locating the velocimeter at a point on the y-axis permitted measurement of U_z and U_r, which could be followed by nozzle rotation by 90 deg to place the point on the x-axis, and translation of the velocimeter for measurement of U_z and U_θ. The redundant measurement of U_z provided a check to assure the same point was being interrogated. In practice, data were acquired for circumferential traverses of the flow as achieved by rotating the nozzle in 5-deg increments for each of eight radial positions. Data from all radial placements of the measurement volume along one axis were first acquired, followed by repeat circumferential traverses with the volume on the second axis. A numerically-controlled milling machine bed was used to position the velocimeter. The actuation of this bed and the rotary table, and the collection/storage of the velocimeter data were governed by an Apple IIe microcomputer equipped with 128K of RAM. Reference marks were used to initialize the rotary table; a fine wire target, inserted into the nozzle precisely on its centerline, was used to zero the position of the velocimeter. Operation of the system was completely automated; approximately 30 sec were required to acquire, process and store data for 512-point PDFs on each of the two channels, and to position the equipment to the next measurement station.

TEST RESULTS

The test program described above studied eight model aerating nozzle configurations in order to determine the airflow characteristics produced by them. The magnitude of data collected for the twelve measurement planes indicated in Table 1 is too great to fully discuss in this single paper. The focus here will be to describe many features of the airflow established by the Baseline configuration and then to describe how the subsequent nozzle configurations altered it. Detailed analyses of the turbulence properties of these flows will be considered in another publication.

Baseline Configuration Airflow

The airflow produced 0.060-in. downstream from the Baseline configuration is represented by the isometric contour plots depicted in Fig. 6. The first row of contours reflect the data acquired for numerous circumferential traverses with the measurement volume located to sense axial and tangential velocities; the second row reflects measurements for axial and radial velocity. Data for the first plot of each row, axial velocity, were obtained independently and indicate the degree of repeatability achieved in the measurement and positioning systems. While only qualitative, these profiles convey an important sense of the complex flow exiting this nozzle. All of the profiles were nearly axisymmetric as expected, with regions of high turbulence generation

occurring in the outer shear layers. These and other features are quantified by the plots contained in Fig. 7 which display the circumferentially-averaged values for the velocity and turbulence measurements at each radial station. The "error bars" indicate a one standard deviation limit of the 72 data averaged at each radius.

These average radial profiles demonstrate the high degree of axisymmetry achieved and indicate the magnitude of the measured quantities. The axial velocity was center peaked and therefore gave no indication that the swirl generated by this nozzle produced a center recirculation zone. Axial velocities approaching 170 ft/sec were in agreement with the airflow pressure loss. Integration of the axial velocity over the nozzle area determined the air massflow distribution and hence provided another indicator of flow uniformity. Following the practice for fuel spray distribution, the percentages of flow in 45-deg sectors were calculated; the highest was less than 12.6 pct, extremely close to the ideal value of 12.50 pct. The airflow uniformity was in fact much better than observed for the spray results for this configuration (depicted in Fig. 3a). The spray analysis found up to 13.8 pct of the fuel in one sector despite attempts to precisely control both the air and fuel. Since the velocity measurements indicated that a high degree of airflow control was achieved, the spray pattern variations must have resulted from fuel path effects. Even with fuel annular gap variations less than 0.001 in. a noticably nonuniform pattern was produced. This conclusion is consistent with the finding cited above that the fuel gap does have a strong influence on circumferential uniformity.

Positive tangential velocities indicated the expected clockwise (viewing downstream) swirl. In the outer regions of the flow the tangential velocities greatly exceeded the axial velocities with the opposite relation near the center. Together the axial and tangential velocities were used to calculate local swirl angles and a swirl number for the flow. The radial variation of swirl angle for the Baseline is depicted in Fig. 8. The depicted swirl angle was calculated from a horizontal traverse across the nozzle at a downstream distance of 0.060 in. Because of the geometry and velocity relationships, the clockwise swirl was discerned as a positive swirl angle along the negative x-axis and as a negative swirl angle along the positive x-axis; in fact, the entire flow was swirling clockwise. The calculated angle was near to the measured vane turning angle (50 deg) for the outer regions decaying to much lesser levels near the core. The swirl number, often used as an indicator of vortex breakdown in the flow, is the ratio of the angular momentum and the product of the axial thrust and a characteristic radius. The swirl number calculated for this configuration was based on the ratio of angular momentum to axial momentum; no account was made of the pressure thrust. Based upon the radius at which the axial velocity dropped to zero, the swirl number was 0.62. There are various definitions and approximations to the swirl number (Ref. 3); for some cases a vortex breakdown and resulting central recirculation zone would be expected for this calculated swirl number. Such a separation was not evident indicating such a single parameter did not sufficiently characterize these complex swirling flows.

Positive radial velocities indicated flow directed toward the centerline of the nozzle. The radial velocities (Figs. 6 and 7) were much lower than the others and registered a greater variation in magnitude (i.e., greater standard deviation), especially near the center regions of the flow. The RMS fluctuations of the radial velocity were nearly equal to, or exceeded, the mean radial velocity. These radial velocity data show that near the nozzle face, flow from the outer swirler was directed inward while the core-swirler air moved outward; the zero radial velocity region was near to the radius of the annular fuel gap. It was likely that the interaction of these streams contributed to the radial velocity variations, a flow situation which ought to aid in fuel atomization. It appeared that the wakes from the swirler vanes also contributed to the flow variations. Figure 9 depicts the measured radial velocity and turbulence data around the nozzle at radial positions of 0.1 in. and 0.3 in.; the former is within the core flow while the latter is in the outer swirling stream. Although of differing magnitude, periodic variations of the radial velocity and fluctuation were observed, with six local peaks evident for the innner flow and fourteen in the outer flow in direct correspondence to the number of swirler vanes; harmonic analyses also identified these as dominant modes. The magnitude of these variations was greater for the inner flow, consistent with the greater deviations and turbulence indicated above. These observations were also consistent with the fuel spray results which indicated that variations on the inner swirler had a greater impact on patternation than variations on the outer swirler. It was argued that inner swirler variations were effectively more intense because they were confined to a smaller flow area. These velocity data confirm that potentially similar wake disturbances had a greater influence on the inner flow.

Except for the outer shear region, the turbulence appeared isotropic with component RMS fluctuations of approximately 20 ft/sec. When compared to the total velocity vector, the turbulence intensity was 16 to 20 pct over the bulk of the flow with a 60 pct intensity registered in the outer shear region.

Altered Configurations

The mis-aligned aircap configuration inclined the outer swirler and endcap by 2.5 deg from true axial. As described above, however, the nozzle was mounted to the rotary table by a flange attached to the endcap. Therefore, as mounted, the endcap was axially aligned while the inner components of the nozzle deviated by the 2.5 deg. The velocity profiles 0.060 in. downstream from the nozzle were axisymmetric. Figure 10 displays the mean radial profiles for axial velocity for this configuration and the Baseline. The standard deviation in the core region averaged 2.6 ft/sec for the mis-aligned configuration and 4.3 ft/sec for the Baseline. Clearly the presence of the 2.5 deg mis-aligned core swirler flow was not sensed; the bulk airflow was dominated by the outer flow. The fuel spray pattern produced by this configuration was not axisymmetric however (Fig. 3c). The pattern was shifted approximately 0.18 in. off center, which for a measurement plane 2.5 in. downstream, translated to a 4 deg deviation. More importantly, the pattern was not only shifted but also skewed to result in a very nonuniform fuel mass flux. Three regions of higher fuel mass flux were discerned in the fuel patternation. Therefore, an altered interaction of the air and fuel streams at the filming lip was probably a stronger influence on the resulting pattern than the alignment. Detailed studies within the nozzle would be necessary to document this effect.

Two configurations were studied to determine the influence of reducing the number of vanes in either the inner or outer swirler. The fuel spray formed by the reduced vanes outer swirler configuration (Fig. 3d), displayed seven regions of high fuel mass flux in direct correspondence to the number of swirler vanes. Figure 11 contains the velocity and turbulence contours determined for the airflow produced by this configuration. Again, seven distinct regions of high air flux are evident. This is particularly true for the radial velocities where strong cyclic variations between inward and out-bound flow were sensed. This latter feature is more clearly presented in traverses for radial velocity and fluctuation obtained at radial positions of 0.15 and 0.35 in. (Fig. 12). The seven distinct cycles discerned for both radii indicated the spread of the influence over the entire flow. The velocity variations imposed by the removal of alternate outer swirler vanes (equivalently, increasing the gap-to-cord ratio in the swirler) were most prominent for the radial velocity because it had the lowest magnitude. Periodic variations in both the axial and tangential velocities were also present. Analyses of these velocity components suggested that the fuel mass flux variations corresponded to the regions of increased axial velocity. The patternation data were fuel mass flux and not fuel concentration values; regions of high airflow velocity convected higher flow rates of fuel. At the radius of maximum variation, the total velocity ranged from 167 ft/sec to 138 ft/sec. This variation occurred at a radial position of 0.25 in. or 55 pct of the full flow radius. The fuel patternation of this configuration contained maximum fuel flux variations at a radius of 1 in. or 50 pct of the fuel spray radius. The ratio of the maximum to minimum mass flux at this radius was approximately 1.7, much greater than the corresponding air velocity ratio of 1.2. Therefore, while regions of high axial flow likely did convert higher local fuel flow rates, a fuel-air interaction in the nozzle must have occurred to further enhance this effect. It is important to note that these influences were imposed in the vicinity of the nozzle exit but were not apparent in the velocity distributions further downstream from the nozzle. Figure 13 depicts velocity contours in a plane 2.5 in. downstream from the nozzle. Regular variations resulting from the number of swirl vanes could not be discerned. Notice also that the radial velocity was largely negative, indicating flow away from the centerline. Hence, while the airflow signature decayed, its influence on the fuel flux leaving the nozzle persisted. The flow characteristics observed for the configuration with the reduced number of core swirler vanes were similar to those described for the outer swirler variation. That is, the use of a three-vane swirler resulting from removal of alternate vanes from the core swirler produced a flow field which reflected the three vanes. All four swirlers used--the 14-vane and 7-vane outer swirler, and the 6-vane and 3-vane inner swirlers--produced cycles in the velocity profiles, particularly the radial profiles.

Two configurations used outer swirlers with each trailing edge altered to produce either a sharp edge (knife edge) or a blunt (square) edge; the Baseline configuration had rounded trailing edges. Velocity data were acquired only 0.060 in. downstream of the nozzle in an attempt to sense a significant difference in the turbulence levels produced by these configurations. Patternation data acquired previously indicated that only small differences were produced from the use of these differing trailing edges. Figure 14 displays mean radial profiles for the axial, tangential, and radial turbulence levels for these three configurations. No regular influence was discerned; no particular trailing edge shape appeared to generate greater or lesser turbulence levels. Therefore, there appears to be no need (from a fuel circumferential patternation point of view) to achieve highly streamlined trailing edges on conventional swirlers.

A nozzle configuration was assembled which included two six-vane core swirlers in tandem. For this configuration, the core air pipe was extended upstream to accept the two swirlers; the velocity and turbulence characteristics of this altered Baseline (i.e.,

extended-core Baseline) were essentially the same as the original Baseline configuration. The two core swirlers were mounted to place the trailing edge of the upstream vanes in the center of the gap at the inlet plane to the downstream swirler. That is, the swirlers were oriented to place the wake regions from the upstream swirlers in the inlet flow to the downstream swirler. The purpose of this configuration was to determine if these upstream disturbances could be discerned in the velocity and turbulence characteristics at the nozzle exit. A comparison of the contour plots and the mean radial profiles for these quantities contained no components produced by the upstream-most swirler. As for the Baseline configuration, the presence of flow disturbances was most easily detected by examining the traverses for radial velocity and turbulence as displayed in Fig. 15 at radial positions of 0.1 and 0.3 in. Fourteen cycles of the radial velocity and turbulence can be observed at the outer radius in response to the fourteen vanes in the outer swirler. Less than six cycles are observed for radial velocities at 0.1 in., a trend similar to that observed for the Baseline configuration (Fig. 9a); harmonic analyses revealed no organized variation near 12 Hz. This result suggests that the swirler itself is the dominant influence on the velocity and turbulent fields downstream of it; turbulent disturbances occurring upstream of the swirler appeared not to be transmitted through it. Similarly, it would be expected that reasonable variations in the turbulence levels upstream of the fuel nozzle would not significantly alter the fuel atomization and distribution process; of course, extreme deviations as might be experienced during compressor stall or surge would clearly be transmitted through the swirler and strongly influence the fuel pattern.

CONCLUSIONS

Detailed measurements of the airflow and turbulence have been made downstream of several configurations of a model aerating fuel nozzle. The nozzle assemblies included a symmetric baseline and others which purposefully altered the airflow by mis-aligning swirlers, changing the number of vanes in a swirler, or contouring the vane trailing edge.

1. The acquired data indicated that very symmetric airflow profiles can be achieved supporting the position that nozzle patternation quality is more dependent on the fuel distribution in the nozzle.

2. Directed (e.g., mis-aligned) airflows can shift the fuel patternation by convecting higher fuel fluxes along new trajectories. Such cases are accompanied by a new fuel-air interaction within the nozzle which often has a greater influence in distorting the fuel distribution than the mis-alignment.

3. Significant variations in the airflow exiting the nozzle can mix out within relatively short distances. The influence of these variations on the fuel distribution persists, however.

4. The flow in the swirler passages dominate in establishing the velocity and turbulence field downstream of it. Upstream disturbances are not easily transmitted through it; practical changes of the edge condition result in minor variations. Hence, spray atomization and distribution are insensitive to such effects.

REFERENCES

1. Rosfjord, T. J. and S. Russell: Influences on Fuel Spray Circumferential Uniformity. AIAA Paper 87-2135. June 1987.

2. McVey, J. B., S. Russell and J. B. Kennedy: Characterization of Fuel Sprays Using a High Resolution Patternator. AIAA Paper 86-1726. June 1986.

3. Gupta, A. K., D. G. Lilly and N. Syred: Swirling Flows. Abacus Press, 1984.

ACKNOWLEDGEMENTS

This study was performed at UTRC under the sponsorship of the U.S. Air Force Aero-Propulsion Labortory, Wright-Patterson Air Force Base, Ohio (Contract F33615-85C-2515); the Program Managers were Ms. Ruth Sikorsky and Mr. Royce Bradley. The authors were appreciative of the fine efforts of Dr. John McVey, Mr. Lou Chiappetta, and Mr. Richard Roback in the acquisition and analysis of these data. The continuing support of UTRC studies and capabilities by UTC/Pratt & Whitney is also appreciated.

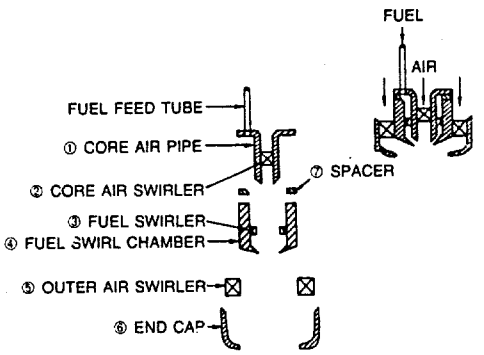

Fig. 1 Model aerating nozzle

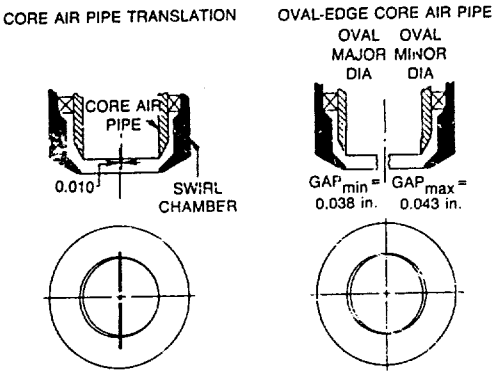

Fig. 2 Configurations altering fuel gap

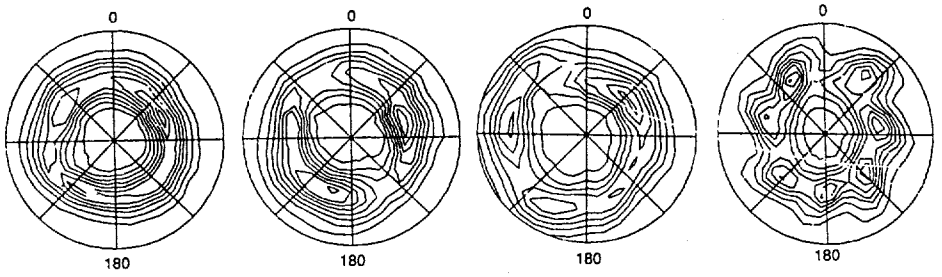

Fig. 3 Spray contour

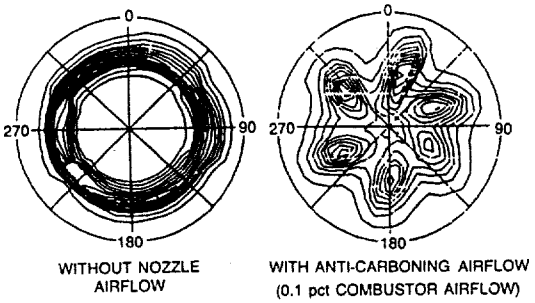

Fig. 4 Influence of minor airflow on pressure-atomizing nozzle

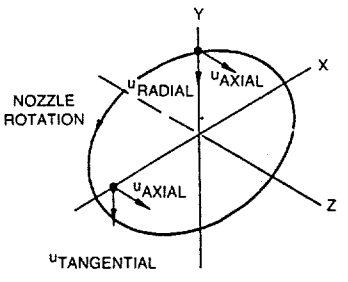

Fig. 5 Velocity measurement positioning

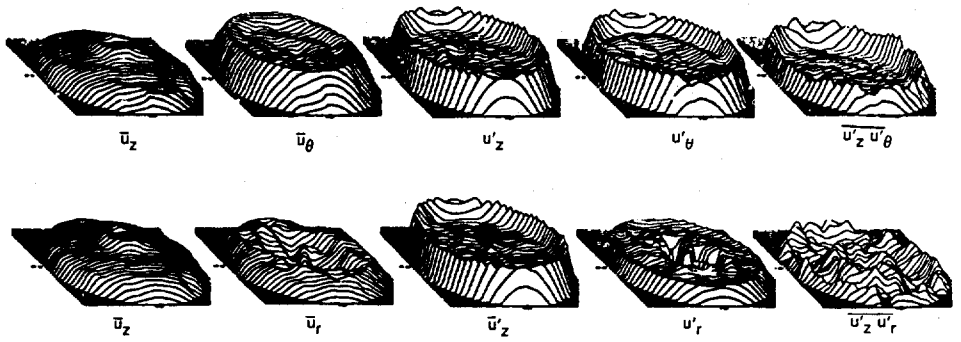

Fig. 6 Velocity and turbulence contours for baseline (z = 0.060 in.)

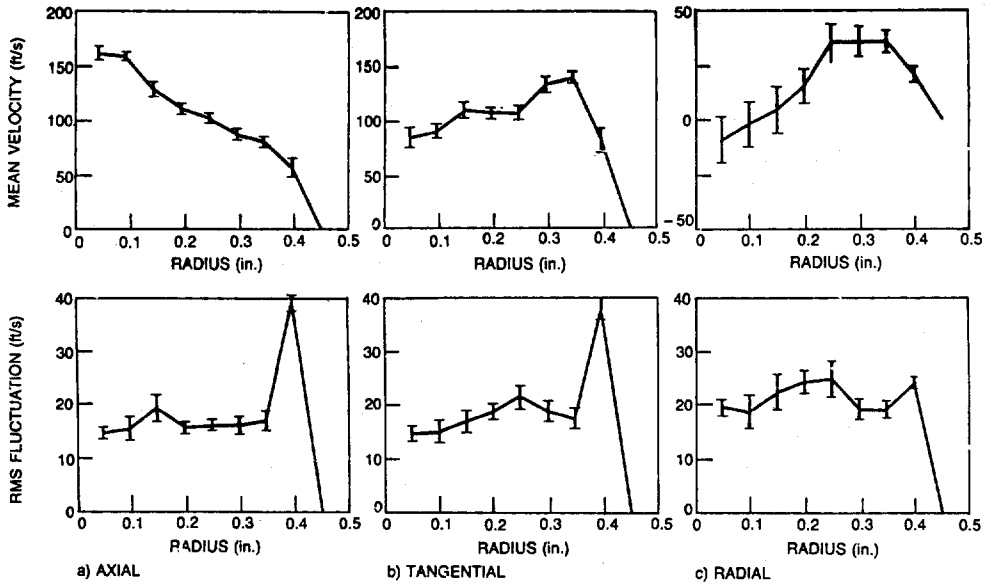

Fig. 7 Mean radial profiles for baseline (z = 0.060 in.)

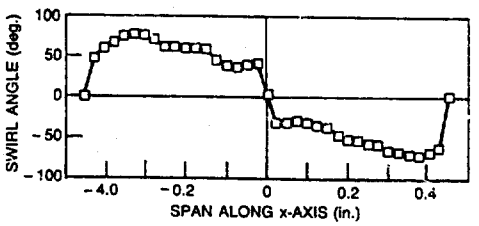

Fig. 8 Local swirl angles for baseline (z = 0.060 in.)

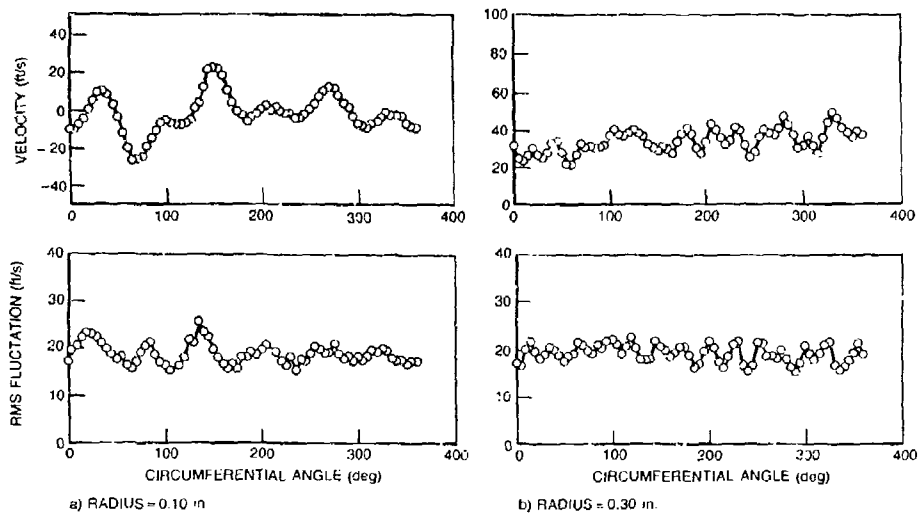

Fig. 9 Radial velocity signatures for baseline (z = 0.060 in.)

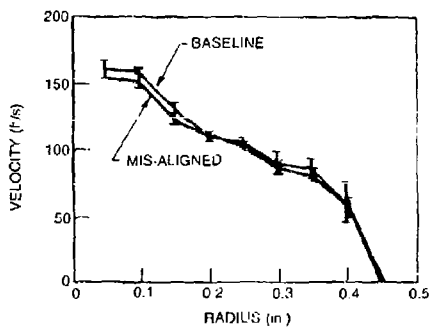

Fig. 10 Comparison of axial velocity profile for baseline and mis-aligned aircap (z = 0.060 in.)

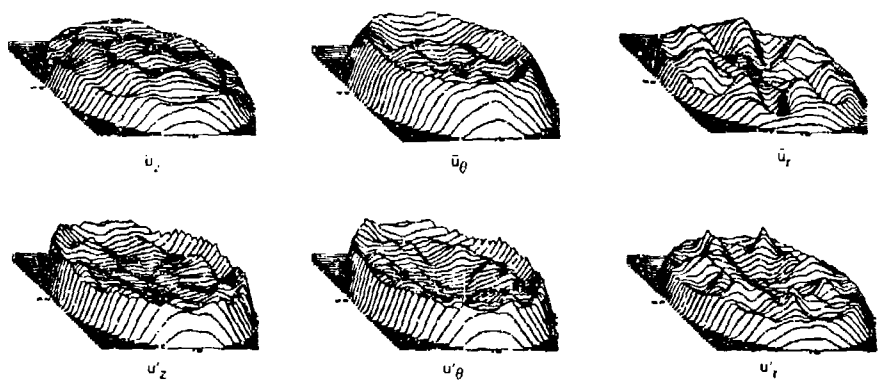

Fig. 11 Velocity and turbulence contours for reduced-outer vane (z = 0.060 in.)

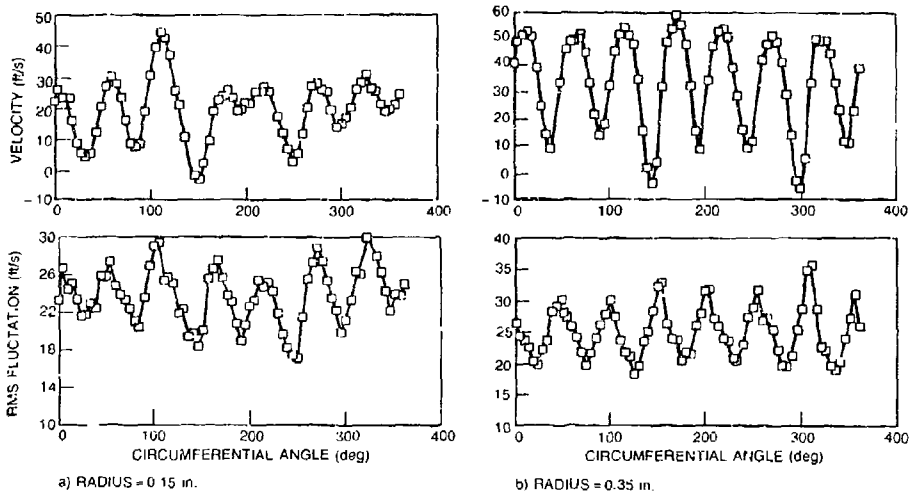

Fig. 12 Radial velocity and turbulence signatures for reduced outer-vane (z = 0.060 in.)

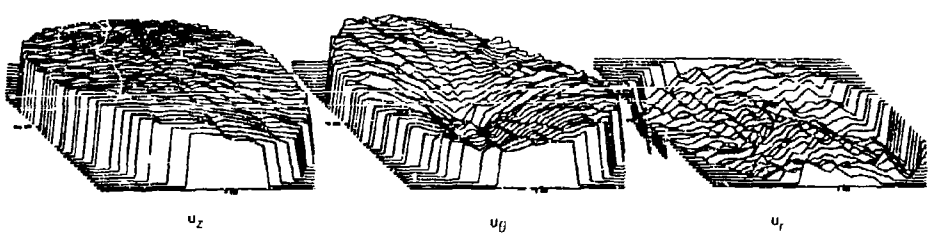

Fig. 13 Velocity contours downstream of reduced-outer-vane (z = 2.50 in.)

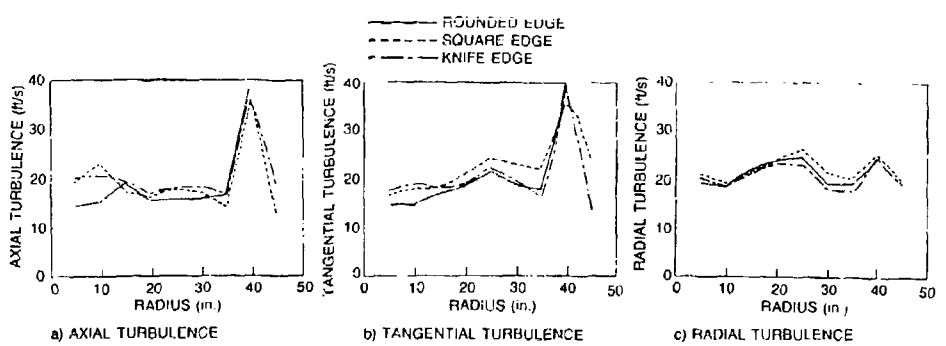

Fig. 14 Comparison of turbulence levels produced by different swirler trailing-edge shapes

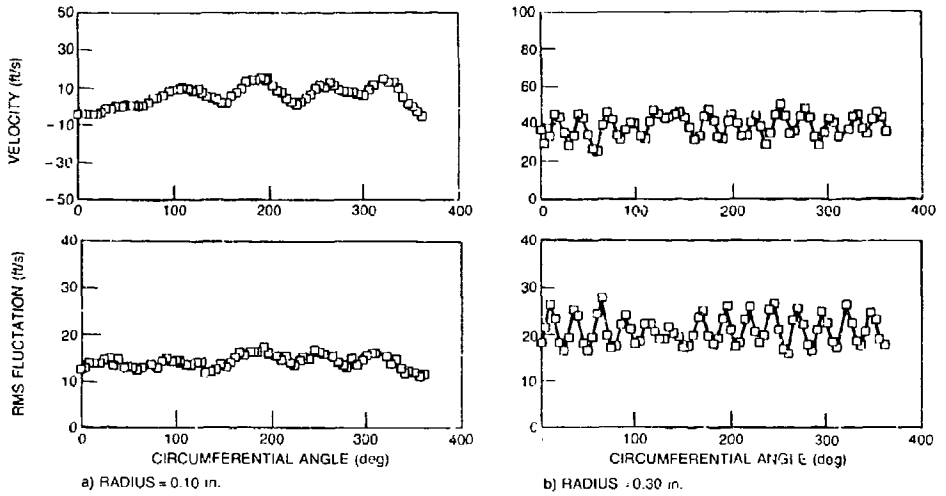

Fig. 15 Radial velocity and turbulence signatures for Tandem-Core-Swirler (z = 0.060 in.)

DISCUSSION

G.Winterfeld, GE:

Do you use curved blades in the core air swirler?

What is the mass ratio of the outer air flow?

Author's Reply

The core swirler vanes are straight while the outer swirler vanes are curved (but not twisted). This is smaller to a practical aerating nozzle that formed the design guide. The massflow ratio was approximately 3/1 (outer-to-inner).

MULTIPLE SCATTERING EFFECTS IN DROP SIZING OF DENSE FUEL SPRAYS BY LASER DIFFRACTION

Ömer L. Gülder
National Research Council of Canada
Division of Mechanical Engineering, M-9
Ottawa, Ontario K1A 0R6, Canada

SUMMARY

The purpose of the reported work is to present practical schemes to correct the effect of multiple scattering in a dense drop field on the measured distribution parameters by laser light scattering based spray sizing techniques. An experimental study, involving multi-modal distributions and drop fields which can not be adequately described by single-mode two-parameter distributions, is described. Data from the experimental program were employed to develop empirical expressions to correct the measured spray parameters at high obscuration levels. Accuracies of the proposed expressions are acceptable for engineering applications, and comparable to the accuracies involved in conversion of light scattering data to drop size information.

LIST OF SYMBOLS

C_d	correction factor for Sauter mean diameter, D_{32}/D'_{32}
C_v	correction factor for volume mean diameter, D_{30}/D'_{30}
C_ω	correction factor for ω, ω/ω'
D_{30}	apparent volume mean diameter, μm
D_{32}	apparent Sauter mean diameter, μm (=SMD)
D'_{30}	actual volume mean diameter, μm
D'_{32}	actual Sauter mean diameter, μm
D_i	apparent diameter below which is the 10 % of the spray volume
D_j	apparent diameter below which is the 50 % of the spray volume
D_n	apparent diameter below which is the 90 % of the spray volume
S	apparent span of the distribution,defined by Eq.(6)
ϕ	percent obscuration
ω	apparent ratio of the percentage volume of the spray in the smaller drop size mode to that of in the larger size mode for bi-modal distribution
ω'	actual ratio of the percentage volume of the spray in the smaller drop size mode to that of in the larger size mode for bi-modal distribution

INTRODUCTION

Ignition and combustion of fuel sprays are dynamic phenomena which are strongly influenced by the drop size and drop size distribution in addition to thermo-fluidmechanics of the combustion system and the chemical structure of the fuel. Also pollutant formation, especially that of soot, in spray diffusion flames is dependent on the spray characteristics, among other parameters. For this reason, to be able to measure, with reasonable accuracy, drop size and size distribution in fuel sprays of propulsion systems has become one of the major objectives in the field of spray combustion.

For drop size and drop size distribution measurements in transient and steady flow fuel sprays, use of laser light scattering techniques has many advantages over the other diagnostic techniques. Details of a recent study comparing the reliability of different techniques has been reported by Dodge [1]. The forward light scattering (Fraunhofer diffraction) technique utilizes the scattered light in the forward direction by the drops in the spray [2]. The shape of the resulting scattered light intensity profile provides the information necessary for determining the drop sizes and distributions. However, there exists two important problem areas associated with light scattering techniques. The first one is related to the inversion of light scattering data to drop size distributions, and the second one is related to the problem of multiple scattering in dense sprays. The latter problem arises when the interdrop spacing is very small such that the scattering characteristics of a drop in the spray depend on the relative positions and sizes of the neighboring drops, and when the probe volume length (i.e., the optical path of the incident laser beam) is long enough so that a considerable portion of the photons are scattered more than once through the probe volume before they reach the detector lense.

For sprays exhibiting Rosin-Ramler, log-normal, or normal drop size distributions, the Malvern instrument provides acceptable data, and for dense sprays, available correction schemes can be used to take care of multiple scattering effects [3]. However, some sprays display drop size distributions which can not be described by any of the single-mode two-parameter distributions, and some sprays exhibit multi-modal distributions [4]. For such sprays, Malvern has the *model-independent* option. Although the details of the inversion algorithm are not known, and some doubts exist related to the reliability of the inversion method [5,6] , our measurements with calibrated latex spheres using the model-independent mode provided quite acceptable results. An alternative approach is to use the Shifrin inversion technique to obtain model-independent size distribution from the light scattering data [7].

The effect of multiple scattering on model independent results has not been investigated systematically. The mathematical model developed by Hamidi and Swithenbank [8], to correct the effect of multiple scattering for any type of size distribution has not been extensively tested against experimental data, and some problems related to the formulation have been recently discussed by Gomi [9].

This work reports the results of an experimental program conducted to obtain data and a corrective scheme for model-independent and bi-modal distributions for the concentrations corresponding to the obscuration levels of 50 to 98 % for the diffraction based spray sizing systems.

EXPERIMENTAL

Measurements were made in a magnetically stirred cell similar to the one described by Hamidi and Swithenbank [8], to study the effects of multiple scattering on drop size and drop size distribution in drop fields with model-independent and bi-modal size distributions. Mono-size latex spheres (eight sizes from 7 μm to 100 μm), and aluminum oxide particles (five distributions, largest diameter around 250 μm) were used to design model-independent and bi-modal size distributions of different characteristics. A very dense suspension of each distribution of latex spheres was first prepared with deionized and filtered water. This sample solution was then added to the stirred cell, containing filtered water, to the desired concentration level. Thus, it was possible to obtain a series of concentrations corresponding to obscuration levels from 15 to 98 %, for the same drop size distribution. For aluminum oxide particles, methyl alcohol was used as the suspension liquid in the cell, and particles were added into the cell by a spatula. A Malvern 2600 spray sizer was used for the measurements utilizing the model-independent mode for data inversion, and most of the experiments were repeated with a modified beam expander with which the beam diameter was reduced from 9 mm down to 4 mm.

RESULTS

The ultimate effect of multiple scattering due to relatively high density of the drop field is to reduce the obtained mean drop size with increasing obscuration of the incident laser beam. For the nine bi-modal distributions, with which extensive data have been compiled, variation of the Sauter mean diameters is shown in Figure 1. The data obtained for single-mode and tri-modal distributions follow the same trend. For obscurations below approximately 45-55 %, the light energy and drop size distributions correspond to, within the experimental error range, the actual distributions.

In order to show the effect of multiple scattering on light energy, and final drop size distributions, data on three drop fields will be presented. The first of these three distributions is a bi modal one, obtained by mixing the the two different distributions of aluminum oxide particles. Obtained light energy distributions, Figure 2, do not give any clue towards the nature of drop size distribution, and exhibit single-mode light energy distributions at all obscurations. With increasing obscuration, however, the light energy distribution shifts towards larger detector ring numbers, Figure 2, resulting in smaller mean drop diameters, Figure 3.

The second distribution we will discuss is, again, a bi-modal one, but obtained by mixing two practically mono-size latex spheres. The resulting light energy distributions at different obscurations are shown in Figure 4. These distributions carry the signatures of a bi-modal type drop size distribution. With increasing multiple scattering, light energy distribution shifts towards larger detector ring numbers. This results in, in addition to a reduction in obtained mean drop size, an increase in the percentage drop volume in the smaller drop size mode of the bi-modal distribution with increasing obscuration, Figure 5.

Figure 6 illustrates the light energy distributions at different obscuration levels for a tri-modal distribution obtained by mixing three mono-size latex spheres. Even at very high obscurations, the multi-modal nature of the drop field can be easily seen from the shape of the light energy distributions. Corresponding drop size distributions are shown in Figure 7.

EMPIRICAL EQUATIONS AND DISCUSSION

The empirical expressions presented in this section were developed by curve fitting to the experimental data using multiple regression methods.

The correction equation for the Sauter mean diameter is

$$C_d = 1.35 * e^{F_1 + F_2} \tag{1}$$

where C_d is the ratio of the measured Sauter mean diameter, D_{32}, to the actual one, D'_{32}. F_1 and F_2 are given as follows

$$F_1 = -0.1184(D_{32}/100)^2 + 13.122\phi/D_{32} - 5.7474\phi/D_{32}^{0.5} \tag{2}$$

$$F_2 = 2.2389\phi^8 - 2.6077\phi^9 \tag{3}$$

where ϕ is the percentage obscuration.

The correction equation for the volume mean diameter is

$$C_v = 0.1639C_d^{0.7738}D_{30}^{-0.0760}e^{0.0165\phi/D_{30}^{0.5}} + 1.9413C_d \tag{4}$$

where C_v is the ratio of the measured volume mean diameter, D_{30}, to the actual one, D'_{30}

For bi modal size distributions, as mentioned before, the effect of multiple scattering manifests itself as an increase in the percentage volume of the drops in the smaller size mode, as the obscuration percentage increases. If we define ω as the ratio of percentage volume of the spray in the smaller drop size mode to that of in the larger drop size mode, then the correction equatio for ω is

$$C_\omega = 1.048/[C_d^{1.37} S^{0.157} \phi^{0.00525 S^3}] \tag{5}$$

where C_ω is the ratio of measured ω to the actual value, ω'. S is the measured value of the span defined as

$$S = (D_n - D_t)/D_f \tag{6}$$

where D_t, D_f, and D_n are the spray diameters below which are the 10, 50, and 90 % of the spray drop volume, respectively. The saddle point was taken as the reference to divide the two modes.

Figure 8 shows the variation of the correction factor for Sauter mean diameter with obscuration for different mean diameters. Although , the percentage obscuration is dominating the change in correction factor, the effect of Sauter mean diameter is not negligible. One interesting aspect of Eq.(1) is that, C_d is independent of the spray distribution width parameter. This is in contradiction to previous empirical models for Rosin-Rambler distributions [3,10] , and for log-normal distribution [3], which include terms for the distribution width parameter dependency of the correction factor for the Sauter mean diameter. A distribution width parameter, in terms of span S, had been included in our regression exercise, but C_d did not show any correlation with S. Same discussion applies for Eq.(4).

Figure 9 shows the correction factors for Sauter mean diameter predicted by Eq (1) versus measured ones. Correlation coefficient is 0.96 and mean error is around ± 3.5 %. Similar values have been obtained for the Eqs.(4) and (5), Table.1.

The validity ranges of the corrective equations for model-independent and bi-modal distributions are limited to :

$$10\mu m < D_{32} \leq 100\mu m$$

$$15\mu m < D_{30} \leq 120\mu m$$

$$0.7 \leq S \leq 4$$

$$0.3 \leq \omega \leq 3.5$$

$$0.5 < \phi \leq 0.98$$

Table 1
Regression statistics for the empirical expressions.

	Eq (1)	Eq.(4)	Eq.(5)
Correlation coefficient, R	0.96	0.83	0.97
Standard deviation of residuals,σ	0.046	0.056	0.054
Mean absolute error, %	3.5	3.4	3.5

Although the ultimate correction scheme should be obtained through modeling of multiple scattering of the light by a polydisperse drop field, as demonstrated by Hirleman [11] , Gomi [9], and Hamidi and Swithenbank [3], there exists two concerns related to the immediate application of these models. The first concern is related to the appropriateness of the selected physical model to describe the multiple scattering, which can only be justified by a rigorous testing of the numerical predictions against experimental data. As discussed by Gomi [9], this validation has not been demonstrated yet. The second concern is a more practical issue: unless simplified to easily managable algorithms, the existing models may not be suitable for use in data processors and PCs used with light scattering systems, even main frame computer runs can be prohibitive [9]. The present empirical approach does not shed any light on the physics of multiple scattering in dense drop fields, but it is simple and easy to use , and accurate within the specified range.

CONCLUDING REMARKS

An experimental study, to predict the effect of multiple scattering in a dense drop field on the measured model independent and bi modal distribution parameters, has been described. Obtained data were employed to develop empirical expressions to correct the measured spray parameters at high obscuration levels, with light scattering based spray sizing instruments. Accuracies of the proposed correction equations are acceptable for engineering applications, and comparable to the accuracies involved in conversion of light scattering data to drop size information.

REFERENCES

1. Dodge, L.G.,Comparison of Performance of Drop-Sizing Instruments, *Applied Optics*,**26**,(1987), 1328-1341.

2. Swithenbank, J., Beer, J.M., Abbot, D., and McCreath, C.G., A Laser Diagnostic Technique for the Measurement of Droplet and Particle Size Distributions, *AIAA Progress in Astronautics and Aeronautics*,**53**, (1977), 421-447.

3. Felton, P.G., Hamidi, A.A., and Aigal, A.K., Measurement of Drop Size Distribution in Dense Sprays by Laser Diffraction, *Proc. 3rd Int'l. Conference on Liquid Atomisation and Spray Systems*, Institute of Energy,London, 1985, IVA/4/1 - IVA/4/11.

4. Gülder, Ö.L., Temporally and Spatially Resolved Drop Sizing of Dense Diesel Sprays, *ASME Paper No. 87-FE-5*, American Society of Mechanical Engineers, 1987.

5. Bayvel, L.P., Knight, J.C., and Robertson, G.N., Application of the Shifrin Inversion to Malvern Particle Sizer , Paper presented at *Int'l Symp. on Optical Particle Sizing*,.Rouen, France, 12-15 May, 1987.

6. Dodge, L.G., Rhodes, D.J., and Reitz, R.D., Drop-size Measurement Techniques for prays : Comparison of Malvern Laser-Diffraction and Aerometrics Phase/Doppler, *Applied Optics*,**26**, (1987), 2144 2154.

7. Bayvel, L.P., and Jones, A.R., Electromagnetic Scattering and Its Applications, Applied Science Publishers, Essex, 1981.

8. Hamidi, A. A., and Swithenbank, J., Treatment of Multiple Scattering of Light in Laser Diffraction Measurements Techniques in Dense Sprays and Particle Fields, *J. Institute of Energy*, June (1986), 101-105.

9. Gomi, H., Multiple Scattering Correction in the Measurement of Particle Size and Number Density by Diffraction Method, *Applied Optics*, **25**, (1986), 3552-3558.

10. Dodge, L.G., and Biaglow, J.A., Effect of Elevated Temperature and Pressure on Sprays for Simplex Atomizers, *ASME Paper No. 85-GT-58*, American Society of Mechanical Engineers, 1985.

11. Hirleman, E.D., Modelling of Multiple Scattering Effects in Fraunhofer Diffraction Particle Size Analysis, *Combustion Institute/Western States Section, Paper No. WSCI-86-17*, 1986.

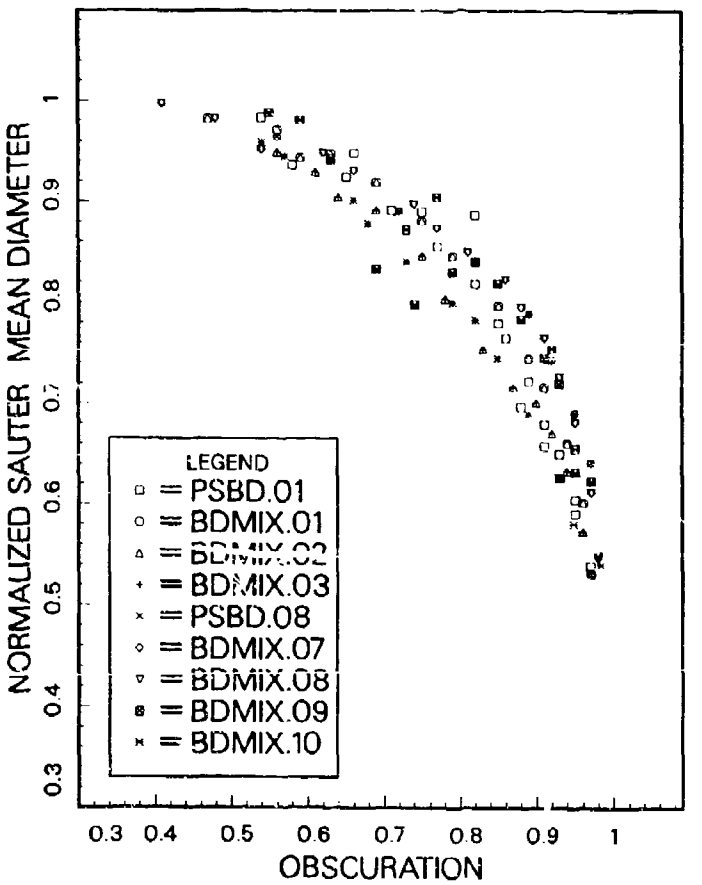

Fig.1 Variation of Sauter mean diameter with obscuration for bi-modal size distributions.

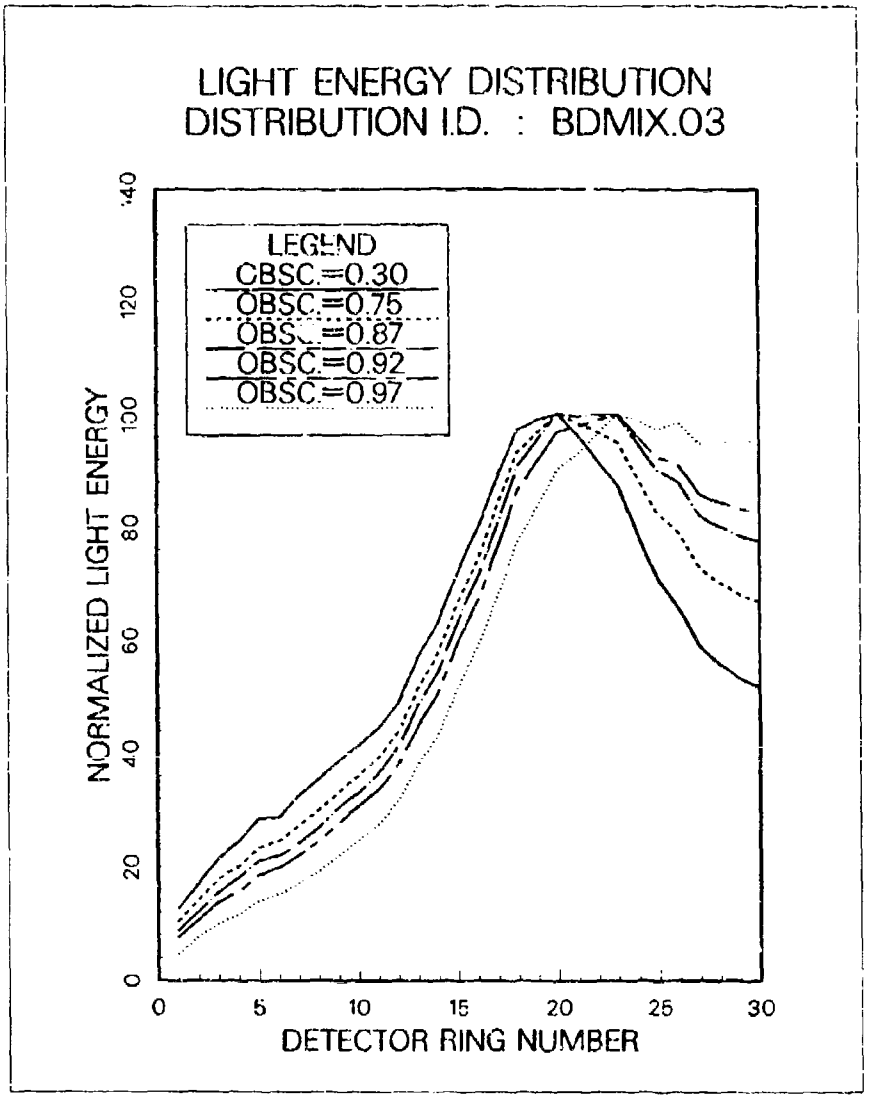

Fig. 2 Light energy distributions for a bi-modal drop field obtained by mixing two different aluminum oxide particle distributions.

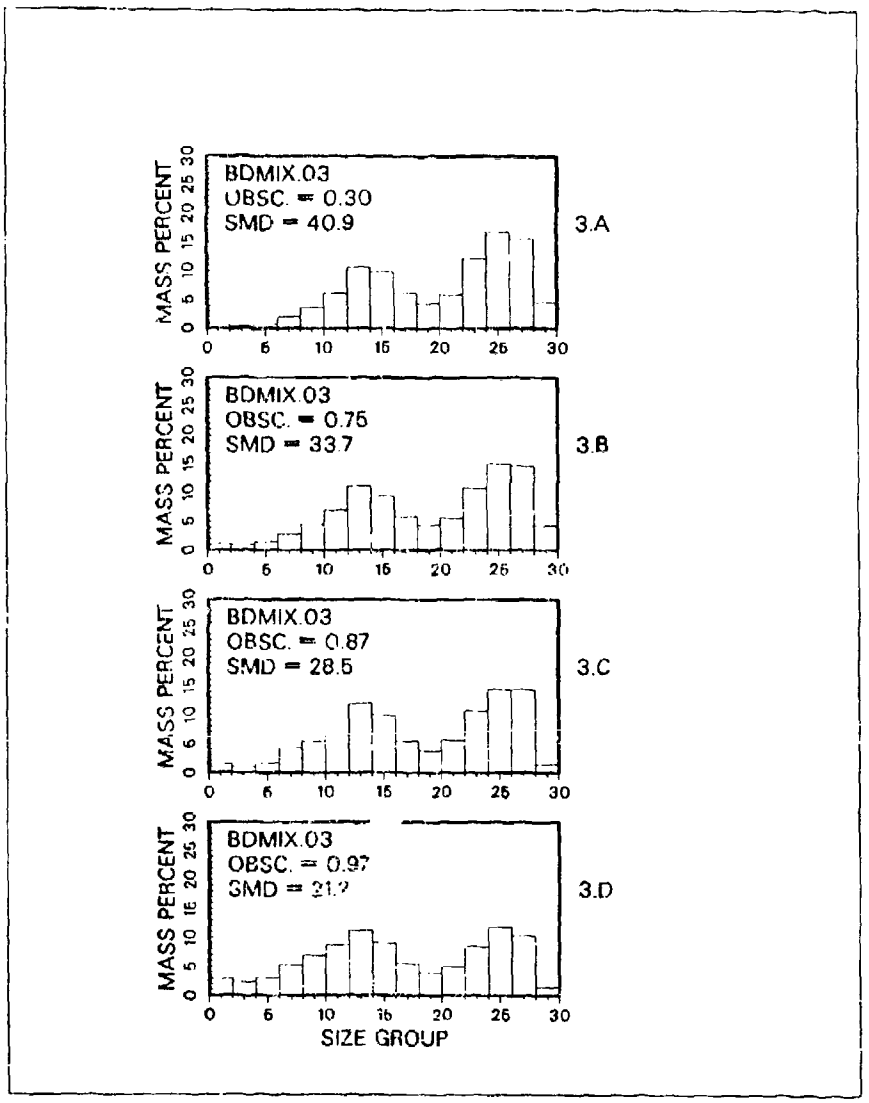

Fig.3 Change of drop size distribution with obscuration for the drop field of Fig.2.

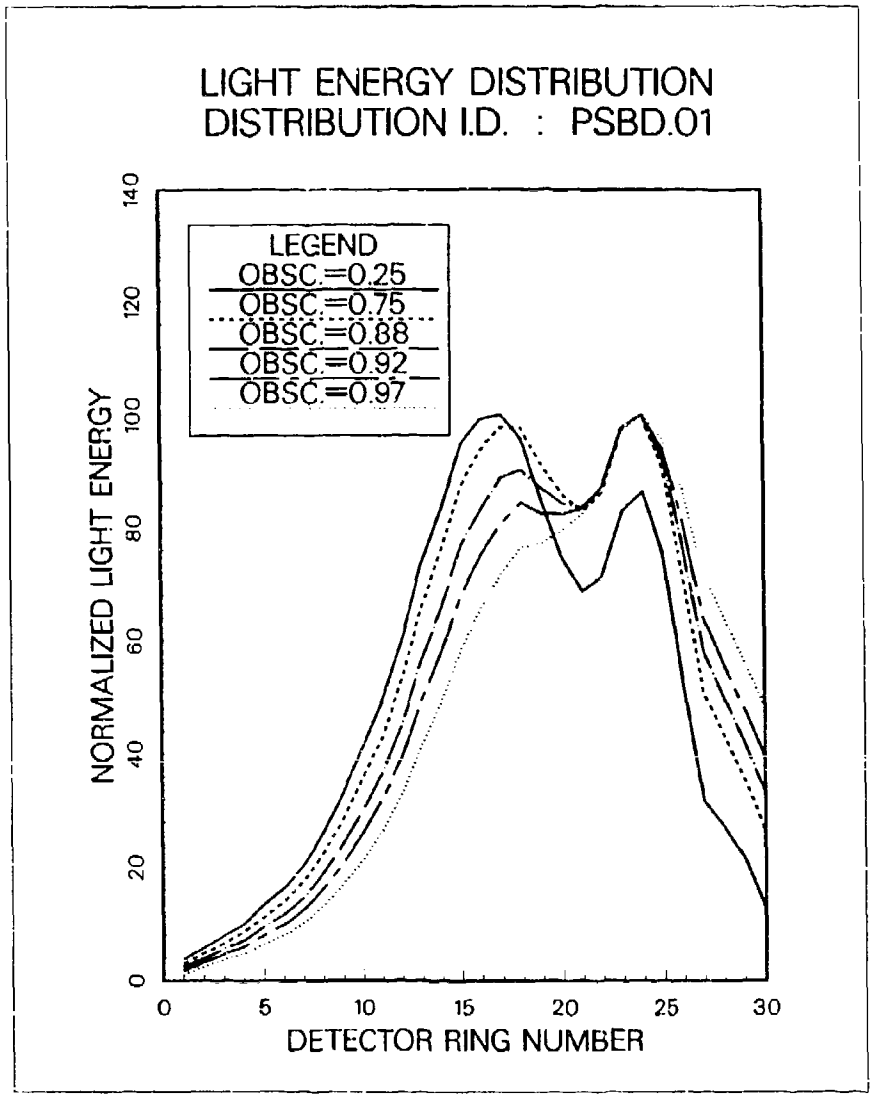

Fig.4 Light energy distributions for a bi modal drop field obtained by mixing two mono-size latex spheres.

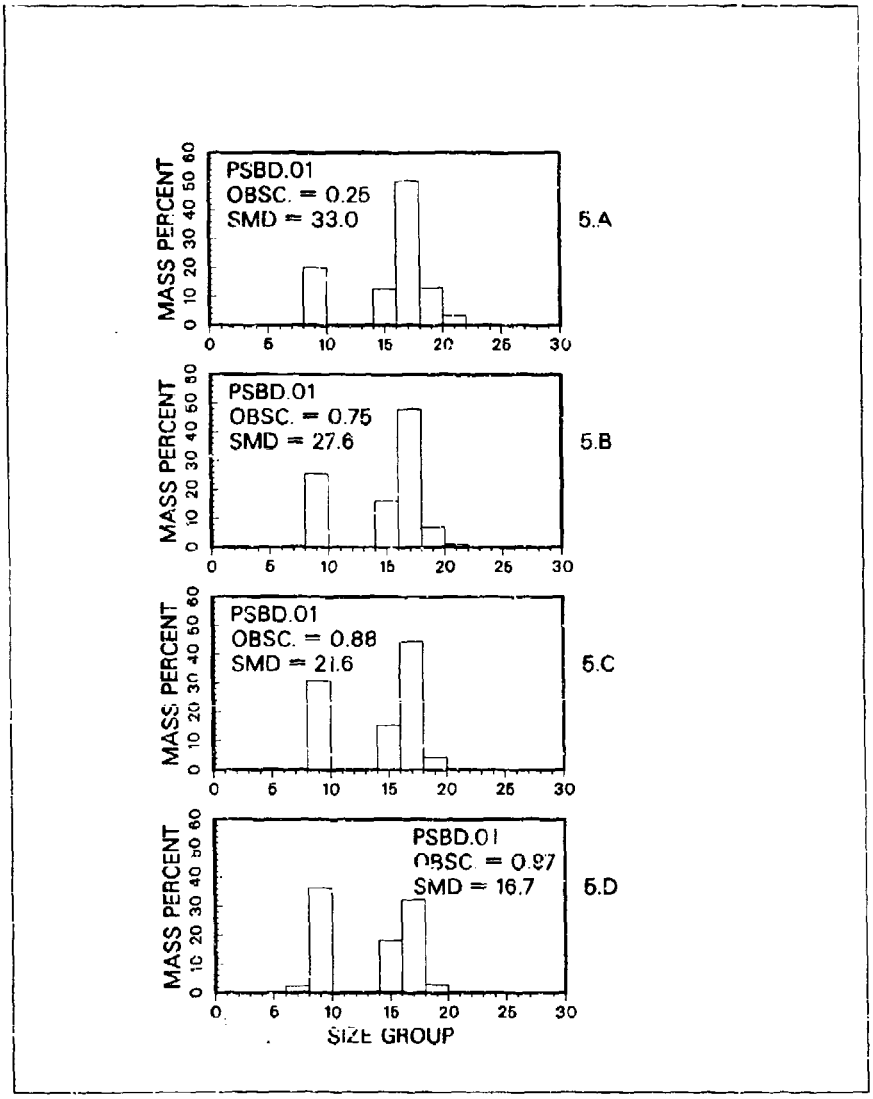

Fig.5 Change of drop size distribution with obscuration for the drop field of Fig.4.

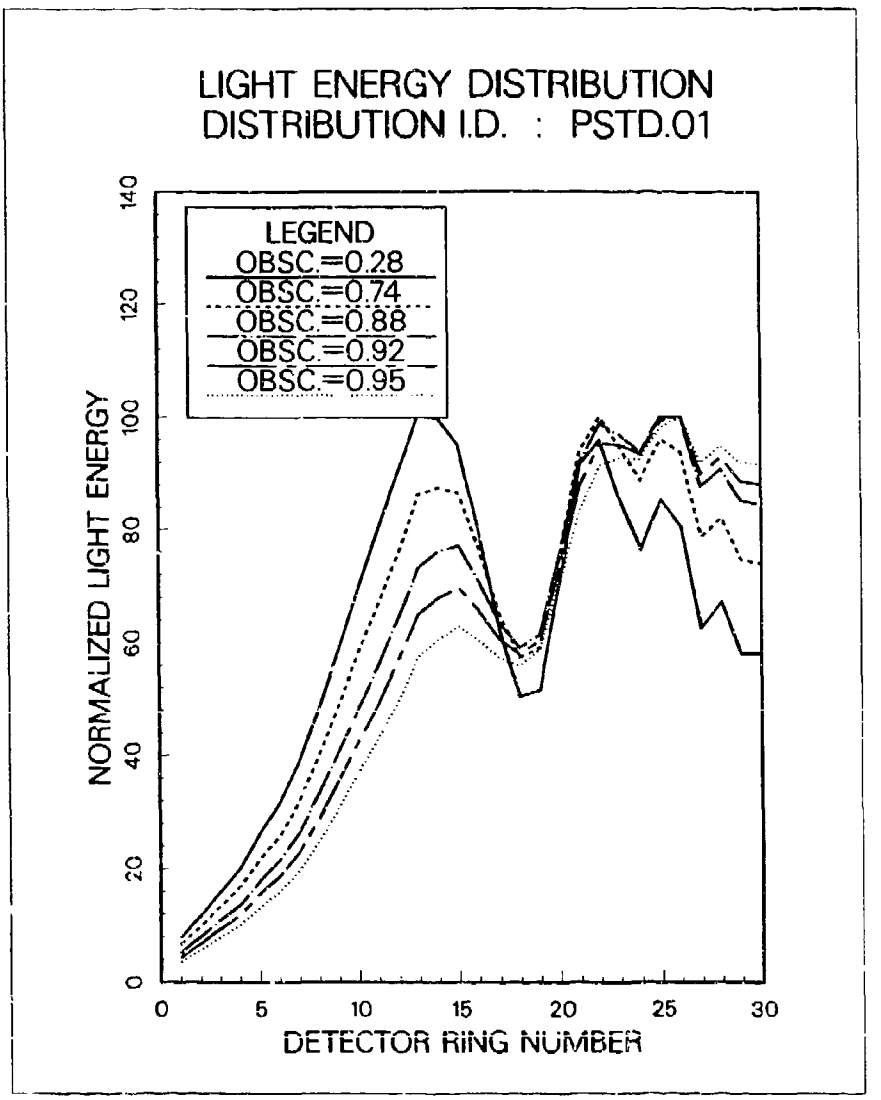

Fig.6 Light energy distributions for a tri-modal drop field obtained by mixing three mono-size latex spheres.

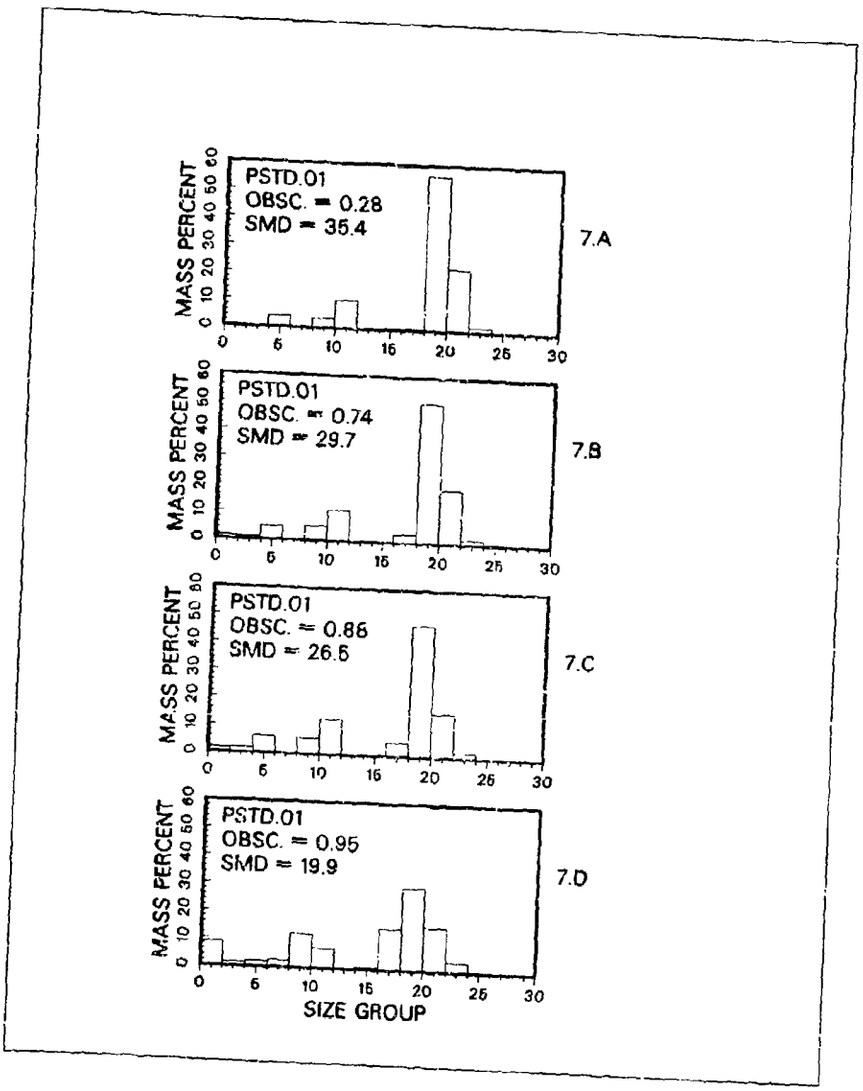

Fig.7 Change of drop size distribution with obscuration for the drop field of Fig.6.

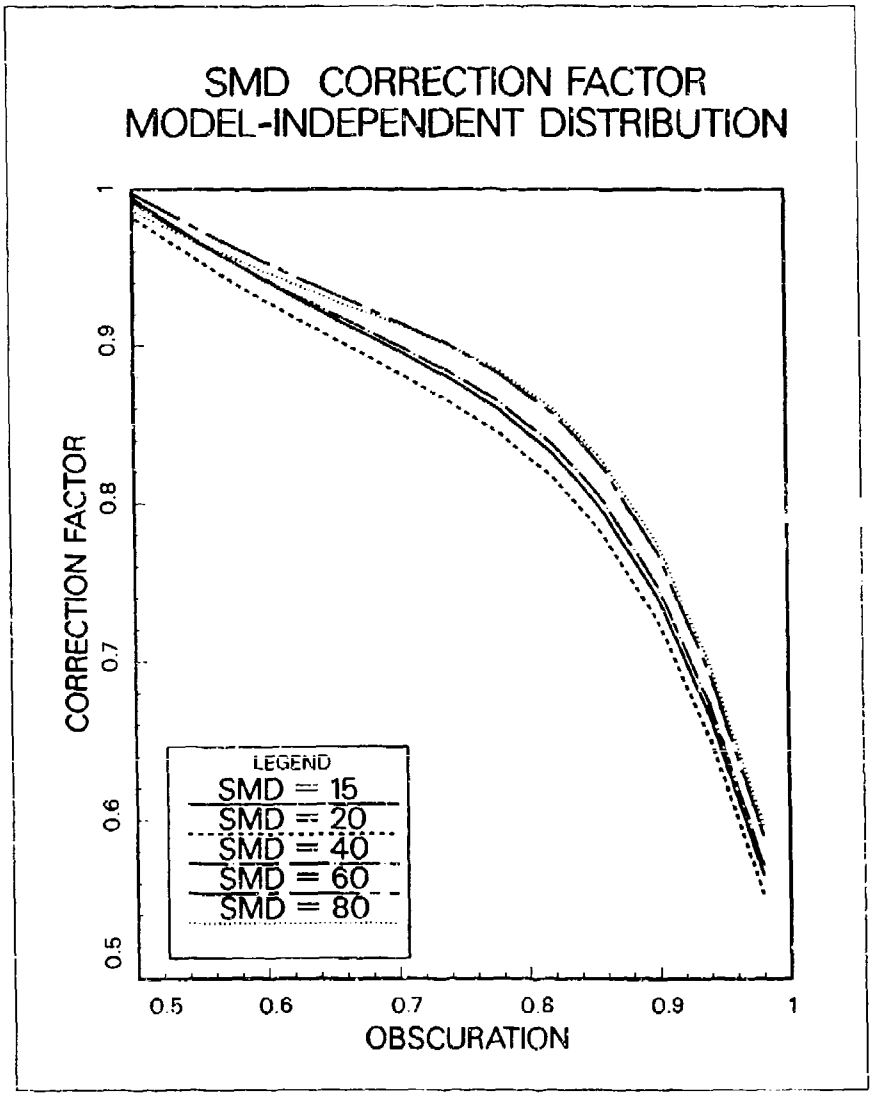

Fig.8 Predicted correction factors for the Sauter mean diameter as a function of obscuration and apparent Sauter mean diameter.

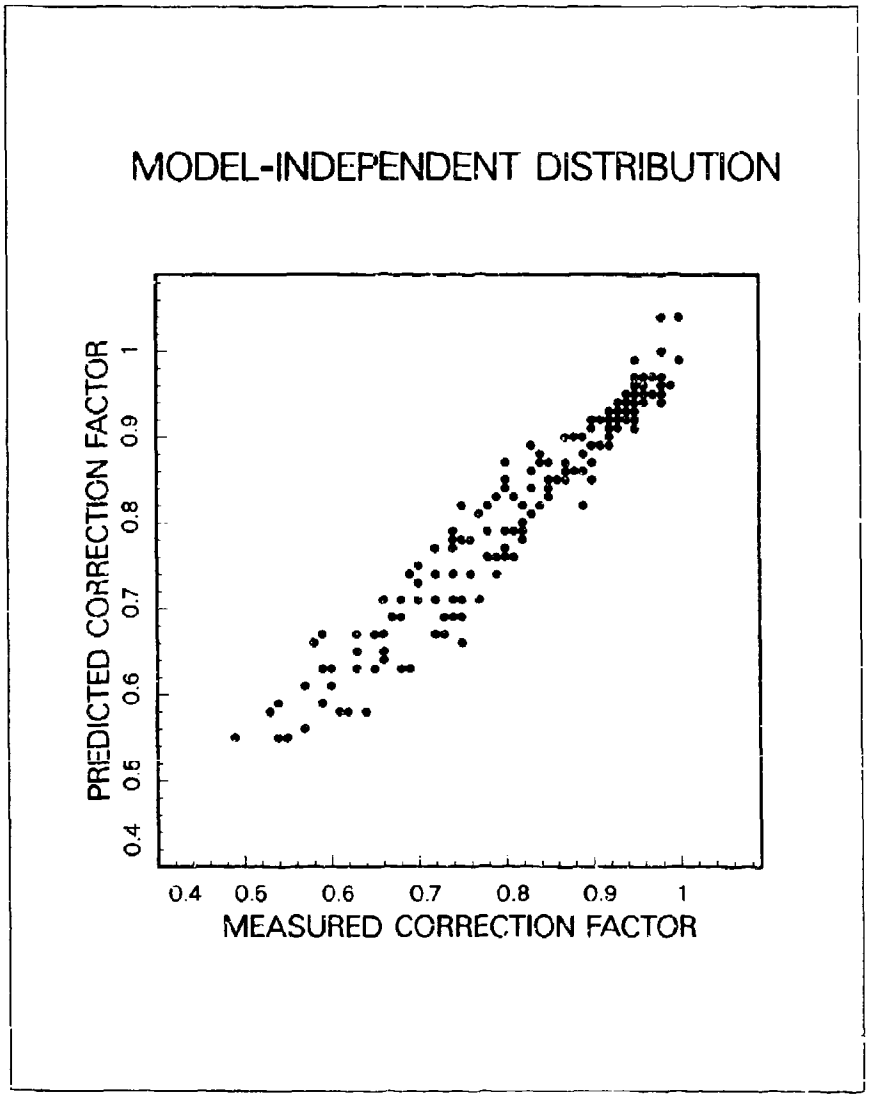

Fig.9 Predicted correction factors for Sauter mean diameter by Eq.(1) versus measured ones.

DISCUSSION

J.E.Peters, US

Your correction for SMD was derived using bi-modal and tri-modal size distributions. How well will it work for sprays that have realistic size distributions such as Rosin-Rammler or upper limit distribution functions?

Author's Reply

Data used for the derivation of correction expressions included single-mode distributions as well as multi-modal ones. The principal application of the described corrections scheme is to correct the distributions (single or multi-modal) of dense sprays obtained through the Malvern "model-independent" algorithm, and through the Shifrin inversion technique. I believe that it is a risky practice to force given distribution data to fit into Rosin Rammler or upper-limit type two-parameter distribution functions, with the rationale that these functions are presumably realistic. Existence of model-independent distributions (single-mode or multi-modal distributions which can not be adequately described by two-parameter distribution functions) is not a scarce probability; these type of distributions are frequently encountered in transient fuel sprays, and in high pressure full core sprays. The present correction scheme has not been rigorously tested for upper-limit, log-normal, and normal distributions. Limited tests with Rosin-Rammler distributions (3 distributions) were satisfactory. However, present expression for SMD gives different correction factors as compared to those obtained by expressions for Rosin-Rammler distributions reported in the literature (e.g., ref. 3 of this paper).

A.K.Jasuja, UK

The correction scheme has been derived on what are nearly stationary particles. Fuel sprays feature particles that are moving generally at high velocities. Can the correction scheme be applied to the fuel spray case as it is or does it need some modifications?

Author's Reply

The optical drop sizing techniques based on Fraunhofer diffraction are insensitive to the movement of drops. Therefore, the correction scheme presented does not need any modification. However, if any modification is applied to the measured distribution to prevent bias due to non-equal velocities (hence, non-equal residence times of the drops in the probe volume) of different sizes of drops, the same modification should be applied to the corrected distribution.

Influence of Operating Conditions on the Atomization and Distribution of Fuel by Air Blast Atomizers

M. Cao, H. Eickhoff

DFVLR,
Institut für Antriebstechnik
Postfach 90 60 50
Linder Höhe
5000 Cologne 90
Federal Republic of Germany

F. Joos, B. Simon

MTU Motoren- und Turbinen-Union
München GmbH
Postfach 50 06 40
Dachauer Straße 665
8000 Munich 50
Federal Republic of Germany

Summary

The performance of a gas-turbine combustion chamber depends essentially on the distribution of the fuel in the primary zone. Ignition, stability of combustion, wall temperatures, and smoke and pollutant emission are all affected.

Maintaining a fixed geometry, the droplet size and spray angle under variation of the air pressure drop at constant temperature were measured using two test liquids in an air blast atomizer system. Correlation equations were provided for both variables. Known correlations were confirmed for the droplet size. The spray angle is pressure-related, increasing very rapidly with increasing pressure.

Notation

AFR	-	Air fuel ratio
d_N	m	Characteristic nozzle diameter (d_N = 1)
m_1	kg/s	Air flow through nozzle
m_2	kg/s	Purging air flow
n	-	Exponent of Rosin-Rammler distribution
P_A	MPa	Air pressure
ΔP_A	kPa	Air pressure drop
r_1	mm	Nozzle exit radius
r_2	mm	Collector radius
S	mm	Distance between the nozzle and the collector
SMD	um	Sauter diameter
We	-	Weber number = $\frac{2 \Delta P_A}{\sigma_L} d_N$
α_{50}	degree	Angle within which 50% of the fuel is injected
σ_L	N/m	Surface tension of liquid

1 Introduction

The testing of gas-turbine combustion chambers under realistic operating conditions is very elaborate and expensive, requiring high pressures and great mass flows of hot air. Traversing instrumentation for measuring the temperature, pressure and composition of the exhaust at the combustor outlet must be provided.

For this reason, the effort is made to conduct as many of the combustor tests as possible under operating conditions at reduced pressure, preferably even at atmospheric pressure. The measurement of the gas temperatures and emissions is then much simpler because there is no need for pressure-resistant traverse-type instrumentation. Also, the air requirement is more modest. This reduces the costs of the test. However, to avoid inaccuracies, the test results must be transferable to full operating conditions.

As is known, mass and heat transfer are affected by pressure, gas radiation and reaction rates increase, phase and chemical equilibria change and air forces multiply. Since all these phenomena play a role in the combustion process, it is difficult to see what differences occur in combustion chamber testing at atmospheric pressure and at above-atmospheric pressure.

In the present investigation, therefore, mainly the influence of pressure on the fuel-injection system is considered. Systems in which the degree of atomization depends on the shear forces of the air, known as air blast atomizers, are particularly sensitive. A system of this type is investigated here.

2 Test Setup

2.1 Experimental nozzle

Air blast atomization has the advantage that fuel and air are pre-mixed early, and acceleration of the fuel droplets at the separation edge by the air ensures good heat and mass transfer, as large differences in the droplet and air flow velocities prevail from the very beginning of atomization. This is a prior condition for rapid vaporization.

The arrangement of the air blast atomization system is illustrated schematically in figure 1. The fuel is transferred via a simplex nozzle to the inside surface of a venturi. A swirled airflow forces the fuel film to the end of the venturi, where it is atomized into fine droplets at the pre-film separation edge, where there is an outer and inner airflow, with the outer flow being swirled in the opposite direction to the inner flow. The air leaving the nozzle flows around the contour of the combustor dome. This flow pattern, important for the spray characteristics, is observable in water-simulation tests and can be demonstrated mathematically. Figure 2 shows the calculated isothermal flow downstream of the nozzle, determined by a two-dimensional flow-field calculation. It can be clearly seen that the whole of the flow of air leaving the nozzle flows radially outwards and becomes attached to the rear wall. This behaviour remains constant throughout the operating range.

The purposes of the air blast atomization system are the following:

- To atomize the fuel in very fine droplets
- To generate a stabilizing recirculation zone
- To generate high turbulence for the mixing of the air, fuel and recirculated exhaust gases
- To ensure homogeneous distribution of the fuel in the primary zone of the flame tube.

In contrast to other fuel-injection system, such as a pressures atomization system for example, the purpose of the air blast atomizer is not merely to generate very fine droplets. It must also generate a large stabilizing recirculation zone, and this is achieved in particular by the radial flow of the swirled air on discharge. The atomized fuel follows the flow of air to a greater or lesser extent, depending on the strength of the interaction. This interaction determines both the droplet size and the fuel distribution in the primary zone of the combustor.

The droplet size and fuel distribution are examined more closely below.

2.2 Droplet measurement

The droplet size was measured with the aid of the apparatus depicted in figure 3. To enable the droplets to be measured at increased pressure as well, a double-walled container with variable-diameter air discharge line is used. The air stream m_1 is the atomization air, whereas air stream m_2 is required for purging the observation windows. This container can be used for pressures of up to 10 bar.

The droplets were measured using an optical procedure based on the light-diffraction principle. Details of this method can be found in reference /1/. This procedure suffers from inherent difficulties if the spray-cone becomes optically too dense, which occurs preferably under high-pressure conditions. Thus, to reduce the optical density, the laser beam was focused on one half of the spray cone via a tube. The light intensity was evaluated on the basis of the Rosin-Rammler function for the droplet-size distribution. As liquids, water and kerosine were used.

2.3 Measurement of fuel distribution

The measurement of the local distribution of the fuel was carried out using the same apparatus as for the droplet-size measurement, but without the optical tube for diffraction measurement, which was replaced by a fuel collector vessel downstream of the nozzle. The distance S between the collector and the nozzle could be adjusted by means of a threaded rod (figure 4). The collected fuel was weighed with the resulting mass flow being determined as a function of the distance S. This allowed the volume of fuel, injected at a certain angle, to be determined, where the following relation between the spray angle and the distance S, corresponding to the geometrical conditions shown in figure 5, results:

$$\alpha = 2 \arctan \frac{r_2 - r_1}{S}$$

where r_2 is the radius of the fuel collector und r_1 is the radius of a reference cross-section of the nozzle. If the collector is positioned immediately next to the nozzle, the spray angle is 180°, decreasing to zero with distance of the collector from the nozzle.

In the experimental arrangement chosen, the flow through the nozzle is affected to a greater or lesser extent, depending on the position of the collector. At least, a marked effect will occur when the collector is located very close to the nozzle. But, because of the nature of the flow field of the fuel injector nozzle, this effect decreases very rapidly with increasing distance of the collector to the nozzle. As already mentioned, the air flowing from the nozzle becomes attached to the rear wall of the test cell, and is disturbed by the collector only at very short distances. The low-pressure region occurring downstream of the nozzle is filled, however, not by the recirculation of the nozzle air, but by air from the collector. This is possible since the collector is connected with the test cell via side openings.

3 Results

3.1 Droplet size

A series of measurements was made with water and with kerosine, varying the air pressure and relative pressure drop via the nozzle in each case. The influence of viscosity and the air-fuel ratio was not investigated, since this is already known well enough from the literature. The literature shows that the droplet size does not depend on the viscosity, if the higher-viscosity liquids are excluded /2/. This finding is confirmed in more recent investigations /3/, where it is demonstrated that up to 33 cP the viscosity has no effect on the droplet size. Ref. /2/ also shows that the effect of the air-fuel ratio can be ignored as long as it is not less than 3:1. In the present case, the AFR was in the region of 7.7:1, in other words a value at which it was expected to have had little influence on the droplet size, and this was confirmed by several random verifications.

The influence of the air pressure and the relative pressure drop on the Sauter diameter of the spray cone is represented in figure 6 for kerosine and water. Because the shear forces of the air play a major role in the atomization of the fuel, the droplet size decreases with increasing drop in pressure. Similarly, because of the accompanying higher air density, higher pressures lead to a marked reduction in the droplet size.

These findings apply qualitatively to both liquids. Quantitatively, as expected, there are major differences. Under identical conditions, the Sauter diameters are nearly twice as great with water as with kerosine.

As can be seen in figure 7, the values for water and air correlate with a certain scatter over the reciprocal value of the Weber number We, according to

$$SMD = 6.7 \left(\frac{1}{We}\right)^{0.5} \qquad (1)$$

where the Weber number is defined as $We = \frac{2\ \Delta p_A}{\sigma_L} d_N$ in which the characteristic diameter d_N is kept constant and taken to be equal to 1. For this We-number, correlation represents 83% the measurements with better than ± 25% fluctuation. The relatively large scatter is caused by insufficient variation in the surface tension, represented by only two liquids. Furthermore, it must be remembered that the method of measurement used is not free of errors. Ref. /4/ provides an estimation of the error involved in the measurement of the droplet size by the diffraction method, according to which the relative error is approximately 11%.

In the light-diffraction procedure, the result of the measurement is represented in a Rosin-Rammler distribution of the spray, in which, as is known, the distribution is represented not only by a characteristic diameter, such as the SMD for example, but also as to two-parameter distribution by the exponent n. If the SMD alone is stated, the so-characterized distribution is comparable with others if the exponent n remains constant.

The dependence of the exponent n on the We number is shown in figure 8. It varies only slightly, increasing as the We number increases. The functional relationship is

$$n = 4.1\ We^{0.16}$$

This means that increasing We number produces somewhat closer scatter in the droplet size.

The finding for SMD shows good correspondence with the relevant investigations as per references /2/ and /3/, where the Sauter diameter is correlated by the relation $SMD \sim (\sigma_L / \Delta p_A)^b$ and where the exponent b lies between 0.45 and 0.6.

3.2 Local fuel distribution

Determination of the amount of liquid atomized under different angles results in a cumulative frequency curve over the spray angle (figure 9). To enable this curve to

be characterized by a single value, the angle α_{50}, at which 50% of the fuel is injected, has been introduced.

Approximately 60 measurements were made at different pressures and relative pressure drops, using two different liquids, plotting a cumulative frequency curve and determining the angle α_{50} in each case.

The results were correlated using the following relationship:

$$\alpha_{50} = 0.065 \left(\frac{\Delta P_A}{P_A}\right)^{0.423} p_A^{0.61} \, AFR^{0.36} / \sigma_L^{0.186} \qquad (2)$$

This equation correlates 80% of the measurements within a scatter of ± 15% (figure 10). In the same way as the mean SMD, the spray angle α_{50} very much depends on the relative pressure drop and the absolute air pressure as well as on the surface tension, giving rise to the suspicion that in this case also, the droplet size is of significance. Comparison of equation 2 with equation 1, however, reveals clear differences between the exponents. Furthermore, there is an additional dependence of the fuel flow or the AFR at constant air flow.

On the basis of a selected series of measurements, the behaviour of the spray angle depending on the air pressure, pressure drop and the AFR is illustrated below.

3.2.1 Air-fuel ratio

The AFR was varied by varying both the air mass flow, i.e. the pressure drop via the nozzle, and the fuel flow rate. The influence of the AFR on the spray angle α_{50} is shown in figure 11. The angle becomes smaller with decreasing AFR, i.e. with increasing fuel content of the mixture. This applies to a very similar extent with both large and small pressure drops irrespective of the test liquid. The larger liquid content increases the amount of inert liquid to be accelerated by the air, meaning that the acceleration of the individual droplets becomes lower. Consequently, this leads to a change in the spray angle because the flow of air downstream of the nozzle is subject to a marked radial directional change, which is followed by the droplets decreasingly as the strength of the aerodynamic forces acting on them weakens. Figure 11 also illustrates how well the measurements are approximated by the correlation. Under the realistic conditions of AFR of 5 - 10:1 the degree of error is less than 12%.

3.2.2 Pressure drop

The relative air pressure drop was varied between 2 and 12%. The relationship between the spray angle α_{50} and the pressure drop for three different pressures at constant AFR is shown in figure 12. As the pressure drop increases, the angle grows noticeably, and all the more so as the pressure increases. Clearly, under these conditions the fuel droplets increasingly follow the air as it flows radially outwards.

For the technically interesting range of 3% pressure drop, equation 2 represents the effect of pressure drop on the spray angle with an error of less than 10%.

3.2.3 Air presssure

The air pressure was varied between 0.1 and 0.4 MPa at constant relative pressure drop. Its influence on the spray angle α_{50} is shown in figure 13. As the air pressure increases, the spray angle increases and approaches a limiting value, which is reached when the direction of flow of the fuel droplets fully coincides with that of the air. Evidently, under normal combustor conditions ($\Delta P_A/P_A \approx 3\%$), this value will be reached already at the relatively low pressure of 0.4 MPa, since at this pressure the spray angle α_{50} is in the region of 160°. With the present geometry of the test cell, it is not possible to have a spray angle greather than 180°.

Since the air temperature was constant in the tests, the density of the air depended solely on the pressure. Hence, the spray angle α_{50} is plotted against the density ratio of liquid to air in figure 14. In this case, the liquid used was water, meaning that similar spray angles to those obtained using kerosine are only reached at smaller density ratios.

In combustion chamber tests the air is normally preheated to the compressor discharge temperature and as a result, at the same pressure, the air density is about half that in the spray tests here. Consequently, the spray angle in these tests would have been influenced by pressures higher than 0.4 MPa, were it not for the fact that under combustion conditions the fuel droplets lose mass to evaporation along their flight path, and follow the air stream more rapidly.

It remains to be noted that already at relatively low pressure as mentioned above, the influence of the present air blast atomization system on the pressure-dependence of combustion can be ignored, but that under atmospheric conditions, however, it is not possible to obtain representative results.

3.2.4 Influence of droplet size on the spray angle

The ability of the droplets to follow the air flow depends on the size of the droplets, where smaller droplets follow the flow better than large ones. It can thus be assumed that the the spray angle α_{50} will also be affected by the mean SMD of the spray. To verify this, the Sauter diameter from equation 1 is introduced into the correlation acc. to equation 2, resulting in the following relationship:

$$\alpha_{50} = \frac{\left(\frac{\Delta p_A}{p_A}\right)^{0.237} \cdot p_A^{0.414} \cdot AFR^{0.36}}{SMD^{0.372}}$$

This equation shows that the spray angle decreases as the SMD increases, which, in view of the stronger impulse of the large droplets, is a reaction that was to be expected. As a rule in combustor testing, the relative flame tube pressure drop is maintained constant irrespective of the test pressure. Therefore the droplet size mainly depends on the absolute pressure drop, and with increasing test pressure not only the droplet size, but also the fuel distribution varies. The influence of the Sauter diameter on the fuel distribution is of the same order as the influence of pressure. The significance of the relative pressure drop is small because, the relative pressure drop remains more or less constant, also if the combustion chamber is operated under differing pressure conditions, .

4 Conclusions

Using an air blast atomizer as an example, the influence of pressure and test liquids on the droplet size and fuel distribution is illustrated. It is well known that both have a marked effect on the combustion process and the related factors such as wall temperatures, smoke behaviour, coke formation, stability of combustion and temperature distribution at the combustor outlet. The pressure was regularly found the exert a marked influence on the above criteria, for example when tests at atmospheric pressure are compared with those at higher pressures. There are various reasons for this, such as the greather flame radiation, accelerated thermal and mass transfer or higher reaction rates. But it is revealed that these phenomena alone are not sufficient to account absolutely for the change in behaviour between operation at atmospheric and at higher pressure. An attempt was therefore made to investigate the spray behaviour of the air blast atomizer in relation to absolute pressure in a test set-up at constant air temperature without combustion.

This revealed the following:

- The droplet size, represented by the SMD, can be correlated well with the absolute pressure drop, where the exponent of this relationship corresponds well with exponents derived from measurements according to the literature.

- The mean spray angle α_{50} changes markedly with air pressure. This has two causes, firstly the pressure-related mass inertia of the droplets, and secondly the pressure- and relative pressure drop-related aerodynamic forces of the air acting on the droplets. Whilst the mass inertia of the droplets assists them maintain their direction of motion, the aerodynamic forces tend to force the droplets to change direction, insofar as the flow directions of the air and droplets differ. Such conditions usually prevail when the air is strongly swirled by the nozzle.

- The two causes can be separated. The influence of pressure on the spray angle α_{50}, resulting from the aerodynamic forces, is of similar magnitude to that resulting from the droplet size.

- In contrast to the droplet size, the spray angle also depends on the AFR, because of the interaction between the fuel and air downstream of the nozzle. As the amount of fuel in the mixture increases, the aerodynamic forces acting on the droplets decrease, and the spray angle grows smaller.

- If, for safety reasons, the atomization tests are carried out using water instead of fuel, the conditions must be adapted according to whether the droplet size or the spray angle is being investigated.

5 Acknowledgement

Part of the work reported was financed by the Federal German Ministry of Research and Technology. This support is gratefully acknowledged.

6 References

/1/ Kayser, A., Pita, G.P.A., "Die Industriefeuerung" Vulkan Verlag, Essen, Heft 21, pp 26-39 (1981)

/2/ Lefebvre, A.H., "Gas Turbine Combustion", Hemisphere Publ. Corp., Washington, New York, London (1983)

/3/ Aigner, M., Wittig, S., "Swirl and Counterswirl Effects in Prefilming Airblast Atomizers" ASME Paper No 87-GT-204 (1987)

/4/ Schneider, M.H. "Investigation into the Influence of Atomization on the Evaporation of Liquid Fuels in Turbulent Spray Flames" (in German) Thesis, TH Darmstadt (1986)

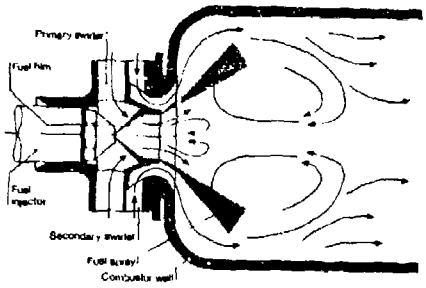

Fig. 1: Scheme of an Air Blast Atomizer

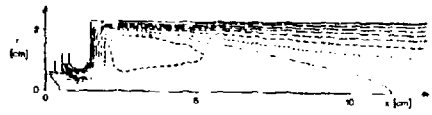

Fig. 2: Streamfunction of the Computed Flow Field behind the Atomizer

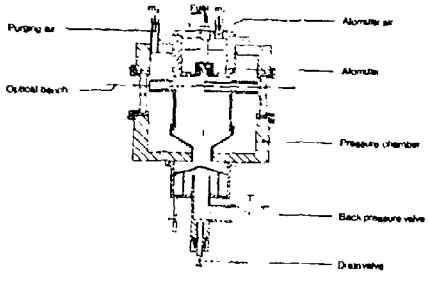

Fig. 3: Apparatus for the Determination of the Droplet Size Distribution

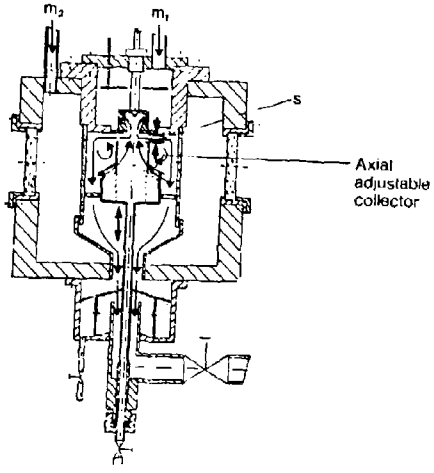

Fig. 4: Apparatus for the Determination of the Spray-Angle Distribution

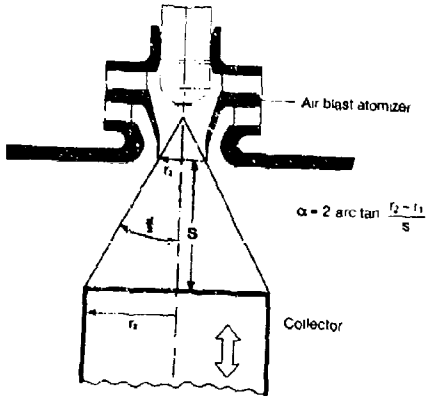

Fig. 5: Determination of Spray Angle from the Geometrical Dimensions

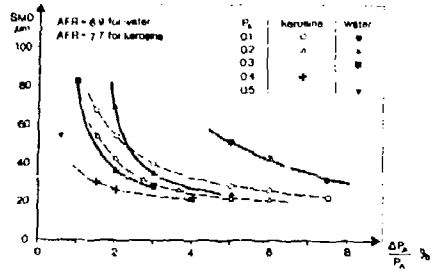

Fig. 6: Influence of Varying Atomizer Air Pressure Drop and Ambient Air Pressure on Spray Mean Droplet Size

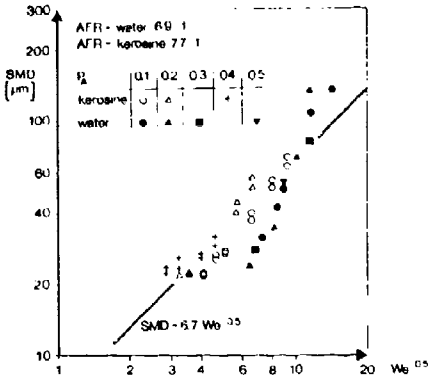

Fig. 7: Effect of Weber Number on Mean Droplet Size

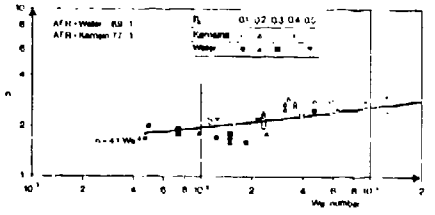

Fig. 8: Effect of Weber Number on the Exponent "n" of the Rosin Rammler Distribution

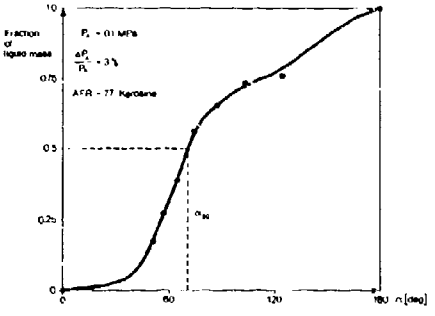

Fig. 9: Measured Spray Angle Distribution Curve

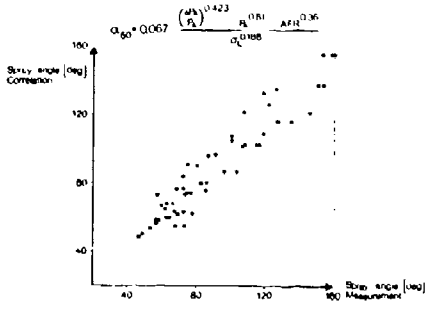

Fig. 10. Correlation for the Mean Spray Angle α_{50}

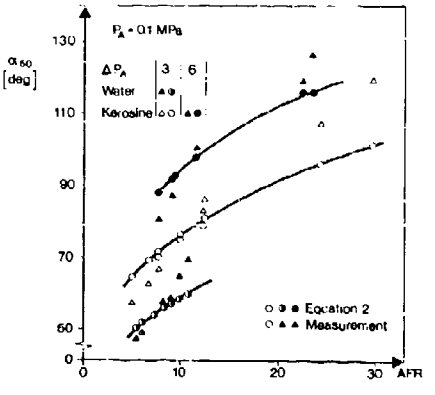

Fig. 11: Effect of Air/Liquid Ratio on Mean Spray Angle α_{50}

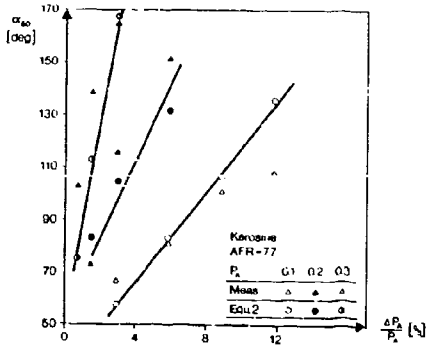

Fig. 12: Effect of Atomizer Air Pressure Drop Upon Mean Spray Angle

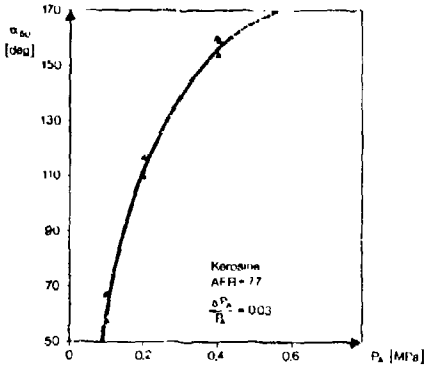

Fig. 13: Effect on Ambient Air Pressure on Mean Spray Angle α_{50}

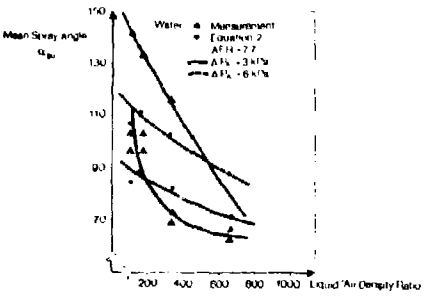

Fig. 14: Effect of Liquid/Air Density Ratio Upon Mean Spray Angle α_{50}

DISCUSSION

A.Lefebvre, US

Your analysis of the factors governing spray angle and the variation of spray angle with combustion operating conditions has much to commend it.

However, it is not made clear in your paper that the equation you have derived for spray angle applies only to the atomizer/swirler configuration you have tested, and could give misleading results if applied to other fuel nozzle/air swirler combinations.

Author's Reply

It was not the intention of our papers to derive a spray angle equation suitable for all types of atomizers. What we wanted to show is that there is a masked influence of air pressure on the spray angle according to the given equation for atomizer/swirler combinations, where the atomizer is surround by a strong swirler. This was also pointed out in the conclusions.

SPRAY PERFORMANCE OF A VAPORISING FUEL INJECTOR

A. K. Jasuja
School of Mechanical Engineering
Cranfield Institute of Technology
Cranfield
Bedford, MK43 OAL

H.C. Low
Rolls Royce plc
P.O. Box 3
Filton
Bristol, BS12 7QE
UK

SUMMARY

The purpose of this paper is to examine the spray performance of a vaporiser fuel injector of a type that has accumulated extensive service experience in sub - and supersonic commercial and military aircraft applications. Spray performance data covers a wide range of operating conditions including the effects of fuel quality as well as the atomizing air temperature. The chief objective is to further not only the current level of understanding regarding the fundamental functional aspects of vaporiser technology but also the data base for future designs.

INTRODUCTION

Effective fuel-air mixture preparation is now widely recognised as being of paramount importance in order to achieve satisfactory combustor performance. This is acknowledged to be the case in the context not only of the current but to an even greater extent for the future generation of gas turbine engines with their inherently more demanding operational requirements of pressure, temperature, fuel flexibility/flow range and pollution control. The mechanism through which bulk fuel is transformed into a spray of droplets and the factors influencing their behaviour need to be well understood if sprays featuring optimum characteristics as well as satisfactory interaction with the combustor primary zone environment are to be generated. This has resulted in a considerable amount of research activity in recent years focusing attention upon the structure of spray emanating from fuel injectors. However, with very few exceptions (Refs 1-3) these studies have been restricted to pressure and airblast atomised sprays, largely at ambient air conditions.

This paper is devoted to an examination of the spray performance of a vaporising fuel injection system of a type that has been used extensively by Rolls-Royce in sub-and supersonic commercial and military aircraft applications. The modern annular vaporising chamber concept depicted in Figure 1 is fully described in Ref 4. The continuing effectiveness of the vaporiser is demonstrated by its having achieved substantial trouble-free service life, 2300 hours to date, in the Olympus 593 engine featured in Concorde. Confidence in its future is illustrated by its current use in the RB199 engine in Tornado as well as by its selection for the EJ200, the Euro Jet Fighter for the next century. Whilst the vaporising fuel injector has demonstrated highly competitive combustion/emissions performance thus far, its projected useage under more arduous conditions of operation has prompted a thorough re-appraisal of the fundamental functional aspects of vaporiser technology.

It transpires that the corridor of satisfactory vaporiser operation (eg. adequate mechanical integrity without significant smoke, carbon accretion etc) narrows with increasing compressor exit temperature. Extreme caution therefore needs to be exercised in the selection of the air-to-fuel ratios (AFR) that the vaporiser is designed to operate with, especially at fuel rich conditions. Of particular relevence to the design process is the development of an in-depth understanding of the mechanistic as well as the operational behaviour of the vaporising injector through a series of well-planned and executed experiments under non-combusting and combusting conditions. Some of the results pertaining to the vaporiser efflux obtained during the course of such studies are the subject of this paper.

EXPERIMENTAL

At the very outset it was felt that the use of imaging cum laser diffraction techniques should prove beneficial in obtaining experimental data that would shed adequate light on the mechanistic/operational behaviour of the vaporising style of fuel injector. Short duration spark photography was expected to identify the character of the efflux at the point of exit from the vaporiser tutes under non-combusting and combusting conditions whereas the laser diffraction technique was to provide quantitative information regarding the spray structure vis-a-vis the drop size. Futhermore, the well established, non-intrusive nature of the two techniques selected for experiments offered the prospect of meaningful and reliable results.

The test hardware and experimental technique employed in the spark photographic investigation were largely as described in Ref 1. A single vaporiser sector cut from a typical annular combustor was fitted with transpiration cooled sidewalls and modified to permit optical access to the vaporiser efflux zone (figures 2,3). A heat exchanger was installed in the vaporiser fuel delivery line to enable the fuel temperature effects to be investigated in this study.

The argon arc light source and associated optics provided a parallel beam of light which illuminated the spray for a duration of approximately 300 ns and a focused shadow of the 'frozen' efflux was cast in the plane of the film. The current exercise featured a light source of increased power (ca. X1.5) to that of the Lunartron unit used in the previous tests - thus offering the prospect of more reliable data. The shadowgraphy technique was applied to combusting and non-combusting effluxes at air pressures upto 1300 kPa.

The experimental set up utilised for spray drop size measurements was similar to that used in Ref. 5. Non-vitiated, hot air was generated by using electrical resistance heating in combination with counter-flow type of heat exchanger unit connected to a kerosine fired slave combustor. The mass flow of hot air that was surplus to requirement bypassed the vaporiser working section. An orifice plate to BS1042 was installed as close as practically possible to the measurement section to enable the air mass flow monitoring. A thermocouple was located just upstream of the vaporiser air inlet. Air pressure drop across the vaporiser was measured by a manometer and all drop size tests were carried out at near atmospheric pressure.

The vaporiser as well as the fuel injector geometry for the drop size study was basically identical to that deployed for the spark photographic assessment. The fuel supplied to the injector was at ambient temperature and the relevant flow conditions were achieved by using calibrated flow meters.

Spray drop size measurements were carried out by utilising a commercially available particle sizer - Malvern Instruments Model 2200. Briefly, the instrument is based upon the well established principle of diffractive scattering of a collimated, coherent and monochromatic beam of light in the forward direction as a result of its passage through the test spray. The instrument uses a Helium - Neon laser as the light source while a multi-element, concentrically configured, semi-circular ring detector monitors the scattered light signals. Through a process of iteration a dedicated microcomputer arrives at a drop size distribution that exhibits a computed light energy distribution close to that actually measured. The computed versus measured light energy distribution comparisons can be performed for a range of assumed drop size distributions - notably Rosin - Rammler, log - normal, model - independent, etc.

In house and commercially developed light diffraction instruments have been used extensively for gas turbine fuel spray research in recent years. Drop size data reported in the open literature, thus far however, has been confined mainly to injectors spraying in ambient air conditions due to considerations of cost and complexity. Some exposure had nevertheless, been achieved in the use of such optical techniques for twin-fluid atomised spray studies in elevated air pressure environments (Refs. 6 and 7). By contrast there was almost a total dearth of similar exposure to twin-fluid atomised spray studies under conditions of elevated air temperature. Preliminary tests with hot air revealed the pattern of light scattering in the proximity of the optical axis to be significantly different from that for the ambient temperature tests. This change in light scattering pattern was observed to follow the air temperature, increasing with an increase in air temperature and vice versa. Furthermore, the problem seemed to be just as severe even in the absence of liquid fuel injection. From analysis of the scattering data, it became apparent that the laser beam was being diffused/steered in the vicinity of the optical axis. Refractive index variations resulting from temperature gradients are responsible for the generation of additional scattering cells. Consequently, the overall scattering pattern is a combination of that due to liquid droplets as well as the thermal effects. The procedure adopted during the tests was to record the background light scattering levels at each of the working temperatures in the absence of liquid fuel injection as the reference. This was followed by the test run wherein the fuel was injected and the subsequent drop size analysis took account of the background light levels at the relevant air inlet temperature thus effectively countering the beam steering problem.

Effects of fuel quality upon vaporiser performance were confined in both studies to aviation kerosine and gas oil. Relevant properties of the two fuels are listed in table 1.

RESULTS AND DISCUSSION

The primary objective of the parametric exercise reported here was to study the effect of air, fuel and injector variables upon vaporiser performance in a combusting and non-combusting environment. This was expected to improve not only the level of knowledge regarding the detailed structure of the two-phase efflux emanating from the vaporising fuel injector but also the design capability for future applications. Futhermore, the availability of such experimentally determined representative data could also enhance the prospect of its being usefully correlated with some key aspects of combustion performance.

Spray Imaging

This technique is generally capable of detecting the very high frequency variations to which all fuel injectors are subjected. The photographs presented in this paper feature a magnification of approximately three and give a good account of the average situation at each test condition. The zone illuminated by the spark is shown in figure 3.

Effect of Combustion

The comparison made between the effluxes at non-burning (no vaporisation situation) and burning conditions, plate 1(a) and 1(b) respectively, highlights the significance to fuel preparation process of the heat transfer from the reacting gases to the vaporiser walls. A detailed semi-empirical assessment of the external heat transfer processes with allowances for turbulence enhancements of the convective and radiative fluxes inferred an upper limit of 50 percent for the degree of vaporisation at this burning condition. This is borne out by the experimental results.

Effect of Fuel Temperature

Fuel temperatures significantly higher than ambient occur at all engine conditions as a result of the fuel being used as the coolant medium in lubricating oil coolers. The effect this has on the fuel preparation process within the vaporiser at idle conditions is also evident in Plate 1,(b) versus (c). A comparison between plates 1(c) and 1(a) reveals the degree of vaporisation under combusting conditions with hot fuel to be of the order of 80 percent. This is broadly in line with the predicted value at these conditions.

Effects of Vaporiser AFR, Inlet Air Temperature

It is clear from Plate 2 that increases in AFR have a beneficial influence upon the spray quality. Since such improvements are translated into higher combustion efficiencies and lower smoke/carbon levels it is extremely important that as high a vaporiser air throughput as is compatible with integrity should be employed.

Similarly, the degree of vaporisation and fineness of the spray improve with increasing inlet air temperature (Plate 3). Provided that the air temperature is above the boiling range of the fuel at a given pressure, this mechanism of fuel heating is very effective considering the short residence times involved. These results suggest an intimate physical contact between the fuel and air within the vaporiser. This is a direct consequence of the complex internal aerodynamics (see plate 4) necessary to ensure that all internal surfaces of the device are well scrubbed by the two phase mixture (Ref. 8).

Effect of Pressure

The spark photographic investigation has been extended to examine the vaporiser efflux at high pressures. As expected the mottled background (schlieren effect seen in all combusting effluxes) became increasingly dense at higher pressures eventually causing a degree of obscuration beyond which no useful information could be derived by this approach. The working range of the technique was thus defined as between ambient pressure and 1300 kPa.

The efflux for a typical AFR and inlet air temperature at this pressure limit is presented in Plate 5. Although the ability of the technique to detect droplets at these pressures is unknown, it is fair to claim a high degree of vaporisation at this condition bearing in mind that here there is a four-fold increase in fuel flow over the idle condition.

From a simple analysis of the two phase flow through the device at these conditions it is clear that the heat energy of the airstream alone is sufficient for this to be the case. Autoignition precluded comparisons of burning and non-burning effluxes at this pressure.

A very modest carbon accretion on the vaporiser outlet is evident at this condition.

Effect of Injector Geometry

The 4-jet fuel injector was conceived as a solution to the problem of potentially damaging thermal gradients resulting from the deletion of stem cooling air on the Olympus 593 vaporiser (Figure 4). Although its introduction in service has not proven necessary with the identification of improved materials, this fuelling arrangement may make a worthwhile contribution to gaseous emissions and smoke/carbon control at more arduous operating conditions.

An investigation of its effect on efflux quality (Plate 6) confirmed the potential benefits of doubling the number of fuelling points. The more even fuel coverage of the vaporiser stem walls is translated into an improved fuel distribution at the outlet and furthermore at high inlet air temperatures the more intimate fuel/air contact is reflected in higher degrees of vaporisation relative to the standard 2-jet system. Such improvements in fuel preparation prior to combustion may prove necessary to maintain smoke and carbon deposition at acceptable levels for advanced cycle engines.

Effect of Fuel Quality

It is desirable that the vaporising fuel injector exhibits satisfactory fuel flexibility/multi-fuel capability to adequately cope with the potential concerns regarding the quality of gas turbine fuels in future as well as under emergency situations. Consequently to determine the sensitivity of the vaporiser fuel preparation process to fuel type, efflux measurements were made while burning a poor quality gas oil. A direct comparison with the performance on standard aviation kerosine is made in Plate 7. From a simple calorimetric viewpoint, the lower degrees of vaporisation seen with the gas oil are not surprising. However, it has been demonstrated recently in a series of alternative fuel engine tests that the penalty incurred in idling efficiency as a result of such a deterioration in spray quality is less than 0.05 percent.

An important point to note is that at the engine idle condition (Plate 7, Condition A) no evidence of carbon deposition on the vaporiser is seen with the gas oil. Furthermore, boroscope inspections of the engine combustor after extended running on similar and even poorer quality fuels over the entire operating range revealed no significant carbon accretion on the vaporiser or anywhere else within the combustor. It was discovered possible, however, to generate substantial deposits on the vaporiser stem and outlet tube at certain conditions not encountered during engine operation (Plate 7, Condition B). The level of deposition shown represents an equilibrium situation.

The overall impression that emerges from the spark photographic work and engine test programme is that the vaporising combustor is remarkably insensitive to fuel type.

Dropsize Measurements

Before the main investigation could proceed, the location of the drop size measuring station had to be selected carefully in order to ensure meaningful results. Measurements that are made too close to the vaporiser outlet will be misleading because the mechanism of droplet/spray formation will not have proceeded to its natural completion. Equally, measurements too far downstream from the outlet will also be unsatisfactory due to the possible influence of such secondary effects as droplet coalescence and evaporation. Experimental data in this study was obtained at two stations located some 3 and 6 centimetres from the vaporiser outlet. The 3 centimetre station was relevant to the combustor head/vaporiser geometry while the other station was selected to ensure compatibility with the bulk of other work carried out at the spray laboratories. Drop size data relating to the 3 centimetre station is presented in the subsequent sections while reference 9 features the full data.

Effect of AFR

Figure 5 depicts the influence that the vaporiser AFR has upon its Sauter Mean Diameter (SMD) performance for a range of air inlet temperatures with kerosine as the spray medium. An increase in vaporiser AFR can be observed to result in an improved spray quality, although the degree of improvement diminishes at higher levels of air inlet temperature as well as AFR. This reinforces the spark photographic study finding that higher values of AFR are conducive to the attainment of improved combustion performance. From these results it is evident that caution needs to be exercised in selecting the design point AFR. Excessively large values of AFR may result in some of the additional air not actually contributing to improved spray/combustion performance along with the added risk of thermal distress at high power conditions.

Effect of Air Pressure Drop

Engineers are faced with the perennial demand of having to design gas turbine combustors that will operate satisfactorily with a minimum of air pressure drop. This in turn requires that careful attention be devoted to the vaporiser air flow features in order to achieve the best possible level of spray performance that is compatible with required degree of wall cooling. Figures 6 and 7 illustrate the influence that vaporiser air pressure drop has upon spray quality. Clearly, the higher the available air pressure drop the superior the drop size performance although the degree of this superiority can be seen in both the figures to diminish somewhat at higher levels of air inlet temperature. Both the above performance trends are, generally speaking, akin to those already established for conventional air blast atomisers (Ref. 6,7).

Effect of Air Temperature

The influence of air temperature on mean drop size is shown in figure 8 where SMD is plotted against vaporiser inlet air temperature for a range of AFRs at a constant air pressure drop of 5 percent. Higher air temperature can clearly be seen to yield significantly finer sprays.

Such a powerful effect of air temperature upon mean dropsize performance is in agreement with the findings of the imaging study. The airblast atomisation study of Rizkalla and Lefebvre (Ref. 10) is the only other attempt, to the best of the authors' knowledge, at exploring the effect of air temperature upon twin-fluid atomised spray quality. However, their work was limited to a maximum air temperature of 424°K and the interpretation of results somewhat difficult due to the combined variations in AFR and air inlet temperature. Futhermore, they made no comment whatsoever regarding the problem of beam steering. Their results showed a linear increase in SMD when the air temperature was raised in conjunction with a reduction in AFR. In view of the

foregoing, however, it is perhaps inappropriate to draw comparisons between the two studies. In general though, the effect of air temperature upon spray quality would be expected to be somewhat stronger for the vaporising type of fuel injection system relative to the air blast due largely to the considerations of residence time and internal aerodynamics.

Effect of Fuel Quality

Figure 9 illustrates the effect of fuel quality upon vaporiser mean drop size performance over a range of inlet air temperatures. At air temperatures close to ambient, the change in spray media from kerosine to gas oil leads to an increase in SMD due largely to an increase in absolute viscosity alone - the effects of changes in surface tension, density and distillation range being relatively insignificant. As the air temperature rises, the difference in spray quality is a consequence of the combined influence of absolute viscosity and distillation range differences. These results do not, however, provide an insight into their relative importance from the viewpoint of SMD. On the face of it, the viscosity sensitivity of the vaporising fuel injector at air temperatures close to ambient does not appear to exhibit any marked difference relative to that observed for airblast systems. Furthermore, the vaporiser fuel injector is free from small orifices which may be prone to blockage due to gumming while operating on poorer quality fuels.

Effect of Injector Geometry

As stated before, the modified 4 jet fuel injector of figure 4 offers the prospect of reducing thermal gradients in the inlet section of the vaporiser tubes relative to the basic 2 jet injector. Figure 10 allows a comparative assessment of their spray performance at two different levels of air pressure drop. As might be expected and indeed observed in the imaging study the 4 jet injector is exhibiting a somewhat superior drop size performance as a result of more intimate fuel and air interaction. This is backed up by liquid film studies that show a more even coverage of the inside walls in the vaporiser inlet stem area (Ref. 9).

CONCLUDING REMARKS

The choice of imaging cum laser diffraction techniques for examining the spray performance of the vaporiser fuel injector has turned out to be a satisfactory one. A testimony to that effect is provided by the aforegoing sections of the paper that feature detailed and extensive experimental data covering a wide range of combusting as well as non-combusting conditions. The two techniques complement each other to yield a balanced insight into the phenomenological as well as the operational behaviour of the vaporiser - thus helping to advance significantly the state of knowledge regarding this style of fuel injector. Many of the uncertainties have been minimised if not entirely dispelled.

The results presented in this paper reveal that despite its mechanical and geometric simplicity, the vaporising fuel injector achieves high degrees of atomization, vaporisation and pre-mixing at engine idle conditions. Extension of these results to higher power conditions as typified for example by take off air pressures and temperatures would indicate further improvements in mixture preparation. In addition, the vaporiser seems to be remarkably insensitive to fuel type - coping admirably with gas oil.

The vaporising fuel injector exhibits spray performance trends that are generally similar in character to those already observed on conventional airblast atomizers - for example an improvement in spray quality with increases in AFR and air pressure drop whilst an increase in fuel viscosity having a somewhat adverse effect. A noteworthy exception to this general similarity being the stronger influence exerted by the air temperature upon the dropsize performance of the vaporiser due largely to considerations of residence time and internal aerodynamics. It is hardly surprising therefore, that the vaporising fuel injector is able to deliver highly competitive combustion/emissions performance.

REFERENCES

1. Low, H C, Recent Research on the Efflux of the Rolls-Royce Vaporiser Fuel Injector AGARD-CP-353, Paper 11, October 1983

2. Rosfjord, R J and Briehl, D, 'Evaluation of Fuel Injection Configurations to Control Carbon and Soot Formation in Small GT Combustors', AIAA Paper AIAA-82-1175, June 1982

3. Vezhba, I, 'Experimental Investigation of Fuel Evaporation in the Vaporising Elements of Combustion Chambers', NASA TM-75383, February 1979

4. Sotheran, A, The Rolls-Royce Annular Vaporiser Combustor, ASME Paper 83-GT-49, March 1983

5. Jasuja, A K, 'Atomization of Crude and Residual Fuel Oils', ASME Journal of Engineering for Power, Vol. 101, No. 2, April 1979, pp 250-258.

6. Jasuja, A K, 'Airblast Atomisation of Alternative Liquid Petroleum Fuels Under High Pressure Conditions', ASME Journal of Engineering for Power, Vol. 103, July 1981, pp 514-518

7. Jasuja, A K, 'Plain - Jet Airblast Atomisation of Alternative Liquid Petroleum Fuels Under High Ambient Air Pressure Conditions', ASME Paper No. 82-GT-32

8. Sotheran, A, 'Recent Advances in Vaporiser Fuel Injection Technology', 1983 Tokyo International Gas Turbine Congress

9. Jasuja, A K, 'Vaporiser Research Studies', Unpublished School of Mechanical Engineering Reports, Cranfield Institute of Technology, August 1983 and February 1986

10. Rizkalla, A A and Lefebvre, A H, 'The Influence of Air and Liquid Properties on Airblast Atomisation', Transactions of the ASME, Journal of Fluids Engineering September 1975, pp 316-320

ACKNOWLEDGEMENTS

The loan of Malvern Particle Sizer by Ruston Gas Turbines Ltd. for the dropsize study as well as the support and interest of those individuals who have made this paper possible is gratefully acknowledged. One of the authors (AKJ) wishes to thank the Institution of Mechanical Engineers for the award of a travel grant in connection with the paper presentation.

TABLE 1

PROPERTY	KEROSINE	GAS OIL
Density in kg/m^3 at 15^0C	797	863
Absolute Viscosity in Ns/m^2 at 15^0C	0.0013	0.0053
Surface Tension in N/m at 20^0C	0.027	0.0299
Distillation Range, ^0C	152-236	188-342

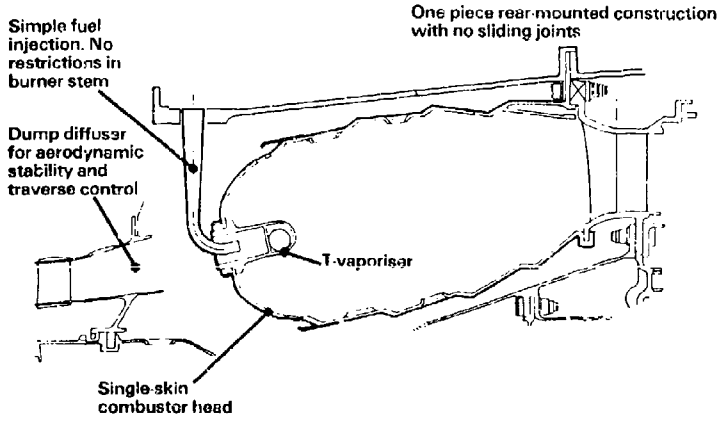

FIG. 1 ANNULAR VAPORISING CHAMBER

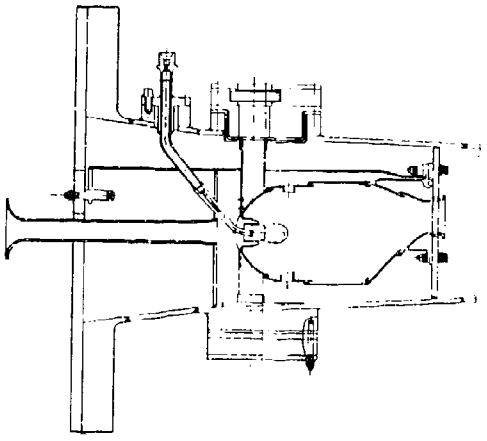

FIG.2. TEST UNIT

FIG.3.

ZONE ILLUMINATED BY SPARK

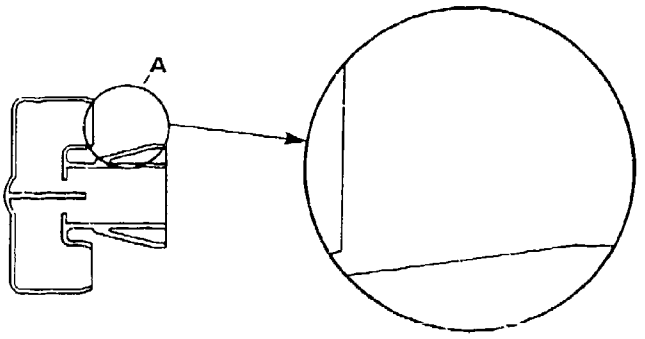

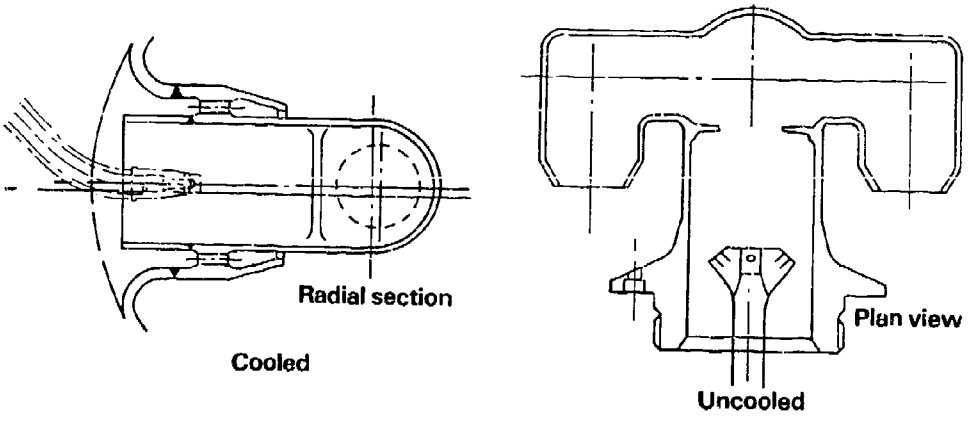

FIG. 4 VAPORISER CONFIGURATIONS

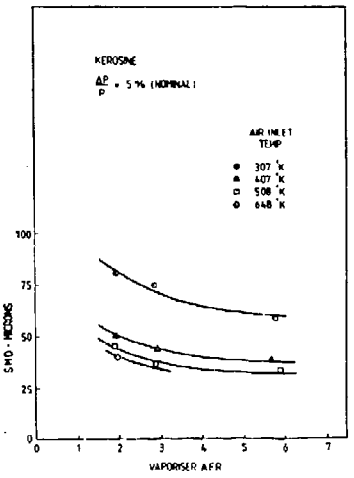

FIG 5 EFFECT OF VAPORISER A/F R UPON DROPSIZE

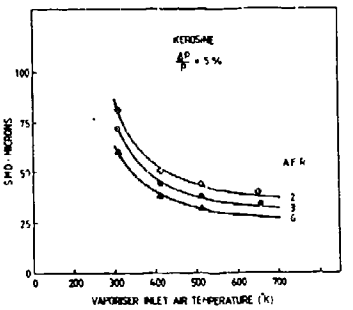

FIG 8 EFFECT OF VAPORISER INLET AIR TEMPERATURE

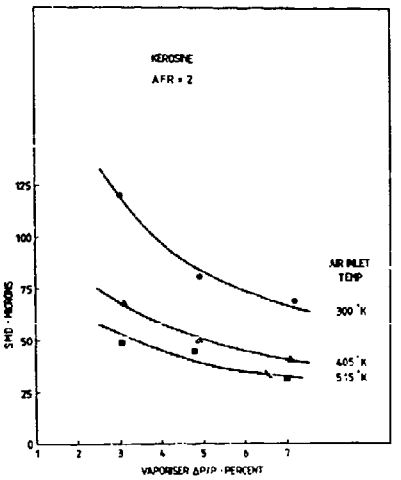

FIG 6 EFFECT OF VAPORISER PRESSURE DROP

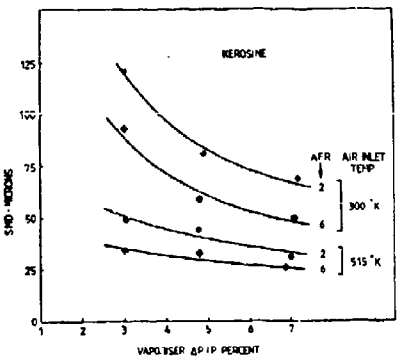

FIG 7 EFFECT OF VAPORISER PRESSURE DROP

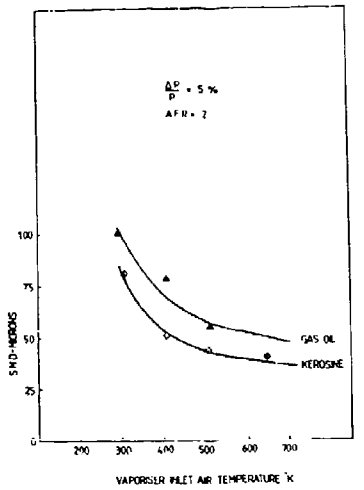

FIG 9 EFFECT OF FUEL QUALITY

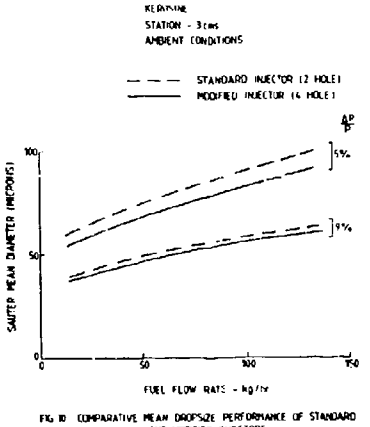

FIG 10 COMPARATIVE MEAN DROPSIZE PERFORMANCE OF STANDARD AND MODIFIED INJECTORS

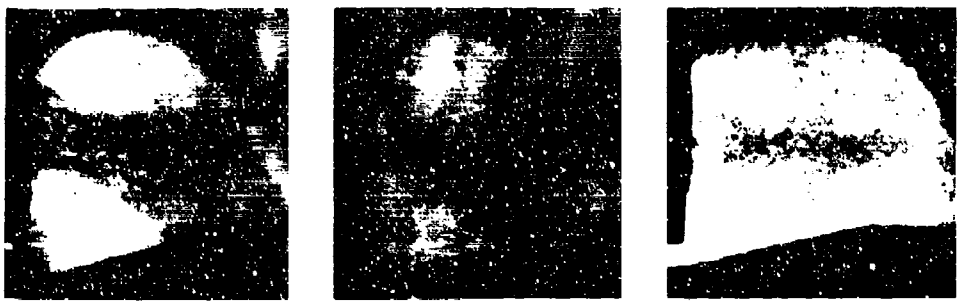

(a) T_{fuel} = 300°K, (NC) (b) T_{fuel} = 300°K, (C) (c) T_{fuel} = 423°K, (C)

Plate 1 Combusting(C) Versus Non-Combusting (NC) at 380 kPa; Effect of T_{fuel}

(a) AFR = 6:1 (b) AFR = 5:1 (c) AFR = 4:1

Plate 2 Combustion at 380 kPa - Effect of AFR

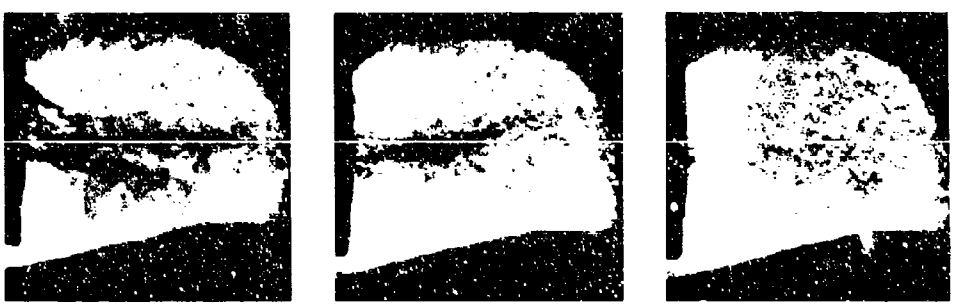

(a) T_3 = 453°K (b) T_3 = 523°K (c) T_3 = 573°K

Plate 3 Combustion at 380 kPa - Effect of T_3

(a) Effect of weir plates

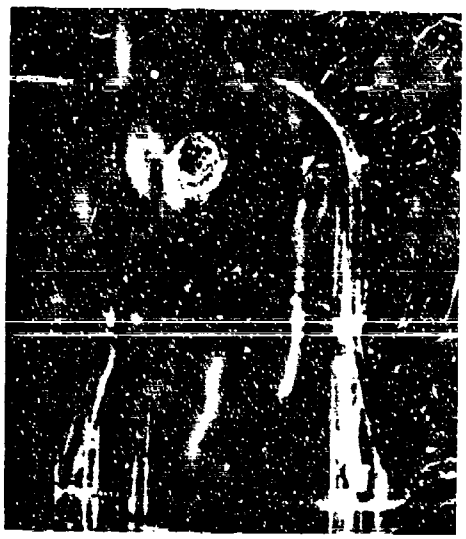

(b) View on 'A'

Plate 4 Vaporiser Internal Flows

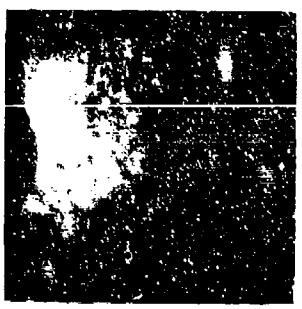

Plate 5 Combustion at 1300 kPa

(a) Two-Jet Injector (b) Four-Jet Injector

Plate 6 Combustion at 360 kPa - Effect of Injector Geometry

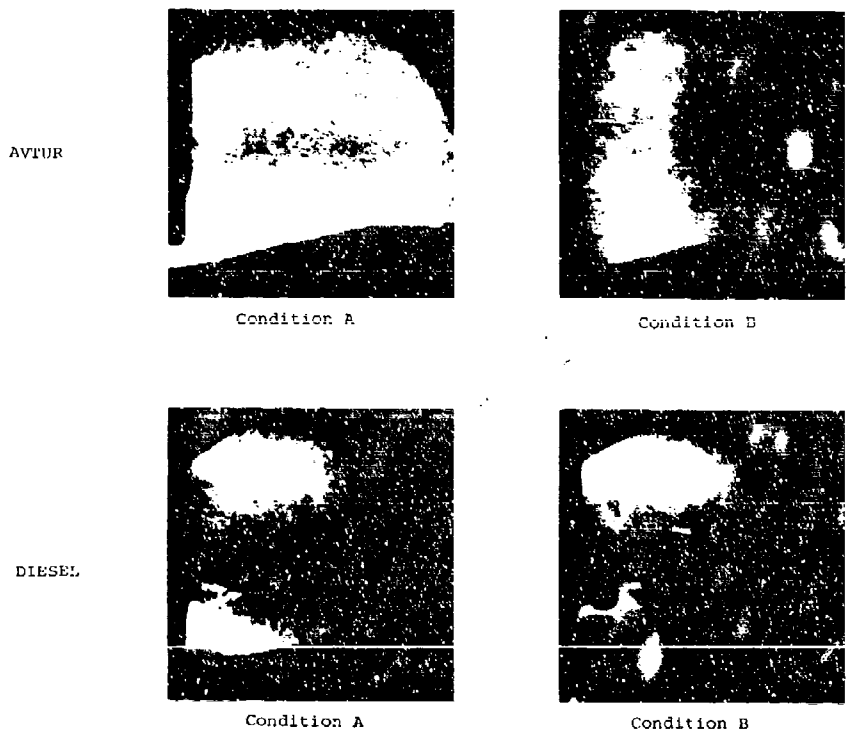

Plate 7 Combustion at 380 kPa - Effect of Fuel Quality

DISCUSSION

A.H.Lefebvre, US

You state that increase in inlet air temperature has a beneficial effect on atomization. Surely this is because, for a constant value of ΔPa/Pa, an increase in air temperature raises the velocity through the vaporizer. It is this higher velocity that enhances atomization, not the higher temperature which, in fact, has an adverse effect on atomization.

Author's Reply

The tests reported in Plate 3 were carried out at a constant ΔPa/Pa and this indeed meant that an increase in temperature resulted in an increase in air velocity. However, the magnitude of the improvement in atomization/degree of vaporization due to a temperature rise of 70°C (Plate 3(b) vs 3(a)) cannot simply be explained by the small increase in air velocity (calculated to be 7 percent). The improved spray quality is, therefore, clearly due to intimate contact between the fuel and the hot air within the vaporizer.

Question

You quote 5 percent as being typical of the pressure drop across a vaporizer. If this is true it represents a basic drawback to the vaporizer system in comparison to the airblast atomizer which functions very satisfactorily with pressure drops of half this value.

Author's Reply

Combustor design is based upon wall pressure drop rather than injector pressure drop. For a given wall loss the pressure drop across the vaporizer is no greater than that across a typical airblast atomizer. The value of five percent quoted in the text arises because the feed to the vaporizer does not incur any diffuser loss. In reverse flow combustors where this is obviously not the case, the vaporizer operates very satisfactorily at pressure drops of less than half this value. In general, though, such comparisons can only be meaningful if performed for the same application/duty.

Question

Your conclusion that the atomizing performance of the vaporizer is comparable to that of an airblast atomizer is difficult to justify on the basis of your experimental data most of which were obtained at values of ΔPa/Pa that would be considered unacceptably high for an airblast/nozzle.

Author's Reply

See the reply above.

Question

Have you attempted experiments or calculations to assess the relative merits of these two devices at comparable operating conditions? Fuel vaporization may have much to commend it, but the design features employed to achieve vaporization (random impingement of fuel drops on tube walls, inbuilt pressure losses in bends, etc.) must merely impair performance when the "vaporizer" is operating in an atomizing mode.

Author's Reply

Fuel vaporization, which is clearly high, obviously has much to commend it. Furthermore, the results indicate that the design features do not impair performance in the atomizing mode. However, assessment of relative merits of the vaporizing and airblast injectors under comparable conditions is hampered by

i) differences in injector physical scales

ii) differences in operating conditions — for example lack of satisfactory data regarding the effect of air temperature on airblast atomized sprays

iii) lack of reliable and somewhat universal dropsize correlation — those developed thus far being specific to a given airblast atomizer geometry etc.

G.Grienche, FR

Firstly, I thank you very much for these very interesting experimental results on vaporizers; there are very few. Have you tried to calculate some aspects of fuel droplet motion and evaporation inside the vaporizer and to compare them with experimental results?

Author's Reply

Degrees of vaporization at the outlet have been calculated for two different vaporizer designs and results agree very well with experimental observations. Such calculations, inevitably, have to take into account the heat transfer to fuel as it flows through the vaporizer tubes.

Question

How did you handle the beam steering problem, due to density gradients, in determining the mean diameter?

Author's Reply

The problem of beam steering was tackled by recording the background light signal levels at each of the working air temperatures without liquid fuel injection. Experimental runs featuring fuel injection used these background light levels as the reference — hence effectively countering the beam steering problem.

C.Sanchez Tarifa Sener, SP

In military engines, operational conditions in the combustion chambers will often have gas pressure higher than the critical pressure of the fuel. I would appreciate your view on the possible influence of this effect on the performance of your vaporizing injector.

Author's Reply

Vaporizing combustors do indeed experience pressures well above the critical pressure of the fuel, but in service operation at such conditions need not and has not compromised the integrity/performance of the vaporizer. As at all conditions the fueling level must be sufficient to ensure mechanical integrity of the device. With regard to fuel preparation the effect will be minimal.

H.Pfost, GE

There was little difference in combustion effeciency comparing ketosine with diesel. Any measurements of NO_x emission with respect to the grade of fuel?

Author's Reply

NO_x emissions were measured in the series of engine tests referred to in the text. No increase was observed in tests with the gas oil.

THE CHARACTERIZATION OF COMBUSTION BY FUEL COMPOSITION - MEASUREMENTS IN A SMALL CONVENTIONAL COMBUSTOR

by
D. Kretschmer & J. Odgers
Département du génie mécanique
Université Laval
Québec, QC Canada G1K 7P4

Summary

In a continuing programme on the effects of fuel properties on combustion, some 20 pure hydrocarbons and synthesized fuels were tested at atmospheric conditions in a one third scale version of an aircraft type combustor. This combustor used a Simplex type pressure jet atomizer. Each fuel was burned over a range of air/fuel ratios, and at each condition, a full exhaust gas analysis was done, exhaust temperature distribution was measured, as also weak extinction. The results and their implications are discussed.

1. INTRODUCTION

These tests form part of a large programme aimed at examining which fuel properties are most cogent in determining combustion behaviour. The objectives are detailed in [1], the only major change in the present work being the substitution of the transparent combustor by a small conventional, downstream injection combustor having a Simplex pressure jet atomizer. Whereas in the earlier work changes in droplet size were very limited, in the present work the use of the Simplex atomizer has resulted in considerable variation of droplet size. Thus, whilst the previous work could be thought of as largely representing chemical effects, it was anticipated that the present work would be reflective of the 'physical' effects.

2. COMBUSTOR AND TEST RIG

The combustor is one of a set of three geometrically similar combustors originally purchased for size scaling experiments. The largest is referred to as the 'Full Scale', the two others as the 'Half Scale' and the 'Third Scale'. It is the latter combustor which has been used here. A schematic is given in Fig. 1.

The test rig was very similar to that used for the transparent combustor [1], except that there was no requirement for atomization air. Combustion air was supplied at close to atmospheric pressure by a rotary compressor and metered by a calibrated venturi nozzle. Fuel was metered by a Pierburg volumetric flow meter, and except for fuel temperature, all temperatures were measured using Chromel/Alumel thermocouples. Flame temperature measurement within the combustor were attempted using a modified red/green brightness pyrometer. Carbon was determined using a filter paper stain technique to yield the smoke number [2]. The gas analysis train and the gas sampling techniques were identical to those in [1], and the gases determined were - CO_2, CO, HC, O_2, NO, & NOx.

The atomizer had a nominal flow number (FN) of 0,33 as defined by -

$$FN = \text{Flow(Imp. gal/h)}/\text{pressure(psig)}^{0,5} \quad (1)$$

The atomizer was recalibrated by Pratt & Whitney Canada using a standard 'Stoddard Solvent', and the results are summarized in Table I.

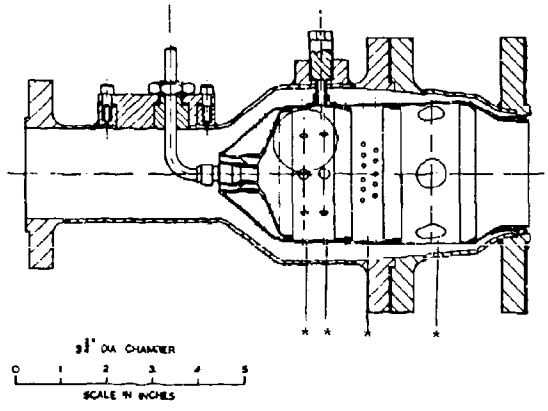

Fig. 1 SCHEMATIC OF COMBUSTOR AND CASING
* Positions of thermocouples

Table I
Atomizer Calibration

ΔP_f psig	FN	SMD µm x = 0,5	1,0	1,5 inches *
230	0,349	59	34	36
83	0,353	61	53	47
37	0,356	89	72	63
9,2	0,334	177	235	239

* distance from sprayer face.

Based upon correlations given in [3], the molar mass of the Stoddard Solvent was estimated as being 0,15 0,01 kg/mol, and the surface tension was estimated as 26 2 dyn/cm. A standard formula used to predict the SMD is -

$$SMD = 62\ (FN)^{0,2}\ \nu^{0,2}\ \sigma^{0,6}\ \rho^{0,2}\ p_j^{-0,32} \qquad (2)$$

with SMD in μm, ν in cSt, σ in dyn/cm, ρ in g/cm³ and p in psig. Assuming a value of 26 dyn/cm, we have :

P_j	37	83	230	psig
SMD	115	89	64	μm from Eqn. (2) (at x = 0)
SMD	112	80	64	μm Experiment extrapolated to x = 0

It is felt that the above comparison of predicted and measured results justifies the use of Eqn. (2) for the prediction of the SMD's for any of the various fuels used in the tests. For practical reasons the equation was rearranged and modified to give the SMD at x = 0,5 inches from the sprayer face. The final version used was - $SMD = 5,744\times10^{-6}\ \nu^{0,2}\ \sigma^{0,6}\ \rho^{0,515}\ m_f^{-0,63}$ (all in SI base units).

As previously [1], the calibration of the unit was performed using JP-4 fuel. The results were compared with predictions made using the following equations:

$$\lg(\lg(1/\eta)) = 0,911\ \lg \Psi - 0,55\ n + A \qquad (3)$$

with n = 2Φ for Φ ≤ 1 and 2/Φ for Φ > 1, all values being taken in the combustion zone. The derivation of Eqn (3) and a discussion of its application is given in [4]. Based upon the cited value for A of -0,215 [4] a comparison of predicted and measured combustion efficiencies is possible (Table II). Bearing in mind the uncertainty of A, the agreement, both in form and in absolute value, is considered to be satisfactory and to confirm the principle of volumetric scaling.

Table II

$\Phi_{overall}$	Efficiency measured	Efficiency predicted
0,211	94,6 %	94,8 %
0,288	97,2	9[illegible],6
0,331	97,6	95,7
0,354	97,2	94,7

The nominal operating conditions for the above tests and for all others discussed below are -

Pressure - 111 kPa Air mass flow - 110 g/s
Inlet temperature - 350 K Fuel flow - varied.

The fuels used in these experiments were restricted to those listed as 'Mixed Fuels' in [1]; their properties are also listed in the same reference.

3. TESTS WITH BASE FUEL

In order to establish repeatability and reproducibility, four test series were done using the base fuel (41). The results (which are considered to be satisfactory for this type of combustor) are given in Table III and Fig. 2 which illustrate the repeatability and reproducibility respectively. The separately metered air and fuel indicated a maximum difference of 2,5 % between the values measured for the air/fuel ratio and those indicated by the mass balance derived from gas analysis. This also was considered to be an acceptable agreement.

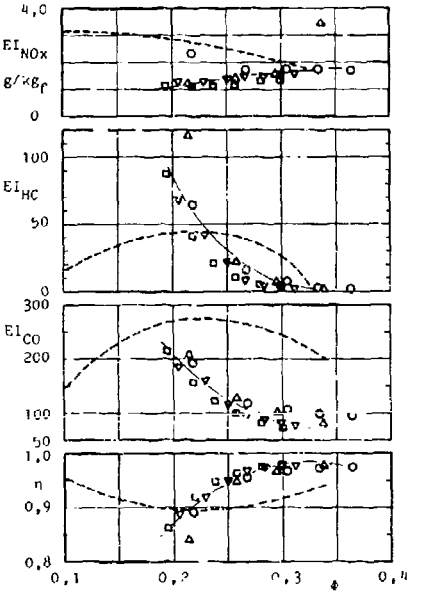

Fig. 2 COMBUSTION CHARACTERISTICS AND REPRODUCIBILITY OF TEST RESULTS - BASE FUEL (41)
Dotted Line - results from [1]

Table III

REPEATABILITY OF TESTS

Scan	CO_2 %	CO %	HC ppm	NOx ppm	NO ppm	O_2 %	T_4 K
1	3,75	0,208	87,9	-	6,2	14,97	1057
2	3,72	0,213	95,3	19,7	-	14,89	1058
3	3,76	0,207	80,6	-	6,4	15,01	1059
4	3,72	0,211	97,7	18,8	-	15,01	1059
5	3,76	0,207	85,5	-	5,9	14,95	1055
6	3,72	0,211	87,2	18,9	-	15,00	1061

Also shown in Fig. 2 are the performance curves for the same fuel tested in the transparent combustor [1]. The difference in the form of curves indicates the effect of air-blast (near constant drop size) and combustor geometry. The explanation for the form of the curves from the transparent combustor has been given in [1]. The form of curves given by the 1/3 scale combustor is typical of any pressure-jet fuel system and reflects both loading and droplet size effects. At a first glance it would appear that the conventional combustor is somewhat more efficient than the air-blast system, this in spite of the larger droplets and the higher Mach number (0,04 as opposed to 0,02). However if the fuel loadings of the two systems are examined, then the transparent combustor is about 2,5 times heavier loaded then the conventional combustor. Thus, one would estimate that at the same fuel loading the performance of the transparent combustor would be considerably better than the present can. It was concluded that the performance with Base Fuel was acceptable and typical of combustors using pressure jet atomization.

4. TESTS USING OTHER FUELS

Space restrictions do not permit the experimental data to be quoted, neither in tabular form nor as curves such as Fig. 2. The form of the curves for all of the fuels tested was very similar to those of Fig. 2, only the levels of the curves differed. The operating conditions selected did not prove conducive to ignition testing.

4.1 Combustion efficiency

All fuels were burned at, nominally, the same air loading, but the fuel loading was varied by changing the overall equivalence ratio over the approximate range of $0,2 \leq \phi \leq 0,4$.

In ref. [1] it was remarked that there was a trend of the measured combustion efficiencies with the average boiling points of the fuels tested in the transparent chamber. In the present test series one might expect that this trend would again be noted, and indeed it is (Fig. 3). The points plotted on Fig. 3 were obtained by reading off the values at the two equivalence ratios from the curves of the basic experimental data. In fact, the dependence upon boiling point is far more pronounced than in the previous case. Also there is the general observation that those fuels which have the higher boiling points also yield the largest droplets. If this is so, then it is probable that the results would also correlate against droplet

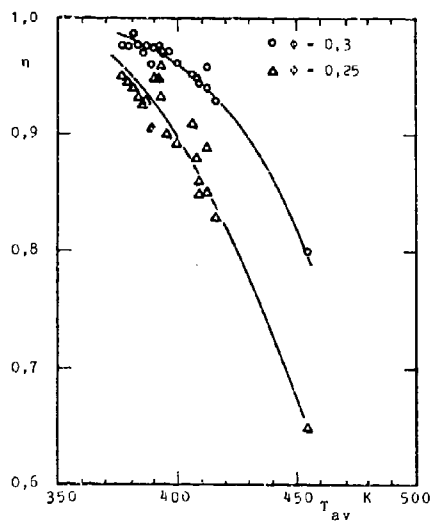

Fig. 3 RELATIONSHIP BETWEEN COMBUSTION EFFICIENCY AND AVERAGE BOILING POINT

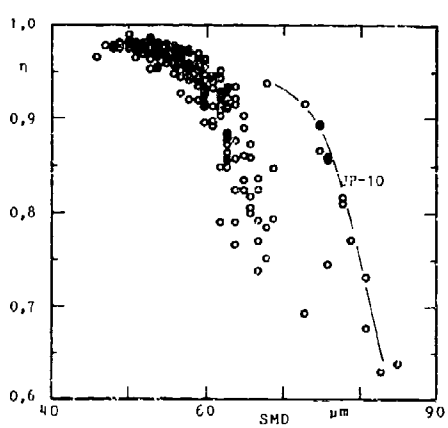

Fig. 4 RELATIONSHIP BETWEEN COMBUSTION EFFICIENCY AND DROPLET SIZE

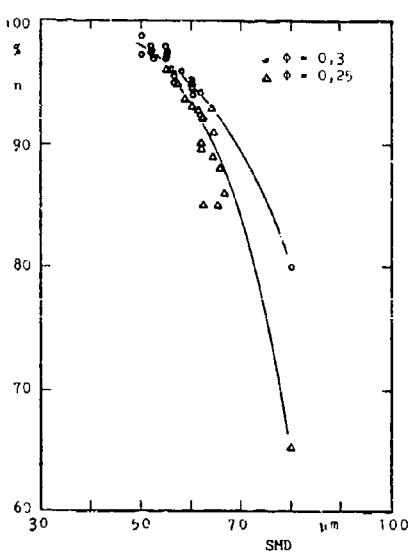

Fig. 5 RELATIONSHIP BETWEEN COMBUSTION EFFICIENCY AND DROPLET SIZE

diameter. This is clearly indicated in Fig. 4 which gives a plot of all the data. How[illegible] this mass of points tends to obscure trends and so the data were evaluated for the two equivalence ratios of 0,25 and 0,30 so as to compare with Fig. 3. The results are demonstrated in Fig. 5. Clearly both Figs. 4 and 5 show a marked effect of SMD upon combustion efficiency. Moreover the closeness of the two curves on Fig. 5 suggests that the droplet diameter is more important than the boiling point since it tends to eliminate the effects of equivalence ratio. It is concluded that the predominant effects are due to droplet size, the small separation in Fig. 5 indicating the existance of some secondary effects.

In Ref. [1] a relationship was established between the ratio of CO to unburned hydrocarbons at the exhaust and the combustion efficiency, significantly improved by introducing a function of the equivalence ratio within the primary zone. A tentative explanation of this latter term was that, in reality, the dependence was one of temperature, and in turn, this suggested that the flame zone behaved as though it were at least partially premixed. Figure 6 plots the results from the present tests. The correlation has about the same scatter as that of the previous work but without the need to employ the equivalence ratio function as additional parameter. A tentative explanation is that in the conventional combustor the Simplex atomizer gives rise to droplet diffusion flames which then show relatively little sensitivity to the zone mean equivalence ratio. What remains in doubt is whether the behaviour in the transparent combustor was due to the very small droplets which behaved as a pseudo-gas or whether the behaviour was brought about by the intimate mixing of the air and droplets occasioned by the use of air-blast, or to some combination of the two.

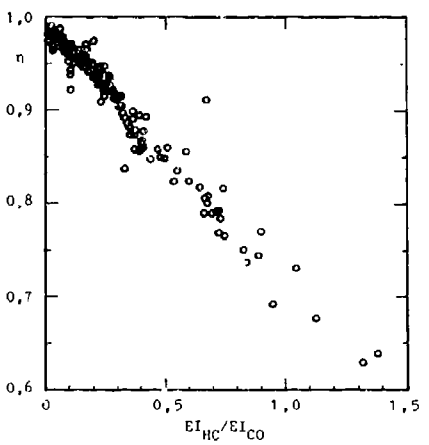

Fig. 6 RATIO OF HYDROCARBON TO CO EMISSION INDICES

In Ref. [4] a correlation was derived for the combustion efficiency of several combustors operated over a range of conditions. This took the form -

$$\lg(\lg(1/\eta)) = K_1 \times \lg(\dot{m}_f/Vp^n) + K_2 \times n + K_3 \qquad (4)$$

Although most of the combustors were conventional, one of them was a vaporizer chamber and another was a high velocity combustor. No specific term was included to represent possible droplet effects. It was decided to attempt an improvement of the correlation (Eqn. 4) by including a term to represent the effect of droplet size. Since the combustor operated with a constant volume and at constant pressure, the new correlation became -

$$\lg(\lg(1/\eta)) = 2{,}920 \lg \dot{m}_{f,300K} + 1{,}422\, n + 35{,}28\times10^{3} \times SMD + 2{,}556 \qquad (5)$$

All units are SI base units. The fuel mass flow in kg/s is corrected to 300 K using -

$$\lg\left(\dot{m}_{f,300}/\dot{m}_f\right) = 3{,}054\, y^{-1{,}205} - 1{,}2327\, y^{-1{,}205} \times \lg T_3$$

$n = 2\Phi$ for $\Phi \leq 1$ or $2/\Phi$ for $\Phi > 1$, $y = \Phi$ for $\Phi \leq 1$ and $y = 1$ for $\Phi > 1$, Φ being taken as the mean for the recirculation zone. Figure 7 compares the measured values of inefficiency $(1 - \eta)$ with those calculated using Eqn (5). The standard deviation of the inefficiency was 0,268 which is considered to be reasonably satisfactory for most purposes.

4.2 Pollutants

Carbon monoxide and hydrocarbons

The success in correlating the combustion efficiency gave some hope for the correlation of the amounts of carbon monoxide and hydrocarbons within the exhaust. In fact, the form of equation obtained to correlate the carbon monoxide emissions index very closely resembled that of Eqn. (5).

$$\lg EI_{CO} = 2{,}316 \lg \dot{m}_{f,300K} + n + 12{,}6\times10^{3} \times SMD + 6{,}49 \qquad (6)$$

In Eqn. (6) all values are in SI base units. The comparison of the calculated and measured emission indices is given in Fig. 8. Apart from 4 points (part of one single test series - indicated by triangles) the data appear to yield a satisfactory correlation. The standard deviation (including the 'out' points) is 0,180.

As might be expected the hydrocarbons in the exhaust showed little evidence of any relation to the type of correlation based upon a reaction rate equation, such as those of Eqns. 5 & 6. The major factors affecting the presence of hydrocarbons showed to be those parameters which defined evaporation rates. In addition to the droplet size and the average boiling point of the fuel, it was found necessary to include the transfer number and the hot gas temperature. Thus the correlation took the form -

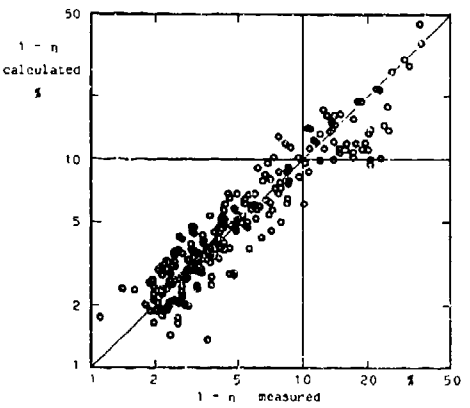

Fig. 7 COMBUSTION EFFICIENCY CORRELATION

$$EI_{HC} = 10^{18,85} \times T_{av}^{7,76} \times T_{\phi}^{-8,84} \times \left(\frac{(SMD)^2 \times \rho}{\ln(B + 1)}\right)^{2,09} \qquad (7)$$

and a fair agreement (Fig. 9) was obtained from EI = 1 (a loss of 0,1 % due to HC) to EI = 500 (a loss of 50 % due to hydrocarbons). All values in Eqn. (7) in SI Base Units.

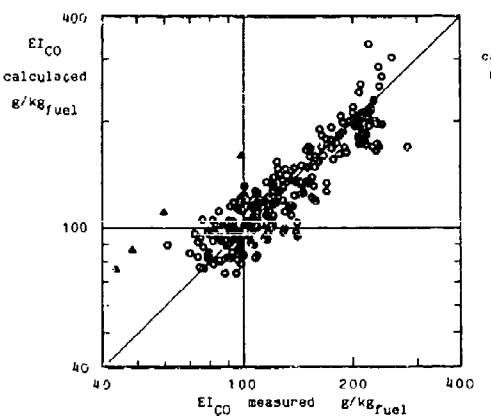

Fig. 8 EXHAUST CARBON MONOXIDE

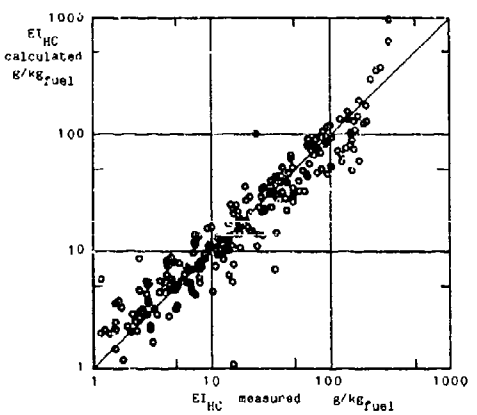

Fig. 9 EXHAUST HYDROCARBONS

Figure 10 plots the measured combustion efficiency loss (total) against the individual losses. Obviously there is a strong relationship, and it takes the usually observed form and magnitude [5]. If the overall combustion efficiency is known, the hydrocarbon content may be expressed as -

$$\lg\left(EI_{HC}/1000\right) = 1 - 1,1247\ (1 - \eta)^{-0,2964} \qquad (8)$$

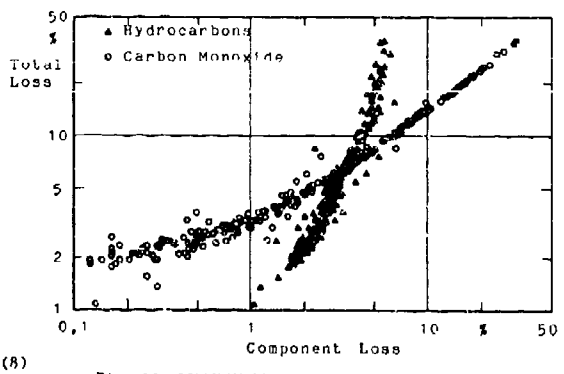

Fig. 10 POLLUTANT/EFFICIENCY RELATIONSHIP

Oxides of Nitrogen

In all cases the observed oxides of nitrogen were very low (even lower than for the transparent combustor [1]). Because of this, the accuracy of measurement is not thought to be very good (± 0,5 EI). If one assumes that both systems are diffusion flames, then according to the correlation given in [1] -

$$EI_{NOx} = 29 \times e^{-21670/T} \times p_3^{0,66} \times (1-e^{-150\tau}) \qquad (9)$$

where T is the adiabatic dissociated flame temperature. For the transparent combustor, a definite trend of the effective residence time was found with equivalence ratio; the weaker the mixture, the longer the time. If the present system functions as a pure droplet flame one would anticipate that it would not be so sensitive to equivalence ratio as the transparent combustor. In fact, one finds this to a fair degree. However, the important scatter of the experimental values tends to hide any real trends. Because of this, it was decided to mean the values for each fuel regardless of equivalence ratio (see Table IV).

In an attempt to use Eqn. (9), an effective residence time was calculated for fuel 41 using the appropriate values for the stoichiometric flame temperature and the inlet pressure. The result indicated that all fuels should be between 1,46 (fuel 41) and 1,63 (fuel 43) g/kg of fuel. Since this difference is smaller than the actual scatter for any given fuel, this attempt remained inconclusive. A much simpler method of prediction which takes no account of residence times is given by an empirical curve in [6]. This curve which plots the NOx emission index against the maximum flame temperature is a summary of many practical gas turbines, with and without water/steam injection, as well as several laboratory systems, premixed or with droplet combustion. Taking into account all fuels and their respective flame temperatures, this curve indicated a minimum value for the EI of 1,5 ± 0,6 and a maximum of 2,4 ± 1 g/kg. All the results fall within this range of scatter and almost all the measured values, too. No discernable relationship could be seen in the ratios of NO to NOx.

Table IV

VALUES OF NO AND NOx

Fuel	EI_{NO}	EI_{NO}/EI_{NOx}	EI_{NOx}		
	mean	mean	minimum	mean	maximum
41	0,84	0,58	1,1	1,46	2,4
42	1,23	0,84	0,9	1,47	3,1
43	1,39	0,68	1,1	2,04	3,0
44	1,01	0,56	1,1	1,79	2,0
45	1,07	0,55	1,0	1,94	3,2
46	0,82	0,51	1,1	1,60	2,0
47	1,26	0,60	1,3	2,10	2,5
48	0,86	0,53	1,3	1,62	2,3
49	1,01	0,62	1,2	1,62	3,4
50	1,74	0,78	1,7	2,23	3,2
53	0,68	0,38	1,4	1,78	2,2
54	0,63	0,33	1,5	1,93	2,3
55	0,52	0,37	1,2	1,41	1,8
56	0,50	0,25	1,7	2,03	2,3
57	0,50	0,24	1,7	2,08	2,4
58	0,65	0,46	1,0	1,42	2,2
59	0,58	0,41	1,1	1,43	1,7
60	0,83	0,46	1,3	1,80	2,3
61	0,48	0,26	1,5	1,85	2,2
62	0,61	0,45	1,1	1,37	1,8
63	0,55	0,38	1,1	1,45	1,8
01	0,65	0,36	1,3	1,80	2,2

NB. all value of EI as g of NO_2 per kg fuel.

Exhaust Carbon

The results of the carbon measurements were considered to be so interesting as to warrant a separate publication [2]. Consequently, only a summary will be given here. During the present test series, due to the small quantities of soot which were formed at the operating conditions, the necessary time, which would have been needed to obtain a measurable sample, rendered it economically impossible to determine the smoke using a gravimetric technique. Hence, a filter paper stain technique was decided upon. A Whatman GF/A filter paper was clamped in a double conical holder, and a known mass of exhaust gas (21 g calculated as air) was metered through the paper. The resultant stain was then measured in terms of reflectivity using a Pacific Scientific RG-4600 reflectometer. The results were then expressed in terms of Smoke Number (SN in % reflectivity change).

In earlier work [7] the influence of temperature had been described in terms of combustor inlet temperature. This had appeared to give a satisfactory correlation since (for the data available), for any given engine, any one operating condition was confined to a single air/fuel ratio, and hence changes due to air/fuel ratio were not evident. Because of the behaviour with changes in air/fuel ratio noted in the present work it was felt that the combustor exit temperature would be more representative of the burn-out region than the inlet temperature, and additionally, the exit temperature would reflect changes in inlet temperature and flame temperature changes due to changes in fuels. A careful analysis of the experimental data showed that the exponent for the exit temperature was the same as that used before for the inlet

temperature. The new correlation group now became -

$$EI_C = f\ [\{p_3/(O/C)\}^{2,7}\ (H/C)^{-5,45}\ T_4^{-8,66}\}] \quad (10)$$

or writing (10) in terms of operating conditions -

$$SN = f_1\ [X_1]$$

$$X_1 = \frac{1}{A/F + 1} \times \left(\frac{p_3(1 - h)^3}{A/F \times h^2}\right)^{2,7} \times T_4^{-8,66} \quad (11a)$$

$$EI_C = f_2\ [X_2]$$

$$X_2 = \left(\frac{p_3(1 - h)^3}{A/F \times h^2}\right)^{2,7} \times T_4^{-8,66} \quad (11b)$$

where $T_4 = T_3 + h(T_4^* - T_3)$ and $T_4^* = T_4$ at $h = 100$ %.

In [2] the new correlation has been applied to the data of the present work as well as to published data from 8 other combustors. The data pertinent to the present work are plotted in Fig. 11.

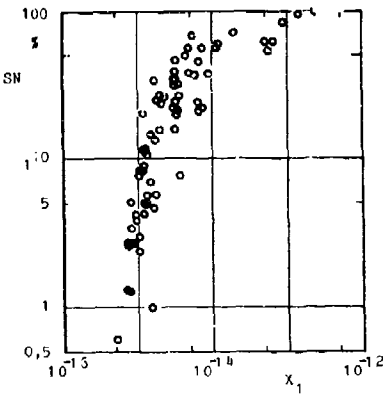

Fig. 11 SMOKE CHARACTERISTICS

Attempts to modify the correlation group so as to include any effects of fuel molecular structure have so far not met with any great success, althought there is some evidence that there are trends with the hydrogen saturation factor S_H, and that additionally, there may be small effects due to aromaticity. Apart from the above terms, the only other determined property which was found to show even a trend with the measured smoke number was, as might be expected, the value of the Smoke Point of the fuels. The trend was not satisfactory for correlation purposes.

4.3 Flame temperature measurements

It was attempted to measure flame temperatures and emissivities in the primary zone using a red-green brightness temperature technique. A red brightness pyrometer (wavelength 645 nm) was modified in the National Defence Laboratories (Ottawa) so as to include a green filter (547 nm), and a suitable calibration was performed.

Two-colour pyrometry has been successfully applied to gas turbine combustors over a range of from 0,2 to 7,5 MPa [8 & 9], and red brightness temperatures had been measured successfully in an identical combustor to that used here over a pressure range of from 0,1 to 3,3 MPa [10]. Under these circumstances the selection of this instrument seemed entirely reasonable.

Visually the flames ranged from blue to yellow, the former flames characteristic for the paraffinic fuels, the latter for those with aromatic additions. However, most of the flames were insufficiently opaque to produce satisfactory results, the green temperatures being by far too high due to the interference of the blue radiation caused by water vapour and carbon dioxide. As a result of this, analysis has been postponed until further results, using more aromatic fuels, are obtained.

4.4 Wall temperature measurements

For the determination of the flame tube wall temperatures nine thermocouples were attached in three rows of three (see Fig. 4). Due to the very high temperature gradients encountered (up to 150 K/cm) the accuracy of placement is somewhat limited. In spite of this, the results are fairly promising. The mean values at any given axial location agreed quite well with predictions using the technique described in [11], however, no full analysis will be done until more data have been obtained.

4.5 Weak extinctions

Weak extinctions were determined at the end of each test by gradually reducing the fuel flow until the flame commenced to be unsteady. At this point the ignition was switched on and the fuel further reduced. After a little while the igniter was switched off. If the flame remained lit, the plug was again fired and the fuel further reduced until extinction occurred when the spark was arrested. At this point the plug was re-fired and the fuel increased a little. By this means it was possible to determine the minimum self sustaining fuel flow below which the flame always extinguished. This defined the weak extinction.

Table V lists the appropriate data. The parameter f_θ described in [12]

$$f_\theta = \frac{m_f}{m_{41}} = \left[\frac{f_{s,f}}{f_{s,41}} \times \frac{q_{n,f}}{q_{n,41}} \times \frac{m_{a,f}}{m_{a,41}} \times \frac{\ln(1+B_{41})}{\ln(1+B_f)}\right]^{0,53} \times \left(\frac{\rho_f}{\rho_{41}}\right)^{0,92} \times \left(\frac{\sigma_f}{\sigma_{41}}\right)^{0,47} \times \left(\frac{\nu_f}{\nu_{41}}\right)^{0,16} \quad (12)$$

did not correlate the data in as satisfactory a manner as might have been anticipated. However, it obviously had an interplay since a very good correlation of the data was obtained by plotting $(\Phi_{w,f}/\Phi_{w,41})/f_\theta$ against $(\rho_f/\rho_{41})^{0,8} \times (q_{n,f}/q_{n,41})$ as in Fig. 12. Why the weak extinction should be a function of what approaches to the heating value per unit volume of liquid is not clear. It could be that the density is only representative of some other property of the fuel (e.g. volatility, viscosity, surface tension, or any combination thereof), and further analysis will be attempted in the future when other data become available.

TABLE V

LIMITS

Fuel	$\Phi_{w,f}$	$\Phi_{w,f}/\Phi_{w,41}$	f_θ	$\frac{\Phi_{w,f}/\Phi_{w,41}}{f_\theta}$
41	0,101	1,0	1,0	1,0
42	0,199	1,970	5,222	0,377
43	0,117	1,158	1,857	0,624
44	0,120	1,188	1,952	0,609
45	0,093	0,921	1,079	0,854
46	0,093	0,921	1,190	0,774
47	0,093	0,921	1,365	0,675
48	0,101	1,000	1,032	0,967
49	0,104	1,030	1,302	0,791
50	0,110	1,089	1,667	0,653
53	0,109	1,079	1,698	0,635
54	0,105	1,040	1,571	0,662
55	0,096	0,950	1,111	0,855
56	0,094	0,931	1,175	0,792
57	0,104	1,030	1,206	0,854
58	0,102	1,010	1,238	0,816
59	0,102	1,010	1,365	0,740
60	0,101	1,000	1,365	0,733
61	0,097	0,960	1,111	0,864
62	0,100	0,990	1,302	0,760
63	0,117	1,010	1,460	0,692

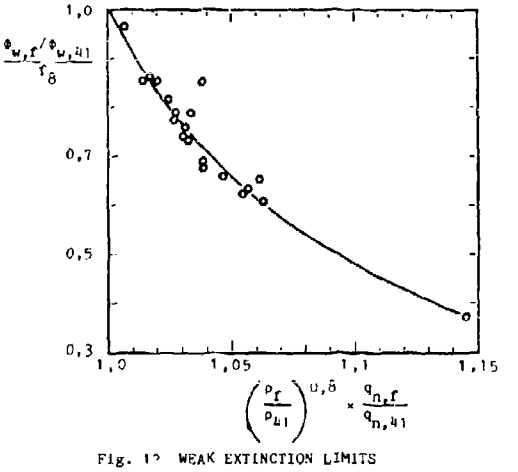

Fig. 12 WEAK EXTINCTION LIMITS

4.6 Exhaust temperature distribution

As with the transparent comtustor [1], the exhaust temperature distributions, based upon the dimensionless temperature rise, are very similar for all fuels and at all operating conditions. The results again indicate that the exhaust pattern is governed by the air/fuel patternation as defined by the injector and the combustor air distribution. The preservation of the patternation shows a stable air/fuel distribution, and experience with other combustors suggests that this same patternation would persist if the chamber was operated at higher pressures. Indeed, since at high pressure conditions all the fuels would operate at close to 100 % efficiency, it is likely that the exhaust temperature distributions would even be more similar.

5. GENERAL COMMENTS

Clearly a significant amount of combustion data has been logged in the course of the present work, and not all of the data have been fully analysed yet. The major reason for this is that some of the trends noted require confirmation by the use of fuels which will extend property variations. A similar requirement was found for the transparent combustor.

Both programmes have shown the inadequacy of Mach number scaling and have proven the reaction volume scaling for small combustors. This could be of considerable interest to the manufacturers of small engines. Both units also demonstrate the adequacy of the NOx prediction techniques used. With regard to combustion efficiency and pollutants the units differ in that the Simplex injection system shows much more dependence upon droplet characteristics than the air-blast system used previously. Weak extinction correlations differ for the two units and, although not proven, one is tempted to attribute this to the two different injection systems.

At atmospheric pressure the carbon found within the exhaust has been too small to be measured gravimetrically. The use of a filter paper stain technique showed visible differences between the fuels

and enabled the carbon to be assessed quantitatively. The exhaust temperature distribution shows little difference from one fuel to another, and it would appear that any possible fuel effects may be neglected. Because of flame transparency it has not proved possible to determine primary zone flame temperatures. No success was had in establishing a correlation for ignition.

6. NOMENCLATURE

A/F	air/fuel mass ratio	B	transfer number
EI	emission index - g/kg fuel	FN	flow number - $(I.G./h)/psig^{0,5}$
f_s	stoichiometric fuel/air mass ratio	f_θ	weak extinction correlation group
H/C	atomic hydrogen/carbon ratio	h	hydrogen mass fraction in fuel
K	a constant	m	mass flow - kg/s [lb/s]
n	= 2Φ for Φ ≤ 1, = 2/Φ for Φ > 1	O/C	atomic oxygen/carbon ratio
p	pressure - Pa [atm]	p_3	inlet pressure - Pa
p_j	atomizer pressure [psig]	q_n	net calorific value - MJ/kg
S_H	hydrogen saturation factor = $h_f/h_{corresponding\ paraffin}$		
SMD	Sauter mean diameter - m [μm]	SN	smoke number - %
T_{av}	volume average boiling point - K	T_3	inlet temperature - K
T_ϕ	adiabatic flame temperature - K	T_4	outlet temperature - K
V	combustion volume - m^3 [ft^3]	X	a smoke correlation group
x	distance from atomizer face - [inch]	y	= Φ for Φ ≤ 1, = 1 for Φ > 1
η	combustion efficiency	Y	fuel loading = m_f/Vp^n - $[lb/(s\cdot ft^3\cdot atm^n)]$
Φ	equivalence ratio $A/F_{stoich.}$ / A/F_{actual}	Φ_w	Φ at weak extinction
ν	kinematic viscosity - m^2/s [cSt]	σ	surface tension - N/m [dyn/cm]
ρ	density - kg/m^3 [g/cm^3]	τ	time - s

Suffixes: a air, f fuel.

7. REFERENCES

[1] Odgers, J. & Kretschmer, D.: **The Characterization of Combustion by Fuel Composition, 1 - Measurements in a Small Transparent Combustor**, 70th AGARD Meeting, Combustion and Fuels in Gas Turbine Engines, Chania Gr., 19-23 Oct. 1987.

[2] Kretschmer, D. & Odgers, J.: **Exhaust Carbon - The Effects of Fuel Composition**, 8th Intern. Symp.on Air Breathing Engines, Cincinnati, 15-19 June 1987.

[3] Odgers, J. & Kretschmer, D.: **Tests on Five Different Aircraft Fuels and the Correlation of their Physical Properties**, Université Laval, Combustion Laboratories, report jo 100, Sept. 1981.

[4] Odgers, J. & Carrier, C.; "Modelling of Gas Turbine Combustors - Considerations of Combustion Efficiency and Stability", **Trans. ASME, J. Engineering for Power**, 95A, April 1973, pp 105/113.

[5] Opdyke, G. jr: Discussion in **Emissions from Continucus Combustion Systems**, Cornelius, W. & Agnew, W.G., Eds., Plenum Press, 1972, pp 309/310.

[6] Odgers, J. & Kretschmer, D.; **The Prediction of Thermal NOx in Gas Turbines**, 1985 Intern Gas Turbine Symp. & Exhibition, Beijing, 1-7 Sept. 1985, ASME Paper 85-IGT-126.

[7] Odgers, J. & Kretschmer, D.; "Some Fuel Effects on Carbon Formation in Gas Turbine Combustors", **Canad. Aeron. & Space J.**, 28, Dec. 1982, 4, pp 327/338.

[8] Hill, W.E. & Dibelius, N.R.; **Measurement of Flame Temperature and Emittance in Gas Turbine Combustors**, ASME Paper 70-GT-19.

[9] Davis, L.B., Farrell, R.A. & Hill, W.E.; **Total Radiation and Two Color Flame Temperature in Industrial Gas Turbine Combustion Systems**, ASME Paper 76-HT-57.

[10] Marsland, J., Winter, J. & Odgers, J.; **The Effects of Flame Radiation on Flame Tube Metal Temperatures**, Proc. 12th Symp. (Intern.) on Combustion, The Combustion Institute, 1969, pp 1265 ff.

[11] Kretschmer, D. & Odgers, J.; **A Simple Method for the Prediction of Wall Temperatures in Gas Turbines**, ASME Paper 78-GT-90.

[12] Sampath, P., Gratton, M., Kretschmer, D. & Odgers, J.; "Fuel Property Effects Upon Exhaust Smoke and the Weak Extinction Characteristics of the Pratt & Whitney PT6A-65 Engine", **Trans. ASME, J. Engineering for Gas Turbines & Power**, 108, Jan 1986, pp 175/181.

ACKNOWLEDGEMENTS

The Authors extend their grateful thanks to the National Defence Canada who financed the present work. Additional thanks are also due to the group of undergraduate students who operated the test rig for the experiments.

DISCUSSION

A.Williams, UK

Have you made any measurements of the composition of hydrocarbons in the products and is there any correlation with the nature of the parent fuel?

Author's Reply

Our hydrocarbon measurements are solely in terms of 'total hydrocarbons' using an F.I.D. They are calculated in terms of the parent hydrocarbon.

A.Lefebvre, US

Your equation for NO_x contains an exponential temperature dependence. Was this obtained from theory or experiment? If the latter, what range of residence times did the experimental data cover?

Author's Reply

The residence time effect is discussed in Ref. [5] of the paper No.41. From memory I think the times investigated were about 1 to 6 ms. Much of the experimental data were taken from NASA reports of experiments in pre-mixed, pre-vaporized reactors, and other stirred reactor work plus some from 'real' combustors. Theoretically the exponential function may also be justified from the approach to equilibrium.

A.M.Mellor, US

Is the discrepancy associated with combustion efficiency versus SMD (Figure 4) for JP-10 associated with its narrow boiling range?

Author's Reply

I do not think so, because two or three of the fuels used here were pure compounds having only a single boiling point (i.e. no range). In recent work many more pure substances have been introduced with no effect. We believe it is due to (a) very large droplets combined with (b) a low volatility and (c) the degree of unsaturation. We have recently investigated a correlation involving these three terms and initial results suggest a significant reduction in the scatter of results. However, the new correlation has not yet been 'finalized'.

LIMITES D'EXTINCTION PAUVRE DE LA RECHAUFFE D'UN TURBOREACTEUR

par

Madame A.Cadiou
ONERA
Fort de Palaiseau
91120 Palaiseau
France

Résumé

La combustion dans un foyer de rechauffe est stabilisée en aval d'accroche-flammes et le processus de stabilisation dépend des paramétres suivants : nombre de Mach, température, pression et richesse de l'écoulement, géométrie de l'accroche-flammes. Les études expérimentales effectuées permettent d'accéder à un paramètre de corrélation englobant l'effet du nombre de Mach et de la température.

Quant à l'effet de la géométrie : dans le cas d'accroche-flammes linéaires en écoulement bidimensionnel le profil de l'accroche-flamme est le paramètre géométrique déterminant.

Une étude expérimentale détaillée de la zone de combustion dans le sillage d'accroche-flammes annulaires dans un écoulement axisymétrique a mis en évidence l'effet d'un autre paramètre géométrique en plus du profil, le diamètre moyen de la gouttière annulaire constituant l'accroche-flammes. Les résultats expérimentaux obtenus au cours de cette étude permettent de préciser les mécanismes de stabilisation de la flamme par des obstacles annulaires.

FLAME STABILIZATION IN A REHEAT COMBUSTOR

abstract

In a reheat burner, combustion is stabilized with flameholders. The stabilization depends on the following parameters : Mach number, temperature, pressure and equivalence ratio of the flow, flameholder geometry.

Many experimental measurements have allowed the calculation of a correlating parameter including the Mach number and the temperature.

For the geometry, studies on linear stabilizers in 2-dimensionnal flows have shown that the height of the stabilizer is a convenient parameter.

An accurate experimental study of the recirculation zone downstream annular flameholders in an axisymetric flow have pointed out the effect of an another geometrical parameter, the diameter of the flameholder. The experimental results have improved our knowledge of the flame stabilization mechanism downstream annular flameholders.

NOMENCLATURE

H hauteur de l'accroche-flamme

H* H/hauteur de l'anneau unique (40 mm)

$\dot{m}$ débit massique d'air

M nombre de Mach en amont de la rechauffe

T température en amont de la rechauffe

V vitesse en amont de la rechauffe

X coordonnée axiale : distance à l'accroche-flamme

Φ richesse du mélange air-kérosène

η_c rendement de combustion

1. INTRODUCTION

Les dispositifs de postcombustion mis en place sur des avions visent à une augmentation très forte de la poussée pendant un temps relativement court.

Cet accroissement de poussée est obtenu par combustion de kérosène en aval de la turbine. La combustion conduit en effet à une augmentation de la température des gaz éjectés et donc de leur vitesse d'échappement et de la poussée qui s'en déduit.

Les caractéristiques de fonctionnement de la rechauffe sont telles que l'on sort du domaine classique de définition des chambres de combustion : la pression est relativement faible, de l'ordre de 2 ou 3 bars, la vitesse et la température en amont de la rechauffe sont élevées (V = 140 m/s ; T = 800°C). D'autre part, le dispositif de rechauffe doit induire le minimum de pertes de charge, car rechauffe éteinte, il est totalement inutile.

Ces considérations ont conduit à utiliser le principe de stabilisation des flammes au moyen d'obstacles pour le foyer de rechauffe. En effet, un obstacle dans un écoulement produit un sillage turbulent comportant immédiatement en aval une zone de recirculation nécessaire à la stabilisation de la combustion (fig. 1, [1]). Les gaz frais forment une couche limite au contact du stabilisateur jusqu'au point de décollement où cette couche rencontre une couche analogue formée de gaz brûlés induite par la recirculation. En ce point il y a contact entre les gaz frais et les gaz brûlés : à travers la surface de séparation ont lieu des transferts de chaleur qui provoquent l'inflammation des gaz frais. Les gaz nouvellement enflammés restituent ensuite de la chaleur aux gaz brûlés de la zone de recirculation, compensant ainsi la perte de chaleur précédente. L'extinction a lieu lorsque la quantité de chaleur cédée à la zone de recirculation devient inférieure à la quantité de chaleur nécessaire au maintien de cette zone à une température suffisante. L'extinction dépend donc uniquement des phénomènes ayant lieu juste en aval de l'accroche-flamme. La zone plus en aval qui assure la propagation de la combustion n'a aucun effet sur la stabilité.

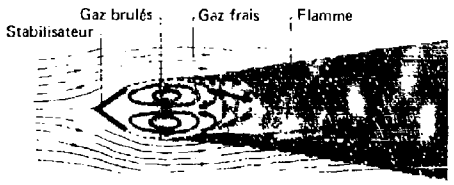

Fig. 1 – Stabilisation et propagation de la flamme.

La définition d'un système de rechauffe comprend la définition géométrique de l'obstacle appelé accroche-flammes, du canal dans lequel sera placé cet obstacle et des injecteurs de kérosène carburant l'air vicié issus de la turbine et l'air pur venant du fan. Cette définition doit être faite de façon à optimiser les performances de la rechauffe c'est-à-dire de façon à avoir :

- une valeur du rendement de combustion aussi proche de 1 que possible pour une longueur de canal toujours limitée par les applications ;
- une perte de charge relativement faible afin de ne pas augmenter d'une façon sensible la consommation spécifique du moteur lorsque la rechauffe n'est pas en service ;
- un large domaine de fonctionnement afin d'assurer la stabilité de la combustion pour les différentes conditions rencontrées au cours du vol.

Les recherches sur la rechauffe effectuées à l'ONERA ont pour objectif de fournir aux constructeurs des éléments utilisables au stade avant-projet et en particulier l'effet des paramètres aérothermochimiques et géométriques sur les performances de la combustion. C'est une partie des travaux en cours à l'ONERA sur ce sujet et plus particulièrement celle ayant trait aux limites d'extinction

pauvres, c'est-à-dire à la stabilité de la rechauffe, qui est présentée ici.

Les paramètres qui influencent l'extinction sont la vitesse, la température et la richesse de l'écoulement en amont de la rechauffe ainsi que la géométrie de l'accroche-flamme. Afin de s'affranchir des paramètres relatifs à la carburation, celle-ci est effectuée au moyen d'un grand nombre de points d'injection situés loin en amont de l'accroche-flamme afin d'avoir dans le plan des obstacles une répartition aussi homogène que possible du combustible.

Après une description globale du montage expérimental les résultats obtenus avec des accroche-flammes de forme annulaire ainsi qu'une tentative de corrélation seront présentés. Une étude détaillée de la combustion dans la zone de recirculation a toutefois été nécessaire pour expliquer des anomalies apparentes.

2. DESCRIPTION DU MONTAGE EXPERIMENTAL

Les figures 2 et 3 représentent respectivement un turboréacteur équipé d'un dispositif de rechauffe intégrée au raccordement du moteur et le montage expérimental sur lequel sont relevées les conditions d'extinction de la rechauffe. Le banc d'essai reproduit les mêmes niveaux de température et de vitesses que ceux du moteur.

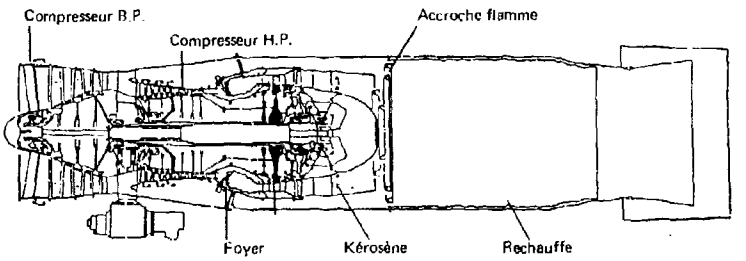

Fig. 2 – Schéma d'un turboréacteur équipé de rechauffe.

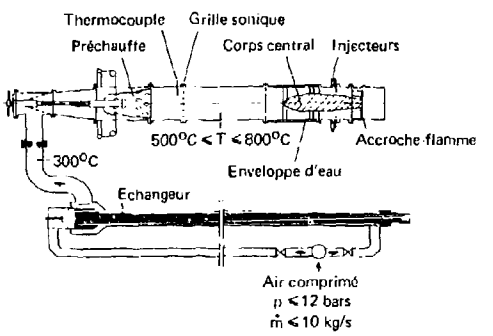

Fig. 3 – Schéma du montage expérimental.

L'air comprimé est fourni par trois compresseurs : le débit maximal est de 10 kg/s sous une pression dont la valeur peut être modulée jusqu'à 12 bars.

Cet air est chauffé dans un échangeur de chaleur jusqu'à 300°C. Il pénètre ensuite dans une chambre de combustion correspondant au foyer principal du turboréacteur.

La température de l'écoulement à la sortie de chambre peut être ajustée à une valeur quelconque comprise entre 500°C et 800°C. Les variations sont obtenues en agissant sur le débit de combustible.

Une grille sonique située en aval homogénéise les vitesses dans la conduite.

Un corps central simule le cône de fuite du dernier étage de turbine.

L'injection de carburant pour la rechauffe est faite au moyen de 24 tubes radiaux percés de 5 orifices de 0,6 mm. Ces orifices sont orientés à contre-courant ; les jets de kérosène sont brisés sur un bouclier afin d'assurer un bon mélange air-kérosène.

L'accroche-flamme est situé 345 mm en aval de l'injection dans le plan de l'extrémité aval du corps central.

Le diamètre du canal de rechauffe est égal à 300 mm. La longueur utilisée lors des études d'extinction est sensiblement égale à 1 diamètre. Un canal relativement court permet d'observer la

combustion et de détecter aisément l'extinction.

Les mesures faites sur ce montage sont les suivantes :

- un col sonique en amont de la chambre de combustion équipé d'une prise de pression statique et d'un thermocouple permet de calculer les valeurs du débit d'air ;
- un thermocouple chromel-alumel placé en amont de l'injection de kérosène fournit la température de l'écoulement amont rechauffe ;
- deux débitmètres à turbine sont utilisés pour enregistrer les débits de kérosène de la chambre de combustion et de la rechauffe.

L'extinction pauvre est obtenue en réduisant progressivement le débit de kérosène alors que le débit d'air la température de l'écoulement amont rechauffe et la pression conservent respectivement une valeur constante. Les valeurs du nombre de Mach, de la richesse rechauffe, ainsi que des principaux paramètres de l'écoulement sont calculés en temps réel, enregistrés et affichés sur moniteur au moment de l'extinction.

3. RESULTATS SUR LES LIMITES D'EXTINCTION

Les résultats présentés ici concernent les deux accroche-flammes des figures 4 et 5. Celui de la figure 4 est formé d'une gouttière annulaire unique de diamètre moyen 200 mm et de hauteur 40 mm. Celui de la figure 5 comporte deux gouttières annulaires concentriques et coplanaires de diamètres moyens 250 mm et 150 mm et de hauteur 20 mm. Les deux accroche-flammes conduisent au même taux de blocage de la section droite de canal.

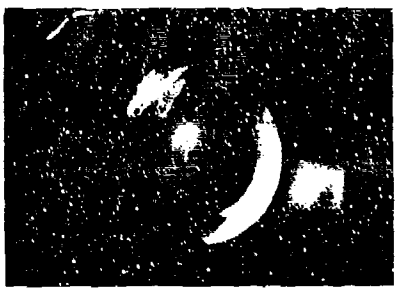

Fig. 4 — Photographie de l'accroche-flamme constitué d'un anneau unique avec combustion en aval.

Fig. 5 — Photographie de l'accroche-flamme constitué de deux anneaux avec combustion en aval.

L'extinction a été déterminée dans le cas de combustions à la pression atmosphérique pour les conditions suivantes :

- température de l'écoulement amont

  $500°C \leq T \leq 800°C$

- nombre de Mach de l'écoulement amont

  $0,15 \leq M \leq 0,40$

- richesse de rechauffe

  $0,03 \leq \varphi \leq 0,53$

Les résultats sont rassemblés sur les figures 6, 7 et 8.

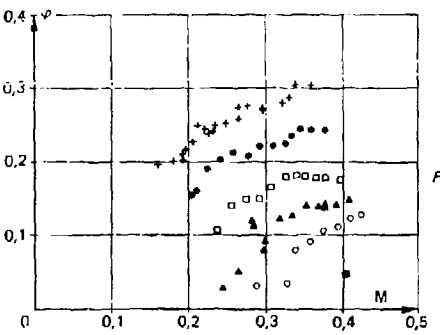

Fig. 6 — Richesse d'extinction en fonction du nombre de Mach et de la température de l'écoulement pour l'anneau unique.

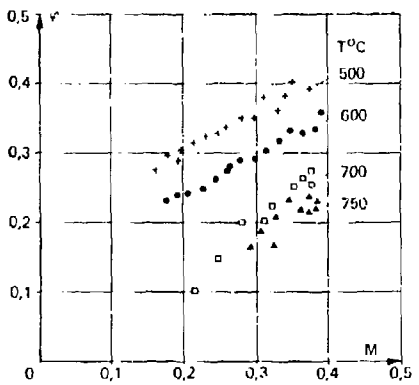

Fig. 7 – Richesse d'extinction en fonction du nombre de Mach et de la température de l'écoulement pour le petit anneau.

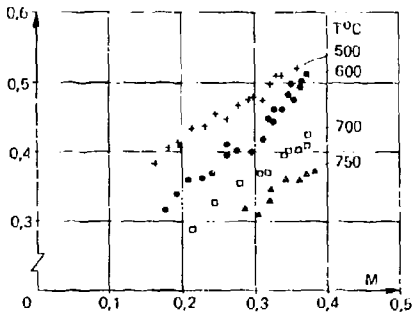

Fig. 8 – Richesse d'extinction en fonction du nombre de Mach et de la température de l'écoulement pour le grand anneau.

Les différents points d'extinction sont représentés par la richesse de la rechauffe φ en fonction du nombre de Mach M. Les points correspondant à une même valeur de la température de l'écoulement amont sont représentés au moyen d'un même symbole.

Dans le cas du système d'accroche-flamme constitué par deux anneaux coplanaires de même hauteur, l'extinction en aval de ces deux anneaux n'est pas simultanée : pour un couple de valeurs déterminées, nombre de Mach, température, lorsque la richesse rechauffe est progressivement réduite, le grand anneau s'éteint toujours avant le petit anneau et l'écart de richesse correspondant est de l'ordre de 30 %.

Il ressort de l'examen général de ces figures que :

- pour une valeur constante de la température la richesse d'extinction augmente lorsque le nombre de Mach augmente ;
- pour une valeur constante du nombre de Mach l'augmentation de température conduit à une diminution de la richesse d'extinction.

4. CORRELATION DES LIMITES D'EXTINCTION

La stabilité de la combustion en aval d'accroche-flammes a fait l'objet de nombreuses études et différents auteurs ([2], [3], [4]) ont proposé des formules de corrélation pour interpréter l'effet des principaux paramètres : température, pression, vitesse, dimension caractéristique de l'accroche-flammes, taux de blocage de l'écoulement.

Dans le cas des expériences effectuées, la pression a une valeur pratiquement constante égale à la pression atmosphérique et les deux accroche-flammes correspondent à une même valeur du taux de blocage 0,38. Les trois paramètres dont les variations influent sur les limites de stabilité sont la température, le nombre de Mach et la géométrie des anneaux.

A la suite de calculs préliminaires et compte tenu des paramètres de corrélation trouvés dans la littérature, il est apparu qu'une expression de la forme

$$\varphi = f\left(\frac{M}{\sqrt{T}\ exp\,(T/n)}\right)$$

permet l'obtention d'une corrélation satisfaisante susceptible d'interpréter pour chaque accroche-flamme l'effet de la température et du nombre de Mach amont pour une valeur de n égale à 300.

On a représenté sur les figures 9, 10 et 11 les points d'extinction obtenus pour chaque accroche-flamme en utilisant comme coordonnées la richesse d'extinction φ et le groupement :

$$\frac{M}{\sqrt{T}\ exp\,(T/300)}$$

Chaque figure révèle un groupement satisfaisant des différents points qui justifie l'utilisation du paramètre de corrélation.

L'effet de la géométrie sur les limites d'extinction a fait l'objet d'études antérieures dans le cas d'obstacles linéaires, de grands allongements pour lesquels l'écoulement environnant était pratiquement bidimensionnel. Il ressort de ces études que le paramètre géométrique essentiel dont dépend l'extinction est la longueur de la zone de recirculation [3]. Dans le cas de plusieurs obstacles de

formes homothétiques les longueurs des zones de recirculation sont proportionnelles aux hauteurs H de ces obstacles et le paramètre de corrélation incluant simultanément l'effet de la température amont et de la géométrie a pour expression :

$$\frac{M}{H\sqrt{T}\,exp\,(T/300)}$$

Cette expression ne peut pas être utilisée dans le cas d'anneaux concentriques de même hauteur. La figure 12 représente une tentative de corrélation : au lieu d'avoir une courbe unique il y en a trois, la courbe de l'anneau de hauteur 40 mm se situant entre les courbes des deux anneaux de hauteur 20 mm.

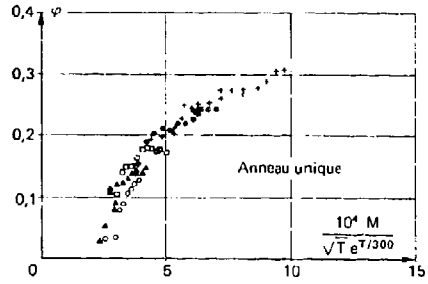

Fig. 9 – Evolution de la richesse d'extinction en fonction du paramètre de corrélation.

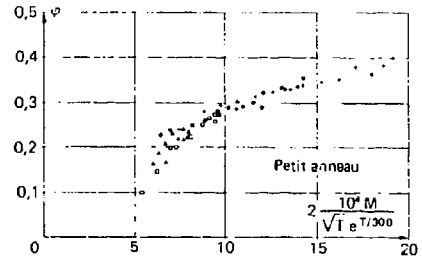

Fig. 10 – Evolution de la richesse d'extinction en fonction du paramètre de corrélation.

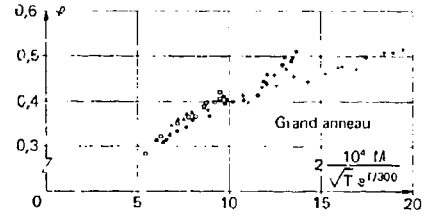

Fig. 11 – Evolution de la richesse d'extinction en fonction du paramètre de corrélation.

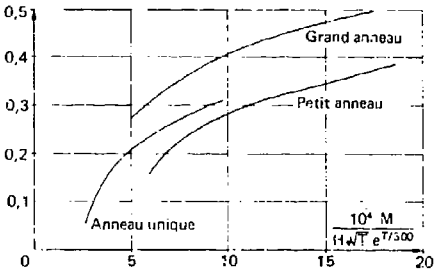

Fig. 12 – Corrélation des limites d'extinction. Effet de la géométrie

Ce résultat paradoxal a été à l'origine d'une étude détaillée de la combustion au voisinage immédiat des accroche-flammes dans le cas des deux anneaux concentriques.

5. ETUDE DE LA COMBUSTION EN AVAL DES DEUX ANNEAUX

La première explication à envisager lors de la constatation de richesses d'extinction distinctes pour deux obstacles de même profil placés dans un même écoulement est une hétérogénéité de cet écoulement en température ou en richesse.

Les mesures de température effectuées dans le canal de rechauffe ont conduit à des profils de température relativement plats présentant des valeurs identiques au niveau du petit et du grand anneau. Pour connaître la richesse locale dans l'écoulement une sonde ponctuelle de prélèvement d'échantillon de gaz de combustion a été utilisée. Cette sonde a été placée dans le creux de l'accroche-flamme. L'échantillon de gaz prélevé est amené jusqu'à des analyseurs de gaz qui mesurent les concentrations en CO, CO_2, CxHy et NOx. La mesure des composés carbonés permet de calculer la richesse locale. Les résultats obtenus avec ces prélèvements ont mis en évidence une légère hétérogénéité : le petit anneau est dans une zone plus riche que le grand anneau mais la différence relative n'est que de 15 pour cent ce qui n'explique pas l'écart de trente pour cent obtenu sur les richesses d'extinction.

Une autre explication à cet écart aurait pu être la suivante : la procédure d'essai est telle que l'extinction du petit anneau et celle du grand anneau ne se déroulent pas dans des conditions équivalentes ; l'extinction du grand anneau se produit alors qu'il y a combustion derrière le petit anneau ; pour l'extinction du petit anneau par contre il n'y a plus de combustion derrière le grand anneau. La différence d'extinction entre les deux anneaux s'expliquerait par une variation de vitesse dans le canal due à l'obstruction créée par la combustion. Pour éliminer cette explication des mesures d'extinction sur le grand anneau sans combustion en aval du petit anneau ont été effectuées et ont conduit aux mêmes résultats que les précédentes expérimentations.

Afin de comprendre l'organisation de la combustion derrière l'accroche-flamme, la sonde de prélèvement a été placée dans l'écoulement avec combustion non plus pour mesurer une richesse mais un rendement de combustion ainsi que les différentes espèces présentes. Les premières mesures ont été effectuées dans la portion centrale du sillage de chacun des deux anneaux et suivant une direction parallèle à l'axe de l'écoulement, elles ont permis en particulier de déterminer l'évolution longitudinale du rendement de combustion en aval du grand et du petit anneau.

Les résultats sont présentés graphiquement sur la figure 13 en fonction de l'abscisse réduite x/H : les deux courbes présentent le même aspect avec toutefois un changement important d'abscisse. Les points qui suivent méritent d'être soulignés :

1) au voisinage immédiat de chaque accroche-flamme le rendement présente une valeur constante et égale à 1 pour :

   $0 \leq x/H \leq 1,5$ dans le cas du grand anneau,
   $0 \leq x/H \leq 3$ dans le cas du petit anneau ;

2) plus en aval, le rendement décroit jusqu'à la valeur minimale $\eta = 0,84$. Cette valeur est obtenue respectivement pour :

   $x/H = 6,25$ dans le cas du grand anneau.
   $x/H = 9,25$ dans le cas du petit anneau ;

3) au-delà des valeurs précédentes de x/H le rendement de combustion augmente progressivement.

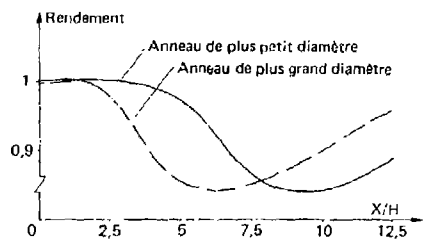

Fig. 13 – Evolution du rendement en fonction de la distance à l'accroche-flamme x rapportée à la hauteur de l'anneau pour : $\dot{m} = 2,5$ kg/s – $T = 800^{\circ}C$ – $\varphi = 0,52$.

Or, juste en aval de l'accroche-flamme il y a une zone de recirculation constituée par des gaz brûlés qui permet la stabilisation de la flamme. On peut donc penser qu'il existe une proportionnalité entre la zone de rendement 1 et la zone de recirculation.

A égalité de hauteur H il apparait ainsi que l'organisation de l'écoulement avec combustion en aval de l'accroche-flamme n'est pas la même dans le cas des deux anneaux étudiés et que la zone de recirculation est plus étendue dans le cas du petit anneau que dans le cas du grand anneau.

Quant aux concentrations en CO, CO_2 et CxHy leurs variations en fonction de x sont représentées sur les figures 14 et 15. Près de l'accroche-flamme, en aval, il n'y a pas d'hydrocarbures imbrûlés et la quantité de CO est égale à la quantité présente à l'équilibre thermochimique (dans les mêmes conditions de richesse et de pression). Dans la zone de recirculation le temps de séjour du mélange air-kérosène est suffisant pour que les réactions chimiques soient très avancées et donc que la composition des produits de combustion soit très proche de la composition à l'état d'équilibre thermochimique correspondant. Par contre, en aval de la zone de recirculation la configuration de l'écoulement change. On trouve une zone où les gaz brûlés n'ont pas un degré d'avancement élevé. Les concentrations en monoxyde de carbone et en hydrocarbures imbrûlés augmentent en fonction de x. Après avoir atteint une valeur maximale, elles diminuent. Cela correspond à la zone de propagation de la combustion.

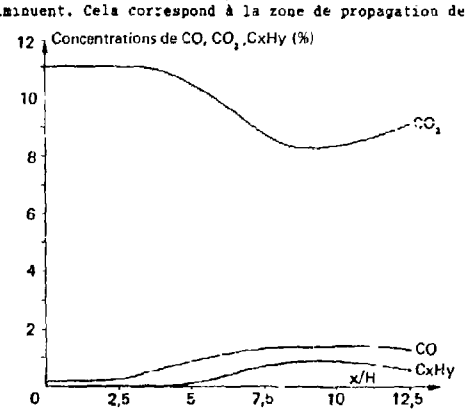

Fig. 14 – Evolution des concentrations en CO, CO_2 et CxHy en fonction de la distance à l'accroche-flamme rapportée à la hauteur de l'anneau pour le petit anneau et pour $\dot{m} = 2,5$kg/s $T = 800^{\circ}C$ – $\varphi = 0,52$.

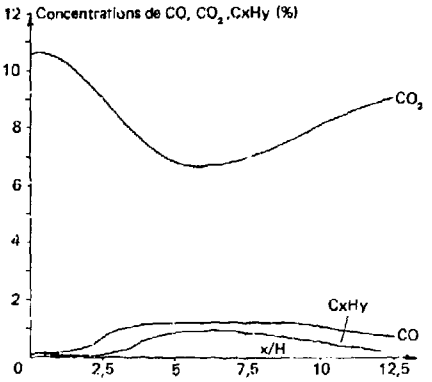

Fig. 15 – Evolution des concentrations en CO, CO_2 et CxHy en fonction de la distance à l'accroche-flamme rapportée à la hauteur de l'anneau pour le grand anneau et pour : $\dot{m}$ = 2,5kg/s T = 800°C – φ = 0,52.

Les résultats obtenus par comparaison des rendements sur les deux anneaux ont conduit à définir une autre expérimentation permettant de confirmer les longueurs distinctes de zones de recirculation sur ces deux stabilisateurs. La longueur de ces zones est mesurée de la façon suivante : on injecte du sodium sous forme d'une solution aqueuse saturée en chlorure de sodium à la limite de la zone de recirculation. Le sodium devient émissif à haute température et donne une très nette coloration jaune. Si le point d'injection se situe en dehors de la zone de recirculation la coloration fuit vers l'aval avec l'écoulement. En revanche, s'il se situe à l'intérieur de la zone de recirculation le sodium est entraîné en amont vers l'accroche-flamme et la coloration jaune envahit toute cette zone. On peut ainsi définir les contours de la zone de recirculation.

Cette méthode a été mise en oeuvre par A. MESTRE [1].

L'expérimentation a permis de dessiner la figure 16 où sont représentées les deux anneaux avec leurs zones de recirculation respectives en coupe.

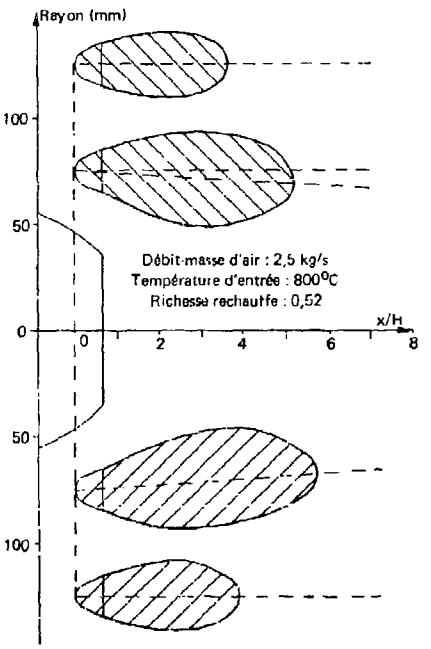

Fig. 16 – Forme des zones de recirculation déterminée expérimentalement par injection de sodium.

Ces résultats confirment ce qui avait été entrevu lors des mesures de rendement, à savoir que les zones de stabilisation de la combustion en aval des deux anneaux n'ont pas la même longueur.

6. CONCLUSION

Les observations et les mesures faites au cours des expérimentations sur les accroche-flammes constitués de un seul anneau et de deux anneaux ont permis de montrer que l'extension des corrélations obtenues avec les accroche-flammes linéaires placés dans des écoulements bidimensionnels à des accroche-flammes annulaires dans des écoulements axisymétriques est possible pour ce qui concerne l'effet de la vitesse et de la température sur les limites de stabilité mais se révèle plus difficile pour l'effet de la géométrie.

Pour les accroche-flammes linéaires le paramètre géométrique significatif est la longueur de la zone de recirculation elle-même proportionnelle à la hauteur du stabilisateur, c'est cette grandeur géométrique qui est utilisée avec succès dans les corrélations de stabilité. En présence d'accroche-flammes annulaires et probablement à cause de l'axisymétrie de l'écoulement et du stabilisateur, les zones de recirculation qui se développent en aval de deux obstacles de hauteurs identiques mais de rayons distincts, ont des longeurs différentes.

Pour ces accroche-flammes, qui se rapprochent plus de la configuration utilisée sur un moteur que les accroche-flammes linéaires, la hauteur de l'obstacle se révèle insuffisante pour caractériser la stabilité.

Au stade actuel de l'étude il nous est encore impossible de préciser le paramètre géométrique significatif. Un certain nombre d'expérimentations et de calculs sont encore nécessaires pour cela.

Mais les résultats présentés ici fournissent également un certain nombre de renseignements qui améliorent la connaissance des phénomènes de stabilisation par obstacle et nous permettront d'améliorer la modélisation de la combustion afin qu'elle reflète encore mieux les phénomènes réels très complexes.

REFERENCES

[1] - A. MESTRE
"Etude des limites de stabilité en relation avec la résistance des obstacles à l'écoulement".
AGARD Combustion Researches and Reviews Butterworths, London, 1955.

[2] - M.V. HERBERT
"A theoretical analysis of reaction rate controlled systems : part I".
Combustion Researches and Reviews Butterworth, London, 1957.

[3] - D.R. BALLAL, A.H. LEFEBVRE
"Weak extinction limits of turbulent flowing mixtures".
ASME 1979, vol 101, Journal of Engineering for power.

[4] - WANG JIA-HUA, CHANG YING ZOU
"Experimental research on the mechanism of flame stabilization in two phase mixture".
American Institute of Aeronautics and Astronautics, 1983.

DISCUSSION

G.Winterfeld, GE

From the old studies of flame stabilization in the fifties and sixties (e.g., E.E.Zukowski), it is well known that the length of the recirculation zone is one of the prime geometric parameters for correlating stabilization results (residence time in the flow along recirculation zone). This length is strongly influenced by the geometry of the flame holder system and the blockage it causes between the outer wall and the centre body. Could you comment on the effect of blockage generated by your system of flame holders?

Author's Reply

The blockage has a strong influence on the lean blow out. Its effect has been quantified in previous studies. The value of this blockage doesn't appear in our correlating parameter because we have used flame holders having the same blockage: the single annular flame holder and the 2 annular flame holders have the same cross section. We have not studied the influence of the blockage on the lean blow out limits, only the influence of the Mach number, the temperature and the flame holder geometry.

A.Lefebvre, US

Many previous workers have studied the flame stabilizing properties of single, two-dimensional flame holders. What makes your research especially interesting and useful is that you employ fully annular flame holders, sometimes alone and sometimes in conjunction with one or two other annular flame holders. Thus your test rig simulates much more closely the actual engine configuration. I would like to ask if the flames supported on the different gutters burn independently of each of them or if one flame zone interacts with an adjacent flame zone, thereby raising the combustion efficiencies of both zones.

Author's Reply

When we observed the different lean blowouts with the two annular flame holders we first made different hypotheses. The first was to suppose that the upstream flow was not homogeneous. However, the temperature and equivalence ratio measurements led to the conclusion that this was not a convenient reason.

The second hypothesis was that there was an influence of the combustion downstream of the little annular flame holder on the combustion downstream of the large one. In order to know if this was true or not we have done measurements of lean blow out limits on the large annular flame holder without combustion downstream of the little annular flame holder. The results obtained were equal to the previous one. We can conclude that there is no influence on the lean blow out limits. There is no interaction between recirculation zones of different flame holders. Downstream, interaction can occur and this has no influence on lean blow out.

J.Odgers, CA

With reference to Figure 13, I presume the change (reduction) in combustion efficiency as one goes downstream from the gutters is due to a dilution effect brought about by the relative recirculation zones. Is this correct?

Author's Reply

In the recirculation zone, just downstream of the flame holder, the combustion products have a large residence time. For this reason, the combustion efficiency is equal to 100%. But downstream of this zone there is mixing between combustion products and fresh gases and therefore, because of this dilution, the combusting efficiency decreases and then increases in the propagation zone of combustion.

HIGH PERFORMANCE TURBOFAN AFTERBURNER SYSTEMS

A Sotheran*
Rolls-Royce plc
Filton, Bristol
England

ABSTRACT

The modern turbofan afterburner is characterised by its high boost and efficiency and by its compact geometry which is achieved by locating the flameholding baffles immediately downstream of the turbine exhaust plane at the confluence of the engine core and bypass gas streams. At the confluence, the stream divider may be a simple cylinder or it may be of lobed configuration to encourage mixing between the two gas streams in the downstream jet pipe in order to improve the unboosted thrust of the engine. Obviously the geometry of the afterburner hardware must be adapted to suit the choice of mixed or unmixed configurations. In flight, selection of the afterburner must be fast and reliable under all flight conditions with times to full thrust of the order of only a second or two. Both the light up and the subsequent acceleration to full thrust are expected to be smooth with no excessive initial thrust jump. Synchronisation and matching of the afterburner fuel with the variable final nozzle must be accurate at all times to maintain the engine turbomachinery on its required running lines. The afterburner must always be free of combustion driven pressure oscillations which can occur either in cross stream modes, which destroy engine hardware in fractions of a second, or in longitudinal modes which can also be mechanically damaging and, in some instances, cause fan surge and other intolerable effects in the engine. The afterburner must incorporate appropriate measures to avoid various potential thermal problems including fuel boiling and gumming in the supply manifolds and excessive heat transfer to the jet pipe and aircraft engine bay.

INTRODUCTION

The so-called 'propelling' nozzle of a jet engine is somewhat misnamed since its function is to act as a throttle on the engine air flow to establish the engine turbomachinery on its required running lines, and the aerodynamic forces acting on it are always in the rearward direction. Far from providing the propulsive forward thrust of the engine, the nozzle is actually a drag on the installation. Some of this drag is, of course, recovered when a divergent second stage is provided to the nozzle but this never amounts to more than a small proportion of the rearward force. The value of afterburning to the engine cycle is that, by increasing the volume of the turbine exhaust gases, it provides an extra, or, more usually, an alternative means to throttle the engine airflow which incurs no drag penalty and is easily varied and very powerful in its effect. The simplest use of an afterburner is to slightly uprate an engine provided with only a fixed mechanical nozzle. The resulting additional thrust is approximately what would be obtained, without afterburning, by the use of a smaller nozzle but without incurring the additional drag of the small nozzle. The degree of boost achievable in this way, if any, depends on the particular characteristics of the engine turbomachinery and on the prevailing flight condition. At best, it is restricted to low values. High boost afterburners may use this minor effect, when it is effective, but their chief purpose is to provide compensatory thermal throttling of the engine whilst the variable nozzle, which is an essential adjunct to a high boost system, is progressively opened to high degrees. The object of opening the nozzle is, of course, to reduce its drag and it is this reduction in nozzle drag which is the source of afterburner boost.

It is obviously not necessary that the degree of afterburning provided should always precisely compensate for the nozzle opening, that is to exactly maintain the turbomachinery on the same running line whether the afterburner is on or off. There is often a fuel consumption or thrust advantage in operating the boosted engine either under or over restored relative to the unboosted case, that is as if operating "dry" (unboosted) with a relatively larger or smaller nozzle. The 'equivalent dry nozzle area' or EDNA value, expressed as a percentage deviation from the unboosted nozzle area is a convenient means to indicate the prevailing engine or fan running line in the boosted case.

There is a further option, whenever afterburning is selected, of increasing the engine thrust by a core engine "throttle push" that is by increasing the turbine entry temperature. The term "afterburner boost" is sometimes used to indicate the total (engine plus afterburner) increase in thrust between afterburner on and afterburner off but in this paper it denotes only the contribution from the afterburner and is quoted as a percentage of the prevailing "dry thrust" of the engine, that is the thrust which the engine would deliver if it were operating without afterburning but at the same turbine entry temperature and with its nozzle set at the prevailing EDNA value.

AFTERBURNER CONFIGURATIONS

The earliest Rolls-Royce turbofan afterburners (Figure 1) were termed mix-then-burn systems because they featured a stream mixer, of about one jet pipe diameter in length, between the engine and the afterburner proper. Its purpose was to mix the turbine and bypass gas streams ahead of the flameholders to avoid the obvious and, at the time, novel problems of promoting burning in the cold gases of the engine bypass stream. Instead, similar flameholding and fuel injection arrangements to those used in earlier turbojet afterburner systems were provided and these, it was anticipated, would be appropriate for operation in what was intended to be a fully mixed gas stream at near turbojet temperatures.

Stream mixing can, of course, be a thermodynamic benefit to the engine cycle in itself but its value at military engine bypass ratios depends strongly on the aircraft application in which the engine is employed. Whilst the mixing always gives a constant if modest improvement in the engine dry thrust, any additional pressure losses which the mixer generates

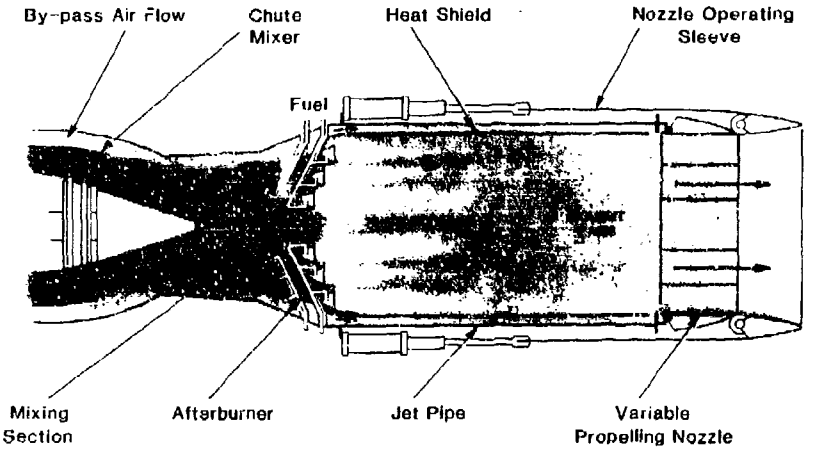

FIG 1 THE MIX-THEN-BURN AFTERBURNER

result in a thrust deficit which is variable with flight condition and which can more than eliminate the mixing benefits (Figure 2). The pressure loss deficit is a strong function of nozzle pressure ratio but is not important, for instance, during high altitude, high speed flight. In applications in which this flight mode dominates, the use of mixing could clearly be beneficial.

The mix-then-burn afterburner achievas its objectives fairly satisfactorily but at the expense of a relatively long jet pipe. It has also proved to be prone to the instability known as afterburner buzz or rumble, to which turbofan afterburners are particularly susceptible, at intermediate to high levels of boost. In fact the boost which is safely available from the mix-then-burn afterburner is limited by the appearance of buzz and the fuel schedule has to be set down accordingly. Buzz is a longitudinal "organ pipe" pressure oscillation which can become established between either the fan or the turbine and the nozzle with frequencies between about 50 and 150 Hz depending on the type of buzz established, the flight condition, the afterburner fuelling level and so on. Its causes and avoidance are discussed in later sections.

In the next afterburner evaluated at Rolls-Royce, a stream mixing arrangement was retained but, to save engine length and weight, a flameholder system was

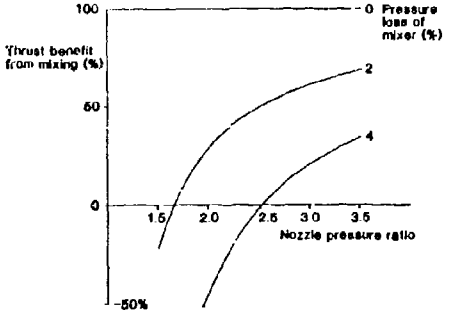

FIG 2 MIXING BENEFITS VERSUS NOZZLE PRESSURE RATIO

chosen which could double as the stream mixer in the afterburner off case. In this paper this system is referred to as the "mix-and-burn system".

The mix-and-burn afterburner system uses an adaptation of a cold stream burner device which has been employed in various applications in Rolls-Royce engines, for instance in ramjets and in "PCB", for boosting the front nozzle thrust of the Pegasus vectored thrust engine (Reference 1). In its afterburner configuration the mix-and-burn system features a pilot burner at the downstream end of the splitter which divides the bypass and turbine streams at turbine exhaust (Figure 3). The pilot is a simple annular gutter and is separately fuelled by direct injection into its wake through a variation of the "vaporiser" fuel injector employed in Rolls-Royce military core combustors (Reference 2). The distinguishing feature of the mix-and-burn afterburner is a system of Vee-shaped "longerons" which extend from the annular pilot across the bypass stream at a narrow angle to the flow (Reference 3). The wakes of the longerons are contiguous with that of the annular pilot and hence fill with flame whenever pilot fuel is selected. The main bypass stream fuel injectors are located in the slots between the longerons acting as the ignition source for this fuel. For the turbine stream, an arrangement of plain V-baffles with upstream fuel injectors is employed.

With afterburner off, the action of the bypass stream longerons is to turn the flow radially inwards through an angle dependent on the angle and circumferential blockage they present to the approaching flow. Meanwhile, the turbine stream gases tend to lift outwards into the wakes of the longerons, thus generating a large interface between the two streams to encourage the required high level of stream mixing. Mixing efficiencies of the order of 85% are measured for this system at the engine nozzle which is about 1.25 pipe diameters from the end of the stream mixer.

The burning performance of the mix-and-burn system is high and, in terms of both boost and efficiency, matches that of the earlier mix-then-burn configuration fairly closely. However, once again afterburner buzz imposes an upper limit to the thrust which can be safely extracted from the system and, although this is very high, it is believed that this system could never deliver the near stoichiometric nozzle temperatures which are targeted for modern afterburners. Accordingly, the mix-and-burn afterburner has never been developed beyond a short

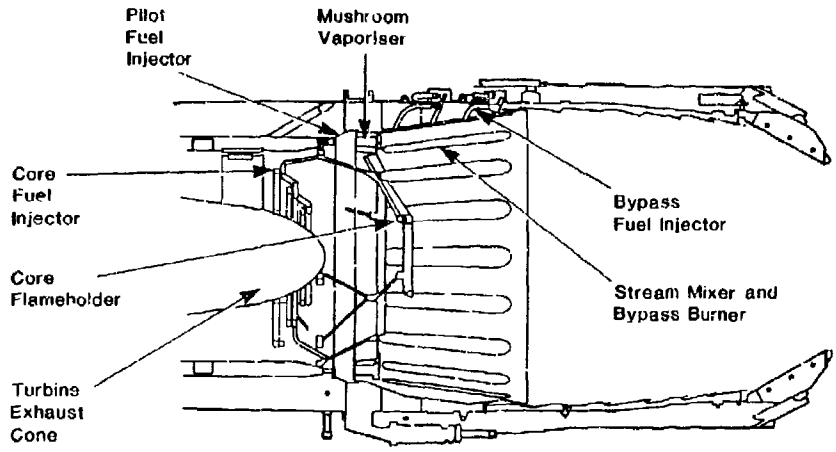

FIG 3 THE MIX-AND-BURN AFTERBURNER

programme of exploratory engine and full scale rig evaluations.

The cause of the mix-and-burn system's proneness to afterburner buzz is believed to be a strong inward migration of the bypass fuel, which is generated in the first place by the cross-duct movements of the two gas streams.

Accurate fuel placement and control of fuel movements are always difficult to achieve in cold stream burners since, ahead of the flames, the fuel droplets tend to remain unevaporated and to move ballistically,that is without following the gas stream around bends and obstacles in the flow, so that their trajectories are always uncertain and often end in impact with the duct walls or with other hardware. For this reason, in Rolls-Royce cold stream burners, the fuel injectors are usually located between rather than upstream of the flameholders, which would otherwise tend to operate awash with liquid fuel, so that the fuel is injected directly into the burning zones. However, an inevitable consequence of "direct" fuel injection, from between the flameholders rather than ahead of them, is that the flameholder wake flames need to be provided with their own separate supply of fuel (Figure 4). The use of "wake" and "fill" fuel stages is another feature of all Rolls-Royce cold stream burners to date.

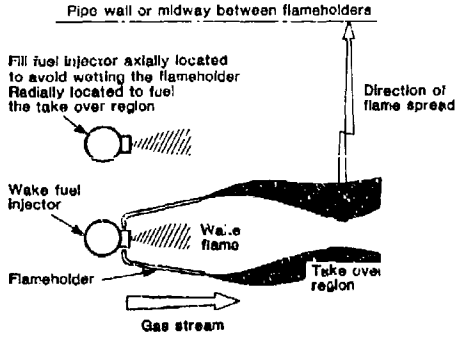

FIG 4 COLD STREAM FUEL INJECTION SYSTEMS

In the case of the mix-and-burn afterburner, when the main bypass stream fuel in injected into the system from between the longerons, it immediately assumes the radially inward motion of the local gas stream and, despite the fact that the fuel enters the flame and must evaporate very quickly, significant proportions of it continue towards the centre of the jet pipe when the bypass gases, in which they are intended to burn, turn axially rearward towards the nozzle. The measured effect of this is a concentration of fuel on the jet pipe centre line which, coupled with the incomplete mixing of the gas streams at the upstream end of the jet pipe, leads to very high local values of fuel/air ratios and, as further explained in the next section, the relative proneness to afterburner buzz already mentioned. As as alternative to the mix-and-burn system and especially when there is no operational advantage in stream mixing, it is advantageous to dispense with mixing altogether in order to ensure the aerodynamic conditions and the control over fuel movements which are needed to best ensure that buzz is avoided. The most recent Rolls-Royce afterburners are of this type and are designed specifically to discourage stream mixing. However, despite the measures taken to avoid forcing the mixing, significant amounts nevertheless occur due to natural diffusion of the streams into each other. Because of this effect, this afterburner is termed the mix/burn system. A full description is deferred to a later section.

AFTERBURNER BUZZ IN THE OLYMPUS 22R SYSE

Although afterburner buzz is usually associated with fairly recent turbofan engines, it is by no means confined to this type, and, as early as 1961, the phenomenon was encountered in a Rolls-Royce turbojet engine, the Olympus 22R, during bench engine investigations into a quite separate engine instability.

Since the appearance of buzz during flight seemed a real, if remote, possibility on this engine and its possible consequences were believed to be potentially very damaging, a full enquiry into its fundamental causes was initiated (Reference 4). From the start of the investigation it was known that the possibility of buzz arose in the Olympus 22R because of the nature of its fuel control system. This introduced the fuel in consecutive stages, with each fuel injection stage feeding one of the afterburner's annular flameholders. The control system was designed to deliver the scheduled fuel irrespective of the back pressure from the fuel injection system

and this meant that, if one fuel injector failed to be selected, due to a faulty valve, for instance, its intended share of the fuel would be automatically divided between the injectors already operating. As a consequence their flameholders would receive significantly more fuel than their scheduled flow and it was this circumstance which, it was found, could generate buzz.

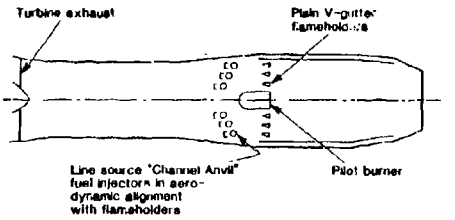

FIG 5 THE OLYMPUS 22R TURBOJET AFTERBURNER

The Olympus 22R afterburner (Figure 5) features three, concentric, annular flameholders, of plain V-baffle section, each served by a "channel-anvil" fuel injector located about 70mm directly upstream. The channel-anvil fuel injector (Figure 6) is a ring manifold from which the fuel is injected in an upstream direction into a downstream facing channel. The fuel spreads circumferentially in the channel which therefore acts as a line source of fuel and provides a very uniform supply along its length. An important secondary advantage of the channel anvil injector is that the fuel ring is externally cooled by the injected fuel which helps to suppress internal boiling in the ring and the instabilities in fuel supply and burning which this causes. In the cross stream or, in the present case, the radial direction, the channel anvil develops a peak in the fuel concentration in line with itself and this peak

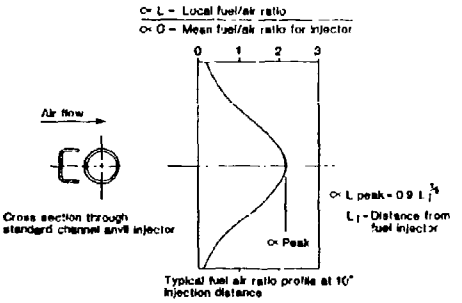

FIG 6 THE FUEL DISTRIBUTION FROM THE CHANNEL ANVIL FUEL INJECTOR

reduces at increasingly remote distances downstream. At any fixed distance downstream of the fuel injector (L_I), the radial fuel distribution is constant over practical ranges of gas conditions and fuel flow and the half-width (W) of the spray is given by the simple expression

$$W = 0.9\ L_I^{1/2}$$

where the half-width is defined by the stations where the local fuel concentration is half the peak value.

This simple characteristic allows the fuel injection distance to be chosen to optimise the distribution of fuel at the flameholder station since the fuel may be spread evenly across the gas stream or, alternatively, concentrated at the flameholders by siting the fuel injectors either relatively far or close upstream.

The operating characteristics of an afterburner which are influenced by the uniformity of the fuel distribution are the thrust boost at which maximum efficiency is achieved, the lean operating limits and, as will be seen, the system's buzz characteristics. All of these characteristics are strongly influenced by the fuel air ratio local to the flameholder station. With channel-anvil fuel injection, peak efficiency, lean blow off and afterburner buzz occur at, respectively, stoichiometric, 30% stoichiometric and 150% stoichiometric conditions at the flameholder. In general, therefore, the fuel injection length can be chosen to maximise afterburner efficiency at the boost required by the engine application, but with possible overriding limitations determined by the fuel (or boost) turn down requirements and by the risk of buzz.

The value of the flameholder fuel air ratio at buzz onset (50% above stoichiometric) was determined in the series of experiments on the Olympus 22R engine referred to earlier in which it was deduced that an excess of fuel air ratio beyond this value at any single flameholder was a sufficient condition for buzz. The tests were made in an altitude test cell at various simulated flight conditions. The main hardware changes evaluated during the tests were to the fuel injectors, of which several types in addition to the channel anvil injectors were used. The injectors were located at various distances from the flameholders to vary the fuel concentrations at the flameholder station and, during the tests, the fuel to single and various combinations of fuel injectors was increased until the buzz instability was detected. As already noted, it was found that, in every example of buzz onset, the fuel to some flameholder had been raised to the critical level and this applied irrespective of the prevailing gas conditions in the jet pipe or the prevailing level of heat release in the pipe - although the latter obviously influenced the amplitude of the instability once it had been generated. This is illustrated in Figure 7 which shows buzz amplitude versus a fuel concentration parameter which indicates the peak fuel air ratio at the flameholders. It shows how buzz always appears at a fixed local fuel air ratio but thereafter responds to the number of flameholders in operation, that is to the total quantity of fuel supplied to the system.

Because of the nature of the Olympus 22R engine cycle and its afterburner control system, the only jet pipe gas stream property which was variable with flight condition during these tests was the gas pressure so that no information on the influence of inlet gas

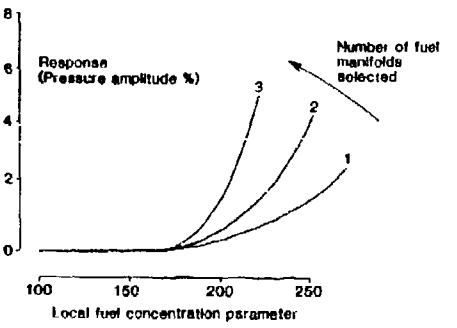

FIG 7 THE BUZZ CHARACTERISTICS OF THE OLYMPUS 22R

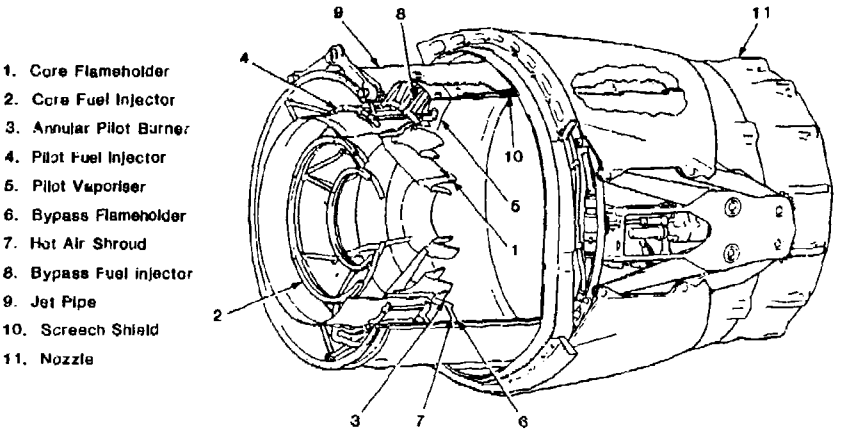

FIG 8 THE MIX/BURN AFTERBURNER

stream velocity, temperature or vitiation on buzz onset was obtained, nor were the effects of pipe acoustics investigated. Nevertheless the results help to explain why buzz has seldom been reported in turbojet afterburners but seems to be a common feature of turbofan systems. In turbojet afterburners it is a relatively simple matter to achieve a uniform fuel distribution at the flameholders and, even in a very high boost system, it is never necessary to fuel beyond a mean or local stoichiometric level. Thus it is only in the event of a fuel control system failure, such as described earlier, that local fuel air ratios rise to anything like buzz provoking levels. In normal circumstances turbojet afterburners operate within a 50% margin, at least, of buzz provoking fuel air ratios. The situation is quite different in a mixed turbofan where, because of the lower inlet gas temperature, afterburner fuelling levels can be 30% to 40% higher than a turbojet of the same total air flow. Meanwhile the vitiation of the turbine exhaust stream is 15%-20% higher than that of a turbojet of the same turbine exit temperature (the extra representing the work extracted to drive the outer fan). Local fuel and fuel air ratio concentrations are therefore much higher in turbofan systems than in turbojets and any failure to distribute the afterburner fuel in strict accordance to the local stream requirements can instigate buzz.

THE MIX/BURN AFTERBURNER

As first specified, the two main requirements of the mix/burn afterburner were that it should deliver very high thrust boosts, of the order of 75% at take off, and that it should do so in an extremely confined geometry (Figure 8). The length allowed between the turbine and the throat of the variable nozzle was approximately 1.75m. The pipe diameter allowed at the afterburner inlet station was fairly generous so that, although the gas velocities at this station vary considerably as the engine bypass ratio adjusts with the prevailing flight condition and EDNA value, they are never high enough to jeopardise the burning stability of the flameholders within the required flight envelope of the system. Shortly downstream of the flameholders, however, it was necessary to taper the jet pipe very steeply in order

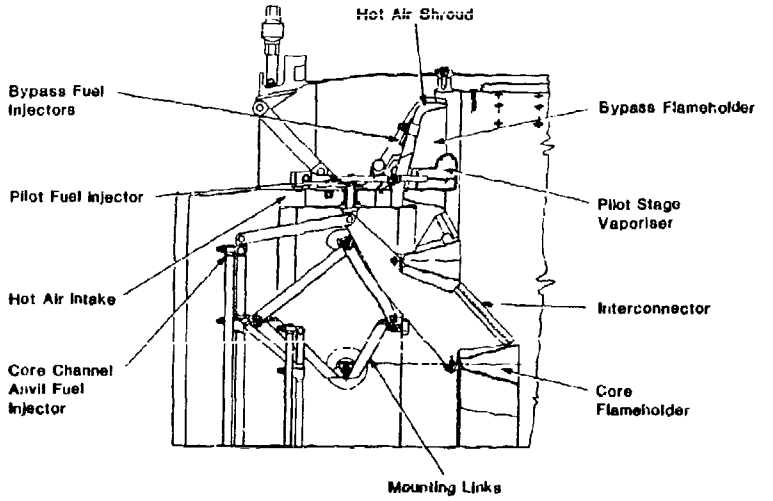

FIG 9 THE MIX/BURN AFTERBURNER

to accommodate the nozzle actuation system and a thrust reverser between the jet pipe and the boat tail lines of the aircraft. The effect of the pipe taper is, of course, to increase the internal gas velocities relative to the cylindrical pipe case and, since all gas stream heating generates total pressure losses which increase with stream velocity, the eventual consequence is a significant loss in the afterburner boost for a fixed nozzle gas temperature. To compensate for this the afterburner must be designed and developed either to complete its burning relatively early in the tapered pipe or to achieve a correspondingly higher nozzle temperature. In either case the tapered pipe increases the difficulty of meeting the afterburner objectives.

It has already been explained that, because of previous experience of afterburners which were designed to encourage vigorous mixing between the bypass and turbine gas streams, a principle objective of the mix/burn system was to discourage large scale movements of either stream across the jet pipe. To achieve this the mix/burn system was designed as two separate systems intended to operate more or less independently of each other. This allowed each system to be arranged to suit the conditions of its own gas stream, and, in the case of the turbine stream, for a simple turbojet afterburner to be adopted, similar to that of the Olympus 22R engine.

In the mix/burn system (Figures 8 and 9) it features two concentric and inter-connected annular vee-shaped baffles each fuelled by an upstream channel-anvil fuel injector. Flameholders and injectors are separately link-mounted to an enclosing outer cylinder to allow unrestricted and independent thermal expansion of the various rings and the whole assembly is located within the engine exhaust annulus. The geometric details of the system are chosen to ensure clean aerodynamics throughout the system with accurate alignment of the fuel injectors with the flameholders. An overriding requirement of the system was to avoid afterburner buzz within the operational range of afterburner fuel flows and the buzz avoidance rules explained above were used to achieve this effect.

For the bypass system, a cold stream burner was obviously required and the usual Rolls-Royce combination of wake-fuelled flameholders and coplanar "fill" or main fuel injector was adopted. The flameholder arrangement is of an annular vee-shaped baffle from which radial baffles extend across the bypass stream. Vaporiser fuel injectors are provided at each intersection of the radial and annular baffles (Figure 10).

Although the bypass and turbine stream afterburners of the mix/burn system are intended to operate independently of each other, nevertheless the close proximity of the hot turbine stream is used to aid burning stability in the bypass stream where the temperature can fall as low as 300 K at extremes of the flight envelope. To achieve this, a small proportion of the hot gases is collected ahead of the turbine stream flameholders (Figure 10) and ducted to feed the bypass stream vaporisers and, indeed to enshroud the whole of the bypass flameholder system so that its wake flame is fed wholly and only with hot turbine stream gases. This has the effect of giving the whole of the mix/burn afterburner the burning stability characteristics of a turbojet afterburner as well as providing considerable assistance to the propagation of the main burning across the cold bypass stream.

Early experience of the vaporiser fuel injection used in the bypass afterburner was not encouraging until it was realised that the wake system behind the array of interconnected annular and radial baffles was divided into quite distinct flow zones with no guaranteed interchange of gases between them. Before this was established it was assumed that the whole of the wake region was effectively a single zone subject to vigorous and random cross-movement of gases. Accordingly, the pilot fuel was fed into the wakes through "mushroom vaporisers" (Figure 11) in a fairly simple fashion.

Subsequently these were replaced by L-shaped vaporisers with various provisions to ensure that all parts of the wake system were adequately fuelled. One such feature is an internal baffle which divides the vaporiser air flow between inner feed holes to the annular baffle and outer feed holes to the radial baffles. The total airflow through the vaporiser is metered by an internal orifice ahead of the baffle. The fuel flow is injected just downstream of the metering orifice, where the gas velocities are at their highest, and equal quantities of fuel are directed to either side of the vaporiser baffle. The fuel air mixture is finally ejected from the vaporiser through a system of small holes located to feed the wake of the annular baffle and various zones of the radial baffle wake. Without the separate feeds to the wake zones a full wake flame could not be guaranteed.

For the main bypass fuel injectors, an array of six fan sprayers, three along each side of the radial baffles, was eventually adopted (Figure 10). The number and disposition of these injectors were

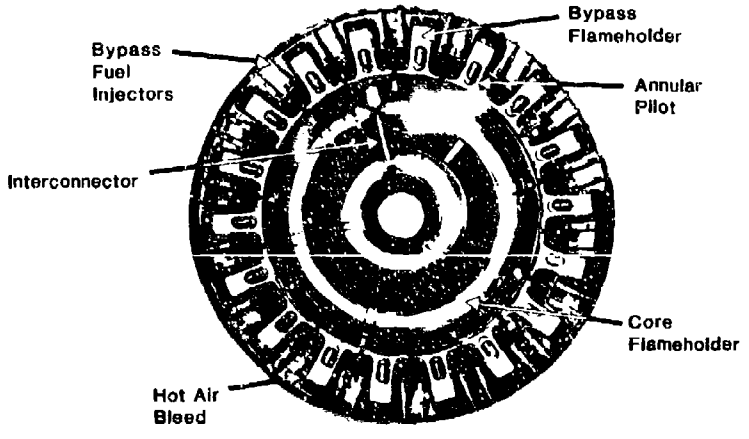

FIG 10 THE MIX/BURN AFTERBURNER

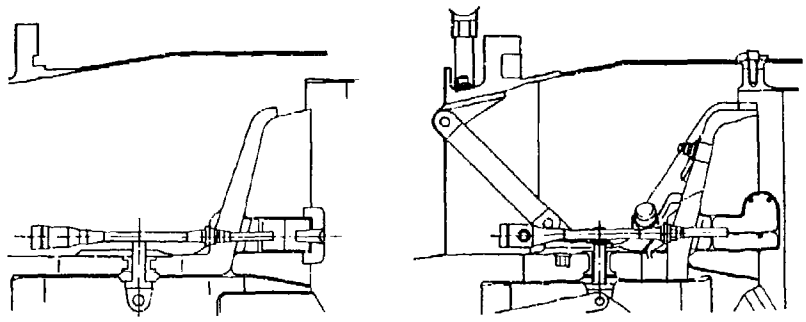

Mushroom Vaporiser

L-Shaped Vaporiser

FIG 11 THE PILOT BURNER FUEL INJECTION

developed on a sector burning rig reproducing a section of the annular baffle and two radial baffles. In general it was found that a configuration which is conducive to high heat release and combustion efficiency is also relatively prone to buzz, whilst, for instance, if the fuel injectors are located sufficiently far from the flameholders then both the efficiency and the proneness to buzz is reduced. An advantage of coplanar fuel injection is that it allows the placement of the main fuel to be relatively accurately optimised to achieve the best possible compromise between heat release, efficiency and buzz.

The fanspray fuel injector was chosen because it proved to be the best of several fuel injectors which were evaluated. The fan sprayers were originally developed for use in the "plenum chamber burner", to augment the front nozzle thrust of the Pegasus engine. They are an adaptation of the swallow tail gas jet and, when employed for liquid fuel injection, they produce a fan shaped, thin sheet of fuel which quickly disrupts into a spray of fine droplets.

FUEL STAGING

To achieve the very fast selections and accelerations required of the mix/burn afterburner a relatively simple, two stage fuel feed system was employed. The first stage supplies fuel to the pilot baffle only and the second stage provides the rest, that is to the turbine stream channel anvil fuel injectors and to the bypass stream fan spray fuel injectors. The pilot fuel is not modulated with the pilot's lever but, on afterburner selection, is metered as a fixed function of the prevailing turbine stream air flow to establish a constant fuel air ratio in the afterburner gutter wakes. The main fuel modulates with the pilot's lever from a minimum flow, which is set to just keep the manifolds full of fuel against the natural drainage, to maximum flow which, over large parts of the flight envelope, gives approximately stoichiometric nozzle gas temperatures. This arrangement ensures that all afterburner accelerations can proceed without the hesitations which would inevitably result if they began with any parts of the fuel injection system yet to be filled. The division of the main fuel injection stage between the turbine and bypass gas streams is not, of course, fixed but varies with the engine bypass ratio around the aircraft flight envelope.

AFTERBURNER SELECTION AND IGNITION

The previous section describes how, once selected, all parts of the fuel injection system remain full and in operation whatever the degree of afterburning selected by the pilot. The requirements of the selection procedure are to fill the fuel injection system, to establish the minimum afterburner flows described above, to open the nozzle to the matching area and, finally, to light the system.

In a turbofan engine there is direct communication between the afterburner and the fan by way of the bypass duct so that any mismatch of the afterburner fuel with the nozzle area setting is immediately felt by the fan, whose running line rises or falls depending on the direction of the mismatch. Afterburner light ups inevitably involve a degree of mismatch since ignition is always instantaneous and much too fast for any practicable nozzle actuation system to follow. The effect of the light up is, of course, to thermally throttle the fan flow and to raise its running line towards surge. To compensate for this effect and to eliminate any possibility of fan surge on afterburner light up, the nozzle of the mix/burn afterburner is pre-opened to its minimum boost area before the fuel is ignited. The fan running point therefore falls on afterburner selection but is immediately restored when the afterburner lights.

The manifold filling procedures in the mix/burn system is in two phases - a 'fast prime' phase which nearly fills the fuel system very quickly and a slow prime stage which completes the process. These arrangements ensure that fuel never reaches the burning zones at fast prime rates which, once again, could over restore and, perhaps surge the fan.

Ignition in the mix/burn afterburner is by 'hot streak' in which a small quantity of fuel is injected into the main combustor and briefly generates a flame through the turbine which is long enough to ignite the afterburner fuel. Experience of hot streak ignition in early gas turbine engines was not always satisfactory, especially when large quantities of fuel were injected slowly into the primary zone of the main combustor. Not surprisingly these measures could severely damage the turbine. Modern practise is to inject the fuel at the downstream end of the combustor towards the turbine and to use very small quantities (Figure 12). With these provisions, the system is safe and extremely reliable.

Engine	Flow
Avon	250 ccs in 2 secs
Olympus-22R	250 ccs in 0.4 secs
RB145	30 ccs in 0.6 secs
RB168-25R	48 ccs in 0.3 secs
RB199	20 ccs in 0.25 secs

FIG 12 HOT STREAK FUEL FLOW RATES

TWIN OPEN LOOP CONTROL OF THE AFTERBURNER FUEL AND NOZZLE

The afterburner selection times specified for the mix/burn afterburner were felt, when the system was designed, to be too fast to allow automatic 'closed loop' control of the nozzle to match the fuel modulations. In closed loop control, whenever the afterburner fuel is modulated an error signal from the engine, for instance ir. the turbine pressure ratio, is used to vary the nozzle area in such a way as to restore the engine turbomachinery to the required running line. The responses in such a system are inevitably time consuming and hence limit the rate at which the fuel flow can be modulated. To avoid these delays in the mix/burn afterburner, the fuel flow and nozzle area are separately controlled to pre-scheduled values which suit the prevailing flight and engine running conditions and give the degree of boost selected by the pilot.

The chief ramification of twin open loop control for the afterburner system results from the fact that the schedules and control system sequences must be chosen to ensure that schedule errors and mismatches which inevitably occur during the fast transients are always safe and tend to lower the fan running line rather than raise it towards surge. The resulting high EDNA values increase the engine bypass ratio and the gas velocities through the afterburner and both of these effects tend to degrade the afterburner performance and reduce its burning stability.

The full sequence of afterburner selection and acceleration procedures are shown in Figure 13. Originally it was intended that the selection would not proceed beyond light up without a positive indication from a u/v flame detector but this has not proved to be a necessary feature. However, if the engine running line, as indicated by the turbine pressure ratio, should deviate too far from normal, then the selection is terminated and the system is shut down.

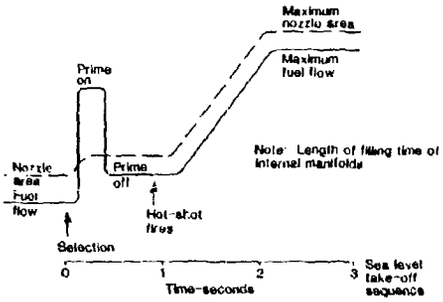

FIG 13 THE LIGHT-UP SEQUENCE

JET PIPE AND HEAT SHIELD

The jet pipe of the mix/burn afterburner is a titanium fabrication and is protected from the afterburner flames by a two piece heat shield which is fabricated in a heat resistant nickel based alloy. Design of the heat shield is inherently more difficult than that of the jet pipe which is essentially a cool running, fairly simple pressure drum. Against this, the heat shield not only operates much hotter than the jet pipe, and must be mounted from it by means which allow differential expansions between them, it also has to withstand pressure loads which vary with flight conditions and the degree of afterburning selected and which switch from expansive to implosive along its length.

Many systems have been devised to accommodate these circumstances with varying degrees of success in terms of durability, weight, complication and so on. The mix/burn afterburner uses simple cylindrical sections which are conventionally film cooled. The cooling rings provide the stiffness required to withstand any pressure loads which the heat shield may experience, including afterburner flame out cases. They are comparatively heavy in themselves but allow a simple and light mounting system of bolts and radial pins which are attached to the jet pipe and locate in holes and slots in the heat shield sections.

The forward section of the heat shield is perforated to provide acoustic suppression of the high frequency, cross stream pressure oscillations (screech) to which all high boost afterburner systems are prone.

COMPARATIVE PERFORMANCE

The performance of the three afterburner systems described in previous sections is compared in Figures 14-17. Figure 14 shows the burning stability in terms of the excess nozzle area or EDNA value which the afterburners can withstand without extinction versus the prevailing jet pipe pressure. The plot indicates not only steady burning stability but also the extreme conditions at which the afterburner can be 'handled', that is selected or turned up or down without risk of extinction, since it is during handling that high EDNA values are experienced.

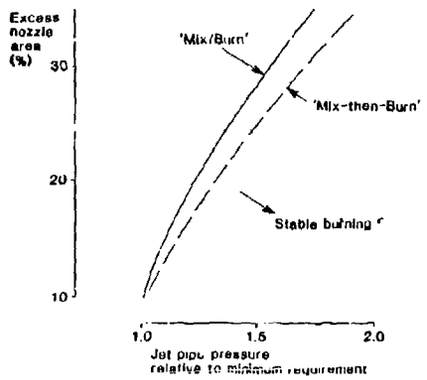

FIG 14 BURNER STABILITY

Unexpectedly the superiority of the mix/burn afterburner diminishes with reducing pressure

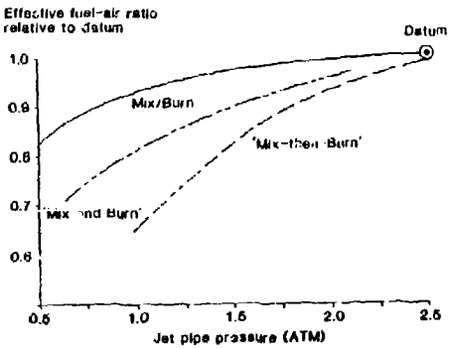

FIG 15 MAXIMUM AFTERBURNER FUEL AIR RATIO

possibly indicating that, even with the assistance from the hot stream provided by the mix/burn afterburner the contribution of the bypass stream burner to high altitude boost and burning stability reduces at very low pressures.

Figures 15 and 16 show how the highest fuel air ratios at which the three afterburners can be operated and their peak efficiencies are affected by jet pipe pressure. In all cases the effects are increasingly important as pressure reduces below 2 atmospheres but the mix/burn system is easily the least sensitive to pressure and maintains its performance to much lower levels than the other systems.

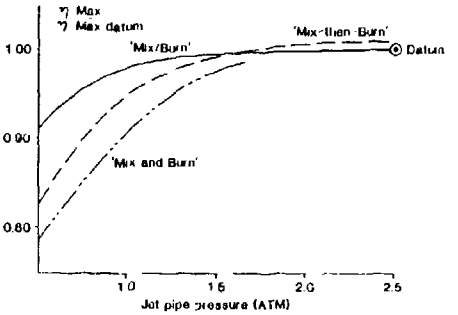

FIG 16 AFTERBURNER EFFICIENCY

Figure 17 shows the buzz characteristics of the three afterburners and illustrates the increasing degree of control exerted over the fuel placement within the successive systems. In the mix/burn system, the two types of buzz which can be provoked depending on whether the bypass or the core gas stream is over fuelled are particularly distinct. The fuel air ratio at which each stream is provoked into buzz is virtually independent of the fuel supplied to the other stream indicating the absence of any exchange of fuel between the two. Clearly this does not apply to the other systems where cross-stream movements of fuel or gas add to the buzz proneness of both streams and lower the total fuel air ratio at which buzz free operation is possible.

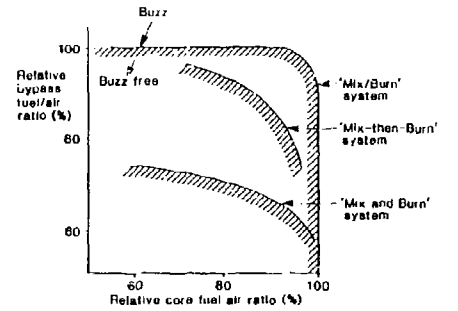

FIG 17 AFTERBURNER BUZZ CHARACTERISTICS

The buzz fuel air ratios of the mix/burn system are well in excess of the maximum levels required for steady operation of the afterburner and allow considerable excursions above these levels during the fast accelerations demanded of the system.

FUTURE REQUIREMENTS

The current trend in military engine cycles is towards high and even stoichiometric turbine entry

However, none of the alternative materials match the comparative ease of manufacture and flexibility of application of the high duty metal alloys they are intended to replace and most have serious incidental defects for instance in their oxidation resistance or high temperature strengths. As a result both the type and form of the material employed must be selected and developed to suit its precise application whilst the manner in which the item achieves its aerodynamic or thermodynamic function must usually be adjusted either to protect the material or to secure maximum advantage from its improved properties.

REFERENCES

1. Sotheran, A
'Some Aspects of Plenum Chamber Burning'
Combustion and Heat Transfer in Gas Turbine Systems, Pergamon Press, Oxford, 1971, Norster, ER ed.

2. Sotheran, A
'The Rolls-Royce Annular Vaporiser Combustor'
Trans ASME, J Eng Gas Turbines and Power, Vol 106, No.1, pp 88 – 95, January 1984.

3. Rowe, R A
'Preliminary Development of a Longitudinal Vortex Combustor', Internal Rolls-Royce Report (unpublished).

4. Lewis, J S
'The Effect of Local Fuel Concentrations on Reheat Jet Pipe Vibrations'
Combustion in Advanced Gas Turbine Systems, Pergamon Press, Oxford, 1968, Smith I E ed.

Comparison of the Performance of a Reverse Flow Annular Combustion Chamber under Low and High Pressure Conditions

F. Joos, B. Simon
MTU Motoren- und Turbinen-Union München GmbH
Postfach 50 06 40
Dachauer Str. 665
8000 Munich 50
Federal Republic of Germany

Abstract

Combustor development testing is usually carried out under different pressure conditions; low-pressure burning tests for the optimization of the fuel distribution inside the combustor and high-pressure tests for demonstrating the desired performance.

Comparison of the results under these two test conditions often reveals discrepancies, especially in wall temperatures and exit temperature patterns, which cannot be attributed simply to the greater flame radiation and heat-release rate associated with the tests at high pressure. Another cause, in particular, lies in differences in the fuel distribution in the primary zone as a function of pressure conditions. This phenomenon will be demonstrated by measurements and 3D 2-phase flow-field calculations.

Nomenclature

FAR	-	Fuel-air ratio
p	bar	Pressure
SMD	µm	Sauter mean diameter
T_3	K	Combustor inlet temperature
T_m	K	Average temperature
X	mm	Axial distance between nozzle outlet and calculation plane

Introduction

Reverse-flow combustion chambers contribute to the compactness of a gas-turbine engine because they can be installed outside of the turbine. However, this advantage is offset by a number of disadvantages.

The large diameter of the combustion chamber results in a large flame-tube surface area to be cooled. Furthermore, relatively large spacing between the fuel nozzles is required, because the number of nozzles cannot be increased at will. Consequently, a fuel injection system for uniform distribution of the fuel between the nozzles is required.

For developing such a system, it is usual to conduct tests at atmospheric pressure, followed by testing of the chosen design at pressures encountered in service.

Experience shows that the knowledge gained from testing at atmospheric pressure can be applied only conditionally as far as the operating condition is concerned. For instance, the atomization properties of the nozzles vary in relation to the air pressure, regarding both the atomization of the fuel /1, 2, 3/ and the distribution by each nozzle /4/. Marked increases in the wall temperatures of the flame-tube have also been observed /3, 5/. In addition, the exit gas temperature patterns are different at the higher service pressure /6/.

Some of the effects of an increase in the operating pressure are explained below with the aid of tests and flow-field calculations. Because the possibilities for conducting tests at elevated pressure are limited, in each case, the measurements at atmospheric pressure are compared with calculations at a pressure of 1 bar, allowing the results to be checked qualitatively. The influence of pressure is then extrapolated analytically.

Testing

The experimental reverse-flow combustor is illustrated in figure 1. It is provided with 13 air-blast atomizer nozzles, where each nozzle consists of two contrarotating swirlers. The task of the swirlers is to create a stabilizing recirculation flow and

high turbulence, as well as to atomize the fuel. The inner and outer walls of the flame-tube are each provided with two rows of 78 holes. In both cases, cooling is effected via 3 cooling films. Connected to the flame-tube is a similarly-cooled exhaust bench.

The combustor was tested under various conditions up to the design values (p = 13 bar, T_3 = 670 K, FAR = .026). To allow comparison with the 3D flow-field calculations, measurements had also to be made in the middle of the flame-tube. In this case, to be able to accomodate all probes, testing had to be carried out without the exhaust bench and only at atmospheric pressure.

The set-up for this test is illustrated in figure 2. Gas measurements to determine the local FAR were possible in any plane with a single probe. It was also possible to scan the temperature distribution at the end of the flame-tube by means of a thermo-couple probe.

The flow-field within the flame-tube was assessed by water-simulation tests, in which the flame-tube was represented as a 90° sector to the scale of 2:1 in plexiglass. The flow pattern was recorded at various meridional light-section planes with a video camera.

Aerothermal model

The code used to calculate the flow-field and the temperature-field of the combustor is the NREC adaptation /7/ of an AiResearch code.

INTERN is a three-dimensional finite-difference code capable of solving the elliptic partial differential equations for the conservation of mass, momentum, energy and chemical species. It applies to both laminar and turbulent, two-phase or single-phase, steady reacting flows. It employs a k-ε two equation model for turbulence, a two-step chemical kinetic model for heat release, an option of a Lagrangian or an Eulerian model for fuel droplet transport, and an eddy break-up model for the effects turbulence has on reaction rates. Its numerical approach uses an implicit, upwind differencing scheme. The rate of convergence of the iterative solution procedure has been enhanced by the incorporation of a cyclic tridiagonal matrix algorithm into the code.

The calculation grid consists of 41 x 33 x 27 lines in a cylindrical coordinate system with 24,138 grid-points in the calculation field (figure 3). The flame-tube walls are approximated in stair-step boundaries. The calculation time was approximately 1 - 5 hours CPU time using an IBM computer. The calculations were made in different blocks, verifying the convergence and varying the relaxation factors and/or adapting the solution strategy to the given requirements in each case.

The boundary condition at the nozzle outlet is represented in figure 4. The circumferential component of the velocity is established with the aid of the nozzle swirl parameter under the assumption of a forced vortex, whilst the radial component is determined in accordance with the nozzle discharge-opening contour. The axial component is calculated from the mass flow as a plug-flow profile.

To introduce the liquid fuel, the fuel film at the atomization edge is split into 10 spray-cone rays with each ray consisting of 5 different droplet size ranges. The droplet distributions were taken from /1/. The individual fuel-cone rays are added to the airflow-field at a spray angle of 90° at low initial velocity.

The dilution air flows in perpendicular to the wall.

Results and discussion

Flow-field in the combustor

For the qualitative assessment of the calculated flow-field in the combustor, ample results from water-simulation tests are available. The main flow pattern is represented in figures 5 and 6. In contrast to the calculated flow-field, the arrows serve simply to show the direction of flow and are not an indication of the flow-velocity level.

Figure 5 shows the calculated and the measured flow-field in meridional section through the swirler. Qualitatively, the measured flow-field corresponds with the calculated field. In both cases the swirling air leaves the nozzle radially without separation. The strong swirl generates a typical recirculation vortex, which is limited by the dilution air streaming through the first row of holes. In the measurement, smallish unsteady vortex areas were observed in the recirculation zone, which are represented in the calculation by a single large vortex, because the calculation procedure is not capable of recording transitory effects.

The measured meridional section between the nozzles is compared with the calculation in figure 6. In this area the recirculation vortices of two adjacent nozzles meet, creating an axial flow over the whole cross-section. At this level the measured flow pattern likewise shows good correspondence with the calculation. Areas of separation form downstream of the jets of dilution air, can be required both in the measurement and the calculation.

Fuel distribution

The course of the fuel droplets from the spray-point to complete evaporation can be seen in figure 7, in which all trajectories are shown in projection at the plane of the nozzle. At a pressure of 1 bar the calculated spray-cone trajectory remains more-or-less within the set angle of 90° for a distance of approximately 10 mm in the axial direction, whereas at 13 bar pressure a marked radial deviation occurs (figure 7). Despite the length of the trajectories, it should be understood that the major part of the fuel is already evaporated a long way from the end of the trajectory.

The greater expansion of the spray-cone at elevated pressure was also observed in measurements made in the atomization experiments /4/. In the present model tests as well as the tests acc. to ref. /4/, this expansion may be attributable to the greater aerodynamic forces and the smaller fuel droplets.

The influence of pressure on the amount of fuel evaporated at one axial position downstream of the nozzle is shown in figure 8. The calculation at atmospheric pressure (figure 8a) reveals a fuel-rich area at the nozzle and at the sector edges. In contrast, at 13 bar the distribution of the evaporated fuel is much more homogeneous at the same axial position at a level generally more rich in fuel (figure 8b). This fuel-rich homogeneous mixture results from the more rapid evaporation that occurs at 13 bar because of the smaller droplets. In addition, even if only to a slight extent, the wider spray angle also contributes to the homogeneity of the primary zone.

The measured FAR distribution at the end of the primary zone at atmospheric condition is compared with the corresponding calculation in figure 9. Qualitatively, the measured FAR distribution (figure 9a) shows good agreement with the calculated values (figure 9b). Both the relatively weak region in the right-hand half of the sector and the area more rich in fuel in the left-hand half are represented. Admittedly, the absolute values differ markedly from one another. This is attributable essentially to the very simplified reaction model, which does not simulate the many intermediate products still present in the primary zone. Nevertheless, the qualitatively satisfactory correspondence indicates that the flow-field in the primary zone has been calculated realistically.

Apart from the spray-angle, one of the main influences on the homegeneity of the primary zone is the droplet-size distribution in connection with a favourable air-flow-field.

Gas temperature

In figure 10 the isotherms measured at the flame-tube outlet under atmospheric conditions are compared with the calculated values.

The measured isotherm-fieled has hot spots at the sector edges and a relatively cool area in the centre. These hot sector edges are caused by the fuel-enriched swirler air, which flows radially outward from the swirler and is then deflected rearward in the axial direction by the impingement of the flows from the two neighbouring swirlers. The fuel reacts during this axial movement, whilst cooler, leaner flows predominate in the sector centre. Qualitatively, there is good correspondence between the measurement and the calculation.

If one looks at figure 10 closely it becomes apparent that the left-hand hot region is considerably more extensive than the right-hand one. The cooler sector centre appears to be slightly twisted, and this twist, where a symmetrical isothermal-field was expected, also shows in the calculation. It is caused by a slight swirl about the combustor axis in the primary zone as a result of the bend in the duct. The occurrence of this secondary swirl is clearly recognizable in the flow-field of the axial plane directly at the nozzle outlet (figure 11). The flow from the nozzle-swirl area is favoured by the annulus wall, curved in the direction of swirl. On the other side of the swirler this bend acts against the swirl flow. Consequently, the swirl, which is eccentric in relation to the flame-tube axis, has a swirl superimposed upon it that is slightly centric to the axis.

This twist also causes the shift in the lean region of the FAR distribution at the end of the primary zone.

Qualitatively, the differences between the 1 bar and 13 bar isotherm-fields are only insignificant.

The radial temperature distribution at the end of the flame-tube is plotted in figure 12. The measured temperature distribution under atmospheric conditions (figure 13) corresponds satisfactorily with the calculation with the exception of a maximum near the duct wall. This temperature maximum is attributable partly to the fuel distribution in the primary zone, but above all to the addition of the air from the 2nd row of holes, not fully compensated for in the calculation.

Although the fuel distribution in the primary zone changes markedly with increase in pressure, the effect on the temperature distribution at the end of the flame-tube is insignificant.

Influence of pressure on the wall temperature

A known cause of the temperature increase at the flame-tube wall in relation to pressure is certainly the increased gas radiation. Another cause is to be found in the effect of fuel treatment.

In figure 13, the calculated gas temperatures at a pressure of 1 bar are compared with the measured wall temperatures in the atmospheric tests. The wall temperatures provide only qualitative conclusions about the temperature of the gas close to the wall, because they are affected by both the two sided thermal transfer and the gas radiation.

Nevertheless, in figure 13, both the calculation and measurement exhibit a constant increase in the temperature as far as the sector edge. Around the nozzle, the temperatures are relatively low.

As shown in figure 14, a pressure of 13 bar results in a totally different behaviour. The calculated isotherm-field in figure 14 b exhibits relatively high gas temperatures already close to the swirler outlet. The isotherms are concentric to the swirler. The temperatures increase again toward the sector edge. The measurement also indicates very high wall temperatures at the swirler outlet. The temperature decrease toward the sector edge is attributable to the stronger cooling of the flame-tube between the swirlers.

The comparison shows that, qualitatively, the wall-temperature behaviour is as would be expected with the given gas-temperature distribution.

These calculations show that, in addition to the gas radiation, the better atomization of the fuel under elevated pressure has an essential effect on the wall temperature in the primary zone. Furthermore, the larger spray-angle makes for a more homogeneous mixture distribution. Associated with the higher reaction rates, markedly higher gas temperatures occur in the vicinity of the swirler outlet.

Conclusion

The influence of the air pressure on the flow- and temperature-field as well as on the wall temperature of a reverse-flow combustion chamber is investigated with the aid of both experiments and a 3D flow-field program.

Qualitatively, the calculated flow-field corresponds well with the field known from water-simulation tests. The measured outlet temperature profile was calculated satisfactorily. The FAR distribution at the end of the primary zone corresponds qualitatively with the measurements. This correspondence is almost certainly attributable to the realistic calculation of the flow-field. It is qualitatively shown that the marked increase in wall temperature under elevated pressure, observed in the experiments, is attributable to the better fuel treatment under these conditions and to the larger spray-angle. Because of the quicker evaporation, the smaller fuel droplets result in more rapid combustion immediately at the swirler outlet. In association with better thermal transfer under pressure because of radiation, this may well be the cause of the higher wall temperatures observed.

Despite the relatively wide grid mesh in the calculation of the flow-field and the simplified model of the nozzle air and dilution air flow, it was possible to explain the phenomena observed in the experiments with the aid of the calculations.

However, further development of both the physical model and of the numerical solution is required to permit more reliable determination of the temperature patterns and the gas values.

Acknowledgement:

The work was supported by the Federal German Ministry of Research and Development. This support is gratefully acknowledged.

References

/1/ A. Rizkalla, A.H. Lefebvre

The Influence of Air and Liquid Properties on Air Blast Atomization
J. Fluids Eng. Vol. 97 No. 3 pp 316 - 320, 1975

/2/ T. Sattelmayer, S. Wittig

Internal Flow Effects in Prefilming Air Blast Atomizers: Mechanisms of Atomization and Droplet Spectra, ASME 86-GT-150

/3/ A.H. Lefebvre, Gas Turbine Combustion
McGraw-Hill 1983

/4/ H. Eickhoff, M. Cao, F. Joos, B. Simon

Influence of Operating Conditions on the Atomization and Distribution of Fuel by Air Blast Atomizers

70th Symp. of the Propulsion and Energetics Panel, AGARD; 1987

/5/ A.H. Lefebvre, M. V. Herbert

Heat Transfer Processes in Gas-Turbine Combustion Chambers

Proc. Inst. Mech. Eng. Vol. 174 No. 12
pp 463 - 473, 1960

/6/ The Design and Development of Gas Turbine Combustors
Report No. 1344, 1980, NREC, Woburn, MA

/7/ The Design and Development of Gas Turbine Combustors; Computing System Report No. 1420, 1986, NREC, Woburn, MA

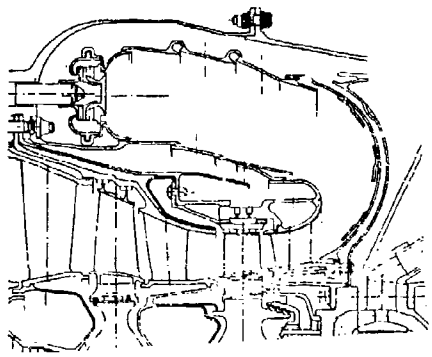

Fig. 1: Reverse-flow combustor

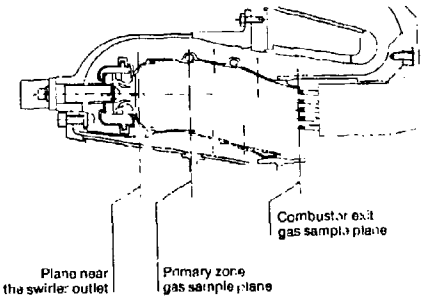

Fig. 2: Combustor used for testing under atmospheric conditions

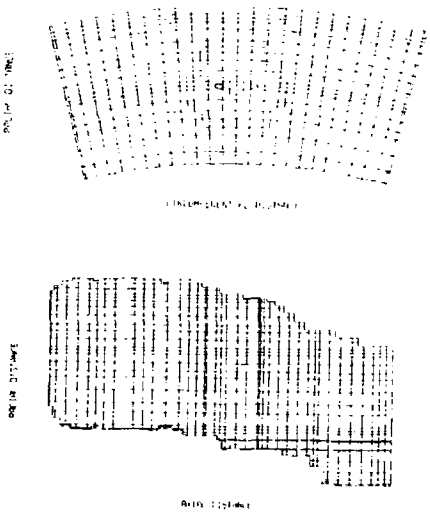

Fig. 3: Grid used in the calculations

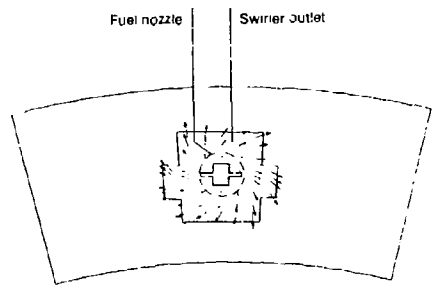

Fig. 4: Boundary condition of the velocity field at the nozzle exit

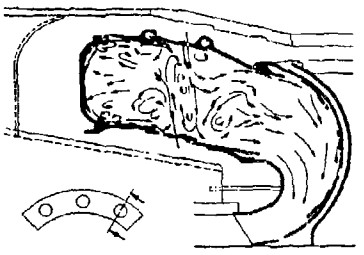

a) Flow pattern in the water flow rig test

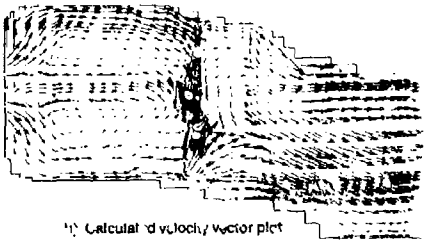

b) Calculated velocity vector plot

Fig. 5: Flow-field in the axial section through the nozzle in the water-simulation tests and the calculations with chemical reaction

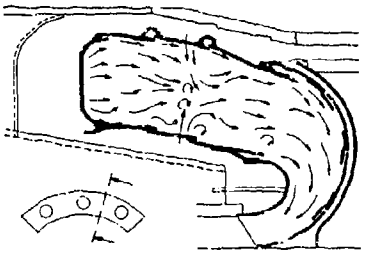

a) Flow pattern in the water flow rig test

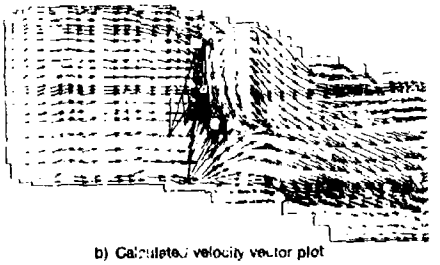

b) Calculated velocity vector plot

Fig. 6: Flow-field in the axial section between the nozzles in the water-simulation tests and the calculations with chemical reaction

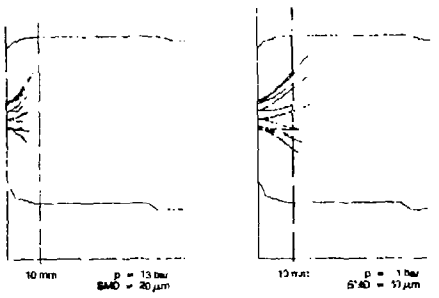

Fig. 7: Trajectories of the liquid fuel up to complete evaporation at 1 and 13 bar air pressure

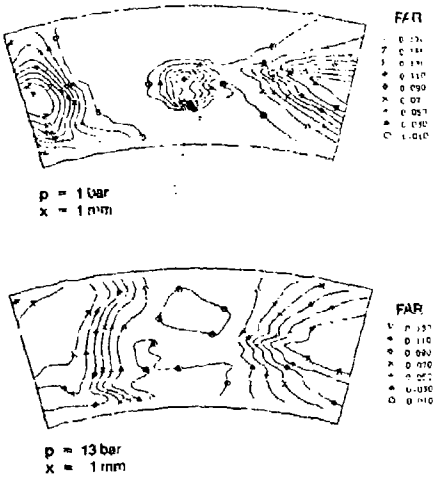

Fig. 8: FAR distribution of the evaporated fuel in the immediate vicinity of the nozzle exit

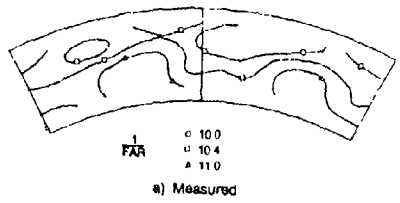

a) Measured

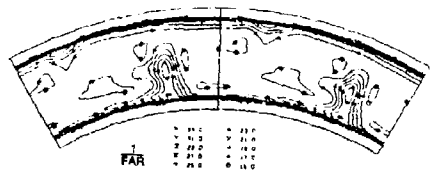

b) Calculated

Fig. 9: FAR distribution at the end of the primary zone; comparison between measurement and calculation

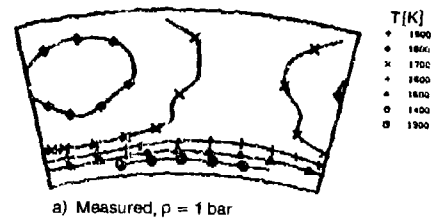

a) Measured, p = 1 bar

b) Calculated, p = 1 bar

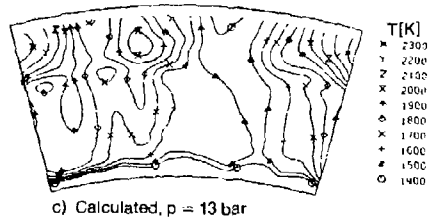

c) Calculated, p = 13 bar

Fig. 10: Isotherm-field at flame-tube exit at 1 bar air pressure; comparison between measurement and calculation

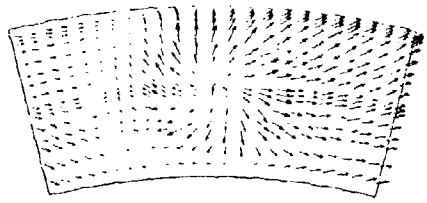

Fig. 11: Flow-field in radial section in the immediate vicinity of the nozzle exit in the calculation with chemical reaction

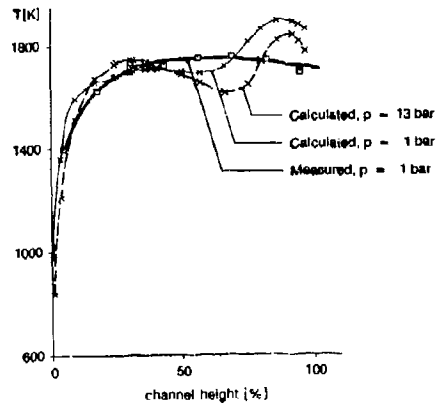

Fig. 12: Averaged temperature profile at the flame-tube exit; comparison between measurement and calculation

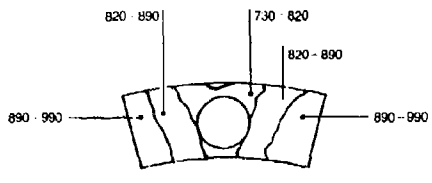

a) Measured wall temperature [K], p = 1 bar

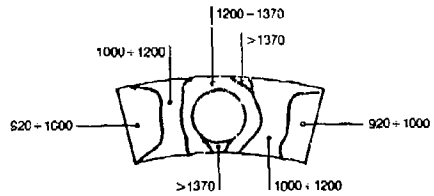

a) Measured wall temperature [K], p = 13 bar

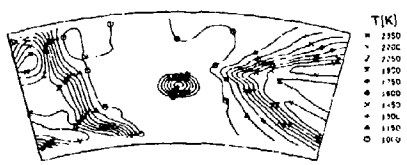

b) Calculated gas temperature field near the wall, p = 1 bar, x = 1 mm

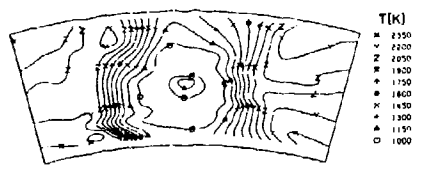

b) Calculated gas temperature field near the wall, p = 13 bar, x = 1 mm

Fig. 13: Comparison of the isotherm-field of the calculated gas-flow with the measured wall-temperature distributions at 1 bar air pressure

Fig. 14: Comparison of the isotherm-field of the calculated gas-flow with the measured wall-temperature distributions at 13 bar air pressure

DISCUSSION

G.Grienche, FR

You have presented a good prediction of the radial temperature profiles at the flame tube exit. Have you calculated with your aerothermal model the evolution of this profile in the bend from the flame tube exit to the turbine nozzle?

Author's Reply

The calculation of the velocity – and temperature field in the bend is just going on with a two-dimensional axis symmetric model with body fitted coordinates. First comparison shows a good agreement between the calculated and the measured radial temperature.

The measured pattern factor of these test combustors was approximately 0.33 at the exit of the flame tube and 0.29 at the exit of the bend.

L.Galfetti, IT

With reference to the chemical submodel implemented in the numerical code, you mentioned a two step overall scheme. What are the chemical species and the kinetic parameters considered?

Author's Reply

The chemical reaction scheme of the evaporated fuel implemented in the code is:

$$C_8H_{16} + 8O_2 \rightarrow 8CO + 8H_2O$$

$$2CO + O_2 \rightarrow 2CO_2$$

This reaction is often used by other codes too, and is well documented in Ref.7.

FLOW CHARACTERISTICS OF A MODEL ANNULAR COMBUSTOR

by

A F BICEN, D TSE AND J H WHITELAW

Imperial College of Science and Technology
Fluids Section
Department of Mechanical Engineering
London SW7 2BX United Kingdom

ABSTRACT

Measurements are reported of the velocity and passive scalar characteristics of the isothermal flow in a model combustor which comprises a T-vaporiser and two rectangular sectors of an annular combustor similar to one used in small gas-turbine engines. Mean temperatures have also been obtained in a reacting flow with an overall equivalence ratio similar to that of take-off conditions. The results were obtained with a combination of laser velocimetry, thermocouples and probe techniques and quantify the effects of flow asymmetries in the vaporiser fuel arrangement and of different alignments of the primary holes with respect to the vaporiser position. Flow visualisation results are also included to indicate the general features of the combustor flow.

The isothermal results show that the primary zone is characterised by a vortex driven by the film-cooling flows and limited in its downstream extent by the primary jets. The vortex has forward streamwise velocity peaks in the lower part of the combustor which are in line with the primary jets and backward velocity peaks in the upper part corresponding to the gaps between the primary holes. The T-vaporiser distributes the fuel into the shear layers of the velocity profiles and a small asymmetry in the vaporiser flow can still be detected up to ten diameters downstream of the plane of the vaporiser exits. Temperature results indicate two hot regions in the primary zone which are in line with vaporiser exits and positioned close to the upper wall. Changes in the position of the primary holes in a range from 0 to 1/2 pitch are shown to result in poorer mixing. The hot regions at the combustor exit move from the centre plane as the primary holes are moved and the hot region on one side bifurcates as a consequence of the lower dilution jet and results in exit temperature distributions which are asymmetric about the centre plane.

1. INTRODUCTION

This investigation was undertaken to establish the velocity and passive scalar characteristics in a flow configuration of direct relevance to an annular combustor and, by so doing, to assist the development of calculation methods which involve numerical, turbulence and scalar transport assumptions. It is similar to that of reference 1 but involves a more practical annular arrangement which comprises a T-vaporiser (reference 2) and two rectangular sectors representing the primary and upstream dilution zones of a combustor used in helicopter engines. The investigation emphasises isothermal flow and makes use of probes and laser velocimetry to determine the velocity and passive scalar characteristics. The effect of flow asymmetry in the fuelling device and its relative position with respect to the primary holes are determined to establish the importance of flow and geometric changes which can occur as a consequence of combustion and flight cycle and mean temperature measurements are presented to demonstrate how fuel is transported downstream and can be affected by the cross-stream alignment of the primary holes.

Related experiments with much simplified geometries have been reported previously in, for example, references 3 and 4. In reference 3, the effects of alignment of a row of holes in the cross-stream direction were investigated in a wind tunnel flow and, in reference 4, geometric and flow asymmetries were examined in an arrangement with a closed upstream end. The present measurements provide similar information in a combustor.

The following section describes the combustor and the instrumentation and experimental uncertainties. The third section presents the results and discusses them with the purposes of the above pragraph in mind. Summary conclusions are stated in a final section.

2. FLOW CONFIGURATION AND INSTRUMENTATION

The model combustor is shown in Figure 1 and corresponds to two rectangular sectors of the Gem-60 combustor used in helicopter engines. The usual reverse-nozzle has been removed and the reverse-flow casing replaced by plenum chambers which allow the same back pressure on the outer surfaces of the combustor. The model includes three film-cooling slots near the head, from which 33.5% of the total mass flow enters and drives a vortex in the primary zone. This vortex is limited in its downstream extent by a row of primary jets issuing from the lower wall, which constitutes 15% of the total mass flow. Further downstream, two additional film-cooling slots and opposed dilution jets, representing 14.5 and 33% of the total flow respectively, maintain a cool downstream wall and the required pattern factor in the exit plane. The combustor makes use of a T-vaporiser mounted on the head with its exits in line with two of the five primary holes as shown in Figure 1. With the isothermal flow experiments, the

vaporiser transported air at a rate of 4.5% of the total mass flow and corresponded to a momentum similar to that of fuel at the take-off condition. In the combustion experiments, natural gas (94% CH_4) was delivered at a rate which led to an air-fuel ratio of 17. The combustor was arranged in the flow rig of Figure 2 which permitted separate control and measurement of the bulk flow to the two sides of the combustor and to the vaporiser at near atmospheric conditions. The mass flow rates and velocities associated with the primary and dilution holes are given in Table 1 and Table 2 records the dimensions of the holes and film-cooling slots which also comprised rows of holes.

The concentration of a passive scalar was measured in isothermal flow by adding a trace of helium with a volumetric concentration of around 5% to the air flowing to the T-vaporiser. Samples of gas were drawn through a total head probe of 1mm outside diameter and passed to a katharometer which was able to determine the helium concentration with a precision of 2% of the full-scale reading. Tests to establish the influence of sampling rate suggested that the overall measurement accuracy was of this order of magnitude except inside the recirculating flow region where probe interference could cause larger errors.

Velocity information was obtained by a laser-Doppler velocimeter similar to that described in reference 5. It made use of diffraction grating optics together with a 5mW helium-neon laser and forward-scattered light. The geometrical features of the optical system are given in Table 3. The flow was seeded with atomised silicone oil and the signals from a photomultiplier were processed with a frequency counter interfaced to a microcomputer which calculated mean and rms values of the local velocity with an overall precision better than 2 and 5%, respectively.

Temperature measurements were obtained with thermocouples made from 80μm platinum/13%-rhodium and platinum wires butt welded to minimise conduction effects. The signal was digitised and the mean temperature was evaluated by a microcomputer which, according to reference 6, is closely related to the unweighted average. The probable uncertainty in the mean value was of the order of 5% and arose mainly from radiation losses, reference 5. Flow visualisation, similar to that of reference 4, was also used to obtain a rapid overview of the flow and to guide the choice of the location of measurement with the above instrumentation.

More detailed consideration of measurement uncertainties can be found in references 4-7. They are insufficient to affect the conclusions drawn on the basis of results presented and discussed in the following section.

3. RESULTS AND DISCUSSION

This section is divided into two parts. The first is concerned with the velocity and passive scalar measurements obtained in the isothermal flow and the second presents the temperature measurements with the discussion emphasising the influence of different alignments in the cross-stream direction of the primary holes within the combustor and at its exit plane.

3.1 Isothermal Flow

The general nature of the flow can be deduced from Figure 3 which presents flow visualisation results in five vertical planes. On the centre plane and at $z = \pm$ 28mm, the primary jets impinge on the upper wall with a near vertical trajectory and a recirculation pattern, driven mainly by the film-cooling jets, is contained between the primary jets and head of the combustor. At z = 14mm, the impingement of the opposed dilution jets divides the larger-diameter upper jet and causes the flow on the upstream side of the jet axis to be directed downwards as a consequence of the greater upper jet momentum. The part of the jet directed towards the exit is nearly horizontal. The result at z = -14mm corresponds to a plane where only the upper dilution jet is present and it impinges on the lower wall. Cross-stream flows can also be deduced from the apparent stagnation regions, for example at z = 28mm and between the dilution holes and so can small regions of recirculation, for example near the bottom dilution jet at z = 14mm.

Figures 4-8 present velocity measurements at various stations chosen to quantify the features of the flow associated with the vaporiser, the primary zone, the primary jets, the dilution jets and the convergence of the exit region. Figures 4-6 characterise the primary zone and quantify the primary recirculation with forward streamwise velocity peaks in the lower part of the combustor corresponding to the primary holes and in the upper part corresponding to the gaps between the primary jets. This difference occurs because the film-cooling slot on the upper wall and immediately downstream of the primary jets provide sufficient mass flow to fill the gaps between the jets. The perturbations in the flow and velocity distributions at x = 11mm of Figure 4 in the lower half are due to the flow from the vaporiser which distributes the fuel into the shear layers of the velocity profiles. Figure 6 shows that the normal component of velocity is upwards and in line with the primary jets issuing from the lower wall. The forward flow into the lower half of the combustor is comparatively uniform with a maximum velocity of around 30% of the maximum jet velocity. The streamwise normal stresses are generally lower and more uniform than those in the normal direction and indicate that the primary jets are responsible for large production of turbulence at this station. The streamwise turbulence intensity is around 10% in the regions of maximum forward velocity.

Downstream of the dilution holes, Figure 7, the flow is in the downstream direction with streamwise velocity maxima corresponding to planes of opposed dilution jets. The planes of the single dilution holes correspond to minima in the streamwise component of velocity and to maxima in the downward normal velocity. These characteristics remain downstream of the exit plane, Figure 8, but are considerably dampened. The contraction towards the exit has not accelerated the flow in the upper region of the combustor to the maximum value below the midplane. The rms profiles at the exit are comparatively uniform and of lower magnitude than those of Figure 7. It is evident that most of the turbulence energy has been produced upstream of the exit plane by the various jet flows and their interaction.

Distributions of the non-dimensional passive scalar, based on concentrations of the helium tracer, are shown in Figure 9 for three vertical planes. The emphasis is on the region upstream of the dilution jets where the higher values allowed accurate measurements and, as would be expected, the flow is symmetric about the centre plane. This implies that, in the primary zone of a combusting flow, high temperatures will coincide with the plane of the vaporiser exits and cool regions will occur near the centre plane, as verified in the following subsection. Figures 3 and 4 provide partial support for this result in that the former shows little evidence of cross-stream flow in the primary zone and the latter suggests that the fuel jets are absorbed by the primary jets in the same planes.

The effects of flow asymmetry in the vaporiser-fuel arrangement on the velocity and scalar characteristics are quantified in Figures 10 and 11. The symmetric and asymmetric streamwise velocity profiles at the vaporiser exits are also shown in Figure 10 where it can be seen that the former are skewed outwards. The asymmetric exit profiles were caused by a small blockage in the T-junction of about 10% of the exit diameter and result in asymmetries of about 15% in the velocity distributions in the lower part of the combustor as shown in Figure 10. The asymmetry in velocity profiles is important only in the region near the lower wall but the passive scalar profiles are more affected, Figure 11, with the asymmetry extending beyond the primary holes.

3.2 Temperature Field

The cross-plane distributions of mean temperature obtained with the symmetric fuelling arrangement in the primary zone and exit plane are shown in Figure 12. They are reproduced in Figures 13 and 14 to facilitate comparison with those obtained with different arrangements of the primary holes in the cross-stream direction with respect to the vaporiser position. As expected from the isothermal flow results with the in-line arrangement of the primary holes and vaporiser exit, the maximum temperatures, which exceed 1950K, occur in the upper part of the primary zone and are in line with the vaporiser exits, Figure 12. This general pattern is maintained at the exit plane with a slight shift of the high temperature regions towards positive z values caused by the two lower dilution jets.

The effect of moving the primary holes by lateral distances up to 1/2 pitch is noticeable in the primary zone and at the exit of the combustor as shown in Figures 13 and 14, respectively. A small change (by 1/8 pitch) in the primary hole position causes a significant reduction in the size of the hot regions in the primary zone with comparatively low temperatures particularly near the centre plane, indicating poor mixing of fuel with air. Although the horizontal positions of the hot regions are not affected, they have moved downwards by about 20% of the combustor height in all misaligned cases and, at the exit, the hot regions have shifted from the centre plane and become out of line with the vaporiser exits. As a result, the hot region on the negative z half has been bifurcated by the lower dilution jet.

4. CONCLUSIONS

The main findings of the investigation may be summarised as follows:

1. With isothermal flow, the primary zone of the combustor is characterised by a vortex driven by the film-cooling jets and limited in its downstream extent by the primary jets. The vortex has forward streamwise velocity peaks in the lower part of the combustor which are in line with the primary jets and backward velocity peaks in the upper part corresponding to the gaps between the primary holes. The T-vaporiser distributes fuel into the shear layers of the velocity profiles.

2. In the dilution zone, the streamwise velocity profiles exhibit peaks in the planes of impinging jets. The cross-stream gradients of the profiles induce rapid mixing and at 0.1 combustor length downstream of the exit both mean and rms velocity profiles have become much more uniform.

3. A small blockage in the T-junction of the vaporiser, of about 10% of its diameter causes a 15% asymmetry in velocity profiles in the lower part of the primary zone. The effect on passive scalar distributions is greater and is detectable beyond the primary holes.

4. Temperature measurements in combusting flow indicate two regions with values in excess of 1950K, close to the upper wall and in line with the vaporiser exits in the primary zone; this pattern is maintained at the combustor exit.

5. The lateral position of the primary holes influences primary and exit temperature

distributions. As they are moved, by up to 1/2 pitch, the hot regions in the primary zone decrease and move downward by about 20% of the combustor height and exit temperature distributions become more asymmetric about the centre plane.

ACKNOWLEDGEMENT

The authors are glad to acknowledge financial support from Rolls Royce PLC and from the Procurement Executive of the Ministry of Defence. Discussions with Mr J Gardiner of Rolls Royce were of particular benefit to the work.

REFERENCES

1. Toral H and Whitelaw J H "Velocity and Scalar Characteristics of the Isothermal and Combusting Flows in a Combustor Sector Rig", Combustion and Flame, V 45, p 251, 1982.

2. Sotheran A "The Rolls-Royce Annular Vaporiser Combustor", Journal of Engineering for Gas Turbines and Power, V 106, p 88, 1984.

3. Khan Z and Whitelaw J H "Vector and Scalar Characteristics of Opposing Jets Discharging Normally Into a Cross-Stream", Int Journal of Heat and Mass Transfer, V 23, p 1673, 1980.

4. Sivasegaram S and Whitelaw J H "Flow Characteristics of Opposing Rows of Jets in a Confined Space", Proc I Mech E, V 200, p 71, 1986.

5. Bicen A F, Heitor M V and Whitelaw J H "Velocity and Temperature Measurements in a Can-Type Gas-Turbine Combustor", AGARD-CP-399, Paper 14, 1986.

6. Heitor M V, Taylor A M K P and Whitelaw J H "Simultaneous Velocity and Temperature Measurements in a Premixed Flame", Experiments in Fluids, V 3, p 323, 1985.

7. Heitor M V and Whitelaw J H "Velocity, Temperature and Species Characteristics of the Flow in a Gas-Turbine Combustor", Combustion and Flame, V 64, p 1, 1986.

TABLE 1 Air Flow Split and Jet Velocities of Model and GEM-60 Combustor at Take-off Condition

Item	Model Combustor		GEM 60 Combustor	
	% ṁ	U/ms^{-1}	% ṁ	*U/ms^{-1}
Top Dilution Holes	25.4	66.2	25.9	67.8
Primary Holes	14.9	62.1	15.6	66.8
Bottom Dilution Holes	7.5	62.1	7.6	66.2

* Values are calculated assuming a discharge coefficient of unity and based on the mass flow rate scaled down using $\dot{m}\sqrt{T}/AP$ parameter with atmospheric conditions

TABLE 2 Geometric Details of Combustor

(Figure 1 identifies the flow entries by number)

Cooling Slots	Slot Height/ mm.	No of Holes	Dia./ mm.	Pitch/ mm.
2	1.65	21	2.25	5.91
3	1.38	24	2.00	5.20
4	1.38	24	1.65	5.20
5	1.60	18	2.40	6.84
7	1.10	18	1.65	6.84

Primary and Dilution Holes	Hole Dia./ mm.	No of Holes	Pitch/ mm.
1	6.2	4	28
6	4.6	5	28
8	4.6	2	56

Vaporiser	Exit Dia./ mm.
9	5
10	5

TABLE 3 Characteristics of Laser Velocimeter

Half angle of beam intersection	7.5°
Fringe spacing	4.75μm
Diameter of control volume at $1/e^2$ intensity level	152μm
Length of control volume at $1/e^2$ intensity level	2.3mm
Number of fringes	31

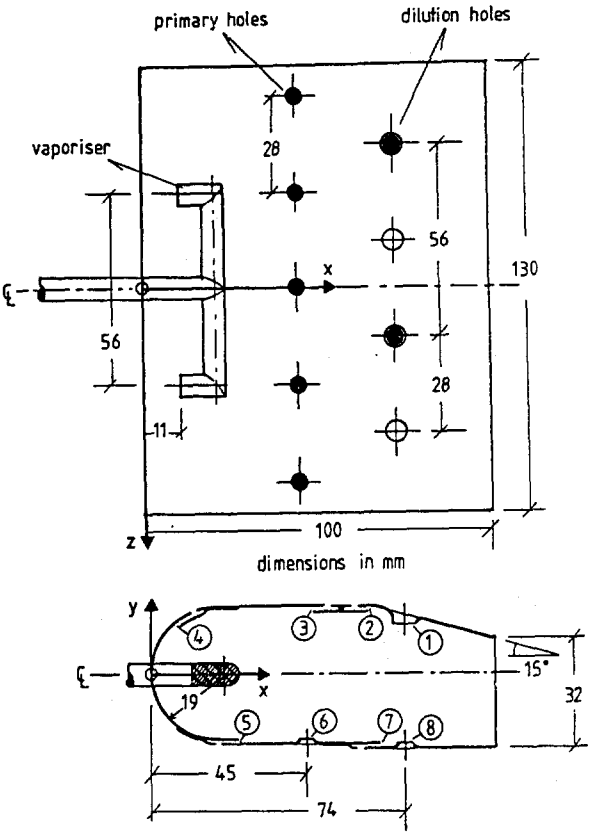

Figure 1 Combustor geometry.

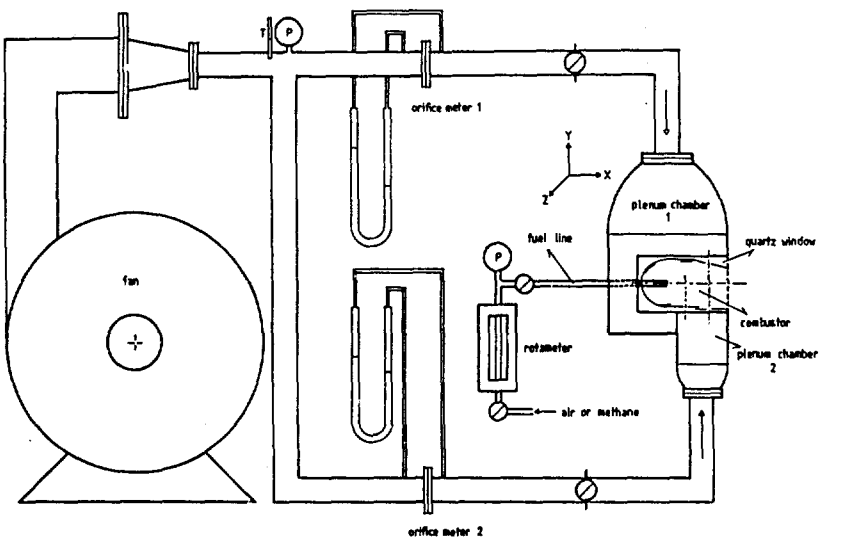

Figure 2 Diagram of flow rig.

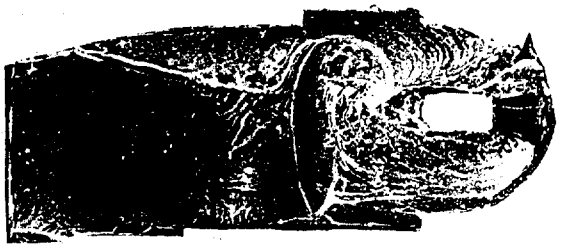

z = +28 mm

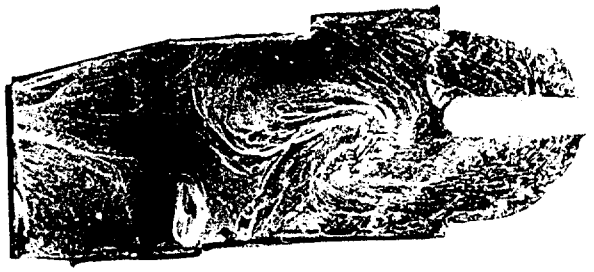

z = +14 mm

z = 0 mm

z = -14 mm

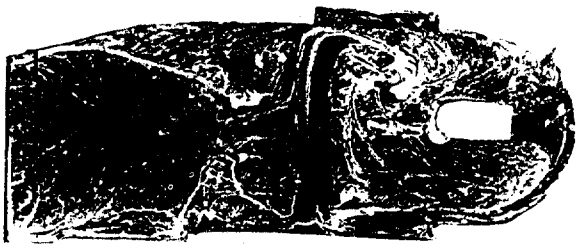

z = -28 mm

Figure 3 Flow visualisations

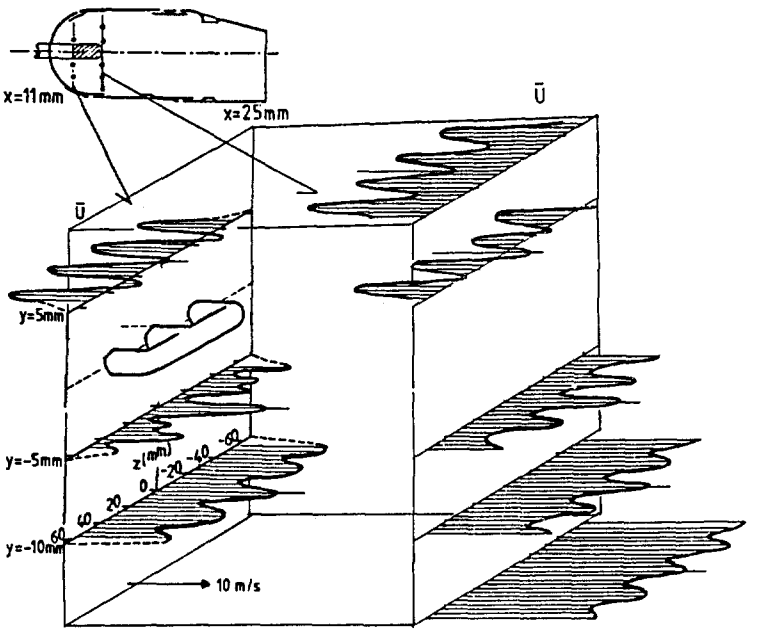

Figure 4 Mean profiles of streamwise velocity near combustor head.

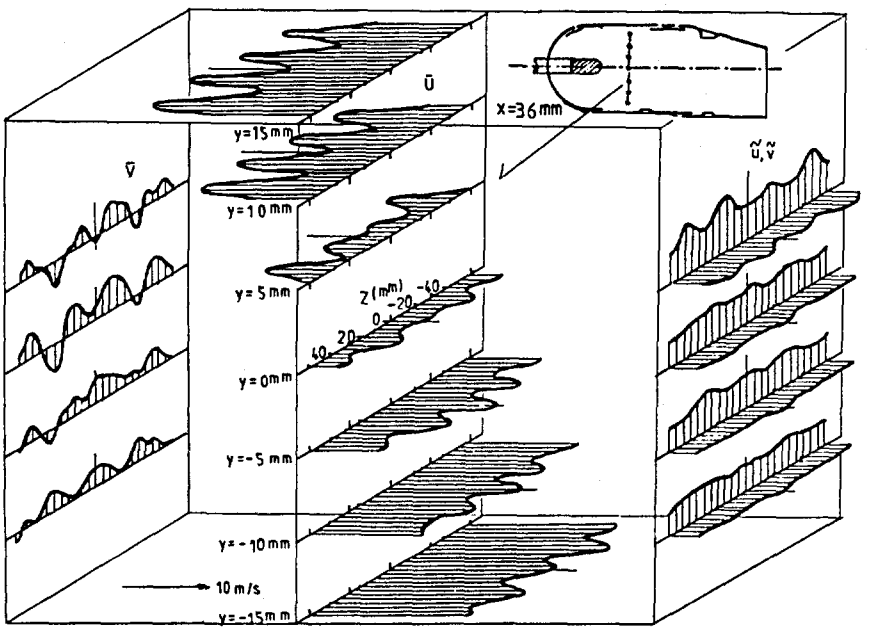

Figure 5 Mean and rms profiles of streamwise and normal velocity in primary zone.

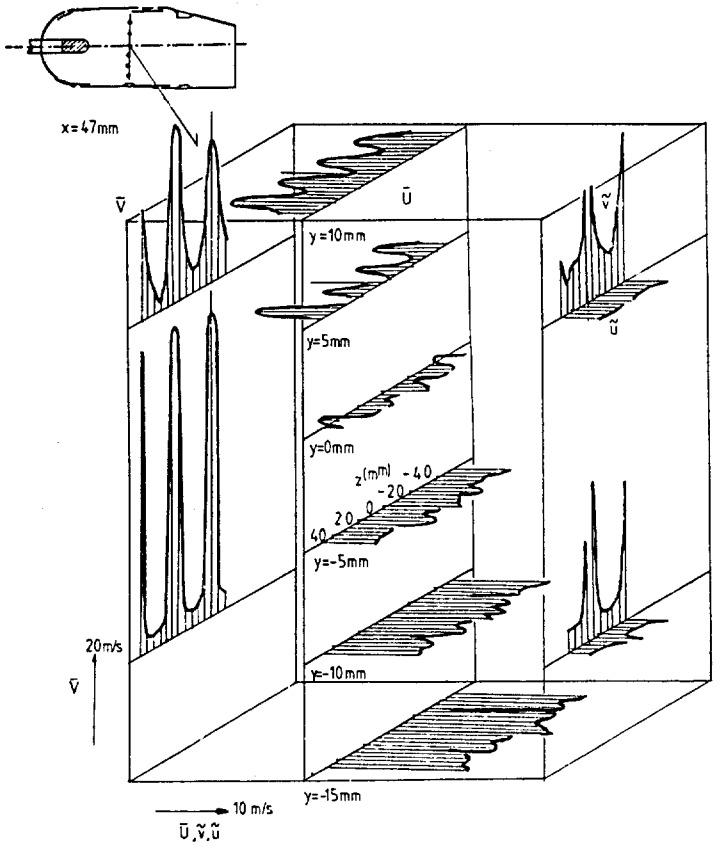

Figure 6 Mean and rms profiles of streamwise and normal velocity in plane of primary jets.

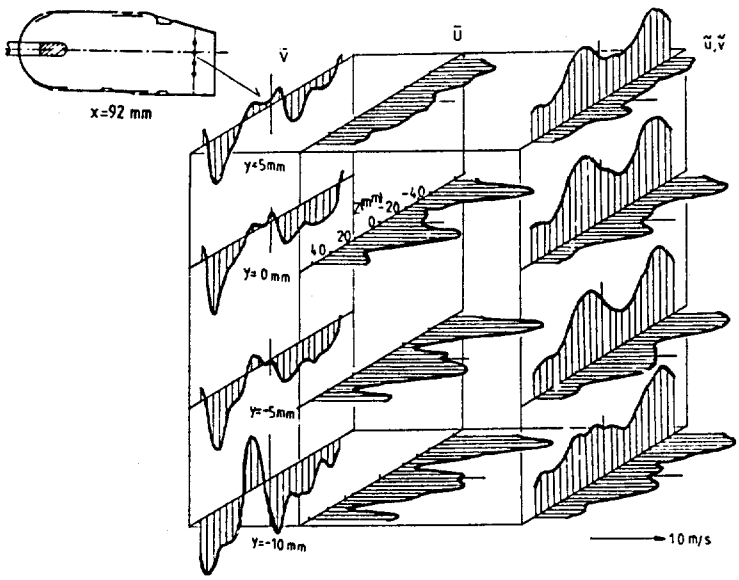

Figure 7 Mean and rms profiles of streamwise and normal velocity in dilution zone.

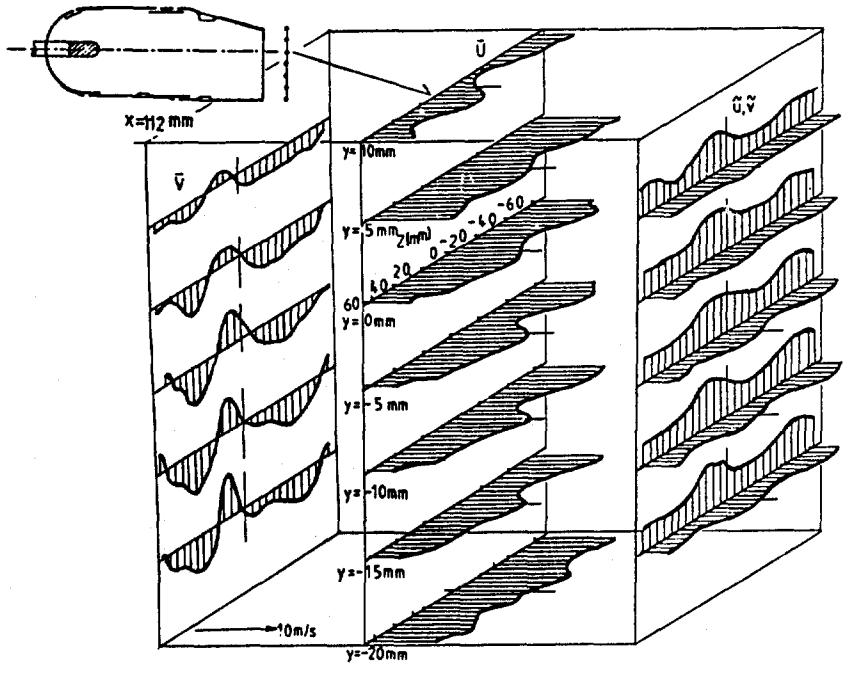

Figure 8 Mean and rms profiles of streamwise and normal velocity at combustor exit.

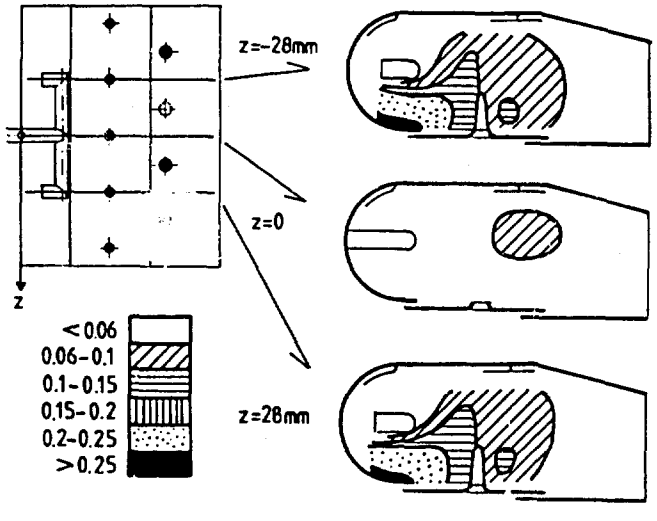

Figure 9 Normalised distributions of passive scalar.

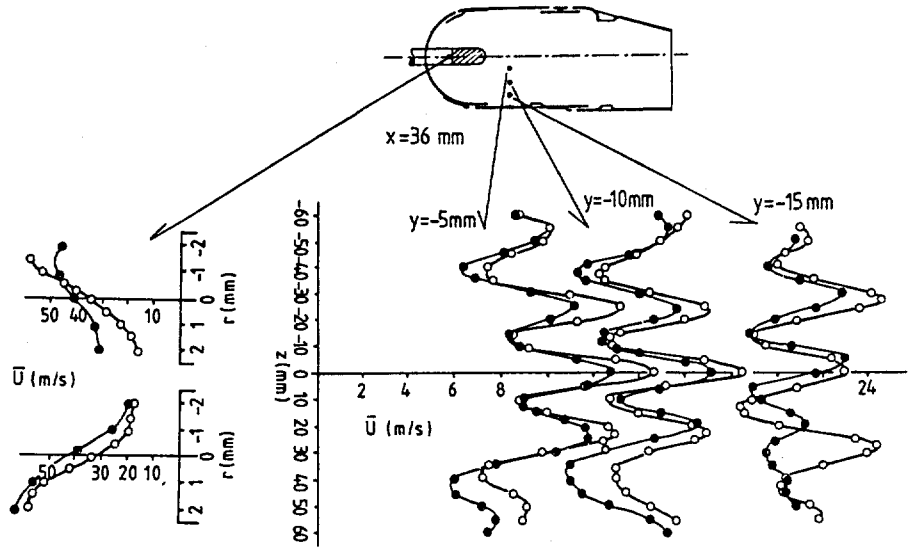

Figure 10 Effect of flow asymmetry in vaporiser fuel arrangment on combustor velocity characteristics.
(●) asymmetric vaporiser flow.
(o) symmetric vaporiser flow.

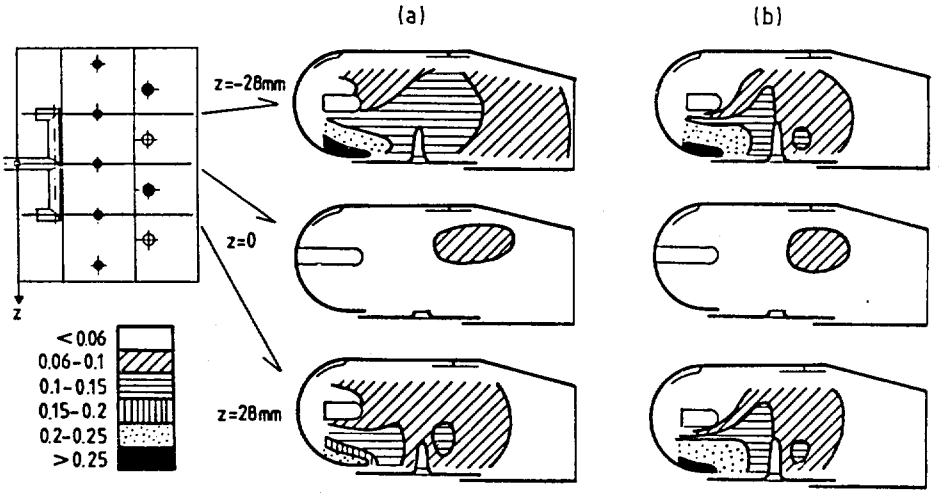

Figure 11 Effect of flow asymmetry in vaporiser fuel arrangement on passive scalar characteristics.
(a) asymmetric vaporiser flow.
(b) symmetric vaporiser flow.

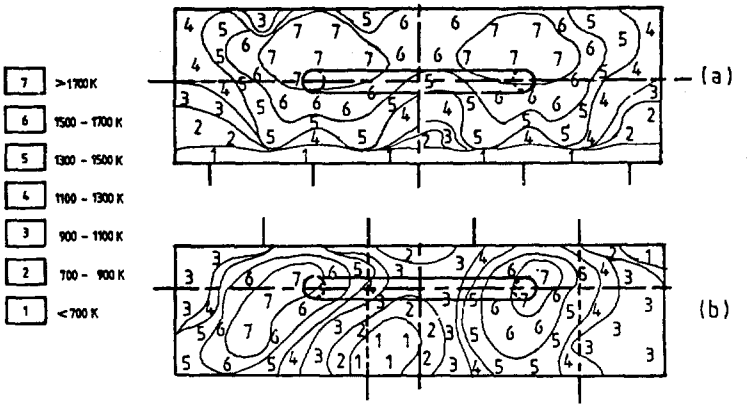

Figure 12 Cross-plane distributions of mean temperature
(a) primary zone
(b) exit plane.

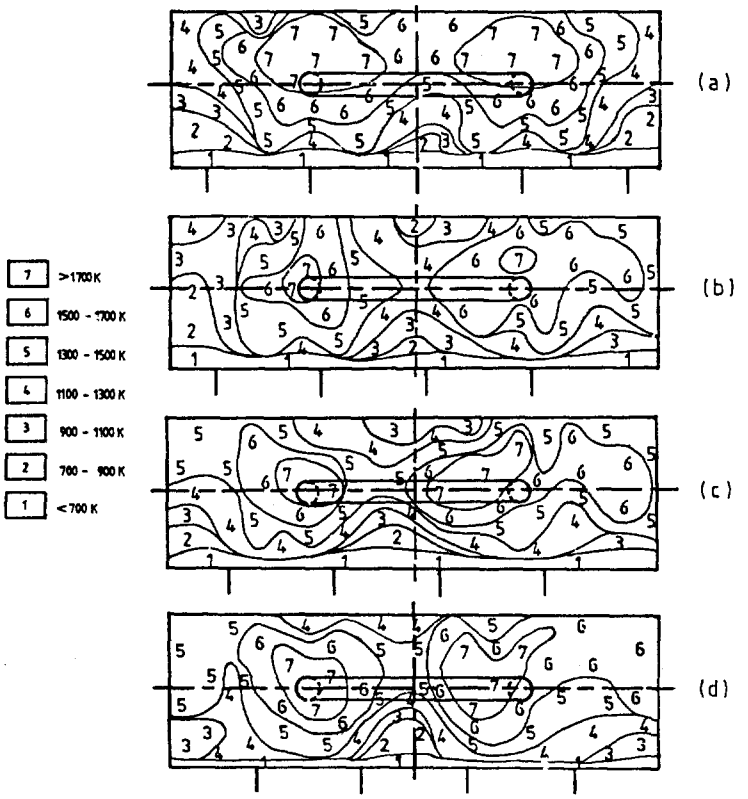

Figure 13 Effect of alignment of primary holes with vaporiser position on primary zone temperature.

(a) usual alignment
(b) 1/8 pitch alignment
(c) 1/4 pitch alignment
(d) 1/2 pitch alignment

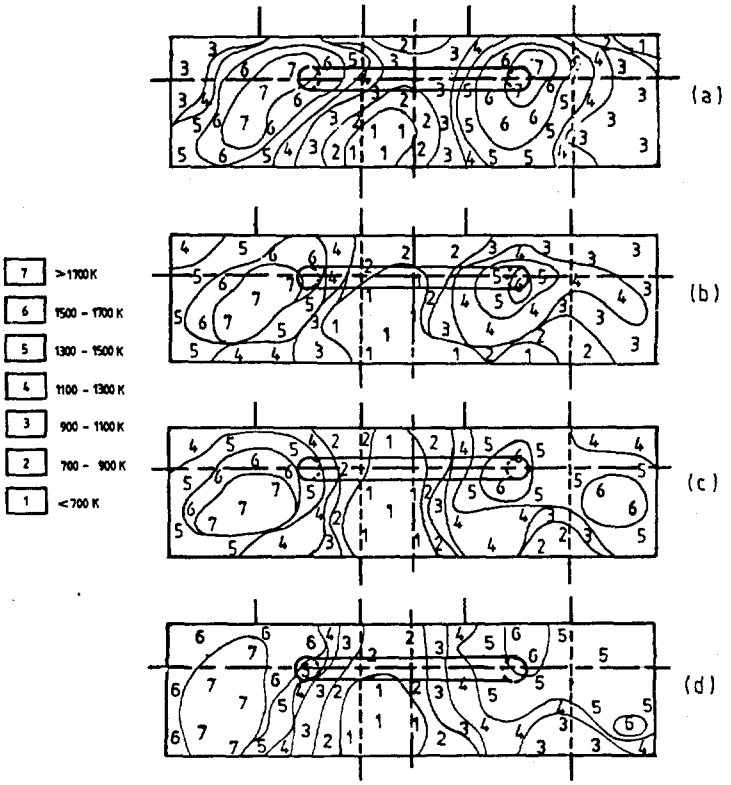

Figure 14 Effect of alignment of primary holes with vaporiser position on exit plane temperature.

(a) usual alignment
(b) 1/8 pitch alignment
(c) 1/4 pitch alignment
(d) 1/2 pitch alignment

DISCUSSION

C.G.W.Sheppard, UK

Do you have any particular reason for using helium to trace gas in the isothermal "passive scaler" experiment? An alternative is to use ethylene at low concentrations — this has a relative molecular mass close to that of air, so avoiding any relative molecular diffusion effects. Ethylene is inexpensive and can be measured at vey low concentrations using standard flame ionization detector unburned hydrocarbon analyzers. (Reference: Chlebour, P.V., et al, Comb. Sci and Tech., circa 1981.)

Author's Reply

In the highly turbulent flow in which these measurements were made, I do not believe that molecular diffusion effects are of any significance at all. The helium trace technique was used because it is a cheap, simple and a well tried and understood technique.

FUEL EFFECTS ON FLAME RADIATION AND HOT-SECTION DURABILITY

by

Dr C.A.Moses
Southwest Research Institute
6220 Culebra Road
San Antonio, Texas 78284, USA

Mr P.A.Karpovich
US Naval Air Propulsion Center
1440 Parkway Avenue
Trenton, New Jersey 08628, USA

ABSTRACT

This paper summarizes the results of recent combustor experiments relating to fuel effects on combustor durability and analyzes them with respect to Navy aircraft operations and maintenance. By combining life-ratio models with data on mission profiles, models were developed that predict the impact of flying an aircraft on a fuel of reduced hydrogen content in terms of the combustor life lost in flying a typical mission. To determine the effect of decreasing hydrogen content on maintenance requirements, the life-ratio models were combined with data obtained from maintenance depots on combustor life along with information on the importance of combustor life in determining engine overhaul schedules. From this, it was possible to identify which engines/aircraft would be most affected by decreases in hydrogen content, and at what point increases in maintenance requirements are likely to be realized.

INTRODUCTION

Since 1980, the U.S. Naval Air Propulsion Center (NAPC) has been developing the concept of an Alternate Test Procedure (ATP) for the qualification of future Navy aviation fuels. The purpose of the ATP is to ensure the compatibility of current aircraft with fuels of the future as fuel specifications evolve to accommodate new crude sources and refining techniques. The underlying thought is that it will be easier to qualify the fuel than it will be to re-qualify all of the aircraft. Another role of the ATP will be to assess the potential impact of using non-aviation fuels in emergencies so that rational decisions can be made concerning operations and maintenance to maximize readiness.(1,2)

One of the fuel properties of concern is the hydrogen content. Figure 1 shows the historical trend of hydrogen content for F-44 (JP-5) and F-76 (NDF)*. This shows that the fleet-average hydrogen content for F-44 is gradually drifting down to the recommended minimum meaning that many fuels are below that level. The hydrogen content of F-76 and other diesel fuels which could be condidates for aviation use in emergencies is not controlled and rarely measured. Figure 1 shows that the hydrogen content of F-76 is about 0.3-0.5 wt% lower than F-44 and decreasing as well.

The concern over the reduction in hydrogen content stems from the potential impact on hot-section durability. This paper presents the results of an NAPC study at Southwest Research Institute (SwRI) on the fuel effects on hot-section durability and the potential impact on operations and maintenance. First, several aspects of hot-section durability will be discussed. Then the results from the Navy and Air

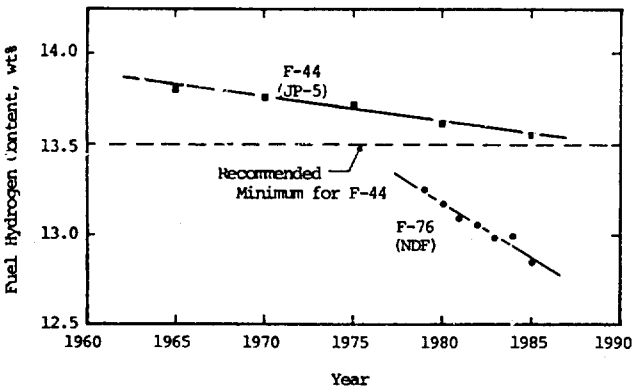

FIGURE 1. HISTORICAL TREND OF HYDROGEN CONTENT IN F-44 (JP-5) AND F-76 (NDF) - FLEET AVERAGE

*The values for F-44 prior to 1980 and for F-76 were developed from correlations with other fuel properties.(15)

Force combustor programs (3-14) on the fuel effects on liner temperature will be summarized along with the resulting predictions on liner durability. Finally, the significance of liner durability on engine overhaul is addressed to see the potential impact of fuel changes on operations and maintenance.

DISCUSSION

Hot-Section Durability

The term hot-section durability refers in general to the life of the combustor and the high-pressure turbine section. Variations in fuel composition and properties can affect the life of these components insofar as they affect flame radiation and hot streaks. In stationary gas turbines, hot corrosion from metal contaminants and erosion from large combustion-generated particulates are of concern, but these are relatively minor in aircraft gas turbines.

Hot streaks are non-uniformities in the high-temperature gas flow. These are minimized by the combustor design for normal operation but can be caused or aggravated by fuel-related problems. Fuels with high viscosity can sufficiently degrade atomization so as to reduce the efficiency and uniformity of the fuel-air mixing. More likely are deformations in the fuel spray caused either by deposits within the fuel atomizer due to thermal stability problems or by carbon deposits on the outside face. If the hot streaks impinge on the combustor wall, they obviously lead to higher local temperatures and shorter life. If they are not mixed out of the flow by the dilution jets, they can impinge on the stationary turbine vanes reducing their life. The rotating blades are generally less sensitive to hot streaks because they tend to experience average temperatures due to their rotation.

Radiation is not considered as a significant heat load to the rotating blades because they are effectively shielded by the stationary guide vanes. The vanes, however, are exposed to the flame radiation except in reverse-flow combustors like the T53 and T76. The radiation heat load to the vanes is not as great as that to the liner wall and dome because the viewing angle is much smaller and because some of the radiation is absorbed by cooler gases in the dilution zones. The impact on vane durability is further lessened by the fact that the life is usually limited by thermal fatigue cracking on the trailing edge of the blade, a region which sees much less radiation than the leading edge. The remainder of this discussion will therefore address only liner durability.

The primary effect of fuel changes on combustor life is due to increases in flame radiation and the resulting changes in combustor liner metal temperatures. Flame radiation primarily comes from combustion-generated soot in the primary zone of the combustor. Design factors such as combustor pressure and the fuel/air distribution of the primary zone determine the general soot-forming characteristics of a combustor, but the effects of variations in fuel properties have been shown to be significant with respect to liner life.

High metal temperatures and gradients in the combustor liner result in high stresses which lead to warping and the formation of cracks. High temperature oxidation or burnout can occur, but usually only after warping has disturbed the flow in such a way as to aggravate the metal temperature. Each time a combustor goes from a low temperature to a high temperature and back, the stresses change and, like repeated bending stresses, eventually lead to the initiation of a crack. This failure mode is termed low-cycle thermal fatigue (LCF) and is the dominant failure mode in almost all combustor liners. Figure 2 illustrates typical power excursions in the mission of a Navy fighter aircraft.(16) Liner metal temperatures follow these power changes.

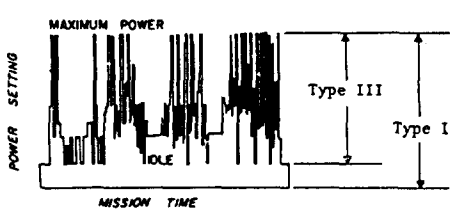

FIGURE 2. POWER REQUIREMENTS DURING COMBAT MANEUVERS OF A NAVY FIGHTER AIRCRAFT (from ref. 16)

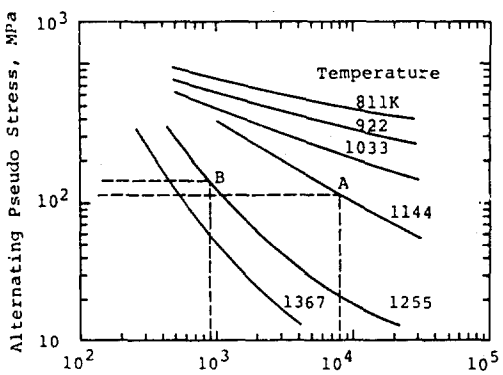

FIGURE 3. FATIGUE DIAGRAM

The two significant engine cycles for most aircraft are the Type I cycles (off to max power to off) and the Type III cycles (idle to max power to idle). Type II cycles include going to supersonic conditions. Type I and II cycles cause more damage than Type III because the change in liner temperature is much greater going from a cold-start condition to maximum power. The ratio of the damage severity varies with engine type; it is strongly influenced by the temperature of the compressor discharge air which cools the liner, the local maximum liner temperatures, and the temperature gradients within the liner as well as the materials. These ratios vary from around 1.5:1 to 50:1 and will be further addressed later.

If the maximum liner temperature is increased beyond its nominal design, by an increased radiant heat load for example, then the basic stress level is increased, and cycle-life-to-failure is decreased from the design life. This can be illustrated by Figure 3 which is a fatigue diagram for a modern, high-temperature alloy typically used in combustor liners.(17) Using an extreme example for clarity on the diagram, consider a combustor liner with a metal temperature of 1150K and a design life of 8000 cycles (Point A). If the temperature were increased by 100K due to an increase in flame radiation, then the stress will increase a proportionate amount (Point B). The associated cycle life is only about 900 cycles or 11% of the original life. A more realistic case would be a 30K temperature increase leading to about a 40% loss in life. The importance of this radiative heat load to the liner depends upon the relative magnitude of the convective heat load and the agressiveness of the cooling mechanisms. The viewing angle of the combustion zone is also important so that aft panels and turbine vanes/blades are less affected by changes in flame radiation than the dome and primary zone. However, since the highest liner temperatures are often found in the aft panels, even small increases in heat load can be significant to life.

Soot Formation

Soot is formed in fuel-rich, high-temperature regions of the primary zone. Most of this soot is consumed in the leaner regions downstream of the primary zone, with perhaps 1-2% exiting the combustor and engine as exhaust smoke. The soot is in thermal equilibrium with combustion gases; in the regions of generation, this would be close to the stoichiometric flame temperature, around 2500-2600K (4500-4700R). The soot radiates as a black body according to T^4, and is the largest source of radiation heat flux to the liner.

Soot formation is dominated by engine design factors because of the importance of air-fuel mixing. Combustion pressure plays an important role because, as this pressure increases, the cone angle of the fuel spray is reduced thus concentrating the fuel even more and hindering the mixing process. More soot is formed at the high power conditions because both the combustion pressure and the fuel-air ratio are highest. Figures 4a&b illustrate this by showing the independent effects of pressure and fuel-air ratio on flame radiation for the T700. Note also the level of the non-luminous radiation due to CO_2 and H_2O.

The high power operating conditions are therefore the most important at which to evaluate the fuel effects on liner durability. At these conditions, not only are the soot and radiation levels the highest, but the liner temperatures are already at the highest levels in the mission cycle. For most aircraft this would be the sea-level takeoff condition (SLTO). For supersonic aircraft the sea-level "dash" condition is also important since the combustion pressures are higher than at SLTO as are the measurements of radiation and liner temperature.

Fuel Effects on Soot Formation: The question of which fuel properties are important in soot formation has been an active topic of discussion for the last ten years or so. For distillate fuels in the range of F-40 through F-54/F-76 (JP-4 through DF-2/NDF), there is general agreement that soot formation is controlled by gas-phase

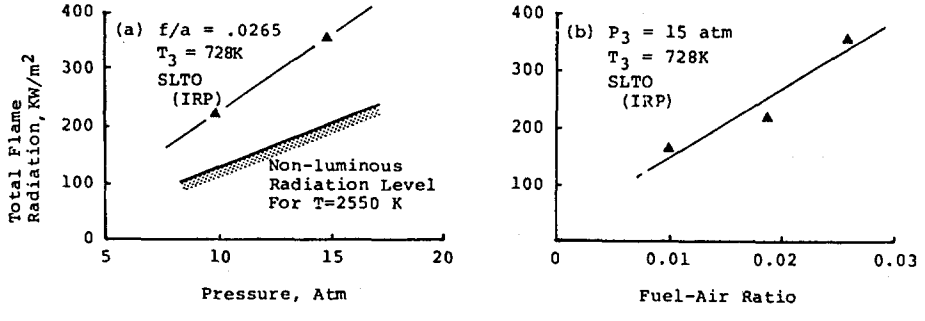

FIGURE 4. EFFECTS OF COMBUSTOR PRESSURE AND FUEL-AIR RATIO ON FLAME RADIATION FOR T700

kinetics and the properties which affect droplet lifetime, i.e., viscosity and boiling-point distribution, have very little affect on soot formation. This may be somewhat surprising in light of the importance of fuel-air mixing, but evaporation processes are controlling only at ignition and idle where soot formation is minimal.

The major controversy has been whether hydrogen content is the controlling parameter or if aromatic structures, especially polycyclic aromatics (PCA) such as naphthalenes, are important. This will be examined for several combustors representing different design technologies. Table 1 summarizes the Navy combustors plus the Air Force combustors which have been tested. (Also shown are the reference numbers which for convenience will be left out of the text.) In the Air Force programs, the range of fuels covered the spectrum of F-40, F-34, and F-54 (JP-4, JP-8, and DF-2); these were blended to different hydrogen contents using both single-ring and double-ring aromatics as well as end-point extenders. The Navy tests did not cover as broad a range of properties, but the selection was sufficient to address the concerns of Navy aviation fuels since the scope of F-44 and F-76 (JP-5 and NDF) is less than that of the Air Force fuels.

TABLE 1. SUMMARY OF COMBUSTOR TESTING FOR FUEL EFFECTS

Engine	Navy Aircraft	Navy Tested	Air Force Tested	% Navy Inventory(1)	Reference
J52	A-4-A-6			9.2	
J57/TF33	F-8		X	-	8
J79(HS)(2)	F-4		X	3.6	3
J79(LS)(3)	F-4		X	3.4	6
J85	F-5,T-38		X	2.1	7
T53	H-1	X		0.6	12
T56	C-2,C-130	X		47.2	10
	E-2,P-3				
T58	H-2,C-3,H-46			10.5	-
	H-52				
T64	C-8,C-115,H-53			3.6	
T76	OV-10	X		0.9	13
T400	H-1		(4)	3.1	-
T700	H-60	X		2.7	11
TF30	F-14,A-7	X		6.5	9
TF34	S-3		X	1.7	14
TF39	---		X	-	7
TF41	A-7		X	2.2	5
F100	---		X	-	8
F101/(F110)	F-14		(5)	-	4
F402	AV-8	(6)		0.7	-
F404	A/F-18	X		2.3	11

(1) As of January 1985.
(2) High smoke version, J79-10A and J79-17A.
(3) Low smoke version, J79-10B and J79-17C.
(4) The T400 consists of two PT6 engines geared together; the PT6 combustor tested by the Air Force was a significantly different configuration.
(5) F110 is programmed for F-14 retrofit; the combustor is the same as the F101 except for the atomizers.
(6) Testing not yet completed.

The J79(HS) is a good example of an older design technology using multiple-can combustors with a rich primary zone that produces high soot and smoke levels. Figure 5 is taken from the report of the fuels effects study on that combustor. Shown is the liner temperature rise above the compressor discharge temperature. The peak temperatures at the high-power conditions of SLTO and supersonic dash are the most critical, and the fuel effects can be seen to have caused an increase in liner temperature of over 50K. It can be seen from these data that there is no consistent effect of either aromatics or volatility/viscosity.

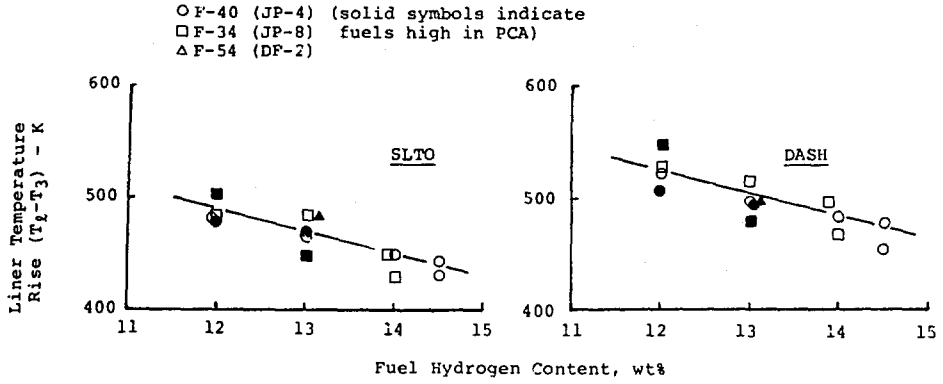

FIGURE 5. EFFECT OF FUEL PROPERTIES ON LINER-TEMPERATURE RISE FOR J79(high smoke)

The J79(LS) is a later model of the above engine which incorporates improved liner cooling for longer life and a leaner primary zone and air-blast atomization for improved mixing to reduce soot formation and smoke. Figure 6 presents the peak liner temperatures for this combustor and as found above, there are no consistent trends due to the presence of dicyclic aromatics or to viscosity and volatility. Since the compressor discharge temperature, T_3, is the same for both models, comparing the data from Figures 5 and 6 shows that the liner of the later model is about 150K cooler than the older model, but the fuel sensitivity is about the same for both.

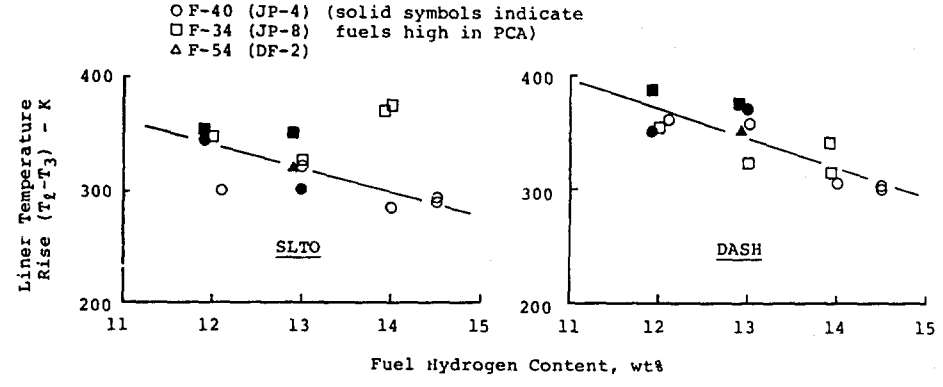

FIGURE 6. EFFECT OF FUEL PROPERTIES ON LINER-TEMPERATURE RISE FOR J79(low smoke)

The TF41 is another example of an older technology engine with can combustors, but with significantly higher pressure ratio than the J79, 22 vs. 13.5 atm. Figure 7 presents the peak combustor liner temperatures at SLTO for the same fuels used in the J79 studies. All of the data points are well correlated except the two JP-8 fuels at 12 and 13 wt% hydrogen blended with multi-ring aromatics; these two produced significantly higher liner temperatures. Strangely enough the JP-4 fuels blended with these same compounds in about the same concentrations did not result in higher temperatures. For this engine the question is perhaps of little consequence since the life-limiting region is in the transition duct between the combustor and the turbine section; in this region, the temperatures were insensitive to any fuel changes.

The T56 engine has the largest population in the Navy inventory; it is used primarily in the P-3 aircraft, but also in the C-2, E-2, and C-130 aircraft. These aircraft have significantly different mission cycles which affect the sensitivity of combustor life to fuel properties. In the T56 study, liner temperature measurements and flame radiation were not well correlated to fuel properties. However, in an earlier study, Blazowski showed that T56 liner temperatures were well-correlated with hydrogen content over the range of 10-16 wt%.(18) In the T56 report, the life-limiting region was stated to be the transition duct between the combustor and turbine inlet; in that location, as with the TF-41, the temperatures were insensitive to fuel changes.

The combustors in the TF30 are can-type, but made of louvered rings for film cooling. Combustor life is limited by LCF cracks at the seam between louvers because one piece is exposed to the flame radiation while the other is shielded and remains

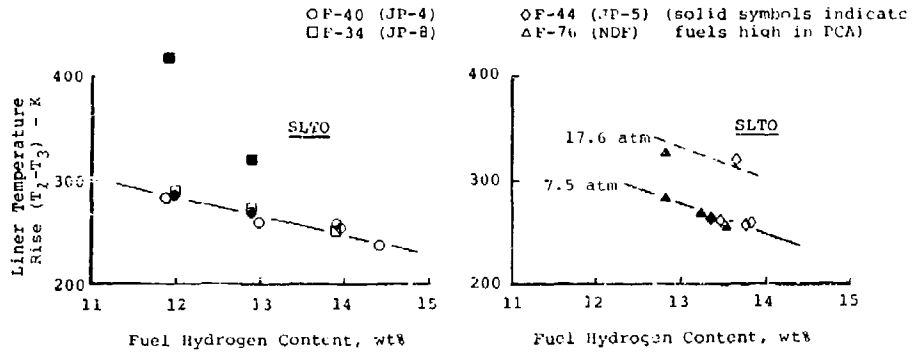

FIGURE 7. EFFECT OF FUEL PROPERTIES ON LINER TEMPERATURE RISE FOR TF41

FIGURE 8. EFFECT OF FUEL PROPERTIES ON LINER TEMPERATURE RISE FOR TF30

cooler, thus increasing the strain. Test-to-test variations in fuel-air ratio were found to have significant affects on liner temperature. When corrections were made for these variations, the fuel property best correlated to increases in liner temperature, as well as flame radiation, was found to be hydrogen content. Figure 8 shows this for the SLTO conditions.

The J85 engine represents older annular combustors of punched-louver design and low pressure ratio. The liner temperature data from both the combustor rig and full engine were very erratic, and apparent fuel effects were inconsistent even among thermocouples at the same axial location. The exhaust smoke data were quite consistent, however, and showed a pronounced increase with decreasing hydrogen content so the soot formation was assumed to follow the same trend. It was concluded that the convective heat transfer is quite complex, and the inconsistencies were due to variations in the internal gas temperature distribution.

The TF34, T700, and F404 are all state-of-the-art annular combustors designed for long life. Generally, with machined-ring combustors, it is possible to identify specific cooling rings which are the life-limiting regions and calculate life predictions for those areas. To illustrate the sensitivity of flame radiation to hydrogen content, Figures 9 and 10 show the data from the T700 and F404 studies at the SLTO condition. The F404 was operated under flow conditions scaled to 4 atm because of limitations in the air factory; the sensitivity to hydrogen content may not be accurate for that reason, but the dominance of this fuel property is again obvious. The radiation data for the TF34 had a correlation coefficient of 0.92 with hydrogen content. The liner temperatures in these combustor studies followed the same trends.

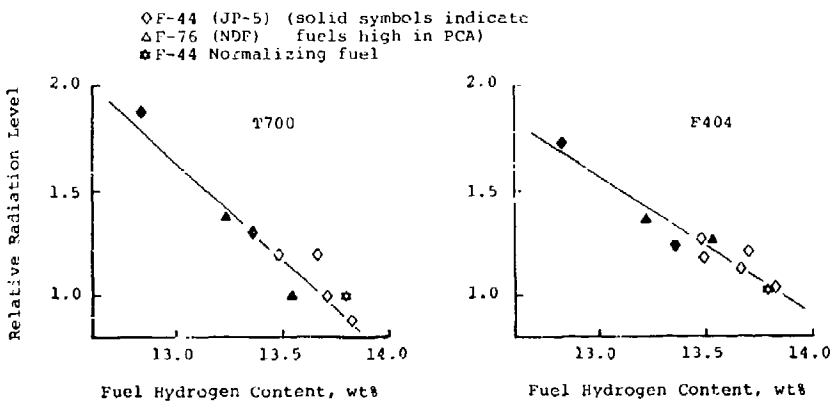

FIGURE 9. SENSITIVITY OF PRIMARY ZONE RADIATION TO HYDROGEN CONTENT FOR T700

FIGURE 10. SENSITIVITY OF PRIMARY ZONE RADIATION TO HYDROGEN CONTENT FOR F404

A simple hydrogen correlation is not always adequate to correlate the radiation and temperature-rise data. Fuels with high concentration of naphthalenes sometimes result in higher values of radiation and temperature rise. Naegeli, et al. (19) have shown in a high-pressure laboratory combustor that the importance of naphthalenes varies with operating conditions with more soot being produced at conditions of lower pressure, temperature, and residence time in the primary zone. When a naphthalene effect has been seen in the full-scale combustor tests, they have been either at isolated conditions which were not realized at other conditions, e.g., F100 cruise condition, or not consistent among the fuels, e.g., TF41. In the cases where such effects were seen, the naphthalene contents were blended to abnormally high concentrations, 14-25%, although the majority of the engines showed no apparent sensitivity even at these same high concentrations. Typical values in jet fuels are less than 3%, and for diesel fuels less than 5%. In combustor tests with fuels of more moderate naphthalene concentrations, hydrogen content has been consistently shown to be the dominant fuel factor in correlating flame radiation and liner temperature increases. Where deviations have existed in liner temperature data, they have not been correlatable to fuel properties and were generally caused by variations in operating conditions or hardware changes such as replacing atmomizers leading to changes in mixing patterns.

It is therefore concluded that for the purposes of relating changes in fuel properties to combustor life, hydrogen content is a sufficient parameter for light and middle distillate fuels such as jet fuel, diesel fuel, and home heating oil.

LCF Life Models

The effect of reduced hydrogen content on LCF life can be determined in one of three ways:

1. Extensive LCF engine tests on a number of fuels.

2. Combustor rig testing to determine the effects of changing fuel properties on liner temperature, and the use of the liner temperature profile data to predict LCF life using sophisticated finite-element computer codes to calculate thermal stresses in life-limiting regions.

3. Using the simplified methodology developed in the SwRI ATP study to predict the effect of reduced hydrogen content on LCF life.

The first approach would be the most comprehensive but prohibitively expensive because of the number of tests required for statistical confidence. The second approach was used in most of the combustor studies; the results are very significant for those engines and much less costly than the first approach. The third approach is much less sophisticated than the second but uses a similar rationale for the effect of temperature on stress and cycle life of liner metals; it is meant to be used where liner temperature data are not available but estimates on life cycle ratio are desirable. It can also be applied where data on fuel effects on liner temperatures are available, but a sophisticated computer code to predict life effects is not.

The simplified methodology was developed under subcontract by Felz and Kenworthy at General Electric (G.E.).(17) The basic assumption is that the pseudo-elastic stress, σ, is proportional to the thermal gradient and that this in turn is proportional to changes in $(T_\ell - T_{coolant})$, where T_ℓ is the peak liner metal temperature and the coolant temperature is the compressor discharge temperature, T_3. Then,

$$\sigma_b = \sigma_a \frac{T_{\ell,b} - T_3}{T_{\ell,a} - T_3} = \sigma_b \left[\left(\frac{T_{\ell,b} - T_{\ell,a}}{T_{\ell,a} - T_3} \right) - 1 \right]$$

The temperature term inside the parentheses is simply the parameter developed by Blazowski (18) to correlate liner temperature data where the subscripts a and b correspond to the reference fuel and the test fuel respectively. This parameter effectively uses the liner thermocouple as a radiation sensor assuming that convective heat transfer does not change as the fuels change. Working curves were developed to predict the reduced cycle life using the current thermal cycle life and the Blazowski parameter as input. The thermal cycle life can be estimated from the design life or from current maintenance experience combined with the mission profile. The Blazowski parameter can either be obtained from experimental data or estimated from data of similar designs. Specific details are found in Reference 17.

Initial verification of the model was obtained by comparing the life-ratio predictions for the two models of the J79 engine with the predictions from G.E.'s thermal stress analysis code. These comparisons are shown in Figure 11 and are considered very good considering the simplicity of the model. The simplified model was compared to the Pratt & Whitney (P&W) model using the temperature data and the thermal cycle life from the F100 report. Figure 12 compares the two predictions of life ratio. Since this comparison is also very good, it is concluded that the simplified model gives essentially similar results to that of the more sophisticated finite-element computer codes if the same cycle life and temperature sensitivity to hydrogen content are used.

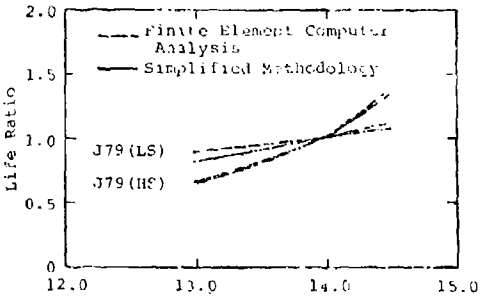

FIGURE 11. COMPARISON OF ANALYTICAL METHODOLOGIES TO PREDICT THE EFFECTS OF FUEL HYDROGEN CONTENT ON COMBUSTOR LINER LIFE

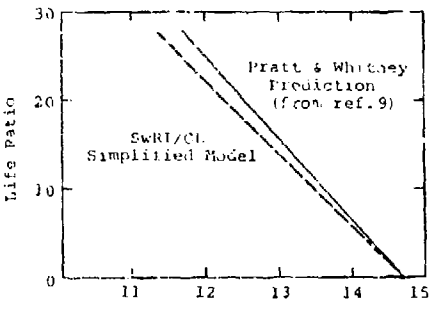

FIGURE 12. COMPARISON OF LCF LIFE RATIO MODEL PREDICTIONS FOR THE F100 ENGINE

The successful application of the model to other engines is therefore expected to be dependent only on the accuracy of establishing, or assuming, the liner temperature sensitivity with hydrogen content and the thermal cycle life of the engine for its mission mix. The equivalence ratio for Type III to Type I cycles for LCF damage depends greatly on design and experience; it therefore represents a potential weakness in all LCF models.

LCF Life Predictions: Predictions of the effect of decreasing fuel hydrogen content on the LCF life of combustors fall into two categories:

- Those engines which the manufacturer has made predictions based on finite-element analysis and liner-temperature data from fuel impact studies.
- Those engines for which the SwRI/GE simplified methodology is applied.

The manufacturer's model predictions were used where they exist, because they are considered superior. Since the two modeling approaches have been shown to be in good agreement, the two will be combined in the presentations.

Table 1 summarized the combustor programs to date, indicating that there are six combustors for which liner-temperature data do not exist, i.e., J52, T58, T64, T400, F110, and F402. The combustor of the F110 is the same as that for the F101 except that the atomizers have been changed to pressure atomizers. For the purposes of this study, the F101 results were used. While the materials and cooling schemes are apparently the same, the flame radiation levels and the sensitivity of flame radiation to soot formation may be different. The use of the F101 model is the best that can be done at this time without F110 data to compare. The simplified methodology was used for the other five combustors. It was also used for the T53, T56, T76, T700, TF34, TF41, and F404, using the liner-temperature data from those combustor programs.

Two items of information are needed to apply the SwRI/GE model:

- The thermal cycle life of the combustor,
- The sensitivity of liner-temperature to variations in the hydrogen content of the fuel.

Thermal-Cycle Life: The thermal-cycle life of each combustor was determined by combining the following information and data on each engine/airframe:

- manufacturer's data on design life and field life
- engine/combustor maintenance schedule
- average mission length
- typical mix of thermal cycles in a mission
- equivalence ratio of Type I and Type III thermal cycles

This information is summarized in Table 2.

The estimates of the LCF thermal cycle life for all of the engines are also summarized in Table 2. They range from 500-600 thermal cycles for older engines such as the J52 and J79(HS) to around 4000 cycles for newer engines like the TF34, T700, and F404. Also, it is apparent that Component Improvement Programs (CIP) have extended the life of several combustors like the T58, T64, and J79.

Liner Temperature Sensitivity: For the purposes of the SwRI/GE model, liner temperature is expressed using the liner temperature parameter defined by Blazowski.(16) Where liner temperature data exist for various fuels, this parameter is evaluated

TABLE 2. SUMMARY OF THERMAL CYCLE AND LINER LIFE DATA

Engine	Aircraft	Liner Repair Life (Hours)	Average Mission Length	Missions to Repair	Mission Cycle Mix per 1000 hours Type I	Type III	LCF Damage Equiv.	Effective Type I Cycles per 1000 hrs	LCF Cycle Life
J52	A-4	750	1.9	395	524	4480	39:1	639	480
	TA-4	750	1.8	417	560	5052	39:1	690	518
	A-6	750	1.8	417	571	3500	39:1	660	495
	EA-6	750	1.9	395	525	4441	39:1	639	479
J79-10A	F-4	600	1.9	316	525	4063	2:1	2556	1533
J79-10B	F-4	1200	1.9	632	525	4063	2:1	2556	3066
J85	T-2	800	1.5	533	666	4027	2:1	2680	2144
T53	UH-1, AH-1	3600	1.9	1895	(534)	(3176)	(13:1)	778	2800
T56	C-2, E-2	5000	5.0	1000	200	---	cs=0.32	264	1320
	C-130	5000	6.3	794	158	---	cs=0.65	261	1305
	P-3	5000	11.0	455	91	---	cs=0.23	112	560
T58-8,-10	SH-2 (also	600	3.2	188	317	3246	2:1	1934	1160
T58-5,-16	H-3, H-46)	1200	3.2	375	311	3246	2:1	1934	2320
T64-6	CH-53	1200	1.3	923	744	1475	2:1	1482	1778
T64-411		2400	1.3	1846	744	1475	2:1	1482	3557
T76	OV-10	3000	3.0	1000	333	(1000)	(13:1)	416	1230
T400	AH-1	2000	1.9	1053	534	2176	(13:1)	778	1556
T700	SH-60	1833	3.2	573	311	3246	2:1	1934	3545
TF30	A-7	(550)	2.1	262	465	4164	39:1	591	325
	F-14	550	1.4	393	715	7211	39:1	900	495
TF34	S-3	1500	2.6	577	381	4113	2:1	2437	3656
TF41	A-7	750	2.1	357	485	4298	13:1	816	612
F10/F101	F-14	not estab.	1.5	not estab.	648	6504	2:1	3940	not estab.
F402	AV-8A(tact.)	300	1.3	230	770	4615	(3:1)	2810	843
	AV-8A(trng)	(2000 counts)	1.0	(100)	1000	9000	(4:1)	9000	900
F404	F/A-18	1030	1.9	542	525	5455	1.5:1	4161	4286

NOTES:

1. Numbers in parentheses are based on estimates from similar designs or missions where data were not available.
2. For the T56, the number of effective thermal cycles was calculated from a cycle severity parameter (Ref. 20) which is an estimate of the LCF damage of the rest of the mission compared to the Type I cycle at takeoff.

directly from that data. Where such data do not exist, a value can be estimated from combustor data of similar design, i.e., materials, cooling, and primary zone fuel-air ratio. Such a correlation developed by Blazowski (18) for older combustors with rich primary zones had a value of about 0.15 for a change in hydrogen content of 1 wt%. Combustors with leaner primary zones generally have values less than this. Also, different locations on a liner will have different values depending on the relative importance of radiation heat transfer; when possible the parameter should be evaluated in the life-limiting region.

Table 3 summarizes the temperatures, T_f and T_3, temperature increase, ΔT, and the Blazowski parameter, β, for the combustors considered here. The values listed are for the life-limiting region of the combustor where that has been identified in the respective reports. An "e" or "d" is used to designate whether the value is estimated or from data. The newer engines showed the highest temperature rise for a decrease in hydrogen content of 1 wt%:

T700	44K
TF34	59
F404	45

The F101 was the exception to this with an increase of only 24K. Several of the older engines had similar temperature increases of about 35K, i.e., T53, T56, and TF30. These are reflected in the life predictions summarized in the next discussion.

Summary of LCF Life Prediction: The results of the combustor LCF life predictions, whether by the SwRI/GE model or from the engine manufacturers, are summarized in Figure 13; Figure 13a is for turboprop and turboshaft engines while Figure 13b is for turbojet and turbofan engines. Solid lines are used for predictions that used data from combustor programs for the liner temperature sensitivity to hydrogen content; this includes all of the predictions made by the engine manufacturers plus several where the data were used in conjunction with the simplified model. The short-dashed lines are used for the engines where no liner temperature data were available, and the Blazowski correlation was used. The F110/F101 is shown as a line of long dashes since the F101 life prediction is being used to estimate the F110 life.

The engines which show the greatest impact are the newer General Electric engines, TF34, T700, and F404. This is because of the larger temperature increases measured on the life-limiting panels during the combustor programs for those engines. At the time of this writing, General Electric has not published the final report for the

TABLE 3. SUMMARY OF TEMPERATURE DATA FOR LCF MODEL CALCULATIONS

Engine	T_3(°K)	T_4(Ref.)	$\Delta T(\Delta H=1 wt\%)$	$\beta(\Delta H=1 wt\%)$
J52	-	-	-	0.15 e
J79-10A	664	1114	22	0.05 d
J79-10B	664	974	8	0.04 d
J85	588	880	5	0.025 d
T53	586	1119	33	0.06 d
T56	623	860	35	0.15 d
T58	591	-	-	0.15 e
T64	689	-	-	0.15 e
T76	630	947	47	0.15 d
T400	586	-	-	0.15 e
T700	741	983	44	0.18 d
TF30	744	1003	36	0.14 d
TF34	753	1075	59	0.18 d
TF41	765	996	20	0.09 d
F110/F101	829	1180	24	0.07 d
F402	-	-	-	0.15 e
F404	800	1150	45	0.13 d

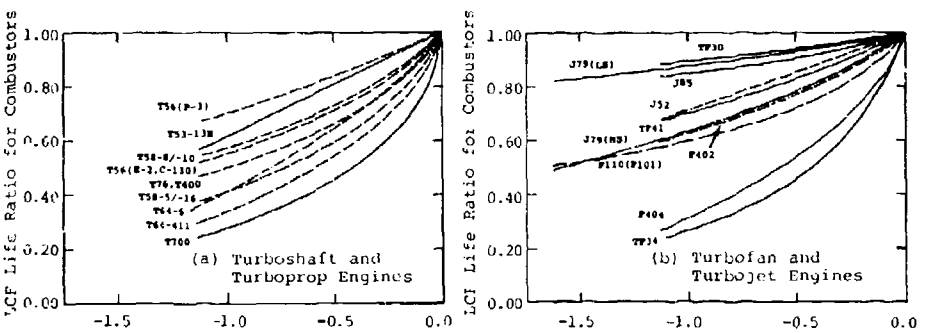

FIGURE 13. EFFECT OF CHANGING FUEL HYDROGEN CONTENT ON COMBUSTOR LCF LIFE RATIO

T700 and F404, so these predictions are from the simplified method. The TF34 report gave a prediction of a 95% reduction in the life of the 3rd outer panel for a decrease in hydrogen content of 2.25 wt%; the prediction curve from the simplified model shown in Figure 13b would be in the neighborhood of that value if extrapolated to $\Delta H = -2.25$ wt%.

It is important to note that, at best, these predictions are based on data from combustor rigs, not engine data. In some cases the operating conditions were not real but scaled to reduced pressure. In other cases the conditions were not constant as the fuels were changed or atomizers were changed between fuels. The resultant set of combustor LCF life predictions, however, seem to be as consistent a set as can be developed at this time from the diverse sources of information, given some of the vagaries in temperature sensitivities and knowledge of liner life in hours and cycles.

It is of interest to compare the predicted life reductions with increases in liner temperature for the different combustors. Figure 14 shows the liner temperature rise and the corresponding LCF life ratio for a reduction in fuel hydrogen content of 1.0 wt%; the data shown here are only for the combustors where liner temperature data were available, not the ones where T=T(H) was estimated. With the exception of one point, for the TF-30, there is a surprisingly good correlation (r^2=0.94) considering the preceding comments. Generalizing from this for cases where data are not available, it could be estimated that every 10K rise in liner temperature results in about a 13% loss in life.

Impact on Flight Operations and Maintenance

The concern of this problem in hot section durability is the reduction in the life of the combustor and the effect on maintenance, i.e., inspection and repair times, not the threat of a catastrophic failure during a mission. Crack initiation and propagation is the net effect over hundreds of missions. The air that "leaks" into the combustion chamber at these uncontrolled locations distorts the flow patterns, especially that of the cooling air. The excess cooling through the crack means a reduction in cooling air everywhere else. Also the exhaust temperature pattern factor can be

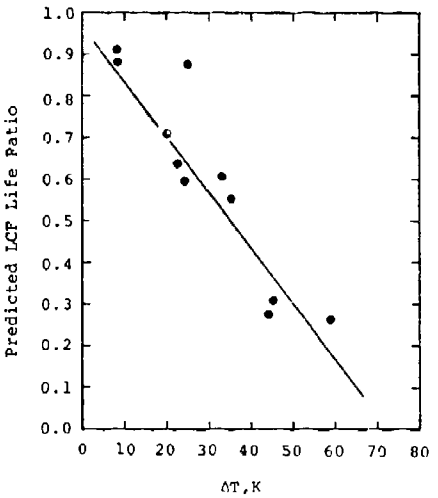

FIGURE 14. CORRELATION OF PREDICTED LIFE RATIO WITH LINER TEMPERATURE RISE

degraded. In the extreme it is possible that the liner wall could distort or even collapse inward under the pressure differential across the liner, but in reality this never happens because the inspection times are established to prevent the problem of excessive air leakage, long before the time of wall failure. It is important, therefore, to consider the impact of reduced hydrogen content on these scheduled inspection and/or repair times.

The presentation of life ratio could be an overstatement of the impact because it effectively assumes the engine is suddenly going to be operated only on a fuel of low hydrogen content, when, in fact, the aircraft may use hundreds of different fuels of varying hydrogen content over its life. It is, therefore, of interest to see the effect of operating an engine for one hour or one mission on a fuel of reduced hydrogen content, i.e., if a mission is flown on a fuel of reduced hydrogen content, by how much has the combustor life been reduced? Relationships for this are easily developed from the information in Figure 13. For example, if the life ratio for a given hydrogen content is 0.5, then each hour/mission on the emergency fuel will result in the same distress as two hour/missions on the reference or base fuel, i.e., a high quality JP-5.

Figure 15 illustrates these results by showing the number of missions/hours on a reference JP-5, e.g., with hydrogen content of 13.8 wt%, corresponding to one mission/hour on JP-5 with reduced hydrogen content for an equivalent amount of LCF damage. As an example, consider the effect of a reduction in hydrogen content of 1.0 wt%. Operating an F-18 aircraft with the F404 engine for one mission on a fuel with only 12.8 wt% hydrogen will produce the same LCF damage to the combustor as 3.2 missions on a JP-5 with 13.8 wt% hydrogen; thus, 2.2 missions would be lost out of the life of the combustor as compared to the repair life of 542 missions shown in

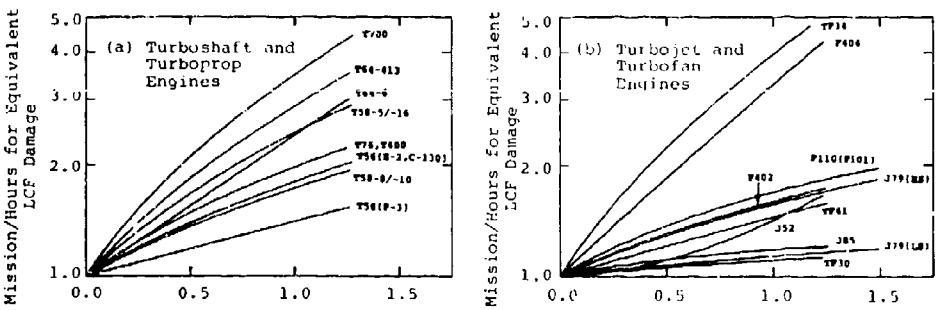

FIGURE 15. MISSION LIFE FOR EQUIVALENT COMBUSTOR LCF DAMAGE USING FUELS OF LOWER HYDROGEN CONTENT

Table 2. In contrast, operating an F-14 with the TF30 engine for one mission on this low-hydrogen fuel would be equivalent to only 1.1 missions; here the loss would be only a tenth of a mission as compared to a repair life of 393 missions. Put in this either maintenance or readiness. It is only as such operation becomes normal practice that the impact will become evident.

The results from this study can also be used to investigate the impact on readiness and maintenance as operations on low-hydrogen fuel become the norm. This can be done by applying the predicted life ratios from Figure 13 to the combustor life and comparing the results with the scheduled maintenance for the hot section. Where hot-section maintenance is driven by combustor life, the impact will be direct. However, if hot-section maintenance is determined by something else, e.g., turbine blades, and if combustor life is much longer, then there will be only a minimal impact on maintenance until the combustor life is reduced to that of the other components. This is because the combustor liner is routinely repaired when the hot-section maintenance is performed.

This will be illustrated with several examples. Consider first the case where engine overhaul is not determined by combustor life. Figures 16-19 illustrate the relationships between the predicted life curves for the T56, T53, TF41, and T64 combustors and the scheduled inspection or repair times.

Figure 16 for the T56 illustrates an example in which no impact is predicted even for an extreme reduction in average hydrogen content of 1.5 wt%. For this engine, the hot-section repair time is dictated by another component with a life much shorter than that of the combustor. Figure 16 also illustrates the effect of installations of the engine in different aircraft; the P-3 flies very long missions and thus has fewer thermal cycles per 1000 flight hours than the E-2 and C-130 aircraft.

Figure 17 compares the predicted liner life with repair time for the T53 engine. For this engine, a reduction of 1.5 wt% hydrogen would begin to impact maintenance requirements as the predicted liner life becomes less than the current engine repair time.

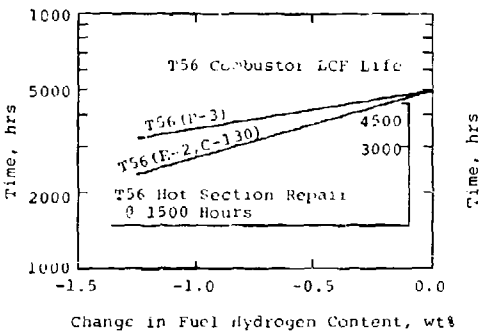

FIGURE 16. IMPACT OF CHANGING FUEL HYDROGEN CONTENT ON T56 MAINTENANCE

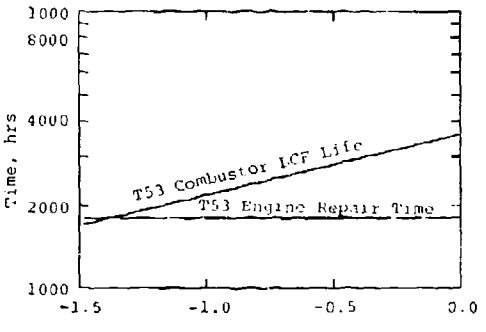

FIGURE 17. IMPACT OF CHANGING FUEL HYDROGEN CONTENT ON T53 MAINTENANCE

Figure 18 illustrates an example where an impact on maintenance may begin at a reduction in hydrogen of around 1.2 wt%. The figure also shows that there will be several hot-section inspections before significant crack growth would occur with the lower hydrogen fuels so there should be no loss of confidence in the flight-worthiness of these engines. A similar impact statement can be made for the TF34.

Figure 19 illustrates a case where continued product development has improved the life of the combustor and resulted in a more tolerant engine. The T64-6B inspections will have to be more frequent as the average hydrogen content drops more than 0.5 wt%. The T64-416 has a longer combustor life which is not defined as yet, but is significantly longer than the scheduled time. Similar impact diagrams can be made for other combustors which are not life-limiting.

For the TF30, T58, J79, J85, and F402 engines, scheduled maintenance and/or overhaul is determined largely by combustor life, and a direct impact would be expected. Figure 20 presents the projected impact on these times. For the TF30, J85, and J79-10B, the life reductions are relatively small, and even a reduction in hydrogen content of 1 wt% is not expected to have a significant impact on maintenance requirements.

For the older J79-10A, decreases of more than 0.5 wt% might begin to create a noticeable change in the liner condition at the 600-hour overhaul. The T58 and F402 engines are the ones projected to have the most serious impact, especially the F402 which has a very short life (100-300 hours). In each of these cases, the life ratio

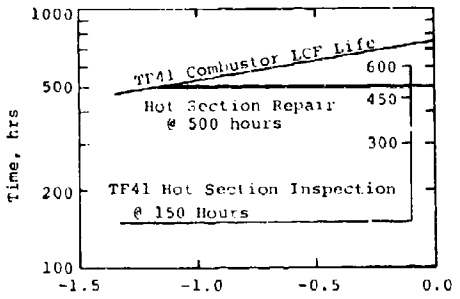

FIGURE 18. IMPACT OF CHANGING FUEL HYDROGEN CONTENT ON TF41 MAINTENANCE

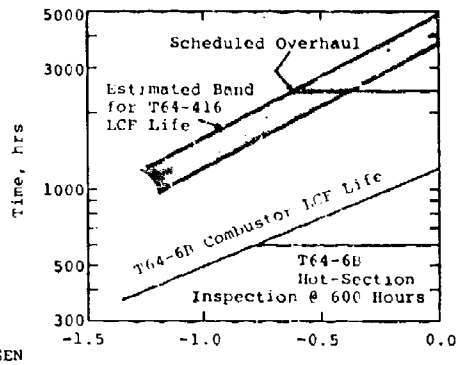

FIGURE 19. IMPACT OF DECREASING FUEL HYDROGEN CONTENT ON T64 MAINTENANCE

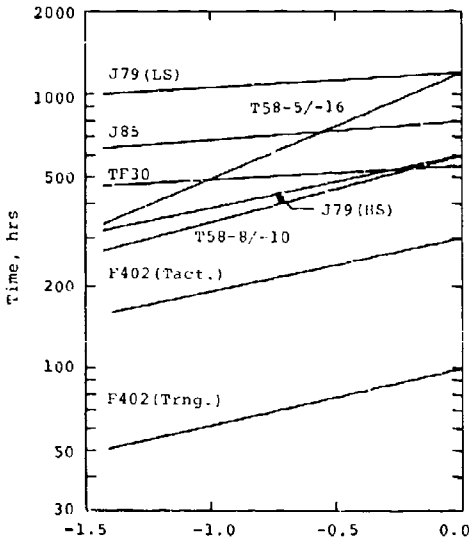

FIGURE 20. IMPACT OF DECREASING FUEL HYDROGEN CONTENT ON ENGINE/COMBUSTOR MAINTENANCE

models were based on assumed sensitivities of liner temperature to hydrogen content; these engines would be prime candidates for fuel impact programs to verify or improve the liner temperature estimates.

This brief analysis would seem to explain why the Navy has not experienced any significant increase in hot section or combustor maintenance over the last decade even though the hydrogen content of JP-5 has decreased, at least in local areas. Flying a few missions sacrifices a relatively small number of hours of combustor life. Even as the average hydrogen content continues to fall, for most engines it would have to drop at least 0.5 wt% from current levels before any impact is projected. Two engines showing significant effects, i.e., T58 and F402, were cases where the liner temperature sensitivities had to be estimated so the projections may be too severe.

SUMMARY AND CONCLUSIONS

1. For the purposes of controlling soot formation and the resultant impact on combustor liner life, hydrogen content is considered to be a sufficient fuel property to control in JP-5.

2. The simplified model for predicting the effects of reduced hydrogen content on LCF life ratio has been shown to produce results comparable to the more sophisticated finite-element computer models of both General Electric and Pratt & Whitney when appropriate values for liner temperature sensitivity and thermal cycle life are used.

3. The effects of reduced hydrogen content on LCF life depend upon the mission profile and can vary significantly for the same engine in different applications. Examples are the more benign mission cycle of the P-3 vs. the C-130 and the more vigorous use of engine power during flight training with the AV-8 Harrier as compared to its use in the squadron.

4. Based on the combustor rig data for liner temperatures and the analyses of that data, there are several engines for which the predicted LCF life ratio of the combustor is significantly reduced for a decrease of 1 wt% in fuel hydrogen content. However, flying a few missions will not seriously affect the life or maintenance requirements of any engine in the fleet. The most serious cases and the predicted loss in liner life for flying a mission on 12.8% vs 13.8% hydrogen fuel are as follows:

Engine	Hours of Combustor Life Lost for One Mission	Percent of Combustor Life Lost for One Mission
T58-5/-16	7.8	0.7
T58-8/-10	5.6	0.9
T64-6	3.2	0.5
J79(high smoke)	3.0	0.5
F402(Tact.)	2.9	0.7
F402(Trng.)	1.6	1.6

Engine overhaul is determined by combustor life for all of these engines. For all other engines the impact on combustor life for one mission on a fuel with 1 wt% less hydrogen would be less than 0.5% of combustor life.

5. It is only when operations on JP-5 of low hydrogen content becomes the norm that increases in maintenance requirements will become apparent. The engines expected to be first affected are:

T58
F402
J79(high smoke)

The TF34 LCF life is very sensitive to hydrogen content, but it is apparently a long life combustor. A conservative estimate predicts an impact on maintenance may begin at a decrease in hydrogen content of 0.4 to 0.5%. The maintenance on the T76 and T64 engines probably would not be affected until hydrogen decreases between 0.5 and 1.0%. The J79-10B, J85, and TF30 engines may see minor increases in maintenance, 10% or less, and the maintenance requirements on the T53, T56, and TF41 engines will be unaffected by decreases in hydrogen content. Statements cannot be made about the effects for newer, long-life engines such as the T700, F404, and F110 because maintenance requirements have not been established.

REFERENCES

1. Moses, C.A., et al., "An Alternate Procedure to Qualify Fuels for Navy Aircraft, "NAPC-PE-55C, Naval Air Propulsion Center, Trenton, NJ, August 1981.

2. Moses, C.A., et al., "Development of an Alternate Test Procedure to Qualify Fuels for Navy Aircraft, Phase II," NAPC-PE-145C, Naval Air Propulsion Center, Trenton, NJ, August 1984.

3. Gleason, C.C., et al., "Evaluation of Fuel Character Effects on J79 Engine Combustion System," AFAPL-TR-79-2015, Wright-Patterson AFB, Dayton, OH, June 1979.

4. Gleason, C.C., et al., "Evaluation of Fuel Character Effects on F101 Engine Combustion System," AFAPL-TR-79-2018, Wright-Patterson AFB, Dayton, OH, June 1979.

5. Vogel, R.E., et al., "Fuel Character Effects on Current High Pressure Ratio, Can-Type Turbine Combustion Systems," AFAPL-TR-79-2072, Wright-Patterson AFB, Dayton, OH, April 1980.

6. Gleason, C.C., et al., "Evaluation of Fuel Character Effects on J79 Smokeless Combustor," AFAPL-TR-80-2092, Wright-Patterson AFB, Dayton, OH, November 1980.

7. Oller, T.L., et al., "Fuel Mainburner/Turbine Effects," AFAPL-TR-81-2100, Wright-Patterson AFB, OH, May 1982.

8. Russell, P.L., "Fuel Mainburner/Turbine Effects,"AFAPL-TR-81-2061, Wright-Patterson AFB, September 1982.

9. Beal, G.W., "Effect of Fuel Composition on Navy Aircraft Engine Hot Section Components," NAPC-PE-74C, Naval Air Propulsion Center, Trenton, NJ, May 1983.

10. Reider, S.B., et al., "Effect of Fuel Composition on Navy T56 Aircraft Engine Hot Section Components," NAPC-PE-88C, Naval Air Propulsion Center, Trenton, NJ, November 1983.

11. Morton, H.L., "Effects of Fuel Composition on Navy Aircraft Engine Hot Section Components," NAPC-PE-117C, Naval Air Propulsion Center, Trenton, NJ, December 1983.

12. Rutter, S., "Effect of Fuel Composition on T53-L-13B Hot Section Components," NAPC-PE-92C, Naval Air Propulsion Center, Trenton, NJ, January 1984.

13. Ball, I., et al., "Fuel Property Effects on the Operational Characteristics of the Navy T76 Engine," NAPC-PE-100C, Naval Air Propulsion Center, Trenton, NJ, April 1984.

14 Abreu, M., "Fuel Character Effects on the TF34-100 Combustor," AFAPL-TR-84-2040, Wright-Patterson AFB, Dayton, OH, June 1985.

15. Technical Data Book--Petroleum Refining, Procedure 2B6.1, pg. 2-25, American Petroleum Institute, New York, NY, 1982.

16. Cote, S.M., and Byers, J.L., "Operational Environment of Naval Aircraft Gas Turbines," Journal of Aircraft, Vol. 16, No. 10, p. 729, October 1979.

17. Foltz, H.L., and Kenworthy, M.J., "A Procedure for Evaluating Fuel Composition Effects on Combustor Life," ASME Paper No. 82-GT-296, May 1982.

18. Naegeli, D.W., et al., "Sooting Tendencies of Fuels Containing Polycyclic Aromatics in a Research Combustor," Journal of Energy, Vol. 7, No. 2, p.168, MarchApril 1983.

19. Blazowski, W.S., and Jackson, T.A., "Evaluation of Future Jet Fuel Combustion Characteristics," AFAPL-TR-77-93, Wright-Patterson AFB, Dayton, OH, July 1978.

20. Curry, C.E., and Korn, J., "Aspects of the T56 Power Section Usage/Operating Cost," AIAA Paper No. 83-1408, June 1983.

DISCUSSION

T.Rosfjord, US

I believe your translation of fuel effects data to practical implications (e.g., maintenance) is very worthwhile. For small variations of fuel properties – as likely will be seen in aviation fuels – hydrogen content is a good indicator. If derivative engines were used for power generation, a broader range of fuels might be used, and a more inclusive fuel property indicator is required. At UTRC, we have seen naphthalene content to be important for such very poor quality fuels. We also have seen, through excellent data correlation, that smoke point is an indicator which covers fuel ranging from aircraft quality to very poor. What is your opinion on the use of smoke point as a fuel chemical property indicator?

Author's Reply

The smoke point test was originally developed to control the smoking tendency of lamp oils burned on the wicks of kerosene lamps. It has proved to be an adequate quality control for jet fuels although no one seems to understand why. Many are dissatisfied with the poor precision of the test, while others question whether its laminar diffusion flame is relevant to gas turbine combustion. This question becomes more significant as the viscosity of the fuel increases and/or the vapour pressure decreases since the wicking and evaporation rates become more controlling in the overall combustion process. Therefore, I would be less comfortable using smoke point with lower quality fuels unless I knew its relationship to the specific combustor in question.

Likewise with naphthalene content. Combustion research by my staff has shown that naphthalenes can be important to soot formation beyond the effect of their lower hydrogen content, i.e., possibly due to nucleation of unbroken ring structures. However, this contribution is dependent upon the operating conditions of the combustor, i.e., temperature, density, and residence time. In experiments which emphasized variations in fuel composition at constant hydrogen content, soot formation in our Phillips 2-inch research combustor was found to be quite sensitive to naphthalenes, tetralins, anthracene, etc. In contrast, when these same fuels were burned in our T-63 combustor, soot formation was found totally insensitive to these polynuclear aromatics. As I remember, smoke point could be correlated fairly well to flame radiation data from the 2-inch combustor at given operating conditions, but it would have been poorly correlated with the T-63 data since, at a constant hydrogen content, the flame radiation did not vary. Incidentally, in the T63 combustor, even the flame radiation data from heavy distillate and residual fuels correlate with hydrogen content.

Therefore, if I were an engine manufacturer interested in the operation of derivative engines on "very poor quality" fuels, I would want to evaluate hydrogen content, smoke point, naphthalene content, etc., for their relevance to that engine at real operating conditions, not scaled, over a range of fuels, and establish a meaningful fuel specification or quality control for that engine. Determining the effects of change operating conditions on the fuel effects would also be beneficial in that it would provide guidance on how to use marginal fuels in emergencies. Lastly, I would do this for each engine type, since I doubt that there would be many, and not try to generalize. If all fuel measures are of equal merit, I would choose hydrogen content because it is the most accurate and precise over all fuels without limitations or caveats. But if it isn't adequate, and smoke point is for some unknown reason, then by all means smoke point should be used.

J.Odgers, CA

For your hydrogen content range, I agree entirely that hydrogen content is very satisfactory for soot correlation. However, for lower hydrogen contents, structural effects do occur and this we represent by the hydrogen saturation factor. From 114 fuels (H6.7 to H6.52) we found smoke point to be less representative than hydrogen alone or hydrogen combined with hydrogen saturation factor.

THE PERFORMANCE OF A SURROGATE BLEND IN SIMULATING JP-4 IN A SPRAY-FUELED COMBUSTOR

G.S. Samuelsen, Professor
C.P. Wood, Associate Development Engineer

UCI Combustion Laboratory
Department of Mechanical Engineering
University of California
Irvine, California 92717

Summary

A surrogate fuel has been developed to simulate the atomization and combustor performance of a practical, distillate JP-4. The surrogate is comprised of fourteen pure hydrocarbons and formulated based on the distillation curve and compound class composition of the distillate parent. In previous work, the atomization performance (evaluated in terms of the atomization quality in an isothermal chamber), and the combustor performance (evaluated in terms of the velocity and thermal fields in a spray-fueled combustor) were found to be equivalent for the parent and surrogate JP-4. The present study address the sooting performance of the two fuels, as well as two reference fuels (a JP-5 and isooctane) of purposefully disparate properties. The sooting performance of the parent and surrogate JP-4 are nearly identical, and distinctly different from that of either the JP-5 or the isooctane. The surrogate represents, as a result, an attractive fuel blend for the study of fuel compositional effects on the sooting performance of petroleum fuels in spray-fueled combustor.

Introduction

Fuel flexibility is a viable and realistic approach to assure adequate availability of aviation fuel through this century. To achieve this position, the relationship of fuel properties and composition to combustion hardware performance and durability must be identified more precisely.

Future fuels (relaxed-specification fuels from petroleum sources and alternative fuels from nonpetroleum sources) are anticipated to contain increased amounts of aromatics as well as increased aromatic complexity. To accommodate an increased fuel aromaticity, the production of soot from combustors operating on relaxed-specification and alternative fuels must be reduced. Toward this end, experimental evidence is needed to define the effects which fuel properties and combustor operating conditions have on soot formation and burnout.

Practical fuels are chemically complex, and the partitioning of the individual hydrocarbon species that comprise such fuels is difficult and fraught with ambiguity. In contrast, the use of a fuel surrogate comprised of pure hydrocarbons has the advantage of allowing the fuel composition to be accurately controlled and monitored.

A surrogate would also provide an attractive fuel for the development and verification of computational codes. The modeling of evaporation rates would be, for example, more tractable and the effect of fuel composition on evaporation rates would be more readily identified and interpreted.

In a previous study [1], the rationale for the composition and blending of a surrogate to represent a distillate JP-4 was developed. In addition, (1) the surrogate blend was formulated, and (2) the atomization and combustion performance of a practical distillate JP-4, a surrogate of the JP-4, and two reference fuels (a JP-5 and isooctane) were compared. Atomization performance was evaluated in an isothermal chamber, whereas combustion performance was assessed by in-flame measurements of the velocity and temperature fields acquired in a swirl-stabilized modal laboratory combustor. Both the atomization and the combustor performance of the parent JP-4 and its surrogate were remarkably similar whereas the performance of the two reference fuels were distinctly different. The present study compares the sooting performance of the surrogate and parent JP-4, and references this sooting performance to that of two fuels of widely different physical and chemical properties.

Experiment

Combustor. The combustor employed is a model axisymmetric can combustor (ASCC) developed in a series of tests [2,3]. The configuration is presented in Figure 1. The ASCC features an aerodynamically controlled, swirl stabilized recirculation zone to simulate important features of practical combustors (e.g., swirl and highly turbulent recirculation). It consists of an 80 mm I.D. cylindrical stainless steel tube that extends 32 cm from the plane of the nozzle. Rectangular, flat windows (35 x 306 mm) are mounted perpendicular to the horizontal plane on both sides of the combustor tube to provide optical access for the laser measurements. A set of swirl vanes (57 mm O.D.) are concentrically located within the tube around a 19 mm O.D. centrally positioned fuel delivery tube. Dilution and swirl air are metered separately. The dilution air is introduced through flow straighteners in the outer annulus. The swirl air passes through swirl vanes with 100 percent blockage which imparts an angle of turn to the flow of 60°.

For the results reported here, the fuels are burned at an overall equivalence ratio of 0.3, corresponding to a primary zone equivalence ratio of approximately 0.8 with the current combustor geometry. The combustor is operated at atmospheric pressure and a bulk reference velocity of 7.5 m/s. The ratio of swirl-air to dilution-air is 1.5 by mass. Prior to introduction into the combustor, both swirl and dilution air are heated to 100°C. The nozzle is a twin-fluid, air-assist atomizer [4], operated in the

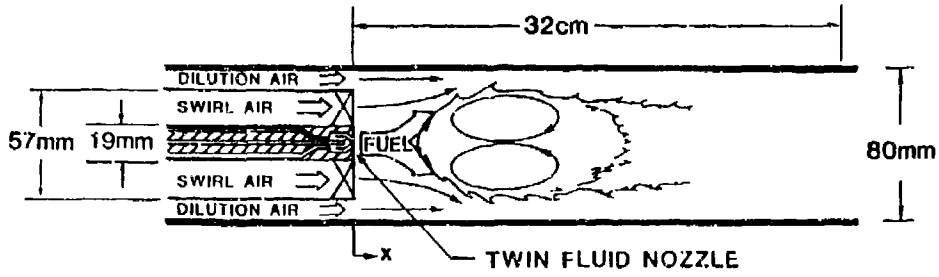

Figure 1 Axisymmetric Can Combustor[4]

present experiment at a nozzle air-to-fuel mass ratio of 2.7. This is in contrast to a ratio of 3.0 for the previous study in which the atomization quality of the nozzle, and the combustor velocity and thermal fields were characterized [1]. The soot measurements were made at the reduced air-to-fuel mass ratio to provide sufficient soot particulate light scattering levels upon which to make interfuel comparisons.

Optical Soot Probe. The method adopted for the point measurement of soot particle size is scattered intensity ratioing. Figure 2 depicts the optical and data processing layout of the intensity ratioing instrument relative to the ASCC. Laser lines from a 5-watt Argon Ion laser (Spectra Physics Model 165), operating in the TEM_{00} (i.e., Gaussian) mode, are separated by a dispersion prism to resolve the 0.488 μm (blue) line at a power of ~300 mW. This line is focused within the combustor through optical windows to a 95 μm waist by a 250 mm focal length, f/5 lens. Scattered light at 60° and 20° is collected, collimated, and focused to two photomultiplier tubes (RCA Model 8575) with pinhole apertures of 200 μm.

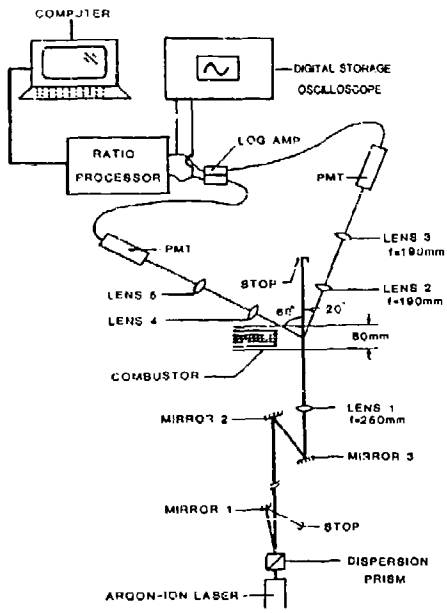

Figure 2 Intensity Ratioing Instrument

The output current from each photomultiplier tube is directed to a dual channel logarithmic amplifier (Spectron Development Laboratories Model LA-1000) which converts the negative current to a positive voltage. The logarithmic amplifier has a response function of +2 volts change in output for every decade change in input. This 2-volts-per-decade response allows the compression of 3 orders of magnitude of scattering intensity into a 6 volt range of signal to the processing electronics.

The amplified signals are then directed simultaneously to a 50 MHz digital storage oscilloscope (Nicolet Model 4094A with a Model 4175 Time Base) and an intensity ratio processor (Spectron Development Laboratories Model RP-1000). The digital oscilloscope is used to monitor signal quality during both calibration and experimental work, and to archive temporal histories of particulate light scattering for later analysis.

The intensity ratio processor determines the intensity ratio of incoming scattering signals and converts the ratio to a digital word to be fed to a microcomputer (Apple IIe). However, in contrast to the previous study that relied on the intensity ratio processor for data processing, the present study emphasizes the acquisition of time-resolved scattering histories obtained with the digital oscilloscope digitizing at 1.00 MHz.

Results

Velocity and Thermal Fields: Prior Results. For perspective, the velocity and thermal field data obtained and compared in the previous study [1] are summarized here. The velocity fields of the four fuels are presented in Figure 3. The fields are virtually the same except at the x/R=1.00 station (Figure 4). Here the velocity profiles vary depending on the evaporation rates of the fuels. Isooctane is completely evaporated, and the profiles represent the gas velocity (Figure 4a). The JP-5, which has the lowest volatility of the four fuels, exhibits significantly higher velocities (in excess of 60 m/s), reflecting the persistence of high velocity droplets at this station. The volatility of the JP-4 parent and surrogate lies between the isooctane and JP-5. Although droplets still persist for the JP-4 fuels, the drop size is smaller (due to the higher evaporation rate relative to the JP-5), and the local velocities are, as a result, lower. Note the remarkable correspondence between the JP-4 parent and surrogate (Figure 4b).

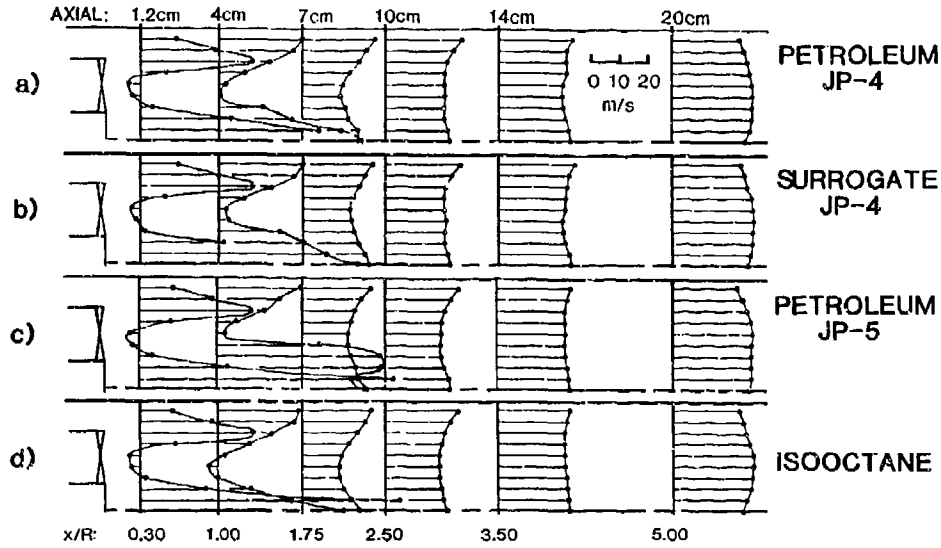

Figure 3 Mean Axial Velocity Fields[1]
(a) Petroleum JP-4
(b) Surrogate JP-4
(c) Petroleum JP-5
(d) Isooctane

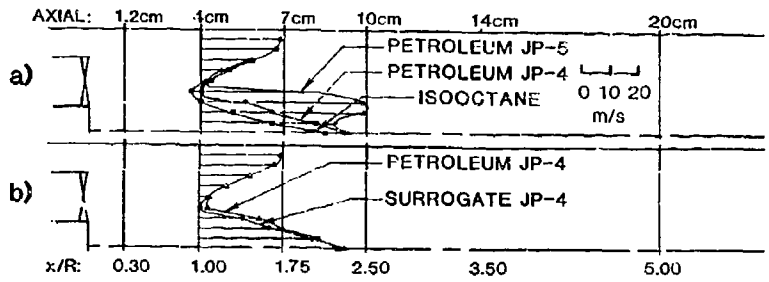

Figure 4 Mean Axial Velocity Fields at x/R=1.00[1]
(a) Petroleum JP-4
Petroleum JP-5
Isooctane
(b) Petroleum JP-4
Surrogate JP-4

The thermal fields are presented in Figure 5. The JP-4 parent and surrogate are again remarkably close whereas JP-5, the fuel with the most disparate physical and chemical properties, exhibits a significantly different result.

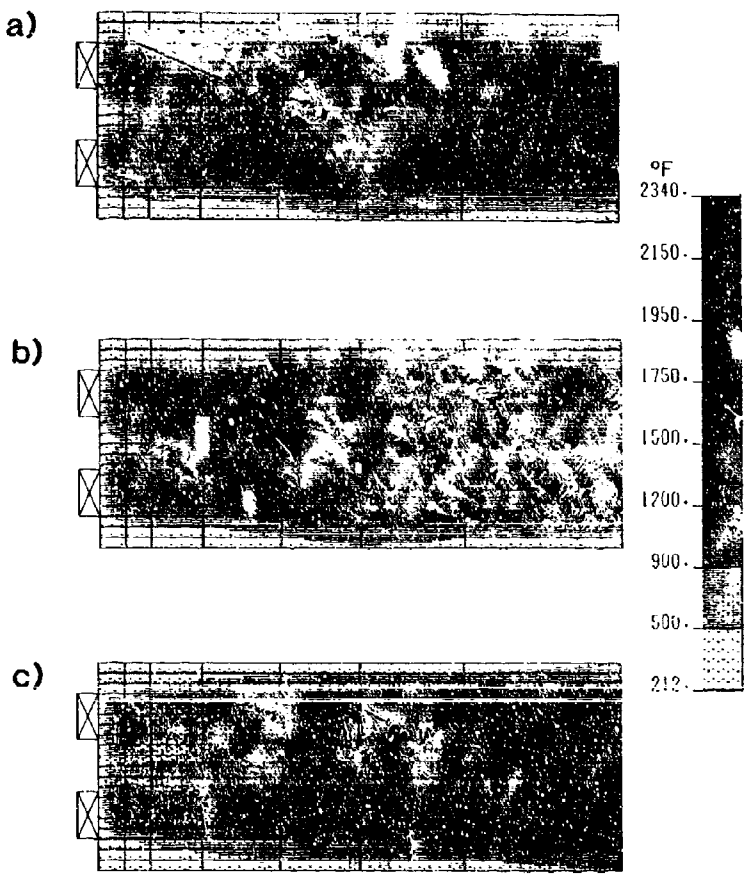

Figure 5 Thermal Fields[1]
(a) Petroleum JP-4
(b) Surrogate JP-4
(c) Petroleum JP-5

Sooting Propensity. Time-resolved scattering histories of light scattering at $\lambda = 0.488 \mu m$ made with the Intensity Ratioing System at angles of 20° and 60°, are presented in Figure 6 for the parent JP-4, the surrogate JP-4, the JP-5, and isooctane at X/R=5.00. Each digital record presents the logarithmic (base 10) scattered intensity versus time for a duration of 8.00 milliseconds.

An important feature of the scattering histories depicted in Figure 6 is the relatively long time duration of the individual scattering events. Figure 6a has a scale bar showing the durations of scattering events arising from single submicron particle traverses of the laser beam at velocities of 1 and 10 m/s (note the mean axial velocity at X/R=5.00 is 25 to 30 m/s.) Thus, the total duration of the major scattering events depicted here are inconsistent with an event arising from individual submicron particles traversing the optical probe volume. Instead, the scattering events appear to arise from packets of particle laden gas with characteristic dimensions of 1.5 to 20 mm. The relatively smooth nature of the major scattering events suggests many particles reside in the probe volume at one time, which is also consistent with the intensity of the scattered signals.

The light scattering histories for petroleum JP-4, JP-5, and isooctane (Figures 6a, c, and d respectively) show significant differences among these three fuels. The degree of scattering activity (defined as the number of scattering events, or peaks, occurring within the 8 millisecond scattering history displayed in each figure) increases significantly from isooctane to JP-5 as hydrogen wt% decreases and aromatic content increases. This increased scattering activity is directly associated with an increase in sooting. In contrast, the scattering fingerprint of the surrogate (Figure 6b) is virtually indistinguishable from that of the petroleum JP-4 (Figure 6a).

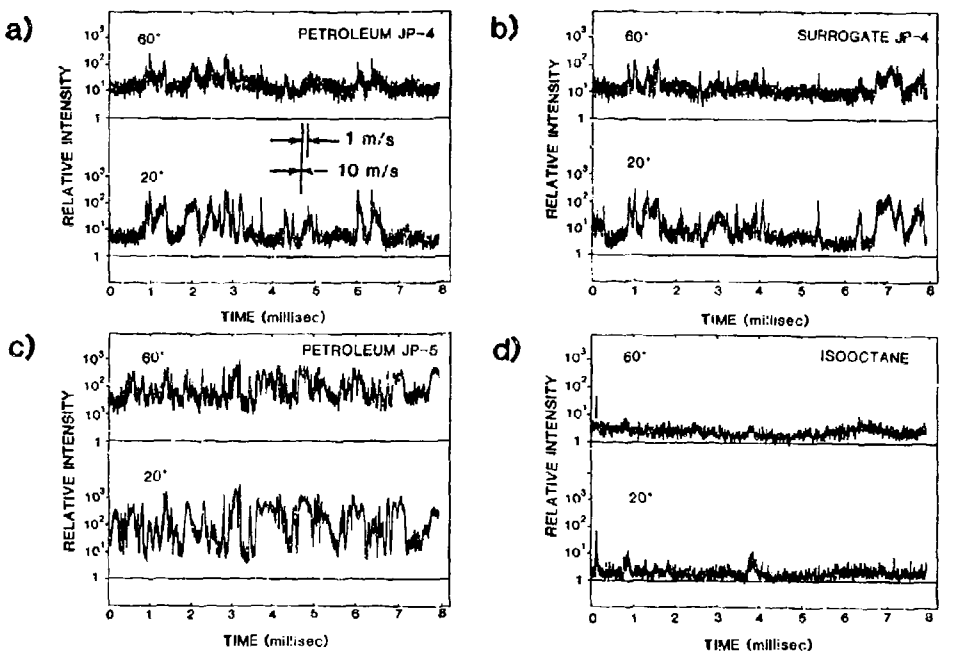

Figure 6 Sooting Propensity
(a) Petroleum JP-4
(b) Surrogate JP-4
(c) Petroleum JP-5
(d) Isooctane

A second criteria by which the sooting propensity of the fuels can be evaluated is flame background. In particular, the flame background at $\lambda = 0.438\ \mu m$ (i.e., the background signal level upon which the particulate scattering events ride) is the contribution from particulate blackbody emission within the field of view of the collection optics, and is a measure of relative flame radiation levels among these fuels. This background contribution is always greater at 60° because the optical path length is greater by a factor of approximately 1.9 relative to 20°. A comparison of the flame background contribution at 60° shows JP-5 > petroleum JP-4 > isooctane by factors of 14:5:1, respectively. Again, the surrogate flame background contribution, at a factor of 5, is identical to the parent JP-4.

Summary

A previous study established the effectiveness of a fuel surrogate blend of 14 pure hydrocarbons to simulate the combustor performance of a practical, distillate JP-4 in terms of the velocity and thermal fields in a spray-fueled model combustor. The present study demonstrates that the sooting behavior is also nearly identical. This is in direct contrast to two reference fuels of disparate properties (a JP-5 and isooctane), both of which display a distinctly different sooting behavior in contrast to the parent and surrogate JP-4, and to each other. The approach used in the formulation of the surrogate, based on replicating the distillation curve and class compound partitioning of the parent, is an effective approach in the preparation of a fuel that can be used for (1) the acquisition of data for combustor code verification and development, and (2) the study of fuel compositional effects on the sooting propensity of practical fuels.

Acknowledgments

This study is supported by the Air Force Engineering and Services Center, Research and Development Directorate, Environics Division (Air Force Contract FO-8635-86-C-0309), with the cooperation of the Naval Air Propulsion Center. The United States Government is authorized to reproduce and distribute reprints for governmental purposes notwithstanding any copyright notation hereon. The authors gratefully acknowledge (i) the contributions of Jack Brouwer, Scott Drennan, and Randy Smith in the collection and presentation of the data, (ii) Lou Crain and Jim Cox of PDA Engineering in Santa Ana, California, for the computer graphical representation of the thermal fields, (iii) the cooperation of Hal Simmons and Parker Hunnifin in the provision of the liquid fuel injector used in the ASCC, and (iv) Verna Bruce for the preparation of the manuscript.

References

1. Wood, C.P., McDonell, V.G., Smith, R.A., and Samuelsen, G.S., "Development and Application of a Surrogate Blend in Simulating the Performance of a Practical Distillate Fuel in a Spray-Fired Combustor," submitted to the AIAA Journal of Propulsion and Power, 1987.

2. Brum, R.D. and Samuelsen, G.S., "Assessment of a Dilute Swirl Combustor as a Bench Scale, Complex Flow Test Bed for Modeling, Diagnostics, and Fuels Effects Studies," presented at the AIAA/SAE/ASME Joint Propulsion Conference, AIAA paper 82-1263, Cleveland, June, 1982.

3. Brum, R.D., and Samuelsen, G.S., "Two-Component Laser Anemometry Measurements of Non-Reacting and Reacting Complex Flows in a Swirl-Stabilized Model Combustor," Experiments in Fluids, Vol. 5, 1987, pp. 95-102.

4. Wood, C.P. and Samuelsen, G.S., "Optical Measurements of Soot Size and Number Density in a Spray-Atomized, Swirl-Stabilized Combustor," ASME Journal of Engineering for Gas Turbines and Power, Vol. 107, No. 1, 1985, pp. 38-47.

5. Wood, C.P., Smith, R.A., and Samuelsen, G.S., "Spatially-Resolved Measurements of Soot Size and Population in a Swirl-Stabilized Combustor," Twentieth Symposium (International) on Combustion, The Combustion Institute, 1985, pp. 1083-1094.

DISCUSSION

A.Williams, UK

You showed that the substantiation of a small amount on N-hexane by 1-pentene in the surrogate blend significantly increased the soot yield. What effect did this have on the percent weight hydrogen content and does this have implications on the use of the hydrogen content alone to define fuel sooting tendencies?

Author's Reply

The data to which you refer are preliminary and, while presented to demonstrate the potential utility of the surrogate in exploring the dependency of sooting on constituents doped into the fuel, are not formally included in the manuscript. You are correct that, in the example given, the doping of 1.5% volume 1-pentene in substitution for 1.5 volume n-hexane did increase the sooting propensity as measured by a ratioing processor in a model axisymmetric can combustor devoid of wall jet injection. While we are working to verify the repeatability and accuracy of these measurements, we find (in both the model axisymmetric can combustor and in a model three-dimensional can combustor with wall jet injection) that fuel preparation, nozzle operating conditions (in particular the atomizing air) fuel air mixing in the dome region, and wall jet mixing in the secondary zone can dominate the production of soot independent of the hydrogen content alone. The change in percent weight hydrogen of the blend is negligible for the 14.4% level of the base surrogate.

RADIATION FROM SOOT-CONTAINING FLAMES

G. M. Faeth, J. P. Gore and Y. R. Sivathanu
Department of Aerospace Engineering
The University of Michigan
Ann Arbor, MI 48109-2140, U.S.A.

SUMMARY

The thermal radiation properties of turbulent soot-containing diffusion flames are considered, treating: scalar structure, excluding soot; soot properties; and turbulence/radiation interactions. The laminar flamelet concept, implying universal correlations of scalar properties as a function of mixture fraction (found from analysis or measurements of laminar flames) appears to be effective for estimates of scalar structure needed for analysis of flame radiation. Extension of the laminar flamelet concept to soot volume fractions (the soot property needed for radiation predictions) has also been encouraging; however, universality is cruder than for gas properties due to effects of finite-rate chemistry. Turbulence/radiation interactions were studied by comparing radiation predictions based on statistical simulation of scalar properties along a radiation path (stochastic analysis) with conventional results using time-averaged properties along the path. Stochastic predictions of spectral radiation intensities are found to be 40-100 percent higher than mean-property predictions in luminous turbulent diffusion flames, suggesting significant effects of turbulence/radiation interactions.

LIST OF SYMBOLS

a	acceleration of gravity
C_j	constants in turbulence model
d	burner exit diameter
$e_{\lambda b}$	blackbody monochromatic emissive power
f	mixture fraction
f_v	soot volume fraction
g	square of mixture fraction fluctuations
I_λ	spectral radiation intensity
k	turbulence kinetic energy
K_λ	spectral absorption crossection
L_e	dissipation length scale of eddy
$P(f)$	probability density function of f
r	radial distance
Re	burner Reynolds number
s	distance along optical path
Sc	laminar Schmidt number
S_ϕ	source term
T	temperature
u	axial velocity
v	radial velocity
x	height above burner
ϵ	rate of dissipation of turbulence kinetic energy
λ	wavelength
μ	laminar viscosity
μ_{eff}	effective viscosity
μ_t	turbulent viscosity
τ_λ	spectral transmittance
ρ	density
σ_j	turbulent Prandtl/Schmidt number
ϕ	generic property, fuel-equivalence ratio

Subscripts

c	centerline
o	burner exit condition
∞	ambient condition

Superscripts

$(-)$, $(\cdot)$	time averaged mean and root-mean-square fluctuating quantity
$(\tilde{-})$, $(\tilde{-})''$	Favre-averaged mean and root-mean-square fluctuating quantity

1. INTRODUCTION

Radiation from turbulent diffusion flames is an important aspect of heat transfer in combustors and exhaust plumes of aircraft propulsion systems, internal combustion engines, furnaces, industrial flares, and unwanted fires. Motivated by these applications, a series of studies concerning the structure and radiation properties of nonluminous turbulent diffusion flames were recently completed in this laboratory (1-8). Encouraging predictions of flame structure were obtained using the conserved-scalar formalism along with the laminar flamelet concept for relating scalar properties to the conserved scalar (9-13). Stochastic methods for predicting flame radiation were also developed, which provided reasonably good agreement with experimental findings, as well as insight concerning effects of turbulence/radiation interactions. The present paper describes extension of this work to luminous (soot-containing) turbulent diffusion flames, involving both measurements and predictions of flame structure and radiation properties. Results of several studies are briefly described, additional details are reported elsewhere (14-16).

Several reviews treat aspects of flame radiation: Tien and Lee (17) summarize the radiative properties of flame environments, Faeth and coworkers discuss the radiation properties of turbulent flames (18,19), and Goody (20) and Ludwig et al. (21) consider computations of the radiative properties of gases and particles. Thus, the following review of earlier work will be limited to three issues relating to luminous turbulent flames, as follows: scalar structure, excluding soot; soot properties; and turbulence/radiation interactions.

The laminar flamelet concept has been successful for estimating the scalar properties needed to predict radiation for nonluminous turbulent diffusion flames, as noted earlier. The concept is based on the observations of Bilger (11) and Liew et al. (12,13) that the concentrations of major gas species are nearly universal functions of mixture fraction (the fraction of mass which originated from the burner) within laminar diffusion flames. Some variation of these functions, termed state relationships (2), are observed in regions of high flame stretch, associated with points of flame attachment and extinction (12,13). Minor gas species, like radicals and pollutants, also display less tendency for universal state relationships (22). However, regions of attachment and extinction are generally only a small fraction of most flame fields, and minor gas species generally have little effect on flame radiation properties; therefore, these exceptions still leave a significant range of conditions where the state relationships can provide a useful connection between scalar properties and mixture fractions. The laminar flamelet concept is applied to turbulent flames by assuming that turbulent flames correspond to wrinkled laminar flames, and have the same state relationships. When this approach is appropriate, the difficulties of complex flame chemistry in turbulent environments are replaced by relatively routine analysis or measurements for laminar flames having the same initial and ambient states as the turbulent flames.

State relationships for major gas species have been prepared for laminar nonhydrocarbon fuels, and for weakly sooting hydrocarbon fuels, all burning in air, as follows: hydrogen (7,11), carbon monoxide (6), methane (2,8,11), propane (3) and n-heptane (11). Local thermodynamic equilibrium is generally observed for the nonhydrocarbon fuels and in the fuel-lean region for the hydrocarbon fuels. However, hydrocarbon fuels depart significantly from local thermodynamic equilibrium for fuel-rich conditions, due to slow chemical processes associated with fuel decomposition, soot formation and soot oxidation. Nevertheless, scalar properties still correlated reasonably well for weakly sooting hydrocarbons, providing the state relationships needed for use of the laminar flamelet concept (2,3,8,11).

In view of the added complexities of soot chemistry, extension of the laminar flamelet concept, if appropriate, would be particularly valuable for finding the scalar properties needed to analyze the radiation properties of luminous (soot-containing) turbulent flames. Flame radiation is predominantly in the infrared, at wavelengths longer than 1000 nm, while soot particles are generally smaller than 100 nm; therefore, the Rayleigh limit for small particles is acceptable for estimating the spectral absorption coefficients of soot and scattering can be ignored (17). In this situation, the only soot properties needed for radiation analysis are the refractive indices and volume fractions of soot. The refractive indices of soot are relatively independent of the original fuel, and values have been reported in the literature (17,23). Thus, soot volume fractions are the soot property that must be found from flame structure predictions, in order to analyze radiation from luminous flames.

Several earlier studies of soot containing turbulent flames (24-27) provide some evidence that soot volume fractions might be correlated with mixture fractions, yielding soot volume fraction state relationships for a useful range of flame conditions. Kent and Bastin (24) observed that soot concentrations within turbulent acetylene/air diffusion flames become relatively independent of residence time, for sufficiently-long residence times, suggesting that a quasi-equilibrium condition typical of a correlation between soot properties and mixture fraction was being approached. Later, Kent (25) found that characteristic soot volume fractions (a parameter related to maximum soot volume fractions in a turbulent flame) were relatively independent of fuel residence times for sufficiently long residence times; and were related to the same parameter found in laminar flames for a variety of fuels. Becker and Liang (26,27) studied turbulent sooting flames for a wide range of conditions. They found that the soot generation efficiency (defined as the mass percentage of fuel carbon which was converted to soot and emitted from the flames) also became relatively independent of flame conditions for sufficiently-long residence times. Based on these observations, it seems worthwhile to pursue whether state relationships are observed for scalar properties, including soot volume fractions, in soot-containing turbulent diffusion flames.

Another issue concerning the radiation properties of luminous turbulent diffusion flames involves effects of turbulence/radiation interactions. Mean scalar properties are generally used to compute flame radiation; however, turbulent fluctuations make this practice questionable since radiation properties are nonlinear. Assuming a gray gas, Cox (28) finds that radiance values can be more than twice predictions based on mean temperature. Kabashnikov and Kmit (29) treat combined effects of fluctuating absorption coefficient and temperature, reaching similar conclusions. Past work in this laboratory, examined effects of turbulence/radiation interactions for nonluminous flames, yielded a more complex outcome (1-8). Radiation predictions for stochastic simulation of scalar properties along a path were compared with predictions based on time-averaged scalar properties along the path. Findings indicated relatively small effects of turbulence/radiation interactions for carbon monoxide/air (6) and methane/air (4,8) flames, while effects comparable to (28,29) were observed for hydrogen/air (7) flames. Grosshandler and Vantelon (30) similarly find large effects of turbulence/radiation interactions, using stochastic simulations with prescribed probability density functions of scalar properties along the radiation path, for both nonluminous and luminous turbulent diffusion flames. Based on these findings, turbulence/radiation interactions appear to be appreciable for turbulent diffusion flames; prompting further consideration of the phenomenon during the present investigation.

The objectives of the present investigation were to examine whether state relationships needed for use of the laminar flamelet concept existed for a useful range of flame conditions, and to evaluate effects of turbulence/radiation interactions, in luminous turbulent diffusion flames. Ethylene/air and acetylene/air flames were studied, since these fuels provide strongly luminous flames which have been considered by others (24-27,31-33). Flame structure and radiation measurements were completed, and compared with predictions based on methods developed during earlier studies of nonluminous flames (1-8). Auxiliary measurements in laminar flames, to find state relationships, are also reported.

The paper begins with descriptions of experimental and theoretical methods, including the measurement of state relationships. This is followed by comparison of predictions and measurements of flame structure for the turbulent flames. The paper concludes with consideration of predicted and measured radiant absorption and emission properties.

2. EXPERIMENTAL METHODS

Test Apparatus. The turbulent flame apparatus was identical to the arrangement used to study nonluminous flames (1-8). The fuels were injected vertically upward from a round burner passage having an exit diameter of 5 mm. The flames burned within a screened enclosure, in order to reduce effects of room disturbances. The flames were attached at the burner exit, using a small coflow of hydrogen, similar to Becker and Liang (26,27).

The laminar flame apparatus involved vertical upflow of coflowing fuel and air, similar to the arrangement used by Santoro et al. (31). Fuel flowed from the central tube (14.3 mm diameter) while air flowed from a concentric outer tube (102 mm diameter). Both passages contained layers of beads and honeycomb to insure uniform flow at the burner exit. The flow field was shielded by a 115 mm diameter quartz cylinder, surmounted by a fine-mesh screen, to reduce effects of drafts.

Test Conditions. Table 1 provides a summary of test conditions for the turbulent flames. Two flames (each) were considered for ethylene and acetylene. All flows had relatively high Reynolds numbers and were turbulent at the burner exit. Initial Richardson numbers were relatively low; however, effects of buoyancy were still important.

The flames are similar to the longer residence time flames studied by Becker and Liang (26,27); corresponding to Richardson ratios on the order of 10^3, or characteristic residence times of 90-160s (based on definitions of these parameters of Becker and Liang). Thus, the present flames are in the plateau region observed in (26,27), where radiative heat loss fractions and soot generation efficiencies are nearly independent of the burner flow rate.

Instrumentation. The following measurements were made in the turbulent flames: mean and fluctuating streamwise velocities, mean concentrations of major gas species, laser extinction, soot volume fractions, spectral radiation intensities, and radiative heat fluxes. Velocities were measured across the burner exit (x/d = 2), at [illegible] the axis, using a single-channel laser-Doppler anemometer. These measurements were time averages, with uncertainties 95 percent confidence) less than 5 percent for mean velocities and less than 10 percent for velocity fluctuations (14,15).

Mean concentrations of major gas species in the turbulent flames were measured by sampling with a 6.3 mm diameter water-cooled probe and analysis with a gas chromatograph. At high soot concentrations, the probe tended to clog with deposited soot: measurements at such conditions are not reported in the following. Uncertainties in mean species concentrations (95 percent confidence) are less than 15 percent in the flaming region, but are higher in the overfire region as combustion product concentrations become small (14-16). Concentration measurements were similar in the laminar flames, except that a quartz microprobe having an inlet diameter of 0.1-0.2 mm, operating with choked flow at the inlet, was used to obtain better spatial resolution.

Mixture fractions were computed from the species concentration measurements, based on the measured concentrations of carbon and oxygen while assuming that carbon/hydrogen ratios were preserved throughout the flow field. Uncertainties in mean mixture fractions (95 percent confidence) were ~ 20, ~ 50 and ~ 100 percent at f = 0.04, 0.004 and 0.0005 (16).

Laser extinction measurements (514.5 and 632.8 nm) were used to study absorption by soot in the turbulent flames. Uncertainties in these measurements (95 percent confidence) are less than 10 percent (14,15)

Laser extinction measurements were also used to measure soot volume fractions in the laminar flames, following the deconvolution technique reported by Santoro et al. (31). The refractive index correlation of Dalzell and Sarofim (23) was used during these calculations. Uncertainties in these measurements (95 percent confidence) are estimated to be less than 20 percent (14,15).

Turbulent fluctuations had only a small effect on laser extinction measurements for the present flames; therefore, the extinction measurements were deconvoluted to provide time-averaged soot volume fractions in the turbulent flames. Uncertainties (95 percent confidence) are as follows: acetylene, 15 percent at 4 ppm and 300 percent at 0.06 ppm; ethylene, 20 percent at 0.5 ppm and 300 percent at 0.004 ppm. Uncertainties are roughly proportional to soot volume fractions in the intervening region.

Spectral radiation intensities were measured with a monochromator, viewing roughly 10 mm diameter (1.2° field angle) horizontal paths through the axis of the flames. A combination of gratings and order-sorting filters provided observations in the 1200-5500 nm wavelength range with resolutions of 80 and 230 nm at the low and high ends of this range. Uncertainties of these measurements (95 percent confidence) were less than 15 percent.

Radiative heat fluxes were measured at points around the turbulent flames using a gas-purged, water-cooled radiometer (150° viewing angle with a sapphire window which attenuates radiation having wavelengths longer than 5500 nm). Uncertainties of these measurements (95 percent confidence) were less than 10 percent (14,15).

3. THEORETICAL METHODS

Flame Structure. Analysis of flame structure and radiation properties was similar to methods used for nonluminous flames (1-8). Major assumptions of the structure analysis are as follows: low Mach number boundary-layer flow with no swirl; equal exchange coefficients of all species and heat; buoyancy only affects the mean flow; and negligible radiant energy exchange between various portions of the flame. Except for the last, these assumptions are either justified by the test conditions or by acceptable performance for similar diffusion flames. The present flames, however, lose an unusually large fraction of their chemical energy release by radiation (30-60 percent), suggesting significant energy exchange within the flames as well. Nevertheless, the assumption was adopted, as a first approximation, to avoid the complications of combined structure and radiation analysis. Under these assumptions, the conserved-scalar formalism can be used, relating all scalar properties to the mixture fraction through the laminar flamelet state relationships.

Turbulence properties were found using the Favre-averaged formulation of Bilger (10), but with specific modifications and empirical constants due to Jeng and Faeth (2). The governing equations can be written in the following generalized form (2):

$$r\,\partial/\partial x(\bar{\rho}\tilde{u}\tilde{\phi}) + \partial/\partial r(r\bar{\rho}\tilde{v}\tilde{\phi}) = \partial/\partial r(r\mu_{eff,\phi}\,\partial\tilde{\phi}/\partial r) + r\,S_\phi \qquad (1)$$

where $\phi = 1, \tilde{u}, \tilde{f}, k, \varepsilon$, or g. The formulation is based on Favre (mass-weighted)-averaged quantities, defined as follows (10):

$$\tilde{\phi} = \overline{\rho\phi}/\bar{\rho} \qquad (2)$$

where the overbar represents a conventional time average. Expressions for $\mu_{eff,\phi}$ and S_ϕ appearing in Eqs. (1) are summarized in Table 2, along with all empirical constants. The constants were established by matching predictions and measurements for constant and variable density round jets (2); however, they are not much different from values originally proposed by Lockwood and Naguib (9) for round-jet flames.

Under present assumptions, instantaneous scalar properties are only functions of the instantaneous mixture fraction through the state relationships $\phi(f)$. Given $\phi(f)$, the Favre-averaged mean and variance of scalar flow properties are found from the mass-averaged (Favre) probability density function of f, $\tilde{P}(f)$, as described by Bilger (10). For example, the expression for $\tilde{\phi}$ is as follows:

$$\tilde{\phi} = \int_0^1 \phi(f)\,\tilde{P}(f)df \qquad (3)$$

Noting that the time-averaged probability density function of f, $\overline{P}(f)$, is given by

$$\overline{P}(f) = \overline{\rho}\,\widetilde{P}(f)/\rho(f) \tag{4}$$

under present assumptions, time-averaged scalar properties become (10):

$$\overline{\phi} = \overline{\rho}\int_0^1 (\phi(f)/\rho(f))\,\widetilde{P}(f)df \tag{5}$$

The value of $\overline{\rho}$, needed to integrate Eqs. (1), can be found by setting $\phi = 1$ in Eq. (5). Predictions are not very sensitive to the functional form chosen for $\widetilde{P}(f)$; a clipped Gaussian function was used, similar to past work (1-9). The most probable value and variance of $\widetilde{P}(f)$ are found from the following identities:

$$\widetilde{f} = \int_0^1 f\,\widetilde{P}(f)df; \qquad g = \int_0^1 (f-\widetilde{f})^2\,\widetilde{P}(f)df \tag{6}$$

where both $\widetilde{f}$ and g are known from the solution of Eqs. (1).

The prescription of initial and boundary conditions, and numerical solution of the equations was similar to earlier work (1-8) and is described elsewhere (14,15).

State Relationships. State relationships for major gas species for the acetylene/air and ethylene/air diffusion flames were obtained from measurements in the laminar flames. The concentrations of major gas species for acetylene are plotted as a function of fuel equivalence ratio (a single-valued function of mixture fraction) in Figs. 1 and 2. Various radial positions, axial positions and burner flow rates were considered, but only the last variable is identified to reduce clutter of the figures. Predictions based on the assumption of local thermodynamic equilibrium (assuming no solid carbon present and adiabatic combustion) also appear on the figures; these results were obtained using the Gordon and McBride (35) code. The measurements approximate local thermodynamic equilibrium for fuel-lean conditions, but depart appreciably from local thermodynamic equilibrium for fuel-rich conditions. However, properties in the rich region still yield reasonably universal correlations as a function of fuel-equivalence ratio, providing state relationships needed for the laminar flamelet approximation.

State relationships for major gas species for ethylene/air diffusion flames are illustrated in Fig. 3. The results for this fuel are very similar to acetylene, as well as to earlier findings for more weakly sooting hydrocarbon/air diffusion flames (2,3,8,11).

State relationships for soot volume fractions were studied using measurements in laminar diffusion flames and in the overfire (lean) region of the turbulent diffusion flames. Findings for acetylene are illustrated in Fig. 4. Consider the results for the laminar flames first. The highest concentrations of soot are confined to a relatively narrow range of mixture fractions, yielding a soot spike just on the fuel-rich side of the stoichiometric condition. The spike appears due to the competition between soot formation, for rich conditions, and soot oxidation, as stoichiometric conditions are approached. Species concentrations could not be measured in the soot spike; therefore, mixture fractions were estimated by interpolating plots of mixture fraction as a function of radial distance for a given height above the burner. The uncertainty of this procedure is highest near the burner exit. Except for results at the lowest positions (x = 14 and 16 mm), where finite-rate chemistry and errors in the interpolation procedure may be factors, the results are crudely universal, although the correlation is clearly not as good as for major gas species, illustrated in Figs. 1 and 2. However, the divergence from universality of the laminar measurements illustrated in Fig. 4 was not felt to be large in view of experimental uncertainties and the status of current capabilities for predicting soot concentrations in turbulent flames. Therefore, a correlation of the soot volume fraction state relationship for fuel-rich conditions was fitted by averaging data at each mixture fraction – excluding results at the lowest two positions – as shown in Fig. 4.

For acetylene, the highest Reynolds number laminar flame and the turbulent flames were all sooting; therefore, state relationships must also be found for fuel-lean conditions. Measurements in the overfire region of the turbulent flames, illustrated in Fig. 4, were used to find this portion of the state relationship. Within experimental uncertainties, shown as brackets on the figure, the results suggest that reaction of soot is quenched at a particular soot volume fraction and mixture fraction, followed by passive mixing of soot in the lean region. This implies a constant volumetric soot generation coefficient (defined as the volume of soot emitted from the flame per unit mass of carbon in the fuel), yielding the correlation of the lean portion of the state relationship (called the soot mixing region) illustrated in Fig. 4.

Relating time-averaged measurements in a turbulent flame to instantaneous properties associated with a state relationship is questionable; therefore, potential effects of turbulent fluctuations are illustrated in Fig. 4, by cross-plotting predictions of time-averaged soot volume fractions (based on the state relationship) as a function of Favre-averaged mixture fractions (which approximates sampling), in an attempt to simulate the measurements. There was little effect of burner Reynolds number or height above the burner on this correlation for acetylene; therefore, a single predicted line serves all the measurement conditions. This line merges with the state relationship for very lean conditions, where effects of turbulent fluctuations are small, but is biased above the state relationships as stoichiometric conditions are approached, due to the presence of the soot spike. In general, the measurements exhibit similar trends.

Results concerning the soot volume fraction state relationships for ethylene are illustrated in Fig. 5. The laminar results for fuel-rich conditions are similar to acetylene, exhibiting a large soot spike. These results are crudely universal, with greatest departures seen for the lowest positions, where finite-rate chemistry and the extrapolation procedure to find mixture fractions may be factors. These findings were correlated similar to acetylene, including a soot mixing region for lean conditions, as shown in the figure.

Measurements for the lower Reynolds number turbulent ethylene flame, illustrated for lean conditions in Fig. 5, are similar to the findings for acetylene. The results fall along the soot volume fraction state relationship for low mixture fractions, where effects of turbulent fluctuations are small. As the mixture fraction increases toward stoichiometric, the measurements are biased upward from the state relationships, similar to the turbulent flame predictions. In this case, the predictions indicate a much larger effect of biasing due to turbulent fluctuations, and greater variation of the degree of biasing with burner Reynolds number and height above the burner, since the soot spike is much higher in comparison to soot concentrations in the lean region for ethylene than for acetylene. This behavior may be responsible for the larger degree of data scatter as stoichiometric conditions are approached for the low Reynolds number turbulent flame.

In contrast, the results for the high Reynolds number ethylene flame, illustrated in Fig. 5, exhibit much less conformity to the soot volume fraction state relationship in the soot mixing region. Even at low mixture fractions, where effects of turbulent

fluctuations are small, the scatter of the measurements exceeds experimental uncertainties. This behavior could indicate failure of the laminar flamelet concept for soot volume fractions due to effects of finite-rate chemistry. The high Reynolds number turbulent ethylene flame has the shortest characteristic residence time of all the turbulent flames; while Becker and Liang (26,27) find that larger characteristic residence times are needed to reach the plateau region for soot generation efficiencies for ethylene than acetylene. Since characteristic residence times vary for different paths through the flame, this would imply different soot volume fractions when soot oxidation is quenched; and different correlations of soot volume fractions as a function of mixture fraction during passive mixing in the lean portion of the flame. Thus, results illustrated in Fig. 5 suggest potential for a soot volume fraction state relationship for sufficiently long characteristic residence times, with possible breakdown of this condition for the high Reynolds number flame. More precise experimental results are needed to confirm this conjecture; for lack of an alternative, however, the correlation illustrated in Fig. 5 was used for subsequent radiation calculations.

Flame Radiation. Spectral radiation intensities were found using the Goody statistical narrow band model with the Curtis-Godson approximation for inhomogeneous gas paths, following Ludwig et al. (21). This involves solving the equation of radiative transfer

$$\partial I_\lambda / \partial s = \rho K_\lambda ((e_{\lambda b} / \pi) - I_\lambda \qquad (7)$$

along a path through the flame. All paths eminated from a cold boundary; therefore, I_λ (0) was negligible. The computer program RADCAL, developed by Grosshandler (36), was used for these calculations; considering the gas bands of CO_2, CO, H_2O and CH_4, as well as continuum radiation from soot at the small-particle limit.

Turbulence radiation interactions were either ignored, by basing predictions on time-averaged mean scalar properties evaluated from Eq. (5); or considered, using a stochastic method due to Jeng et al. (4). The stochastic method involved dividing the radiation path into dissipation-scale sized eddies, as follows (37):

$$L_e = C_\mu^{3/4} k^{3/2} / \varepsilon \qquad (8)$$

Each eddy was assumed to have uniform properties at each instant. The probability density function of mixture fraction for each eddy was randomly sampled to provide a realization of scalar properties along the path, in conjunction with the state relationships. Spectral radiation intensities were then computed for each realization, similar to the mean-property method, averaging sufficient realizations to obtain the time-averaged spectral intensity. All properties needed for the stochastic solution are available from the structure analysis; therefore, the procedures is closed (4).

Radiative heat fluxes were computed using the mean-property method, in conjunction with the discrete-transfer approach of Lockwood and Shah (38). This involved summing spectral intensities for 120 paths through the flame, to cover the field of view of the sensor; and for the wavelength range having significant radiance, after allowing for the cut-off of the sapphire window of the sensor (500 - 5500 nm).

4. RESULTS AND DISCUSSION

Flame Structure. Only a sample of predictions and measurements of flame structure will be considered, in order to indicate the capabilities of the structure analysis. Additional results can be found in (14-16). Predicted and measured mixture fraction distributions for the turbulent acetylene/air flames are illustrated in Fig. 6. Results are plotted as a function of r/x at various heights above the burner exit. The flame tips (based on the location of the mean stoichiometric mixture fraction along the axis) are reached at x/d ~ 75 and 80 for the low and high Reynolds number flames. Favre-averaged predictions are shown, however, the differences between Favre- and time-averaged mixture fractions are less than 15 percent. The degree of density weighting of the measurements is unknown. The agreement between predictions and measurements is reasonably good, typical of similar comparisons for nonluminous flames (1-8). Largest discrepancies are observed at x/d = 130 for the low Reynolds number flame; they are probably due to ambient disturbances that are difficult to control for strongly-buoyant flows far from the burner exit.

Predicted and measured mean and fluctuating streamwise velocities and mean gas species concentrations along the axis of the high Reynolds number acetylene flame are illustrated in Fig. 7. Time-averaged velocities were measured, while the analysis only provides Favre-averaged velocities; differences between these averages are less than 10 percent for mean velocities, but time-averaged velocity fluctuations can be up to 40 percent greater than Favre averages near the flame tip (22). Furthermore, $\tilde{u}''$ has been estimated from k assuming isotropic turbulence; for typical levels of anisotropy near the axis of turbulent diffusion flames, $\tilde{u}''$ would be roughly 20 percent higher (22). In view of these considerations, the comparison between predicted and measured velocities is reasonably good. The analysis provides both Favre- and time-averaged values of mean scalar properties but differences between the two are not large. The comparison between predictions and measured species concentrations is reasonably good, typical of results for nonluminous flames (1-8), suggesting comparable performance of the state relationships for gas concentrations for the heavily sooting acetylene flame.

Predicted and measured time-averaged soot volume fractions in the turbulent acetylene flames are illustrated in Fig. 8. Trends with respect to position and Reynolds number are predicted reasonably well, using the single soot volume fraction state relationship. The greatest differences between predictions and measurements are observed near the edge of the flow at x/d = 53. This could be due to the mixing analysis, since mixture fraction widths are underestimated at this position, see Fig. 6. However, similar to the laminar flames, soot levels in the lean region may be lower than the state relationship for positions relatively near the burner.

Results for the ethylene flames were similar, aside from somewhat poorer predictions of mixing levels, indicated by the mixture fraction distributions. The state relationships for gas species performed reasonably well. Predictions of soot volume fractions were also reasonably good, in spite of the significant data scatter seen in Fig. 5 for the correlation of the soot volume fraction state relationship. Taken together, the structure predictions were sufficiently encouraging to proceed with consideration of flame radiation properties, discussed next.

Monochromatic Transmittivities. Predictions and measurements of laser extinction by soot, for the high Reynolds number turbulent acetylene flame, are illustrated in Fig. 9. Measurements at 514.5 and 632.8 nm are consistent with the reciprocal-wavelength dependence of extinction coefficients at the small-particle limit, justifying this approximation in the analysis. Three sets of predictions for extinction at 632.8 nm are shown: (1) the stochastic method with the complete soot volume fraction state relationship, denoted STOCH, B.T.; (2) the stochastic method, but ignoring the soot mixing region of the soot volume fraction state relationship, denoted STOCH, N.B.T.; and (3) the mean-property method with the complete soot volume fraction state relationship, denoted MEAN, B.T. The stochastic and mean-property predictions using the complete soot volume fraction state relationship are nearly the same, indicating small effects of turbulence/radiation interactions for extinction by soot. The role of soot in the lean region can be seen by comparing results with and without the soot mixing portion of the state relationships. Results at the upper positions

show that neglecting the soot-mixing region causes substantial underestimation of extinction. In contrast, measurements at the lowest position are better represented by omitting the soot mixing region, which could be an indication that the turbulent flames do not emit much soot into the lean region, near their base, similar to the laminar flames.

Predictions and measurements of laser extinction by soot, for the high Reynolds number turbulent ethylene flame, are illustrated in Fig. 10. These results are for 632.8 nm, with predictions using the complete soot volume fraction state relationship. Like acetylene, there is little difference between predictions using the mean property and stochastic methods, suggesting small effects of turbulence/radiation interactions for extinction. Also, similar to acetylene, predictions underestimate transmittivities near the burner, which may indicate lower levels of soot emission into the lean region than positions nearer the tip of the flame. However, recalling that this flame exhibited poorer agreement with the soot volume fraction state relationships than all the other flames, see Fig. 5, the comparison between predictions and measurements is encouraging.

Spectral Radiation Intensities. Measurements and predictions of spectral radiation intensities, for the high Reynolds number turbulent acetylene flame, are illustrated in Fig. 11. These results are for horizontal paths through the axis of the flame, at locations before, near, and after the flame tip (which is at $x/d \approx 70 - 80$). Predictions are based on the complete soot volume fraction state relationship, both ignoring and considering effects of turbulence/radiation interactions.

The spectra in Fig. 11 are dominated by continuum radiation from soot, however, gas bands at 1140, 1870, 2700 and particularly 4300 nm can still be seen. Differences between mean property and stochastic predictions suggest significant effects of turbulence/radiation interactions, with stochastic predictions being 40-100 percent higher than mean property predictions near peak spectral intensities in the continuum portions of the spectra. Since the extinction results exhibited little effects of turbulence/radiation interactions, the nonlinearity of the Planck function with temperature is probably the main cause of this behavior. The comparison between predictions and measurements is encouraging, particularly for the stochastic approach. Discrepancies are largest at the highest position, where inaccuracies in the temperature predictions are probably responsible for the problem (15). This region is generally fuel-lean for the entire optical path; therefore, the flow tends to absorb energy emitted from high temperature regions, since it contains appreciable concentrations of soot and other absorbers in the infrared. Thus, actual temperatures are probably greater than present predictions, which are based on the assumption that a uniform fraction of the chemical energy release is lost from all portions of the flame. Furthermore, spectral intensities in the continuum are very sensitive to flow temperatures in this region: for example, a 5 percent temperature increase caused roughly a 50 percent increase of the spectral intensity at 1770 nm. Such effects are most apparent when the flame has a high radiative heat loss fraction (59 percent in this case), suggesting significant energy exchange by radiation within the flame as well. Coupled structure and radiation analysis are required to remove this deficiency.

Measurements and predictions of spectral radiation intensities, for the high Reynolds number turbulent ethylene flame, are illustrated in Fig. 12. Similar to acetylene, spectral intensities for horizontal paths through the flame axis are shown, at locations before, near and after the flame tip (which is at $x/d = 90 - 100$). While the spectra are still dominated by continuum radiation from soot, the gas bands are more prominent than for acetylene, since ethylene has much lower soot concentrations. The agreement between the stochastic predictions and the measurements are somewhat better for ethylene than for acetylene, even though the correlation of the soot volume fraction state relationship was poorest for this ethylene flame, cf. Figs. 4 and 5. This is probably due to lower levels of radiant energy exchange within the ethylene flame, due to its lower radiative heat loss fraction, which is more representative of the approximations of the analysis. Differences between mean property and stochastic predictions suggest significant effects of turbulence/radiation interactions in the ethylene flame, similar to acetylene.

Radiative Heat Fluxes. Measurements and predictions (using the mean property method) of radiative heat flux distributions near the turbulent ethylene flames are illustrated in Fig. 13. These results are for a detector facing the flame axis and traversing vertically at a distance of 575 mm from the axis. Radiative heat fluxes are highest near the flame tip (ca. $x = 500$ mm or $x/d = 100$ for the high Reynolds number flame, and slightly nearer to the burner exit for the low Reynolds number flame). Reducing the Reynolds number causes predicted radiative heat fluxes to drop in a proportional manner, even though the state relationships for scalar properties are taken to be the same for both flames. This is due to the smaller dimensions of the lower Reynolds number flame, caused by increased effects of buoyancy. The mean property method tends to underestimate the measurements, while predicting trends with respect to position and burner Reynolds number reasonably well. This behavior follows from the performance of this approach concerning spectral radiation intensities, suggesting that use of the stochastic method would yield better quantitative agreement with measurements. Other findings concerning radiative heat fluxes in the present luminous flames yield similar conclusions (14, 15).

5. CONCLUSIONS

Major conclusions of the study are as follows:

1. Consideration of both laminar and turbulent flames suggests nearly universal state relationships for major gas species concentrations in soot-containing ethylene/air and acetylene/air diffusion flames.

2. State relationships for soot volume fractions in the laminar and turbulent flames were much less universal than gas concentrations, particularly at short residence times where effects of finite rate kinetics were noted. Nevertheless, use of universal soot volume fraction state relationships for each fuel yielded encouraging predictions of flame radiation properties, while circumventing the complexities of soot chemistry in a turbulent flame environment. Further evaluation of the concept, for a wider range of fuels and flame conditions, appears to be warranted.

3. Effects of turbulence/radiation interactions were significant for radiation emission from soot, but were not very important for radiation absorption in the visible, based on comparison of mean-property and stochastic predictions.

4. The performance of predictions of scalar structure for the luminous flames were similar to earlier findings for nonluminous flames (1-8). However, radiation predictions for acetylene flames were generally poorer than for the nonluminous flames, or even the luminous ethylene flames. The main reason for this behavior is the high radiative heat loss fraction for acetylene flames (ca. 60 percent). This implies significant energy exchange within the flames, which is not considered in the current analysis. Coupled structure and radiation analysis should be considered to remove this deficiency.

REFERENCES

1. Jeng, S.-M., Chen, L.-D. and Faeth, G.M. The Structure of Buoyant Methane and Propane Diffusion Flames. Nineteenth Symposium (International) on Combustion. The Combustion Institute, Pittsburgh, 1982, pp. 349-358.

2. Jeng, S.-M. and Faeth, G.M. Species Concentrations and Turbulence Properties in Buoyant Methane Diffusion Flames. J. Heat Transfer, Vol. 106, 1984, pp. 721-727.

3. Jeng, S.-M. and Faeth, G.M. Predictions of Mean Scalar Properties in Turbulent Propane Diffusion Flames. J. Heat Transfer, Vol. 106, 1984, pp. 891-893.

4. Jeng, S.-M., Lai, M.-C. and Faeth, G.M. Nonluminous Radiation in Turbulent Buoyant Axisymmetric Flames. Comb. Sci. and Tech., Vol. 40, 1984, pp. 41-53.

5. Jeng, S.-M. and Faeth, G.M. Radiative Heat Fluxes Near Turbulent Buoyant Methane Diffusion Flames. J. Heat Trans., Vol. 106, 1984, pp. 886-888.

6. Gore, J.P., Jeng, S.-M. and Faeth, G.M. Spectral and Total Radiation Properties of Turbulent Carbon Monoxide/Air Diffusion Flames. AIAA J., Vol. 25, 1987, pp. 339-345.

7. Gore, J.P., Jeng, S.-M. and Faeth, G.M. Spectral and Total Radiation Properties of Turbulent Hydrogen/Air Diffusion Flames, J. Heat Transfer, Vol. 109, 1987, pp. 165-171.

8. Gore, J.P., Faeth, G.M., Evans, D. and Pfenning, D. Structure and Radiation Properties of Large-Scale Natural Gas/Air Diffusion Flames. Fire and Materials, in press.

9. Lockwood, F.C. and Naguib, A.S. The Prediction of the Fluctuations in the Properties of Free, Round-Jet Turbulent Diffusion Flames. Combustion and Flame, Vol. 24, 1975, pp. 109-124.

10. Bilger, R.W. Turbulent Jet Diffusion Flames. Prog. Energy Combust. Sci., Vol. 1, 1976, pp. 87-109.

11. Bilger, R.W. Reaction Rates in Diffusion Flames. Combustion and Flame, Vol. 30, 1977, pp. 277-284.

12. Liew, S.K., Bray, K.N.C. and Moss, J.B. A Flamelet Model of Turbulent Non-Premixed Combustion. Comb. Sci. and Tech., Vol. 27, 1981, pp. 69-73.

13. Liew, S.K., Bray, K.N.C. and Moss, J.B. A Stretched Laminar Flamelet Model of Turbulent Nonpremixed Combustion. Combustion and Flame, Vol. 56, 1984, pp. 199-213.

14. Gore, J. P. and Faeth, G.M. Structure and Spectral Radiation Properties of Turbulent Ethylene/Air Diffusion Flames. Twenty-First Symposium (International) on Combustion, The Combustion Institute, Pittsburgh, in press.

15. Gore, J.P. and Faeth, G.M. Structure and Radiation Properties of Luminous Turbulent Acetylene/Air Diffusion Flames. J. Heat Transfer, in press.

16. Sivathanu, Y.R., Gore, J.P. and Faeth, G.M. Scalar Properties in the Overfire Region of Sooting Turbulent Diffusion Flames. Combustion and Flame, submitted.

17. Tien, C.L. and Lee, S.C. Flame Radiation. Prog Energy Combust. Sci., Vol. 8, 1982, pp. 41-59.

18. Faeth, G.M., Gore, J.P., Chuec [illegible] S. and Jeng, S.-M. Radiation from Turbulent Diffusion Flames. Ann. Rev of Numerical Fluid Mechanics, Hem[illegible]ere Publishing Corp., Washington, in press.

19. Faeth, G.M. Heat and Mass Transfer in Flames. Eighth International Heat Transfer Conference, Hemisphere Publishing Corp., Washington, Vol. 1, 1986, pp. 151-160.

20. Goody, R.M. Atmospheric Radiation Theoretical Base. Clarendon Press, Oxford, Vol. 1, 1964.

21. Ludwig, C.B., Malkmus, W., Reardon, J.E. and Thomson, J.A. Handbook of Infrared Radiation from Combustion Gases. NASA SP-3080, Washington, 1973.

22. Faeth, G.M. and Samuelsen, G.S. Fast-Reaction Nonpremixed Combustion. Prog. Energy Combust. Sci., Vol. 12, 1986, pp. 305-372.

23. Dalzell, W.H. and Sarofim, A.F. Optical Constants of Soot and Their Application to Heat-Flux Calculations. J. Heat Transfer, Vol. 91, 1969, pp. 100-104.

24. Kent, J.H. and Bastin, S.J. Parametric Effects on Sooting in Turbulent Acetylene Diffusion Flames. Combustion and Flame, Vol. 56, 1984, pp. 29-42.

25. Kent, J.H. Turbulent Diffusion Flame Sooting - Relationship to Smoke-Point Tests. Combustion and Flame, Vol. 67, 1987, pp. 223-233.

26. Becker, H.A. and Liang, D. Total Emission of Soot and Thermal Radiation by Free Turbulent Diffusion Flames. Combustion and Flame, Vol. 44, 1982, pp. 305-318.

27. Becker, H.A. and Liang, D. Soot Emission, Thermal Radiation, and Laminar Instability of Acetylene Diffusion Flames. Combustion and Flame, Vol. 52, 1983, pp. 247-256.

28. Cox, G. On Radiant Heat Transfer from Turbulent Flames. Comb. Sci. Tech., Vol. 17, 1977, pp. 75-78.

29. Kabashnikov, V.P. and Kmit, G.I. Influence of Turbulent Fluctuations on Thermal Radiation. J. Appl. Spect., Vol. 31, 1979, pp. 963-967.

30. Grosshandler, W.L. and Vantelon, J.P. Predicting Soot Radiation in Laminar Diffusion Flames. Comb. Sci. Tech., Vol. 44, 1985, pp. 125-141.

31. Santoro, R.J., Semerjian, H.B. and Dobbins, R.A. Soot Particle Measurements in Diffusion Flames. Combustion and Flame, Vol. 51, 1983, pp. 203-218.

32. Beier, R.A., Pagni, P.J. and Okoh, C.I. Soot and Radiation in Combustion Boundary Layers. Comb. Sci. and Tech., Vol. 39, 1984, pp. 235-262.

33. Newman, J.S. and Steciak, J. Characterization of Particulates from Diffusion Flames. Combustion and Flame, Vol. 67, 1987, pp. 55-64.

34. Magnussen, B.F. An Investigation into the Behavior of Soot in a Turbulent Free Jet C_2H_2 - Flame. Fifteenth Symposium (International) on Combustion. The Combustion Institute, Pittsburgh, 1975, pp. 1415-1425.

35. Gordon, S. and McBride, B.J. Computer Program for Calculation of Complex Chemical Equilibrium Compositions, Rocket Performance, Incident and Reflected Shocks, and Chapman-Jouget Detonations. NASA SP-273, Washington, 1971.

36. Grosshandler, W.L. Radiative Heat Transfer in Nonhomogeneous Gases: A Simplified Approach. Int. J. Heat Mass Trans., Vol. 23, 1980, pp. 1447-1459.

37. Shuen, J.-S., Solomon, A.S.P., Zhang, Q.-F. and Faeth, G.M. Structure of Particle-Laden Jets: Measurements and Predictions. AIAA J., Vol. 23, 1985, pp. 396-404.

38. Lockwood, F.C. and Shah, N.B. A New Radiation Solution Method for Incorporation in General Combustion Prediction Procedures. Eighteenth Symposium (International) on Combustion, The Combustion Institute, Pittsburgh, 1981, pp. 1405-1414

ACKNOWLEDGEMENTS

The research described in this paper was supported by the Center for Fire Research of the National Bureau of Standards, Grant No. 60NAN135D0576, with B.J. McCaffrey serving as NBS Scientific Officer.

Table 1 Summary of Test Conditions[a]

Fuel	Ethylene		Acetylene	
Reynolds number[b]	6,370	12,740	5,300	9,200
u_0 (m/s)[c]	17.0	33.9	10.5	18.1
Heat release rate (kW)	13.5	27.0	10.5	18.1
Radiative heat loss (%)	36.0	34.4	57.0	59.0

[a] Flow discharged vertically upward from of 5 mm diameter round passage in still air. Commercial grade fuels.

[b] $Re = u_0 d/\nu$ based on fuel properties at the burner exit.

[c] Average gas velocity at burner exit.

Table 2 Summary of Turbulence Model Parameters

ϕ	Term	S_ϕ
1	-	0
2	$k - \kappa_k$	$\alpha(P - \varepsilon)$
3	$(\varepsilon - \kappa_\varepsilon) + (\varepsilon_0 - \varepsilon_0)$	0
4	$k - (\rho_0 \varepsilon_0^2)$	$\mu_t (\partial \bar{u}/\partial r)^2$ - $\rho\varepsilon$
5	$k - (\rho_0 \varepsilon_0)$	$(C_{g_1} \mu_t (\partial \bar{u}/\partial r)^2 - C_{g_2} \rho\varepsilon)(\varepsilon/k)$
6	$(\alpha - \alpha_0) - (\rho_0 \varepsilon_0)$	$C_{g_1} \mu_t (\partial^2 \bar{u}/\partial r^2 - C_{g_2} \beta g \sigma_t$

κ_k	κ_ε	κ_α	$C_{g_1} = C_{g_2}$	σ_k	σ_ε	$\sigma_\varepsilon = \sigma_\alpha$	S_α
0.09	1.44	2.8	1.87	1.0	1.3	0.7	0.7

$\kappa_\varepsilon = \kappa_\varepsilon + \kappa_\varepsilon$

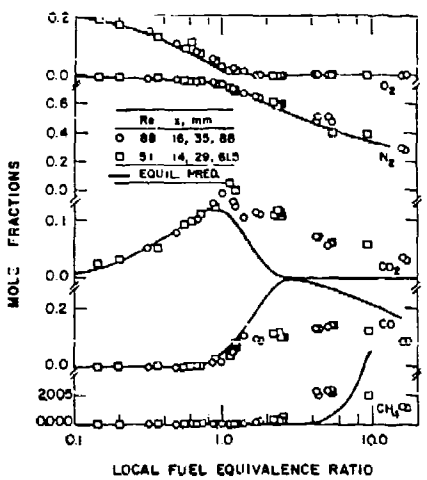

Fig. 1 State relationships for gas species in acetylene/air diffusion flames

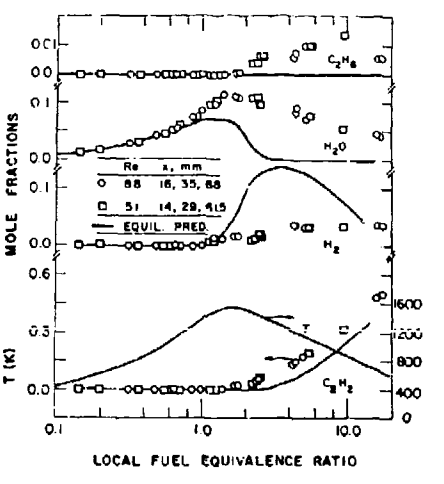

Fig. 2. State relationships for gas species in acetylene/air diffusion flames (continued)

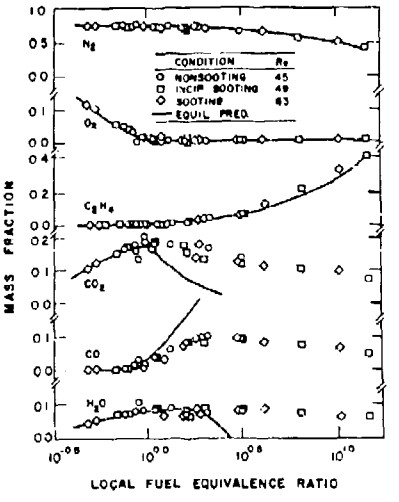

Fig. 3 State relationships for gas species in ethylene air diffusion flames

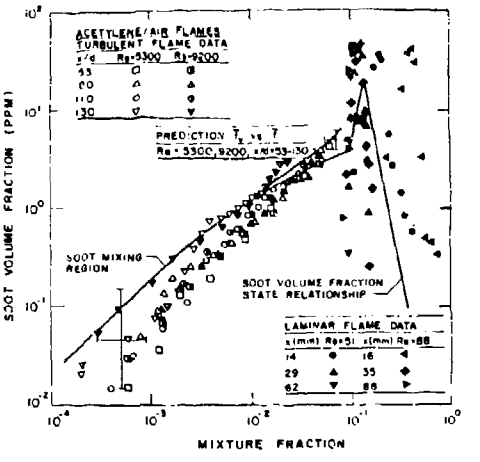

Fig. 4 Correlation between soot volume fractions and mixture fractions for acetylene air diffusion flames

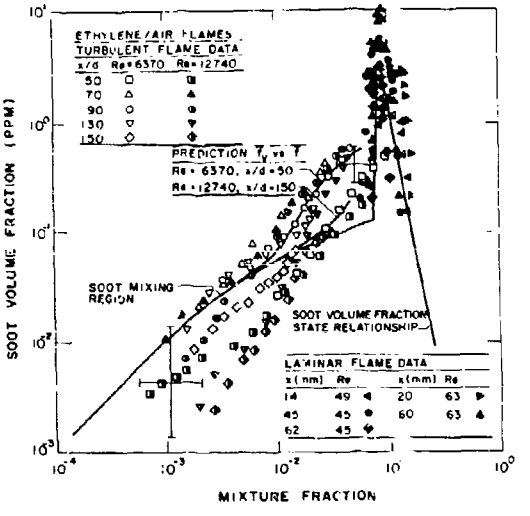

Fig. 5 Correlation between soot volume fractions and mixture fractions for ethylene air diffusion flames

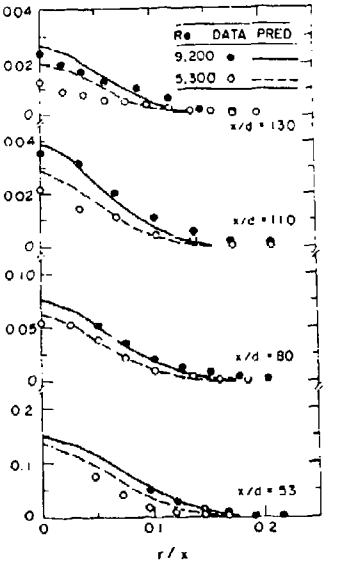

6 Mixture fraction distributions in the acetylene air diffusion flames

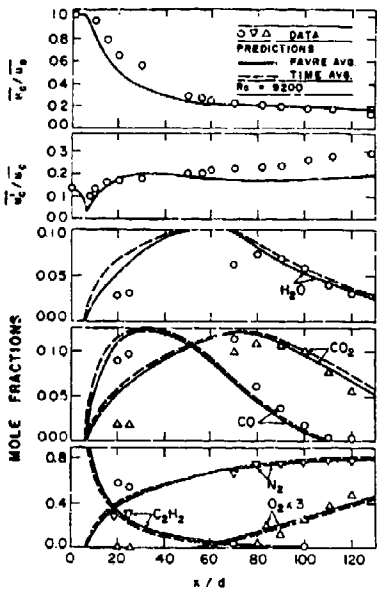

Fig. 7 Structure predictions and measurements along the axis of an acetylene/air diffusion flames. Re = 9200.

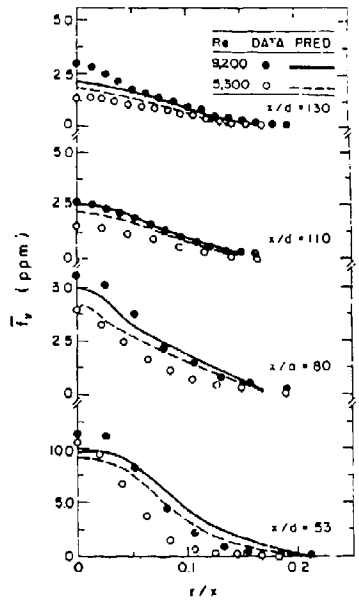

Fig. 8 Soot volume fraction distributions for the acetylene/air diffusion flames.

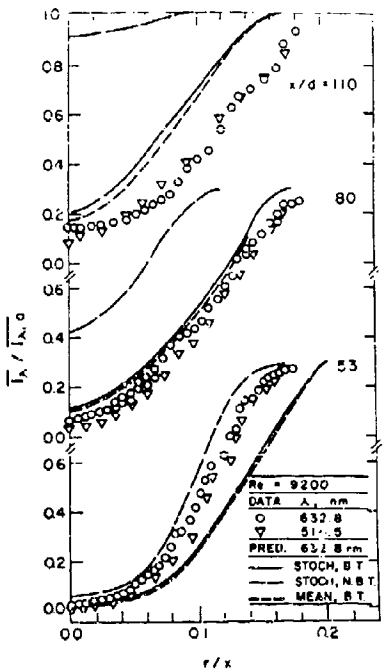

Fig. 9 Monochromatic transmittancies for an acetylene/air diffusion flame. Re = 9200.

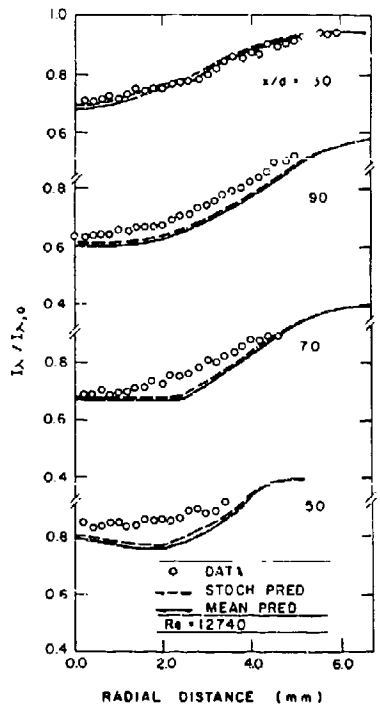

Fig. 10 Monochromatic transmittancies for an ethylene/air diffusion flame. Re = 12740.

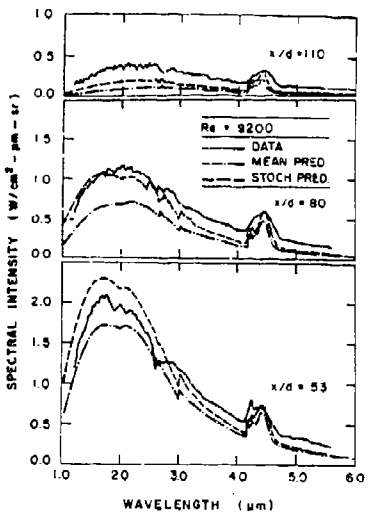

Fig. 11 Spectral radiation intensities for an acetylene/air diffusion flame: Re = 9200.

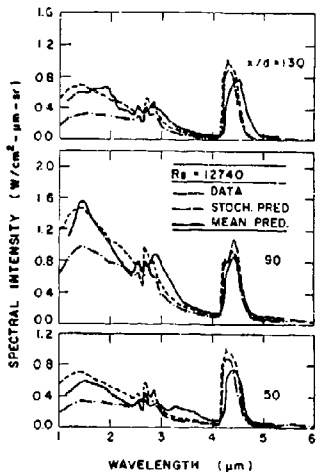

Fig. 12. Spectral radiation intensities for an ethylene/air diffusion flame: Re = 12740.

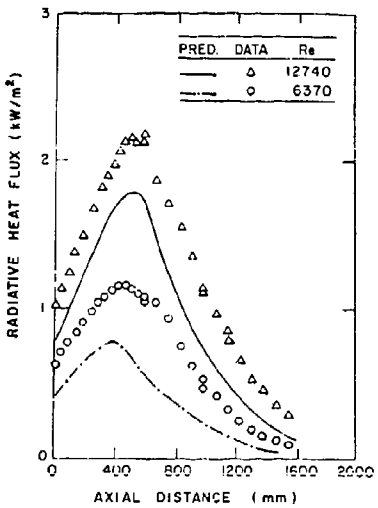

Fig. 13 Total radiative heat flux distributions along the axis of the ethylene/air flames.

DISCUSSION

P.N.Wild, UK
Do you think this type of modelling is applicable to spray combustion problems?

Author's Reply
While I have never used it for spray combustion, I think that it should work, because the spray tends to be located in regions which are quite rich, and are fairly widely separated from the flame zone itself which sets up that chemistry.

J.J.McGuirk, UK
Don't you think it is rather surprising that you can get away with a single scalar description to characterize heat loss?

Author's Reply
I don't really know what the heat loss was from the laminar flames. We have looked at the solution of the enthalpy equation for these flames, and it had little effect on the radiation prediction. We will investigate further.

S.Candel, FR
Do you take the radiative transfer into account when you calculate the temperature profile?

Author's Reply
We assume that every point in the flame loses 60% of the chemical energy released, and based on the knowledge of that enthalpy and the composition you can calculate the temperature.

S.Candel, FR
What happens beyond the tip of the flame? Can you still use the mixture fraction at that point?

Author's Reply
We continue on with the same state relationships.

O.Gulder, CA
Why did you select these two particular fuels, since they are not aviation fuels?

Author's Reply
We took ethylene because there were considerable data from other investigators, and acetylene because it is inexpensive and much data is available also.

FLAMELET CHEMISTRY MODELLING OF SOOT FORMATION FOR RADIATION PREDICTION IN COMBUSTOR FLOW FIELDS

Moss, J.B., Stewart, C.D and Syed, K.J.

School of Mechanical Engineering,
Cranfield Institute of Technology, Cranfield, Bedford MK43 0AL

SUMMARY

The development of generalised models for radiative heat transfer in the gas turbine requires the detailed prediction of the turbulent scalar fields, most notably for temperature, the principal gaseous species (fuel, CO, CO_2 and H_2O) and particulate soot. Mixing limited descriptions of the turbulent combustion process have proved quite successful in modelling the effects of heat release on the flowfield. However, the chemical aspects of the problem - fuel-specific features and the multi-component composition - are poorly reproduced.

Laminar flamelet modelling, in which the underlying scalar relationships in turbulent combustion are determined from 'exact' laminar flame calculation or experiment, currently offers the best prospect for incorporating realistic complex chemistry into the computations.

A strategy is described to extend laminar flamelet modelling of turbulent non-premixed hydrocarbon combustion to include a simplified mechanism for soot formation. In the absence of a widely applicable multi-step kinetic mechanism the formation rate must be inferred from detailed measurement but comparatively comprehensive flowfield modelling is necessary to distinguish fluid mechanic and chemical kinetic effects and hence interpret the observations in model terms. The effects of nucleation, surface growth and agglomeration are accommodated in a simplified form in equations describing the evolution of soot mass fraction and number density in the flame. Local measurements of soot volume fraction by laser extinction and mixture fraction by microprobe mass-spectrometric sampling in planar laminar diffusion flames, burning heavily sooting fuels of ethylene and kerosine, are reported and have then been modelled and predicted computationally in order to generate the basic flamelet relationships necessary for subsequent incorporation in turbulent flowfield calculations.

A further programme of measurements with these fuels burning at elevated pressure is underway and preliminary results up to pressures of 3 atmospheres are reported.

INTRODUCTION

Confidence in the capabilities of computational fluid dynamics to simulate plausibly the key features of the flow in complex gas turbine geometries continues to grow. Improvements relative to such numerical aspects as computational mesh generation and difference schemes (cf., Leonard (1979)) have been matched by a greater concern for the limitations of physical intuition derived from more traditional non-reacting turbulent flows and accordingly the development of models which better reflect the interaction between turbulence and combustion chemistry (Libby and Williams (1980)). Given also the wider availability of major computing facilities, numerical simulation can play an increasingly important role in the design process. The paucity of information routinely available from within the combustor - and the restricted insights possible from exit plane traverses and water analogy tests - make detailed numerical simulation of the primary zone, for example, a highly prized goal. Accordingly a shift in emphasis is discernible in modelling studies; away from the prediction of pollutant emissions in the exhaust and towards the detailed local prediction of those properties with, for example, direct implications for combustor durability and life. These embrace, amongst others, soot formation and its implications for the radiative component in liner heat transfer, the concern of the present paper.

Targetting on the detailed prediction of temperature, gaseous composition and soot in the more inhomogeneous zones within the combustor requires that we confront the problem of modeling turbulent combustion chemistry at the necessary level of detail. In practical flows this task has been approached largely in one of two ways. If the emphasis is on heat release and its impact on the velocity field rather than chemical composition, then the chemistry may be considered to be sufficiently rapid that small-scale turbulent mixing is the rate controlling process whence the fuel disappearance rate can be prescribed in terms of turbulent flowfield properties alone. Such approaches are commonly referred to as 'eddy-break-up' models (after Spalding (1971)). An equally robust alternative is to combine a conserved scalar approach (cf., Bilger (1980)) with the assumption that the chemistry is again fast and that local chemical equilibrium prevails throughout the flowfield. Mixture fraction, or normalised fuel-air ratio, is a conserved property - free from the immediate effects of combustion chemistry - which can be readily determined throughout the turbulent flowfield and so characterise the process of scalar mixing. Whilst multicomponent chemical equilibria may then be readily computed (Gordon and McBride (1971)), the compositions so calculated are largely inappropriate to highly inhomogeneous, fuel-rich combustion regimes in which finite rate chemical kinetics prevail. Additional concerns, the effects of practical fuels and of soot formation, for example, are excluded by such strategies. A more responsive approach to these problems is provided by laminar flamelet modelling (Peters (1984), Liew et al (1984b)).

The direct incorporation of chemical kinetic calculations within the framework of three-dimensional turbulent flowfield prediction is a lengthy, and hence computationally expensive task even for much simplified global reaction schemes (Pope (1985), for example). The laminar flamelet approach separates these two aspects - turbulent flowfield calculation and detailed combustion chemistry - restricting the latter to a small number of once-for-all, 'exact' laminar flame calculations or to prescription from experiment. At the microscopic level within the turbulent flame, combustion is a molecular process dominated by the interplay between heat and mass transfer and chemical kinetics. The flamelet approach assumes that at this level the processes in the turbulent and laminar non-premixed flames are substantially the same and further that the turbulent flame may be viewed as comprising an ensemble of laminar-like flamelets. The detailed structure of laminar flames can be determined computationally for chemistry of arbitrary complexity - at least to the extent that the kinetic mechanism is well-established - or can be analysed in detail experimentally. If the flamelet structure is described in conserved scalar space (mixture fraction), rather than physical space, a substantial measure of similarity is evident in the data from different locations in the same flame or different flame configurations.

Moss (1987) describes the application of this approach to the more complex hydrocarbon fuels of practical interest. Figure 1 illustrates the flamelet profile for kerosine-air non-premixed combustion, computed using a semi-global fuel disappearance step of the form

$$C_n H_m + \tfrac{1}{2} n\, O_2 \longrightarrow nCO + \tfrac{1}{2} m\, H_2$$

supplemented by a detailed mechanism for the oxidation of CO and H_2 (cf., Liew et al (1984a)). A variety of rate expressions for fuel disappearance steps of this form have been reported (cf., Westbrook and Dryer (1984)); the profiles illustrated have used the chemical rate expression of Edelman and Fortune (1969) although other alternatives have been investigated (Askari-Sardhai (1987)).

Once the basic flamelet profile has been established as a function of mixture fraction, $\phi_\alpha = \phi_\alpha(\zeta)$, say, it may be stored as a library file to be simply called during the turbulent flowfield calculation. The statistical character of the turbulent mixing process is accommodated in the prediction of mixture fraction, ζ. Favre-average balance equations for the mean and variance of mixture fraction, which are free of any chemistry,

$$\frac{\partial}{\partial x_j}\left(\bar{\rho}\tilde{u}_j\tilde{\zeta}\right) = \frac{\partial}{\partial x_j}\left(\frac{\mu_T}{\sigma_\zeta}\frac{\partial\tilde{\zeta}}{\partial x_j}\right) \qquad (1)$$

$$\frac{\partial}{\partial x_j}\left(\bar{\rho}\tilde{u}\,\widetilde{\zeta''^2}\right) = \frac{\partial}{\partial x_j}\left(\frac{\mu_T}{\sigma_\phi}\frac{\partial\widetilde{\zeta''^2}}{\partial x_j}\right) + 2\frac{\mu_T}{\sigma_\phi}\left(\frac{\partial\tilde{\zeta}}{\partial x_j}\right)^2 - 2\,\bar{\rho}\,\frac{\varepsilon}{k}\,\widetilde{\zeta''^2} \qquad (2)$$

are then added to those of a similar form for continuity, momentum, energy, turbulence kinetic energy and its dissipation rate. From their simultaneous solution at discrete points throughout the computational domain, a probability density function $\tilde{P}(\zeta)$ can be constructed which describes the distribution of instantaneous values of ζ realised at these points. The average composition at each point may then be determined simply by quadrature, namely

$$\tilde{\phi}_\alpha = \int_0^1 \phi_\alpha(\zeta)\,\tilde{P}(\zeta)\,d\zeta \,. \qquad (3)$$

(flamelet profile) (pdf for mixture fraction)

The approach has been described extensively in the references cited and the brief outline presented here seeks simply to emphasise that it is particularly attractive for the modelling of complex chemistry, and for present purposes soot, because the level of detail introduced in the laminar flamelet does not compromise the flowfield computation.

Soot Formation in Laminar Flamelets

The complexities of soot chemistry in flames are formidable. Whilst a measure of concensus is discernible in the several comprehensive reviews of the subject reported in recent years (c.f. Haynes and Wagner (1981)) a detailed mechanism with confidently documented elementary steps is not available. For purposes of combustor flowfield prediction the prescription of the microscopic processes, embodied in the laminar flamelet, must therefore be empirically determined. The experimental approach to this problem is described in the following section but it is appropriate to review briefly here what kind of data is sought and how it is to be interpreted and applied.

The strategy which most closely parallels that applied to the gaseous composition outlined earlier is simply to specify soot mass (or volume) fraction as a function of mixture fraction through a laminar diffusion flame, analogous to the species profile $\phi_\alpha(\zeta)$. Such an approach has been reported by Gore and Faeth (1986) with a view to radiation prediction from fires but there are evident shortcomings in such an extension to soot. Whilst heat release chemistry is fast and the rates of molecular transport in the flame are all broadly comparable, whence a measure of similarity for gaseous species

in mixture fraction space is to be expected, the same reasoning will not apply to particulate soot. The chemical rates for key processes - nucleation, surface growth and coagulation, for example - differ widely and are controlled by quite different mechanisms, whilst mass diffusion for the particulate phase may be negligible. Without this simplification the goal of the laminar flame experiment must therefore be less direct and specifically be the identification of an appropriate soot formation rate as a function of mixture fraction, $\dot{w}_s(\zeta)$, which will provide a compact source term for the turbulent flowfield prediction of average soot mass fraction of the form

$$\bar{\dot{w}}_s = \int_0^1 \dot{w}_s(\zeta)\, P(\zeta)\, d\zeta.$$

Direct measurements of soot volume fraction in a laminar flame are therefore insufficient in themselves. They must be interpreted in the light of a model which can be carried over to the turbulent flame. Of the simpler models of soot formation available in the literature we have adopted the essential features of that due to Gilyaretdinov (1972). The impact of the processes of nucleation, surface growth and coagulation on soot mass fraction, ms, and number of density, n, are represented by the equations

$$\frac{d}{dt}\left(\frac{n}{N_o}\right) = \underset{\text{(nucleation)}}{\alpha(\zeta)} - \underset{\text{(coagulation)}}{\beta(\zeta)\left(\frac{n}{N_o}\right)^2} \qquad (4)$$

$$\frac{dm_s}{dt} = \underset{\text{(surface growth)}}{\gamma(\zeta)n} + \underset{\text{(nucleation)}}{\delta(\zeta)} \qquad (5)$$

where the respective rates α, β, γ,δ are explicit functions of local density ρ, temperature T, parent fuel concentration X_c and N_o is Avogadro's number (6×10^{26}),

$$\alpha = C_\alpha \rho^2 T^{1/2} X_c \exp\left[-T_\alpha/T\right]$$

$$\beta = C_\beta T^{1/2}$$

$$\gamma = C_\gamma \rho T^{1/2} X_c \exp\left[-T_\gamma/T\right]$$

$$\delta = C_\delta \alpha / C_\alpha$$

where $C_{\alpha,\beta,\gamma,\delta}$ are fuel-type dependent constants and T_α, T_γ are activation temperatures. These parameters will be determined empirically.

The flexibility of such a simple model to acccommodate different fuels and working pressures will emerge in the light of comparisons between prediction and experiment. For this purpose eqns. (4) and (5) must evidently be incorporated into the complete laminar flowfield prediction described more fully later.

Experimental Detail

A Wolfhard-Parker burner has been constructed in both two- and three-slot configurations (cf., fig. 2), producing a substantially two-dimensional thin flame suitable for line-of-sight, but effectively localised, laser extinction measurements of soot volume fraction. Similar geometries have been successfully investigated experimentally in sooting studies at atmospheric pressure by Kent and Wagner (1982) and Smyth et al (1985), amongst others. The slots are 4.8 cm in length and 0.7 cm in width in the case of the 2-slot burner and again 4.8 cm in length for the 3-slot burner but with widths of 9 mm and 6 mm for the outer air slots and central fuel slot respectively. The transmitted intensity of the low power He-Ne laser beam (at 633 nm), aligned parallel to the reactant slots, is measured by the silicon photo- detector as the slot burner is traversed perpendicularly to the beam. The variation in soot concentration through the flame, from fuel-rich ($\zeta = 1.0$) to air ($\zeta = 0$) streams, gives rise to an absorption profile which is readily interpreted in terms of the distribution for soot volume fraction (Kerker (1969)). Whilst the two-slot burner produces a more uniform and extensive curved two-dimensional flame sheet, the absence of an enclosed flame tip leads to excessive soot deposition in downstream regions which in turn causes experimental difficulties and therefore the majority of measurements reported here were made in the more traditional, over- ventilated three-slot geometry. Excessive carbon build-up on the stabilising gauzes and sampling probes has proved a particular problem for heavily sooting fuels, for example ethylene and kerosine, and during high pressure operation.

The burner operates satisfactorily with both gaseous and pre-vaporised liquid fuels. The small, but steady, fuel supply in the latter case (~ 0.6 g/min) is provided by a fine spray into a resistively heated brass chamber, positioned beneath the fuel slot at a working temperature some 100 K in excess of the fuel boiling point. Flow smoothing in the slots and shield flow is effected by filling the cavities with glass beads. The complete burner assembly is mounted on a motorised traverse inside a cylindrical pressure vessel designed to withstand pressures not exceeding 15 bar. Typical air and fuel flow velocities are 10 cms^{-1} and 1.8 cms^{-1} respectively.

As we indicated in the previous section the key to the approach lies in the characterisation of the relationship between soot volume fraction and a conserved scalar, the mixture fraction ζ. The latter is determined in the present experiments by mass spectrometric microprobe sampling. Given the particular importance of temperature in soot formation, the sampled composition data are supplemented by fine wire

thermocouple (50μm Pt - Pt/Rh) measurements of temperature. Probe sampling through small orifices (~ 0.2 mm) in the presence of significant quantities of soot is naturally difficult. Determination of local mixture fraction and detailed species profiles, though comparatively straightforward in the higher H-C ratio fuels (cf., data for CH_4 in fig. 3), has therefore been abandoned in favour of the simpler, more direct, measurement of mixture fraction alone. A second quartz probe, mounted inside the sampling probe, supplies excess oxygen to the sampled gases which, in conjunction with a heated platinum catalyst, then converts all the carbon present, even in fuel-rich regions in which there is unburnt fuel, to carbon dioxide. The peaks at mass numbers corresponding to CO_2 and N_2 are then monitored by the mass spectrometer (VG Micromass) and from their ratio the carbon element mass fraction is derived. This strategy has proved satisfactory over the range of mixture fractions, typically $\zeta_{st} < \zeta < 0.3$, for which there is significant soot formation.

The spacing of the probes and laser beam is held fixed as the burner, and hence the flame, is traversed relative to them. Soot build-up on the thermocouple is minimised by rapid one-sided traversing from air to fuel and effectively making transient measurements. The response time of the mass spectrometer makes this strategy inappropriate however to the composition measurements. The probe is located at each measuring point for approximately 30 seconds in critically sooting regions. To date most of the data has been obtained at atmospheric pressure and, for ease of handling in the preliminary experimental phase, with ethylene as fuel. Stable flames have however been burnt up to pressures of 7 bar and some measurements will be reported in the following section at 3 bar.

Measurements and Model Interpretation

Results from a typical combined thermocouple and laser extinction traverse are illustrated in fig. 4. The centre-line temperature and laser absorption level will evidently increase with height until the flame tip is reached. In the steady-state laminar diffusion flame it is the variation of soot volume fraction with height which diagnoses the rate of soot formation, identified in eqns. (4) and (5). Soot volume fraction is inferred from the relative transmitted intensity, I/I_o, of radiation at wavelength λ using the standard expression

$$f_v = \frac{\lambda \ln(I_o/I)}{36\pi L}\left[\frac{(n^2 - \kappa^2 + 2)^2 + 4n^2\kappa}{n\kappa}\right] \qquad (7)$$

where n,κ denote the complex refractive index $n - i\kappa$. Some uncertainty surrounds these latter parameters and in particular the imaginary component, depending on both the nature of the soot and the method of measurement. The values employed in the present study, 1.92 - 0.45i, were taken from the recent experiments of Mullins and Williams (1987).

The variation of volume fraction with height, represented by the peak value and the spread in mixture fraction space, is illustrated by fig. 5 for ethylene fuel burning at atmospheric pressure. With the exception of the flame base, where limited quenching and fuel-air intermixing occurs, the local peak value increases steadily with height in the flame (and hence elapsed time). The spread of the sooting regime in mixture fraction space is seen to decrease with increasing height, essentially through the progressive reduction on the rich side which accompanies downstream mixing. There is also some evidence of a progressive displacement of the peak volume fraction towards stoichiometric mixture fraction. Substantially higher levels are observed with kerosine as fuel in fig. 6 (approximately two-fold greater at comparable heights) but the variation with height shows evidence of saturation at a soot volume fraction of ~ 1.5×10^{-5}. This appears to be a function of the particular experimental conditions; fuel depletion and mixing, rather than oxidation, are envisaged as the principal reasons for this eventual diminution in formation rate.

It is clear from these data that there is an intimate link between the experimental configuration and the observations. If a simplified representation of the formation rate is to be inferred from such experiments, a complete flowfield simulation is required which couples both detailed scalar and velocity fields.

If a simple plug flow model is employed, in which soot production occurs along lines of constant mixture fraction, then the various rates identified in eqns (4) and (5) are time-independent functions of mixture fraction. They can therefore be integrated readily and analytic solutions for soot number density and mass fraction growth along the 'reactor' can be deduced. In particular, we find that

$$n = \sqrt{\frac{\alpha(\zeta)}{\beta(\zeta)}}\ \tanh\left\{\sqrt{\alpha(\zeta)\beta(\zeta)}\ \ t\right\} \qquad (8)$$

$$m_s = \rho_s f_v = \frac{\gamma(\zeta)}{\beta(\zeta)} \ln\left\{\cosh\left[\sqrt{\alpha(\zeta)\beta(\zeta)}\ \ t\right]\right\} + \delta(\zeta)t$$

If the rates for nucleation, surface growth and agglomeration in eqn. (6) are evaluated using a laminar flamelet profile to describe ρ, T, X_c as functions of mixture fraction, then the evolution of soot volume fraction, f_v, with time (and by implication height) is as illustrated in fig. 7. Detailed discussion of the flamelet profile and the choice of constants C_i ($i = \alpha, \beta, \gamma, \delta$) in eqn. (6) is deferred until later. The features to note here are the essentially linear growth of f_v with tir and the narrow range of mixture fraction over which the soot formation is predicted to occur. The dominant influence in the model proposed is evidently the temperature.

Such results are simply illustrative however. The flame is clearly not a plug flow reactor and if the soot model is to be calibrated against experiment a more plausible representation of the distribution of properties within the flame is necessary. The laminar flame on the Wolfhard-Parker burner has therefore been simulated in two-dimensions using a modified version of GENMIX (Spalding (1977). Figure 8 illustrates the computed flow pattern for the ethylene-air flame. The flowfield is substantially similar to that reported by Smyth et al (1985) from detailed flow visualisation.

The predicted streamlines and lines of constant mixture fraction, as expected, are not parallel. Fuel depletion in particular leads to a flow pattern in which a fluid element experiences a range of local mixture fraction states within the regime of experimental interest. The numerical simulation of the sooting flame must therefore embed the mechanism (eqns. (4)-(6)) in this more complex flowfield.

The conservation equations for x-momentum, mixture fraction and soot mass fraction assume, in laminar parabolic flow, the general form

$$\rho u \frac{\partial \phi}{\partial x} + \rho v \frac{\partial \phi}{\partial y} = \frac{\partial}{\partial y}\left(\frac{\mu}{\sigma_\phi} \frac{\partial \phi}{\partial y} \right) + S_\phi \qquad (9)$$

where S_ϕ denotes the source term appropriate to the property

$\phi(S_u = -\frac{dp}{dx} + (\rho - \rho_o)g;\ S_\zeta = 0\ ;\ S_{m_s} = \rho\left[\frac{dm_s}{dt}\right])$. Diffusional transport, represented by the diffusivity μ/σ_ϕ, is assumed to be negligible in the case of the particulate soot. Combustion chemistry is incorporated in the form of the flamelet, for ethylene-air for example, illustrated in fig. 7. This is determined using a semi-global mechanism of the form described earlier and computed using the approach described by Liew et al (1984). For the purposes of these preliminary calculations the soot formation mechanism is treated as trace chemistry, decoupled from that of the heat release, but occurring in fluid elements which are transported through the flowfield having spatially-varying scalar properties. The temperatures measured experimentally, including a thermocouple radiation correction, are substantially lower than those predicted in the adiabatic flamelet model - measured T_{max} ~ 1980K compared with an adiabatic flame temperature T_{ad} ~ 2360K. We are evidently not in a position as yet to calculate such laminar flame structure including the effect of luminous flame radiation, but the sensitivity of the soot formation mechanism to temperature, alluded to earlier, makes its neglect potentially significant. The experimental temperature profile (cf., fig. 7) has therefore been incorporated in the present simulation.

The six undetermined constants in the mechanism, eqn. (6), have been subject to casual numerical experimentation and fitted to the laser extinction data reported in fig. 5. The comparison between prediction and experiment shown in fig. 9 is obtained with the following parameter values

$$\begin{aligned} C_\alpha &= 1.7 \times 10^{8} \\ C_\beta &= 10^{9} \\ C_\gamma &= 4.2 \times 10^{-17} \\ C_\delta &= 2.57 \times 10^{10} \end{aligned} \qquad (10)$$

and activation temperatures

$$\begin{aligned} T_\alpha &= 46.1 \times 10^{3} \text{ (nucleation)} \\ T_\gamma &= 12.6 \times 10^{3} \text{ (surface growth)} \end{aligned}$$

The choice of these values, and in particular that of the activation temperatures, was guided initially by the values reported by Gilyazetdinov (1972). Both the evolution of peak soot volume fraction with height and the spread in mixture fraction space are plausibly reproduced. The location of the soot peak in mixture fraction space is also predicted to shift to lower values with increasing height in the flame. The experimental evidence, cf., fig. 10, is a little ambiguous but broadly confirms the overall trend.

Further optimisation of the model parameters is clearly possible but the values cited were obtained readily and the level of agreement achieved is very encouraging. Of the two key steps necessary to develop this model for the gas turbine combustor, namely to accommodate kerosine as fuel and operation at elevated pressures, we consider the latter to be the more challenging. This has therefore been the focus of recent experimental studies. Both laminar flame stability and the probe sampling difficulties attendant on the enhanced soot yield complicate the experimental task. A gradualist approach has been adopted to detailed data acquisition although qualitative observations up to

pressures of 7 bar do not indicate fundamental obstruction. Fig. 11 shows the evolution of soot volume fraction in the ethylene-air flame to a pressure of 3 bar. The measurements were made on flames of approximately the same size by maintaining a fixed fuel mass flow rate, however the air flow rates were varied to retain flame stability. From the discussion presented earlier it is evident that a detailed flowfield simulation is necessary if the soot formation rate is to be distinguished from flowfield effects specific to particular flame geometries. The detailed investigation of the flamelet approach applied to sooting flames at elevated pressure is continuing and will be reported more fully later but it is instructive at this stage to infer the pressure dependence of the growth rate simply with downstream distance, namely df_v/dx, accepting that the transformation to the formation rate, df_v/dt, is flowfield-dependent and not trivial. Comparison of this rate of soot growth at increasing pressure then suggests a pressure dependence of $p^{1.5}$. In broadly similar laminar flame experiments a pressure exponent of $n = 1.2$ was inferred from measurements of peak integrated soot volume fraction across an axisymmetric flame, again with ethylene as fuel, by Flower and Bowman (1986). The effects of path integration introduced in this data, coupled with flowfield uncertainties, make more detailed comparisons with the present results extremely difficult however. Measurements of soot volume fraction alone appear comparatively uninformative if they are not linked to a model which distinguishes chemical kinetic and fluid dynamic effects. The present study is far from complete but we have attempted to demonstrate a systematic approach to soot modelling which admits continued development with further experimental and computational modelling input.

Conclusions

A strategy has been identified to extend laminar flamelet modelling of turbulent combustion chemistry by embracing a simple representation of soot formation. This approach is designed to permit the ready incorporation of soot mass fraction into the framework of turbulent flowfield computation for purposes of detailed temperature and radiation prediction.

The six model parameters controlling the proposed rate processes for nucleation, surface growth and agglomeration are determined by a comparison between detailed model prediction for a simulated two-dimensional laminar diffusion flame and experimental measurement on a Wolfhard-Parker burner.

The flamelet model emphasises the importance of the relationship between soot formation rate and mixture fraction. Simultaneous measurements have therefore been made of local soot volume fraction by laser attenuation, mixture fraction by microprobe sampling and temperature by fine wire thermocouple. The burner is designed to operate with both gaseous and liquid fuels and data is reported for both ethylene and kerosine, primarily at atmospheric pressure but some preliminary measurements are also described at elevated pressures.

Both prediction and experiment emphasise that soot formation is restricted to a comparatively narrow range of mixture fractions ($0.06 < \zeta < 0.2$). The particular importance of temperature is illustrated by the activation temperatures for nucleation and surface growth, 46.1×10^3 and 12.6×10^3 (K) respectively, inferred from the data for ethylene-air combustion. The limited measurements at a pressure of 3 bar suggest a pressure-dependent soot formation rate of the form $p^{1.5}$.

Acknowledgement

The experimental programme is being conducted under a research agreement with the Procurement Executive of the Ministry of Defence (RAE, Pyestock). K.J. Syed holds a CASE research studentship, jointly sponsored by the Science and Engineering Research Council and British Gas. The interest and support of these bodies are gratefully acknowledged.

References

Askari-Sardhai, A. (1987). Laminar Flamelet Modelling of Turbulent Combustion Chemistry for Practical Fuels. PhD Thesis Cranfield Institute of Technology (in preparation).

Bilger, R.W. (1980). Turbulent Flows with Non-Premixed Reactants in Turbulent Reacting Flows, Springer.

Edelman, R. and Fortune, O. (1969). A Quasi-global Chemical Kinetic Model for the Finite Rate Combustion of Hydrocarbon Fuels, AIAA Paper 69-86.

Flower, W.L. and Bowman, C.T. (1986). Soot Production in Axisymmetric Laminar Diffusion Flames at Pressures from One to Ten Atmospheres, Paper presented at Twenty-first Symp. (International) on Combustion, Munich.

Gilyazetdinov, L.P. (1972). The Kinetics and Formation Mechanism of Carbon Black during Thermal Decomposition of Hydrocarbons in the Gas Phase, Khim. Tverd. Topl. 3, 103.

Gordon, S. and McBride, B. (1971). Computer Program for Calculation of Complex Chemical Equilibrium Compositions, Rocket Performance, Incident and Reflected Shocks, and Chapman-Jouguet Detonations. NASA SP-273.

Gore, J.P. and Faeth, G.M. (1986). Structure and Spectral Radiation Properties of Turbulent Ethylene/Air Diffusion Flames, Paper presented at Twenty-first Symp. (International) on Combustion, Munich.

Haynes, B.S. and Wagner, H. Gg. (1981). Soot Formation, Prog. in Energy and Comb. Sci. 7, 229.

Kent, J.H. and Wagner, H. Gg. (1982). Soot Measurements in Laminar Ethylene Diffusion Flames, Comb. and Flame 47, 53.

Kerker, M. (1969). The Scattering of Light and Other Electromagnetic Radiation, Academic Press, New York.

Leonard, B.P. (1979). A Stable and Accurate Convective Modelling Procedure Based on Quadratic Upstream Interpolation, Comp. Meths. Appl. Mech. Eng. 19, 59.

Libby, P.A. and Williams, F.A. (1980) ed. Turbulent Reacting Flows, Springer.

Liew, S.K., Bray, K.N.C. and Moss, J.B. (1984a). A Stretched Laminar Flamelet Model of Turbulent Non-premixed Combustion, Comb. and Flame 45, 199.

Liew, S.K., Bray, K.N.C. and Moss, J.B. (1984b). Predicted Structure of Stretched and Unstretched Methane-Air Diffusion Flames in Prog. in Astronautics and Aeronautics, Vol. 95, p.

Mitchell, R.E., Sarofim, A.F. and Clomburg, L.A. (1980). Experimental and Numerical Investigation of Confined Laminar Diffusion Flames, Comb. and Flame 37, 337.

Moss, J.B. (1987). Modelling Combustion Chemistry for Practical Fuels in Engine Flowfield Computations. Proc. I.Mech. Conf. Combustion in Engines, C02/87 p.175.

Mullins, J. and Williams, A. (1987). The Optical Properties of Soot: A Comparison between Experimental and Theoretical Values. Fuel, 66, 277.

Peters, N. (1984). Laminar Diffusion Flamelet Models in Non-premixed Turbulent Combustion, Prog. in Energy and Comb. Sci. 10, 319.

Pope, S.B. (1985). PdF Methods for Turbulent Reactive Flows. Prog. in Energy and Comb. Science 10, 119.

Smyth, K.C., Miller, J.H., Dorfman, R.C., Mallard, W.G. and Santoro, R.J. (1985). Soot Inception in a Methane/Air Diffusion Flame as Characterized by Detailed Species Profiles, Comb. and Flame 62, 157.

Spalding, D.B. (1971). Mixing and Chemical Reaction in Steady Confined Turbulent Flames. Thirteenth Symp. (International) on Combustion, Combustion Institute, p.649.

Spalding, D.B. (1977). GENMIX - A General Computer Program for Two-Dimensional Parabolic Phenomena, Pergamon.

Westbrook, C.K. and Dryer, F.L. (1984). Chemical Kinetic Modelling of Hydrocarbon Combustion, Prog. in Energy and Comb. Science 10, 1.

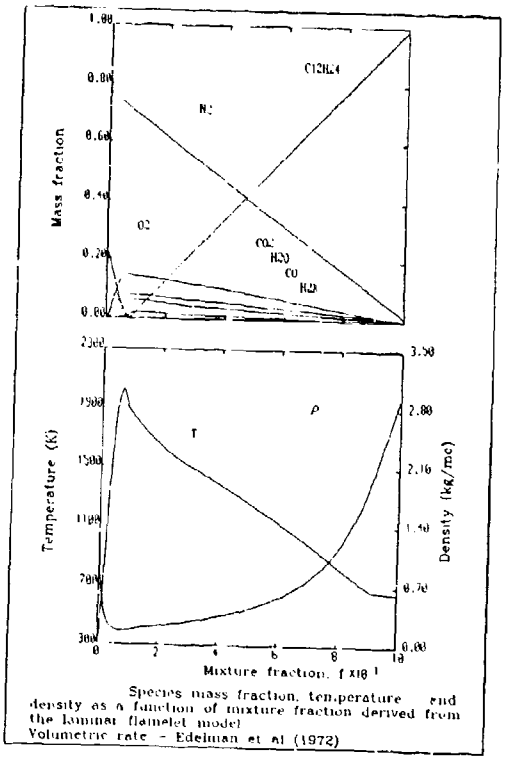

Species mass fraction, temperature and density as a function of mixture fraction derived from the laminar flamelet model
Volumetric rate - Edelman et al (1972)

Figure 1. Laminar flamelet profile for gaseous kerosine-air combustion computed using the quasi-global scheme.

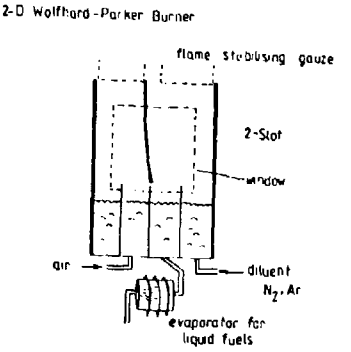

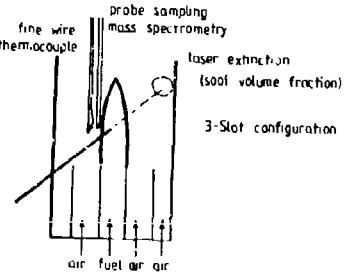

Figure 2. Two- and three-slot Wolfhard-Parker burner configurations.

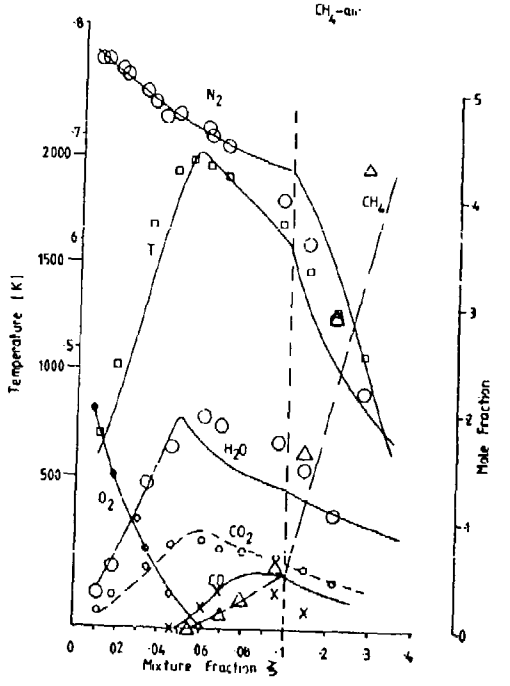

Figure 3. Experimentally-determined laminar flamelet profile for methane-air, compared with that inferred from the measurements in an axisymmetric flame by Mitchell et al (1980).

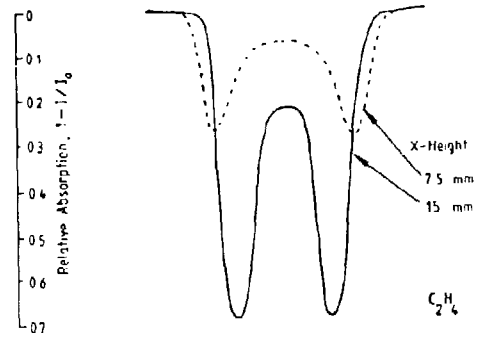

Figure 4. Typical laser extinction and thermocouple traverses through the laminar flame.

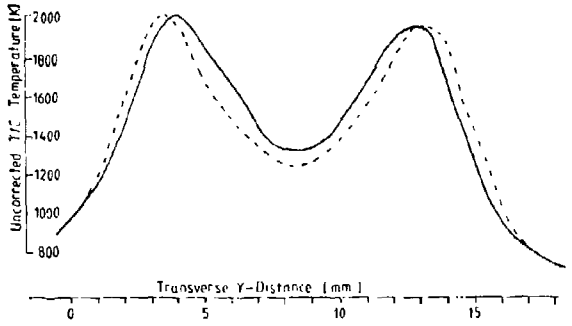

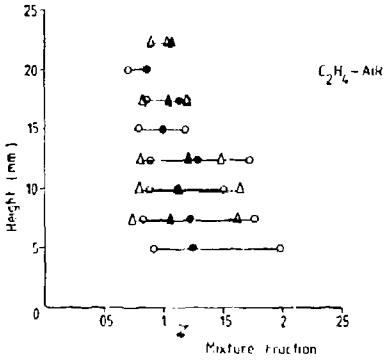

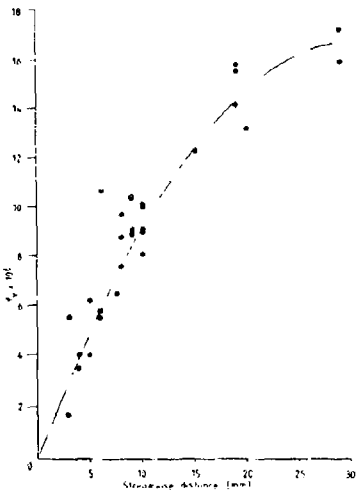

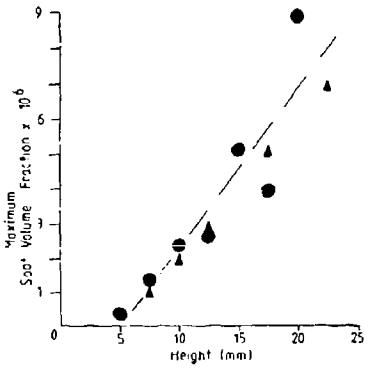

Figure 5. The variation of soot volume fraction with height in the ethylene air flame; (a) the spread of the distribution (upper/lower bound and peak value) in mixture fraction space (b) peak value; ●, ▲ duplicated experiments.

Figure 6. The variation of peak soot volume fraction with height in the 2-slot kerosine-air flame.

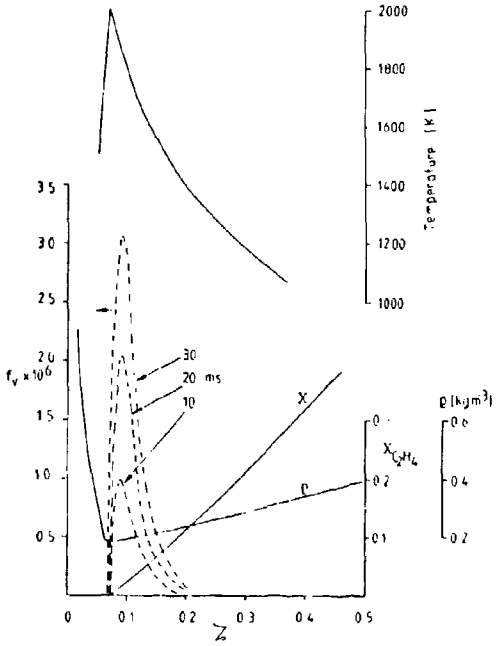

Figure 7. The ethylene-air flamelet for temperature, mixture density and fuel mole fraction and the soot volume fraction predicted by the analytic model (eqn. (8)).

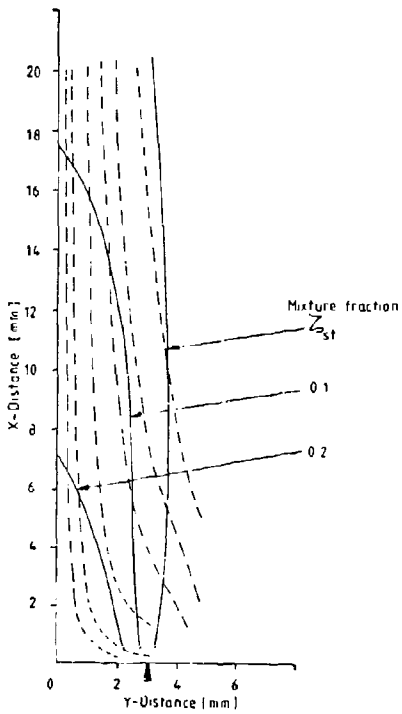

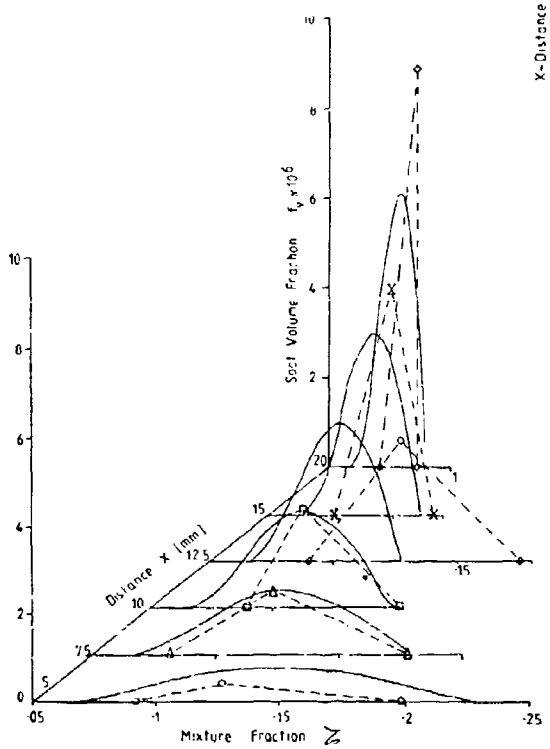

Figure 8. The computed flow pattern for the 3-slot burner, relative to the mid-plane of the fuel slot; --- streamlines, contours of constant mixture fraction.

Figure 9. Comparison between model prediction (solid lines) and experiment at different heights in the ethylene-air flame.

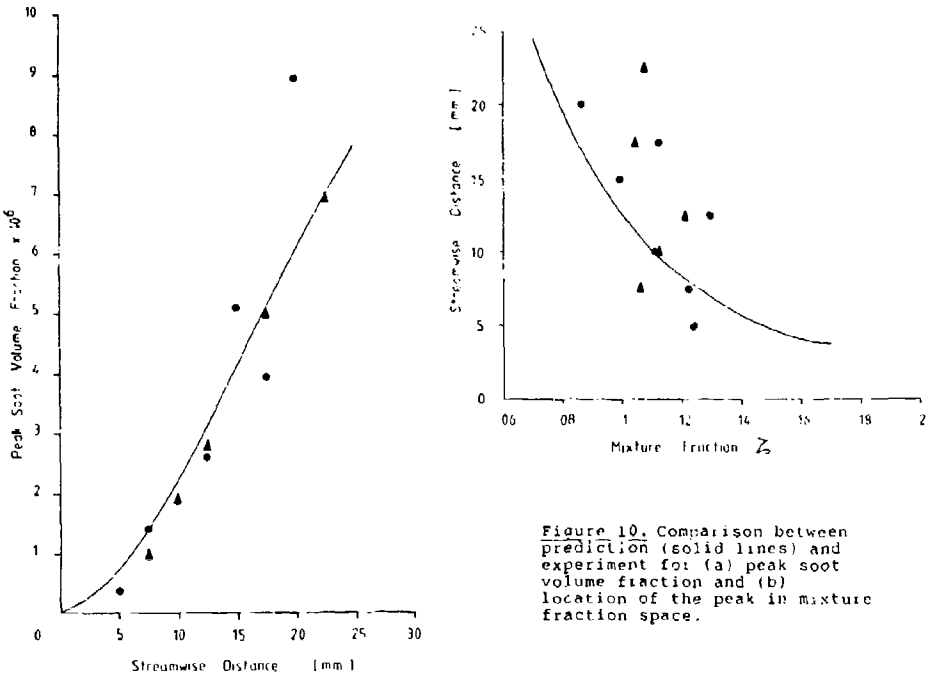

Figure 10. Comparison between prediction (solid lines) and experiment for (a) peak soot volume fraction and (b) location of the peak in mixture fraction space.

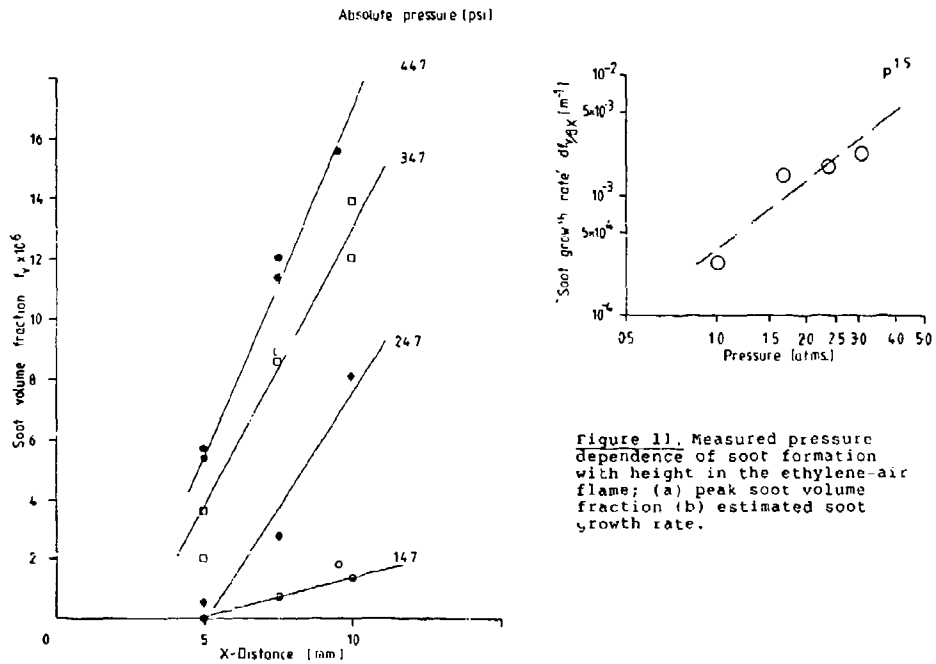

Figure 11. Measured pressure dependence of soot formation with height in the ethylene-air flame; (a) peak soot volume fraction (b) estimated soot growth rate.

DISCUSSION

O.Gulder, CA

Do you have any speculation between the temperature profile you showed and that presented by Prof. Faeth.

Author's Reply

If one clearly has to do the radiation calculation for the laminar flame before you can infer the model properties, then we are in a Catch-22 situation. We have, to some extent, circumvented that by using a measured temperature profile, which of course contains some radiative loss.

G.Faeth, US

The calculation that we did was based on the heat loss from the turbulent flame, which is the relevant parameter in the radiation calculations in the turbulent flame.

RADIATION TRANSFER IN GAS TURBINE COMBUSTORS

by

M.G. CARVALHO AND P.J.M. COELHO

Instituto Superior Técnico
Mechanical Engineering Department
1096 Lisbon Portugal

SUMMARY

The present paper is concerned with the prediction of the local flow, heat-transfer and combustion processes inside a three-dimensional can combustor chamber of a gas turbine. A three-dimensional numerical solution technique is used to solve the governing time-averaged partial differential equations and the physical modelling for the turbulence, combustion and thermal radiation.

The heat transfer modelling is emphasised in this paper. A method to calculate the distribution of temperature, radiative heat flux and total heat flux of the liner is described. The implications of neglecting radiative heat transfer in gas turbine combustion chamber calculations are discussed. The influence of working pressure on the radiative heat transfer is investigated comparing the radiative heat flux and the temperature distribution of the liner for three different working pressures: 5, 15 and 25 bar.

1. INTRODUCTION

For many years the design of gas turbine combustion chambers was based on the use of empirical models correlating overall performance with simple global parameters such as inlet air conditions, fuel/air ratio or chambers volume. This approach was relatively successful for combustors of essentially similar shape dictated by the need for its lenght and frontal area to remain within the limits set by other engine components, by the necessity for a diffuser to minimize pressure loss, and by the requirement of a liner to provide stable operation over a wide range of air/fuel ratios [1].

In the last two decades, awareness of the limitations of energy resources, on one hand, and pollutant emissions regulations, on the other, have imposed additional constrains leading to the need to optimise the design of combustion equipment, including gas turbine combustors. Together with these limitations all combustors should satisfy the following requirements: high combustion efficiency, uniformity of outlet gas temperature to maximize the life turbine blades and nozzle guide vanes, wide stability limits, low pressure loss, reliable and smooth ignition, durability and minimum cost.

The improvement of the performance and the need to satisfy all the listed requirements cannot be achieved by traditional methods. A more fundamental approach is needed. So in the last years a great effort has been developed, both in the experimental field and mathematical modelling, to increase the knowledge about the phenomena occuring in the combustors. Experimental methods are expensive and slow whereas mathematical models, whose implementation has been possible due to the advent of powerful digital computers, are easily, quickly and economically adaptable to different geometric configurations and load conditions. However the large number of complex phenomena present in the combustor such as a tri-dimensional turbulent flow, swirl, chemical reaction, radiation, soot and, for liquid fuels, atomization and vaporization taking place in a complex geometry, makes the modelling rather difficult. Due to this complexity many of the results obtained by mathematical models have only achieved qualitative agreement but, even in this case they are very useful since they provide guidance as to the directions in which a design should be modified in order to meet the design objectives, hence reducing considerably the number of experimental tests required to achieve a satisfactory design.

Due to the multiplicity of phenomena involved, little atention has been paid to radiative heat transfer, as it was thought to be a small percentage of the total heat release by the chemical reactions and there was no means by which it could be reliably calculated. However, if the goal is the calculation of the liner wall temperatures, thermal stresses and liner durability an accurate means of prediction of the radiant heat flux is needed. Furthermore the accurate assessments of pollutant emissions necessitate fairly precise knowledge of radiant heat transfer rates as the models for predicting the emissions of carbon monoxide, unburned hydrocarbons and oxides of nitrogen require an accurate description of gas temperature distributions in all regions of the combustor [1]. Besides, over the past 30 years, pressure ratios have increased markedly in order to improve thermal efficiency, and it seems probable

that they will continue to do so. This increase in pressure raises the amount of heat transfered to the liner walls by radiation.

Almost all the authors who used mathematical models for gas turbine combustors did not calculate thermal radiation based on the argument that it is very small compared with the heat released by the combustion.

Boysan et al [2] used a flux model to account for the effects of radiation in a gas turbine combustor solving three second-order linear differential equations for the fluxes in the axial, radial and tangential directions. The contribution of radiation was considered in the enthalpy equation through a source term calculated from those fluxes. The study was carried out at atmospheric pressure. The authors did not specify the kind of boundary condition used for the calculation of the radiation heat transfer, nor discuss its influence on the results.

Lockwood et al [3] used the "discrete transfer" radiation prediction procedure of Lockwood and Shah [4] for the computation of the radiation transfer in a combustor can. The authors assumed adiabatic flame and they did not solve for the enthalpy equation. The distribution of temperature was determinated as a function of the instantaneous mixture fraction using the equilibrium method of Gordon and McBride [5].

Therefore the effects of the radiative heat transfer on the flow, temperature field and chemical reaction were not accounted for. The radiative heat fluxes to the walls were calculated aposteriori assuming an uniform wall temperature equal to the inlet air temperature. They have concluded that the total radiation heat transfer to the walls was less than 1/4 % of the energy supplied to the combustor justifying the adiabatic assumption on which the flow and reaction calculations were based.

Carvalho et al [6] performed a similar study as the previous one, using also the "discrete transfer" method for the prediction of radiative heat transfer in a can combustor. However in this case, the authors solved the enthalpy equation with a source term accounting for the heat transfered by radiation. The wall temperature was assumed uniform and equal to the inlet air temperature. Two sets of predictions were made for pressures of 6 and 25 bar. Radiative wall heat fluxes increased markedly with the pressure.

In the present paper the "discrete transfer" method of Lockwood and Shah is also used. The principal contribution of this paper is the calculation of the wall temperature distribution which was assumed in the previous works. In order to calculate the wall temperature distribution, we use, for the calculation of the radiative heat transfer, a boundary condition based on the energy balance of the wall, similar to the one described by Lefebvre [1]. This balance is applied to each control volume adjacent to the wall and it is based on empirical correlations for the calculation of external convection and radiation, on the wall law for the calculation of internal convection and on the "discrete transfer" method for the calculation of internal radiation. The enthalpy equation is solved and a source terms accounting for the radiation heat transfer is included. Instantaneous gas compositions are determined as a function of the instantaneous mixture fraction using the equilibrium method of Gordon and McBride [5].

Predictions of wall temperature, radiative heat fluxes and total heat fluxes distributions are presented and discussed. The influence of the pressure ratio is analised comparing the solutions obtained for three different working pressures: 5, 15 and 25 bar.

2. FLOW CONFIGURATION

The geometry of the combustion chamber studied is sketched in Figure 1. The combustor has 18 separated burners. As the geometry of the combustor repeats itself every 20^{o}, and the flow pattern also, only a single 20^{o} section of the chamber is studied. Gaseous fuel (propane) enters the combustor through the inner of two annular rings. It was assumed to enter in the form of a conical jet of 90^{o} included angle. The combustion air is introduced through a concentric annular ring. Two streams of cooling air enter close to the inner and outer annulus walls simulating the cooling ring flows which actually are discharged parallel to the walls. Secondary and dilution air are introduced through round holes in the inner and outer annulus walls as shown in Figure 1. The air has been specified as entering only with a radial velocity component through these holes. Three sets of operating conditions were studied, keeping an overall air/fuel ratio of approximately 60 and varying combustors pressure, inlet temperature and mass flow rates according to Table 1.

TABLE 1 - THE OPERATING CONDITIONS

	Case 1	Case 2	Case 3
Pressure [bar]	5	15	25
Inlet Air Temperature [K]	400	600	750
Inlet Fuel Temperature [K]	300	400	500
Primary Air Mass Flow Rates [Kg/s]	0.233	0.466	0.621
Cooling Air Mass Flow Rate [Kg/s]	0.146	0.292	0.398
Secondary Air Mass Flow Rate through the Holes [Kg/s]	0.114	0.227	0.304
Dilution Air Mass Flow Rate through the Holes [Kg/s]	0.172	0.341	0.456
Mass Flow Rate of Fuel [Kg/s]	0.011	0.022	0.0295
Primary Air Axial Inlet Velocity [m/s]	40	40	40
Fuel Axial Inlet Velocity [m/s]	25	22.2	22.2

3. PHYSICAL MODELLING

The governing transport equations for the mean motion of a turbulent three-dimensional flow were applied in the cylinder polar coordinate form:

Continuity:

$$\frac{1}{r}\frac{\partial}{\partial r}(\rho r v)+\frac{1}{r}\frac{\partial}{\partial \theta}(\rho w)+\frac{\partial}{\partial x}(\rho u)=0 \tag{1}$$

Momentum:

$$\rho\left(v\frac{\partial v}{\partial r}+\frac{w}{r}\frac{\partial v}{\partial \theta}-\frac{w^2}{r}+u\frac{\partial v}{\partial x}\right)=-\frac{\partial p}{\partial r}-\left[\frac{1}{r}\frac{\partial}{\partial r}(r\tau_{rr})+\frac{1}{r}\frac{\partial}{\partial \theta}\tau_{r\theta}-\frac{\tau_{\theta\theta}}{r}+\frac{\partial \tau_{rx}}{\partial x}\right] \tag{2}$$

$$\rho\left(v\frac{\partial w}{\partial r}+\frac{w}{r}\frac{\partial w}{\partial \theta}+\frac{vw}{r}+u\frac{\partial w}{\partial x}\right)=-\frac{1}{r}\frac{\partial p}{\partial \theta}-\left[\frac{1}{r^2}\frac{\partial}{\partial r}(r^2\tau_{r\theta})+\frac{1}{r}\frac{\partial \tau_{\theta\theta}}{\partial \theta}+\frac{\partial \tau_{\theta x}}{\partial x}\right] \tag{3}$$

$$\rho\left(v\frac{\partial u}{\partial r}+\frac{w}{r}\frac{\partial u}{\partial \theta}+u\frac{\partial u}{\partial x}\right)=-\frac{\partial p}{\partial x}-\left[\frac{1}{r}\frac{\partial}{\partial r}(r\tau_{rx})+\frac{1}{r}\frac{\partial}{\partial \theta}(\tau_{\theta x})+\frac{\partial}{\partial x}(\tau_{xx})\right] \tag{4}$$

Here v, w and u represent the velocities in the (r, θ, x) cylindrical-coordinate directions; and ρ and p are the density and pressure, respectively. The τ's represent the combined laminar and turbulent stresses; these are supposed to be related to velocity gradients by way of an isotropic effective viscosity, μ_t. The latter is derived at each point from:

$$\mu_t = C_\mu \rho k^2/\varepsilon \tag{5}$$

where C_μ is a constant of the model; and k and ε are derived from their differential transport equations. The turbulence-energy equation is:

$$\rho\left(v\frac{\partial k}{\partial r}+\frac{w}{r}\frac{\partial k}{\partial \theta}+u\frac{\partial k}{\partial x}\right)=\frac{1}{r}\frac{\partial}{\partial r}\left(r\frac{\mu_t}{\sigma_k}\frac{\partial k}{\partial r}\right)+\frac{1}{r}\frac{\partial}{\partial \theta}\left(\frac{\mu_t}{\sigma_k}\frac{\partial k}{r\partial \theta}\right)+\frac{\partial}{\partial x}\left(\frac{\mu_t}{\sigma_k}\frac{\partial k}{\partial x}\right)+G_k-\rho\varepsilon \tag{6}$$

where σ_k is another universal turbulence constant and G_k represents the volumetric rate of generation of k and can be expressed in terms of velocity gradients and the

turbulent viscosity. The dissipation-rate equation is:

$$\rho(v\frac{\partial\varepsilon}{\partial r}+\frac{w}{r}\frac{\partial\varepsilon}{\partial\theta}+u\frac{\partial\varepsilon}{\partial x})=\frac{1}{r}\frac{\partial}{\partial r}(r\frac{\mu_t}{\sigma_\varepsilon}\frac{\partial\varepsilon}{\partial r})+\frac{1}{r}\frac{\partial}{\partial\theta}(\frac{\mu_t}{\sigma_\varepsilon}\frac{\partial\varepsilon}{r\partial\theta})+\frac{\partial}{\partial x}(\frac{\mu_t}{\sigma_\varepsilon}\frac{\partial\varepsilon}{\partial x})+C_1\frac{\varepsilon}{k}G_k-C_2\rho\frac{\varepsilon^2}{k} \tag{7}$$

where C_1, C_2 and σ_ε are all turbulence constants.

The model constants appearing in the above equations were assigned the following values, taken unchanged from Launder and Spalding [7]: C_μ=0.9, C_1=1.44, C_2=1.92, σ_k=1.0 and σ_ε=1.3.

The combustion model is based on the assumption that the reaction rates associated with the fuel oxidation have time scales very short compared with those describing the transport processes. Using the assumption of "fast" chemical reaction, chemical equilibrium prevails. Assuming also that all species and heat diffuse at the same rate and that the heat loss to the surrounds can be neglected compared with the heat transfer released by chemical reacting then instantaneous gas composition can be determined as a function of a strictly conserved scalar variable. Any conserved scalar may be chosen and here we used the mixture fraction f defined as the mass fraction of fuel present both burnt and unburnt. Instantaneous gas composition was determined from f using an equilibrium model based on the minimization of the free energy. The computer code developded by Gordon and McBride [5] was used and the results were tabulated for 1000 values of f from pure air (0) to pure fuel (1). Instantaneous temperature field was calculated from the instantaneous enthalpy field which was correlated with instantaneous misture fraction field assuming the relations used by Carvalho [8].

In a turbulent flow, the mixture fraction will fluctuate and, because of the nonlinearity of the relationships, knowledge of its mean value is insufficient to allow the determination of the mean values of such quantities as density and temperature, etc.

We adopt a statistical approach to describe the temporal nature of the mixture fraction fluctuations. The time-averaged value of any property ϕ solely dependent on f can then be determined from:

$$\bar{\phi}=\int_0^1\phi(f)P(f)df \tag{8}$$

In the present work we have assumed the "clipped normal" probability density function [9] which is characterized by just two parameters, and the mean square of the fluctuations $g\equiv\overline{(f-\bar{f})^2}$. These variables, f and g, also obey modelled transport equations of the form:

$$\rho(v\frac{\partial f}{\partial r}+\frac{w}{r}\frac{\partial f}{\partial\theta}+u\frac{\partial f}{\partial x})=\frac{1}{r}\frac{\partial}{\partial r}(r\frac{\mu_t}{\sigma_f}\frac{\partial f}{\partial r})+\frac{1}{r}\frac{\partial}{\partial\theta}(\frac{\mu_t}{\sigma_f}\frac{\partial f}{r\partial\theta})+\frac{\partial}{\partial x}(\frac{\mu_t}{\sigma_f}\frac{\partial f}{\partial x}) \tag{9}$$

$$\rho(v\frac{\partial g}{\partial r}+\frac{w}{r}\frac{\partial g}{\partial\theta}+u\frac{\partial g}{\partial x})=\frac{1}{r}\frac{\partial}{\partial r}(r\frac{\mu_t}{\sigma_g}\frac{\partial g}{\partial r})+\frac{1}{r}\frac{\partial}{\partial\theta}(\frac{\mu_t}{\sigma_g}\frac{\partial g}{r\partial\theta})+\frac{\partial}{\partial x}(\frac{\mu_t}{\sigma_g}\frac{\partial g}{\partial x}) \tag{10}$$

$$-Cg_1\,\mu_t\left[(\frac{\partial f}{\partial x})^2+(\frac{\partial f}{\partial r})^2+(\frac{1}{r}\frac{\partial f}{\partial\theta})^2\right]+\frac{Cg_2}{k}\rho\varepsilon g=0$$

where Cg_1 and Cg_2 are additional adjustable parameters.

The mixture specific enthalpy may be defined by:

$$h\equiv\int_0^T\sum_{\text{all }j}m_jC_{pj}(T)dT+m_{fu}H_{fu}+m_{CO}H_{CO}+m_{H_2}H_{H_2} \tag{11}$$

where C_{pj} is the constant-pressure specific heat of a species j.

Density is determined from the equation of state:

$$\rho=p(RT\sum_{\text{all }j}m_j/M_j)^{-1} \tag{12}$$

where p is pressure, R_o is the universal gas constant, and M_j is the molecular weight of species j. Since the m_j's, as well as T, are all functions of f, the time-averaged density for use in the mean flow equations is again determined from (8).

Treatment of the Radiation Transfer

The "discrete transfer" radiation prediction procedure of Lockwood and Shah [4] has been utilized in this study. This method combines ease of use, economy and flexibility of application. This last feature is of particular importance in the real world of geometrically intricate combustion chambers. The claimed advantages of the method have now survived the rigours of several industrial applications, see [10] and [11] for example.

The "discrete transfer" method is founded on a direct solution of the radiation transfer equation for a direction $\underset{\sim}{\Omega}$ which runs:

$$\frac{dI}{ds} = (k_g + k_s)\left(\frac{E}{\pi} - I\right) \tag{13}$$

where I is the radiation intensity in a $\underset{\sim}{\Omega}$ direction, s is distance, $E \equiv \sigma T_g^4$ is the black body emissive power, and k_g and k_s are respectively the gas and soot absorption coefficients. The scattering terms do not appear, although they are easily accomodated, since the only particulate matter present in the present application is the soot particles which are much too small to scatter significantly. Many radiation methods are based on the solution of the much more complex integro-differential equation which results when equation (13) is rewritten for the whole solid angle Ω. In our opinion this is unsatisfactory since the numerical solution treatment of such an equation is necessarily very elaborate

We prefer to solve the much simple equation (13) within discretisation $d\Omega_j$ of the whole solid angle Ω about selected directions $\underset{\sim}{\Omega}$. Assuming that E, k_g and k_s are constant over a finite distance increment δs, equation (13) may be integrated to yield the simple recurrence relation:

$$I_{n+1} = \frac{E}{\pi}\left(1 - e^{-(k_g+k_s)\delta s}\right) + I_n\, e^{-(k_g+k_s)\delta s} \tag{14}$$

where n and n+1 are successive locations along $\underset{\sim}{\Omega}$ separed by the increment δs. The relation is applied along the chosen $\underset{\sim}{\Omega}$ from known conditions at point Q, say, (either guessed or pertaining to those of the previous iteration) on one wall to the point of impegement, P say, of the direction $\underset{\sim}{\Omega}$ on an opposite wall.

If the hemisphere above P is discretized into subangles $\delta\Omega_r$, within which the intensity is considered to be uniform, the energy flux arriving at P is:

$$q_{+,p} = \int_{\pi} I_p\, \underset{\sim}{\Omega} d\Omega \approx \sum_{\text{all } r} I_{p,r}\, \underset{\sim}{\Omega}_r\, d\Omega_r \tag{15}$$

The wall boundary condition is:

$$q_{-,p} = (1 - \varepsilon_w) q_{+,p} + \varepsilon_w E_w \tag{16}$$

where $q_{-,p}$ is the energy leaving the wall at P, ε_W is the wall emissivity, and $E_W = \sigma T_W^4$ is the wall emissive power. The value of $I_{o,r}$ at point Q, the initial value required for the application of the recurrence relation (14), is $q_{-,p}/\pi$. The net radiation heat flux is of course:

$$q_p = q_{+,p} - q_{-,p} \tag{17}$$

The net heat gain or loss within a small control volume of the flow procedure is:

$$S_R = (I_{n+1} - I_n)\underset{\sim}{\Omega} d\Omega dA \tag{18}$$

where the locations n and n+1 correspond to the "entry" and "exit" of a direction $\underset{\sim}{\Omega}$ into and from a control volume, and δA is the cell wall area projected normal to $\underset{\sim}{\Omega}$. The energy sources S_R are appended to the energy balance equation solved for by the flow code.

The gas absorption coefficient k_g is calculated from the "two grey plus a clear gas" fit of Truelove [12]. Water vapour and carbon dioxide are the prime contributors to the gaseous radiation. The contribution of the carbon monoxide and fuel for the gas absorption coefficient was not considered due to the lack of appropriate data. However, it is though that the total combustor absorption by the fuel and carbon monoxide will be small. The total gas emittance is expressed by:

$$\varepsilon_g = \sum_n a_{g,n}(T)\left[1 - \exp(k_{g,n}(p_w + p_c)L)\right] \tag{19}$$

where the summation n is over the three gases of the assumed mixture, the $k_{g,n}$ are presumed constant with the temperature dependence of the emittance being accomodatedin the weighting coefficients $a_{g,n}$, p_W and p_c are the partial pressures of the water vapour and carbon dioxide and L is the path length. The values of the $k_{g,n}$ and $a_{g,n}$ are tabulated in [12]. The value of k_g required for our calculations is obtained from the pseudo grey gas approximation:

$$\varepsilon_g = 1 - e^{-k_g L} \tag{20}$$

which has worked well in many furnace heat transfer computations (see, e.g. [10]). Since the Truelove correlation was formulated for furnace applications, the predicted mol fractions must be multiply by the current pressure to obtain the correct partial pressures.

We have made no attempt to solve for the soot. Some guidance on how this can be done is offered by [13]. In this paper a review on soot formation and soot oxidation models is presented. The soot formation model of Khan and Greeves [14] and the soot oxidation model of Magnussen and co-workers [15] have been applied successfully in industrial furnaces (see [8], [10], [11]). The work of Khan and Greeves was performed in connection with diesel engines and they present for the constant, C_f appearing in the model, the value of 4.68×10^5 mg/Nms. The value of this constant was tuned by Abbas and co-workers [16] for the case of spray flame combustion inside furnaces and a value of $0{,}1 \times 10^5$ mg/Nms was found to be appropriate. In the aforementioned applications the value for the soot formation constant proposed by Abbas was used. However, there are no information on the value of this constant for high pressures.

The boundary condition necessary for the calculation of the radiative heat transfer was obtained from an energy balance of the liner. Broadly, the liner is heated by radiation and convection from the hot gases inside it; it is cooled by radiation to the outer casing and by convection to the annulus air. Under equilibrium conditions the liner temperature is such that the internal and external heat fluxes at any point are just equal. Loss of heat by conduction along the liner wall is comparatively small and usually may be neglected. Since the liner wall is usually very thin we have neglected the difference between inner and outer liner wall areas. Therefore, under steady-state conditions, the following balance equation can be written:

$$R_1 + C_1 = R_2 + C_2 = K_{12}$$

where subscript 1 refers to internal fluxes and subscript 2 to external fluxes and K_{12} is the conduction heat transfer through a solid liner wall due to a temperature gradient within the wall. Internal radiation, R_1, is calculated from equation (17), while the internal convection C_1 was calculated from Reynolds analogy (e.g. [17]). Calculations of external radiation and convection, R_2 and C_2, were done using the correlations presented by Lefebvre [1].

The calculation procedure may be summarized as follows:

1. As a first guess, the liner wall temperature (flame side) is assumed to be equal to the inlet air temperature.

2. The internal radiation R_1 and internal convection C_1 are calculated.

3. Using the relationship $R_1 + C_1 = R_2 + C_2$, the liner wall temperature (coolant side) is calculated. A non-linear equation has to be solved, as R_2 is proportional to T^4, and the Newton-Raphson's method was used for the solution of this equation.

4. Setting $R_1 + C_1 = K_{12}$, a new value for the liner wall temperature (flame side) is obtained and it is compared with the value used in step 2.

5. Steps 2-4 may be repeated according to a convergence criterium.

4. NUMERICAL SOLUTION PROCEDURE

Method of solution

The finite difference method used to solve the equations entails by subdividing the calculation domain into a number of finite volumes or "cells". The solution algorithm was embodied in a version of TEACH program [18] for three-dimensional recirculating flows. The convection terms were discretized by the Hybrid Central/Upwind method [19]. The velocities and pressures are calculated by a variant of the SIMPLE algorithm [20]. The solution of the individual equations sets was obtained by a form of Gauss-Seidel line-by-line iteration.

Computational details

The equations presented in section 3, together with appropriate boundary conditions, have been applied to the geometry shown in Figure 1. A grid of 19 x 17 x 18 nodes (r, θ, x - directions) was used. The number of iterations required for a convergent solution was around 220, which corresponds to a CPU time of about 50 hours in a Micro VAX II. Convergence was achieved when the normalized residuals for the three momentum equations and mass conservation were less than 2×10^{-3}.

The iterative procedure for the heat transfer calculation was embodied in the SIMPLE algorithm. This calculation was only performed after the residuals of the main variables had attained the value 8×10^{-3} and for every 5 iterations. As described in section 3, this iterative process for the heat transfer calculation consists on: i) starting from a guessed liner wall temperature (flame side); ii) calculating internal radiation and convection; iii) liner wall temperature (coolant side)and again the liner wall temperature, (flame side), which will correct the guessed value.

This iterative procedure was applied to each wall boundary cell of the grid. The difference between the liner temperature (flame side) for two sucessive iterations was calculated for all the boundary cells. The process was considered to have "converged" if the mean value of these differences would be less or equal to 10^{o} C and the maximum value less or equal than 50^{o} C. An under-relaxation factor of 0.2 was used for the temperature.

It was observed that the iterative process for the heat transfer calculation converged very fast. Six iterations were needed for the first time that the procedure was called but this number decreased rapidly to one iteration.

In the present calculations, the computation time is essencially dependent on the time required to evaluate the internal radiation by the discrete transfer method. Thus, the computation time of the present calculations does not increase significantly when compared with calculations with prescribed wall temperatures. The main problem of the method used here for the heat transfer calculation is the lack of suitable correlations for the calculation of external convection. The same problem arises with the calculation of external radiation, but, since external convection is more important than external radiation, errors associated with the external radiation seem not to be important. Though, if a precise prediction of the liner temperature is needed, the equations for the flow and heat transfer for the outer annular region should be solved and the two solution procedures (combustion chamber and outer annular region) should be linked in an iterative fashion as described in the present work.

5. DISCUSSION OF RESULTS

Figure 2 shows the temperature distribution of the backplate (Fig. 2a), inner annular wall (Fig. 2b) and outer annular wall (Fig. 2c) for the conditions identified in Table 1 as case 1 (p=5 bar). The film-cooling air near the outer and inner annulus wall can be identified in the backplate temperature distribution by the presence of the two lines corresponding to low temperature (500 K and 600 K) near to the annular walls and parallel to these walls. In the middle of the backplate there is a region of high gradients as this region is the center of combustion activity. Near the simmetry planes the temperature is higher (900 K) due to the recirculation of hot gases.

The temperature distribution of the two annular walls (Fig. 2b and c) reflects the distribution of the cooling holes. The levels of temperature increase from the burner side to the exit side. Until the location of the second row of holes, the film-cooling air protects the walls avoiding the occurrence of high temperature. But due to diffusion, the cool air will tend to mix with the mainstream and the hot gases from the mainstream will tend to mix with the cool air increasing its temperature. The highest temperatures (800 K) in the annular walls occur near the two corners formed between the exit plane and the simmetry planes. This is due to the fact that the middle region of the exit plane is under the cooling effect of the dilution air from the second row of holes. It is worth noting that the maximum wall temperature is, in this case of about 800 K and the maximum temperature difference is of the order of 300 K.

Figure 3 displays the radiation heat transfer contours to the backplate, inner and outer annular walls for a working pressure of 5 bar (case 1). The heat flux to the three walls is rather uniform. For the backplate (Fig. 3a) the radiative heat flux wavers about a value of 25 KW/m^2, although near the entrance of the film-cooling air the heat flux attains a value of 50 KW/m^2. For the annular walls, it can be seen that the higher values of the radiative heat fluxes can be found in the intermediate region of the combustors between the burner plane and the exit plane. This is a consequence of the higher temperature of the gases in this region, as after the second row of holes, the temperature of the gases decreases due to the effect of the dilution air. The heat transfer to the inner annular wall reflects the distribution of the cooling holes. The heat flux through the holes is more than to the walls but since the holes cover less 5% of the total wall area this fact is not significant.

Figure 4 shows the gas field temperature on a plane perpendicular to the axis of symmetry of the combustor after the second row of holes, near the exit for p=5 bar. The feature of dilution air intrusion is still identified at this location where again cooler air penetration follows the pattern expected from the hole geometry with one cool region near the bottom wall and one near the upper wall. It is known that an uniform exit temperature distribution would be considered ideal in order to maximize the life of the turbine blades and nozzle guide vanes. However, as it can be seen for the present case, the distribution of temperature at the combustor exit is far from uniform as usually happens in all modern high-performance engines.

Figure 5 and 6 show the temperature distribution and the radiative heat fluxes distribution to the combustor walls for a working pressure of 15 bar (case 2). Figure 7 shows the gas field temperature distribution at a plane near the exit for the same pressure. For a pressure of 25 bar (case 3), the temperature and radiative heat fluxes distribution are shown in figures 8 and 9, respectively. Comparing the results

for the different working pressures, it can be concluded that the distributions are qualitatively similar. However, the effect of the presence of the cooling holes in the temperature and fluxes distribution of the annular walls is more pronounced for higher pressures. The levels of temperature and fluxes increase with pressure due to the increase of the temperature of the gases and gas emissivity. The highest wall temperature observed in all cases is of the order of 1100 K. To ensure a satisfatory liner life, it is important to keep temperatures down to an acceptable level. It is generally recognized that for the common used materials the maximum temperature of the liner should not greatly exceed 1100 K [1]. In the cases investigated, temperatures of this order of magnitude only occur for the pressures of 15 and 25 bar near the exit plane where the film cooling is no longer effective.

Figure 10 shows the total heat transfer contours to the backplate, inner and outer annular wall for a pressure of 25 bar. The convective fluxes to the holes were not calculate. So the distribution of heat fluxes near the holes are meaningless. Comparing figures 9 and 10, it can be concluded that, radiation is more important in the primary zone and the convection is more important in the dilution zone. The temperature of the film-cooling air is kept low in the primary zone. Therefore the convective heat transfer to the liner in this region will be small. As the temperature of the film-cooling air increases the convective heat transfer to the liner will increase also.

Figures 11, 12 and 13 show temperature contours for several axial, radial and tangential locations at a pressure of 25 bar. Figure 11a) shows a plane perpendicular to the axis of symmetry of the combustor passing through the first row of holes. The influence of the secondary air entering through these holes can be seen by the penetration of one cooler region into the combustor in each annular wall. The maximum temperature is attained near the center of the plane due to the presence of hot combustion products. The plane shown in Figure 11b) is located near the exit of the combustor. The features of the contours are similar to those of figure 4 (p=5 bar) and figure 7 (p=15 bar) since the location is the same.

Figure 12 shows contours of two constant radius planes, the first passing through the burner centre-line and the second passing close to the outer annular wall. The influence of cooling air entering through the secondary and dilution holes is clearly seen in the second plot but not in the first one. Primary air generates very high gradients in the primary zone, as can be seen in figure 12 a, due to the chemical reaction. Highest temperatures are attained in the secondary zone away from the burner centre-line. In the second plot, figure 12 b, temperature is rather uniform in the primary zone, due to the presence of cooling air. This influence is less important in the intermediate and dilution zones due to the diffusion of the cooling air into the centre of the combustor.

In figure 13, two constant θ planes are presented. In the first plot cooler regions near primary and dilution holes can be identified as well as a cooler region close to the inner and outer annular walls in the primary zone due to the film cooling air. Maximum temperature occurs at the central region of the plane. The second plot shows very steep gradients in the primary zone where combustion takes place and a much more uniform distribution downstream. Cooler regions near the first row of holes can also be seen.

Table 2 shows the radiative, convective and total heat fluxes to the walls for the three combustor pressures investigated. The values of the heat fluxes presented in this table are referred to all the 18 sectors of the combustor. As it can be seen, radiative and convective fluxes are small. The small convective fluxes can be justified by the streams of cooling air close to the annular walls. Although this cooling air deteriorates temperature pattern factor, reduces combustion efficiency and contributes to the presence of pollutants in the exhaust gases [13], its presence is required to reduce wall temperature. Both radiative and convective fluxes increase with pressure, mainly due to the increase of inlet air temperature and gas emissivity. The ratio of these fluxes to the energy supplied to the combustor is about 1% and is almost the same for the three cases studied. However, convective fluxes are sligthly greater than radiative ones.

In our calculations no attempt has been made to account for the presence of soot. Soot would enhance radiative heat transfer mainly at high pressures. However, measurements made by Marsland and co-workers [21] suggest that above 20 bar, soot concentration reach a level such that blackbody radiation is approached. So a further increase in pressure will have little or no effect on the flame radiation.

TABLE 2 - HEAT FLUXES TO THE WALLS [kW]

COMBUSTOR PRESSURE	WALL CONSIDERED	RADIATIVE HEAT TRANSFER	RADIATIVE HEAT TRANSFER/ENERGY SUPPLIED TO THE COMBUSTOR	CONVECTIVE HEAT TRANSFER	CONVECTIVE HEAT TRANSFER/ENERGY SUPPLIED TO THE COMBUSTOR	TOTAL HEAT TRANSFER	TOTAL HEAT TRANSFER/ENERGY SUPPLIED TO THE COMBUSTOR
5 bar	Combustor backplate	6.4	0.07%	9.7	0.11%	16.1	0.18%
	Inner annulus wall	45.4	0.49%	49.0	0.53%	94.4	1.02%
	Outer annulus wall	68.0	0.74%	72.5	0.78%	140.5	1.52%
	Total	119.8	1,30%	131.2	1.42%	251.0	2.72%
15 bar	Combustor backplate	12.3	0.07%	20.3	0.11%	32.6	0.18%
	Inner annulus wall	88.4	0.48%	116.5	0.63%	204.9	1.11%
	Outer annulus wall	131.6	0.71%	172.1	0.93%	303.7	1.65%
	Total	232.3	1,26%	308.9	1.68%	541.2	2.94%
25 bar	Combustor backplate	13.4	0.06%	25.6	0.10%	39.0	0.16%
	Inner annulus wall	96.1	0.39%	120.8	0.49%	216.9	0.88%
	Outer annulus wall	146.2	0.59%	179.8	0.73%	326.0	1.32%
	Total	255.7	1.04%	326.2	1.32%	581.9	2.36%

6. CONCLUDING REMARKS

The present paper describes a prediction procedure for the calculation of the flow, heat-transfer and combustion processes inside a three-dimensional can combustor chamber of a gas turbine. The incorporation into the computational scheme of a technique for calculating the distribution of temperature and heat fluxes in the liner represents the main contribution of this paper. It is believed that is the first time that the temperature and heat fluxes distributions of the liner were calculated. All the previous works have imposed the liner temperature. The accurate assessment of these quantities are an essential prerequisite for the prediction of liner life. The calculation method outlined in the present paper constitutes the only correct way to calculate the liner temperature (a heat balance to the liner linking the heat transfer processes occurring in the combustion chamber with the heat transfer processes occuring in the outer annular region). The main problem of the method used here for the heat transfer calculation is the lack of suitable correlations for the external convection and radiation. For a complete and accurate picture of the heat transfer in gas turbine combustion chambers, the equations for the flow, and heat transfer for the outer annular region should be solved and the two prediction procedures should be linked through the energy balance to the liner. Another cause for concerne is the lack of reliable data for the contribution of the carbon monoxide to the gas absorption coefficient and the lack of a reliable method of predicting the soot concentrations at high pressures and hence the emissivities of luminous flames.

7. REFERENCES

[1] - Lefebvre, A.H., Gas Turbine Combustion. McGraw-Hill, New York, 1983.

[2] - Boysan, F., Ayers, W.H., Swithenbank, J. and Pan, Z., Three-dimensional model of spray combustion in gas turbine combustors. J. Energy, Vol. 6, n° 6, 1982, pp. 368-375.

[3] - Lockwood, F.C., McGuirk, J.J. and Shah, N.G., Radiation transfer in gas turbine combustors. Presented at AIAA 18th Thermophysics Conference, Paper n° AIAA-83-1506, June, 1983.

[4] - Lockwood, F.C. and Shah, N.G., A new radiation solution method for incorporation in general combustion prediction procedures. Proc. 18th Symposium (Int.) on Combustion, The Combustion Institute, 1981.

[5] - Gordon, S. and McBride, B.J., Computer Program for the calculation of complex chemical equilibrium compositions. NASA SP 273, 1971.

[6] - Carvalho, M.G., Durão, D.F.G. and Lockwood, F.C., Computation of thermal radiation for gas turbine conditions. 65th AGARD/PEP Symp. Bergen, 1985.

[7] - Launder, B.E. and Spalding, D.B., Mathemacical Models of Turbulence. Academic Press, New York, 1972.

[8] - Carvalho, M.G., Computer simulation of a glass furnace. Ph.D. Thesis, London University, 1983.

[9] - Lockwood, F.C. and Naguib, A.S., The prediction of the fluctuations in the properties of free, round jet, turbulent diffusion flames. Combust. Flame, Vol. 24, 1975.

[10] - Carvalho, M.G., Durão, D.F.G. and Pereira, J.C.F., Prediction of the flow, reaction and heat transfer in an oxy-fuel glass furnace. Eng. Comput., Vol. 4, nº 1, March 1987, pp. 23-34.

[11] - Carvalho, M.G. and Lockwood, F.C., Mathematical simulation of an end-port regenerative glass furnace. Proc. Instn. Mech. Engrs, Vol. 199,, 1985, pp. 113-120.

[12] - Truelove, J.S., A mixed grey gas model for flame radiation. AERE Harwell Report nº HL 76/3448/KE, 1976.

[13] - Lefebvre, A.H., Flame radiation in gas turbine combustion chambers. Int. J. Heat Mass Transfer, Vol. 27, nº 9, 1984, pp. 1493-1510.

[14] - Khan, I.M. and Greeves, G., A method for calculating the formation and combustion of soot in diesel engines. Heat Transfer in Flames, Ed. Afgan and Beer, 1974, pp. 391-402.

[15] - Magnussen, B.F. and Hjertager, B.H., On mathematical modelling of turbulent combustion with special emphasis on soot formation and combustion. Proc. 16th Symposium (Int.) on Combustion, The Combustion Institute, Pittsburg, 1976.

[16] - Abbas, A.S., Koussa, S.S. and Lockwood, F.C., The prediction of a variety of heavy oil flames. Proc. ASME Winter A. Mtg, Washington, Special Session on Two Phase Combustion Liquid Fuels, Nov. 1981.

[17] - Schlichting, H., Boundary Layer Theory. McGraw Hill, New York, 1968.

[18] - Gosman, A.D., Humphrey, J.A.C. and Vlachos, N.S., TEACH-3E: a general computer program of three-dimensional recirculating flows. Report CHT/76/10, Dept Mech. Eng., Imperial College, 1976.

[19] - Spalding, D.B., A novel finite difference formulation for differential expressions involving both first and second derivatives. Int. J. Num. Meth. Eng., Vol. 4, 1972, p. 551.

[20] - Caretto, L.S., Gosman, A.D., Patankar, S.V. and Spalding, D.B., Two calculation procedures for steady, three-dimensional flows with recirculation. Proc. 3rd. Int. Conf. Num. Meth. Fluid Dynam., Springer-Verlag, New York, 1972, p. 60.

[21] - Marsland, J., Odgers, J. and Winter, J., The effects of flame radiation on flame-tube metal temperatures. Proc. 12th Symposium (Int.) on Combustion, The Combustion Institute, Pittsburgh, 1969, pp. 1265-1276.

ACKNOWLEDGEMENT

The authors whish to thank Dr. J. McGuirk for his useful suggestions on this work. The financial support of Instituto Nacional de Investigação Científica, Lisbon, is aknowledged. The preparation of this paper was expeditated by the speedy typing of Ms. M. Cristóvão and Ms. S. Ribeiro.

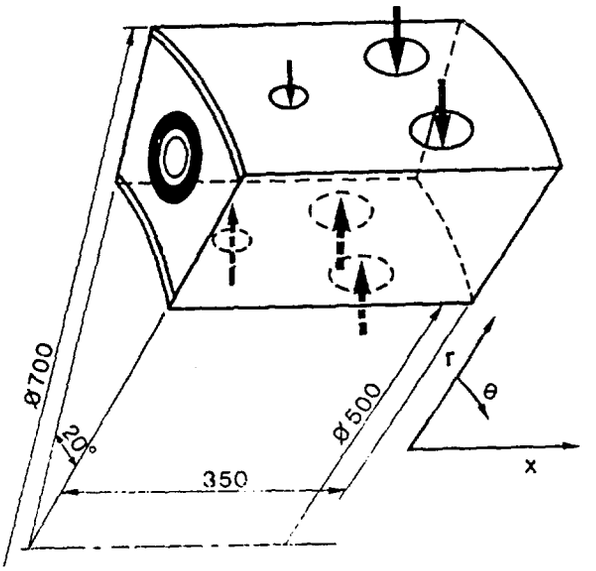

Fig. 1 - Annular combustor geometry

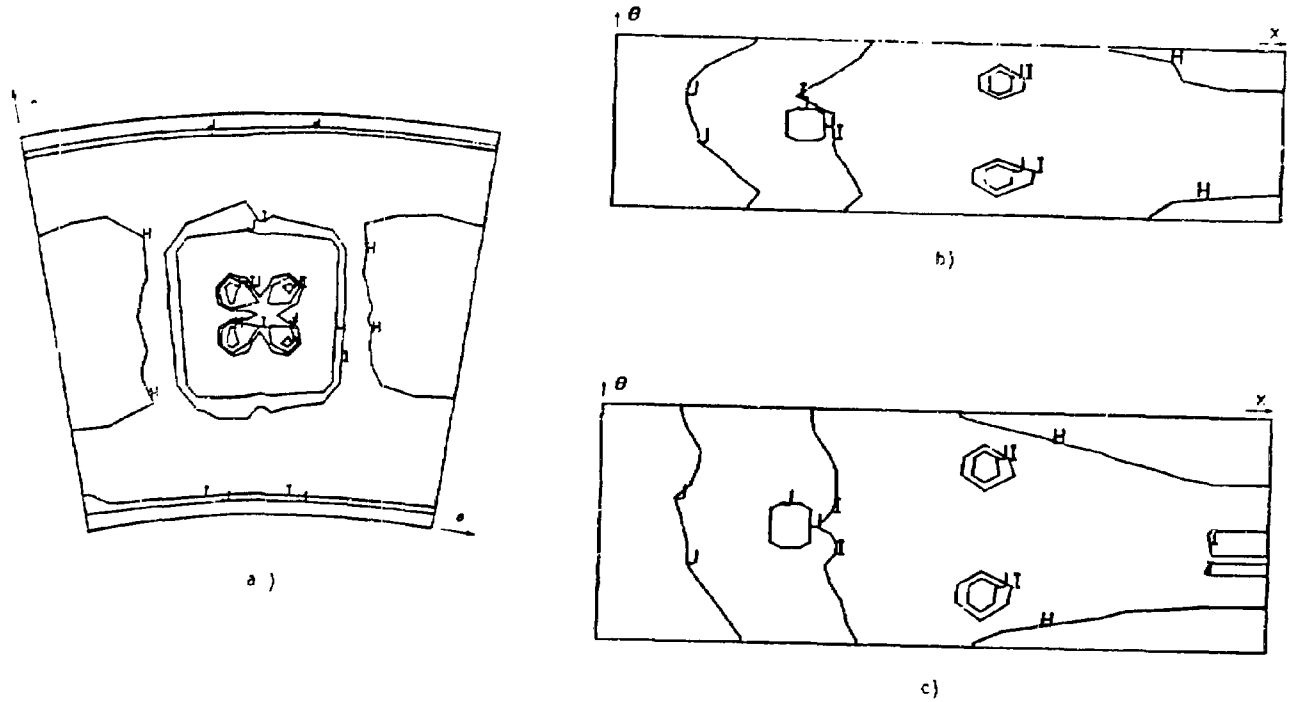

Fig. 2 - Wall temperature distribution: p=5 bar
a) Combustor backplate
b) Inner annulus wall
c) Outer annulus wall
Contours levels [K]:
H=800; I=600; J=500

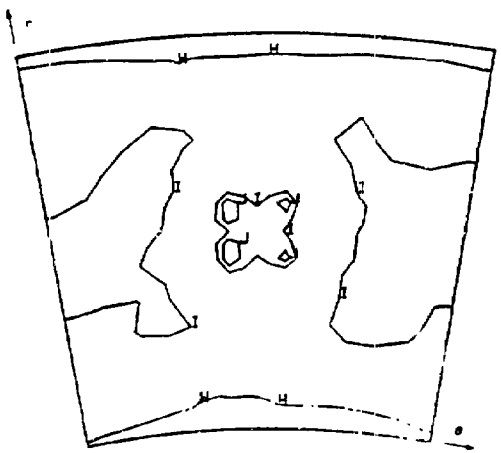

a)

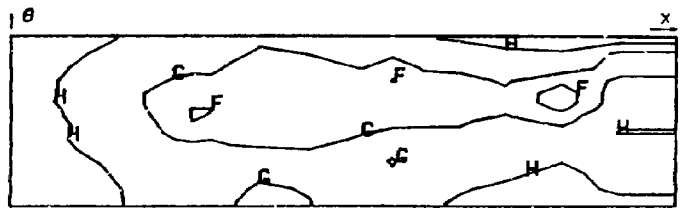

b)

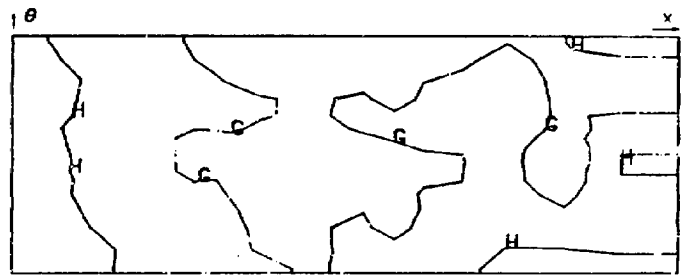

c)

Fig. 3 - Radiative wall heat fluxes: p=5 bar
a) Combustor backplate
b) Inner annulus wall
c) Outer annulus wall
Contour levels [KW/m^2]:
F=150.0; G=100.0; H=50.0; I=25.0; J=10.0

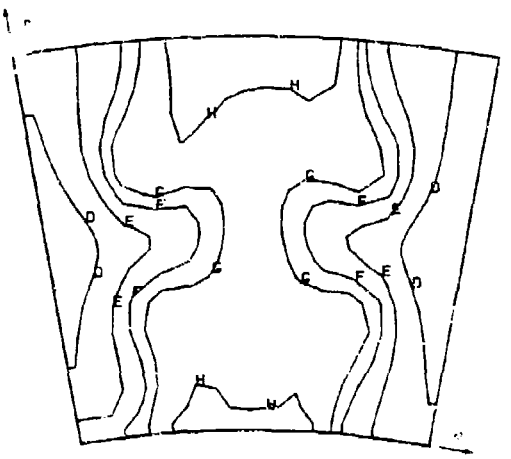

Fig. 4 - Gas field temperature for the plane x=0.34 m; p=5 bar
Contour levels [K]:
D=1500; E=1250; F=1100; G=1000; H=800

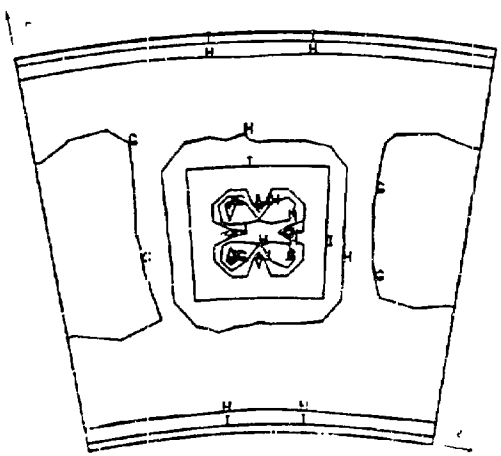

a)

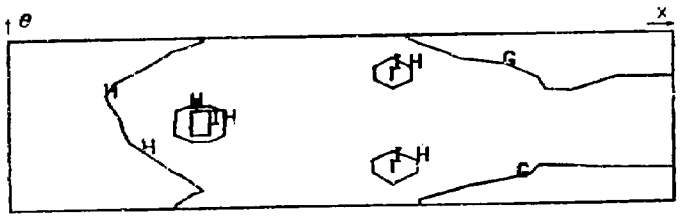

b)

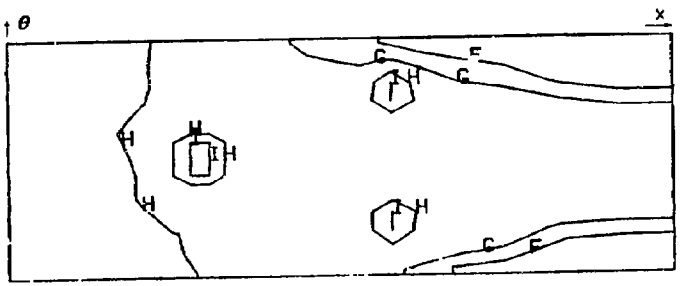

c)

Fig. 5 - Wall temperature distribution; p=15 bar
a) Combustor backplate
b) Inner annulus wall
c) Outer annulus wall
Contour levels [K]:
F=1100; G=1000; H=800; I=600; J=500

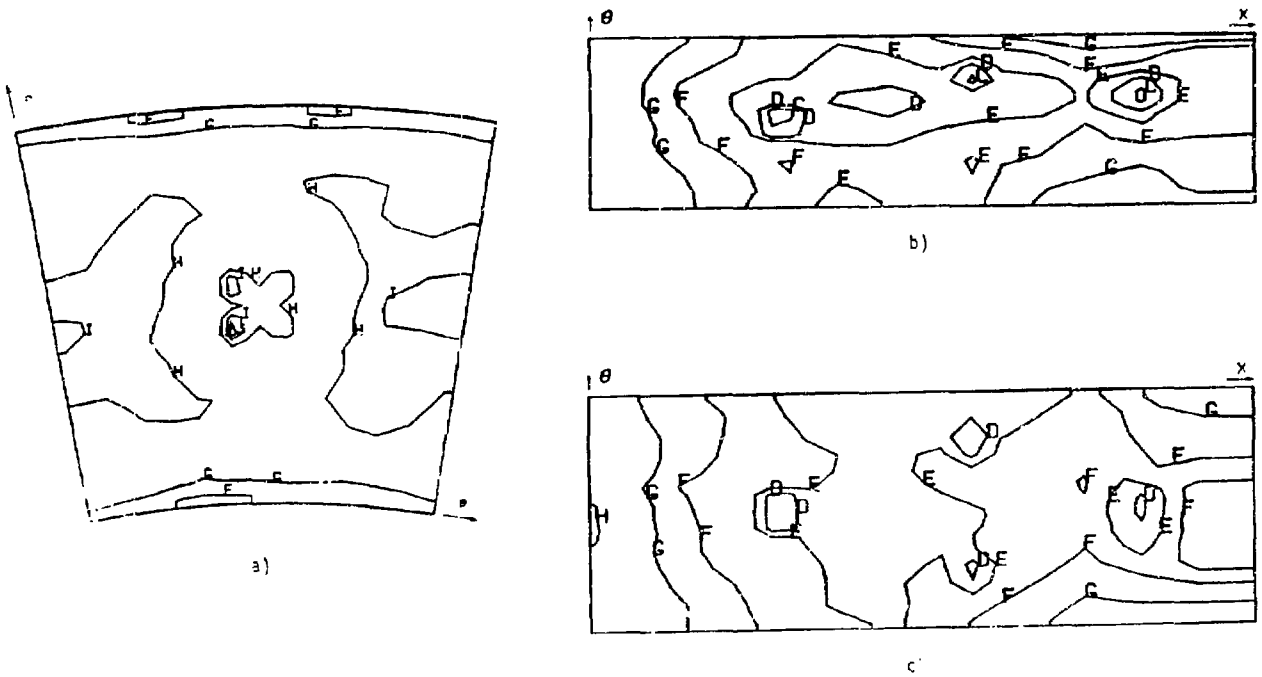

Fig. 6 - Radiative wall heat fluxes; p=15 bar
a) Combustion backplate
b) Inner annulus wall
c) Outer annulus wall
Contour levels [KW/m^2]:
C=300.0; D=250.0; E=200.0; F=150.0; G=100.0; H=50.0;
I=25.0; J=10.0

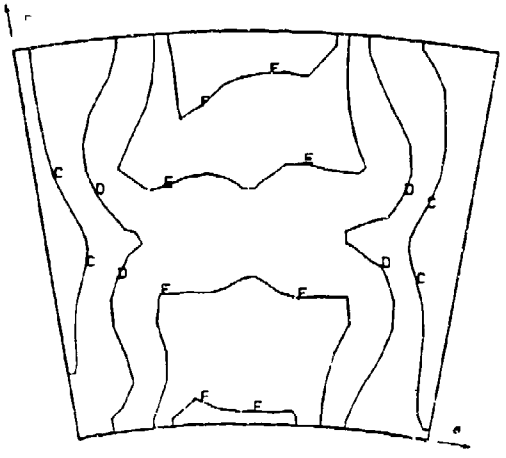

Fig. 7 - Gas field temperature for the plane x=0.32 m; p=15 bar
Contour levels [K]:
C=1750; D=1500; E=1250; F=1100

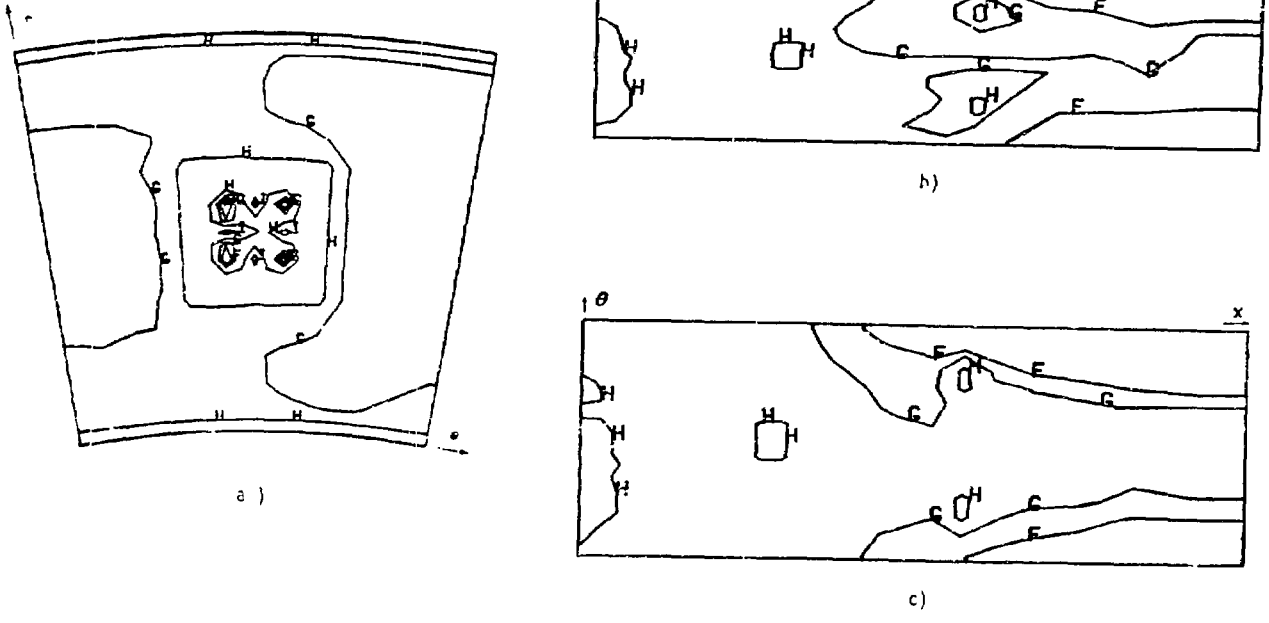

Fig. 8 - Wall temperature distribution; p=25 bar
a) Combustor backplate
b) Inner annulus wall
c) Outer annulus wall
Contour levels (K):
F=1100; G=1000; H=800; I=600

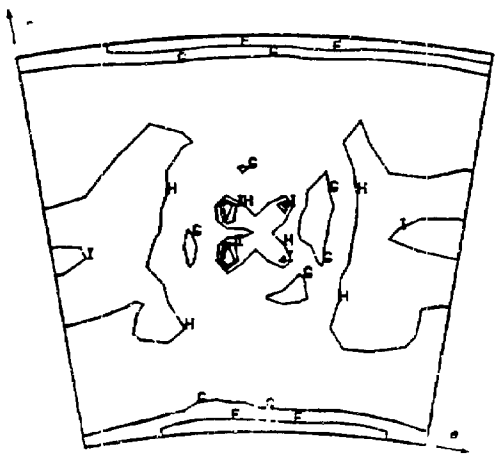

a)

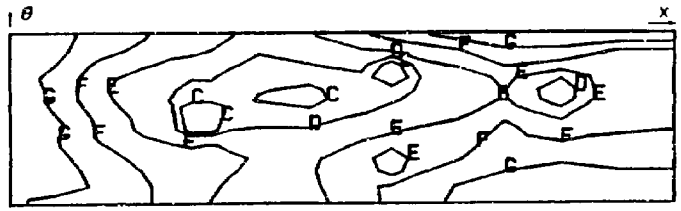

b)

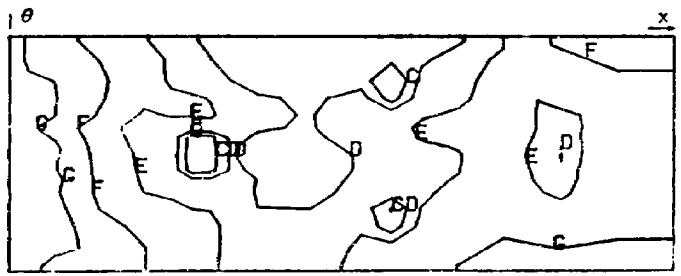

c)

Fig. 9 - Radiative wall heat fluxes; p=25 bar
a) Combustor backplate
b) Inner annulus wall
c) Outer annulus wall
Contour levels [KW/m^2]:
C=300.0; D=250.0; E=200.0; F=150.0; G=100.0; H=50.0;
I=25.0; J=10.0

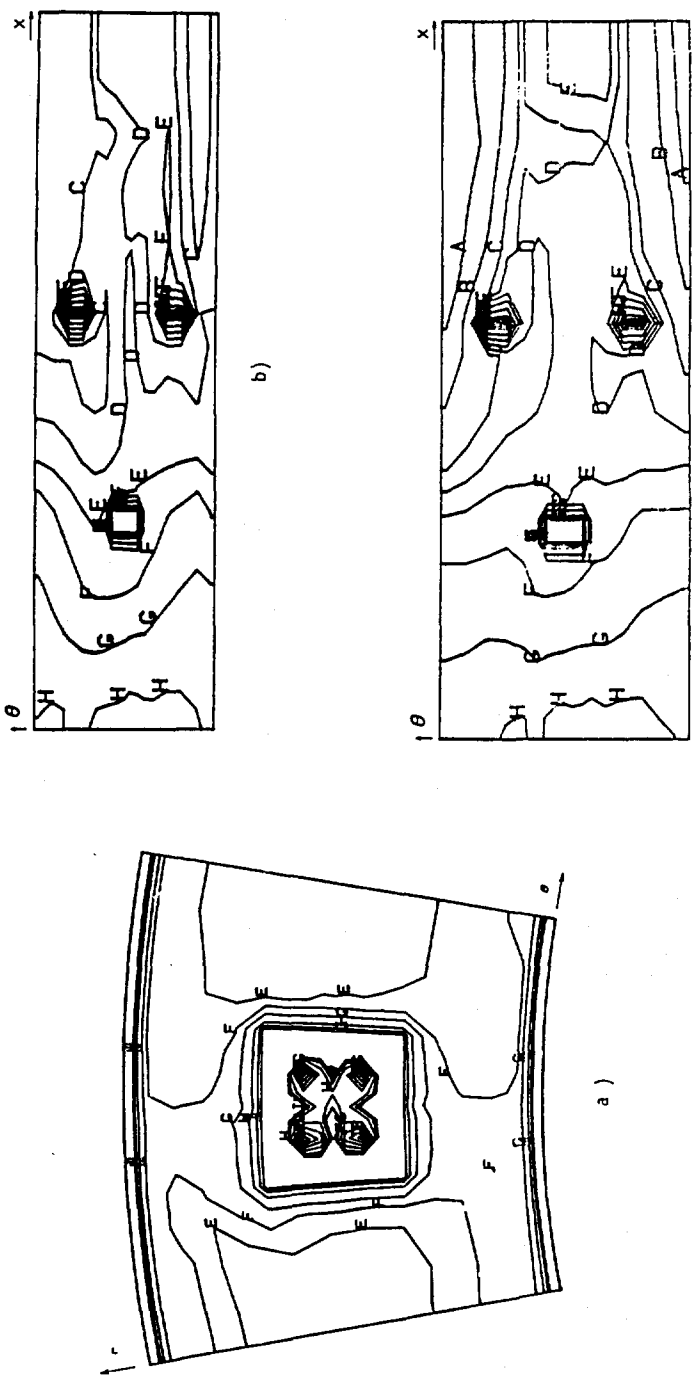

Fig. 10 - Total wall heat fluxes; p=25 bar
a) Combustor backplate
b) Inner annulus wall
c) Outer annulus wall
Contour levels [KW/m^2]:
A=500.0; B=400.0; C=300.0; D=250.0; E=200.0; F=150.0;
G=100.0; H=50.0; I=25.0; J=10.0

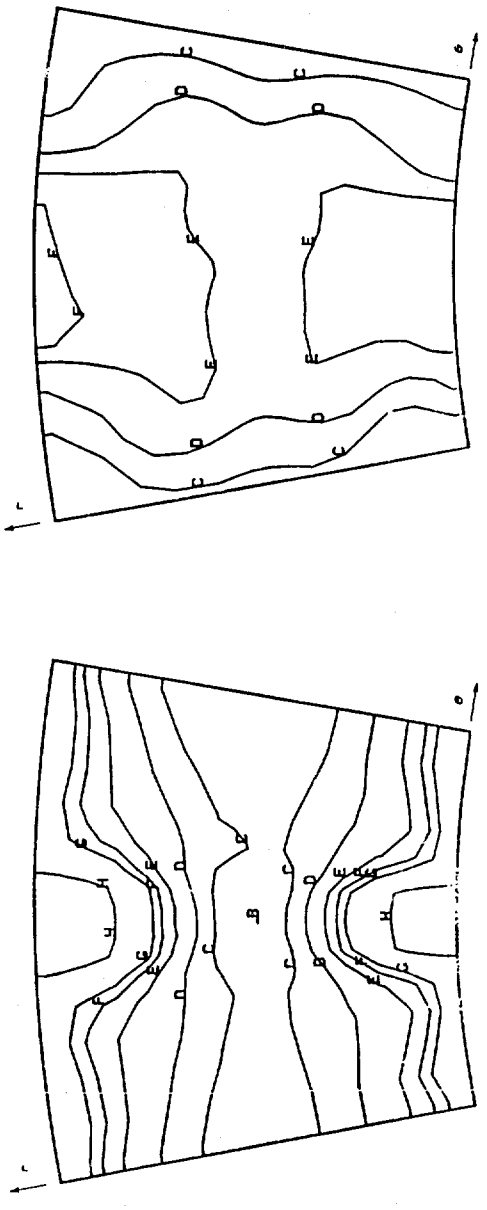

Fig. 11 - Gas field temperature; p=25 bar
a) Plane x=0.105 m
b) Plane x=0.320 m
Contour levels [K]:
D=2000; C=1750; D=1500; E=1250; F=1100; G=1000; H=800

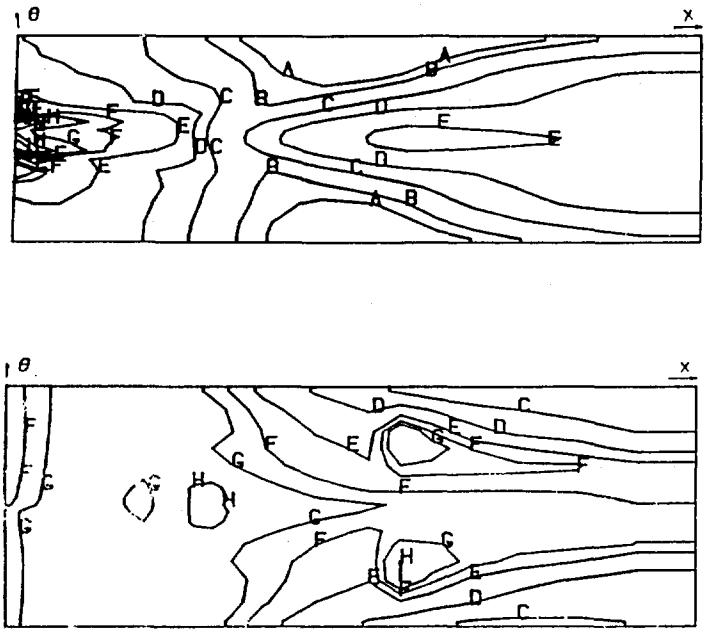

Fig. 12 - Gas field temperature; p=25 bar
a) Plane r=0.344 m
b) Plane r=0.300 m
Contour levels [K]:
A=2100; B=2000; C=1750; D=1500; E=1250; F=1100; G=1000; H=800; I=600; J=500

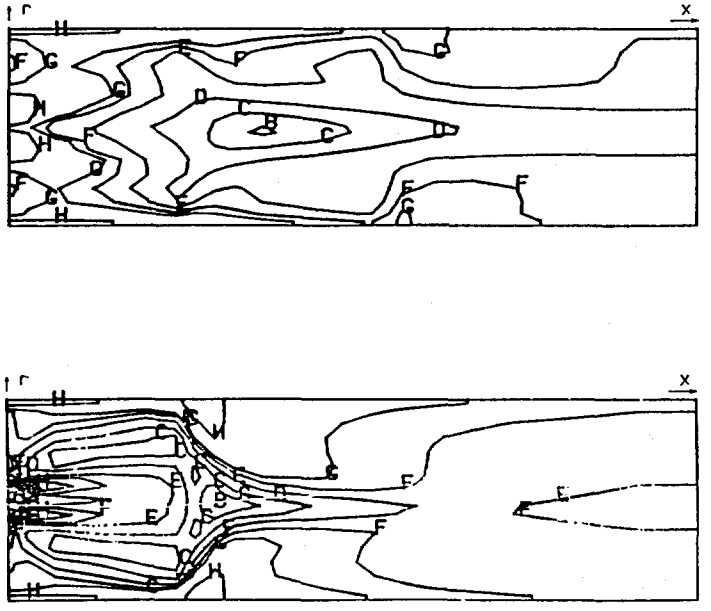

Fig. 13 - Gas field temperature; p=25 bar
a) plane θ=6.7°
b) Plane θ=10.0°
Contour levels [K]:
B=2000; C=1750; D=1500; E=1250; F=1100; G=1000; H=800; I=600

GAS TURBINE SMOKE MEASUREMENT: A SMOKE GENERATOR FOR THE ASSESSMENT OF CURRENT AND FUTURE TECHNIQUES

by

S. P. Girling

Propulsion Department
Royal Aircraft Establishment, Pyestock
Farnborough, Hampshire, GU14 OLS, England

SUMMARY

Smoke measurement from gas turbine engines is one instrumentation technique that remains, literally, a "black-art". Current methods are inaccurate, slow, insensitive and unable to detect transients. A smoke generator has been developed at the Royal Aircraft Establishment, Pyestock, capable of generating by pyrolysis of aviation kerosene, stable levels of smoke for prolonged periods, representative of that from engines. Particle size measurements have enabled the comparison of smokes from different sources and provided a greater understanding of the problems of representative sampling using currently approved methods. Several alternative measurement techniques have been evaluated using the smoke generator, precluding the need for expensive engine testing. This has promoted research into instrumentation that will give a truer indication of particulate criteria of interest to the engine designer and customer, for example true visibility and erosiveness.

1 INTRODUCTION

Developments in gas turbine technology necessitate more powerful, hotter and more compact combustion systems. One result of this is an increased tendency for the combustor to produce smoke, a problem which could be exacerbated even further with future requirements for operation on poorer quality fuels. The measurement of this smoke is important for a number of reasons. It may be visible and thus environmentally and cosmetically undesirable, it may be erosive, limiting turbine life expectancy, and if it is particularly visible or has a significant IR signature it may be hazardous to military operation.

Methods for smoke measurement have developed little in comparison with other exhaust gas analysis techniques, despite the increased importance being placed upon smoke data. The current procedure relies on a filter stain technique which is non-continuous, cannot discriminate between particulate source or characteristics and is open to large sampling and measurement inaccuracies. The lack of both improvements and alternatives is partly due to the difficulties of representative sampling across a wide range of particulate size distributions. However there has also been the lack of availability of a cheap, easily accessible source of smoke with which to undertake instrumentation development. To this end a smoke generator has been developed at RAE Pyestock, capable of producing, cheaply and for long periods, a stable, controllable source of smoke. Critical appraisals of current sampling and measurement techniques have been possible using the smoke generator. In addition, calibrations and cross-correlations have been made against an absolute standard of mass loading of carbon.

Furthermore it is becoming increasingly evident that techniques are required which discriminate between different regions of the particle size spectrum and provide real-time data which are more immediately applicable to a particular design or performance criteria. The smoke generator has been used for the critical assessment of techniques which are likely to fulfil some or all of the above requirements. The most promising of these are optical techniques which are capable of continuous, high temperature, rapid response measurements. However it must be recognised that all methods are in some way dependent upon particle characteristics, whether it be filtration efficiency upon physical size and shape or optical response upon absorption and scattering properties. These characteristics are themselves dependent upon the processes of particle formation and growth, as influenced by variables such as fuel type, combustor design and operating conditions. Thus it is clear that no single technique will be capable of making absolute measurements across the whole spectrum of particle sizes, for applications from combustor development to engine certification.

This paper details the capabilities of the smoke generator and its use in assessing the merits and limitations of both current and future techniques, recognising the above constraints.

2 THE SMOKE GENERATOR

Smoke generators to date have included 2-cylinder petrol engines, oil burners and discharge nozzles seeded with carbon black. These have proved unstable and uncontrollable, producing smokes of unrepresentative mass loadings and size distributions in comparison with those from gas turbines. Recognising these problems, the Pyestock facility generates smoke by the pyrolysis of aviation kerosene, reproducing the basic engine formation processes as far as possible in a practical laboratory system, to ensure representativeness.

2.1 Principles of operation

The layout of the smoke generator is detailed in Fig 1. Aviation kerosene is fed into a pre-vaporising furnace from a variable-drive syringe pump, through a stainless steel capillary. Steady fuel flow is critical to the stability of the smoke output; metered flow rates are typically 0.1 - 0.5 mℓ/hr, so the fuel system is fully purged of air before operation. The capillary is mounted in the furnace in an atmosphere of preheated nitrogen as a carrier gas. From the prevaporiser the fuel/nitrogen mix is passed through a high temperature furnace at 1600°C where pyrolysis of the fuel takes place. Residence time is approximately 0.1s and is sufficient to ensure effective carbon formation at this temperature. The carbon is mixed with air in the sample duct, to give smoke levels representative of those from engines. Air is fed in through a 'dilution furnace' at 300°C, to maintain the smoke sample temperature at 150-180°C. This range is typical of 'in field' sample temperatures where condensation of sample water and unburnt fuel must be prevented.

A swirler at the head of the sample duct generates effective turbulent mixing of the carbon with the dilution air and a honeycomb flow straightener is positioned further downstream to ensure uniform concentrations across the duct when sampling from multiple positions at the duct exit. Excess smoke is vented to exhaust.

Smoke mass loading, the mass of particulate per unit standard volume (µg/ℓ), is a function of fuel flow and dilution air flowrate. Either of these may be used to set the required level, though fuel adjustment ensures a constant air/sample flow ratio is maintained in the duct. Further operational and development details are outlined in Ref 1.

2.2 Capabilities and characteristics

For gas turbine smoke measurement, mass loadings typically encountered are 0.5 - 5.0µg/ℓ. Over this range the smoke generator stability is between ±0.05 to ±0.15µg/ℓ. After a stabilisation period of 10-15 minutes this level of stability can be maintained for a period limited only by the volume of fuel in the syringe (7 hrs at 0.5µg/ℓ to 1.5 hrs at 5.0µg/ℓ). The day-to-day repeatability of mass loading for a given fuel flow is poorer.

Initially, particulate shape and size estimates were made by analysing a smoke sample under a scanning electron microscope. Fig 2 shows the sizes and shapes of the particles collected. The smoke appears to be made up of largely submicron particulates in the range 0.02 -0.1µm with agglomerated chains and clusters up to ∿1.0µm in size. A Differential Mobility Particle Sizer (DMPS) and Aerodynamic Particle Sizer (APS) were used to make more detailed particle size distribution measurements in the size ranges 0.01 - 1.0µm and 1.0 - 15.0µm respectively[2]. Fig 3 shows typical results and confirms that the size distribution is submicron with few particles >1µm. Information on particle size for typical combustion generated smoke is limited; Ref 1 alludes to data in the range 0.02 - 0.12µm for a variety of combustion systems. Measurements using the above instruments were also made on a diesel fuelled gas turbine engine. The results in Fig 4 show;

(a) the bulk of the particles are submicron, but with lower count and volume mean diameters than the smoke generator at an equivalent smoke level. (These are the diameters above and below which lie 50% of the particles, by number and volume respectively).

(b) a significant number of particles >1µm are present which were not present on the smoke generator.

Differences in (a) may be due to fuel type while (b) is likely to be due to the fact that the experimental combustion system on test was one which was prone to the build up and shedding of carbon from the walls of the combustor, thus generating greater numbers of larger particles than would be experienced in a 'clean' system (see 3.2.2). The true representativeness of the smoke generator particle characteristics, as compared to a combustion generated smoke, cannot be easily defined. Besides discrepancies introduced by sampling and measurement techniques for submicron to >1µm particulates, the variability introduced by fuel physical and molecular properties, combustor mechanics, aerodynamics and operating conditions has to date only been objectively (and crudely) studied with reference to smoke visibility or total mass loading.

2.3 Calibration of current techniques

The currently accepted technique for smoke measurement[3] involves filtering a predetermined mass of sample through a white filter paper. The ratio of the reflectance of the filter paper when stained to its white reflectance is a measure of the smoke level. According to the measurement procedure followed, the ratio is defined as an SAE Smoke Number, a Bacharach Number or a Bosch Smoke Number, each of which has been adopted by different sections of the engine industry, broadly speaking aeronautical, industrial/marine and automotive respectively. These measurement scales are arbitrary in that they bear no relation to the physical properties of the smoke. A number of correlations have been derived for the relationships between these scales and mass loading of carbon[1], with a high degree of variability due to the difficulties of representative sampling

over long periods from often unstable sources and the multiple inaccuracies inherent in these filtration techniques (see 3.1). Using the advantage of good stability from the smoke generator over long periods, further correlations between current techniques and mass loading of particulate have been produced. The correlation between mass loading and the accepted filter stain method for aero gas turbines, SAE Smoke Number, is shown in Fig 5.

3 SMOKE MEASUREMENT: CURRENT PROBLEMS AND FUTURE TECHNIQUES

Using the smoke generator a more quantitative assessment than had been previously possible has been made of the inaccuracies inherent in the techniques described in 2.3. This has prompted research into more fundamental and accurate methods which are better suited to providing information of value to the combustor designer and engine customer.

3.1 Smoke sampling and measurement

The techniques outlined in 2.3 rely upon the extraction of a sample from the exhaust gas of the engine or combustion system under test, followed by filtration through a low-grade filter paper. Work on the smoke generator[4] has shown that at typical mass loadings, with the maximum permissible length of sample line, losses of ~25% are caused by particulate diffusion and impaction onto the inner walls. Filter tests[2] showed that for a typical particle size distribution in the range 0.02 - 0.9μm, the filtration efficiency (by mass) of the standard media is ~80%. Furthermore preliminary work with the same filter media[1] indicated errors introduced by poor batch-to-batch repeatability, and poorly defined reflectance measurement procedures, could be of the order of ±10% of the true mass loading. In addition to these cumulative errors of possibly 50%, the technique is cumbersome and non-continuous and as mentioned does not provide a measurement which has any direct significance to the engine designer or customer other than by empirical correlations with physical quantities.

3.2 Future techniques for smoke measurement

3.2.1 Objectives

In spite of the difficulties and inaccuracies cited in 3.1 the current technique has been in service for the past 17 years and only recently have new techniques emerged, which with development could prove to be satisfactory alternatives. "Total smoke" measurements as made by the filter stain techniques are increasingly inadequate as demand grows for information on particulate effects such as erosiveness, exhaust plume visibility and IR radiance. Depending upon the engine application, military or civil, and the performance criteria to be met, future procedures will necessitate some or all of the following capabilities;

(a) sensitivity to submicron particulates (these are primarily produced by high temperature pyrolysis in overrich combustion zones).

(b) sensitivity to larger (>1μm) particulates (these are primarily produced by the deposition of carbon on the interior surfaces of the combustor, with subsequent shedding).

(c) direct plume measurements to obviate sampling inaccuracies

(d) continuous measurements to detect transients

(e) operation in a harsh environment at high temperatures

(f) calibration standards and auditable procedures

The smoke generator has proved an ideal tool with which to assess measurement techniques that fulfil some or all of the above requirements. To date a number of instruments have demonstrated capabilities for qualitative continuous measurements.

3.2.2 Light scattering techniques

Two commercial instruments, the MINIRAM and SIGRIST, have been evaluated using the smoke generator and begun preliminary usage on engine test facilities[5]. The MINIRAM is a single beam instrument measuring total light scattering in the forward angle 45-95°, the SIGRIST dust monitor is a dual beam instrument measuring in the forward angle 7-22°. Neither of these techniques discriminates particle size since they detect the total light scattering from an ensemble of particles crossing a sensing volume. Quantitative data are only currently available through correlations with other techniques. (Manufacturers' calibrations have been made using Arizona road dust and polystyrene latex spheres, both with optical properties dissimilar to carbon particulates). Figs 6 and 7 show the potential of these techniques for continuous smoke monitoring. The 'steady-state' smoke level can be observed as the baseline signal at positions (a) and (b) over and above which carbon shedding can be observed as transient peaks in the instrument

signal. The frequency and intensity of these peaks is a qualitative indication of the severity of the problem. Fig 7 shows a "worst case" situation for an engine which had idled for an extended period, over which time carbon had built up on the inside walls of the combustor. Acceleration to high power at position (x) caused shedding of this highly erosive carbon through the turbine. A 'steady-state' smoke condition was achieved after a period of ~18 minutes.

These techniques are attractive in that they are sensitive to low mass loadings typical of those from combustion systems, they are continuous, have a rapid response, and some instruments can operate at high temperatures. On the other hand dependence upon particulate properties means quantitative, auditable measurements are not currently possible and may limit these instruments to use on combustor development programmes and possibly as engine health monitors.

3.2.3 Light obscuration techniques

In many engine applications the exhaust plume visibility criteria is of prime importance. The opacity of the exhaust must be determined, ie the degree to which the incident light intensity is attenuated by the presence of particles between the light source and detector. Rolls-Royce have developed a technique for opacity measurements by intrusive sampling. While this has a slower response than scattering techniques, by virtue of its large sample cell, its advantages are that it is continuous, repeatable, can operate at elevated temperatures and can be calibrated to a preset transmission level.

To eliminate inaccuracies introduced by sampling from an engine exhaust, new techniques must be developed with the capability for making direct opacity measurements across the plume or exhaust 'stack'. Techniques must be found which are sufficiently sensitive to detect low smoke levels without inconveniently long sample path lengths, and for which optical alignment and cleanliness can be maintained.

3.3.3 Other techniques

Shortfalls in each of the above techniques arise from their dependence upon the physical and optical properties of the sample particulates. As such it will prove difficult to develop an optical method to supersede the filter stain technique that is internationally acceptable and comparable amongst different test facilities. Indeed 'true smoke visibility' measurements may necessitate judgements by trained observers as is the current practice[6,7] for stationary power sources in a number of American states.

Techniques exist which measure particulate mass loading from the change in frequency of an oscillating filter as a result of particulate build-up. Mass is calculable for given filter body characteristics, but the technique is currently too slow or insensitive[8].

Recourse to particle size information is increasingly attractive for research purposes and instruments such as the DMPS and APS offer a great deal in terms of their ability to discriminate particulate characteristics, although for engine testing these techniques are slow and cumbersome. Inertial impaction techniques may be suitable for larger particles, if difficulties of representative sampling can be overcome.

4 CONCLUSIONS

The RAE Pyestock smoke generator provides a cheap, controllable, stable source of smoke, with particulate characteristics similar to those produced by in-service combustion systems. The ability to generate a predetermined steady smoke level for a long period has enabled an accurate calibration and cross-correlation of current methods for smoke measurement. Detailed assessment of the inaccuracies of current techniques, coupled with an increased demand for more fundamental measurements, has led to requirements for methods which are continuous, discriminating and more sensitive. Instruments using principles of light scattering and transmission have been evaluated using the smoke generator and are currently providing diagnostic information on smoke and carbon shedding characteristics from engine test facilities. Development of these into techniques suitable for wider use and to supersede the current internationally accepted filter stain method will involve detailed assessment of their suitability for use in a wide range of test areas from combustion development to engine certification. For each of these areas a better understanding is needed of the fickle nature of smoke particulates, primarily in respect of their formation, growth and oxidation and the effects therein of fuel and combustor variables. As different techniques are adopted this information will enable the sampling, calibration and audit procedures to be tailored to suit specific applications and customer requirements. With an increased understanding of particulate effects, optical techniques will become more widely accepted until more quantitative mass or size based methods are available.

REFERENCES

1 S.P. Girling, C.D. Hurley, 'A smoke generator for the absolute calibration of gas turbine engine smoke sampling and measuring systems.' RAE TM-P1044 Jan.1985

2 J.P. Mitchell, 'Aerosol studies of a kerosene smoke generator and analysis of a gas turbine engine exhaust smoke.' UK AEEW-R2185 March 1987

3 'Aircraft gas turbine engine exhaust smoke measurement.' SAE ARP 1179A

4 C.D. Hurley, R.M. Gittins, 'Smoke losses down exhaust gas sample lines with inlet smoke at 20SN.' RAE Pyestock Combustion Note 023/87

5 S.P. Girling, 'A critical assessment of two commercial instruments for continuous gas turbine smoke measurement.' RAE Pyestock Combustion Note 010/85

6 M. Ringelmann, 'Method of estimating smoke produced by industrial installations.' Rev. Technique 268, June 1898

7 J.D. Coons, et al, 'Development, calibration and use of a plume evaluation training unit.' Jrl. Air Pollution Control Assn.15, May 1965

8 P.R. Shore, R.D. Cuthbertson, 'Applications of a tapered element oscillating microbalance to continuous diesel particulate measurement.' SAE 850405

Reports quoted are not necessarily available to members of the public or commercial organisations.

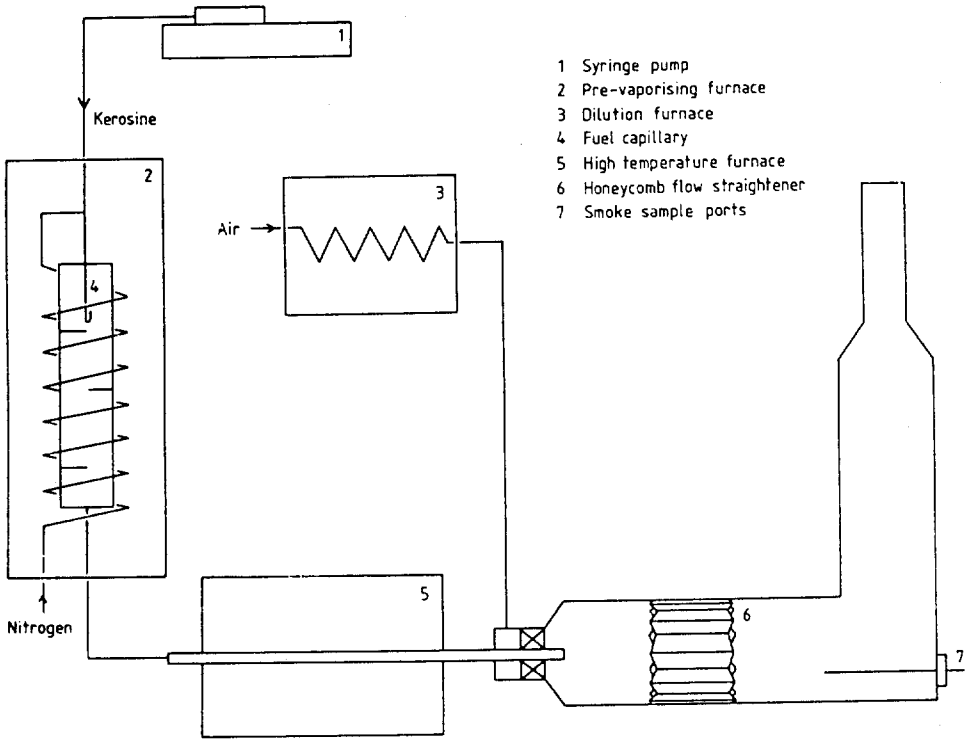

FIG.1 SMOKE GENERATOR LAYOUT

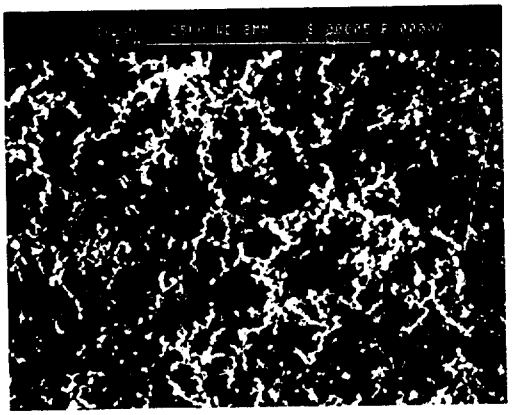

FIG.2 SEM MICROGRAPH OF TYPICAL SMOKE GENERATOR PARTICULATES

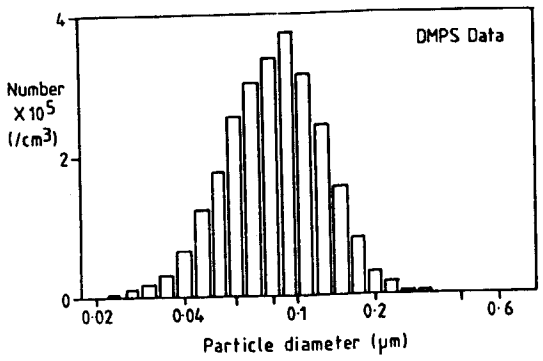

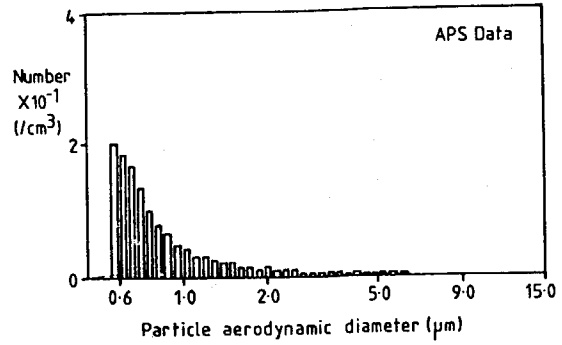

FIG.3 SMOKE GENERATOR TYPICAL PARTICLE SIZE DISTRIBUTION

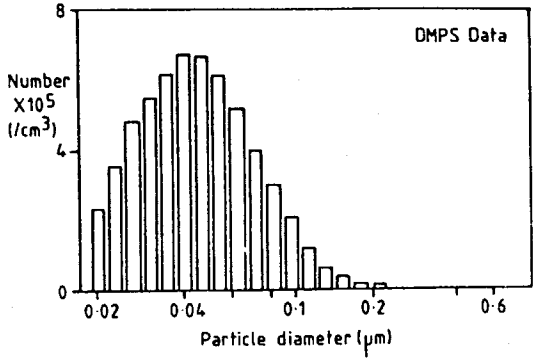

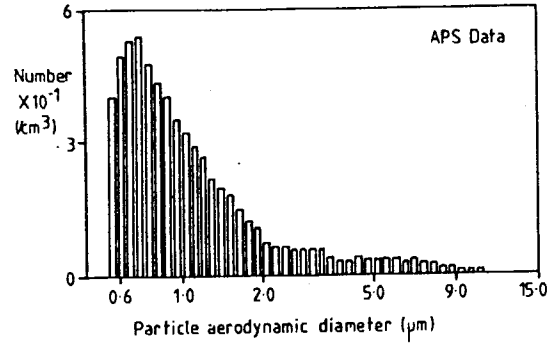

FIG.4 TYPICAL PARTICLE SIZE DISTRIBUTION FROM A DIESEL FUELLED GAS TURBINE ENGINE

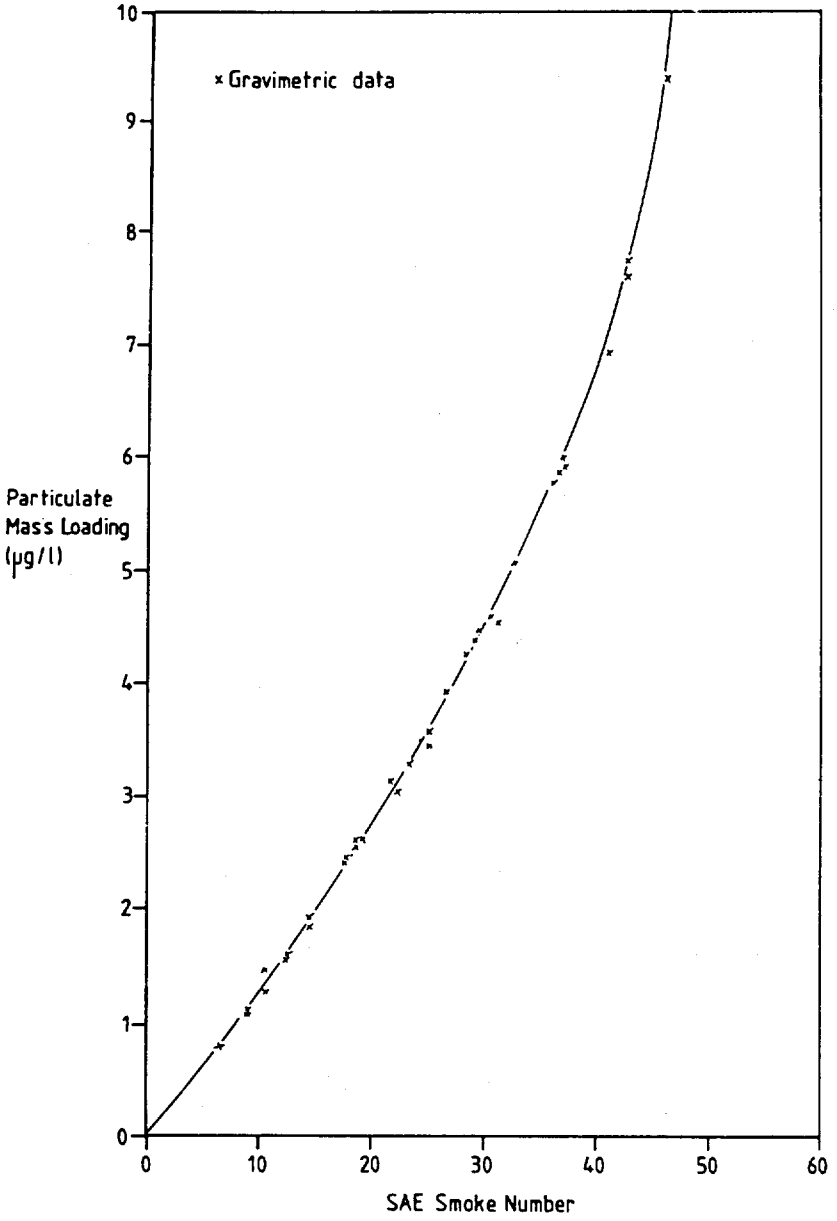

FIG.5 SMOKE GENERATOR GRAVIMETRIC CALIBRATION OF THE STANDARD FILTER STAIN TECHNIQUE[3]

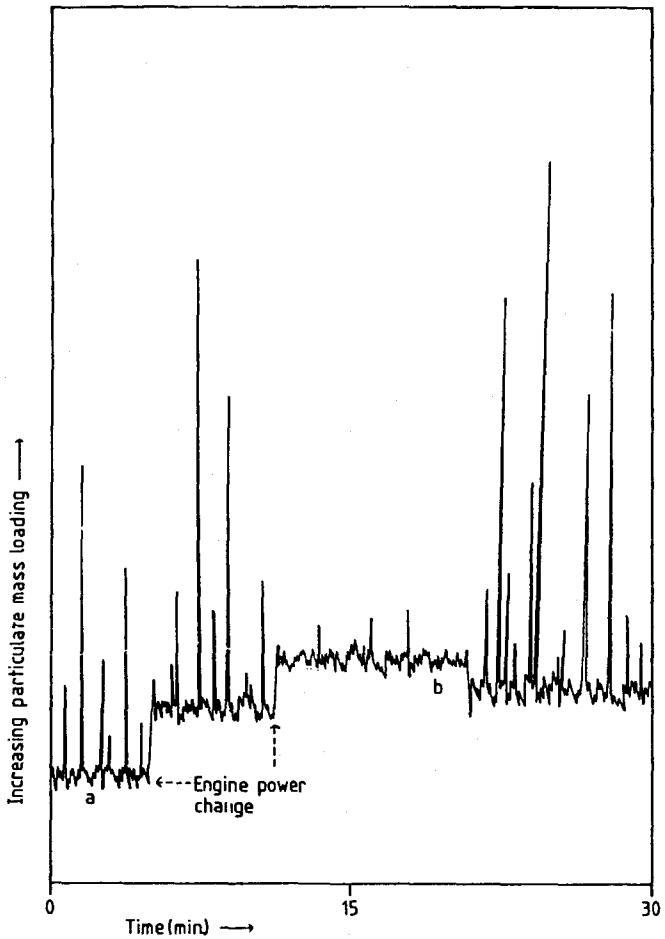

FIG.6 SMOKE AND CARBON SHEDDING MONITORING USING A LIGHT SCATTERING INSTRUMENT

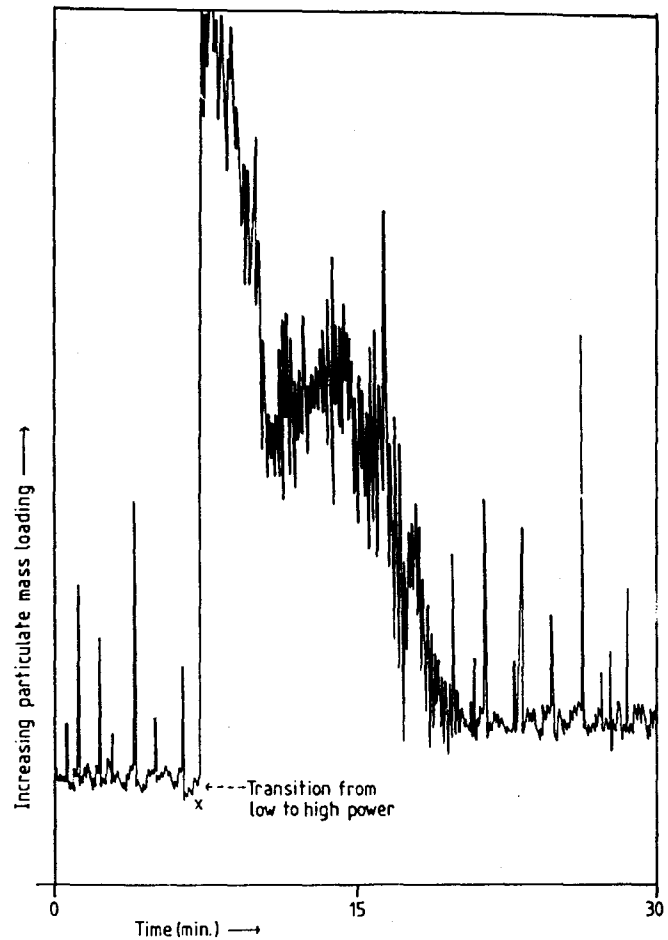

FIG.7 CARBON SHEDDING MONITORING DURING TRANSITION FROM AN EXTENDED PERIOD AT LOW POWER

DISCUSSION

T.Rosfjord, US

For research applications, it is desirable to use a responsive diagnostic which offers more information about the soot — particle size, size distribution, etc. I agree that "stain" techniques will continue to be used for some time, however, in studies at UTRC to obtain simultaneous SAE smoke number and soot mass loading data, we concluded that greater errors are introduced in the mass loading determination. The masses are small and outside influences (e.g. moisture filtration efficiency, etc.) can be important. Will you please indicate the technique you used for mass loading determination?

Author's Reply

Our mass loading was determined grammatically, by sampling through a glass fibre filter paper (estimated 99.9 percent efficiency) for periods of between 15 and 60 minutes. Several SAE measurements were made during the sampling period and averaged for each mass loading determination. Samples were dried to constant weight at 200°C to remove any unburnt hydrocarbons or moisture and after weighing the carbon was burnt off at 500°C and the filter paper reweighed after cooling in a dessicator! Throughout the procedure a blank filter paper was included and corrections made for any mass losses in the paper itself. This sampled volume was measured with a wet-type gas meter and corrected to standard conditions. The scatter in the resulting data was small, less than predicted by error analysis. This was the virtue of being able to sample large masses of carbon from a stable smoke source ($<\pm 1$ SAE.SN) under controlled laboratory conditions.

J.Odgers, CA

Can you suggest lower and higher limits of SAE smoke number? Our experience shows poor repeatability in 0—15 range and poor correlation with mass loadings above SN = 50. Could you please comment?

Author's Reply

We have successfully made smoke measurements as low as 2 SAE-SN, and have found that in cases where the repeatability was poor, it was due more to the smoke source itself than the measurement procedure, with short term instabilities or "transients" biasing the smoke stains. Indeed our experience is that the repeatability is poorer at high levels (>20 SAE-SN) due partly to differences in the white reflectance between papers becoming more significant in the reflectance ratio determination. I quite agree that the correlation with mass loading above 50 SAE-SN is poor, due to the asymptotic nature of the relationship, though the repeatability at these levels can be improved by adopting the four filter method laid down in the recommended practices.

A.Williams, UK

Could you indicate whether there was any indication of the presence of PAH which could be absorbed in the soot particles and released during the soot drying process.

Author's Reply

The soot particulates have not been analyzed for the presence of PAH, the purpose of the drying process in the gravimetric determination of mass loading was, as you indicate, to release any "unburnt" hydrocarbons that might be present.

Particle Size Measurements in Sooting Combustion Systems

by
S. Wittig, H.-J. Feld
Lehrstuhl und Institut für Thermische Strömungsmaschinen
Universität Karlsruhe (T.H.)
Kaiserstr. 12, D-7500 Karlsruhe (West-Germany)

SUMMARY

Radiation effects caused by the presence of soot particles are of dominant influence in gas turbine combustors, especially on the stress distribution in the flame tube. In studying the two-phase flow within and after the combustor experimentally, a wide spectrum of soot particle and fuel droplet sizes is to be considered. Two optical measuring techniques have been used throughout the present work. First, the dispersion quotient (DQ) technique was applied to determine the size of the early soot particles, i.e. in the small-diameter range. The second method, the well established Multiple-Ratio-Single-Particle Counter (MRSPC), was used to measure the larger particle sizes, i.e. fuel droplets and soot. Furthermore, attention was focused on data acquisition- and analysis-techniques. Experimental results were obtained from measurements in a combustor with high concentration of soot particles and in the exhaust gas of a gas turbine.

INTRODUCTION

The knowledge of the particle size and particle density is of major importance to the understanding of the two-phase flow phenomena, the reaction and condensation processes and the mechanisms leading to soot formation especially in thermal turbomachines, i.e. gas turbines and steam turbines. In continuing an earlier study, the present work was predominantly directed towards the two-phase phenomena within gas turbine combustors. Especially the processes occuring in the fuel spray as well as the soot formation and soot particle growth were of major interest. High particle densities beyond 10^{10} particles per cm^3 were to be expected in the lower size ranges up to one micrometer, whereas the particle density is drastically reduced for the larger particle sizes. To avoid any interference, only non-intrusive optical techniques can be employed. At high particle densities optical single particle counters have to be excluded. Here, integrating optical techniques have to be used. Their major disadvantage, however, is a certain loss of information due to the integrating character. On the other hand, their major advantage is the simplicity of application which is demonstrated with the dispersion quotient (DQ) technique used in the present analysis. If detailed information on the local particle size distribution is of interest, such as the droplet sizes in the fuel spray or the soot emission within the exhaust gases, the introduction of an instrument, which provides relatively fast the local size diameter distribution over a wide range, is necessary. With soot emission additional problems arise such as relatively high concentrations, the unknown shape of the particles and the lack of detailed knowledge of the index of refraction. The requirements are largely fulfilled by the MRSPC which is a single particle counter operating over a relatively wide size range and which is largely independent on the refractive index and the shape of the particles. The major emphasis of the present work was the detailed analysis of the two techniques under prototype conditions and their application to gas turbines.

PRINCIPLES OF THE DISPERSION QUOTIENT TECHNIQUE

The principle of the dispersion quotient (DQ) technique is based on the light extinction at different wavelengths by a particle collective. The method which was first suggested by Teorell [1] has been discussed by us at other occasions [2]. Basically, the intensity of a light beam which passes through a particle cloud will be scattered and absorbed. In assuming spherical particles and a monodisperse particle distribution, and in neglecting multiple scattering the light extinction for monochromatic light is described by the following well-known equation [3],

$$I = I_o \cdot \exp(-N \cdot L \cdot \pi r^2 \cdot Q_{ext}(r,\lambda,n)) \qquad (1)$$

where I_o is the intensity of the incident light, I the intensity after transmission through the particle cloud, N the particle density, r the particle radius, $Q_{ext} \cdot \pi r^2$ the extinction cross section, n the complex index of refraction, λ the wavelength of the beam and L the optical path length. The dispersion quotient DQ is obtained by dividing the natural logarithms of the intensity ratios I over I_o of two light beams with different wavelengths which are passing through the identical particle cloud. The unknown particle density N is cancelled and equation 2 is obtained:

$$DQ = \frac{\ln(\frac{I}{I_o})_{\lambda_1}}{\ln(\frac{I}{I_o})_{\lambda_2}} = \frac{Q_{ext}(r,\lambda_1,n)}{Q_{ext}(r,\lambda_2,n)} \qquad (2)$$

It can be seen that at predetermined wavelengths and with known index of refraction the dispersion quotient is a function of the particle radius only. The extinction cross

sections can be calculated by employing Lorenz-Mie theory [4,5]. With the known particle size the particle density can be determined by employing equation 1.

Figure 1 illustrates the dependence of the dispersion quotient on the particle density for three different indices of refraction, assuming that the index of refraction is not a function of the wavelength.

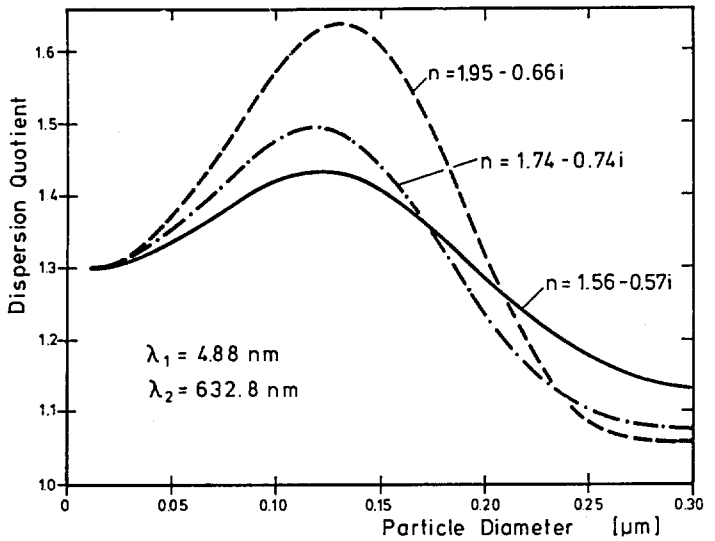

Figure 1: Dispersion quotient as a function of refractive index

It is obvious that the technique is relatively sensitive to changes of the index of refraction. Wittig and Lester [2] and Bro et al. [6] have provided detailed studies on this relation. An additional problem is the observation that the functional dependency between particle size and dispersion quotient is not always unique as can be seen from Figure 1, a fact which is quite important with respect to absorbing particles such as soot. A solution is found by employing a third wavelength as shown in Figure 2.

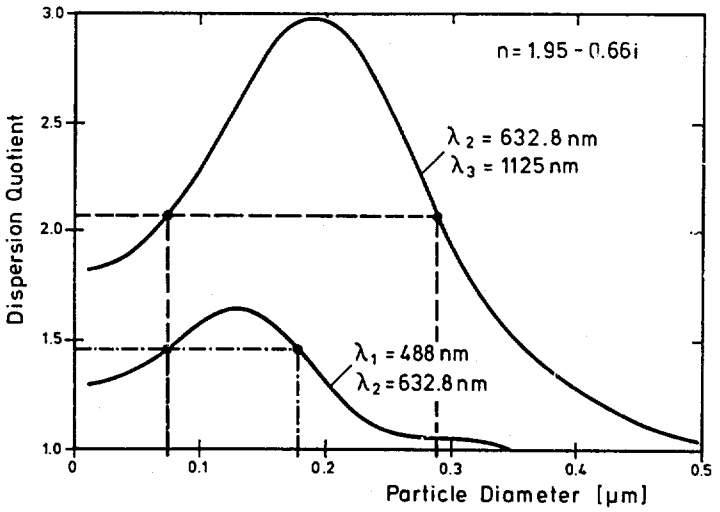

Figure 2: Determination of the particle size by means of three wavelengths

As can be seen, for example, in employing an argon-ion and helium-neon laser (488 nm/633 nm) particle sizes of 75 nm and 180 nm could be present. In utilizing a third wavelength (1152 nm for example) a new dispersion quotient can be measured and the particle size in the present case is determined to be 75 nm.

Up to now, only monodisperse particle distributions were considered. However, the dispersion quotient as a function of particle size can also be calculated for particle size distributions [7,8]. Relative to the mean particle diameter the maximum is changing towards smaller diameters and will be somewhat flatter. This is illustrated in

SOOT MEASUREMENTS IN A SMALL COMBUSTOR

The DQ-method has been employed at the Institute for Thermal Turbomachinery for a variety of processes such as the analysis of unsteady two-phase flows [10] and the measurement of tobacco smoke. As a standard procedure it is employed for the study of soot formation mechanisms in fast homogeneous combustion processes in shock tubes.

In the present investigation direct measurements were made in a small combustor test facility as shown in Figure 5. The measurements were made in two different planes at different equivalence ratios ϕ.

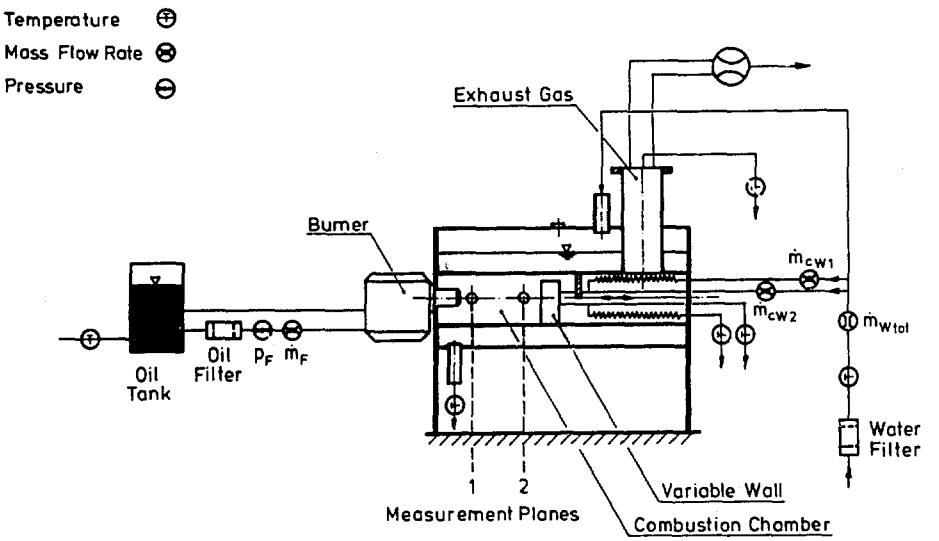

Figure 5: Combustor test facility

It should be noted that the measurements were made without correction for the initial intensity. Improvements, therefore, can be expected if this is incorporated into the instrument. As the index of refraction of the soot formed in an oil-burner is still under discussion, the value n = 1.95 - 0.66i suggested by Senftleben and Benedict [11] was chosen. As the earlier stages of the soot forming process were studied, it is obvious that the positive slope of the curve as shown in Figure 6 was of relevance. Using an argon-ion and a helium-neon laser the curve as shown in Figure 6 was employed in evaluating the particle size.

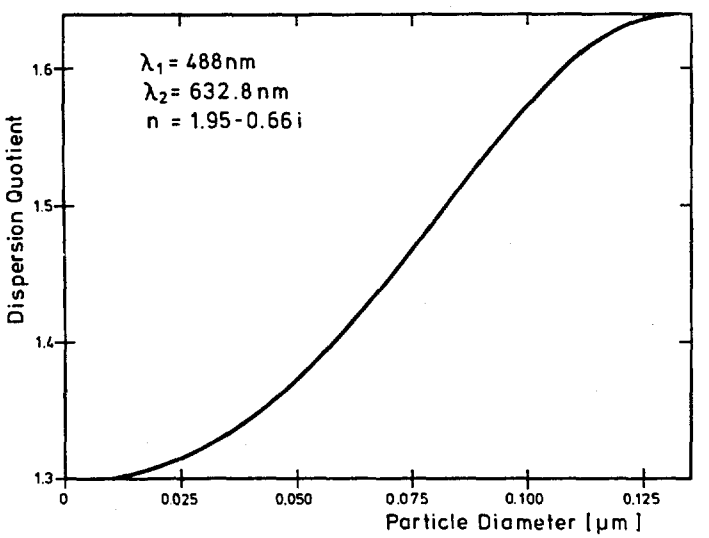

Figure 6: Dispersion Quotient computed from exact solution to Lorenz-Mie theory

The measurements were made in the larger context of a program studying the effects of the fuel spray characteristics on the soot formation and on the pollutant emissions. The pressure of the atomizer as well as the cone angles were changed over wide ranges. It would lead too far in the context of this paper to discuss all the details. It should be noted, though, that the particle diameter is increasing with increasing equivalence ratio as expected. Furthermore, the mean volumetric diameter is considerably higher at a later stage indicating agglomeration processes. However, a variety of influence parameters is to be considered. For example, if the equivalence ratio is increased with constant airflow rate it is obvious that the pressure atomizer induces a higher droplet momentum and thus the structure of the flame is altered. Despite smaller fuel droplet diameters with higher nozzle pressures, increasing soot production is observed due to higher local equivalence. The measurements were highly reproduceable. Detailed tests were made on the influence of the backround radiation, but it was found that its importance is negligible. The results also agree quite well with measurements made at other systems. It should be mentioned that earlier calibration measurements by Wittig et al. [7] yielded extremely high accuracy.

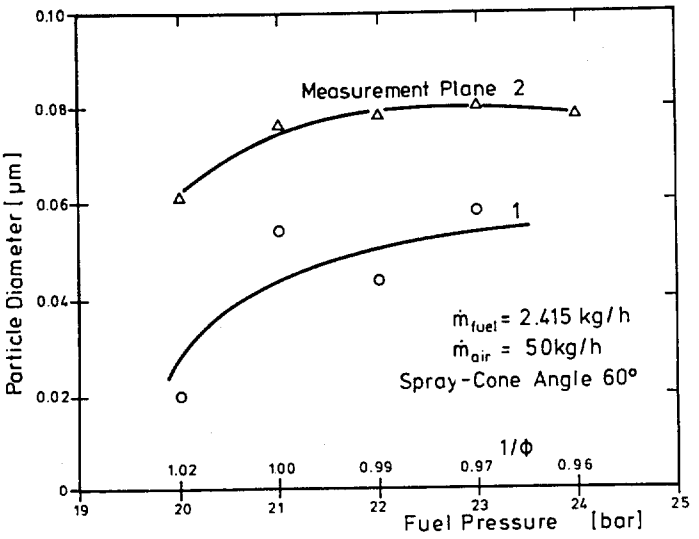

Figure 7: Soot particle size as a function of fuel pressure

THE MULTIPLE RATIO SINGLE PARTICLE COUNTER (MRSPC)

In addition to the measurements of particles in well-defined environments, the determination of the particle emissions in an exhaust gas poses additional requirements on the instrument: A relatively high concentration, the unknown shape of the particle and the generally unknown index of refraction are inducing new difficulties. The requirements can be summarized as follows:

1. In situ, non-intrusive measurements are necessary with high local resolution.
2. The size distribution is to be recorded independently of particle material and shape in the range of interest for emission analysis (.2 micrometer to approximately 10 micrometer).
3. If the particle material such as in droplet measurements is known, the instrument should cover a broader particle size range.
4. The influence of windows, background radiation and changes of index of refraction within the gas atmosphere due to temperature gradients should be negligible.

The multiple ratio single particle counter, described by us at various occasions [12,13,14,15], fulfills these requirements to a large extent. It was developed based on suggestions by Gravatt [16] utilizing basic theoretical concepts introduced by Hodkinson [17].

THEORY AND EXPERIMENTAL CONCEPT OF THE MRSPC

As described earlier, the MRSPC is utilizing the principle of light scattering. Figure 8 illustrates the schematic of the instrument as reported in other studies [12,14]. The light source is an argon-ion laser which is focused on the probe volume by a lens.

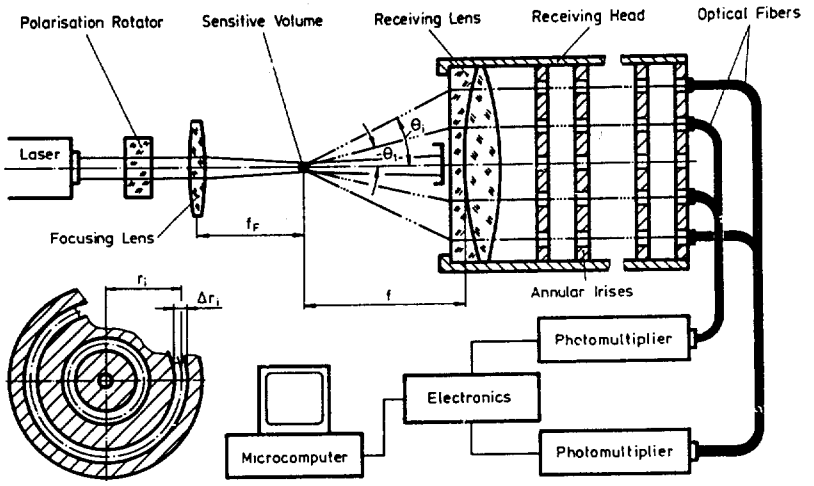

Figure 8: Schematic of the MRSPC

The receiving optics is arranged such that its focal point coincides with that of the focusing lens. In passing through the probe volume, the light scattered by a particle is made parallel by the receiving optics and separated by a sequence of annular irises into four angle regions. The rings of the last iris are equipped with fiber optics which guide the light to the appropriate photomultipliers. The signals which are proportional to the scattered light intensity at the respective angle are processed by the electronics. Here, various control functions are performed and the peaks of the signals are determined. The peaks are digitalized and their ratios are formed using a microcomputer.

The determining equation which describes the power of the scattered light under a predetermined angle range is as follows:

$$P_{s\theta_1} = \frac{I_o \cdot \lambda^2}{4\pi} \left(i_1(\theta_1, \alpha, n) + i_2(\theta_1, \alpha, n) \right) \sin\theta_1 \cdot \Delta\theta_1 \qquad (3)$$

Here P_s is the scattering light power, I_o is the intensity of the initial light irradiating the particle, λ is the light wavelength, i_1 and i_2 are the Mie-intensity functions, $\alpha = \pi \cdot d/\lambda$ the dimensionless particle size and n the complex index of refraction, θ_1 the scattering angle and $\Delta\theta_1$ the size of the angular range which is associated with the mean scattering angle. By forming the ratio of the scattering light power under two angles the influence of the incoming light is eliminated as shown in equation 4.

$$V_{\theta_2/\theta_1} = \frac{P_{S\theta 2}}{P_{S\theta 1}} = \frac{\left(i_1(\theta_2, \alpha, n) + i_2(\theta_2, \alpha, n) \right) \sin\theta_2 \cdot \Delta\theta_2}{\left(i_1(\theta_1, \alpha, n) + i_2(\theta_1, \alpha, n) \right) \sin\theta_1 \cdot \Delta\theta_1} \qquad (4)$$

The ratio, then, is only a function of the particle size, the index of refraction and the angle. The well-known problem of the position of the particle within the light beam as observed in using a TEMoo-laser with Gaussian intensity distribution across the beam diameter thus is largely eliminated due to the formation of the ratio. For example, if only the scattering light power would be recorded, the passage of a particle at different locations through the beam would yield different results.

Figures 9a and 9b illustrate the scattering ratio for two different angle combinations. Also, the effect of the complex part of the index of refraction, i.e. absorbing material, is shown. As can be seen, the oscillations for non-absorbing particles lead to errors in the order of approximately 20 % (compare [14,15]). In other words, if the curve for absorbing material is used as a reference, the error in determining the particle size for material of unknown index of refraction will be below 20 %.

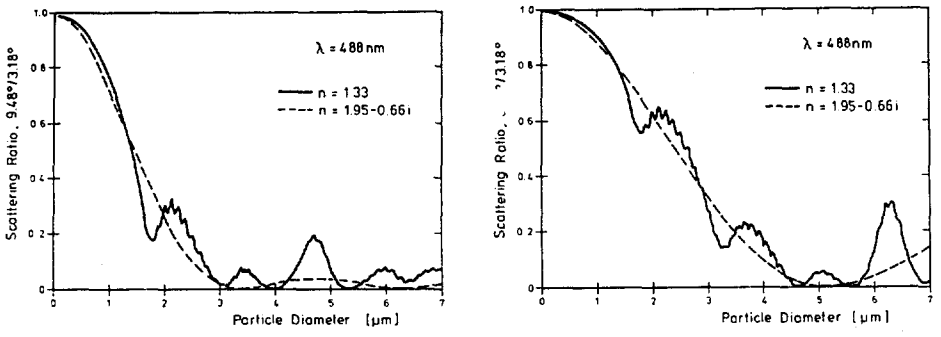

Figure 9: Mie-intensity ratios

It should be noted that despite forming the ratios errors can arise due to the non-uniform size of the probe volume as seen by the receiving optics, i.e. that particles passing through different areas of the probe volume will not necessarily induce identical signals. This fact has been analysed by us in detail at various occasions [15]. In applying appropriate statistical analysis and in optimizing the optical and electronic design this error can be minimized. However, a lower particle size limit has to be recognized.

The maximum size up to which the Mie-intensity ratios of non-absorbing particles oscillate about those of absorbing particles depends on the angle ratios considered. The particle counter used in the present study employs presently four angle ranges with a measurement range from .25 up to approximately 10 micrometers. The influence of the particle shape in this regime is relatively small [15,18]. It, therefore, is possible to employ the MRSPC for the measurement of exhaust gas emissions, whereas its utilization for soot formation measurements is limited. However, Samuelson et al. [19] have been able to apply a modified design for the measurement of soot in its early status. With respect to larger size parameters of particles of known index of refraction, the instrument can be employed. However, as an extremely broad size range is to be determined, the necessary dynamic range of the electronic yields considerable problems.

As has been mentioned earlier one of the problems under consideration was the question of the importance of variation of the index of refraction of the gas between the probe volume and the receiving head. However, as the scattered light is recorded by radial symmetric rings and as such over a relatively large integration regime, strong dependencies on local temperature and thus index of refraction variations are not to be expected. In this series of tests a bimodal particle distribution was used for test purposes. As can be seen from Figure 10 the results employing latex spheres are excellent for cold flow situations. The superposition of the temperature gradient between the probe volume and the receiving optics practically did not change the results as can be seen from Figure 10. The gradients were generated by means of a non-sooting flame of a Bunsen burner with relatively high temperature gradients.

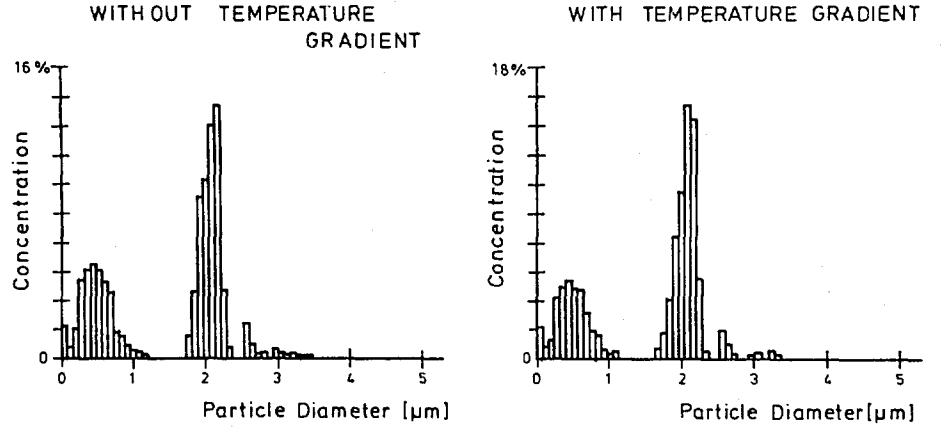

Figure 10: Influence of strong temperature gradients in measuring a bimodal particle size distribution

The importance of strong background radiation can be minimized by using relatively high power lasers and small band filters.

A final source for errors is derived from a high density particle cloud between the probe volume and the receiving optics. The scattered light which is emitted from a particle passing through the probe volume can experience multiple scattering and absorption. The relative extinction can be calculated by using equation 1 and for the case of an assumed optical path length of 127 mm yields the results shown in Figure 11.

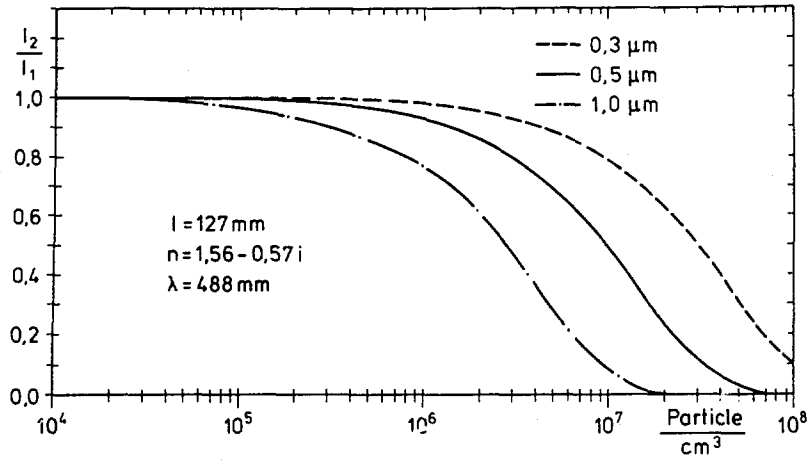

Figure 11: Extinction as a function of particle concentration

As long as the particle distribution is homogeneous, the relative extinction is identical for all angles and thus will not affect the results under ideal conditions. However, at relatively high concentrations and high extinction it was observed that inhomogeneities in the particle distribution will induce significant errors. As can be seen from Figure 11 this effect is of no significance as long as the particle concentration is below 10^6 particles / cm^3.

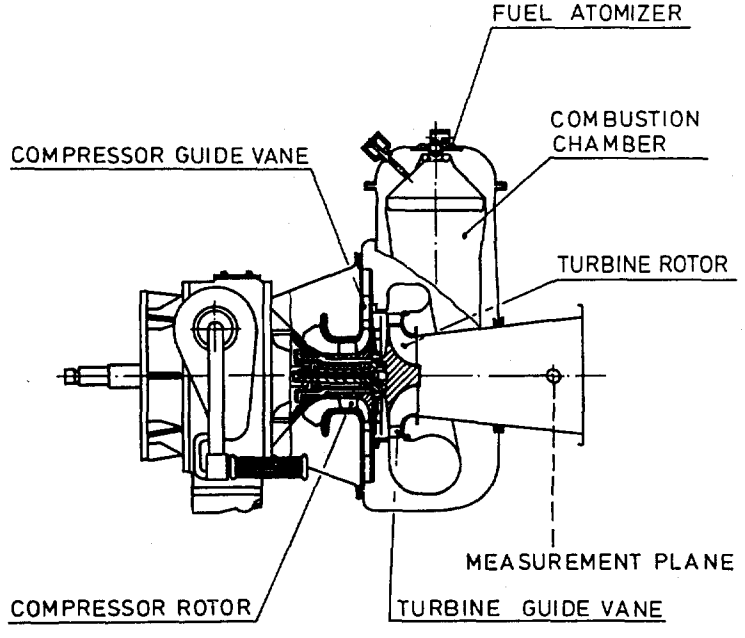

Figure 12: Schematic of the gas turbine DEUTZ T-216

EXHAUST MEASUREMENTS BEHIND A GAS TURBINE

Due to its relatively large dynamic range over approximately two orders of magnitude and its insensitivity to the index of refraction and the particle shape, the MRSPC is ideally suited for exhaust gas measurements. Early attempts were reported by Wittig et al. on studies of automobile smoke emissions [20]. At that time the problems associated with the non-uniform facts of probe-volume on the particle size as well as the dynamic range of the electronics were not fully corrected. The present example illustrates the application of the MRSPC to an exhaust gas measurement on the relatively stringent conditions for exhaust measurements behind a small gas turbine as shown in Figure 12. The location of the measurement plane is indicated in Figure 12. In recording typical samples of 10000 particles the measurement times were approximately a few seconds. The flow velocity of the exhaust gas was - depending on the gas turbine load - between 20 m/s and 60 m/s. Due to the optimization of the data acquisition system the evaluation of the data was practically online. The evaluation time of approximately 1000 particles is slightly about 1 s. The results for a typical experiment in the gas turbine exhaust is illustrated in Figure 13.

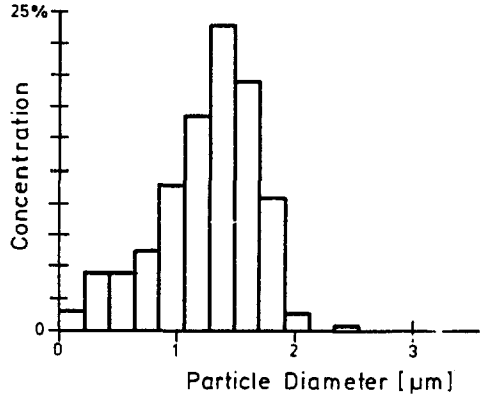

Figure 13: Typical particle size distribution in the exhaust gas of a gas turbine

The particle size distribution shows a mean value of about 1.3 micrometer. The observation that the small particles are practically absent was initially somewhat surprising. At present intensive studies are conducted to analyse the simultaneous measurements of the soot formation process and the subsequent exhaust. However, the present paper was primarily concerned with the technical aspect of the diagnostics.

CONCLUSIONS

In analysing gas turbine combustors, two major problems are arising from the soot formation. First, the soot forming processes that are to be studied require non-intrusive optical instrumentation capable of monitoring large concentrations of very small particles with diameters generally smaller than .5 micrometer. The dispersion quotient technique seems to be well-suited as a diagnostic tool. Its advantages are found in the possibility of monitoring extremely high concentrations, its fairly high accuracy and in its simple handling especially under extreme conditions of a gas turbine combustor. The disadvantages derive from the fact that it is principally an integrating optical technique thus yielding either monodisperse characteristic particle sizes or requiring the assumption of the characteristic type of the distribution. Furthermore, it is relatively sensitive to variations of the index of refraction.

The second major problem arises from the measurement of the soot emissions in exhaust gases after the soot forming processes within the combustor. Here, considerably larger particles of sizes above .2 micrometer at considerably lower concentrations are to be recorded. Under these conditions, the multiple ratio single particle counter leads to excellent results. Despite its limitations with respect to a maximum concentration its major advantages are found in an insensitivity to the index of refraction and to the fact that particles deviating from the spherical shape are recorded with their equivalent optical diameter thus yielding an averaging effect. As it is an actual single particle counter, local particle size distributions can be obtained. Furthermore, it was shown that disturbances such as background radiation and temperature gradients are only of relatively small influence. The capabilities of the instruments were demonstrated using gas turbine combustor flows.

ACKNOWLEDGEMENTS

This work was partially funded by the Stiftung Volkswagen AG. Thanks are due to its program administrator, Dr. Michael Maurer. Furthermore, our colleagues Dipl.-Ing. K. Steinebrunner and Dipl.-Ing. R. Koch as well as cand.phys. H. Zohm and cand.eltec. J. Schorn were extremely helpful in performing the experiments and in designing the optical and electronic systems. The measurements were made in the larger context of the Sonderforschungsbereich "Hochbelastete Brennräume (High Intensity Combustors)" and "Tecflam (Technical Flames)".

REFERENCES

[1] Teorell, T.: Photometrische Messung der Konzentration und Dispersität in kolloiden Lösungen, Kolloid-Zeitschrift, Bd.54 , S. 150ff (1931)

[2] Wittig, S.L.K. and Lester, T.W.: Radical and Chemi-ion Precursors: Electric Field Effects in Soot Nucleation, Advances in Chemistry Series, No 166, J.T.Zung Ed., 167ff.(1978)

[3] Kerker, M.: The Scattering of Light and Other Electromagnetic Radiation, Academic Press, New York (1969)

[4] Mie, G.: Beiträge zur Optik trüber Medien speziell kolloidaler Metallösungen, Ann. d. Physik, H.25, S. 377ff (1908)

[5] Giese, R. H.: Streuung elokromagnetischer Wellen an absorbierenden und dielektrischen kugelförmigen Einzelteilchen und an Gemischen, Z. Astrophysik 51/52 , S. 119ff (1960-1961)

[6] Bro, K., Wittig, S.L.K. and Sweeny, D.W.: In Situ Optical Measurements of Particulate Growth in Sooting Acetylene Combustion, Proceedings of the 12th Intenational Symposium on Shock Tubes and Waves, Ed. by A. Lifshitz and J. Rom, Jerusalem 1980

[7] Wittig, S. L. K.; Zahoransky, R. A. and Sakbani, Kh.: The Dispersion Quotient Technique in Submicron Particle Size Analysis, J. of Aerosol Science, Vol. 12, No 3, p. 183 (1981)

[8] Dobbins, R.A. and Jizmagin, G.S.: Optical Scattering Cross Sections for Polydispersions of Dielectric Spheres, J. Opt. Soc. Am. Vol. 56, No. 10, p. 1345 (1966)

[9] Lester, T.W. and Wittig, S.L.K.: Particle Growth and Concentration Measurements in Sooting Homogeneous Hydrocarbon Combustion Systems, Proceedings of the Tenth International Shock Tube Symposium Kyoto, Japan, p.632 - 639 (1975)

[10] Spiegel, G.H., Zahoransky, R.A. and Wittig, S.L.K.: Homogeneous and Heterogeneous Condensation of Non-ideal Binary Vapour Mixtures in Shock Tube Expansion Flow, Shock Waves and Shock Tubes, Eds. D. Bershader and R. Hanson, Stanford University, p. 775 (1986)

[11] Senftleben, H.; Benedict, E.: Über die optischen Konstanten und die Strahlungsgesetze der Kohle, Ann. d. Physik (IV), 54, p.65 (1917)

[12] Hirleman, E.D. and Wittig, S.L.K.: Laser Application in Particulate Analysis: The Multiple Ratio Single Particle Counter, Laser 77 Opto-Electronics. Conference Proceedings. Ed. by Prof. W. Waidelich, Munich, June 1977

[13] Wittig, S.L.K. und Sakbani, Kh.: Teilchengrößenbestimmung mit dem optischen Vielverhältnis-Partikelzähler im Vergleich mit dem Andersen Sampler, Tagungsband der 6. Fachtagung der Gesellschaft für Aerosolforschung, Sept. 1978 Wien

[14] Wittig, S. und Sakbani, Kh.: Teilchengrößenbestimmung im Abgas eines Heißgaskanals mit Hilfe des prozeßrechnergesteuerten optischen Vielverhältnis-Einzelpartikelzählers (MRSPC). 2. Europ. Symp. "Partikelmeßtechnik" (1979) Nürnberg, Tagungsband S. 166

[15] Sakbani, Kh.: Entwicklung eines Streulicht- Meßverfahrens zur Partikelgrößenspektrometrie, Dissertation Universität Karlsruhe (1983)

[16] Gravatt, C.C.jr.: Real Time Measurement of the Size Distribution of Particulate Matter by a Light Scattering Method, J. of Air Pollution Control Association, Vol 23, No 12, p.1035 (1973)

[17] Hodkinson, J.R.: Particle Sizing by Means of the Forward Scattering Lobe , Applied Optics, Vol.5, p.839 (1966)

[18] Zerull, R.H., Killinger, R., Weiss-Wrana, K.: The Influence of Shape and Structure on the Light Scattering Properties of Aerosols, 1. World Congress Particle Technology. Conference Preprints. Ed. by Prof K. Leschonski. Nürnberg 1986

[19] Samuelsen, G.S., Wood, C.P., Jackson, T.A.: Optical Measurements of Soot Size and Number Density in a Complex Flow, Swirl-Stabilized Combustor, Agard Conference Preprint No. 353 "Combustion Problems in Turbine Engineß, Cesme, Turkey, Oct 1983.

[20] Wittig, S.L.K.; Hirleman, E.D. and Christiansen, J.V.: Noninterfering Optical Single-Particle Counter Studies of Automobile Smoke Emission, Advances in Chemistry Series, No. 166, Evaporation-Combustion of Fuels (1978)

DISCUSSION

O.Gulder, CA
If you change the index of refraction by 10% what would be the effect on measured droplet size? Is it acceptable?

Author's Reply
It depends on the region where you are. If you have small particles, a change of 10% would produce a 20% error. If you have larger particles the error would be somewhat smaller.

LARGE IONIC SPECIES IN SOOTING ACETYLENE AND BENZENE FLAMES

by

Ph.Gerhardt, K.H.Homann, S.Löffler and H.Wolf
Institut für Physikalische Chemie, Technische Hochschule Darmstadt
Petersenstraße 20, D-6100 Darmstadt
Federal Republic of Germany

ABSTRACT

Ionic species with masses from 24 to $1x10^6$ u have been studied in premixed, fuel-rich, low-pressure acetylene and benzene flames by means of a time-of-flight mass spectrometer. Total positive and negative ion concentrations in the flame were also determined by sampling ions from a beam. The mass spectrum of positive poly-yne ions corresponds to two different Poisson distributions for the groups $C_{2n}H_3^+$ and $C_{2n+1}H_3^+$ respectively. These ions are not related to soot formation. The growth of polycyclic aromatic hydrocarbon ions, however, could be followed up to a mass of about $2x10^3$ u where coagulation started resulting in ions of about $4x10^3$ u which then grew further. The relative volume fractions of charged and neutral soot was determined using a method of soot deposition in vacuum. The results can be interpreted by a partial-equilibrium model. Polyhedral carbon ions have been detected as a completely new class of flame ions similar to those found in the laser-evaporation of graphite. C_{60}^+ is the dominant positive ion of this group, while C_{50}^- and a broad distribution of C_{2n}^- with 2n up tc about 210 are characteristic for the negative polyhedral ions.

1. INTRODUCTION

The number density of charge carriers in a hydrocarbon flame is only about $1/10^7$ times that of the total number density. Yet the variety of ionic species is of the same order if not larger than that of the uncharged molecules. Particularly when flames are made fuel-rich both the number of different neutral hydrocarbons with masses greater than that of the original fuel molecule and the variety of heavy ions increase enormously [1]. It is very difficult to follow the process of transition from large hydrocarbon molecules to solid soot particles by only measuring the formation and depletion of uncharged species using e.g. gaschromatography or mass spectrometry or a combination of both. Particularly the large molecules or particles can much easier be detected in the ionized form in which they occur naturally in the flames. The use of an artificial ion source for these particles may be rather inefficient and also changes them by fragmentation. The mass range of the beginning of soot formation has not been satisfactorily explored by measuring only the growth of neutral particles. The growth of ionized species, however, can be followed right through this transition region up to larger particles.

But not only its importance for the understanding of soot formation makes the study of large ions in flames a somewhat exotic but nevertheless fascinating field in combustion science. Their mass and molecular composition with respect to C/H/O can be compared to those of the higher aliphatic and polycyclic aromatic compounds. Many plausible similarities are found since most of the ionic species result from a reaction of an ion with a neutral precursor. But there are also ionic structures which are not possible for uncharged molecules. Very unexpected particles such as the polyhedral carbon ions can be found in sooting flames [2]. Striking differences show up between positively and negatively charged species and for ions in flames from different fuels [3, 4].

2. EXPERIMENTAL METHODS

2.1 The Flames

Premixed, flat low-pressure flames of acetylene/oxygen and benzene/oxygen were used. They burned on water-cooled sintered disk burners of 7.5 cm diameter in a pressure range of 26.6 - 40 mbar. Details of the preparation of the burning mixtures and the stabilization of the flames have been published before [5]. As the structure of these flames is relatively well-known with regard to the concentration profiles of many neutral species and of the temperature [6] they were only sampled for molecular ions and larger charged particles in these studies.

2.2 The Analysis of Charged Species

The method of sampling the flames was always the same but the analysis of the different charged particles varied. Conical quartz probes were used to form a supersonic beam containing the ions. The expansion of the free jet to molecular flow conditions took place under zero electric field [7]. As the masses of the positive and negative ions in the flame covered a very large range different methods of separating and detecting them had to be applied:

(a) To measure the total positive and negative ion number densities in the flame a Faraday detector having a cross section larger than that of the beam was used. It was biased negatively or positively for positive or negative ions, respectively. In addition, ions could be reflected by a grid in front of the detector to which a varying repelling voltage was applied. This energy filter allowed a rough mass analysis of the particles with masses in the range $10^3 \lesssim m \lesssim 5 \times 10^4$ u [8].

(b) For the analysis of charged soot particles with $m \gtrsim 10^4$ u a collimated beam of ions was led through the electric field of a plate capacitor in a second vacuum chamber. A suitable voltage was applied to the plates to deflect the charged particles. After travelling over a field-free length they were deposited together with the uncharged soot particles on an electrically grounded glass plate. From the pattern of the deposits the relative amounts of neutral soot and charged soot of either sign, a rough mass analysis of the particles, and the evidence of doubly charged soot particles were obtained [9].

(c) To gain a better mass resolution of the large molecular ions and also of the small charged soot particles ($m \lesssim 2 \times 10^4$ u) time-of-flight mass spectrometry was applied. Fig. 1 shows a schematic view of the experimental set-up.

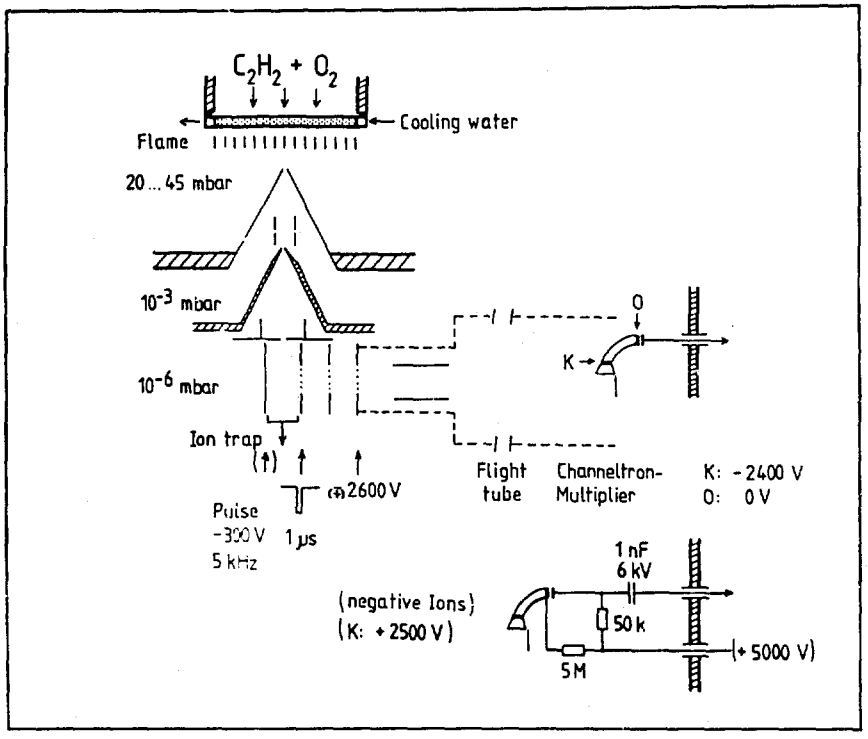

Fig. 1 Scheme of the flame sampling system and the time-of-flight mass spectrometer for heavy positive and negative ions

The ion beam was collimated by a rectangular slit in a skimmer and a second slit into a TOF mass spectrometer. Positive ions were drawn by a -300 V rectangular 5 kHz pulse to an accelerating grid (-2.6 kV) and into a 55 cm long field-free tube. By applying the same negative pulseto the back plate of the deflecting region and reversing the accelerating voltage negative ions could be separated as well. A channeltron electron multiplier served as the detector, the signal of which was amplified and fed into a gated boxcar averager [10].

(d) Using a fourth method described elsewhere mass and velocity analyses of small charged soot particles of either sign in the range $10^3 < m < 10^4$ u were performed by means of a Wien velocity filter combined with an energy discriminator [10] .

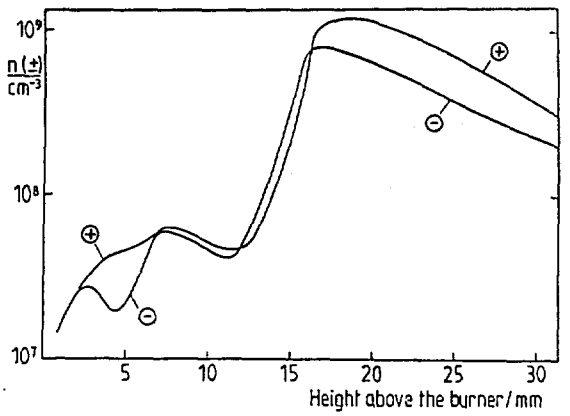

Fig. 2 Profiles of total ion number densities in a sooting C_2H_2/O_2 flame with C/O = 1.05

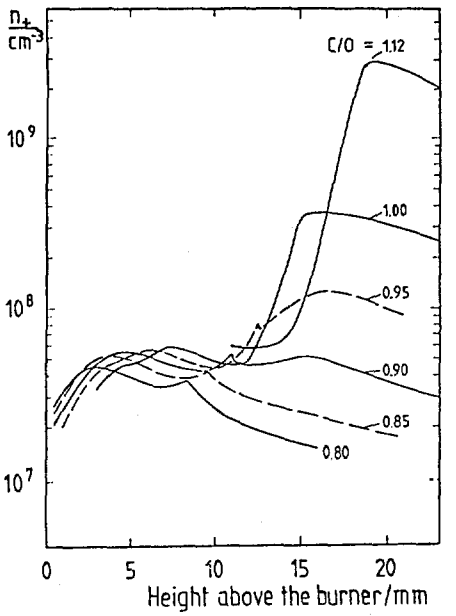

Fig. 3 Profiles of total positive ion number densities in C_2H_2/O_2 flames of different C/O (v_u= 42 cm s^{-1} , p= 27 mbar for both figures)

3. TOTAL NUMBER DENSITIES

Two typical profiles of the total number densities of positively and negatively charged species in a low-pressure slightly sooting C_2H_2/O_2 flame are shown in Fig. 2. The oxidation zone and the soot forming zone can clearly be distinguished by the profiles of charged particles. The ionization is less strong in the oxidation zone (up to about 12 mm of height from the burner) where chemi-ionization of small radicals is the prevailing mechanism of charge generation. The difference in the profiles in this zone can be explained by a relatively high concentration of free electrons which cannot be measured by method (a). In the preheating zone below 2 mm of height electrons are attached to neutral molecules or radicals (see 4.2) because of the low temperature. As the temperature increases large hydrocarbon molecules with high electron affinities such as the poly-ynes are formed from which negative ions can be formed by dissociative attachment causing the free electron concentration to decrease.

At the beginning of the soot forming zone there is a steep increase in the ionization by more than an order of magnitude which is even larger as the flame is made more fuel-rich. After reaching a maximum some mm downstream from the maximum of temperature the ion number densities decrease more slowly by charge recombination. The higher concentration of positively charged particles in the burned gas where the soot particles have grown to a diameter of 5 - 10 nm [11] cannot yet be explained conclusively. The concentration of free electrons should be relatively low but it is unlikely that there is a net positive space charge in the burned gas. The reason for the discrepancy might be that very large positively charged soot particles could not be prevented from reaching the detector when measuring negative ion currents applying method (a). Measurements of energy distributions showed that in this region of the flame positively charged particles are heavier on the average than their negative counterparts. The seeming unbalance of charge becomes smaller with lower maximum flame temperature [12].

Fig. 3 gives an impression of the development of the ionization in the burned gas with increasing C/O ratio. The visual threshold of soot formation in C_2H_2/O_2 flames lies at about 0.95 but the profiles of positive ions indicate that the formation of large and more easily ionizable particles begins at C/O ratios between 0.85 and 0.90. The shift of the profiles to greater distances from the burner with increasing C/O corresponds to a general shift of the flame reaction zone when burning richer mixtures. The small peaks in the profiles are considered artefacts due to an unknown interaction between the sampling nozzle and the flame. This is also observed in the profile of negative ions.

4. INDIVIDUAL GROUPS OF IONS

4.1 Positive Alkapoly-yne Ions

Ions of this kind are derived from the addition of a proton to alkapoly-ynes of the general formula $C_{2n}H_2$ (n = 2,3,4,...) giving alkapoly-ynium ions of the type $C_{2n}H_3^+$ and to alkapolyenyliden radicals (or corresponding carbenes) of the general formula $C_{2n+1}H_2$ (n = 1,2,3,...) giving $C_{2n+1}H_3^+$. Both groups of ions exhibit a mass distribution with one maximum in the enveloping curve. See Fig. 4 which shows these groups of ions in the mass range up to about 170 u at two different heights in a sooting C_2H_2/O_2 flame. Ions up to $C_{14}H_3^+$ can already be found in non-sooting flames. The ions with low odd numbers of C atoms are more abundant than those with low even numbers but this difference vanishes for ions with many C atoms. Therefore the centre of the distribution of the $C_{2n+1}H_3^+$ lies at a lower mass by about one C atom than that of the $C_{2n}H_3^+$. The distribution of both groups of ions can well be described by Poisson distributions. Their centres are shifted to larger numbers of C atoms with increasing height in the flame and with increasing C/O ratio [8] .

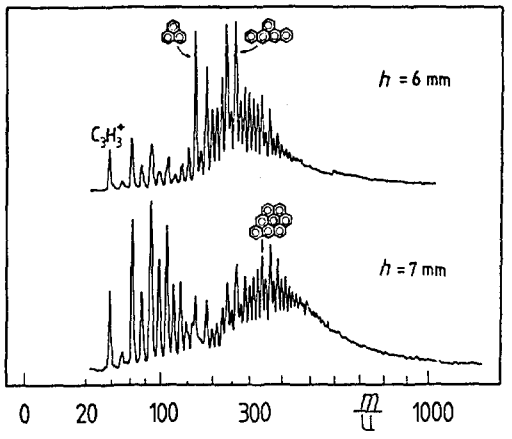

Fig. 4 Mass spectra of poly-yne and PAH ions at two different heights in a sooting C_2H_2/O_2 flame (C/O = 1.12, v_u = 60 cm s^{-1} p = 27 mbar)

Neutral poly-ynes, $C_{2n}H_2$, are a major group of hydrocarbons in fuel-rich and particularly in sooting flames. Of the carbenes, $C_{2n+1}H_2$, only C_3H_2 has been detected till now[13]. The neutral poly-ynes have in common with the respective protonated species that they are formed later than the less unsaturated molecules (ions) and reach their maxima at the end of the oxidation zone or shortly thereafter. In contrast to the ions, however, there is no Poisson distribution of the neutral species, the concentrations of which decrease monotonously with higher number of C atoms, a consequence of their relation by partial equilibria . Furthermore, the series of alkapoly-ynes is guided by acetylene while the $C_2H_3^+$ is practically absent from the flames.

4.2 Light Negative Ions

Much less is known about negative ions in fuel-rich hydrocarbon flames. After the pioneering work of Green [14] Goodings et al. reported about negative ions in methane/oxygen flames [15] and Hayhurst et al. studied acetylene/oxygen flames along these lines [16]. Atmospheric pressure flames were used in all cases.

The two maxima of total negative ionization in the oxidation zone (Fig. 2) can be attributed to different groups of ions. More than 90 percent of the ions in the first maximum are anions of saturated alkamonoacids $C_nH_{2n-1}O_2^-$ ($1 \leq n \leq 6$) of unsaturated acids $C_nH_mO_2^-$ (n = 3-5, m = 2n-3, 2n-5) and of the alkadiacids $C_nH_{2n-3}O_4^-$ ($2 \leq n \leq 6$). Since in a flame ion mass spectrum each ion is represented by only one peak and not by a characteristic fragmentation pattern the formulae have been proposed not only according to the mass. Characteristic mass differences of related peaks due to the CH_2 group and a typical behaviour of the different groups of anions under different burning conditions (C/O ratio, temperature) support this assumption. The decomposition of acid anions at temperatures above 500 to 600 K is the reason for the minimum of the total negative ion concentration at a height of 4 - 5 nm in the flame (see Fig. 2). It must be assumed that these ions decompose into free electrons and neutral molecules or radicals since other anionic products would have been detected. The larger acid anions decompose faster than those with a lower mass.

The negative ions of the second maximum are mainly those derived from the poly-ynes and have the composition $C_{2n}H^-$ and C_{2n}^- ($1 \leq n \leq 10$). They are still present in the burned gas although their concentration decreases after the second negative ionization maximum [8] . The concentrations of the smaller representatives of these groups, C_2H^-, C_2^-, are the only ones that decrease with increasing C/O while those of the ions with more C-atoms increase, the more the larger they are. The over-all concentration of the C_{2n}^- ions is between 10 and 20 % of that of the $C_{2n}H^-$ group depending on the burning conditions.

In contrast to the positive poly-ynic ions those with an odd number of C atoms in the chain are less abundant. While with an even number of C atoms those with one hydrogen atom ($C_{2n}H^-$) are dominating it is the C_{2n+1}^- group that is relatively more frequent than $C_{2n+1}H^-$ ions or even particles with a composition $C_{2n+1}H_2^-$. With increasing chain length

(2n+1 > 7), however, the odd carbon anions with one and two H atoms increase in abundance relative to the C_{2n+1}^- [8].

The general formulae HC_nO^- ($2 \leq n \leq 10$) and C_nO^- ($2 \leq n \leq 4$) can be assigned to other ions in the second maximum. They are ions derived from the respective ketenes. Those with an even number of C atoms are relatively more abundant. Their profiles in the flames suggest that they are thermally more stable than the acid anions but less long-lived than the poly-ynic anions. They are not found at greater heights in the burned gas of sooting flames.

4.3 Aromatic Ions

Aromatic ions in flames were first reported by Calcote et al. [1] and by Delfau et al. [17]. In C_2H_2/O_2 flames with C/O > 0.55 aromatic ions are formed early in the oxidation zone. To these belong the ions with only one aromatic ring system such as the benzylium ($C_7H_7^+$), phenylvinylium ($C_8H_7^+$), phenylpropinylium ($C_9H_7^+$) and the protonated naphthalene ($C_{10}H_9^+$). From its behaviour in the flame the protonated benzene, ($C_6H_7^+$), although not aromatic, can also be counted to this group. These ions decompose or are oxidized still within the oxidation zone at temperatures higher than about 1400 K.

At a C/O ration > 0.6 also aromatic ions with more than one ring appear in the oxidation zone (polycyclic aromatic hydrocarbon ions, PAH ions). First only those with two or three rings are formed. The three-ring ion phenalenylium ($C_{13}H_9^+$, see Fig. 4) is one of the most prominent PAH ions but also ions with a short side-chain such as the naphthylmethylium ($C_{11}H_9^+$) and the vinylphenalenylium ($C_{15}H_{11}^+$) are formed. Two- and three-ring PAH ions also disappear again still within the oxidation zone at about the same temperature as the mono-ring ions, see Fig. 10. With increasing C/O ratio PAH ions with four and more condensed rings appear. In the mass range $\lesssim$ 350 u the abundance of the ions with an even and an odd number of C atoms is alternating, those with an odd number prevailing. In PAH ions with an odd number of C atoms and no side chains the positive charge can be delocalized within the aromatic π-electron system which makes them more stable. Two very noticeable representatives of these are benzo(cd)pyrenylium ($C_{19}H_{11}^+$) and benzo(fg)tetracenylium ($C_{21}H_{13}^+$). With an even number of C atoms the positive charge must be located outside the aromatic ring system.

The mass distribution of the heavier PAH ions can be represented by a Gauss function, the maximum of which is shifted to larger masses with longer reaction time in the flame, see Fig. 4. According to the mass of the most condensed ring systems they contain up to about 50 rings in sooting flames. Ions with four and more rings do not disappear completely at the end of the oxidation zone but can be detected in the burned gas.

Negative aromatic ions have not conclusively been found in acetylene flames. They occur, however, in benzene flames in which case they probably always contain one or two oxygen atoms [1].

4.4 Polyhedral Carbon Ions

Fig. 5 shows three outstanding peaks at the end of the mass spectrum of the positive PAH ions. They belong to another group of large ions which are formed at the end of the oxidation zone in sooting flames and also persist in the burned gas. This group of both positive and negative ions with the composition C_{2n} and $C_{2n+1}H_x$ ($x \leq 2$) has been detected for the first time by us in acetylene and benzene flames [2]. For the positive ions 2n lies between 30 and 90 while for the negative species the range even extends up to $2n \lesssim 210$. Ions with an even number of C atoms are more abundant by factors between 10 and 100 than the neighbouring particles with odd numbers. Probably the same ions but not with such a broad distribution of masses have been found when graphite was evaporated by absorption of intense laser radiation [18]. Since particles with even numbers of C atoms are particularly stable Kroto et al. assume that they must be closed spherical shells of carbon atoms [19] but ellipsoidal structures are possible as well. The closed shells would consist of six- and five-membered carbon rings. We therefore call them polyhedral carbon ions.

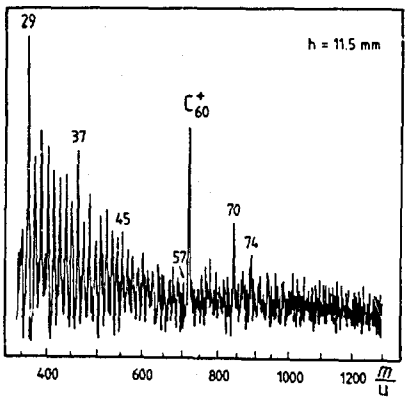

Fig. 5 Three prominent positive polyhedral ions at the end of the PAH ion mass spectrum (C_2H_2/O_2 = 1.0, v_u = 42 cm s^{-1}, p = 27 mbar)

In benzene flames the positive polyhedral ions smaller than C_{60}^+ can better be distinghuished from the heavy PAH ions since the concentration of the latter steeply decreases at the end of the oxidation zone. A mass spectrum is shown in Fig. 6. The most striking observation is the high abundance of the C_{60}^+ ion. Furthermore, C_{44}^+, C_{50}^+ and C_{70}^+ are relatively abundant in accordance with the results of the graphite vaporization experiments. While in acetylene flames the smallest detectable polyhedral ion is

C_{50}^+ there are ions down to C_{30}^+ in benzene flames. The relative abundance of the positive polyhedral ions with a number of C atoms $\gtrsim$ 60 is not much different in benzene and acetylene flames. The total concentration of polyhedral ions is about twice as high in benzene as in acetylene flames when compared at C/O ratios where both flames form the same amount of soot.

The mass distribution of negative polyhedral ions is distinctly different. Examples from an acetylene and a benzene flame are given in Fig. 7a,b. While the ions smaller than C_{60}^- display almost the same relative abundance as the corresponding positive ions the larger ions cover a much more extended mass range up to about C_{210}^-. In benzene flames there is a bimodal mass distribution with maxima at C_{50}^- and C_{82}^- and a minimum at C_{62}^-. C_{60}^- is more abundant than its direct even-numbered neighbours but its intensity cannot be compared to that of C_{60}^+. The mass spectrum of the negative ions heavier than about C_{86}^- is quasi-continuous with no single mass peak standing out. This part is similar in acetylene and benzene flames apart from the somewhat different position of the maximum at C_{88}^- in benzene and at about C_{100}^- in acetylene flames. The branch around C_{50}^- is more pronounced in benzene flames.

A maximum in the distribution both of positive and negative ions with odd numbers of C atoms lies at about $C_{49}H$. For negative ions a weak second maximum was found near $C_{79}H_2^-$ (not discernible in Fig. 7).

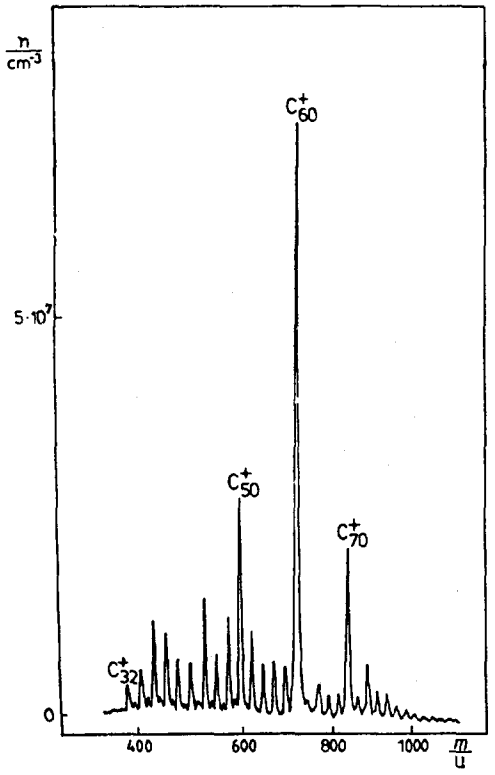

Fig. 6 Mass spectrum of positive polyhedral ions from a benzene/O_2 flame (C/O = 0.76, v_u = 42 cm s^{-1} h = 15 mm, p = 27 mbar)

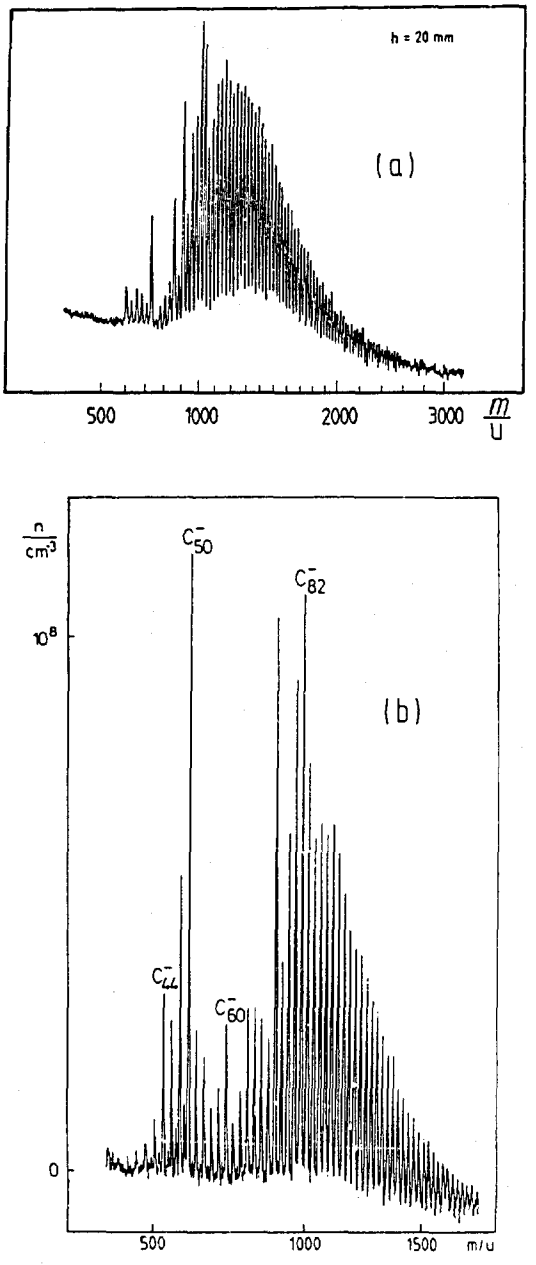

Fig. 7a,b Mass spectrum of negative polyhedral ions from a
(a) C_2H_2/O_2 flame (C/O = 1.12, v_u = 42 cm s^{-1}, p = 27 mbar)
(b) benzene/O_2 flame (C/O = 0.86, v_u = 42 cm s^{-1}, h = 10 mm, p = 27 mbar)

When burning a benzene-d_6 flame no mass shift of polyhedral ions of either sign containing an even number of C atoms was detectable. This confirms the fact that also in flames these particles do not contain hydrogen. There was, however, a hydrogen content in ions of either sign with an odd number of C atoms, $C_{2n+1}H_x$: If $2n \gtrsim 60$ negative ions contain two hydrogen atoms whereas for $2n < 60$ one H atom per ion was observed for most species, particularly for positive ions. Nothing is known so far about the number density of neutral polyhedral carbon in sooting flames but it is very probable that it exists.

5. CHARGED SOOT PARTICLES

With the mass spectrometers used charged soot particles can be distinguished from the molecular ions with a more or less well-defined composition by the following criteria: The charged soot particles occupy the mass range beyond that of the PAH and the polyhedral ions. Their mass distribution is continuous with a smooth enveloping curve.No individual mass peaks can be distinguished as in the case of the polyhedral ions and no particular masses are standing out from the distribution. They are the species with the largest growth rate by far. The variation of their mass distributions indicate both growth by coagulation of large particles and by the addition of small particles. The total ionization increases steeply when they appear and begin to grow.

5.1 Positively Charged

The Figs. 4 and 8 a,b illustrate the development of the mass distribution of the positively charged soot particles in a C_2H_2/O_2 flame. At a height of 6 mm single PAH ions in the mass range 140 to 450 u are clearly visible in the spectrum. At 7 mm the PAH ions with masses lower than about 3×10^2 u have decreased while a continuous background mass distribution which is already indicated at 6 mm develops and is first centered at about 4×10^2 u. At 11 mm (Fig. 8a) the lower mass range is dominated by the poly-ynium ions but the PAH in the mass range 300 to 450 u are still discernible on the left flank of the underlying continuous distribution shown with a lower resolution. Its centre has now moved to about 7×10^2 u while its upper end extends to 2×10^3u. It can clearly be seen that a second maximum in the continuous mass distribution develops at about 4×10^3 u leaving a minimum around 2×10^3 u. The further growth of the continuous distribution with the maximum at 7×10^2 u now does not continue as in the way before. Instead it fades out while its centre is only being shifted to about 1.2×10^3 u. In the same time the larger charged particles grow strongly in concentration and their maximum is shifted to $5 - 6\times10^3$ u extending to 10×10^3 u and leaving still a minimum around 2×10^3 u (see Fig. 8b).

The appearance of a minimum in the mass range around 2×10^3 u which corresponds to 150 - 160 C atoms per particle and of a maximum at about 4×10^3 u in the very early stage of soot formation is an indication of an effective coagulation process of particles with a mass around 2×10^3 u.

The further growth of the soot particles and their mass distribution has been studied by the experimental methods (a), (b), and (d) (see above)[3,10]. The results for the C_2H_2/O_2 flame with C/O = 1.12, v_u = 42 cm s^{-1} are in short: With increasing height in the flame the mass distribution of the positively charged soot particles broadens and its centre is shifted rapidly to larger masses (20 mm: 2×10^4 u; 25 mm: 6×10^4 u; 40 mm: $>3\times10^5$ u ($d \gtrsim 8$ nm). In more fuel-rich flames the growth rate is higher.

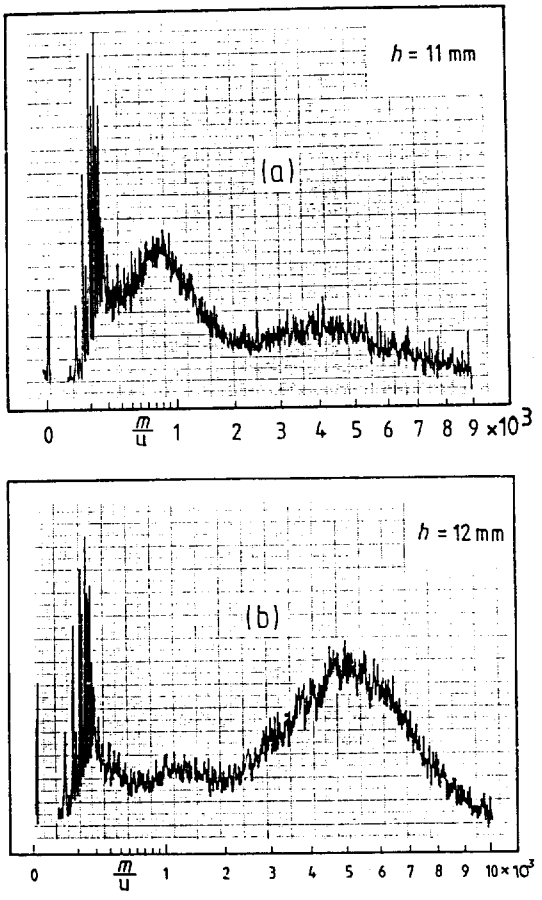

Fig. 8a,b Mass distributions of large positive PAh ions and small charged soot particles at 11 mm (a) and 12 mm (b) in a C_2H_2/O_2 flame showing the effect of coagulation. The resolved peaks on the left are due to poly-yne ions.(Conditions as in Fig. 7a)

5.2 Negatively Charged

Negatively charged soot particles and their mass distribution show a different behaviour. There is no analogous growth of negative PAH ions nor is there a minimum in the mass distribution at 2×10^3 u or a second maximum starting at some thousand mass units as in the case of positively charged soot particles. Mass distributions of large negatively charged particles obtained by energy-discriminating methods have shown that, although the absolute maxima in these distributions remain at a few thousand mass units (mostly polyhedral ions), these distributions develop long and broad tails extending to very large masses with increasing height in the flame. Since the distributions of positively charged particles also become very flat and broad not much difference is found in the distributions of very large particles of either sign if measured above 20 mm of height using methods that can only detect particles with $m > 2\times10^4$ u [9].

5.3 Soot Volume Fractions

The development of the total volume fractions, φ, of charged and neutral soot particles with masses $\gtrsim 2\times10^4$ u ($d \gtrsim 3$ nm) is shown in Fig. 9. The points are experimental values [12] while the full lines have been calculated using a partial-ionization-equilibrium model [9]. Both the experiment and the model show that the ionization of the particles with $m \gtrsim 8\times10^3$ u starts at about 15 mm above the burner, apart from a small fraction of charge that remains on the particles from the non-equilibrium chemi-ionization processes in the oxidation zone. The volume fraction of charged soot increases up to a height of about 40 mm followed by a slow decrease (not shown). In this flame the volume fraction of positively charged soot is larger than that with a negative charge. This deficit of negative charge on the large particles is balanced by the larger number density of negative polyhedral ions and poly-yne ions. At heights larger than 25 mm a small soot fraction carries two elementary positive charges per particle. The calculated concentration of free electrons is low and decreases with temperature.

In sooting flames of lower temperature the soot fractions of either sign are nearly equal. The fraction of negatively charged soot can be increased over that with positive charge by seeding the flame with easily ionizable metal salts, e.g. CsCl [9].

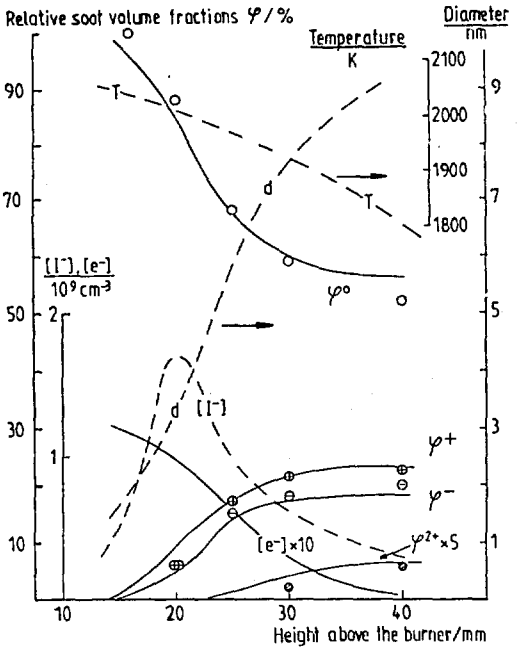

Fig. 9 Experimental and calculated relative volume fractions of charged and neutral soot with experimental curves for the mean particle diameter, d, temperature, T and number density, I, of negative molecular ions. (Conditions as in Fig. 7a)

6. DECAY AND GROWTH OF CHARGED SPECIES IN RELATION TO NEUTRAL HYDROCARBONS

One purpose of the study of charged species in fuel-rich flames is to draw conclusions as to the growth and decay of large neutral hydrocarbons, particularly of those which escape direct observation. By far the main chemical conversions in the flame take place by reactions of neutral particles. This also concerns the formation of higher hydrocarbons and of soot. But since almost every group of related species (poly-ynes, PAH etc.) has its ionic pendent and a great deal of the reactions of ions are ion-molecule reactions the ions being formed and consumed in flames are closely related to the pool of neutral reactants and products.

Similar behaviour in many respects has been found where the profiles of the neutral species and the related ions could be measured separately. But there are also significant differences within and between the groups of neutral and ionic particles. Important reasons for these differences are an enhanced reactivity of most ions, a variation of the proton and electron affinities and the ionization potentials within and between the groups and the demand for local electroneutrality in the flame. The latter has also an influence on the diffusional transport. Because of statistical reasons the differences due to the reactivity and the electrical properties of the particles can be expected to become smaller at higher temperature and with larger particles.

6.1 Poly-yne Ions

Poly-yne ions ($C_{2n(+1)}H_3^+$) are the smallest of the larger hydrocarbon ions in flames. They could be followed up to $C_{24}H_3^+$. Similarities to neutral poly-ynes are the following: They are formed in the hotter region of the oxidation zone and reach their maxima almost simultaneously at the end of it. Their relative rates of consumption downstream from the oxidation zone increase with increasing mass, but absolutely the rate of decay is slow compared to that of the small PAH ions at the end of the oxidation zone so that they still have an appreciable concentration in the burned gas. The difference to the neutral poly-ynes lies in their mass distribution (two Poisson distributions) and its variation with temperature. The experiments indicate that there is a rapid equilibration between the concentrations of the poly-yne ions. Although they are the dominating low-mass positive ions in the region of soot formation they hardly have any relation to it: As direct precursors of charged soot particles, they are too small and as building bricks for growing particles their concentration is far too low compared to that of neutral C_2H_2 and C_4H_2 . As with neutral poly-ynes prolongation of the carbon chain does not lead to the formation of very large ions or molecules, respectively.

6.2 PAH Ions

The next steps of growth can only take place in two dimensions via aromatic systems. Again both growth and decay control the concentration profiles of the aromatic ions although in a way different from those of the poly-yne ions. In the first lower-temperature region of the oxidation zone there is a relatively rapid formation of aromatic ions up to masses considerably larger than those of the largest poly-yne ions. In contrast to the "one-dimensional" poly-yne ions some of the PAH ions attain a more stable structure than others, such as the phenalenylium. As the temperature increases to >1400 K the decay (or oxidation) of the aromatic ions starts but it mainly affects PAH ions up to a mass of about 350 u. These ions reach their maxima at about the same height and decay more or less simultaneously and with a similar rate. It is very probable that poly-yne ions are products of this decay since it takes place in the flame zone where the number density of the poly-yne ions increases. A mere charge transfer to neutral $C_{2n(+1)}H_3$ species cannot be an effective process since the concentration of such radicals is so low that they have not yet been detected in these flames. Fig. 10 shows the decay of a representative small PAH ion in the oxidation zone and its reappearance at great heights in the burned gas together with the profile of a representative poly-yne ion. Thus, the decay of the smaller PAH ions to poly-yne ions seems to be in some way reversible when the temperature in the burned gas has dropped below about 1400 K. The decay of smaller PAH at higher temperature and a reappearance when the burned gas cools has also been observed for neutral PAH [20].

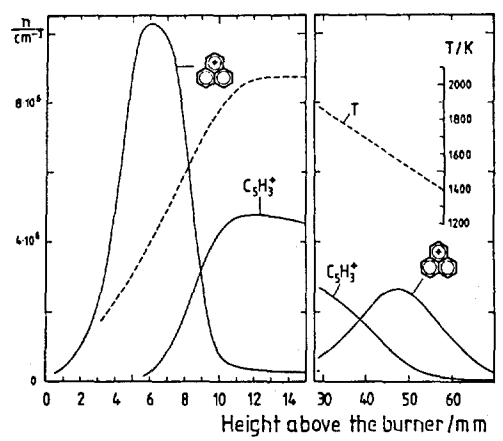

Fig. 10 Decay and reappearance of a small representative PAH ion in relation to profiles of a representative poly-ynium ion and the temperature (Conditions as in Fig. 5)

The larger PAH ions also display maxima in their profiles but these are shifted toward greater heights with increasing mass indicating consumption by growth to larger particles rather than decomposition to smaller ions. There is no more preference for odd-numbered PAH ions but species with a minimum of H atoms are still preferentially formed. During the growth up to a mass of more than 10^3 u no bimodal mass distribution appears. This is an indication for growth mainly by the addition of small hydrogen-poor neutral hydrocarbons enlarging the two-dimensional aromatic system at this stage rather than by coagulation starting a growth in three dimensions.

In the range from naphthalene (128 u) to corenene (300 u) the maximum concentrations of neutral PAH in many sooting flames decrease on the average by one order of magnitude with an increase in mass of about 80 u [21]. The growth and the change in number density of neutral PAH with $m > 300$ u , however, has not yet been observed directly. A single older mass spectrum from a very rich flame covering the range from 350 to 550 u shows that this rough relation is not valid for $m \gtrsim 350$ u [22] The mass spectra of the PAH ions also show that beginning from this mass range the amount of carbon that goes into the larger particles increases.

6.3 Coagulation

Mass growth by coagulation is the next step. That coagulation of soot particles takes place has long been known from the decrease in their number density during growth. But the beginning of the coagulation causing a transient bimodal mass distribution has first been observed by us while measuring the growth of large ionized PAH. At the height where

the coagulation begins (Fig. 8a,b) the strong extra ionization of the growing soot particles has not yet started. Therefore the variation in the number density and the mass distribution of the positively charged particles reflect the variation in the mass distribution also of the uncharged particles. Measurements using method (b) have shown that at this stage the volume fraction of uncharged soot is more than 99 % (see Fig. 9).

6.4 Polyhedral Ions

Formation and decay of polyhedral ions is totally different from that of all other charged species. The principle that can be recognized so far is the following: There is no indication that polyhedral ions grow from smaller aromatic or poly-ynic species. The order of appearance has nothing to do with increasing mass. The polyhedral ions seem to appear as soon as the smallest soot particles have been formed. In benzene flames this occurs already within the oxidation zone. The most stable of the polyhedral ions appear first. The less stable are formed later. In non-sooting flames there are large PAH ions but no polyhedral ions. It is our working hypothesis that the polyhedral ions are formed from the very small soot particles probably by partially oxidative attack as soon as these have begun their three-dimensional growth.

In the zone of maximum temperature and shortly thereafter there is a partial decay (or oxidation) of these ions. The degree of decomposition is largest for the ions that have been formed late, i.e. the less stable. In the region of largest increase of the soot mass where no more oxidation is possible their concentration remains constant, apart from a slight increase of the particularly stable C_{60}. This shows that they are not formed from larger soot particles, that they are comparatively stable at high temperature in a non-oxidizing environment and that they are not re-incorporated into the soot. Their mass range is limited and they do not grow by coagulation with themselves. Further investigations of these interesting carbon species in flames are being undertaken.

This work has received financial support from the Deutsche Forschungsgemeinschaft and the Fonds der Chemischen Industrie which is gratefully acknowledged.

REFERENCES

1. Olson, D.B. and Calcote, H.F., 18th Symp.(Internat.) on Combustion, p. 453, The Combustion Institute, Pittsburgh 1981
2. Gerhardt, Ph., Löffler, S. and Homann, K.H., Chem.Phys.Lett.137, 306 (1987)
3. Homann, K.H. and Ströfer, E.: Soot in Combustion Systems and its Toxic Properties, Lahaye, J. and Prado, G. (eds.), p. 217, Plenum Press, New York 1983
4. Homann, K.H. and Wolf, H., Ber.Bunsenges.Phys.Chem. 87, 1073 (1983)
5. Homann, K.H.,Ströfer, E. and Wolf, H., 62. AGARD Propulsion and Energetics Symposium, Çeşme, Turkey 1983, AGARD Conf.Proc.No. 353, p. 19-1, 1984
6. Bittner, J.D. and Howard, J.B., 18th Symp. (Internat.) on Combustion, p. 1105, The Combustion Institute, Pittsburgh 1981
7. Homann, K.H., Ber.Bunsenges.Phys.Chem. 83, 738 (1979)
8. Gerhardt, Ph., Dissertation D17, TH Darmstadt, 1987
9. Homann, K.H. and Wolf, H., 21th Symp.(Internat.) on Combustion, The Combustion Institute, Pittsburgh 1987 (to be published)
10. Homann, K.H. and Traube, J., Ber.Bunsenges.Phys.Chem. 91, 1987 (to be published)
11. Wersborg, B.L., Howard, J.B. and Williams, G.G., 14th Symp. (Internat.) on Combustion, p. 929, The Combustion Institute, Pittsburgh 1973
12. Wolf, H. Dissertation, TH Darmstadt D17, 1986
13. Kubitza, Ch., Schottler, M. and Homann, K.H., Ber.Bunsenges.Phys.Chem. 91, 1987 (to be published)
14. Green, J.A., 26th AGARD Propulsion and Energetics Panel, Pisa, Italy, AGARD Conf. Proc. No. 8, Vol. I, p. 191 (Wilsted, H.D., Ed.), 1965
15. Goodings, J.M., Bohme, D.K. and Chu-Wai ng, Comb.Flame, 36, 45 (1979)
16. Hayhurst, A.N. and Jones, H.R.N., 20th Symp. (Internat.) on Combustion, p. 1121, The Combustion Institute, Pittsburgh 1985
17. Michaud, P., Delfau, J.L. and Barassin, A., 18th Symp.(Internat.) on Combustion, p. 443, The Combustion Institute, Pittsburgh 1981
18. Rohlfing, E.A., Cox, D.M. and Kaldor, A., J.Chem.Phys. 81, 3322 (1984)
19. Kroto, H.W., Heath, J.R. O'Brien, S.C., Curl, R.F. and Smalley, R.E., Nature, 318, 162 (1985)

20. Bockhorn, H., Fetting, F. and Wenz, H.W., Ber.Bunsenges.Phys.Chem. 87, 1067 (1983)

21. Homann, K.H., 20th Symp. (Internat.) on Combustion, p. 857, The Combustion Institute, Pittsburgh 1984

22. Homann, K.H. and Wagner, H.Gg., 11th Symp. (Internat.) on Combustion, p. 371, The Combustion Institute, Pittsburgh 1967

DISCUSSION

O.Gulder, CA

Would you expect the same sort of profile if you were to have a diffusion flame?

Author's Reply

The profile will not be the same but one knows that in diffusion flames the soot formation starts where the oxidation zone touches the pyrolysis zone, and I wouldn't be astonished if you also see all these ions in diffusion flames.

RATES OF FORMATION OF SOOT FROM HYDROCARBON FLAMES AND ITS DESTRUCTION

J. Mullins, B. Simmons, A. Williams*

* Department of Fuel and Energy, The University of Leeds, LS2 9JT

SUMMARY

In the first part of the paper the equations that have been proposed in the literature to describe the rate of soot formation in hydrocarbon flames are surveyed. Recent work in this laboratory using a shock tube to measure soot formation rates is outlined and the correlation equation proposed compared with that of other workers.

Data on the rate of combustion of soot particles are also outlined and combined with recent measurements in this laboratory to give an overall soot oxidation rate expression.

The two equations are combined to give an expression suitable to describe soot formation and burn out for gas turbines and tested to a limited degree.

1. Introduction

One of the requirements for the successful design of a gas turbine combustor is the ability to predict the concentration of soot particles from a knowledge of the fuel concentrations in the early combustion region, and to predict its burn-out in leaner regions.

The amount of soot produced is generally too small to influence the rate of heat release, and, in principle, its rate of formation can be calculated from a knowledge of the hydrocarbon and oxygen concentrations if an appropriate correlation equation is known. In general, the soot concentration is given by [1]

$$\frac{dc}{dt} = \frac{dc_f}{dt} - \frac{dc_{OXID}}{dt} \qquad (1)$$

where c is the actual soot concentration, dc_f/dt is the rate of soot formation which is a function of hydrocarbon and oxygen concentrations, temperature and pressure; and dc_{OXID}/dt is the rate of oxidation of soot particles which takes place in the leaner zones of the combustion chamber.

Soot formation in flames is generally envisaged as taking place in three conceptually separate consecutive stages. The initial transformation of the original fuel into a particulate system is known as nucleation. The small spherical particles first produced then increase in size in the growth stage (via surface growth and coagulation), and finally, fully grown particles arrange themselves into chains by aggregation [2]. The processes involved are illustrated schematically below:

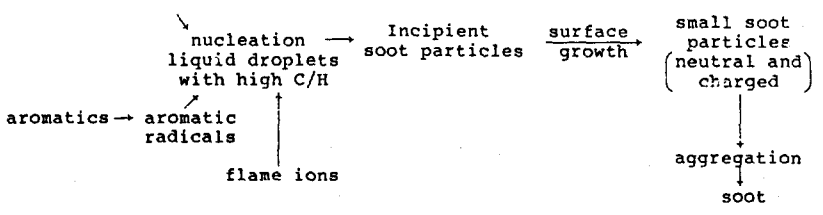

Whilst it is possible to describe the individual steps leading to soot formation [3], in most practical cases it is necessary to employ global kinetics to link the concentration of the initial hydrocarbon to the rate of soot formation.

Tesner et al [4] described the formation of soot particles in an acetylene hydrogen diffusion flame using the branched-chain process of Semenov [5], the radical nuclei formation step being given by:

$$dn/dt = n_o + (f - g)n - g_o Nn \qquad (2)$$

where n is the concentration of active particles, n_o is the spontaneous origination rate of active particles, f is the linear branching coefficient, g is the linear termination coefficient, g_o is the coefficient of linear termination on soot particles and N is the concentration of soot particles. The rate of nuclei formation was related to fuel concentration by the following expression:

$$n_o = 10^{13} N_o e^{-E/RT} \quad (3)$$

where 10^{13} is the assumed frequency factor, N_c is the acetylene concentration, E is the activation energy, R is the gas constant and T is the temperature.

The rate of formation of soot particles was given by:

$$dN/dt = (a - bN)n \quad (4)$$

where a and b are constants.

Essentially the same two-step model was adopted by Magnussen [6] to model soot formation in turbulent flames, good agreement between prediction and experiment being cited for the variation of mean soot concentrations along the axis of pure acetylene flames.

The most generally used expression, derived for direct-injection diesel engine use and therefore applicable to high pressure situations is that due to Khan et al [7]:

$$\frac{dS}{dt} = C \frac{V_u}{V_{NTP}} \Phi_u^3 P_u e^{-E_s/RT_u} \quad (5)$$

where C_s is the soot formation rate coefficient, V_u and V_{NTP} are the volumes of the soot formation zone and cylinder contents at NTP respectively, Φ_u is the local unburnt equivalence ratio, P_u is the partial pressure of unburnt fuel, E_s is the activation energy for soot formation, R is the universal gas constant and T_u is the local temperature for soot formation.

A similar expression was cited by Naegeli et al [8] to correlate relative soot concentrations in a gas turbine combustor:

$$S = A(F/A)^{3.425} \exp(-b/T) \quad (6)$$

where S is the relative soot concentration, A is an arbitrary pre-exponential factor and b is an Arrhenius type temperature coefficient. The relative soot concentration was strongly dependent on the fuel/air ratio, consistent with the equations of Khan et al [7].

More recently, Hiroyasu et al [9] developed a mathematical model for predicting the rate of heat release, the concentration of exhaust nitric oxide and soot in swirl-chamber type (indirect injection) diesel engines. The rate of soot formation was cited as being strongly affected by the concentration of unburned total hydrocarbon in the flame, and was given by:

$$\frac{dS_f}{dt} = A \left(\frac{P_{THC}}{Po_2}\right)^{1.25} .T^{-1.0} \exp\left(\frac{-40,000}{RT}\right) \quad (7)$$

where P_{THC} and Po_2 are the partial pressures of unburned total hydrocarbon and oxygen respectively. The soot oxidation rate incorporated the findings of Nagle and Strickland-Constable [10].

Farmer et al [11] citing previous work [12], presented a similar expression for the rate of soot formation in a jet-stirred reactor:

$$R_F = AT^a C_{HC}^{\ b} C_{O2}^{\ c} \exp(-E/RT) \quad (8)$$

where R_F is the soot formation rate and A, a,b,c, and E are constants. The temperature, hydrocarbon and oxygen concentrations used in the correlation were obtained by experiment [12] with the soot oxidation rate due to Nagle and Strickland-Constable [10] again being used to allow for soot burn out.

Wang et al [13] investigated the combustion kinetics of soot formation for toluene and other selected fuels behind reflected shock waves. For toluene/oxygen/argon mixtures, the following correlation equation was given to describe the apparent rate of soot formation:

$$R_{SOOT}(g/ml.\mu sec) = (5.55E + 10) \cdot \exp\{-41.8/RT + \sigma(-48.1/R) \cdot (1/T - 1/T_m)\} \cdot [C_7H_8]^{2.59} [O_2]^{-0.71} [Ar]^{0.13} \quad (9)$$

where σ is a variable so that both high and low temperature regions are represented, and T_m is the critical temperature (1800 K) above which fragmentation occurs; $\sigma = 0$ if $T < T_m$, otherwise $\sigma = 1$.

Najjar [14] developed a soot model to predict soot formation in the primary zone of a gas turbine combustor [15,16]. Equations are given describing the soot formation

rates applicable to the three gas turbine fuels, kerosine, gas oil and R50. For kerosine, the following expression was given:

$$\frac{dS}{dt} = C(1).[HC].\exp(-12,100/T) - 3x10^{9}.[O_2].[S].\exp(-7,800/T) \qquad (10)$$

where C(1) is a pre-exponential collision factor for soot formation equal to 58 x 10^{14} at 3 atm. and 4.88 x 10^{14} for 10 atm., [HC], [O_2], and [S] are the fuel, oxygen and soot concentrations.

More recently, Simmons and Williams [1,17] investigated the rate of soot formation using a reflected shock tube and expressed the rate of soot formation by the following:

$$\frac{dc}{dt} = \{C_1[RH]^a \exp(-E_1/RT) - C_2[O_2]^b \exp(-E_2/RT)\} - \frac{dc_{OXID}}{dt} \text{ kg m}^{-3} \text{ s}^{-1} \qquad (11)$$

where [RH] and [O_2] are the initial concentrations of hydrocarbon and oxygen respectively, mol m^{-3}; a, b, C_1 and C_2 are constants, E_1 and E_2 are activation energies for pyrolysis and rich oxidation conditions respectively, J mol^{-1}; R is the universal gas constant, J mol^{-1} K^{-1}; T is the temperature, K and dc_{OXID}/dt is the rate of soot oxidation.

The development of this equation forms the basis of the next part of this paper.

2. Experimental Method and Results

A laser beam attenuation technique was used to measure the rates of soot formation and to determine final soot concentrations in experiments involving the pyrolysis and oxidation of benzene, toluene and toluene/n-heptane mixtures in shock-heated gases as described previously [1,17]. The reflected shock tube used is illustrated in Fig. 1 as was essentially that described by Coats and Williams [3]. Both laser detectors were shielded from thermal radiation by narrow bond-pass filters and the laser beams were mechanically chopped at a frequency of 16 kHz to eliminate residual background radiation.

Test gas mixtures employed were diluted by more than 98 mol % of argon, with the test gas pressure maintained at 4.67 x 10^3 Pa for all experiments. All data were obtained in the temperature range of 1500-1950 K and pressures of 2.6 to 3.6 x 10^5 Pa. The experimental data consisted of curves expressing laser beam attenuation as a function of time (inset Fig. 1), measurements of this type were made for benzene, toluene and toluene/n-heptane mixtures under pyrolysis or rich oxidative conditions where ϕ, the equivalence ratio was in the range 6 to 11.

From the laser attenuation records, values of the variation of the soot concentration, c, with time were obtained using the conventional absorbtion and scattering equations:

$$\frac{I}{I_o} = \exp[-K_\lambda tc] \qquad (12)$$

and

$$K_\lambda = \frac{n^2k}{(n^2+n^2k^2)^2 + 4(n^2-n^2k^2+1)} \times \frac{36\pi}{\rho\lambda} \qquad (13)$$

The density of the soot particles was experimentally determined to be 1860 kg m^{-3} for all the soots which is in good agreement with reported values [13,18]. The most detailed recent analysis of the values of n (the real part) and k (the imaginary part) has been by Lee and Tien [19], the variation of n and k given by them is shown in Fig. 2. The observations of Lee and Tien [19] tend to disprove the assumption of Dalzell and Sarofim [20] that room temperature values of n and k are valid at flame temperatures. Recent work in this laboratory [21] tends to confirm the validity of the Lee and Tien [19] data at room temperature, hence their data was used to determine soot concentrations despite the uncertainties still remaining about the high temperature results.

We have proposed [1] the following relationship (which derives from equations 1 and 11 :

$$\frac{dc_f}{dt} = \{C_1[RH]^a \exp(-E_1/RT) - C_2[O_2]^b \exp(-E_2/RT)\} \quad \text{kg m}^{-3} \text{ s}^{-1} \qquad (14)$$

The form of this expression is such that it can deal with oxidizing and pyrolytic situations; also, by setting $dc_f/dt = 0$, it can define the soot boundary (limits) as a function of the gas temperature. However, as outlined previously, the accuracy of this expression is dependent on the validity of the complex refractive index chosen. Furthermore, the initial formation of large polycyclic soot precursors [22] or side-reaction products may significantly interfere with the attenuation calculations. Fig. 3

[23] illustrates both the bathochromic and hyperchromic shifts associated with the increased conjugation in polyaromatic hydrocarbons (PAH) but shows that they can only influence our data if they become very large and this is further developed below.

By comparing soot yield data obtained simultaneously at two wavelengths (632.8 and 1152.0 nm), an attempt was made to determine the variation in total PAH concentration with temperature. Toluene pyrolysis data was obtained using the Lee and Tien [19] values of the complex refractive index of soot derived from Fig. 2 at 300, 1000 and 1600 K. At lower temperatures, the visible results exhibited higher apparent concentrations (SOOT + PAH) than the infra-red (SOOT only), in agreement with the findings of Graham et al [18]. However, at more realistic flame temperatures (1600 K), the visible and infra-red curves yielded no conclusive evidence of any PAH absorbtion. Those observations are consistent with the work of Rawlins et al [22], who concluded that once soot formation takes place, laser attenuation by soot particles renders polycyclic laser attenuation insignificant. The recent findings of Beretta et al [24] lends weight to this conclusion, finding that the molar absorbtivities of PAH's observed in methane/ethene/oxygen diffusion flames decrease with wavelength over the range 250 to 436 nm.

In view of this discussion, the visible and infra-red results were combined by using the Lee and Tien [19] values for the complex refractive index at 1600 K for the relevant wavelengths. Consequently, the rate of soot formation over the pressure and temperature range investigated can be represented thus:

Toluene

$$\frac{dc_f}{dt} = 6.25\times10^5[C_7H_8]^{2.36}\ \exp(-13,400/T) - 2.32\times10^6[O_2]^{1.28} \times \exp(-21,000/T) \qquad (15)$$

Benzene

$$\frac{dc_f}{dt} = 4.68\times10^5[C_6H_6]^{2.02}\ \exp(-14,000/T) - 7.98\times10^4[O_2]^{1.30} \times \exp(-15,000/T) \qquad (16)$$

Toluene/n-Heptane

$$\frac{dc_f}{dt} = 6.25\times10^5[C_7H_8]^{2.36}\ \exp(-13,400/T) + 5.35\times10^{22} \times [C_7H16]^{-3.99}\ \exp(-117,300/T) \qquad (17)$$

Attempts to observe soot formation in pyrolyzing n-heptane/argon mixtures (up to 2 mol %) or low percentage aromatics mixtures similar to turbine fuels proved unsuccessful in our apparatus because of the short path length with no soot formation apparent. Evans and Williams [25] also observed very low soot yields from n-heptane in relation to toluene and benzene.

However, the toluene/n-heptane expression, though adequately describing the range of experimental conditions investigated, does not hold for the condition where no toluene is present. The following expression takes this limitation into consideration:

$$\frac{dc_f}{dt} = F_1[\text{Total Hydrocarbon}]^{2.36}\ \exp(-13,400/T) \qquad (18)$$

For the toluene/n-heptane mixtures investigated at 1800 K, the following data were obtained:

mol % AROMATIC	wt % FUEL HYDROGEN	F_1	MEASURED SMOKE POINT (mm)
100	10.0	6.25×10^5	11
80	11.2	5.31×10^5	13
67	12.0	2.60×10^5	17

The soot yield may be derived from records of the type inset in Fig. 1 where attenuation ceases to increase, reaching a final, stable value. Soot yield (Y_2, kg m^{-3}) data were obtained from the same results that furnished the rate data and yielded the following analogous expressions:

Toluene

$$Y_2 = 5.95\times10^2[C_7H_8]^{2.27}\exp(-14,200/T) - 1.46\times10^5[O_2]^{2.01} \times \exp(-26,600/T) \quad (19)$$

Benzene

$$Y_2 = 95.2[C_6H_6]^{1.64}\exp(-12,300/T) - 1.45\times10^3[O_2]^{1.51} \times \exp(-19,900/T) \quad (20)$$

Toluene/n-heptane

$$Y_2 = 5.95\times10^2[C_7H_8]^{2.27}\exp(-14,200/T) + 1.65\times10^3[C_7H_{16}]^{-2.54} \times \exp(-40,100/T) \quad (21)$$

As before, the toluene/n-heptane expression was modified to the form:

$$Y_2 = F_2[\text{Total Hydrocarbon}]^{2.27}\exp(-14,200/T) \quad (22)$$

For the toluene/n-heptane mixtures investigated at 1800 K, the following data were obtained:

mol % AROMATIC	wt % FUEL HYDROGEN	F_2	MEASURED SMOKE POINT (mm)
100	10.0	5.95×10^2	11
80	11.2	5.57×10^2	13
67	12.0	2.83×10^2	17

The mixtures studied have aromatic contents higher than current aviation fuels, but the data can be extrapolated so that with mixtures with 25% aromatics $F_2 = 1.0 \times 10^2$, and with 20% the value is 0.5×10^2.

3. Comparison of Different Soot Forming Expressions

Ideally, in order to compare the accuracy of the various equations they should be compared with experimental data of soot concentrations which have been measured in conjunction with local concentrations of hydrocarbon and oxygen. No such data seems to be available.

Application of the equations cited in the literature, which for convenience are listed in Table 1, is difficult because often important constants or units are not specified. Of those listed four were selected for comparison and these are given in Table 2.

Rates of soot formation were calculated for equivalence ratios of 5 and 7 between 1600 and 1800 K, and these are listed in Table 2. It seems that there is modest agreement between Khan et al [7], Wang et al [13] and this work. Taking the data for $\Phi = 5$, $T = 1800$ K we find respectively 0.17, 11.16 and 0.43. The results for Najjar [14] are much higher; it is possible that we are not applying this equation correctly because in this type of calculation we cannot include the second term which requires a soot concentration term.

It should be noted that since the Khan et al [7] work was specifically for diesel-like situations its accuracy in other situations may be less accurate. On this basis the results by Wang et al [13] and these presented here seem to be the most accurate, and one must conclude that these form the upper and lower bounds of the limits of accuracy of the rate expressions.

4. Soot Oxidation Rates

Soot particles formed in relatively fuel-rich regions of the combustion chamber may be burned out in subsequent leaner regions.

Few measurements have been made of the burning rates of in-situ flame generated soot. Nagle and Strickland-Constable [10] however deduced a model applicable to carbons generally, this being:

$$R = 12\left[\left(\frac{20\exp(-30{,}000/RT(Po_2))}{1+21.3\exp(4100/RT(Po_2))}\right) X + 4.46\times10^{3}\exp(-15{,}200/RT(Po_2))(1-x)\right] \quad (23)$$

$$\text{where } X = \left[1 + \frac{1.51\times10^{5}\exp(-97{,}000/RT)}{4.46\times10^{-3}\exp(-15{,}200/RT(Po_2))}\right]^{-1}$$

where R is the rate of oxidation/unit area of soot surface, although this is based on an assumption of first order kinetics for the reaction between carbon and oxygen, which is now known not to apply under flame conditions.

Lee, Thring and Beer [26], using in-situ propane flame generated soot, also derived an expression for the burning rate, this being:

$$\text{rate of combustion/unit area} = 1.085\times10^{4}\,\frac{Po_2}{T^{\frac{1}{2}}}\exp\frac{-39{,}300}{RT} \quad (24)$$

although it also follows the Nagle and Strickland-Constable [10] approach to the problem.

Other studies have been undertaken by a number of other groups in related areas. Park and Appleton [27] have studied the oxidation of carbon blacks in a shock tube; Tesner and Tsibulevsky [28], Fenimore and Jones [29] and Garo, Lahaye and Prado [30] have made flames studies; Chan et al [31] have low temperature oxidation studies, Smith [32] and Hargrave et al [33] have considered coal char combustion rates. The results from these workers are compiled in Fig. 4 (based on refs. 27, 31).

It is generally agreed that soot particles are so small (typically 50 to 100 nm) that the rate of oxidation is not limited by diffusion under normal combustion chamber conditions (by typically an order of magnitude) and that the soot is essentially non-porous. In this case the rate of the intrinsic chemical reaction, ρ_i, between the soot surface and oxygen is given by

$$\rho_i = R_i\,[O_2]^m \quad (25)$$

where R_i is the intrinsic rate coefficient and $[O_2]$ is the concentration of oxygen at the surface raised to the reaction order m.

The relationship between R_i and the observed rate of oxidation per unit surface area, ρ_{obs}, may be expressed as:

$$\rho_{obs} = \gamma\,\sigma\,Ag\,R_i\,[O_2]^m \quad (26)$$

where γ is the characteristic particle size defined as the ratio of the particle volume/particle external area, σ and Ag are the density and total surface areas respectively. This applies to soot chains or particles of any shape, but for a spherical particle it becomes

$$\rho_{obs} = m_s\,R_i\,[O_2]^m \quad (27)$$

where m_s is the mass of the soot particle. The value of the reaction order, m, has the value of zero at low temperatures [31] and about 0.5 at flame temperatures [33].

In order to make comparison of the reactivities of different samples, on a same oxygen partial pressure basis, the available data (and not all the information given in Fig. 4 can be used in this way) were normalised by calculating the intrinsic rate coefficient, R_i, and then determining the oxidation rate at an oxygen partial pressure of 101 kPa. This data is given in Fig. 5. It seems that on the basis of all available experimental data the best fit value at flame temperatures is given by:

$$\rho_i = 10^{-2}\exp(-160/RT) \qquad kg/cm^2\,s \quad (28)$$

where the activation energy is in kJ/mol. This can be recast as follows:

Rate of combustion of a single spherical soot particle = $\rho_i\,[O_2]^{\frac{1}{2}}\,\pi d^2$ kg/s

thus $$\frac{dc_{OXID}}{dt} = \frac{6\times10^{2}\,c}{\rho d}\exp\left(\frac{-160}{RT}\right)[O_2]^{\frac{1}{2}} \qquad kg/m^3 s \quad (29)$$

where d is the diameter of the soot particle (m), and ρ is the density (kg/m^3), $[O_2]$ is the O_2 concentration in atm. In applying this equation there are two problems. Firstly the soot particle temperatures may not be the same as the gas temperatures, and secondly the availability of oxygen in turbulent combustion situations (i.e. whether chemical control holds under these conditions).

From a radiation balance it is possible to estimate the soot particle temperature 'overshoot' ($T_p - T_g$) from:

$$\rho_{obs} = h \left[(T_p - T_g) + \varepsilon \sigma (T_p^4 - T_m^4)\right]/\Delta H \qquad (30)$$

where h is the heat transfer coefficient, T_p and T_g the particle and gas temperatures, ε the particle emissivity, ΔH (for combustion to CO) equals 9.781, T_m is the temperature of the surrounding combustor walls. Under gas turbine combustion chamber conditions with low carbon burnout rates it seems that the degree of overshoot is negligible.

As far as turbulent mixing control is concerned one must generally assume in gas turbine situations, which are lean, that turbulent mixing is not a controlling factor.

5. Applications to Gas Turbine Combustion Chambers

In general many treatments of turbulent reacting flows assume that the mean rate of production (or loss) of a chemical species is a function of the mean state. That is, it is equivalent to laminar flow.

The analyses that have been presented here have been based on the assumption that both soot forming and soot burning are chemically controlled. This assumption has been used by Najjar [14] and Edelman et al [12], for both soot forming and soot burning conditions, although, to a certain degree, the expressions that they derived have an inherent turbulence factor incorporated into them.

The present data can be represented by the following expression:

$$\frac{dc}{dt} = \{C_1[RH]^a \exp(-E_1/RT) - C_2[O_2]^b \exp(-E_2/RT)\} - \left\{\frac{6\times10^2\, c}{\rho d} \exp\left(-\frac{160}{RT}\right)[O_2]^{\frac{1}{2}}\right\} \qquad (31)$$

within the temperature range of 1300 to 1850 K. It should be noted that for the burn-out part of the equation it is necessary to know c either by experiment or by calculation using the first term of equation (31).

This equation, and the yield equations, are applicable to premixed or diffusion flames but must be applied to the local concentrations of the reactants. Whilst some researchers [34,35]have incorporated turbulent mixing control steps into the application of such models the choice at present is arbitrary and the straight application of the above equation seems satisfactory but only if local concentrations are employed.

As far as the accuracy of the equations to practical systems is concerned it can be tested in three ways:

(i) We note that if the equation is applied to a model gas turbine combustor [34] using a Jet A1 fuel (13.77% H, 18.3% aromatics, 27 mm smoke point), and assuming a 'local' equivalence of $\phi \approx 7$ we find that the calculated concentration of soot is 0.8×10^{-3} kg m^{-3} using our extrapolated data to a 27 mm smoke point. This may be compared with experimental results [34] of 1.3×10^{-3} kg/m^{-3} for an inlet air fuel ratio of 40/1, and 0.6×10^{-3} kg/m^{-3} for an air fuel ratio of 50/1. Variations in soot yield found here are also consistent with variations in aromatic content of the fuel [36].

(ii) The pressure dependence of the smoke yield is given commonly by the expression [37]: Smoke α P^2. Essentially equation (11) has a form that is consistent with this dependence; this is because the fuel term $(\text{fuel}^{2.36})$ dominates the expression.

(iii) Secondly the form of equation (11) should predict the sooting limits, because at the soot boundary $dc_f/dt = 0$, that is

$$C_1 [RH]^a \exp(-E_1/RT) = C_2 [O_2]^b \exp(-E_2/RT) \qquad (32)$$

which maps out the boundary. Such a boundary is given in Fig. 6 based on ref. 38 where the concentrations indicated refer to toluene. It is clear that our soot boundary is slightly too rich, this indicates probably that the oxygen term (which is derived indirectly) is probably too small. Indirectly this would imply that our rate of soot formation is possibly on the low side by an estimated factor of 2. Clearly more work is required over a wide range of conditions.

ACKNOWLEDGEMENTS

This work is a composite of results from various research projects supported by IEA, Lucas-CAV Ltd, British Gas plc, and SERC.

REFERENCES

1. Simmons, B. and Williams, A., Proceedings of the Combustion Research Conference, Harwell, UKAEA, March, 1986.

2. Calcote, H.F., Soot in Combustion Systems and its Toxic Properties (ed. Lahaye, J. and Prado, G.), Plenum Press, 197, 1983.

3. Coats, C.M. and Williams, A., Seventeenth Symposium (International) on Combustion, The Combustion Institute, 611, 1979.

4. Tesner, P.A., Snegiriova, T.D. and Knorre, V.G., Combustion and Flame, 17, 253, 1971.

5. Semenov, N.N., Problems of Chemical Kinetics and Reactivity, Princeton University Press, New Jersey, 1958.

6. Magnussen, B.F., Particulate Carbon, Formation During Combustion (eds. Siegla, D.C. and Smith, G.W.), Plenum Press, 321, 1981.

7. Khan, I.M., Greeves, G. and Probert, D.M., Air Pollution Control In Transport Engines, Institute of Mechanical Engineers, 205, 1971.

8. Naegeli, D.W., Dodge, L.G. and Moses, C.A., Combustion Science and Technology, 35, 117, 1983.

9. Hiroyasu, H., Yoshimatsu, A. and Arai, M., Institute of Mechanical Engineers, 207, 1982.

10. Nagle, J. and Strickland-Constable, R.F., Proceedings of the Fifth Carbon Conference, 1, 154, 1961.

11. Farmer, R. Edelman, R. and Wang, E., Particulate Carbon, Formation During Combustion (eds. Siegla, D.C. and Smith, G.W.), Plenum Press, 299, 1981.

12. Edelman, R.B., Turan, A., Harsha, P.T., Wong, E. and Blazowski, W.S., Combustor Modelling, AGARD-CP-275, 15-1, 1979.

13. Wang, T.S., Matula, R.A. and Farmer, R.C., Eighteenth Symposium (International) on Combustion, The Combustion Institute, 1149, 1981.

14. Najjar, Y.S.H., J.Inst.E., 148, Sept. 1986.

15. Najjar, Y.S.H. and Goodger, E.M., Fuel, 60, 981, 1981.

16. Najjar, Y.S.H., Fuel, 64, 93, 1985.

17. Simmons, B. and Williams, A. Combustion and Flame, to be published.

18. Graham, S.C., Homer, J.B. and Rosenfeld, J.L.J., Proceedings of the Royal Society, 344, 259, 1975.

19. Lee, S.C. and Tien, C.L., Eighteenth Symposium (International) on Combustion, The Combustion Institute, 1159, 1981.

20. Dalzell, W.H. and Sarofim, A.F., Journal of Heat Transfer, 91, 100, 1969.

21. Mullins, J. and Williams, A., Fuel, 66, 277, 1987.

22. Rawlins, W.T., Cowles, L.M. and Krech, R.H., Twentieth Symposium (International) on Combustion, The Combustion Institute, 879, 1984.

23. DMS UV ATLAS of Organic Compounds, 1, 2, Butterworths, 1966.

24. Beretta, F., Cincotti, V., D'Alessio, A. and Menna, P., Combustion and Flame, 61, 211, 1985.

25. Evans, M. and Williams, A., Fuel, 60, 1047, 1981.

26. Lee, K.B., Thring, M.W. and Beer, J.M., Combustion and Flame, 6, 137, 1962.

27. Park, C. and Appleton, J.P., Combustion and Flame, 20, 369, 1973.

28. Tesner, P.A. and Tsibulevsky, A.M., Combustion, Explosion and Shock Waves, 3, 1963, 1969.

29. Fenimore, C.P. and Jones, G.W., J.Phys.Chem., 71, 593, 1967.

30. Garo, A., Lahaye, J. and Prado, G., Twenty-first Symposium (International) on Combustion, The Combustion Institute, 1987.

31. Chan, M.L., Moody, K.N., Mullins, J. and Williams, A., Fuel, to be published.

32. Smith, I.W., Fuel, 57, 407, 1978.

33. Hargrave, G., Pourkashanian, M. and Williams, A. Twenty-first Symposium (International) on Combustion, The Combustion Institute, 1987.

34. Abbas, A.S. and Lockwood, F.C., J.Inst.E., 112, Sept. 1985.

35. Magnussen, B.F., Hjertager, B.H., Olsen, J.G. and Bhaduri, D., Seventeenth Symp. (Int.) on Combustion, The Combustion Institute, 1383, 1978.

36. Bowden, T.T., Pearson, J.H. and Wetton, R.J., ASME 84-GT-6, 1984.

37. Friswell, N.J., Combustion Science and Technology, 19, 119, 1979.

38. Homan, H.S., Combustion Science and Technology, 33, 1, 1983.

TABLE 1

Soot Forming Equations

EQUATION	SOURCE	EXPRESSION
(5)	Khan[7] et al	$\frac{dS}{dt} = 4.68 \times 10^5 \frac{v_u}{V_{NTP}} \phi_u^3 P_u^{1.8} e^{-20,130/T_u}$
(6)	Naegeli[8] et al	$S = A(F/A^{3.425}) \exp(-29,101/T)$
(7)	Hiroyasu[9] et al	$\frac{dS_f}{dt} = A \left[\frac{P_{THC}}{Po_2}\right]^{1.25} T^{-1.0} \exp\left[\frac{-40,000}{RT}\right]$
(8)	Farmer[11] et al	$R_F = 4.66 \times 10^{14} . T^{-1.94} . C_{HC}^{1.81} . CO_2^{-0.5} . \exp(-32,000/RT)$
(9)	Wang[13] et al	$R_{SOOT}(g/ml\ \mu sec) = (5.55E+10) . \exp(-41.8/RT + a(-48.1/R)(1/T - 1/T_m)) . [C_7H_8]^{2.59} [O_2]^{-0.71} [Ar]^{0.13}$
(10)	Najjar[14]	$\frac{dS}{dt} = 58 \times 10^{14} . (HC) \exp(-12,160/T) - 3 \times 10^9 . (O_2)(S) \exp(-7800/T)$ (KEROSINE (3 atm.))
(11)	Simmons[1] and Williams	$dc_f/dt = 6.25 \times 10^5 [C_7H_8]^{2.36} \exp(-13,400/T) - 2.32 \times 10^6 [O_2]^{1.28} \exp(-21,000/T)$

TABLE 2

Calculated Rates of Soot Formation $kg/m^3 s$

SOURCE	$\phi = 5.0$*			$\phi = 7.0$**		
	1600K	1700K	1800K	1600K	1700K	1800K
Khan et al[7]	0.04	0.08	0.17	0.10	0.23	0.47
Najjar[14] 3 atm	452	705	1047	452	705	1047
Najjar[14] 10 atm	38.0	59.3	88.1	38.0	59.3	88.1
Wang et al[13]	2.59	5.61	11.16	3.79	7.12	14.16
Simmon and Williams[17]	0.77	0.81	0.43	1.07	1.46	1.73

* $\phi = 5.0$ ($[C_7H_8] = 0.150$, $[O_2] = 0.270$ mol m^{-3})

** $\phi = 7.0$ ($[C_7H_8] = 0.150$, $[O_2] = 0.193$ mol m^{-3})

$[Ar] = 20$ mol m^{-3}

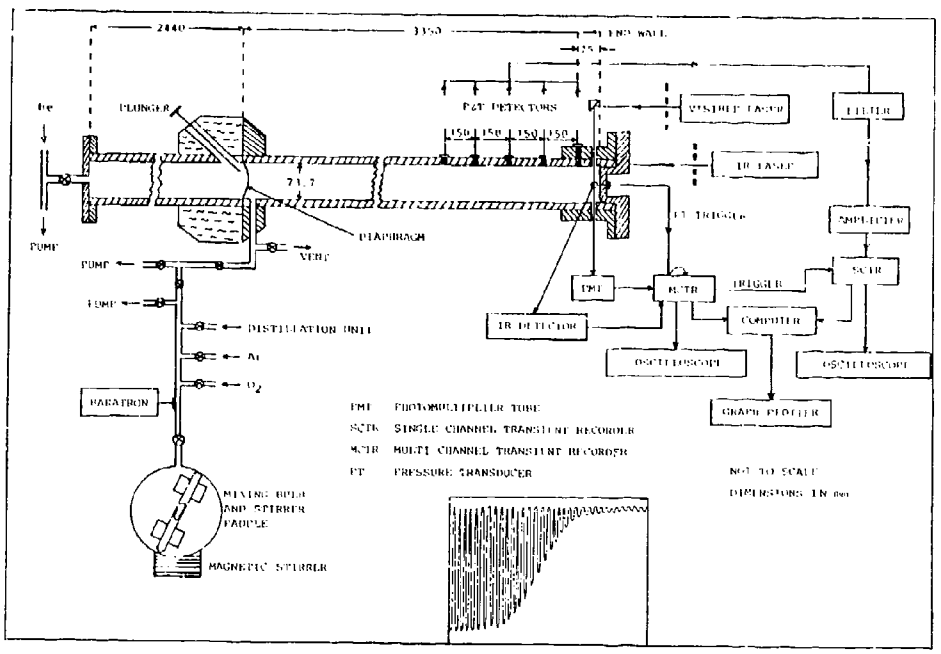

Figure 1. Schematic representation of the shock tube with a typical laser attenuation record illustrated.

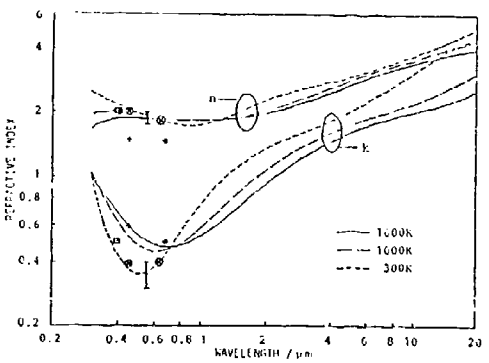

Figure 2. Measured and predicted spectral refractive indices at different temperatures.[19]

{* Propane (room temperature) Dalzell and Sarofim;
+ Propane (room temperature) Dalzell, Williams and Hottel;
I Propane (2 room temperature) Chippett and Gray;
⊡ Acetylene (flame temperature) Chippett and Gray;
× Toluene} (room temperature) Mullins and Williams}[17]
O Methane}

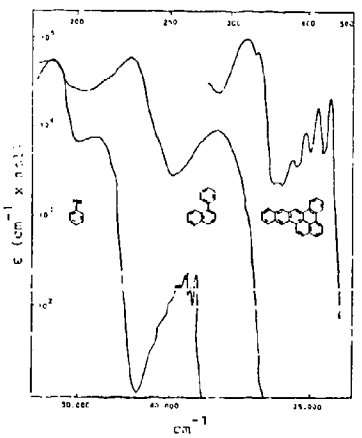

Figure 3. The effect of increasing conjugation on the molar absorbtivity and λ_{MAX} of selected aromatic compounds.[23]

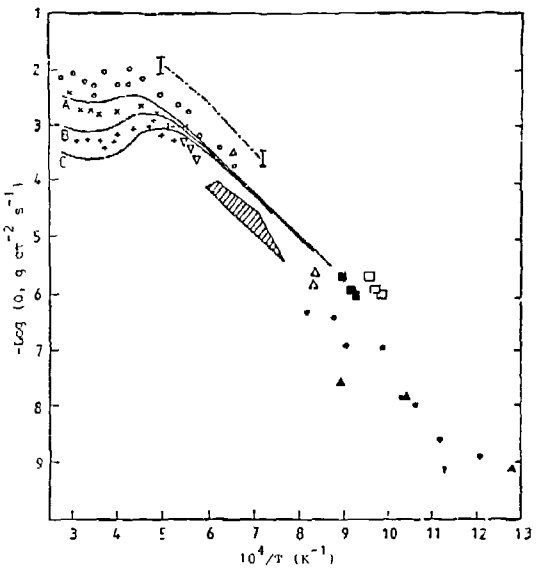

Figure 4. Observed soot oxidation rates versus particle temperature.[31] (□, ■, ●, ▲)[31]; Curves A, B, C[10]; ▨ 26; ○[27]; ⊢·–·–⊣[28]; Δ, ▽[29]; ⊢–⊣[30].

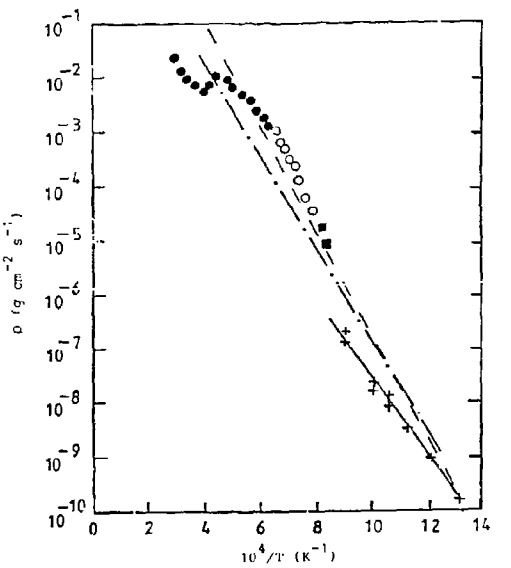

Figure 5. Intrinsic soot oxidation rate at an oxygen partial pressure of 1.01×10^5 Pa.[31]; ○[26]; ●[27]; ■[29]; +[31]; – –[32]; –·–[33].

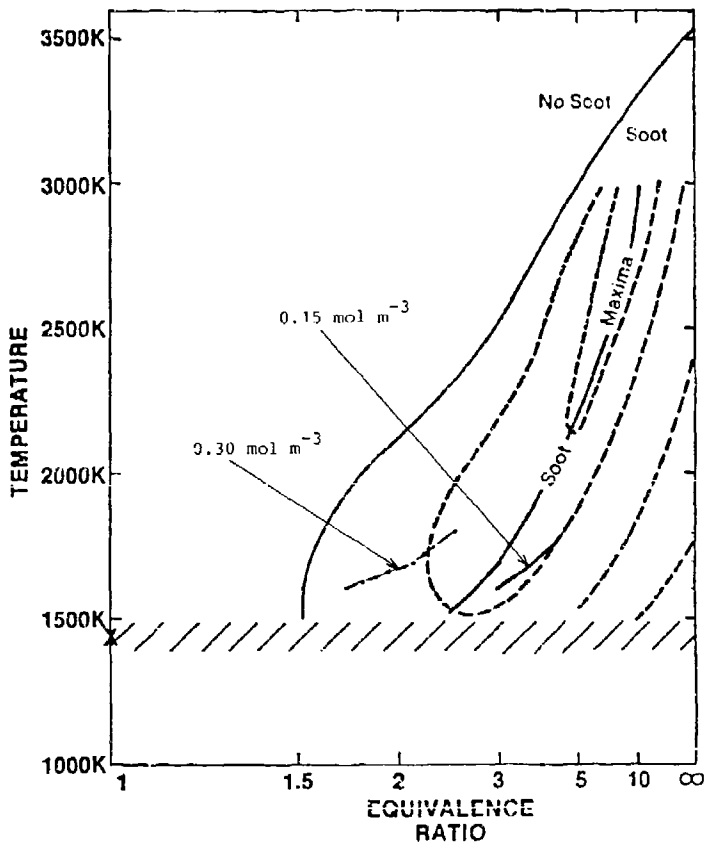

Figure 8. Soot yield trends versus flame conditions.[38]

DISCUSSION

H.May, GE

Did you investigate also the influence of different aromatic structures as Mono — Bi — and Polyaromatics on soot function: ?

Author's Reply

We have not investigated the influence of two or three very aromatic compounds on soot formation because they are not volatile enough to get a sufficient high vapour partial pressure; we hope to heat our shock tube in the future to do this.

A.Ormancey, FR

Dans votre article, vous écrivez que vos essais ont été réalisés jusqu'à une pression de 3.5×10^5 pa. Envisagez-vous de faire des essais sous des pressions plus élevées?

Author's Reply

We appreciate that the pressure range studied is rather limited and we would wish to extend the experiments to higher pressures (and other fuels) to obtain more precise data.

K.H.Homann, GE

If the formation term and the oxidation term in your equation become equal there would be a stationary soot volume fraction. You determined the soot threshold from that condition. What stationary soot volume fraction do you calculate for those conditions and how does this compare with experimental soot volume fractions at the threshold?

Author's Reply

You are correct in stating that when pyrolysis and oxidative terms are equal, this represents a stationary state. However, we would consider that the soot forming boundary is set by the region immediately on the lean side of the boundary shown in Fig.6. In this region there is no soot present if one assumes that this is the equilibrium condition (time independent) with infinite amounts of fuel and oxygen available.

THE INFLUENCE OF PRESSURE ON SOOT FORMATION

by

H.Gg. Wagner
Institut für Physikalische Chemie
Universität Göttingen
Tammannstr. 6,
3400 Göttingen, FRG

SUMMARY

The influence of pressure on soot formation has been investigated for pyrolysis, premixed flames and diffusion flames. Detailed kinetic studies are available for the first two. They show that the essential steps: particle inception, induction time (τ), coagulation and surface growth remain similar for different pressures, also the influence of temperature on the maximum amount of soot formed. τ for pyrolysis depends on the carbon density, strongly on temperature and only slightly on pressure. The coagulation rate constant decreases slightly towards higher pressures. The amount (f_v) of soot formed per cm^3 for a given fuel-air mixture increases with pressure P like P^n. n was found for C_2H_4-air up to 3, for other fuels near one, it depends on pressure. Larger f_v means larger soot particles, larger radiation losses and longer oxidation time at a given temperature and therefore higher chance for smoke emission.

INTRODUCTION

Pressures applied in technical combustion processes range from one (atmospheric pressure) to about 200 bar. The high pressures are reached as maximum pressures in modern Diesel engines, combustion chambers run up to about 30 bar, while stationary burners in general operate closer to atmospheric pressure. In any of these combustion devices soot can be formed if a sufficiently high "carbon concentration" (as fuel or other hydrocarbon) is present in a range of sufficiently high temperature for sufficient time [1].

Soot will be emitted, if the soot particles formed are not oxidized in the combustion process. The oxidation of soot praticles depends strongly on temperature. It is therefore necessary to keep the particles long enough at a high temperature in an oxidizing atmosphere. The influence of the O_2 concentration is not very pronounced, as long as it is above a certain limit, but the size of the soot particles influences the residence time required for total oxidation [1].

Soot emitted through the exhaust system of a combustion device is in general quite different from that product, which is formed within the combustion process. Its appearance depends on its history with respect to temperature, temperature gradients, concentrations, pressure etc. in the exhaust system. This is clearly shown by a comparison of the soot emitted at the valves of a Diesel engine and the smoke leaving the exhaust pipe. This is of importance for discussions about the particulate emission of combustion devices. This later part of soot life will not be considered here. The present paper describes results of investigations about the influence of pressure on soot formation under the well defined conditions of hydrocarbon pyrolysis in shock waves and in laminar premixed flames as well as some results obtained with laminar diffusion flames.

PYROLYSIS

Soot formation in the gas phase has been studied under isothermal conditions in flow systems [2] and in shock tubes [3-11]. For many different fuels experiments have been performed at pressures up to about 7 bar [7,8]. Until now experiments at much high pressures are available only for C_2H_4 and C_2H_2 diluted in rare gas. For these two fuels soot formation has been studied at pressures up to around 250 bar in a wide range of temperature [5,6].

Fig. 1 shows an emission signal for a mixture of C_2H_4 in Ar, taken at a wave-length of 8000 Å at a pressure near 130 bar and temperature of 2100 K, taken through a narrow slit from the side of a high pressure shock tube [6]. This signal is at least at the beginning of the process when $f_v < 10^{-7}$ gr/cm^3 nearly proportional to the amount of soot $f_v = N \cdot \bar{v}$ in cm^3 present per cm^3. N is the number of soot particles per cm^3 and v the mean particle volume. (In the final part of the process shown the Rayleigh condition is not fulfilled anymore.) This emission signal is typical for soot formation. Starting from time zero (front of the incident or reflected shock wave), there is no signal until after a certain induction period τ (the absorption) or emission signal rises. The increase of the signal continues, than it slows down and approaches a nearly horizontal line which is due to a (nearly constant) value of $f_v = f_\infty$. Towards still longer times the signal rises again, however, with a much lower time constant, which is due to a slower process.

The characteristic properties [6,7,8] of this signal are similar for different temperatures, for different fuels and also for different pressures. It is to be expected that this holds also for pressures higher than those used in the experiments described here. For a quantitative evaluation of the signals the optical properties of the soot, the particle size relative to the wave-length, the influence of species other than soot etc. have to be known. Rather independent from these properties are the characteristic times like the induction period or rates as represented by the slope of the signal in Fig. 1 around the turning point.

INDUCTION TIME

The induction time for soot formation in a pyrolysis process is an important property. It is not a uniquelly defined time but it depends to a certain extent on the experimental technique used. This is quite obvious: within this induction period essential parts of the soot formation process happen. The fuel is pyrolysed and during this pyrolysis process many intermediates are formed which again tend to form acetylenes and at sufficiently high carbon concentrations aromatic compounds. Finally the first very small soot particles appear. These compounds absorbe light at different wave-length. This in fact can be used as a rough method to follow the appearance of these species [11,12]. Therefore an induction period determined by absorption around 5000 Å will be shorter than one measured at 8000 Å or in the infrared [7,8]. This complicates a comparison of data from different authors. Even though the absolute data of the τ values determined with different methods differ, their dependences on P or T usually run parallel [5-8].

The temperature dependence of the induction periods for soot formation has been investigated in some detail [3-12]. For a given C atom concentration the τ values show a distinct dependence on the type of fuel [13], but the apparent energies of activation for the different fuels are very similar: The values of τ fall steadily towards higher temperatures as shown in Fig. 2. It is much harder to determine the influence of total pressure and of fuel concentration on soot formation and especially on induction period than that of temperature.

Fig. 2 gives measured induction periods for the pyrolysis of C_2H_2 for pressures from 0.3 to 200 bar and for total carbon concentrations from $2\cdot10^{17}$ to $2\cdot10^{19}$ C atoms per cm^3. The upper line in Fig. 2 represents a set of data from Frenklach et al. [8] for $[C] = 5\cdot10^{17}$ and pressures between 2 and 3 bar (measured at 6728 Å). This line represents the experimental points (not shown here) very well. Within the range indicated by the bar around that line values obtained by [8] for carbon concentrations from $2\cdot10^{17}$ to $2\cdot10^{18}$ C atoms per cm^3 for pressures from 0.3 to 7 bar are located. Part of these data are shown separately in Fig. 3 in order to indicate the influence of various parameters. In the lower part of Fig. 2 data are given which have been obtained in our laboratory [5,6] at pressures from 40 to 200 bar and [C] from $4\cdot10^{17}$ to $2\cdot10^{19}$ atoms per cm^3 by following light emission at 8000 Å. (This emission measurements give results very similar to absorption measurements at the same wave-length as shown in [5].) The three dashed lines are obtained from an approximation used by Frenklach [8] which reads $\tau\cdot[C_2H_2]^{0.84} = 10^{-11.66} e^{(+\,14700/T)}$ calculated for three different C_2H_2 concentrations. There seems to be a good agreement between the experimental results and this approximation and the total variation of τ over two orders of magnitude can be covered by the dependence of τ on the C_2H_2 concentration alone without a separate total pressure influence. There are, however, experiments at high pressure [5,6] with rather low [C] values, which should be higher up in the diagram, if there is not separate influence of pressure on the induction times. The high pressure data alone can in fact be better approximated using a weaker dependence of τ on $[C_2H_2]$ and an additional influence of the total density ρ for example in the approximate [6] form $\tau \sim [C_2H_4]^{-0.3-0.5}\cdot[\rho]^{-0.5-0.3}$. The assumption, that higher pressure, at otherwise similar conditions accelerates the formation of the first small soot particles does not seem to be unreasonable.

For the pyrolysis of C_2H_4 there are data available for pressures from 1 to about 5 bar. They can be represented with an apparent energy of activation of about 40 kcal/mol. Data towards higher pressures have been obtained in our laboratory [5,6] in the range from 9 to 225 bar for $[C] = 2\cdot10^{17}$ to $4\cdot10^{19}$ atoms per cm^3. A presentation of these data in the form $\tau\cdot[C_2H_4]$ as a function of T^{-1} is shown in Fig. 4. As for the pyrolysis of C_2H_2 the approximation of τ for the data presented here and those of other authors can be improved if a dependence of τ on the total density is included. This is indicated by Fig. 5 which shows the induction periods for C_2H_4 pyrolysis for different pressure ranges. Here the apparent energies of activation for τ at different densities show a systematic tendency from low to high total pressures.

For other fuels pyrolysis data are available only at pressures below 10 bar and a set of induction periods as a function of temperature is given in [13]. Some additional data are shown [8] in Fig. 6 for an approximately constant C atom density. The different hydrocarbons exhibit under equal conditions different absolute values of the induction times, with aromatics having low τ values and C_2 hydrocarbons higher ones, an exception is vinylacetylene C_4H_4. The slopes of most of the curves do, however, not differ very much, the influence of hydrocarbon-concentration and total pressure on τ seem to be similar to those mentioned above. (Quantitative data for high pressures are still missing.) The dashed line corresponds to the toluene curve for 0.3 - 0.7 bar, it belongs to a mixture which has equal O_2 and C_7H_8 concentrations. For the 1.9 - 3 bar C_7H_8 curve addition of corresponding amounts of O_2 does not influence the induction period, higher O_2 additions generally reduce τ also for other fuels [8].

For combustion processes operating at high pressure the stoichiometry applied under normal operation conditions does not differ much from that used in burners for lower pressures. Therefore the above mentioned data, even if the influence of fuel concentration and total pressure cannot be precisely separated, do show that the first phase of soot formation is strongly favoured by high pressure.

INFLUENCE OF PRESSURE ON SOOT MASS GROWTH

As shown in Fig. 1, the soot volume fraction f_v (cm^3/cm^3) starts to rise after the induction period and then approaches a "stationary" value f_∞. This second phase of soot formation following the induction period can often be approximated [6,13,14,15] by an empirical expression $df/dt = k_f(f_\infty - f)$. There are two different methods used in the literature in order to characterize the rate of soot growth. For shock tube experiments in which f_∞ can often not be reached because the time available in the shock tube is too short, it is convenient to draw the tangent at the signal in Fig. 1 around the turning point and take the slope at that point as a measure for the rate of soot growth. Another possibility, often used in flames is [1] to determine df_v/dt and plot it as a function of f_v, or to plot $\log(f_\infty - f_v)$ as a function of time. On the basis of the formula mentioned, the first method gives a rate which is nearly equal to $df/dt = kf_\infty$ but includes more of the beginning of the process, while the second method can give k(1/sec) directly, which in flames proved to be a function of temperature which is independent of the fuel structure [14]. This second method puts more weight on the later part of the soot formation process.

An interesting quantity for soot formation is the total amount of soot f_∞ formed from a given fuel carbon concentration, the soot yield. In premixed flames, in a wide range of conditions, this soot yield in the burned gases is small compared to the carbon present as hydrocarbon like acetylenes and other thermodynamically rather stable hydrocarbons [16]. For shock tube pyrolysis experiments, as mentioned above, it is often not possible to reach or even to come close to f_∞ because the observation time is usually less than a few milliseconds. In cases, where f_∞ can be reached as in the high pressure experiments [5,6] reported here within the time available, normal simple optical methods like absorption measurements cannot easily be applied for the determination of the properties of the soot particles, because these may be so large that they are no longer in the Rayleigh regime. It would therefore be necessary to perform laborious angle dependent light scattering experiments with high time resolution in order to obtain the properties of the soot particles [17].

There are two observations, which are of interest in relation to f_∞. Buckendahl [5] in our laboratory found for C_2H_4 pyrolysis in shock waves at high pressure (100-200 bar) that the "rate constant" k_f determined with either one of the above mentioned methods and plotted as a function of temperature pass through a maximum at temperatures between 2000 and 2300 K (depending on C_2H_4 concentration and total pressure).

Shortly afterwards Graham et al. [7] used Laser absorption in order to determine the amount of soot formed during pyrolysis in shock waves. They found especially for aromatic but also for other compounds, that the fraction of carbon atoms transformed into soot after a given time, the soot yield at time t, increases with temperature, passes through a maximum and than decreases towards higher temperatures. This is shown in Fig. 7 for several fuels.

In recent years especially Frenckiach and his colleagues [8] investigated this phenomenon in great detail for different fuels, fuel combinations, and fuel-oxygen systems and found many interesting relations. A strong influence of the carbon concentration on the soot yield curve is shown in Fig. 8 for two concentrations of C_2H_2 as an example [8].

A comparison between Fig. 7 and 8 shows, that the maxima of the soot yield curves for C_2H_2 and for aromatic compounds appear at different temperatures. One may ask, how these bell-shaped curves are "generated". On the low temperature side the shape of these curves is determined by the induction time for soot formation (see Figs. 2,3,4,5). On the high temperature side it is the rate of soot mass growth which reduces f_v present after a certain time. This is nicely demonstrated by the soot yield profiles shown in Fig. 9 for times up to 2.5 ms. (E(m) is a function of the optical properties of the soot particles) in connection with the curves in Fig. 7 und 8 (which are obtained for a certain fixed observation time!). For a temperature of 1587 K (see Fig. 9) the induction time is long, nearly 2 msec, soot growth takes place later. At 1672 K the induction period is shorter, more soot is formed after 2 msec. At 1799 K the induction time is further reduced, the soot yield, however, starts to grow slower. At 2059 K the induction period is still shorter, the turning point is reached rather early and the curve seems to tend towards a rather low soot yield. With further increase of temperature this effect continues. Even in case the rise of these soot yield curves for high temperatures continues, it will take a very long time until a soot yield as that for 1672 or 1799 K is reached. Towards lower temperatures the induction periods increase so that for this and other reasons the growth of soot is slowed down. For C_2 hydrocarbons the situation is quite similar to that for aromatics but "shifted" towards higher temperatures.

The data described above have been obtained at pressures from 0.3 to about 5 bar and the question arises whether the soot formation process will remain similar towards high pressures.

As mentioned before, measurements of the rate of soot formation in pyrolysis up to pressures of 250 bar have been performed for C_2H_4 and for C_2H_2 and carbon-atom densities between $2\cdot10^{17}$ and $4\cdot10^{19}$. Indicator for soot (f_v) has been light absorption at 8000 Å, in most cases, however, light emission around 8000 Å as a function of time. For most of the data to be presented especially those of Geck [6] the measurements have been performed in reflected shock waves, there are, however, data available for pressures up to about 30 bar from incident waves. (For the evaluation of the data the emission signal I_t has been plotted, referred to the signal I_∞ for f_∞ in logarithmic form as a function of time ($\log(I_\infty - I) - t$). The slope of these plots are taken as the "rate constants" k_f for soot growth. It is to be expected that for a number of experiments the radiating medium near f_∞ is no longer optically thin, this may shift the obtained k_f values to a certain extend, but this shift should remain within the experimental uncertainty of the experiments.)

The first order "rate constants" k_f obtained from measurements following pyrolysis of C_2H_2 as well as of C_2H_4 show a typical behaviour as a function of temperature. Starting from low temperatures, 1600 to 1700 K, they increase towards higher temperatures with apparent energies of activation of about 40 kcal/mol. This is very similar to the behaviour of k_f obtained in flames. Above a certain temperature (not reached in flames), however, the curves start to decrease with increasing temperature rather steeply.

Another observation is, that the curves obtained at different total densities and at different fuel concentrations do not fall together in an Arrhenius plot. This is different from the results obtained in flames until now, where fuel structure and concentration seem to have little influence on k_f.

A presentation of measured rate constants k_f for the pyrolysis of C_2H_4 in argon at total pressures up to 250 bar is shown in Fig. 10. Here the measured rate constants are divided by the hydrocarbon density ρ_{HC} in mol/cm^3 so that a second order rate constant $k(HC) = k_f/\rho_{HC}$ cm^3/mol sec results. From this plot it becomes obvious that at the low temperature side the data obtained under different conditions group around a central line with a given slope ($k(HC) \sim 10^{14} \exp - 21000/T$ cm^3/mol sec). Towards higher pressures at first those data obtained at relatively low pressures (and C atom densities!) change direction and tend towards lower values of k(HC). An apparent turn around point lies at 2100 K. For higher pressures this change of the temperature dependence happens at higher temperatures, for 200 bar near 2400 K, it is also influenced by the total carbon-concentration.

A better correlation than that one shown in Fig. 10 can be obtained [6] if instead of the hydrocarbon-density the total density ρ is used to correlate the data. This holds especially for the low temperature part. There an expression $k(\rho) = k_f/\rho = 10^{12.5} \exp(22000/T)$ cm³/mol sec results. One may expect that the correlation can be further improved if both the total density as well as the hydrocarbon-density is included.

Results obtained for the pyrolysis of C_2H_2 in a similar range of conditions are in the same range as that for C_2H_4 with a slightly lower apparent energy of activation and also a somewhat weaker dependence on the total density. The temperature dependence of the k_f values measured for C_2H_4 and C_2H_2 up to high pressures is similar to that obtained on flames at lower pressures.

A rather direct comparison between low and high pressure data can be made for C_2H_2. The k_f curves measured at low pressure [8] show a similar temperature dependence as those obtained at high pressures. The maxima of these low temperature k_f values as a function of temperature seem to be at temperatures slightly below that of the maxima of the bell-shaped soot yield curves, but this can be within the limit of experimental error. It does therefore not seem to be unreasonable to assume that the total soot yield at high pressures shows a similar temperature dependence as that at low pressures. This should, however, be confirmed by independent direct measurements, because emission measurements as a function of temperature do not show a temperature dependence, which shows such a pronounced concentration effect as the bell-shape curves from [7,8]. This could be an indication that the total soot yield is much less than that reported in [7].

Because most of these high pressure measurements have been performed in reflected shock waves the question may arise, how much conversion takes place in the incident wave, before arrival of the reflected wave. In case of C_2H_4 this could be calculated from known data about C_2H_4 pyrolysis [19]. It could also be approximately be determined from the immediate rise of the emission signal after the arrival of the reflected shock wave [6]. At reflected shock wave temperature below 2700 K (about 1300 K in the incident wave) the conversion was only a few percent and it dropped rapidly towards lower temperatures. For pressures up to 30 bar there was good agreement for k_f between data from incident and reflected waves. Less favourable is the situation for the C_2H_2 pyrolysis experiments reported [6].

It should be mentioned that towards temperatures higher than those reported here for the high pressure experiments the conversion of fuel in the incident wave has a strong influence on soot formation in the reflected wave.

From the experiments described above one can see that:

1.) The phenomenology of soot formation in pyrolysis of hydrocarbons at high pressures remains similar to that around atmospheric pressure.

2.) The induction periods for the onset of soot formation are reduced by increasing carbon atom density and by pressure.

3.) The "rate constants" for soot formation, obtained from the expression $df_v/dt = k_f(f_a - f_v)$ can best be represented as being proportional to hydrocarbon or total density over a fairly large temperature range. This means that the "active lifetime" of soot particles with respect to mass growth, which is inversely proportional to k_f, should in the range discussed here be proportional to the total or hydrocarbon density (or some product of total and hydrocarbon density). Towards higher temperatures the k_f values invert their temperature dependence.

4.) It is probable that the soot yield after a given time shows at high pressures a similar behaviour as at normal pressure. Absorption measurements indicate that the soot yield rises with total carbon-atom concentration and very probably also with pressure so that the absolute conversion of carbon into soot can increase rather strongly towards high pressures.

INFLUENCE OF PRESSURE ON SOOT FORMATION IN PREMIXED FLAMES

Laboratory experiments on carbon formation in flames under steady state conditions [1,2,22] have only seldom been extended towards elevated pressures. In bomb experiments it has not always been possible to specify the local conditions during carbon formation because pressure and temperature change within time. In most of the other experiments performed at elevated pressures no detailed information about the process of carbon formation could be obtained [1,20,23].

In a pioneering work McFarlane et al. [21] studied carbon formation in premixed flames of different C_5 and C_6 hydrocarbons for pressures up to 20 bar. The burner they used consisted of a 0.3 inch diameter bundle containing 140 refractory tubes, each 0.008 inch internal diameter and a 0.2 inch diameter bundle containing 32 refractory tubes each 0.006 inch internal diameter. Flow velocities through the refractory tubes were 600 cm/s resp. 5000 cm/s corresponding to mean fresh gas flow velocities within the burner cross section of 17 and 500 cm/sec. The first mentioned flame is called a flat flame, the second one is characterized as "turbulent flame brush". Because the fresh gas flow velocity is higher than the laminar flame velocities of the sooting flames, the flow for the flat flames must also have expanded and the combustion process is strongly influenced by heat losses and by recirculation.

These experiments lead to some important results:

1.) The soot formation threshold for both types of flames are rather similar.

2.) The soot formation threshold varies little with pressure. For the different flames investigated namely n-pentane, iso-pentane, n-hexane, cyclo-hexane, hexene 1, cyclo-hexene, methyl-cyclopentane and benzene in air it shifts very slightly towards stoichiometric mixture with increasing pressure.

3.) For some fuels the soot yield seems to be an optimum at a given fuel-air ratio and it decreases towards leaner and richer mixtures.

4.) The soot yield obtained in the flat flame is reached in turbulent flames only at higher pressures.

5.) The soot yield for a given mixture increases proportional to $P^{2.5}$ to P^{3} for most of the fuels mentioned.

6.) The general behaviour of benzene and cyclo-hexene air flames differs somewhat from that for the other fuels mentioned.

In addition an increase of flame temperature (by exchange of N_2 by Ar) is reported to rise the soot yield. It is important to note, that the analysis of the soot yield has been performed by sampling for a given time and collecting the soot on a filter for further treatment. This does not necessarily measure the soot mass really formed in the flame and Mc Farlanes description of the product formed points into that direction.

As mentioned already the operation of flat flames which can be used for detailed kinetic investigations at elevated pressures causes a number of problems, especially due to the increasing energy density to flame front stability, flow problems and the presence of soot etc. This may be one of the reasons, why so few experiments have been done with one-dimensional flames at elevated pressure.

In this chapter some experiments shall be described, performed with laminar premixed C_2H_4-air flames burning on flat capillary or porous plate burners at pressures up to 5 or 10 bar. This pressure is high enough to observe the influence of pressure on soot formation from free molecular flow to continuum conditions for the coagulation of the particles. On the other hand the extension of the soot formation zone is still large enough to allow optical absorption and scattering measurements for the determination of soot volume fraction f_v, particle number density N and mean particle volume $\bar{v}$. In addition the applicability of the Rayleigh condition can be checked by measurements of the wave-length dependence of the absorption and of the depolarization ratio. Temperature measurements can be performed by Kurlbaum method. As mentioned above problems are caused by flow problems, the formation of vortices in the burned gases and by flame stability, which limit the range of conditions for which measurements can be performed [23].

INFLUENCE OF PRESSURE ON f_∞

Flat flames at elevated pressure are usually not burning under adiabatic conditions, because the flame stability is not good enough and the flames are sensitive to even small disturbances [32,23]. Some energy loss into a hot burner improves the flame front stability and it influences the flame temperature. This flame temperature, characterized by its maximum value T_{max} proved to be a very important parameter also for flames burning at elevated pressure [23].

It is known from experiments performed at normal pressure [1], that for a given stoichiometry of the fuel-air mixture, or a given C/O ratio a reduction of the flame temperature increases the value of f_∞ until at a certain flame temperature (the temperature is usually fixed via the cold gas flow velocity) a maximum of f_∞ is reached [26] (see Fig. 11) With a further reduction of the flame temperature f_∞ starts to decrease. This typical behaviour is related with a clear influence of temperature on the threshold of soot formation [24,25]. Below a certain temperature the (stabilized) flames do not form soot anymore and towards a certain high temperature, at the same C/O ratio f_∞ also tends to zero [26]. At a certain temperature the soot threshold curve exhibits a minimum (minimum C/O ratio for onset of visible soot formation). Going at a fixed value of flame temperature towards higher C/O ratios the values of f_∞ increase strongly (proportional to the 3 to 4^{th} power of the carbon surplus $((C/O)-(C/O)_{thresh})$) [1,2,3,27].

For flames at elevated pressures the situation remains very similar [27]. The threshold curves expand slightly away from the 1 bar curve and the mountain formed by the f_∞ values increases in hight, the dependence on the carbon surplus, however, remains quantitatively similar. It is obvious therefore that a change in temperature away from the maximum for the f_∞ in the direction of the steep fall of the f_∞ mountain can easily cause a strong variation of the dependence of f_∞ on the total pressure.

A typical example for f_v profiles obtained for C_2H_4-air flames burning at 5 bar with two different fresh gas velocities v = 9 and 12 cm/sec is shown in Fig. 12. One can easily recognize that the growth of f_v with time starts very rapidly and approaches a stationary value f_∞. The shape of the different curves for f, N, and v is very similar to that from flames burning at atmospheric pressure. The profiles in Fig. 12 show, that f_∞ can be quite well determined.

A plot of f_∞ measurements for flames with C/O ratios from C/O = 0.65 to C/O = 0.76 as a function of pressure is shown in Fig. 13. The different experimental results for a given C/O ratio can, in a first approximation, be represented by a pressure dependence of about $f_\infty \sim P^{2.5-3}$ which is very close to the results reported by McFarlane [21]. It should be mentioned, however, that the flames compared here burned at different temperatures and this influences the exponent of P. If it would be possible to burn flames of a given C/O ratio and a given flow velocity and temperature the dependence on P would be weaker (exponent for C_2H_4-air from 2 to 5 bar about 1.8 to 2). For flames burning near the maximum of the f_∞ curves in Fig. 11 the influence of P on f_∞ can be described by an exponent which is between 1 and 1.5, that means the total soot yield in that range does not change much with pressure.

At atmospheric pressure the typical dependence of f_∞ on flame temperature mentioned above has been found not only for C_2H_4-air but also for other fuels including C_2H_2 and C_6H_6 [26]. It is on the high temperature side in agreement with earlier results [1] and also with measurements from other authors [24,25]. McFarlane reported a different tendency. This may either be due to the sampling technique used in his experiments or the temperature of his flames is in the "low temperature" range described above.

INFLUENCE OF PRESSURE ON SOOT MASS GROWTH

From the experiments in shock waves the "rate constant" k_f which is a measure for the duration of the "second" part of soot formation appears to depend on total density. Some measurements performed in C_2H_4-air flames by evaluating the measured f_v profiles are given in Fig. 14. The data are taken from a narrow range of flame temperatures [23]. Even if they should have a certain dependence on pressure it is not as strong as that found in shock waves. The absolute values for k_f obtained in these flames, however, center around the figures obtained from an extrapolation of the shock tube data down to low pressures at the same temperature.

This observation can be of some importance for the description of the soot mass growth. The results obtained from flames, where k_f was found to be only a function of temperature support the assumption that the active lifetime of the growing soot particles is essentially determined by the soot particles themself. The tempering of these particles, the decay of the active centers could be rate determining [28,29]. This assumption leads to a quantitative description of soot formation in C_2H_4-air flames. An active lifetime, which is proportional to the total density should hardly be determined by the "solid particles" alone.

COAGULATION

An important step for soot formation in combustion processes is coagulation [1]. At atmospheric pressure the Knudsen number $K_n = 2\lambda/d$ (with λ being the mean free path of the gas molecules and d the particle diameter) for soot formation in premixed flames is usually 10 or larger, and therefore in the free molecular flow regime. For flames burning at elevated pressure and for the high pressure shock tube data described the Knudsen numbers can fall far below 10 and pass into the continuum range. This has certain consequences. The coagulation rates measured at atmospheric pressure usually exceed the theoretical value for ball-shaped molecules by a factor less than ten [1]. Towards higher pressure the data obtained in shock waves came close to theory [7] while the flame data at 5 bar seem to fall somewhat below the calculated values [23]. The reason for this difference requires further investigation.

INFLUENCE OF PRESSURE ON THE PARTICLE NUMBER DENSITY

The measurements of the "final" particle number densities in these flames can be performed with higher accuracy than in shock waves, because the application of different optical techniques is much easier and the time available for the measurements much longer.

For the C_2H_4-air flames burning at elevated pressures, with different C/O ratios and with different flame temperatures the "final particle number density" was found to be between $N = 10^9$ to 10^{10} particles per cm^3 and therefore very close to values found at normal and reduced pressures [23]. A slight systematic variation of N can be explained by the change of the coagulation rate constant for the transition from high to low Knudsen numbers.

The fact, that the "final" N value remains practically independent of pressure means that the variations of the soot mass formed at different burning conditions result in variations of the mean final soot particle volume. It is therefore practically exclusively determined (as long as the flames are sufficiently hot) by the coagulation of the particles.

As in sooting flames burning at atmospheric pressure the soot particles in flames burning at higher pressure are surrounded not only by the components of the water-gas but also by hydrocarbons like acetylenes, methane, and by many other hydrocarbons including polycyclic aromatics. For the C_2H_4-air 5 bar flames presented here, these hydrocarbons contain much more carbon atoms per cm^3 than are present as soot particles. This should, however, change towards high pressures with further increasing soot yield. The situation should become more similar to that in rich benzene flames [23].

The reported measurements about soot formation in laminar flat flames at pressures up to 5 bar give fairly detailed information about the sequence of events involved in soot formation. They cover a pressure range which is not large, but the data up to 5 bar have recently been confirmed at higher pressures. The experimental results about flames burning at elevated pressure show that

1.) As in the pyrolysis experiments described the phenomenology of soot formation in premixed laminar flames burning at elevated pressure remains similar to that at 1 bar.

2.) The "final particle number density" is hardly influenced by pressure as to be expected from the formulas for particle coagulation rates. During soot formation particle coagulation determines the reduction of N with time.

3.) The dependence of f_v on the C/O (or fuel-air) ratio at elevated pressure remains practically the same as that at atmospheric pressure.

4.) Above a certain temperature soot mass f_v decreases with increasing temperature for all C/O ratios within the soot threshold.

5.) The influence of pressure on f_v depends on the fuel. For "hot" C_2H_4-air flames f_v increases with pressure proportional to about $p^{1.5}$ (depending on the burning conditions for which the comparison is made!).

6.) The threshold of soot formation depends on temperature and shifts only slightly towards lower C/O ratio with increasing pressure.

7.) The rate constant k_f obtained at elevated pressure shows a temperature dependence as that found in atmospheric flames and in shock waves. Up to 5 bar no pressure dependence which is outside the limit of experimental error could be measured. (This differs from the high pressure values obtained in shock waves!)

INFLUENCE OF PRESSURE ON DIFFUSION FLAMES

Diffusion flames shall be mentioned for reason of completeness but only briefly. Laminar diffusion flames have been investigated by Miller et al. [32] in the CH_4-air system for pressures up to 50 bar. Based on emissivity measurements, they report an increase of soot yield with pressure roughly proportional to $P^{1.7}$. This trend flattened considerably above 30 bar. Kadota [33] studied soot yield of liquid hydrocarbon droplets up to 10 bar and found a nearly linear increase of soot y[illegible] pressure.

The soot formation in diffusion flames is a rather complicated process because not only soot formation but also its oxidation plays an important role. Recent studies of local soot concentrations, formation rates, particle number densities etc. did show a rather complicated [34-36] interaction of the different zones in a diffusion flame and the strong influence which even slight heat losses or additions by the burner or by radiation can have on the appearance of the flame [34]. It is interesting to note that even though diffusion flames are rather complicated as far as soot formation is concerned, there seems to be a certain lower temperature at which soot formation starts [37] and a temperature below which soot oxidation stops [34].

Recently Flower and Bowman [38] performed detailed studies of ethylene air diffusion flames. For pressures up to 10 bar they found an increase of the soot volume fraction f_v integrated across the diameter of the flame which varied proportional to p^n with $n \approx 1.2$. Towards 10 bar the integral volume fraction measurements begin to fall below this trend indicating a decreasing dependence of f_v on pressure towards higher pressures.

Their experiments further showed that while the formation of soot increases with pressure, the soot oxidation consumes a decreasing fraction of the soot formed. Therefore the tendency to emit smoke rises strongly with increasing pressure. The pictures shown by these authors (Fig. 15) demonstrate that very convincingly. It seems rather obvious [34] that it is essentially the influence of temperature (increasing radiation losses) which, with increasing soot yield reduces oxidation rate for soot particles for higher pressures closer to the burner mouth.

The three topics, the experimental side of which is briefly discussed here do show, that pressure exhibits a strong influence on the formation rate of soot and on the volume fraction of soot finally formed within the process. They also show, that the number of scientific investigations devoted to that important topic is relatively small. Therefore technical problems connected with soot formation in combustion at elevated pressures still have to be handled on a trial and error basis.

REFERENCES

[1] Wagner, H.Gg., 17th Symposium (International) on Combustion, 3-19, The Combustion Institute, Pittsburgh (1979).
Haynes, B.S., Wagner, H.Gg., Progr. in Energy and Comb.Sci. 7, 229 (1981).

[2] Palmer, H.G. in Chemistry and Physics of Carbon, Marcel and Dekker, 1 (1965).
Homann, K.H., Comb.a.Flame 11, 265 (1967).
Homann, K.H. and Wagner, H.Gg., Proc.Roy.Soc. A307, 141 (1968).

[3] Hooker, W.J., 7th Symposium (International) on Combustion, 943, The Combustion Institute, Pittsburgh (1959).

[4] Mar'yasin, I.L., Nabutovsky, Z.A., Kinetics and Catalysis 10, 983 (1969); 11, 706 (1970); 14, 139 (1973).

[5] Buckendahl, W., Diplom Thesis, Göttingen (1970).

[6] Geck, C.C., Diplom Thesis, Göttingen (1975).

[7] Graham, S.C., Homer, J.B., Rosenfeld, J.L.J., Proc.Roy.Soc. A344, 259 (1975);
18th Intern. Shock Tube Symposium 421 (1975);
Graham, S.C., Proc.Roy.Soc. A377, 19 (1981) (there further ref.).

[8] Frenklach, M., Shock Tube Study of the Fuel Structure Effects on the Chemical Kinetics Mechanisms Responsible for Soot Formation, NASA, CR 174661 (1983).
Frenklach, M., Ramachandra, S., Mahila, R.A., 20th Symposium (International) on Combustion, The Combustion Institute, Pittsburgh (1985).
Frenklach, M., Taki, S., Durgaprasat, M.B., Mahila, R.A., Spring Techn. Meeting Western States Section, The Combustion Institute 1983, Combustion and Flame 54, 81 (1983).
Frenklach, M., Taki, S., Mahila, R.A., 19th Symposium (International) on Combustion, The Combustion Institute, Pittsburgh (1983);
20th Symposium (International) on Combustion, The Combustion Institute, Pittsburgh (1985);
21st Symposium (International) on Combustion, The Combustion Institute, Pittsburgh (1987) (there further ref.).

[9] Wang, T.S., Mahila, R.A., Farmer, R.C., 18th Symposium (International) on Combustion, The Combustion Institute, Pittsburgh (1981).

[10] Rawlins, W.T. et al., 20th Symposium (International) on Combustion, The Combustion Institute, Pittsburgh (1985).

[11] Bro, K., Wittig, S.L.K., Sweeney, D.W., 10th Intern.Shock Tube Symp. (1975); SFB Report 1987.

[12] Cundall, R.B., Fussey, D.E., Harrison, A.J., Lampard, D., 11th Intern.Shock Tube Symp. (1977);
Cundall, R.B., Fussey, D.E., Harrison, A.J., Lampard, D., J.C.S., Faraday Trans. I, 74, 1403 (1978).
Cundall, R.B., Fussey, D.E., Harrison, A.J., Lampard, D., J.C.S., Faraday Trans. I, 75, 1390 (1979).

[13] Wagner, H.Gg. in Soot in Combustion Systems, Plenum 171 (1983));
in Particulate Carbon Plenum 1 (1981).

[14] Haynes, B.S., Wagner, H.Gg., Z.Phys.Chem. N.F. 133, 201 (1983).

[15] Harris, S.J., Weinert, A.M., Comb.Sci.and Technology 31, 155 (1983);
19th, 20th, 21st Symposium (International) on Combustion, The Combustion Institute, Pittsburgh (1983, 1985, 1987).

[16] Brei, M., Jander, H., Bunsentagung 1982.
Brei, M., Jander, H., Wagner, H.Gg., Ber.Bunsenges.Phys.Chem. 91, 31 (1987).

[17] D'Alessio, A., DiLorenzo, A., Borghese, A., Beretta, F., Musi S., 16th Symposium (International) on Combustion. The Combustion Institute, Pittsburgh (1967). See also the following Symposium volumes.

[18] Lahaye, J., Prado, C., Chem.Phys. of Carbon 14, 168, Marcel Dekker, New York (1978); see also Symposium on Combustion papers.

[19] Roth, P., Just, T.H., Ber.Bunsenges.Phys.Chem. 71, 1114 (1973).

[20] McArraghers, J.S., Tau, K.J., Comb.Sci. and Techn. 5, 257 (1977).

[21] McFarlane, J.J., Holderness, F.H., Whitcher, F.S.E., Comb.a.Flame 8, 215 (1965).

[22] Tesner, P.A., Fiz Goreniya Vzryva 2, 3 (1979);
Chem.Phys. of Carbon, Marcel Dekker (1984).

[23] Mätzing, H., Dissertation Göttingen (1986);
Mätzing, H., Wagner, H.Gg., 21st Symposium (International) on Combustion, The Combustion Institute, Pittsburgh (1987).

[24] Millikan, R.G., J.Phys.Chem. 66, 794 (1962);
Lucht, R.P., Sweeney, D.W., Laurendeau, N.M., Comb.Sci.and Techn. 37, 93 (1984).

[25] Floßdorf, J., Wagner, H.Gg., Z.Phys.Chem. N.F. 54, 113 (1967).

[26] Hesse D., Diplom Thesis, Göttingen (1983).

[27] Luers, H., Diplom Thesis, Göttingen (1987).

[28] Haynes, B.S., Jander, H., Wagner, H.Gg., Ber.Bunsenges.Phys.Chem. 84, 585 (1980);
17th Symposium (International) on Combustion, 1365, The Combustion Institute, Pittsburgh (1979);
Haynes, B.S., Jander, H., Mätzing, H., Wagner, H.Gg., 19th Symposium (International) on Combustion, 1379, The Combustion Institute, Pittsburgh (1983);
Baumgärtner, L., Jander, H., Wagner, H.Gg., Ber.Bunsenges.Phys. Chem, 87 (1983)
Baumgartner, L., Hesse, D., Jander, H., Wagner, H.Gg., 20th Symposium (International) on Combustion, 959, The Combustion Institute, Pittsburgh (1985).

[29] Homann, K.H., Wagner, H.Gg., Ber.Bunsenges.Phys.Chem. 69, 20 (1965);
Bonne, K., Wagner, H.Gg., Ber.Bunsenges.Phys.Chem. 69, 35 (1965);
Dash, C.J., Comb.a.Flame 61, 215 (1985).

[30] Friedlander, S.K., Smoke, Dust and Haze, Wiley and Sons (1977).

[31] Hidy, G.M., Brock, J.R., The Dynamics of Aerocoll. Systems, Pergamon (1979).

[32] Miller, I.M., NASA, T.P. 1318 (1978);
Maans, H.G., Miller, I.M., NASA, T.P. 1673 (1980)

[33] Kadota, T., Hiroyasu, H., Farazandehmar, A., Comb.a.Flame 29, 67 (1977)

[34] Haynes, B.S., Wagner, H.Gg., Ber.Bunsenges.Phys.Chem, 84, 495 (1980);
Kent, J.H., Jander, H., Wagner, H.Gg., 18th Symposium (International) on Combustion, 1117, The Combustion Institute, Pittsburgh (1981);
Roper, F.G., Comb.a.Flame 29, 219 (1977);
Roper, F.G., Smith, C., Cunningham, A.C., Comb.a.Flame 29, 227 (1977);
Roper, F.G., Smith, C., Comb.a.Flame 36, 125 (1979)

[35] Kern, J., Spengler, G., Erdöl, Kohle, Erdgas, Petrochemie 23, 811 (1970;
Schug, K.P., Mannheimer-Timmat, T., Yaccarino, P., Glassman, I., Comb.Science and Technology 22, 235 (1980);
Glassman, I., Yaccarino, P., Comb.Science and Technology 24, 107 (1980); 18th Symposium (International) on Combustion, 1175, The Combustion Institute, Pittsburgh (1981); 19th, 20th Symposium (International) on Combustion, The Combustion Institute, Pittsburgh (1983, 1985).

[36] Smyth, K.C., Miller J.H., Dorman, R.C., Mallard, W.G., Santoro, R.J., Comb.a.Flame (1986);
Santoro, R.J., Semerjian, H.G., Dobbing, R.A., Comb.a.Flame 51, 203 (1983);
Santoro, R.J., Semerjian, H.G., 20th Symposium (International) on Combustion, 937, The Combustion Institute, Pittsburgh (1985).

[37] Gomez, A., Littmann, M.G., Glassman, I., Comb.a.Flame (1987).

[38] Flower, W.L., Bowman, C.T., Comb.Sci.Techn. 37, 93 (1984);
20th Symposium (International) on Combustion, 1035, The Combustion Institute, Pittsburgh (1985)

[39] Flower, W.L., Bowman, C.T., 21st Symposium (International) on Combustion, The Combustion Institute, Pittsburgh (1987).

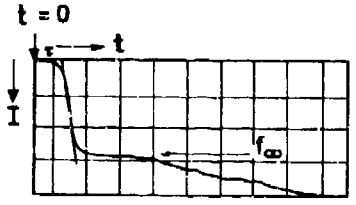

Fig. 1: Emission signal from soot formed in a shock wave. T = 2100 K; ρ = $7.9 \cdot 10^{-6}$ mol/cm³; 0.7 % C_2H_4 in Ar; 200 µs/cm; 200 mV/cm [6].

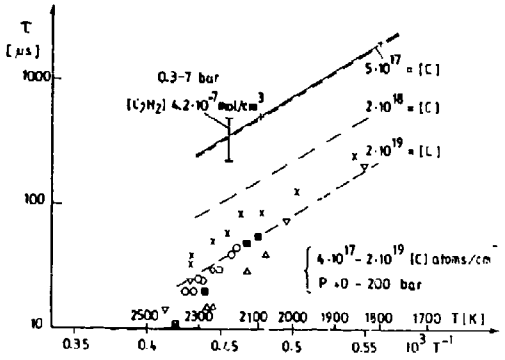

Fig. 2: Induction time τ(µs) for C_2H_2 pyrolysis as a function of temperature for pressures from 0.3 to 200 bar and total C atom densities of $2 \cdot 10^{17}$ - $2 \cdot 10^{19}$. The points around the lowest curve correspond to the experimental conditions given in the figure. The dashed lines are from an approximation by Frenklach [8].

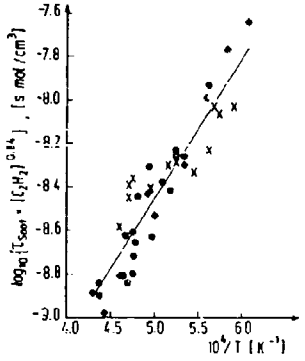

Fig. 3: Induction times τ(µs) multiplied by $[C_2H_2]^{0.84}$ for C_2H_2 pyrolysis measured in the infrared as a function of temperature [8].
x [C] = $5 \cdot 10^{17}$, P = 5-7 bar,
● [C] = $5 \cdot 10^{17}$, P = 1.3-2.7 bar
◆ [C] = $2 \cdot 10^{18}$, P ~ 5-8 bar

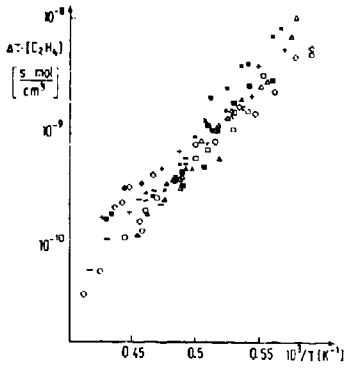

Fig. 4: Induction time τ for C_2H_4 pyrolysisas a function of temperature, $[C_2H_4]$ is 1 % except stated otherwise [6].
□ P = 9-12 bar, ▲ P ~ 35 bar,
■ P ~ 95 bar, 0.5 %, x P ~ 100 bar,
● P ~ 100 bar, 1.2-1.4%,
Δ P ~ 145 bar, 0.5-0.7%,
□ P ~ 210 bar, 1-1.4%,
– incident wave 15-30 bar, 1-1.7 %,
+ P ~ 120 bar[5], P ~ 240 bar[5]

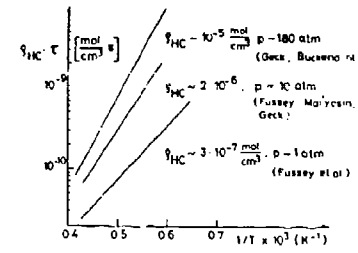

Fig. 5: Induction periods for C_2H_4 as a function of temperature for different pressure ranges [2-6], [12].

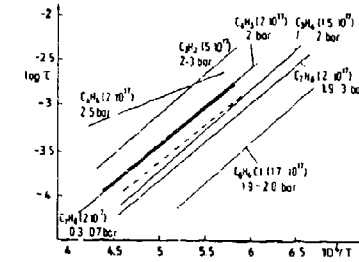

Fig. 6: Induction times for pyrolysis of different fuels. Conditions stated in the figure [8]

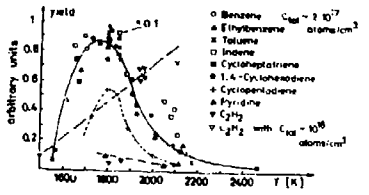

Fig. 7: Soot yield after 2.5 msec for shock wave pyrolysis of the fuels shown in the figure after Graham et al. [7].

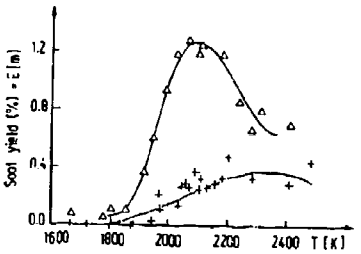

Fig. 8: Soot yield after 1 ms for C_2H_2 as a function of temperature [8].
Δ [C] = $5 \cdot 10^{17}$, P = 2.1-3.1 bar
+ [C] = $2 \cdot 10^{17}$, P = 2.1-3.2 bar

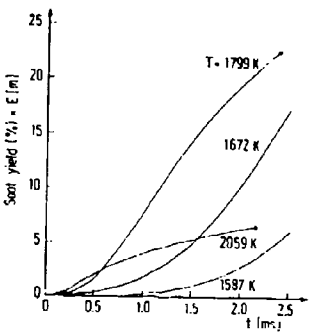

Fig. 9: Soot yield as a function of time for different temperature [6,7,8].

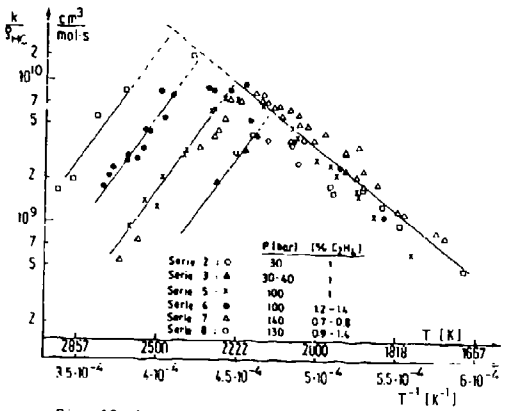

Fig. 10: k_f values divided by the carbon density as a function of temperature for C_2H_4 pyrolysis in argon. The experimental conditions are given in the figure [6].

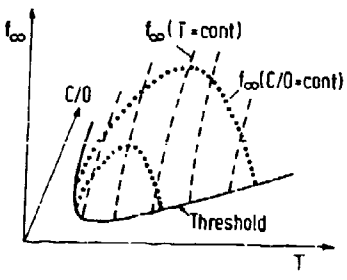

Fig. 11: Soot volume fraction f_∞ for hydrocarbon-air flames (schematic) plotted as a function of C/O ratio and of temperature. The curve in the C/O-T plane represents the threshold for soot formation. Lines parallel to the f_∞-T plane give for a given C/O ratio the f_∞ values. The dashed lines represent the dependence of f_∞ on C/O.

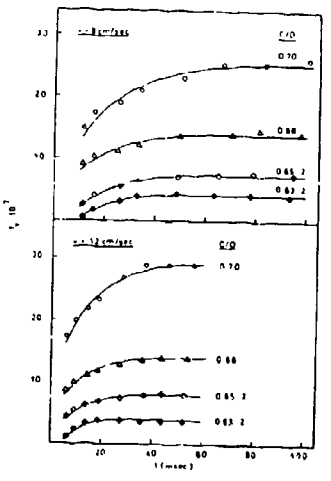

Fig. 12: Profiles of f_v as a function of time in C_2H_4-air flames for different C/O ratios at a pressure of 5 bar [23].

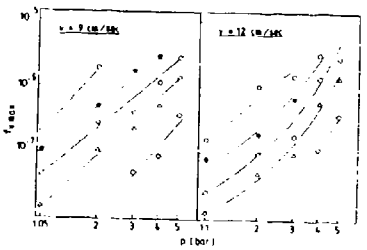

Fig. 13: Soot volume fraction f_s for C_2H_4-air flames as a function of pressure for gas flow velocities of 9 and 12 cm/s for C/O ratios:
◇ = 0.65, Δ = 0.68, ○ = 0.7,
● = 0.73, □ = 0.76 [23]

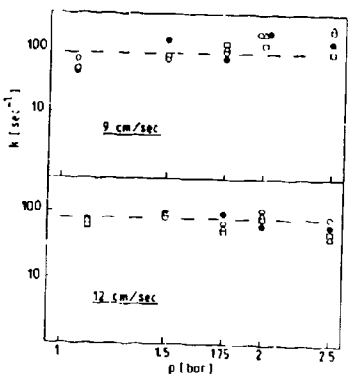

Fig. 14: k_f as a function of pressure for C_2H_4-air flames as a function of pressure (symbols as in Fig. 13) [23].

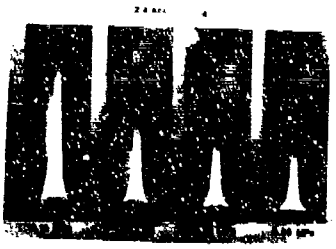

Fig. 15: Photographs of axisymmetric C_2H_4-air flames. Pressures and flow rate are given in the figure. Bright luminosity from soot is visible for each flame. The reduction of length with increasing height demonstrates the earlier onset of soot emission [39].

NUMERICAL MODELS FOR ANALYTICAL PREDICTIONS OF COMBUSTOR AEROTHERMAL PERFORMANCE CHARACTERISTICS

D.L. BURRUS GE, Aircraft Engines, Cincinnati, Ohio.
W. SHYY GE, Corporate Research and Development, Schenectady, New York.
M.E. BRAATEN GE, Corporate Research and Development Schenectady, New York.

SUMMARY

The purpose of this paper is to present an overview of the work performed at GE Aircraft Engines under an ongoing program to develop and improve the sophisticated analytical models for the design and analysis of aircraft turbine engine combustors. This effort has focused on the full three dimensional (3D) elliptic combustor internal flow model. This paper will begin with an introduction and review of the objectives of the program. This will be followed by a discussion of the progress made in the past five years starting with the initial application and assessment of "first generation" 3D combustor models based on cartesian grids, progressing to the development and recent application of an improved "second generation" 3D combustor model based on a body fitted generalized curvilinear grid. Finally, a brief review of planned future modeling activities to be conducted under this program will be discussed.

1. INTRODUCTION

One of the significant ways in which the performance level of aircraft turbine engines has been improved is by the use of higher pressure ratio compressors, and higher turbine inlet temperatures. These approaches have achieved engine performance benefits. They have also resulted in an increasingly hostile aerothermal environment for the engine combustor and turbine components. The escalating cost of experimental component development testing approaches directed towards improving hot section durability and aerothermal performance has necessitated the development of sophisticated combustor design and analysis methods. Early combustor modeling activities at GE focused on the development of one dimensional models, (Reference 1), capable of providing predictions of overall combustor total pressure loss, bulk flowfield quantities stationwise through the burner, and the mass flow level of the various mass injection features of the combustor design. An example of this type of analysis provided by the COBRA program derived from Reference 1, is shown for the GE/SNECMA CFM56 combustor in Figure 1. In general, the sophistication incorporated in this one dimensional model provides accurate predictions of the overall total pressure loss, and the injected mass flow distribution. However, such a model provides little or no predictive information concerning the combustor heat transfer characteristics, the combustor exit gas temperature patterns, or any performance characteristic dependent in the three dimensional nature of the combustor geometry. As such, a need existed for the capability to perform fully 3D analysis of the turbulent reacting internal flowfield of the combustor. The problem of developing suitable analysis approaches was nontrivial. The combustor flow problem is extremely complex involving aspects of complicated geometries coupled with complex flow phenomena.

For many years the lack of computer capabilities prohibited the development of fully 3D combustor aerothermal models. Rapid advances in computer technology within the past ten years have overcome previous limitations permitting the extension of aerothermal models to fully 3D elliptic form suitable for detailed analytical simulation of the internal flowfield of conventional combustor designs. One of the first comprehensive combustor model packages was developed by the Garrett Turbine Company under contract to the United States Army, (Reference 2). In this work many individual analysis procedures were developed and assembled into a complete computerized combustor analysis package. Included in this package was a fully 3D elliptic combustor internal flow model based on a cartesian grid system, a so called "first generation" combustor internal flow model. The availability of this model led to the initiation of a program at GE to examine the usefulness of such a model as applied to real combustor flow problems, and to identify model deficiencies and the needed improvements to provide a "second generation" improved combustor internal flow model.

The anticipated benefits of this program are improved combustor designs with better performance, greater durability, developed in less time and at reduced cost. The development and application of such models will provide much improved engineering understanding of the complex flow features of the gas turbine engine combustor.

2. PROGRAM OBJECTIVES AND APPROACH

The overall objectives of the GE combustor modeling program are to develop improved combustor design and analysis tools to assist engineers in achieving improved combustor designs at reduced development cost. The focus of the combustor modeling program has been the development of the combustor internal flow model. The near term goals have been to develop modeling capability to provide reasonably accurate predictions of combustor exit gas temperature patterns, and liner hot side heat transfer characteristics. These areas of combustor performance are where combustor modeling has the best near term potential to assist engineers in the development of improved

combustors. The development of modeling capability to provide useful predictions of other performance characteristics such as efficiency, gaseous and particulate emissions, as well as flame lightoff and extinction have been pursued in the past with less emphasis. However, the move towards high temperature rise and, ultimately, stoichiometric combustors has demonstrated the need to pursue the development of the physical modeling capabilities to address these performance concerns.

The approach used in this program has been to assess the combustor internal flow models against actual and combustor like flow problems, and, where possible, more definitive experiments of benchmark quality. The key items of concern are accuracy and suitability of the methodology employed, useability, and computational efficiency as related to the cost of the solution. Based on the assessment studies, the strong points of the model are noted, and the deficiencies identified. The next step is to identify and develop the needed modeling improvements. The developed improvements are then incorporated into the model yielding an "improved" combustor internal flow model. The improved model undergoes additional assessment and refinement in a continuous cyclic fashion. After each cycle, the improved model becomes available for application, by engineering, to real combustor flow problems. This approach hastens the introduction of improved modeling capability into the design and development of combustors while further model improvement is taking place.

3. ASSESSMENT OF FIRST GENERATION MODELING CAPABILITY

The assessment of the accuracy and sources of error in the methodology of existing first generation combustor internal flow models was an important first step in justifying the extent of use of the models, and identifying the needed improvements. This effort was conducted in part under an in-house Research and Development program, and in part under the NASA Aerothermal Modeling Phase I Program, Reference 3. The assessments were conducted using 2D parabolic and elliptic, as well as fully 3D elliptic model calculations of definitive test data from the available literature, and data generated as part of the NASA program effort. The assessments performed with the 2D models provided a methodical examination of the numerical techniques and the physics, while work with the 3D models focused on the overall useability and performance as a design analysis tool.

3D MODEL ASSESSMENT

Evaluations of the available 3D modeling capability began with the assessment of the model prepared by the Garrett Turbine Engine Company, Reference 2, and a very similar model prepared by the Northern Research and Engineering Company, Reference 4. The major differences between the two models involves the numerical finite differencing scheme employed. First order accurate upwind differencing is used in the Northern Research model; the "hybrid" differencing scheme in the Garrett model. In the hybrid scheme, second order accurate central differencing is used where the computational cell Peclet number (uAx/ν) has a value of 2 or less. For cells where the Peclet numbers exceed 2, the hybrid scheme reverts to first order accurate upwind differencing to maintain numerical stability. As such numerical diffusion has been introduced into the solution, potentially effecting the accuracy. To support the application of these models, plotting routines to display the calculated results, and improved model input flexibility were developed. This entire modeling package was then referred to as the 3D INTFLOW combustor internal flow model.

The flow problems selected to use in the 3D model assessment study were comprised of simplified combustor like flows for which some definitive experimental data existed. For modeling simple round jet flows in a crossflow with uniform inlet profile characteristics, two sets of experimental data from the work by Walker and Kors (Reference 5) were selected for examination. In addition, experimental test data, obtained as part of the NASA modeling program, for combustor like flows of progressively increasing flow complexity were used. The selection of these simple isothermal nonreacting flow problems permitted assessing the capability of the existing 3D models to accurately predict dilution jet penetration and mixing without the added complication of fuel injection and heat release.

The two experiments selected from the Walker and Kors data represented jet to crossflow momentum ratios of 6.3 and 26.8. The experimental techniques employed mapping out the penetration and mixing of room temperature jets into a heated uncarbureted crossflow. The experimental data consisted of detailed thermocouple measurements at prescribed planes downstream of the jet injection point. In the modeling calculations of the Walker and Kors data three similar grids of 10395, 21000, and 41600 grid mesh points were used to investigate the influence of mesh grid point density on the calculated results. The finest mesh, shown in Figure 2, required computer memory approaching the capacity of the computer system available at the time. Besides the mesh characteristics, these modeling calculations also investigated the sensitivity from varying the inlet and jet boundary conditions for turbulence kinetic energy and length scale, and the prescribed turbulent Schmidt number.

From the results of the modeling calculations on the Walker and Kors data the two available 3D models were shown to predict almost identical jet penetration and mixing characteristics although considerably lower turbulence levels were calculated by the Northern Research model. This result provided support to the claim that the presence of numerical diffusion in the solution arising from the use of first order accurate upwind numerics can dominate over the mixing generated by the turbulence model. As such, it was decided not to make further use of the Northern Research model. Excellent agreement between the model calculation and the experimental test data was demonstrated by use of the "optimum" choice of the model inlet and jet turbulence boundary conditions, Figure 3. Because the Walker and Kors data did not contain information concerning inlet and jet turbulence characteristics, it was not possible to conclude that the levels which produced the best modeling results were fundamentally correct. The investigation of the mesh grid density showed that comparably good agreement for jet penetration and mixing could be achieved for all three grids if the solutions were allowed to be sufficiently converged. As the mesh density increased, the model calculations produced jet shapes, as defined by the temperature contours, which more closely approximated the test data. However, it was apparent that considerable further mesh refinement would be necessary to achieve a "matched" result. The need for very fine meshes, provided the computer capability existed, illustrated another problem with the model. The computer processor time per iteration was shown to generally increase proportional to N, where N is the number of mesh grid points. It was also observed that the number of iteration steps required to achieve convergence increased proportional to $N^{1/2}$. As such the total computer time increases proportional to $N^{3/2}$, making fine grid solutions cost prohibitive.

Additional assessments of the 3D INTFLOW model were performed by modeling selected experiments from the work performed as part of the NASA/GE Aerothermal Modeling Program. The nonreacting experiments represented various dilution patterns penetrating into a cylindrical duct flow. These experiments employed the use of the two temperature trace technique. The penetration and mixing of the jets was documented using detailed thermocouple measurements. For these modeling calculations a coarse grid mesh of 13365 grid points was used, Figure 4. This mesh provided sufficient detail to model the dilution pattern while not requiring excessive computational time. The same turbulence inputs that had produced satisfactory results in the calculations of the Walker and Kors experiments were used in these calculations. A selection of the results from this modeling exercise is shown in Figure 5. In general, the calculated results demonstrated qualitative agreement with the test data. However, there was evidence of over prediction of the jet penetration and slower predicted mixing.

Another of the experiments from this test series involved a GE/SNECMA CFM56 five cup (90°) sector combustor operating with gaseous fuel. All dome and liner cooling flows closed off to reduce the degree of difficulty of modeling a combustor reacting flow problem. A cross section view of this combustor is shown in Figure 6, illustrating the complex geometry of the boundary walls. Experimental test data involved detailed thermocouple measurement at the exit of the combustor. A considerably more detailed grid mesh containing approximately 37000 grid points was used to perform the 3D modeling calculations, Figure 7. Because of the lack of special boundary treatment within the model to address liner wall contours, the modeling simulation featured cylindrical geometry. The inlet swirler velocity characteristics were generated using data from 5-hole yaw probe measurements obtained from CFM56 combustor swirl cup hardware, and manually added to the model input file. The calculated results from this exercise are shown in the form of the velocity field in a side view plane midway between swirl cup centers, Figure 8, and as a comparison with measured exit gas temperature data normalized using the pattern factor parameter, Figure 9. The pattern factor parameter is defined as follows:

$$P_f = \frac{T_{LOCAL} - T_{AVG}}{T_{AVG} - T_3}$$

where T_{LOCAL} is the local gas temperature, T_{AVG} is the average gas temperature at the combustor exit, and T_3 is the compressor discharge temperature. As observed in this comparison, the model did reasonably predict the relative locations of the hot spots in the exit gas temperature field, indicated by the higher levels of the pattern factor parameter. However, once again, the mixing appears to be under predicted as evidenced by the higher levels of calculated pattern factor as compared to the measured test data. The quality of this result is perhaps fortuitous considering the reliability in the accuracy in the measured swirler velocities using an intrusive instrument, and the gross simplification of representing the complex flowpath contours with cylindrical geometries. Calculated velocity magnitudes suffer inaccuracies due to the misrepresentation of the flowpath areas. There was also the issue of the numerical accuracy in this calculation, specifically concerning the introduction of numerical diffusion. As shown in Figure 10, with the grid mesh selected, very little of the computational domain had Peclet number levels below 2. As previously mentioned, the hybrid scheme reverts to first upwinding under these conditions. Hence the bulk of the domain was solved using first order accurate upwind differencing resulting in the introduction of numerical diffusion proportional in magnitude to the ratio of the local Peclet number to a Peclet number of 2. The evidence of considerable numerical error is obvious, demonstrating that within the grid limitations of the existing computer capacity, there was a need for improved numerics.

As an extension of this exercise, the modeling capability of the 3D INTFLOW model

was extended to permit simulation of contoured flowpath boundaries typical of conventional combustor designs. This was accomplished by the introduction of the so called "stairstep" boundary treatment into the model. This approach was selected because it was easy to implement within the cartesian framework of the 3D INTFLOW model. One further modeling improvement involved automating the generation of the inlet swirler velocity boundary conditions thus eliminating the tedious task of generating the model input manually. This improved 3D INTFLOW model was then applied to the same CFM56 combustor flow problem previously modeled using cylindrical geometry. The purpose of this exercise (Reference 6) was to assess the suitability of the stairstep boundary technique in representing complex combustor geometries. To model the CFM56 combustor design, stairstep boundaries were introduced along the outer and inner liner flowpaths, as well as the dome inlet in a way which closely simulates the actual combustor flowpath contours. A side view of the grid mesh used, and the stairstep boundaries representing the combustor geometry is presented in Figure 11. This particular mesh contained 44352 mesh grid points. However, it is obvious from observing this figure that many of the mesh grid points actually lie outside of the stairstep boundaries, and hence, the computational domain. This is one of the immediate disadvantages of the stairstep boundary technique. The calculated velocity fields obtained with this model, in two different side views, are presented in Figure 12. A comparison between the calculated exit gas temperature pattern and the available measured test data is presented in Figure 13. Again the results are displayed as contours of the pattern factor parameter. It is observed from this figure that the magnitude of the hot spots and their locations circumstantially were accurately predicted by the model. In this sense, the result was somewhat improved over the result obtained in the previous modeling calculation employing cylindrical wall boundaries. However, considerable discrepancy is observed in the radial location of the hot spots. The test data suggests they are centrally located within the annulus boundaries, while the model predicted them along the inner boundary.

As a result of this assessment exercise, several observations concerning the use of stairstep boundary treatment were made. The need for treating wall contours was perhaps a foregone conclusion, and the results of this exercise serve to support this. However, the use of the stairstep boundary technique involves significant limitations and/or difficulties. A feature of using stairstep boundaries of particular concern is observed in the flow along the boundary walls. A cascading effect has been introduced into the solution of the flow along the walls. This has resulted from the use of flats (horizontal or vertical sections of the stairstep boundary of more than a single grid cell spacing in length), in the construction of the stairstep boundary. A related difficulty involves the awkwardness in obtaining grid detail along the boundary walls. This particular experimental test configuration modeled did not feature liner wall cooling slots. However, conventional combustor configuration feature numerous liner wall film cooling slots which could not easily or accurately be represented on a stairstep boundary. Any attempt to provide this detail would result in randomly distributed grid concentration, and excessive requirements for computer storage. Another limitation of the stairstep approach was briefly touched on before. The stairstep technique inherently involves considerable amounts of "wasted" mesh grid points. These are the grid points which are present within the cartesian structure of the mesh, but which lie outside the boundaries of the problem. The wasted grid points have no adverse impact on the computational time for the solution, they nonetheless require computer storage. The magnitude of this problem can be severe. In the CFM56 example, only about half of the total mesh grid points actually lie within the problem boundaries. As such, the stairstep boundary approach does not provide for the optimum use of grid or the available computer storage.

ASSESSMENT OF NUMERICAL AND PHYSICAL METHODOLOGY

The combustor aerothermal model can be simplistically regarded as a set of simultaneous partial differential and algebraic equations, a discretization procedure, and a solution algorithm. Physical modeling is contained in the original equations, numerical accuracy in the discretization procedure and solution algorithm, and computation efficiency primarily in the solution algorithm. It is computationally prohibitive and actually unnecessary to study these modeling issues in fully three dimensional flows. Thus a series of one and two dimensional studies were conducted ranging from the analysis of liner uniform coefficient convection diffusion equations to a turbulent recirculation combusting flow. These studies, conducted as part of the NASA/GE Aerothermal Modeling Program, each focused on different aspects of the overall numerical and physical submodel issues to assess their role in the accuracy of the solution. Assessments performed in two dimensions made use of the TEACH code, developed initially at the Imperial College, and the GETREF (GE Turbulent Reacting Flow) code developed at GE.

The first issue studied was the accuracy of the finite difference representations of the convection term. Several schemes for approximating this first order spatial derivative in convection dominated flow were investigated. The relative accuracy and computational efficiency (convergence speed) among the first order accurate upwind scheme, second order accurate central differencing scheme, second order accurate upwind difference scheme, and the QUICK (Quadratic Upstream Interpolation for Convective Kinematics) scheme, were compared against several idealized one or two dimensional model problems, e.g., uniform, constant diffusivity flow with a prescribed source term.

It was shown that in a finite difference simulation with large cell Peclet number, the high wave number Fourier components of the real solutions cannot be evaluated accurately. As a result of this, in a convection dominated flow, if the viscous terms

are required to balance the convection terms in a thin layer close to the downstream boundary due to, for example, the imposition of a Dirichlet type boundary condition, a finite difference approximation can, at best use the truncation errors of the approximations to help damp out the disturbances in that thin layer. The detailed structure of the real solution is unresolved. Even this may or may not be accomplished by a given scheme, and hence for a high cell Peclet number flow the formal order of accuracy, by itself, is a poor criterion by which to judge the performances of different schemes. For example, Figure 14 compares the typical solution profiles along the y direction given by the five schemes for a 2D convection diffusion equation with constant values of u, v, and Pe (Pe = 40, u/v = 2). For Figure 14, the downstream boundary conditions are taken to be the same as the upstream boundary conditions. Figure 15 shows the solution profiles given by the five schemes for the same flow problem, but with zero as the downstream boundary condition; a thin boundary layer normal to the flow direction is formed close to the downstream boundary. Among the five schemes tested in this study; the second order upwind scheme gives the most satisfactory results in general; this scheme, however still exhibits some overshoots in the solution. On the other hand, although both second order central differencing and QUICK are formally of the same order of accuracy as the second order upwind scheme, they fail to enhance the viscous terms properly where needed for a high cell Peclet number flow problem. Noticeable spurious oscillations appear in the numerical solutions. Furthermore, if no boundary layer type region exists in the real solution, the accuracy of the approximating solutions given by QUICK and that by the second order upwind are comparable. The first order upwind scheme is free from unphysical over and undershoots in the solutions for all test problems considered, but fails to give accurate approximations in the presence of a source term and shows too much numerical diffusion in the convection dominated region for multidimentional flow. The skew upwind scheme is able to substantially reduce numerical diffusion by the first order in the cross stream direction but is found to be less satisfactory than the second order upwind scheme. The skew upwind scheme also fails to give accurate solutions in the presence of source terms.

The physical models for turbulence and turbulence chemistry interaction phenomena were studied by comparison of predictions with four benchmark quality axisymmetric experiments. These experiments were: a turbulent nonpremixed jet flame (Reference 7); an annular isothermal dilution jet/chamber flow (Reference 8); an isothermal pipe flow (Reference 9); and a nonpremixed, bluff body stabilized flame (Reference 10). The turbulent jet flame is a shear flow and so a parabolic version of the model was used. An elliptic model was used for the three recirculating flow simulations.

The first simulation establishes the need to account for random compositional and temperature fluctuations. In a shear flow such as this jet flame, the parabolic nature of the governing equations permits the use of sufficient grid points to make the issue of discretization accuracy irrelevant. Thus a more direct assessment of the turbulence, and particularly, the turbulence chemistry interaction model is possible. In addition, the jet flame experiment provided both laser velocimeter and spontaneous Raman scattering data so that the mean, variance, and indeed, the pdf (probability density function) of major species concentrations, temperature, and axial velocity were available. Comparisons of these quantities, many of which are shown in Figures 16 through 20 indicate the accuracy of the single scalar pdf/equilibrium chemistry submodel in accounting for the highly nonlinear "unmixedness" turbulence chemistry interaction. It should be noted that so called adequacy of simpler models such as the eddy breakup scheme is often inferred from far more complicated experiments, e.g., recirculating flows with less precise instrumentation; under these circumstances the turbulence chemistry interaction cannot be isolated and compensating errors frequently occur. Finally it should be noted that the single scalar pdf can be extended to multiscalar pdf descriptions of nonequilibrium flows without added empiricism.

The three recirculating flows are progressively more complex in that more phenomena occur simultaneously. Solutions essentially free from "numerical diffusion" were obtained by increasing grid density until central differencing of the convection term was possible. The isothermal dilution jet/chamber flow provides data for a gas turbine combustion chamber like flow which retains axisymmetric geometry. Comparisons (Figures 21 and 22) indicate that the flow is dominated by the mean pressure gradient rather than by the turbulence. This is evident from the poor agreement in the turbulence kinetic energy profiles and, despite this, the good agreement in the mean axial velocity. However, in a reacting flow the turbulence is important in that besides controlling diffusivity, it interacts nonlinearly with the chemistry to produce a mean density field which enters all the equations.

The co- and counterswirled isothermal pipe flow features strong streamline curvature and consequently, anisotropic turbulence. This cannot be represented by the isotropic eddy viscosity two equation models which are widely used, e.g., k-ε model. On the other hand the full Reynolds stress equations, which could account for anisotropy, involve semiempirical closure for higher correlations, ignore very important issues in the dissipation rate equation, and are computationally very much more expensive. Hence, an algebraic simplification of the Reynolds stress equations, in two dimensions, which finally retains the two equation form with a very complex eddy viscosity, rather than a constant, was derived. This model is more universal than, for example, Richardson Number corrections; it has been used successfully in several recirculating flows. Figure 23 shows centerline axial velocity profiles in this flow with the standard k-ε and the new model; the appearance of a recirculation zone in the latter case confirms its accuracy.

The last flow simulated was an axisymmetric recirculating nonpremixed flame. Combustion, i.e., the turbulence chemistry interaction, was represented by the single scalar pdf described earlier. Again, truncation error analysis and grid densification were used to produce solutions essentially free from numerical diffusion error as observed in Figure 24. The centerline mean axial velocity profile shows reasonable agreement with the data. The measured turbulence kinetic energy profile shows a marked peak at the first stagnation point, which is not predicted. Mean and variance of species concentrations were not measured and so those predictions could not be evaluated. Agreement of mean temperature (Figure 25) is reasonable but it should be noted that in the model temperature is not a primitive variable, that thermocouple data is notoriously difficult to interpret, and that intermittency may affect the pdf in the annular shear layer (y = 0.07 m). The position of the forward stagnation point as a function of the central jet to annular flow velocity ratio (Figure 25) also shows reasonable agreement with the data.

The conclusions made from the assessments of existing first generation combustor internal flow models were clear. The stairstep boundary technique was not a suitable approach for addressing the complex flowpath geometries of conventional combustor designs. Considerable thought went into identifying better alternate approaches for handling the geometry issue. What emerged was the decision to adopt a body fitted coordinate mesh structure using generalized curvilinear coordinates to provide for the greatest flexibility in handling complex geometries. The one and two dimensional axisymmetric studies addressed the issues of stability and accuracy of convection term discretization, the performance of several difference operators in various flows, and the physical modeling of turbulence and turbulence chemistry interactions. These studies all lead to modeling approaches which would result in a more accurate predictive capability in the next generation code for combustor flow.

4. IMPROVED COMBUSTOR MODEL DEVELOPMENT

The conclusions reached as part of the assessment studies of the available first generation modeling capabilities demonstrated the need for significant improvements. As a result of this, a decision was reached to undertake the development of a new improved combustor internal flow model. This second generation combustor model would be based on a generalized body fitted curvilinear mesh structure to provide the required flexibility to model the complex flowpath geometries typical of combustor designs. The new model would have all of the capabilities of the first generation model, plus feature the improvements in numerics and physical submodeling that were identified during the assessment studies. The development of the new model, 3D CONCERT (Cartesian Or Natural Coordinates for Elliptic Reacting Turbulent flows), was conducted at the GE Corporate Research and Development Center. In a parallel effort conducted at the GE Aircraft Engine Business Group, improvements to the first generation model, 3D INTFLOW, were made, and application to actual combustor design and analysis problems was initiated. This approach permitted the near term introduction of improved modeling capability while development of the new combustor model was taking place. It also permitted the identification of further needed modeling improvements and capabilities to be introduced into the 3D CONCERT model as development proceeded.

DEVELOPMENT OF 3D CONCERT MODEL

The major issue behind the development of the new combustor model, 3D CONCERT, involved the inappropriate representation of a complex flowpath such as a gas turbine combustor in a cartesian or cylindrical coordinate system. As such, the development of 3D CONCERT involved constructing a new combustor model comprising state-of-the-art physical submodels and numerical procedures within the framework of a boundary fitted coordinate system. Because the use of the curvilinear coordinate system presented some new challenges in the formulation of the solution algorithm in the CONCERT model, a brief discussion of the formulation is appropriate.

The 3D CONCERT model like the first generation 3D INTFLOW model addresses the solution of the governing conservation equations for a dependent variable ϕ. The governing equations are written in the strong conservation law form in general curvilinear coordinates, as derived in Reference 11. The conservation equations typically can be written in the cartesian coordinates for the dependent variable ϕ in the following form

$$\frac{\partial}{\partial X}(\rho u\phi)+\frac{\partial}{\partial Y}(\rho v\phi)+\frac{\partial}{\partial Z}(\rho w\phi) = \frac{\partial}{\partial X}(\Gamma\frac{\partial\phi}{\partial X})+\frac{\partial}{\partial Y}(\Gamma\frac{\partial\phi}{\partial Y})+\frac{\partial}{\partial Z}(\Gamma\frac{\partial\phi}{\partial Z})+R(x,y,z) \qquad (1)$$

where Γ is the effective diffusion coefficient and R the source term. When new independent variables ξ, η, and γ are introduced. Equation 1 changes according to the general transformation $\xi = \xi(x,y,z)$, $\eta = \eta(x,y,z)$, $\gamma = \gamma(x,y,z)$. The result of this coordinate transformation is to transform the arbitrarily shaped physical domain into a rectangular parallelopiped.

Equation 1 can be rewritten in (ξ,η,γ) coordinates as follows:

$$\frac{\partial}{\partial\xi}(\rho U\phi) + \frac{\partial}{\partial\eta}(\rho V\phi) + \frac{\partial}{\partial\gamma}(\rho W\phi) = \frac{\partial}{\partial\xi}\left[\frac{\Gamma}{J}(q_{11}\phi_\xi + q_{12}\phi_\eta + q_{13}\phi_\gamma)\right] + \frac{\partial}{\partial\eta}\left[\frac{\Gamma}{J}(q_{21}\phi_\xi + q_{22}\phi_\eta + q_{23}\phi_\gamma)\right] + \frac{\partial}{\partial\gamma}\left[\frac{\Gamma}{J}(q_{31}\phi_\xi + q_{32}\phi_\eta + q_{33}\phi_\gamma)\right] + S(\xi,\eta,\gamma)\cdot J \tag{2}$$

where

$$\begin{aligned}
U &= u(y_\eta z_\gamma - y_\gamma z_\eta) + v(x_\gamma z_\eta - x_\eta z_\gamma) + w(x_\eta y_\gamma - x_\gamma y_\eta)\\
V &= u(y_\gamma z_\xi - y_\xi z_\gamma) + v(x_\xi z_\gamma - x_\gamma z_\xi) + w(x_\gamma y_\xi - x_\xi y_\gamma)\\
W &= u(y_\xi z_\eta - y_\eta z_\xi) + v(x_\eta z_\xi - x_\xi z_\eta) + w(x_\xi y_\eta - x_\eta y_\xi)\\
q_{11} &= (y_\eta z_\gamma - y_\gamma z_\eta)^2 + (x_\gamma z_\eta - x_\eta z_\gamma)^2 + (x_\eta y_\gamma - x_\gamma y_\eta)^2\\
q_{22} &= (y_\gamma z_\xi - y_\xi z_\gamma)^2 + (x_\xi z_\gamma - x_\gamma z_\xi)^2 + (x_\gamma y_\xi - x_\xi y_\gamma)^2\\
q_{33} &= (y_\xi z_\eta - y_\eta z_\xi)^2 + (x_\eta z_\xi - x_\xi z_\eta)^2 + (x_\xi y_\eta - x_\eta y_\xi)^2\\
q_{12} = q_{21} &= (y_\gamma z_\xi - y_\xi z_\gamma)(y_\eta z_\gamma - y_\gamma z_\eta) + (x_\xi z_\gamma - x_\gamma z_\xi)(x_\gamma z_\eta - x_\eta z_\gamma)\\
&\quad + (x_\gamma y_\xi - x_\xi y_\gamma)(x_\eta y_\gamma - x_\gamma y_\eta)\\
q_{13} = q_{31} &= (y_\xi z_\eta - y_\eta z_\xi)(y_\eta z_\gamma - y_\gamma z_\eta) + (x_\gamma z_\eta - x_\eta z_\gamma)(x_\eta z_\xi - x_\xi z_\eta)\\
&\quad + (x_\xi y_\eta - x_\eta y_\xi)(x_\eta y_\gamma - x_\gamma y_\eta)\\
q_{23} = q_{32} &= (y_\xi z_\eta - y_\eta z_\xi)(y_\gamma z_\xi - y_\xi z_\gamma) + (x_\eta z_\xi - x_\xi z_\eta)(x_\xi z_\gamma - x_\gamma z_\xi)\\
&\quad + (x_\xi y_\eta - x_\eta y_\xi)(x_\gamma y_\xi - x_\xi y_\gamma)\\
J &= x_\xi y_\eta z_\gamma + x_\gamma y_\xi z_\eta + x_\eta y_\gamma z_\xi - x_\xi y_\gamma z_\eta - x_\gamma y_\eta z_\xi - x_\eta y_\xi z_\gamma
\end{aligned} \tag{3}$$

and $S(\xi,\eta,\gamma)$ is the source term of the governing equation in (ξ,η,γ) coordinates.

A staggered grid system as described in Reference 12 is used in the calculation. The scalar variables (p, ρ, k, ε, etc.) are located at the center of the control volumes, while the velocity components are located on the control volume faces, Figure 26. Finite difference approximations to the conservation laws are obtained by taking the integral of Equation 2 over the control volume and discretizing it, as done in cartesian coordinates. By choosing $\Delta\xi = \Delta\eta = \Delta\gamma = 1$, the resulting form of the governing equations become formally of the same form as the finite difference equations derived in cartesian coordinates. Because of this similarity, the SIMPLE solution procedure is extended to the body fitted curvilinear coordinate system using the methods discussed in Reference 13.

The solution marches sequentially through the momentum, pressure correction, and other scalar equations (such as k, ε), with a maximum allowance being prescribed for updating each dependent variable. This sequential procedure is defined here as the outer iteration cycle. Within each equation, and with the prescribed allowances as the limit, the discretized system of linear equations are also solved iteratively. This procedure is called the inner iteration step. The detailed implementation of the numerical algorithm is discussed in Reference 13.

Second order central differencing is used to approximate the second order derivative terms (diffusion), in the governing equations. For the finite difference approximation to the convection terms, both hybrid differencing and second order accurate upwind differencing are available. The incorporation of the second order upwinding reflects the results of previous assessments of numerical issues.

In the development of the 3D CONCERT model to date, much of the effort has focused on the numerical framework rather than on the development of specific physical submodels. As such, the model at this time considers gaseous fuel injection, the two equation k-ε turbulence model, and "fast" chemistry coupled with a probability density function treatment to account for compositional fluctuations. Elemental rather than molecular species concentrations are considered. Since elements and total enthalpy are conserved, their conservation equations are homogeneous. If all diffusion coefficients are equal the mixture fraction (ψ) is usefully defined as

$$0 \le \psi \equiv \frac{Z - Z_a}{Z_f - Z_a} \le 1 \tag{4}$$

where (a) and (f) refer to air and fuel streams and Z is any elemental mass fraction or total enthalpy. A value of corresponds to a known instantaneous concentration of the elements and total enthalpy. The thermochemical program CREK, (Reference 14) is built into CONCERT to determine the equilibrium density, temperature, and species concentration for each mixture fraction. These equilibrium vectors are then stored as

thermochemical tables for use as required in the solution of the conservation equations. The fluctuations in Φ are represented by the β-probability density function (β-pdf), References 15 and 16. The transport equations for the first two moments of the pdf describing the fluctuations are solved simultaneously with the equations for the pressure correction, momentum, turbulence kinetic energy, and dissipation rate. Thus the local pdf at each point is convoluted with the corresponding equilibrium vector to generate required quantities such as the local mean density. This approach provided improved physical modeling over the treatment of fast chemistry featured in the first generation 3D INTFLOW model.

During the development of the 3D CONCERT model considerable effort went to address the need for improved computational efficiency associated with modeling calculations. In 1985 two studies, Reference 17, were performed to investigate two aspects of computational speedup. The first of these studies explored the use of a direct solver approach within the framework of the curvilinear coordinates. The second study explored the pressure correction equation used in the iterative approach.

In the direct solver investigation, a procedure using sparse matrix techniques for curvilinear coordinates was formulated and evaluated. In this procedure, the continuity equation is directly discretized instead of using the pressure correction equation in the iterative approach. The momentum and continuity equations are combined into a single equation set, linearized by successive substitution, and solved in a fully coupled manner using a sparse matrix technique. The specific details of the formulation of the direct solver approach can be found in Reference 17.

The adopted direct solver approach was implemented into a 2D version of CONCERT to simplify the overall effort. The relative performance of the direct solver, in terms of computational speedup, was assessed against the iterative approach in a series of 2D channel flow calculations. From the results of this study it was demonstrated that curvilinear coordinates make the relative performance between the direct solver and iterative approaches different from what is observed in cartesian coordinates. Increases in grid mesh points penalize the computer storage requirements and the cost, in terms of processor time, of the direct method more severely than the iterative method. For the iterative approach, the amount of processor time per iteration was shown to be proportional to the number of mesh points, N. The direct solver approach did converge more rapidly in terms of the number of iterations. However, the cost in processor time per iteration was found to be proportional to N^2. As such, the straight forward adoption of the direct solver sparse matrix approach was not a viable approach to achieve computational speedup in the 3D CONCERT model. However, the importance of retaining the coupling between the velocity and pressure fields was demonstrated by the vastly superior rate of convergence of the direct solver relative to the iterative method.

The purpose of the second study was to assess the effect in the overall rate of convergence of the iterative approach from the degree of convergence achieved in the solution of the individual equations in the inner iteration step. For typical combustor flows, the pressure correction equation, which is Poisson-like and hence inherently elliptic in nature, needs more iterative steps to converge than the momentum or scalar transport equations which are convection dominated. Typical rates of convergence for the various equations are shown in Figure 27. The use of line-SSOR (Symmetric Succession Over Relaxation) is found to provide substantially faster convergence than point-SSOR for the pressure correction equation. In either case, the pressure correction equation often needs an order of magnitude more iterative sweeps than the momentum and scalar transport equations to reach the same degree of convergence in the inner iterations steps.

In the initial development of CONCERT the linear equations were formulated and solved on a series of 2D planes comprising the 3D solution domain. Only one pass was made through the domain to avoid the need to recompute the coefficients. Although this procedure reduces the required computer storage, it is incapable of solving the linear equations to any arbitrary level of convergence within a given outer iteration. Consequently, a new procedure was developed in which the coefficients are calculated and stored over the full 3D domain. The resulting 3D equations are solved by repeated sweeps of point- or line-SSOR to the desired level of convergence.

The improvement in the overall convergence rate that results from solving the linearized equations at each step to a suitably close convergence is demonstrated by the results shown in Figure 27. Here the decay of the mass residual is shown for both the old and new procedures as a function of the number of outer iterations for a turbulent flow calculation in a curved 3D diffuser with a cross sectional shape varying from circular at the inlet to rectangular at the exit. It is observed that the improved solution of the pressure correction equation, resulting from the new approach investigated, causes the mass residual to decay much more rapidly and smoothly than in the existing procedure. However, in the new approach, more calculations are performed in the inner iteration layer, resulting in the consumption of more processor time per each outer iteration. The overall savings in processor time will not be as good as the improvement in convergence rate. It thus becomes apparent to look at approaches which can improve the computing efficiency of the solution of the pressure correction equation.

The results of these initial studies into improving computational efficiency demonstrated that some sort of compromise between the fully uncoupled iterative ap[illegible]ch

and the fully coupled direct solver approach was needed to achieve meaningful reductions in the computational time. What evolved was the selection of an approach involving a multistep pressure correction algorithm coupled with a multigrid scheme. Efforts in 1986 led to the development and assessment of this approach in the curvilinear coordinate framework of CONCERT.

The multiple step pressure correction algorithm developed is similar in spirit to the PISO (Reference 18) algorithm. The use of general curvilinear coordinates introduces a number of additional terms into the complete form of the pressure correction equation, which appears as:

$$A_P P'_P = A_E P'_E + A_W P'_W + A_N P'_N + A_S P'_S + A_F P'_F + A_B P'_B \qquad (a)$$

$$+((\rho U)_W - (\rho U)_E + (\rho V)_S - (\rho V)_N + (\rho W)_B - (\rho W)_F) \qquad (b)$$

$$+((U')_W - (U')_E + (V')_S - (V')_N + (W')_B - (W')_F \qquad (c)$$

$$+ \Sigma A_{NB} P'_{NB} \qquad (d)$$

Terms (a) and (b) make up the standard pressure correction equation as derived in the SIMPLE algorithm for cartesian coordinates, except that the contravariant velocity components U, V, and W appear in the mass imbalance term (b) here due to the use of a curvilinear coordinate system. Two additional terms also appear, with Term (c) representing a mass imbalance source term resulting from the velocity corrections at the neighboring points (a similar term also appears in the PISO algorithm) and Term (d) representing the additional neighboring points introduced as a result of the use of a nonorthogonal coordinate system. Since the complete pressure correction equation is virtually intractable in this form, approximations must be made to lead to a more suitable form. A predictor-corrector approach, which in Term (c) was evaluated using the corrections from a previous step, was selected as the most viable approach. Dropping Term (d) was found to lead to a more efficient and stable algorithm.

Test runs were made comparing the performance of the algorithm as a function of the number of corrector steps. For a turbulent flow through a rectangular channel with an asymmetric expansion, increasing the number of corrector steps from one to three did lead to an appreciable improvement in the rate of convergence, as shown in Figure 28. However, not as much improvement was noted for the more complicated flow in a typical annular combustor geometry, as shown in Figure 29. The combination of a highly nonorthogonal mesh around the dilution holes, and the strong coupling between the turbulence equations and the flow equations seems to reduce the improvement in convergence rate the new procedure can provide.

The computer time required to solve the pressure correction equation represents a sizable fraction of the total computational effort. Consideration of pressure correction methods with multiple corrector steps means that a number of pressure correction like equations need to be solved at each outer iteration, placing an even higher premium on efficient solution of the pressure correction equation.

In previous studies it was found that the pressure correction equation required many more sweeps of a point-SSOR or line-SSOR method to converge than either the momentum or the scalar transport equations. This is because the pressure correction equation is elliptic in nature while the other equations are convection dominated. It is well known that point and line iterative methods converge rather slowly on elliptic problems, particularly as the number of mesh points becomes large. The multigrid method (Reference 19), has been found to be very useful in accelerating the convergence of these solvers for elliptic equations. Another approach that has proven successful in accelerating the convergence is the, so called, additive correction method, Reference 20. In the approach selected for CONCERT, a multigrid correction method, which is a blend of both of these approaches, is applied to the pressure correction equation, with the goal of reducing the overall computer time required by the flow calculation. Corrections are assumed to be uniform over 2 x 2 x 2 blocks of the fine grid. These blocks make up the control volumes of a coarse grid level of a multigrid scheme. Equations for the corrections are formulated so that the corrected solution satisfies the conservation equations for the control volumes of the coarse grid, in the same way that the corrected solution satisfies the conservation equation over each grid line in the additive correction approach. Since the coefficients of the correction equations on the coarse mesh are merely sums of the fine grid coefficients, the calculation requires very little extra computational effort. In the context of a three dimensional calculation in a nonorthogonal coordinate system, the savings is substantial relative to the effort that is required to compute the coefficients independently for each grid level, as is often done in multigrid methods.

In the adopted approach, the fine grid is solved first, followed by the next coarser level, and finally the coarsest level. At present only these levels are used although extensions to more levels is possible. The generated corrections on the coarsest level are interpolated using trilinear interpolation onto the mid level grid, which is resolved, and finally, those corrections are interpolated back onto the fine mesh completing the cycle. A fixed number of sweeps of the point of line-SSOR procedure

is performed on each grid level. The performance of this multigrid algorithm for the pressure correction equation is illustrated in Figure 30 for a curved duct diffuser flow solved on a 46 x 22 x 22 mesh. The multigrid scheme is observed to provide significant improvement in the convergence rate of the pressure correction equation relative to the single grid.

Another essential step in the development of the 3D CONCERT model involved efforts to develop a generalized curvilinear grid generation method capable of accurately addressing the special features of the combustor geometry such as round dilution holes and cooling slots arbitrarily located on the contoured boundary walls. The special purpose grid generation code developed employs a combined use of elliptic partial differential equations and algebraic interpolation methods to generate the grid system.

The procedure starts by generating a 2D grid mesh on the side contour of the combustor geometry using prescribed grid clustering along the wall boundaries and mesh expansion ratio in the interior region. This 2D system is then rotated about the axis of symmetry (engine centerline), to form a full 3D section with a prescribed mesh spacing in the circumferential direction. A remeshing procedure is employed if there are dilution holes present on either surface. By defining the hole center location, and the hole radius, the elliptic equation method is employed to generate a new grid mesh with satisfactory smoothness over the mesh surface domain while conforming to the shape of the round holes. Any odd number of node points can be assigned within each hole to resolve the necessary details of the dilution jets. After the surfaces are remeshed, all interior mesh points are remeshed, using an algebraic interpolation method, to satisfy the clustering and smoothness requirements.

Figure 31 presents such grid meshes, for an isolated 18^{o} sector of an annular combustor, generated with the code. This figure also provides a comparison of dilution hole treatment within the generated mesh between the rectangular grid scheme used in the older 3D INTFLOW model, and this new curvilinear grid generator. The superiority of this improved approach are obvious. Further development of the curvilinear grid mesh generator is required to improve the grid detail for wall film cooling slots, and to address the 3D features of the inlet dome, especially in the circumferential direction. Work on these grid generation issues will be addressed as part of the continuing development of the 3D CONCERT model.

Having completed the basic development of the 3D CONCERT model, it was time to put it all together into a package usable by the engineering design community. The development of a menu driven "user friendly" package of supporting routines built around the 3D CONCERT model was completed in 1986. The package consists of eleven elemental routines which allow the user to build up a model problem, submit it for execution on a selection of available computers,and a post process the calculated results. Use of the package significantly reduces model set up time. A typical combustor problem can be set up and submitted for execution in about one hour. The preprocessor element of this package automatically generates the file for the 3D CONCERT model. As such, the chances for input errors are also significantly reduced. The execute element generates all of the job control language (JCL) required to submit the job on the designated computer system. This eliminates the need for the user to be familiar with the often complicated JCL required. The package also provides the user with file management to assist in passing information from step to step through the entire process.

With the completion of all initial development aspects of 3D CONCERT, the model was applied to perform a calculation of the internal flowfield for the GE/SNECMA CFM56 engine combustor, Figure 32. The high pressure core system of this engine is currently in use on several aircraft including the 737-300. The combustor configuration modeled represented the standard design. This modeling exercise served as the initial validation and demonstration of the 3D CONCERT model applied to real combustor flow problems. Combustor component test data in the form of detailed thermocouple measurements around the exit annulus was used to compare with the calculated results. A mesh of 52 x 25 x 37 grid points was used in the calculation permitting the use of three levels of multigrid. Illustrations of this grid mesh are presented in Figure 33. The combustor operating conditions including the flow levels through the various combustor mass injection features were decermined from available test data. The combustor inlet swirler and splashplate velocity characteristics were generated using existing experimental test data of axial, radial, and tangential (swirl), velocities at varying radii from the swirl cup axis of symmetry. These data were taken earlier using a five hole yaw probe, and are the same data used to generate the inlet swirler characteristics in the previously performed 3D INTFLOW modeling calculations. The inlet swirler and splashplate velocity features generated in the preprocessor using this data are shown in Figure 34.

This modeling calculation was run for 1250 iterations requiring about 1.75 hours of cpu time on the CRAY XMP-28 computer. The convergence history of the residuals for mass, momentum, and energy indicated that the solution was reasonably converged at this point. Figure 35 presents the calculated velocity field in the plane in line with the inlet swirl cup centers. A blowup of the dome region in line with the swirl cup centers is shown in Figure 36. This blowup view reveals the recirculation zones formed by the interaction of the swirl cup flow and the primary dilution jets. These velocity field results also serve to demonstrate the superior features of the curvilinear mesh used in CONCERT when compared to the earlier results obtained for the same combustor design using the cartesian mesh with the 3D INTFLOW model, Figure 12. In Figure 37 the calculated velocity field and gas temperature patterns at the combustor discharge plane

are presented. For comparison purposes, the measured exit gas temperature patterns obtained from rig testing this combustor are also presented in this figure. This temperature data was obtained from an array of thermocouple measurements around the entire combustor exit annulus, corrected to provide an integrated temperature rise of 99.5% of the ideal value. The presence of vortices in the exit plane flow is evident from this figure. These vortices have their origin from the secondary flows developed with the injection of the secondary dilution air into the combustor. Figure 37 also demonstrates that good agreement was achieved between the predicted exit gas temperatures and the adjusted measurements from the rig test. The modeling calculation does show a little more pattern than is evident from the test data, possible indicating less overall mixing generated by the model than is experienced in the actual combustor. Similar observations have been made in previous modeling studies using the first generation 3D INTFLOW model which, like 3D CONCERT, employs the two equation K-ε turbulence closure model. Another possible contributory cause may be the lack of "total" convergence of the solution. The temperature field is usually the last to completely settle out. Given the crudeness of the boundary condition details supplied to the model for each of the combustor flow injection features, especially the swirl cup, the generated results are clearly quite good.

This modeling exercise has successfully demonstrated the capabilities and superiority over first generation modeling technology provided by the 3D CONCERT model. While further validation of the model at this stage of development is necessary to provide a more thorough checkout, its release to the user community will provide them with an easy to use and very useful analysis tool to assist in the design and development of other aircraft gas turbine engine combustors.

5. PLANNED MODELING IMPROVEMENT ACTIVITIES

The completion of the initial development of the 3D CONCERT model has provided a superior analysis tool to the combustor design community. Efforts to further assess the capabilities of the new combustor model are applied to other GE aircraft gas turbine engine combustor designs are presently underway. These exercises will provide a demonstration of the modeling capabilities and limitations at this stage of development. The model will also begin to be used within the combustor design community as an analysis tool to assist in combustor development efforts. Being that this represents the initial release of the 3D CONCERT model, many modeling issues of concern to the designers have not as yet been addressed within its framework. However the new model does provide a new foundation on which to develop/implement the needed modeling improvements. The list of modeling improvement candidates is seemingly endless. As such, within the scope of this program it is necessary to assign priorities to these issues based on the perceived near term needs, and potential payoffs in selecting which ones to pursue. The following discussions briefly describe some of the modeling improvement activities currently in progress or planned in the near future.

At this time work is nearing completion on an improved release of a 2D/axisymmetric model package version of CONCERT. This package will provide the needed modeling capability to perform flow analysis in diffusers, swirl cups, or any 2D/axisymmetric duct of complex geometry. The ability to perform detailed computational analysis of complex swirl cup flows will provide a very useful tool for the designer to apply in what has generally been regarded as a challenging art. These swirl cup calculations will also provide the needed detailed inlet boundary condition information to supply to the 3D internal flow model. In a recent assessment of this modeling package, the model was applied to perform calculations for a series of 2D diffuser configurations from the Stanford experiments, (Reference 22). The calculated static pressure recovery variation with diffuser area ratio is shown to be in excellent agreement with the experimental results, Figure 38. This exercise also demonstrated the ability of the model to accurately predict which configurations would experience flow separations.

Work has also been progressing on the development of a combustor wall cooling model. This model employs a novel approach in which a boundary layer calculation is linked with the 3D internal flowfield calculation to provide predictions of the liner wall hot side heat transfer characteristics. This capability is needed to achieve improved 3D thermal analysis and life predictions for the combustor liner structures. The adopted boundary layer approach overcomes the deficiencies associated with the wall function treatment used in the 3D internal flow model. In its present state of development the wall cooling model is 2D parabolic in character . Some very initial assessments of this model have been encouraging, (Reference 23). It is planned to extend the model to 3D in the near future.

Compressibility for subsonic flows has already been introduced into the 2D/axisymmetric version of CONCERT and into the 3D version. It will be necessary to develop changes to the existing algorithm to permit transonic and supersonic flow conditions. This added capability will permit the application of the CONCERT modeling technology to high Mach number duct flow analysis such as the aircraft gas turbine engine augmentor system.

A liquid droplet spray modeling capability is presently under development for the 3D CONCERT combustor model. Because of the excessive computational intensity and storage requirements models of considerable complexity are not considered practical within the framework of the 3D model applied as a design tool. Several moderately

complex approaches which account for droplet size, evaporation, and momentum exchange with the surrounding flowfield are being considered, including a refinement to the Lagrangian approach.

Another area of planned activity is to introduce a form of finite rate chemistry into the model. The next level of complexity relative to the fast chemistry treatment currently employed is to add one more scalar variable and have it describe as complicated a kinetic scheme as possible. The two scalar approach has been carried to an advanced stage in hydrogen-air systems (Reference 24). A more complex three scalar model has also been developed for CO/H_2 flames, (Reference 25). The third scalar introduced spans the range between the CO frozen, and in partial equilibrium with the radical pool. Rather than a 2D matrix, the thermochemical system lies in a cube. This model has demonstrated the ability to account for the CO kinetics lagging with respect to the radical pool, and should, therefore, be applicable over a wider temperature range than the two scalar approach. It is planned to pursue the development of this approach for the CH-air system.

In the area of turbulence modeling much has been published about the deficiencies of the two equation K-ε model. Many have suggested the need to adopt the full form of the Reynold's stress equations. However, it is felt that at this time the excessive computational intensity associated with this approach is prohibitive for its introduction into a 3D model design tool environment. A less rigorous approach such as the algebraic stress model, for 2D CONCERT and a Richardson number correction for 3D CONCERT will be pursued as potential near term improvements. These approaches have demonstrated somewhat superior performance over the standard K-ε model, especially in the modeling of flows with high swirls.

Considerable effort and progress were made in providing improved computational efficiency during the development of the 3D CONCERT model. Recent applications of the model to real combustor flow problems has demonstrated a need for yet further improvement. In the near term it is planned to continue to optimize and streamline the coding to take the most advantage of the CRAY XMP-28 system available at GE. Future efforts may see a restructuring of the model to take advantage of parallel processing techniques associated with new computer system designs featuring clustered processor arrangements. The coding is presently undergoing modifications that will permit the use of the CRAY solid state disc device (SSD), as a sort of virtual memory device. In the adopted approach only the five planes of information necessary to generate the inputs to the local computational cells are loaded into the central memory. The rest resides on the SSD which currently has a memory capacity of 32 megawords. When fully implemented calculations using up to 450000 grid points could be solved using just one of the two 4 megaword processors of the current CRAY XMP-28 system. The extreme input/output speed of the SSD will result in very little penalty in total cpu time. This will permit very detailed analysis of flow problems within the currently available computer capacity.

In the area of grid generation, consideration is being given to adopting a zonal or block grid approach for the 3D CONCERT model. In this approach the physical domain is broken up into a number of separate zones. Each zone could be meshed separately as needed. The global flow problem transforms into a number of smaller flow problems. Linking the individual zones together must be done with care to assure that conservation is maintained across the interface boundaries. This approach offers many advantages. One of these is the added flexibility in meshing extremely complex geometries such as multichannel duct flows. Another advantage is the ability to couple with a zonal solution procedure. Different problem zones could be solved with a procedure different and more appropriate than for other zones. An example in point is the planned incorporation of the wall cooling model into the 3D internal flow model. Flow regions near the wall could be established as separate zones from the main internal flow. These boundary zones would be solved using the wall cooling model procedures under development. Yet another advantage of the zonal approach is its suitability to take advantage of parallel processing. One could hypothetically imagine global flow problems broken into a number of zones each solved on a separate processor of a clustered computer system. Another grid generation issue receiving considerable attention is the concept of adaptive grid solutions. The appealing aspect of the adaptive grid method is the ability to adjust the grid in an intelligent way to achieve improved accuracy without resorting to a priori knowledge and intuition of the modeler. An approach for 2D flow problems based on the concept of equidistribution has been developed, and has undergone considerable examination (Reference 26). As an example, the flow configuration shown in Figure 39 is a two dimensional planar channel flow with a one sided sudden expansion. The flow is isothermal and turbulent with an inlet Reynolds number of 2.5×10^5. This figure shows the original uniform and resulting adaptive grid systems and the numerical solutions obtained for each. It is seen from this figure that the adaptive grid solution yields a much sharper velocity gradient in the free shear layer region. The scale of flow variations in the lower wall region is also better resolved by the adaptive grid which has clustered more grid points there. As to the skewness of the mesh that can be introduced by the adaptive grid procedure, studies have shown that no noticeable effect on the overall numerical accuracy resulted. The development of a multi dimensional adaptive grid approach suitable for the 3D CONCERT model is a planned future improvement.

During the development of the 3D CONCERT model considerable effort went into addressing issues concerning the useability of the model. In its present form, the 3D CONCERT modeling package is an easy to use stand alone flow analysis tool. As a further significant improvement in this area, efforts to develop a comprehensive combustor

aerothermal workstation built around the 3D and 2D/axisymmetric CONCERT models have just been initiated. When completed the engineering workstation will provide the combustor design community a packaged and managed system with which the user will be able to perform a complete development study of a combustor from the preliminary design right through to predictions of the combustion system performance. The workstation data management will be compatible with existing mechanical design workstations to allow pertinent information to be passed between design groups. This workstation system will greatly enhance engineering productivity in the design and analysis of combustion systems.

6. CONCLUDING COMMENTS

The combustor aerothermal modeling technology development program has made considerable progress to date. Knowledge has been gained through the application and assessment of modeling technology to a wide variety of combustor flow problems, and through the development of the new second generation model 3D CONCERT. These activities have also demonstrated the usefulness of modeling technology, plus obtained acceptance within the combustor design community.

The payoffs to be obtained from the efforts of this program have only recently begun to be realized. It is felt that the modeling capability available at this time provides very useful and accurate predictions of the combustor internal flow features, and the exit gas temperature patterns . This useful capability will play a significant part in the reduction of lengthy and costly development testing efforts to achieve acceptable exit gas temperature patterns. It is clearly understood that many important modeling issues have yet to be addressed. The continued development and introduction of modeling improvements to address these issues will further enhance combustor modeling capabilities providing even greater benefits to the combustor design community. The ultimate payoff of these efforts becomes significantly improved engineering productivity in the design and development of combustion systems with overall superior performance achieved at considerably reduced costs. This represents the ultimate objective of the combustor aerothermal modeling technology development program.

LIST OF REFERENCES

1. Samuel, B.P., "A Jet Engine Combustor Design Analysis Suitable for Electronic Computers," ASME Paper 61-WA-305 (1961).

2. Mongia, H.C., et al., "Combustor Design Criteria Validation," UATL-TR-78-55A, 55B, 55C, February 1979.

3. Kenworthy, M.J., Correa, S.M., and Burrus, D.L., "Aerothermal Modeling Phase I Final Report," NASA CR-168296, November 1982.

4. "The Design and Development of Gas Turbine Combustors - Phase II Basic Computing System," VOL Report No. 1420, Northern Research and Engineering Corporation.

5. Walker, R.E. and Kors, D.L., "Multiple Jet Study Final Report," NASA CR-121217, June 1973.

6. Kenworthy, M.J. and Burrus, D.L., "Internal Flowfield Calculations for Annular Combustor Configurations," AIAA 84-1168.

7. Lapp, M., Drake, M.C., Penney, C.M., Pitz, R.W., and Correa, S.M., "Turbulent CO/H_2N_2 Jet Diffusion Flame in Coflowing Air," DoE *contract Report DE-AC04-78 ET 13146, 1983.

8. Green, A. and Whitelaw, J.H., "Measurements and Calculations of the Isothermal Flow in Axisymmetric Models of Combustor Geometries," J. Mech. Eng. Sci., 22,119, 1980.

9. Vu, B.T., and Gouldin, F.C., "Flow Measurements in a Model Swirl Combustor," AIAA Paper No. 80-007, 1980.

10. Lightman, A.J., Richmond, R.D., Magill, P.D., Krishnamurthy, L., Roquemore, W.M., Bradley, R.P., Strutrud, J.S. and Reeves, C.M., "Velocity Measurements in a Bluff-Body Diffusion Flame," AIAA Fifteenth Thermophysics Conference, Snowmass, Colorado, AIAA-80-1544, 1980.

11. Vinokur, M., "Conservative Equations of Gas Dynamics in Curvilinear Coordinate Systems," Journal of Computational Physics, Volume 14, pages 105 - 125, 1974.

12. Patankar, S.V., "Numerical Heat Transfer and Fluid Flow," Chapter 6, McGraw-Hill, New York, 1980.

13. Shyy, W., Tong, S.S., and Correa, S.M., "Numerical Recirculating Flow Calculation Using a Body Fitted Coordinate System," Numer. Heat Transfer 8, pages 99 - 113, 1985.

14. Pratt, D.T. and Wormeck, J.J., "CREK: A Computer Program for Calculation of Combustion Reaction Equilibrium and Kinetics in Laminar or Turbulent Flow," WSU-ME-TEL-76-1, Washington State University, 1976.

15. Richardson, J.M., Howard, H.C., and Smith, R.W., "The Relation Between Sampling Tube Measurements and Concentration Fluctuations in a Turbulent Gas Jet," Fourth Symposium (International) on Combustion, pages 814 - 81 , 1953.

16. Rhodes, R.P., Harsha, P.T., and Peters, C.E., "Turbulent Kinetic Energy and Analysis of Hydrogen-Air Diffusion Flames," ACTA Astronauti I, pages 443-470, 1974.

17. Shyy, W., and Braaten, M.E., "Comparison of Iterative and Direct Solution Methods for Viscous Flow Calculations in Body Fitted Coordinates," International Journal for Numerical Methods in Fluids, Volume 6, pages 325 - 349, 1986.

8. Braaten, M.E., Shyy, W., and Correa, S.M., "A Numerical Study of Flow in a Combustion with Dilution Holes," AIAA 86-0057, 1986.

19. Issa, R.I., "Solution of the Implicitly Discretized Fluid Flow Equations by Operator Splitting," Journal of Comp. Physics, Volume 62, pages 40 - 63, 1986.

20. Settari, A. and Aziz, K., "A Generalization of the Additive Correction Methods for the Iterative Solution of Matrix Equations," SIAM Journal of Numerical Analysis, Volume 10, pages 506 - 521, 1973.

21. Hackbusch, W., and Trottenberg, U. (Editors), "Multigrid Methods, Lecture Notes in Mathematics, Volume 960, Springer-Verlag, Berlin, 1982.

22. Reneau, L.R., Johnston, J.P., and Kline, S.J., "Performance and Design of Straight Two Dimensional Diffusers," Report PD-8, Department of Mechanical Engineering, Stanford University, 1964.

23. Mehta, J.M. and Burrus, D.L., "A Numerical Method to Predict Gas Turbine Combustor Film Slot Cooling Effectiveness," 8th International Symposium on Air Breathing Engines, June 1987.

24. Janicka, J., and Killman, W., "A Two Variable Formula for the Treatment of Chemical Reactions in Turbulent H_2-Air Diffusion Flames," 17th International Symposium on Combustion, The Combustion Institute, Pittsburgh, Pennsylvania, pages 421 - 430, 1978.

25. Correa, S.M., "A Model for Non-Premixed Turbulent Combustion of CO-H_2 Jets," 9th International Symposium of Combustion Processes, Wisla-Jawornik, Poland, 1985.

26. Shyy, W., "An Adaptive Grid Method for Navier-Stokes Flow Computation," Applied Mathematical Computations, 1986.

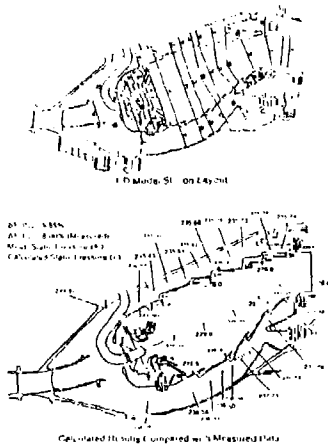

Figure 1. 1D COBRA Model and Predicted Results for CFM56 Combustor.

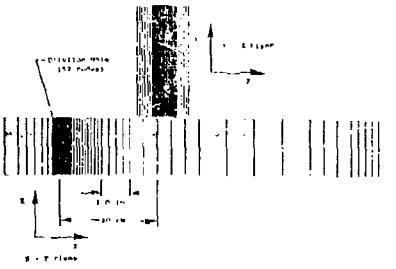

Figure 2. 50 x 26 x 32 Grid Mesh for 3D INTFLOW Model of Walker/Kors Dilution Jet Experiments.

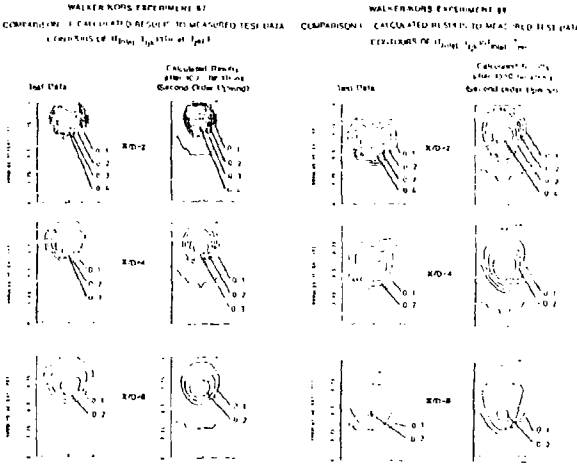

Figure 3. 3D INTFLOW Model Results for Walker/Kors Dilution Jet Experiments.

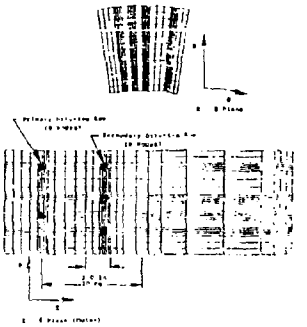

Figure 4. Coarse Grid Selection for Calculations of NASA/GE Experimental Test Configurations.

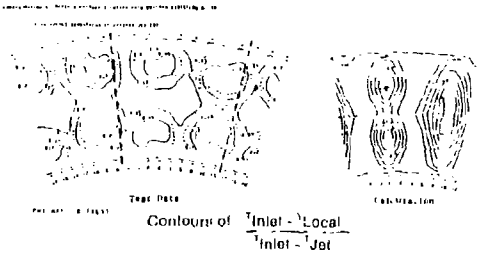

Figure5. Comparison of Measured and Calculated Results for Experimental Test Configuration 4.

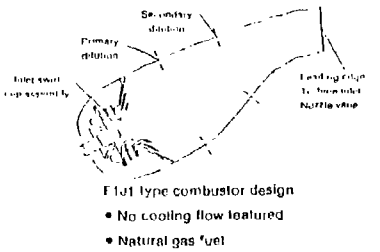

Figure 6. Modified CFM56 Sector Test Configuration.

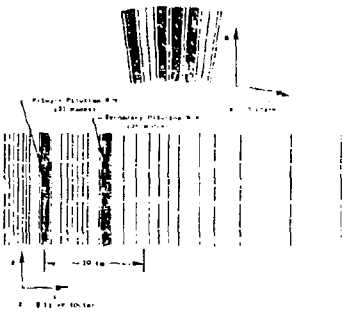

Figure 7. 40 x 21 x 38 Grid Mesh Used for Cylindrical Wall Model of Modified CFM56 Sector Combustor.

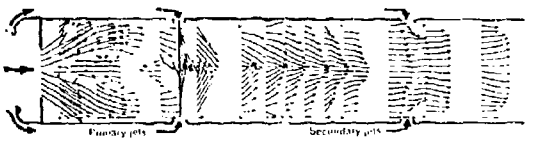

Figure 8. Calculated Velocity Field for a Combustor Using 3D INTFLOW Model (Without Stairstep Boundary Treatment).

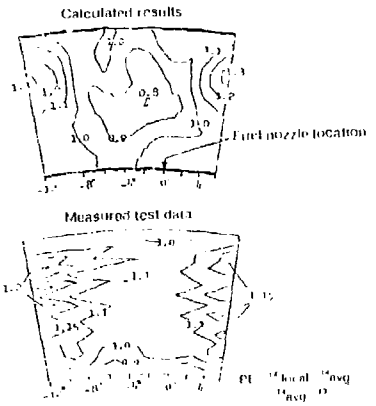

Figure 9. Calculated 3D INTFLOW Results for CFM56 Modified Combustor Using Cylindrical Liner Walls.

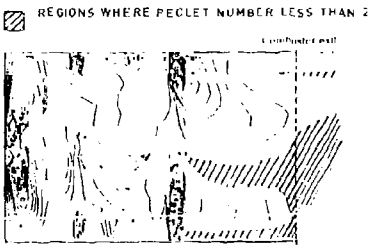

Figure 10. Calculated Y-Peclet Numbers for 3D INTFLOW Model of Modified CFM56 Sector Combustor.

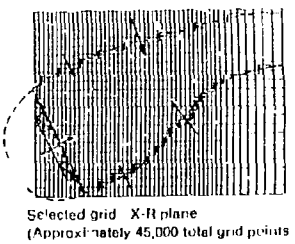

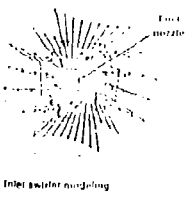

Figure 11. Grid Mesh with Stairstep Boundary Treatment Model of Modified CFM56 Sector Combustor.

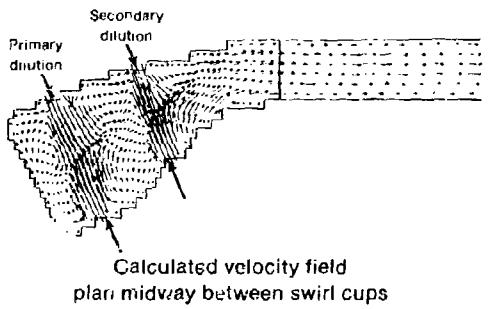

Figure 12. Calculated Results from 3D INTFLOW Model (Velocity Field).

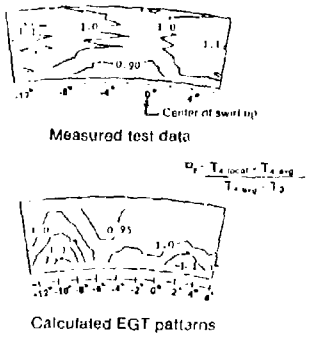

Figure 13. Calculated Results from INTFLOW Model (EGT Patterns).

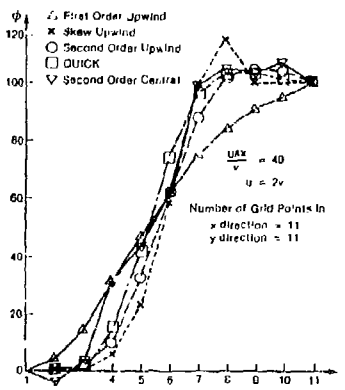

Figure 14. Numerical Solutions at X = 1 - 2Δx (Downstream Boundary Conditions: Gradient of $\phi = 0$ in Streamwise Direction).

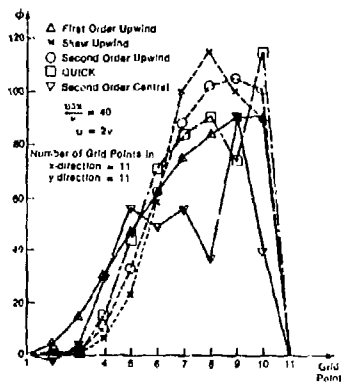

Figure 15. Numerical Solutions at X = 1 - 2Δx (Downstream Boundary Conditions: $\phi = 0$).

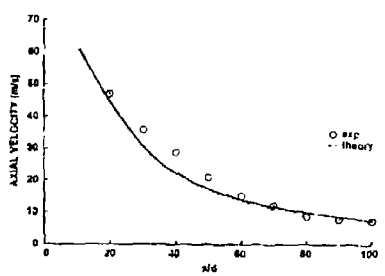

Figure 16. Centerline Profile of Axial Velocity.

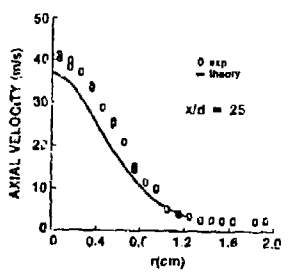

Figure 17. Radial Profile of Axial Velocity.

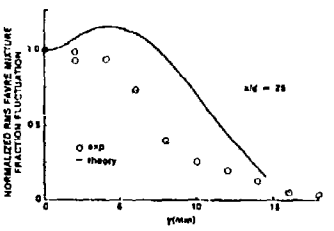

Figure 18. Radial Profile of Favre-Averaged Variance in Mixture Fraction.

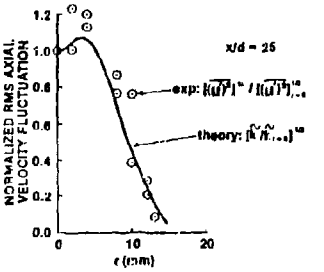

Figure 19. Radial Profile of Turbulence Kinetic Energy.

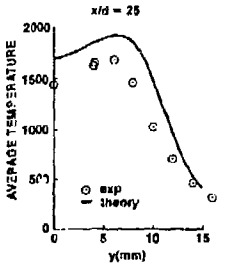

Figure 20. Radial Profile of Favre-Averaged Mean Temperature.

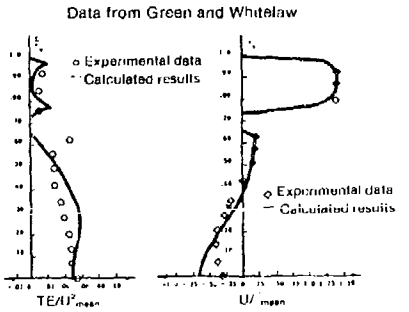

Figure 21. Radial Profile of Turbulence Kinetic Energy and Mean Axial Velocity at x/r_o = -0.61.

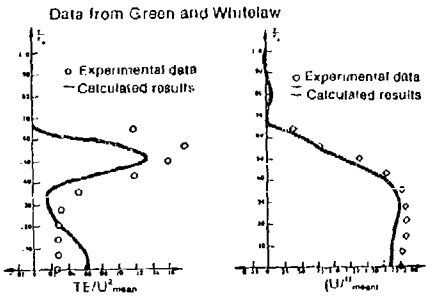

Figure 22. Radial Profile of Turbulence Kinetic Energy and Mean Axial Velocity at x/r_o = 2.7.

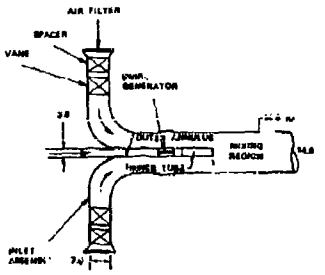

Figure 23a. Experimental Flow Assembly Schematic.

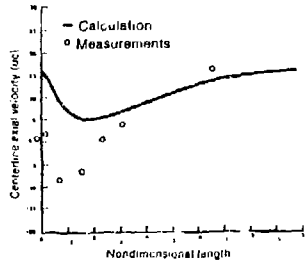

Figure 23b. Centerline Profile of Axial Velocity for Counterswirl Flow, k-ε Model.

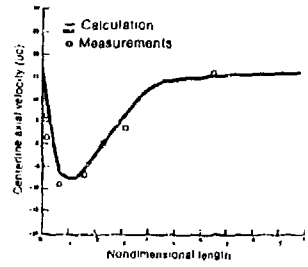

Figure 23c. Centerline Profile of Axial Velocity for Counterswirl Flow, Algebraic Stress Model.

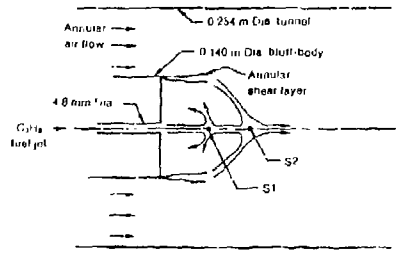

Figure 24a. Schematic of AFAPL Axisymmetric Bluff Body Flame Experiment.

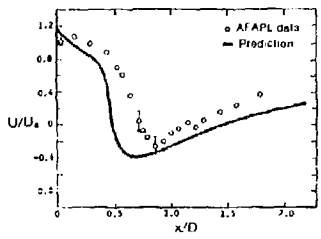

Figure 24b. Centerline Axial Velocity.

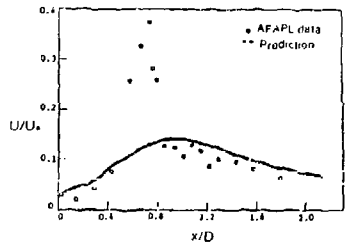

Figure 24c. Centerline Turbulence Kinetic Energy.

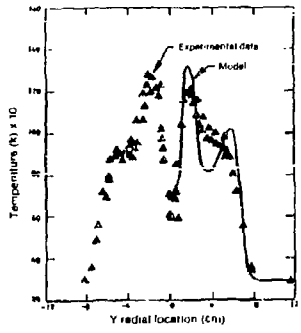

Figure 25a. Radial Temperature Profile at X/b = 0.43.

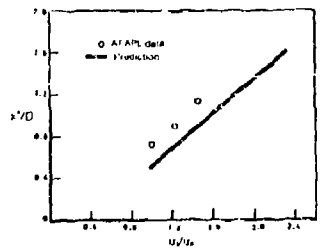

Figure 25b. Location of First Stagnation Point for Higher Jet Velocities.

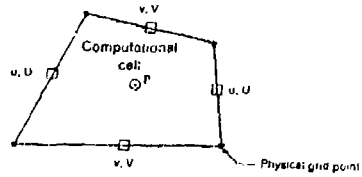

Figure 26. Staggered Grid Arrangement for CONCERT.

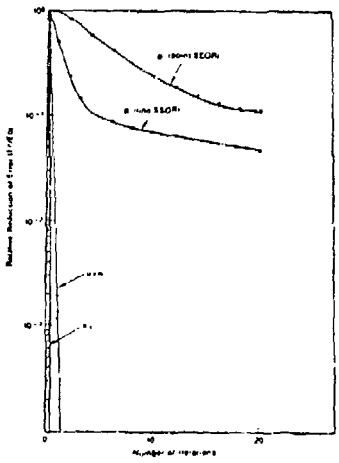

Figure 27a. Reduction of Error for the Various Equations.

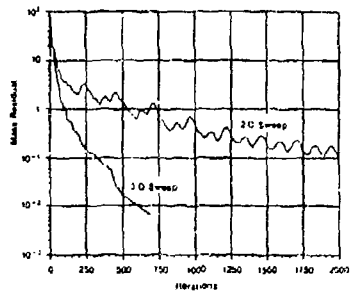

Figure 27b. Convergence Histories of Old and New Algorithms.

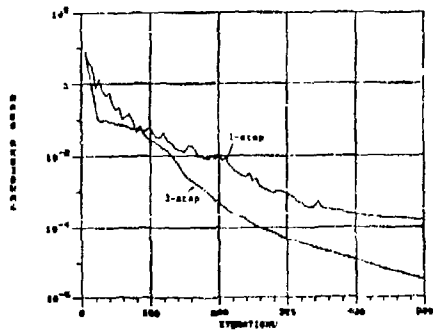

Figure 28. Comparison Between 3 Step and 1 Step Pressure Correction Methods for Turbulent Flow in a Rectangular Channel with an Axisymmetric Expansion, Re = 10^6.

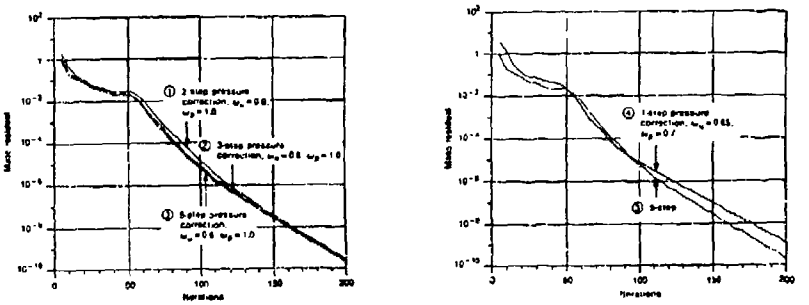

Figure 29. Effect of Pressure Correction Steps on Convergence Rate, Isothermal Flow in Combustor Configuration, 13x13x13 Grid, S = 0.6, Re = 10^4, 3 Level Point-SSOR (10% Tolerance) for Pressure, 1 Level Point-SSOR for all Other Equations.

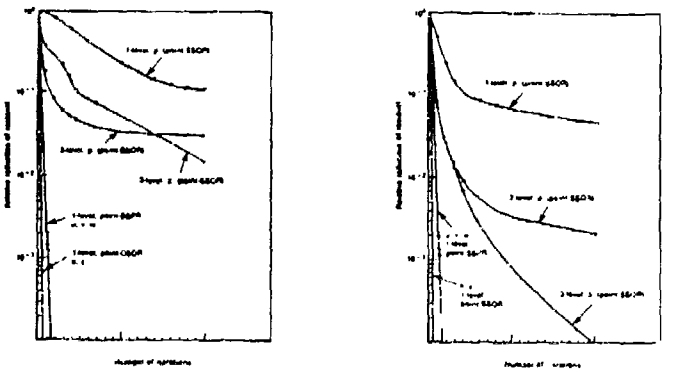

Figure 30. Typical Reduction of Residuals for the Various Equations Using Single or Multigrid Solver.

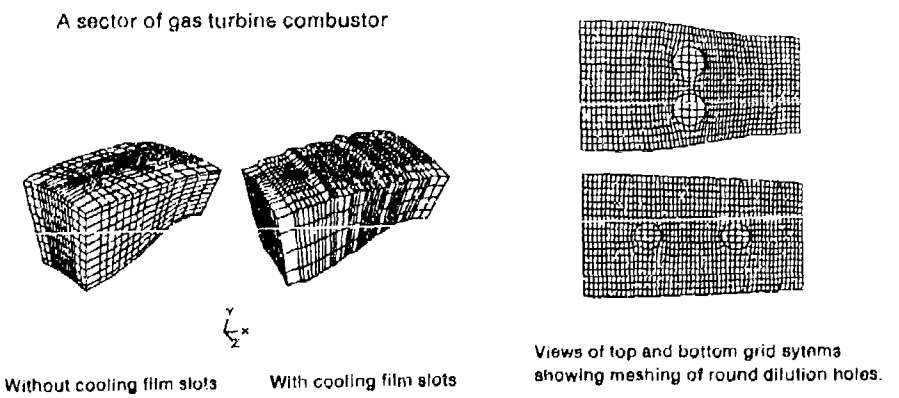

Figure 31. Curvilinear Grid Meshes for 3D CONCERT Modeling.

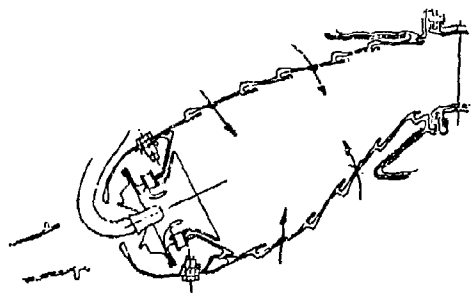

Figure 32. CFM56 Engine Combustor.

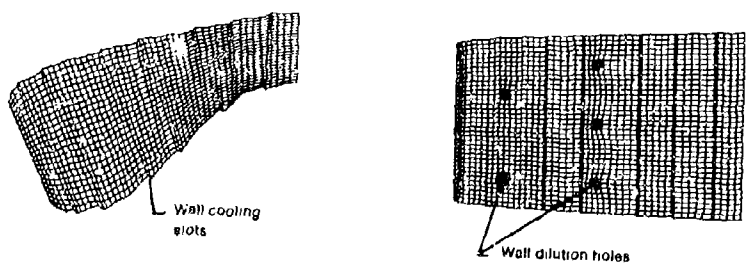

Figure 33. CFM56 Engine Combustor Model Grid Mesh (3D CONCERT).

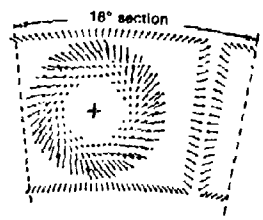

Figure 34. CFM56 Engine Combustor Inlet Swirler/Splashplate Modeling (3D CONCERT) Viewed from Forward Looking Aft.

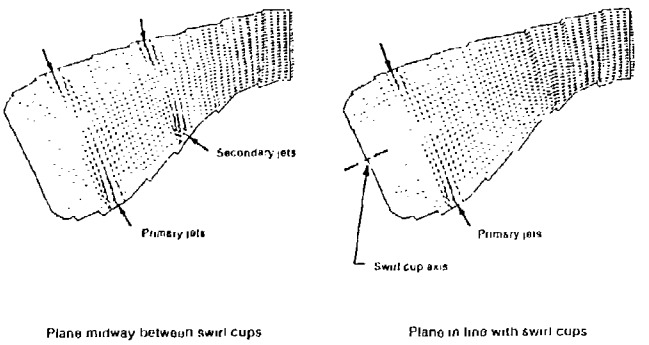

Figure 35. Calculated Velocity Field for CFM56-2 Combustor (3D CONCERT).

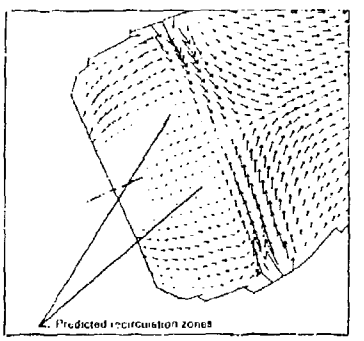

Figure 36. Blowup View of Dome Region in Line with Swirl Cups.

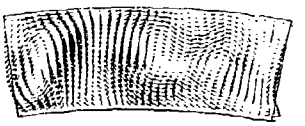

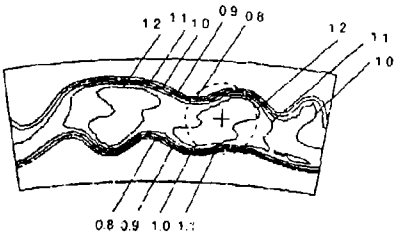

Calculated exit gas temperatures (P_t) $P_t = \frac{T_{local} - T_3}{T_{4,avg} - T_3}$

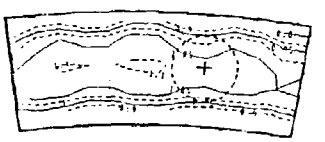

Measured exit gas temperatures (P_t)

Figure 37. Calculated Exit Velocity Field and Exit Gas Temperatures for CFM56-2 Combustor (3D CONCERT).

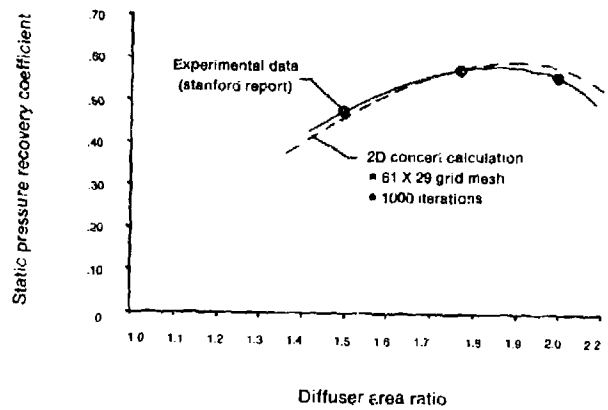

Figure 38. Comparison of Calculated vs. Measured Results for 2D Diffuser.

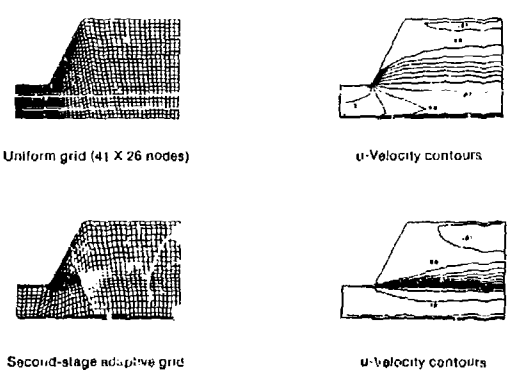

Figure 39. Grid Systems and Calculated Solutions for Flow in Expansion Channel (14x26 Grid), Re = 2.5 x 10^5.

DISCUSSION

G.Winterfeld, GE

You showed an impressive list of improvements of your modelling techniques; however, you still have to validate the codes against the exit temperature distribution. If you don't reproduce the time history of development of the temperature profiles inside the combustor, the validation of the codes remains rather by chance. Do you plan also to improve the experimental test case of the original combustor, not only models of parts of the combustor. Can you please comment on that point?

Author's Reply

Yes. I understand that we have a supporting test program using a variety of experimental techniques to acquire a benchmark quality data base. We will take data in reacting flow fields.

T.Rosfjord, US

After a 3D combustor calculation has been performed, how do you judge whether the predictions are 'good enough?" Do you target for a combustion efficiency? Emissions? Liner hot spots?

Author's Reply

In response to this question, we are presently focusing our modelling development to provide engineers with reasonably accurate predictions of the combustor exit gas temperatures. In particular, we are looking at the capability to predict EGT pattern changes resulting from dilution pattern or film cooling changes. This we feel is the greatest near term usefulness of modelling technology. In assessing how good is good enough, we have applied the new 3D model to a series of actual combustor flow problems for which EGT data is available, documenting pattern changes arising from dilution changes. What we are looking for here is, did the model predict the correct trends in the pattern changes, and are changes in hot spot levels correctly predicted? The examples presented represent a range in the quality of the prediction obtained to date for what would be considered useful for engineering design and development.

J.McGuirk, UK

I would like to comment on your statement that you currently only use a second order upwind scheme in the momentum equations. This means you use first order, numerically diffused, methods in the turbulence model equations and for mixture fraction. In several flows calculated at Imperial College, we have observed that it is equally necessary to use false diffusion free schemes in the turbulence equations and it is *very important* in the equation for mixture fraction, since this is a conserved scalar, and has no source terms to offset false diffusion effects.

Author's Reply

The selection of second order upwinding was based on a detailed assessment of hybrid, quick, skew upwind and several others. In this assessment second order upwind was not the best performer in each case studied. However, it represented an approach with formal second order accuracy unconditionally stable for all values of cell Peclet number and was straightforward to implement in the curvilinear coordinates. It does however exhibit under/over shoots due to its non-conservative nature. As such we employ it only for the convective terms in the momentum equation. As you point out, we have thus created a situation in which we solve the scalar and turbulence equations with hybrid numerics. It would be more rigorous to develop a bounded technique for second order upwinding and apply. In the solution of all the governing equations your comments are appreciated and we shall consider further numerical improvements of this kind.

J.B.Moss, UK

It is disconcerting to those of us working in combustion modelling, for example, as distinct from combustor modelling to find so many code developments proceeding in parallel without ranking of requirements or sensitivities. If we were to distinguish four elements: numerical procedures (difference schemes, mesh generation, solution algorithms); turbulence modelling, turbulence-chemistry interaction modelling; two-phase flow effects — what would be your ranking of priorities? The all-singing all-dancing code makes molecular testing and validation quite impossible.

Author's Reply

In reviewing my response, keep in mind that the objective of this project is the development of a combustor model which can provide useful predictions of gross internal flow features (exit gas temperature patterns), easy and economical to apply for the average combustor design engineer. To respond to this question we presently have a plan for future modelling activities which covers all of those areas you mentioned plus some others. We are presently working on several items from this large list. These are the things we feel we have the greatest near term need for. In selecting these items we have assessed the benefits and risks involved. Since our program is very small in scope we are looking for the best near term benefits with low risk involvement. As such, our list includes.

- 2 phase modelling capability to model fuels, droplet effects and perform low power analysis.
- 3D parabolic wall cooling model to couple with 3D elliptic internal flow calculation to provide a rigorous prediction of the flow/heat transfer characteristics at the walls.
- 2D/Axisymmetic model for analysis of swirl cup flows. We will implement 2 phase flow capability and improved turbulence modelling in this code prior to implementing the improvements in the 3D model.

A STATUS REPORT ON GAS TURBINE COMBUSTION MODELING

by

Hukam C.Mongia
Allison Gas Turbine Division
General Motors Corporation
PO Box 420 -- Speed Code T-14
Indianapolis, Indiana 46206-0420, USA

ABSTRACT

To effectively use multidimensional models for gas turbine combustor design and development activities, a method is presented to compute several thermal performance parameters including CO, unburned hydrocarbon, NO_x and smoke emissions; lean blowout and ignition fuel/air ratios, and pattern factor. To further improve modeling accuracy, advances are required in numerics and physical submodels of turbulence and spray transport processes. A status report is presented on the ongoing Allison modeling activities.

I. INTRODUCTION

Since the first two successful applications [1] of multidimensional combustion models to aid the design and development of gas turbine combustors, a number of combustion systems have been designed using the empirical/analytical design methodology as summarized in Reference 2. An extensive model assessment activities were conducted under a NASA sponsored program and reported in Reference 3. The major conclusions of References 2 and 3 are:

(1) current multidimensional combustion models provide qualitatively good comparison with measurements; and therefore they can be used as an adjunct to the conventional empirical design approach.

(2) Any further improvement in the predictive accuracy of analytical combustion models is predicated on accomplishing the following:

- o collect a benchmark quality data
- o develop numerical schemes with significantly lower numerical inaccuracy
- o conduct a systematic evaluation of current physicochemical models of turbulent reactive flows; and if needed, develop and validate new models
- o mathematical simulation of practical gas turbine combustor hardware

(3) Multidimensional models cannot realistically predict a number of design parameters including burner exit pattern factor; liner hot streaks; gaseous emissions (CO, unburned hydrocarbons and NO_x); exhaust smoke; lean blowout and ignition characteristics. Consequently, the combustion models have been used to provide qualitative guidance in arriving at innovative design concepts.

Since January 1984, Allison Gas Turbine Division of General Motors Corporation has been working hard in addressing the model deficiencies identified above under company and government sponsored programs. Some of these activities are reported in References 4 through 13.

Section II presents a second-generation combustor design system that predicts most of the combustor design parameters; this capability represents a significant improvement over the first generation design system based on Reference 1. Section III presents briefly the development of advanced numerical schemes[5,6], followed by turbulence model validation[7-9] in Section IV. Considerable effort is being expended at Allison [10-13] on spray formation and transport processes as described in Section V, followed by summary in Section VI. From this one can conclude that although some progress is being made in the modeling of turbulent combustion processes, much more needs to be done to improve the accuracy of multidimensional reacting flow calculations.

II. SECOND GENERATION COMBUSTOR DESIGN SYSTEM

The first generation combustor design procedure as outlined in Reference 1 has been very useful for developing a number of advanced combustors[2] that exhibited significant technology advances in combustor ΔT, heat release rate, L/H, pattern factor, lean blowout, ignition, liner cooling air flow requirement, wall temperature gradient, gaseous and smoke emissions. However due to many reasons, the analytical models have provided only qualitative guidance during combustor design and development phases.

Simple semi-analytical correlations have been successfully developed by Lefebvre[14] and Mellor[15] and their associates to predict combustor overall design parameters. Table 1, for example, presents a set of the correlations recommended by Professor Lefebvre. These correlations have evolved over a number of years and are based on the vast amount of experimental data for a number of engine combustors. Since these expressions have given good quantitative agreement with data over a wide range of operating conditions, they probably include most of the key parameters that govern the operation of the combustor. Professor Lefebvre has been able to correlate data from different combustors with a set of empirical constants C_1 through C_4 and C_8. However, to achieve this, engineering approximations have been made to fix some of the constants (e.g., f, f_c, $(f/a)_{st}$, V_c, and V_{ev}) whereas other constants (e.g., C_5, C_6, and C_7) vary from combustor to combustor. This approach has been very useful to correlate the available data and gain insight. Further work is needed to predict the effect of the design details (e.g., combustor dome, nozzle and primary jet details - vane angles, spray cone, airflow splits, primary orifice size and spacing) on combustor performance.

To predict accurately the combustion efficiency, CO, unburned hydrocarbons, NO_x and soot, significant improvements are required in numerics and turbulent spray combustion models; and this may take many years. Even then some sort of modeling will be required to predict other design parameters, e.g., pattern factor, lean blowout and ignition. Therefore, an alternative approach that combines the best of semi-analytical and multidimensional combustion modeling techniques may be very useful. In addition, improved calculation procedures are needed to accurately define the combustor liner boundary conditions, the near-wall hot-side convective flux, and radiative heat loading.

Table I.
Semianalytical Correlations Recommended by Professor Lefebvre[14].

$$CO = \frac{C_1 \; W_{a3} \; T_{PZ} \; e^{-C_2/T_{PZ}}}{P_3^{1.5} \; (V_c - V_{ev}) \; (\frac{\Delta P_L}{P_3})^{0.5}}$$

$$UHC = \frac{C_3 \; W_{a3} \; T_{PZ} \; e^{-C_4/T_{PZ}}}{P_3^{1.5} \; (V_c - V_{ev}) \; (\frac{\Delta P_L}{P_3})^{0.5}}$$

$$NO_x = C_4 \; P_3^{1.25} \; e^{0.01 \; T_{ST}} \; (\frac{V_c}{W_{a3} \; T_{PZ}})$$

$$S_F - S_{OX} = (18 - H)^{1.5} \; P_3^{2.0} \; (\frac{F/A}{f W_{a3} \; T})_{PZ} \; [C_5 - C_6 (\frac{0.0011 \; T}{F/A})_{SZ}]$$

$$\eta_c = \eta_\theta \; \eta_{ev} \; \eta_{mix}$$

$$\eta_\theta = 1 - \exp \; [-0.042 \; P_3^{1.3} \; \frac{V_L}{f_c W_{a_3}} \; e^{\frac{T_c}{400}}]$$

$$\eta_{ev} = 1 - \exp \; [-36 \times 10^6 \; \frac{P_3 \; V_c \; \lambda_{eff}}{T_c^2 \; D_o^2 \; f_c \; W_{A3}}]$$

$$\eta_{mix} = f \; [(\frac{P_3 A_L}{W_{a3} \; T_3^{0.5}}), \; (\frac{\Delta P_L}{P_3})^{0.5}]$$

$$LBO \; F/A = C_7 \; (\frac{f \; W_{a3}}{V_c \; P_3^{1.3} \; e^{13/C30}}) \; (\frac{D_o^2}{\lambda_{eff}})_{LHV}$$

$$FF = 1 - e^{-C_8 P_L / (\frac{\Delta P_L}{Q_{ref}})(L_L - L_{av})}$$

A second-generation combustor design system, as shown in Figure 1, is being developed at Allison. This approach has given good agreement with data from a number of combustors as discussed in the following paragraphs.

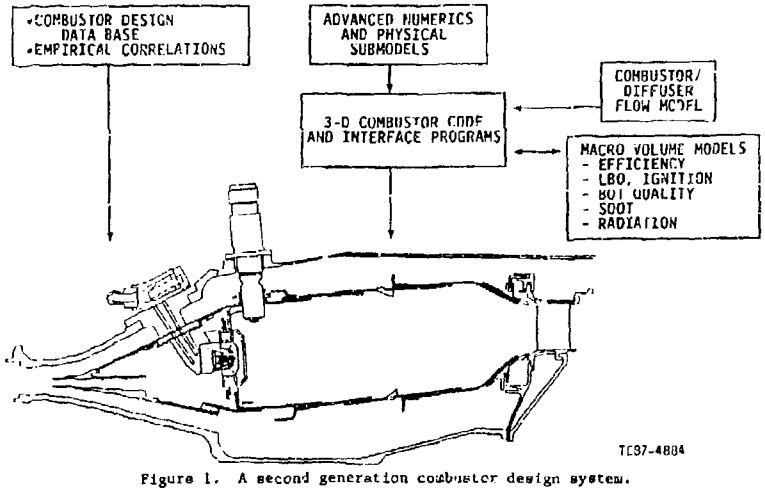

Figure 1. A second generation combustor design system.

Table II presents the macrovolume correlations that have been used to predict CO, unburned hydrocarbons, NO_x, soot concentration, combustion efficiency, pattern factor, and lean blowout fuel/air ratios. The expressions within the square brackets (as predicted by the 3-D combustor model) are summed over each of the control volume unit. The seven independent empirical constants of Table II need to be fitted with the available combustor data base. It is hoped that one set of these constants will fit the entire data base. To date, a number of engine combustors have been used for validating this approach. A typical comparison is discussed in the following paragraphs for three classes of combustors, namely can-annular, inline and reverse flow annular combustors.

Figure 2 presents typical measured CO emission index for inline and reverse flow annular and can-annular combustors as denoted by open circles, squares and diamonds; the corresponding predictions are shown in solid symbols. The comparison covers over a broad range of engine operation from idle to maximum power. The agreement is good. Similarly, the comparison between predictions and data is good for unburned hydrocarbons, NO_x and smoke as shown in Figures 3, 4, and 5, respectively.

Lean blowout fuel/air ratios during startup and at idle points, and pattern factor can be presented as a function of a number of parameters. Figure 6 presents the LBO data (open symbols) as a function of $V_R\delta\theta$ where V_R, δ and θ represent liner reference velocity, compressor discharge pressure and temperature, respectively. Model predictions (denoted by solid symbols) agree well with data. Figure 7 presents predicted and measured pattern factor values of different combustors as a function of $(\Delta P/q_3)\ L/H$ where $\Delta P, q_3$, L and H are combustor liner pressure drop, compressor discharge dynamic head, combustor liner length and channel height, respectively. Again good correlation is obtained between data and predictions.

Table II.
Macrovolume Expressions.

CO: $$\frac{A_1}{P_3^{1.5}}\left[\frac{M_A M_B T\, e^{-0.005T}}{V\left(1-\frac{M_{ev}}{M_f}\right) T_u^{0.5}}\right]_{ijk}$$

UHC: $$\frac{A_2}{P_3^{2.5}}\left[\frac{M_A M_B T\, e^{-0.00345T}}{V\left(1-\frac{M_{ev}}{M_f}\right) T_u^{0.5}}\right]_{ijk}$$

NO_x: $$A_3 P_3^{1.25}\, e^{0.01T_{st}}\left[\frac{V}{T}\frac{M_B}{M_A}\right]_{ijk}$$

Soot Formation

$$S_F:\ A_4\,(18-H)^{1.5}\,P_3^{2.0}\left[\frac{(F/A)\,M_B}{T\,M_A\,T_u^{0.25}}\right]_{ijk}$$

Soot Oxidation

$$S_{ox}:\ A_5\,(18-H)^{1.5}\,\frac{P_3^{2.0}}{V}\left(\frac{F/A}{T}\right)_{PZ}\left[\frac{V\,e^{0.0011T}}{M_A\,F/A}\right]_{ijk}$$

$$\eta_c = \eta_\theta\,\eta_{ev}\,\eta_{mix}$$

$$\eta_\theta:\ 1-\exp\left(-A_6 P_3^{1.3}\left[V\frac{M_B}{M_A}e^{\frac{T}{400}}\right]_{ijk}\right)$$

$$\eta_{ev}:\ 1-\exp\left(-A_7\left[\frac{M_f}{M_{ev}}M_B\right]_{ijk}\right)$$

$$\eta_{mix}:\ 1-\exp\left(-\frac{A_8}{V}\left[\frac{T_u V}{M_A}\right]_{ijk}\right)$$

LBO F/A: $$\frac{A_9}{LHV}\,P_{3design}\left(\frac{W_{a3}}{P_3^{1.3}e^{T3/300}}\right)\left(\frac{t}{F}\right)_{PZ}\left[\frac{M_{ev}}{T}\frac{M_B}{M_A M_f}\right]_{ijk}$$

PF: $$1-e^{-A10/\left(\frac{L_L-L_{ev}}{D_L V}\left[\frac{T_u^{0.5}V}{M_A}\right]_{ijk}\right)}$$

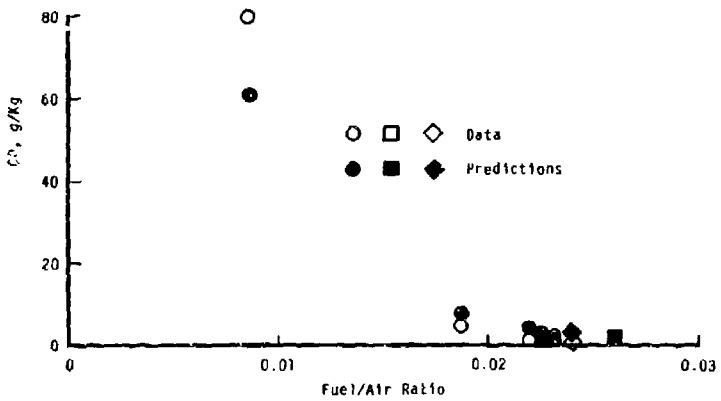

Figure 2. Predicted and measured CO (carbon monoxide) emission index for in-line and reverse-flow annular and can-annular combustors.

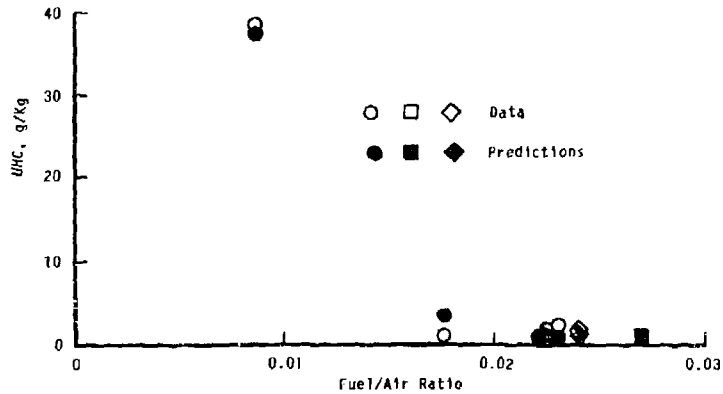

Figure 3. Predicted and measured unburned hydrocarbons emission index for in-line and reverse-flow annular and can-annular combustors.

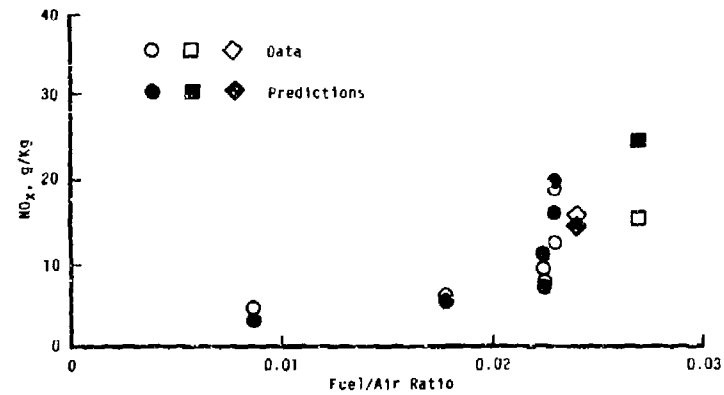

Figure 4. Predicted and measured NO_x emission index for in-line and reverse-flow annular and can-annular combustors.

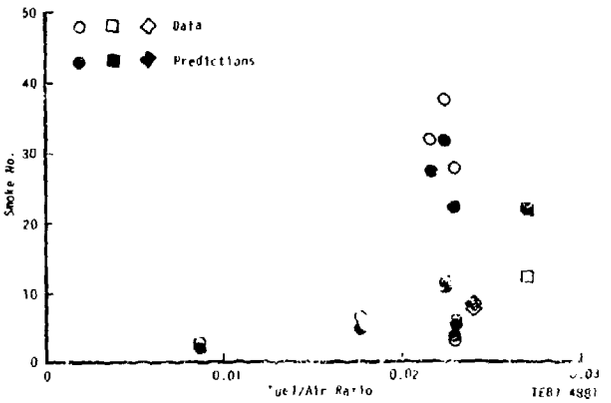

Figure 5. Predicted and measured SAE smoke numbers for in-line and reverse-flow annular and can-annular combustors.

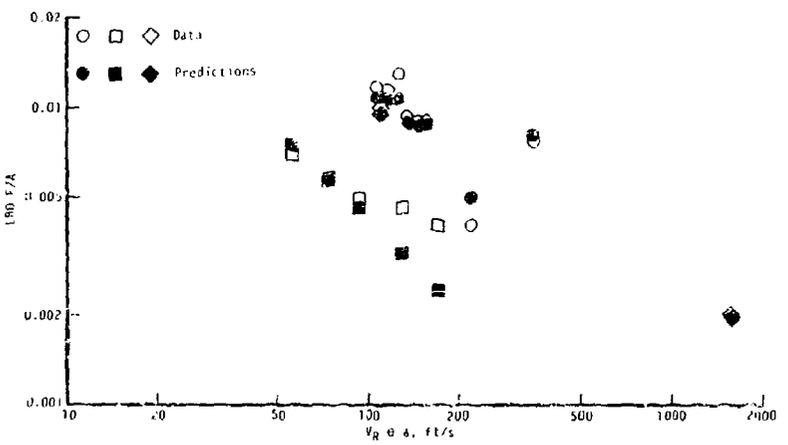

Figure 6. Predicted and measured lean blowout fuel/air ratios of in-line and reverse-flow annular and can-annular combustors.

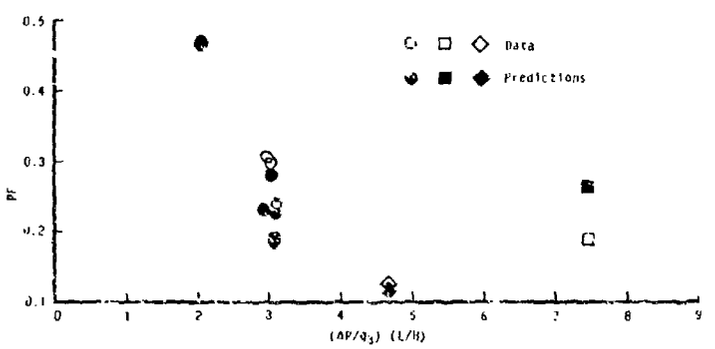

Figure 7. Predicted and measured patterns factors of in-line and reverse-flow annular and can-annular combustors.

Combustor liner durability is affected by liner wall temperature levels and gradients and attendant thermal induced stresses. It is therefore important to accurately predict liner hot streaks and how they are influenced by combustor design details. To obtain accurate estimate of liner wall temperature, it is essential to include the radiation flux contribution from its various combustor zones onto each wall segment. This can be easily done when the detailed 3-D combustor flow field is known. Radiation flux to a wall segment ℓ is given by $R_\ell = 0.5\ \sigma\ (1+\epsilon_w)\ \sum[F\ \epsilon_g\ T^{1.5}\ (T^{2.5} - T_{w\ell}{}^{2.5})]_{ijk}$. Here σ, ϵ_w, ϵ_g, F, T and $T_{w\ell}$ are Stefan-Boltzmen constant, wall emissivity, gas emissivity, radiation view factor, gas and wall temperatures, respectively. Simple expressions are used for computing convection contribution to and from the wall. Such a procedure has given good correlation with measured data.

Figures 8 and 9 are typical predicted wall temperature contours for the outer and inner diameter liner walls of an inline through flow annuler combustor; the results shown are for a one-nozzle sector un-

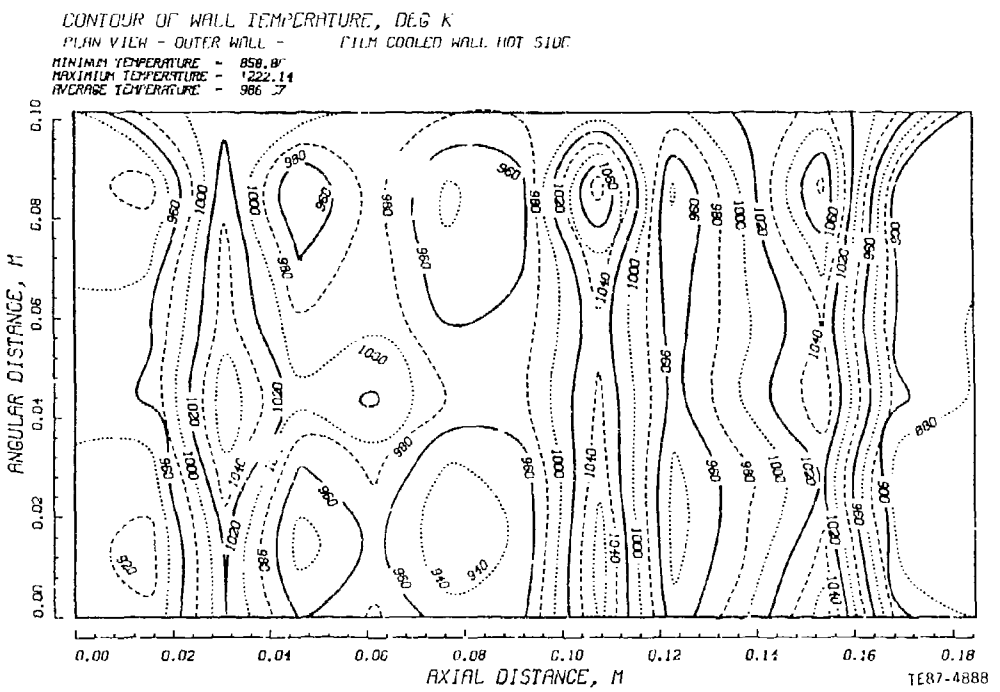

Figure 8. Typical predicted outer diameter liner wall temperature distribution.

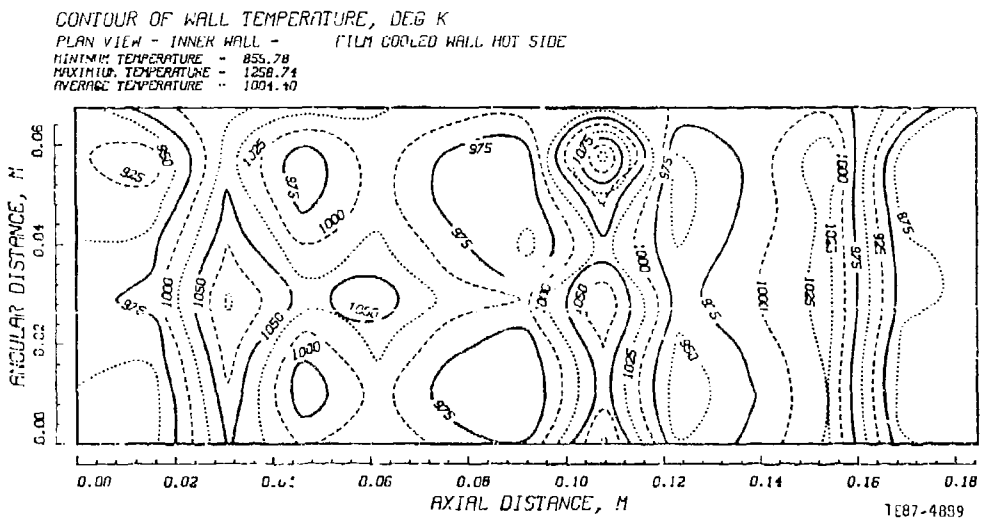

Figure 9. Typical predicted inner diameter liner wall temperature distribution.

wrapped. From these figures one can see a number of hot and cold spots. For example, the predicted average OD wall temperature (from Figure 8) is 986°K whereas the maximum wall temperature is 1222°K.

III. ADVANCED NUMERICAL SCHEMES

Over the past two decades significant advances have been made in numerical schemes in regard to discretization, profile assumptions and solution algorithms. A limited literature review is given in References 5 and 6, where the details are presented on the two advanced numerical schemes for application to gas turbine combustor flows. These schemes are briefly described in the following paragraphs.

For most practical problems, the central differencing scheme (CDS) would be ideally suited if it were unconditionally stable. The CDS is a simple second-order accurate scheme which is easy and straightforward to implement. However, for grid Peclet numbers larger than 2, the CDS can lead to over- and under-shoots and is unstable. The hybrid (upwind/CDS) scheme is stable for all Peclet numbers but suffers from excessive false diffusion. An alternate scheme named CONDIF (for COntrolled Numerical Diffusion with Internal Feedback) has been devised[5] to have unconditionally positive coefficient and still maintains the essential features of the CDS and its second-order accuracy.

CONDIF employs the central differencing when $P_e \leq 2$. At points where $P_e > 2$ and the dependent variable varies monotonically, a modified central differencing scheme is used. Otherwise, the upwind scheme is used. CONDIF employs numerical diffusion just enough to ensure stability based internally on the field distribution of the variable rather than switching to upwind differencing as soon as P_e exceeds 2. Since upwinding is done only at relatively few grid points, CONDIF essentially maintains the second-order accuracy of the central differencing scheme.

Another advanced numerics called flux-spline that has been developed[6] is based on a linear variation of total flux (convection and diffusion) between two grid points. This represents an improvement over the assumption of uniform flux used in hybrid schemes. The linear flux variation leads to an expression that includes the effect of multidimensionality as well as the source terms. Consequently, the numerical error is reduced.

An attractive feature of CONDIF and flux spline schemes is that their extension to three-dimensional flows is relatively straightforward. The resulting finite difference equations involve only seven points as opposed to 27 points used in many skew upwind schemes.

Both of these schemes have been used to solve a variety of analytical, 2-D laminar and turbulent flows[5,6]. As an example, results for a square driven cavity are presented here. This flow is characterized by a strong recirculation zone typical of many physical situations. The problem was solved with a uniform 22 x 22 grid using different scheme; and the results were compared with a very fine grid (82 x 82) hybrid solution. The velocity profiles at the midsection of the cavity are shown in Figure 10. Both CONDIF and flux spline show improvement over the hybrid scheme; e.g. solution of flux spline with (22 x 22) grid compares well with (82 x 82) grid hybrid solution

In addition to the need for improved numerical accuracy, an important aspect of the fluid flow calculations is the treatment of interlinkages between various transport equations. This issue is especially important in the primitive variable formulation for incompressible flows since the momentum and continuity equations are coupled through the pressure field but no explicit equation exists for the evaluation of pressure.

Normally the equations are solved in a segregated manner and the velocity pressure coupling is handled using the SIMPLE algorithm or its variants. In this approach the continuity and momentum equations are combined to obtain an equation for pressure (or a related quantity) and the equations are solved in a decoupled manner. The success of this approach depends heavily on a proper choice of the under relaxation factors. Moreover, the convergence rate deteriorates significantly beyond a certain number of grid points.

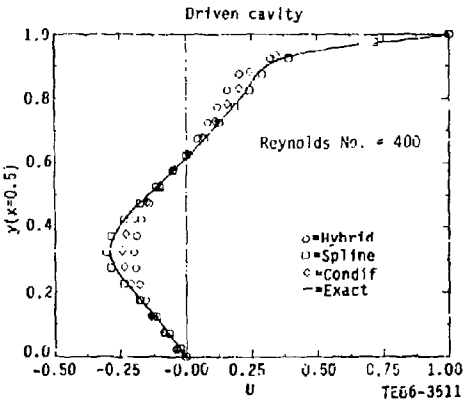

Figure 10. Velocity profiles at the midsection of the cavity.

An alternate to the SIMPLE-like approach is to solve the equation in a coupled manner. For this purpose coupled solvers with point, line, or direct whole domain inversion have been developed. Here, we will discuss whole domain inversion technique wherein a direct solution of the whole set of continuity and momentum equation is obtained. Thus, the coupling between the various equations is implicitly retained. The velocities and pressures are updated simultaneously and iterations are required only for resolving the nonlinearities in the equations. Our approach, similar to that of Vanka, and Braaten, uses the Yale sparse matrix package (YSMP) for inverting the matrix. YSMP solves the linear system equation AY = B by a sparse matrix variation of the LU decomposition procedure, where L and U are the lower and upper triangular matrices. Even though the cost of matrix inversion is large, the total computation cost is rather small due to the few number of iterations required to achieve convergence.

Previous work on the direct inversion technique (DIT) has been limited to lower-order schemes, e.g. hybrid. We have combined DIT with flux spline differencing technique so that more accurate numerical predictions can be obtained at computer costs comparable with current numerics.

To demonstrate the advantage of this scheme over the SIMPLE-Hybrid based scheme, a number of problems have been calculated. Here we present the results of two problems (laminar flow in a driven cavity, and turbulent flow over a backward facing step) in regard to the saving in computer time for the same level of numerical accuracy. Table III summarizes the results which show that for the driven cavity problem the current scheme with 82 x 82 grids is comparable in accuracy with 22 x 22 grids of flux-spline and direct solver; the former requires 572 seconds whereas the latter takes 6 seconds of CPU time, giving a speed factor of 95 or 99% reduction in computer time. For the turbulent backward facing step problem, the speed factor of 15 corresponds to a 93% reduction in computer time.

Table III.
Flux spline with a direct solution algorithm.
IBM 3081 CPU time, seconds (Grid)

Test Problem	SIMPLE and Hybrid	Flux spline and Direct Solver	Speed factor
Laminar Driven Cavity R_e = 400	572 (82 x 82)	6 (22 x 22)	95
Backward facing step Turbulent Flow	890 (62 x 32)	58 (42 x 22)	15

IV. TURBULENCE MODELING

A number of turbulence modeling investigations have been reported over the years for application to gas turbine combustion flow fields; and these have included the use of k-ε, Reynolds stress algebraic and differential models (RSA, RSD). These investigations have contributed significantly in identifying the strength and weaknesses of the models, and it is generally agreed that although general features of the flow field are well predicted by the second-order closure models, a systemetic validation effort is required to further improve these models and to develop advanced models. A good quality data is obviously needed in addition to advanced numerics to assess model accuracy.

The k-ε model is the simplest model that is suitable for recirculating flow calculations. This model achieves closure by using a gradient transport model for Reynolds stresses by using an isotropic eddy viscosity. For the flows where the isotropic eddy viscosity assumption is not valid, the k-ε is either modified (to include the effect of low Reynolds number, streamline curvation and swirl) or replaced by algebraic stress models (RSA). RSA can be classified into two categories: equilibrium (RSA/E) and nonequilibrium models. RSA/E is based on a local equilibrium assumption whereby the convection and diffusion terms are neglected compared to the local production and dissipation of turbulence. In the nonequilibrium models the convection and diffusion terms are approximated, e.g. Mellor and Yamada[16] (RSA/MY) and Rodi[17] (RSA/R).

In the flow situations where it is not possible to approximate or neglect convection and diffusion terms, the six Reynolds stress transport equations along with at least one length scale equation, e.g. ε-equation, need to be solved (RSD).

The results of a number of RSA and RSD turbulence models have been compared with available data during the last two years with the SIMPLE-Hybrid based computer code. Figure 11 shows a typical comparison of the three turbulence models (k-ε, algebraic stress model and Reynolds stress model) with the mean axial velocity profiles measured by Johnson and Bennett[18] at X = 13, 51, 102, 152, 203, 254 and 305 mm, respectively.

Although the agreement between models and predictions is enccuraging, one cannot make any definite conclusions about which of the three turbulence models is superior because a number of issues still need to be resolved, e.g. numerical accuracy, boundary conditions and accuracy of the data. This is currently under progress, e.g. grid independent solution with the k-ε model for two 2-D recirculating flow cases is presented in Reference 6. We will continue our effort to establish how far second-order closure models can be extended for application in gas turbine design method.

In parallel we have been working on developing a joint probability density function (PDF) transport equation approach for solving recirculating swirling flow problems as encountered in gas turbine combustors. This effort[9] is based on the extension of the PDF transport approach of Professor Pope and his associates[19] that has been validated with a number of simple flows with and without reaction. The PDF approach involves the solution of the evolution equation of the velocity-composition joint PDF. The joint PDF, $f(\underline{V}, \psi, \underline{x}, t)$, is the probability density of the simultaneous event $\underline{U}(\underline{x}, t) = \underline{V}$ and $\phi(\underline{x}, t) = \psi$, where $\underline{U}$, ϕ, $\underline{x}$ and t denote velocity vector, a set of scalars, spatial coordinates and time, respectively. The PDF approach is ideally suited for solving complex reacting flows due to the following reasons:

- significantly less computer time will be required compared to direct numerical simulations
- since convection, variable density, chemical reaction rates, and mean pressure gradients appear in closed form, many of the closure issues of current turbulent combustion models are avoided altogether
- the approach is extendable to multistep chemical reactions most appropriate for JP fuels
- a realistic stochastic spray combustion simulation can be easily incorporated in the joint PDF approach

A multiyear PDF effort is currently underway to settle a number of issues involving modeling, solution strategy, numerics and validation. The feasibility of the approach has recently been demonstrated[9] as applied to a backward facing step. Figure 12 through 14 show typical comparison of predictions with the measured data of Pronchick and Kline[20]. The calculations were made with k-ε, RSA, RSD and PDF models for a uniformly distributed 52 x 32 grid. All four turbulence models show essential features of the axial velocity field as shown in Figure 12. Here X denotes $x-x_R/x_R$, where x is the axial distance from the step and X_R is the reattachment length. Similarly, PDF, RSA and RSD give general trends of $\langle u'^2 \rangle$, $\langle v'^2 \rangle$ and $\langle u'v' \rangle$ as shown in Figures 13, 14 and 15. Like the second-order closure models, work is in progress to further improve PDF calculations.

V. ATOMIZATION AND SPRAY TRANSPORT PROCESSES

Gas turbine combustor performance, durability and fouling are strongly influenced by fuel injector design and its interaction with swirler and dome detail design. It is therefore important to fully understand various processes occuring within and around the fuel nozzle. The specific areas that are being addressed include aerodynamics within the complex passages of the atomizer, fuel filming, ligament formation and breakup, atomization, convection and diffusion transport of spray droplets, evaporation, mixing and combustion.

The predictions of air flow velocities within the nozzle passage was originally carried out using a body-conforming, curvilinear orthogonal grid[7]. Now it is done with a more generalized nonorthogonal coordinate system that also includes coupling between the injector, swirler and the shroud. The liquid film thickness is calculated based on the interfacial friction factor between the airstream and liquid film. The breakup of the liquid sheet into ligaments and drops is governed by the balance of the forces caused by air velocity, surface tension, liquid inertia and viscosity. The time needed for the disturbance wave to grow to maximum value at breakup is determined from the resulting equation of motion. The average length of ligaments and initial droplet size are calculated through an iterative procedure. The secondary atomization is based on the rate of removal of fluid stripped off the surface by the high velocity stream.

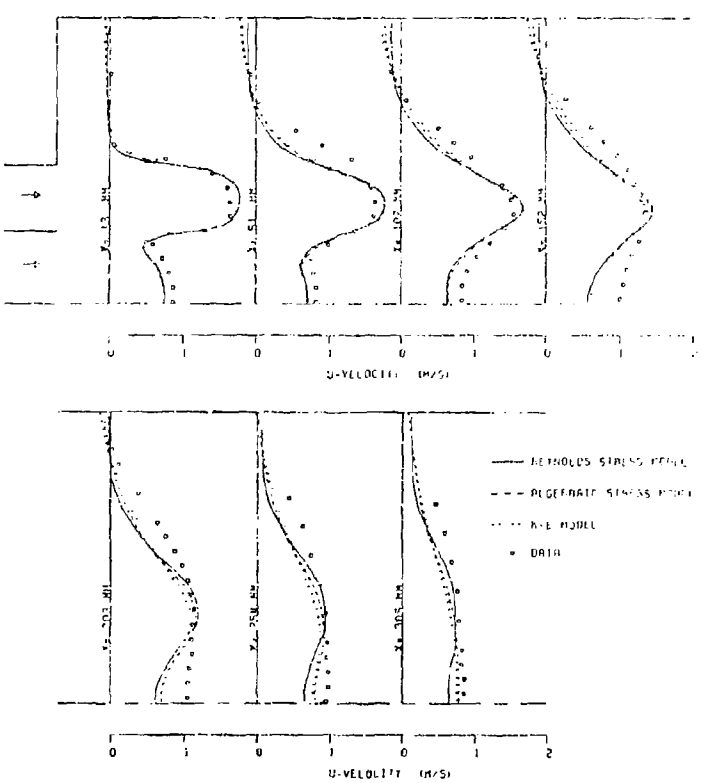

Figure 11. Comparison of turbulence models with measured mean axial velocity profiles of Johnson and Bennett[18].

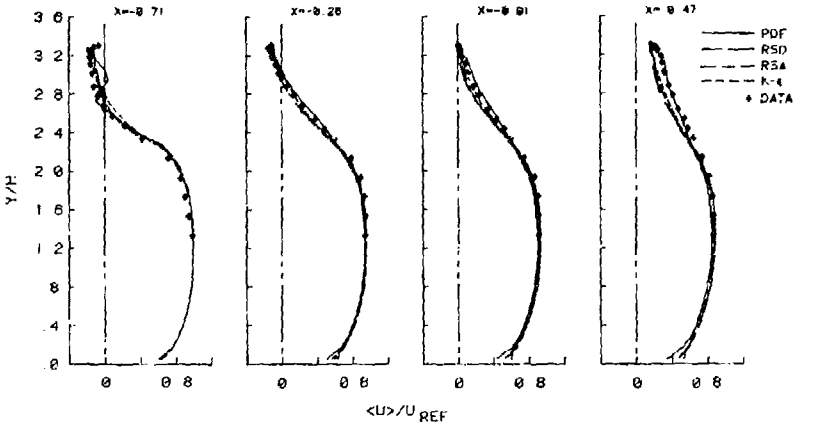

Figure 12. Predicted and measured axial velocity profiles.

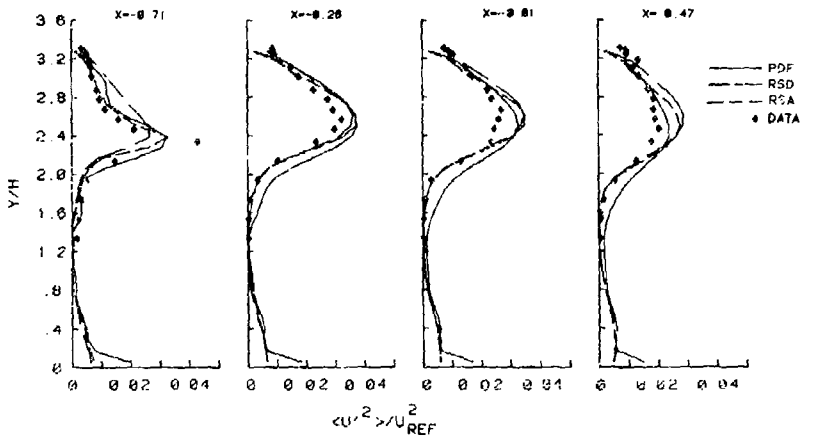

Figure 13. Predicted and measured $\langle u'^2 \rangle$ profiles.

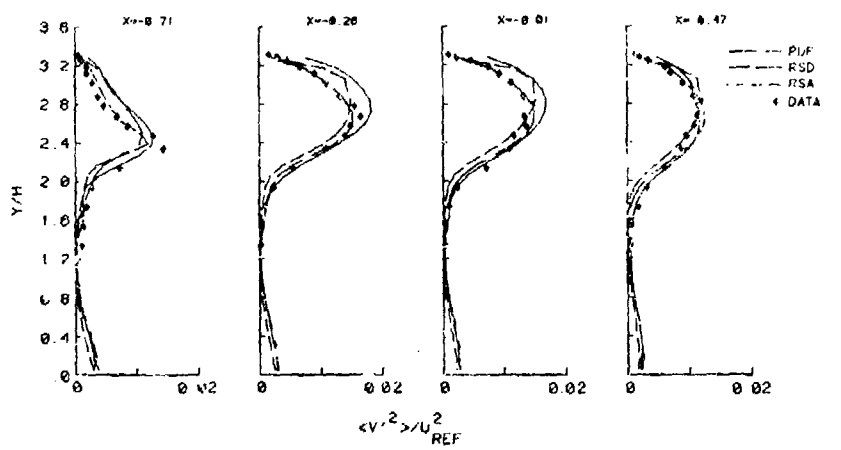

Figure 14. Predicted and measured $\langle v'^2 \rangle$ profiles.

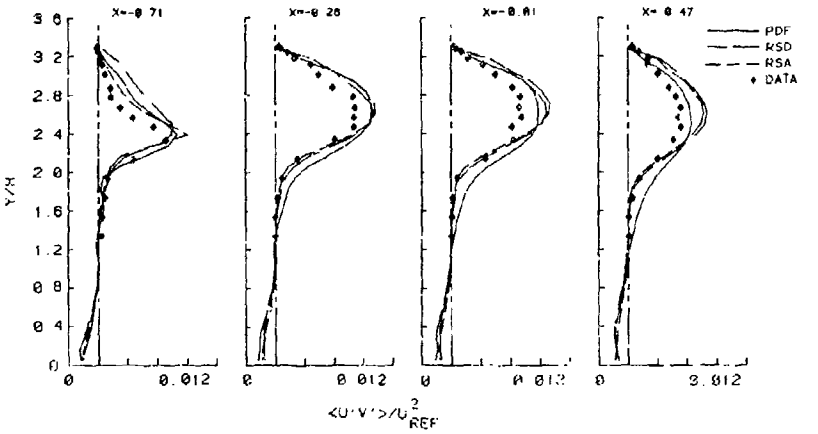

Figure 15. Predicted and measured (u'v') profiles.

The spray dynamics model consists of a fully-coupled combination of Lagrangian droplet and Eulerian gas phase calculations. The Lagrangian model includes the effects of the gas turbulence on droplet dispersion as described by Gosman and Ioannides[21]. The Eulerian treatment of the fluid is based on the two-phase k-ε model that accounts for the extra energy dissipation due to the presence of the droplets within the carrier phase[10].

To validate nozzle airflow calculation procedure, detailed near-nozzle airflow field has been mapped for a total of eight nozzles with a two-color, four-beam LDA system. Reference 7 presents a comparison between measurements and predictions for the four simulated nozzles. A typical comparison for an airblast nozzle[13] is shown in Figure 16 for X/D = 0.1 and 1.0, where D is the nozzle shroud exit diameter and X the axial distance downstream from the nozzle exit. The calculations were done with the standard k-ε model.

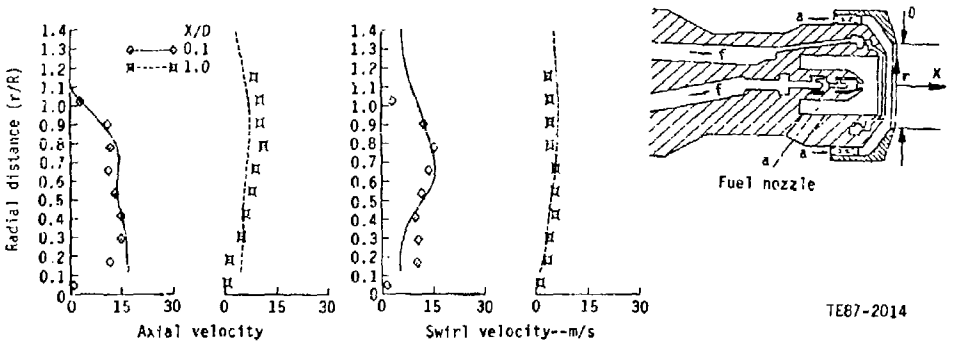

Figure 16. Comparison between predicted and measured axial and swirl velocity profiles.

The spray dynamics model was used to predict the pressure atomizer spray data of Batchalo et al[22] who used a Phase/Doppler analyzer to measure axial and radial velocity components, droplet number density and size distribution. Figure 17 shows a typical comparison between predictions and data at 5 mm downstream from the injector. This test configuration is too complicated in that the boundary conditions are not well defined in addition to measurement uncertainties. Nevertheless, the agreement can be considered qualitatively good.

In our more recent investigation[12] a well defined test configuration has been studied. The developing regions of an unconfined axisymmetric turbulent jet with and without glass beads of 105 micron diameter have been investigated experimentally and analytically with two mass loading ratios, LR = 0.2 and 1.0. A two-component Phase/Doppler system was used to map out the flow field for both phases including number density, and two orthogonal components of velocity for both phases.

Figures 18 and 19 show comparison between predictions and measurements for two loading ratios (LR = 0.2 and 1.0) in regard to gas axial velocity, particle axial and radial velocity components, and particle number density. The calculations are shown for both deterministic (DT) and stochastic (ST) treatments

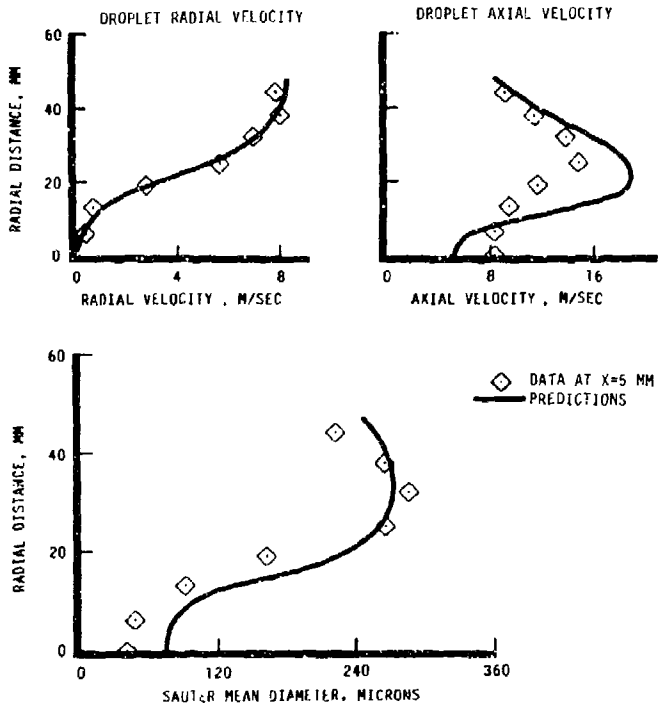

Figure 17. Comparison between predicted and measured data[22].

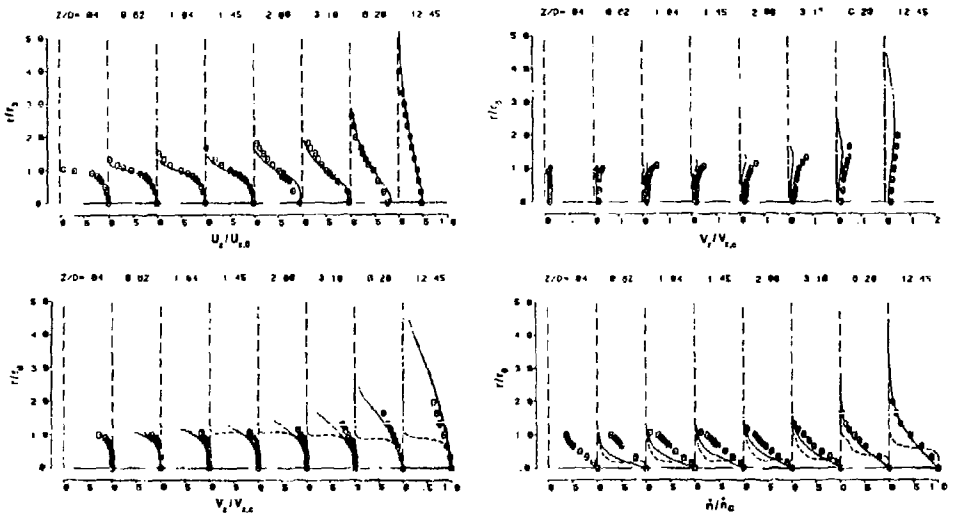

Figure 18. Radial profiles of normalized gas axial velocity, particle axial and radial velocity components, and particle number density at loading ratio, LR=0.2. ———— stochastic treatment ------- deterministic treatment

of the particles. In these calculations, the two-phase k-ε model was used. Both DT and ST treatments give nearly the same gas axial velocity profiles. However for the particle quantities including radial and axial velocity components, and number density ST treatment gives better agreement with data than DT. As loading ratio increases from 0.2 to 1.0 (Figure 18 versus Figure 19), the correlation gets worse indicating more modeling work need to be done in the near jet exit region which is of interest in gas turbine combustors.

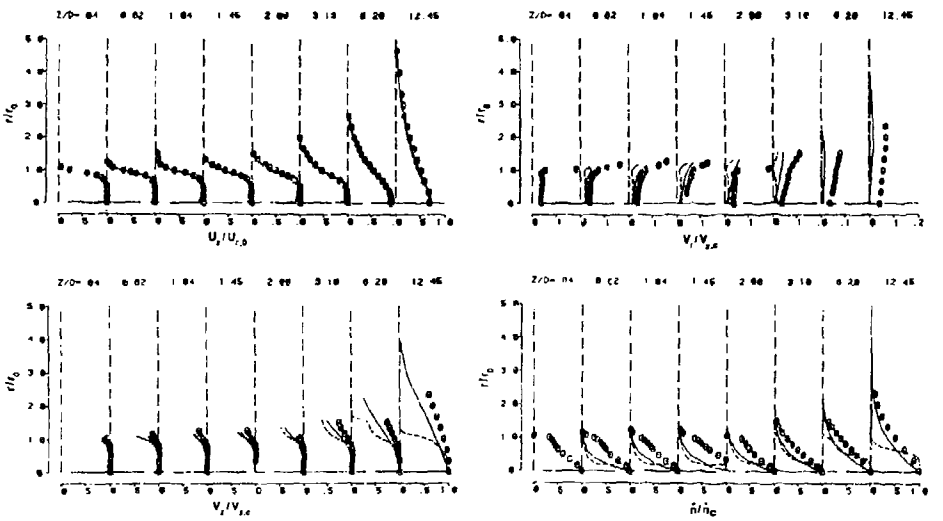

Figure 19. Radial profiles of normalized gas axial velocity, particle axial and radial velocity components, and particle number density at loading ratio, LR=1.0. ———— stochastic treatment -------- deterministic treatment

VI. SUMMARY

Multidimensional gas turbine combustion modeling involves a number of physicochemical processes, and these will have to be sorted out individually and in combination. Robust, reliable, accurate and computationally efficient numerical schemes need to be developed. In addition, one must determine how to use the detailed combustor internal aerothermal calculations to aid the combustion system design process.

A unique calculation procedure has been developed that combines the 3-D combustor model output with macrovolume expressions to compute design parameters and wall temperature distribution. This approach has been calibrated with a number of gas turbine combustors.

Some advances have been made in numerics, turubulence and spray formation/injection modeling. Work is continuing in further validating these models with the benchmark quality data currently being produced under the NASA sponsored Aerothermal Modeling Phase II activities.

REFERENCES

1. Mongia, H. C. and Smith, K. F., "An Empirical/Analytical Design Methodology for Gas Turbine Combustor," AIAA Paper 78-998, 1978.
2. Mongia, H. C., Reynolds, R. S., and Srinivasan, R., "Multidimensional Gas Turbine Combustion Modeling: Applications and Limitations," AIAA J., V24 n6, June 1986, pp 890-904.
3. Srinivasan, R., et al, "Aerothermal Modeling Program Phase I Final Report," NASA CR-168243, August 1983.
4. Rizk, N. K., and Mongia, H. C., "Gas Turbine Combustor Design Methodology," AIAA Paper 86-1531, 1986.
5. Runchal, A. K., Anand, M.S. and Mongia, H. C., "An Unconditionally-Stable Centeral Differencing Scheme for High Reynolds Number Flows," AIAA Paper 87-60, 1987.
6. Patankar, S. V., Karki, K. C. and Mongia, H. C., "Development and Evaluation of Improved Numerical Schemes for Recirculating Flows," AIAA Paper 87-61, 1987.
7. Sultanian, B. K. and Mongia, H. C., "Fuel Nozzle Air Flow Modeling," AIAA Paper 86-1667, 1986.
8. Nikjooy, M., et al, "k-ε Turbulence Model Assessment with Reduced Numerical Diffusion for Coaxial Jets," Submitted for Publication.
9. Anand, M. S., Pope, S. B. and Mongia, H. C., " A PDF Method for Turbulent Recirculating Flows," Presented at U.S.-France Joint Workshop on Turbulent Reactive Flows, July 6-10, 1987 at Rouen, France.
10. Mostafa, A. A. and Mongia, H. C., "On the Turbulence-Particles Interaction in Turbulent Two-Phase Flows," AIAA Paper 86-215, 1986.
11. Mostafa, A. A. and Mongia, H. C., "Eulerian and Lagrangian Predictions of Turbulent Evaporating Sprays," AIAA Paper 86-452, 1986.
12. Mostafa, A. A., Mongia, H. C., McDonnell, V. G., and Samuelsen, G. S., "On the Evolution of Particle-Laden Jet Flows: A Theoretical and Experimental Study," AIAA Paper 87-2181, 1987.
13. Rizk, N. K., Mostafa, A. A. and Mongia, H. C., "Modeling of Gas Turbine Fuel Nozzles," AMD-Vol 81 (1986), ASME Winter Annual Meeting, 7-12 December 1986.
14. Lefebvre, A. H., "Influence of Fuel Properties on Gas Turbine Combustion Performance," AFWAL-TR-84-2104, January 1985.
15. Plee, S. L. and Mellor, A. M., "Characteristic Time Correlation for Lean Blowoff of Bluff-Body Stabilized Flames," Combustion and Flame V35, pp 61-80 (1979).

16. Mellor, G. L. and Yamada, T., "Development of a Turbulence Closure Model for Geophysical Problems," Review of Geophysics and Space Physics, 20 (1982), pp 851-87.
17. Rodi, W., "A New Algebraic Relation for Calculating the Reynolds Stresses," ZAMM, 56 (1976), pp 219-221.
18. Johnson, B. V. and Bennett, J. C., "Mass and Momentum Turbulent Transport Experiments with Confined Coaxial Jets," NASA CR-165574, 1981.
19. Pope, S. B., "PDF Methods for Turbulent Reactive Flows," Progress in Energy and Combustion Science, 11 (1985), pp 119-192.
20. Pronchick, S. W. and Kline, S. J., "An Experimental Investigation of the Structure of Turbulent Reattaching Flow Behind a Backward-Facing Step," Stanford University Report MD-42, 1983.
21. Gosman, A. D. and Ioannides, E., "Aspects of Computer Simulation of Liquid Fueled Combustors," AIAA Paper No. 81-0323, (1981).
22. Datchalo, W.D., Houser, M. J. and Smith, M. J., "Evolutionary Behavior of Sprays Produced by Pressure Atomizers," AIAA Paper No. 86-0296 (1986).

DISCUSSION

J.McGuirk, UK

I notice in the PDF transport equation results you showed for the backward facing step that there still seems significant statistical error present in the velocity profile in the reverse flow zone. Is this an indication that the sample size in the Monte Carlo ensemble is not large enough? Also, what is the relative cost of performing this calculation compared with, say a K-E or Reynolds Stress Transport model?

Author's Reply

The kink in the U-velocity profile in the reverse-flow region is not a result of the sample size in the Monte Carlo ensemble, which, incidentally, is adequate. It should be noted that the calculation were peformed using a novel approach which combines conventional finite-difference calculations with the Monte Carlo calculations (see Reference 9 in the paper). The kink in the velocity profile is a consequence of the error in the derivatives of the Reynold stresses which appear as source terms in the momentum equations in the finite difference calculations. The components of the Reynolds stresses are supplied by the Monte Carlo in the form of bi-cubic spline fits, which are subsequently differentiated to obtain the source terms. Small errors in the spline-fit are amplified when differentiated. Since the papers (Reference 9 and the present work) were written, we have significantly improved the accuracy of the spline fits with considerable reduction in error in the derivatives derived from them.

The number of particles usd in the Monte Carlo simulation was 100,000. While the Monte Carlo calculations were performed on a CRAY-XMP the finite difference calculations were performed on an IBM 3084. Taking into account the difference in execution speeds between the machines, we deduce that the PDF calculations take a factor of 2 to 4 more CPU time that calculations with conventional models (K-E, RSA, RSD). More details can be found in Reference 9. A precise comparison of the execution speeds for the various models has not been performed and cannot be performed free of biases in coding, vectorization, etc. The important conclusion is that the Monte Carlo calculations for 2-D recirculating flows are quite affordable.

We would like to point out that forming splines consumes the majority of the CPU time in Monte Carlo calculations. The time required for the present PDF calculations reflects a successful effort in reducing the CPU time by judiciously modifying the Monte Carlo algorithm to drastically reduce the frequency of forming splines without affecting the modelling of the PDF transport equation.

3-DIMENSIONAL GAS TURBINE COMBUSTOR MODELLING

by

P.N. WILD*, F. BOYSAN*, J. SWITHENBANK and X. LU

The Department of Chemical Engineering and Fuel Technology,
The University of Sheffield,
Sheffield, S1 3JD
UK

SUMMARY

A mathematical model of the finite difference type is employed to predict the three dimensional reacting flows within realistic combustor geometries. Both algebraic stress and k - ε sub-models have been employed for turbulence, together with combustion models of the Magnussen type and a detailed fuel spray model. A Lagrangian type model for the calculation of residence time distribution has also proved useful in validating the predicted flow fields. Modelling is carried out for a cylindrical combustor can and for a sector of an annular gas turbine burner. Both of these possess swirl stabilised primary zones. Experimental measurements of gas velocity, combustor residence time distribution, composition and temperature have been employed for model validation and results obtained to date have been encouraging.

NOMENCLATURE

A = Combustion Model Constant

C_D = Droplet Drag Coefficient

C_p = Gas Specific Heat Capacity at Constant Pressure

C_{pd} = Droplet Specific Heat Capacity

D_d = Droplet Diameter

h = Enthalpy

k = Kinetic Energy of Turbulence

L = Latent Heat of Vaporization

M_i = Molecular Weight of Species i

m_i = Mass Fraction of Species i

N = Number of Trials

p = Pressure

R = Gas Constant

R_{co} = Rate of CO Consumption by Chemical Reaction

R_{fu} = Rate of Fuel Consumption by Chemical Reaction

S_h = Enthalpy Source Term Due to Chemical Reaction

S_s = Species Source Term Due to Chemical Reaction

T = Temperature

t = Time

$\mathbf{u}$ = Velocity Vector

u_i = Time Average Velocity Component

$\tilde{u}_i$ = Instantaneous Velocity Component

u_i' = Fluctuating Component of $\tilde{u}_i$

u_{id} = Droplet Velocity Component

*The authors are now with Flow Simulation Ltd., 146 West Street, Sheffield, England

δ_{ij} = Kronecker Delta

ϵ = Dissipation Rate of k

η = Gaussian Distributed Random Number

λ = Gas Thermal Conductivity

ρ = Density of Gas

ρ_d = Density of Liquid Phase

τ = Turbulence Time Scale

Subscripts

co Carbon Monoxide

d Droplet

fu Fuel

k Kinetic Energy of Turbulence

o Oxidant

s Chemical Species

ϵ Dissipation Rate of k

INTRODUCTION

The mathematical modelling of reacting flow, using finite difference techniques, is now well established. The k - ϵ model, which is the simplest practical turbulence model, together with the simplest combustion models (based on the fact that chemical reaction proceeds at a much greater rate than does turbulent mixing) have often proved adequate. Such models are increasingly being put to use by industry, allowing prediction of overall flow patterns and temperature distributions, for example Priddin [1]. Reviews of the techniques and their application to gas turbine technology can be found in many of the recent publications, [2, 3]. Less well developed are: computationally tractable combustion models capable of predicting pollutant formation; models capable of predicting the effect of fuel atomizer performance on the combustion process; the use of higher order turbulence closures which might overcome the problems often encountered with two equation models in strongly swirling flows.

Application of models to modern gas turbine combustor geometries, with complicated wall boundaries and many discrete inlets, is also an area undergoing development. Approaches here range from the direct solution of the governing equations in cartesian or cylindrical polar coordinate systems to the use of general two and three dimensional non orthogonal grids, for example Thompson [4]. The former technique requires the least computational effort but has the disadvantage of only approximating the shape of many curved boundaries. Additionally it often results in an inefficient distribution of grid nodes within the flow field.

This paper presents the findings of studies carried out at Sheffield in applying finite difference techniques to two realistic three dimensional combustor geometries. The combustors employed are a crylindrical can with swirl stabilised primary zone and an annular combustion chamber. The same computer code, written for solution of problems in cylindrical or cartesian coordinates with arbitrary boundary conditions, has been employed in both cases. (This was a variant of the FLUENT code). The coupling together of more than one finite difference grid has made modelling of the annul[illegible]stor possible, without the need for more sophisticated gridding methods. In this [illegible]me efforts have been made to assess the usefulness of an algebraic stress turbulence closure for the reacting flow problem and, for the liquid fuelled combustor can, a detailed fuel spray model is included. A Magnussen type model [5, 6] has been employed for chemical reaction since it has proved to give reasonable results in earlier studies and is easily incorporated with the droplet model. The extension of the reaction model to a two step chemistry allows some estimate of CO formation in the combustors.

For validation, experimental studies have also been performed with both combustor geometries. Measurements of gas composition, temperature and exit velocity are compared with model predictions. In addition residence time distribution measurements have been made using the method described by Topps [7] and Ewan et al [8]. These are compared with the results of a Lagrangian type prediction method and provide a convenient means of flow field validation.

1. THE MATHEMATICAL MODEL FOR THE GAS PHASE

For the prediction of isothermal flow fields within the combustion chambers, the equations requiring solution are those for conservation of mass and momentum in their time averaged form. Since the process of Reynolds decomposition and time averaging results in unknown correlations of the fluctuating velocity components, a turbulence model is also required. Using the k - ε model requires the solution of two additional transport equations, those for kinetic energy of turbulence, k, and its dissipation rate ε. The set of governing equations is given in appendix A (equations A1 to A6). For compactness cartesian tensor notation has been employed to present the formulation. The use of an algebraic stress turbulence model (ASM) requires additional algebraic relationships for the six Reynolds stresses (appendix A). In the present ASM formulation the partial differential equations have been retained in their k - ε model form.

The prediction of single phase reacting flow requires further transport equations for the time averaged species concentration and enthalpy. Turbulent diffusion is modelled here by analogy with Fick's law. That is the gradient diffusion assumption is assumed, the method adopted by most workers for large 3-dimensional calculations. Heat capacity data and the gas law are also required in order to relate gas density, temperature, and enthalpy. The equation set is summarised in appendix B. The approach adopted here has been to retain Reynolds decomposition and to neglect density fluctuations, a procedure which is consistent with the frequently used density weighted averaging method. Finally the reacting flow model requires a means of providing the time average source terms present in species and enthalpy equations. As is well known, when the flow is turbulent the source terms due to chemical reaction cannot be determined using the Arrhenius rate equations alone. The present work employs an eddy dissipation model based on the method of Magnussen and Hjertager [5]. A two step reaction mechanism has been modelled

$$C_xH_y + \left(\frac{x}{2} + \frac{y}{4}\right)\left(O_2 + nN_2\right) \longrightarrow xCO + \frac{y}{2}H_2O + \left(\frac{x}{2} + \frac{y}{4}\right)nN_2 \qquad (1)$$

$$xCO + \frac{x}{2}\left(O_2 + nN_2\right) \longrightarrow xCO_2 + \frac{x}{2}nN_2 \qquad (2)$$

Reaction rates for the two steps were determined by

$$R_{fu} = \left[\!\left[A_1 \rho m_{fu} \frac{\varepsilon}{k},\ A_1 \frac{\rho m_o \varepsilon}{S_{fu} k} \frac{S_{fu} m_{fu}}{S_{fu} m_{fu} + S_{co} m_{co}},\ R_{fu\ kinetic} \right]\!\right] \qquad (3)$$

$$R_{co} = \left[\!\left[A_2 \rho m_{co} \frac{\varepsilon}{k},\ A_2 \frac{\rho m_o \varepsilon}{S_{co} k} \frac{S_{co} m_{co}}{S_{fu} m_{fu} + S_{co} m_{co}},\ R_{co\ kinetic} \right]\!\right] \qquad (4)$$

A is a model constant and the subscript 'kinetic' denotes the rates determined by the Arrhenius equations. S_{fu} and S_{co} are the stoichiometric oxidant : fuel mass ratios for the combustion reactions. These have been included in order to account for the fact that the two reactions are simultaneously competing for available oxygen. The operator [[...]] takes the smaller of the terms within and allows combustion to be controlled by: the Arrhenius formula; the dissipation of oxygen containing eddies or the dissipation of fuel eddies. Once the rates R_{fu} and R_{co} are known, the required source terms are determined from knowledge of stoichiometry and the heat of combustion.

2. THE DROPLET PHASE MODEL

The Lagrangian formulation employed here, has the advantage over other methods of being grid independent and not requiring solution in regions where all the droplets have evaporated. The fuel spray is simulated by a statistically representative ensemble of droplets. These are given a range of discrete injection velocities and sizes to represent the distributions produced by the atomizer. Lagrangian equations are then solved for droplet motion, droplet heating and evaporation. In simulating droplet motion only the drag force acting on the droplet is considered, effects of droplet - droplet interaction are neglected. The equation for droplet motion is then

$$\frac{du_{id}}{dt} = -\frac{18\mu}{\rho_d D_d^2}\frac{C_D Re}{24}\left(u_{id} - \tilde{u}_i\right) \qquad (5)$$

u_{id} denotes the component of droplet velocity, D_d is the droplet diameter and ρ_d is its density. The droplet Reynolds number, Re, is defined

$$Re = \frac{\rho D_d}{\mu} |u_d - u| \tag{6}$$

and C_D is a Reynolds number dependent drag coefficient. C_D is assumed to be that for a solid sphere and is obtained for the appropriate Reynolds number using the correlations of Morsi and Alexander [9]. The instantaneous droplet location is computed by integration of the equation

$$\frac{dx_i}{dt} = u_{id} \tag{7}$$

To account for the effect of turbulence on the trajectory of a droplet a stochastic technique is used. This employs simulation with random numbers. Many trials must be performed for each droplet, so that the time averaged effect of turbulence can be simulated. At each trial the instantaneous gas velocity, $\hat{u}_i$, is constructed from the time mean and fluctuating components, u_i and u'_i. It is assumed that the fluctuating velocity prevails for a time period equal to the lifetime of the fluid eddy which the particle is traversing. This is expressed in terms of the local kinetic energy of turbulence and its dissipation rate, Hinze [10].

$$\tau = \frac{C\mu^{0.75}}{2^{0.5}} \frac{k}{\epsilon} \tag{8}$$

The magnitude of the fluctuating velocities are assumed to possess a Gaussian distribution and are related to the root mean fluctuations by

$$u'_i = \eta \left(\overline{u'^2_i} \right)^{1/2} = \phi \left(2k/3 \right)^{1/2} \tag{9}$$

where η is a Gaussian distributed random variable. Values of u_i derive directly from the solution of the gas phase. Equation (7) is solved and at the end of each time period, τ, a new value of u' is generated. The simulation is stopped when a particle; evaporates, escapes from the flow field or impinges on a wall. The next trial can then be performed.

In the modelling of droplet evaporation it is assumed that droplet temperature rises, as a result of convective heat transfer, until the boiling point is reached. A uniform temperature within the droplet and a single boiling point are assumed. Heat up is governed by the equation

$$\frac{dT}{dt} = 6\lambda \left(2 + 0.6\, Re^{1/2}\, Pr^{1/3} \right) \frac{T - T_d}{\rho_d D^2 C_{pd}} \tag{10}$$

which is due to Ranz and Marshall [11]. λ is the gas thermal conductivity. T_d and C_{pd} are droplet temperature and specific heat respectively. After reaching the boiling point evaporation begins. Fuel vapour is distributed to the gas phase along the particle trajectory and droplet diameter decreases. Evaporation is described by

$$\frac{dD_d}{dt} = \frac{8\lambda}{2\, \rho_d\, C_p\, D_d} \ln \left[1 + \frac{C_p}{L} \left(T - T_d \right) \right] \left[1 + 0.23\, Re^{1/2} \right] \tag{11}$$

which is taken from the work of Wise and Agoston [12].

In order that gas and liquid phases may interact, droplet source terms are introduced into the gas phase equations. These account for fuel species, mass, momentum and enthalpy exchange between the phases. On completing the droplet simulation the source terms are updated. For example the mass source term is computed, for each droplet and each finite difference cell, as

$$\left[\frac{m_{in} - m_{out}}{m} \right] \frac{\dot{m}}{N}$$

m denotes the initial droplet mass while subscripts in and out denote values at entry and exit from the computational cell. $\dot{m}$ is the fuel mass flow rate associated with a droplet and N is the number of trials in the stochastic simulation. Gas and droplet simulations may be performed alternately until a converged solution is obtained. The simulation procedure is summarised in figure 1.

3. MODEL FOR THE PREDICTION OF RESIDENCE TIME DISTRIBUTION (RTD)

Knowledge of the different life times for which fluid exists inside a combustion chamber, is a useful diagnostic tool as well as a means of model validation. The RTD may be determined from a calculated 3-dimensional flow field, by simulating the injection of a tracer gas pulse at a suitable inlet and by applying equation (12) to compute the normalised response.

$$E(t) = \frac{C(t)}{\int_0^\infty C(t)dt} \tag{12}$$

Where E is the residence time distribution and C is the tracer gas exit concentration. Modelling can be achieved using a finite difference procedure and solving the time dependent equation for conservation of a passive scaler. However the code used in the present study is formulated for the solution of steady state problems. Furthermore, in determining an RTD, solution at all points in the flow field is not necessary, values of concentration only being required at the combustor exit plane. A Lagrangian method employing stochastic particle tracking is therefore most convenient.

It is possible to represent a diffusion process by a stochastic differential equation of the following form

$$X_i(t+\delta t) - X_i(t) = D_i(X(t), t)\delta t + \left[B(X(t),t)\right]^{\frac{1}{2}}\left[W_i(t+\delta t) - W_i(t)\right] \tag{13}$$

in the limit as $\delta t \longrightarrow 0$. Where $X_i(t)$ represents a position vector at time t, $W_i(t)$ is a standard Wiener process, D_i and B are specified functions, known respectively as the coefficients of drift and diffusion. X_i then describes the motion of a computational particle through space. If many of these particles exist at a point $X_i(0)$ at time t = 0 then the distribution of particle concentration, ϕ at some time $t > 0$ obeys the equation

$$\frac{\partial}{\partial t}\phi + \frac{\partial}{\partial x_i} D_i\phi = \frac{1}{2}\frac{\partial^2}{\partial x_i^2} B\phi \tag{14}$$

The Wiener process employed in the above theory can be considered to be made up of discrete time steps, δt, in the limit as $\delta t \longrightarrow 0$.

$$W_i(t_n) = \delta t^{1/2} \sum_{l=1}^{n} \eta_l \tag{15}$$

where $t_n = n\delta t$ and η_l denotes a set of independent standardised random variables. (l=1, ...n). This concept is employed in the numberical solution.

In a similar manner to the droplet model, equations 13 and 15 can be employed to produce a particle trajectory. The procedure is

1) Select initial particle coordinates, X_i, and a suitably small time step δt.

2) Obtain k, ε, u_i and the gradient of diffusivity from the finite difference solution of the gas phase and use these to calculate the appropriate D_i and B.

3) Compute the new particle coordinates after the time interval δt.

$$X_i \longrightarrow X_i + D_i\delta t + B^{1/2}\delta t^{1/2}\eta \tag{16}$$

where η is obtained from a Gaussian distribution random number generator.

4) Repeat from step 2) to produce the particle path.

To obtain a residence time distribution, an injection point is selected and many particle trajectories are generated. The time required for each computational particle to travel from injection point to combustor exit is recorded. This data is then used to construct the cumulative distribution function, F(t). F(t) is defined as the fraction of material in the exit stream with residence time less than t. It is related to the residence time distribution function by

$$F(t) = \int_0^t E(t)dt \tag{17}$$

The RTD may be obtained by curve fitting F(t) and differentiating. For the latter, a least squares cubic spline fit has proved satisfactory.

4. THE COMBUSTION CHAMBERS AND EXPERIMENTAL MEASUREMENTS

The combustor can employed in this work is shown in figure 2. It is a Lycoming experimental burner on which a number of previous studies have been performed. For example [13, 14]. As can be seen, the burner postesses a single centrally located pressure jet fuel atomizer, a primary swirler and 3 sets of injection holes. Experimental studies have involved fuelling the can with kerosene and operating with atmospheric discharge. Temperature profiles, at the exit and within the combustor, have been measured using unshielded platinum - platinum rhodium thermocouples. Exit velocity measurements using uncooled pitot probes, have also been performed.

The annular chamber used in the present work is an F101 main burner. Figure 3 shows a section through the combustion chamber and figure 4 shows details of one of its 20 primary zone swirl assemblies. The entering air flow supplies the dome and two combustor passages. Part of the dome flow enters the combustion zone through the two stage counter rotating swirlers. Further air provides impingement cooling of the splash plate and hot side film cooling. Part of the flow diverted to the liners is employed as film cooling and the remainder enters through sets of injection holes. For this geometry experimental measurements have been made using a 3 sector (54 degree) test rig. Studies have been performed for isothermal flow in the combustor and with the combustor fuelled on propane gas. All tests have been performed at atmospheric pressure. No data has yet been obtained for the liquid fuel system. In the isothermal flow study, residence time distributions were measured by injecting pulses of mercury vapour into the chamber. Exit concentration was then measured using the vapour's ability to absorb ultra violet light. By repeating the experiment many times, time average responses were obtained. Equation 12 could then be used to compute RTD's. The results in this form are independent of the actual size of the tracer pulse and are suitable for comparison with model prediction. The experimental apparatus is illustrated in figure 5. The probe, figure 5 (a), is suitably positioned in the combustor and an electric spark is passed across its two mercury amalgam electrodes to generate the vapour pulse. A photomultiplier detects absorption of ultraviolet light at the combustor exit and a micro computer is employed to log the data. Further experimental details can be found in the publications of Topps [7] and Ewan et al [8]. For the reacting flow studies, thermocouple and gas sampling probes were again used to obtain internal and combustor exit profiles.

5. NUMERICAL SOLUTION

For solution of the gas phase equations, the SIMPLE algorithm and hybrid differencing, [15], were employed. In solving the Lycoming combustor problem a cylindrical polar coordinate system was used. 30 grid nodes were used in the axial direction together with 16 and 7 nodes in the radial and angular directions respectively. Symmetry allowed modelling to be confined to a single 60 degree sector of the chamber, this being bounded in the angular direction by planes of cyclic symmetry. It was necessary to model the conical primary zone wall by 10 steps in the grid. The fuel spray was modelled with 10 discrete droplet sizes. 10 discrete angles of injection represented the hollow cone spray.

In the case of the annular combustor, a cylindrical polar coordinate system was again employed. Modelling used two separate flow fields. For the primary zone swirler assembly a cylindrical field was employed, with 18, 16 and 38 cells in the axial, radial and angular directions respectively. A separate annular field modelled the main body of the chamber, symmetry allowing the solution to be confined to a single 18 degree combustor sector. This second flow field used 42, 35 and 23 grid nodes in the axial, radial and angular directions respectively. The computer code allowed the two flow fields to be treated in turn by the solution algorithm. However, since the swirling flow causes recirculation into the primary zone swirl cup, it was necessary to completely couple the two solutions. This was achieved by repeatedly solving the two flow fields and transferring boundary conditions between the two. The approach is illustrated in figure 6. For this problem the curved liner surfaces were modelled by the use of a stepped wall approximation.

6. RESULTS

Figure 7 shows predicted velocity vectors for reacting flow in the Lycoming combustor. These are for a slice in the plane of the injection holes. Strong recirculation in the primary zone and steep penetration of the entering air jets can be seen. Figure 8 (a) compares predicted and measured exit temperatures and figure 8 (b) compares exit velocity profiles. Use of either a single or two step kinetic mechanism with the Magnussen combustion model was found to have a negligible effect on these predicted exit profiles. All predictions in the Lycoming combustor were made using the ASM turbulence model. This was seen to perform satisfactorily in the reacting flow but gave little improvement over $k - \varepsilon$ model predictions for this case [14]. Figure 9 shows the predicted mean trajectories of fuel droplets in the combustor can. The greatest proportion of fuel is seen to evaporate within the primary zone. However the largest droplets penetrate to the combustor walls where they impinge. It can be seen from the contour plots in figure 9, that the entering fuel spray imparts momentum to the gas in the primary zone and influences the flow field here. The time histories of typical drops are shown in figure 10. The model predicts that there is significant influence of turbulence on the trajectories of the smallest droplets, and this will in turn influence fuel distribution in the combustion zone. The effect is illustrated by the predicted trajectories in figure 11.

Predictions for the annular combustor have, to date, been performed using the k - ε turbulence model in isothermal and reacting flows. Measured residence time distributions for the annular combustion chamber are presented in figure 12. These are compared with predictions of the Lagrangian model described in section 3. The latter was used as a post processor after computation of the combustor flow field. Good agreement between prediction and measurement is obtained for tracer released into the dilution zone. For tracer released into the primary zone, the major features of the distribution are also reproduced. However there is some over prediction of the rate at which the concentration pulse decays. This suggests an under prediction of the effective primary zone volume, a result which may be attributed to using the k - ε model in this strongly swirling flow. Figure 13 shows reacting flow velocity vectors at two axial locations. The interaction of the entering air jets and the asymmetry induced by swirl, are clearly visible. Further visualisation of the flow field has been achieved by simulating fluid particles which follow the flow. These are shown for reacting and isothermal cases in figure 14. In the reacting flow velocities are increased and jet penetration is seen to be reduced. Predicted temperature contours for the reacting case are shown in figure 15. These are at a plane through the centre of the 18 degree sector. Predicted and measured temperatures are compared in figure 16. Predicted and measured gas compositions appear in figure 17. Modelling results are generally in good agreement with measurement. Discrepancies at the exit plane may be attributed to the stepped wall approximation for the inner liner surface.

7. CONCLUSION

* A code, suitable for use with arbitary geometries in cylindrical or polar coordinates, has been applied to the modelling of a can and an annular combustion chamber. A technique for the coupling together of finite difference grids has made possible the modelling of a difficult primary zone geometry.

* A detailed spray model has been presented for liquid fuelled systems. This includes the influence of turbulence on fuel droplet trajectory, an effect which appears significant in some cases.

* A two step kinetic scheme, together with a Magnussen type model for determining reaction rate, has been able to give some indication of pollutant formation inside the combustors.

* An algebraic stress turbulence model has proved satisfactory for combustor simulation. However, further study is required in order to demonstrate any real advantage over two equation models in reacting flows of the type studied here.

* The measurement and simulation of residence time distributions has proved helpful in model validation. The technique will be especially useful in complicated geometries where direct measurements of velocity and turbulence levels can be difficult to obtain.

8. ACKNOWLEDGEMENTS

The authors would like to acknowledge the use of the FLUENT computer code supplied by Creare Inc. Hanover, New Hampshire, and Flow Simulation Ltd., Sheffield, England.

The USAF is also acknowledged for its support of work on the turbulence closures.

9. REFERENCES

1. Priddin, C.H., and Coupland, J., "Impact of Numerical Methods on Gas Turbine Combustor Design and Development", Presented at the Winter Annual Meeting of the ASME, Anaheim, CA, 1986.

2. Mongia, H.C., Reynolds, R.S., and Srinivasan, R., "Multidimensional Gas Turbine Modelling", AIAA Journal, Vol. 24, No. 6 1986, pp. 890-904.

3. Shyy, W., Correa, S.M., and Braaten, M.E., "Computational Models for Gas-Turbine Combustors", Presented at the Winter Annual Meeting of the ASME, Anaheim, CA, 1986.

4. Thompson, J.F., "A Survey of Grid Generation Techniques in Computational Fluid Dynamics", American Institute of Aeronautics and Astronautics, Paper AIAA-83-0447, 1983.

5. Magnussen, B.F., and Hjertager, B.H., "On Mathematical Modelling of Turbulent Combustion with Special Emphasis on Soot Formation and Combustion", Proceedings of the 16th Symposium (International) on Combustion, The Combustion Institute, 1976, pp. 719-727.

6. Magnussen, B.F., Magnussen, F., and Lilleheie, N.I., "Eddy Dissipation Concept Simulation of Hydrogen-Air Turbulent Diffusion Flame", Report of the Division of Thermodynamics, The Norwegian Institute of Technology, Trondheim, Norway, 1985.

7. Topps, J.E.C., "An Optical Technique for the Investigation of Flow in Gas Turbine Combustors", Proceedings of the 17th Symposium (International) on Combustion, The Combustion Institute, 1978, pp. 347-353.

8. Ewan, B.C.R., Boysan, F., and Swithenbank, J., "Closing the Gap Between Finite Difference and Stirred Reactor Modelling Procedures", Proceedings of the 20th Symposium (International) on Combustion, The Combustion Institute, 1984, pp. 541-547.

9. Morsi, S.A., and Alexander, A.J., "An Investigation of Particle Trajectories in Two Phase Flow Systems", Journal of Fluid Mechanics, Vol. 55, 1972, pp. 193-208.

10. Hinze, J.O., Turbulence, McGraw Hill, 1959.

11. Ranz, W.E., and Marshall, W.R., "Evaporation From Drops", Chemical Engineering Progress, Vol. 48, No. 3, 1952, pp. 141-146.

12. Wise, H., and Agoston, G.A., "Burning of a Liquid Droplet", Literature on the Combustion of Petroleum, American Chemical Society, Washington D.C., 1858.

13. Swithenbank, J., Turan, A., Felton, P.G., and Spalding, D.B., "Fundamental Modelling of Mixing, Evaporation, and Kinetics in Gas Turbine Combustors", AGARD CP-275, 1979.

14. Boysan, F., Ayers, W.H., Swithenbank, J., and Pan, Z., "Three Dimensional Modelling of Spray Combustion in a Gas Turbine Combustor", Journal of Energy, Vol. 6, No. 6, 1982, pp. 368-375.

15. Patankar, S.V., Numerical Heat Transfer and Fluid Flow, Hemisphere Publishing Corporation, McGraw Hill Book Company, 1980.

APPENDIX A. EQUATIONS OF THE GAS PHASE MODEL

Conservation of mass

$$\frac{\partial}{\partial x_i}(\rho u_i) = 0 \tag{A1}$$

Conservation of momentum

$$\frac{\partial}{\partial x_i}\left(\rho u_i u_j + \overline{\rho u'_i u'_j}\right) = -\frac{\partial \sigma_{ij}}{\partial x_i} \tag{A2}$$

$$\sigma_{ij} = p\delta_{ij} - \mu\left[\frac{\partial u_i}{\partial x_j} + \frac{\partial u_j}{\partial x_i}\right] + \frac{2}{3}\mu\frac{\partial u_i}{\partial x_j}\delta_{ij} \tag{A3}$$

k - ε Turbulence Model

$$\frac{\partial}{\partial x_i}(\rho u_i k) = \frac{\partial}{\partial x_i}\left[\frac{\mu+\mu_t}{\sigma_k}\frac{\partial k}{\partial x_i}\right] + P - \rho\varepsilon \tag{A4}$$

$$\frac{\partial}{\partial x_i}(\rho u_i \varepsilon) = \frac{\partial}{\partial x_j}\left[\frac{\mu+\mu_t}{\sigma_\varepsilon}\frac{\partial \varepsilon}{\partial x_i}\right] + C_1\frac{\varepsilon}{k}P - C_2\rho\frac{\varepsilon^2}{k} \tag{A5}$$

$$\mu_t = 0.09\,\rho k^2/\varepsilon \tag{A6}$$

(Modelling coefficients take the values

$C_1 = 1.44$ $C_2 = 1.92$ $\sigma_k = 1.0$ $\sigma_\varepsilon = 1.3$)

Algebraic relationships for the Reynolds stresses

$$\overline{u'_i u'_j} = \frac{2}{3}k\delta_{ij} + \frac{1 - C}{P/\varepsilon - 1 + C'}\frac{k}{\varepsilon}\left[P_{ij} - \frac{2}{3}P\delta_{ij}\right] \tag{A7}$$

$$P_{ij} = -\left[\overline{u'_i u'_k}\,\frac{\partial u_j}{\partial x_k} + \overline{u'_j u'_k}\,\frac{\partial u_i}{\partial x_k}\right] \qquad (A8)$$

$$P = 1/2\ P_{ii} \qquad (A9)$$

(C and C' are model constants given the values 0.55 and 2.2 respectively.)

APPENDIX B. EQUATIONS FOR GAS PHASE REACTING FLOW

Equation for the Conservation of Enthalpy

$$\frac{\partial}{\partial x_i}\left(\rho u_i h\right) = \frac{\partial}{\partial x_i}\left[\frac{\mu+\mu_t}{\sigma_h}\,\frac{\partial h}{\partial x_i}\right] + S_h \qquad (B1)$$

Equation for Conservation of Chemical Species

$$\frac{\partial}{\partial x_i}\left(\rho u_i m_s\right) = \frac{\partial}{\partial x_i}\left[\frac{\mu+\mu_t}{\sigma_s}\,\frac{\partial m_s}{\partial x_i}\right] + S_s \qquad (B2)$$

The equation of state

$$\rho = p\ /\ RT \sum_j m_j/M_j \qquad (B3)$$

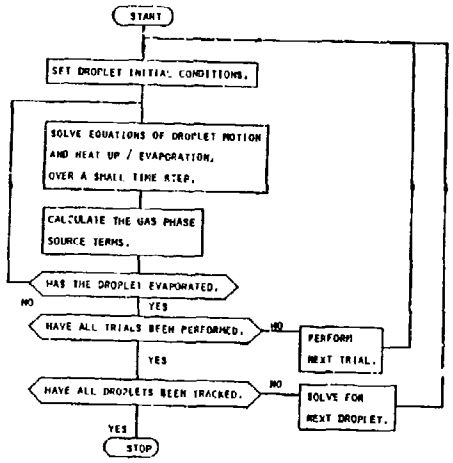

FIGURE 1. ALGORITHM FOR THE DROPLET MODEL.

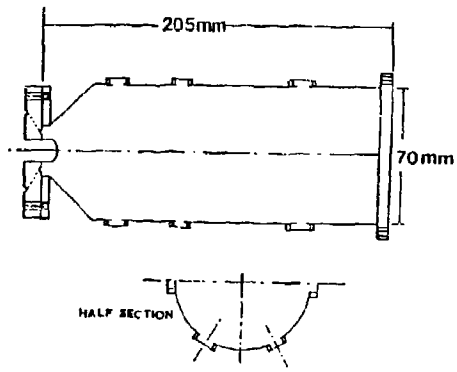

FIGURE 2. THE LYCOMING COMBUSTOR CAN.

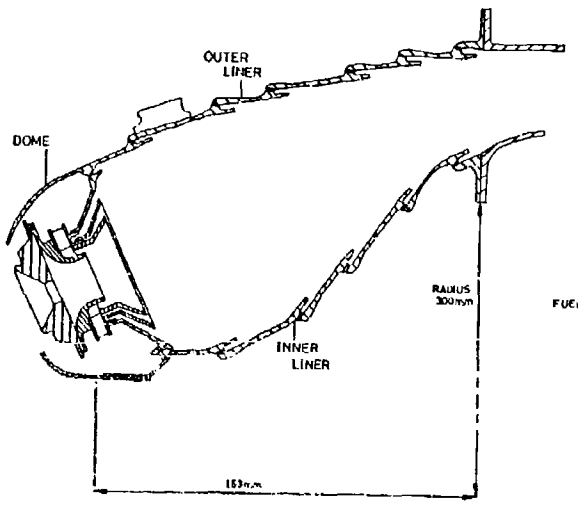

FIGURE 3. THE ANNULAR COMPUSTION CHAMBER.

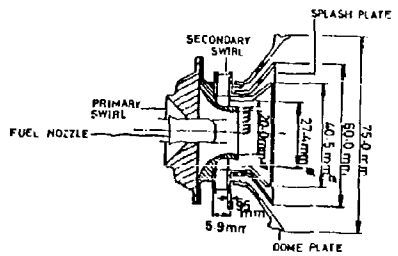

FIGURE 4 THE PRIMARY ZONE SWIRL ASSEMBLY.

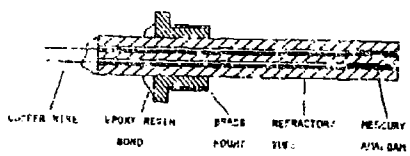

FIGURE 5(A) THE MERCURY SPARK ELECTRODE.

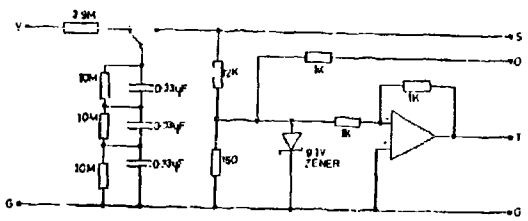

FIGURE 5(B) THE R.T.D. MEASUREMENT SYSTEM SPARK UNIT.

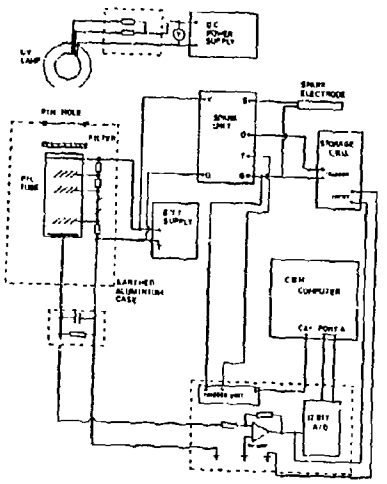

FIGURE 5 (C) THE RTD MEASUREMENT SYSTEM.

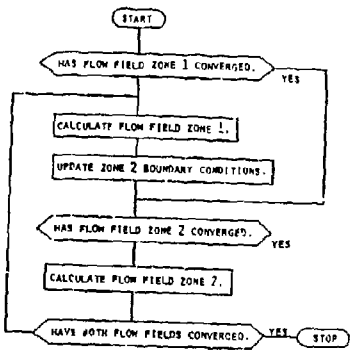

FIGURE 6 ALGORITHM FOR THE COUPLING OF FINITE DIFFERENCE GRIDS.

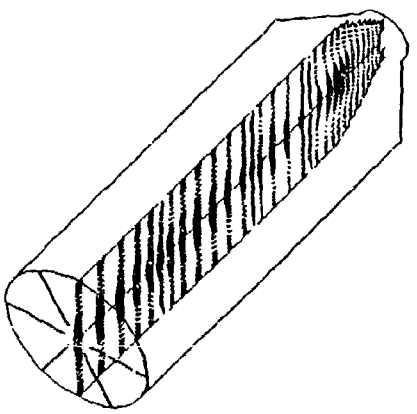

FIGURE 7 PREDICTED VELOCITY VECTORS FOR REACTING FLOW IN THE LYCOMING COMBUSTOR.

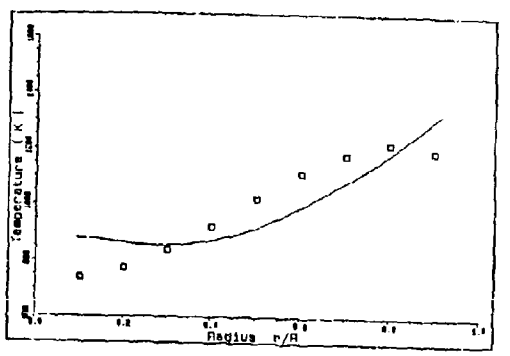

FIGURE 8 (A) LYCOMING COMBUSTOR EXIT TEMPERATURE,
□ EXPERIMENT — PREDICTION

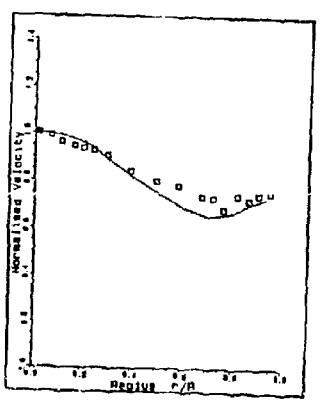

FIGURE 8 (B) LYCOMING COMBUSTOR EXIT VELOCITY.

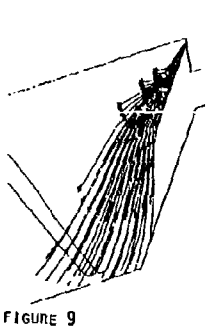

MEAN DROPLET TRAJECTORIES.
DROPLET DIAMETERS 20 TO 190 MICRONS.

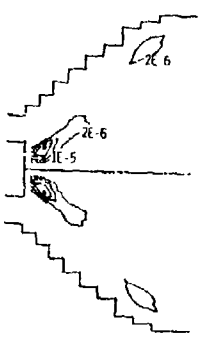

CONTOURS OF X MOMENTUM EXCHANGE.
(KG.M/SEC/SEC)

FIGURE 9

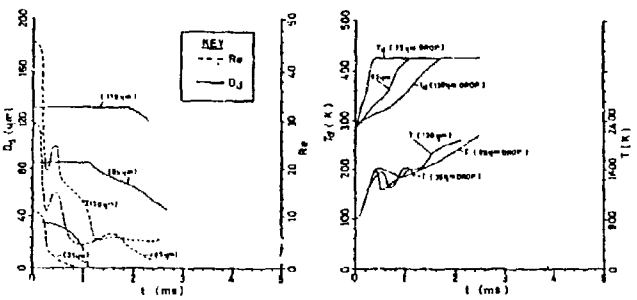

FIGURE 10 TYPICAL DROPLET TIME HISTORIES.

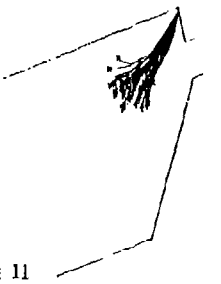

FIGURE 11
THE EFFECT OF TURBULENCE ON 45 MICRON DROPLETS.

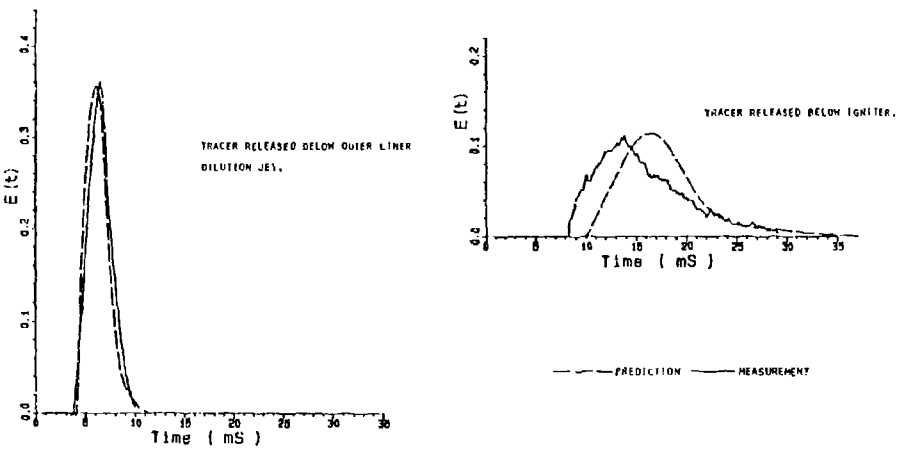

FIGURE 12 PREDICTED AND MEASURED RESIDENCE TIME DISTRIBUTIONS FOR ISOTHERMAL FLOW IN THE ANNULAR COMBUSTOR.

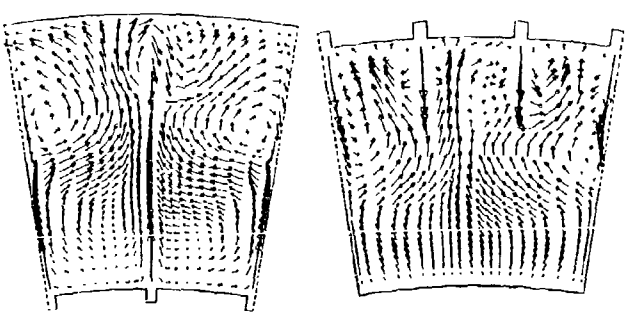

FIGURE 13 REACTING FLOW VELOCITY VECTORS FOR THE ANNULAR COMBUSTOR.

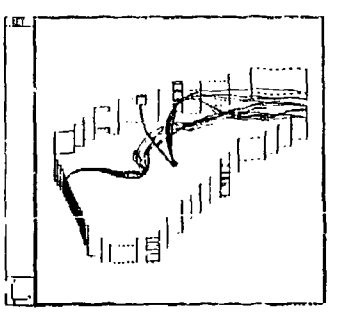

FIGURE 14 (A)
TRACER PLUMES FOR ISOTHERMAL FLOW IN THE ANNULAR COMBUSTOR.

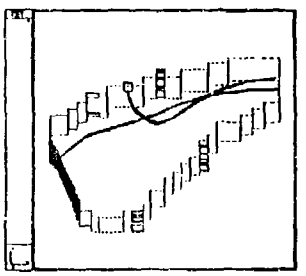

FIGURE 14 (B)
TRACER PLUMES FOR REACTING FLOW IN THE ANNULAR COMBUSTOR.

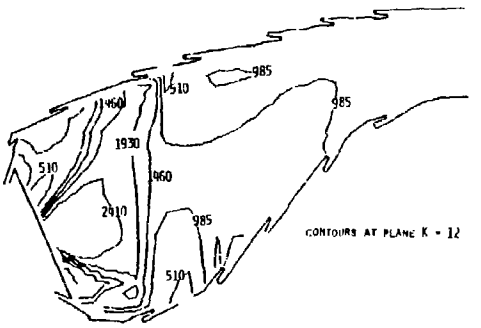

FIGURE 15 PREDICTED TEMPERATURE IN THE ANNULAR COMBUSTOR. (KELVIN)

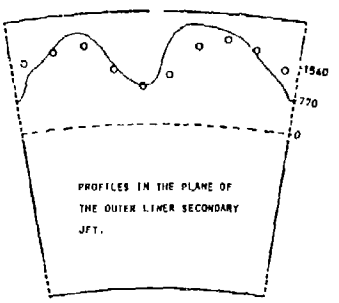

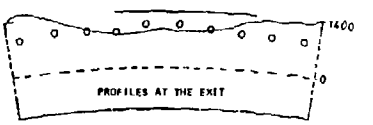

—— PREDICTION O MEASUREMENT

FIGURE 16 PREDICTED AND MEASURED TEMPERATURES IN THE ANNULAR COMBUSTOR. (K)

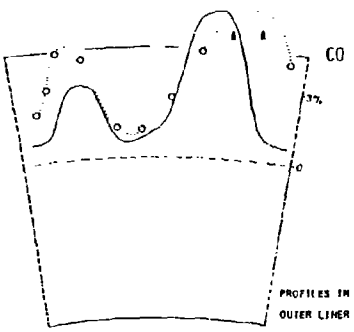

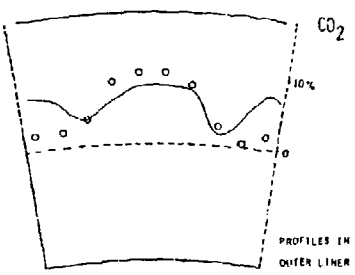

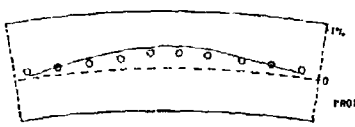

—— PREDICTION O MEASUREMENT

FIGURE 17 PREDICTED AND MEASURED GAS COMPOSITION FOR THE ANNULAR COMBUSTOR.

DISCUSSION

J.McGuirk, UK

I understand from the equations in your paper that you evaluate the mean density from the gas law using the mean temperature. This means that you are ignoring density fluctuations; in the primary zone where the fluctuations are large and the density/temperature relationship non-linear, this can lead to errors of up to a factor of two, so if you are getting the right answers, it will be for the wrong reason.

You use a mixing limited two-step reaction scheme — do you know at how many points you are mixing rate limited and at how many you use a kinetic expression!

Author's Reply

(1) The transport equations employed are essentially density weighted in form and density weighted quantities are predicted. Yes, densities are computed from mean temperature. This is a modelling assumption which we have found satisfactory in a wide range of combustion applications. To directly include temerature fluctuations requires additional modelling assumptions which have their own uncertainties. (2) Most heat release is confined to a small region in the primary zone and here the reaction is almost mixing controlled.

B.Noll, GE

(1) How many droplet trajectories did you calculate to achieve a stationary solution (in a statistical sense) for the fuel propagation.

(2) Which convergence criterion do you use to stop the iteration procedure which accounts for droplet/gas phase-interaction?

(3) How many "outer" iterations were necessary to achieve overall convergence?

Author's Reply

(1) The spray in the 60 degree combustor sector was represented by 100 droplets with discrete injection angles and diameters. Fifty trials of these droplets were performed in the stochastic simulation. (2) The residuals employed to test for convergence are those for the gas phase equations. Since the two phases are coupled this automatically ensures correct results for the disperse phase. (3) Twenty iterations of the gas phase calculation were performed between each droplet simulation. At the present time no attempt has been made to optimize this solution parameter.

J.B.Moss, UK

The level of agreement between prediction and experiment for scalar properties (CO and temperature) obtained with the Magnussen-adapted eddy break up model is impressive (even for the exit plane) but surprising given its limited physical and chemical content. The two-step chemistry (which is "laminar"?) is largely cosmetic since it can operate over only a restricted flow regime in the combustor, I assume. Are the model parameters generally applicable or specific to the application? What values are assumed for A1, A2, Rfu kinetic, Rco kinetic?

Author's Reply

The constants A1 and A2 are given the value 0.4. Rfu kinetic etc. are obtained from an Arrhenius expression. Since the operator [1...1] takes the smallest of the terms within, the two step model does operate in the turbulent regime. Constants were taken from the literature and no attempt was made to adjust or tune these.

Finally, I think that the reason for so many workers obtaining satisfactory results when using combustion models of the eddy dissipation type, stems from the fact that combustor, and therefore heat release, is restricted to a narrow region in the primary zone. The fine details of the processes occurring here are therefore not important in determination of the overall combustor flow field.

Modelling issues with perceived higher risk in providing a significant payoff are deferred to future activities. Our thinking here is to let these concepts evolve within the University environment. We would then be in a position to easily implement them into our model.

ON THE APPLICATION OF FINITE-DIFFERENCE TECHNIQUES FOR THE COMPUTATION OF THE FLOW FIELD IN GAS TURBINE COMBUSTORS WITH COMPLEX GEOMETRIES

by
S. Wittig, H.-J. Bauer and B. Noll
Lehrstuhl und Institut für Thermische Strömungsmaschinen
Universität Karlsruhe (T.H.)
Kaiserstr. 12, D-7500 Karlsruhe 1 (West-Germany)

SUMMARY

A finite-volume method is presented for solving the time-averaged two-dimensional Navier-Stokes equations in non-orthogonal curvilinear coordinates. In contrast to most existing codes, a non-staggered grid is employed for the discretization of the momentum equations avoiding the onset of pressure- and velocity oscillations by additional steps. In a first step, turbulent transport is taken into account by the standard k, ε-model. As a test-case, the turbulent flow through a model combustor with variable cross-sectional area and dilution air jets is considered. The results of the computations are compared with measurements as well as with finite-difference calculations of other available codes utilizing orthogonal coordinates especially adapted for this geometry. The advantages of the new non-orthogonal approach are demonstrated. It is shown that the proposed mathematical model serves as a powerful tool for the computation of turbulent separated flows in ducts with complex geometries pertinent to modern gas turbine combustors, especially those of the reverse-flow type.

NOMENCLATURE

a_i	coefficients of discretization equation
b	coefficient of discretization equation
B	boundary
c	velocity
C_i	constant of turbulence model
d_u	coefficient of correction equation for U
D_S	additional diffusion source-term
G_k	volumetric production rate of turbulent kinetic energy
h	enthalpy
H	duct height
J	Jacobian
J	momentum flux ratio
k	turbulent kinetic energy
l	distance between injection slot and slope
p	pressure
Pe	Peclet number
Pr	Prandtl number
q_i	geometric coefficient of transport equation
Re	Reynolds number
S	source-term
u	velocity component in x-direction
U	convective term normal to control-volume interface (ξ=const)
v	velocity component in y-direction
V	convective term normal to control-volume interface (η=const)
Γ	diffusion coefficient
ε	dissipation rate of k
η	curvilinear coordinate
μ	dynamic viscosity
ξ	curvilinear coordinate
ρ	density
σ_k	constant of turbulence model
σ_ε	constant of turbulence model
φ	dependent variable

Subscripts

e	eastern cell interface
E	eastern grid-point (or boundary)
eff	effective
j	jet
n	northern cell interface
N	northern grid-point (or boundary)
P	grid-point under consideration
s	southern cell interface
S	southern gid-point (or boundary)
w	western cell interface
W	western grid-point (or boundary)
x	partial derivative with respect to x-coordinate
y	partial derivative with respect to y-coordinate
ξ	partial derivative with respect to ξ-coordinate
η	partial derivative with respect to η-coordinate
∞	inlet

Superscripts
up upwind scheme
HOS higer-order scheme
* estimated
' correction
- average

INTRODUCTION

The continuing improvement of the thermal efficiency and of the specific thrust in modern jet engine design is directly dependent on the rise of the pressure ratio and the turbine inlet temperature. As a consequence, the combustor dimensions are reduced. In addition, even with higher temperature levels, lower pressure losses as well as complete combustion of the fuel with low emissions are a necessity. Furthermore, velocity profiles which are matched to the turbine requirements for high reliability are of interest. In predicting the performance of the combustor, a fairly accurate knowledge of the velocity within the combustor is required. In an attempt to reduce the high cost for a detailed experimental analysis it is necessary to utilize newly developed analytical and numerical tools in combination with available correlations in the design process. In recent years, various numerical codes for the three-dimensional description of the flow field have been developed. Continuing effort, however, has to be addressed towards relatively complex geometries.

Up to now two- and three-dimensional finite difference schemes for the description of the turbulent combustor flow have been used at the Institute for Thermal Turbomachinery employing orthogonal, i.e. in general cartesian or cylindrical, grids. Relatively simple geometries such as the flow through a plane duct with normal injection of the dilution air [1] or the swirling flow through a duct with constant circular cross-section [2] can be described with these codes. However, real gas turbine combustors deviate more or less from these simple geometries. A typical example is the reverse-flow combustor of a small helicopter engine, where the 180 -bend induces considerable influence on the velocity, turbulence and temperature field.

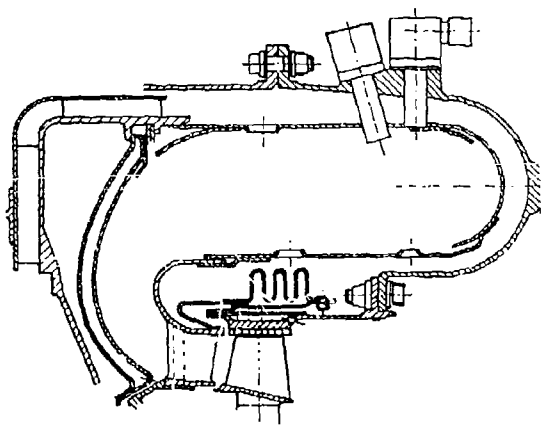

Fig. 1: Typical reverse-flow combustor

Up to now, in using orthogonal grids the boundaries of a complex flow field had to be approximated by a sequence of steps [3,4]. The shortcomings of this procedure are obvious. In addition to the fact that the boundary representation is insufficient, it is fairly difficult to take into account gradients normal to the wall. In addition, in the case of three-dimensional flows this method leads to a highly uneconomical utilization of storage space. In arriving at a high accuracy, the grid density in the area of the steps has to be sufficiently high which generally leads to an unnecessary high number of grid-points in the other areas resulting in excessive computation times. In extreme cases such as shown in Fig. 1 it is almost impossible to apply a conventional orthogonal grid.

In the present study, therefore, a new finite-difference method using a body fitted curvilinear and generally non-orthogonal grid for two-dimensional turbulent elliptic flows has been derived based on the experiences with the earlier codes. The transport equations in the physical domain are solved in the $\xi\eta$-space discretized by an equally

spaced cartesian coordinate system (Fig. 2). One advantage of this technique is that the relatively simple discretization of partial differential equations is largely conserved.

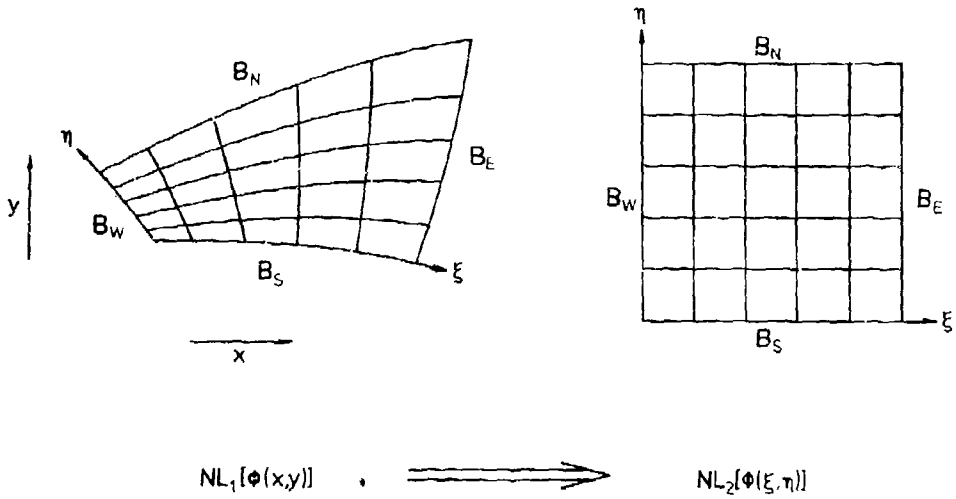

Fig. 2: Physical and transformed computational domain

It can be seen that all grid-points are considered and an efficient use of storage space and computational time is possible. Principally, it is possible to increase the local density of the grid in areas with large gradients and to consider gradients normal to the boundary. In selecting appropriate grid distribution, the so-called 'numerical diffusion' which is observed with oblique flow vectors can be reduced.

Obviously, additional effort in programming is required in utilizing body-fitted coordinates. Cross-derivative terms in the transformed differential equations are to be considered and generally staggerd grids are not suitable as will be illustrated later.

GRID-GENERATION

In generating an appropriate computational grid it is necessary that the boundaries of the grid with that of the flow field are identical. As will be shown later it is necessary to calculate the cartesian x/y-coordinates for each point ξ/η (see Fig. 2). In following Thompson et al. [5] the curvilinear coordinates have to satisfy the Laplace equations with the appropriate boundary conditions.

$$\xi_{xx} + \xi_{yy} = 0 \qquad\qquad \eta_{xx} + \eta_{yy} = 0 \qquad (1)$$

In exchanging the dependent and independent variables a new system of differential equations is obtained which leads to a curvilinear orthogonal grid. Adding additional terms on the right-hand side of the Laplace equation it is possible to achieve a locally denser or a stretched grid. However, the orthogonality is not conserved under these conditions. Thompson, for example, used this principle in generating a grid for the flow around an airfoil. In the present work this grid-generating program was adapted to internal flow problems by changing the boundary conditions.

Computational grids which are produced accordingly - i.e. following equation (1) - satisfy similarly to the potential and stream function of a potential flow the Laplace equation, i.e. stream lines and potentials are identical with the lines η = const. and ξ = const. of the grid. An oblique flow with respect to the control-volume interfaces is avoided in domains with potential flow character and thus the numerical diffusion is minimized. However, this technique which requires the solution of a non-linear differential system for the grid-generation is relatively cumbersome. For practical considerations, it is relatively difficult to position the grid-lines to predetermined measurement planes despite the possibilities of increasing their local density or in stretching the lines. Generally a sequence of iterative steps is necessary.

Another possibility for generating body oriented computational grids which is much simpler is to predetermine grid-lines of two boundaries such as $B_H(\eta = \eta_{max})$ and B_B ($\eta = 1$), to connect the boundary lines using straight lines (ξ = constant) and to define the grid-spacing analytically [6]. It is obvious, that this method allows for a rapid grid-generation. The resulting grids, however, show - under certain conditions - strongly non-orthogonal regimes. This is to be taken into account in the transformation of the transport equations. Fig. 3 illustrates various grids for the calculation of the flow through a reverse-type combustor which were generated with the techniques described here. Fig. 3d especially shows the grid-geometry for the case of rotational symmetry.

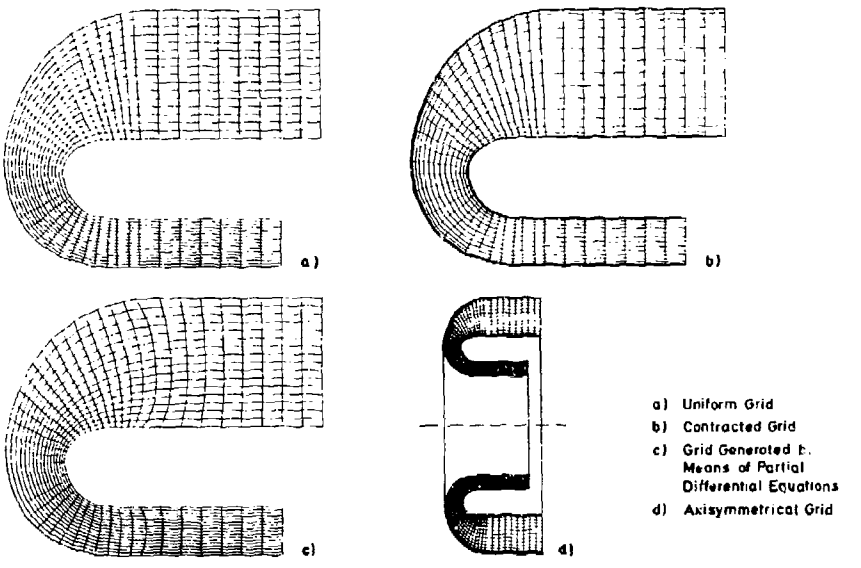

Fig. 3: Computational grids - reverse-flow combustor

TRANSFORMATION OF THE TRANSPORT EQUATIONS TO A CURVILINEAR COORDINATE SYSTEM

In cartesian coordinates the partial differential equation of a general transport property can be formulated in the usual way:

$$\underbrace{\frac{\partial}{\partial x}(\rho^* u^* \phi) + \frac{\partial}{\partial y}(\rho^* v^* \phi)}_{\text{convection}} = \underbrace{\frac{\partial}{\partial x}(\Gamma \frac{\partial \phi}{\partial x}) + \frac{\partial}{\partial y}(\Gamma \frac{\partial \phi}{\partial y})}_{\text{diffusion}} + \underbrace{S(x,y)}_{\text{source-term}} \qquad (2)$$

All terms which arise in addition to convection and diffusion are grouped in the source-term. The partial differentials of equation (2) can be replaced by derivatives of the new coordinates ξ and η [5]. A new transport equation is the result which can be grouped in analogy to equation (2) in a convection-, a diffusion- and a source-term.

$$\underbrace{\frac{\partial}{\partial \xi}(\rho^* U^* \phi) + \frac{\partial}{\partial \eta}(\rho^* V^* \phi)}_{\text{convection}} = \underbrace{\frac{\partial}{\partial \xi}[\frac{\Gamma}{J}(q_1 * \frac{\partial \phi}{\partial \xi} - q_2 * \frac{\partial \phi}{\partial \eta})] + \frac{\partial}{\partial \eta}[\frac{\Gamma}{J}(-q_2 * \frac{\partial \phi}{\partial \xi} + q_3 * \frac{\partial \phi}{\partial \eta})]}_{\text{diffusion}} + \underbrace{S(\xi,\eta)*J}_{\text{source-term}} \qquad (3a)$$

$$J = \begin{vmatrix} x_\xi & x_\eta \\ y_\xi & y_\eta \end{vmatrix} = x_\xi y_\eta - x_\eta y_\xi \tag{3b}$$

$$q_1 = x_\eta^2 + y_\eta^2 \tag{3c}$$

$$q_2 = x_\xi x_\eta + y_\xi y_\eta \tag{3d}$$

$$q_3 = x_\xi^2 + y_\xi^2 \tag{3e}$$

$$U = u^* y_\eta - v^* x_\eta \tag{3f}$$

$$V = v^* x_\xi - u^* y_\xi \tag{3g}$$

The terms q_1 and J which are observed in equation (3) are determined by the geometrical derivatives of the curvilinear grid in the cartesian domain x_ξ, y_ξ, x_η, y_η. q_2 is a measure for the orthogonality of the grid and it disappears for orthogonal grids and with it the mixed derivatives of the diffusion term in equation (3). The importance of the geometrical derivatives and of the velocities u and v is illustrated in Fig. 4.

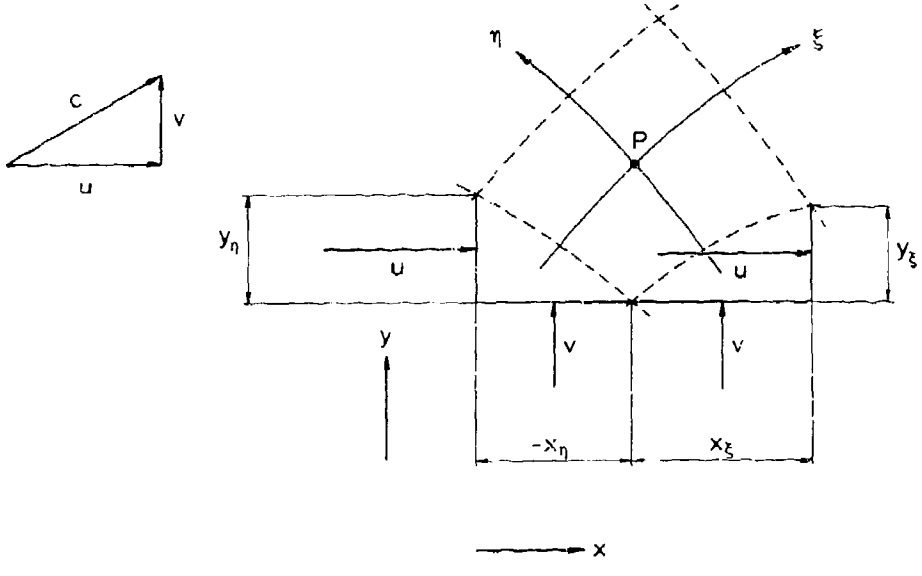

Fig. 4: Geometric derivatives and velocity components at the control-volume considered

The interface area of a control-volume is determined by the geometric derivatives x_ξ, y_ξ and x_η, y_η. ρ^*U and ρ^*V represent the convective fluxes across the respective interfaces of the control-volume. In conserving the consistency of the method, the geometric derivatives are directly determined from the grid-coordinates by a differentiation of the first order and not by differentiation of higher order.

Equation	ϕ	Γ	S
Momentum x-Direction	u	μ_{eff}	$\frac{1}{J}[\frac{\partial}{\partial\xi}[\frac{\Gamma}{J}(y_\eta^2*\frac{\partial u}{\partial\xi} - y_\xi y_\eta*\frac{\partial u}{\partial\eta} + x_\eta y_\xi*\frac{\partial v}{\partial\eta} - x_\eta y_\eta*\frac{\partial v}{\partial\xi})]$ $+ \frac{\partial}{\partial\eta}[\frac{\Gamma}{J}(y_\xi^2*\frac{\partial u}{\partial\eta} - y_\xi y_\eta*\frac{\partial u}{\partial\xi} + x_\xi y_\eta*\frac{\partial v}{\partial\xi} - x_\xi y_\xi*\frac{\partial v}{\partial\eta})]$ $- y_\eta*\frac{\partial}{\partial\xi}(p + \frac{2}{3}*\rho*k) + y_\xi*\frac{\partial}{\partial\eta}(p + \frac{2}{3}*\rho*k)\}$
Momentum y-Direction	v	μ_{eff}	$\frac{1}{J}[\frac{\partial}{\partial\xi}[\frac{\Gamma}{J}(x_\eta^2*\frac{\partial v}{\partial\xi} - x_\xi x_\eta*\frac{\partial v}{\partial\eta} + x_\xi y_\eta*\frac{\partial u}{\partial\eta} - x_\eta y_\eta*\frac{\partial u}{\partial\xi})]$ $+ \frac{\partial}{\partial\eta}[\frac{\Gamma}{J}(x_\xi^2*\frac{\partial v}{\partial\eta} - x_\xi x_\eta*\frac{\partial v}{\partial\xi} + x_\xi y_\eta*\frac{\partial u}{\partial\xi} - x_\xi y_\xi*\frac{\partial u}{\partial\eta})]$ $- x_\xi*\frac{\partial}{\partial\eta}(p + \frac{2}{3}*\rho*k) + x_\eta*\frac{\partial}{\partial\xi}(p + \frac{2}{3}*\rho*k)\}$
Energy	h	$\frac{\mu_{eff}}{Pr_{eff}}$	0.
Turbulence	k	$\frac{\mu_{eff}}{\sigma_k}$	$G_k - \rho*\varepsilon$
	ε	$\frac{\mu_{eff}}{\sigma_\varepsilon}$	$\frac{\varepsilon}{k}(C_1*G_k - C_2*\rho*\varepsilon)$
			$G_k = \frac{\mu_t}{J^2}*\{2[(y_\eta*\frac{\partial u}{\partial\xi} - y_\xi*\frac{\partial u}{\partial\eta})^2 + (x_\xi*\frac{\partial v}{\partial\eta} - x_\eta*\frac{\partial v}{\partial\xi})^2]$ $+ (x_\xi*\frac{\partial u}{\partial\eta} - x_\eta*\frac{\partial u}{\partial\xi} + y_\eta*\frac{\partial v}{\partial\xi} - y_\xi*\frac{\partial v}{\partial\eta})^2\}$

Table 1: System of differential equations

Tab. 1 summarizes the diffusion coefficients and source-terms for the momentum equations, the energy equation and the equations for the turbulence parameters of the k,ε-model which is employed for the closure of the system of equations.

As can be seen from Tab. 1, the momentum equations for the velocity components of the cartesian coordinate system u (x-direction) and v (y-direction) are solved even after the transformation. Other authors tend to formulate the momentum equations for the covariant velocity components. In the case of non-orthogonal computational grids, however, the momentum equations are quite complicated and the discretization becomes expensive. These techniques generally are, therefore, restricted to orthogonal grids [7].

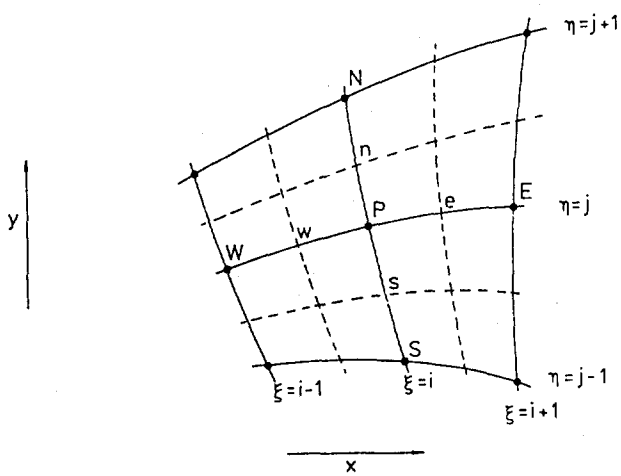

Fig. 5: Typical control-volume for curvilinear coordinate systems

The differential equation is transformed into a difference equation by integrating over each control-volume (Fig. 5) with $\Delta\xi = \Delta\eta = 1$. In discretizing the diffusion-terms of the general transport equation, the so-called central-difference scheme is used. Here, the gradient of the property ϕ at an interface of the control-volume is calculated directly from the adjacent grid-points. It should be noted that with the mixed derivatives of equation (3) the values at the corners of the control-volumes are required which have to be calculated by appropriate interpolation from the four adjacent grid-points. As the solution of the system of equations is based on a five-point difference-star it is impossible to consider these terms directly: they have to be accounted for by additional source-terms. This approach reduces the convergence characteristics of the method and additional interpolation errors can arise. It, therefore, is advisable to employ grids which have only slight deviations from the orthogonality, which, however, is frequently in contrast to the necessities of the flow geometry.

Considerable difficulties are observed with the discretization of the convective terms of the transport equations. Here, the transport property itself at the cell's boundary is required. The use of the central-difference scheme for Peclet numbers Pe > 2 can result in an instability of the solution procedure. A simple alternative is found in the well-known upwind scheme. Here, the transport property is defined at the cell boundary using that of the upwind positioned grid-point. This scheme is quite stable. Its major drawback, however, is the onset of numerical diffusion.

A scheme which excludes these discretization errors, is the so-called 'QUICK scheme' that has been originally proposed by Leonard [8]. This scheme uses two grid-points upstream and one downstream for interpolation of the unknown value at the control volume interface. As the direct incorporation of that scheme into the finite difference procedure can lead to instabilities for large Peclet numbers (Pe > 8/3) similarly to the case of the central-difference scheme, a different method is used, which has been presented by Elbahar [1] and improved by Noll [2]. In this method, commonly known as 'flux-splitting technique', the convective terms are first calculated by the upwind scheme. In a second step, the difference between the convective fluxes determined by the upwind scheme and those by the QUICK scheme are added to the source term. Using this method, it is also possible to include other higher-order disretization schemes (HOS) such as the aforementioned 'central-difference scheme' or the so-called 'linear upwind scheme' without strongly affecting the stability of the solution procedure. The convective flux at the e (-eastern) side of a control volume under consideration, can then generally be written as

$$(\rho^*U^*\phi)_e^{HOS} = (\rho^*U^*\phi)_e^{upw} + (\rho^*U^*\Delta\phi)_e \tag{4a}$$

and in the case of QUICK being the higher-order scheme for $\rho^*U > 0$

$$\Delta\phi_e = (\phi_W-\phi_P)^*f_{eWP} + (\phi_E-\phi_P)^*f_{eEP} \tag{4b}$$

$$f_{eWP} = \sqrt{\frac{((x-x_P)^2+(y-y_P)^2)^*((x-x_E)^2+(y-y_E)^2)}{((x_W-x_P)^2+(y_W-y_P)^2)^*((x_W-x_E)^2+(y_W-y_E)^2)}} \tag{4c}$$

$$f_{eEP} = \sqrt{\frac{((x-x_W)^2+(y-y_W)^2)^*((x-x_P)^2+(y-y_P)^2)}{((x_E-x_W)^2+(y_E-y_W)^2)^*((x_E-x_P)^2+(y_E-y_P)^2)}} \tag{4d}$$

Comparisons of calculations employing the different discretization schemes described (upwind, linear upwind, central-difference and QUICK) with experimental investigations of typical combustor flows show that the best agreement between measurement and computation is achieved using the QUICK scheme [6,10,11].

On discretizing the differential equations, the value of the general transport variable ϕ can be expressed for each control volume by the values of the four adjacent cells.

$$a_P\phi_P = a_E\phi_E + a_W\phi_W + a_N\phi_N + a_S\phi_S + b \tag{5a}$$

$$a_P = a_E + a_W + a_N + a_S + S_P \tag{5b}$$

$$b = S^*J^*\Delta\xi^*\Delta\eta + D_s \tag{5c}$$

$$D_s = f(q_2, J, \Gamma, \phi) \tag{5d}$$

The resulting system of algebraic equations is solved in this program by a line Gauss-Seidel method [9].

For closure of the system of equations an additional equation for the pressure is needed. In the code presented here, Patankar's 'SIMPLE-algorithm' is used mainly in evaluating the pressure by an estimated pressure-distribution and a 'pressure correction equation'. Starting with an approximation p^* of the correct pressure field p the momentum equations are solved. The resulting velocities u^* and v^* generally do not satisfy continuity. Therefore, a velocity correction u' and v', respectively, is added in order to satisfy the continuity equation. An equation similar to the momentum equations can be derived for the velocity correction with the gradient of pressure correction being the source term. Introducing this equation into the discretized continuity equation, an equation for the pressure correction can be derived which is mainly determined by the 'mass-flux source term'

$$b = (\rho_w * U_w^* - \rho_e * U_e^*) * \Delta\eta + (\rho_s * V_s^* - \rho_n * V_n^*) * \Delta\xi \tag{6}$$

The calculated corrections are subsequently added to the estimated velocity and pressure fields, respectively, which now satisfy both the momentum equations and the continuity equation.

If pressure and velocities are located at the same grid-points, the calculated pressure field and velocity field can show strong checkerboard oscillations although a converged solution is obtained. This is caused by a decoupling of pressure and velocity in the discretized momentum equations where the pressure gradient at a considered grid-point is determined only by the values at the adjacent grid-points and not by the pressure at the grid-point itself. As a remedy in the case of cartesian or cylindrical coordinate systems Patankar [9] proposes the use of a 'staggered grid' shifting the control volumes for the momentum equations by a half grid spacing in x-direction and y-direction for u and v, respectively. This leads to a strong coupling of pressure and velocity because now the pressure gradient in the momentum equations is determined by directly adjacent grid-points. Furthermore, the velocities are located exactly at the interfaces of the control-volumes for the pressure correction equation where they are needed to calculate the mass-flux source term.

Shyy et. al. [12] use a 'staggered grid' in their finite difference method on curvilinear coordinate systems too. In this case, however, the control volumes for the calculation of the velocities are now staggered in ξ-direction (for u) and in η-direction (for v). In considering the mass-flux source term of the pressure correction equation (6) it is obvious (compare Fig. 4) that in regions where lines ξ = const are nearly perpendicular to the x-direction or lines η = const to the y-direction the staggered grid will not lead to the desired effect. The convective term U at the eastern interface, for example, is exclusively determined by the cartesian velocity component v in y-direction which is only known at the northern and southern cell interface. Similarly, the pressure source term in the momentum equations (see Tab. 1) is no longer determined by directly adjacent grid points. Therefore, in such regimes this kind of staggered grid is not advantageous as oscillations of pressure and velocity can not be prevented.

In the code presented, a different method of avoiding the onset of oscillations is employed which was proposed first by Rhie and Chow [13] and later used in a slightly modified manner by Peric [14]. Here, the cartesian velocity components in x- and y-direction are located at the same grid-points as the pressure. The convective terms U and V at the cell interfaces are calculated by suitable interpolation of the cartesian velocities at the grid-points. Subsequently the averaged values of the convective terms U and V are corrected by means of local pressure gradients, e.g. for the eastern interface

$$U_e = \overline{U}_e + \overline{d_{u,e}} * \left(\frac{p_E^* - p_P^*}{\Delta\xi} - \overline{p}_{\xi,e}^* \right) \tag{7a}$$

$$d_u = \Delta\eta * \left(\frac{y_\eta^2}{a_u} + \frac{x_\eta^2}{a_v} \right) \tag{7b}$$

This procedure was found to be quite stable and up to now oscillations of pressure and velocity have been successfully suppressed. Another advantage of the use of a 'nonstaggered grid' is that the complexities of the program are reduced as the coefficients have to be evaluated for one grid only and not for three different grids as is the case for a 'staggered grid'.

EXPERIMENTAL VERIFICATION

As a test case for the quality of the newly developed finite difference code on curvilinear coordinate systems use was made of measurements in a turbulent flow through a plane combustor model with convergent cross-section and normal injection of dilution air.

A schematic view of the complete experimental facility and the employed data acquisition system is shown in Fig. 6. Air from the compressor is subdivided into the primary and the mixing jet flow. Adjustable valves and standard orifice meters facilitate control and volumetric flow measurements within the ducts, respectively. Both, the primary air and the secondary air flow through settling chambers fitted with turbulence grids. The primary air enters the test section of 300 mm x 100 mm cross-sectional inlet area through a nozzle with a contraction factor of 20.8. The secondary air is normally injected by a slot in the bottom wall prior to a slope of 90 mm length and 43 mm height contracting the flow area as illustrated in Fig. 7. At six discrete measurement planes it is possible to attach a probe traversing mechanism. The measurement of the velocity field has been done by means of a calibrated five-hole probe with a diameter of 2.9 mm. A detailed description of that miniature probe can be found in [2]. Computer assisted data acquisition is necessary as a large matrix of data is obtained and has to be analyzed.

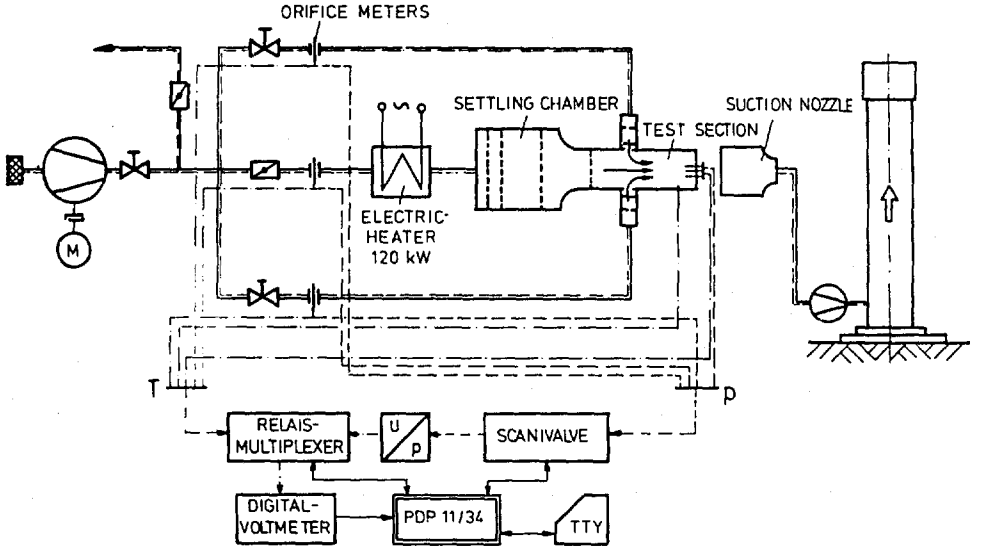

Fig. 6: Experimental set-up

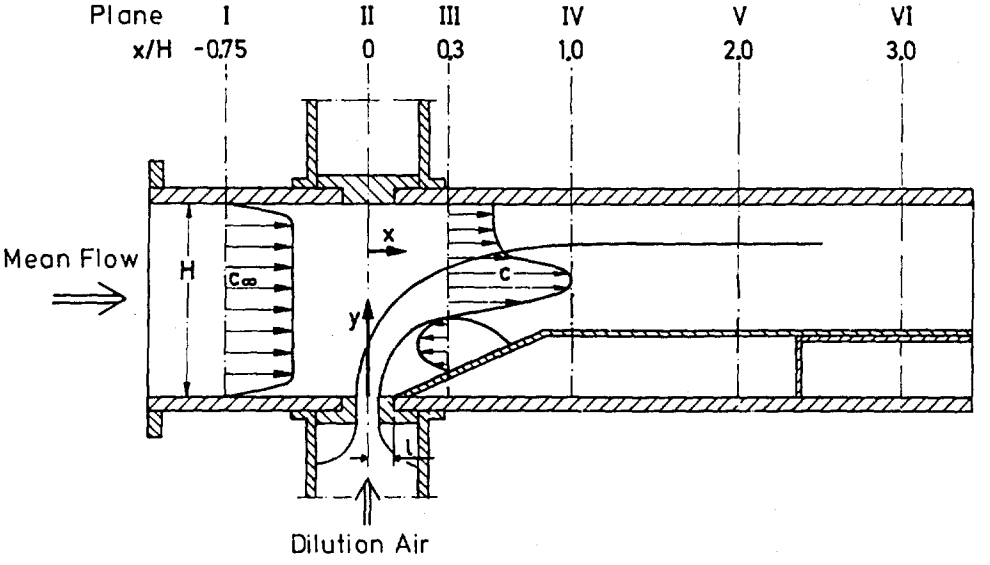

Fig. 7: Test section with convergent flow area

The flow through the described combustor model has been calculated with the newly developed finite-difference method using curvilinear coordinates as well as with the conventional code using cartesian coordinates (s. [3]). Both programms employed a grid of 54 x 38 grid-points. Fig. 8 illustrates the combustor-fitted curvilinear grid.

Fig. 8: Curvilinear computational grid

The cartesian grid discretizes the convergent part of the combustor by discrete orthogonal steps. Grid-points located at the lower right hand side are skipped and not used for the flow calculation. In Fig. 9 this part of the model combustor is shown enlarged for both computational grids.

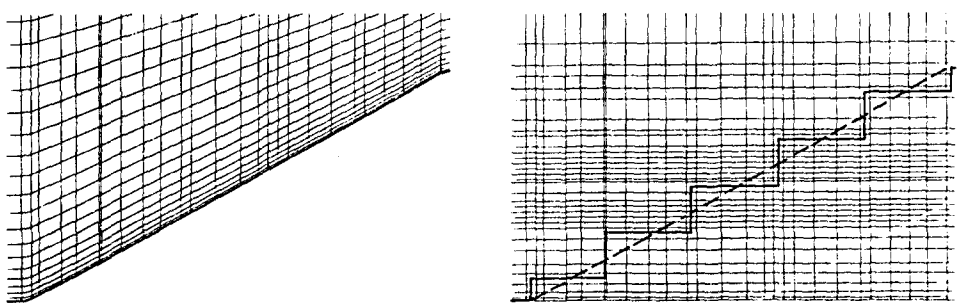

Fig. 9: Discretization of the slope

Fig. 10 shows the measured velocity distribution along the model combustor for a momentum flux ratio $J = \rho_j/\rho_\infty * (v_j/u_\infty)^2$ of 20.5 for an axial distance l between injection slot and beginning of the slope of 15 mm.

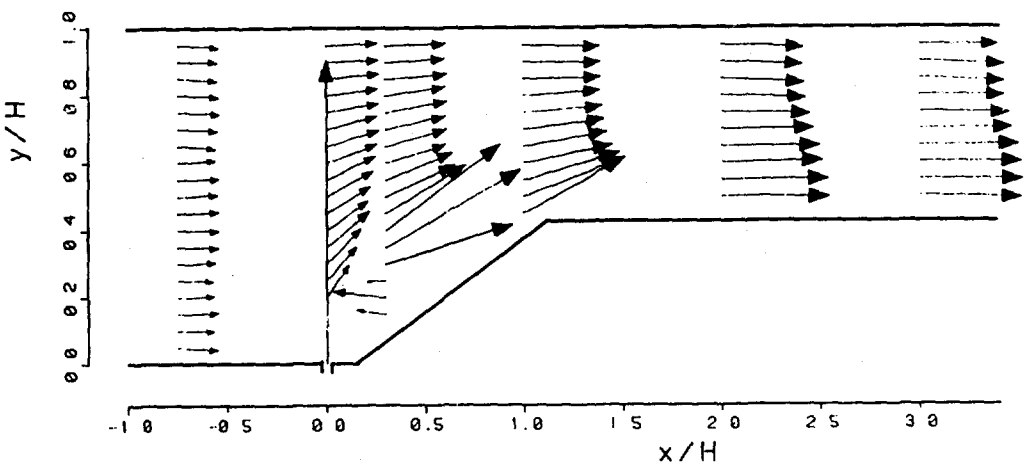

Fig. 10: Measured velocity distribution

Although the flow is accelerated in the convergent section of the duct adjacent to the injection slot, an extensive recirculating zone can be observed. The calculated velocity fields (see Fig. 11) which have been obtained by employing the finite-difference program using curvilinear computational grids generally show the same characteristics. However, the two numerical results differ clearly: In using the QUICK scheme for the discretization of the convective terms in the momentum equations, the depth of penetration of the dilution air is slightly increased and the length of the recirculating zone is enlarged.

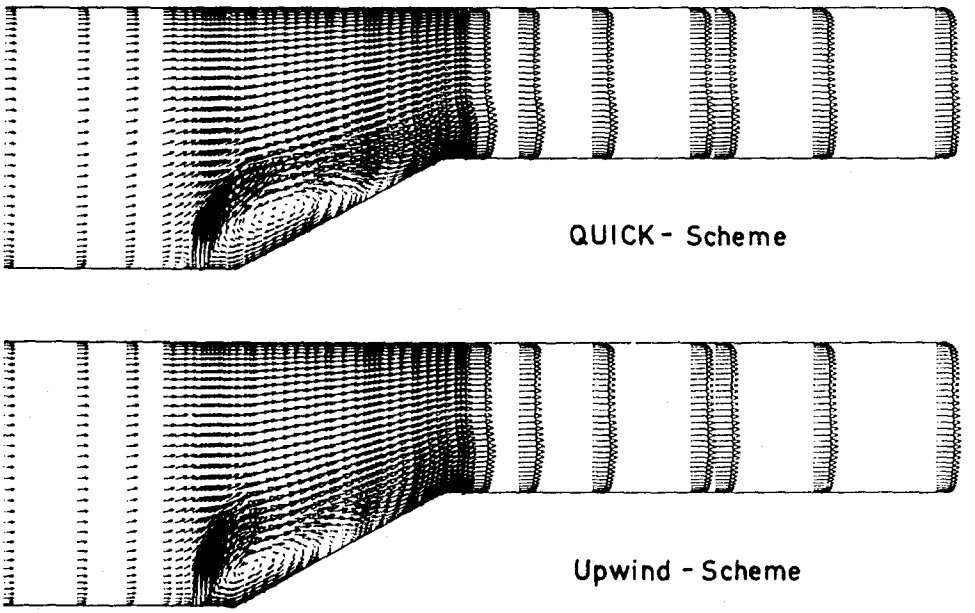

Fig. 11: Calculated flow field

On comparing measurement and calculations for several discrete measuring planes directly as illustrated in Fig. 12, the results obtained are quite satisfactory.

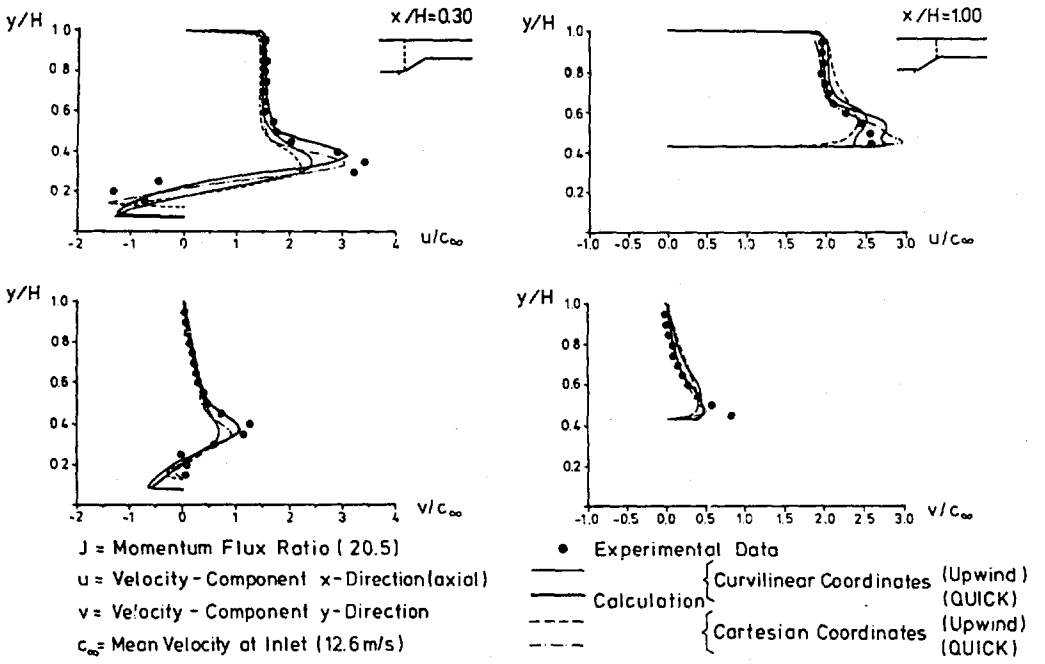

Fig. 12: Comparison of experimental and computational results

The best agreement with the experimental data is achieved for both numerical methods using cartesian or curvilinear coordinates in the case of utilizing the QUICK scheme for the convective terms. As should be noted, the new finite difference code leads to even slightly better results. On using the simpler upwind scheme, the steep velocity gradients are smoothed and the maximum values of velocity can not be obtained. This is due to the intensive oblique flow with respect to the grid within the recirculating zone and the resulting 'false diffusion'. The fictitious better agreement in predicting the velocity minimum close to the boundary by the method using cartesian coordinates is caused by the local approximation of the boundary. At the position x/H = 0.3 the step is protruding into the duct for a certain amount (see Fig. 9) and thus the velocity profile is shifted upwards.

The comparison of the finite-difference method using curvilinear coordinates with measurements and with conventional finite-difference methods illustrates that the newly developed calculation procedure is at least of comparable accuracy for relatively simple flow geometries. However, its entire potential is demonstrated for such geometries which can not be considered by the existing methods to a reasonable expense. As an example, the flow in a combustor type diffuser with centre-body is calculated with the method presented [15] without changing the program source code: the previously generated body-fitted computational grid had to be read in and the appropriate boundary conditions had to be defined.

CALCULATION OF THE FLOW IN A REVERSE-FLOW COMBUSTOR

As an other example for a flow which can not be calculated by other existing conventional finite-difference methods, the calculation of the flow in a reverse-flow combustor of a small helicopter engine (see Fig. 1) is presented.

Fig. 13 shows the calculated flowfield within the axisymmetric duct for a Reynolds number of $Re = 1.3*10^5$. The computation has been performed for a computational grid consisting of 47 x 17 grid-points with the grid-lines beeing contracted towards the boundary (see Fig. 3d).

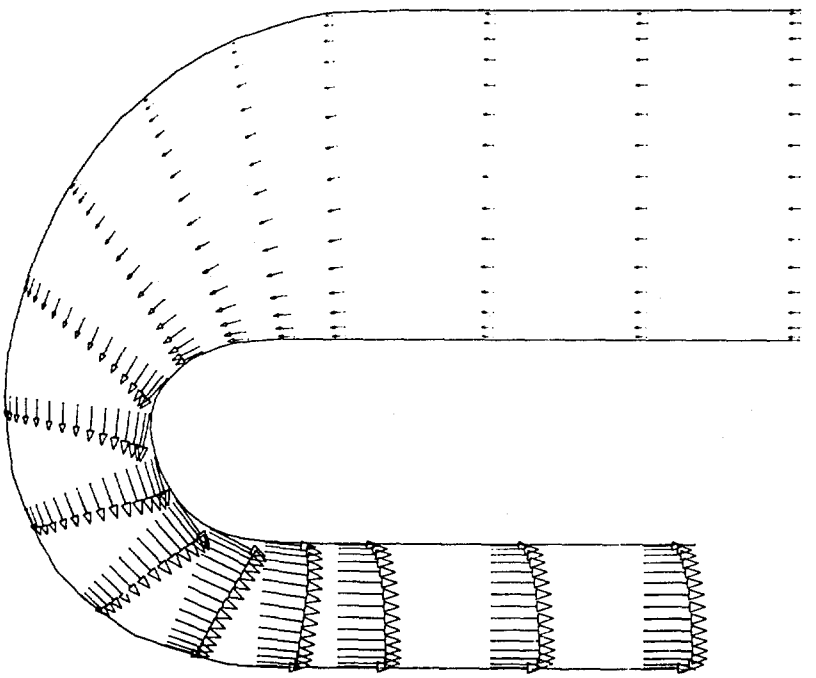

Fig. 13: Calculated velocity field in the 180 deg. bend of a reverse-flow combustor

Due to the decrease of the duct hight in flow direction in combination with the decreasing mean radius the flow is strongly accelerated within the bend. In spite of the strong curvature of the internal duct side, a separation of the flow at the bend exit is prevented by this acceleration. The flow in the bend shows potential vortex character, as the circumferential velocity increases towards the internal side (suction side) of the duct while the boundary layers are quite thin due to the acceleration of the flow. At the bend exit the maximum of the velocity is shifted in direction of the external duct side caused by centrifugal forces.

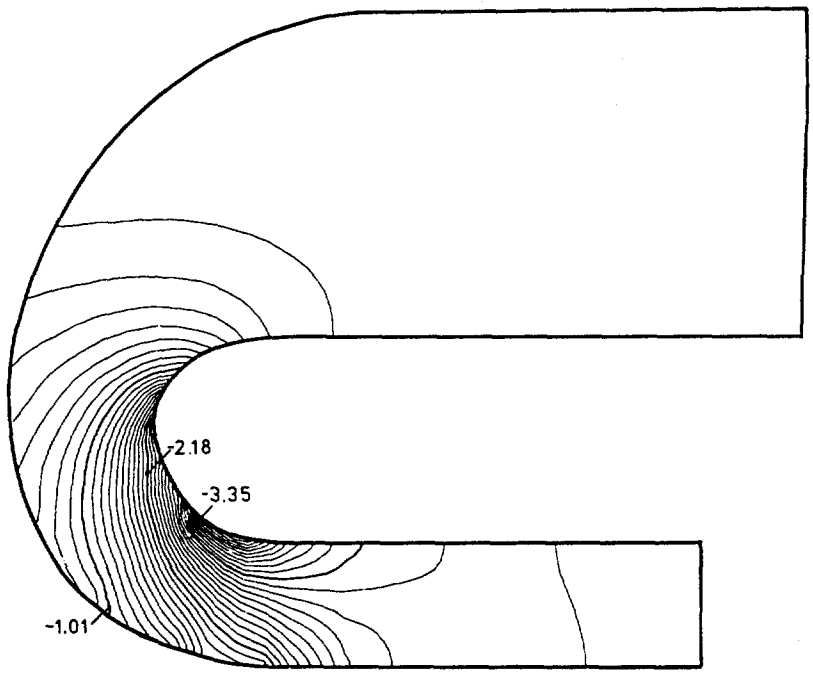

Fig. 14: Calculated pressure distribution

Fig. 14 illustrates the calculated pressure field pertinent to the flow field. The isobars in the bend show the typical behaviour of a potential vortex superposed by a flow acceleration. The pressure minimum at the bend exit with subsequent increase of pressure due to the local flow deceleration is obvious.

CONCLUSIONS

A newly developed difference scheme for the calculation of two-dimensional turbulent and elliptic combustor flows has been introduced which provides the discretization of the geometry of the flow field by body-fitted curvilinear grids. These grids can be generated either analytically or by the numerical solution of elliptic differential equations. An orthogonality has not to be assumed. The transport equations to be solved are transformed appropriately to the curvilinear coordinate system generated. As the differential equations principally do not change their character during the transformation it is possible to apply previously derived methods of discretization and thus can be solved. In discretizing the convective terms of the transformed transport equations the relatively simple upwind scheme and the more elaborate QUICK scheme were employed. It was found, that staggered grids did not exclude oscillations of the calculated pressure and velocity field for all flow geometries. A non-staggered grid, therefore, was employed. Oscillations of the solutions were avoided using a correction of the convective terms along the boundaries of the control-volumes using local pressure gradients. In addition, the obvious advantage of non-staggered grids is the resulting simplicity of the program's structure. An elaborate check of the reliability of the program was initiated. The comparison with calculations using a conventional cartesian grid were quite favourable. Furthermore, measurements in a combustor-type flow were conducted for validation. In demonstrating the capabilities for application under real conditions, a reverse-flow combustor of complex geometry was analysed.

ACKNOWLEGEMENTS

The present work was supported by a grant of the German National Science Foundation (Deutsche Forschungsgemeinschaft, DFG) within the larger context of the Sonderforschungsbereich 167 'High Intensity Combustors'.

REFERENCES

[1] Elbahar, O.M.F.:
Zum Einfluß von Kühlluftstrahlen und Mischzonengeometrie auf die Temperaturprofilentwicklung in Gasturbinenbrennkammern. Dissertation, Universität Karlsruhe, 1982

[2] Noll, B.E.:
Numerische Berechnung brennkammertypischer Ein- und Zweiphasenströmungen. Dissertation, Universität Karlsruhe, 1986

[3] Wittig, S.L.K., B.E. Noll, O.M.F. Elbahar and U. Willibald:
Einfluß von Mischluftstrahlen auf die Geschwindigkeits- und Temperaturverteilung in einer Querströmung. VDI-Berichte, Nr. 487, paper presented at VDI-Tagung 'Thermische Strömungsmaschinen', Köln, June 1983, pp. 161-169

[4] Wittig, S.L.K., R. Kutz, B.E. Noll and K.-H. Platzer:
Development of Temperature-, Velocity- and Concentration-Profiles in a Curved Combustor. AGARD-CP-353, 1983

[5] Thompson, J.F., F.C. Thames and C.W.Mastin:
Curvilinear Coordinate Systems For Solution of Partial Differential Equations on Fields Containing Any Number of Arbitrary Two-Dimensional Bodies. NASA Contractor Report No. 2729, 1977

[6] Wittig, S., H.-J. Bauer and B.E. Noll:
Zwei- und dreidimensionale Strömungsvorgänge - Entwicklung des Strömungszustandes in Brennkammern bei komplexer Geometrie. Forschungsbericht, SFB 167 'Hochbelastete Brennräume', Teilprojekt B1, 1987, pp. 279-324

[7] Moore, J. and J.G. Moore:
A Calculation Procedure for Three -Dimensional, Viscous, Compressible Flow. Part I and II, Journal of Fluids Engineering, Vol. 101, 1979, pp. 415-422 and 423-428

[8] Leonard, B.P.:
A Stable and Accurate Convective Modelling Procedure Based on Quadratic Upstream Interpolation. Computer Methods in Applied Mechanics and Engineering, 19, 1979, p. 59

[9] Patankar, S.V.:
Numerical Heat Transfer and Fluid Flow. Hemisphere Publishing Corporation, Washington, 1980

[10] Noll, B.E.,S. Wittig and K. Steinebrunner:
Numerical Analysis of the Flame-Stabilizing Flow in the Primary Zone of a Combustor. Proc. of the 2nd ASME/JSME Thermal Engineering Joint Conference, Vol. 1, Honolulu, Hawaii, 1987, pp. 151-159

[11] Elbahar, O.M.F., B.E. Noll and S.L.K. Wittig:
Investigation of the Flow-Field and Temperature Profiles in Gas Turbine Combustors: The Results of Three Finite Difference Schemes. Paper presented at the 6th Intern. Conf. on Mechanical Power Engineering, Menoufia-University, Cairo, 27.-29. Sept., 1986

[12] Shyy, W., S.S. Tong and S.M. Correa:
Numerical Recirculating Flow Calculation Using a Body-Fitted Coordinate System. General Electric, Technical Information Series, Report No. 84CRD027, 1984

[13] Rhie, C.M. and W.L. Chow:
Numerical Study of the Turbulent Flow Past an Airfoil with Trailing Edge Separation. AIAA-Journal, Vol. 21, No. 11, 1983, pp. 1525-1532

[14] Peric, M.:
A Finite-Volume Method for the Prediction of Three-Dimensional Fluid Flow in Complex Ducts. PhD Theses, University of London, 1985

[15] Wittig, S., S. Kim and R. Hestermann:
Verlustarme stabilisierende Diffusoren im Übergangsteil und in der Primärzone hochbelasteter Brennkammern. Forschungsbericht, SFB 167 'Hochbelastete Brennräume', Teilprojekt B3, 1987, pp. 367-391

NUMERICAL MODELING OF COMBUSTION PROCESSES IN GAS TURBINES

by

L. Galfetti
Dipartimento di Energetica
Politecnico di Milano
Piazza Leonardo da Vinci, 32
20133 Milano, Italy

M. Belli
Dipartimento di Meccanica
Università degli Studi della Calabria
87030 Arcavacata di Rende (Cs), Italy

C. Bruno
CNR-CNPM
Viale F. Baracca, 69
20068 Peschiera Borromeo (Mi), Italy

SUMMARY

The indications coming from fundamental turbulence research have been incorporated in combustor modeling without a systematic analysis of their effect on predictions. In this work comparisons are presented between finite rate (overall) kinetics and equilibrium in their influence on the structure of the recirculation region attached to a disk flame-holder. The effect of including density gradient terms in the k-epsilon turbulence model is also examined. The results indicate that the fluidynamic field may determine whether equilibrium or kinetics produces higher temperatures, and that the temperature difference predicted with the two approaches tends to become small with increasing pressure. The effect of introducing density gradients has a moderate effect on temperatures.

LIST OF SYMBOLS

a	air inlet annulus thickness
A	air
C_i	constants in turbulence model
D	combustor can diameter
ER	equivalence ratio
F	fuel
G	free energy
HC	hydrocarbon
K	turbulence kinetic energy
K_p	equilibrium constant
m	reaction order
n	reaction order
p	pressure
R	universal constant of gas
RJ	ramjet
SCRJ	supersonic combustion ramjet
t	time
T	temperature
U	velocity
V	velocity
Y_k	mass fraction of species k
ϵ	rate of dissipation of turbulence kinetic energy
μ_t	turbulent viscosity
ρ	density
σ_i	turbulent Prandtl/Schmidt number

Subscripts and superscripts

max,min	maximum, minimum
ref	reference
"	fluctuating quantity
~	Favre-averaged mean quantity

1. INTRODUCTION

Much progress in gas turbine combustor modeling has been accomplished in recent years /1-3/, mainly by appropriate modeling of the turbulence phenomena of importance and of the reactive zone structure. Notwithstanding its shortcomings, the turbulent flowfield is described in most works by the k-epsilon model; however, work by Jones /4/ has resulted in the introduction of additional terms in the 'standard' equations to account for density changes due to combustion. Besides, the Favre-averaging procedure has won wide acceptance over the more traditional time-averaging in writing conservation equations for both scalar and vectorial quantities.

At the moment use of Favre-averaged scalar equations, however, is dictated more by expediency than by real need: in fact, LDV measurements of velocity components are indeed 'Favre-averaged', and are immediately compared to predictions. Scalars, such as enthalpy or species mass fractions are usually obtained from CARS-type measurements, supplying the time-averaged value of the quantities /5/. Mathematical difficulties in dealing with two different averaging techniques in the same equation are still severe, and no solution is in sight yet. However, Favre-averaging is in many respects an advancement. The structure of the reactive zone and the statistical description of combustion processes has been the object of many investigations /6/. Historically, modeling of the reactive terms has moved from global or semiglobal time- or Favre-averaged rate equations through equilibrium assumption, to flamelet models involving PDF (requiring rather time-consuming measurements under difficult conditions /2,7/.

The combustor modeling community has followed all these developments trying to incorporate them in its computer codes; the speed of change has been rather fast, however, and often there has not been the time to sit back and evaluate the many suggestions and novelties coming from the fundamental research. In particular, there has not been yet a consistent evaluation/comparison of the different approaches available; some papers have used the 'standard' TEACH code for the turbulent flowfield, adding a mixed global/equilibrium kinetics to it /8/; other works have accounted for density gradients in the k-epsilon equations while using global kinetics to describe combustion /9,10/. It is of interest therefore to try to assess in a systematic way the effects of these modeling choices on the results, and to compare them with available combustor measurements.

The purpose of this paper is twofold: to compare predictions obtained using global kinetics for the fuel/air reaction and equilibrium assumption, and to compare predictions obtained with the 'standard' k-epsilon turbulence model and that including density and pressure gradient terms. To uncouple the problem from the particular combustor design, a basic geometry was chosen, consisting of a disk flameholder in a cylindrical can. This is the simplest possible geometry that is still capable of generating intense turbulent recirculation.

Section 2 contains details of the geometry used and the operational parameters employed in the computer runs; Section 3 gives the essentials of the mathematical model; results and their discussion are reported in Section 4.

2. GEOMETRY AND CONDITIONS

Combustor can geometry is shown in Fig. 1. Two L/D ratios were used, i.e., L/D=1.5 and 2.5: the first was adopted for all equilibrium calculations, as the overall fuel consumption rate was faster and a shorter combustor length required for combustion completion. With finite-rate kinetics the total length needed was longer; dictating a larger number of grid points in the axial direction. The ratio between air inlet annulus thickness, a, and can diameter D was kept constant and equal to 0.1505, with D=0.25 m.

The advantages of such cavity shape are as follows: geometry is simple, with only primary air mixing; combustor shape and design are essentially those of the model combustor used at AFWAL by Roquemore et al. /11/ in their simulations and experiments, so that comparisons are possible; this geometry is also interesting for ramjet combustor modeling, where research is also in progress.

Conditions used in the simulations were the following: the fuel was gaseous C_3H_8, for which global kinetic data were available and that approximates the reactive behavior of higher HC (using methane, a much more likely candidate for RJ and SCRJ was considered and discarded because of its rather special kinetics); inlet air temperature ranged from 900 to 1100 K and inlet fuel temperature between 350 and 450 K; the inlet air and fuel velocities ranges were 40-120 and 20-50 m/s respectively. Pressure was varied between 1

and 9 bar. With these choices the air Reynolds number varied between 50,000 to 400,000.

3. MATHEMATICAL MODEL

The model uses a standard 2-D TEACH solver /12/ modified to include multiply-connected surfaces capability. Chemical kinetics may be either generalized (i.e., capable of simulating elementary steps), or global/overall; alternatively, thermochemical equilibrium may be imposed to find species concentrations and temperatures in the presence of chemical reactions.

All dependent variables use the Favre-averaging formulation; for the two velocity components, this makes comparison with LDV measurements very convenient. In fact, preliminary runs of the model without chemical reactions ('cold' runs) yielded velocity fields in close agreement with both predictions and LDV measurements obtained by Roquemore et al. /11/. Comparison with temperature measurements would require transforming Favre-averaged temperatures into conventional time-averaged temperatures, and because of the scarce data was not attempted.

The effect of density changes due to the heat release has been accounted for by including the modified k-epsilon model proposed by Jones /4/ and later employed by Jones and McGuirk /2/ and Jones and Whitelaw /13/.

3.1 k-epsilon Equations

Inclusion of the extra terms due to density and pressure gradients results in the equations for k and epsilon shown in Fig. 2. The terms depend on the product of the density and pressure gradients: therefore, in subsonic flows their magnitude is essentially determined by density gradients. For diffusion flames the introduction of these terms may cause numerical problems near the interface between the fuel jet and the surroundings during the first iterations starting from an initial guess of the field. This is due to the sharp radial density gradients near the flameholder fuel injection hole, that demand either a finer local mesh along the radii near x = 0, or introduction of these terms after a number of iterations large enough that those gradients have been smoothed down. This second approach was implemented here. Typically, about 0(10) iterations were performed prior to the activation of the density gradient terms in both k and epsilon equations.

3.2 Overall Kinetics

Rather than using a flamelet model coupled to PDF approach, global kinetics was investigated using Favre-averaged concentrations and temperatures in the rate expression. The rate was taken from /14/, dealing with premixed HC/air flame propagation, and has the form

$$\frac{d\,[\tilde{F}]}{dt} = 8.6\times10^{11}\,[\tilde{O}_2]^{\,m}\,[\tilde{F}]^{\,n}\,\exp(-30{,}000/\,R\tilde{T}),\ \frac{\text{mole}}{\text{cm}^3\text{s}} \qquad (1)$$

where m = 1.65 and n = 0.1. However, this fit works well only in a relatively narrow range of equivalence ratios ER. The n << 1 exponent tends in fact to predict unphysically high rates in the fuel-lean zones of the mixing region(s). To avoid this, the exponent n was made a function of the local ER, following a suggestion by Riva implemented in /15/. The fit for n that gave the best results over the broadest range of pressures was:

$$n = n_{ref} + (n_{max} - n_{ref})\,\frac{ER(x,y) - ER_{ref}}{ER_{min} - ER_{ref}} \qquad (2)$$

where n_{ref}=0.1, n_{max}=0.5, ER_{ref}=0.5, and ER_{min}=0.

3.3 Thermochemical equilibrium

In this mode, besides C_3H_8, O_2, N_2, CO_2, H_2O, the model includes also CO, OH and H_2. The species concentrations are predicted using fits for the equilibrium constant $K_p = K_p(T)$, resulting in functional relationships of the type

$$Y_k = f\,[ER(x,y)] \qquad (3)$$

The fits are valid between 700 and 3000 K. The equilibrium calculations are bypassed

entirely either for F/A (0.001 (very lean mixture) or if A/F (0.01 (very rich) /16/. Besides, for propane fuel and if ER) 3, the combustion products are assumed to be only CO and H_2.

Using the model in the equilibrium mode, the solution procedure becomes as follows: starting from an initial guess, compute the momenta transport. With the flowfield already updated, compute equilibrium values for species Y_k and enthalpy; next, compute the enthalpy transport, and from updated p, Y_k and h and old density, update the temperature inverting the fit for the enthalpy as a function of temperature and species mass fractions. Last the density is also updated from the equation of state.

In both equilibrium and overall kinetics calculations there is a modeling approximation inherent to using [Favre-] averaged quantities. In the case of finite-rate kinetic, fuel and oxygen fluctuations, that would tend to reduce the average value of the rate itself, are not accounted for; in the equilibrium approach, the approximation consists in evaluating equilibrium constants K_p at an averaged temperature. In both cases the dependence of the approximation on temperature is exponential: for the finite -rate case, in the Arrhenius term of (1); for the equilibrium case, in the Van't Hoff dependence of the equilibrium constant on free energy

$$\frac{\partial(\ln K_p)}{\partial T} = - \frac{\Delta G}{RT^2} \qquad (4)$$

so that the error in both cases is of the same order.

4. RESULTS

Table 1 shows the matrix of the runs performed and the values adopted for the parameters changed.

The structure of the recirculation region was investigated at first using the equilibrium approach. Figure 3 shows the predictions of the velocity field in the centerbody combustor for different fuel and air flow rate ratio. Streamlines indicate that the formation of one or two vortices, and their extension, depends on the ratio between the air and fuel inlet momenta. The interaction of the central and annular jets is responsible of changes in the flame structure; Figs. 3a and 3b show the condition where the annular jet dominates the flow field, while Fig. 3c relates to a condition where neither jet dominates the velocity field. In Fig. 3a the air inlet momentum, greater than the fuel inlet momentum, creates a dominant outer vortex; however, since the two inlet momenta are essentially of the same order of magnitude, the fuel jet creates also a second inner vortex. Fig. 3b shows, instead, formation of only one vortex, due to air momentum, while the fuel is rapidly entrained as soon as it exits the injector. The strong gradients in the upper region of the vortex are responsible for high turbulence levels and, consequently, for high conversion to products and heat release, as shown in Fig. 5. Air and fuel inlet velocity are equal in the case of Fig. 3c. An upper clockwise vortex and a well developed counterclockwise vortex are formed, due to the same inlet velocity of air and fuel. In such situation turbulence levels are quite low, turbulent transport is poor and the combustor efficiency is bad, as seen in Fig. 8a.

These predictions were compared with those obtained with finite kinetics assumption under the same operating conditions. Results are reported in Fig. 4. A detailed comparison shows a negligible influence of the approach chosen on the velocity field.

A different conclusion is reached when temperature fields are compared. Starting with test case 25 (p=5 bar, inlet air velocity=120 m/s, inlet fuel velocity=25 m/s), the fluidynamic field is shown in Fig. 3b (equilibrium assumption) and in Fig. 4b (overall kinetics assumption). For the same test case 25, Fig. 5a shows isothermal contour lines obtained for thermochemical equilibrium and Fig. 5b isotherms predicted with the finite kinetics assumption. Significant differences exist in the two temperature fields. In both cases the hot gas region is localized at the bottom side of the annulus region. This is a physically realistic conclusion considering that such region contains a strong shear layer, characterized by high velocity gradients and high turbulence levels. Transport of fuel and oxidant is favoured, and so in both equilibrium and finite kinetics assumption the largest temperature is reached. An interesting feature of the two solutions is that the temperature field for the finite kinetics case is higher than for the equilibrium case. The opposite conclusion may be drawn when the temperature fields of test case 16 (Fig. 6) are examined: in such situation the finite kinetics temperature field (Fig. 6b) is lower than that pertaining to equilibrium (Fig. 6a). The reason of

this apparently nonintuitive behavior has to be found in the influence of turbulence: high turbulence levels, associated with high inlet momenta, favor the heat release process in the kinetic approach, since faster mixing produces larger regions where fuel and oxygen concentrations are sufficiently high to activate the global finite-rate kinetics. In low turbulence level situations, poorer mixing results in either too low fuel or too low oxygen concentrations, and finite rate kinetics, at least in the global formulation used here, cannot 'take off'. This is not so for the equilibrium case, in which temperature increases no matter how small the fuel and oxygen present. Therefore, the heat release process is favored by the equilibrium approach. It is important to underline that such differences in the temperature field do not significantly influence the velocity field and this may be relevant in comparing experimental measurements and numerical predictions.

According to these different temperature fields, different fields in carbon dioxide distribution are observable. For test case 25 the carbon dioxide field is shown in Fig. 7a (equilibrium) which has to be connected to Fig. 5a and in Fig. 7b (finite kinetics) which has to be connected to Fig. 5b. From a qualitative point of view the structure is the same in both cases: the highest concentrations are associated with the highest temperatures, the trend in the region of the fuel inlet is similar in the two cases, and so is also the CO2 distribution from the annular region to the centerline. However, at least for this particular set of input data, quantitative differences exist locally.

To further investigate the effect of the two considered approaches, the structure of the recirculation region has been correlated to the combustion products field. For the thermochemical equilibrium case (test case 16, Fig. 8a) streamlines are shown superimposed to the chemical species field: the dashed region shows where fuel dominates. Concentration is related to the density of dots: high density corresponds to high concentration. As the fuel diffuses from the central fuel jet outwardly, it decelerates by entraining air at high temperature; the region between vortices is the most favorable to products formation in that equivalence ratio is closer to the stoichiometric value. Combustion products thus provide a source of heat and ignition for the fuel from the central jet: as the picture shows, most of these products are distributed radially along and close to the combustor face, and reaching close to the inlet air transported by the annular jet. Diffusion of fuel and of combustion products is quite poor; the low inlet velocities are responsible for low turbulent gradients, which govern turbulent diffusion. This general picture is confirmed when finite kinetics is assumed. Aside from differences in the temperature field, general trends do not change; for example low turbulent gradients are seen when looking at the velocity field shown in Fig. 8b. The bad efficiency of the combustor, operating at these conditions, is indicated by Figs. 8c and 8d in which fuel and carbon dioxide mass fractions respectively are shown for the overall kinetics assumption. Fig. 9a shows for the equilibrium case, streamlines superimposed to the chemical species field for the test case 6 (p=3 bar; inlet air velocity=50 m/s; inlet fuel velocity=20 m/s). Compared to the previous case, the different structure of the recirculation region and combustion products shot a different behavior of the combustor: the fuel is completely entrained in the recirculation region and the mass fractions at the outlet section of the combustor are represented only by the combustion products. Fig. 9 also shows the comparison between the equilibrium (Fig. 9b) and finite kinetics (Fig. 9c) temperature field. Differences have to be ascribed to the above mentioned phenomena. Again, carbon dioxide fields (Fig. 9d for the equilibrium case and Fig. 9e for the finite kinetics case), are correlated to the temperature field.

The effect of pressure on the temperature field for the two cases of thermochemical equilibrium and finite kinetics are shown in Fig. 10a-c and Fig. 11a-c respectively. Equilibrium computations were performed at p=3 bar (case 6, Fig. 10a), p=5 bar (case 17, Fig. 10b) and p=9 bar (case 27, Fig. 10c). No significant temperature variations nor consistent changes in the spatial distribution of isothermal lines can be observed. Finite kinetics computations are shown for p=1 bar (case 4, Fig. 11a), p=3 bar (case 10, Fig. 11b) and p=5 bar (case 25, Fig. 11c). A different structure of the temperature field is detectable going from 1 to 4 bar; at higher pressures, going from 3 to 5 bar, for the same operating conditions, the temperature field does not show significant changes, also from a quantitative point of view. This is due to the effect of concentration on kinetics. In fact while pressure has a direct effect on density and concentrations, changing the reaction rate (1) with a n=m power, it has a much milder effect on equilibrium predictions, that depend essentially on temperature. In order to evaluate what is the best approach - finite kinetics or thermochemical equilibrium - vs pressure change, experimental measurements are needed spanning a realistic pressure range.

Preliminary results obtained to investigate the influence of density gradients terms included in the K-ε eqs, were obtained for 'cold' (unreacting) conditions at pressure of

1,3 and 5 bar, and for combustion conditions at pressure of 1 bar and for a low ratio between air and fuel inlet momentum. For such conditions investigated the effect is almost negligible. This is realistic from a physical point of view because such operating conditions are not responsible for extended regions of high density gradients. In fact, density gradients are associated with slow mixing between fuel jet and surrounding air; increasing pressure increases also fuel jet momentum (or Reynolds number). Thus, at higher pressures the jet will tend to remain more 'coherent', and this will cause sharper density gradients over larger regions. Fig. 12 compares the temperature field obtained with the k-ε standard model (Fig. 12a) with that obtained implementing the k-ε model (Fig. 12b) modified to include the density gradients source terms. The temperature field is almost the same and the same conclusion may be drawn for the turbulent kinetic energy field, when comparing the standard k-ε approach (Fig. 12c) with the modified k-ε approach (Fig. 12d). Similar conclusions are obtained from the comparison of the cold flow field predicted at 3 or 5 bar. Work is currently being done to check whether these preliminary results apply also at higher pressure and especially under reactive conditions.

CONCLUSIONS

Conclusions from the work performed so far and presented here are as follows:

1. implementing equilibrium or overall kinetics does not affect significantly the recirculation region;
2. the temperature field is instead affected by this choice, and so are major species. However, highest temperatures and largest conversion ratios are not necessarily associated with equilibrium assumption and depend instead on the structure of the velocity field;
3. differences in temperature and mass fractions due to the choice of equilibrium or finite-rate kinetics tend to diminish at higher pressures;
4. preliminary results at p=1 bar indicate that introducing density gradients terms inside k-epsilon equations for reactive cases has a minor effect on all variables; at p=3 and 5 bar this is also true at least for the nonreactive case tested.

REFERENCES

1. Bray, K.N.C., "The Interaction Between Turbulence and Combustion", in: Seventeenth International Symposium on Combustion, The Combustion Institute, Pittsburgh, 1978, pp. 223-233.
2. Jones, W.P., and McGuirk, J.J., "Mathematical Modelling of Gas-Turbine Combustion Chambers", AGARD CP-275, 1979.
3. Syed, S.A., Chiappetta, L.M., and Gosman, A.D., "Error Reduction Program", NASA CR-174776, 1985.
4. Jones, W.P., "Models for turbulent flows with variable density and combustion", Von Karman Institute for Fluid Dynamics, Lecture Series 1979-2, Rhode Saint-Genese, Belgium, 1979.
5. Greenhalgh, D.A., personal communication, 1987.
6. Libby, P.A., and Williams, F.A., editors, "Turbulent Reactive Flows", Springer-Verlag, Berlin, 1980.
7. Aguirre-Saldivar, R.G., "Two Scalar Probability Density Function Models for Turbulent Flames", PhD Thesis, Dept. of Mech. Engin., Imperial College, London, 1986.
8. Raju, M.S., and Sirignano, W.A., "Spray Computations in Centerbody Combustor", to appear in: Proceedings of the 2nd ASME-JSME Thermal Engineering Joint Conference, Honolulu, Hawaii, March 1987.
9. Khalil, E.E., "Modelling of Furnaces and Combustors", Abacus Press, Tunbridge Wells, Kent, 1982, p. 52.
10. Hutchinson, P., Khalil, E.E., and Whitelaw, J.H., "RS190: The measurement and calculation of furnace-flow properties", AERE Report R 8710, Harwell, U.K., 1977.
11. Roquemore, W.M., Bradley, R.P., Stutrud, J.S., Reeves, C.M., Obringer, C.A., and Britton, R.L., "Utilization of Laser Diagnostics to Evaluate Combustor Models", AGARD CP-353, 1984.
12. Gosman, A.D., and Ideriah, F.J.K., "TEACH-T: A General Computer Program for Two-Dimensional, Turbulent, Recirculating Flow", Dept. of Mechanical Engineering Report, Imperial College, London, 1976.
13. Jones, W.P., and Whitelaw, J.H., "Calculation Methods for Reacting Turbulent Flows: A Review", Comb. and Flame, Vol. 48, 1982, pp. 1-26.
14. Westbrook, C.K., and Dryer, F.L., "Simplified Reaction Mechanisms for the Oxidation of Hydrocarbon Fuels in Flames", Comb. Sci. and Technol., Vol. 27, 1981, pp. 31-43.

15. Sirignano, W.A., Rivo, G., Tong, A., Abramzon, B., and Mo[illegible]i, K., "Spray Combustion: A Driving Mechanism for Ramjet Combustion Instability", presented at the 23rd JANNAF Combustion Meeting, NASA/Langley Research Center, Hampton, VA, Oct. 21, 1986.
16. Olikara, C., and Borman, G.L., "A Computer Program for Calculating Properties of Equilibrium Combustion Products with Some Applications to I.C. Engines", SAE Paper 750468, 1975.

ACKNOWLEDGEMENTS

This study was performed under the sponsorship of Progetto Finalizzato Energetica, CNR-ENEA, contratto CNR.

CASE	P (bar)	V_{air} (m/s)	V_{fuel} (m/s)	T_{air} k	T_{fuel} k	kev	EQ
1	1	40	25	1000	450	•	
2		80					
3		100					
4		120					
5	3	40			450	•	
6		50	20		350		•
7		80					•
8			25		450		
9		100					
10		120					
11					350		
12	5	40			450	•	
13		50	20	900			•
14				1100			
15					350		•
16		50	50	1000	450		•
17			25				•
18		80	20		350		
19			25		450		•
20				1100			
21				900			
22				1100	350		
23				900			
24				1000			
25		120			450		•
26					350		
27	9	50			450		•

Tab. 1 Matrix of the runs performed

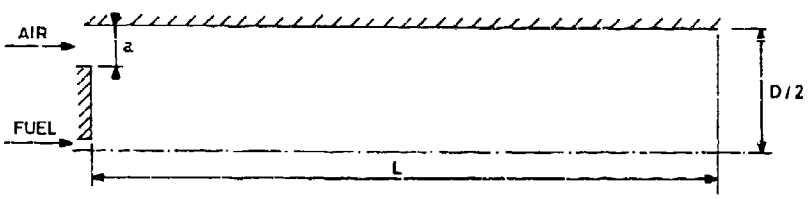

Fig. 1 Combustor can geometry used in this study

$$\rho\frac{\partial k}{\partial t}+\rho\tilde{U}_j\frac{\partial k}{\partial x_j}=\frac{\partial}{\partial x_j}\left\{\left[\frac{\mu_t}{\sigma_k}+\mu\right]\frac{\partial k}{\partial x_j}\right\}-\rho\widetilde{u_i''u_j''}\frac{\partial\tilde{U}_i}{\partial x_j}-\frac{\mu_t}{\rho^2}\frac{\partial\rho}{\partial x_i}\frac{\partial\rho}{\partial x_i}-\rho\epsilon$$

$$\rho\frac{\partial\epsilon}{\partial t}+\rho\tilde{U}_j\frac{\partial\epsilon}{\partial x_j}=\frac{\partial}{\partial x_j}\left\{\left[\frac{\mu_t}{\sigma_\epsilon}+\mu\right]\frac{\partial\epsilon}{\partial x_j}\right\}-C_1\frac{\epsilon}{k}\left[\rho\widetilde{u_i''u_j''}\frac{\partial U_i}{\partial x_j}+\frac{\mu_t}{\rho^2}\frac{\partial\rho}{\partial x_i}\frac{\partial\rho}{\partial x_i}\right]-C_2\rho\frac{\epsilon^2}{k}$$

Fig. 2 Equations for k and epsilon including the extra terms due to density and pressure gradients (Ref. 2,4,13)

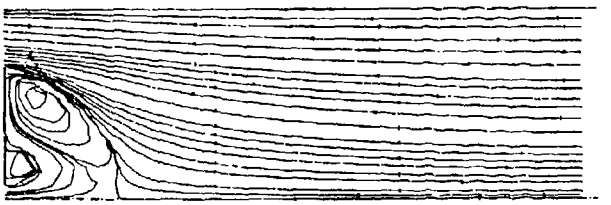

Fig. 3a

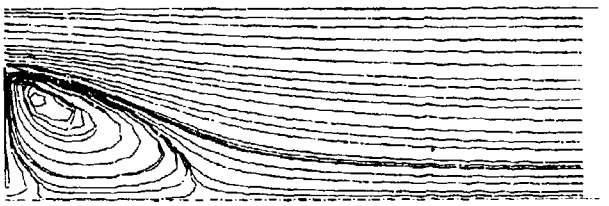

Fig. 3b

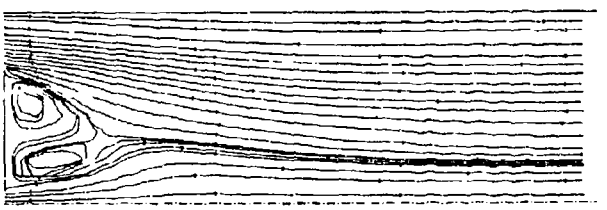

Fig. 3c

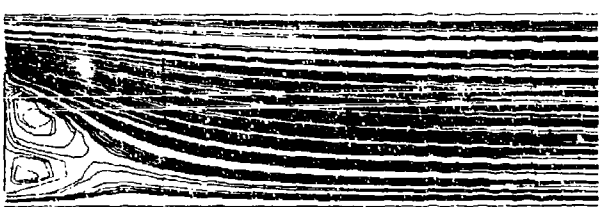

Fig. 4a

Fig. 4b

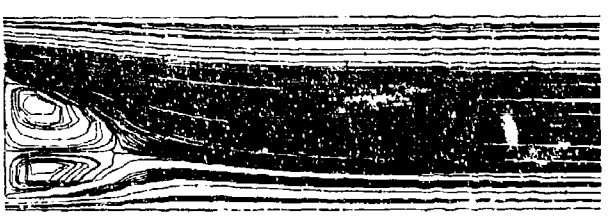

Fig. 4c

Figs. 3 and 4 Streamlines field (Fig. 3: equilibrium; Fig. 4: overall kinetics)
3a and 4a case 17 (p = 5 bar; inlet velocities: air = 50 m/s; fuel = 25 m/s)
3b and 4b case 25 (p = 5 bar; inlet velocities: air = 120 m/s; fuel = 25 m/s)
3c and 4c case 16 (p = 5 bar; inlet velocities: air = 50 m/s; fuel = 50 m/s)

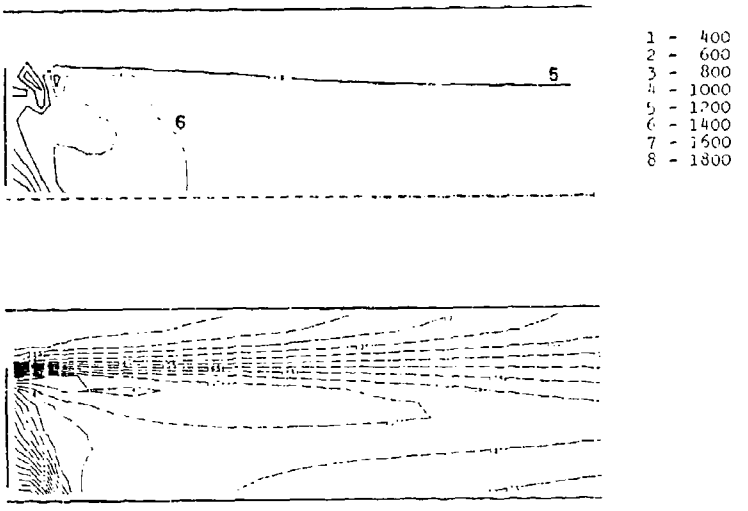

Fig. 5 Isothermal contour lines. Test case 2b
5a Thermochemical equilibrium assumption
5b Overall kinetics assumption

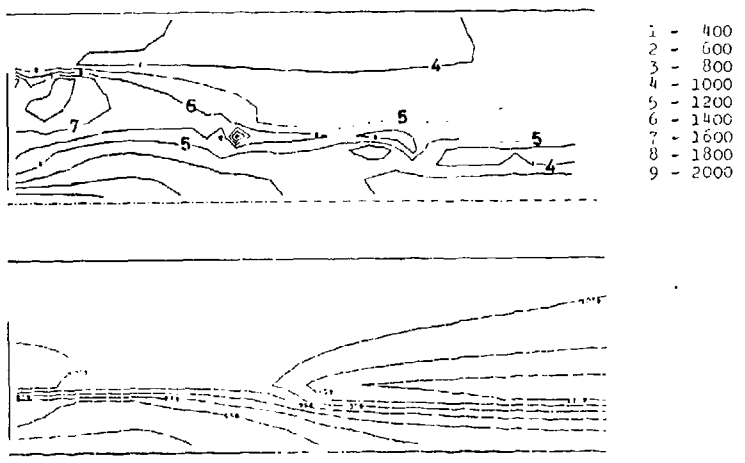

Fig. 6 Isothermal contour lines. Test case 1b
6a Thermochemical equilibrium assumption
6b Overall kinetics assumption

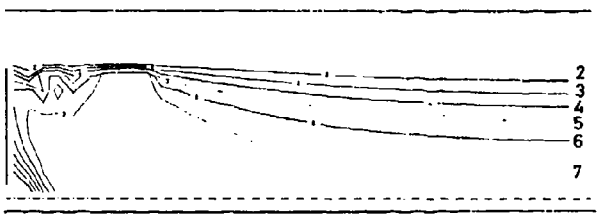

Fig. 7a

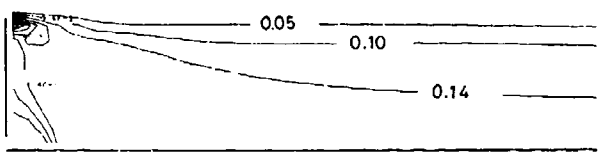

Fig. 7b

Fig. 7 Carbon dioxide fields. Test case 25
7a Thermochemical equilibrium assumption
7b Overall kinetics assumption

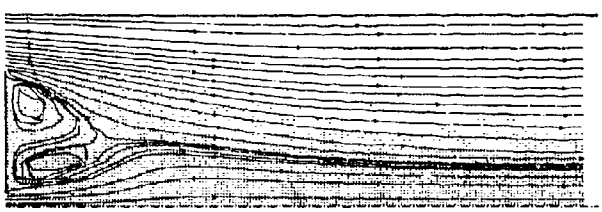

Fig. 8a

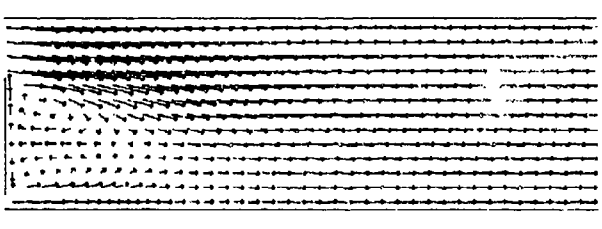

Fig. 8b

Fig. 8c

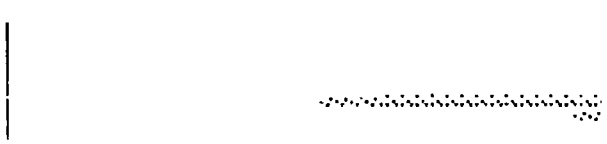

Fig. 8d

Fig. 8 Test case 16 8a Streamline and chemical fields 8b Velocity field
8c Fuel mass fraction field 8d Carbon dioxide mass fraction field

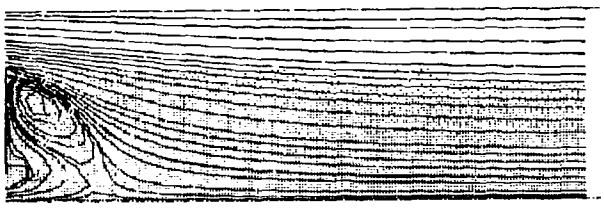

Fig. 9a

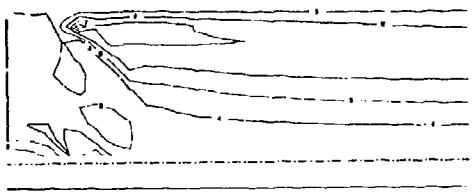

1 - 400
2 - 600
3 - 800
4 - 1000
5 - 1200
6 - 1400
7 - 1600

Fig. 9b

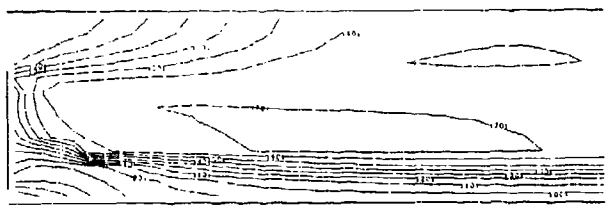

Fig. 9c

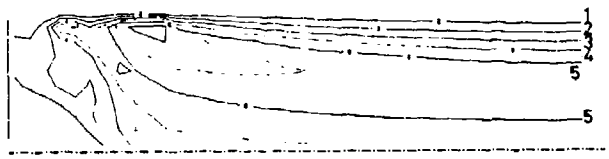

1 - 0.02
2 - 0.04
3 - 0.06
4 - 0.08
5 - 0.10
6 - 0.12
7 - 0.14

Fig. 9d

Fig. 9e

Fig. 9 Test case 6 (p = 3 bar; inlet air velocity = 50 m/s; inlet fuel velocity = 20 m/s)
9a Streamlines and chemical species field (equilibrium assumption)
9b Temperature field (equilibrium assumption)
9c Temperature field (overall kinetics assumption)
9d Carbon dioxide field (equilibrium assumption)
9e Carbon dioxide field (overall kinetics assumption)

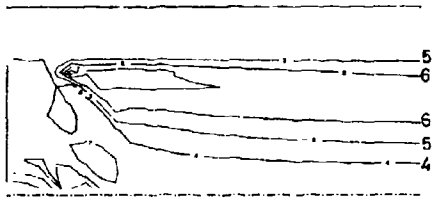

1 - 400
2 - 600
3 - 800
4 - 1000
5 - 1200
6 - 1400
7 - 1600
8 - 1800

Fig. 10a

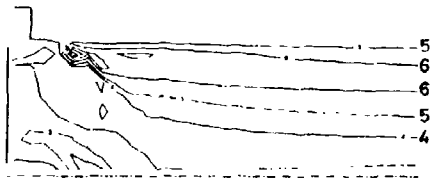

1 - 400
2 - 600
3 - 800
4 - 1000
5 - 1200
6 - 1400
7 - 1600
8 - 1800
9 - 2000

Fig. 10b

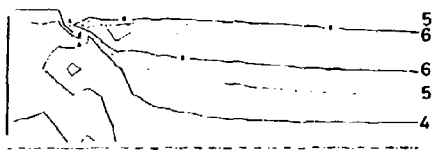

1 - 400
2 - 600
3 - 800
4 - 1000
5 - 1200
6 - 1400
7 - 1600

Fig. 10c

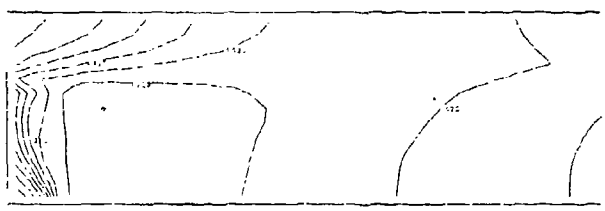

Fig. 11a

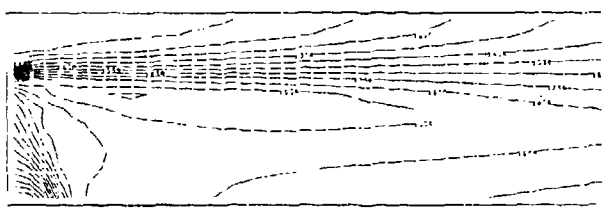

Fig. 11b

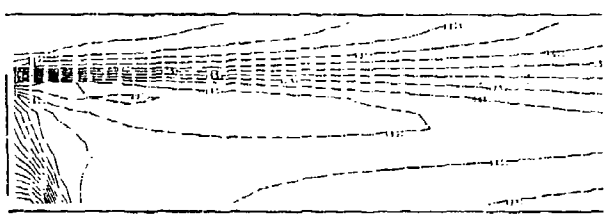

Fig. 11c

Fig. 10 and Fig. 11 Effect of pressure on the temperature field.
(Fig. 10: equilibrium; Fig. 11: overall kinetics)

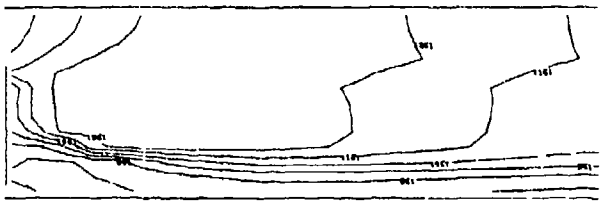

Fig. 12a

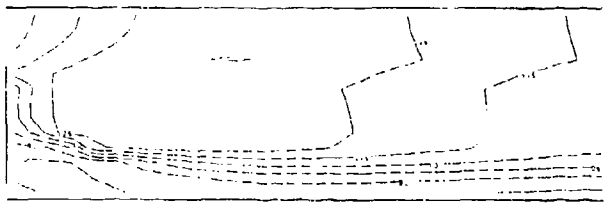

Fig. 12b

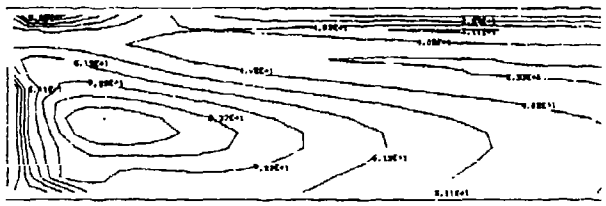

Fig. 12c

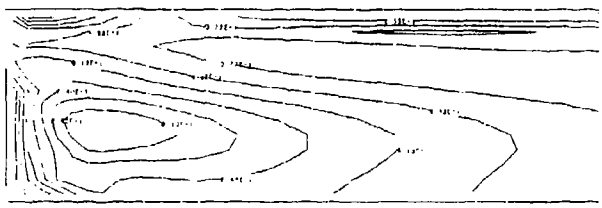

Fig. 12d

Fig. 12 Comparison between k-epsilon standard model and k-epsilon model modified to include pressure and density gradients source terms.

12a Temperature field. Test case 1. Overall kinetics assumption. k-ε standard model

12b Temperature field. Test case 1. Overall kinetics assumption. k-ε modified model

12c Turbulent kinetic energy field. Test case 1. Overall kinetics assumption. k-ε standard model

12d Turbulent kinetic energy field. Test case 1. Overall kinetics assumption. k-ε modified model.

DISCUSSION

M.Nina, PO

Would you comment on the range of equivalence ratios you used in the tests and its effect regarding the different submodels proposed?

Author's Reply

The range of the (global) equivalence ratios for the tested cases is between 0.2 and 0.6. The comparisons shown, between the thermochemical equilibrium assumption and the overall kinetics assumption, were obtained for the same operating conditions and therefore for the same value of the equivalence ratio. The effects of the (global) equivalence ratios were not systematically investigated. Attention was focused instead on the local equivalence ratio in order to correlate its value with the formation of combustion products.

3D Combustor Predictions - A comparison of Equilibrium and Laminar Flamelet Chemistry Models

By

J J McGuirk
Fluids Section
Department of Mechanical Engineering
Imperial College of Science and Technology
London SW7 2BX United Kingdom

ABSTRACT

Numerical calculations are reported of the three-dimensional reacting flow inside a can-type combustor geometry. Several flow features found in current combustor designs are included, a swirl driven primary zone and a single row of radially inward dilution air jets. The particular aspect of the mathematical formulation given special attention concerns the model for the chemical reaction. Alternative descriptions of the instantaneous thermochemistry are adopted which correspond to either full chemical equilibrium or the laminar flamelet approach. In the latter case the flamelet structure is taken over from published calculations of laminar propane-air diffusion flames. All other aspects of the mathematical model such as numerical discretisation and solution algorithm, turbulence model and turbulence/chemistry interaction are common in the predictions obtained (the two equation k-ε model and a β-function pdf have been used).

The results obtained indicate that the predicted flow patterns are essentially the same for both chemistry models, even though differences of almost 100% are observed for the instantaneous density field . In terms of predicted gas temperature and levels of species concentrations, more significant differences are observed. This is particularly so for CO and H_2 where the changes introduced by the laminar flamelet description andobserved in open jet diffusion flame predictions are borne out by the present calculations. In particular, the primary zone levels of CO and H_2 are significantly reduced. The predictions with both models indicate however a deficiency in the representation of CO burn out and it is probable this will require an alternative chemistry description. Finally, although the calculations have used an unstrained laminar flame description, predictions of the mean scalar dissipation rate are presented to assess the likelihood of local quenching due to flame stretching. Some uncertainty exists in selecting a critical maximum value, and in transferring from the mean value to the instantaneous state; nevertheless, the current predictions seem to imply that significant local extinction is unlikely in the present flow, except for some fuel rich regions very close to the injection location.

1. INTRODUCTION

Much work is currently underway which is intended to lead to the development of three-dimensional mathematical models for the flow and chemical reaction inside gas-turbine combustion chambers. The complexity of the physical and chemical events in combusting flow means however that the formulation of a complete mathematical model is by no means easy. Even for the simplified case of gaseous fuels, such models must be constructed from several components comprising sub-models for turbulent transport, for the instantaneous thermochemical description, and (to allow the necessary simulation of turbulence/chemistry interaction) a further model is required to prescribe the statistics of the scalars which determine the state of reaction (usually in the form of a probability density function (pdf),. This combination leads to a closed set of partial differential equations which must then be solved, using computational fluid dynamic techniques, in a manner which offers robustness, geometric flexibility, numerical accuracy and computational efficiency. Examples may be found in the literature of the extent to which the development of such calculation procedures has progressed, e.g. Reference 1, but it is clear from review papers on turbulent combustion (see Reference 2) that none of the components of the overall model may be said to be in an entirely satisfactory state or to have reached an optimum level. The present paper concentrates on just one of the above aspects, namely the chemistry sub-model, and attempts to compare two alternative descriptions at the level which is considered currently feasible within the constraints of a three-dimensional numerical simulation.

Most combustion models for gas-turbine combustors adopt the so-called conserved scalar approach. For non-premixed flames, the assumptions of negligible heat losses due to radiation, low Mach numbers and equality of all diffusive transport coefficients allows all thermochemical state variables to be expressed in terms of any conserved scalar such as an element mass fraction. Conventionally the mixture fraction is chosen to describe the gas state. Further, if recognition is taken of the fact that combustors operate predominantly at high inlet temperatures and pressures, then it may be assumed that all chemical kinetics are very fast compared to the

time scales of turbulent mixing or residence times associated with convective transport. This leads to the "fast chemistry" approximation implying that it is admissible to assume (instantaneous) chemical equilibrium composition appropriate to the local mixture fraction value. Modelling the consequences of turbulent fluctuations on the chemical composition is then reduced to describing the fluctuations of the mixture fraction. This is conventionally carried out by presuming knowledge of the probability density function (pdf) for the conserved scalar usually in terms of a well-defined assumed form described by a small number (commonly) of free parameters. This is the full chemical equilibrium model and is one of the two models considered below.

Whilst the above approach can lead to successful prediction of some features of combustor flows, it has been observed to produce an overprediction of such aspects as carbon monoxide concentration, particularly under conditions of locally fuel rich zones (see Reference 3). Additionally, any phenomenon which is inherently non equilibrium and dependent on finite rates (e.g. the quenching of CO burnout reactions) clearly cannot be predicted using the model just described. In recent years, the requirement for low emissions levels has placed demands on combustor designers which have had to be met by costly trial and error experimentation (Reference 4) since no models have been developed for use in 3D combustor flows to provide accurate information of this type. Extensions of chemistry models to include finite rate effects have been made, but the introduction of additional scalars which describe the instantaneous state has forced the use of a multi-dimensional joint pdf. The construction of this using assumed shape forms is either computationally expensive (Reference 5) or has involved assumptions such as statistical independence of the scalars (Reference 6) which might adversely influence the predictions and which are not strongly supported by evidence. Many of the above problems are avoided if a transport equation for the joint pdf itself is devised and solved, although additional and different modelling problems are thereby introduced. Reference 7 describes the most advanced application of this type to a free turbulent diffusion flame (in fact the joint pdf for velocity and two scalars was used). The technique is promising, although the closure models used are still under test. For 3D combustor calculations, such models are clearly premature as all reported calculations to date have been to problems which have allowed the significant simplification of negligible probability of one velocity component assuming negative values. This has allowed marching solution algorithms to be used, and has nevertheless led to computing times of order of one hour.

An alternative to these multi-scalar descriptions has emerged over the last few years, and is usually termed the laminar flamelet approach. In this type of model the single conserved scalar formulation is extended to include non equilibrium effects. Originally this was based on experimental observations (Reference 8) that measured temperature and species compositions in undisturbed laminar diffusion flames, when plotted against mixture fraction, provided unique and alternative relationships to those devised assuming equilibrium. The calculations of Reference 9 were the first to use an experimentally deduced laminar flame structure to show that, by assuming turbulent diffusion flames consist of a collection of laminar flames, the above-mentioned overprediction of CO in methane air open turbulent flames could be remedied. Similar results were reported for propane air flames in References 10 and 11, but now the laminar flame structure was deduced not from experiments, but from a one-dimensional transient laminar flame calculation which invoked a semi-global reaction mechanism involving a global fuel disappearance step followed by a comprehensive mechanism for the oxidation of CO and H_2. This laminar flamelet model detailed in Reference 10 is the second chemistry model used in the calculations which follow.

The laminar flamelet approach has been extended (see References 12 and 13) to account for the fact that in a turbulent flow the flamelets will be stretched and distorted by the turbulence. This modification allows such effects as local flame quenching and hence local pre-mixing to occur in turbulent diffusion flames. The parameter which is assumed to characterise the flame stretching process is the instantaneous scalar dissipation rate (proportional to the square of the instantaneous scalar gradient). Following this approach involves providing a set of flame structure profiles in terms of both mixture fraction and scalar dissipation rate. In addition, a joint pdf is (in principle) required, although many workers have to date assumed statistical independence between mixture fraction and its dissipation rate which has simplified this aspect of the model (a log normal distribution has usually been used for the scalar dissipation rate). Although some evidence is starting to emerge for the benefits to be gained by including the influence of flame stretch, it is not yet clear how this can be achieved in an optimum manner in a complex flow calculation. Accordingly, this version of the flamelet model is not used in the present work, although some attempt is made to examine the values of the mean scalar dissipation rate which emerge as part of the current predictions, to see if these imply conditions close to the values of the dissipation rate believed to be large enough to cause local extinction (References 10 and 12).

The following section details the mathematical model used in the present work and presents a brief description of the solution algorithm adopted and a few computational details. Section 3 outlines the particular combustor configuration chosen to examine the two chemistry models mentioned above and sets out a detailed comparison on the basis of predicted flow and species parameters. Summary conclusions are stated in the final section.

2. MATHEMATICAL MODEL

The equations governing continuity and conservation of momentum and mixture fraction may be written for steady high Reynolds number flows as follows:

$$\frac{\partial}{\partial x_i}(\bar{\rho}\tilde{U}_i) = 0$$

$$\frac{\partial}{\partial x_j}(\bar{\rho}\tilde{U}_i\tilde{U}_j) = -\frac{\partial \bar{p}}{\partial x_i} - \frac{\partial}{\partial x_j}(\bar{\rho}\widetilde{u_i u_j})$$

$$\frac{\partial}{\partial x_j}(\bar{\rho}\tilde{U}_j\tilde{f}) = -\frac{\partial}{\partial x_j}(\bar{\rho}\widetilde{u_j f})$$

Density weighted averaging has been preferred since this leads to simpler equation forms in variable density flows. Closure of these equations requires the provision of a model for the turbulent transport (Reynolds stresses and scalar fluxes). The two equation $\tilde{k}$-$\tilde{\varepsilon}$ model is used in the calculations performed here, for combusting flows the form of the model used in Reference 3 has been adopted:

$$-\bar{\rho}\widetilde{u_i u_j} = \mu_t\left[\frac{\partial \tilde{U}_i}{\partial x_j} + \frac{\partial \tilde{U}_j}{\partial x_i}\right] - \frac{2}{3}\delta_{ij}\left[\bar{\rho}\tilde{k} + \mu_t\frac{\partial \tilde{U}_k}{\partial x_k}\right]$$

$$-\bar{\rho}\widetilde{u_j f} = \frac{\mu_t}{\sigma_t}\frac{\partial \tilde{f}}{\partial x_j}$$

$$\mu_t = C_\mu \bar{\rho}\frac{\tilde{k}^2}{\tilde{\varepsilon}}$$

$$\frac{\partial}{\partial x_j}(\bar{\rho}\tilde{U}_j\tilde{k}) = \frac{\partial}{\partial x_j}\left(\frac{\mu_t}{\sigma_k}\frac{\partial \tilde{k}}{\partial x_j}\right) - \bar{\rho}\widetilde{u_i u_j}\frac{\partial \tilde{U}_i}{\partial x_j} - \frac{\mu_t}{\bar{\rho}^2}\frac{\partial \bar{\rho}}{\partial x_j}\frac{\partial \bar{p}}{\partial x_j} - \bar{\rho}\tilde{\varepsilon}$$

$$\frac{\partial}{\partial x_j}(\bar{\rho}\tilde{U}_j\tilde{\varepsilon}) = \frac{\partial}{\partial x_j}\left(\frac{\mu_t}{\sigma_\varepsilon}\frac{\partial \tilde{\varepsilon}}{\partial x_j}\right) - C_{\varepsilon 1}\frac{\tilde{\varepsilon}}{\tilde{k}}\left[\bar{\rho}\widetilde{u_i u_j}\frac{\partial \tilde{U}_i}{\partial x_j} + \frac{\mu_t}{\bar{\rho}^2}\frac{\partial \bar{\rho}}{\partial x_j}\frac{\partial \bar{p}}{\partial x_j}\right] - C_{\varepsilon 2}\bar{\rho}\frac{\tilde{\varepsilon}^2}{\tilde{k}}$$

The standard set of constants as given in Reference 14 have been used throughout together with a constant turbulent Prandtl number of 0.7.

As described below, the construction of the pdf of mixture fraction also requires values for the variance of the mixture fraction at all points in the flow. This is obtained from its own modelled transport equation:

$$\frac{\partial}{\partial x_j}(\bar{\rho}\tilde{U}_j\widetilde{f''^2}) = \frac{\partial}{\partial x_j}\left(\frac{\mu_t}{\sigma_t}\frac{\partial \widetilde{f''^2}}{\partial x_j}\right) + 2\frac{\mu_t}{\sigma_t}\left(\frac{\partial \tilde{f}}{\partial x_j}\right)^2 - C_D\bar{\rho}\frac{\tilde{\varepsilon}}{\tilde{k}}\widetilde{f''^2}$$

It should be noted that the last term in this equation is the modelled term for the mean scalar dissipation rate and introduces an additional model constant C_D whose value is 2.0 in the calculations reported here.

In lieu of the chemistry models to be used, as described in the previous section, all thermochemical state variables are presumed known as unique functions of f on an instantaneous basis, i.e.

$$\phi_i = \phi_i(f)$$

where ϕ_i may stand for gas density, temperature or the mole fraction of any species present. The functional form represented by these relations is very commonly non-linear, and, because the mixture fraction fluctuates, the local mean value of any state variable must be calculated from

$$\tilde{\phi}_i = \int_0^1 \phi_i(f)\,\tilde{p}(f)\,df$$

where $\tilde{\rho}\,\tilde{p}(f)$ is the density weighted probability density function for f. Adopting the assumed-shape approach, this pdf is specified using a Beta function, viz:

$$\tilde{p}(f) = \frac{f^{a-1}(1-f)^{b-1}}{\int_0^1 f^{a-1}(1-f)^{b-1}\,df}$$

where the exponents a and b are given by:-

$$a = \tilde{f}\left[\frac{\tilde{f}(1-\tilde{f})}{\widetilde{f''^2}} - 1\right] \quad , \quad b = \frac{(1-\tilde{f})}{\tilde{f}}\,a$$

i.e. these are uniquely specified at any point if the mean and variance of the mixture fraction are known. The mean density appearing in the transport equations may be obtained from this density weighted pdf using:-

$$\bar{\rho} = \left[\int_0^1 \frac{1}{\rho(f)}\,\tilde{p}(f)\,df\right]^{-1}$$

The functions $\phi_i(f)$ and $\rho(f)$ describing the instantaneous thermochemical information have been obtained using either the technique of Reference 15 for the equilibrium model or the tabulated data included in Reference 10 for the laminar flamelet model. In both cases propane fuel has been assumed. This has necessitated the use, in the equilibrium model only, of a rich flammability limit at an equivalence ratio of 2.5 (as recommended in Reference 16) and the supression of solid carbon. These modifications are required to enable pure fuel to exist in the equilibrium model for rich mixtures (it would otherwise break down to a mixture of solid carbon, H_2 and CH_4), and to reduce the very large levels of CO produced by the equilibrium model for equivalence ratios larger than 2.5. The version of the equilibrium model used is identical to that used in Reference 16 for an open turbulent propane air jet flame. All calculations have assumed a pressure of two atmospheres, the laminar flamelet detailed kinetic calculations tabulated in Reference 10 are actually for atmospheric pressure, but evidence of changes in flamelet structure with pressure included in the same work imply that such a small increase in pressure level would not lead to any significant changes.

Examples of the differences between these two models for the instantaneous functions ϕ_i are shown in Figures 1-3. In the first the variation of gas density and temperature over mixture fraction space are compared. The minimum density near the stoichiometric value of f is very similar in both models, but differences approaching a factor of 2 are observed on both lean and rich sides, with the flamelet model producing the larger density values. The most striking changes in the temperature curves are a reduction of the maximum temperature by some 300 degrees in the flamelet model compared to the equilibrium, and the existence of significantly higher temperatures in the flamelet model on the rich side of stoichiometric leading to a much less peaked distribution. The CO and CO_2 comparisons in Figure 2 illustrate the result, mentioned in the previous section, that the high CO levels produced by the equilibrium model on the rich side are reduced by the flamelet description (by a factor of four in the present case) with corresponding increases in the CO_2 mole fractions. A second point to note is the presence of CO in the flamelet model below stoichiometric, whereas the equilibrium model implies negligible CO; this has implications for the prediction of emission levels. Finally, Figure 3 presents a comparison of oxygen and hydrocarbon (propane) mole fractions; here the differences are much less between the two models. The single point worthy of note is the slight interpenetration of fuel and oxygen curves in the flamelet model, for equilibrium a clear separation between finite levels of O_2 and fuel exists.

The equations described in this section have been solved using a finite volume technique incorporating hybrid differencing for the approximation of the convection terms. A standard pressure-correction method has been used to handle the pressure velocity coupling. The calculations have been performed with cylindrical polar co-ordinates and any irregular boundaries in this system were approximated via a simple castellated approach; comparisons between this method and a body fitted curvilinear calculation for the isothermal flow in the geometry considered showed negligible differences. The grid used in most calculations possessed 42x22x21 nodes in the x,r and θ directions (19,000 nodes in all). The grid disposition was non-uniform and chosen to give optimum resolution of the expected high shear regions. Calculations were performed on an Amdahl 470 V8 machine; typical storage and CPU requirements to obtain a converged solution for a combusting flow were 2 Mbytes and 45 mintues CPU time.

3. RESULTS AND DISCUSSION

The model combustor geometry for which the current tests have been made is shown in Figure 4. A simple can type geometry is used with an internal diameter of 76mm and an overall length of 170mm. The combustor head contains a 45° swirler and a fuel injector which allow air and fuel (propane gas) to enter the primary zone. The swirl number used in the present calculations was 0.85. In setting the inlet conditions for flow through the swirler, flat profiles were assumed, but an allowance was made for vane blockage decreasing swirler effective area (by about 15%) by increasingly the hub radius accordingly. The fuel was assumed to enter in the form of radial jets from the outer surface of the injector which protruded slightly (about 3mm) in the axial direction; for the moment discrete fuel jets have not been assumed, but rather for simplicity the fuel enters as an annular ring possessing only radial momentum. A tilted combustor backplate is followed at x=48mm, by a single row, of six dilution air jets of diameter 8mm. Circumferential uniformity has been supposed so that only a 60° cydically repeating sector containing one jet at θ=30° was calculated. A discharge coefficient of 0.6 was assumed in fixing velocity boundary conditions at the jet holes. Wall cooling air enters the combustor along the can periphery at a uniform effective transpiration rate. Finally, the air flow split between the several features is given on Figure 4, together with the overall air/fuel ratio for the combustor, which corresponds to an overall equivalence ratio of 0.41.

Figure 5 presents results for both isothermal and burning flow in terms of centre-line velocity development. The increase in the maximum backflow velocities on reaction is about 40% accompanied by a downstream shift. The zero velocity location remains about the same however; the larger velocities in the downstream part are indicative of the lower gas densities due to reaction. The differences between the two chemistry models is rather slight in the primary zone upstream of the jets (about 10% maximum) indicating that the mean density fields must be predicted to be quite similar. At the can exit differences of some 20% occur with the laminar flamelet model giving rise to lower velocities; this is in accord with the instantaneous curves which show larger densities in the flamelet model. Other features which are influenced only via a bulk property such as mean density shown similar trends; the predicted mixture fraction field for example shows changes of order 20% in the near fuel injector region and at exit differences are of order 10% with the flamelet predictions showing a slightly more mixed out profile shape.

The changes in flow field structure due to combustion are further illustrated in Figures 6 and 7. These show, for two planes one axial (θ=30°, jet entry) and one radial (x=48mm), predicted streakline patterns for weightless particles tracked through the respective planes for a time of 0.4 msec (Figure 6) and 0.2 msec (Figure 7). The primary zone vortex is clear to see in both isothermal (6a) and burning (6b) calculations (only equilibrium results are included due to the close similarity observed above). Two features may be noted on closer inspection: under burning conditions the swirler air seems to penetrate slightly further axially before being forced against the combustor backplate and, perhaps due to this, the dilution jet penetration is slightly less radial in the combusting flow. In spite of this, in both cases, almost complete penetration is obtained to the can centre-line before the jet fluid acquires finite swirl momentum (see Figure 7a and 7b); some evidence exists for larger jet spreading in the case of combustion, but on the whole the flow structure is rather similar.

It may be expected that properties such as gas temperature and composition are more sensitive to changes in the chemistry model. These features of the current predictions are examined in Figures 8 to 10 for the two stations in the primary zone marked on Figure 4. Station I is halfway between swirler exit and dilution jet entry and station II is at the jet entry cross-section, at station I the flow is still fairly axi-symmetric, but at station II significant three dimensionalities occur and predictions are examined for two θ planes, one through the jet centre-line and one mid-way between jets. Figure 8 indicates that the temperature predicted by the two models at the first station can differ by up to 300K. The maximum temperatures are only some 50K different and are in the same radial location, but nearer the centre-line the flamelet model predicts considerably lower temperatures. The waviness in the equilibrium predictions occurs because at this location there are two positions where the mixture fraction goes through a stoichiometric value, and the fluctuations are not large enough to stoooth out the profiles; this also happens in the flamelet predictions but because of the slightly different mixture fraction field, not at the station plotted. Further downstream the temperature comparisons for the between jets plane (9a) shows much similarity with the earlier profiles, not surprisingly since this plane forms the exit route from the primary zone. For the plane through the jets, the jet entry can be clearly identifed with the low temperatures down to a radius of about 30mm, subsequently the shape of the profile is similar in both models, with again the equilibrium model showing higher temperatures.

The most important species concentration to examine in the present context is the CO mole fraction; this is shown for the two station II planes in Figure 10. The between jets profile (10a) displays differences which are in keeping with observations made in Reference 9 for open jet diffusion flames. In fuel rich regions, the flamelet model produces CO levels considerably lower than the equilibrium model and more in keeping with values expected from measurements in this kind of flow (Reference 17); closer to the fuel injector similar behaviour prevails. The comparison between H_2 mole fractions shows exactly the same differences. Note also that the maximum CO levels differ by a factor of 3 which is a reduction from the instantaneous curves, and this is probably the effect of scalar fluctuations. In the equilibrium model, practically zero CO exists at exit, the maximum value being about 120ppm. For the flamelet model, however, under the conditions of this calculation, a maximum mole fraction at exit of some 10,000 ppm was obtained. These figures illustrate that neither of these models is capable of predicting CO emission levels since values more like 1000 ppm might be

expected (Reference 17). Since the flamelet model was found to agree well with laminar diffusion flame data at the equivalence ratios existing at the combustor exit (see Reference 10), then it is clear that additional non-equilibrium effects may be present in the present flow field which contains rapid air addition. This may require direct finite rate effects to be taken into account before reasonable emissions may be predicted.

Finally, although unstretched laminar flamelet profiles have been used here, it is instructive to examine to what extent flame stretch might influence the present predictions. Figure 11 quantifies this by examining the predicted mean scalar dissipation rate (the final term in the modelled scalar variance equation divided by the mean density) for the θ=30^0 plane. High values are, not surprisingly, obtained in the region of fuel injection where scalar gradients are large, but also in the shear layer bordering the upstream edge of the inflowing dilution jet. Reference 13 quotes a value of about 50 $secs^{-1}$ to be necessary to imply significant stretching leading to local quenching. If this value is taken then only a very small region near the fuel injector is implied as being affected by the present calculations. A much lower value (5 $secs^{-1}$) is given in Reference 12, but even this would not include even 25% of the primary zone volume. These remarks should however be taken with some caution since no allowance has been made to take fluctuations into account in this assessment, to examine over what region the instantaneous scalar dissipation rate might exceed these critical values. This would require some assumption as to the probability distribution for the scalar dissipation rate and has not yet been attempted. Further, it may also be that quenching in only a small but critical region near the fuel injection is sufficient to cause changes over a much larger area, but this conjecture awaits confirmation from further calculations.

4 CONCLUSIONS

The main findings of the current work may be summarised as follows:

1. For a combustor flowfield containing many typical features a laminar flamelet model has been successfully incorporated allowing a quantitative comparison with the commonly used equilibrium approach

2.Little changes in the predicted mean density field were observed on changing the chemistry model, leading to differences of only some 10-20% in such quantities as mean velocity and mixture fraction predictions.

3.Much larger differences were observed in predicted gas temperatures (up to 400K) and species compositions. CO and H_2 levels in particular were significantly reduced in the fuel rich regions of the primary zone, as was expected from open diffusion flame calculations.

4. Neither model could predict reasonable emission levels of CO and further attention is plainly needed here to incorporate finite rate kinetic effects for combustor flows.

5. Although the flow-field predicted corresponded to the high intensity loading and large fluctuations found in typical combustors, relatively little evidence was found for large flame stretch effects, although only preliminary and incomplete investigations could be made on this issue.

6. The flamelet approach did seem to improve the realism of the primary zone representation, although final confirmation of this requires comparison with experimental data, and this is planned for future work.

AKNOWLEDGEMENTS

The author would like to acknowledge many useful discussions on this and related work with staff at RAE (Pyestock); Dr C Hurley especially has provided much useful information of particular benefit to this work.

REFERENCES

1.Coupland, J. and Priddin C. "Modelling the flow and combustion in a production gas turbine combustor" Turbulent Shear Flows, Vol 5, Eds L Bradbury et al, Springer Verlag. (1986).

2. Jones, W.P. and Whitelaw, J.H. "Modelling and measurements in turbulent combustion" 20th Symposium (International) on Combustion, pp.233-249, The Combustion Institute. (1984).

3.Jones, W.P. and McGuirk, J.J. "Mathematical modelling of gas-turbine combustion chambers" AGARD Conference Proceeding CP-275 (1979).

4.Bhangu, J.K., Snape, D.M. and Eardley, B.R. "The design and development of a low emissions transply combustor for the civil Spey engine" AGARD Conference Proceedings CP-353 (1983)

5.Aguirre-Saldivar, R. "Two scalar probability density function models for turbulent flames" PhD. thesis, University of London, (1987).

6.Correa, S.M. "A model for non-premixed turbulent combustion of CO/H_2 jets" IX International Symposium on Combustion Processes, Poland, (1985).

7.Pope, S.B. and Correa, S.M. "Joint pdf calculations of a non-equilibrium turbulent diffusion flame" 21st Symposium (International) on Combustion, The Combustion Institute, (1986).

8.Bilger, R.W. "Reaction rates in diffusion flames", Combustion and Flame, vol 30, pp.227-284 (1977).

9.Liew, S.K., Bray, K.N.C. and Moss, J.B. "A flamelet model of turbulent non-premixed combustion" Combustion Science and Technology, vol 27, pp.69-73, (1981).

10. Liew, S.K., Moss, J.B. and Bray, K.N.C. "Flamelet modelling of chemical closures in turbulent propane air combustion" Report TP-84-1, School of Mech Eng, Cranfield Institute of Technology, (1984).

11. Askari-Sardhai, A., Liew, S.K. and Moss, J.B. "Flamelet modelling of propane-air chemistry in turbulent non-premixed combustion" Combustion Science and Technology, vol 44, pp89-95 (1985).

12.Peters, N. "Laminar diffusion flamelet models in non-premixed turbulent combustion", Progress in Energy and Combustion Science (1984).

13. Liew, S.K., Bray, K.N.C. and Moss J.B. "A stretched laminar flamelet model of turbulent non-premixed combustion", Combustion and Flame, vol 56, pp. 199-213, (1984).

14. Launder, B.E. and Spalding, D.B. :"The numerical computation of turbulent flows", Computer Methods in Applied Mechanics and Engineering, vol 3, pp. 269-289, (1974).

15. Gordon, S. and McBride, B.J. "Computer program for calculation of complex chemical equilibrium compositions" NASA SP273 (1971).

16. Godoy, S. "Turbulent diffusion flames" PhD thesis, University of London (1982).

17. Hurley, C. "Private communication" (1987).

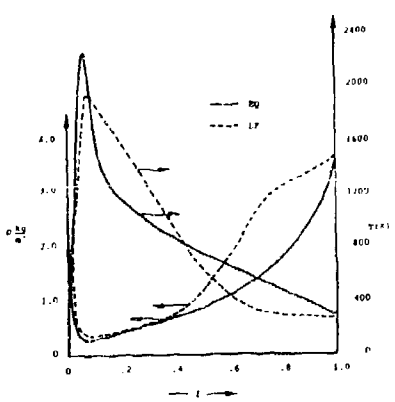

Figure 1 Density and Temperature, two chemistry models

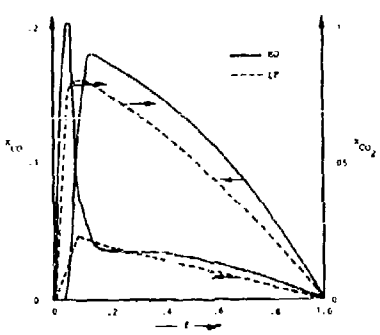

Figure 2 CO and CO_2 mole fraction, two chemistry models

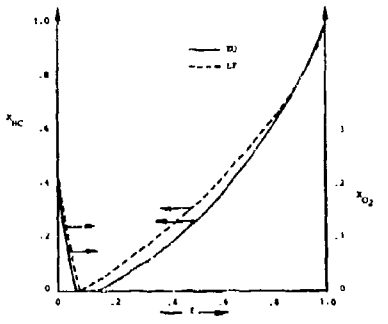

Figure 3 O_2 and Hydrocarbon mole fractions, two chemistry models

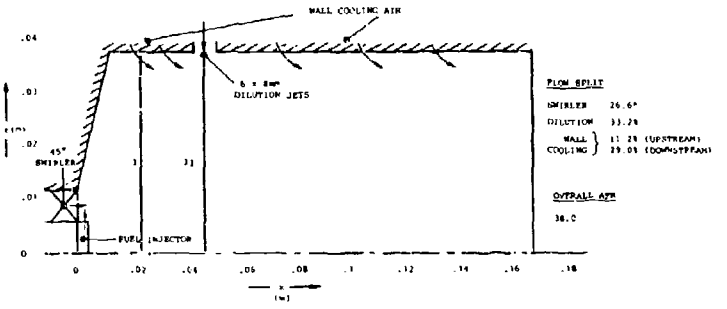

Figure 4 Combustor geometry and flow conditions

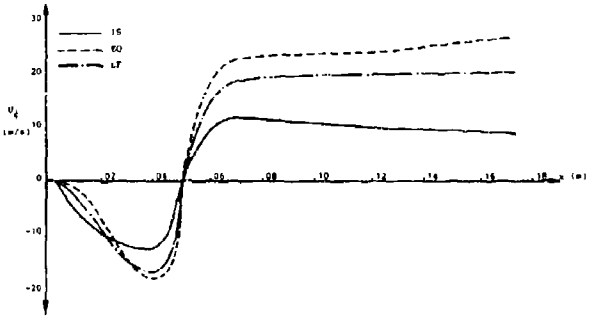

Figure 5 Axial velocity profile along combustor centre- line isothermal and reacting flow.

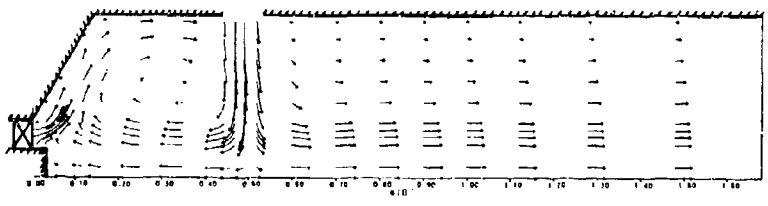

Figure 6a Predicted streaklines, $\theta = 30^{o}$, isothermal flow.

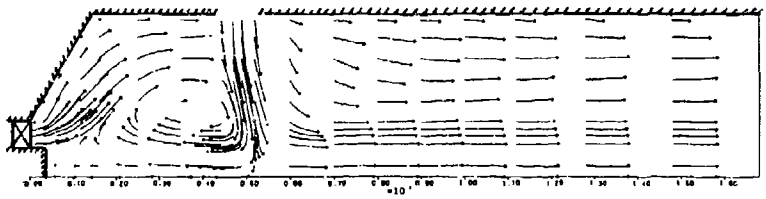

Figure 6b Predicted streaklines, $\theta = 30^{o}$,combusting flow.

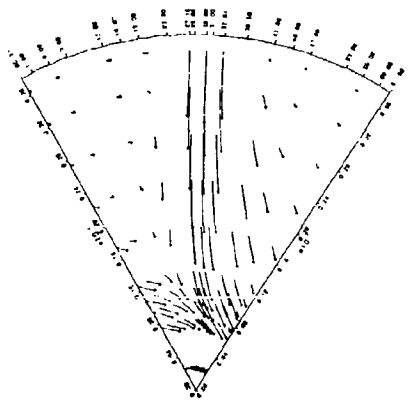

Figure 7a Predicted streaklines, x=48mm, isothermal flow.

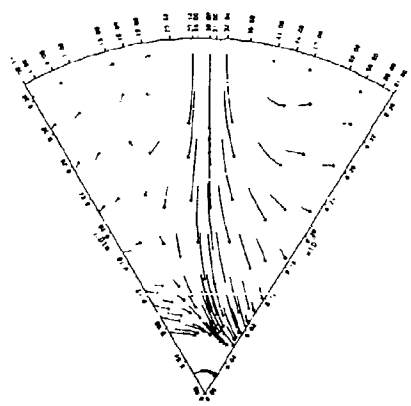

Figure 7b Predicted streaklines, x=48mm, combusting flow.

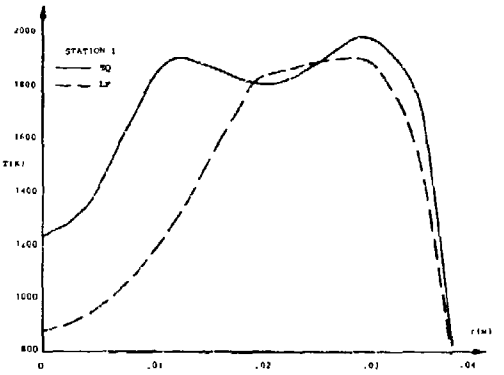

Figure 8 Temperature profile at station I.

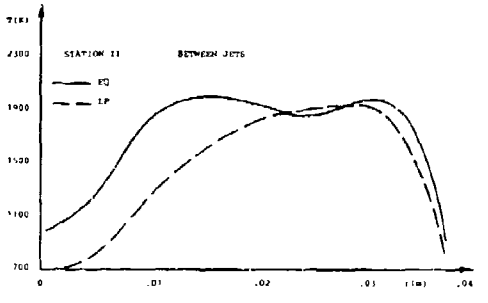

Figure 9a Temperature profile at station II, $\theta = 0^{o}$.

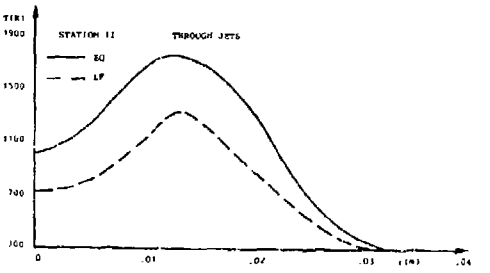

Figure 9b Temperature profile at station II, $\theta = 30^{o}$.

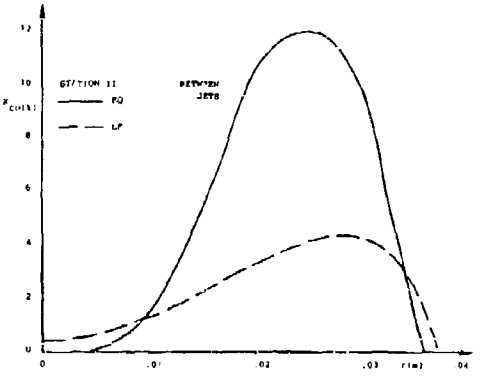

Figure 10a CO mole fraction profile at station II, $\theta = 0^{o}$.

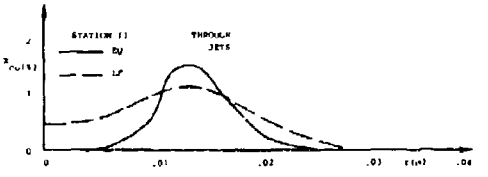

Figure 10b CO mole fraction profile at station II, $\theta = 30^{o}$.

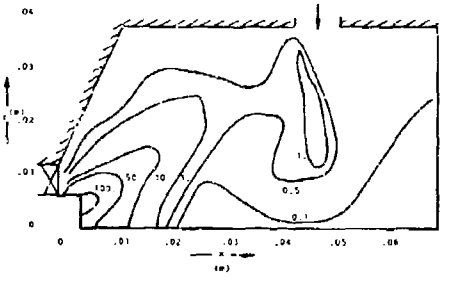

Figure 11 Predicted mean scalar dissipation rate, $\theta = 30^{o}$.

DISCUSSION

H.Eickhoff, GE

Do you have criteria for the laminar flamelet model to apply to conditions typical of gas turbine combustion in terms of scales of length and time, which are characteristic of the turbulence and of the flamelets?

Author's Reply

I have been assured that the Reynolds and Damkohler numbers are similar in gas turbine combustors to those occurring in turbulent jet diffusion flames, where the laminar flamelet model has been shown to work well. I have not performed any additional calculations to examine the applicability of the flamelet approach to combustor flows in particular.

P.H.Wild, UK

Can you say how dependent your predictions are on the form of the assumed PDF? How well can a 2 parameter model represent this PDF? For example at the point where the primary jet enters the flow field and where intermittency in mixture fraction might be expected.

Author's Reply

The predictions are known to be *very* sensitive to the use of a PDF in the first place; the neglect of a PDF can cause large changes to the flow field and its effect on mean temperature and species composition. Some comparisons have been made between the use of a B-function and a dipped Gaussian form for the PDF; the results show some solid differences, but nothing as large as neglecting the functions altogether. As long as the PDF shape is not bi-modal, then in principle a B-function can represent a wide range of shapes; how accurately this is achieved depends on the correctness of the prediction of the mean and variance of the scalar. For a combustor flowfield, we have no evidence based on experimental measurements that the variance is predicted well. It is possible to modify the PDF to allow for intermittence effects although this is much more likely to be important in free jet diffusion flames than in a confined, highly turbulent combustor flow.

A.Williams, UK

The existing data for flamelets calculations comes from quite large laminar diffusion flames. We have burned very small gaseous stationary diffusion flames rated at about 0.25W (which we claim to be the smallest stationary flame possible) and there is a considerable change in behaviour compared with larger flames. There is a greater influence of fuel/oxidant interpenetration with consequential effects on CO and smoke. Would you please comment on whether you believe that this approach may be useful in turbulent combustion.

Author's Reply

I believe there is evidence in the current predictions that the laminar flamelet profile used is not ideal for this kind of flow; it underpredicts CO shifts in rich regions and overpredicts considerably in lean regions. It is difficult to know whether this is due to an inappropriate flamelet profile, or due to a limitation of the flamelet approach altogether for combustor flowfields. I do not know whether the flamelet profiles you are referring to would remedy these defects, but it is difficult to see why data from very small flames should be more relevant to combustor flows than large laminar flame data. Much more relevant would be a flamelet profile derived from a laminar flame which approached the rapid rates of dilution found in combustor flows, although it is difficult to conceive of such a flow. Even if this were possible, the laminar flame calculations might no longer collapse to give a unique flamelet.

THE EFFECT OF PARTICLE PROPERTIES ON RADIATIVE HEAT TRANSFER

Em. Kakaras, M. Founti and N. Papageorgiou
Thermal Engineering Section, Mechanical Engineering Department,
National Technical University of Athens, Greece.

NOMENCLATURE

a_n, b_n	optical coefficients (complex)
B	mass density (particle loading) (kg/m³)
C_{ext}	equivalent extinction cross-section (m²)
C_{sca}	equivalent scattering cross-section (m²)
d	particle diameter
I	radiative intensity (W/m²)
J_λ	black-body radiative intensity distribution (Plank's function)
K_A	absorption coefficient (m^{-1})
K_{sca}	scattering coefficient (m^{-1})
K_{ext}	extinction coefficient (m^{-1})
L	equivalent thickness (m)
m	particle refractive Index = $n-in^{(1)}$
N	particle number density (m^{-3})
Qsca	scattering efficiency
Qext	extinction efficiency
$Q_{b,sca}$	back-scatter efficiency
T	temperature (°K)
X	particle parameter = $\frac{\pi d}{\lambda}$

Greek symbols

$\Delta\ell$	mean free path between particles
λ	wavelength
ρ	density

1. INTRODUCTION

Radiative heat transfer in combustion chambers is strongly influenced by the presence among the gaseous combustion products of solid particles of various size and chemical composition such as soot, char and fly-ash. The particle parameters of these products are of great importance for the calculation of radiative heat transfer and insufficient knowledge of their magnitude can often lead to erroneous simplifications. The importance of absorption or scattering phenomena in radiative transfer is also sometimes misinterpreted.

It is the aim of this work to provide computational data in order to demonstrate and explain the importance of solid particles, present in the combustion products, on absorption and scattering phenomena occuring in the radiative heat transfer.

2. THEORETICAL CONSIDERATIONS FOR THE CALCULATION OF RADIATIVE HEAT TRANSFER IN PARTICLE-LADEN FLOWS

It is generally accepted that the radiative behaviour can be well represented by the emissivity, ε. The emissivity of a mixture of substances is calculated from

$$\varepsilon_{1+2} = 1-(1-\varepsilon_1)(1-\varepsilon_2)$$

For the general case of the mixture of combustion products we have

$$\varepsilon_{tot} = 1-(1-\varepsilon_{gas})(1-\varepsilon_{soot})(1-\varepsilon_{char})(1-\varepsilon_{ash}) \quad (/1/) \qquad (1)$$

The gas emissivity ε_{gas} depends on the CO_2 and H_2O concentrations, pressure and temperature and is calculated from well known relations [(/1/,/2/,/3/)].

In order to evaluate the solid-particle emissivities an one-dimensional, two-flux model has been used for the solution of the transfer equation of radiative intensity in a slab (Fig.1), a technique which has also been applied by many authors (/4/,/5/,/6/,/7/,

/8/,/9/).

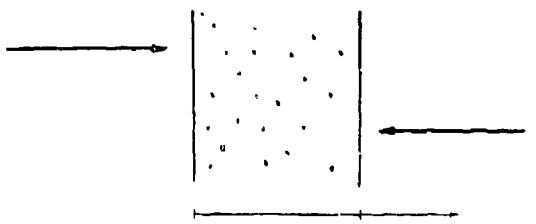

Fig.1 : 2-Flux model for a particle slab.

$$\frac{dI_+}{dx} = (-K_E.I_+ + K_{f.s}I_+ + K_{Bs}I_- + K_A.\frac{\sigma T^4}{\pi})$$

$$\frac{dI_-}{dx} = (-K_E.I_- + K_{f.s}I_- + K_{Bs}I_+ + K_A.\frac{\sigma T^4}{\pi}) \qquad (2)$$

The particle emissivity has been calculated as

$$\epsilon_p = \frac{I+(L)-I-(L)}{\sigma.\frac{T^4}{\pi}} \qquad (3)$$

Neglecting the scattering effects we find the well known expression:

$$\epsilon = 1-\exp(-K_A.L) \qquad (4)$$

3. OPTICAL CHARACTERISTICS OF SOLID PARTICLES

Because of the insufficient data existing for the various chars occuring in combustion, our efforts have been focussed on the more accurate calculation of soot and ash emissivities.

3.1 Fly-ash Particles

The applicability of Mie-theory for the calculation of absorption, scattering or extinction coefficients (K_A,K_S,K_E) can only be justified after investigation of the ratio $\frac{c}{\lambda}$ (/10/,/11/) where c = Δt-d with the definition of the sympbols given in the beginning of the paper.

It should be noted that when $\frac{c}{\lambda} < 0.3$, single-particle characteristics can be used for particle clouds.

The theoretical coefficients $K_{A,S,E}$ can be calculated from

$$K_i = N.\frac{\pi d^2}{4}.\overline{Q_i} \qquad (5)$$

For every wavelength, the optical efficiency $Q_{i,\lambda}$ is calculated according to the Mie-theory from the following relations (/12/,/13/):

$$C_{sca} = (\frac{\lambda^2}{2\pi}) \sum_{n=1}^{\infty} (2n+1)\{|a_n|^2+|b_n|^2\} \quad , \quad Q_{sca} = \frac{C_{sca}}{\frac{\pi d^2}{4}} \qquad (6)$$

$$C_{ext} = (\frac{\lambda^2}{2\pi}) \sum_{n=1}^{\infty} (2n+1)\{Re(a_n+b_n)\} \quad , \quad Q_{ext} = \frac{C_{ext}}{\frac{\pi d^2}{4}} \qquad (7)$$

$$Q_{B,sca} = \frac{1}{X^2} \left| \sum_{n=1}^{\infty} (2n+1)(-1)^n(a_n-b_n) \right|^2 \qquad (8)$$

The results of this calculation (see Fig.2) have been compared with the experimental data of /14/,/15/ and have shown a very good agreement in Q_{ext} and Q_{sca} and a slight overestimation of $Q_{B,sca}$.

$Q_{i,\lambda}$ has been integrated on the black-body emissive power distribution J_λ, giving

$$\bar{Q}_i = \frac{\int_0^\infty Q_{i,\lambda} \cdot J_\lambda \cdot d\lambda}{\int_0^\infty J_\lambda \cdot d\lambda} \qquad (9)$$

This integration led to a temperature dependence of $\bar{Q}_i$, as it is shown in Figure 3.

3.2 Soot Particles

The efficiency factors for soot particles can be generally calculated from the Mie-theory. Due to the small diameter of the soot particles, the Rayleigh theory has also been tested here. Computations have been performed for extinction, absorption and scattering cross-sections according to three different theoretical concepts:

- The Mie-theory as described by eqn.(6),(7),(8).
- The Rayleigh theory which is applicable for small particles (/13/).
- Widely used approximations suggested by Hawksley et al.(/3/,/16/,/17/), considering only the absorption efficiency factor.

The obtained monochromatic results were integrated according to eqn.(9). The existing differences between the Mie and Rayleigh theory for the cases of small wavelengths ($\lambda \leq 2\mu m$) became negligible with increasing wavelength (Fig.4). The integration however over the black-body intensity distribution function causes serious discrepancies between the two assumptions leading to an overestimated value for Q_{sca} according to Rayleigh theory (Fig.5, 5a).

4. RESULTS AND DISCUSSION

According to the previous analysis, we could determine the following parameters as the most important factors influencing the solid particle emissivity.

- The particle size parameter, $X = \frac{\pi d}{\lambda}$
- The particle refractive index, $m = n\text{-}in^{(1)}$
- The equivalent thickness, L (mean beam length)
- The forward to backward scattering ratio
- Particle number density N ($1/m^3$) or mass density, B (kg/m^3)
- Particle density, ρ

The effects of these parameters on the particle emissivity as well as on the total emissivity of a particle-gas mixture have been investigated, and a sample of the results is presented here.

Figures 6 and 7 present the variation of particle emissivity with and without scattering versus loading for various temperatures. From these figures together with further calculations performed with loadings greater than 0.5 kg/m^3 can be seen that, for both with and without scattering, the particle emissivity tends to a constant value for loadings beyond 0.8 kg/m^3 which remains temperature dependent, as it is also indicated by equation (9).

The calculations of Figure 8 show that, as the optical density is increased, the effects of scattering become more important for the particle emissivity than for the cases without scattering. Namely, scattering effects can only be neglected in calculation procedures for low values of optical densities.

It should be noted here, that the isotropic scattering assumption usually overestimates the scattering effects for large particles. This can be seen from comparisons with experimental data for fly-ash particles, extracted from ref./7/. However, neglecting scattering-effects totally, can lead to more serious errors than assuming isotropic scattering.

Figure 9 presents the total emissivity dependence for various particle loadings of gas/fly-ash mixtures. It can be seen that for particle loadings below 0.05 kg/m^3, as the temperature increases the total emissivity decreases. For particle loadings above this value the temperature dependence is negligible. The observed temperature dependence is the result of two counter-affecting phenomena: of the known reciprocal influence of the temperature increase on the gas emissivity (i.e. for gases, as the temperature is increased emissivity decreases) and of the analogous influence of temperature on the particle emissivity (i.e. for particles, increasing the temperature increases also the emissivity) as shown in figures 6 and 7.

In Fig.10 the dependence of soot emissivity on temperature is presented. As it is shown the soot emissivity increases with increasing temperature. The practical independence between scattering and soot emissivity is confirmed from the related table.

5. CONCLUSIONS

• The important factors affecting the radiative behaviour of particles in particle-laden flows have been established and investigated.

• Scattering effects can only be neglected in calculation procedures for low values of optical densities.

• For particle loadings above 0.05 kg/m³ the total-emissivity becomes temperature independent for Fly-ash particles.

• For particle loadings above 0.8 kg/m³ the particle emissivity is no longer affected by the increase of loadings for Fly-ash particles.

• Detailed calculation of soot emissivity has shown, that scattering phenomena are of no practical importance on soot emissivity.

REFERENCES

/1/ Vortmeyer-Richter-Michelfelder. VDI-Wärmeatlas Kap. K. Abs. Kc, Kd., 4. Auflage 1984.

/2/ P.B. Taylor-P. Docherty. Zone Method for Heat Transfer Calculations, Parts 2 and 4., HTFS DR33 Part 2 1973, Part 4 1985.

/3/ J.M. Béer - P.J. Foster - R.G. Siddal. Calculation Methods of Radiative Heat transfer., HTFS DR22, December 1971.

/4/ F. Biermenn-D. Vortmeyer. Wärmestrahlung staubhaltige Gase., Wärme und Stoffübertragung Bd.2, pp.193-202, 1969.

/5/ D. Grouset-R. Debufat. Radiative Heat Transfer Calculation for Pulverized Coal Combustion; Application of Lorenz Mie Theory, 8th Int. Heat Transfer Conference, S. Fran. Ca. 17/22.8.86.

/6/ P. Biermann. Wärmestrahlung staubhaltiger Gase in Dampfkessln., Dissert. TU Stuttg., 1968.

/7/ D. Köneke. Kühlung und Erhitzung von Gas-Feststoff Strömen., Dissert. UNI Dortm., 1983.

/8/ R.K. Avery-A.R. Jones. Scattering of Grey Body Radiation by Clouds of Spherical Particles, Int. J. of Energy, pp.7[illegible], 1982.

/9/ M.Q. Brewster-C.L. Tien. Examinati of the Two-Flux Model for Radiative Transfer in Particulate Systems., Int.J. Heat Mass Transfer, Vol.25, No.12, pp.1905-1907, 1982.

/10/ M.Q. Brewster-C.L. Tien. Radiative Transfer in Packed Fluidized Beds: Dependent Versus Independent Scattering., Journal of Heat Transfer, Vol.104, pp.573-579, 1982.

/11/ B.L. Drolen-C.L. Tien. Independent and Dependent Scattering in Packed-Sphere Systems., 4th Joint Thermoph. Heat Transfer Conf., New York ASME, pp.1-7, 1986.

/12/ M. Kerker. Scattering of Light and other Electr. Radiation. Academic Press, 1969.

/13/ C.F. Bohren-D.R. Huffman. Absorption and scattering of light by small particles, Wiley, 1983.

/14/ R.P. Cupta-T.F. Wall-J.S. Truelove. Radiative Scatter by Fly Ash in Pulverized Coal Furnaces: Application of the Monte Carlo Method to Anisotropic Scatter, Int. J. of Heat and Mass Transfer, Vol.26, No.11, pp.1649-1660, 1983.

/15/ G. Gouesbet-G. Grehan-B. Matheu. Single scattering characteristics of volume elements in coal clouds., Applied Optics, Vol.22, No.13, pp.2038-2050, 1983.

/16/ M.A. Field D.W. Gill - B.B. Morgan - PGW Hawksley. Combustion of Pulverized Coal , BCURA 1967.

/17/ P.G.W. Hawksley. BCURA monthly Bulletin 14 Parts 4 and 5, 1952.

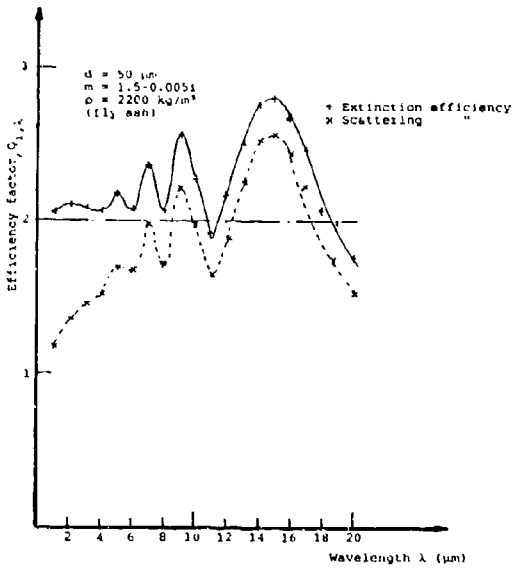

Fig.2 : Extinction and scattering efficiencies as related to wavelength λ.

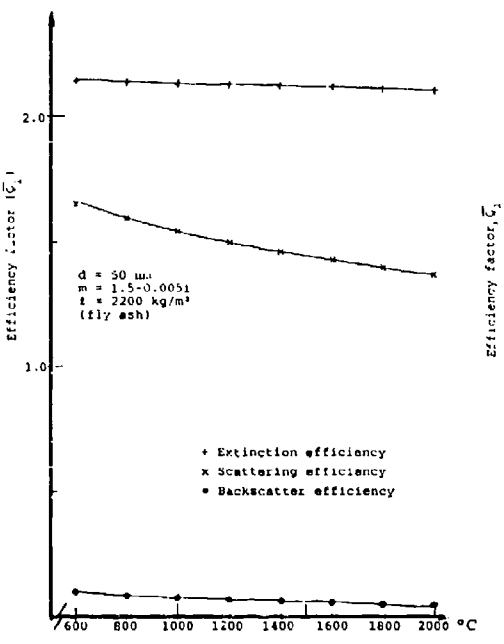

Fig.3 : Variation of average efficiencies for fly-ash particles with temperature.

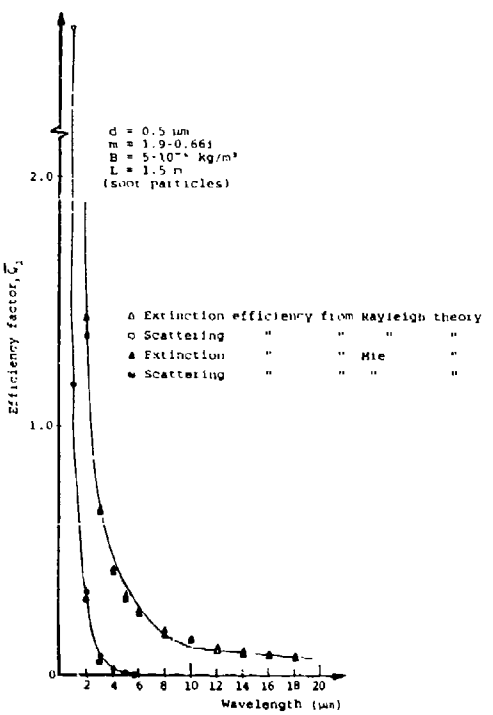

Fig.4 : Variation of extinction and scattering efficiencies for soot particles with wavelength λ.

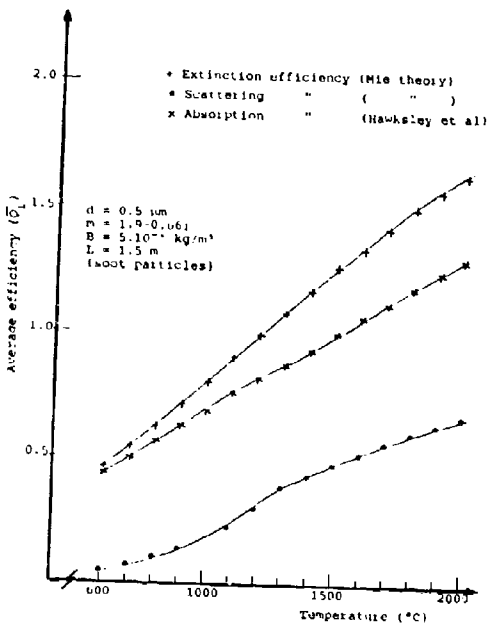

Fig.5 : Variation of average efficiencies for soot particles calculated from Mie theory, with temperature.

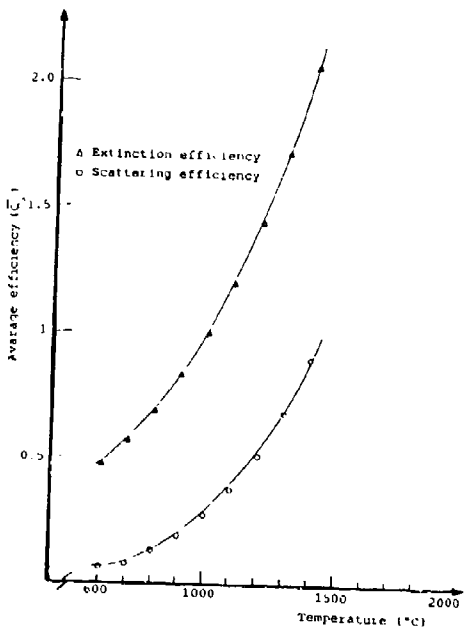

Fig.5a : Variation of average efficiencies for soot particles calculated from Reyleigh theory with temperature.

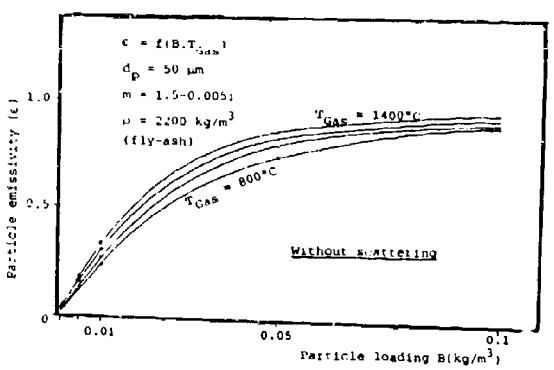

Fig.6 : Variation of particle loading versus emissivity without scattering.

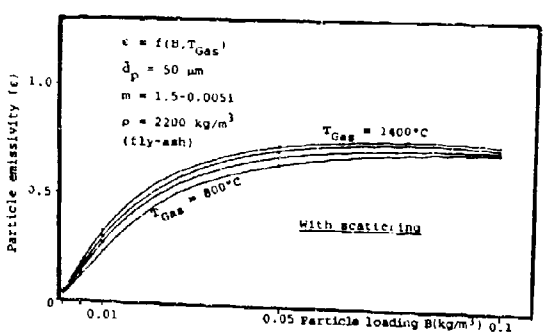

Fig.7 : Variation of particle loading versus emissivity with scattering.

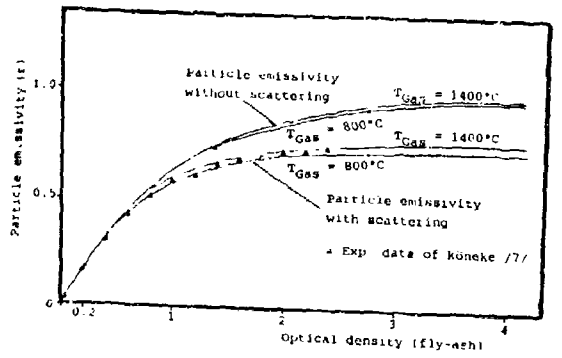

Fig.8 : Effect of optical density on particle emissivity with and without scattering.

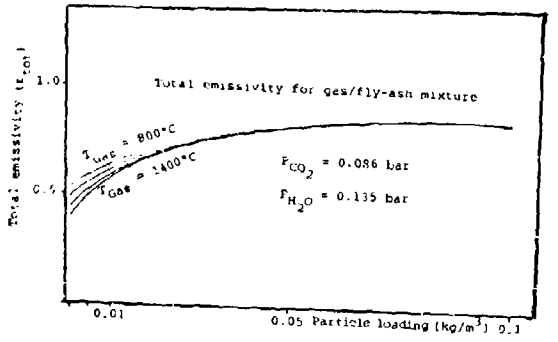

Fig.9 : Effect of particle loading on the total emissivity of gas/fly-ash mixture.

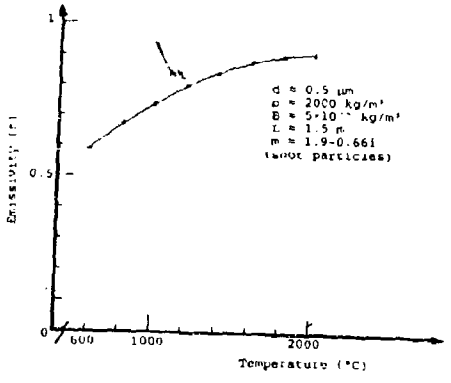

Fig.10 : Variation of soot emissivity with temperature.

Temperature °C	Soot emissivity	
	with scattering	without scattering
600	0.59398	0.59516
800	0.68753	0.68795
1000	0.75866	0.75877
1200	0.81076	0.81081
1400	0.84858	0.84859
1600	0.87590	0.87590
1800	0.89571	0.89571
2000	0.91036	0.91036

FLAMELET MODELING OF TURBULENT PREMIXED FLAMES

N. Darabiha, V. Giovangigli*, A. Trouvé=, S.M. Candel+ and E.Esposito

E.M2.C Lab., CNRS and Ecole Centrale des Arts et Manufactures,

92295 Châtenay-Malabry, France

Abstract

This paper describes some aspects of our effort to analyze turbulent combustion on the basis of an extension of the coherent flame model initially proposed by Marble and Broadwell.

At this stage the model comprises a local description (flamelets) and a global representation of the turbulent flow-field including a balance equation for the mean flame area per unit volume.

The flamelets are non-adiabatic premixed strained flames, a model suggested by Libby, Liñan and Williams. Complex chemistry calculations have been carried out for a large number of propane-air flames and a large data-base of flamelets is being constructed. These calculations provide consumption rates, extinction and ignition characteristics which are used in the global turbulent calculation to model the mean reaction terms. Numerical results obtained for turbulent premixed flames stabilized in a duct are discussed.

Experiments performed on a model combustor provide distributions of the mean heat release rate. These distributions are compared with those determined numerically. This comparison indicates that the coherent flame description accounts for important features found in the experiment.

1. INTRODUCTION

Many recent studies of turbulent combustion are based on flamelet models. In these models the turbulent reaction zone is viewed as a collection of laminar flame elements (flamelets) embedded in the turbulent stream (Williams 1975, Carrier et al. 1975, Marble and Broadwell 1977, 1979, Peters 1984, 1986, Bray 1986, Spalding 1978, Brey et al. 1984, Clavin and Williams 1982).

An advantage of this concept is that it essentially decouples complex chemistry calculations from the turbulent flow description. Chemical kinetics and multi-component transport properties may be treated separately and the results of the local flamelet analysis are then included in the calculation of the turbulent flow field. In practical applications a flamelet library (data base) is first constructed and provides specific properties such as the consumption rates per unit flame area, ignition and extinction conditions that are required in the computation of the turbulent flow field. Because chemical kinetics are explicitely treated it is expected that this approach will be able to describe its influence on the turbulent flame structure.

Flamelet models are believed to provide a viable description of turbulent combustion in the range of large Damkohler numbers and for flows characterized by typical length scales which are much larger than the typical flame thickness (Peters 1986, Bray 1986, Borghi 1985, Williams 1985). Another limit of the flamelet regime may result from quenching mechanisms due to the turbulent fluctuations. According to some authors (Borghi 1985, Williams 1985, Peters 1986) the turbulent flame structure is modified if the kolmogorov length scale ℓ_k becomes larger than the flame thickness. It is indicated that in that situation the smallest eddies enter into the inner flame structure and that the rates of strain associated with these eddies locally quench the flamelets. This is a regime of distributed reaction in which the flamelets have lost their identifiable structure. While some authors believe that this regime cannot be described by flamelet models, others suggest that flame quenching and the subsequent mechanisms and modifications of the reactive flow may be treated with flamelet descriptions. The question is not settled because very little is actually known on the structure of the turbulent small scales and on their interaction with flames. This point may be examined with detailed numerical simulations but the current understanding remains essentially intuitive and speculative. Relevant contributions dealing with these aspects are due to Williams (1975, 1985), Broadwell and Breidenthal (1982), Peters (1984, 1986), Borghi (1985), Bray (1986). Further comments on the problem of flame quenching and on its modelling are given in Section 2 of this paper.

While the domain of application of flamelet models cannot be precisely defined at this time one may say that such models are generally valid in the range of large Damkohler numbers. The typical turbulent scale must also be much larger than the flame thickness. These two conditions are certainly satisfied in many practical situations and flamelet models are relevant at least in a portion of the domain of operation of IC engines and of continuous flow combustors. Leaving aside further discussions of this point let us consider some of the problems encountered in the construction of flamelet models. These problems are related to the basic ingredients of such models :

(1) The laminar flamelet submodel (or submodels) providing the local structure and properties of the reactive elements.
(2) The description of the turbulent flow based on dynamic equations for the flow variables and the main species and the relevant closure rules.
(3) The rule or rules or additional balance equations which are flamelet submodels into the turbulent flow description.

+ Also with ONERA, 92322 Chatillon
= On leave, Department of Mechanical Engineering, U.C. Berkeley, Berkeley CA.
* Also with UA 868, CNRS, Université de Paris VI, 75252 Paris

(4) Any additional submodel accounting for chemical reactions taking place outside the flamelets.

There are many alternative ways of specifying these elements. Some methods are reviewed in Peters (1984, 1986) and in Bray (1986). Our own work is based on the coherent flame model initially proposed by Marble and Broadwell (1977) for the analysis of nonpremixed combustion. Fundamental ideas of this model are also contained in an earlier study due to Carrier, Fendell and Marble (1975). These investigations suggest that turbulent combustion of unmixed reactants is controlled in the early stages by a competition between straining of the flame elements and mutual annihilation of flame area due to the interaction of neighbouring reactive elements. The coherent flame model recognizes some other important features of turbulent combustion such as the production of flame area by stretching and its destruction by flame shortening (mutual annihilation). Because these mechanisms are important in the large scale coherent motions found in turbulent shear flows, the model accounts in some sense for these organized fluctuations.

Our own effort has been to extend the coherent flame description to premixed flow configurations (Candel et al. 1982, Darabiha 1984, Darabiha et al. 1986, Darabiha et al. 1987a) and to explore its potential in nonpremixed situations (Veynante et al. 1986, Lacas et al. 1987). The present paper reports on our progress in this entreprise. The current state of the model is described and comparisons between calculations and experiments are provided in the case of a turbulent flame stabilized in a duct. From the many experiments performed in this configuration we will only examine the flow structure obtained from schlieren visualizations and spatial distributions of the light emission from C_2 radicals. These distributions may be interpreted as giving a qualitative mapping of the local mean heat release in the turbulent flame and they are compared with distributions of the mean source terms obtained from the model. This comparison has obvious imperfections but it also constitutes an original test of turbulent combustion models. It is of special interest because it deals with the mean source term appearing in the right hand side of the energy balance equation. This differs from the more common tests performed in the literature on velocity, temperature and species mass fractions all of which are only indirectly related to the modeled source terms. Because these variables are the outcome of an integration process they are less sensitive to the modeling assumptions and do not allow a direct evaluation of the combustion models and do not give access to the source terms. Accurate representations of the mean source terms are however essential if one wishes to describe the effects of chemical kinetics or Reynolds number on the structure of the turbulent flame.

To provide the proper background to this study the basic elements of the coherent flame model are reviewed in Section 2. Special attention is devoted to the balance equation describing the transport of flame area. This equation put forward by Marble and Broadwell is derived and adapted to the premixed flow case. Production of flame area by stretch and destruction by mutual annihilation are given further consideration. The effect of flame quenching on the balance of flame area is discussed and a model is proposed for this mechanism.

Important features of strained premixed flames with complex chemistry are examined. Calculations of strained propane-air flamelets under adiabatic and non adiabatic conditions are discussed.

Experimental results for premixed ducted flames are presented in Section 3. Results of calculations for the same configuration are presented in Section 4 and compared to the measurements contained in Section 3.

2. BASIC ELEMENTS OF THE COHERENT FLAME MODEL

The coherent flame model adopts the view that the turbulent reaction field may be described as a collection of laminar flamelets. The flamelets are transported and distorted by the turbulent stream but each flamelet retains an identifiable structure. In this sense the flamelets remain "coherent" (i.e. organized). A rough sketch of this situation is given in fig. 1. A flamelet embedded in this flowfield is essentially effected by the local strain rate. The flamelet structure is modified and the local reaction rate per unit flame area may be obtained from an analysis of strained laminar flames. The simplest geometry allowing this analysis is shown in fig. 1c.

The turbulent motion and the associated field of strain rates also has the effect of increasing the available density of flame surface. The production of flame area is balanced by various destruction mechanisms such as flame shortening (mutual annihilation of adjacent flamelets) and flame quenching.

The basic elements of the coherent flame description are now reviewed. We will focus on aspects which are most specific and apparently less well known such as the balance of flame area.

2.1 Turbulent Flow description

The description of the turbulent reacting flow employs standard mass-avereged balance equations. Using standard notations to designate the density, velocity components, pressure enthalpy and species mass fractions these equations may be cast in the form :

Overall mass

$$\partial\bar{\rho}/\partial t + \partial\bar{\rho}\tilde{V}_k/\partial x_k = 0 \qquad (1)$$

Momentum

$$\partial\bar{\rho}\tilde{V}_j/\partial t + \partial\bar{\rho}\tilde{V}_k\tilde{V}_j/\partial x_k = -\partial\bar{P}/\partial x_j + \partial(-\rho\widetilde{V_k''V_j''})/\partial x_k \qquad (2)$$

Energy

$$\partial\bar{\rho}\tilde{h}_t/\partial t + \partial\bar{\rho}\tilde{V}_k\tilde{h}_t/\partial x_k = \partial\bar{P}/\partial t + \partial(-\rho\widetilde{V_k''h''})/\partial x_k - \sum_{i=1}^{N} h_{f_i}^{\circ}\bar{\dot{w}}_i \qquad (3)$$

Species

$$\partial\bar{\rho}\tilde{Y}_i/\partial t + \partial\bar{\rho}\tilde{V}_k\tilde{Y}_i/\partial x_k = \partial(-\bar{\rho}\widetilde{V_k''Y_i''})/\partial x_k + \bar{\dot{w}}_i \qquad (4)$$

In writing these equations for high Reynolds number flows it has been assumed that molecular fluxes could be neglected with respect to the turbulent fluxes.

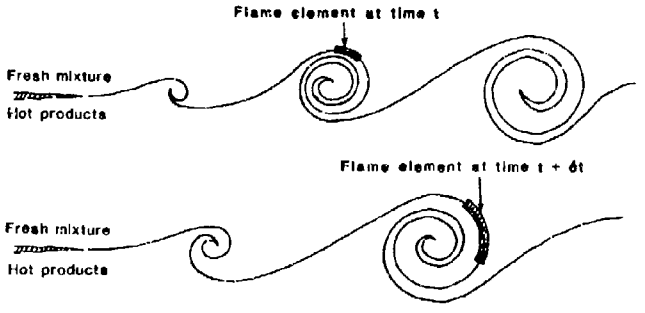

a) Production of flame surface by the strain rate

b) Flame annihilation process

c) Local model of the strained premixed flame element

Figure 1

Two distinct types of closure models are required to obtain a complete set of balance equations. The first closure model concerns the momentum, enthalpy and species transport terms (i.e. $-\rho\widetilde{V_k''V_j''}$, $-\rho\widetilde{V_k''h''}$, $-\rho\widetilde{V_k''h''}$). A conventional second order closure based on transport equations for the turbulent kinetic energy and the dissipation is used in this study. These equations have well known imperfections but they are provisionally adopted because they provide an acceptable description of turbulent transport in simple flow configurations.

The second closure model concerns the mean reaction terms $\bar{\dot{w}}_i$. The corresponding closure problem has been the subject of many studies and research in this area is reviewed in the monography of Libby and Williams (1980) and in articles due to Borghi (1979), Bray (1980, 1986), Peters (1984, 1986) Jones and Whitelaw (1982). An up to date discussion of the problem is also contained in Williams (1985).

Standard models for the mean source terms are based on probability density functions (PDF). A pdf shape is presumed or calculated. In certain formulations the pdf describes a single parameter like a

progress variable : $p(c, \underset{\sim}{x})$. The pdf then gives the distribution of this variable at each point of the flow and the mean source terms are evaluated as integrals of the source terms weighted by the PDF

$$\tilde{\dot{w}}_i = \int \dot{w}_i \, p(C ; \underset{\sim}{x}) \, dC \tag{5}$$

The coherent flame description provides an alternate solution to the closure problem. The mean reaction rates are deduced from a consideration of the mean flame area per unit volume $\tilde{\Sigma}_f$. The consumption rate per unit flame area are also calculated and the mean source terms are obtained by combining these two quantities. These elements are now considered in more detail.

2.2 Balance equation for the flame area per unit volume

The balance equation for the density of flame area plays an essential role in the coherent flame description. This equation is now established in the case of premixed combustion (see Darabiha et al. 1987b). If Σ represents the material surface per unit volume it can be shown that the balance equation of the mean value of Σ has the following form:

$$\underset{1}{\partial \bar{\rho} \tilde{\Sigma} / \partial t} + \underset{2}{\partial \bar{\rho} \tilde{V}_k \tilde{\Sigma} / \partial x_k} = \underset{3}{\partial (- \bar{\rho} \widetilde{V_k'' \Sigma''}) / \partial x_k} - \underset{4}{\bar{\rho} \widetilde{n_i n_j S_{ij}} \Sigma} \tag{6}$$

The turbulent flux of the surface density which appears in the third term of this expression may be modeled like the other turbulent fluxes by making use of the turbulent viscosity μ_T and the mean gradient of $\tilde{\Sigma}$

$$- \bar{\rho} \widetilde{V_k'' \Sigma''} = \mu_T / \sigma_\Sigma \, \partial \tilde{\Sigma} / \partial x_k \tag{7}$$

where σ_Σ is a Schmidt number for the surface density.

The last term in equation (6) is more unusual. It represents the mean variations of surface density produced by the local strain rates. Following Marble and Broadwell (1977) this term may be modeled by

$$- \bar{\rho} \widetilde{n_i n_j S_{ij}} \Sigma = \bar{\rho} \, \varepsilon_s \tilde{\Sigma} \tag{8}$$

where ε_s designates a mean strain rate. According to this model the surface density Σ increases linearly with the mean strain rate. In simple shear flows (mixing layers, jets, wakes) the strain rate may be related to the mean velocity gradient in the transverse direction

$$\varepsilon_s = \alpha \left| \partial \tilde{u} / \partial y \right| \tag{9}$$

where α is a constant. In more complex flows it is more appropriate to deduce the strain rate ε_s from the turbulent kinetic energy and from the dissipation rate

$$\varepsilon_s = C_s \, \varepsilon / k \tag{10}$$

where C_s is a constant. An alternate method for prescribing this strain rate consists of estimating the scalar dissipation rate χ and assuming that ε_s is proportional to this quantity. The mean scalar dissipation rate may be obtained from (see for example Peters 1984)

$$\chi = C_\chi \varepsilon / k \; \widetilde{z''^2} \tag{11}$$

where $C_\chi = 2$ and $\widetilde{z''^2}$ designates the mass average of the square of the fluctuations of a conserved scalar. This last quantity is usually determined by solving an additional transport equation.

The mean scalar dissipation χ may also be derived from a modeled transport equation as given for example by Borghi and Dutoya (1979).

Leaving aside any further discussion of this aspect, one finds that the transport equation for the mean surface density $\tilde{\Sigma}$ may be cast in the form

$$\partial \bar{\rho} \tilde{\Sigma} / \partial t + \partial \bar{\rho} \tilde{V}_k \tilde{\Sigma} / \partial x_k = \partial ((\mu_T / \sigma_\Sigma) \partial \tilde{\Sigma} / \partial x_k) / \partial x_k + \bar{\rho} \, \varepsilon_s \tilde{\Sigma} \tag{12}$$

In fact this equation does not describe all the mechanisms which determine the balance of flame area. Indeed the elements of flame area cannot be identified with material surfaces because they are in relative motion with respect to the local flow. One may however neglect this displacement because the flame velocities are usually small when compared to the flow velocities.

Furthermore it is indicated by Marble and Broadwell that flame area disappears when two adjacent flame elements interact and consume the intervening reactants. Finally in certain situations the flame element is located in a field of high strain rates and it may be extinguished. This process causes the dissipation of flame area. To represent these mechanisms one has to include additional terms in the transport equation describing $\tilde{\Sigma}$. The balance equation for the density of flame area $\tilde{\Sigma}_f$ will take the general form

$$\left\{\begin{array}{c}\text{Rate of change}\\ \text{of } \widetilde{\Sigma}_f\\ (1)\end{array}\right\} = \left\{\begin{array}{c}\text{Turbulent diffusion}\\ \text{of } \widetilde{\Sigma}_f\\ (2)\end{array}\right\} + \left\{\begin{array}{c}\text{Production of}\\ \text{by strain}\\ (3)\end{array}\right\} - \left\{\begin{array}{c}\text{Dissipation of } \widetilde{\Sigma}_f\\ \text{caused by extinction}\\ (4)\end{array}\right\} - \left\{\begin{array}{c}\text{Dissipation of}\\ \widetilde{\Sigma}_f \text{ by mutual}\\ \text{annihilation}\\ (5)\end{array}\right\} \qquad (13)$$

The first two terms are similar to those obtained for the material surface density.

The third term has to be modified because local conditions of temperature mass fractions and strain rate influence the production of flame area. Whereas a material surface submitted to strain is augmented, this may not be the case for the flame surface. If for example the strain rate is too high extinction will occur, no flame area will be produced and in some cases the flame surface density will be decreased.

Another process which may limit the production of flame area is the absence of one of the reactants. For instance in the recirculation region the gases are near chemical equilibrium and no heat production occurs.

Other mechanisms may limit the production of flame area but those mentioned are among the most important. The production term $\bar{\rho}\varepsilon_s\widetilde{\Sigma}$ must be moderated to account for these processes. In the general case, for adequate values of the strain rate, mass fractions and temperature the production term keeps its standard form $\bar{\rho}\,\varepsilon_s\,\widetilde{\Sigma}_f$. When these values are outside the domain in which a flame may develop, the production term will vanish. The domain Ω of possible flames is derived from the local flamelet analysis. If $f_\Omega(\varepsilon_s, Y_l, T_b)$ designates a function which vanishes outside Ω and is equal to one inside Ω then the production of flame area may be cast in the form $\bar{\rho}\,\varepsilon_s\,f_\Omega\,\widetilde{\Sigma}_f$.

According to this expression flame area is produced if the flame existence is assured.

If the local strain rate is very high the local flamelets are quenched and the strain rate does not create flame area. In that situation the strain rate will actually participate in the destruction of flame surface. This mechanism is expected to occur when the strain rate ε_s exceeds a certain critical value ε_{sc} which depends on the local conditions and is determined from the local flamelet analysis. In that circumstance the flame area will disappear in proportion to the strain rate itself. A model for this destruction term is of the form $\gamma_c\,\bar{\rho}\,\varepsilon_s\,h(\varepsilon_s-\varepsilon_{sc})\,\widetilde{\Sigma}_f$

where h is the Heaviside function and γ_c is a constant. One may also argue that the rate of destruction of flame area is proportional to the difference between the strain rate and the critical strain rate. In that case the destruction term becomes

$$\gamma_c\,\bar{\rho}\,(\varepsilon_s-\varepsilon_{sc})h(\varepsilon_s-\varepsilon_{sc})\,\widetilde{\Sigma}_f$$

In both cases the net result of the production and destruction terms (3) and (4) appearing in eq. (13) will be a decrease of the flame surface density when ε_s exceeds ε_{sc} .

It is not difficult to take into account the fact that the strain rates found at a certain point in the turbulent stream are distributed in a finite range around the mean value. This is achieved with a probability density function like that proposed by Peters (1984) or Bray (1986). When such a PDF is introduced the transition between production and dissipation of flame area is more progressive.

Dissipation of flame area is also due to the mutual annihilation of adjacent flame elements. Flamelets coming at a close distance consume the intervening reactant and this shortens the available flame area. This mechanism is well illustrated by the theoretical work of Marble (1985), Karagozian and Marble (1986) and by some recent calculations of Laverdant and Candel (1987a, 1987b).

A model for this process may be established on the basis of a simple argument due to Marble and Broadwell. Their derivation is easily extended to the premixed case. Consider now two flamelets seperated by combustion products. The distance between these two elements will tend to increase and mutual annihilation will not occur. On the other hand if fresh reactants seperate the two flamelets the reaction fronts progress towards each other, the reactants are consumed and mutual annihilation takes place. Now consider the mean distance between the flamelets. This distance is of the order of $1/\widetilde{\Sigma}_f$. If $\widetilde{X}_i$ designates the volume fraction (the molar fraction) of one of the main species involved in the reaction, then the effective distance occupied by this species is $l_i = \widetilde{X}_i/\widetilde{\Sigma}_f$. Let v_{Di} designate the volume rate of consumption of the i-th species per unit flame area (this quantity has the dimensions of a velocity). This species is consumed at the rate v_{Di} and it disappears in a characteristic time

$$\tau_{Di} = l_i / v_{Di} = \widetilde{X}_i /(v_{Di}\,\widetilde{\Sigma}_f)$$

The rate of annihilation of flame area associated with the consumption of the i-th species is then proportional to

$$\widetilde{\Sigma}_f / \tau_{Di} = v_{Di}\,\widetilde{\Sigma}_f^{\,2} / \widetilde{X}_i$$

The rate of flame annihilation associated with the consumption of the main species involved in the reaction is then of the form

$$\sum_{i=1}^{N} (v_{Di} / \widetilde{X}_i)\,\widetilde{\Sigma}_f^{\,2} \qquad (14)$$

When the main species are a fuel F and an oxidizer O, the flame shortening term is proportional to

$$(v_{Do} / \widetilde{X}_o + v_{DF} / \widetilde{X}_F)\,\widetilde{\Sigma}_f^{\,2} \qquad (15)$$

This term is evaluated per unit volume. The flame shortening term is proportional to the square of the flame surface density and to a weighted sum of the consumption velocities of the main species.

It is now possible to write a complete balance equation for the flame surface density :

$$\partial\bar{\rho}\tilde{\Sigma}_f/\partial t + \partial\bar{\rho}\tilde{V}_k\tilde{\Sigma}_f/\partial x_k = \partial((\mu_T/\sigma_\Sigma)\partial\tilde{\Sigma}_f/\partial x_k)/\partial x_k + \bar{\rho}\,\varepsilon_s\,f_\Omega\,\tilde{\Sigma}_f$$
$$- \gamma_e\,\bar{\rho}\,(\varepsilon_s - \varepsilon_{se})h(\varepsilon_s - \varepsilon_{se})\,\tilde{\Sigma}_f \qquad (16)$$
$$- \beta\,\bar{\rho}\,(\nu_{Do}/\tilde{X}_o + \nu_{DF}/\tilde{X}_F)\,\tilde{\Sigma}_f^{\,2}$$

where may be estimated as

$$\varepsilon_s = \alpha\,(\tilde{S}_{ij}\tilde{S}_{ij})^{1/2} \quad \text{or} \quad \varepsilon_s = C_s(\varepsilon/\kappa)$$

In these expressions $\alpha, \beta, \gamma_e, C_s$ are constants and σ_Σ is a Schmidt number for the flame surface density.

The volume rate of consumption per unit flame appearing in this expression are obtained from the local flamelet analysis.

2.3 Determination of the mean reaction rates

Knowing the mean flame surface density $\tilde{\Sigma}_f$ and the consumption rates per unit flame surface one may easily determine the mean consumption terms per unit volume :

$$\tilde{\dot{w}}_F = -\bar{\rho}\,\nu_{DF}\,\tilde{\Sigma}_f$$
$$\tilde{\dot{w}}_O = -\bar{\rho}\,\nu_{Do}\,\tilde{\Sigma}_f \qquad (17)$$

These simple expressions may be refined if one takes into account the fact that the local flamelets correspond to a distribution of strain rates. The probability density function describing the distribution of the strain rates $P_s(\varepsilon_s)$ may be presumed and the mean consumption terms per unit volume take the general form

$$\dot{w}_i = -\rho\,\Sigma_f \int \nu_{DF}(\varepsilon_s)\,p_S(\varepsilon_s)\,d\varepsilon_s \qquad (18)$$

A slightly more complex expression is also obtained if one assumes that the burnt gas temperature which arises in the local flamelet analysis is also distributed around its mean value.

2.4 The flamelet model

An idea shared by all flamelet models is that the strain rate imposed by the turbulent flow on the laminar flame elements plays an essential role. The flamelets are strained by the turbulent motion, their inner structure is modified and the consumption of reactants and the heat release rate per unit flame area are affected. Large strain rates may lead to partial or total extinction of the flamelets. The simplest example illustrating the effect of strain rate is that of a diffusion flame in the fast chemistry limit. It is easily shown that in this limit the rate of reaction is augmented when the strain rate is increased (see Carrier et al. 1975). It is actually found that the consumption rates per unit flame area increase like $(D\varepsilon_s)^{1/2}$ where D is a diffusion coefficient. The strain rate augments the flow of gases to the flame sheet and the reaction rate is enhanced. This process is limited by finite chemical rates of reaction and for high strain rates the flame may be cooled by the rapid convection of fresh material and it may be extinguished.

Notable analyses of strained diffusion flames are due to Carrier et al. (1975), Linan (1974), Tsuji (1982), Law (1984). The case of premixed strained flames is considered by Klimov (1963), Buckmaster and Ludford (1983), Libby and Williams (1981, 1983, 1984), Libby et al. (1983).

Many studies of premixed strained flames are based on activation energy asymptotics. Numerical calculations are due, among others, to Smooke et al. (1986), Giovangigli and Candel (1986), Darabiha et al. (1986), Giovangigli and Smooke (1985). Detailed chemistry calculations are now being performed by many groups. Dixon-Lewis et al. (1984) compare calculations of methane-air diffusion flames. Complex chemistry is also used in the studies of Marble and Brodwell (1977, 1979), Liew et al. (1984), Rogg et al. (1986) and Giovangigli and Smooke (1986).

The structure and properties of strained propane-air flames with complex chemistry are examined by Darabiha et al.(1987a). The basic flamelet model and the main results of this study are reviewed in this section. The presentation will essentially focus on the effect of strain and hot stream temperature on the flamelet structure and extinction/ignition characteristics.

A strained premixed laminar flame in a counterflow of fresh reactants and burnt gases is considered as shown in Fig. 2. The system is modeled by employing a boundary layer approximation (see Darabiha et al. 1987a).

The local flamelet model depends on three parameters ε_s, T_b and ϕ. The quantity ε_s denotes the strain rate, T_b represents the temperature in the burnt gas stream and ϕ is the equivalence ratio of the incoming fresh reactant stream. The strain rate is a measure of the "stretch" in the flame due to the imposed flow, ϕ is a measure of the relative proportion of fuel and air in the reactant stream and T_b represents how much the incoming burnt products have gained or lost energy subsequent to their creation, by a mechanism inoperative within the flamelet. Whenever these products have neither gained nor lost any energy, the temperature T_b is the so called adiabatic flame temperature T_{ad}. We will refer to this case as the "adiabatic" case, whereas the situations $T_b > T_{ad}$ and $T_b < T_{ad}$ are referenced as "superadiabatic" and "subadiabatic". These terms characterize the history of the burnt gases and not the flamelets which do not exchange heat with the surroundings.

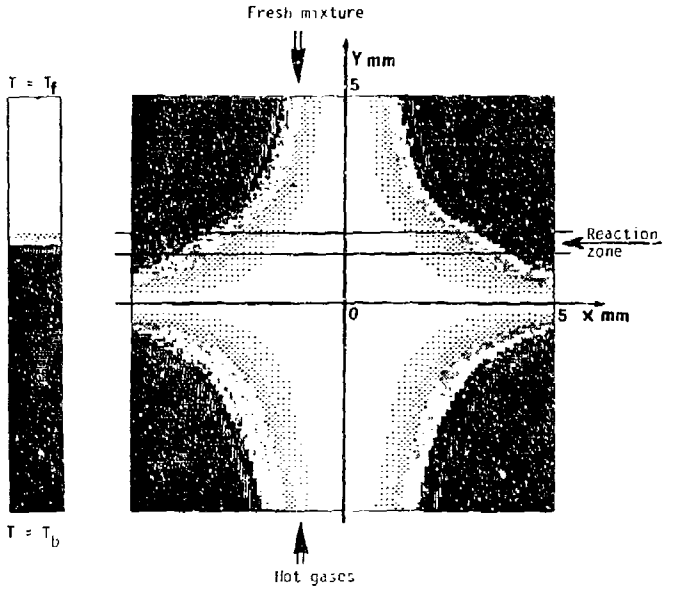

Figure 2

Our goal is now to study the dependence of the solution on the parameters ε_s and T_b for propane-air mixtures.

The solution method used to determine the flamelet structure combines a phase-space, pseudo-arclength continuation method, Newton-like iterations and global adaptive gridding. Thermodynamic and transport properties are determined with CHEMKIN and TRANSPORT packages developed by Kee et al. (1980 , 1985). (Details may be found in Giovangigli and Smooke 1987a,b,c, Smooke 1982 and Giovangigli and Darabiha 1987.)

The flamelet data base may be constructed by performing continuation sequences with respect to the strain rate for different values of the burnt gas temperature. It is possible in this way to investigate the dependence of the propane-air flame on ε_s and T_b. Typical calculations done for an equivalence ratio of $\phi = 0.75$, a fresh reactant stream temperature of $T_f = 300°K$ and a pressure p of one atmosphere are now described. The reaction mechanism for the propane-air system is taken from Warnatz (1983, 1985). It involves 33 species and 126 reactions.

Based on the theoretical work of Libby, Linan and Williams (1983) it is anticipated that the burnt gas temperature T_b will play an important role in the extinction process. In particular, depending on the value of T_b, a flame subject to varying strain rates may undergo abrupt ignition or extinction transitions involving altered locations of the reaction zone and altered creation of product.

To investigate this solution multiplicity, the heat release rate h per unit flame area is plotted in figure 3 as a function of the strain rate ε_s for different temperatures T_b. These curves show that for flames with product stream having elevated enthalpies, i.e., a sufficiently large T_b, the heat release rate varies continuously with ε_s. On the other hand, for flamelets with sufficiently cooled product streams, i.e., a sufficiently low T_b, there are abrupt ignition and extinction transitions and the characteristic response curve is S-shaped. The upper branch corresponds to standard flame structures, the lower branch to extinguished solutions and the intermediate branch to unstable solutions. It is found that the first extinction point is reached at about $T_b = 1550$ K and for $\varepsilon_s = 800$ sec^{-1}. The corresponding flame front locations are presented in figure 4. These plots show that during ignition or extinction transitions there are abrupt flame front location and peak temperature changes. These results are in

excellent qualitative agreement with the theoretical work of Libby, Liñan and Williams (1983).

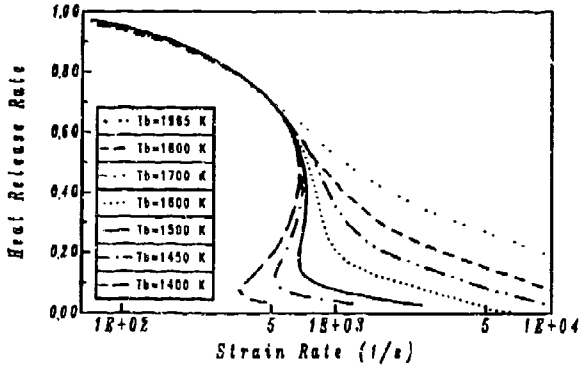

Figure 3

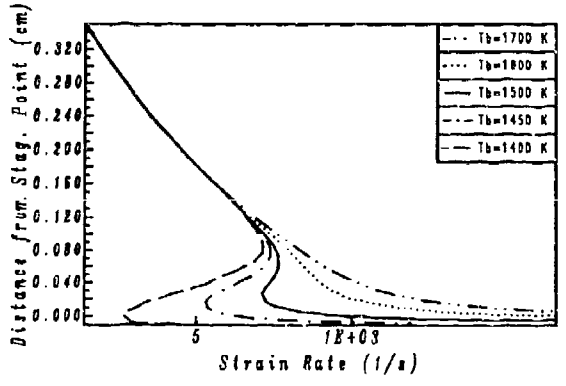

Figure 4

3. EXPERIMENTS ON TURBULENT DUCTED FLAMES

3.1 Experimental configuration

The experimental set up used in this study is shown in Fig. 5. A mixture of air and propane is injected through a long duct into a rectangular combustor. The height, depth and length of this element are respectively 50, 100 and 300 mm. The inlet plane comprises a V-gutter flame holder placed at the duct center and producing a 50 % blockage. The upper and lower combustor walls are made of thick ceramic material while the lateral walls are transparent artificial quartz windows. A stainless steel structure holds the various parts together. Ignition of the premixed stream is obtained with a spark plug. The plug may be lowered down behind the flameholder, it is activated and removed from the chamber after ignition. Combustion is then stabilized by hot gases recirculating behind the V-gutter.

The stabilizer may be set into a pitching motion with an electromechanical shaker as shown in Figure 5 but this device is not used in the present study.

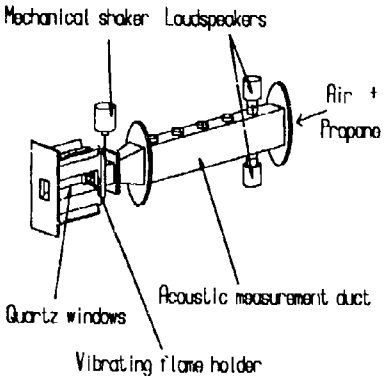

Figure 5

3.2 Schlieren visualization and C_2-radical light emission measurements

It is intructive to first examine the flame structure using spark Schlieren photographs.

For the whole range of Reynolds numbers considered in this paper $Re_H < 10^5$ (the Reynolds number is based on the stabilizer height, on the velocity at the lips and on the cold flow viscosity), the flow in the flame zone is dominated by large scale coherent vortices. A typical case is shown in Fig. 6. The small fluctuations observed in the recirculation zone are due to a small leak between the flameholder and the window leading to some spurious burning of the mixture near the wall. These vortices resemble those found in studies of non reactive two dimensional shear layers (for example Brown and Roshko 1974). There are however some distinctive features. It is observed in particular that the initial small scale vortices formed near the stabilizer lips are perfectly rolled up in a succession of "cat's eye" patterns (Fig. 6). However at a greater distance from the stabilizer the inner boundary of the vortex patterns disappears and a core of relatively uniform gases is formed on the hot side of the flame. This behavior is a direct consequence of the competition taking place in the vortices between the production of flame area by stretch and its destruction by mutual annihilation.

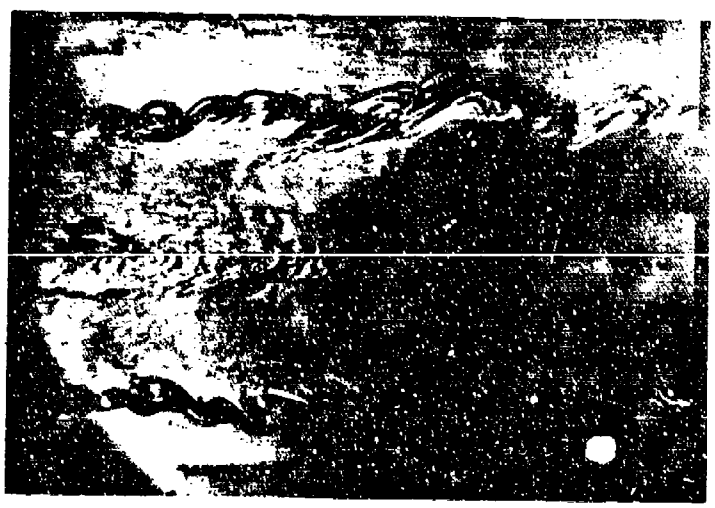

Figure 6

While exact measurements of the local energy release are not available many observations indicate that the light radiated by the combustion zone is related to the reaction intensity and hence to the heat-release process. Certain radicals like C_2, CH, OH appear almost exclusively in reactive zones and their concentration is always small. Hence the self absorption of the light emitted by these radicals is not important and the radiated light intensity is directly related to the reaction rate or equivalently to the heat release rate (see Poinsot et al. 1987 for further discussion of this point and an application to the analysis of the nonsteady heat release under unstable combustion).

While a linear relation between the heat release source term and the light emission from free radicals has been proved in some special situations it may be safely stated that a monotonic relation exists between these two quantities. The measurement of the mean heat release source term relies on this assumption. The emission band used to this purpose is the (0,0) C_2 band at a wavelength λ = 5165 A. This wavelength is isolated in the emission spectrum with a narrowband interferential filter ($\Delta\lambda \simeq$ 50 A). The light emitted by the flame is collected by an f = 54 mm convex lens located at 100 mm from the combustor center plane. The light beam is then filtered and the filtered light intensity is detected by a photomultiplier through a 1 mm diameter pinhole to provide a local measurement ; the emitting area actually seen by the detector has a diameter of about 1 mm. The detector output is amplified, low pass filtered to prevent aliasing and transmitted to a PDP 11/23 computer through an 8 channel 12 bit A/D converter. This computer also controls the optical system displacement in the vertical and horizontal directions. The photomultiplier scans a grid comprising 3000 points. At each point $\underline{x}$ of this grid, 1000 data samples are acquired and averaged. This process yields the spatial distribution of the mean light emission $I(\underline{x})$.

Spatial distributions of the light emitted by C_2 radicals are displayed in figures 7a and b. The first map (Fig. 7a) corresponds to a Reynolds number of Re_H = 46000 and an equivalence ratio of Φ =0.6. At low values of Φ , concentrated regions of reaction are observed in the vicinity of the flame holder. For Φ = 0.6 these regions form at a close distance and a merged reaction zone is observed. For higher values of the equivalence ratio the reaction regions are shifted downstream and further apart from each other.

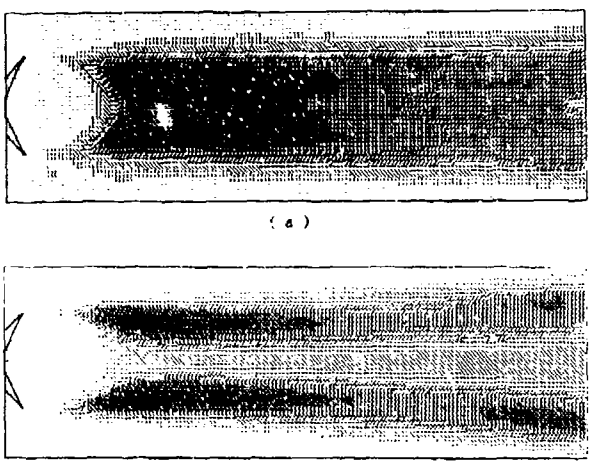

(a)

(b)

Figure 7

Consider now the light emission map obtained for a higher value of the mass flow rate and of the equivalence ratio (Fig. 7b). In this case the flame angle decreases slightly and the maximum of the heat release rate is shifted upstream.

A systematic exploration of the flow regimes (Derabiha et al. 1987b) indicates that the equivalence ratio and the Reynolds number have a notable influence on the flame structure. The modifications associated with these two parameters are not extensively documented in the previous literature (see Libby et al. 1987 for a review of the available data, Zukoski and Marble 1955 for an early analysis of the influence of the Reynolds number on the wake transition behind a flame stabilizer). It is however important to retrieve this behavior in the numerical modeling of the flame.

4. NUMERICAL RESULTS AND DISCUSSION

Numerical results obtained for the combustor geometry described in the previous section are now discussed. These results may be compared to the experimental data presented in Section 3. All calculations

correspond to a single set of constants (standard values are adopted for the k- ϵ model ($C_\mu = 0.09$, $c_1 = 1.44$, $c_2 = 1.92$, $\sigma_k = 1$, $\sigma_\epsilon = 1.3$, $\sigma_T = 0.7$) and the constants involved in the balance of flame area are :

$$\sigma_\Sigma = 1 , \quad C_s = 1 , \quad \gamma_c = 1 , \quad \beta = 1 .$$

No effort was expended to adjust these parameters but some improvements are possible. The calculations are carried with a time dependent finite difference implicit code developed at ONERA and described by Dupoirieux and Scherrer (1985).

The coherent flame description was introduced in the code in place of the preexisting "Eddy-Break Up" model.

Taking into account the mean flow symetry the computation is performed on a domain extending from the combustor axis to the wall. The finite difference grid is nonuniform in the axial direction and comprises 21 vertical and 63 horizontal nodes.

The reacting flow calculations are initiated by introducing a temperature spot with a Gaussian shape and a localized distribution of flame surface density in the recirculation zone of the cold flow. It turns out that the temperature spot is sufficient to start the reaction, the initial distribution of flame surface may be chosen arbitrarily.

The inlet temperature is 300 K, and the ambient pressure at the combustor exhaust is atmospheric. Results presented correspond to a stationary flow configuration which is obtained after 2000 time step iterations after ignition. The typical CFL number used in the calculations is 7.

To compare the numerical results with the experimental results, we have displayed in Figure 8a the fuel consumption rate distribution in the combustor using a scale of grey symbols. This figure corresponds to an inlet velocity of 15 m/s, a mass flow rate of $\dot{m}_0 = 69$ g/s and a fresh mixture equivalence ratio of $\Phi = 0.6$. The fuel consumption is essentially concentrated in a region located at about 40 mm from the flame holder edge. The maximum value is 1.59 kg/m^3/s. Note that for clarity the geometry of the plot is distorted, the vertical scale differs from the horizontal one. The ratio of the combustor height to the combustor length is 0.357 in the figure while it is 0.166 in reality. However the numerical results may be directly compared with the experimental distributions (Fig. 7a).

The fuel consumption rate diminishes progressively in the downstream direction. There is no consumption of fuel near the horizontal walls. This result is in agreement with the experimental observations of the C_2 radiall light emission (Fig. 7a). The main difference between these two results is that the calculation predicts heat release in the recirculation zone. This is at variance with the experiment and also with common knowledge. This difference may be explained in various ways. One may argue for example that the turbulent diffusion of flame area is overestimated and that the Schmidt number should be increased. A detailed examination of the distribution of fuel indicates that a certain amount of this species penetrates into the recirculation region and burns in that region. This indicates an important weakness of the gradient diffusion modeling used in the calculation.

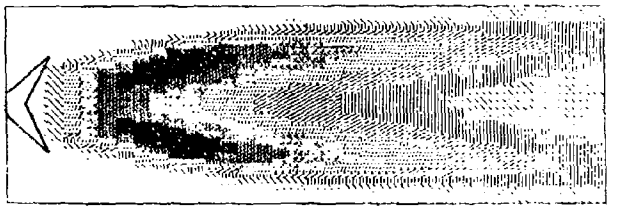

(a)

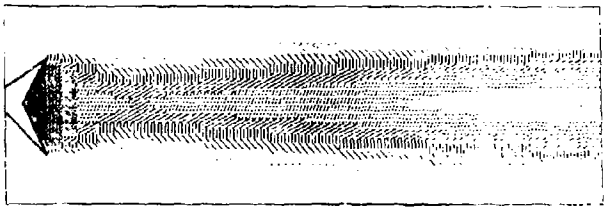

(b)

Figure 8

Figure 8b displays the temperature distribution in the combustor for the same conditions (v_I = 15

m/s, $\dot{m}_a$ = 69 g/s, Φ = 0.6). The hot recirculation zone has the maximum temperature slightly above 1700 K. The temperature then diminishes on the combustor axis. In the middle of the chamber and on this axis the temperature is about 1000 K. Near the combustor exhaust the temperature increases and reaches 1400 K. Near the walls, the temperature slowly increases in the axial direction and the temperature profile at the exhaust has not reached a uniform state.

Another calculation is performed for an equivalence ratio of Φ = 0.75 and an inlet velocity of 22 m/s (corresponding to a mass flow rate $\dot{m}_a$ = 100 g/s). Figure 9a displays the distribution of the mean consumption rate of fuel. Comparing this figure with the previous calculation it is found that the length of the reaction region diminishes but its location is almost the same. This result agrees with the experimental observations (see Fig. 7b). We note that the maximum fuel consumption rate reaches a value of 2.14 kg/m^3/s which is greater than that of the previous calculation. This change is due in part to the higher value of the equivalence ratio and it also corresponds to a change in the spatial distribution of the mean reaction rate term.

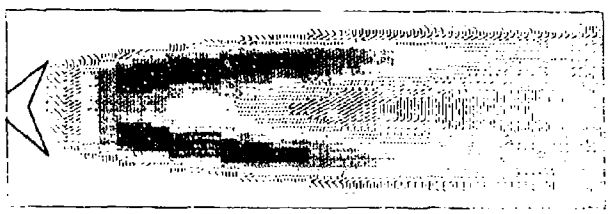

(a)

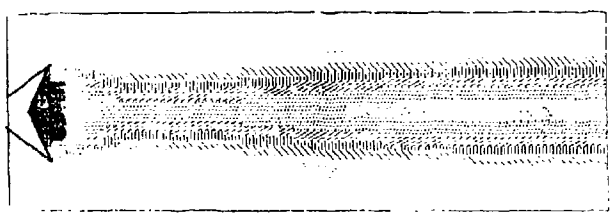

(b)

Figure 9

Figure 9b represents the distribution of the temperature for this calculation (Φ = 0.75, $\dot{m}_a$ = 100 g/s). The temperature in the recirculation zone reaches 2000 K instead of 1700 K in the previous calculation. On the jet axis, the temperature diminishes less rapidly to about 1300 K. It increases in the downstream direction. In this region the temperature varies from about 400 K to 1500 K.

The agreement between calculated and measured mean heat release terms is not perfect but qualitative features and trends are retrieved. In view of these results one may ask if the flamelet description is indeed applicable to the ducted flame configuration considered in this paper.

As indicated in the introduction a precise answer to this question cannot be given but some information may be obtained from an examination of the Barrère-Borghi-Peters phase diagram. This diagram defines the different regimes in premixed turbulent combustion in terms of two dimensionless parameters :

(1) the ratio of the local turbulent length scale to a typical flame thickness ℓ_T / ℓ_l
(2) the ratio of the local velocity fluctuation to the laminar flame speed v'/v_F.

A simplified phase diagram adapted from Peters (1986) is shown in Figure 10. In this plot lines of constant Damkohler number are parallel and make a 45° angle with the horizontal axis. The line Da = 1 separates the region of homogeneous combustion corresponding to well stirred reactors (Da < 1) from the region of corrugated flamelets and distributed reaction zones (Da > 1).

Conditions which exist at each point of the grid representing the combustor in a typical calculation are indicated in the diagram. The domain defined in this way is located below the Da = 1 line and, it therefore belongs to the region of corrugated flamelets and distributed reaction zones. The domain covers regions where the flamelets are well defined and other regions where extinction takes place.

From this discussion it may be concluded that the flamelet model will be applicable if it includes a proper description of flame quenching and subsequent mechanisms. The present model accounts for this aspect at least in some sense but it certainly requires some further refinements.

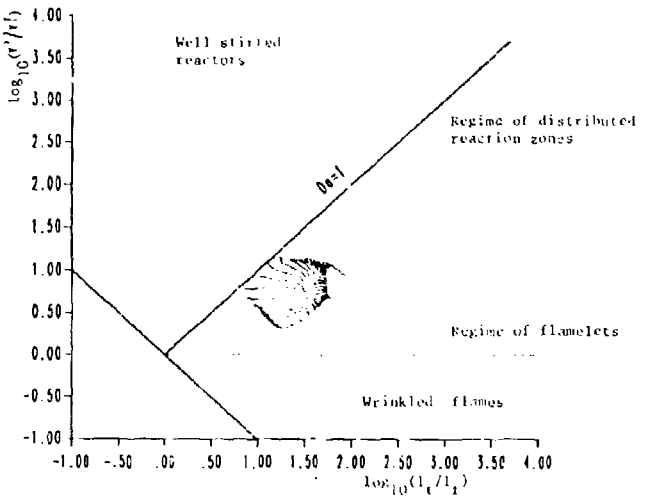

Figure 10

5. CONCLUSION

A description of premixed turbulent ducted flames is proposed on the basis of the coherent flame model. This model initially proposed by Marble and Broadwell for turbulent diffusion flames is extended to the premixed situation.

The balance equation which fixes the amount of flame area per unit volume is derived from basic principles and a consideration of important mechanisms which participate in the production and destruction of flame surface. These mechanisms (flame stretch, extinction, flame shortening) are illustrated by recent experimental observations and numerical calculations. The local flamelet structure of strained premixed flames with complex chemistry is discussed and extinction/ignition properties of these flames are examined.

Numerical calculations based on the coherent flame description are carried for turbulent flames stabilized in a duct. The results are compared with experiments performed on a model combustor. It is shown that the spatial distributions of the mean heat release computed in the model are similar to the distributions of the light intensity emitted by C_2 radical. This indicates that the model, in its present form, already provides a suitable description of turbulent ducted flames. Imperfections are also made evident but the structure of the model allows refinements and improvements at various levels.

ACKNOWLEDGMENTS

This work was supported in part by contracts from SNECMA and DRET. The anonymous views included in the paper were obtained with the help of Frank Bourienne. The authors wish to acknowledge many discussions with François Lacas, Drs Denis Veynante and Thierry Poinsot. We would also like to thank E. Djavdan and F. Maistret for their help in the computation.

References

Borghi, R., and Dutoya, D. (1979). On the scales of the fluctuations in turbulent combustion. 17th Symposium (International) on Combustion, Combustion Institute, 235-244.

Borghi, R. (1979). Models of turbulent combustion for numerical predictions. Prediction Methods for Turbulent Flows. Lecture Series 1979-2, Von Karman Institute, Rhode St Genese, Belgium.

Borghi, R. (1985). On the structure and morphology of turbulent premixed flames. Recent Advances in the Aerospace Sciences. C. Casci, ed. Plenum Press, New York, 117-138 .

Bray, K.N.C. (1980). Turbulent flows with premixed reactants. Turbulent Reacting Flows. Topics in Applied Physics Vol. 44, P.A. Libby and F.A. Williams ed. Springer Verlag, New York.

Bray, K.N.C, Libby, P.A., and Moss, J.B. (1984). Flamelet crossing frequencies and mean reaction rates in

premixed turbulent combusti . Comb. Sci. and Tech. 41, 143-172.

Bray, K.N.C. (1986). Methods of including realistic chemical reaction mechanisms in turbulent combustion models. Second workshop on modelling of chemical reaction systems. Heidelberg, Aug. 1986.

Broadwell, J.E., and Breidenthal, R.E. (1982). A simple model of mixing and chemical reaction in a turbulent shear layer. J. of Fluid Mech. 125, 397-410.

Brown, G.L. and Roshko A. (1974). On density effects and large structure in turbulent mixing layers. J. of Fluid Mech. 64 , 775-816.

Buckmaster, J.D., and Ludford, G.S.S. (1983). The theory of laminar flames. Cambridge University Press, Cambridge.

Candel, S.M., Darabiha, N., and Esposito E. (1982). Models for a turbulent premixed dump combustor. AIAA Paper 82-1261, AIAA, New York.

Carrier G.F., Fendell, F.E., and Marble, F.E. (1975). The effect of strain rate on diffusion flames. SIAM J. of Appl. Math. 28, 463-500.

Clavin, P., and Williams, F.A. (1982). Effects of molecular diffusion and thermal expansion on the structure and dynamics of premixed flames in turbulent flows of large scale and low intensity. J. Fluid Mech. 116, 215

Darabiha, N. (1984). Un modèle de flamme cohérente pour la combustion prémélangée: Analyse d'un foyer turbulent à élargissement brusque. Doctoral Thesis. Ecole Centrale des Arts et Manufactures, Châtenay-Malabry, France.

Darabiha N., Candel, S.M., and Marble, F.E. (1986). The effect of strain rate on a premixed laminar flame. Comb. Flame 64, 203-217.

Darabiha, N., Giovangigli, V., Candel, S.M., and Smooke, M.D. (1987a). Extinction of strained premixed propene-air flames with complex chemistry. Submitted to Comb. Sci. and Tech.

Darabiha, N., Giovangigli, V., Trouvé, A., Candel, S.M. and Esposito, E. (1987b). Coherent flame description of turbulent premixed ducted flames. Presented at the USA-France Workshop on Turbulent Combustion , Rouen, France, July 1987.

Dixon-Lewis, G., David, T., Gaskell, P.H., Fukutani, S., Jinno, H., Miller, J.A., Kee, R.J., Smooke, M.D., Peters, N., Effelsberg, E., Warnatz, J., and Behrendt, F. (1984). Calculation of the structure and extinction limit of a methane-air counterflow diffusion flame in the forward stagnation region of a porous cylinder. Twentieth Symposium (International) on Combustion, The Combustion Institute, Pittsburgh, 1893.

Dupoirieux, F., and Scherrer, D. (1985). Methodes numériques à convergence rapide utilisées pour le calcul des écoulements reactifs. Conference on Simulation of the Combustion Phenomena, INRIA, Sophia Antipolis, France.

Giovangigli, V., and Smooke, M.D. (1985). Calculation of extinction limits for premixed laminar flames in stagnation point flow. Yale Univ. Rep. ME-105-85. Submitted to J. Computat. Phys.

Giovangigli, V., and Candel, S.M. (1986). Extinction limits of premixed catalysed flames in stagnation point flows. Comb. Sci. and Tech..

Giovangigli, V., and Smooke, M.D. (1986). Calculation of critical points in flames. Second workshop on modelling of chemical reaction systems, Heidelberg, Aug. 1986.

Giovangigli, V., and Darabiha, N. (1987). Vector computers and complex chemistry. Presented at SIAM Meeting on Numerical Combustion. San Francisco, March 1987.

Giovangigli, V., and Smooke, M. (1987a). Extinction limits for premixed laminar flames in a stagnation point flow. J. Comp. Phys. 68, 327-345.

Giovangigli, V., and Smooke, M. (1987b). Extinction limits of strained premixed laminar flames with complex chemistry. Comb. Sci. and Tech., in press.

Giovangigli, V., and Smooke, M. (1987c). Adaptive continuation algorithms with application to combustion problems. Submitted to Appl. Numerical Methods.

Jones, W.P. and Whitelaw, J.H. (1982). Calculation methods for reacting turbulent flows: a review. Comb. Flame 48, 1-26.

Karagozian, A., and Marble, F.E. (1986) Study of a diffusion flame in a stretched vortex. Comb. Sci. and Tech. 45, 65.

Kee, R.J., Miller, J.A., and Jefferson, T.H. (1980). CHEMKIN : A general - purpose problem - independent, transportable fortran chemical kinetics code package. SANDIA Rep SAND 80-8003, Sandia Lab., Livermore.

Kee, R.J., Warnatz, J., and Miller, J.A. (1983). A fortran computer code package for the evaluation of gas-phase viscosities, conductivities, and diffusion coefficients. SANDIA Nat. Lab. Report, SAND 83-8209.

Klimov, A.M. (1963). Laminar flame in a turbulent flow. Zhurnal Prikladnoi Mekhaniki Tekhnicheskoi 3 , 49-58.

Laca, F., Zikikout, S., and Candel, S. (1987). A comparaison between calculated and experimental mean source terms in non premixed turbulent combustion. AIAA 87-1782.

Laverdant, A., and Candel, S.M. (1987). Numerical calculations of a diffusion flame vortex interaction. Submitted to Comb. Sci. and Tech..

Laverdant, A., and Candel, S.M. (1987). Computation of diffusion and premixed flames rolled-up in vortex structures. AIAA Paper 87-1779.

Law, C.K. (1984). Heat and mass transfer in combustion : fundamental concepts and analytical techniques. Progr. in Energy and Comb. Sci. 10, 295-318.

Libby P.A., Sivasegaram, S., and Whitelaw J.H. (1986). Premixed Combustion. Progr in. Energy and Comb. Sci. 12, 393-405.

Libby, P.A., and Williams, F.A. (1980). Fundamental aspects in turbulent reacting flows. Topics in Applied Physics, Vol. 44, P.A. Libby and F.A. Williams ed. Springer Verlag, New York.

Libby, P.A., and Williams, F.A. (1981). Structure of laminar flamelets in premixed turbulent flames. Comb. Flame 44, 287

Libby, P.A., and Williams, F.A. (1983). Strained premixed laminar flames under nonadiabatic conditions. Comb. Sci. and Tech. 31, 1.

Libby, P.A., Linan, A., and Williams, F.A. (1983). Strained premixed laminar flames with nonunity Lewis numbers. Comb. Sci. and Tech. 34, 257-293.

Libby, P.A., and Williams, F.A. (1984). Strained premixed laminar flames with two reaction zones. Comb. Sci. and Tech. 37, 221.

Liew, S.K., Bray, K.N.C., and Moss, J.B. (1984). A stretched laminar flamelet model of turbulent non-premixed combustion. Comb. Flame 56, 199-213.

Linan, A. (1974). The asymptotic structure of counterflow diffusion flames for large activation energies. Acta Astronautica 1, 1007.

Marble, F.E. (1985). Growth of a diffusion flame in the field of a vortex. Advances in Aerospace Science, C. Casci, Ed. Plenum Press, New York, 395-413.

Marble, F.E., and Broadwell, J.E. (1977). The coherent flame model for turbulent chemical reactions. Project Squid Rep. TRW-9-PU.

Marble, F.E., and Broadwell, J.E. (1979). A theoretical analysis of nitric oxide production in a methane-air turbulent diffusion flame. EPA Tech. Rep.

Peters, N. (1984). Laminar diffusion flamelets model in non-premixed turbulent combustion. Progr. in Energy and Comb. Sci. 10, 319-339.

Peters, N. (1986). Laminar flamelet concepts in turbulent combustion. 21st Symposium (International) on Combustion.

Poinsot, T.J., Trouvé A.C., Veynante, D.P., Candel, S.M., and Esposito, E. (1987). Vortex driven acoustically coupled combustion instabilities. J. Fluid Mech. 177, 265-292.

Rogg, B., Behrendt, F., and Warnatz J. (1986). Turbulent non-premixed combustion in partially premixed diffusion flamelets with detailed chemistry. 21st International Symposium on Combustion, Munich, Aug. 3-8, 1986.

Smooke, M.D. (1982). Solution of burner stabilized premixed laminar flames by boundary value methods. J. Computat. Phys. 48, 72.

Smooke, M.D., Puri, I.K., and Seshadri, K. (1986). A comparison between numerical calculations and experimental measurements of the structure of a counterflow diffusion flame burning diluted methane in diluted air. Yale Univ. Rep. ME-101-86.

Spalding, D.B. (1978). The influence of laminar transport and chemical kinetics on the time mean reaction rate in a turbulent flame. Seventeenth Symposium (International) on Combustion. The Combustion Institute, Pittsburgh, 431

Tsuji, H. (1982). Progr. in Energy and Comb. Sci. 8, 93

Veynante, D., Candel, S.M., and Martin, J.P. (1986). Coherent flame modelling of chemical reaction in a turbulent mixing layer. Second workshop on modelling of chemical reaction systems, Heidelberg, Aug. 1986.

Warnatz, J. (1983). The mechanism of high temperature combustion of propane and butane. Comb. Sci. and Tech. 34 177-200.

Warnatz, J. (1985). Private communication.

Williams, F.A. (1975). A review of some theoretical combustions of turbulent flame structure AGARD Conf. Proc. 164, p. II 1.1.

Williams, F.A. (1985). Combustion theory. 2nd ed. Benjamin/Cummings, Menlo Park.

Zukoski, E.E., and Marble F.E. (1955). The role of wake transition in the process of flame stabilization on bluff bodies. Comb. Research and Rev., Butterworths Scientific Publications, London.

Figure captions

Fig. 1 Schematic representation of physical processes described in the coherent flame model.
(a) Production of flame area by the field of strain rates
(b) Mututel annihilation of adjacent flamelets
(c) Strained laminar flamelet model.

Fig. 2 Strained flame geometry

Fig. 3 Heat release rate per unit flame area plotted as a function of the strain rate for different hot stream temperatures. The curves are monotonic when T_b exceeds 1530 K, they take an S-shape below that value. The vertical scale is divided by 10^8 J/m^3/s.

Fig. 4 Reaction zone location plotted as a function of the strain rate for different hot stream temperatures. The curves are monotonic when T_b exceeds 1530 K, they take an S-shape below that value.

Fig. 5 Experimental configuration. A mixture of air and propane is injected through a long duct into a rectangular combustor inlet plane comprises a V-gutter flame-holder placed at the duct center and producing a 50 % blockage.

Fig. 6 Spark schlieren photographs of the wake of the flameholder.
$\dot{m}_a$ = 67.5 g/s, $\dot{m}_F$ = 3.4 g/s, Φ = 0.79, Re_H = 46500
Reaction takes place over a broad spatial domain and the burning structures form a regular pattern and their size grows uniformly.

Fig. 7 Spatial distributions of the light emitted by C_2 radicals. The distributions are plotted on a scale of grey levels. The darkest symbol corresponds to the maximum light emission, the lightest symbol represents the minimum light intensity.
(a) Re_H = 46000, Φ = 0.6, $\dot{m}_a$ = 69 g/s
(b) Re_H = 68000, Φ = 0.75, $\dot{m}_a$ = 100 g/s

Fig. 8 Spatial distributions obtained by numerical calculation of (a) the fuel consumption rate and (b) the temperature for $\dot{m}_a$ = 69 g/s and equivalence ratio of Φ = 0.6. Part 'a' of this figure may be compared to Fig. 7a.

Fig. 9 Spatial distributions obtained by numerical calculation of (a) the fuel consumption rate and (b) the temperature for $\dot{m}_a$ = 100 g/s and equivalence ratio of Φ = 0.75. Part 'a' of this figure may be compared to Fig. 7b.

Fig. 10 Simplified version of the Barrère-Borghi-Peters diagram showing the different regimes of premixed turbulent combustion. Conditions existing at each point of the computational grid are plotted in this diagram.

DISCUSSION

J.B.Moss, UK

The critical strain rate which defines extinction on your "S-curve" is 1/800 seconds. This value is large (more than an order of magnitude) when compared with values emerging in non-premixed flame studies (Peters and Williams, Liew et al, Bilger, for example). Why are your values so much larger and is this expected in premixed flames to such a degree? How relevant are the modelled turbulence properties k (turbulence kinetic energy) and E (viscous dissipation rate) to the local strain rate employed in your laminar calculations?

Author's Reply

I would like to thank Prof. Moss for asking these interesting questions.

The magnitude of the critical strain rates corresponding to extinction is strongly dependent on the flame configuration being studied as well as on the operational parameters (field type, equivalence ratio, cold gas temperature, hot gas temperature...). In the present case, the calculations pertain to a counterflow of fresh mixture and hot combustion products. (The temperature of the hot stream is equal or differs from the adiabatic flame temperature.) Such flames are more resistant to stretch than diffusion flames.

Another reason which may be invoked to explain the difference in the critical values obtained by different groups is perhaps less evident. In many studies (Liew et al, Peters, Bilger) the critical values are given for the scalar dissipation X. It is implicitly assumed that this quantity is proportional to the strain rate. The proportionality factor connecting these two quantities is, however, not clear to me. In any event, I am more inclined to consider that the flamelets embedded in the turbulent flow really sense the strain rate associated with the turbulent fluctuations.

The determination of this strain rate is as usual a difficult problem. Our choice has been to determine a *mean strain rate* as a ratio of the rate of dissipation to the turbulent kinetic energy. It is then a good idea to use a pdf to obtain the distribution of strain rates at each local point as suggested by Liew et al, Bray and Peters.

MODELISATION DE LA STABILISATION D'UNE FLAMME TURBULENTE PREMELANGEE, EN AVAL D'UNE MARCHE PAR UNE METHODE LAGRANGIENNE

A. GIOVANNINI
ONERA/CERT/DERMES
BP 4025 31055 TOULOUSE
FRANCE

RESUME

Les calculs sont réalisés, pour la géométrie de la marche descendante, par résolution numérique des équations de Navier Stokes non moyennées, en utilisant une méthode Lagrangienne du type singularités.

La combustion des gaz prémélangés est modélisé en utilisant le concept de flamme mince séparant gaz brûlés et mélange qui sont traités comme deux milieux incompressibles. L'exothermicité de la réaction est représentée à l'aide de sources volumiques placées à proximité du front de flamme. L'avancement de celle-ci est réalisé par advection, et normalement, avec une vitesse de combustion fonction non seulement de l'état thermodynamique du mélange, mais aussi de la courbure locale du front et de son étirement.

Ainsi, l'aérodynamique de la combustion peut-être discutée, sous l'aspect des structures cohérentes, et les vitesses comparées aux expériences de Pitz et Daily avec et sans réaction chimique.

INTRODUCTION

L'aérodynamique des écoulements recirculés est un des problèmes les plus difficiles de la mécanique des fluides. En particulier, les méthodes classiques de fermeture des équations de la turbulence se sont révélées inaptes à la prédiction de ces écoulements. En effet, ceux-ci sont fortement instationnaires et les structures tourbillonnaires présentes interagissent entre elles depuis les plus petites issues de l'instabilité de la couche cisaillée, du type Kelvin-Helmholtz et donc à l'échelle de l'épaisseur de la couche limite amont, jusqu'aux plus grosses de même dimension que la zone recirculée.

Cette difficulté de modélisation est renforcée par l'introduction d'une réaction de combustion à cause de sa "raideur" dans le temps (cinétique chimique rapide) et dans l'espace (fronts minces) ; mais aussi de la forte non linéarité du terme de source d'Arrhénius dans les équations.

Le processus physique correspondant, appelé interaction aérodynamique-combustion, est encore mal connu et doit faire l'objet à la fois d'études théoriques et expérimentales.

Nous avons voulu présenter ici un calcul instationnaire réalisé par une méthode Lagrangienne du type vortex (R.V.M)* couplé à un algorithme de combustion utilisant S.L.I.C et S.L.I.C-V.O.F.**, et comparer les résultats avec les expériences de Pitz et Daily.

1 - CALCUL AERODYNAMIQUE

1.1 Présentation

L'équation la plus générale du vecteur tourbillon $\vec{\zeta}$ obtenue par transformation des équations de Navier Stokes s'écrit :

$$(1) \qquad \frac{D(\vec{\zeta}/\rho)}{Dt} = \frac{\vec{\zeta}}{\rho}.\,\vec{\nabla U} + \frac{\mu}{\rho^2}\,\nabla^2\vec{\zeta} - \frac{\vec{\nabla\rho}\wedge\vec{\nabla\rho}}{\rho^3}$$

advection étirement diffusion source

Dans le cas d'un écoulement plan 2D, incompressible, cette expression se simplifie, sous forme adimensionnelle :

$$(2) \qquad \frac{D\zeta}{Dt} = \frac{\partial\zeta}{\partial t} + \vec{u}\,.\,\nabla\zeta = \frac{1}{Re}\,\nabla^2\zeta$$

Comme le montre la figure 1, la vitesse $\vec{U}$ est décomposé en 2 parties, une potentielle $\vec{U}_p$ et une rotationnelle $\vec{U}_\zeta$ satisfaisant séparément la condition de glissement aux parois, alors que physiquement, la vitesse totale $\vec{U} = \vec{U}p + \vec{U}\zeta$ satisfait à la condition d'adhérence. La composante potentielle U_p est obtenue par transformation conforme (Schwartz-Christoffel) du plan physique, en demi plan supérieur du domaine complexe. Des éléments de vorticité (segments de densité tourbillonnaire constante) sont créés à la paroi, et transformés en tourbillons, induisant un champ de vitesse calculé analytiquement à l'aide de la loi de Biot-Savart filtrée par un noyau de dimension r_o.

La procédure générale utilise le principe de l'éclatement d'opérateurs pour résoudre l'Eq.(2). Les éléments sont déplacés par convection et leur mouvement au hasard, avec un écart type dépendant du nombre de Reynolds, modélise le terme de diffusion.

Pour de plus amples détails, le lecteur est renvoyé aux travaux de A. CHORIN Réf. 1 et 2 .

1.2 Calculs

O.H. HALD [3], J.T. BEALE and A. MAJDA [4], C. MARCHIORO and M. PULVIRENTI [5] ont établi les preuves de convergence de cette méthode par rapport aux équations de Navier Stokes en milieu infini. On ne possède pas de preuve complète en écoulement interne, avec génération de rotationnel et on doit donc mener prudemment les experiences numériques afin de juger de sa crédibilité.

A la suite d'essais numériques et sur les conseils de Y. GAGNON et A. GHONIEM [6], les résultats présentés sont obtenus avec un schéma d'avancement des tourbillons d'ordre 2 en temps (RUNGE-KUTTA), un pas de temps $\Delta t = 0{,}2$, une discrétisation des éléments tourbillonnaires $\Delta l = 0{,}04$ et une taille de noyau $r_o = 0{,}08$. La précision est d'ordre 2 en temps et en espace, et l'éclatement d'opérateur donne un taux de convergence proportionnel à $\frac{\Delta t}{Re}$, intéressant pour les écoulements turbulents.

* R.V.M. : Random Vortex Method
** S.L.I.C.-V.O.F. : Single Line Interface Calculation - Volume of Fluid

I.3 Résultats

Sur la figure n° 2 représentant des champs instantanés de rotationnel et de vitesse, pendant une phase de développement, on note tout d'abord une croissance stable de la recirculation.

Après un temps réduit de 10, on observe une déstabilisation due à 2 effets :

- l'amplification des oscillations de la couche cisaillée qui entraîne la cassure du tourbillon principal (1) en deux parties (1) et (2), la partie (2) étant convectée vers l'aval.
- la respiration du tourbillon contrarotatif (3) dans le coin de la marche qui éjecte le tourbillon principal (1) vers l'écoulement direct et favorise ainsi l'engouffrement de fluide depuis le point de détachement à travers la zone (4) à très basse vitesse.

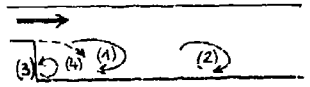

Lorsque le régime est établi, on a présenté figures n° 3 et 4, une séquence de champs instantanés de rotationnel, de vitesses et de lignes de courant mettant en évidence la dynamique des grosses structures. En règle générale, le tourbillon principal grossit, atteint une taille critique et est coupé en deux parties dont l'une s'échappe vers l'aval, induisant des fluctuations importantes du point de recollement ($\simeq$ 3 fois la hauteur de marche). L'échelle de temps de ce phénomène est grande comparée à l'instabilité de couche cisaillée. Mais on ne retrouve pas une périodicité nette pour ce phénomène et les analyses de Foutier pour le signal de vitesse en un point donnent un spectre à bande large, comme remarqué expérimentalement par S.W. PRONDCHIK et S.J. KLINE (7).

Sont ensuite présentées, figure n° 5, les vitesses moyennes, avec comparaison aux mesures de R. PITZ et J. DAILY (8) et les lignes de courant moyennes. Toutes ces grandeurs et en particulier la vitesse de retour maximum ainsi que l'extension de la zone recirculée sont en bon accord.

II - CALCUL DE COMBUSTION

II.1 Introduction

La plupart des flammes d'intérêt industriel brûlant dans des conditions d'écoulement turbulent et souvent ce processus est stabilisé par une zone de recirculation induisant des vitesses plus faibles. Par rapport à la classification des flammes de prémélange, on se place dans la zone où les échelles intégrales de la turbulence ℓ_T sont plus grandes que l'épaisseur de la flamme e_T. De plus, la vitesse de combustion laminaire U_L étant plus petite que l'énergie cinétique turbulente $k^{1/2}$, on est dans le régime de flammes plissées avec formation de poches (figure n° 6).

En général, la turbulence fait croître le taux de combustion dVb/dt par augmentation de la surface de contact entre gaz frais et brûlés, mais aussi par l'étirement local des particules fluide qui favorise l'échange turbulent. On introduit alors une pseudo-vitesse de combustion turbulente U_T différente de U_L par le rapport de la surface de contact A_f à la surface moyenne $\bar{A}$.

$$(3) \qquad \frac{U_T}{U_L} = \frac{A_f}{\bar{A}}$$

Dans la littérature, si l'on reprend figure n° 7, les corrélations proposées pour cette quantité, on observe que ces valeurs sont > 1 et on note une forte dispersion des courbes dues aux échelles de la turbulence et aux nombres de Reynolds turbulents considérés.

Les calculs numériques relatifs à la combustion dans ce régime d'écoulement turbulent sont délicats. Les difficultés viennent :

- du modèle de turbulence proprement dit s'il est monoéchelle,
- du modèle de combustion turbulence, la loi d'Arrhénius étant fortement non linéaire et faisant intervenir les fluctuations d'espèces chimiques et de température,
- de la présence de larges gradients de vitesse et de masse volumique rendant l'utilisation de grilles Eulériennes difficiles et induisant soit des instabilités, soit de la diffusion numérique à moins que l'on n'utilise des maillages plus resserrés, des corrections de flux ou des grilles adaptatives.

II.2 Modèle physique

Le modèle utilisé est basé sur l'algorithme SLIC et les principales hypothèses sont les suivantes :

- le milieu est supposé composé de 2 milieux incompressibles : le mélange (u) et les gaz brûlés (b) séparés par un front de flamme mince convecté par l'écoulement et se propageant avec une vitesse normale U_N.
- les gaz frais traversant la flamme subissent une dilatation à cause de l'exothermicité de la réaction et un terme de source volumique apparaît dans l'équation de continuité correspondant au passage d'une masse fixée Δm de fluide de la masse volumique ρ_u à ρ_b.
- la cinétique chimique est infiniment plus rapide que tous les temps caractéristiques de l'écoulement.
- les effets de compressibilité sont négligés : les ondes acoustiques se propageant infiniment vite et l'interaction des gradients tangentiel de pression et normal de masse volumique n'étant pas prise en compte. La modélisation de ce terme (Eq. 1) en milieu infini a été faite par M. PINDERA (8), mais son ordre de grandeur dans notre cas est difficile à apprécier.

a) suivi de l'interface

Le suivi d'un front Lagrangien est difficile à cause des discontinuités, pointes et repliements que l'on rencontre lorsqu'une interface est étirée ou lorsque deux interfaces se coupent.

La méthode appliquée ici s'inspire de travaux bien connus comme SLIC et SLIC-VOF dus à W. NOH and P. WOODWARD (9), A. CHORIN (10), C.W. HIRT and B.D. NICHOLS (11), A. GHONIEM (12). Le domaine physique est divisé en cellules carrées de coté h_c et la position (forme du front de flamme) est reconnue pour chaque

cellule (i,j) en considérant les fractions brûlées $f_{i,j}$ des cellules voisines (figure n° 8).

d) dynamique de l'interface

La position du front de flamme $\overline{r}_f$ est régie par l'équation de propagation :

$$(4) \quad \frac{d\overline{r}_f}{dt} = \overline{u} + U_N \cdot \overline{u}_f$$

et les deux opérateurs, advection et combustion sont donc successivement appliqués :

- advection

pour une cellule i,j, le bilan pour la fraction brûlée $f_{i,j}$ s'écrit :

$$(5) \quad h_c^2 \frac{d}{dt}(f_{i,j}) + (u_f\, h_c)_{i-1/2,j}^{i+1/2,j} + (v_f\, h_c)_{i,j-1/2}^{i,j+1/2} = 0$$

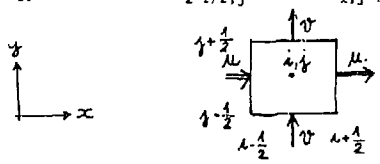

Pendant chaque pas de temps de combustion Δt_c, les deux derniers termes qui représentent le flux à travers les faces de la cellule, sont évalués par le calcul des vitesses u et v sur une grille décalée.

L'interface est déplacée en 2 pas fractionnaires suivant x et y et une reconnaissance de forme est opérée.

- combustion

La flamme se déplace et du gaz frais est consommé à une vitesse normale U_N. Pour les écoulements instationnaires, P. CLAVIN et G. JOULIN [13] ont montré qu'une quantité scalaire unique, l'étirement total, contrôle la propagation. Cet étirement est composé de 2 parties : une représentant l'effet de la géométrie du front de flamme (courbure R) et l'autre, la non uniformité de l'écoulement au voisinage de la flamme (tenseur du taux de contrainte).

La loi correspondante proposée s'écrit :

$$(6) \quad \frac{U_N}{U_L} = 1 + \frac{\mathcal{L}}{U_L}\left(\frac{U_L}{R} - \frac{1}{\sigma}\frac{d\sigma}{dt}\right)$$

La courbure R est évaluée comme dans la référence [11] (SOLA-VOF), au noeud le plus près du front côté gaz frais, d'après les valeurs de la fraction brûlée dans les 8 cellules voisines. L'étirement local $1/\sigma\ d\sigma/dt$ qui se réduit en 2D à $dU_\sigma/d\sigma$ (U_σ étant la vitesse tangente au front σ), se calcule toujours du côté gaz frais, par interpolation des vitesses.

c) exothermicité

Les particules fluides sont accélérées lorsqu'elles traversent le front de flamme, avec un rapport d'expansion ρ_u/ρ_b. Cet effet est modélisé en plaçant des sources volumiques caractérisées par un vitesse $U_s = U_N/2\ (\rho_u/\rho_b - 1)$ dont l'intensité $\Delta_{i,j}$ est facilement reliée à la variation de fraction brûlée pendant Δt_c.

$$(7) \quad \Delta_{i,j} = \frac{h_c^2}{2}\left(\frac{\rho_u}{\rho_b} - 1\right)\frac{\Delta f_{i,j}\ \text{brûlée}}{\Delta t_c}$$

Les sources sont discrétisées et placées juste derrière le front de flamme du côté des gaz brûlés. Sur la figure n°1, une troisième contribution à la vitesse U_ϕ apparaît et est évaluée par un traitement analogue aux tourbillons $\overline{U}_\xi$.

II.3. Calculs

Les calculs suivants ont été réalisés dans le cas d'un prémélange pauvre de propane et d'air, de richesse 0,57 correspondant à un rapport d'expansion de 5 et une vitesse de combustion laminaire réduite $U_L/U_\infty = 0{,}015$. La longueur de Markstein $\mathcal{L}$ intervenant dans (Eq. 6) a été prise égale à 0,005. Le pas de temps de combustion $\Delta t_c = 0{,}025$, la taille des cellules carrées $h_c = 0.05$ et les conditions initiales sont un écoulement aérodynamique établi et une fraction brûlée $f_{i,j} = 1$ dans la zone recirculée $y \leq h$.

II.4. Résultats

La figure n° 9 compare l'évolution dans le temps du taux de combustion relatif au débit amont en phase d'établissement, ceci pour une loi de propagation constante $U_N = U_L$ et la loi variable de l'équation 6. Cette comparaison est complétée par la figure n° 10 représentant une séquence des champs de vitesse et de position de flamme. On constate que le taux de combustion est plus élevé et en conséquence, la flamme plus plissée pour la loi de Clavin et Joulin dont la forme semble plus réaliste si l'on se réfère aux visualisations par ombroscopie correspondantes de A. GANJI et R. SWAYER [14]. Après établissement du processus de combustion, on a représenté figure n° 11, une comparaison des champs de vitesse instantanés avec et sans combustion. On remarque donc une flamme fortement plissée avec création de poches de produits frais par l'écoulement rotationnel, poches qui se consument ensuite assez rapidement. Pour ce cas, nous trouvons un rapport $U_1/U_L = 2{,}9$ qui semble en accord avec les résultats de P. CLAVIN et F. WILLIAMS [15], avec une préturbulence au niveau de la position moyenne de la flamme de 9 %. Près de la sortie, les vitesses sont plus grandes et il en résulte un gradient de pression adverse dans la zone de recollement plus petit que dans le cas non réactif.

Ainsi, comme le montrent les expériences de D.M. KHUEN [16], dont les résultats sont présentés figure n° 12, l'effet d'exothermicité, imposant un gradient de pression adverse moins important, réduit la longueur de recirculation. Cette réduction est évaluée d'après nos résultats à 2 fois la hauteur de la marche.

De plus, si l'on rassemble les résultats de la littérature (figure n° 13) sur l'évolution de la longueur de recollement xR/h en fonction du nombre de Reynolds basé sur la hauteur de marche et si l'on porte les résultats de R. PITZ et J. DAILY en combustion, avec une viscosité évaluée à la température moyenne de la couche cisaillée, on obtient un glissement sur l'axe des abscisses, se traduisant par une diminution de R_e dans le rapport $(\overrightarrow{\rho u/\rho b})^{1,5}=4$. On se trouve donc, pour ces nombres de Reynolds entre 10^3 et 10^4, dans une zone où les longueurs recirculées sont aussi plus faibles. On peut donc aussi penser que le comportement initial de la couche cisaillée et sa croissance jouent un rôle important.

Finalement, nous avons comparé figure n° 14, les champs de vitesse moyennés sur 60 pas de temps successifs avec les expériences de PITZ et DAILY. Nous obtenons une réduction de la longueur recirculée de xR/h = 7,15 à 4,7 et une augmentation correspondante du débit volume recirculé Q_R/Q_0 obtenu par intégration des vitesses dans la recirculation de 13,5 % à 17,5 % mettant en évidence des vitesses plus fortes en combustion au droit de la marche.

III- CONCLUSION

L'effet des grosses structures tourbillonnaires sur le front de flamme, son plissement et la création de poches de gaz frais peuvent être étudiés de manière fondamentale par ce type de méthode instationnaire et Lagrangienne, couplée à un algorithme de reconnaissance de forme très performant. Il semble que la loi de propagation variable de P. CLAVIN et G. JOULIN donne de meilleurs résultats concernant la longueur et la position de la flamme, les vitesses et l'extension de la zone recirculée.

Pour l'avenir, des comparaisons plus détaillées doivent être menées, en utilisant plus de pas de temps de calcul pour les statistiques turbulentes et en mettant en oeuvre expérimentalement des écoulements bidimensionnels et des visualisations instantanées de front de flamme.

Cette étude a été partiellement financée par la DRET (Direction des Recherches et Etudes Techniques du Ministère des Armées), par la Convention d'Etudes n° 86 002.

REFERENCES

1. A.J. CHORIN
Numerical study of slightly viscous flow
J.F.M. 1973 Vol. 57 pp 785-796

2. A.J. CHORIN
Vortex sheet approximation of boundary layer
J. Comp. Phys. 1978 Vol. 27 pp 428-442

3. O.H. HALD
The convergence of vortex methods part II
S.I.A.M. J. Num. Anal. 1979 Vol. 16 pp 726-755

4. J.T. BEALE and A. MAJDA
Rates of convergence for viscous splitting of N.S. equations
Math. of Comp. 1981 Vol. 37 pp 243-260

5. C. MARCHIORO and M. PULVIRENTI
Hydrodynamics in 2D and vortex theory
Com. Math. Phys. 1982 Vol. 84 pp 483-503

6. A. GHONIEM and Y. CAGNON
Numerical investigations of recirculating flow at moderate Reynolds Numbers
AIAA paper 1986 n° 86-0370

7. S.W. PRONDCHIK and S.J. KLINE
An experimental investigation of the structure of a turbulent reattaching flow behind a backward facing step
Stanford University Report 1983 MD 42

8. M. PINDERA
On the aerodynamics of flames
Ph. D. Thesis University of California Berkeley

9. C.W. NOH and P. WOODWARD
SLIC Single Line Interface Calculations
5th International Conference on Numerical Methods in Fluid Dynamics 1976 pp 330-339

10. A. CHORIN
Flame advection and propagation algorithm
J. Comp. Phys. 1980 Vol. 35 pp 1-11

11. C.W. HIRT and B.D. NICHOLS
Volum of Fluid (VOF) method for the dynamic of free boundaries
J. Comp. Phy. Vol. 39 pp 201-225

12. A. GHONIEM
Effect of large scale structures on turbulent flame propagation
Combustion and Flame,June 1986 Vol. 64 pp 321-336

13. P. CLAVIN et G. JOULIN
Premixed flames in large scale and high intensity turbulent flow
Le journal de Physique-Lettres 1983 Tome 44 n° 1 pp 1-11

14. A. CANJI and R. SWAYER
An experimental study of the flow field of a 2D premixed turbulent flame
AIAA J. July 1980 Vol. 18 n° 7 pp 817-824

15. P. CLAVIN and F.A. WILLIAMS
J.F.M. 1982 Vol. 116 pp 251-282

16. P.N. KHUEN
AIAA Journal March 1980 Vol. 18 n° 3

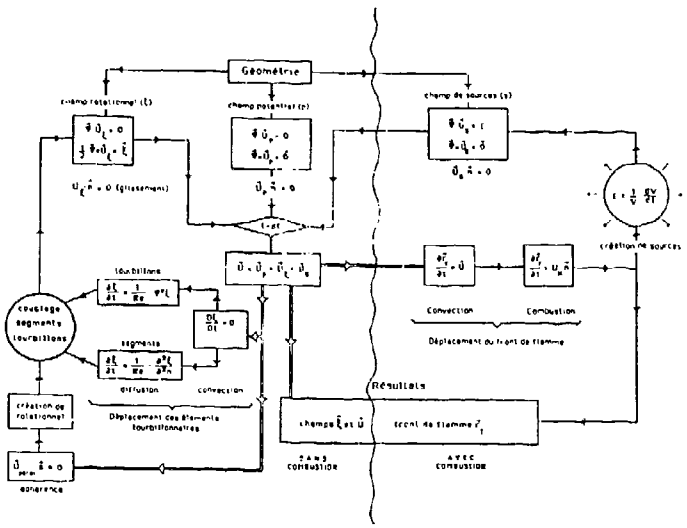

FIGURE 1 : ORGANIGRAMME DE CALCUL

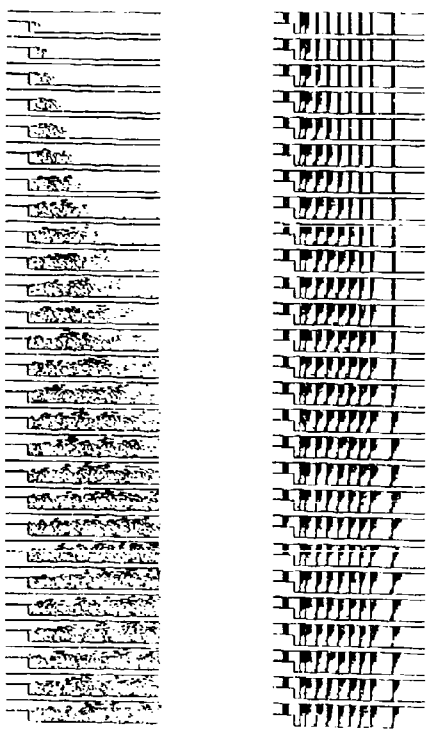

FIGURE 2 :

DEVELOPPEMENT DE L'ECOULEMENT :
CHAMPS DE ROTATIONNEL ET DE VITESSE

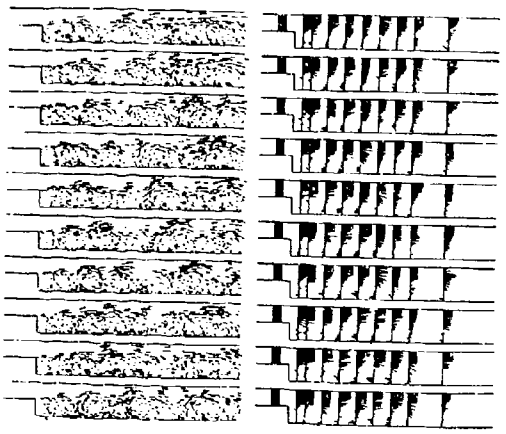

FIGURE 3 : ECOULEMENT ETABLI :
SEQUENCE DE CHAMPS ROTATIONNEL ET DE VITESSE

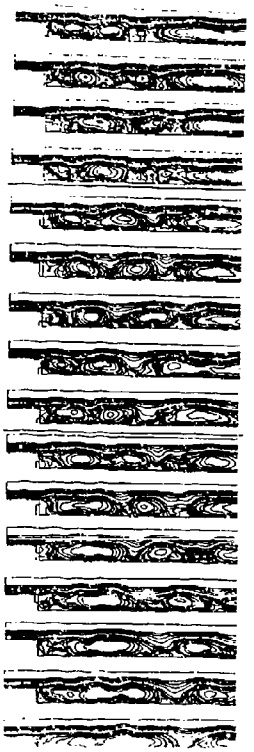

FIGURE 4 :
ECOULEMENT ETABLI :
SEQUENCE DE LIGNES DE
COURANT

FIGURE 5 : GRANDEURS MOYENNES
VITESSES
LIGNES DE COURANT
COMPARAISON AVC L'EXPERIENCE

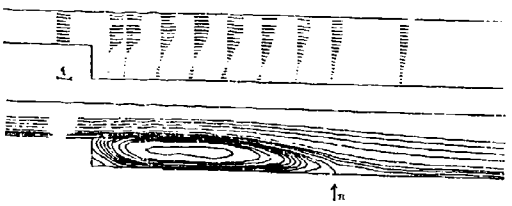

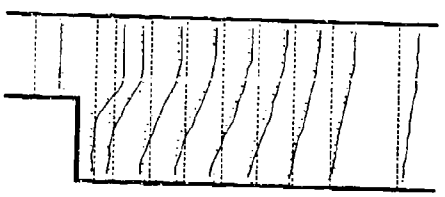

calcul RVM
experience Pitz & Daily

CHEMICAL CHARACTERISTICS

u_L : laminar normal burning velocity of the fresh mixture
e_L : laminar flame thickness
$\tau_C = \frac{e_L}{u_L}$ characteristic time of the laminar flame

TURBULENCE CHARACTERISTICS

k : turbulent kinetic energy
l_t : integral length scale
$\tau_t = \frac{l_t}{u'}$ characteristic turbulent time
$\tau_K = \left(\frac{\nu}{\varepsilon}\right)^{1/2}$ Kolmogorov time
η : Kolmogorov microscale
R_{T_P} : critical Reynolds number for pockets formation

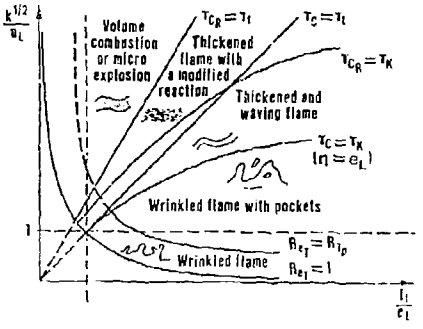

FIGURE 6 : CLASSIFICATION DES FLAMMES TURBULENTES DE PREMELANGE
D'APRES M. BARRERE ET R. BORGHI

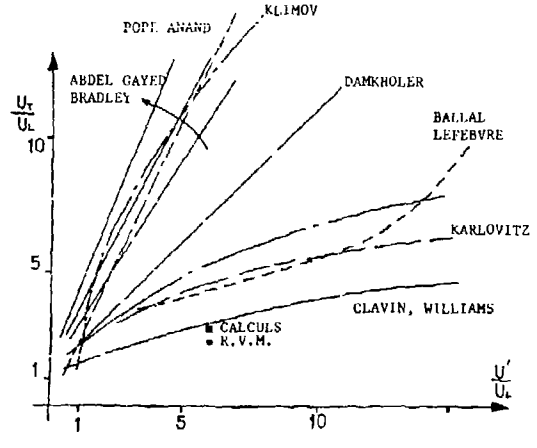

FIGURE 7 : VITESSE DE COMBUSTION TURBULENTE : CORRELATIONS DE LA LITTERATURE

FIGURE 9 : EVOLUTION DU DEBIT VOLUME BRULE AU COURS DU CALCUL :
LOIS D'AVANCEMENT CONSTANTE ET VARIABLE

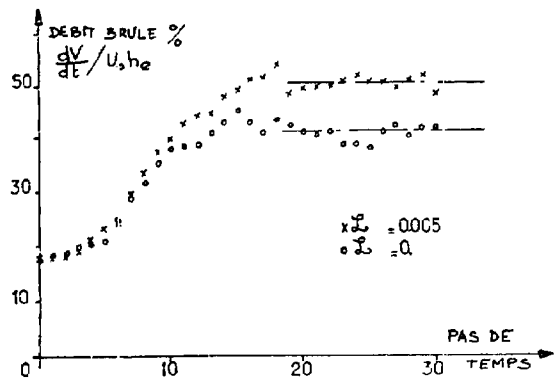

FIGURE 10 : CHAMPS DE VITESSE ET FRONT DE FLAMME

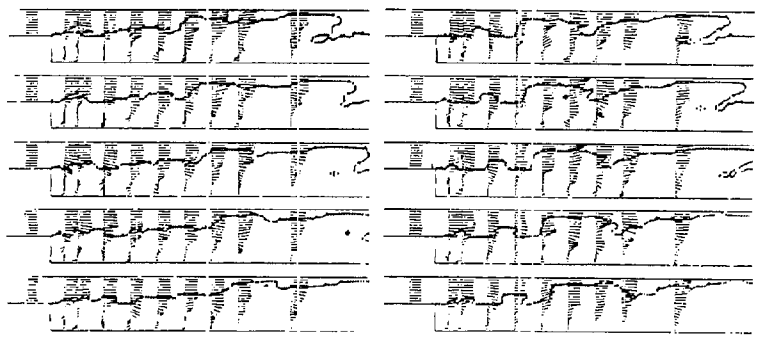

LOI D'AVANCEMENT CONSTANTE LOI D'AVANCEMENT VARIABLE

FIGURE 8 : RECONNAISSANCE DE LA POSITION DE L'INTERFACE

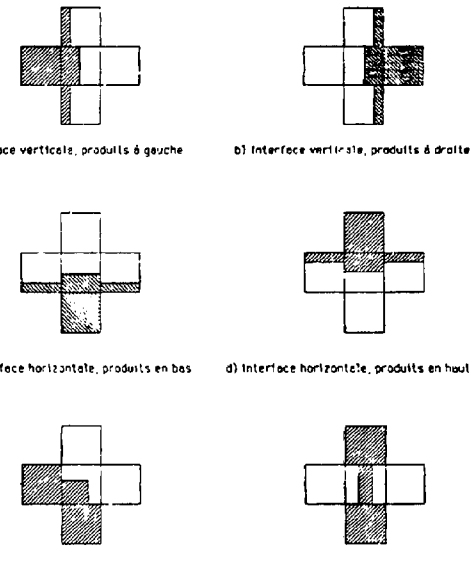

a) interface verticale, produits à gauche

b) interface verticale, produits à droite

c) interface horizontale, produits en bas

d) interface horizontale, produits en haut

e) coin rectangulaire

f) bande

FIGURE 11 : CHAMPS DE VITESSE ET FRONTS DE FLAMME

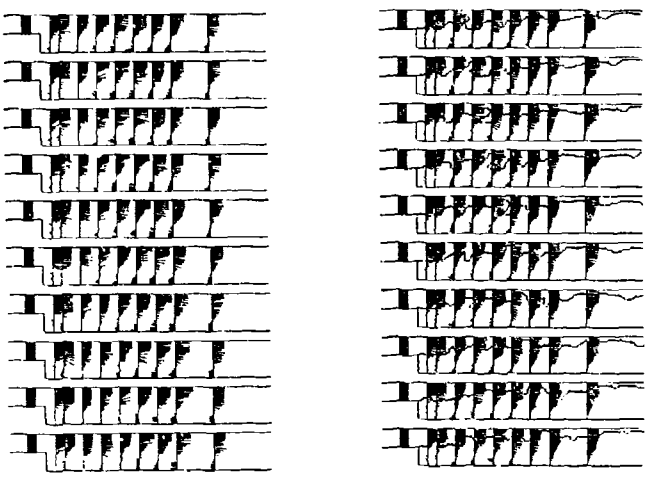

SANS COMBUSTION AVEC COMBUSTION

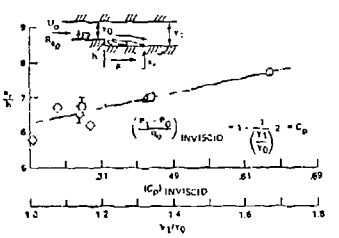

Fig. 1 Effect of adverse pressure gradient on reattachment distance for parallel-walled channels

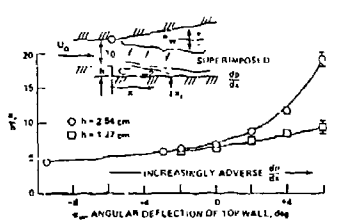

Fig. 3 Reattachment location where a pressure gradient is superimposed on the flow over a rearward-facing step; $U_0 = 45$ m/s.

FIGURE 12 : INFLUENCE DU GRADIENT DE PRESSION EXTERNE DE RECOLLEMENT

D'APRES D.M. KHUEN (AIAA Journ. Vol 18 N° 3 Mars 80)

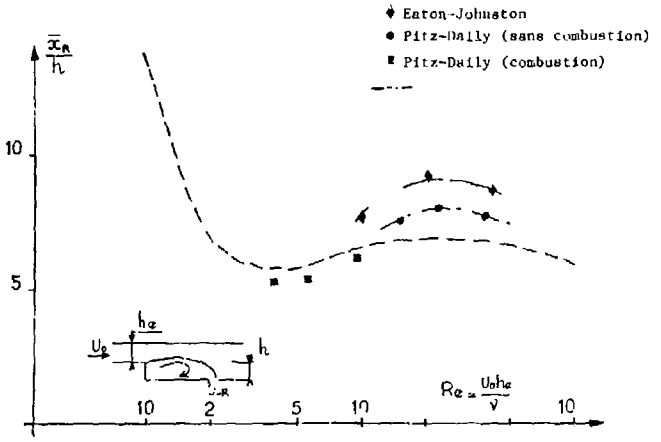

FIGURE 13 : LONGUEURS DE RECIRCULATION

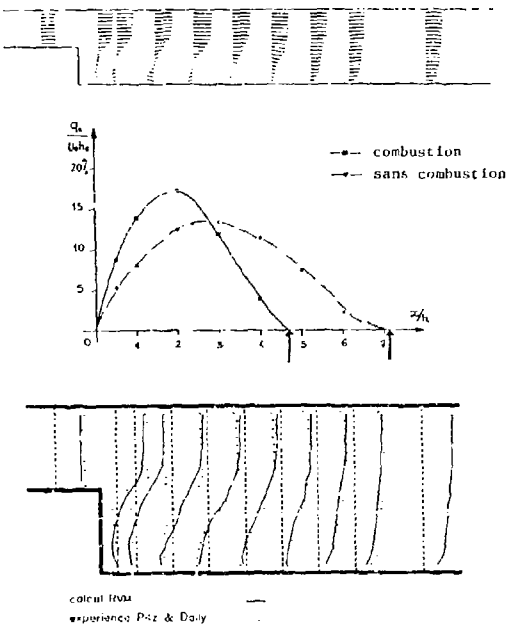

FIGURE 14 : GRANDEURS MOYENNES : AVEC COMBUSTION : CHAMPS DE VITESSE
DEBIT RECIRCULE
COMPARAISON AVEC L'EXPERIENCE

NUMERICAL MODELLING OF PREMIXED FLAMES IN GASEOUS MEDIA

B. LARROUTUROU

INRIA
Sophia-Antipolis
06560 VALBONNE
FRANCE

ABSTRACT: We present numerical methods and numerical results for the propagation of premixed flame fronts in a two-dimensional gaseous flow. The study is restricted to simple rectangular geometries, and considers both open and closed vessels. The methods use essentially finite-element approximations and adaptive gridding procedures. The results include curved flame propagation, cellular front instabilities and quenching phenomena due to non adiabatic walls.

1. INTRODUCTION

The purpose of this paper is to present some recent developments in the field of the numerical investigation of gaseous combustion phenomena. Most of the calculations reported below concern two-dimensional premixed flame propagation problems, and use *adaptive gridding* techniques in order to reduce the computational cost while resolving accurately the small length scales within the flame thickness.

The advantages of an adaptive moving grid for an accurate and low-cost solution of flame propagation problems are now well established. Since the combustion and diffusion inside the thin reaction and preheat zones within the flame thickness determine the flame speed, the temperature and the species mass fractions must be computed accurately in these regions; on the other hand, these variables are almost constant in wide regions apart from the flame, and efficiency dictates to use a coarse computational mesh there. A non uniform adaptive grid whose dense region follows the propagating flame is therefore necessary for an accurate and low-cost simulation of the phenomenon.

We briefly present in this paper some one- and two-dimensional adaptive mesh methods specifically designed to improve the solution of stiff (multi-scale) combustion problems, and illustrate them by showing several numerical results. These results include the cellular instabilities of a flame front, and the extinction of premixed flames propagating in a channel with non adiabatic walls; these two phenomena are studied in the framework of the simplified thermo-diffusive model. We also present some more realistic results showing a flame propagating in a compressible low Mach number compressible flow.

2. ONE-DIMENSIONAL MOVING GRID METHODS

We begin by presenting some adaptive procedures for the simulation of an unsteady planar premixed flame propagating in an infinite tube. More precisely, assuming for simplicity that a single one-step chemical reaction $A \rightarrow B$ takes place in the gas (but the methods remain efficient when more complex chemical effects are taken into account; see [16]), we solve the following system of normalized Lagrangian equations:

$$\begin{cases} T_t - T_{xx} = \Omega(T,Y) \ , \\ Y_t - \frac{1}{Le} Y_{xx} = -\Omega(T,Y) \ , \end{cases} \tag{2.1}$$

where T is the gas temperature, Y the reactant mass fraction, Le its Lewis number (see [17]). The normalized reaction rate Ω is given by:

$$\Omega(T,Y) = \frac{\beta^2}{2Le} Y \ exp[\frac{-\beta(1-T)}{1-\alpha(1-T)}], \tag{2.2}$$

β being the reduced activation energy of the reaction (also called the Zeldovich number), and α being a positive heat release parameter. The boundary conditions associated to equations (2.1) are classical:

$$\begin{cases} T \rightarrow 0, \ Y \rightarrow 1 \ \text{ as } x \rightarrow -\infty \ \text{ (fresh mixture)}, \\ T \rightarrow 1, \ Y \rightarrow 0 \ \text{ as } x \rightarrow +\infty \ \text{ (hot gases)}. \end{cases} \tag{2.3}$$

2.1 In several previous studies of problem (2.1)-(2.2), we have used a mesh whose nodes move at each time t with the same velocity $V(t)$. In other words, the grid is traveling as a rigid body in order to follow the propagating flame. The grid velocity $V(t)$ can simply be taken equal to the instantaneous average flame speed, given by:

$$V(t) = -\int_{x_0}^{x_N} \Omega(T,Y)(x,t) \ dx \ , \tag{2.4}$$

where $[x_0, x_N]$ is the computational domain (see [13], [14]). A better choice is to evaluate the grid velocity according to some physical conservation principle (see [15]): more precisely, we choose the nodes velocity $V(t)$ such that the thermal energy contained in the computational domain remains exactly constant (up to round-off errors) during the calculation: $\int_{x_0}^{x_N} T = Constant$. We then get, instead of (2.4):

$$V(t) = \frac{-\int_{x_0}^{x_N} \Omega(T,Y)(x,t)dx + T_x(x_0) - T_x(x_N)}{T(x_N) - T(x_0)} \ . \tag{2.5}$$

This method revealed to be very efficient and gave very satisfactory results for several one-dimensional problems (see [13], [14], [15], [16]).

2.2 More recently, we have applied to a simple one-dimensional flame propagation problem some of the adaptive moving grid methods developed by J. M. Hyman and the author (see [11]). In these more sophisticated methods, each of the computational nodes moves at each time step with its own velocity. One way to compute the nodes velocities is to use a "mesh function" w, which reflects the local goodness of the mesh (i.e. the accuracy of the spatial approximation and the local mesh regularity). Such a

mesh function is often used in time-dependent calculations, to change the grid at some time levels and generate a new adapted mesh by equidistributing w: the adapted mesh (X_i) satisfies:

$$W_{i+1/2} = \int_{X_i}^{X_{i+1}} w \;=\; Constant \;\text{ for all } i\;, \tag{2.6}$$

(see [14] and the references therein). The mesh function w can also be used to evaluate the nodes velocities and dynamically adapt the grid: for instance, the mesh points velocities can be determined at each time step by solving the tridiagonal system (see [11], [12]):

$$W_{i+1/2}\frac{\Delta \dot{X}_{i+1/2}}{\Delta X_{i+1/2}} - W_{i-1/2}\frac{\Delta \dot{X}_{i-1/2}}{\Delta X_{i-1/2}} = -\frac{1}{\tau}(W_{i+1/2} - W_{i-1/2})\;, \tag{2.7}$$

where $\Delta \dot{X}_{i+1/2} = \dot{X}_{i+1} - \dot{X}_i$ and where $\tau > 0$ is a grid relaxation time.

Figures 1 and 2 show the results of a calculation using 30 mesh points and solving (2.1)-(2.2) for $Le = 1$, $\beta = 10$ and $\alpha = 0.8$. At time $t = 0$, the 30 nodes are uniformly spaced in a domain of length $x_N(0) - x_0(0) = 20$; then, they move according to equation (2.7). Figure 1 shows the trajectories of the mesh points, and figure 2 shows the (steady-state) temperature and reaction rate profiles and the nodes distribution at the end of the computation. This promising method is currently extended to two-dimensional problems.

3. NON ADIABATIC CURVED FLAMES

In collaboration with F. Benkhaldoun and B. Denet, we have investigated the propagation of a premixed flame in a rectangular channel with non adiabatic walls, in the framework of the well-known thermo-diffusive model, which has been used for a long time by the physicists to study flame propagation phenomena in which the gas flow does not play a primary role (see [1], [18], [19]). More precisely, considering a tube of width L, we solve the normalized reaction-diffusion equations:

$$\begin{cases} T_t = \Delta T + \Omega(T,Y)\;, \\ Y_t = \frac{1}{Le}\Delta Y \;-\; \Omega(T,Y)\;, \end{cases} \tag{3.1}$$

in a rectangle $[a,b]\times[0,L]$. Equations (3.1) are associated with the following boundary conditions:

$$\begin{cases} T(a,y,t) \;=\; 0\;,\;\; Y(a,y,t) \;=\; 1 \;\text{ (fresh gases)}\;, \\ T_x(b,y,t) \;=\; 0\;,\;\; Y_x(b,y,t) \;=\; 0 \;\text{ (burnt gases)}\;, \end{cases} \tag{3.2}$$

and:

$$\frac{\partial Y}{\partial n} = 0\;, \frac{\partial T}{\partial n} = -K.T\;, \tag{3.3}$$

on the walls $y = 0$ and $y = L$. The last condition represents a thin poorly conducting wall whose outer surface is maintained at the fresh mixture temperature $T_f = 0$; n is the outer unit normal on the channel wall, and K is a normalized heat loss parameter.

As expected from a physical point of view, we observe that the time-dependent flame eventually extinguishes if the heat loss coefficient K is large enough, say $K > K_{lim}$. On the other hand, when $K \leq K_{lim}$, the solution converges to a steady non adiabatic curved flame (see figure 3). Moreover, it appears from our numerical experiments that the extinction value K_{lim} of the heat loss parameter varies as the inverse of the reduced activation energy β of the reaction; the same result was found analytically in a one-dimensional setting (see [7]), but there exists no similar analysis of flame quenching in a multi-dimensional context.

These two-dimensional calculations use a finite-element approximation on an adaptive moving grid. The grid moves at each time step as a rigid body, as explained in Section 2.1. Moreover, at some time levels during the computation, the grid is changed to a better adapted mesh. In order to realize this "static adaption" in a simple way, we use a computational mesh which is divided into horizontal straight lines, and employ the one-dimensional equidistributing procedure (2.6) on each of these lines (see [2], [4] for the details). The adaptive mesh corresponding to the steady curved flame of figure 3 is shown on figure 4.

4. THERMO-DIFFUSIVE CELLULAR INSTABILITIES

We now consider the adiabatic thermo-diffusive model (with $K = 0$ in (3.3)). It is known from the asymptotic analyses for large activation energies that the planar flame is unstable to two-dimensional perturbations for some values of the Lewis number and of the reduced activation energy, and that cellular instabilities then appear (see [18], [19]). In fact, solving this problem is not an easy computational task, because these instabilities occur on a time scale which is much larger than the flame transit time (defined as the ratio of the asymptotic flame thickness to the asymptotic flame speed), and they appear only if the channel width is sufficiently large compared to the flame thickness. The numerical study of this phenomenon therefore requires an efficient (vectorized) adaptive computer code.

We have computed these instabilities using a semi-implicit version of the finite-element technique briefly described in the previous section, in collaboration with F. Benkhaldoun (see [5]). We also have investigated the same problem in collaboration with H. Guillard and N. Maman using a pseudo-spectral approximation (see [9]). In this latter case, we use an expansion in Fourier series in the y-direction, associated to an adaptive finite-difference formulation in the x-direction (the Neumann conditions (3.3) at the walls are then replaced by a periodicity assumption). This pseudo-spectral method (which might of course be less easy to employ and less efficient in the case of a more complex geometry) uses highly vectorized fast Fourier transforms routines, and reveales to be very accurate and efficient for the problem under consideration.

The typical evolution of the isotherms is shown in figure 5 for $Le = 0.7$ and $\beta = 10$; the last view corresponds to the steady state.

5. TWO-DIMENSIONAL COMPRESSIBLE REACTING FLOWS

We now end this paper by considering more realistic systems of governing equations describing two-dimensional premixed flames.

We still assume that the mixture is made up of only two species A and B, and that the single irreversible one-step reaction $A \longrightarrow B$ takes place in the gas. For the sake of simplicity we also neglect the viscous and external forces effects. We will then consider the following system of equations (see [6], [20]):

$$\begin{cases} \rho_t + \vec{\nabla}.(\rho\vec{V}) = 0 \ , \\ (\rho u)_t + \vec{\nabla}.(\rho u\vec{V}) + p_x = 0 \ , \\ (\rho v)_t + \vec{\nabla}.(\rho v\vec{V}) + p_y = 0 \ , \\ \rho c_p T_t + \rho c_p \vec{V}.\vec{\nabla}T = \vec{\nabla}.(\lambda\vec{\nabla}T) + p_t + \vec{V}.\vec{\nabla}p + Q\omega(T,Y) \ , \\ \rho Y_t + \rho\vec{V}.\vec{\nabla}Y = \vec{\nabla}.(\rho D\vec{\nabla}Y) - m\omega(T,Y) \ , \\ mp = \rho RT \ . \end{cases} \tag{5.1}$$

In this system, ρ is the mixture density, u and v are the components of the velocity $\vec{V}$, p is the pressure; T is the temperature, c_p is the constant pressure specific heat of the mixture, λ the thermal conductivity, Q the heat released by the chemical reaction and ω is the (dimensionalized) rate at which this reaction proceeds. Moreover, Y is the mass fraction of the reactant A, D is its molecular diffusion coefficient, and m is the molecular mass of the reactant.

5.1 In order to numerically investigate the solutions of this system, we use a slightly different formulation. We introduce the variable E as the sum of the internal and kinetic energy ($E = \rho c_v T + \frac{1}{2}\rho(u^2+v^2)$, c_v being the constant volume specific heat), and rewrite equations (5.1) in conservative form as:

$$\begin{cases} \rho_t + (\rho u)_x + (\rho v)_y = 0 \ , \\ (\rho u)_t + (\rho u^2 + p)_x + (\rho uv)_y = 0 \ , \\ (\rho v)_t + (\rho uv)_x + (\rho v^2 + p)_y = 0 \ , \\ E_t + [u(E+p)]_x + [v(E+p)]_y = \vec{\nabla}.(\lambda\vec{\nabla}T) + Q\omega(T,Y) \ , \\ (\rho Y)_t + (\rho Yu)_x + (\rho Yv)_y = \vec{\nabla}.(\rho D\vec{\nabla}Y) - m\omega(T,Y) \ , \\ mp = \rho RT \ . \end{cases} \tag{5.2}$$

It can be noticed that the left-hand side of the four first equations in (5.2) exactly form the classical Euler equations for perfect gas inviscid flow. Starting from this observation, and because these hyperbolic terms play a major role in a reacting flow described by (5.2), we use a numerical approach based on an upwind finite-element solver developed at INRIA for the Euler equations. This solver uses a finite-volume upwind formulation on an unstructured finite-element triangulation, with a second-order approximation of the flux terms (using a MUSCL-type interpolation and slope limiters; see [8] for the details). For the remaining terms in (5.2) (namely, the diffusive and reactive terms in the energy equation and all terms in the mass fraction equation), we simply use a classical mass-lumped finite-element formulation. For the time integration, we use either a forward-Euler explicit scheme, or a semi-implicit formulation in which

the "Euler terms" are treated using a linearized backward-Euler implicit scheme. We refer the reader to [3], [10] for more details about this numerical approach, which has been developed in collaboration with F. Benkhaldoun, A. Dervieux, G. Fernandez, H. Guillard and A. Habbal.

5.2 An example calculation is shown on figure 6, for the propagation of a flame inside a closed square vessel. In this experiment, the mixture is initially cold and at rest, to ignite the gas, we impose a hot temperature on a segment of the upper boundary (the remaining walls are assumed to be adiabatic). The flame begins to propagate with a spherical shape, and then interacts with the lateral walls and tends to become planar while propagating downward. The strong expansion of the gases after ignition appears on the left upper view of figure 6. This calculation was realized with a preliminary explicit non adaptive version of the computer code: it can therefore be noticed that the physical parameters have been chosen in order to obtain a relatively thick flame so that the problem can be adequately solved with a uniform non adaptive mesh.

5.3 Figures 7 to 10 concern a different physical problem. We consider a steady curved flame in a rectangular open tube; an inflow of fresh mixture is introduced at the left end of the channel, and the flame is ignited and anchored at a hot point B located on the upper wall. Two different adaptive procedures are used in combination with the finite-volume/finite-element scheme described above:

(i) We first employ the adaptive procedure mentioned in Section 3: the two-dimensional mesh is divided into parallel straight lines for which a one-dimensional equidistributing method is used. The steady-state isotherms, the reaction rate contours and the corresponding adapted triangulation presented in figure 7 show that the reaction zone is again well resolved by the algorithm. The comparison with the results obtained on a uniform mesh with twice as many nodes is much conclusive (see figure 8).

(ii) An alternate approach is based on progressive mesh enrichment by element division. More precisely, after a first calculation on a coarse mesh, we divide each triangle in which the reaction rate ω is larger than a given value into four new triangles (each triangle in the first row of undivided triangles is then also divided into two or three subtriangles, in order to obtain an admissible finite-element triangulation). This enrichment can be applied several times in a row: in the calculation whose results are shown on figures 9 and 10, the triangulation is enriched three times for various levels of ω. Again, the comparison with the coarse mesh results of figure 8 shows that the mesh refinement highly improves the resolution in the flame region.

6. CONCLUSION

We have presented a sample of methods presently developed at INRIA for combustion calculations. These methods range from pseudo-spectral approximations for some fundamental flame propagation problems in simple rectangular geometries to finite-element methods on unstructured grids for the solution of the full system of governing equations of a compressible reacting flows.

We hope to have shown that adaptive gridding techniques are now efficient tools for the numerical simulation of thin premixed flames in one or two space dimensions. Although several further improvements still need to be investigated, we think that the development of these procedures has now come to a point when they can be used to improve the numerical solution of industrial combustion problems.

REFERENCES

[1] G. I. BARENBLATT, Y. B. ZELDOVICH, A. G. ISTRATOV, Prikl. Mekh. Tekh. Fiz., **2**, p. 21, (1962).

[2] F. BENKHALDOUN, B. DENET, B. LARROUTUROU, "Numerical investigation of the extinction limit of curved flames", to appear.

[3] F. BENKHALDOUN, A. DERVIEUX, G. FERNANDEZ, H. GUILLARD, B. LARROUTUROU, "Some finite-element investigations of stiff combustion problems: mesh adaption and implicit time-stepping", Proceedings of the NATO advanced research workshop on Mathematical modelling in combustion and related topics, Brauner Schmidt-Lainé eds., to appear, (1987).

[4] F. BENKHALDOUN, B. LARROUTUROU, "Explicit adaptive calculations of wrinkled flame propagation", to appear in Int. J. Num. Meth. Fluids..

[5] F. BENKHALDOUN, B. LARROUTUROU, "A finite-element adaptive investigation of two-dimensional flame front instabilities", to appear.

[6] J. D. BUCKMASTER, G. S. S. LUDFORD, "Theory of laminar flames", Cambridge Univ. Press, Cambridge, (1982).

[7] P. CLAVIN, "Dynamic behavior of premixed flame fronts in laminar and turbulent flows", Prog. Energy Combust. Sci., **11**, p. 1, (1985).

[8] F. FEZOUI, "Résolution des équations d'Euler par un schéma de Van Leer en éléments finis", INRIA Report 358, (1985).

[9] H. GUILLARD, B. LARROUTUROU, N. MAMAN, "Numerical investigation of cellular flame instabilities using pseudo-spectral methods", to appear.

[10] A. HABBAL, A. DERVIEUX, H. GUILLARD, B. LARROUTUROU, "Explicit calculations of reactive flows with an upwind finite-element hydrodynamical code", INRIA Report, to appear.

[11] J. M. HYMAN, B. LARROUTUROU, "Dynamic rezone methods for partial differential equations in one space dimension", Los Alamos Report LA-UR-86-1678, (1986).

[12] J. M. HYMAN, B. LARROUTUROU, "On the use of adaptive moving grid methods in combustion problems", Proceedings of the Second workshop on modelling of chemical reaction systems, Springer-Verlag, to appear.

[13] B. LARROUTUROU, "Utilisation de maillages adaptatifs pour la simulation de flammes monodimensionnelles instationnaires", Numerical simulation of combustion phenomena, Glowinski Larrouturou Temam eds., Lect. Notes in Phys., **241**, pp. 300-

312, Springer Verlag, Heidelberg, (1985).

[14] B. LARROUTUROU, "Adaptive numerical methods for unsteady flame propagation", Combustion and chemical reactors, Ludford ed., Lect. in Appl. Math., **24**, (2), pp. 415-435, AMS, Providence, (1986).

[15] B. LARROUTUROU, "A conservative adaptive method for unsteady flame propagation", to appear.

[16] B. LARROUTUROU, "Explicit adaptive numerical solution of non stiff combustion problems with complex chemistry", to appear.

[17] N. PETERS, "Discussion of test problem A", Numerical methods in laminar flame propagation, Peters Warnatz eds., Notes in Num. Fluid. Mech., **6**, pp. 1-14, Vieweg, Braunschweig, (1982).

[18] G. I. SIVASHINSKY, "Diffusional-thermal theory of cellular flames", Comb. Sci. Tech., **15**, pp. 137-145, (1977).

[19] G. I. SIVASHINSKY, "Instabilities, pattern formation and turbulence in flames", Ann. Rev. Fluid Mech., **15**, pp. 179-199, (1983).

[20] F. A. WILLIAMS, "Combustion theory", second edition, Benjamin Cummings, Menlo Park, (1985).

ACKNOWLEDGEMENTS: Most of the numerical calculations reported in this paper are the results of fruitful collaborations between the author and F. Benkhaldoun, B. Denet, A. Dervieux, G. Fernandez, H. Guillard, A. Habbal and N. Maman at INRIA, and J. M. Hyman at Los Alamos.

Figure 1: Trajectories of the moving nodes for $t \leq 4.5$.

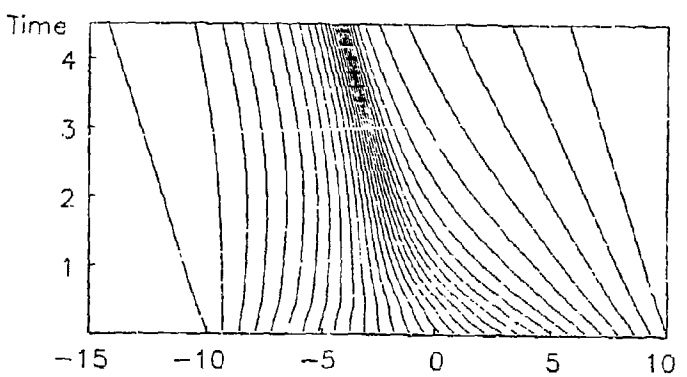

Figure 2: Steady planar flame: temperature and reaction rate profiles.

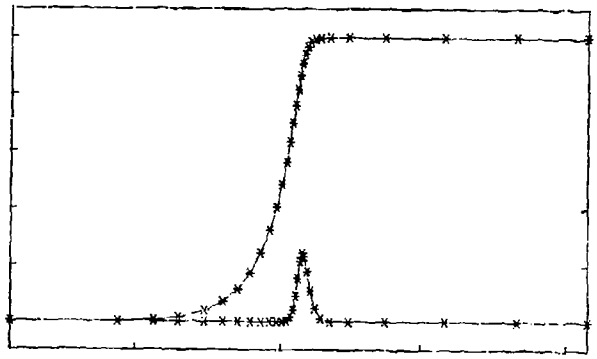

Figure 3: Steady non adiabatic curved flame: temperature, mass fraction and reaction rate contours.

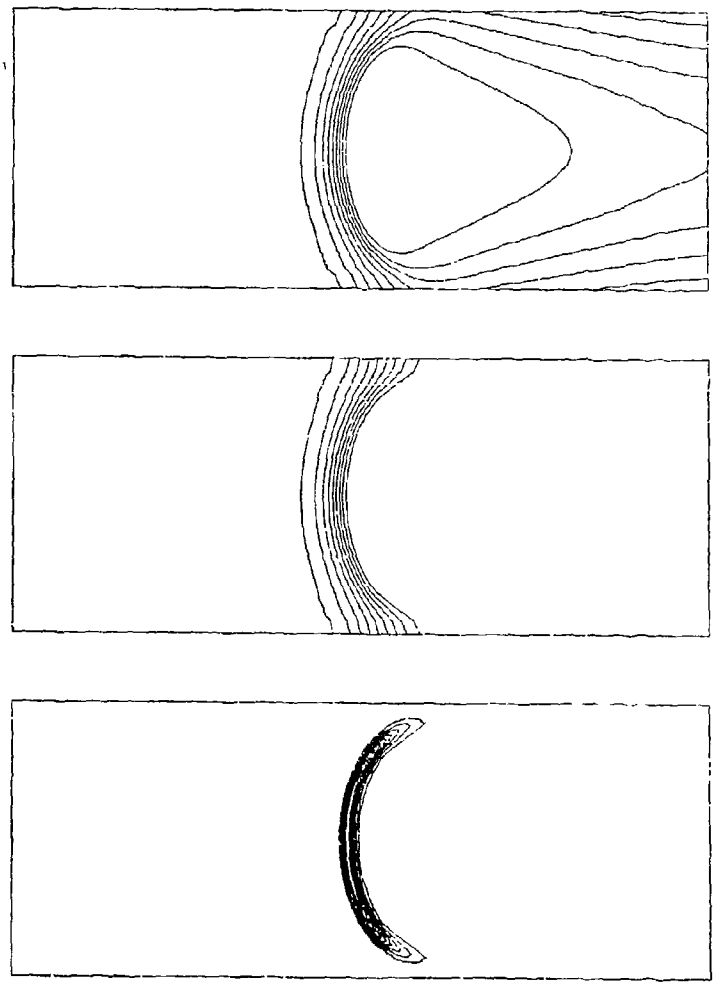

Figure 4: Steady non adiabatic curved flame: reaction rate contours and corresponding adaptive grid in the lower half of the tube.

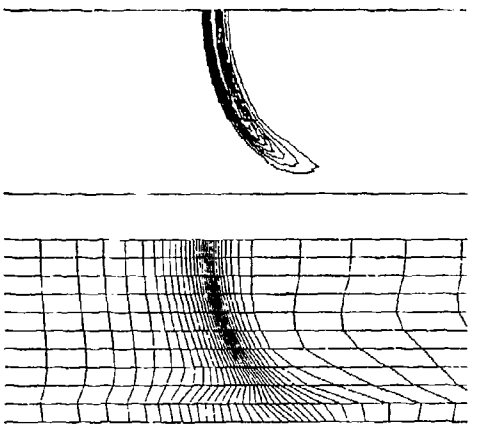

Figure 5: Thermo-diffusive flame instabilities: isotherms at four successive time levels.

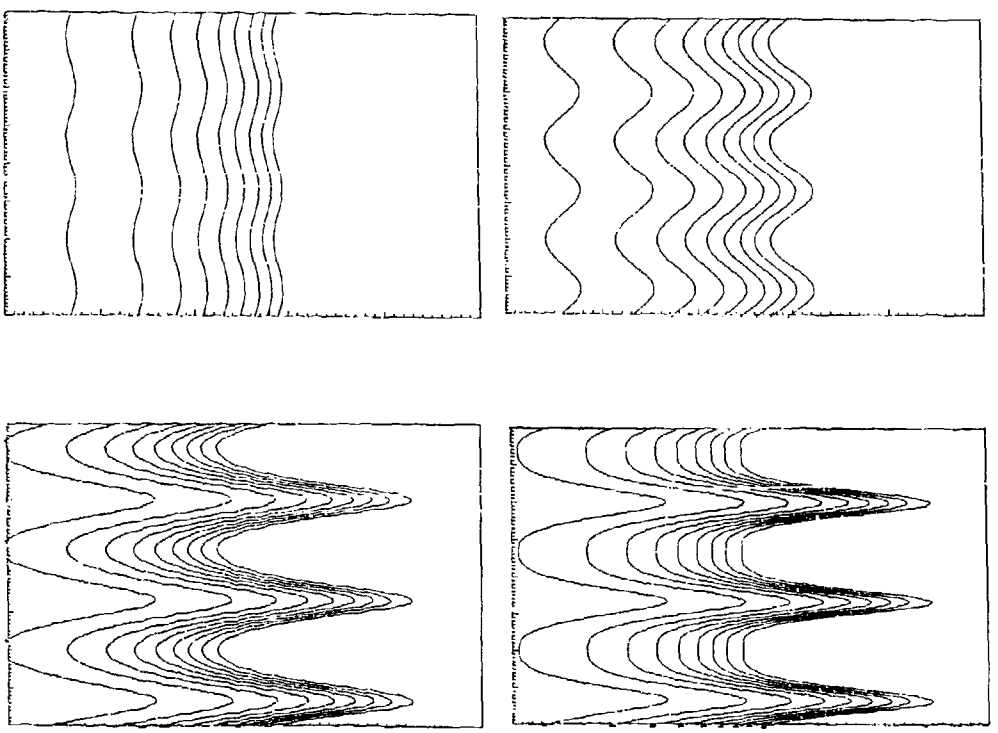

Figure 6: Flame propagation in a closed vessel: velocity field and mass fraction contours at four successive time levels.

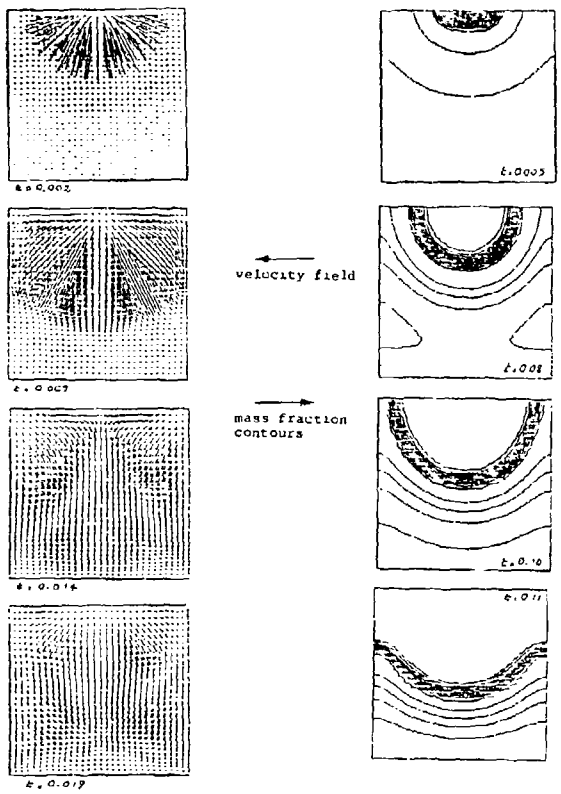

Figure 7: Thermally anchored flame: steady-state isotherms and reaction rate contours on an adaptive 31x11 mesh.

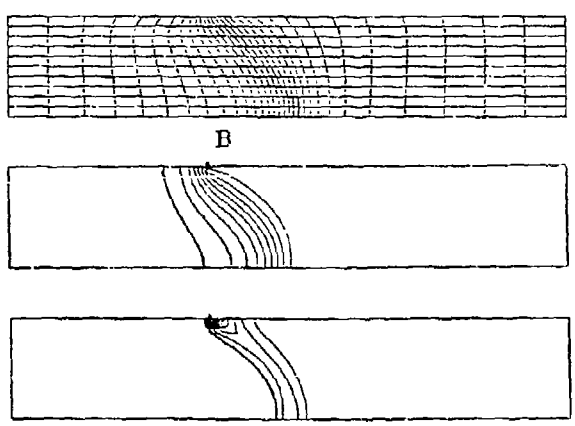

Figure 8: Thermally anchored flame: steady-state isotherms and reaction rate contours on a uniform 61x11 mesh.

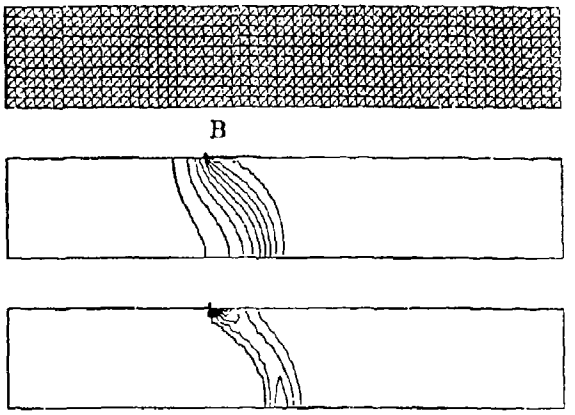

Figure 9: Thermally anchored flame: blow-up of the steady-state reaction rate contours on an enriched mesh (1472 nodes).

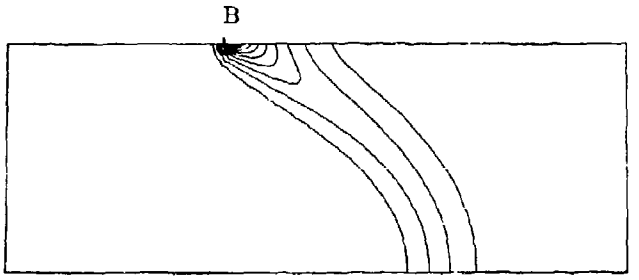

Figure 10: Thermally anchored flame: blow-up of the enriched triangulation.

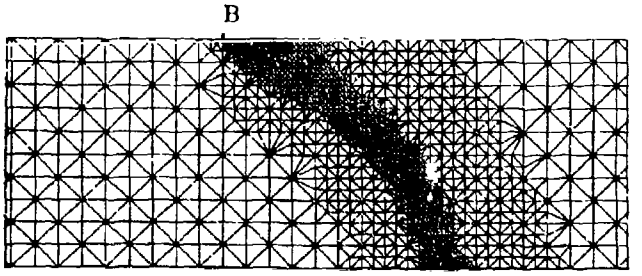

DISCUSSION

Scherrer, FR

L'utilisation des techniques de déplacement de maillage ne risque-t-elle pas de causer des déformations trop importantes du maillage?

Réponse d'Auteur

Si pour des raisons de précision (ou de stabilité du schéma) on veut éviter des déformations trop importants du maillage, il est possible d'inclure des termes géométriques dans les procédures d'adaptation du maillage. Ces termes tendront à produire le maillage le plus régulier ou le plus orthogonal possible. (e.g. J.U.Brackbill & Saltzmann J.S.J. Comp. 46 342 (1982) et Numerical Grid Generation, J.Thompson ed. Elsevier NY (1982).

GASEOUS PREMIXED FLAMES IN NON-UNIFORM FLOWS

P. CAMBRAY, B. DESHAIES, G. JOULIN
U.A. 193 C.N.R.S., E.N.S.M.A., Rue Guillaume VII, 86034 Poitiers Cedex (France)

A theoretical analysis /1/ led to an evolution law for a flame front propagating in a non-uniform flow when the scales of the non-uniformity of the flow are well larger than the flame thickness. This law gives the local burning velocity of the flame front as a function of the "flame stretch" which can be split in two parts, one accounting for the geometry of the front and the other for the non-uniformity of the flow. In such a law, all the physico-chemical properties of the mixture are lumped in only two scale factors.
A theoretical determination of one of these two scale factors (i.e. the so called Markstein length) is developed in a first part of the present paper. In a second part an experimental test of the evolution law is presented in different flame and flow configurations, which leads to experimental values for the two scale factors in the case of lean propane-oxygen-nitrogen mixtures. Finally experimental and theoretical values are compared.

NOMENCLATURE

B pre-exponential constant ; Eq.(3)

C_p mixture specific heat at constant pressure ; Eq.(3)

D coefficient of binary diffusion of the reactant into the upstream mixture

$D_{th}=\lambda_u/\rho_u C_p$: thermal diffusivity of the upstream mixture

E activation energy ; Eq.(3)

J,K integrals defined in Eq.(5)

L Markstein length ; Eq.(1)

$Le=D_{th}/D$: Lewis number

$\ell_T=D_{th}/u_{ad}$: adiabatic flame thickness

n normal coordinate to the flame front ; Eq.(3)

$\underline{n}$ unit normal to the flame front ; Eq.(1)

$Mk=L/\ell_T$: Markstein number

R perfect gas constant ; Eq.(3)

R_1, R_2 : flame front principal radii of curvature ; Eq.(1)

s binary thermal diffusion factor, between the reactant and the mixture, Eq.(4)

T temperature

$\underline{U}$ upstream velocity vector, extrapolated at the flame front position ; Eq.(1)

u_n normal flame velocity, relative to the upstream gas ; Eq.(1)

$U_n = u_n/u_{ad}$: reduced normal flame velocity

u_{ad} burning speed of the unstretched, planar flame ; Eq. (1)

Y reactant scaled mass fraction, Eq.(5)

z axial coordinate

$\beta = E(T_{ad}-T_u)/RT_{ad}^2$: Zel'dovich number ; Eq.(8)

β_{eff} effective Zel'dovich number ; Eq.(7)

$\gamma = (T_{ad}-T_u)/T_{ad}$: scaled reaction enthalpy ; Eq.(4)

ζ reduced flame stretch defined in Eq.(9)

$\theta = (T-T_u)/(T_{ad}-T_u)$: scaled temperature increment ; Eq.(5)

λ mixture heat conductivity ; Eq.(3)

$\Lambda = \lambda/\lambda_u$, Eq.(5)

ρ mixture density ; Eq.(3)

Subscripts

u upstream mixture
ad computed at the adiabatic flame temperature T_{ad}
R computed at the reaction temperature T_R

I - INTRODUCTION

The burning velocity of a premixed flame propagating in a non-uniform flow is widely known to be dependent on the hydrodynamic conditions experienced by the flame via the so-called flame stretch since the pioneering works of Karlovitz et al. /2/ and Markstein /3/.
Such a property is evidenced by the basic theory of P. Clavin and G. Joulin /1/ which moreover gives an expression for the local flame burning velocity u_n as a function of the flame stretch i.e. :

$$u_n = u_{ad} + L\,(u_{ad}\,(\frac{1}{R_1}+\frac{1}{R_2}) + \underline{n}\,.\,\underline{\underline{\gamma u}}\,.\,\underline{n}) \qquad (1)$$

In this equation $(1/R_1 + 1/R_2)$ is the flame front mean curvature (defined to be positive when the center of curvature is located within the fresh mixture). $\underline{\underline{\gamma u}}$ is the rate-of-strain tensor in the fresh mixture extrapolated to the flame front and $\underline{n}$ is the unit vector normal to the flame front.
In such an equation for the flame burning velocity u_n all the physico-chemical properties of the mixture are lumped in only two scale factors :

- the burning velocity u_{ad} of the flame in absence of any stretch or curvature effect (the burning speed of the ideal "one - dimensional planar flame"),
- the coefficient of proportionality relating the change in flame speed to stretch and curvature effects, i.e. the so-called Markstein length L.

The first part of the present paper deals with a theoretical determination of the Markstein number $Mk = L/\ell_T$ (i.e. the Markstein length scaled by the flame thickness) including the case of lean mixtures of an heavy hydrocarbon (without any restriction about the order of magnitude of Le - 1 and of Soret coefficient s). An explicit equation relating the Markstein number Mk to physico-chemical parameters of the mixture (activation energy of the overall chemical process, expansion ratio, effective Lewis number, heat conductivity and heat capacity of the mixture) is given.

In a second part an experimental test of Eq.(1) is done. In cases of lean propane-oxygen-nitrogen mixtures, which are usually considered as representative of lean mixtures of heavy hydrocarbons. By using a large number of steady flame and flow configurations (i.e. of flame

stretches) experimental values of the reference burning velocity u_{ad} and of the Markstein number Mk are obtained.

Finally the experimentally found value of the Markstein number is compared with the one computed from the equation obtained in the first part of the present paper. A surprisingly good agreement is obtained between the two.

II - THE MARKSTEIN NUMBER : A THEORETICAL DETERMINATION

To obtain estimates of the Markstein length involved in (1), we need to introduce a combustion model, then to solve the corresponding conservation equations in various situations of weak stretches and curvatures.

II.1 - Model

We assume that the burning process may be represented as an overall, one-step, irreversible reaction :

$$\text{Fuel} + \text{Oxidizer} \rightarrow \text{Products} + \text{heat} \qquad (2)$$

and we restrict our attention to fuel-lean mixtures. The changes in oxidizer mass fraction are neglected (lean mixture), the effects due to the closeness to stoichiometry being briefly evoked in Section IV. An inert gas (e.g. N_2) is also assumed to be present in the mixture, in large excess.
We further assume that the reaction rate may be modelled by a δ-function, the weight of which being chosen such that the normal component $\lambda\, \partial T/\partial n$ of the conductive heat flux undergoes the jump :

$$\left(\lambda \frac{\partial T}{\partial n}\right)_- - \left(\lambda \frac{\partial T}{\partial n}\right)_+ = (2\, Le\, B\, C_p\, \lambda_R\, \rho_R^2\, \sqrt{T_R}\, e^{-E/RT_R}\, R^2 T_R^4/E^2)^{1/2} \qquad (3)$$

across the reaction sheet, along which the fuel mass fraction vanishes (all the symbols involved in (3) and the subsequent formulae are defined in the nomenclature). The expression (3) for the overall rate of heat release per unit area of reaction sheet has been selected so as to ensure that it gives the same adiabatic flame speed u_{ad} as the leading order asymptotic result /4/, when the Arrhenius law is adopted. Notice that the dependence ($\propto \sqrt{T}$) on temperature of the collision frequency has been retained as the only T-dependence of the pre-exponential factor of the Arrhenius law, and that an overall reaction order of 2 has been selected (hence the factor ρ_R^2) to obtain no pressure dependence of u_{ad}, as it is nearly the case for the C_3H_8-N_2-O_2 mixtures used in our experiments /5/. Finally, among the various molecular mechanisms of heat and mass transport, we only retain the conduction of heat, along with the Fickian and thermal diffusions of the fuel. In particular, the Dufour mechanism is omitted, because it only gives a very small contribution to the heat flux /6/, as well as the multicomponent diffusion effects, since they only mildly affect the Markstein length as estimated by asymptotic models /4/, for dilutad enough lean mixtures of propane. By the same token, λ, C_p, ρD and the thermal diffusion coefficient s may be safely considered as composition independent (across the flame) and are assigned values corresponding to the diluent or to diffusion into it.
Even though (3) leads formally to the same value of u_{ad} as the leading order asymptotic analyses, which postulate $E/RT_R \gg 1$, and the form of (3) is suggested by such analyses, we do not need here to assume that the activation temperature E/R is very large. For this reason, no a priori assumption on the magnitude of Le - 1 and the Soret coefficient s needs to be introduced.

II.2 - Results

A remark worthnoticing is that a purely phenomenological or geometrical interpretation of the constitutive law (1) would a priori assign different values L_1 and L_2 to the coefficients of $u_{ad}(1/R_1 + 1/R_2)$ and $\underline{n} \cdot \underline{\underline{\nabla U}} \cdot \underline{n}$. However, it is readily checked that the Markstein lengths corresponding to the present δ-model have a common value, L, irrespective of the values assigned to the physico-chemical parameters characterizing the mixture. This is best shown by considering a steady, adiabatic spherical flame, for which $\underline{n} \cdot \underline{\underline{\nabla U}} \cdot \underline{n} = -2\, u_{ad}/r_F$ and the effects of stretch and curvature are found to cancell each other for any value of the flame radius r_F. To compute L, it is thus enough to consider a weakly stretched planer flame in a stagnation flow. For this one-dimensional configuration, a straightforward - albeit lengthy - computation yields :

$$Mk_{\delta\text{-model}} = J(\gamma) + \frac{\beta_{eff}}{2} K(Le,s,\gamma) \qquad (4)$$

for the "Markstein number" $Mk = L/\ell_T$ where :

$$J(\gamma) = \int_0^1 \frac{d\theta A}{1 - \gamma + \gamma\theta}\,, \qquad (5)$$

$$K(Le,s,\gamma) = \int_0^1 \frac{A(1-\gamma)}{1 - \gamma + \gamma\theta} \left(1 + \frac{\gamma - 1}{\theta}\right) d\theta$$

In (5), $A(\theta,\gamma)$ stands for λ/λ_u when expressed in terms of $\gamma = (T_{ad} - T_u)/T_{ad}$ and $\theta = (T - T_u)/(T_{ad} - T_u)$; the reduced fuel mass fraction $Y = y/y_u$ is given in terms of θ by the linear ODE :

$$\frac{dY}{d\theta} = Le\, \frac{Y - 1}{\theta} + \frac{sY}{\theta + 1/\gamma - 1}\,, \quad Y(1) = 0 \qquad (6)$$

which involves the Lewis number Le and the Soret coefficient s corresponding to the Fickian and thermal diffusions of the fuels into the diluent. The "effective" Zel'dovich number β_{eff} is defined by:

$$\beta_{eff} = \frac{T_{ad} - T_u}{T_{ad}} \left(\frac{E}{RT_{ad}} + \frac{\partial \log \lambda/\lambda_u}{\partial \log T_{ad}} + \frac{3}{2} - \frac{2T_{ad}}{T_{ad} - T_u}\right) \qquad (7)$$

and measures the fractional change of the rate of heat release, given by (3), as the reaction temperature T_R varies about T_{ad}. The integral J(Y) accounts for the density changes across the flame, whereas K(Le,s,Y) measures the stretch-induced variations in reaction temperature : $T_R - T_{ad} = (T_{ad} - T_u)\, K(Le,s,\gamma)(1/R_1 + 1/R_2 + \underline{n}.\underline{\underline{\nabla U}}.\underline{n}/u_{ad})$; we note that $K(1,0,\gamma) = 0$. The above expression of the Markstein number Mk can be compared with that given by an asymptotic theory /4/ /6/, namely :

$$Mk_{asym} = J(\gamma) + \frac{\beta}{2}(Le-1)\, \frac{\partial K}{\partial Le}(1,0,\gamma) + \frac{\beta}{2}\, s\, \frac{\partial K}{\partial s}(1,0,\gamma) \qquad (8)$$

which assumes that $\beta \equiv E(T_{ad} - T_u)/RT_{ad}^2 \to \infty$ and that $\beta(Le-1)$ and βs are O(1) quantities. Equation (8) is merely an expansion of (4)-(7) for $\beta \to \infty$, $Le-1 \sim s = O(1/\beta)$. Therefore, comparing (8) and (4)-(7) can give informations on the accuracy of the former, when neither the reciprocal Zel'dovich number, nor (Le-1) nor s are vanishingly small quantities, a case of practical interest especially when heavy hydrocarbons or very light fuels are involved.

III - THE MARKSTEIN NUMBER : AN EXPERIMENTAL DETERMINATION

III.1 - Experimental setup

For sake of simplicity the experimental test of Eq.(1) and determination of the Markstein number have been performed using axisymmetric flows and flame shapes. The experimental setup described elsewhere /7/ is sketched in Fig. 1 : the reactive mixture flows out of a cylindrical tube and then impinges on a flat stagnation surface. Using such an experimental device different kinds of axisymmetrical flames (ranging from classical flat flames in stagnation flow to inverted curved flames) can be stabilized at sufficiently large distances from both the burner exit and stagnation surface to avoid a thermal coupling.

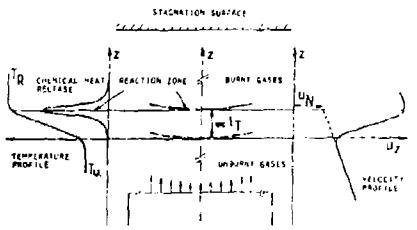

FIG. 1 SCHEMATIC REPRESENTATION OF THE FLOW FIELD.

Laser Doppler Velocimetry (L.D.V.) and laser tomography /8/ are used to measure the local velocity of the fluid and to visualize the shape of the flame front respectively. For that purpose the gaseous reactive mixture is seeded with small oil droplets (typical diameter $\sim 1\mu m$ - boiling point ~ 600 K).

A 3-axe, computer-controlled, motorized translator is used to displace the burner. This computer is also used to compute and store in real time, the mean flow velocity, its standard mean deviation, the digitized coordinate of the measurement point, as well as a digitized video picture of the flame.

III.2 - Experimental methodology

To simplify the experimental procedure all the measurements have been so far performed along the axis of symmetry ; as a consequence, the influence of the stretch effects on the flame burning velocity has been evidenced at the tip of the flame.

When specialized to the axis of symmetry equation (1) reads as :

$$U_n = 1 + Mk.\varepsilon \qquad (9)$$

where the non-dimensional flame burning velocity U_n and non-dimensional toral flame stretch ε are given by :

$$U_n = \frac{u_n}{u_{ad}} \quad , \quad \varepsilon = (2\,\frac{\ell_T}{R}) + (\frac{\ell_T}{u_{ad}}\,\frac{du_z}{dz}) \qquad (10)$$

The Markstein number Mk is defined as in the previous section ($Mk = L/\ell_T$). $2/R$ is the mean flame curvature at its tip and du_z/dz is the gradient along the z axis (axis of symmetry) of the z component of the fresh mixture velocity extrapolated to the flame front. These two quantities can be easily obtained for different flames and flows configurations (i.e. for different flame stretches) using the digitized video pictures of the flames and L.D.V. measurements along the axis of symmetry. If the corresponding local flame burning velocity u_n can be measured for each configuration the linear dependence of u_n on the flame stretches ε inferred from Eq.(9) can then be tested. In case of a reasonable agreement the values of the Markstein number as well as of the reference flame speed u_{ad} can be obtained for a given mixture.

III.3 - The flame burning velocity u_n

A priori, there exists a difficulty in an experimental determination of the local flame burning velocity u_n. Indeed, in the non-uniform flows in which the flames are stabilized, the velocity of the flow has a different value at each point of space.

It should be noticed that even if the typical length scale of the velocity gradient remains larger than the flame thickness, a change in the definition of u_n involving a spatial translation of the order of the flame thickness induces a change in the value of u_n of the same order of magnitude as the second term featuring in the right hand side of Eq.(1).

Thus in order to make a consistent comparison between theoretical and experimental values of the Markstein number Mk, the experimental determination of the local flame burning velocity u_n has to employ the same definition as in /1/.

In /1/ and in the analysis leading to (4) - (7) the local flame burning velocity u_n is the value of the normal component of the velocity prevailing in the unburned (cold) mixture, extrapolated - along the normal to the flame - to the inner reaction zone (cf. Fig. 1 and 2).

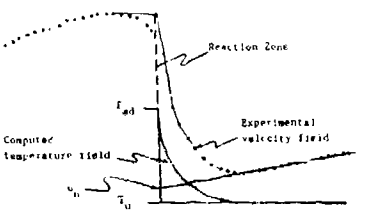

FIG. 2 - REACTION ZONE LOCATION.

From the asymptotic point of view adopted in paper /1/ or as it is a priori assumed in the theoretical part of the present paper, this reaction zone appears to be a discontinuity (when compared to all the other length scales of the problem) where upstream, chemistry-free outer temperature profile reaches the combustion temperature. We have adopted this definition of the reaction zone to determine the flame burning velocity u_n (cf. Fig. 2).

Since an attempt to measure the temperature profile by using thermal probes has exhibited too large perturbations of the flame position and shape, we currently use an indirect procedure to obtain the reactive zone position.

i) a temperature field is computed via a numerical integration of the chemistry-free balance equations under the constant pressure approximation ; we used as boundary conditions the controlled injection temperature and the requirement that the calculated velocity field agrees with the one measured in the cold region of the unburned gas flow and at the beginning of the preheat zone (i.e. for $T < 600$ K),

ii) then the position of the reaction zone is obtained as the abscissa where the computed temperature reaches the constant pressure adiabatic combustion temperature.

Notice that, since this integration is done along the axis of symmetry and a first order approximation for small curvature and small velocity gradient effects is used, a computation of the temperature field requires to solve mass and energy balance equations only. Following the aforementionned definition of u_n, the x component of the fresh mixture velocity outside of the flame is extrapolated to the reaction zone abscissa. This gives the value of the flame burning velocity u_n at the tip of the flame.

These indirect determinations of the reaction zone location and of the local flame burning velocity u_n have been checked in some experiments by using a direct experimental procedure. For that purpose experiments were performed with reactive gaseous mixtures seeded with submicronic refractory solid particles. In that way velocity profiles are obtained in the hot part of the flame.

Thus, and as shown in Fig. 2, a way to determine the reaction zone location is to extrapolate the experimental velocity profile from its inflection point located in the acceleration region, to a value equal to the maximum value measured in the hot part of the flame.

A comparison between this direct estimate of the reaction zone position and the one resulting from the aforementionned indirect procedure is given in Fig. 2. It should be noticed that the complete agreement between the results of these two methods evidenced by Fig. 2 is partially due to the scale of this figure. But, at any rate, these two procedures do not introduce a significant difference in the determination of the flame burning velocity u_n. The resulting discrepancy in the values obtained for the flame burning velocity never exceeds 5%.

III.4 - Results

Up to now three reactive mixtures have been used, i.e. :

$C_3H_8 + 6.25\ O_2 + x\ N_2$ (equivalence ratio r=0.8±1%)

with :

x_1=32.8 (mixture 1; dilution ratio: d_1=0.160)
x_2=24.3 (mixture 2; dilution ratio: d_2=0.154)
x_3=36.0 (mixture 3; dilution ratio: d_3=0.148)

For each mixture different sets of experiments have been performed. For each of these sets of experiments the reduced flame burning velocity $U_n = u_n/u_{ad}$ has been plotted as a function of the total non-dimensional flame stretch ε. For one set of experiments a value of the reference flame speed u_{ad} was obtained as the one for which the least-square linear fit of $U_n = f(\varepsilon)$ was equal to 1 for ε = 0. Together with the value of u_{ad} a value of the Markstein number was obtained as the slope of the least square linear fit. In this way a mean value of the reference flame speed u_{ad} was computed from all the sets of experiments involving the same mixture, together with a typical dispersion around this mean value.

By this means the following results are obtained :

mixture (1)	u_{ad} = 8 ± 5%	(m/s)
mixture (2)	u_{ad} = 9.7 ± 5%	
mixture (3)	u_{ad} = 12 ± 5%	

As for the Markstein number, the different values we found from all the sets of experiments do not indicate a systematic variation due to the mixture composition, but instead seem only to be representative of a random dispersion around a mean value.

This mean value was determined by plotting all the sets of experimental results $U_n = f(\varepsilon)$ on the same figure ; to this end we used the value of the reference burning velocity u_{ad} as previously obtained as a scaling factor for the flame speed U_n and flame stretch ε corresponding to the same set of experiment. Such a plot of all the experimental results is presented in Fig. 3. The slope of the least-square linear fit of $U_n = f(\varepsilon)$ gives a mean value of the Markstein number corresponding to the three mixtures we used, i.e.

$$Mk = 8 \pm 1.5$$

The dispersion we indicate for the Markstein number is the result of a comparison between the mean value and those deduced from the different sets of experiments.

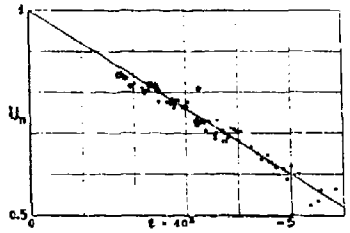

FIG. 3 - REDUCED FLAME BURNING VELOCITY VERSUS TOTAL STRETCH.

LESS (○) MORE (●) THAN 25 % OF CURVATURE EFFECTS IN THE TOTAL FLAME STRETCH.

To conclude this section it should be noticed that:

- in accordance with Eqs(1) and (9), the flame burning velocity dependence on geometrical effects (i.e. flame curvatures), and hydrodynamical effects (i.e. normal gradients of the fresh mixture velocity fields) involves the same proportionality coefficient, i.e. a single Markstein number
- down to a decrease of 50% in the flame burning velocity a linear dependence of this velocity on flame stretches is observed (Fig. 3).

IV - COMPARISON THEORY/EXPERIMENTS

Over the range of dilution ratios used in the experiments, the adiabatic flame temperature only varies by about 100 K and the resulting variations in $\gamma = (T_{ad}-T_u)/T_{ad}$ are too small to cause significant variations (± 0.2) in the theoretical estimate (4) - (7) of the Markstein number Mk ; accordingly, the central value T_{ad} = 1690 K (mixture 2) has been selected when drawing the comparison.

As for the Lewis number Le and the thermal diffusion factor s, we used the values Le = 1.64 and s = +0.48 recommended by Garcia-Ybarra et al. /6/, which correspond to the Fickian and thermal diffusions of propane into nitrogen ; the uncertainty on these figures is at least 5%, especially on s. The specific heat C_p has been taken as constant, and the variations of the heat conductivity λ, assumed to be that of air, with temperature are taken into account by a second order polynomial fit of the values quoted in /9/. Finally, we used the value E = 37700 kcal/mole given in /5/ for the activation energy of lean propane-air mixtures ; inspection of the literature, however, yields rather scattered figures, and the uncertainty on E has been estimated to be about ± 5000 kcal/mole.

Then, Eqs (4) - (7) yield

$$Mk = 8.0 \pm 10\%,$$

the quoted uncertainty on Mk resulting from those on E, Le, s and the variation in γ. The agreement with the experimental figure is surprisingly, and unexpectedly, good.

The following further remarks may be put forward. The difference between β_{eff} (Eq.(7)) and the usual Zel'dovich number β is of the same order of magnitude as the uncertainty to which β_{eff} is known from the values of E available in the literature : with the presently adopted law for $\lambda(T)$, $\beta_{eff} - \beta \simeq \gamma$. Thus the asymptotic theories, which neglect this small difference ($\simeq 10\%$), are not much in error about this particular point. About the dependence of Mk on Le and α, comparing (4) - (7) with (8) reveals that (8) overestimates significantly the dependence on Le (when Le exceeds one significantly), and that a more accurate prediction can be obtained from (8) if (Le - 1) is replaced by (Le - 1)/Le.

Finally it may be pointed out that the theoretical result (4) - (7) can be generalized to account for the depletion of oxygen (the abundant reactant) as well and the corresponding effects of molecular transports ; the resulting shift in Mk has been estimated to be between - 0.5 and - 1, but a more accurate evaluation and many very accurate experiments are needed to decide whether this shift is indeed significant and can be measured.

- *This work was carried with a financial support of the DRET under contract n°85/130.*

REFERENCES

/1/ P. CLAVIN and G. JOULIN (1983) "Premixed flames in large-scale, high intensity turbulent flows", Journal de Physique-Lettre, L1-L12.

/2/ B. KARLOVITZ, D.W DENNISTON, D.H. KNAPSCHAEFER and F.E. WELLS (1953) "Studies on turbulent flames", 4th Symposium (Int.) on Combustion, pp.613-620, Williams and Wilkins Company, Baltimore.

/3/ G.H. MARKSTEIN (1964) "Non-steady flame propagation", Pergamon Press.

/4/ P. CLAVIN (1985) "Dynamic behavior of premixed flames in laminar and turbulent flows", Prog. Energy Comb. Sci., pp.1-59.

/5/ C.R. FERGUSON, J.C. KECK (1977) "On laminar flame quenching and its application to spark ignition engines", Comb. and Flame, 28, pp.197-205.

/6/ P. GARCIA-YBARRA, C. NICOLI, P. CLAVIN (1984) "Soret and dilution effects on premixed flames", Comb. Sci. Tech., 40, pp.41-53.

/7/ P. CAMBRAY, D. DESHAIES (1987) "Experimental investigation of stretch and curvature effects on premixed flame burning velocities", Concilium Analitanum super ignis opera, p.6.19, the Combustion Institute - Sezione Italiana.

/8/ L. BOYER (1980) "Laser tomographic method for flame front movement studies", Comb. and Flame, 39, pp.321-323.

/9/ A.J. REYNOLDS (1971) "Thermofluid Dynamics", Wiley Intersciences.

DISCUSSION

S.Candel, FR

(1) Did you have any problems in measuring the velocity in the reactive zone with laser Doppler veocimetry? More specificaliy how did you deal with the large beam deflections caused by the large temperature gradients existing in that region?

(2) How did you choose the value Le = 1.64 for your propane/O_2/N_2 mixture? I find this value somewhat low.

(3) Did you measure the gas temperature in the hot products? Is this temperature equal or different from the adiabatic flame temperature?

Do you have an estimate of the heat losses from the flame zone (in particular the heat flux into the stagnation plate)?

Author's Reply

(1) The indirect procedure (cf § III.3) chosen to locate the reaction zone and to obtain u_n requires to measure the flame curvature (1/R), the upstream velocity gradient, the room temperature and the minimum value of u_z along the axis of symmetry (but *not* the exact location of that minimum). These needed quantities are not affected by beam deflection. Then an outer, upstream velocity profile is computed along with the corresponding chemistry-free temperature profile. This computed u_z profile is found to agree with the experimental one for $T < 600$ K; b. yond, a slight discrepancy is observed, but we cannot decide whether it is due to beam deflection or to the fact that chemistry comes into play. At any rate, the determinations of the reaction zone location, then of u_n, are not affected.

(2) The value Le = 1.64 is that recommended in /6/, but in the theoretical evaluation of M_k, Le has been assigned an uncertainty of 5%. We further note that $M_k \cong J + a(1 - 1/Le) + b.s$, where J, a and b are almost Lewis-Number-independent; increasing Le beyond 1.64 would not change the theoretical estimate of M_k significantly.

(3) Yes, the burned gas temperature has been measured, with a thermocouple. Within the experimental uncertainty, the measured value does not differ from that (T_b) predicted by the theory. Since Le > 1 and s>0, T_b is lower than the adiabatic flame temperature T_{ad}, even without any loss to the downstream wall; the stretch-induced change in reaction temperature, $\gamma T_{stretch}$, is about $\varepsilon(T_{ad} - T_u)$. For flat flames an overestimate of the change in reaction temperature, δT_{wall}, due to conduction to the stagnation plate can be obtained by approximating ρu, by a linear law between the front and the wall. This gives:

$$-\delta T]_{wall} \cong \frac{2(T_{ad} - T_{wall})\, e^{-D^2/\ell_b}}{\sqrt{2\pi}D/\ell_b \,\mathrm{erf}\,(\sqrt{D/2\ell_b})}$$

where $\ell_b = \bar{\lambda}/\rho_u u_n C_p$, $\bar{\lambda} < \lambda(T_b)$ being an average value of the heat conductivity in the downstream region; D is the flame distance to the wall. For the most stretched flame in Fig.3, $\varepsilon \cong -5.10^{-2}$, $D \cong 1$ cm; with $\bar{\lambda} \leq \lambda(T_b)$ one obtains $-\delta T_{stretch} \cong 5.10^{-2}(T_{ad} - T_u)$ and $-\delta T_{wall} < 2.10^{-4}(T_{ad} - T_u)$. The last figure shows that conduction to the wall is negligible for $-\varepsilon < 5.10^{-2}$ i.e. for all the data used in Fig.3, since D increases with decreasing stretch. However, $-\delta T_{wall}$ increases very rapidly with decreasing D's, hence with increasing stretches, thereby possibly being responsible for the extinction found at $\varepsilon \cong -0.5.10^{-2}$ (not shown in Fig.3); this point is the subject of current studies.

MODELISATION ET ETUDE EXPERIMENTALE D'UN ECOULEMENT REACTIF CONFINE AVEC INJECTION PARIETALE

P. Bruel, M. Champion, M. Boutouili, J.C. Ballet
Laboratoire d'Energétique et de Détonique, U.A. 193 au C.N.R.S.
E.N.S.M.A., rue Guillaume VII, 86034 Poitiers Cedex (FRANCE)

RESUME

La combustion turbulente d'un prémélange injecté dans un canal 2-D est étudiée sur les plans numérique et expérimental. Dans le cas des forts taux de soufflage un modèle de combustion turbulente avec fermeture du second ordre pour les transports de masse et d'énergie a été développé en tenant compte de résultats antérieurs obtenus dans le cas d'écoulements réactifs de cisaillement de structure plus simple. Le code de calcul correspondant a été testé par comparaison d'une part avec la solution exacte dans le cas d'un écoulement de Couette, et d'autre part avec les résultats expérimentaux obtenus sur le champ des vitesses dans le canal 2-D.

NOMENCLATURE

c	température réduite $\frac{T - T_u}{T_{ad} - T_u}$
c''	fluctuation de température réduite
C_f	coefficient de frottement $\frac{\tau_p}{\frac{1}{2}\rho_e u_e^2}$
D	coefficient de diffusion moléculaire
DCFL	le pas de temps numérique est égal à DCFL fois le pas du temps correspondant au critère CFL
F	taux de soufflage $\frac{\rho_p v_p}{\rho_e u_e}$
h	demi-hauteur du canal
NDT	nombre de pas de calcul effectué
P_o	pression statique de référence
Re_{2h}	nombre de Reynolds de l'écoulement $\frac{\rho_e u_e 2h}{\mu}$
T_{ad}	température adiabatique de combustion du prémélange
T_u	température du prémélange injecté
T_∞	température des gaz brûlés de l'écoulement principal
u_e	composante longitudinale de la vitesse à l'extérieur de la couche limite ou sur le plan axial horizontal du canal 2-D
u_p	vitesse de la paroi dans le cas de l'écoulement de Couette
u''	fluctuation de la composante longitudinale de la vitesse
v_p	vitesse d'injection du prémélange
v''	fluctuation de la composante transversale de la vitesse
w	taux de production chimique
ox	direction longitudinale
oy	direction transversale
δ	épaisseur de la couche limite turbulente
δ_{scv}	épaisseur de la sous-couche visqueuse
μ	coefficient de viscosité dynamique
Ψ	richesse du prémélange
ρ_o	masse volumique de référence
ρ_e	masse volumique correspondant à l'écoulement principal
ρ_p	masse volumique du prémélange injecté
τ_p	expression du frottement à la paroi $\mu \frac{\partial u}{\partial y})_{paroi}$

1. INTRODUCTION

Dans la zone primaire des foyers de turboréacteurs, la combustion est stabilisée par recirculation de gaz brûlés dans les gaz frais. Les phénomènes élémentaires qui contrôlent ce processus dépendent des valeurs relatives du temps caractéristique des réactions chimiques d'une part et du temps de mélange entre

gaz frais et gaz brûlés d'autre part.Dans le cas où les réactions chimiques sont très rapides (grand nombre de Damkholer) le processus est contrôlé par la dynamique de l'écoulement (mélange turbulent) et ses interactions avec des fronts de flamme minces localisées dans les interfaces entre gaz frais et gaz brûlés (produits de combustion). Ce cas limite de la combustion turbulente est étudié au Laboratoire d'Energétique et de Détonique dans une expérience de combustion dans une conduite bidimensionnelle avec injection pariétale de gaz frais dans un écoulement principal de gaz brûlés. Un certain nombre d'études expérimentale et numérique ont déjà été consacrées au développement de la couche limite avec injection du mélange réactif /1/ /2/ dans des cas où le taux d'injection est relativement petit.

Cette communication présente les premiers résultats obtenus dans le cas général d'une injection quelconque où ni l'aspect confiné de l'écoulement ni d'éventuelles recirculations ne peuvent être négligés. Les travaux présentés dans cette présente publication sont décrits en distinguant trois parties:

- l'établissement d'un modèle du second ordre applicable à un écoulement elliptique,
- la mise au point du code de calcul correspondant,
- l'obtention d'une base de données expérimentales dans le cas d'un écoulement dans un canal bidimensionnel avec injection pariétale de prémélange hydrocarbons-air.

2. DESCRIPTION DU MODELE DU SECOND ORDRE

Dans un premier temps nous avons traité le cas des écoulements réactifs isenthalpiques, où la combustion est caractérisée par une variable d'avancement c (température réduite ou fraction massique des gaz brûlés) variant de 0 à 1. L'ensemble des équations moyennes qui représentent l'écoulement réactif turbulent est alors :

$$\frac{\partial}{\partial t}(\bar\rho\,\tilde c) + \frac{\partial}{\partial x}(\bar\rho\,\tilde u\,\tilde c) + \frac{\partial}{\partial y}(\bar\rho\,\tilde v\,\tilde c) - \frac{\partial}{\partial x}\left(\overline{\rho D\frac{\partial c}{\partial x}}\right) - \frac{\partial}{\partial y}\left(\overline{\rho D\frac{\partial c}{\partial y}}\right)$$

$$+ \frac{\partial}{\partial x}\left(\overline{\rho\,u''c''}\right) + \frac{\partial}{\partial y}\left(\overline{\rho\,v''c''}\right) = \bar\omega \qquad (1)$$

$$\frac{\partial}{\partial t}(\bar\rho\,\tilde u) + \frac{\partial}{\partial x}(\bar\rho\,\tilde u^2) + \frac{\partial}{\partial y}(\bar\rho\,\tilde v\,\tilde u) - \frac{\partial}{\partial x}\left(\overline{\frac{4}{3}\mu\frac{\partial u}{\partial x}}\right) - \frac{\partial}{\partial y}\left(\overline{\mu\frac{\partial u}{\partial y}}\right) + \frac{\partial}{\partial x}\left(\overline{\frac{2}{3}\mu\frac{\partial v}{\partial y}}\right)$$

$$- \frac{\partial}{\partial y}\left(\overline{\mu\frac{\partial v}{\partial x}}\right) + \frac{\partial}{\partial x}\left(\overline{\rho u''^2}\right) + \frac{\partial}{\partial y}\left(\overline{\rho u''v''}\right) = -\frac{\partial\bar p}{\partial x} \qquad (2)$$

$$\frac{\partial}{\partial t}(\bar\rho\tilde v) + \frac{\partial}{\partial x}(\bar\rho\,\tilde u\tilde v) + \frac{\partial}{\partial y}(\bar\rho\,\tilde v^2) - \frac{\partial}{\partial x}\left(\overline{\frac{4}{3}\mu\frac{\partial v}{\partial x}}\right) - \frac{\partial}{\partial y}\left(\overline{\mu\frac{\partial v}{\partial y}}\right) + \frac{\partial}{\partial y}\left(\overline{\frac{2}{3}\mu\frac{\partial u}{\partial x}}\right)$$

$$- \frac{\partial}{\partial x}\left(\overline{\mu\frac{\partial u}{\partial y}}\right) + \frac{\partial}{\partial x}\left(\overline{\rho\,v''u''}\right) + \frac{\partial}{\partial y}\left(\overline{\rho\,v''^2}\right) = -\frac{\partial\bar p}{\partial y} \qquad (3)$$

où $V(\tilde u,\tilde v)$ est le champ moyen de vitesse (en moyenne de Favre) et $\bar p$ le champ de pression. L'équation d'état est alors :

$$P\rho_o/(1+\tau\,\tilde c) = P_o\,\bar\rho/(1+\tau) \qquad (4)$$

où l'indice o caractérise les gaz brûlés et τ est le facteur d'expansion thermique :

$$\tau = \frac{T_{ad} - T_u}{T_u} \qquad (5)$$

u étant relatif au prémélange frais.

Suivant le modèle BML /3/ le taux de production chimique moyen est :

$$\bar\omega = K\,\frac{\tilde c(1-\tilde c)}{\bar\tau} \qquad (6)$$

où $\bar\tau$ est un temps caractéristique de la turbulence.

En ce qui concerne la fermeture des termes de flux turbulents de masse et d'énergie $\overline{\rho\,u''c''}$ et $\overline{\rho\,v''c''}$ et des composantes du tenseur de Reynolds $\overline{\rho\,u''^2}$, $\overline{\rho\,v''^2}$, $\overline{\rho\,u''v''}$, les remarques préliminaires suivantes doivent être faites :

- Le modèle BML appliqué aux flammes planes /4/5/, c'est-à-dire la résolution du système (1)-(3) dans le cas d'un écoulement monodimensionnal, en tenant compte d'une fonction densité de probabilité $P(c,u_k;x)$ bimodale en c, a montré l'existence de diffusion à contre gradient et d'une production d'énergie cinétique ($\overline{\rho\,u''^2}$, $\overline{\rho\,v''^2}$) à travers la flamme, qui ne pouvaient être pris en compte qu'en résolvant les équations de bilan pour les flux turbulents et les composantes du tenseur de Reynolds.

L'extension du modèle BML au cas des écoulements de cisaillement, notamment au cas de la couche limite turbulente réactive avec injection du prémélange /6/9/ a montré que les flux turbulents pouvaient s'écarter

sensiblement du modèle gradient (tel que $\overline{\rho v'' c''} \sim - \mu_t \, \partial \tilde{c}/\partial y$ par exemple où μ_t est un coefficient de viscosité turbulente), et que le calcul prédit l'existence de diffusion à contre gradient ($\overline{\rho v'' T''} > 0$ dans la couche limite) dans certains cas d'écoulement nonisenthalpique /9/. Par ailleurs il apparaît que, la production de turbulence par cisaillement étant dominante dans un tel écoulement, la tension de Reynolds et la contribution $\rho u''^2$ de l'énergie cinétique turbulente sont correctement évaluées par une fermeture de type gradient.

Tenant compte de ces résultats différents sur l'évaluation des flux turbulents d'une part et sur celle des composantes du tenseur de Reynolds d'autre part, nous avons été conduits à envisager la fermeture des équations (1)-(3) de la façon suivante :

Les composantes $\rho u''u''j$ sont telles que :

$$\overline{\rho u'' u''}_j = \frac{2}{3} \left(\bar{\rho} \, \tilde{k} + \mu_T \frac{\partial \tilde{u}_k}{\partial x_k} \right) \delta_{ij} - \mu_t \left(\frac{\partial \tilde{u}_i}{\partial x_j} + \frac{\partial \tilde{u}_j}{\partial x_i} \right) \qquad (7)$$

ce qui introduit l'énergie cinétique turbulente $\tilde{k}$.

Le calcul des flux se fait par l'intermédiaire des équations de bilan :

$$\frac{\partial}{\partial x_k} \left(\bar{\rho} \, \tilde{u} \, \overline{\rho u_i'' c''}/\bar{\rho} \right) + \frac{\partial}{\partial x_k} \left(\overline{\rho u_i'' u_k'' c''} \right) = - \overline{\rho u_k'' c''} \frac{\partial \tilde{u}_i}{\partial x_k} - \overline{\rho u_i'' u_k''} \frac{\partial \tilde{c}}{\partial x_k}$$

$$- \overline{c'' \frac{\partial p}{\partial x_i}} + \overline{u_i w} - \bar{\rho} \, \tilde{\varepsilon}_{ic} \qquad (8)$$

où $\tilde{\varepsilon}_{ic}$ est la fonction de dissipation visqueuse.

La méthode de fermeture choisie pour ces équations découle de l'application de la théorie BML. L'introduction d'une pdf bimodale conduit tout d'abord à :

$$\overline{c''} = \tau \frac{\tilde{c}(1-\tilde{c})}{1+\tau \tilde{c}} \qquad (9)$$

$$\overline{u_i w} = - \tilde{w} \frac{\overline{\rho u_i'' c''}}{\bar{\rho} \, \tilde{c}(1-\tilde{c})} (\tilde{c} - \phi_m) \qquad (10)$$

où ϕ_m est une constante

et

$$\overline{\rho u_i'' u_k'' c''} = \frac{(1 - 2\tilde{c})}{\bar{\rho}} \frac{\overline{\rho u_i'' c''} \, \overline{\rho u_k'' c''}}{\tilde{c}(1-\tilde{c})} \qquad (11)$$

Par ailleurs $\tilde{\varepsilon}_{ic}$ est exprimée par :

$$\bar{\rho} \, \tilde{\varepsilon}_{ic} = k_{ic} \frac{1+\tau}{1+\tau \tilde{c}} \overline{\rho u_i'' c''} \qquad (12)$$

Les équations (9)-(12) ont été utilisées et testées dans le cas d'un écoulement réactif elliptique, simple : une flamme stabilisée au voisinage d'un point de stagnation /11/.

3. METHODE DE CALCUL

La mise au point d'un code de calcul applicable aux écoulements stationnaires elliptiques ou 2-D instationnaires paraboliques a été faite en 3 étapes qui peuvent être décrites comme il suit :

- mise au point de la méthode numérique dans le cas d'un écoulement incompressible non réactif et validation par application à un écoulement connu,
- étude de la sous couche visqueuse et des taux de frottement de la paroi. Résolution du problème posé par la prise en compte d'une injection pariétale,
- mise en place du système complet d'équations tel qu'il est décrit au paragraphe précédent, et application au cas de l'écoulement dans un canal 2-D avec injection du prémélange frais.

La méthode implicite aux différences finies utilisée est celle développée initialement par BEAM et WARMING /12/ et peut être brièvement décrite comme il suit :

Les équations y sont résolues sous la forme conservative suivante :

$$\frac{\partial f}{\partial t} + \frac{\partial F}{\partial x} + \frac{\partial G}{\partial y} = S \qquad (13)$$

où S représente l'ensemble des termes source.

Ces équations sont résolues par factorisation d'opérateurs associée à une linéarisation des termes conservatifs de la forme suivante :

$$\left(\frac{\partial M}{\partial x}\right)^{(n+1)} = \left(\frac{\partial M}{\partial x}\right)^{(n)} + \frac{\partial (A^{(n)} . (f^{(n+1)} - f^{(n)}))}{\partial x} + O(\Delta t^2) \qquad (14)$$

où $A^{(n)}$ est la matrice Jacobienne telle que :

$$A_{ij}^{(n)} = \frac{\partial M_i^{(n)}}{\partial f_j} \qquad (15)$$

et la discrétisation temporelle s'écrit :

$$f^{(n+1)} = f^{(n)} + \frac{\Delta t}{2} \left(\left(\frac{\partial f}{\partial t}\right)^{(n)} + \left(\frac{\partial f}{\partial t}\right)^{(n+1)} \right) \qquad (16)$$

La discrétisation spatiale étant de type centré, les équations (13) se ramènent à un système tridiagonal par blocs, chaque bloc étant une matrice carrée dont l'ordre est le nombre de fonctions inconnues. En ce qui concerne le problème traité dans cet article, les fonctions inconnues sont $\tilde{\rho}$, u, v, $\bar{p}$, $\tilde{c}$, $\tilde{k}$, $\tilde{\varepsilon}$ si on envisage une fermeture de type gradient et $\tilde{\rho}$, u, v, $\bar{p}$, c, k, $\overline{\rho u''c''}$, $\overline{\rho v''c''}$ dans le cas plus général décrit au paragraphe précédant.

Les conditions limites utilisées au voisinage des parois solides sont les conditions d'adhérence : $\tilde{u} = \tilde{v} = c = 0$ $k = \overline{\rho u''c''} = \overline{\rho v''c''} = 0$. Ceci nécessite la prise en compte de la sous couche visqueuse par le calcul. Pour cela le maillage est transformé par le changement de variable suivant /13/ :

$$\bar{x} = x$$

$$\bar{y} = 1 - \frac{Ln[\beta+1 - (y/h))/(\beta-1 + y/h)]}{Ln\ [(\beta+1)/(\beta-1)]}$$

$$1 < \beta < \infty$$

où h est la demi-hauteur du canal.

Cette transformation conduit à une accumulation des points pour les petites valeurs de y et permet donc de tenir compte d'une sous couche visqueuse très fine par l'intermédiaire d'un nombre de points de calcul qui peut varier entre 5 et 10 (cf. figure 2).

En plus des conditions de parois un point important concerne les conditions limites à utiliser lorsqu'il y a injection de prémélange. Afin d'imposer un débit d'injection (c'est-à-dire pour éviter tout phénomène de refoulement) les contraintes suivantes ont été choisies :

$$u = 0, \qquad T = T_u$$

$$P_1^{(n+1)} = P_2^{(n)} + \delta P$$

les indices inférieurs notent les points de maillage, et supérieur le pas de temps. δP est ici un incrément de pression variant avec x mais non avec t.

Un calcul avec injection se déroule de la façon suivante :

i) à t = 0 les profils de vitesse dans le canal sont tels que :

$$u(y) = \min(u^+ = y^+,\ u^+ = \frac{1}{k} Ln\ y^+ + 5.25,\ \frac{u}{u_{axe}} = (y/h)^{1/6})$$

où $u^+ = \frac{u}{u_\tau}$ $\qquad u_\tau = \left(\frac{\tau_p}{\rho}\right)^{1/2}$

$$\tau_p = \left(\mu \frac{\partial u}{\partial y}\right)_{y=0}$$

où k est la constante de von KARMAN /14/

ii) à $t = t_{inj} > 0$ lorsque l'écoulement turbulent est établi dans le canal, on commence à injecter.

A ce moment les conditions d'entrée dans le canal (x=o) sont à débit fixé.

Avant d'effectuer un calcul complet, il a été nécessaire de procéder à des tests de validation du code de calcul en écoulement laminaire puis turbulent. Ces tests portent principalement sur la précision des résultats obtenus, par comparaison avec la solution exacte, dans le cas d'un écoulement couette, et la rapidité de convergence vers cette solution en fonction du maillage et du pas de temps. Par ailleurs, en

ce qui concerne les écoulements turbulents des tests ont été effectués sur les comportements des grandeurs et en particulier du champ de vitesse à la paroi.

Nous donnons ici les résultats de ces études préliminaires de validation :

1 - Application de la méthode au calcul d'un écoulement de Couette.

On considère l'écoulement d'un fluide à température constante dans un canal 2-D. A t = 0, le fluide est immobile et la paroi supérieure du canal se met en mouvement (vitesse u_o). Le pas de temps Δt choisi pour faire ce calcul est un multiple du pas déterminé à l'aide du critère CFL[P]/16/ :

$$(\Delta t)_{CFL} = \frac{1}{\frac{|u|}{\Delta x} + \frac{|u|}{\Delta y} + a_o \sqrt{\frac{1}{\Delta x^2} + \frac{1}{\Delta y^2}} + 2\nu \left(\frac{1}{\Delta x^2} + \frac{1}{\Delta y^2}\right)}$$

qui est en général limité par l'acoustique.

En toute rigueur l'évolution instationnaire exacte ne pourra être représentée qu'en prenant un pas de temps égal au maximum à $(\Delta t)_{CFL}$. C'est le calcul représenté sur la figure 3a où une comparaison avec la solution exacte du problème est établie.

Dans les 3 figures suivantes (fig. 3b, c, d) l'état stationnaire u/u_o = 1 - y/h est obtenu avec différents pas de temps, jusqu'à $\Delta t = 50\ (\Delta t)_{CFL}$. L'évolution instationnaire est de plus en plus mal représentée mais en revanche l'état stationnaire est obtenu pour un nombre de pas de temps (NDT.Δt) de plus en plus petit. Les figures 4.a et 4.b montrent l'erreur relative faite sur le calcul du champ de vitesse en fonction du maillage.

2 - Calcul d'un écoulement turbulent dans un canal 2-D.

On considère maintenant l'écoulement turbulent établi dans un canal 2-D de hauteur 2 h. Le nombre de Reynolds Re_{2h} est calculé pour une viscosité ν dépendant de la température du fluide.

La comparaison des champs de vitesse u calculé et mesuré est effectuée sur la figure 5.

En ce qui concerne la sous-couche visqueuse une étude fine a été faite sur l'évolution du profil de vitesse $u^+ = f(y^+)$ et du coefficient de frottement $C_f(Re_{2h})$ avec u^+ et y^+ définis précédemment, le coefficient de frottement étant défini par /17/ :

$$C_f = \frac{\bar{\tau}_p}{\frac{1}{2}\rho_e u_e^2}$$

Les résultats sont illustrés par les figures 6.a et 6.b qui correspondent à des calculs faits avec une dizaine de points dans la sous couche visqueuse (utilisant la transformation (17)). L'évolution de l'épaisseur de la sous-couche visqueuse en fonction du nombre de Reynolds Re_{2h} est décrite par la figure 6.a et celle du coefficient du frottement par la figure 6.b.

4. RESULTATS EXPERIMENTAUX

Les mesures ont été effectuées à l'aide d'un montage expérimental schématisé sur la figure 7 et qui comporte en série :

. un générateur de gaz chauds, constitué par une chambre de combustion dont les produits sont mélangés à de l'air frais pour en abaisser la température T_∞.

. une veine d'expérimentation de longueur 40 cm.

. un canal d'évacuation des gaz.

La paroi inférieure de la veine d'expérience est constituée d'une plaque poreuse à travers laquelle est injecté le mélange frais propane-air et les autres parois sont garnies de matériaux réfractaires. Dans ces conditions une zone de combustion turbulente est stabilisée à une distance de 2 à 3 cm au-dessus de la paroi, pour un nombre de Reynolds de l'écoulement principal suffisamment élevé.

Les mesures du champ de vitesse sont faites par l'intermédiaire d'une chaîne A.D.L. en ensemençant l'écoulement principal et l'écoulement (injecté) de gaz frais avec des particules de TiO_2 /18/. Deux configurations non réactive puis réactive ont été choisies, chacuns pour deux taux d'injection différents: 4 et 7%. Les profils de vitesse longitudinale dans le cas d'une injection d'air froid sont donnés sur la figure 8.a. Pour F = 7% le profil apparaît comme totalement décollé. Les fluctuations quadratiques moyennes correspondantes sont celles données sur la figure 8.b. Une comparaison montre que ces fluctuations de vitesse sont peu modifiées par l'injection, du moins dans le cas envisagé ici de forts taux de soufflage.

Le cas réactif est illustré par les figures 9.a et 9.b. La figure 9.a montre que le décollement du profil de vitesse se fait de façon similaire au cas sans combustion, mais en revanche l'accélération des gaz dus au dégagement de chaleur est clairement mise en évidence, principalement dans le cas où F = 7%. Comme le montre la figure 9.b pour des taux de soufflage supérieure à 4%, l'effet de l'injection sur les fluctuations de vitesse dans le canal est pratiquement négligeable.

5. CONCLUSION

Partant des résultats obtenus dans le cas d'écoulements de cisaillement simples, un modèle de combustion turbulente s'appuyant sur une fermeture du second ordre pour les transports turbulents de masse et d'énergie a été développé dans le cas d'écoulements de type elliptique. La validation de ce modèle a été effectué jusqu'à maintenant sur deux types de tests : la comparaison d'une part avec l'établissement d'un écoulement de Couette et d'autre part avec un écoulement turbulent dans un canal 2-D. Le calcul complet dans ce canal avec injection d'un prémélange est en cours.

REMERCIEMENTS

Cette étude a été effectuée dans le cadre du contrat n° 85-126 avec la Direction des Recherches, Etudes et Techniques.

REFERENCES

1 - MEUNIER S., Combustion turbulente en couche limite avec injection pariétale d'un mélange frais, Thèse de Docteur-Ingénieur, Université de Poitiers, 1982.
2 - BRAY KNC, LIBBY KNC, AIAA Journal, 19, 11, 1976.
3 - LIBBY P.A., BRAY K.N.C., AIAA Journal, 19, 1981.
4 - BRAY K.N.C., LIBBY P.A., MASUYA G. and MOSS J.B., Comb. Sci. and Tech., 25, 1981.
5 - BRAY K.N.C., LIBBY P.A.and MOSS J.B., Comb. and Flame, 61, 1985.
6 - CHAMPION M., LIBBY P.A., Comb. Sci. and Tech., 38, 1984.
7 - CHAMPION M., Comb. Sci. and Tech., 44, 1965.
8 - BRAY K.N.C., CHAMPION M., DAVE N. and LIBBY P.A., Comb. Sci. and Tech., 46, 1985.
9 - BRAY K.N.C., CHAMPION M. and LIBBY P.A., Comb. Sci. and Tech., sous presse 1987.
10 - MEUNIER S., CHAMPION M. et BELLET J.C., Comb. and Flame, 50, 1983.
11 - BRAY K.N.C., CHAMPION M. and LIBBY P.A., Comb. and Flame, soumis pour publication, 1987.
12 - BEAM R.M., WARMING R.F., AIAA Journal, 16, 4; 1978.
13 - ANDERSON D.A., TANNEHILL J.C. and PLETCHER R.H., Computational Fluid Mechanics and Heat transfer, Hemisphere Pub. 1984.
14 - HINZE J.O., Turbulence, Mac Graw Hill Ed. 2nd Edition 1972.
15 - ANDREWS G.R., BRADLEY D. and LWAKABAMBA S.B., Comb. and Flame, 24, 1975.
16 - VANDROMME D. HA MINH H. , Solution of the compressible Navier Stokes equations, Applications to complexe turbulent flows. Rapport TELET, 1986.
17 - SCHLICHTING H., Boundary layer theory, p. 38, Mc Graw-Hill, 1968.
18 - MOSS J.B., Comb. Sci. Tech., 22, pp. 119-129, 1980.

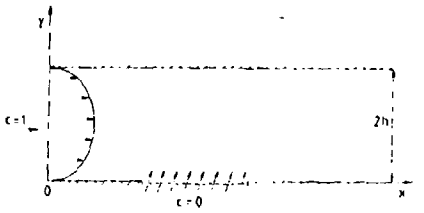

Fig. 1 - Configuration bidimensionnelle étudiée.

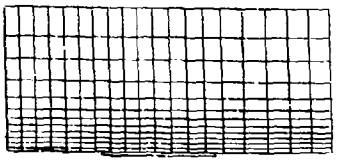

Fig. 2a - Maillage du domaine physique.

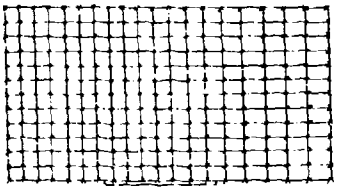

Fig. 2b - Maillage du domaine de calcul.

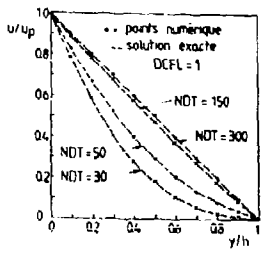

Fig. 3a - Calcul d'un écoulement de Couette (DCFL = 1)

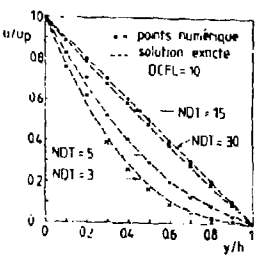

Fig. 3b - Calcul d'un écoulement de Couette (DCFL = 10)

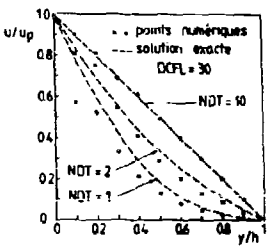

Fig. 3c - Calcul d'un écoulement de Couette (DCFL = 30)

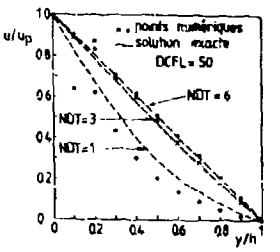

Fig. 3d - Calcul d'un écoulement de Couette (DCFL = 50)

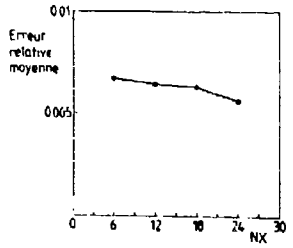

Fig. 4a - Calcul d'un écoulement de Couette : Influence sur l'erreur relative par rapport à la solution exacte du nombre de noeuds dans la direction ox.

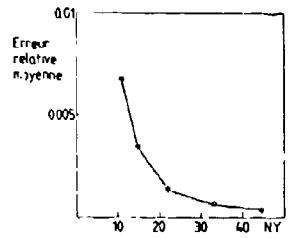

Fig. 4b - Calcul d'un écoulement de Couette : Influence sur l'erreur relative par rapport à la solution exacte du nombre de noeuds dans la direction oy.

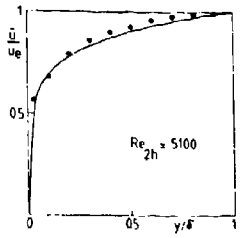

• points expérimentaux
— courbe numérique

Fig. 5 - Calcul d'un écoulement turbulent dans un canal 2D : Profil de vitesse moyenne, comparaison avec l'expérience.

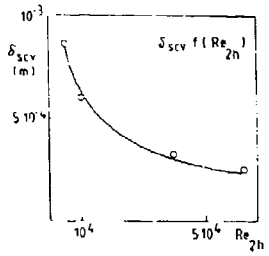

Fig. 6a - Calcul d'un écoulement turbulent dans un canal 2D : Influence du nombre de Reynolds de l'écoulement sur l'épaisseur de la sous-couche visqueuse.

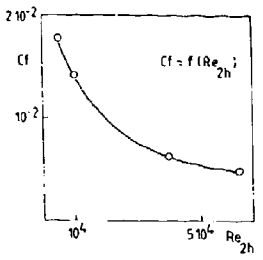

Fig. 6b - Calcul d'un écoulement turbulent dans un canal 2D : Influence du nombre de Reynolds de l'écoulement sur le coefficient de frottement.

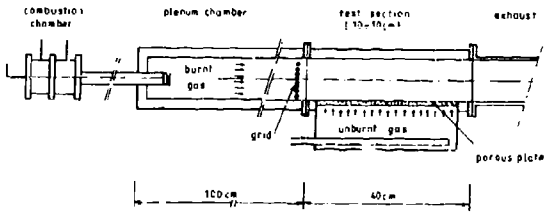

Fig. 7 - Dispositif expérimental.

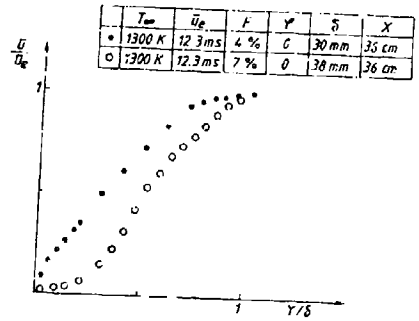

Fig. 8a - Ecoulement dans un canal 2D avec injection d'air froid, profil expérimental de vitesse moyenne.

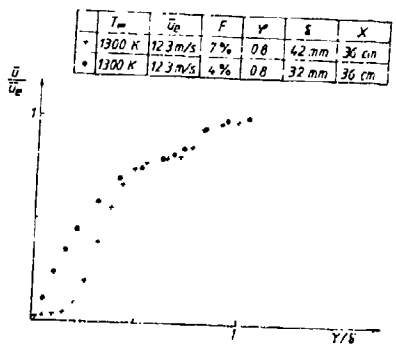

Fig. 9a - Injection d'un prémélange air-propane : profil expérimental de vitesse moyenne.

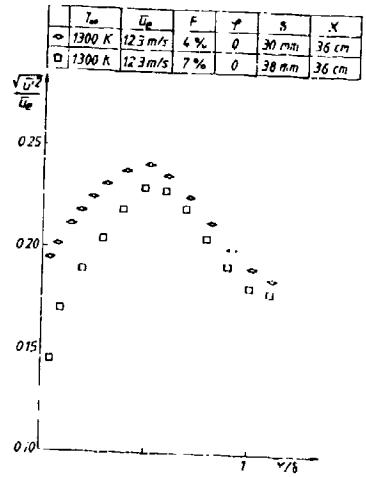

Fig. 8b - Ecoulement dans un canal 2D avec injection d'air froid, profil expérimental des fluctuations quadratiques moyennes de vitesse longitudinale.

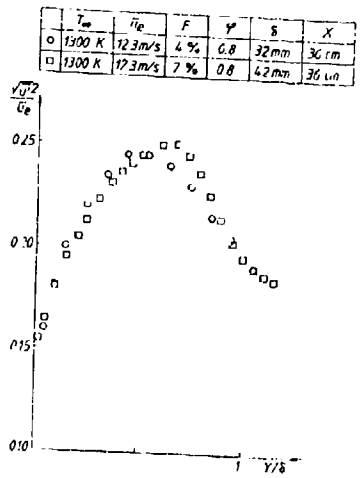

Fig. 9b - Injection d'un prémélange air-propane : profil expérimental des fluctuations quadratiques moyennes de vitesse longitudinale.

Modelling of CO Oxidation in Dilution Jet Flows

Chleboun, P.V.[+], Hubbert, K.P.[*], and Sheppard, C.G.W.[x]

+ formerly of Rolls-Royce plc, now at:
Racal Defence Electronics (Radar) Limited, Walton-on-Thames, Surrey, KT12, 3PS.
* formerly of Leeds University, now at:
Proudman Oceanographic Laboratory, Bidston Observatory, Merseyside, L43 7RA.
x Department of Mechanical Engineering, Leeds University, Leeds LS2 9JT, UK.

SUMMARY

Existing equilibrium chemistry and laminar flamelet computer codes are inadequate for calculation of "post-flame" carbon monoxide burn-up in gas turbine combustion chamber dilution zones. The amount of reaction occurring in such zones is small, but significant in terms of CO emissions, especially under low power conditions. A method has been developed, based on a "small departure from equilibrium" concept, which shows promise in modelling dilution zone carbon monoxide oxidation rate. The procedure, when incorporated into the Rolls-Royce PACE program, still only requires specification of a one-dimensional probability function and entails just one extra conservation equation. Output data have been compared with those measured experimentally in an idealized dilution zone.

LIST OF SYMBOLS

c	CO mass fraction
c_e	equilibrium CO mass fraction
C_{g2}	constant in dissipation equation
f	fuel fraction
f''	favre averaged fluctuation of f
k	turbulent kinetic energy
r_{CO}	rate of formation of CO mass fraction
t	time
u_i	velocity in direction i
x_i	coordinate in direction i
$A(E)$	CO "driving function"
CO	carbon monoxide
CO_e	equilibrium carbon monoxide
COEI	carbon monoxide emission index
D	departure of CO mass fraction from equilbrium
P(f)	probability density function for fuel fraction
S_c	schmidt number
ε	turbulent energy dissipation rate
ρ	density
μ	laminar viscosity
Γ_{eff}	effective diffusion coefficient
χ	scalar dissipation
$\bar{}$	time averaged
$\tilde{}$	favre averaged
[i]	molar concentration of species i

INTRODUCTION

Recent years have seen much progress in the mathematical modelling of gas turbine combustion chambers. These models generally use finite difference algorithms for the solution of mass, momentum and energy conservation equations, with k-ε or alternative turbulence sub-models (1). Early variants of such programs generally invoked the infinitely fast chemistry assumption; that reaction proceeds instantaneously to thermochemical equilibrium as gases mix. Coupled with the assumptions of equal species and thermal diffusivities, and negligible heat loss to the surroundings, the instantaneous thermodynamic state can then be expressed in terms of a single conserved scalar. Local mean values of species mass fractions, temperature etc. can then be determined for turbulent flow in terms of this scalar, integrated for some probability density function (pdf). Programs of this type, such as the Rolls-Royce PACE code initially developed by Jones and Priddin (2), have been successfully applied to (for example) compute combustor turbine entry temperature profiles (3).

The "instantaneous equilibrium" concept is likely to prove inadequate for gas turbine combustor primary zones, where reaction is incomplete (4). More recent developments using the "laminar flamelet" approach to express species concentrations, heat release and temperature in terms of a single reaction progress variable offer a more realistic approach (5). However, it is unlikely that either equilibrium or laminar flamelet models could accurately predict burner carbon monoxide (CO) concentrations with, and emissions from, a dilution zone. Oxidation of CO proceeds at a much slower rate than the reactions associated with the initial breakdown of the hydrocarbon fuel, at a rate comparable with transport processes. Clearly the equilibrium model is not valid in these circumstances; CO emissions are well above equilibrium levels (6). It is also unlikely that a flamelet

model can cope with a chemical reaction rate dominated process in a post reaction zone, as already burned gases try to approach a new chemical equilibrium following the mixing of dilution air.

Even for simple hydrocarbons, chemical reaction mechanisms are complex and uncertain; similarly rate constants for constituent reactions are subject to wide tolerances. It is not considered practical to incorporate even a simplified hydrocarbon reaction scheme (7) into a three dimensional iterative code, such as the PACE computer program, in order correctly to model CO oxidation for engineering applications. In addition to the chemical uncertainties, density would need calculation at every node in each iteration step; also the reaction rate would be very dependent on the (unknown) pdf of temperature. However, the output of combustion products from a modern high efficiency gas turbine combustor primary zone is characterized by low unburned hydrocarbon levels - such that the principal hydrocarbon reaction proceeding in the dilution zone is the oxidation/recombination/quenching of carbon monoxide. Under these conditions CO oxidation may be considered in terms of a single, uncoupled, reaction. In the currently reported work, CO oxidation in an idealized gas turbine combustor dilution zone has been modelled using a variant of the Rolls-Royce PACE computer code. This version incorporates a "small departure from equilibrium" CO oxidation sub-model - along the lines suggested by the work of Bilger (8).

The computations have been carried out for the idealized dilution zone shown in Fig. 1. This facility comprises a 175 mm diameter turbular burner; it has a primary zone which burns propane and an extended intermediate zone to allow essentially uniform conditions to be attained at entry to a dilution zone. The dilution zone has eight, annulus fed, 25.4 mm plain dilution holes. The facility, together with its associated gas analysis and other instrumentation, have been described more fully in an earlier publication (9). Computed CO concentrations are compared with those obtained using the standard PACE equilibrium chemistry sub-model, and with some preliminary experimental data.

CARBON MONOXIDE OXIDATION

Westenberg (10) has suggested that lean premixed hydrocarbon-air combustion may be considered to occur in two stages. Initially, free atoms and radicals are generated; these react very rapidly with the fuel, converting the carbon content to CO. In this first phase of burning most heat release occurs, such that the adiabatic flame temperature is approached. This condition is particularly likely to obtain in the mixing zone of the current test chamber, where combustion efficiency exceeds 90% at entry to the dilution zone. Westenberg also suggested that fast bimolecular reactions would result in radicals such as OH and H rapidly approaching their equilibrium concentrations at the adiabatic flame temperature. It was suggested that the somewhat slower oxidation of CO to CO_2, as well as NO formation, could be considered to occur in a second stage of combustion - of effectively constant temperature and radical concentrations. In this later phase of burning, the principal CO oxidation reaction is given by (10):

$$CO + OH \rightleftharpoons CO_2 + H \qquad (1)$$

For this reaction, invoking carbon conservation it can be shown that (10,11):

$$\frac{d[CO]}{dt} = -k_1 [OH]_e \left\{ 1 + \frac{[CO]_e}{[CO_2]_e} \right\} \left([CO] - [CO]_e \right) \qquad (2)$$

where k_1 is the forward rate constant for the reaction and [i] represents the molar concentration of species i.

The term $-k_1[OH]_e$ is, via temperature dependence, a strong function of equivalence ratio (or fuel fraction). For lean mixtures, at moderate temperatures, $[CO]_e \ll [CO_2]_e$. Hence the CO oxidation rate is simply a function of the departure of CO from its equilibrium concentration and the fuel fraction. Equation (2) may be recast in terms of mass fractions (11,12):

$$r_{CO} = A(f) \cdot D \qquad (3)$$

where A(f) represents those terms which are functions of fuel fraction (f) and D is the departure of the CO mass fraction from equilibrium, i.e.

$$D = c - c_e \qquad (4)$$

where c, c_e are the CO and equilbrium CO mass fractions, respectively.

TURBULENCE MODELLING OF CO OXIDATION

Since the driving potential for the CO reaction is so dependent on equivalence ratio, it is to be expected that in a turbulent reacting flow the temporal variation in fuel fraction will have a significant effect on the mean CO oxidation rate. The CO species conservation equation is:

$$\rho \frac{\partial c}{\partial t} + \rho u_i \frac{\partial c}{\partial x_i} - \frac{\partial}{\partial x_i}\left\{ \frac{\mu}{Sc} \cdot \frac{\partial c}{\partial x_i} \right\} - \rho r_{CO} = 0 \qquad (5)$$

From Eqs. (4) and (5), one may derive a conservation equation for the departure of the CO mass fraction from its equilibrium level, D:

$$\rho \frac{\partial D}{\partial t} + \rho u_i \frac{\partial D}{\partial x_i} - \frac{\partial}{\partial x_i}\left\{\frac{\mu}{Sc}\frac{\partial D}{\partial x_i}\right\} - \rho A(f)D - \frac{\mu}{Sc}\frac{\partial f}{\partial x_i}\frac{\partial f}{\partial x_i}\frac{\partial^2 c_e}{\partial f^2} = 0 \qquad (6)$$

which, favre averaged (or mass weighted) for steady state flow, yields:

$$\tilde{\rho u}_i \frac{\partial \tilde{D}}{\partial x_i} - \frac{\partial}{\partial x_i}\left\{\Gamma_{eff}\frac{\partial \tilde{D}}{\partial x_i}\right\} - \overline{\rho A(f)D} - \left\{\overline{\frac{\mu}{Sc}\frac{\partial f}{\partial x_i}\frac{\partial f}{\partial x_i}\frac{\partial^2 c_e}{\partial f^2}}\right\} = 0 \qquad (7)$$

In dilution zones, particularly that modelled in the present work, local values of D are determined by the mixing conditions in the primary zone; they are only weakly dependent on the instantaneous value of the fuel fraction. Hence A(f) is assumed to be statistically independent of D. The last term in Eq. 7 represents a source term due to mixing and contains the scalar dissipation χ,

where, $$\chi \equiv \frac{2\mu}{\rho Sc}\cdot\frac{\partial f''}{\partial x_i}\cdot\frac{\partial f''}{\partial x_i}$$

since, $$\frac{\partial f''}{\partial x_i} \gg \frac{\widetilde{\partial f}}{\partial x_i} \text{ and so, } \frac{\partial f}{\partial x_i} \simeq \frac{\partial f''}{\partial x_i}$$

where f'' is the turbulent fluctuation in the fuel fraction,

$$\text{i.e.} \qquad f = \tilde{f} + f''$$

Now χ and $\partial^2 c_e/\partial f^2$ are assumed to be statistically independent (β) and χ is modelled according to Spalding (13),

$$\text{i.e} \qquad \tilde{\chi} = C_{g2}\bar{\rho}\frac{\varepsilon}{k}\widetilde{f''^2} \qquad (8)$$

where Cg_2 is an empirical constant which also appears in the modelled equation.

With these assumptions, the modelled equation for the conservation of the departure from equilibrium of the CO mass fraction becomes:

$$\underset{I}{\tilde{\rho u}_i \frac{\partial \tilde{D}}{\partial x_i}} - \underset{II}{\frac{\partial}{\partial x_i}\left\{\Gamma_{eff}\cdot\frac{\partial \tilde{D}}{\partial x_i}\right\}} - \underset{III}{\overline{\rho A(f)}.\tilde{D}} - \underset{IV}{\frac{1}{2}C_{g2}\bar{\rho}\frac{\varepsilon}{k}\widetilde{f''^2}\left(\overline{\frac{\partial^2 c_e}{\partial f^2}}\right)} = 0 \qquad (9)$$

where, $$\overline{A(f)} = \int_0^1 A(f)P(f)df \qquad (10)$$

$$\left(\overline{\frac{\partial^2 c_e}{\partial f^2}}\right) = \int_0^1 \left(\frac{\partial^2 c_e}{\partial f^2}\right)P(f)df \qquad (11)$$

and P(f) is a one dimensional pdf describing the variation of f for the flow.

INCORPORATION INTO THE ROLLS-ROYCE PACE PROGRAM

The evaluation of A(f), $\partial^2 c_e/\partial f^2$ and c_e as functions of f was performed using a chemical equilibrium program similar to that of Gordon and McBride (14). The rate constant, k_1, was calculated using the values of Baulch et al. (15). The mean values of $\partial^2 c_e/\partial f^2$, A(f) and c_e were calculated in the PACE program using a standard Simpsons rule integration routine. The mean value of c_e was calculated from:

$$\tilde{c}_e = \int_0^1 c_e P(f)df \qquad (12)$$

The mean CO mass fraction was then calculated from

$$\tilde{c} = \tilde{c}_e + \tilde{D} \qquad (13)$$

A β-function pdf, as normally employed in the PACE program, was used; the transport equations were solved for the favre mean and variance of the fuel fraction.

PHYSICAL SIGNIFICANCE OF THE TERMS IN THE MODELLED EQUATION

In Eq. 9, terms I and II represent the convection and diffusion of the departure from equilibrium $\tilde{D}$, by the mean and turbulent motions. Term III represents the change in the departure from equilibrium due to chemical reaction. The multiplier term A(f) is shown plotted as a function of the fuel fraction, f, in Fig. 2; A(f) has been calculated for the fuel (propane), burner pressure (atmospheric), air and fuel temperatures (323 and 311K) appropriate to the burner shown in Fig.1.

This term clearly becomes important as stoichiometric conditions are approached (f = 0.06), where the equilibrium CO concentration and the adiabatic flame temperature are highest. Chemical reaction causes D to decrease, hence A(f) is negative. For overall lean conditions A(f) only becomes significant for high values of the fuel fraction variance, which is used in the calculation of the pdf over which A(f) is integrated.

Term IV represents the creation of non-equilibrium concentrations due to mixing, as described earlier. The equilibrium CO mass fraction (c_e) is low for lean mixtures, but increases very rapidly as stoichiometric conditions are approached (f = 0.06). It then rises more gradually to a maximum (at f = 0.15) before again falling, at first rapidly and then more gently towards zero for very rich mixtures. The resultant effects on $\partial^2 c_e / \partial f^2$, which appears in the mixing source term (IV in Eq.9), are shown in Fig. 2. The initial spike is associated with the rapid change in gradient as c_e rises abruptly towards the stoichiometric condition; the negative spike at the rich fuel fraction of 0.16 is similarly associated with the rapid fall in c_e for this mixture.

MODELLED CONDITIONS

Calculations were principally conducted for a mean primary zone equivalence rate of 0.38 (corresponding fuel fraction = 0.024); a condition representative of idling conditions, albeit at the atmospheric pressure restriction imposed by the burner being modelled. The primary and dilution air mass flow rates considered were .22 and .15 kgs^{-1} respectively.

The computational mesh used was 47 x 22 x 15 (x, y, θ), with the axial (x) grid lines concentrated in the region of the jet, the circumferential (θ) grid lines evenly spaced and the radial (y) grid lines chosen to avoid centreline convergence problems and to give greater accuracy in the wall region. Uniform (flat) profiles were assumed for all variables at both the dilution jet and the axial flow entry plane (75 mm upstream of the dilution jet centreline), except for CO concentrations; the latter were assumed equal to those experimentally measured at entry to the dilution zone.

The form of the mixing source term in the CO oxidation model was such that the effects of the inlet k and ε values were significant. Therefore some care was taken to ensure that realistic boundary condition values were used. A value of 33 m^{2}s^{-2} was used for k at the inlet to the main flow, consistent with the data reported earlier under similar conditions (9). The boundary value of ε was fixed at 900m^{2}s^{-3}, based on mixing length hypotheses in a duct. At the dilution jet entry boundary, values of k and ε were set at 10.6 and 700 respectively, these were based on mean calculated values from an earlier computation of the flow in the annulus (11).

Since the mean CO oxidation rate was sensitive to the pdf in fuel fraction, itself based on modelled fuel fraction mean and variance values, and since the mechanism being modelled was the quenching of the CO reaction, it was clearly important to set valid values for these boundary conditions.

For the non reacting flows reported earlier (9), for the identical geometry, r.m.s. temperature fluctuations of 55 K about a mean value of 715 K were typical at the axial flow entry plane. Under those conditions, the (adiabatic flame) temperature could be expected to be directly related to fuel fraction (f). Based on such a relationship between temperature and f, and the assumption that the ratio of $\tilde{f}$ to $\widetilde{f''^2}$ was the same for the earlier and current experimental conditions, an inlet value of $1.23.10^{-5}$ was adopted for the variance of fuel fraction ($\widetilde{f''^2}$) at the entry plane (11).

RESULTS

(a) Equivalence ratio 0.38

The measured combustion efficiency at the dilution zone entry plane was well above 90%, and the unburned hydrocarbon levels were low (< 200 ppm). It was therefore reasoned that heat release associated with any additional CO oxidation within the dilution zone would be small, and have minimal effect on the general character of the flow. Hence, in calculating the main mean flow features the standard PACE turbulent chemical equilibrium model was used. Computed streamlines, fuel fraction, and variance in fuel fraction distributions, for an axial plane through the centre of a dilution jet, are shown in Fig. 3. Corresponding data for a plane midway between two dilution jets are given in Fig. 4. The flow proved very similar to that for the low dilution jet flow case reported in reference (9). The low momentum dilution jet is swept back by the cross flow, such that the core of the flow close to the burner centreline remains largely undiluted until well downstream of the dilution jet plane. The distributions for $\widetilde{f''^2}$ clearly show regions of intense mixing activity at the leading edge of the jet, and to a lesser extent in the vortex behind the jet, as noted previously (9).

Shown in Fig. 5(a) are experimentally measured and computed fuel fractions, along radial lines in the axial plane through a jet centreline, at axial stations 75 mm upstream (entry) and 200 mm downstream (exit) of the plane of the dilution jets. The measured entry fuel fraction was essentially constant, the equivalent exit value showed some dilution at the burner centreline and more dilution with increasing radius - as suggested in Fig. 3. However, the measured exit fuel fraction was generally higher, and the maximum dilution occurred at a radius closer to the burner wall, than computed. This is consistent with the computation of greater dilution jet penetration observed before (9). Contours of CO concentration, computed using the method outlined previously, are shown in Fig. 6 for the two axial planes considered. The reductions in CO concentration along the burner centreline are largely due to further oxidation, as dilution at the centreline has been shown to be small, Figs. 3 and 4. In the regions closer to the dilution jet trajectory, the low CO concentrations are associated more with dilution than oxidation. Computed and experimental CO concentrations along radial lines at entry and exit from the dilution zone, corresponding to the fuel fractions shown in Fig. 5(a), are presented in

Fig. 5(b). The CO concentration at the entry plane is essentially constant in the central core of the flow, with some fall in the region closer to the wall. There is no corresponding fall in fuel fraction with increased radius, Fig. 5(a). It therefore seems most likely that the reduced CO concentration near the wall is associated with a lower temperature caused by heat loss to the wall. The measured inlet CO profile was also used to define the entry plane CO in the theoretical model. The corresponding experimental exit plane CO concentration shows a considerable reduction in mole fraction at the centreline, but that this reduction is smaller with increased radius. The lower centreline CO concentration is a result of further oxidation within this relatively undiluted region, the fall in CO concentration at the outer radii is more associated with dilution of quenched flow. This is shown more clearly in Fig. 7(a), where the CO levels are plotted in terms of emission index (gm CO per kg parent fuel) in an attempt to remove the dilution factor. The additional oxidation of CO in the central flow is evident; the apparently anomalous higher exit than entry COEI at the outer radius is likely to be associated with (high CO level) fluid quenched and transported by the dilution jet wakes to this region. If the upstream CO concentration had been subject to pure dilution (with no further oxidation), its downstream profile would be identical with that of any other conserved scalar. Then, for approximately uniform CO upstream concentration, one would have expected a downstream profile similar to that of $\bar{f}$ in Fig. 5(a), with a high CO concentration in the central flow and lower concentrations in the outer regions - quite opposite to the trend noted experimentally.

Exit plane CO concentrations, computed using the method outlined in this paper may be compared with the experimental values in Figs.5(b) and 7(a). The predicted trend is reasonably correct, more clearly so in terms of the emission index, although the computed concentrations are lower than the experimentally obtained values. The computed results are however, clearly closer to reality than one would have obtained by assuming pure dilution of the upstream CO, or by using the standard equilibrium chemistry model; this yields essentially zero CO concentrations throughout the dilution zone.

b. Equivalence ratio 0.9

As discussed previously, the bulk of the work has been for a simulated "idle" condition with equivalence ratio 0.38. However, some computations have been effected for an equivalence ratio of 0.9 at entry to the dilution zone - a condition more representative of full power, albeit at the same mass flow rates and pressure as before.

To date is has not proved possible to operate the test facility at this condition without overheating the intermediate zone. However, it was considered instructive to run the computer program for this condition in order to see if any quenching occurred upon dilution air addition. In the computations the revised values of $\bar{f}$, $\bar{f''^2}$, k and ε used for the axial flow were 0.0545, 6.5×10^{-5}, 42.6 and 1320 respectively. Uniform entry plane conditions, with CO concentrations at this plane equal to the relatively high equilibrium level, were assumed. Shown in Fig. 8 are the resultant computed streakline plots, mean and variance of the fuel fraction, CO and departure from equilibrium contours for an axial plane through the centre of a dilution hole. The latter have been plotted because, for these conditions the approach to equilibrium proved very rapid; the CO and equilibrium (CO_e) concentration contours hence look very similar, such that the departure from equilibrium contours are more informative. The only significant departures from equilibrium occur in the intense mixing regions, principally at the leading edge of the jet. Here rapid mixing results in partial quench of the CO oxidation, preventing the CO concentration falling fully to the lower levels appropriate to the local lower equivalence ratio. Shown in Fig. 7(b) are the computed CO and CO_e concentrations (in terms of emission index) along a radial line at the exit plane. These concentrations are high in the central richer and hotter flow, falling towards the outer wall as the dilution air mixes in. Although the CO levels are close to those at equilibrium, the differences (especially in the outer and cooler regions) are significant in terms of emissions standards. At the high pressure experienced by real combustors at full power conditions, one might expected a more rapid approach to equilibrium; since the CO oxidation rate is pressure sensitive (4,16).

DISCUSSION

The degree of agreement between computed and the limited experimental CO data currently available is considered encouraging. Part of the disagreement for the $\phi = 0.38$ case results from shortcomings in the scalar transport modelling, as previously reported (9) and as illustrated here in Figs. 3 and 5(a). The greater computed jet penetration and coherence will result in incorrect calculation of axial flow dilution, with higher temperatures maintained longer and consequently lower CO concentrations.

A sensitivity analysis of the effect of entry plane variance in fuel fraction has shown that the CO level for the flow close to the dilution zone centreline is sensitive to this parameter (11). The region of flow strongly affected by the dilution jets is less sensitive to the entry plane value of $\bar{f''^2}$, since this is overwhelmed by the turbulence generated in the jet shear layers. Experimental data for fluctuation in fuel fraction (or at least temperature) are clearly needed for the correct burner conditions, as the method used to estimate these may be inadequate. Alternatively one might include the upstream burner in the computational solution domain, or carry out separate calculations for this burner.

The solution technique developed is considered to have greater potential for predicting CO emissions than chemical equilibrium or laminar flamelet methods. It also has the

considerable benefits of requiring the solution of only one additional conservation equation and of needing specification of just a one-dimensional pdf - unlike multiple chemical reaction kinetic schemes. In the computations reported here, using the solution to similar problems to define the starting conditions, to perform 100 iterations for all the turbulent flow variables (including the Beta function turbulent equilibrium evaluation of the mean density) took 3.5 MB and 45 CPU minutes on an IBM 3081 mainframe computer.

The outlined solution method is only applicable to CO burnout, such as that in a dilution zone; its assumptions make it inapplicable to a highly reactive region, such as a primary zone. In order to apply the method to the dilution zone of a practical burner, as opposed to the highly idealized one used in the present study, it would be necessary to closely specify the dilution zone entry boundary conditions. Those generated by a program using an equilibrium chemistry model may well prove adequate for variables other than CO. However, equilibrium primary zone exit CO concentrations would certainly be incorrect at idling conditions; those generated by a laminar flamelet model might be more appropriate.

CONCLUSIONS

The small departure from equilibrium CO oxidation model offers a cost effective means of calculating super-equilibrium CO emissions. The procedure, when incorporated into a conventional finite difference computer code, such as PACE entails the solution of just one additional conservation equation (of standard form) and requires only a one-dimensional pdf.

For an idealized gas turbine combustor dilution zone, operating at an inlet equivalence ratio typical of idling conditions, the method is capable of generating solutions in good qualitative and reasonable quantitative agreement with the limited experimental data available. The computations are more realistic than those generated using a chemical equilibrium model.

At the higher equivalence ratios typical of full power conditions, a much closer approximation to thermochemical equilibrium CO levels is likely. However, the method used is capable of predicting departures of CO concentration from equilibrium which may be significant in terms of emissions standards.

REFERENCES

1. Jones, W.P. and Launder, B.E., "The prediction of laminarisation with a two equation model of turbulence", Int. J. Heat and Mass Trans. Vol 15, 1972, p301.
2. Jones, W.P. and Priddin, C.H., "Prediction of the flowfield and local gas composition in gas turbine combustors", XVII Symp. (Int.) on Combustion, Pittsburgh, The Combustion Institute, 1978.
3. Coupland, J. and Priddin, C.H., "Modelling the flow and combustion in a production gas turbine combustor", 5th Symp. on Turbulent Shear Flows, 1985.
4. de Chair, R.S., Sheppard, C.G.W. and Whittaker, M., "A note on carbon monoxide oxidation with particular reference to gas turbine combustion", Comb. Sci. and Tech. Vol 12, 1976, p245.
5. Liew, S.K., Bray, K.N.C. and Moss, J.B., "A flamelet model of turbulent non-premixed combustion", Comb. Sci. and Tech. Vol. 27, 1981, p69.
6. Verkamp, F.J., Verdouw, A.J. and Tomlinson, J.G., "Impact of emission regulations on future gas turbine engine combustors", AIAA Paper 73- 77, 1973.
7. Hautman, D.J., Dryer, F.L., Schug, K.P. and Glassman, I., "A multiple-step overall kinetic mechanism for the oxidation of hydrocarbons", Comb. Sci. and Tech. Vol. 25, 1981, p219.
8. Bilger, R.W., "Effects of kinetics and mixing in turbulent combustion", Comb. Sci. and Tech. Vol. 19, 1979, p89.
9. Chlebour, P.V., Nasser, S.H., Sebbowa, F.B. and Sheppard, C.G.W., "An investigation of the interaction between multiple dilution jets and combustion products", AGARD CP 353 1984, Paper No. 26.
10. Westenberg, A.A., "Kinetics of NO and CO in lean premixed hydrocarbon air flames", Comb. Sci. and Tech., Vol. 4, 1971, p59.
11. Chlebour, P.V., "Mathematical modelling relevant to gas turbine combustion, Ph.D. Thesis, in preparation, Leeds University 1987.
12. Hubbert, K.P., "Mixing and combustion in jets relevant to gas turbine burners", Ph.D. Thesis, in preparation, Leeds University, 1987.
13. Spalding, D.B., "Concentration fluctuations in a round turbulent free jet", Chem. Eng. Sci., Vol. 26, 1971, p95.
14. Gordon, F. and McBride, B.J., "Computer program for calculation of complex chemical equilibrium compositions, rocket performance, incident and reflected shocks, chapman-jougeut detonations", NASA SP273, 1971.
15. Baulch, D.L., Drysdale, D.D. and Lloyd, A.C., "High temperature reaction rate data", Leeds University, 1968.
16. Sheppard, C.G.W., "A simple model for CO oxidation in gas turbine combustors", Comb. Sci. and Tech. Vol. 11, 1975, p49.

ACKNOWLEDGEMENTS

The encouragement lent by Arthur Sotheran and the financial assistance of Rolls-Royce are gratefully acknowledged. Kevin Hubbert was supported by an SERC/Rolls-Royce CASE studentship. Thanks are also due to the contribution made by Derek Bradley in discussions on the work.

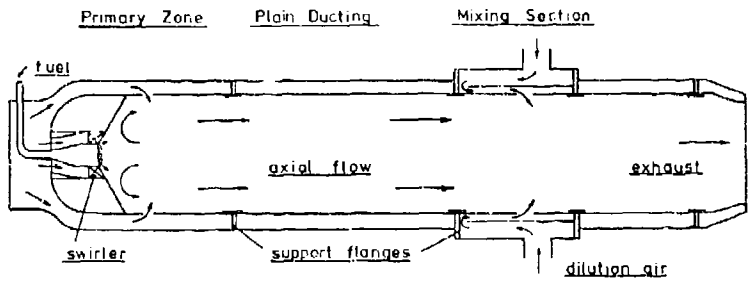

FIG.1. DIAGRAMMATIC REPRESENTATION OF COMBUSTOR DILUTION JET MIXING FACILITY

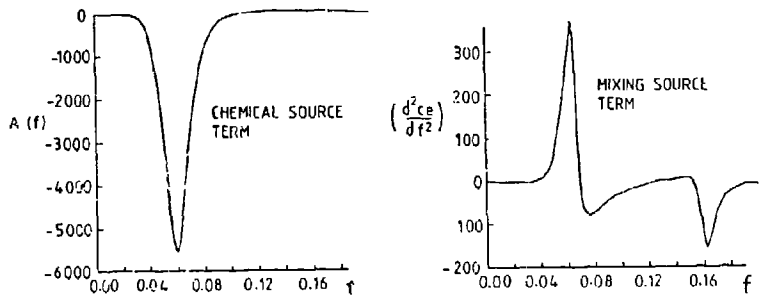

FIG.2. CHEMICAL AND MIXING SOURCE TERM VARIATION WITH FUEL FRACTION

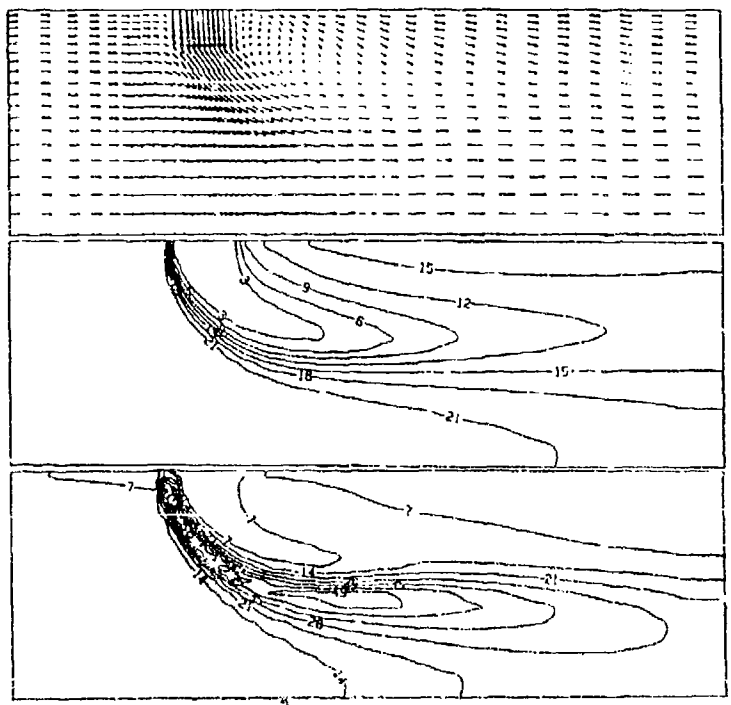

FIG.3. COMPUTED DATA FOR AXIAL PLANE THROUGH JET FOR ϕ = 0.38

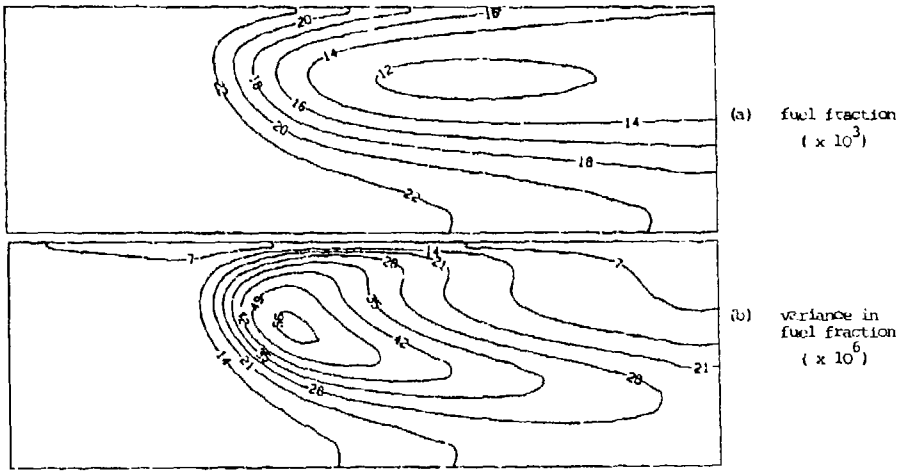

FIG.4. COMPUTED DATA FOR AXIAL PLANE BETWEEN JETS FOR ϕ = 0.38

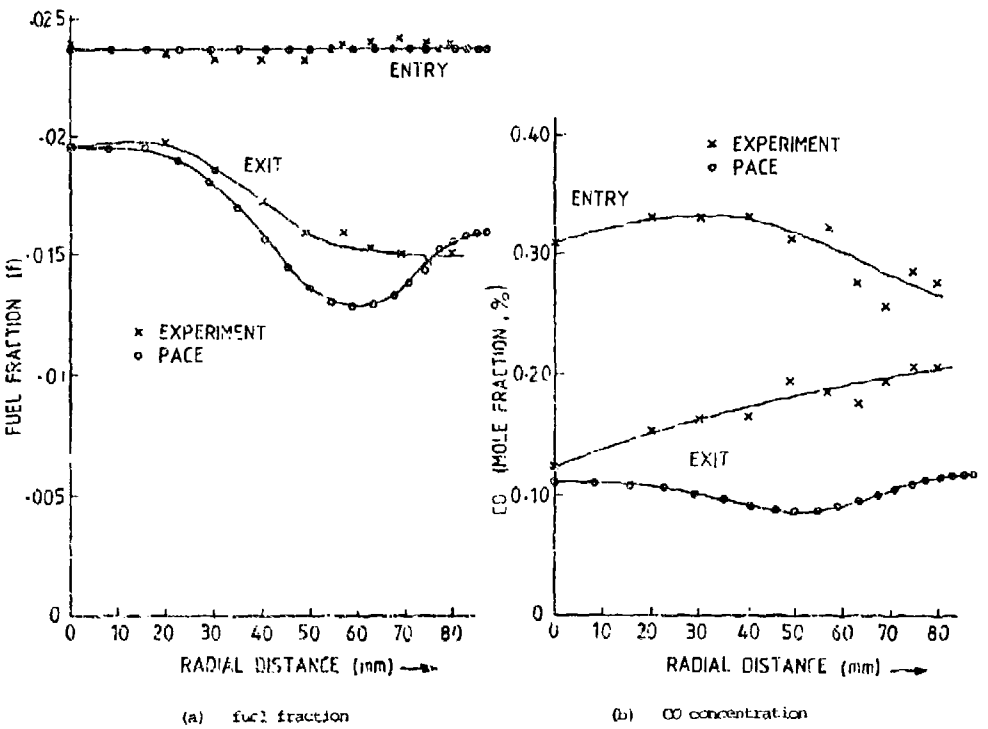

FIG.5. EXPERIMENTAL AND COMPUTED DATA FOR RADIAL LINES AT ENTRY AND EXIT PLANES

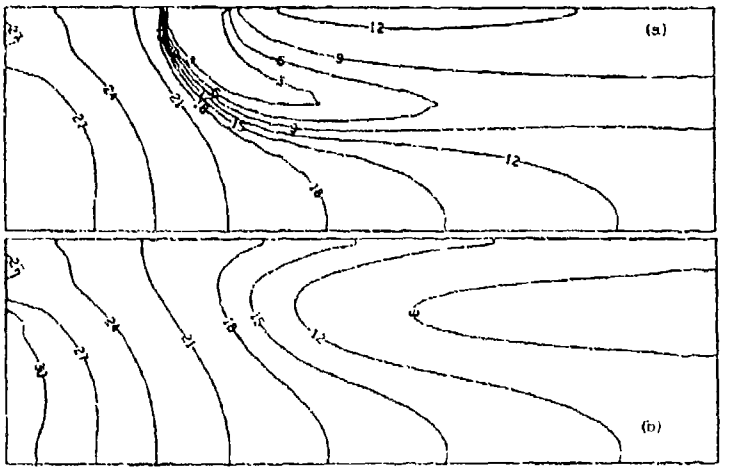

FIG.6. CO CONCENTRATION CONTOURS FOR AXIAL PLANES (a) THROUGH A DILUTION JET, AND (b) BETWEEN TWO JETS, FOR ϕ = 0.76

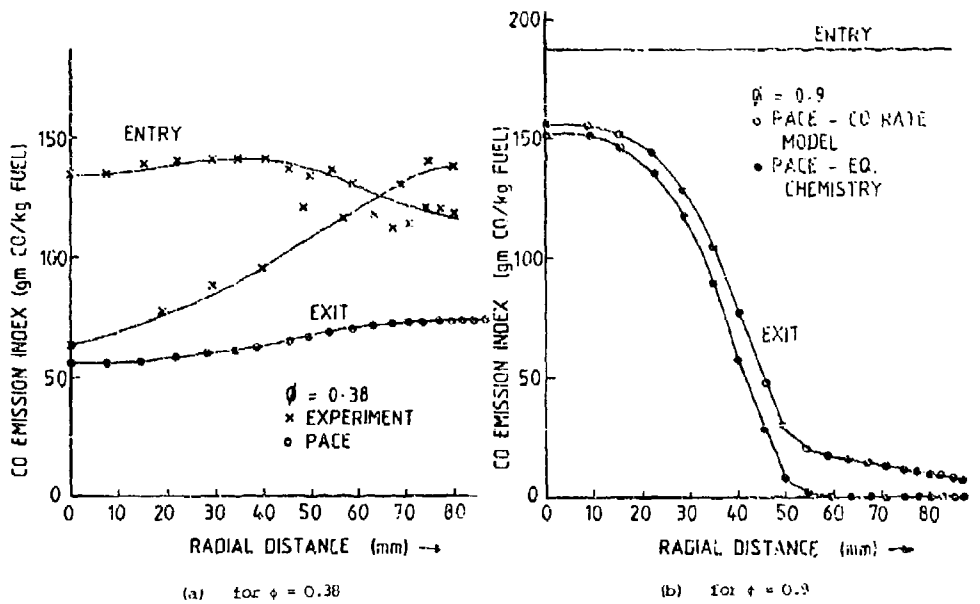

FIG.7. CO EMISSION INDEX VARIATION ALONG RADIAL LINES AT ENTRY AND EXIT PLANES

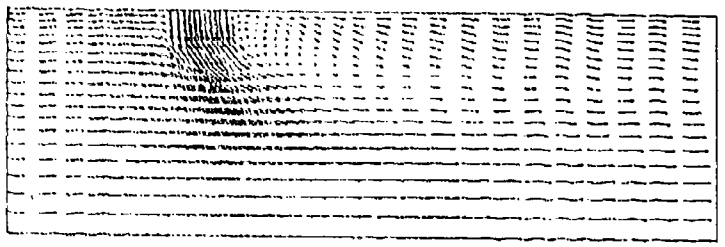

(a) streaklines

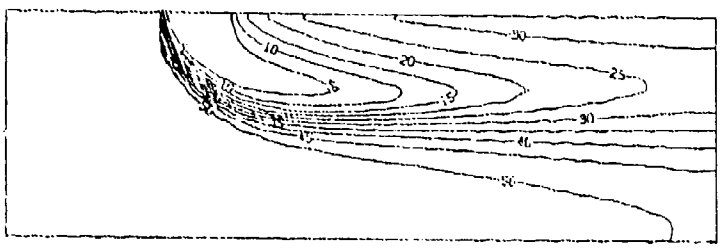

(b) fuel fraction (x 10^3)

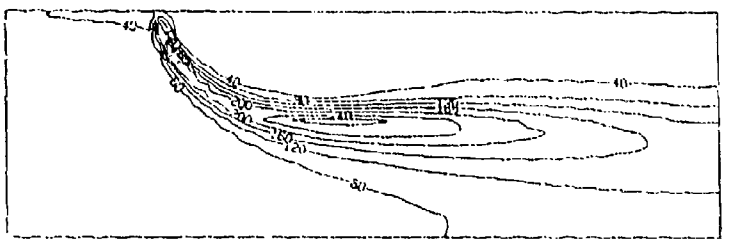

(c) variance in fuel fraction (x 10^6)

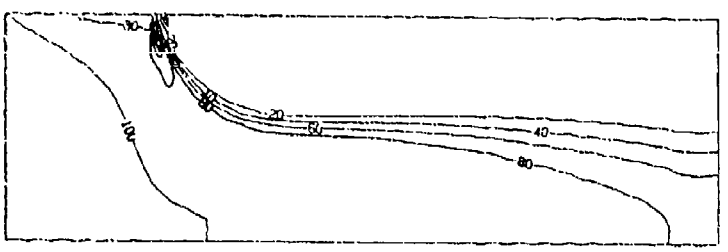

(d) CO concentration (x 10^4)

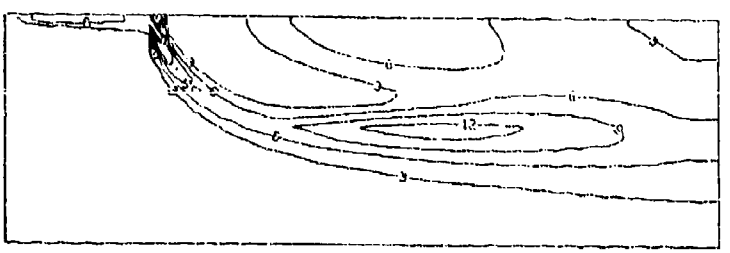

(e) departure of CO from equilibrium concentration (x 10^4)

FIG.8. COMPUTED DATA FOR AXIAL PLANE THROUGH JET FOR ξ = 0.9

DISCUSSION

J.Hanspal, UK

Why is it that experimental data are error-bar free? This is a feature not only for your presentation but most others. Does it mean that the errors are smaller than the data symbols? If not, it is very important to include them for relative comparison between experimental theory.

Author's Reply

The experimental data presented are only preliminary — insufficient data were collected to justify such error bars. Much more data is now being accumulated, and this will have error bars!

J.Odgers, CA

Your "flame" temperature term appears to be a function of equivalence ratio only. Do you take into account the effects of inlet temperature?

Author's Reply

The temperature used is the local adiabatic flame temperature. Since this is a function of both local equivalence ratio and reacted temperature, the air inlet temperature is automatically taken into account.

EFFET DE LA CONVECTION SUR L'EVAPORATION ET LA COMBUSTION D'UNE GOUTTE DE COMBUSTIBLE

par Dominique SCHERRER

Office National d'Etudes et de Recherches Aérospatiales
29, avenue de la Division Leclerc
92320 CHATILLON (France)

Résumé

On présente une étude numérique de la combustion d'une goutte dans un écoulement gazeux. Le principe de la méthode réside dans la résolution des équations de bilan instationnaires dans les deux phases par une technique implicite de volumes finis. Les résultats obtenus pour la loi de vaporisation sont comparés avec la loi semi-empirique de Ranz-Marshall : un accord satisfaisant est trouvé seulement dans le cas d'une vaporisation sans combustion, à un nombre de Reynolds suffisant. Les autres résultats sont les suivants :

- la traînée de la goutte est sensiblement diminuée par la vaporisation,
- les effets instationnaires dans la phase gazeuse disparaissent presque complètement du fait de la convection (exception faite de ceux éventuels liés à une cinétique de réaction finie, qui n'ont pas été étudiés ici),
- les vitesses induites à l'intérieur de la goutte ne sont pas suffisantes pour rendre négligeables les effets instationnaires dus au transfert de chaleur dans la phase liquide.

INFLUENCE OF THE CONVECTION ON EVAPORATION AND COMBUSTION OF A FUEL DROPLET

Abstract

A numerical model is presented for the combustion of a droplet in a gaseous flow. The method is based on the integration of the unsteady balance equations in the two phases. It uses a finite volumes implicit scheme. The results for the vaporization law are compared with the empirical law of Ranz-Marshall : a good agreement is found only in the case of pure vaporization (without combustion) at a sufficient Reynolds number. The other results are the following :

- the drag of the droplet is decreased by the vaporization,
- the unsteady effects in the gaseous phase become negligible with convection (except those due to finite rate reaction which are not studied here),
- the velocities inside the droplet are not sufficient to neglect the unsteady effects due to heat transfert in the liquid phase.

1. INTRODUCTION

Le calcul des écoulements réactifs dans les chambres de combustion fait très souvent appel à un modèle de combustion de goutte. C'est en particulier le cas dans les moteurs Diesel, les moteurs fusées et les turbomachines, le combustible étant injecté dans la chambre sous forme de gouttelettes issues de la pulvérisation de jets liquides. Les nombreux travaux effectués sur la combustion d'une goutte sont résumés dans les articles de revue de A. Williams [1], Faeth [2], C.K. Law [3] et Sirignano [4]. Malgré le nombre et l'importance de ces travaux, le modèle le plus utilisé reste la célèbre "loi du D^2", valable en l'absence de convection et issue de la théorie analytique déjà ancienne due à Godsave [5]. Cette loi stipule que, dans le cadre de certaines hypothèses (quasi-stationnarité, Lewis = 1, flamme infiniment mince), le carré du diamètre de la goutte diminue linéairement avec le temps : $d_b^2/dt = -K$, K étant

fonction de la diffusivité, de l'énergie apportée par les gaz chauds environnants et par la réaction chimique, et de la chaleur de vaporisation de la goutte. Dans le cas où la goutte est placée dans un écoulement gazeux de vitesse non nulle, Frössling, puis Ranz et Marshall [6] ont établi de façon semi-empirique que le taux d'évaporation instantané était multiplié par un facteur ne dépendant que du nombre de Reynolds et du nombre de Prandtl : $d\rho^3/dt = -K\ C(Re, Pr)$ avec $C = 1 + 0,3\ \sqrt{Re}\ Pr^{1/3}$. Cette loi repose évidemment sur les hypothèses parfois discutables de la "loi du D^2" et de plus l'expression du facteur correctif C n'a été établie que pour des cas de vaporisation sans combustion, mais sa facilité d'emploi et l'absence de modèles simples plus réalistes expliquent son utilisation quasi-exclusive. A défaut de mieux, il convient au moins de bien connaître l'influence des hypothèses de la "loi du D^2" ainsi que le domaine de validité de la correction de Ranz-Marshall. A cet effet, l'intérêt d'une simulation numérique est évident car elle permet de prendre en compte, simultanément ou non, tous les phénomènes physiques et chimiques en stationnaire ou en instationnaire. C'est cette approche qui a été choisie ici.

Une première étude, portant sur l'influence des hypothèses de la "loi du D^2" dans le cas d'une goutte immobile, a fait l'objet d'une publication antérieure [7]. Elle a mis en évidence l'importance des effets instationnaires dans la phase liquide (chauffage de la goutte), mais aussi dans la phase gazeuse lorsque la pression est élevée : dans ce cas, le temps de diffusion entre la goutte et la flamme ne peut plus être négligé par rapport à la durée de vie de la goutte, ce qui se traduit par un déphasage important entre la vaporisation et la combustion.

L'étude présentée ici porte sur l'influence de la convection (vitesse relative gaz-goutte) sur la combustion d'une goutte. Dans un premier temps, on présentera des résultats stationnaires sur la validité de la correction de Ranz-Marshall, et sur la traînée d'une goutte en combustion. Dans un second temps, on examinera deux aspects instationnaires liés à la convection : l'influence des vitesses internes sur le chauffage de la goutte, et l'effet d'une fluctuation de vitesse des gaz environnants. Bien que le modèle puisse les prendre en compte, les effets de la convection liés à une cinétique de réaction finie ne sont pas étudiés ici. Dwyer et Sanders [8] ont montré dans une étude récente que dans le cas d'une vitesse de gaz élevée et d'une réaction lente, ils se traduisaient par une flamme épaissie pouvant même se situer entièrement dans le sillage de la goutte.

2. CARACTERISTIQUES ET HYPOTHESES DU MODELE

L'objectif est ici l'étude du terme de convection $C = (dD^2/dt)/(dD^2/dt)_{vapot}$ et sa comparaison avec l'expression de Ranz-Marshall. Ce terme étant a priori indépendant du terme de diffusion $(d\rho^2/dt)_{vap}$, on se contente de l'étudier dans le cas de produits fictifs dotés de caractéristiques physicochimiques simplifiées. Ces simplifications ne sont toutefois pas intrinsèques au modèle et il est donc possible de s'en affranchir. Le principe de la modélisation est l'intégration numérique des équations de bilan instationnaires dans les deux phases liquide et gazeuse.

2.1. Phase gazeuse

- La phase gazeuse est traitée comme un fluide compressible visqueux.

- Les équations sont les équations de bilan de masse, quantité de mouvement et énergie. Elles incluent les termes de convection et de diffusion, les forces de pression et de viscosité, et les termes sources dus aux réactions chimiques. Elles sont écrites en coordonnées curvilignes, les lignes isocoordonnées définissant le maillage (fig. 1). Ce maillage suit la goutte dans son déplacement et dans la régression de son diamètre. Les vitesses sont exprimées par rapport au repère naturel lié à ce système de coordonnées. L'accélération de la goutte, donc du repère, est calculée à chaque instant en intégrant les forces de pression et de frottement exercées par le gaz sur la goutte.

- Les espèces chimiques en présence sont le combustible, l'oxydant et les produits de combustion, représentés par une seule espèce chimique.

- La réaction chimique est à une seule étape et à cinétique finie, choisie suffisamment rapide pour rester dans le cadre de l'hypothèse de flamme mince.

- La chaleur spécifique, la diffusivité de masse, la conductivité thermique et la viscosité sont indépendantes de la température et de la composition chimique.

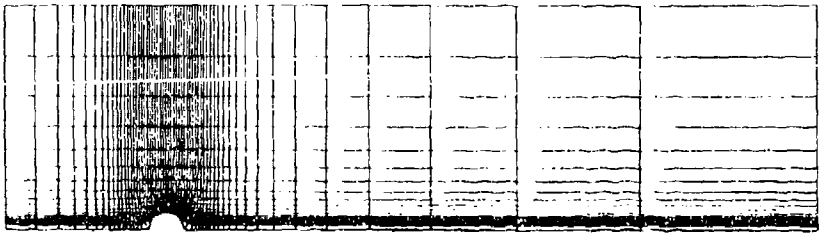

FIG. 1 - Maillage de la phase gazeuse

2.2. Phase liquide

- La phase liquide est traitée comme un fluide incompressible visqueux.

- Les vitesses au sein de la goutte sont définies par un tourbillon de Hill [10], qui est une solution exacte des équations de Navier-Stokes stationnaires, donnée par l'expression de la fonction de courant $\Psi = 1/2\ Ar^2(a^3-r^3)\sin^2\theta$, où a est le rayon de la goutte et A l'intensité du tourbillon. Cette hypothèse est justifiée par la valeur souvent élevée du nombre de Prandtl dans un liquide, ce qui permet de supposer que la diffusion de quantité de mouvement est quasi-stationnaire par rapport à la diffusion de la chaleur. L'inertie de la goutte est toutefois prise en compte par le calcul de l'intensité du tourbillon, obtenue à chaque instant en écrivant le bilan instationnaire de l'énergie cinétique de rotation de la goutte. Dans le milieu convectif ainsi défini, les températures sont calculées par le bilan instationnaire d'énergie sensible. Comme pour la phase gazeuse, cette équation est écrite en coordonnées curvilignes liées au maillage. Celui-ci (fig. 2) est évidemment construit de façon à se raccorder au maillage de la phase gazeuse.

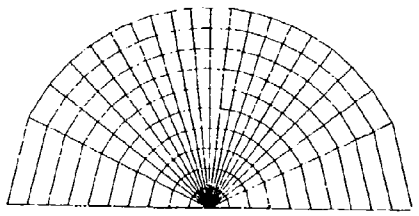

FIG. 2 - Maillage de la phase liquide

2.3. Interface liquide-gaz

- La continuité de la composante tangentielle de la vitesse est imposée à l'interface liquide-gaz. Il convient de noter que la représentation des vitesses dans la goutte par un tourbillon de Hill ne permet pas d'imposer également la continuité de la contrainte de cisaillement, ce qui ne devrait pas avoir d'effet notable sur les résultats dans la mesure où le bilan d'énergie global est correct.

- L'équilibre liquide-vapeur à la surface de la goutte est maintenu par une cinétique de vaporisation très rapide : $\Phi_{vap} = K\left[P_{sat}(T_{l,s}) - P_{vap}\right]$

- Le flux de chaleur arrivant sur la goutte sert d'une part à échauffer la goutte, d'autre part à la vaporiser :

$$\lambda_g\left(\frac{\partial T}{\partial r}\right)_{g,s} = \lambda_l\left(\frac{\partial T}{\partial r}\right)_{l,s} + L\,\Phi_{vap}$$

3. METHODE NUMERIQUE

Une des principales difficultés d'une telle étude réside dans la méthode numérique à mettre en oeuvre, tant pour la discrétisation spatiale que pour la technique d'integration en temps. Ces difficultés sont liées aux singularités de l'écoulement (point d'arrêt en amont de la goutte), à la présence de gradients élevés, et surtout à la coexistence de phénomènes dont les temps caractéristiques ont des ordres de grandeur très différents. Dans de telles conditions, seules les méthodes implicites sont envisageables, les méthodes explicites étant limitées en pas de temps par des critères de stabilité prohibitifs.

On a utilisé ici la méthode des directions alternées, avec un schéma entièrement implicite couplant entre elles toutes les équations. La linéarisation des termes non linéaires permet de traiter également ces termes en implicite. La discrétisation spatiale est basée sur la méthode des volumes finis centrés à maillage décalé, les cas de calcul à vitesse élevée nécessitant toutefois un décentrement amont des termes de convection.

4. RESULTATS

Le domaine de calcul est constitué par un tube cylindrique de révolution sur l'axe duquel est située la goutte. Les conditions imposées à l'entrée du tube sont l'enthalpie d'arrêt, la pression d'arrêt et la composition chimique. A la sortie, on impose la pression statique. La mise en vitesse de l'écoulement est obtenue en augmentant la pression d'arrêt et l'enthalpie d'arrêt à l'entrée. Dans tous les cas de calcul présentés ci-après, les principales grandeurs caractéristiques sont les suivantes :

- nombre de Lewis : 1
- nombre de Prandtl : 0,73
- coefficient de transfert de Spalding : B = 6 pour un écoulement "froid" (T_∞ = 500 K)
  23 pour un écoulement "chaud" (T_∞ = 3000 K)
- diamètre de la goutte : 100 µm

4.1. Résultats stationnaires

4.1.1. Description des différents régimes

Les resultats stationnaires sont obtenus pour une goutte fixe placée dans un écoulement de vitesse, température et composition chimique constantes. La température initiale de la goutte est égale à sa température de vaporisation, ce qui permet de supprimer la période de chauffage. Le rayon de la goutte est maintenu artificiellement constant.

Les figures 3, 4 et 5 représentent les champs de vitesse et les isothermes pour un nombre de Reynolds égale à 10, 100 et 200 respectivement. La température de l'écoulement amont est égale à 500 K, qui est aussi la température de vaporisation de la goutte. Pour les faibles valeurs du nombre de Reynolds (inférieure à 20), le régime de combustion est essentiellement diffusif : la flamme prend une forme elliptique mais reste assez éloignée de la surface de la goutte ; la vitesse normale du gaz à la surface de la goutte est comparable à la vitesse de l'écoulement amont (fig. 3). Pour les grands nombres de Reynolds (entre 50 et 100), la flamme est pratiquement collée à la goutte dans sa partie amont, et très étirée dans sa partie aval, car la diffusion ne peut plus remonter l'écoulement ; le régime de combustion est alors essentiellement convectif ; la vitesse normale du gaz à la surface de la goutte est nettement inférieure à la vitesse de l'écoulement amont (fig. 4). Lorsque le nombre de Reynolds dépasse 150, il apparait derrière la goutte une zone de recirculation qui modifie la forme des isothermes (fig. 5) : ceci se traduit par une légère augmentation des gradients thermique et chimique dans cette région, donc par une augmentation du débit vaporisé. Cette augmentation reste toutefois limitée car la majeure partie de la vaporisation a lieu sur la moitié amont de la surface de la goutte, comme le montre la figure 6 qui représente le taux de vaporisation en fonction de l'angle pour différents nombres de Reynolds.

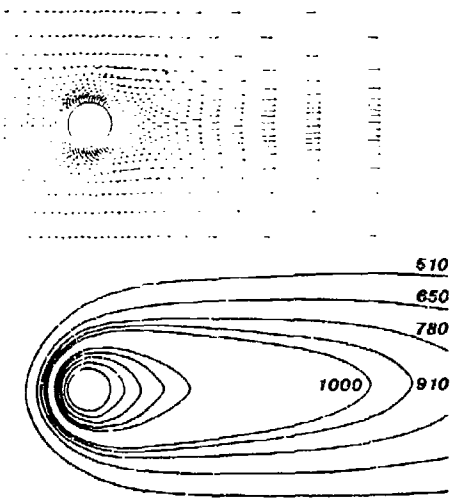

FIG. 3 - Champ de vitesses et isothermes
Re = 13

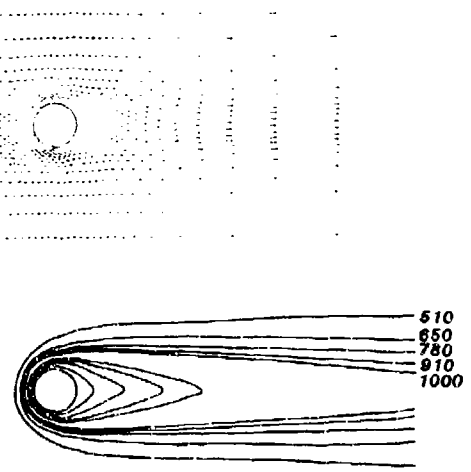

FIG. 4 - Champ des vitesses et isothermes
Re = 90

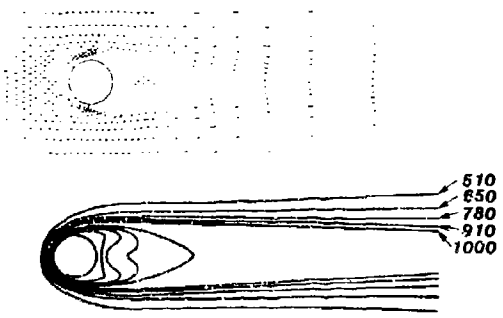

FIG. 5 - Champ des vitesses et isothermes
Re = 200

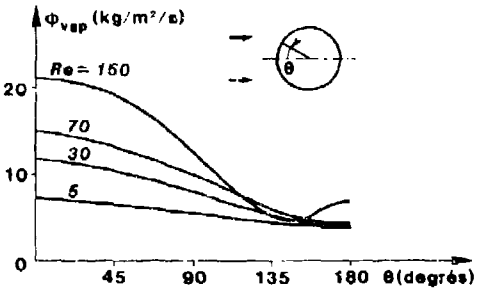

FIG. 6 - Variation du débit vaporisé en fonction de l'angle pour différents Reynolds

4.1.2. Evaluation du terme de convection C en fonction du nombre de Reynolds

Comme on l'a vu plus haut, le terme de convection est défini par :

$$C = \frac{d\,D^2}{dt} \Big/ \left(\frac{d\,D^2}{dt}\right)_{v=0}$$

La loi empirique de Ranz-Marshall, établie pour des cas de vaporisation sans combustion, donne $C = 1 + 0{,}3\ \sqrt{Re}\ Pr^{1/3}$, Re étant le nombre de Reynolds et Pr le nombre de Prandtl.

La figure 7 représente la comparaison entre cette loi et les résultats du modèle numérique, pour un écoulement chaud (3000 K) et pour un écoulement froid (500 K). Dans les deux cas, on note un écart important (allant jusqu'à 30 %) pour les faibles valeurs du nombre de Reynolds (inférieures à 10). Cet écart s'explique sans doute par le fait que le choix d'une loi en $\sqrt{Re}$ est basé sur l'existence d'une couche limite mince, ce qui n'est pas le cas à faible nombre de Reynolds. Pour les nombres de Reynolds élevés, l'accord est satisfaisant dans le cas d'un écoulement chaud, mais on note une différence assez sensible dans le cas de l'écoulement froid. Le cas de l'écoulement chaud étant assez proche d'une vaporisation sans combustion, l'accord entre le modèle numérique et la loi de Ranz-Marshall était prévisible dans ce cas. Dans le cas d'un écoulement froid, l'écart entre le modèle numérique et la loi de Ranz-Marshall peut s'expliquer par la forte diminution de densité liée à l'augmentation de température dans la flamme. On constate qu'on retrouve un accord satisfaisant dans tous les cas si dans la loi de Ranz-Marshall on remplace le nombre de Reynolds par un Reynolds modifié calculé à l'aide de la densité des gaz dans la flamme plutôt qu'à l'infini amont (fig. 8). La loi de Ranz-Marshall ainsi modifiée s'écrit :

$$C' = 1 + 0.3\ \sqrt{Re_m}\ Pr^{1/3} \quad \text{avec} \quad Re_m = \frac{\rho_f\, V_\infty\, D}{\mu} = Re\ \frac{\rho_f}{\rho_\infty}$$

Cette modification est évidemment sans effet en l'absence de combustion.

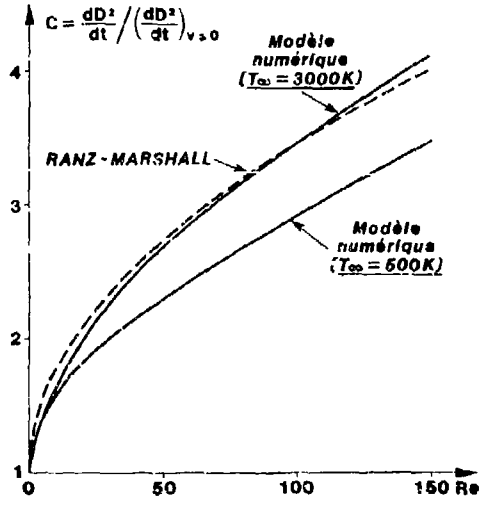

FIG. 7 - Terme de convection en fonction du nombre de Reynolds : comparaison entre le modèle numérique et la loi de Ranz-Marshall

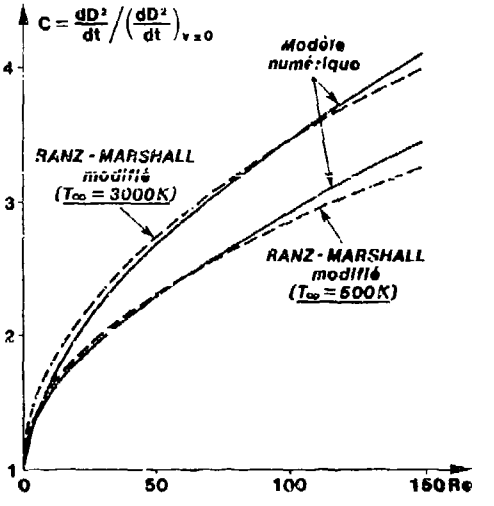

FIG. 8 - Terme de convection en fonction du nombre de Reynolds : comparaison entre le modèle numérique et la loi de Ranz-Marshall modifiée

4.1.3. Evaluation de la traînée de la goutte

La traînée de la goutte peut être calculée numériquement en intégrant sur la surface de la goutte la projection sur l'axe des forces de pression et de frottement, ces deux termes pouvant être calculés séparément. Un premier calcul effectué dans le cas d'une sphère solide dans un écoulement froid non réactif s'est avéré en bon accord avec la loi de traînée expérimentale exprimant le coefficient de traînée en fonction du nombre de Reynolds :

$$C_D = 24/Re\ (1 + 0{,}15\ Re^{0{,}687})$$

La figure 9 représente la loi de traînée obtenue par le modèle numérique pour une goutte en combustion dans un écoulement chaud (T_∞ = 3000 K). On constate que dès que le nombre de Reynolds dépasse 20, la partie frottement de la traînée s'annule presque complètement alors que la partie pression n'est pas affectée. Ceci est dû au soufflage de la couche limite par le débit vaporisé. Ce soufflage n'est efficace que si la couche limite est mince c'est-à-dire approximativement pour les nombres de Reynolds supérieurs à 20. La partie pression de la traînée n'est pas affectée car le débit vaporisé reste faible par rapport au débit arrivant sur la goutte. Pour des taux de vaporisation plus importants, il pourrait apparaître un effet de propulsion dû au fait que la vaporisation a lieu surtout dans la région du point d'arrêt amont : celà se traduirait par une augmentation de la traînée de pression.

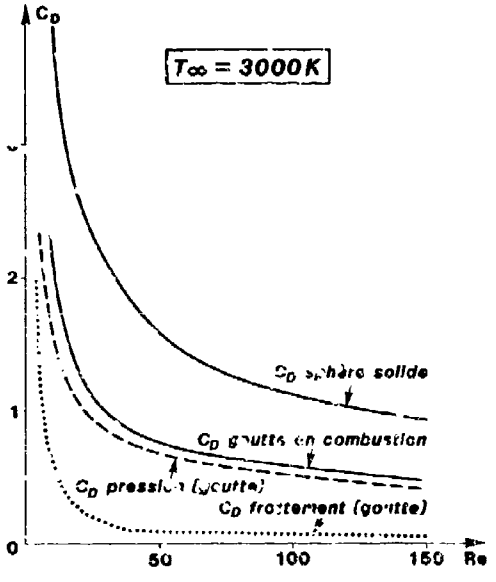

FIG. 9 - Coefficient de traînée d'une goutte en combustion dans un écoulement chaud

4.2. Résultats instationnaires

4.2.1. Etude de la période de chauffage de la goutte

On considère généralement que les vitesses à l'intérieur de la goutte ont pour effet d'uniformiser sa température pendant la période de chauffage de la goutte. Dans ce cas, celle-ci peut être prise en compte dans la loi de Ranz-Marshall de façon relativement simple. Sirignano [9] a montré que cette hypothèse était peu réaliste, ce que confirment les résultats de calcul effectués pour un nombre de Reynolds égal à 30. La figure 10 représente en fonction du temps le carré du diamètre ainsi que les températures minimale et maximale dans la goutte. Par rapport au cas d'une goutte initialement chaude, la durée de vie de la goutte est presque multipliée par deux : la période de chauffage de la goutte a donc une importance considérable, et ce d'autant plus que la pression est proche de la pression critique du combustible, ce qui est le cas de ce calcul. La figure 11 représente les isothermes dans la goutte, à un instant situé vers la moitié de la durée de vie de la goutte. On constate qu'elles ont pratiquement la forme des lignes de courant : celles-ci étant des lignes fermées, la convection ne permet pas de transmettre la chaleur vers le centre du tourbillon, ce qui explique la non-uniformité des températures dans la goutte. Ce résultat serait évidemment réalisé en cause si la représentation des vitesses internes par un tourbillon de Hill s'avérait peu réaliste, ce qui est possible.

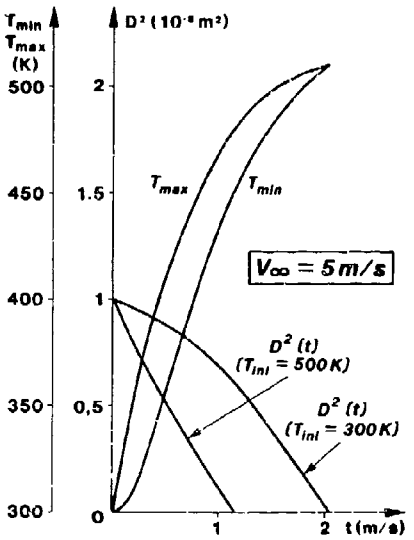

FIG. 10 - Influence du chauffage de la goutte : carré du diamètre, températures minimale et maximale de la goutte en fonction du temps pour un écoulement de vitesse

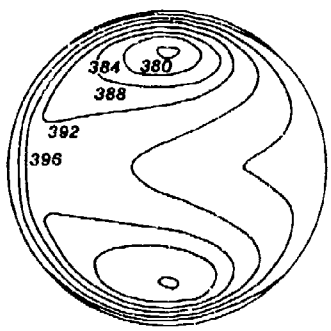

FIG. 11 - Isothermes dans la goutte Re = 30

4.2.2. Effet de fluctuations de la vitesse des gaz

Les fluctuations de vitesse de l'écoulement gazeux sont obtenues en faisant varier la pression d'arrêt et l'enthalpie d'arrêt de telle sorte que la vitesse suive une loi sinusoïdale. Des calculs ont été effectués pour différentes valeurs du nombre de Reynolds allant de 10 à 100, à des fréquences comprises entre 2000 et 10 000 Hz, et avec une amplitude égale à la moitié du niveau moyen. Les résultats ont montré que la réponse du débit vaporisé à de telles fluctuations se faisait sans gain et avec un retard très faible dont l'ordre de grandeur est égal à D/V_∞, D étant le diamètre de la goutte et V_∞ la vitesse de l'écoulement. Cette réponse peut donc être considérée comme quasi-stationnaire.

5. CONCLUSION

L'utilisation d'un modèle numérique bidimensionnel a permis d'effectuer l'étude de l'effet de la convection sur la combustion d'une goutte. Les principaux enseignements de cette étude sont résumés ci-dessous :

- lorsque le nombre de Reynolds est supérieur à 10, la loi de Ranz-Marshall a été confirmée par les résultats numériques dans le cas où l'énergie apportée par la réaction chimique est faible par rapport à celle apportée par l'écoulement amont. Une extension de la loi de Ranz-Marshall basée sur les résultats numériques a permis de tenir compte de la diminution de densité au niveau de la flamme lorsque l'énergie apportée par la réaction n'est pas faible devant celle apportée par l'écoulement ;

- la vaporisation de la goutte diminue sensiblement sa traînée lorsque le nombre de Reynolds est supérieur à 20 ;

- en accélérant tous les phénomènes de transport, la convection rend négligeables les effets instationnaires dans la phase gazeuse, à l'exclusion éventuelle de ceux liés à une cinétique de réaction finie, qui n'ont pas été étudiés ici. Par contre, les vitesses induites à l'intérieur de la goutte ne suffisent pas à uniformiser instantanément sa température, et les transferts de chaleur dans la goutte restent donc un aspect instationnaire non négligeable et difficile à prendre en compte de façon simple. Il faut de plus garder à l'esprit que, dans la réalité, les gouttes de petite taille sont rapidement entraînées par l'écoulement et on retrouve alors l'aspect instationnaire lié à la lenteur de la diffusion en phase gazeuse lorsque la pression est élevée.

Sur le plan quantitatif, ces résultats demandent à être étendus au cas le plus général de produits ayant des caractéristiques physico-chimiques quelconques. Ainsi, la dépendance des coefficients de transfert avec la température et la composition chimique impose d'utiliser dans la loi de Ranz-Marshall et dans la loi de traînée des valeurs moyennes judicieuses qu'il convient de préciser.

REFERENCES

[1] - WILLIAMS A., "Combustion of droplets of liquid fuels : a review", Combust. Flame, vol 21, pp. 1-31, 1973.

[2] - FAETH G.M., "Current status of droplet and liquid combustion", Prog. Energy Combust. Sc., vol 3, pp. 191-224, 1977.

[3] - LAW C.K., "Recent advances in droplet vaporization and combustion", Prog. Energy Combust. Sc., vol 8, pp. 171-201, 1982.

[4] - SIRIGNANO W.A., "Fuel droplet vaporization and spray combustion theory", Prog. Energy Combust. Sc., vol 9, pp. 291-322, 1983.

[5] - GODSAVE G.A.E., "Studies of the combustion of drops in a fuel spray : the burning of single droplets of fuel", 4th Symposium (Int.) on Combustion, Williams and Wilkins, pp. 818-830, Baltimore 1953.

[6] - RANZ W.E., MARSHALL W.R., Chem. Engr. Prog., vol 48, pp. 141-146, 173-190, 1952.

[7] - SCHERRER D., "Combustion d'une goutte immobile : étude numérique de l'influence des hypothèses conduisant à la "loi du D^2"", La Recherche Aérospatiale n° 5, pp. 311-322, 1985.

[8] - DWYER H.A., SANDERS B.R., "A detailled study of burning fuel droplets", 21st Symposium (Int.) on Combustion, 1986.

[9] - SIRIGNANO W.A., PRAKASH S., "Theory of convective droplet vaporization with unsteady heat transfer in the circulating liquid phase", Int. J. Heat Mass Transfer, vol 23, pp. 253-268, 1980.

DISCUSSION

C.Sanchez Tarifa Sener, SP

When modelling droplet combustion under forced convection conditions, the existence of the extinction limit of the envelope flame should be taken into account, which is a function of the Reynolds number, and the existence of a wake flame above this limit.

B.Noll, GE

How accurate are your results and how did you determine the accuracy?

Author's Reply

It is difficult to evaluate the global accuracy. The spatial scheme is second order accurate, except for high velocities which necessitate an upwind first order scheme for the convection. This should not cause an important error because the gradients in the concerned direction are very low.

B.Simon, GE

In your very detailed investigation you regarded difusion and convective transport. Do you believe that at very high temperatures, e.g. 3000K, the radiative heat transfer can be neglected?

Author's Reply

The radiative heat transfer at high temperature becomes important. But the temperature gradients are so important that they remain predominant.

ANALYSIS OF THE FLOW THROUGH DOUBLE SWIRL AIRBLAST ATOMIZERS

BY

E. Blumcke*, H. Eickhoff*, C. Hassa*, J. Koopman*

*Institut für Antriebstechnik, DFVLR, Postfach 90 60 58, D-5000 Köln 90, W-Germany

SUMMARY

In this contribution the flow field resulting from a counterswirl airblast atomizer has been investigated numerically and experimentally. The flow pattern shows the typical features of a swirling flow with an inner recirculation zone. Comparison of calculated results with experimental data shows that general features of the flow can be predicted with reasonable accuracy.

The propagation of the spray downstream from the atomizer has been investigated theoretically using a deterministic flow model for the liquid phase. The predictions demonstrate the influence of operating conditions on the spray characteristics.

1. INTRODUCTION

In gas turbine combustion chambers airblast nozzles are often used for fuel atomization, because they produce a fine spray over a wide range of operation. This requirement is particularly well fulfilled by counterswirl atomizers /1/. It is therefore the goal of this investigation to study the effects of swirl on the flow field as well as on the dispersion of fuel by application of theoretical as well as experimental methods. Here we are especially interested in the evaluation of an existing computer model in its ability to represent the rather complex features of the flow pattern of such a device.

A reverse flow annular combustor with a counterswirl nozzle is shown in Fig.1, /2/. The lower part shows a magnification of the nozzle. The counterrotating airstreams produce a mixing layer with strong shearing forces, that efficiently atomize the liquid film into a fine spray. The flow-field of the combustor is strongly dependent on the flow through the nozzle. For that reason the calculations are started already at the entrance of the swirl channels. Since a prescription of boundary values at the upstream boundary of the computational mesh is needed, further difficulties are introduced by the uncertainties of this step which are discussed in the second chapter.

In the following part of the paper, the theoretical basis of the flow models are briefly outlined and some features of the program used (CPTR) are highlighted. During the design of the experiment, special care was taken to reproduce the essential properties of an airblast atomizer and to gain optical access for LDA measurements at the points of interest. The experiment is described in the third chapter. The results of prediction and experiment are discussed and compared in the fourth chapter. Pressure and pressure loss are important parameters regarding the dispersion of fuel in the combustion chamber. Measurements of dropsize distributions are taken as the starting point of the two phase flow calculations. Their results are discussed in chapter five.

2. THEORY

Gas phase

The turbulent swirling flow is assumed to be stationary and axisymmetric. It is fully described by the conservation equations for mass and momentum. Using time averaged quantities and the standard K- ε -model, the equations are closed after prescription of suitable boundary values.

Block profiles are used as inlet conditions for velocity, turbulence energy and dissipation. The influence of these profiles on the calculated flow field, as well as the geometry of the swirler are discussed in the next chapter.

Liquid phase

On the assumption of a dilute spray, i.e. without droplet interactions the equations of table 1 are valid. The relevant forces acting on a drop are the aerodynamic drag force, the centrifugal force and the Coriolis force, which are in balance with the inertial force. In this representation, the forces are normalized with the droplet mass, thus loosing their dependence on droplet diameter with the exception of the aerodynamic drag force, which keeps an inverse proportionality. The deterministic droplet trajectories are defined by diameter and position for n droplet classes. The dropsize distributions are taken from measurements by Cao et al. /3/ made with the Fraunhofer diffraction particle sizer of Kayser /4/. In this instrument, photomultipliers are used as detectors which by virtue of their high sensitivity enable "frozen" measurements of the particulate flow. The measurements were evaluated with a two-parameter Rosin-Rammler model for the dropsize distribution. Information about the choice of initial droplet position and momentum is given in chapter five.

Numerical solution procedure

The calculations with the finite volume program are made using the Hybrid /5/ and the Quick /6/ discretization scheme. The Hybrid scheme uses a first order interpolation for the convective terms, whereas the Quick scheme uses a third order interpolation. On the assumption of the validity of the used physical model, the Quick scheme yields generally a better agreement of prediction with measurement. The equations for the pressure correction are solved using the pressure implicit operator (PISO) predictor corrector technique developed by Issa /7/. Local relaxation factors are calculated with the method of Neuberger /8/. The TDMA procedure working in alternating directions solves the resulting system of linear equations.

An example of a flow-field prediction for a rather complex geometry is depicted in Fig. 2. It is a measuring apparatus for the determination of local fuel concentration in the chamber /3/. This arrangement is explicitly treated in the fifth chapter.

The fine computational mesh typically had 70 x 49 nodes. To verify the mesh-independence of the computer solutions, the mesh was further refined. More details of the CPTR program are given in reference /9/.

3. EXPERIMENT

The schematic layout of the experimental facility is given in Fig. 3. The liquid tracer particles with a diameter of less than a micron follow the flow and its fluctuations sufficiently. The pressure drop of the nozzle is measured against atmospheric pressure. Thanks to its modular structure, the model allows different nozzles to be built in. The combustion chamber wall is made out of lucite, thus giving unrestricted optical access.

Velocities are measured by Laser-Doppler-Anemometry (LDA). A commercial four beam two color LDA (TSI model 9100-7) working in backscatter is used. The measurement volume has a size of 53 μm x 1 mm. The signals are frequency shifted and downmixed before being evaluated by counters and microcomputer. The signal-to-noise ratio (SNR) for all points shown is better than 10 db, with 2000 samples taken per point resulting in a reproducibility of better than 10 % for rms velocity values. The counters are operated in the controlled processor mode, thereby the time between samples is larger than 10 times the average between validated data. The total time of a measurement varied between 50 sec and 3 min according to the flow situation.

In the current setup of the LDA, either the tangential or the radial velocity components are measured together with the axial component. In the first case, the measurement points are on the axis of the cylinder parallel to the optical axis of the instrument, in the second case on the axis perpendicular to that, thus lying on the sidelines of a 90° sector. On the assumption of axial symmetry of the flow, the axial velocity component has the same value on both measurements. Since there are 6 swirlers, the verification of axial symmetry was done with repeated measurements, performed on the model being rotated 15° respectively 30°. These points are specially marked in the plots of the velocity profiles. A comment about the influence of these dimensional effects is given in the next chapter.

Model nozzle

Airblast nozzles actually used in combustors are very complex. Hence a simplified version of the nozzle was built, incorporating the essential features of the actual atomizer, Fig. 1, above all two separate channels producing a counterswirling air stream. Another important part is the nozzle diffusor, which, during the present stage of our investigation, has not been incorporated because of optical access ability at the atomizing lip. The model has been scaled to enhance the capability of the LDA to resolve the flow field with the desired accuracy. The use of straight channel walls has the twofold advantage of gaining optical access to the nozzle itself and of avoiding uncertainties in the discretization of the governing equations.

The outlet of the model combustor is radial to establish a well defined downstream boundary without reverse flow. In Fig. 4 the model nozzle is depicted with its main dimensions. The ratio of primary to secondary air is 1 over 2.25, a value comparable to those actually used. As a consequence of upscaling, the mass flow is augmented to a level, where the velocities at the atomizing lip reach values, that are commonly seen in airblast atomizers. With this concept the influence of swirl on the flow pattern is investigated at first numerically.

4. RESULTS AND DISCUSSION

Flow patterns

The choice of inlet conditions at the exit of the swirlers has strongly influences on the flow field, especially the prescribed level of the tangential velocity components. Its velocity profile on the inlet cross section of the swirlers shown in Fig. 5a is not known. Their configuration was taken from the nozzle of Fig. 1. Note that there are sharp turns in the flow path from the plenum through the swirler. That will force the flow to separate and to modify the swirler outlet profile. That is taken into account in the computation by the reduction of the effective swirler outlet cross section, thereby increasing the swirl intensity. A 30 ... 40 % blockage has been observed experimentally in such configurations /10/.

The influence of this partial blockage of both swirl channels is demonstrated in Fig. 6. Without blockage no central recirculation is observed, Fig. 6a. Increased inlet

blockage, i.e. augmentation of swirl intensity produces an inner recirculation zone, as can be seen in Fig. 6b, that is getting stronger and finally with 60 % inlet blockage supresses the corner vortex (Fig. 6c). Inlet boundary values were not adjusted with respect to a comparison between measurement and calculation. The flow observed in the experiment has a corner vortex and an inner recirculation zone and corresponds qualitatively with the flow in Fig. 6b, that is compared with the experimental data.

Comparison of prediction with measurement

The measurements show the typical features of a swirling flow. The three velocity components are measured on three cross sections, the first being 2 mm downstream of the atomizing lip. In Fig. 7I a weak reverse flow can be seen on the axis at that height. For the inner as well as the outer stream, the maxima of the axial velocity component are found in the vicinity of the atomizing lip. The wake flow profile observed at z = 2 mm is lost at z = 19 mm (plane II), Fig. 7II. The maximum of the axial velocity component moves out and flattens on its way downstream, Fig. 7III.

Profiles of the tangential velocity component from three measuring planes are shown in Fig. 8. The development of the flow shows a unidirectional swirl at z = 19 mm. The last part of figure 8 shows an already strongly equalized profile of the tangential velocity component. But there are also three-dimensional effects showing up of the measurements, on the profile of the axial as well as tangential velocity component.

As was already mentioned above, measurements have been repeated at different circumferential positions. Comparison of the general reproducibility of the measurements with the considerable differences between some points above the secondary channel leads to the conclusion, that departures from axial symmetry start in the secondary air channel (see Fig. 5). An explanation for these irregularities given by Roback and Johnson /11/ ascribes this to wake effects from the swirlers.

Calculations have been performed with the Hybrid (-) and the Quick (-'-) scheme. There were but minor differences in the solutions. The width of the inner recirculation zone as well as the corner vortex are again correctly calculated. The reversal of the swirl direction is predicted further downstream than shown by the measurements. The profiles of the velocity components at the last measurement plane are again well represented.

The discrepancies in the results can be explained by the combined influence of the uncertainties of the K-ε - model in swirling flows especially with counterswirl, uncertainties in the choice of inlet conditions and three-dimensional effects in the flow, on top of that there are the above mentioned uncertainties of LDA measurements in highly turbulent flows. Bearing in mind the complex nature of the flow, this comparison shows, that it is indeed possible to predict fairly well the flow pattern through a counterswirl nozzle into a tubular combustor. That is the prerequisite for two-phase flow calculations, that superpose the movement of the droplets onto the gaseous flow.

5. RESULTS OF THE TWO-PHASE FLOW CALCULATIONS

Flow Field

The spray characteristics of the nozzle in Fig. 1, are the major issue of this chapter. They have been studied numerically. Its flow field is represented by the streamline plot an Fig. 9a. On the magnified part, a vector plot shows the velocity field. The stream separates quickly into a part following the walls of the chamber and in the inner recirculation zone reaching into the nozzle because of the high expansion ratio and the strong swirl to which it is subjected. The well developed velocity profiles at the entrance of the chamber (see Fig. 10) underline the necessity to start the calculation already at the entrance of the swirl channels. In the course of the investigations of this nozzle, Cao et al. /3/ also performed measurements of the local fuel concentration in the chamber with a sampling bin. It is movable in the axial direction. The sampled fluid was weighted and the mass flow was determined as a function of bin position. The calculation of the flow field with the sampling device at a fixed axial position showed that the flow within the nozzle is only marginally influenced. Hence the atomization process remains unchanged. The flow in the chamber shows a different situation. The air is sucked into the bin by the openings of the sampling device and flows out through the fronted opening. In spite of the considerable perturbation of the flow pattern, the spray characteristics of the nozzle have not changed much.

Droplet trajectories

The dispersion of the spray is characterized by droplet trajectories (see Fig. 11). The spray is approximated by 15 size classes at three initial positions. On Fig. 11, the diameter varies between 10 μm and 220 μm. The drops are started at the atomizing lip with a negligible initial momentum. The calculations show a great sensitivity of the spray dispersion on the initial position. The reasons can be found in the different acceleration rates of the droplets in the region of steep velocity gradients. The numerical predictions show, that the spray dispersion can be represented with a droplet sample initially distributed over one quarter height of the primary channel as can be seen in Fig. 11.

Spray characteristics

The pressure and the pressure loss influence the atomization quality by the changes in shearing stresses. Increasing shear acting on the liquid film produces a finer spray.

Smaller drops will follow the flow more easily than the bigger ones, that will follow their initial direction with only minor changes.

Figure 12 shows what happens, if the chamber pressure is increased from 1 bar (Fig. 12a) to 2 bar (Fig. 12b) and 4 bar (Fig. 12c). The relative pressure drop was held constant and with that the velocities at the atomizing lip. Further data are listed on table 2. From the above discussion it is clear, that the droplet trajectories are stronger deflected with increasing pressure and thus reach the wall earlier. Trajectories on Fig. 13 are calculated for a pressure of 2 bar and demonstrate the influence of pressure loss on spray dispersion (6 KPa in Fig. 13a and 3 KPa in Fig. 13 b). The clear difference in spray dispersion can be explained by the generation of a finer spray with a higher pressure loss, getting to the wall faster.

6. CONCLUSIONS

By comparison with experimental data it has been demonstrated, that the complex flow-field developing in counterswirl airblast atomizers can be predicted with reasonable accuracy. The quality of the numerical code has been shown. However, additional work remains to be done with respect to the experiments as well as concerning the physical model of turbulent transport of particles. Special attention will be given to the initial conditions at the swirler outlet and to threedimensionality of the flow.

7. REFERENCES

/1/ M. Aigner
Charakterisierung der bestimmenden Einflußgrößen bei der luftgestützten Zerstäubung: Physikalische Grundlagen und meßtechnische Erfassung.

/2/ K. Trappmann, MTU München GmbH
Design Characteristics of a New Generation Turboshaft Engine.
ISABE - 85 - 7047

/3/ M. Cao, H. Eickhoff, F. Joos, B. Simon
Influence of Operating Conditions on the Atomization and Distribution of Fuel by Air Blast Atomizers.
70th AGARD-PEP-Meeting, Crete, 1987.

/4/ A. Kayser
Zur optischen Messung der Tropfengrößenverteilung bei der Zerstäubung von Brennstoff.
Chemie-Ing.-Techn. 49, Heft 10

/5/ D.B. Spalding
A Novel Finite Difference Formulation for Differential Expressions Involving Both First and Second Derivatives.
Int. J. for Num. Meth. in Eng., Vol. 4, 1972

/6/ A. Pollard, A. Siou
The Calculation of Some Laminar Flows Using Various Discretisation Schemes.
Computer Methods in Applied Mechanics and Eng. 35, 1982

/7/ R.I. Issa
Solution of the Implicity Discretized Fluid Flow Equations by Operator-Splitting.
J. of Comp. Phys. 62, 1986

/8/ A.W. Neuberger, A.U. Chatwani, H. Eickhoff, J. Koopman
Selection of Relaxation Factors for Computing Steady State Turbulent Flows.
Proc. 3rd Conference Numerical Methods in Laminar and Turbulent Flows, Seattle, 1983

/9/ A.U. Chatwani, H. Eickhoff, J. Koopman, A.W. Neuberger
Computation of Practical Turbulent Reactive Flows.
A User's Guide for Code CFTR. DFVLR - AT, Köln, 1982

/10/ F. Joos, private communication

/11/ R. Roback, B.V. Johnson
Mass and Momentum Turbulent Transport Experiments with Confined Swirling Coaxial Jets.
NASA-CR-168252, 1983

table 1: droplet equations

$$\frac{dx}{dt} = u$$

$$\frac{dr}{dt} = v$$

$$\frac{du}{dt} = \frac{3}{4} \cdot \frac{C_D \cdot Re_D \cdot \mu_f}{\rho_D \cdot D^2} (U - u) - \frac{1}{\rho_D} \left(\frac{\partial p}{\partial x} \right)_f - g$$

$$\frac{dv}{dt} = \frac{3}{4} \cdot \frac{C_D \cdot Re_D \cdot \mu_f}{\rho_D \cdot D^2} (V - v) - \frac{1}{\rho_D} \left(\frac{\partial p}{\partial r} \right)_f + \frac{w^2}{r}$$

$$\frac{dw}{dt} = \frac{3}{4} \cdot \frac{C_D \cdot Re_D \cdot \mu_f}{\rho_D \cdot D^2} (W - w) - \frac{v \cdot w}{r}$$

$$Re_D = \frac{\rho_f \cdot |W - w| \cdot D}{\mu_f}$$

$$C_D = \frac{24}{Re_D} \left(1 + 0.15 \cdot Re_D^{0.687} \right) \quad ; \quad Re_D < 1000$$

$$C_D = 0.44 \quad ; \quad Re_D \geq 1000$$

table 2: two phase flow calculations

medium: kerosine
total droplet classes: 45
diameter groups: 15
initial locations: 3
initial droplet velocity components: u = 3 m/sec, v = 0 m/sec, w = 3 m/sec

chamber pressure (bar)	pressure drop (KPa)	D50 (µm)	diameter range (µm)
1	3	58	10 - 220
2	6	34	5 - 110
4	12	30	5 - 90
2	3	76	10 - 250

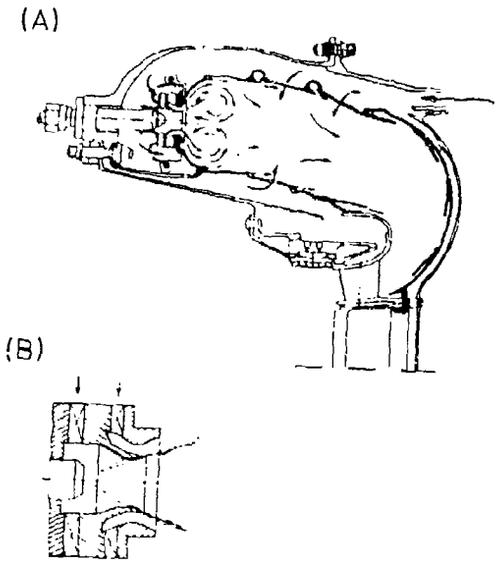

Fig. 1: (A) Reverse-Flow Annular Combustor
(B) Actual Counter-Swirl Atomizer Design

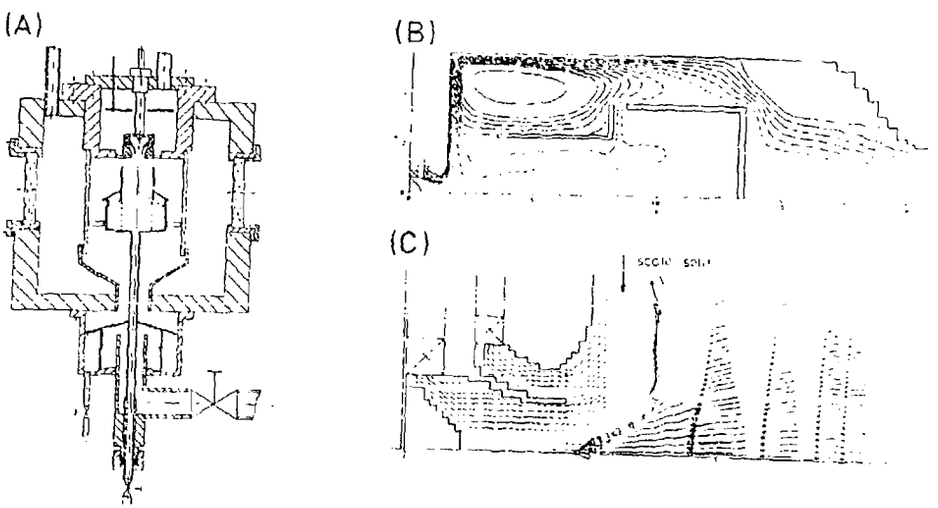

Fig. 2: (A) Pressure Vessel for Fuel Distribution Measurement
(B) Streamlines: Combustion Chamber with Fuel Sampling Bin
(C) Enlarged Nozzle

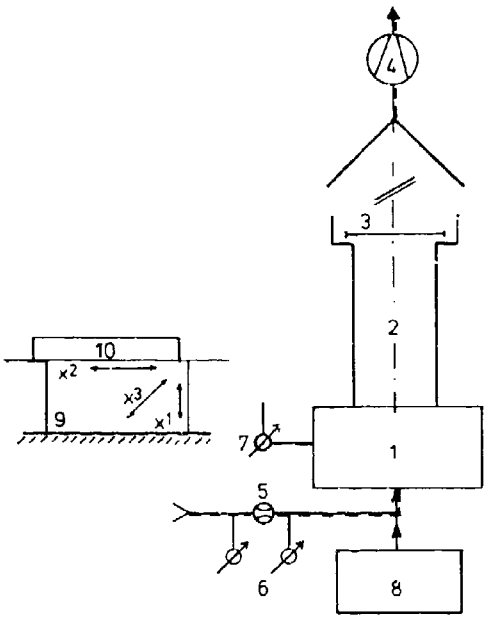

Fig. 3 a: Identification of Numbered Items in Figure 3

1 Plenum and Model Nozzle
2 Combustion Chamber
3 Radial Outlet
4 Blower
5 Critical Nozzle
6 Absolute Pressure Manometer
7 Differential Pressure Manometer
8 DFVLR Particle Generator
9 Traversing Gear
10 LDA

Fig. 3: Schematic Representation of the Experiment

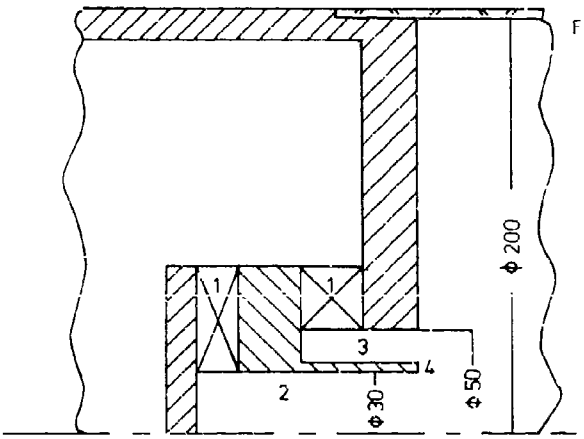

Fig. 4 a: Identification of Numbered Items in Figure 4

1 Swirler
2 Inner Swirl Channel
3 Outer Swirl Channel
4 Atomizing lip

Fig. 4: Model Nozzle

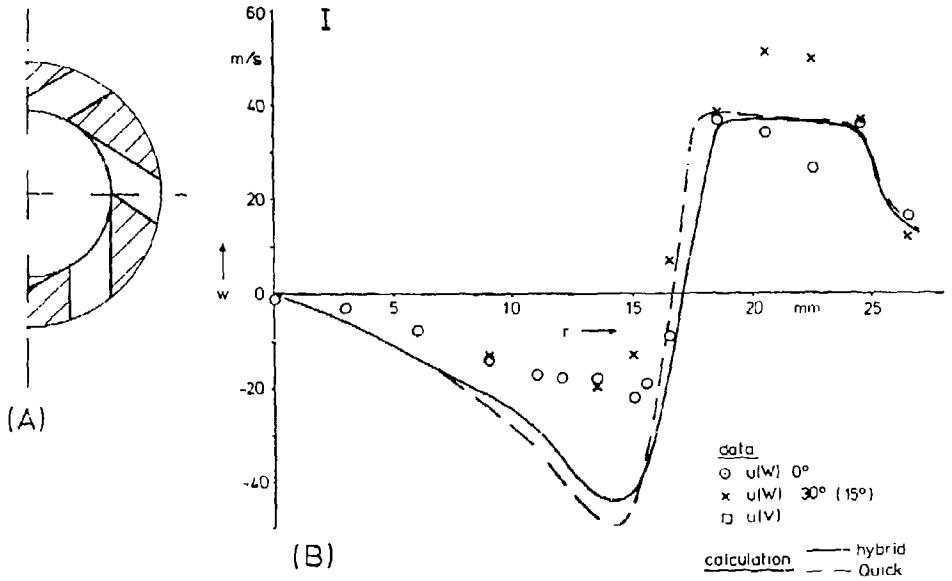

Fig. 5: (A) Sectional View of the Swirler
(B) Swirl Velocity Profile - Experiment and Calculation

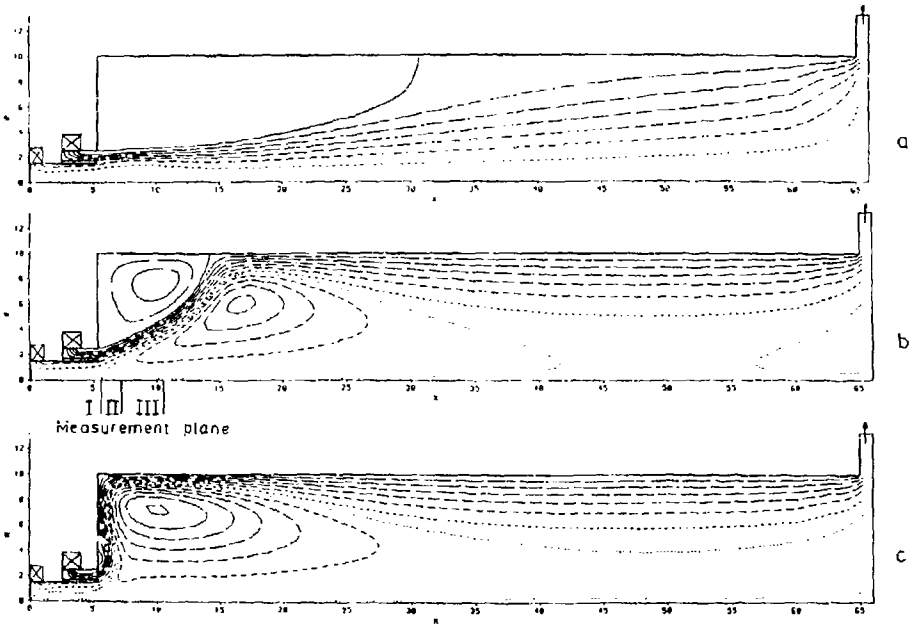

Fig. 6: Calculated Flow Patterns

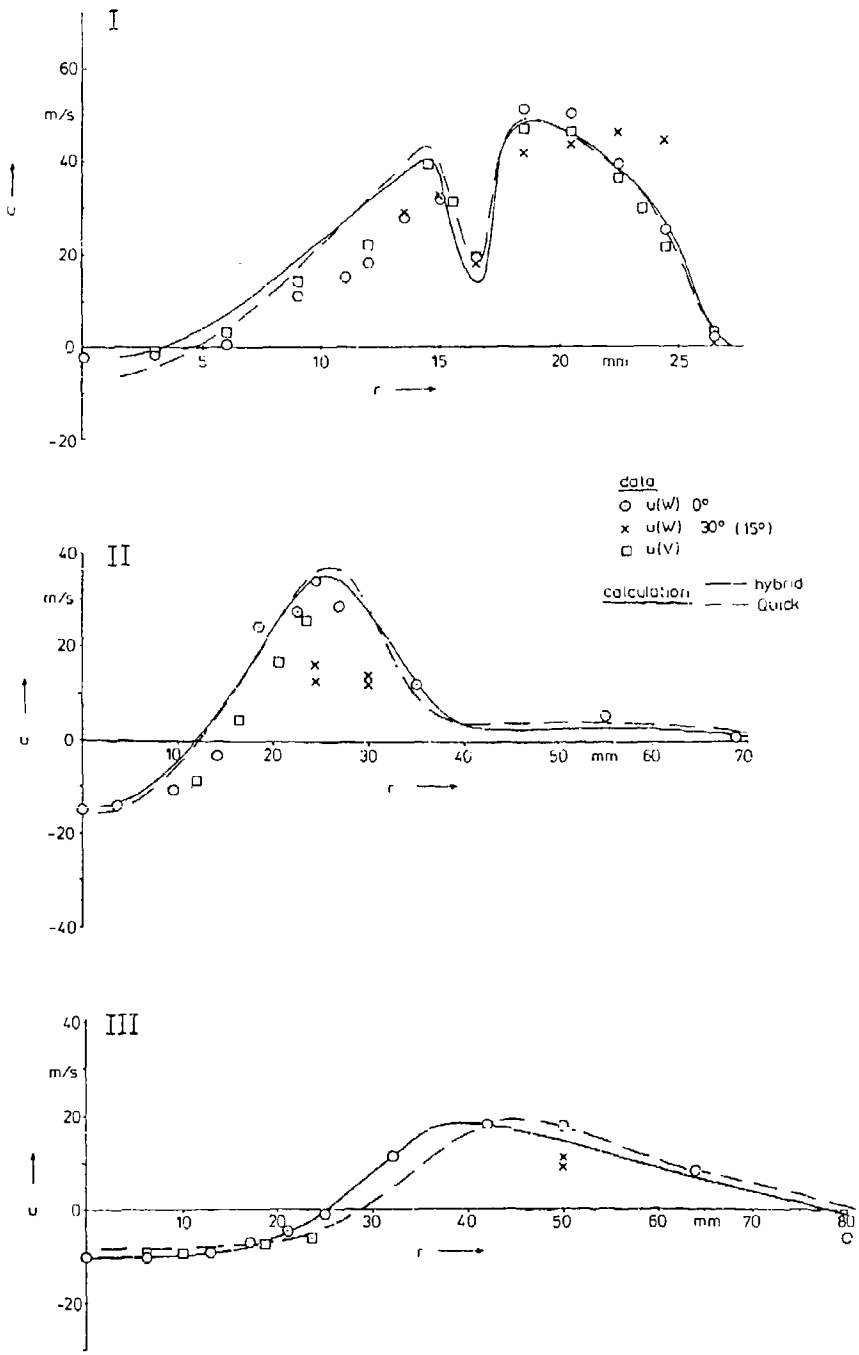

Fig. 7: Axial Velocity Profiles - Experiment and Calculation

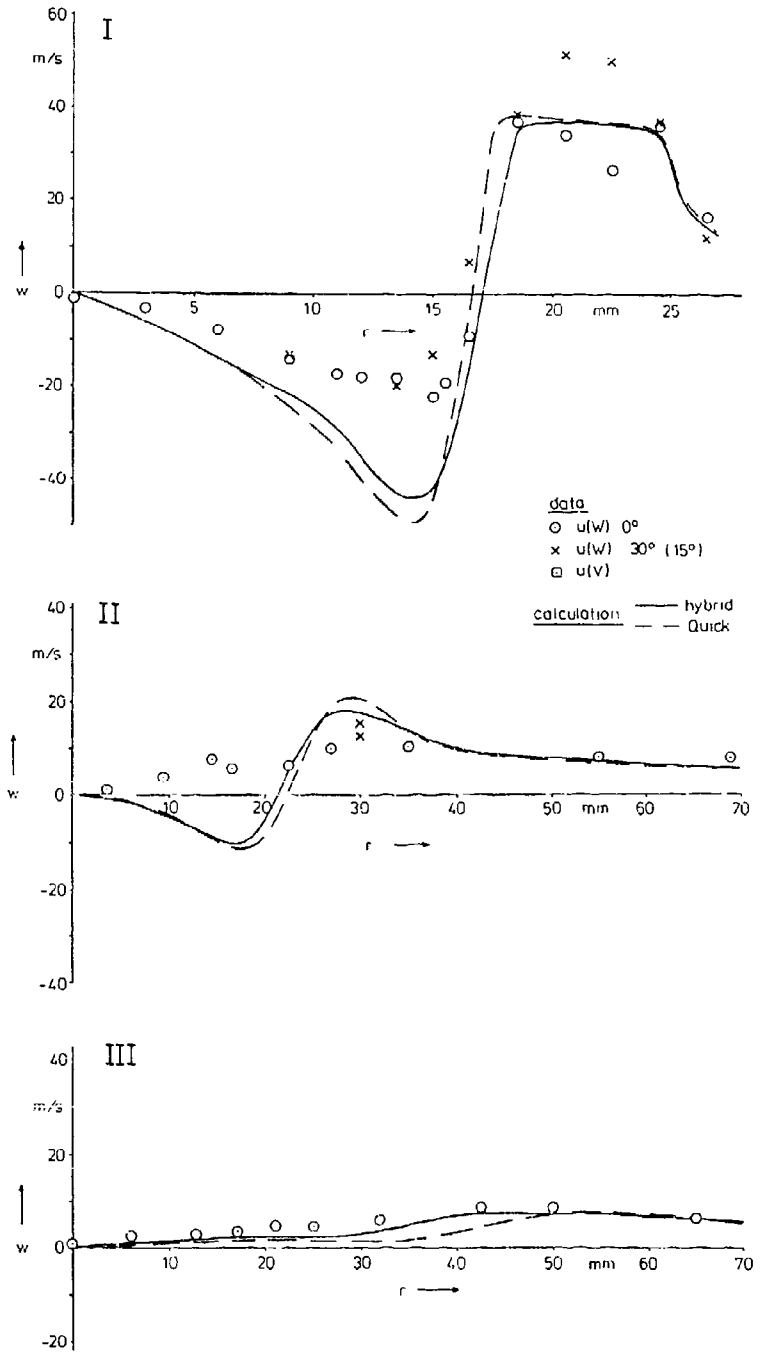

Fig. 8: Swirl Velocity Profiles - Experiment and Calculation

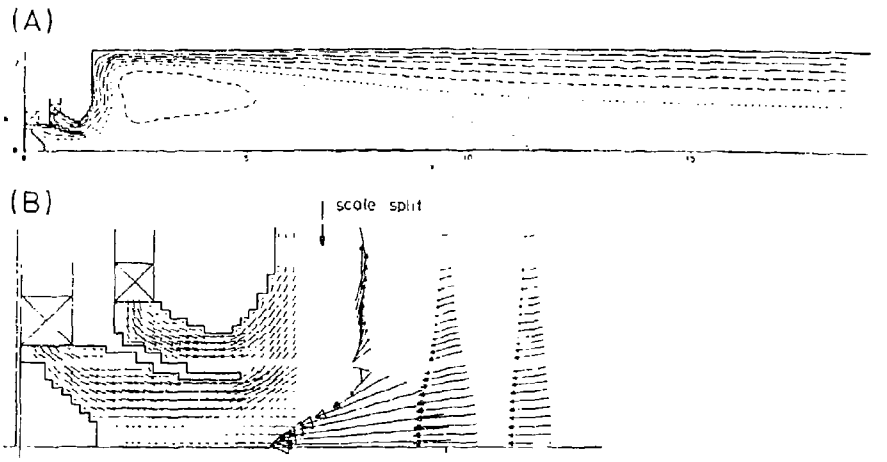

Fig. 9: (A) Streamlines: Combustion Chamber
(B) Enlarged Nozzle

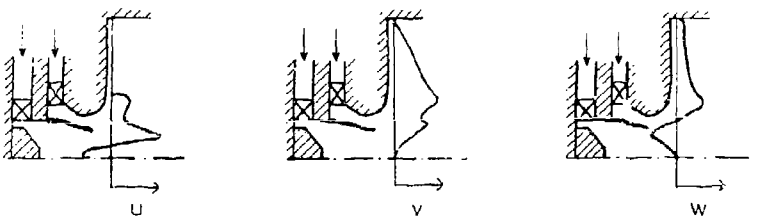

Fig. 10: Velocity Profiles at the Combustion Chamber Entry

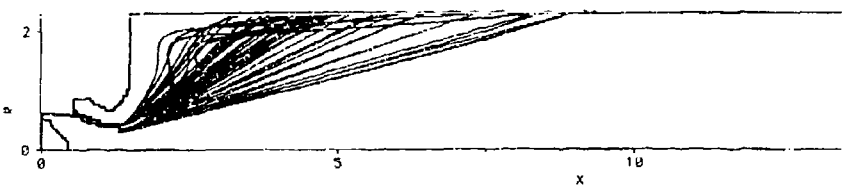

Fig. 11: Droplet Trajectories

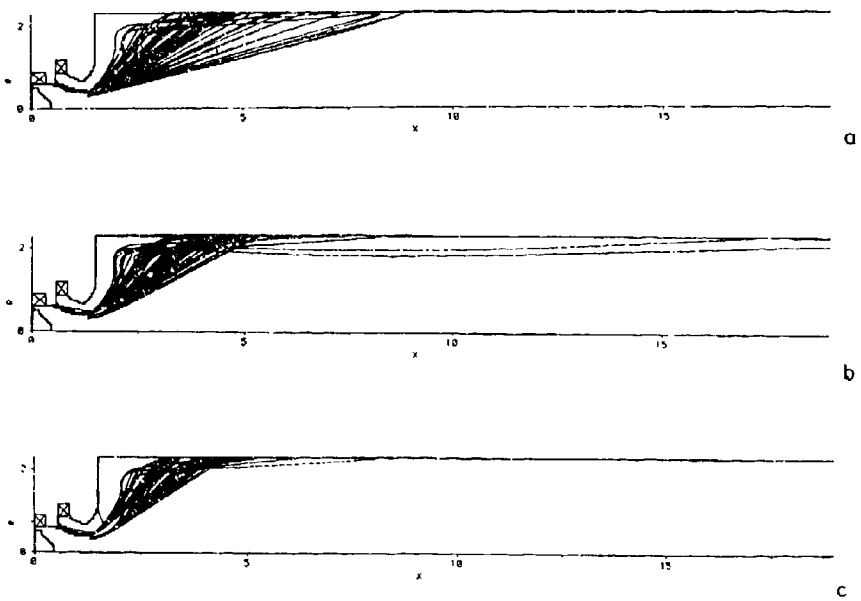

Fig. 12: Influence of Pressure on the Distribution of Fuel

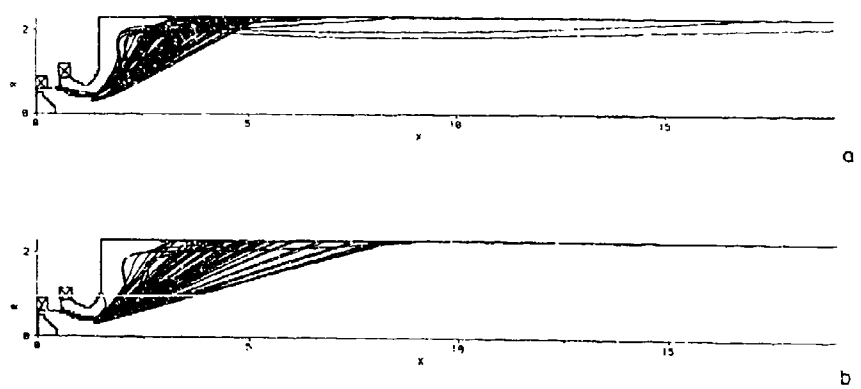

Fig. 13: Influence of Pressure Drop over the Nozzle on the Distribution of Fuel

DISCUSSION

S.Candel, FR

I did not quite understand how the blockage develops and how it affects the flow pattern. Could you provide some further comments on these two aspects.

Author's Reply

We don't know the shape of the velocity profiles at the swirler outlet, therefore block profiles are used. We assume that sharp turns in the flow path from the plenum through the swirler will force the flow to separate and to modify the swirler outlet profiles.

This is taken into account in the computation by a reduction of the geometric swirler outlet cross section, that is to say, by a partial blockage of the swirler outlets.

This blockage affects the flow pattern in the chamber by an increase in swirl intensity.

J.McGuirk, UK

Just a further comment on this issue of blockage. In working swirlers at Imperial College, we have noticed similar problems and effects, which are made even worse and more difficult to handle numerically due to circumferential variance in gap widths between the vanes.

Author's Reply

Thank you for this comment, Mr McGuirk. We hope to get some more insight into this subject by LDA measurements of the swirler outlet profiles.

We will repeat these measurements at different circumferential positions and then start a three dimensional flow field calculation to study the influence of these three dimensional profiles on the axisymmetric flow in the chamber.

THE BEHAVIOUR OF SYNTHETIC FUELS IN A SMALL TRANSPARENT COMBUSTOR

by

J. Odgers & D. Kretschmer
Département du Génie Mécanique
Université Laval
Québec, QC Canada G1K 7P4

Summary

In a continuing programme on the effects of fuel properties on combustion, some 20 pure hydrocarbons and synthesized fuels were tested at atmospheric conditions in a small transparent combustor. This combustor used a very effective air assist atomizer, such that droplet size was nearly constant. Each fuel was burned over a range of air/fuel ratios, and at each condition, a full exhaust gas analysis was done, exhaust temperature distribution was measured, as also flame radiation and weak extinction. The results and their implications are discussed.

1. INTRODUCTION

Over the past several years a large number of combustion tests have been conducted using fuels derived from Tar Sand deposits, Oil Shales, and Coal and within several different combustion systems. The results obtained from this work have been very useful in determining the kinds of problems likely to occur when using such fuels, and they indicate that many of the changes observed during combustion can be defined largely in terms of the liquid droplet diameter and/or the fuel hydrogen content. However, certain workers in the field have expressed doubts that the droplet size characteristics and hydrogen will yield the prediction accuracy necessary for some purposes (e.g. the degree of pollution at high combustion efficiencies), and there have been observations that other properties involving fuel composition and structure might well have important secondary effects in defining the combustion behaviour as a whole and, in particular, items such as carbon formation and flame extinction. The complex nature of real fuels makes it very difficult to decide which components are responsible for the observed behaviour: for instance, the possible effects of the various aromatic compounds in the fuel have been argued unsuccessfully for some considerable time.

The present experiments are part of a large programme designed to obviate the nature of supposition in determining effects due to fuel composition. In brief, some 20 different hydrocarbon compounds have been tested in a small combustion chamber at the same operating conditions. A synthetic fuel was created by mixing five paraffins so as to emulate the major physical characteristics of a JP-4 type fuel. To this "Base Fuel" one or more of the other hydrocarbons was added, and the operating conditions were repeated. Hence it was easy to observe any change in combustion behaviour due to the additional component(s). The tests described here utilised a small transparent combustor employing a very effective air-blast atomizer such that the droplet size changed very little from fuel to fuel (SMD range about 14 to 17 μm). Thus, in the present series, any effects due to droplet size virtually could be eliminated. The effects of droplet size have been studied in some detail in another set of experiments carried out using a small combustor having a Simplex atomizer and reported in [1].

2. COMBUSTOR AND TEST RIG

A schematic of the combustor and its major dimensions is given in Fig.1. Full details of its development have been published elsewhere [2]. The test rig runs at atmospheric pressure; it is fully instrumented for air and fuel flow, inlet air and fuel temperatures, outlet temperature distribution, full gas analysis to EPI standards or better (CO, CO_2, HC, O_2, NO, NOx), exhaust carbon by Smoke Number method, flame radiation within the primary zone, and additionally, the transparent nature of the combustor enabled visual observations of the flame to be made.

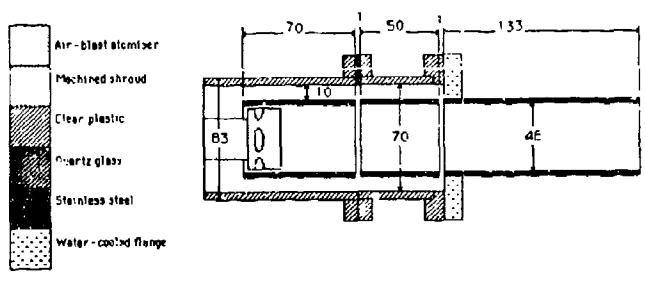

Fig. 1 SCHEMATIC OF TRANSPARENT COMBUSTOR

JP-4 is a typical aircraft gas turbine fuel, and the combustor was developed using this fuel. No attempt was made to optimize the performance, the chamber being considered as satisfactory when it yielded stable combustion over the range of test conditions and with a combustion efficiency of approximately 90 %. To attain this it was necessary to operate the combustor at a casing Mach number somewhat less than the design value. The reason for this is attributed to the incompatibility of reaction scaling and aerodynamic scaling. For most large combustors it is the aerodynamic demands (particularly pressure loss) which define the size of the combustor, and usually there is an excess of reaction time, but as the combustor decreases in size the control of combustion efficiency switches to reaction rate, due to the decreased residence time. For a given inlet temperature, aerodynamic control uses m/D^2p for the scaling group; for reaction control the group is m/D^3p^n. It was found that at atmospheric pressure the latter group controlled, and it became necessary to operate with a decreased Mach number in order to attain good stability and acceptable values of combustion efficiency. The droplet size of the fuels was of the order of 15 μm, so that this was not considered to be a large factor in determining the combustion efficiency.

3. FUELS AND THEIR PROPERTIES

The use of JP-4 for development was acceptable, but the complexity and variability of its composition did not recommend it as a suitable standard. Consequently, an attempt was made to synthesize a Base Fuel (BF) from a mixture of paraffins such that the new fuel had approximately the same major physical properties as JP-4. Consideration of availability and economics led to the following paraffin mixture: hexanes 10%, heptane 20%, isooctane 50%, decane 10%, and dodecane 10% by volume. A comparison of the two fuels is given in Table I.

Although there are obvious differences between the two fuels, it was decided that they were sufficiently similar for the Base Fuel (No. 41) to be acceptable as the new standard for test comparison. Table II lists the fuel compositions used for the present experiments, and Table III gives the range of major properties. It is considered that the range of properties covers more than the variations that are observed (or anticipated) for alternative fuels for aircraft derived from coal, oil shales, or tar sands. It would have been nice to have included 2- or 3- ring aromatic compounds, but these did not seem to be available at an economic price.

Table I

Property	Units	JP-4	Base Fuel
Molar Mass	kg/mol	0,115	0,114
Hydrogen	% by mass	14,3	15,9
Density at 288 K	kg/m³	775	703
Distillation ASTM D-86			
Initial Boiling Point	K	385	360
10% distilled	K	400	364
50% distilled	K	429	373
90% distilled	K	465	465
Final Boiling Point	K	499	477
Viscosity at 303 K	cSt	0,90	0,69
Surface tension at 298 K	dyn/cm	23,0	19,6

4. TESTS WITH BASE FUEL

In order to establish the test repeatability and reproducibility, two test series were done using the Base Fuel. These were performed at the beginning and end of the tests on fuels 42 to 63 inclusive (excluding 51 & 52). The results are given in Table IV and Fig. 2 which illustrate respectively the repeatability and reproducibility.

Normally six readings were taken for each experiment. Scans 1 & 2 were ignored, and a mean value was used based upon the remaining four scans. NO and NOx were recorded alternately (i.e. three readings each), and usually the mean of the last two readings was used. The exhaust temperature (T_4) shown in Table IV is just a sample reading, but it exhibits typical variations for any single point. Temperatures were averaged in the same way as the compositions. It is considered that the repeatability of the data is quite satisfactory.

The reproducibility is given in curve form in Fig. 2, and once again the results are considered to be very satisfactory. Approximately six months elapsed between the two tests. The same experimental technique was applied for all subsequent tests. An interesting feature is the form of the combustion efficiency curve. A tentative explanation was given in [2]. Further considerations suggest an alternative (and more likely) explanation. The weakness of the first explanation lay in the asumption that the effect was at least partially caused by changes in droplet size. Examination of all the operating conditions for all of the fuels suggests that the droplet size varied only from 14,6 to 16,7 μm. These diameters are very close to those for which the air/fuel mixture will burn as thought it was a vapour [3], and this would negate some of the arguments put forward in [2]. An alternative explanation based upon the flame observations is offered here. The combustor is cylindrical in shape, with a reaction zone (primary) largely generated by the centrally located shrouded primary baffle plus secondary effects due to the penetration of the air which is introduced annularly at the end of the zone. Observations of the transition from weak to rich mixtures (within the reaction zone) showed the following effects (especially observable with the yellow

Table II

Fuel Compositions

Pure Fuels

No	Type	No	Type
1	JP-4	22	t-amylbenzene
24	butylbenzene	25	cyclohexane
26	cyclohexene	27	decalin
28	decane	30	dicyclopentadiene
31	dodecane	32	heptane
33	iso-hexanes	34	methylcyclohexane
35	iso-octane	36	octene-1
37	isopropylbenzene	38	tetralin
39	toluene	40	o-xylene
42	JP-10	114	RJ-6

Mixed Fuels

No	Composition
41	28(10) 31(10) 32(30) 33(10) 35(50)
43	23(10) 41(60) 42(30)
44	23(20) 41(50) 42(30)
45	23(10) 41(90)
46	23(25) 41(75)
47	23(40) 41(60)
48	36(25) 41(75)
49	30(12,5) 36(12,5) 41(75)
50	30(25) 41(75)
53	38(25) 41(75)
54	27(25) 41(75)
55	25(25) 41(75)
56	26(25) 41(75)
57	25(25) 26(25) 41(50)
58	39(25) 41(75)
59	35(25) 41(75)
60	24(25) 41(75)
61	34(25) 41(75)
62	40(25) 41(75)
63	22(25) 41(75)

N.B. Numbers in brackets are % by volume.

Table III

Range of Fuel Properties

Property	Symbol	Units	minimum	maximum
Molar Mass	M	kg/mol	0,078	0,170
Hydrogen Content	%H	% mass	7,69	16,28
Density at 288 K	ρ	kg/m³	679	1022
Calorific Value (net)	q_n	MJ/kg	40,14	44,74
Distillation ASTM D-86				
Initial Boiling Point	IBP	K	317	478
5% distilled	T_5	K	338	480
10% distilled	T_{10}	K	338	481
30% distilled	T_{30}	K	339	482
50% distilled	T_{50}	K	339	512
70% distilled	T_{70}	K	339	538
90% distilled	T_{90}	K	341	539
Final Boiling Point	FBP	K	355	550
Volume average	T_{av}	K	339	507
Flash Point	FP	K	245	351
Smoke Point	SP	mm	7	51
Surface Tension at 298 K	σ	dyn/cm	18,6	36,3
Parachor	[P]	(cgs)	220	502
Viscosity at 298 K	ν	cSt	0,63	5,05
SMD	$d_{2,3}$	μm	14,6	16,7
Saturation Factor	S_H	-	0,428	1

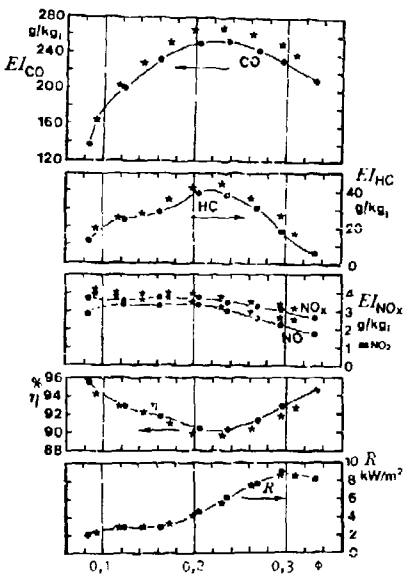

Fig. 2 COMBUSTION CHARACTERISTICS AND REPRODUCIBILITY OF TEST RESULTS Base Fuel (41)

Table IV
Repeatability of Tests

Scan	CO_2 %	CO %	HC ppm	NOx ppm	NO ppm	O_2 %	T_4 K
1	4,56	0,432	42	16	-	18,9	578
2	4,26	0,351	44	-	11	18,9	578
3	4,22	0,344	44	13	-	18,9	581
4	4,21	0,339	44	-	10	18,9	579
5	4,20	0,337	39	13	-	19,0	582
6	4,21	0,342	39	-	9	18,9	583

flame produced by aromatic fuels such as benzene):

a) At weak conditions ($\Phi_{overall} \leq 0,1$) combustion appeared to be limited to a region bounded by the wall of the baffle and within the recirculation zone downstream of the baffle, but still within the boundary of the shroud.

b) As the mixture richened ($0,1 < \Phi_{overall} \leq 0,2$), the shroud of the baffle became dull red, and the flame began to assume a yellow colour and to burn downstream of the recirculation zone.

c) Further richening produced bright red heat at the shroud, and the flame appeared to occupy the whole of the reaction zone and to penetrate well into the secondary zone.

Based upon these observations, and ignoring any droplet effects, the combustion efficiency characteristics may be explained in the following manner -

i) At the weak conditions the reaction zone is burning at $\phi < 1$, and hence the flame is within an oxygen rich region, and due to the intimate mixing of fine droplets and air, the reaction rate is sufficiently high so as to yield a high overall efficiency. However, any unburned fuel leaving the reaction zone is quenched in the secondary zone and appears as exhaust hydrocarbons.

ii) As the mixture richens, the baffle recirculation zone becomes overloaded and burns inefficiently. At this stage the fuel/temperature combination in the secondary zone is still insufficient to burn the excess fuel, and the efficiency decreases at the combustor outlet.

iii) Further richening pushes more fuel into the secondary zone, but at the same time, the temperature is increased such that the fuel continues to burn downstream of the main reaction zone, thereby augmenting the overall efficiency.

The net result of all this is to yield a curve of efficiency such as that illustrated in Fig. 2. The unburnt components, hydrocarbons and carbon monoxide, reflect this behaviour in the form of their respective curves, as also the oxides of nitrogen and flame radiation.

5. TESTS WITH OTHER FUELS

Space restrictions do not permit the experimental data to be quoted, neither tabularized nor in the form of curves such as Fig. 2. However, the form of the curves for all the fuels examined was very similar to those of Fig. 2, only the levels of the curves differed. There were some differences in visual observations. The transparent blue flames were yielded by paraffin type fuels, and the opaque yellow flames by the aromatics, as in accord with flame observations elsewhere. All the flames, regardless of colour, exhibited the hot baffle phenomena described above.

5.1 Ignition Observations

At the conditions of test, all fuels ignited easily and, apparently, they ignited outside their burning limits, the flame being stabilized by the energy release from the plug. In these cases, when the plug was extinguished, so was the flame. This suggests that the ignition system is so (relatively) powerful that it is not a limiting feature with a system such as this, which behaves as though it were premixed, but, unfortunately, it also means that the reults are not correlatable in any way.

5.2 Combustion efficiency

For premixed combustion, there is a widespread assumption that the chemical nature of the fuel has little effect on the rate of combustion. Briefly, this hypothesis assumes that the hydrocarbon very rapidly breaks down into hydrogen and carbon monoxide. Because of its great reactivity, the hydrogen burns almost as fast as it is formed, and as a result of this, throughout the reaction period the hydrogen concentration is always low. Since the rate of destruction of carbon monoxide is slower than the rate of formation, it builds up in concentration until all the hydrocarbon has been destroyed. This constitutes the so-called first stage of the process. The second, and final, stage is the combustion of the relatively slow-burning carbon monoxide. It may be assumed that this latter stage governs the overall rate of the process. If the stoichiometry of the various hydrocarbon/air mixtures is examined in this light then it will be remarked (a) that the relative amounts of carbon monoxide formed are little different for a very wide range of hydrocarbons and (b) that the reaction temperatures are generally similar (for many hydrocarbons ± 1,5 %). For these reasons it is often presumed that the reaction rates of most premixed hydrocarbon flames will be very similar. The two-stage premise has been assumed for a number of reaction rate models to describe combustion since the kinetics of the CO/H/O system are claimed to be known with fair accuracy, whereas the hydrocarbon breakdown is so complex (and rapid) as to be almost unmanageable.

If the two-stage theory really is applicable, then it would be expected that flame speeds and combustion efficiencies of hydrocarbons would be relatively insensible to fuel changes. The flame speeds of various hydrocarbon/air mixtures are in fair accord with the above suppositions, especially when the fuels are saturated or have a long chain. It should be noted that the two-stage hypothesis only applies to major species and that it is quite possible that minor and transitory species may be more sensitive to fuel variation (e.g. aldehydes, ketones, carbon etc.).

From what has been said above, it would be reasonable to presume that since the present system is thought to approximate to a pre ixed system, then there would be little difference between the various fuels with respect to combustion efficiency characteristics. As previously noted, the curves are similar in form, but the levels differ.

Figure 3 plots the variation of combustion efficiency versus the average boiling points of the fuels

for an overall equivalence ratio of $\phi = 0{,}1$. There is obviously a trend, but whether it is solely due to boiling point (volatility) or whether there is/are some other factor(s), which may be a function of the boiling point, is a mute point. Similar curves were obtained for other equivalence ratios (0,2 & 0,3). In an attempt to shed light on the role of boiling point, Figs. 4, 5, & 6 were constructed. They show the variation of combustion efficiency with equivalence ratio for a number of fuels of similar boiling points but with quite different hydrogen contents. These results strongly suggest that the major influence upon efficiency is truly one of boiling point.

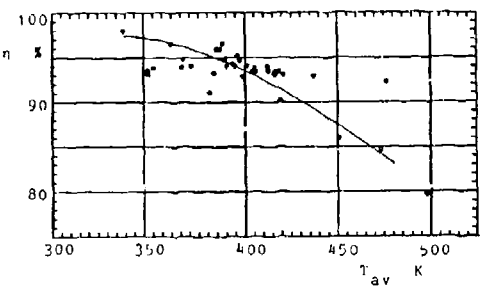

Fig. 3 COMBUSTION EFFICIENCY - VOLATILITY RELATIONSHIP

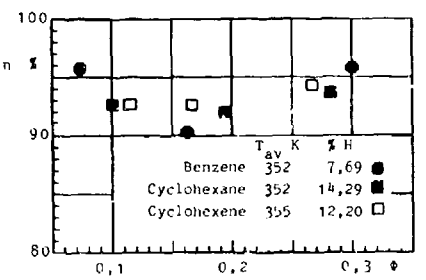

Fig. 4 COMBUSTION EFFICIENCIES OF "CONSTANT" BOILING MIXTURES

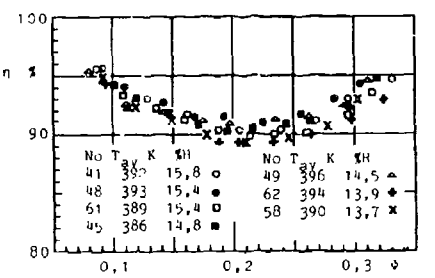

Fig. 5 COMBUSTION EFFICIENCIES OF "CONSTANT" BOILING MIXTURES

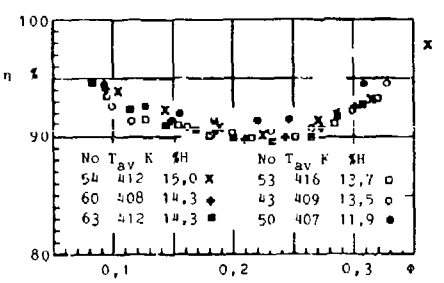

Fig. 6 COMBUSTION EFFICIENCIES OF "CONSTANT" BOILING MIXTURES

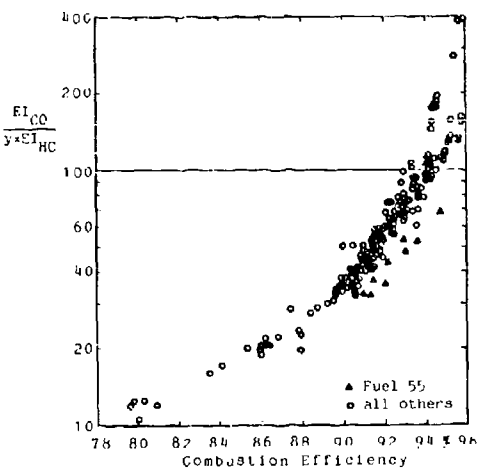

Fig. 7 POLLUTANT CHARACTERISTICS OF HYDROCARBON FUELS

Further confirmation is provided by the data in Fig. 7 which plots the combustion efficiency versus the ratio of emission indices $EI_{CO}/(yEI_{HC})$ where y is the estimated function of equivalence ratio within the primary zone ($y = \phi$ for $\phi \leq 1$, and $y = 1$ for $\phi \geq 1$). The fact that almost all the points lie within the same scatter band suggests that fuel effects have only a small part to play in the establishment of the ratio. This latter appears to depend upon combustion efficiency and equivalence ratio only and therefore suggests a dependency upon temperature and/or oxygen availability only. The only exception appears to be fuel No. 55 (25 % cyclohexane, 75 % BF), and no explanation for this is forthcoming.

The tendency (Fig. 3) for the combustion efficiencies to attain a maximum value (for a given ϕ) suggests that the role of chemical reaction is significant in reaching the 'final' value. This limiting value (about 95 %) is not out of accord with the reaction rate based upon the combustion zone loading.

In view of the above evidence, one is forced to the conclusion that the trend noted is predominantly

one of boiling point, and that fuel chemical effects are small. Although this has been generally accepted, there is still a school of thought that suggests that structure (aromaticity, chemical bonding etc) still plays a role. The difficulty is to define a term which is representative of these various effects. If one uses aromatic content then benzene, toluene, and xylene are all 100 % aromatic, but obviously have different structures. Again, how does one compare an aromatic fuel with an olefin or a cyclo-paraffin? In an attempt to overcome these difficulties a term (Hydrogen Saturation - S_H) has been defined for use in these laboratories. The hydrogen saturation has been defined as the ratio of the number of hydrogen atoms in the fuel to the number of hydrogen atoms in the paraffin having the same number of carbon atoms. Thus, for instance, for benzene, toluene, and xylene:

	Benzene	Toluene	Xylene
Formula	C_6H_6	C_7H_8	C_8H_{10}
Corresponding Paraffin	C_6H_{14}	C_7H_{16}	C_8H_{18}
Hydrogen Saturation	6/14 = 0,429	8/16 = 0,500	10/18 = 0,556

For commercial fuels the value of S_H can readily be shown to be given by:

$$S_H = \frac{6h}{1 + h + 0{,}012/M} \qquad (1)$$

where h is the mass fraction of hydrogen in the fuel and M the molar mass of the fuel (kg/mol). It is conceded that the saturation value cannot be fully representative of all effects. For instance, it cannot distinguish between isomers (e.g. octane and iso-octane) nor between classes of compounds having the same formula (e.g. olefins and corresponding ring saturates), nor has it been considered for fuels other than hydrocarbons. Despite these limitations, recent work in these laboratories has shown the usefulness of this function. As a first example it has been applied to the results obtained here for measured combustion efficiencies. If the efficiency data from Fig. 3 are plotted against $T_{av} / S_H^{0,25}$ Fig. 8 results. The results show less scatter than the plot given in Fig. 3 and suggest that the fuel composition plays a secondary role in the determination of the combustion efficiency. It is felt that this role may become more important the closer the efficiency approaches to 100 % since the very high values may be entirely reaction rate controlled. This is a factor which might assume great importance from the pollution view point.

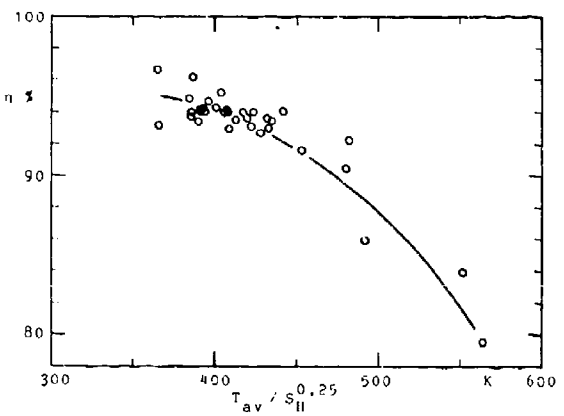

Fig. 8 COMBUSTION EFFICIENCY CORRELATION ϕ = 0,1

5.3 Pollutants

Much of what has been said with respect to combustion efficiency applies, also, to the amounts of hydrocarbons and carbon monoxide found within the exhaust. The amounts of carbon monoxide appear to be independent of fuel type (Fig. 9). This would be anticipated if these quantities were determined by chemical reaction rates and confirms previous work carried out using well stirred reactors [4]. The hydrocarbon content (Fig. 9) shows a trend with boiling point. This confirms the assumption that hydrocarbons are largely due to unburned droplets as the volatility decreases. If the results are plotted against $T_{av} / S_H^{0,25}$, as in the case of the combustion efficiency, there is some reduction of scatter (Fig. 10), however, the influence of structure is slight.

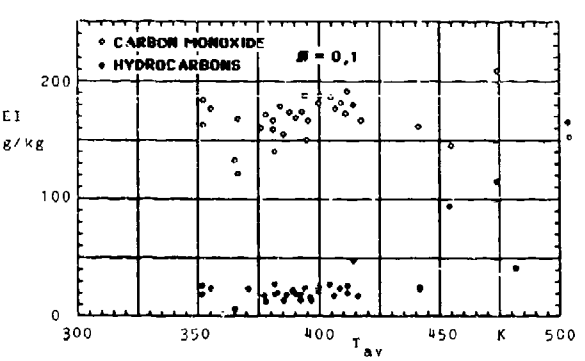

Fig. 9 CO & HC EMISSION INDEX CHARACTERISTICS VARIATION WITH AVERAGE BOILING POINT

The reduction of scatter is mainly noticeable for the hydrocarbons, as would be anticipated.

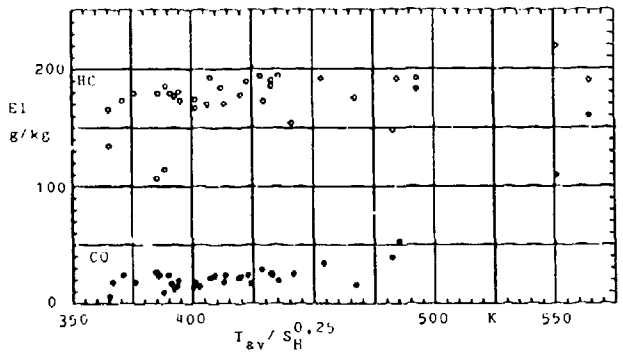

Fig. 10 CO & HC EMISSION INDEX CHARACTERISTICS INFLUENCE OF VOLATILITY AND SATURATION

The prediction of NOx has been made using a formula developed and described in [5]. The equation takes the form -

$$EI_{NOx} = 29 \times e^{-21670/T} \; p_3^{0,66} \left(1 - e^{-250\tau}\right) \qquad (2)$$

where T = adiabatic flame temperature (dissociated) K
p_3 = combustor inlet pressure Pa
τ = available NOx formation residence time s

The major difficulty is to define the NOx formation time. It is normal to take one or more experimental values to determine the time constant and then to utilize such values for future predictions. Because of its effect upon reaction temperature and, indirectly, the size of the burning zone, the apparent NOx formation time is often a function of equivalence ratio. To assess this function, the data pertinent to Fuel 41 (Base Fuel) were analysed and the following equation was derived -

$$\tau = 0,0129 \cdot 0,0266\ \Phi \qquad (3)$$

Substituting (3) in (2) yields -

$$EI_{NOx} = 5,824 \times 10^{4} \times e^{-21670/T} \left(1 - e^{6,65\ \Phi - 3,225}\right) \qquad (4)$$

Since the flame is a diffusion flame, T used is calculated for $\Phi = 1$. The measured versus predicted values are given in Table V for the various fuels.

Examination of Table V suggests that the correlation is not perhaps as accurate as it might be. However, it should be mentioned that at these conditions, and with the low NOx values measured, the experimental accuracy is probably no better than ± 1 g/kg of fuel. Accepting this, the prediction becomes very satisfactory.

The ratios of NO to NOx are difficult to analyse, again because of the low values which do not make for a high experimental accuracy. If equilibrium is assumed at temperatures higher than about 1000 K then virtually all NOx should be in the form of NO. The operating conditions of the test rig give exhaust mean temperatures from about 600 to 1100 K. If equilibrium is assumed at these temperatures then the NO/NOx ratio should range (correspondingly) from about 1 at $\Phi_{overall} > 0,3$ to about 0,4 at $\Phi_{overall} = 0,1$. In fact, between $\Phi = 0,1$ to $\Phi = 0,3$ the trend of the experimental data is to the contrary, although at conditions weaker than $\Phi = 0,1$ there is evidence of a sharp decline in the NO/NOx ratio. This would suggest that the final value is a frozen one, the approach to equilibrium being dictated by the rate(s) of reaction.

At the weak operating conditions, the temperatures in the secondary and dilution zones are too low to lead to high rates of oxidation of NO to NO_2, therefore, the original high ratio of NO/NOx is frozen. As the equivalence ratio increases, these zone temperatures also increase, however not sufficiently so as to produce new NO. These increased temperatures lead to an increase in the rate of the oxidation reaction and lower values of NO/NOx. Of course, after staying in the atmosphere for some considerable time, the NO becomes almost totally converted to NO_2.

Although flame radiation cannot be categorized as a pollutant, it has been included here because of its association with carbon formation. Visual observation of the flames (confirmed by still-photography) showed marked differences in the flame luminosity. Paraffinic flames, such as those of the Base Fuel, were always blue, even at rich conditions, and it was obvious that there was little or no carbon in the flame

at any condition. In contrast, flames of fuels containing high percentages of aromatics were bright yellow at all conditions indicating the presence of considerable soot formation. Fuels with low aromatic content, and others which were non-aromatic, but still unsaturated, gave intermediate colours between blue and yellow.

Despite these visual observations the amount of carbon found in the exhaust was too small to be measured gravimetrically, and even the filter-paper stain technique only indicated trace quantities, so that quantitative measurements were not possible.

It was thought that the flame radiation might represent the carbon formation within the flame since for any given equivalence ratio the flame temperatures of the various fuels differed only by small amounts. The measured radiation ($\Phi_{overall} = 0,3$) was correlated by means of the following equation –

$$R = 4,33 \{[M \ln(B-1)/h]^{2,75} \times S_H\}^{0,875} \quad (6)$$

where R is the radiation in kW/m², M the fuel molar mass in kg/mol, h the fractional hydrogen content, and B the transfer number

$$B = \frac{1575 - 0,5\ T_{av}}{T_{av} - 118}$$

Figure 11 illustrates the calculated versus the measured values as well as the essential statistical data. Bearing in mind the accuracy of the measurements (10 %) the correlation is thought to be satisfactory. The molar mass and the transfer number may be taken as representing the physical effects upon the radiation. For instance, the transfer number may be taken as representative of volatility, and it could be supposed that volatility reflects upon the combustion efficiency (i.e. gas temperature) in the reaction zone, the higher the volatility of the fuel the higher the efficiency and the higher the flame temperature and, therefore, the radiation. Hydrogen content and hydrogen saturation may represent composition and structural effects. The more hydrogen, the less carbon and, hence, less soot formation (radiation). As before, the saturation factor is representative of the fuel structure, and it may be considered to be a measure of the effects due to bonding, ring structure, etc. In the context of the present work, this is the first time that it has been possible to detect possible effects due to structural differences that have not been masked by hydrogen content. One would expect the value of S_H in Eqn. (6) to have a negative exponent; however, it does have a strong relationship with hydrogen content and the positive exponent found in the

Table V

Fuel	EI_{NOx} g/kg$_{fuel}$							
	$\Phi = 0,1$		$\Phi = 0,2$		$\Phi = 0,25$		$\Phi = 0,3$	
	Pred.	Meas.	Pred.	Meas.	Pred.	Meas.	Pred.	Meas.
23	6,24	4,1	5,91	3,3	5,50	2,9	4,92	2,6
25	4,30	4,4	3,96	3,2	3,68	3,1	3,30	3,2
26	5,38	4,6	4,95	4,0	4,61	3,9	4,13	3,8
34	4,23	6,2	3,89	4,9	3,62	4,6	3,24	4,3
36	4,91	7,0	4,52	5,8	4,21	5,2	3,77	4,9
38	5,40	4,8	4,97	2,8	4,63	2,4	4,14	2,3
39	5,86	4,3	5,39	3,2	5,02	2,9	4,49	2,7
40	5,53	4,2	5,09	2,2	4,73	1,9	4,24	2,1
41	3,99	3,6	3,67	3,7	3,42	3,5	3,06	3,0
42	4,40	4,4	4,06	3,8	3,77	3,2	3,38	2,9
43	4,48	3,3	4,12	3,2	3,83	3,1	3,43	2,8
44	4,26	3,7	3,92	3,3	3,65	3,0	3,27	2,9
45	4,11	2,8	3,78	3,0	3,52	2,8	3,14	2,4
46	4,26	3,5	3,93	3,5	3,65	3,0	3,26	3,0
47	4,46	4,4	4,11	4,0	3,82	3,7	3,41	3,0
48	4,16	4,3	3,83	3,6	3,56	3,4	3,18	3,0
49	4,24	3,4	3,91	3,2	3,64	3,0	3,25	2,9
50	4,48	3,5	4,12	3,0	3,83	2,8	3,43	2,7
53	4,19	4,7	3,86	3,5	3,59	3,1	3,21	2,9
54	4,33	3,7	3,99	3,3	3,71	3,2	3,32	3,1
55	3,99	3,4	3,67	3,7	3,42	3,5	3,05	3,1
56	4,21	4,8	3,88	4,1	3,61	3,8	3,22	3,7
57	4,21	3,9	3,88	3,5	3,61	3,2	3,22	3,2
58	4,19	4,5	3,86	3,9	3,59	3,6	3,21	3,1
59	4,11	3,9	3,78	3,3	3,52	3,0	3,14	2,9
60	4,16	3,7	3,83	3,3	3,56	3,0	3,18	2,9
61	3,99	3,5	3,67	3,6	3,42	3,4	3,05	3,1
62	4,19	4,0	3,86	3,6	3,59	3,1	3,21	2,8
63	4,12	4,5	3,80	3,7	3,53	3,5	3,16	3,1
114	4,76	3,5	4,38	3,7	4,07	3,1	3,64	2,9

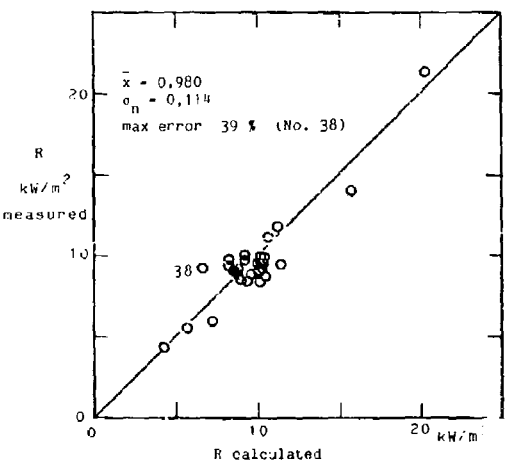

Fig. 11 FLAME RADIATION CORRELATION

correlation analysis may well represent a compensation for an 'overkill' exponent for the hydrogen content.

It would be reasonable to expect that the flame radiation might relate to the carbon content and/or smoke points of the fuels. A plot of radiation versus smoke point shows no relationship whatever. It is suggested that a possible reason for this is that both exhaust smoke and the smoke point are more indicative of carbon burn-out than carbon formation, whereas the reverse is the case for flame radiation.

5.4 Weak Extinctions

To measure the equivalence ratio at weak extinction, after the test rig had been operated at steady conditions, the fuel was turned down until a slight instability was noted, which gave the signal of approaching extinction. At this point the ignition plug was switched on, and the fuel was further reduced. After a little while the plug was turned off. If the flame remained alight, the plug was again fired and the fuel further reduced until, on arresting the spark, the flame was extinguished. At this point the plug was re-fired and the fuel increased by a small amount. By this means it was possible to define the difference between a flame which was just self-sustaining and one which was not. This defined the weak extinction.

Because of the use of air-assist atomization, the combustor exhibits many of the characteristics of a premixed system and/or a gaseous diffusion system, and hence it seems likely that the weak extinctions might depend partly upon droplet (physical) characteristics and partly upon the chemical composition of the fuels.

For a simple pressure-jet atomizer the weak extinction characteristics have been shown to correlate with [6] -

$$f_8 = \frac{\dot{m}_f}{\dot{m}_{41}} = \left[\frac{f_{s,f}}{f_{s,41}} \times \frac{q_{n,f}}{q_{n,41}} \times \frac{\dot{m}_{a,f}}{\dot{m}_{a,41}} \times \frac{\ln(1+B_{41})}{\ln(1+B_f)} \right]^{0,53} \times \left(\frac{\rho_f}{\rho_{41}} \right)^{0,92} \times \left(\frac{\sigma_f}{\sigma_{41}} \right)^{0,47} \times \left(\frac{\nu_f}{\nu_{41}} \right)^{0,16} \qquad (7)$$

If the air mass flow is constant then -

$$\frac{\Phi_f}{\Phi_{41}} = \left[\frac{f_{s,f}}{f_{s,41}} \times \frac{q_{n,f}}{q_{n,41}} \times \frac{\ln(1+B_{41})}{\ln(1+B_f)} \right]^{0,53} \times \left(\frac{\rho_f}{\rho_{41}} \right)^{0,92} \times \left(\frac{\sigma_f}{\sigma_{41}} \right)^{0,47} \times \left(\frac{\nu_f}{\nu_{41}} \right)^{0,16} \qquad (8)$$

where f_s is the stoichiometric fuel/air mass ratio — q_n the net calorific value
B the transfer number — ρ the density
σ the surface tension — ν the kinematic viscosity
index f refers to the fuel under consideration, index 41 to the Base Fuel (as reference).

If the combustion behaves as a premixed (or a gaseous diffusion) system then it might be possible to correlate the extinction data using the technique described in [7]. In this technique, the reaction zone equivalence ratio (Φ_L) is correlated by means of a series of equations -

$$\Phi_L = 0,725 \times X^{-1,3} \qquad (9) \qquad X = 10^{-3} \times \frac{\beta\, q}{C_p^* \, y} \qquad (10) \qquad \beta = 0,24\, T_0/298 + 0,76 \qquad (11)$$

$$y = 2,457 - \left(\psi_H + \psi_O - 0,63 \right)^{1,22} \qquad (12)$$ where T_0 is the unburned gas temperature in K,

q is the net molar calorific value in J/mol; C_p^* is the specific heat of the products of complete combustion of one mole of fuel (at 298 K) in J/(mol$_{fuel}$ K); ψ_H and ψ_O are the respective molar fractions of hydrogen and oxygen in the fuel.

Neither of the two sets of correlation equations gave a satisfactory correlation, and it seemed obvious that the combustor was functioning in between a droplet flame and a premixed flame and hence was not accessible to a satisfactory description by either correlation.

Since fuel volatility had already been shown to play a role in the attainment of combustion efficiency and flame radiation, it seemed likely that some volatility function might lead towards a correlation. Accordingly the groups -

$$\frac{\Phi_w/\Phi_{w,41}}{\Phi_{f8}/\Phi_{f8,41}} \quad \text{and} \quad \frac{\Phi_w/\Phi_{w,41}}{\Phi_L/\Phi_{L,41}}$$ were plotted as functions of the fuel transfer number B. Both correlations exhibited distinct trends, although the f_8 function was more pronounced. A further improvement of the f_8 correlation was obtained by the inclusion of the saturation factor S_H. This is demonstrated in Fig. 12.

It is concluded that the weak extinctions are largely controlled by the physical properties of the fuel, especially those associated with droplet size and evaporation, but that once again, fuel structure effects play a minor role.

5.5 Exhaust Temperature Distribution

The exhaust temperature distribution was determined by means of an array of 17 thermocouples situated at the exit of the combustion chamber. As described in detail in [8], the effect of changing the air/fuel ratio for any one fuel has very little effect upon the temperature distribution.

Visual inspection of the temperature distributions had suggested that there was little, if any, change in patternation due to the use of different fuels [8]. To test this, in a more quantitative way, the following technique was applied:

a) For each of the fuels an operating condition was selected which approached to $\phi_{overall} = 0,3$.
b) At this condition, the mean outlet temperature was calculated based upon the experimental value of equivalence ratio and the combustion efficiency as determined by gas analysis.
c) Each thermocouple temperature was then divided by this mean temperature. Thus for any one fuel a representative dimensionless temperature distribution could be obtained.
d) The dimensionless temperature for each individual thermocouple was examined statistically for all fuels. These results are presented in Table VI.

Table VI shows that there is little alteration in the outlet temperature distribution as the fuels are changed. This clearly emphasizes the dominance of the air & fuel flow patterns over the fuel properties. However, in order to examine the possibility of secondary trends, the ratio of the maximum to the minimum temperature measured for each individual fuel was plotted against several different fuel properties. No effect was noted for structure properties such as hydrogen content, saturation factor, etc, but there was an indication of a slight trend with the average boiling point. Presently this is not considered to be sufficiently confirmed to warrant further analysis.

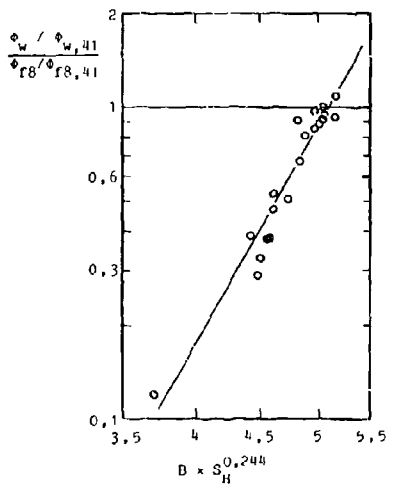

Fig. 12 WEAK EXTINCTION CORRELATION

Table VI

EXHAUST PLANE TEMPERATURE DATA

TC No.	Temperature ratio T/T_{mean} Minimum	Maximum	Average	Stand. Dev. %
1	1,18	1,29	1,24	1,83
2	1,09	1,23	1,15	3,11
3	1,04	1,16	1,10	2,36
4	1,10	1,21	1,15	2,61
5	1,22	1,35	1,27	2,56
6	1,14	1,26	1,20	2,26
7	0,93	1,07	1,00	2,88
8	0,90	1,03	0,98	2,81
9	1,05	1,18	1,09	3,36
10	1,07	1,22	1,14	3,40
11	0,86	1,03	0,96	2,89
12	0,80	0,97	0,88	3,22
13	0,90	1,00	0,94	2,47
14	0,87	0,98	0,90	2,48
15	0,94	1,09	1,03	2,88
16	0,76	0,90	0,84	2,99
17	0,75	0,84	0,80	2,24

Bearing in mind the results of Table VI it seems that fuel effects upon traverse quality may be regarded as negligible. This is perhaps a little surprising since it infers that neither fuel properties nor droplet size variations, nor reasonable variations in combustion efficiency, play any role in the exhaust temperature distribution, and it thus appears that only the combustor geometry, initial fuel distribution (i.e. fuel atomizer geometry), and air distribution govern the outlet pattern.

6. CONCLUSIONS

a) At the conditions of operation (ambient temperatures and pressures) the effects of changing equivalence ratio have been determined for 41 different fuels. The parameters determined were (1) combustion efficiency, (2) pollutants CO, HC, NO, NOx, (3) flame radiation, (4) weak extinctions, (5) exhaust temperature distribution. Ignition data were not obtained due to the efficiency of the igniter, which ignited even mixtures outside the extinction limits. Exhaust carbon concentrations were too low to be measured gravimetrically, and even the filter paper staining was too low for quantitative measurements.

b) Despite the very low droplet diameters (= 17 µm), a trend was observed between the measured combustion efficiency and the average boiling point of the various fuels. A small improvement of the correlation of the efficiency with boiling point was brought about by the inclusion of a term involving the hydrogen saturation factor.

c) A good relationship was observed between the group EI_{CO}/ y EI_{HC} and the combustion efficiency for all fuels at all equivalence ratios.

d) The oxides of nitrogen can be satisfactorily predicted using the equation -

$$EI_{NOx} = 5{,}824\times10^{4} \times e^{-21670/T} \left(1 - e^{6{,}65\Phi - 3{,}225}\right)$$

e) The ratio NO/NOx was determined for each operating point, but no clear picture has emerged.

f) Flame radiation measurements within the primary zone have been found to correlate with -

$$R = 4{,}33 \left\{[M \ln(B-1)/\pi]^{2{,}75} \times S_H\right\}^{0{,}875}$$

g) A flame extinction correlation was found which is similar to that observed previously but modified by the use of the hydrogen saturation factor to the power 0,244.

h) No fuel effects have been detected upon the exhaust temperature distribution which remains remarkably constant for all conditions examined thus proving the dominance of combustor geometry and air flow distribution over the variants due to fuel changes.

i) The improvement in several of the correlations by the inclusion of the hydrogen saturation factor suggests that fuel composition (and structure) does play a small role in the combustion behaviour. However, to fix the magnitude of this role with certainty will probably require special testing and, probably, the inclusion of new fuels having even wider variations of composition than those examined here.

j) The use of an efficient air blast atomizer means that the combustor functions as a partially premixed system.

6. REFERENCES

[1] Kretschmer, D. & Odgers, J.: **The Characterization of Combustion by Fuel Composition: 2 - Measurements in a small Conventional Combustor**, Paper to 70th AGARD meeting, "Combustion and Fuels in Gas Turbine Engines", Greece, 19 - 23 Oct 1987.

[2] Kretschmer, D., Odgers, J. & Daigle, G.; **A Small Transparent Combustor for Alternative Fuel Characterization**, AIAA Paper 86-0368, 24th Aerospace Meeting, Reno, 6-9 Jan 1986.

[3] Burgoyne, J.H. & Cohen, L.; "The Effects of Drop Size on Flame Propagation in Liquid Aerosols", **Proc. Roy. Soc. A225**, 1954, p. 375.

[4] Kretschmer, D. & Odgers, J.; "Modelling of Gas Turbine Combustors - A Convenient Reaction Rate Equation", **Trans. ASME J. Eng. for Power 94A**, 1972, 3, pp 173/180.

[5] Odgers, J., Kretschmer, D.; **The Prediction of Thermal NOx in Gas Turbines**, ASME Paper 85-GT-126, Beijing Intern. Gas Turbine Symp. & Expos., 1-7 Sep 1985.

[6] Sampath, P., Gratton, M., Kretschmer, D. & Odgers, J.; "Fuel Property Effects Upon Exhaust Smoke and Weak Extinction Characteristics of the Pratt & Whitney PT6A-65 Engine", **Trans. ASME J. Eng. for Power 108**, Jan 1986, pp 175/181.

[7] Odgers, J., Kretschmer, D. & Halpin, J; "Weak Limits of Premixed Gases", **Trans. ASME J. Eng. for Power 107**, Jan 1985, pp 10/17.

[8] Odgers, J. & Kretschmer, D.; **The Combustion Behaviour of a Range of Fuels Tested in a Small Transparent Combustion Chamber**, Université Laval, Combustion Laboratories, Dépt. du genie mécanique, Report Jo 144, Apl 1985.

7. ACKNOWLEDGEMENTS

The authors whish to acknowledge the support of the Canadian National Defence, who financed the first series of experiments (fuels 41 to 63), and of the Canadian National Science and Engineering Research Council, who have provided the research grant for the additional tests on all the other fuels. Additional thanks are also due to the group of undergraduate students who operated the test rig for the experiments.

A Small Annular Combustor of High Power Density, Wide Operating Range and Low Manufacturing Cost

by

K.H. Collin

KHD Luftfahrttechnik GmbH
D-6370 Oberursel, Germany

SUMMARY

A short description will be given of the design and manufacturing philosophy, testing and optimization of a combustion chamber. The features and design layout of the burner are characterized by the requirements for a low cost propulsion system for an unmanned flight vehicle, such as RPV and drones. Rig test results for the ignition and the performance over a wide operating range will be discussed. Ignition by hot gas from a cartridge as well as experiences with testing this combustor in the demonstrator turbojet engine will be described.

1. INTRODUCTION

The requirements, established for a combustion chamber layout which is reported in this paper, differ significantly from those of usual gas turbine combustors.

The life of the reference turbojet engine is limited to a few hours only. This therefore does not demand low wall temperatures of the liner as number one priority. But extremely light weight and small size for the burner were to be achieved for a jet engine, which is intended to fit the very narrow installation envelope of the fuselage. This led to a high power density of the burner volume. Good combustion efficiency, ignition reliability and flame stability combined with low fabrication cost are required to get reasonable life-cycle-cost.

The development phases of the combustion chamber up to it's installation in the demonstrator engine will be described. In detail the following topics will be discussed:

- Fuel preparation and combustion.
- Test and optimization of the burner system with a segmented model and of the ignition system with a hot gas cartridge.
- Design and test of a full flow combustor.
- Analyses of test results and subsequent redesign of an improved combustor.
- Burner investigation in the demonstrator engine.

2. FUEL PREPARATION AND COMBUSTION

The mission profile of the unmanned flight vehicle and the resulting design parameters of the engine, which emphasizes low cost /1/, define the operating range of the burner. Fig. 1 shows operating parameters versus engine rotor speed (rpm).

To ensure reliability in ignition, high flame stability and good burner efficiency as well as low manufacturing cost, design criteria were used which were based on experiences made by the development of an earlier KHD combustion chamber /2/. This combustor was successfully tested at DFVLR-Porz /3/ /4/ in a wide range of applications.

The concept of this burner was to swirl air with single air jets combined with fuel injection by a simple spray nozzle. This nozzle has been located in the middle of the air swirler as shown in Fig. 2. The air jet guaranteed a good mixing of air and fuel spray. The high air swirl effected intense recirculation, which in turn promotes improved flame stability and good fuel preparation by high entrainment of hot gaseous reactants.

Further development of this premixing system in connection with an annular burner led to the features of a combustion chamber as will be discussed in this paper. 16 mixing cups with spray nozzles were installed on the front of the annular combustion liner as can be seen in Fig. 3. The burning zone was thus divided in 16 parts reducing combustion length by intensiv recirculation and fast mixing. This concept created a combustion quality, which gave an uniform temperature distribution at the burner outlet.

The large swirl at the outlet of the cups and the following sudden expansion into the annular flame tube caused on one hand a quick circumferential flame propagation around the burner, therefore only one ignitor location was needed. On the other hand the counter clockwise impulse of the swirls between the cups induced high turbulence which improved mixing and flame stability, too.

To predict the flow patterns in the actual combustor computations with a finit element computer program CPTR /5/ were made to optimize swirl intensity and cup locations. But for these computations several simplifications had to be introduced because the real flow distribution is of three, while the computer program is of the two dimensional type. Therefore burner optimization was mainly done empirically. For these investigations a segmented combustion chamber was selected.

3. TEST AND OPTIMIZATION OF THE BURNER SYSTEM IN A SEGMENTED TEST MODEL AND OF THE IGNITION SYSTEM WITH A HOT GAS CARTRIDGE

For the initial investigation and development of the combustion system a segmented combustion chamber was built. This burner comprized 4 segments, each of them equipped with 3 premixing cups in the primary zone. Similarly the annular flame tube was segmented into 4 parts, each part manufactured with a different arrangement of dilution air holes.

During any single test only one part of the segments was flowed by air and fuel. Several combinations of cups and liners could therefor be tested. Fig. 4 shows the cross section of the segmented burner and the instrumentation at the end of the burner. Fig. 5 shows the cup arrangement. The cups had different geometry of holes, inclination angle and number of holes. The feature of the dilution holes arranged in the flame tube for all four segments are shown in Fig. 6. These holes were varied for the optimization of air flow entrainment as well as concerns manufacturing techniques.

In the first test phase the burner segment was tested with openended burner outlet for flame visibility. The flame observation were recorded by colour photography. For example Fig. 7 shows flame photographs with one cup liner arrangement for the same fuel air ratio but different flow velocity. High influence of the segment endwalls was observed, so that only the middle cup could be used for definition.

Further tests were then done with a pressurized combustor to measure temperature and pressure distribution at the outlet. The best combustion and temperature distribution were observed for a 40° inclination angle of the primary air holes combined with a liner type equipped with a few large holes which were plunged. But this liner hole configuration showed vibrations of low frequency. Therefore a modified arrangement of the holes was defined and assembled for the full flow test burner.

The segmented burner rig finally was used for cartridge ignition tests. To fulfil the starting requirements the design goal was to find a cartridge for both: cranking and ignition. A cartridge was developped which simultaneously gives hot gas for fuel ignition and deliveres jet impuls for rotational accelleration of the turbine. The first ignition attemps went wrong. The high inert hot gases from the cartridge injected into the fuel air mixture at the cup quenched the flame and foiled the ignition. After using hot gas to glow a pipe, which was immersed into the fuel air mixture and then guiding the gas of the cartridge downstream into the annular volume, ignition and flame stability was achieved.

4. DESIGN AND TEST OF THE FULL FLOW COMBUSTER

For the exact simulation of all actual operating conditions a combustion chamber for tests was built using the knowledges of the segmented burner test model. The detail of the burner and the arrangement of the measurement devices are shown in Fig. 8. This burner was installed at the DFVLR-Porz combustor test facility. This test facility is described in /6/. Fuel to each spray nozzle was supplied from outside the combustion chamber to control and shut off single nozzles if required. Fig. 9 shows the fuel supply arrangement. Four spark ignitors were assigned at four cups and equally spaced. These could be used together as well as separately. At the burner outlet three measurement rakes for temperature at 4 radii and three rakes for pressure at 5 radii were installed. By traversing these rakes temperature and pressure distribution could be recorded.

5. ANALYSES OF TEST RESULTS AND SUBSEQUENT REDESIGN OF IMPROVED COMBUSTOR

Testing was carried out as concerns:

- Ignition behaviour
- Temperature distribution
- Pressure distribution
- Emission measurements

Fig. 10 shows the ignition behaviour of the burner.

Fuel air ratio and air mass flow, the latter being proportional to flow velocity, were changed during ignition tests. The air inlet temperature was varied from 8 to 56 °C dependend on the test facility range. For the ignition a lower limit for fuel air ratio of $\dot{m}_B/\dot{m}_L \geq 0{,}025$ was found.

In line with the compressor characteristic the ignition range is 10 to 40 % engine speed. That means a large starting window is open to start the engine at different flight conditions.

The ignition tests were done with fuel JET-A1. No influences of ignitor location and ignitor number were observed, therefore further ignition procedures were made by using one ignitor only.

The temperature distribution at the burner outlet for the design point is shown in Fig. 11.

The pattern factor as determined from measurements

$$PAT = \frac{T_{max} - T_{mean}}{T_{mean} - T_{in}}$$

was calculated to be 23 %.

The temperature distribution as a mean value over the radii is shown in Fig. 12. The temperature scatter is here ± 100°.

The measured pressure distribution is shown in Fig. 13.

The highest pressure was measured at large radii caused by centrifugal forces. However, in wall proximity the cooling flow overcomes this centrifugal force resulting larger pressure fluctuation. At radius $r_2/r_3 = 0,83$ the greatest pressure fluctuation was observed. At this point a high velocity exiting at the cup area succeeds a lower velocity between the cups. But here it has to be reported, that the measurement rakes could not be turned in their own axis. So the change of flow direction could not be measured. The total pressure loss of the combustion chamber was found to be 4.5 %.

To determine quality of the combustion the exhaust emissions were measured and the burning efficiency was calculated by the emission indices of HC and CO.

Fig. 14 shows the results of this investigation for ISA-SL ambient conditions. The reduction of burning efficiency and increase in parts of unburned fuel below 90 % engine speed depend on insuffient fuel atomization. Fuel flow and therefore fuel pressure are too small for each spray nozzle to produce a high rate of fine droplets. For application of the burner other than the aformentioned mission the atomization in the operating range can be improved by shutting off some spray nozzles.

6. BURNER INVESTIGATION IN THE DEMONSTRATOR ENGINE

The results from the burner rig investigation are mainly that:

- large compressor diffusor outlet velocity will cause a nonuniform inlet flow to the cups of the burner which increases the burner's pressure loss. This could be improved by reducing the diffusor outlet velocity.

- To get a smooth radial temperature distribution for suitable blade life the flame tube holes were changed to reduce the temperatur at the hub to meet the material properties of the turbine blades.

With this experience in hand a combustion chamber for test in a demonstrator turbojet engine was conceived and built. With a burner arrangement as shown in Fig. 15 an engine testing was started. To date serveral starts and operating hours have been successfully run with air jet starting and a high energy spark plug ignitor. Tes s will be continued edding hot gas ignition and crank start.

This design approach will now allow for minimum parts and low cost manufacture such as:

- Investment cast air swirlers for the primary air with integrated fuel nozzle adapter.

- Inner and outer flame tube made from simple sheet metal and welded parts.

- A hydroformed torus into which cups are brazed.

- Holes laser cut into the flame tube and plunged in one step into the plane sheet. This then is rolled cylindrically-respectively conically.

All these manufacturing methods reduce the cost to a minimum.

7. CONCLUSIONS

The sequence of burner development described here for a very specific application shows that by systematically applieing a modern design method an efficient, cost effective component can be obtained.

Only two burner constructions were needed for tests. The first one was the segment burner to optimize the geometric design, the second one the full flowed burner to check the operating profile of the engine.

Design of the combustion chamber with the following principles

- fuel preparation in a premixing chamber,
- air swirler with holes to create single suction air jets,
- division of the combustion zone in several parts, here 16, seperated and controlled by swirling a well defined fuel air ratio in the cups,
- and finally provision of high turbulence in the annular part of the burner,

yields a excellent flame stability and combustion efficiency as well as an uniform temperature distribution to satisfy the requirements for this burner application.

Without doubt more work has to be and will be done in order to improve the wall cooling effectiveness for a longer life of the combustor liner, however the layout principles need not to be changed.

However there is scope for perfection of our, as yet less then perfect, analytical tools.

For continued progress in the future it is a prerequisite to establish better computer simulation. Specially 3D-Programs easy to handling, capable to describe the fuel preparation and combustion as well as flow is what we need.

8. REFERENCES

/1/ Uwe Dammel
Advances In Technology For Low Cost Turbomachinery -
A Potential To Enhance The Economy Of Future Propulsion System For General And Helicopter Aviation
VIIIth ISABE Cincinnati, Ohio,
June 1987, Proceedings S. 753-757

/2/ Karl-Heinz Collin
Kleinbrennkammer für weiten Betriebsbereich nach dem Auslegungsprinzip der Freistrahlwirkung
DGLR-Tagung 1977-066.

/3/ H.-D. Distelrath, K. Rath, H. Wiegand
Über die Eignung einer Hochdruckbrennkammer zur Simulation des heißen Abgasstrahls in einem Modelltriebwerk
DFVLR IB 351-4 79

/4/ S. Bartmann e.A.
Abgasverhalten einer Hochdruckbrennkammer bei Strömung mit Wärmezufuhr
DFVLR 1977

/5/ A.V. Chatwani, H. Eickhoff, S.W.T. Koopmann, A.W. Neuberger
Computation of Practical Turbulent Reactive Flows A User's Guide for code CPTR
DFVLR Sept. 1989

/6/ G. Kirschey, R. Wagner
Full Annular Combustor Test Facility For High Pressure/ High Temperature Testing
AGARD Conference Proceeding No. 293

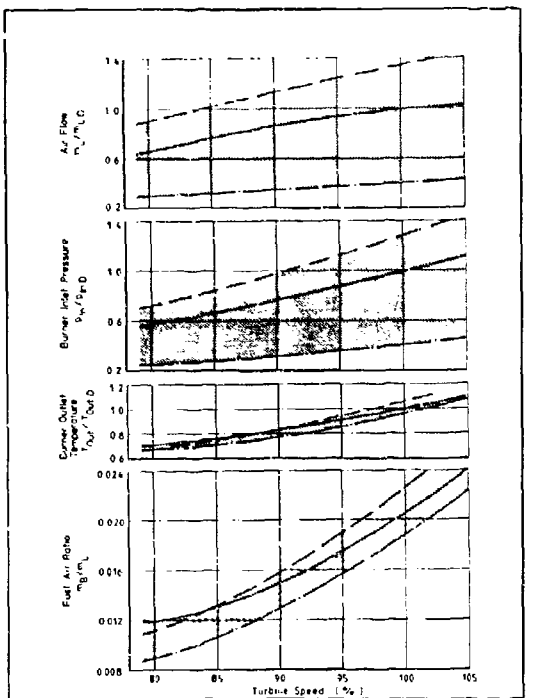

Fig. 1 Required Operating Range of the Burner

KHD Luftfahrttechnik GmbH

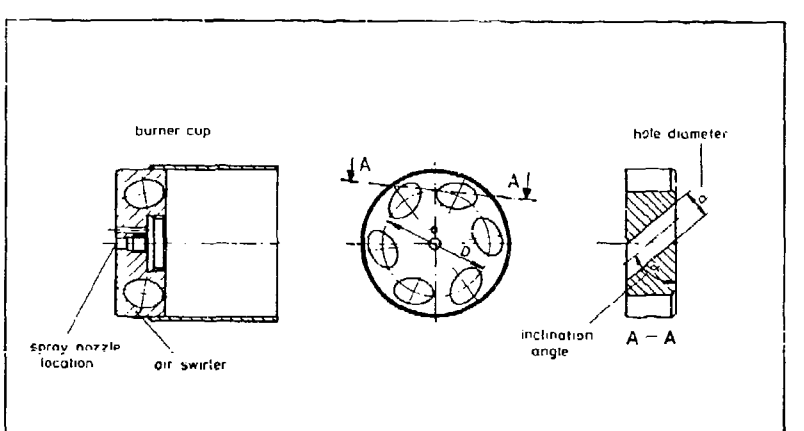

Fig. 2 Primary Air Flow Device

KHD Luftfahrttechnik GmbH

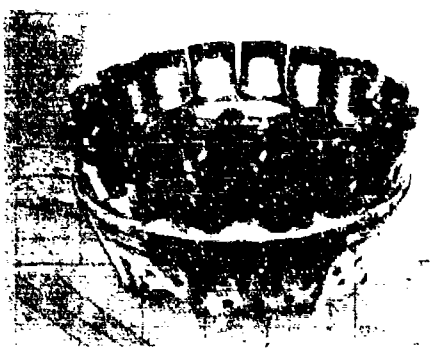

Fig. 3 Combustion Chamber for Demonstrator Engine

KHD Luftfahrttechnik GmbH

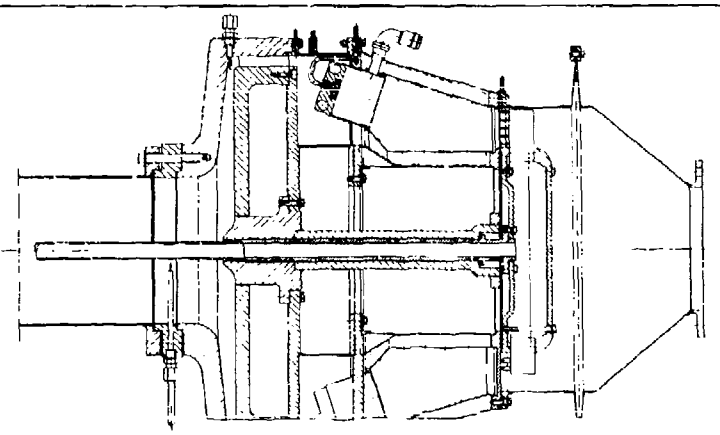

Fig. 4 Cross Section Test Rig for Combustor Segments

KHD Luftfahrttechnik GmbH

Fig 5 Combustor Segments Cups Arrangement

KHD Luftfahrttechnik GmbH

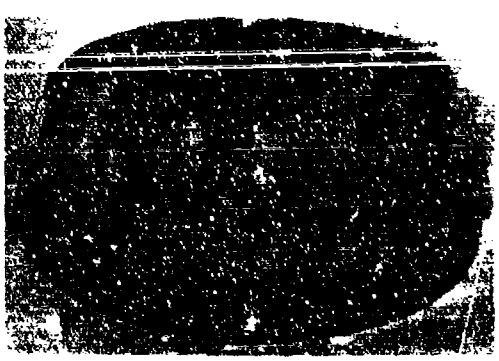

Fig 6 Combustor Segments Dilution Holes Arrangement

KHD Luftfahrttechnik GmbH

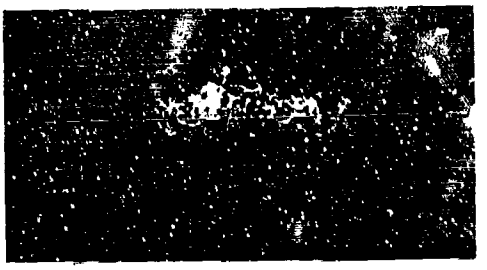

fuel air ratio = 0.0255

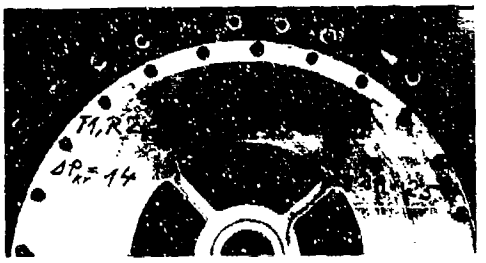

fuel air ratio = 0.0255

Fig 7 Combustor Segment Test at Ambient Pressure
Flame Photographs

KHD Luftfahrttechnik GmbH

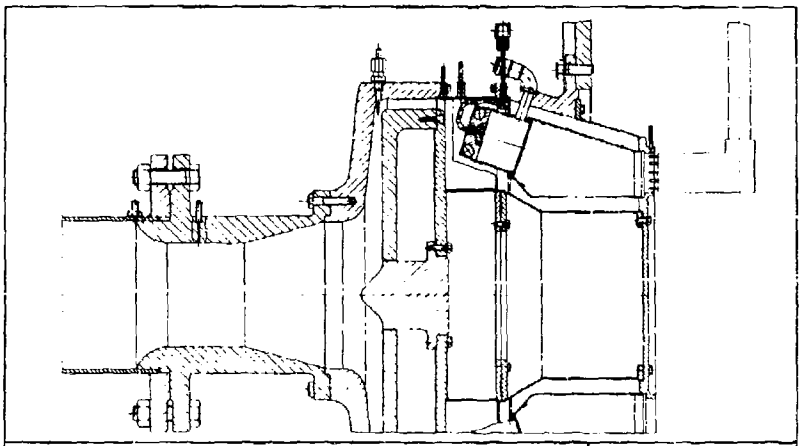

Fig. 8 Cross Section of Complete Combustion Chamber

KHD Luftfahrttechnik GmbH

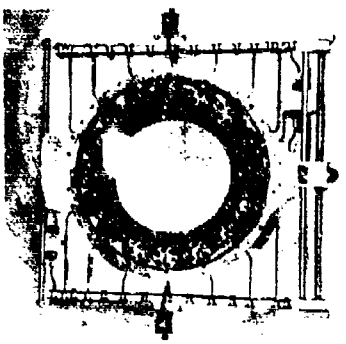

Fig. 9 Fuel Supply Arrangement

KHD Luftfahrttechnik GmbH

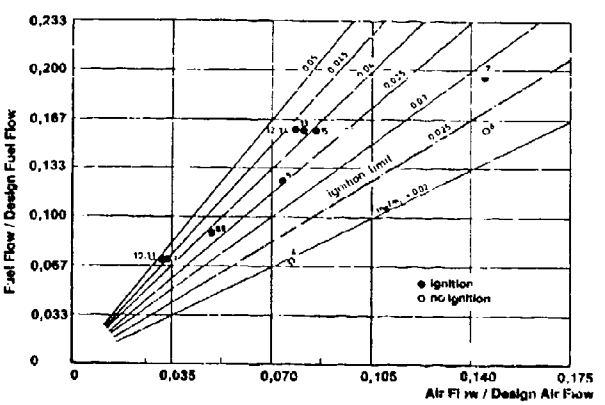

Fig 10 Ignition Behavior of the Burner

KHD Luftfahrttechnik GmbH

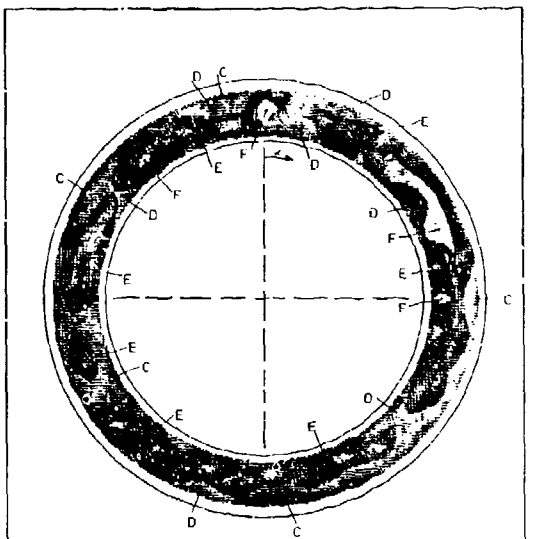

Fig.11 Temperature Distribution at Combustor Exit

KHD Luftfahrttechnik GmbH

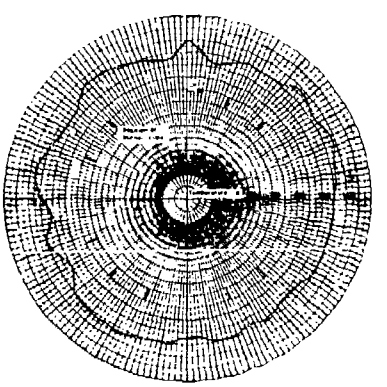

Fig 12 Temperature Distribution at Combustor Exit as mean Value over the Radii

KHD Luftfahrttechnik GmbH

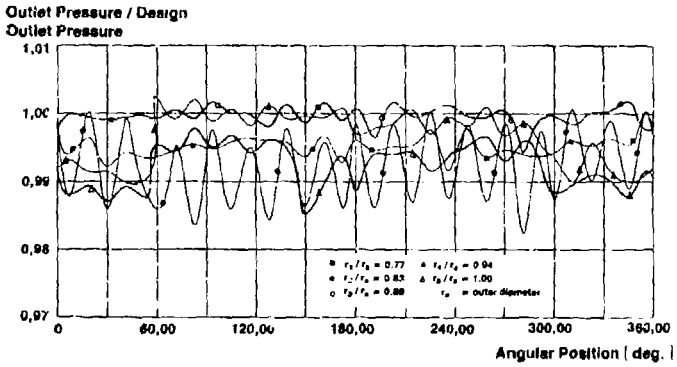

Fig 13 Pressure Distribution at Combustor Exit

KHD Luftfahrttechnik GmbH

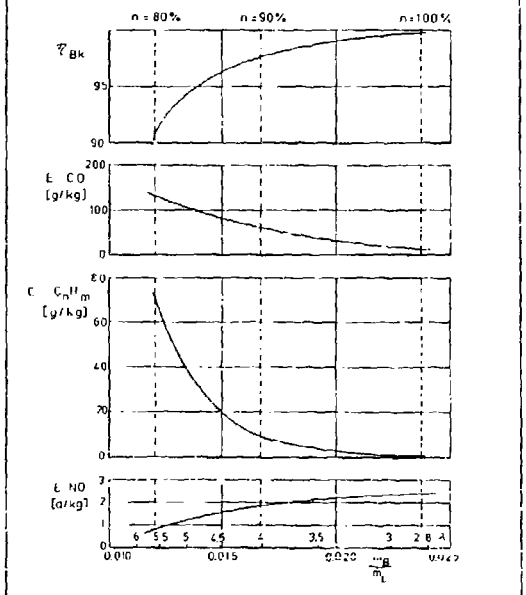

Fig. 14 Emission of Pollutants

KHD Luftfahrttechnik GmbH

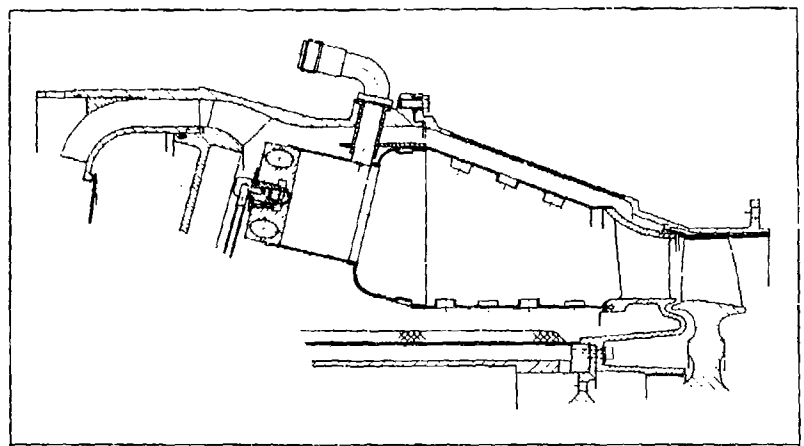

Fig. 15 Cross Section Combustion Chamber for Demonstrator Engine

KHD Luftfahrttechnik GmbH

DISCUSSION

B.Simon, GE
What was the pressure drop across your flametube?

Author's Reply
The pressure drop was 5%.

REPORT DOCUMENTATION PAGE

1. Recipient's Reference	2. Originator's Reference	3. Further Reference	4. Security Classification of Document
	AGARD-CP-422	ISBN 92-835-0465-8	UNCLASSIFIED

5. Originator Advisory Group for Aerospace Research and Development
North Atlantic Treaty Organization
7 rue Ancelle, 92200 Neuilly sur Seine, France

6. Title

COMBUSTION AND FUELS IN GAS TURBINE ENGINES

7. Presented at

the Propulsion and Energetics Panel 70th Symposium held in Chania, Crete, Greece, on 19–23 October 1987.

8. Author(s)/Editor(s)	9. Date
Various	June 1988
10. Author's/Editor's Address	**11. Pages**
Various	544

12. Distribution Statement This document is distributed in accordance with AGARD policies and regulations, which are outlined on the Outside Back Covers of all AGARD publications.

13. Keywords/Descriptors

Afterburner	Fuels
Alternative fuels	Gas turbines
Atomization of fuels	Radiation
Combustion	Soot formation
Droplet distribution	Spray performance

14. Abstract

The Conference Proceedings contain 41 papers presented at the Propulsion and Energetics Panel 70th Symposium, on Combustion and Fuels in Gas Turbine Engines, which was held 19–23 October 1987 in Chania, Crete, Greece.

The Symposium was arranged in the following sessions: Alternative Fuels and Fuel Injection (9); Combustor Development (7); Soot and Radiation (10); and Combustor Modelling (15). The Technical Evaluation Report is included at the beginning of the Proceedings. Questions and answers of the discussions follow each paper.

The aim of the meeting was to review the progress made in the area of combustion and fuels in gas turbine engines since the last AGARD-PEP Meeting on this subject in 1983.

AGARD Conference Proceedings No.422 Advisory Group for Aerospace Research and Development, NATO COMBUSTION AND FUELS IN GAS TURBINE ENGINES Published June 1988 544 pages The Conference Proceedings contain 41 papers presented at the Propulsion and Energetics Panel 70th Symposium, on Combustion and Fuels in Gas Turbine Engines, which was held 19–23 October 1987 in Chania, Crete, Greece. The Symposium was arranged in the following sessions: Alternative Fuels and Fuel Injection (9); Combustor Development (7); Soot and Radiation (10); and P.T.O	AGARD-CP-422 Afterburner Alternative fuels Atomization of fuels Combustion Droplet distribution Fuels Gas turbines Radiation Soot formation Spray performance	AGARD Conference Proceedings No.422 Advisory Group for Aerospace Research and Development, NATO COMBUSTION AND FUELS IN GAS TURBINE ENGINES Published June 1988 544 pages The Conference Proceedings contain 41 papers presented at the Propulsion and Energetics Panel 70th Symposium, on Combustion and Fuels in Gas Turbine Engines, which was held 19–23 October 1987 in Chania, Crete, Greece. The Symposium was arranged in the following sessions: Alternative Fuels and Fuel Injection (9); Combustor Development (7); Soot and Radiation (10); and P.T.O	AGARD-CP-422 Afterburner Alternative fuels Atomization of fuels Combustion Droplet distribution Fuels Gas turbines Radiation Soot formation Spray performance
AGARD Conference Proceedings No.422 Advisory Group for Aerospace Research and Development, NATO COMBUSTION AND FUELS IN GAS TURBINE ENGINES Published June 1988 544 pages The Conference Proceedings contain 41 papers presented at the Propulsion and Energetics Panel 70th Symposium, on Combustion and Fuels in Gas Turbine Engines, which was held 19–23 October 1987 in Chania, Crete, Greece. The Symposium was arranged in the following sessions: Alternative Fuels and Fuel Injection (9); Combustor Development (7); Soot and Radiation (10); and P.T.O	AGARD-CP-422 Afterburner Alternative fuels Atomization of fuels Combustion Droplet distribution Fuels Gas turbines Radiation Soot formation Spray performance	AGARD Conference Proceedings No.422 Advisory Group for Aerospace Research and Development, NATO COMBUSTION AND FUELS IN GAS TURBINE ENGINES Published June 1988 544 pages The Conference Proceedings contain 41 papers presented at the Propulsion and Energetics Panel 70th Symposium, on Combustion and Fuels in Gas Turbine Engines, which was held 19–23 October 1987 in Chania, Crete, Greece. The Symposium was arranged in the following sessions: Alternative Fuels and Fuel Injection (9); Combustor Development (7); Soot and Radiation (10); and P.T.O	AGARD-CP-422 Afterburner Alternative fuels Atomization of fuels Combustion Droplet distribution Fuels Gas turbines Radiation Soot formation Spray performance